10TH ANNIVERSARY
2015 - 2025

International Journal of BIOPRINTING



ISSN: 2424-7723 (Print)
ISSN: 2424-8002 (Online)
Volume 11·Issue 5
October 2025

ACCSCIENCE PUBLISHING

ACCSCIENCE PUBLISHING

International Journal of Bioprinting

Print ISSN: 2424-7723

Online ISSN: 2424-8002

International Journal of Bioprinting is an international journal covering the technology, science and clinical application of the broadly defined field of Bioprinting. Bioprinting is defined as the use of 3D printing technology with materials that incorporate viable living cells or biological elements to produce tissue or biotechnological products. We are interested in the scientific topics spanning all stages of bioprinting process from concept creation to fabrication and beyond.



Scan to access website:

Scan to submit papers:

About the Publisher

AccScience Publishing is a publishing company based in Singapore. We publish a range of high-quality, open-access, peer-reviewed journals and books from a broad spectrum of disciplines.

Contact Us

Managing Editor
ijb.office@accscience.sg

AccScience Publishing
9 Raffles Place, Republic Plaza 1 #06-00 Singapore 048619.

Volume 11 • Issue 5 • October 2025
ISSN 2424-7723 (print) ISSN 2424-8002 (online)

INTERNATIONAL JOURNAL OF BIOPRINTING

Editor-in-Chief

Chee Kai Chua

Singapore University of Technology and Design, Singapore

ACCSCIENCE PUBLISHING

Access Science Without Barriers

Full issue copyright © 2025 AccScience Publishing
All rights reserved. Without permission in writing from the publisher, this full issue publication in its entirety may not be reproduced or transmitted for commercial purposes in any form or by any means, electronic or mechanical, including photocopying, recording, or any information storage and retrieval system. Permissions may be sought from ijb.office@accscience.sg.

Article copyright © Respective Author(s)
See articles for copyright year. All articles in this full issue publication are open-access. There are no restrictions in the distribution and reproduction of individual articles, provided the original work is properly cited. However, permission to reuse copyrighted materials of an article for commercial purposes is applicable if the article is licensed under Creative Commons Attribution-NonCommercial License. Check the specific license before reusing.

INTERNATIONAL JOURNAL OF BIOPRINTING

ISSN: 2424-7723 (print)
ISSN: 2424-8002 (online)

Editorial and Production Credits

Publisher: AccScience Publishing
Managing Editor: Ivanna Gao
Editorial Assistants: Puva Ramakrishnan, Flora Kang
Production Editor: Puva Ramakrishnan
Special Issue Commissioning Editors: Shirley Song, Terra Shi
Article Layout and Typeset: Bsmart Publishing (India)

For all advertising queries, contact ijb.office@accscience.sg.

Supplementary file

Supplementary files of articles can be obtained at https://accscience.com/journal/IJB/11/5.



Disclaimer

AccScience Publishing is not liable to the statements, perspectives, and opinions contained in the publications. The appearance of advertisements in the journal shall not be construed as a warranty, endorsement, or approval of the products or services advertised and/or the safety thereof. AccScience Publishing disclaims responsibility for any injury to persons or property resulting from any ideas or products referred to in the publications or advertisements. AccScience Publishing remains neutral with regard to jurisdictional claims in published maps and institutional affiliations.

International Journal of Bioprinting

Editorial Board

Editor-in-Chief

Chee Kai Chua
Singapore University of Technology and Design, Singapore

Associate Editors

Wai Yee Yeong
Nanyang Technological University, Singapore

Jiankang He
Xi'an Jiaotong University, China

Amit Bandyopadhyay
Washington State University, USA

Liliang Ouyang
Tsinghua University, China

Maling Gou
Sichuan University, China

Yongqiang Hao (Clinician)
Shanghai Jiao Tong University School of Medicine, China

Xiaoxiao Han
Hunan University, China

*Editorial Board Members**

Jason A. Burdick, *USA*
Shweta Agarwala, *Denmark*
Eben Alsberg, *USA*
Anthony Atala, *USA*
Douglas B. Chrisey, *USA*
Andrea Barbetta, *Italy*
Mikhael Bechelany, *France*
Martin Birchall, *UK*
Mohd Fauzi Mh Busra, *Malaysia*
Paulo J.D.S. Bártolo, *Singapore*
Christian Celia, *Italy*
Ming-Wei Chang, *UK*
Maria Chatzinikolaidou, *Greece*
Jun Chen, *Australia*
Daniel Chen, *Canada*
Boris Chichkov, *Germany*
Dong-Woo Cho, *Korea*
Gianluca Ciardelli, *Italy*
Jeremy Crook, *Australia*
Cédric Delattre, *France*
Rui Domingues, *Portugal*
Dennis Douroumis, *UK*
Nileshkumar Dubey, *USA*
Tal Dvir, *Israel*
Eleonora Ferraris, *Belgium*
Sanjay Garg, *Australia*
Antonio Gloria, *Italy*
Manuela Gomes, *Portugal*
Brunella Grigolo, *Italy*
Michinao Hashimoto, *Singapore*
Charlotte A. E. Hauser, *Saudi Arabia*
Dong Nyoung Heo, *Korea*
Raymund E. Horch, *Germany*
Geun Hyung Kim, *Korea*
Richard James Bibb, *UK*
Jinah Jang, *South Korea*
Jingchao Jiang, *China*
Qing Jiang, *China*
Hyun-Do Jung, *Korea*
Lifeng Kang, *Australia*
Ali Khademhosseini, *USA*
Moon Suk Kim, *South Korea*
Jangho Kim, *South Korea*
Bahattin Koç, *Turkey*
Dimitrios A. Lamprou, *UK*
Junmin Lee, *South Korea*
Jin Woo Lee, *South Korea*
Shulamit Levenberg, *Israel*
Khoon Lim, *Australia*
Ki-Taek Lim, *South Korea*
Fengyuan Liu, *UK*
Xiao Liu, *Australia*
Veronica MacChi, *Italy*
Carmelo De Maria, *Italy*
Elena Martínez Fraiz, *Spain*
Laurence Meagher, *Australia*
Ferry Melchels, *Australia*
Nikolaos Michailidis, *Greece*
David K. Mills, *USA*
Vladimir Mironov, *Russia*
Mario Moisés Alvarez, *Mexico*
Maurice N Collins, *Ireland*
Makoto Nakamura, *Japan*

Seung Yun Nam, *Korea*
Roger Narayan, *USA*
Insup Noh, *Korea*
Ali Nokhodchi, *UK*
J.M.A.C. de Oliveira, *Portugal*
Aleksandr Ovsianikov, *Austria*
Sang-Hyug Park, *Korea*
Sungsu Park, *South Korea*
Alokesh Pramanik, *Australia*
Aldo R. Boccaccini, *Germany*
Michael Raghunath, *Switzerland*
Anabela Raymundo, *Portugal*
Shinji Sakai, *Japan*
Thomas Scheibel, *Germany*
Cijun Shuai, *China*
Swee Leong Sing, *Singapore*
Kedong Song, *China*
Jie Sun, *China*
Zhonghua Sun, *Australia*
Ergün Süleyman, *Germany*
Ibrahim Tarik Ozbolat, *USA*
Savas Tasoglu, *Turkey*
S. Vijayavenkataraman, *UAE*
Giovanni Vozzi, *Italy*
Liqiang Wang, *China*
Yin Xiao, *Australia*
Seung-Schik Yoo, *USA*
Barbara Zavan, *Italy*
Ioanna Zergioti, *Greece*
Yu Shrike Zhang, *USA*
Yi Zhang, *China*
Wei Zhu, *China*
Hala Zreiqat, *Australia*

Assistant Editor

Jia An, *Singapore*

Youth Editorial Board Members

Tanveer Ahmad, *Saudi Arabia*
Shivesh Anand, *USA*
Gokhan Bahcecioglu, *USA*
Gianluca Cidonio, *Italy*
Wangwang Ding, *China*
Giovanni Falcone, *Italy*
Ruben Foresti, *Italy*
Gabriele Maria Fortunato, *Italy*
Farnaz Ghorbani, *UK*
Paola Serena Ginestra, *Italy*
Xulin Hu, *China*
Anna Jezierski, *Canada*
Yiting Lei, *China*
Lan Li, *China*
Huixin Liang, *China*
Elena Marcello, *Italy*
Wei Long Ng, *Singapore*
Egor Osidak, *Russia*
Chenxi Peng, *Australia*
Rúben Pereira, *Portugal*
Mohammadmajid Sepantafar, *USA*
João Carlos Silva, *Portugal*
Yogendra Pratap Singh, *India*
Thiago Domingues Stocco, *Brazil*
Binbin Sun, *China*
Aitor Tejo-Otero, *Spain*
Danlei Zhao, *China*
Hui Zhu, *China*

*Editorial Board Members as of October 15, 2025

ACCSCIENCE PUBLISHING

Volume 11 | Issue 5 | October 2025 | Page 1 – 463 |

International Journal of Bioprinting

https://accscience.com/journal/IJB

CONTENTS

REVIEW ARTICLES

1 **Advances and challenges in three-dimensional bioprinting of bone organoids: Materials, techniques, and functionalization strategies**
Longfei Wu, Junjie Zhao, Jiwei Huang, Pengfei Huang, Haiyan Zhao

23 **Advances in decellularized extracellular matrix bioinks for regenerative medicine applications**
Jugal Kishore Bupesh Raja, Giselle Y. Díaz, Fynn S. Owen La Boucan, Madeleine A. Perry, Sravya Tekumalla, Tharaka Srinatha Dunuwilla, Venkatagiri Krishnamoorthy Bupesh Raja, Stephanie M. Willerth

46 **Bioprinting strategies for skeletal muscle regeneration: Advances in bioinks, technologies, and functional reconstruction**
Xiaoguang Liu, Miaomiao Xu, Huiguo Wang, Lin Zhu

68 **Advances in *in vitro* blood–brain barrier models: Integrating bioprinting with microfluidic chips for compound evaluation**
Yating Du, Zezhi Li, Xiang Li, Jianping Xie

98 **A multidisciplinary review on footwear 3D printing: From biomechanics to therapeutics**
Kijung Kim, Hyunji Kim, Wonjae Hwang, Yoonseo Choi, Keewon Kim, Jooeun Ahn, Howon Lee

122 **From cells to organs: Technical challenges of two-photon polymerization in biomedical engineering**
Yanzhe Fu, Mingming Huang, Jiayong Wei, Xiang Ding, Bosong Yu, Jiebo Li, Jianmin Han, Lizhen Wang, Yubo Fan

RESEARCH ARTICLES

154 **Three-dimensional-printed hydrogel scaffolds with neuregulin-1 sustained-release microspheres for enhanced dedifferentiation and myelin regeneration in peripheral nerve injury**
Guanhua Zhang, Enpeng Song, Peng Yu, Jie Wei, Yaqiong Wang, Jie Liu, Hou Bo

178 **3D-bioprinted placenta-on-a-chip platform for modeling the human maternal–fetal barrier**
Yazhi Sun, Henry H. Hwang, Chandana Tekkatte, Scott A. Lindsay, Anelizze Castro-Martinez, Claire Yu, Isabella Saldana, Xuanyi Ma, Omar Farah, Mana M. Parast, Louise C. Laurent, Shaochen Chen

197 **Macro–micro analysis of the physical and biological properties of 3D-printed hydroxyapatite/β-tricalcium phosphate scaffolds with varying polyvinyl alcohol concentrations**
Zhitao Yin, Yutong Chen, Guang Yang, Shuaishuai Wang, Bingbing Wang, Yue Zhao, Xujing Zhang, Yan Xu

217 **Inkjet bioprinting of NE-4C neural progenitor cells with enhanced neuronal differentiation via retinoic acid treatment**
Xinda Li, Xiaolei Guo, Jinzhou Feng, Lihua Chen, Huan Xiong, Ruxiang Xu, Tao Xu

231 **Multi-material bioprinting using a helical mixer for fabricating fibers with controlled composition**
Reza Gharraei, Donald J. Bergstrom, Xiongbiao Chen

266 **Low-concentration GOQD-functionalized Ti6Al4V scaffolds enhance osteogenesis and angiogenesis for vascularized bone regeneration**
Duoling Xu, Song Yang, Chao Wang, Shujun Li, Wentao Hou, Jie Wu, Leyi Liu, Dongsheng Yu, Huancai Lin, Wei Zhao

284 **Preparation and biocompatibility of 3D-printed partially degradable Ta–Mg interpenetrating composites**
Jingchao Xu, Yanru Zhang, Shuixian Guo, Yue Yang, Jinwei Yu

301 **3D-printable alginate-MoS_2-AgNW hydrogel bioink for dual-mode wearable capacitive biosensors**
Suraj Shinde, Kang Hyeon Kim, Omkar Pawar, Omkar A. Patil, Sooman Lim, Han Eol Lee

315 **Pyridinium-based acrylate additives for multifunctional 3D-printable photosensitive resins with antibacterial, antistatic, and high-strength properties**
Qiaoling Zhang, Tongyi Wu, Taojun Lin, Xiangqin Ding, Zhiwei Zhang, Jianqing Liang, Rong Li, Xiaomin Zhang, Guoqiao Lai, Qiu Chen

333 **Dual-nozzle 3D-printed calcium sulfate/polylactic acid scaffold incorporating linezolid microspheres for effective repair of femoral condyle defects in rats**
Xiaojie Tang, Chenxu Li, Yanan Wang, Hai Huang, Tongshuai Xu, Shannan Cao, Changlin Lv, Xiaofan Du, Shuqing Chen, Wenkang Yang, Jiale Shao, Yukun Du, Yongming Xi

350 **Thermally tunable and biodegradable copolymer ink for 3D-printed implantable drug delivery depots**
Yun Geun Jeong, Joon Yeong Park, Moon Hee Lim, James J. Yoo, Sang Jin Lee, Moon Suk Kim

371 **Personalized 3D-printed tantalum-coated titanium alloy pelvic reconstruction prosthesis for complex pelvic defects: A prospective randomized controlled trial**
Zhaoyang Ran, Boran Pang, Yulin Tian, Dinghao Luo, Junxiang Wu, Lei Wang, Kai Xie, Jingke Fu, Liang Deng, Wei Li, Yongqiang Hao

385 **Bioprinting and *in vitro* characterization of alginate–gelatin constructs incorporating human umbilical vein endothelial cells for potential cardiac tissue engineering**
Farinaz Ketabat, Reza Gharraei, Alex Guinle, Nicole J. Sylvain, Michael E. Kelly, Ildiko Badea, Xiongbiao Chen

408 **3D-printed aerogel scaffolds with sodium para-aminosalicylate-encapsulated liposomes for intelligent drug delivery**
Kefeng Wang, Yutong Chen, Yan Xu, Subramanian Sundarrajan, Zhitao Yin, Jingtao Hu, Jian Chao, Shun Zhang, Miaomiao Zheng, Seeram Ramakrishna

431 **3D-printed patient-specific titanium implant for mandibular reconstruction with local drug release: Optimization, *in vivo* evaluation, and functional assessment**
Chiao-Min Chang, Shao-Fu Huang, Hsuan-Wen Wang, Lu-Yi Yu, Tzu-Huan Huang, Chun-Liang Lo, Chun-Li Lin

CASE STUDY

451 **Customized 3D-printed prosthesis for reconstruction of complex bilateral traumatic knee bone defects: A case report**
Gang Zhao, Yongqiang Zhang, Longfei Liu, Longxin An, Futian Zhang, Da Huo, Xuecheng Sun, Xiaoming Yang, Naibo Feng

COMMENTARY

460 **From platelet-rich plasma to personalized implants: A commentary on "3D-printed vascularized biofunctional scaffolds for bone regeneration"**
Hyun-Do Jung

ACCSCIENCE PUBLISHING

International Journal of Bioprinting

REVIEW ARTICLE

Advances and challenges in three-dimensional bioprinting of bone organoids: Materials, techniques, and functionalization strategies

Longfei Wu[1], Junjie Zhao[1], Jiwei Huang[1], Pengfei Huang[1], and Haiyan Zhao[2]*

[1]Department of Orthopedics, The First Clinical Medical College of Lanzhou University, Lanzhou, Gansu, China

[2]Department of Orthopedics, The First Hospital of Lanzhou University, Lanzhou, Gansu, China

Abstract

The use of three-dimensional (3D) bioprinting to construct bone organoids holds significant promise in bone tissue engineering due to its potential to replicate complex structures for research and regenerative medicine. This technology enables the creation of precise 3D structures through layer-by-layer deposition of bioinks guided by digital models. However, challenges remain in achieving functional bone organoids, especially in bioink design, vascularization, and cell viability preservation. To address these issues, various printing techniques such as extrusion, inkjet, light-curing, and microfluidic printing have been explored, but further advances are needed to improve the quality and functionality of printed bone organoids. This review assesses the current state of research on the application of 3D bioprinting techniques for the construction of bone organoids, focusing on the selection of bioinks, scaffold materials, and the role of cells and growth factors. Despite notable progress, significant challenges remain in optimizing the mechanical properties of bioinks, enhancing vascularization, and mimicking the dynamic physiological environment of bone tissue. The main objective of this study is to explore the technical challenges and opportunities in the construction of functional bone organoids through 3D bioprinting, aiming to provide insights into future directions for overcoming these obstacles and improving bone tissue regeneration applications.

Keywords: Bone organoids; Bioink; Three-dimensional bioprinting; Tissue engineering; Vascularization

***Corresponding author:**
Haiyan Zhao
(wulf2024@lzu.edu.cn)

Citation: Wu L, Zhao J, Huang J, Huang P, Zhao H. Advances and challenges in three-dimensional bioprinting of bone organoids: Materials, techniques, and functionalization strategies. *Int J Bioprint*. 2025;11(5):1-22. doi: 10.36922/IJB025190183

Received: May 6, 2025
Revised: June 24, 2025
Accepted: July 1, 2025
Published online: July 1, 2025

Copyright: © 2025 Author(s). This is an Open Access article distributed under the terms of the Creative Commons Attribution License, permitting distribution, and reproduction in any medium, provided the original work is properly cited.

Publisher's Note: AccScience Publishing remains neutral with regard to jurisdictional claims in published maps and institutional affiliations.

1. Introduction

Bone tissue, as the body's structural support system, serves multiple functions such as protecting internal organs, maintaining body shape, facilitating movement, and regulating mineral metabolism. However, the skeletal system often faces challenges from injury, aging, and disease, resulting in bone defects and loss of function. Bone defects not only seriously affect patients' quality of life but also place a heavy burden on healthcare systems and society. With the global aging population, the incidence of skeletal diseases is increasing, especially large-scale bone defects due to fractures, tumors, or infections, which have become a critical concern in current clinical medicine.[1]

Bone organoid is a three-dimensional (3D) *in vitro* model that has recently emerged from advances in organoid technology and tissue engineering, aiming to mimic the structure, function, and microenvironment of natural bone tissues and to provide a more accurate platform for investigating bone-metabolism-related disease mechanisms, drug screening, and regenerative medicine applications.[2]

Three-dimensional bioprinting is a technology that fabricates 3D structures through the layer-by-layer deposition of biomaterials guided by digital models. This approach not only enables the printing of biological scaffolds but also simultaneously loads cells, drugs, and other biomolecules into the scaffolds, thereby broadening its applications in tissue engineering and regenerative medicine.[3] In bone tissue engineering, the application of 3D bioprinting technology has been proven to provide personalized and precise solutions for bone defect repair. Printing bone scaffolds with tailored shapes, pore structures, and mechanical properties enhances their ability to support bone cell growth and differentiation, thereby promoting new bone formation. In addition, 3D bioprinting technology can be combined with stem cell technology, genetic engineering technology, and advanced biomaterials to achieve complete bone tissue regeneration.[4]

Currently, despite the remarkable progress of 3D bioprinting technology in bone tissue engineering, there are still multifaceted challenges in constructing bone organoids. These include designing bioinks with optimal biocompatibility and appropriate mechanical properties, engineering large-scale vascular networks in organoids, maintaining cell viability throughout the printing process, and ensuring the long-term stability and biological functionality of the printed organoids.[5,6]

This article focuses on the application and advancements of 3D bioprinting technology in the construction of bone organoids. It provides a comprehensive review of the development of this technology within the field and analyzes the current challenges and future directions. The article firstly introduces the basic principles of 3D bioprinting, the types of technologies and their applications in bone organoid printing, followed by a discussion on the design requirements of bone organoids, the selection and optimization of cell carrier ink, the challenges faced by vascularization, and the optimization of the structure during the printing process. Lastly, the article analyzes the limitations of existing technologies and explores prospective developments, such as novel biomaterials, multifunctional bioinks, and the clinical translation of this technology. The aim of this review is to present the latest advances in 3D bioprinting applications for bone organoids, offering valuable insights for researchers and clinicians, and to serve as a useful reference to guide future research and clinical practice.

2. Overview of three-dimensional bioprinting technologies

2.1. Principles of three-dimensional bioprinting

Unlike traditional 3D printing, the core of 3D bioprinting extends beyond precise structural fabrication to emphasize cell viability, tissue growth, differentiation, and ultimate biological function.[7] The fundamental steps include digital design, ink selection, layer-by-layer printing, and post-printing culture (Table 1). The process begins with digital model design, which translates medical data into 3D structures through the use of computer-aided design software.[8] In computer-aided design software, designers are able to customize the scaffolds of bone organoids according to specific requirements. For example, scaffold porosity must balance mechanical support with adequate space for cell growth.[9] Bioink, the core component of 3D bioprinting, primarily consists of cells, support materials, and growth factors. Choosing the right bioink is crucial for printing high-quality bone organoid scaffolds (Figure 1). Suitable bioinks must meet several requirements, including biocompatibility, mechanical properties, degradability, and the ability to support cell growth and differentiation.[10,11] Following bioink selection, the 3D model is sliced into

Table 1. Key stages and parameters in bone organoid construction

Stage	Main operations	Key parameters	Influencing factors	Reference
Digital model design	Computer-aided design modeling, pore optimization	Porosity, mechanical strength	Data resolution, software parameters	[8]
Ink selection	Mixing cells, biomaterials, and growth factors	Viscosity, rheology, and biocompatibility	Cell type, biomaterial properties	[10]
Three-dimensional printing	Layer-by-layer deposition, crosslinking, and curing	Printing resolution, curing speed	Printing speed, environmental temperature	[12,13]
Post-culturing	Cell culture, dynamic stimulation	Cell proliferation, differentiation, and vascularization	Mechanical stimulation, growth factors	[15,16,18]

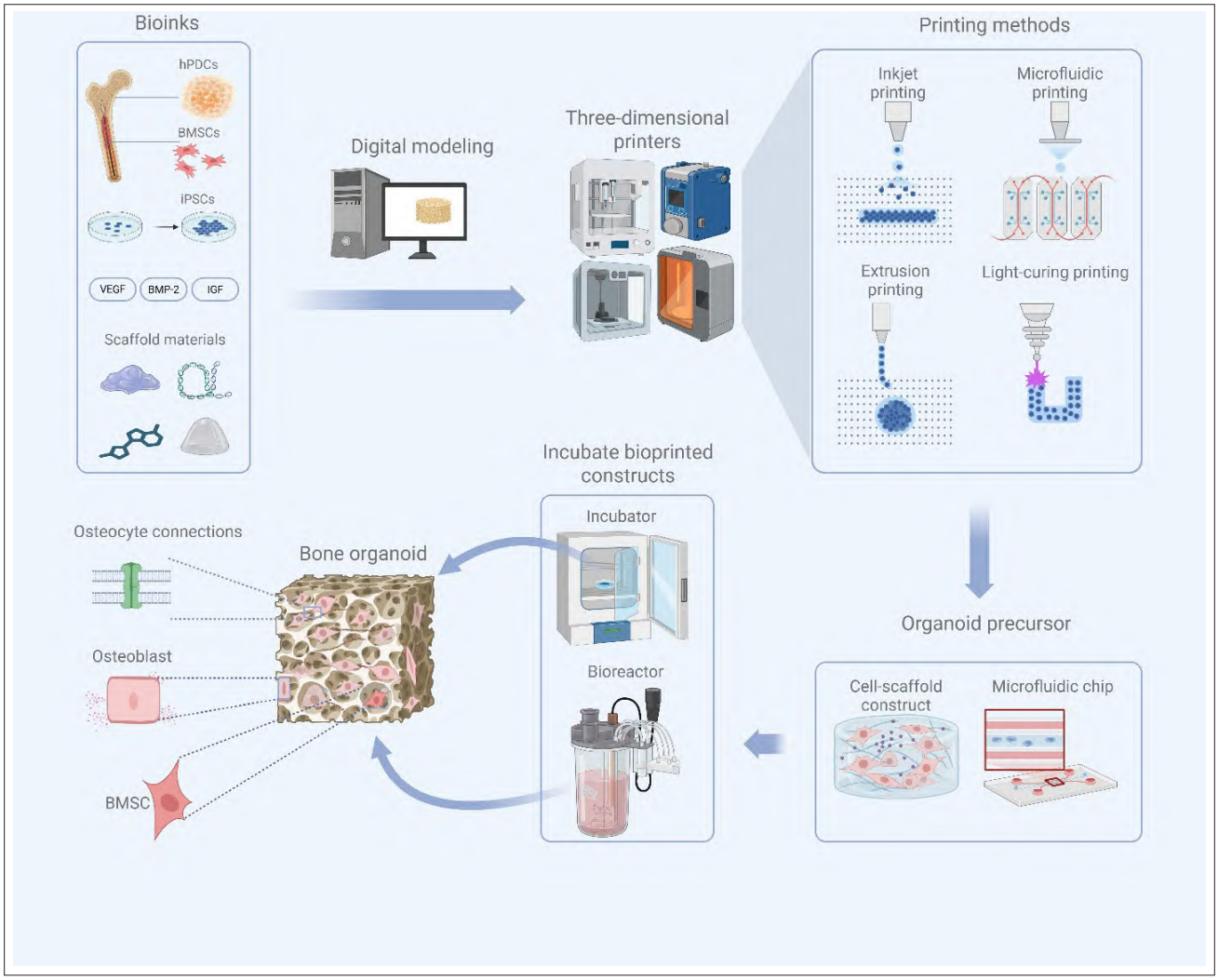


Figure 1. Workflow of three-dimensional (3D) bioprinting for bone organoid construction. The process begins with the selection of bioinks, which include cells, growth factors, and biomaterials. Subsequently, a suitable printing method is chosen based on computer-assisted design modeling. The printed bone organoid precursors are then placed into bioreactors or incubators for further maturation. Finally, the process results in the cultivation of fully matured bone organoids. Schematic diagram created by the authors. Abbreviations: BMSCs, bone marrow mesenchymal stem cells; BMP-2, bone morphogenetic protein-2; hPDCs, human periosteum-derived cells; IGF, insulin-like growth factor; iPSCs, induced pluripotent stem cells; VEGF, vascular endothelial growth factor.

a series of two-dimensional slices, which are printed sequentially. Each layer is printed to ensure structural stability and cellular viability. After each layer is printed, the new ink layer forms a bond with the preceding layer, and the quality of the bond between layers directly affects the overall stability and structural integrity of the print.[12] Certain 3D bioprinting technologies perform a curing process after each layer to stabilize the morphology and mechanical properties of the print. The curing process transforms the bioink from a liquid to a solid state through ultraviolet (UV) light, laser, calcium ions cross-linking, or chemical agents to ensure good bonding between each layer. Poor bonding between layers may lead to fragile scaffolds and affect the normal growth and distribution of cells, especially in biological scaffolds.[13] Therefore, the temperature, humidity, printing speed, and curing process during the printing process must be precisely controlled to ensure proper bonding between each layer. Scaffolds after 3D bioprinting are usually placed in cell culture tanks or bioreactors that mimic the *in vivo* environment by supplying the cells with the required nutrients, oxygen, and growth factors for organoid development.[14,15] In addition, dynamic culture systems such as rotating bioreactors, fluidic culture systems, and microfluidics can be used to provide cells with the required fluid shear, pressure, and flow environment[16] (Figure 1). In 3D bioprinting, scaffolds

serve not only as physical supports for cell growth but also as dynamic structures whose degradation synchronizes with the maturation of bone organoids. As new tissue grows and matures, the scaffold material gradually degrades and is replaced by native tissue. This degradation process must be matched with tissue regeneration to ensure continuous support until the scaffold is completely replaced.[17,18] Culturing bone organoids involves complex, long-term processes such as cell proliferation, differentiation, mineralization, and vascularization. Therefore, it is crucial to select scaffold materials that can remain stable over time and not be rapidly degraded to ensure a successful formation of bone organoids.

2.2. Key three-dimensional bioprinting technologies

Extrusion printing is a widely adopted 3D bioprinting technology that uses methods such as pneumatic pressure, mechanical extrusion, or screw drive to propel the bioink to be extruded from a nozzle and deposited onto the print substrate.[19] Once printed, the bioink typically needs to be cured either physically (e.g., by cooling) or by chemical cross-linking to form a stable structure. This printing technique is capable of handling a wide range of materials, including natural hydrogels and synthetic polymers.[20,21] By adjusting the formulation of the bioink, the mechanical properties, degradation rate, and porosity of the scaffold can be customized to meet the needs of different bone organoids printing.[22] However, conventional extrusion printing requires high-temperature melting of biomaterials, which can cause severe thermal damage to the cells in the bioink. Essential cellular components, such as proteins, lipid bilayers, and nucleic acids, are susceptible to denaturation at high temperatures, leading to cell death or loss of function. Even when cells undergo pretreatment prior to printing, thermal stress may still cause irreversible damage. To minimize the effects of high-temperature materials on cells, researchers have increasingly employed low-melting-point biomaterials for printing, thereby reducing thermal damage to cells.[23] Among various 3D bioprinting techniques, extrusion printing technology is able to maintain a high cell density during the printing process. When constructing bone organoids, this high cell density helps to promote cell-to-cell interactions, which are essential for cell differentiation and functionalization. Although high-viscosity bioinks can support high cell density, they may cause mechanical damage to cells during extrusion.[24] Therefore, optimizing the balance between bioink viscosity, fluidity, and cell viability, while ensuring higher cell density, remains a significant challenge in extrusion printing.

Inkjet printing technology utilizes physical principles, such as thermal or piezoelectric jets, to precisely eject liquid bioink through nozzles, forming minute droplets that are deposited onto a print substrate following a preset path. The size and frequency of the droplets are controlled by the printer.[25] Through layer-by-layer deposition, these droplets accumulate to form a 3D structure. Following each layer's deposition, cooling, cross-linking, or other curing methods are often required to ensure the stability of the printed structure. This technology is capable of producing micron-sized droplets with precise control over cell and material deposition, making it suitable for fabricating tiny pores and fine structures. Consequently, inkjet printing is ideally suited for the printing of high-throughput cell arrays that can be used for drug screening, toxicity testing, and drug response studies. In addition, it enables precise deposition of endothelial cells to progressively construct vascular endothelial layers and microtubular structures, resulting in vascularized networks.[26] Vascularization is a key component in the construction of bone organoids, as tissues lacking vascular support cannot receive sufficient oxygen and nutrients. By printing microvascular networks, inkjet printing technology may supply blood perfusion to printed bone and cartilage scaffolds, thereby accelerating tissue growth. To ensure smooth droplet ejection and deposition, bioinks with low cell density are typically required.[27,28] In bone organoid construction, low cell density scaffolds may lead to slower cell proliferation and differentiation, complicating organoid development. Meanwhile, droplet deposition can cause local aggregation, potentially resulting in scaffolds with poor pore connectivity or non-uniform pore sizes, especially when printing scaffolds with larger areas. Addressing these challenges requires optimization of printing parameters and bioink formulations to improve the quality and functionality of the printed scaffolds.

Light-cured bioprinting employs UV or visible light to irradiate photosensitive resins or light-curing hydrogels, triggering photocrosslinking reactions that cure the material into mechanically strong structures. This technology has exceptional printing accuracy, often achieving micron-level resolution. The ability to print at high resolution ensures precise detail in bone organoids scaffolds, promoting cell growth and functional recovery of tissues.[29] Beyond single-cell-type printing, light-cured printing can co-print multiple cells by adjusting printing parameters and material formulations.[30] Further development of this technology is expected to promote vascularization of bone organoids by simultaneously printing different cell types, such as osteoblasts and vascular endothelial cells, in the same scaffold. The intensity of the light source and the exposure time directly affect the curing speed and depth of the photosensitive resin, which in turn determines the precision of light-cured printing.[31] Higher intensity can accelerate the curing

process, but may also lead to uneven curing of the surface, while lower intensity slows curing, affecting the accuracy of the print. The exposure time for each layer needs to be precisely adjusted according to the material properties and layer thickness. Excessive exposure causes over-curing, impairing the adhesion of subsequent layers; conversely, insufficient exposure results in under-curing, affecting the bonding between layers. At the same time, excessive light intensity or prolonged exposure may damage the cells in the bioink, leading to cell death or functional impairment.[32] Therefore, it is critical to adjust the intensity and exposure time of the light source to ensure uniform curing of each layer while preserving cell viability and function, which are critical for the precise construction of complex structures such as bone organoids.

Depending on the light-curing printing technology, the type of light source and curing process vary slightly. Common light-cured printing technologies include stereolithography (SLA), digital light processing (DLP), and confocal lithography. SLA technology uses a laser beam as the light source, which scans the surface of a liquid photosensitive resin to locally initiate curing. With each scan, the laser illuminates the surface of the resin, completing the curing of a single spot.[33] By precisely controlling the laser's scanning path and exposure time, the point-by-point curing forms the structure of each layer, enabling SLA to achieve very high printing accuracy. DLP technology uses a digital light source combined with a liquid crystal display to irradiate and cure the entire layer at once by projection. Unlike SLA's laser point-by-point curing, DLP uses projection technology to cure the entire layer more quickly, making it suitable for printing large-area structures. However, it may exhibit slightly lower accuracy than SLA.[32,34] Confocal lithography combines light-curing printing and confocal microscopy to enable layer-by-layer curing at high precision. Using the light source of a confocal microscope, each part of the photosensitive material is precisely illuminated, ensuring precision and stability of the print. This technology provides greater precision and more intricate detail and is particularly suited for printing microstructures and microvascular networks. Despite the advantages of DLP's full-layer curing, light-cured printing methods are still challenged by slower printing speeds compared to other 3D printing technologies.

Microfluidic printing combines microfluidic technology and bioprinting by precisely controlling fluid flow and droplet generation in microchannels. Utilizing fluid dynamics principles such as pressure difference, surface tension, and capillary action, microfluid printing enables precise layer-by-layer deposition of bioink at the target location to construct complex 3D structures layer by layer.[35–37] The microfluidic channels are designed to precisely control the speed, direction, and flow rate of the liquid flow to ensure stable deposition of bioink during printing, while droplet generation units convert bioink into tiny and uniform droplets by adjusting flow parameters. These droplets are precisely deposited onto the target area during the printing process, allowing for the precise positioning of cells and support materials.[38] The microfluidic channel is able to effectively regulate the frequency and position of droplet generation to ensure uniform distribution of cells in the support. The size, shape, and arrangement of the microfluidic channels directly affect the uniformity of cell deposition and the biological properties of the final printed structure. By optimizing the channel design, microfluidic printing may enable the co-printing of different cell types, ensuring that multiple cells are distributed in the scaffold in a predetermined pattern that promotes cell-cell interactions and functionalization. This precise cell alignment and material deposition can provide ideal support for the construction of complex tissues such as bone organoids. In addition, microfluidic printing technology is able to mimic complex physiological microenvironments in the body, such as blood flow, oxygen, and nutrient supply, through the tailored design of microchannel systems.[39,40] These microenvironmental factors are critical for cell growth, differentiation, and functional recovery. In bone organoid construction, microfluidic printing not only provides ideal physiological conditions but also simulates blood flow and nutrient exchange by regulating fluid flow, ensuring adequate oxygen and nutrient delivery within the scaffold to promote bone tissue growth and maturation. Additionally, microfluidic printing technology enables the controlled release of growth factors by precisely controlling the fluid flow in microchannels. These growth factors can promote the proliferation, differentiation, and mineralization of bone cells. The microfluidic system is able to precisely regulate the release rate and spatial distribution of growth factors according to the scaffold design, thus further accelerating the construction and functional recovery of bone tissue. However, this technology relies on complex microfluidic chips and precise fluid control systems, resulting in high equipment costs and high operational requirements.[41] In addition, optimizing the microchannel design to ensure uniform cell distribution and stable growth factor release still requires further research. These limitations have hindered the widespread application of microfluidic printing in large-scale bone tissue engineering (Table 2).

2.3. Selection and requirements for bioinks

Bioinks are materials specifically designed to be used in bioprinting and usually consist of a matrix material, cells, and growth factors.[42] The scaffolding material provides the supporting structure and space, the cells serve as the

Table 2. Comparison of three-dimensional bioprinting technologies

Technology	Principle	Advantages	Disadvantages	Applications	Outlook	Reference
Extrusion printing	Pushes bioink through a nozzle	High cell density, suitable for many materials	High temperatures may damage cells	Bone scaffolds, high cell density tissues	Low-melting materials to reduce cell damage	[19]
Inkjet printing	Sprays ink in droplets layer by layer	High precision, good for small structures	Low cell density, poor pore connectivity	Cell arrays, vascular networks	Improve pore structure and cell proliferation	[25,26]
Light-cured printing	Uses light to solidify photosensitive materials	High precision, supports multi-cell printing	Light exposure can damage cells	High-precision structures; complex organoids	Better light control to maintain cell viability	[29,31]
Microfluidic printing	Controls fluid in microchannels for precise deposition	Precise control of cell placement and growth	Complex design, requires precise fluid control	Three-dimensional structures; simulate physiological environments	Optimize channels for growth factor release	[35–37]

basic units for building tissues, and the growth factors promote the growth, differentiation, and mineralization of bone tissue by regulating cellular behavior. Depending on the printing technology, the formulation and structure of bioinks may vary.

2.3.1. Scaffold materials

Scaffolding materials constitute a core component of cell carrier bioinks, playing a critical role in providing structural support and a 3D growth environment for cells. They mimic the extracellular matrix (ECM) of natural tissues to create a suitable microenvironment for cells, promoting cell growth, proliferation, differentiation, and functional expression.[43] The selection of scaffold material directly affects the mechanical properties of bone organoids, their degradation rate, bone tissue regeneration efficiency, and the stability and functionality of the final printed structure. Common scaffold materials can be categorized into hydrogels, synthetic polymers, inorganic materials, and composites, each offering unique advantages and disadvantages.

Hydrogels are among the most commonly used scaffolding materials in 3D bioprinting, providing an environment that closely mimics ECM due to their high water content and excellent biocompatibility. Hydrogels can be categorized into two types: natural hydrogels and synthetic polymers. Natural hydrogels, such as gelatin, sodium alginate, and collagen, have good biocompatibility and degradability and offer an ideal environment that supports cell growth and proliferation.[44,45] Gelatin, a natural macromolecule derived from collagen hydrolysis, promotes cell adhesion and proliferation, owing to its biocompatibility and biodegradability; however, its mechanical properties are insufficient, and its rapid degradation may render it unsuitable for long-term support in bone organoids. Sodium alginate, a natural polysaccharide, can be combined with cross-linking agents such as calcium salts to regulate its mechanical properties, making it suitable for bone organoid printing.[46,47] Collagen, as the primary matrix protein in bone tissue, holds potential to promote bone regeneration, although its mechanical properties are weak and insufficient to mimic the hardness of natural bone. Synthetic polymers, with tunable mechanical properties and degradation characteristics, are commonly used to enhance the structural strength of scaffolds.[48] However, they are usually less biocompatible than natural materials. Polyvinyl alcohol has good biocompatibility and mechanical properties, but has a slow degradation rate and poor cellular support. Polyvinylpyrrolidone has moderate mechanical properties and biocompatibility, but has poor degradation properties, and usually needs to be compounded with other degradable materials. By integrating natural hydrogels with synthetic polymers, composite hydrogels are able to combine the advantages of both material classes, retaining the excellent biocompatibility and cellular support of the natural materials while imparting the controlled mechanical properties and degradation characteristics of the synthetic materials.[45,49] The main advantage of these composites lies in the ability to adjust their composition and properties, enabling optimization of biocompatibility, mechanical properties, and degradation rates in bone organoids printing. By adjusting the ratio of natural to synthetic materials, the desired performance can be achieved in different applications. The tunability of composite hydrogels gives them a unique advantage, facilitating the printing of a wide range of bone organoids with optimized biological and mechanical characteristics, thereby promoting their further development in clinical applications. Inorganic materials such as hydroxyapatite (HAP) and tricalcium phosphate are widely used in 3D bioprinting, enhancing the mechanical strength of the scaffolds and promoting the

mineralization of bone tissue.[50,51] HAP, being a key element of the natural bone matrix, promotes the attachment, proliferation, and differentiation of osteoblasts and enhances the bioactivity of the bone organoids; whereas tricalcium phosphate promotes bone mineralization and provides structural support that closely resembles natural bone, fulfilling the requirements for bone regeneration (Table 3).

2.3.2. Cells and growth factors

Human periosteum-derived cells (hPDCs) are a population of cells isolated from the periosteum and possess specific biological properties. These cells are obtained through the enzymatic digestion of periosteal tissues and can be cultured and expanded for research and applications. hPDCs possess multipotent differentiation potential, and under suitable culture conditions, they can differentiate into osteoblasts and chondrocytes, contributing to bone and cartilage formation and repair.[52] In bone tissue engineering, hPDCs are an ideal cell source due to their ability to construct bone organoids or repair bone defects. These cells can also form spheroids or organoids of varying sizes. For instance, when cultured in customized agarose microtiter wells, their diameter can be controlled, ranging from 100 to 150 μm to approximately 300 μm.[53] This size modulation is crucial for 3D bioprinting, as different application scenarios may require different sizes of tissue constructs. During spheroid or organoid formation, hPDCs establish 3D tissue units characterized by intercellular junctions and ECM secretion.[54] These structurally complex spheroids or organoids can be used as basic building blocks for 3D printing, enabling their precise arrangement and assembly into bone organoids with enhanced structural complexity and biological function.

Bone marrow mesenchymal stem cells (BMSCs) are pluripotent stem cells derived from bone marrow, capable of differentiating into various cell types, particularly those of bone, cartilage, and adipose tissues.[55,56] BMSCs have a wide range of applications in tissue engineering, regenerative medicine, and cellular therapies due to their excellent potential for self-renewal, proliferation, and differentiation. BMSCs have strong proliferative capacity and can expand sustainably *in vitro*. Despite the possibility of cellular senescence and differentiation limitation during long-term culture, BMSCs can still maintain proliferative activity for a long time.[57] With appropriate culture conditions, BMSCs can be obtained in large numbers in long-term culture, making them ideal for use as cells for constructing bone organoids. In addition, BMSCs are highly adaptable, responding to different culture conditions and external stimuli during long-term culture. For example, in osteogenic and chondrogenic tissue formation, the culture environment can be adjusted to enhance their differentiation potential.[58] This characteristic allows BMSCs to exhibit considerable versatility in the construction of bone organoids.

Induced pluripotent stem cells (iPSCs) are adult cells that have been transformed into stem cells with multidirectional differentiation potential through genetic reprogramming. They are capable of differentiating into various cell types *in vitro*, including osteoblasts, chondrocytes, and osteoclasts, making them an ideal cellular source for bone organoid construction.[59] Given that iPSCs can be derived from the patient's own cells, they exhibit low immunogenicity and can be used for personalized therapy. In addition, iPSCs can be effectively differentiated into osteoblasts through optimized differentiation conditions, which can be used to construct functional bone tissues in combination with scaffolding materials for bone defect repair or bone organoid development.[60] However, challenges remain regarding the differentiation efficiency and stability of iPSCs, as genetic mutations introduced during reprogramming can compromise their long-term stability and safety.[61] Therefore, it is necessary to further optimize the differentiation induction technique of iPSCs and address issues such as genetic instability to promote their wide application in bone organoid construction.

Human umbilical vein endothelial cells (HUVECs) play a pivotal role in bone organoid vascularization due to

Table 3. Characteristics of scaffold materials for bone organoids

Type	Main components	Advantages	Applications	Reference
Natural hydrogels	Gelatin, alginate, hyaluronic acid	High biocompatibility, biodegradable	Cell scaffolds, bioinks	[44–47]
Synthetic polymers	Polyvinyl alcohol, polyvinylpyrrolidone	High mechanical strength, controllable degradation	Bone scaffolds, cartilage repair	[49]
Inorganic materials	Hydroxyapatite, calcium phosphate	Promote bone mineralization, good mechanical properties	Bone tissue repair	[50,51]
Composite materials	Natural hydrogels + ceramics or synthetic polymers	Combine bioactivity and mechanical properties	Composite bone tissue engineering	[45]

their strong angiogenic potential and compatibility with osteogenic systems. In both direct and indirect co-culture models, HUVECs retain endothelial lineage identity while promoting osteogenic differentiation in BMSCs through paracrine signaling.[62] This reciprocal interaction enhances vascularized tissue formation and is critical for the development of functional bone constructs. In 3D bioprinting strategies, HUVECs can be incorporated into bioinks and co-printed with BMSCs, facilitating their spatial organization along scaffold pores or printed microchannels. These cells can self-organize into tubular networks *in vitro*, recapitulating early vasculature development. By forming such prevascular structures, HUVECs not only improve nutrient transport but also help establish a regenerative microenvironment essential for bone matrix deposition.[63,64] The integration of HUVECs into bioprinted constructs has thus become a cornerstone technique in current vascularization approaches for bone organoids.

Growth factors play multifaceted roles in bone organoids. They not only stimulate the proliferation and differentiation of osteoblasts but also participate in several processes such as bone mineralization, angiogenesis, and tissue remodeling. Bone morphogenetic proteins (BMPs), especially BMP-2 and BMP-7, have been shown to significantly promote the osteogenic differentiation of BMSCs and are widely used in bone regeneration and repair.[65] In addition, osteoblast growth factors are also able to promote the proliferation of osteoblasts, which, in turn, improves the efficiency of bone organoid construction.[66] Mineralization is a key process in bone formation and bone organoids, regulated by growth factors that modulate ECM synthesis and mineral deposition. BMPs facilitate bone formation by stimulating ECM secretion from osteoblasts and promoting mineralization. Transforming growth factor-β and insulin-like growth factor-1 also have a beneficial effect on the synthesis of bone matrix by activating the relevant signaling pathways that enhance the ability of osteoblasts to synthesize collagen and minerals.[67,68] Thus, growth factors are essential for mineralization, especially during the maturation phase of bone organoids. Vascularization poses a significant challenge in constructing bone organoids, particularly for large-scale organoids. The formation of vascular networks is essential to ensure adequate oxygen and nutrient supply to the bone tissue. Vascular endothelial growth factor is a key factor in promoting angiogenesis. It promotes blood supply to bone tissues by facilitating the proliferation and migration of endothelial cells as well as the formation of new blood vessels.[69] The lack of an effective vascular network can result in bone organoids not receiving sufficient nutrients and oxygen, affecting their growth and function. In addition, the construction of bone organoids not only depends on cell proliferation and differentiation but also requires tissue remodeling. Matrix metalloproteinases play an important role in this process by degrading the ECM, providing space for cell migration and growth, and facilitating tissue repair processes.[70] In bone organoids, precise regulation of matrix metalloproteinases promotes new bone formation and accelerates the maturation of bone organoids. However, the clinical application of growth factors still faces certain challenges, such as possible side effects, stability issues, and delivery efficiency. Therefore, the development of improved delivery methods is necessary to optimize their effects in bone organoid engineering.

3. Design and construction of bone organoids

3.1. Basic principles of bone organoid bioprinting

3.1.1. Hierarchical structure

The natural structure of bone tissue is highly hierarchical, and its structural complexity and functionality enable bone tissue to provide strong mechanical support while meeting biological demands. When designing bone organoids, it is important to mimic the hierarchical nature of natural bone tissue as closely as possible to ensure mechanical properties, function, and bioactivity (Figure 2).

Cortical bone provides strength and rigidity to the skeleton and is usually located on the outer surface of bones, characterized by a dense structure. In contrast, cancellous bone provides a larger surface area and microchannels, enhances the elasticity of the bone tissue, supports vascularization, and promotes cell attachment and proliferation.[65,71] Typically, cortical bone regions require higher mechanical strength and rigidity and are, therefore, constructed using materials with higher modulus of elasticity and greater durability. The cancellous bone region, on the other hand, has greater porosity and smaller pore sizes, forming a "honeycomb"-like structure that provides space for cells to grow and supports the formation of a vascular network. The pore structure of the cancellous bone must be precisely designed to ensure proper cell growth, proliferation, differentiation, and vascularization.[72] Materials with greater porosity and better elasticity are often used to mimic the properties of cancellous bone. The use of 3D printing technology allows precise control of the pore structure, thereby improving cell viability and function within this region.[73]

Cartilage tissue functions primarily by reducing friction, absorbing shock, and supporting skeletal motion. When constructing cartilage organoids, the design should focus on the mechanical properties of cartilage, such as low

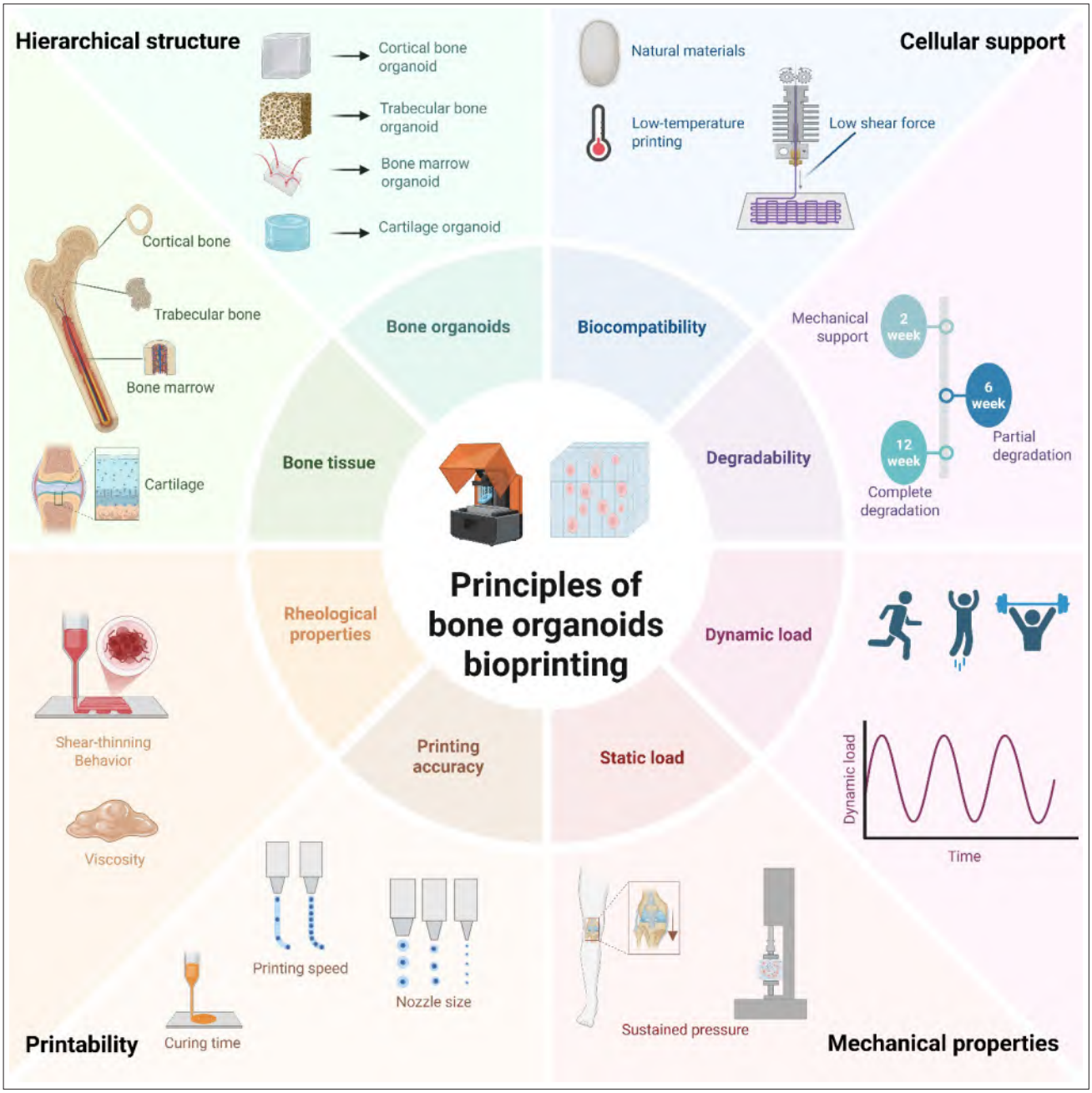


Figure 2. Basic principles of bone organoid bioprinting. This figure illustrates the key principles in designing and constructing bone organoids, focusing on the hierarchical structure, cellular support, printability, and mechanical properties required for bone organoids. Schematic diagram created by the authors.

stiffness, high elasticity, and compressive cushioning.[74] To mimic this property, hydrogel-like materials with excellent hydration and moderate modulus of elasticity are often used. These materials not only mimic the mechanical properties of cartilage but also provide a suitable environment for cell growth to support chondrocyte attachment, proliferation, and differentiation. Due to the relatively simple structure of cartilage tissue and the absence of a vascular network, the selected scaffold materials must mimic the hydration and flexibility of cartilage tissue to ensure that the constructed cartilage can effectively withstand mechanical loads and provide the required cushioning function.[75,76] At the same time, the scaffold's degradation rate must align with the growth of cartilage tissue to maintain the stability of the cartilage layer.[77,78] The connection between cartilage and bone matrix is an essential part in the design and formation

of bone organoids due to their distinct functional and structural properties. Achieving a smooth transition between these tissues in 3D scaffolds will directly affect organoid efficacy. Microfluidic printing technology enables precise gradient control at this interface through regulated inlet flow rates and ink ratios of the microfluidic mixer. By adjusting the gradient parameters according to the structural characteristics and physiological requirements, this technique facilitates the formation of a natural and stable connection between cartilage and bone matrix.[79]

The bone marrow cavity is an important part of bone tissue, containing hematopoietic stem cells, adipocytes, and BMSCs, and playing a key role in bone repair, immune response, and blood circulation.[80] Although fully immunocompetent bone marrow organoids have yet to be realized, the simulation of the medullary cavity, especially in terms of vascularization and intercellular communication, is still an important part of bone organoid construction.[81] 3D bioprinting technology can precisely control the pore structure of scaffolds to create a microenvironment suitable for the growth of bone marrow cavity cells. By using highly porous materials that mimic the spatial characteristics of bone marrow and incorporating materials such as hydrogels and synthetic polymers, the strength and biocompatibility needs of the bone marrow cavity can be met.[82] During printing, bioinks containing hematopoietic stem cells and BMSCs can be printed directly into the scaffold to ensure their uniform distribution and growth. Bioprinting technology also allows for the precise construction of vascular channels to mimic blood flow. Although current technology cannot yet fully mimic the function of bone marrow fluid, the design of microchannels and capillaries establishes a foundational framework for future bone marrow organoid construction. With ongoing technological advances, the integration of microfluidics, immune cells, and multiple types of stem cells holds promise for creating more complex bone marrow function simulations, thereby advancing the construction of bone marrow organoids.

3.1.2. Cellular support

The cell-supportive nature of bioink is reflected not only in its high biocompatibility but also in its ability to degrade harmlessly once the bone organoid has matured.[7,83] First, the chemical composition of the material needs to be compatible with the biological environment to avoid cytotoxicity or inflammatory reactions. Natural polymers like alginate and gelatin are often widely used in 3D bioprinting due to their good biocompatibility. In contrast, synthetic polymers can be chemically modified to improve their hydrogel properties, making them more adaptable to the cell growth environment.[45] In addition, the pH, ionic concentration, and osmotic pressure of bioinks must closely match the physiological environment to ensure cell viability post-printing.[84] The choice of printing method can also impact cell survival. High temperatures during printing can damage cells; therefore, most bioinks require printing at lower temperatures to avoid thermal damage (Figure 2). In particular, extrusion printing technology requires the printing temperature to be maintained below 40°C to avoid overheating-induced cell damage.[85] Other printing methods, such as inkjet, typically operate at lower temperatures, thereby reducing the thermal stress on cells. At the same time, the effect of shear forces may lead to mechanical damage to cells, especially at higher print speeds. Excessive print speeds increase the shear force during material flow, causing stress on the cells. To reduce the shear stress, the print speed should be appropriately reduced, and parameters such as print path and layer thickness must be controlled.[25] By optimizing these variables, it is possible to reduce cell damage during printing and improve cell survival.

The degradation properties of scaffolds directly affect cell differentiation and bone matrix formation. In the early stage of stem cell or precursor cell proliferation, scaffolds must maintain structural stability and provide sufficient support. At this stage, a slower degradation rate is essential to withstand cellular expansion and provide structural support for the new tissue. When cells begin to differentiate and form the initial tissue structure, the degradation rate of the scaffold can be gradually accelerated to accommodate tissue growth. The degradation products at this stage can provide nutrients to the cells while promoting cell differentiation.[51] During the final maturation stage of the bone organoids, the scaffold should gradually undergo complete and harmless degradation to allow the newly formed tissue to stabilize without interference from residual scaffold material.[86] The rate of scaffold degradation can be controlled by adjusting the cross-linking density of the material as well as the printing parameters. Specifically, increasing the material's cross-linking density, layer thickness, and reducing porosity will reduce the scaffold's degradation rate. In contrast, decreasing the cross-linking density, reducing layer thickness, and increasing porosity will accelerate the degradation process.

3.1.3. Printability and mechanical properties of bioinks

Rheological properties are the core parameters for evaluating the printability of bioinks, primarily encompassing viscosity, shear force, and elastic modulus. Viscosity determines the bioink's ability to flow smoothly and maintain the intended structure integrity during the printing process.[87] In 3D bioprinting, the viscosity of

bioink must be balanced within a certain range. When the viscosity is too low, the bioink may flow excessively, failing to maintain the predetermined shape during the printing process and potentially causing undesirable cell displacement or diffusion, which can impair cell localization and proliferation.[88] Another rheological property associated with bioinks is shear thinning, where inks typically experience high shear rates during 3D printing, especially at the nozzle. Bioinks exhibiting good shear thinning demonstrate a reduction in viscosity when subjected to an external force, allowing smooth extrusion through the nozzle and preventing clogging caused by high viscosity.[89–91] This property is particularly beneficial for detailed or high-precision printing, as it enhances print accuracy and structural stability (Figure 2). In addition, another important effect of shear thinning is the rapid recovery of viscosity after extrusion. Once the shear force is removed post-printing, the bioink's viscosity increases promptly, allowing the structure to stabilize quickly and preventing deformation of the structure from affecting the print result.

The printing accuracy and resolution of bioinks directly affect the accuracy of cell and tissue structures generated during 3D bioprinting. During the printing process, the bioink must cure promptly after deposition to form the desired structural morphology.[13,92] If curing occurs too slowly, the printed structure may become unstable; conversely, overly rapid curing can cause nozzle clogging or uneven hardening. Therefore, bioinks require an optimal cure time and hardening rate to ensure that each layer quickly forms a stable structure during the printing process, while maintaining a certain degree of fluidity to ensure accurate printing. Nozzle size and layer thickness during printing directly affect the resolution of the print.[93] Smaller nozzle sizes enable finer structures and higher resolution, but also require lower viscosity and good shear thinning of the ink to avoid clogging. Printing thinner layers enhances detail resolution but increases the stability requirements of the printing process[94,95] (Figure 2). Therefore, controlling the nozzle size and print layer thickness is critical for printing accuracy and resolution. In addition, print speed also affects print resolution. Excessively high speeds may lead to unstable ink flow, compromising print accuracy and detail fidelity. Therefore, appropriate print speeds and optimized print path strategies can ensure accurate printing at high resolutions while maintaining the stability of the printing process.

3.2. Construction process of bone organoids

3.2.1. Cell attachment and proliferation

Appropriate surface roughness has been shown to enhance cell attachment area by improving the contact between the cells and the scaffold, thereby promoting stable cell attachment.[96,97] When the surface of the scaffold is relatively smooth, it may be difficult for cells to form a stable attachment to its surface, while a scaffold with a rough surface can provide more attachment points for the cells (Figure 3). Furthermore, scaffold hydrophilicity is a critical factor affecting attachment; more hydrophilic surfaces can improve cell affinity and facilitate binding between the cell membrane and the scaffold surface.[98] Once stable attachment is established, the cells rapidly enter the proliferation stage and form a preliminary cell population. The porosity, pore size, and distribution of the scaffold directly influence the available space and growth environment for cell proliferation. Larger pores and higher porosity can provide sufficient growth space for cells to expand in a 3D environment.[99] Appropriate pore size also improves gas exchange, nutrient supply, and metabolic waste removal, creating a microenvironment favorable for cell proliferation. For example, micro- or nanopore structures can increase the attachment area of cells, thereby promoting stable cell proliferation.[82] In addition, the connectivity of the scaffold pores is also crucial for the migration and expansion of cells, enabling uniform cell distribution throughout the scaffold's 3D space. In addition, the mechanical properties of the scaffold also play a key role in cell proliferation. Scaffolds with suitable stiffness can highly simulate the mechanical environment of native bone tissue, thereby promoting cell growth.[100] Conversely, scaffolds with insufficient stiffness inhibit cell proliferation, as cells receive inadequate mechanical stimulation, leading to reduced proliferation rates.

3.2.2. Cell differentiation and bone matrix formation

Osteogenic differentiation in bone organoid construction typically involves key signaling pathways, including Wnt/β-catenin signaling, BMPs/transforming growth factor-β signaling, and others. These pathways promote stem cell differentiation into osteoblasts and stimulate the synthesis and mineralization of the bone matrix by activating osteogenesis-related gene expression.[101] To effectively regulate these signaling pathways, researchers can directly add factors such as BMP and Wnt3a into bioinks, which are co-printed alongside cells and scaffold materials (Figure 3). The factors interact with the cells to promote cell differentiation and tissue formation. Furthermore, microfluidic technology can be utilized to introduce microfluidic channels during the printing process to precisely deliver cytokines to specific locations, ensuring their uniform distribution and optimal stimulation of cells. Microenvironmental regulation is also an important factor affecting cell differentiation. Maintaining a low oxygen environment and physiological pH supports osteogenic differentiation.[102] Optimizing these microenvironmental

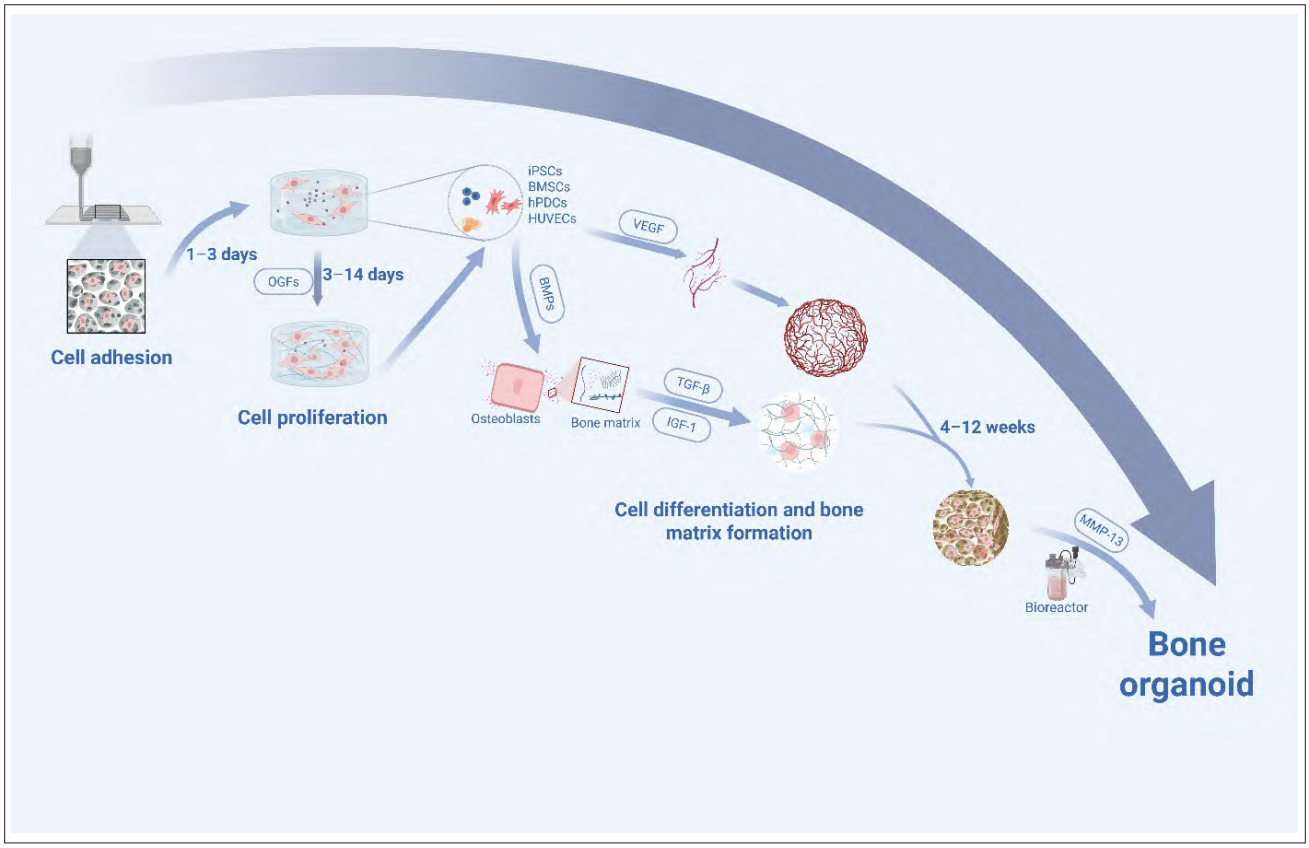


Figure 3. Overview of the bone organoid construction process Cells first adhere to the three-dimensional bioprinted scaffold, where surface roughness and porosity enhance attachment and proliferation. Stem cells then differentiate into osteoblasts and produce bone matrix under stimulation from bone morphogenetic protein (BMP)-2, transforming growth factor-β (TGF-β), and insulin-like growth factor (IGF)-1. Human umbilical vein endothelial cells (HUVECs) promote vascularization in response to vascular endothelial growth factor (VEGF). After 12 weeks of in vitro culture, calcium is stably deposited, and mechanical stimulation from a bioreactor supports final organoid maturation. Schematic diagram created by the authors. Abbreviations: BMSCs, bone marrow mesenchymal stem cells; hPDCs, human periosteum-derived cells; iPSCs, induced pluripotent stem cells; MMP, matrix metalloproteinase; OGFs, osteoblast growth factors.

conditions facilitates the construction of organoids that more closely resemble bone tissue *in vivo*.

After differentiation, osteoblasts undertake the synthesis and mineralization of the bone matrix, a process crucial not only for the structural support and biological functions of bone tissue but also for the mechanical properties and repair capacity of bone organoids.[103] The primary component of the bone matrix is collagen, particularly type I collagen. During collagen secretion, osteoblasts produce collagen fibers that gradually arrange and intertwine into a mesh-like structure, forming the foundational framework of the bone matrix. Glycosaminoglycans constitute another essential component of the bone matrix, conferring elasticity and resistance to compression by interacting with water molecules.[104] During bone repair, glycosaminoglycans help maintain matrix hydration, promote mineral deposition, and support the solidity of the bone matrix. Mineralization represents the final stage of bone matrix formation, imparting stiffness and strength to the tissue. Following the secretion of collagen fibers and other matrix components, mineralization proceeds via deposition of calcium salts, which ultimately transform the matrix into hard bone tissue. Osteoblasts secrete matrix molecules containing calcium ions and phosphates, which interact with the collagen fibers in the bone matrix and gradually deposit HAP crystals, hardening the matrix.[105] Some researchers have incorporated HAP directly into 3D-printed scaffolds as a bioink component, enhancing mechanical strength while accelerating mineralization and increasing matrix hardness.[51,106] Proteins, such as osteocalcin and osteoblastin, secreted by osteoblasts, can regulate the localization and rate of calcium salt deposition. These proteins are particularly important in the early stages of bone matrix deposition, promoting stable deposition of calcium salts and ensuring a homogeneous and orderly mineralization process.[107] In addition, osteocalcin and

bone bridging proteins can be incorporated directly into the scaffold during the early stages of bone matrix formation, enabling more precise control of the process.

3.2.3. Maturation of bone organoids

Bone tissue development involves not only the synthesis and mineralization of bone matrix at the cellular level, but also the gradual acquisition of mechanical competence to bear body weight and dynamic loads. With continuous secretion and deposition by osteoblasts, HAP crystals gradually increase in size and become more evenly distributed, with a significant increase in bone matrix mineralization.[108] Eventually, the mineralized bone matrix provides strong mechanical support, effectively resisting external loads and exhibiting the biomechanical properties of native bone tissue. The mineralization and strength enhancement of the bone matrix is a highly dynamic process involving the synergistic action of osteoblasts and osteoclasts. Osteoblasts contribute to the maturation of the bone matrix by secreting a mineralized matrix, which gradually enhances its hardness and strength. In contrast, osteoclasts regulate the microstructure and mechanical properties of the bone matrix through bone remodeling, a process that removes aged and damaged parts in the bone matrix and provides new deposition space for osteoblasts. This remodeling ensures the adaptability and elasticity of bone tissue under different physiological loads. Osteoblasts are crucial in the maturation of bone organoids, significantly aiding bone matrix reconstruction and adaptation. Their role has been well established in facilitating these processes.[109] However, accurately mimicking osteoclast activity in 3D-printed bone organoids remains a significant challenge. Advances in 3D bioprinting technology are anticipated to ensure precise spatial mapping of osteoclasts within scaffolds. Leveraging high-resolution and multi-material printing capabilities, 3D printing can construct scaffolds that provide a favorable microenvironment for osteoclast growth and functionality. For example, the differentiation and function of osteoclasts can be modulated through inducible factors such as receptor activator of nuclear factor κ B ligand and macrophage colony-stimulating factor, enabling precise control over their activity during bone matrix mineralization and maturation. This dynamic regulation not only facilitates a more physiologically relevant simulation of bone remodeling but also provides a foundation for investigating the intricate cellular crosstalk involved in skeletal homeostasis and pathological bone resorption.

3.2.4. Vascularization strategies in bone organoid

With the maturation of the bone matrix, the formation of a vascular network becomes essential to sustain the viability and metabolic function of the tissue. Vascularization not only facilitates nutrient and oxygen delivery but also plays a pivotal role in maintaining cell viability, removing metabolic waste, and promoting osteogenic maturation within the organoid structure. HUVECs can be co-cultured with BMSCs by encapsulating them in biocompatible hydrogels such as gelatin methacrylate or fibrin.[110] Therefore, in the context of 3D bioprinting, both cell types can be co-printed. These hydrogels provide a favorable matrix environment for endothelial cell self-organization, enabling HUVECs to spontaneously form microvascular networks within the printed constructs.

Beyond single-cell strategies, the incorporation of microvascular fragments (MVFs) has emerged as a promising approach to accelerate vascularization. MVFs are multicellular segments derived from adipose or other vascular-rich tissues and retain intact vessel structures, including endothelial and perivascular cells.[111] When embedded in printable hydrogels and bioprinted into scaffolds, MVFs can rapidly anastomose with host vasculature post-implantation, supporting early perfusion and enhancing tissue survival. Their application has been shown to significantly improve vascular integration and bone regeneration in preclinical models.[112]

Additionally, microfluidic chips offer a complementary *in vitro* strategy for engineering vascular networks in bone organoids. Unlike traditional static co-culture systems, microfluidic platforms can simulate dynamic blood flow and shear stress within precisely patterned channels. Endothelial cells cultured within these channels align and form perfusable capillary-like structures that mimic the hierarchical vascular architecture.[113] When integrated with bioprinted constructs or used as prevascularized modules, microfluidic chips contribute to improved oxygen and nutrient diffusion and offer a controlled platform for investigating vascular–osteogenic interactions.

Beyond preformed constructs, host vessel ingrowth after implantation is also a widely adopted strategy. Instead of relying solely on *in vitro* prevascularized constructs, this approach utilizes the body's intrinsic angiogenic potential to support the gradual infiltration of host-derived blood vessels into the implanted scaffold. After transplantation, the scaffold serves as a physical guide and biochemical microenvironment that encourages endothelial migration, capillary sprouting, and anastomosis with the native vasculature.[114] To facilitate this process, 3D bioprinting can be used to precisely design scaffolds with optimized pore size, interconnectivity, and spatial architecture, which are essential for vessel ingrowth. Unlike artificial vascular networks formed *in vitro*, host-derived vasculature tends to follow physiologically relevant spatial distributions and supports long-term remodeling and integration with

surrounding bone tissue. This strategy is particularly valuable in large bone defects or critical-sized lesions, where robust vascular support is essential for sustained tissue survival, osteogenesis, and integration.[115] Therefore, harnessing host vascular ingrowth through the design of pro-angiogenic 3D-printed scaffolds offers a biologically compatible and translationally promising route toward functional bone organoid development.

3.2.5. Physiological load simulation and functional recovery of bone organoids

Bone tissue is a dynamic structure whose function and morphology are continuously affected by physiological loads. To construct bone organoids with practical clinical relevance, it is essential to consider the role of physiological loads and promote the functional recovery of bone organoids through appropriate mechanical stimulation.[116] Physiological loads include mechanical stimuli such as pressure, tension, and bending that bone tissues experience *in vivo*. These external forces not only affect the physiological adaptation of bone tissues but also critically influence their mechanical properties and repair processes. Mechanical stimulation plays a crucial role in activating the Wnt signaling pathway within osteoblasts, thereby facilitating their proliferation and differentiation. This process not only enhances cellular activity but also strengthens the mineralization of the ECM produced by osteoblasts, ultimately contributing to bone tissue formation and remodeling.[117] In addition, appropriate mechanical loading can regulate the deposition pattern of HAP, promoting its uniform distribution within bone organoids. This uniform mineralization prevents brittleness caused by uneven HAP deposition and improves the overall mechanical integrity of the construct. To replicate the mechanical stimuli endured by bone tissues *in vivo*, a bioreactor can be used in experimental studies to apply periodic compressive loads or tensile loads to the printed scaffolds. Such mechanical conditioning enables cells to perceive and adapt to the external mechanical environment, further optimizing the formation and functional integration of the bone organoids.

4. Challenges

4.1. Challenges in simulating bone tissue structure

The construction of bone organoids aims to mimic the structure and function of natural bone tissues to meet the needs of bone tissue regeneration, disease research, and drug screening. However, due to the physiological complexity of bone tissues, current research emphasizes the creation of functionally specific bone organoids, while complex bone organoids with complete physiological functions have not yet been realized.[101] Current bone organoids are usually constructed for a single tissue, such as cortical bone, cancellous bone, or cartilage, and the integration of multiple tissue types has not yet been achieved. Cortical bone organoids are mostly used for mechanical studies, cancellous bone organoids are more inclined to mimic vascularized microenvironments, and cartilage organoids are mainly used for the study of cartilage injury and degenerative diseases.[118] Due to the significant differences in the structure and cellular composition of these tissues, it remains a technical challenge to integrate different tissues into the same bone organoid model. Future studies could employ bioinks with partitioning properties to accurately reproduce the physical properties of different tissues within a single construct.[79] For example, mineralized biomaterials could be used to print cortical bone with high mechanical strength while combining cell- and growth factor-rich hydrogels to form cancellous bone and bone marrow cavities. In addition, the key to multi-tissue integration lies in the optimization of the transition region between different materials. Establishing a reasonable mechanical gradient between cortical and cancellous bone is essential to improve the overall mechanical stability and physiological adaptability of the composite bone organoid.

The natural bone matrix is fundamentally composed of a composite microenvironment formed by the interweaving of collagen fibers and HAP nanocrystals. However, existing extrusion and light-curing 3D bioprinting technologies, which typically have a resolution of tens to hundreds of microns, fall short of replicating the nanoscale precision required to mimic collagen fiber arrangement.[119] In addition, mineralization of natural bone tissues is regulated by biochemical signals, and existing bioprinting technologies struggle to synchronously guide mineralization during fabrication. Even when mineralization is induced by subsequent culturing, achieving uniform and hierarchical mineral deposition remains challenging. Electrospinning offers a promising complementary approach by utilizing high voltage to generate electrostatic forces that draw polymer solutions or melts into ultrafine fibers, which are then deposited into nanoscale fibrous membranes. The technique can fabricate continuous fibers ranging from nanometers to microns in diameter. Looking ahead, the integration of alternating superposition of electrostatic spinning layers and 3D printing layers holds potential for hierarchical construction, from nanoscale collagen fiber networks to micrometer-scale scaffolds, providing a more physiologically structured support system for bone organoids.[120] Additionally, employing 3D printing to fill electrospun scaffolds could improve cell arrangement and tissue integration efficiency. For instance, 3D printing with bioinks enriched with BMSCs or hPDCs between the nanofiber layers formed by electrostatic

spinning can enhance cell adhesion and osteogenic differentiation potential.

4.2. Vascularization challenges in bone organoid construction

Vascularization of bone tissue is crucial for nutrient transport, oxygen exchange, and waste removal, playing a central role in bone development, regeneration, and homeostasis.[121] However, current strategies for vascularizing bone organoids still face significant technical and biological limitations.

One major challenge is the difficulty in constructing complex microvascular networks using existing 3D bioprinting technologies.[122] Although techniques such as coaxial extrusion and sacrificial molding have shown promise, achieving stable, perfusable lumens with physiologically relevant diameters remains difficult. Printed vascular channels often collapse due to insufficient mechanical support or become occluded by uncontrolled cell proliferation. Moreover, vascular endothelial cells such as HUVECs are highly sensitive to hypoxic conditions, and their survival and function decline in poorly perfused or static environments.[123] Maintaining their viability within dense 3D structures remains a critical bottleneck. In addition, it is difficult to achieve an optimal balance between the biocompatibility and mechanical strength of vascular scaffolds. Materials that support cell adhesion and angiogenesis often lack the stiffness required to preserve lumen structure under dynamic flow conditions.

Another limitation is the lack of functional integration between vascular and osteogenic components. In many constructs, blood vessels form structurally but fail to interact efficiently with bone-forming cells.[124] This lack of paracrine signaling and mechanical communication limits bone matrix maturation and remodeling. Furthermore, reproducing the spatial and temporal dynamics of the native bone microenvironment—including gradients of oxygen, nutrients, and shear stress —remains difficult in static culture systems.

The cell source and heterogeneity of endothelial cells also present challenges. Commonly used HUVECs may not fully represent bone microvascular endothelial phenotypes, and their limited lifespan and variability reduce reproducibility.[125] Meanwhile, achieving vascular anastomosis with host vessels upon implantation remains unpredictable, and inadequate integration can result in central necrosis of the engineered tissue.

Overcoming these challenges will require the integration of advanced bioprinting strategies, dynamic perfusion bioreactors, tissue-specific endothelial cell sources, and real-time functional imaging. Addressing the vascularization bottleneck is essential to developing clinically relevant and physiologically functional bone organoids.

4.3. Inadequate dynamic modeling of the physiological environment

Bone tissues continuously experience complex mechanical stimuli *in vivo*, including fluid shear, cyclic compressive stress, and tensile torsion. However, existing *in vitro* culture environments are mostly static. Even bioreactors currently in use typically provide only a single mechanical stimulus, making it difficult to mimic the real mechanical environment *in vivo*, leading to significant deficiencies in functional maturity and tissue integration of printed bone organoids.[116] For example, mesenchymal fluid shear regulates osteoblast differentiation, and static culture systems fail to provide this critical signal, limiting the formation of mineralized matrix. In addition, conventional bioreactors struggle to precisely regulate mechanical stimuli and nutrient gradients, which affect the growth and functionalization of bone organoids.[126]

These shortcomings can be remedied in the future by developing an intelligent dynamic culture system. In combination with microfluidic mechanical stimulation devices, multi-dimensional mechanical signals can be provided within 3D-bioprinted tissues to enhance cell–matrix interactions. At the same time, the medium flow pattern can be optimized to establish a nutrient gradient closer to the physiological environment and to improve the maturation of bone organoids.[127] Further directions include intelligent bioreactors, combining sensing technology and artificial intelligence algorithms for real-time monitoring, and dynamic regulation of parameters such as mechanical stimulation, pH, and oxygen concentration. Such advancements will enhance the quality of *in vitro* culture of bone organoids and provide a foundation for future clinical translation.

4.4. Limitations in the application of biomaterials

There are still many limitations in the use of current materials for bone organoid bioprinting. Firstly, it is difficult to balance mechanical properties and biocompatibility. Most natural hydrogels have good biocompatibility but low mechanical strength, while synthetic polymers have high mechanical strength but lack cell adhesion sites, which affects cell proliferation and differentiation. Secondly, the degradation rate of materials is difficult to align with bone tissue regeneration. Certain materials degrade too fast, which may lead to insufficient support, while others degrade too slowly, which may increase the probability of bacterial and fungal contamination and lead to experimental failure. In addition, material preparation and printing compatibility issues also affect the efficiency and precision

of 3D bioprinting, and high-performance biomaterials often affect the printing effect due to poor rheology, nozzle clogging, or uneven curing. Incorporating both natural and synthetic polymers into bioink formulations offers a promising strategy to simultaneously enhance scaffold stability and cytocompatibility. However, achieving a homogeneous and structurally robust composite requires precise optimization of surface modifications or synergistic cross-linking techniques. Without such refinements, phase separation may occur, compromising the mechanical properties and long-term stability of the scaffold, which is crucial for biomedical applications. Meanwhile, combining natural materials with synthetic materials often involves multi-step preparation such as freeze-drying, solvent evaporation, and hot pressing. Complex fabrication processes may lead to large differences in compositional homogeneity, mechanical properties, and bioactivity of bioinks, resulting in poor batch stability and reproducibility, affecting their clinical translation.

Temperature-responsive hydrogels and photoresponsive hydrogels exhibit fluidity during printing, facilitating printing operations. After printing, they rapidly transition back to a gel state, significantly improving the stability of the constructed structure. This feature not only ensures the mechanical strength of the material for tissue construction but also effectively prevents cell damage. Given these advantages, temperature-controlled responsive hydrogels are poised to become a primary focus in bioink research. Regarding the construction of composite bioinks, it is necessary to establish a database of the optimal ratios of different natural polymers and synthetic polymers, and establish standardized printing parameters (e.g., nozzle temperature, pressure, printing speed, etc.) for different material systems. Such standardization will reduce inter-experimental variability, thereby improving reproducibility and accelerating the clinical translation of 3D-bioprinted bone organoids.

5. Conclusion

Three-dimensional bioprinting represents a groundbreaking advancement in bone organoids, enabling precise fabrication of biomimetic constructs with tailored biological and mechanical properties. Through innovative bioink formulations and advanced printing techniques, researchers have achieved remarkable progress in replicating the hierarchical structure of bone. The integration of vascular networks via co-printing endothelial cells and the use of dynamic bioreactor systems has further enhanced organoid functionality, bringing us closer to clinically viable solutions for bone regeneration.

Despite these achievements, significant challenges remain. The limited scalability of current bioprinting methods hinders large-scale clinical application, while long-term stability issues related to immune response and scaffold degradation require further investigation. Additionally, fully recapitulating the complex interplay between bone, cartilage, and vascular tissues within a single construct remains technically demanding. Addressing these limitations will be crucial for translating laboratory successes into therapeutic realities.

Looking ahead, future research should prioritize the development of smart, stimuli-responsive bioinks capable of controlled growth factor release, as well as the incorporation of multi-omics data to optimize cellular composition. Combining 3D bioprinting with artificial intelligence-driven design and large-animal validation studies will accelerate progress toward personalized bone repair strategies. As this field evolves, the synergy between engineering innovation and biological insight promises to revolutionize regenerative medicine, offering new hope for patients with critical bone defects.

List of abbreviations

Abbreviation	Full term
3D	three-dimensional
BMP	bone morphogenetic protein
BMSCs	bone marrow mesenchymal stem cells
DLP	digital light processing
ECM	extracellular matrix
HAP	hydroxyapatite
hPDCs	human periosteum-derived cells
HUVECs	human umbilical vein endothelial cells
iPSCs	induced pluripotent stem cells
MVFs	microvascular fragments
SLA	stereolithography

Acknowledgments

Not applicable.

Funding

This publication is partially funded by the National Natural Science Foundation of China (Project Approval number: 82060394), Lanzhou University Undergraduate Education and Teaching Level Improvement Cultivation Project (Project number: lzuyxcx-2022-92), and Lanzhou Talent Innovation and Entrepreneurship Project (Project number: 2020-RC-45).

Conflict of interest

The authors declare no conflict of interest.

Author contributions

Conceptualization: Longfei Wu
Data curation: Jiwei Huang, Pengfei Huang Visualization: Junjie Zhao
Writing – original draft: Longfei Wu, Junjie Zhao
Writing – review & editing: Junjie Zhao, Haiyan Zhao

Ethics approval and consent to participate

Not applicable.

Consent for publication

Not applicable.

Availability of data

Not applicable.

Further disclosure

All four figures in the manuscript, including the graphical abstract, are original works independently created by the author team. The copyright of these figures belongs to all authors, and there is no copyright dispute.

References

1. Salhotra A, Shah HN, Levi B, Longaker MT. Mechanisms of bone development and repair. *Nat Rev Mol Cell Biol*. 2020;21(11):696-711. doi:10.1038/s41580-020-00279-w
2. Wang J, Chen X, Li R, et al. Standardization and consensus in the development and application of bone organoids. *Theranostics*. 2025;15(2):682-706. doi:10.7150/thno.105840
3. Chimene D, Miller L, Cross LM, Jaiswal MK, Singh I, Gaharwar AK. Nanoengineered osteoinductive bioink for 3D bioprinting bone tissue. *ACS Appl Mater Interfaces*. 2020;12(14):15976-15988. doi:10.1021/acsami.9b19037
4. Liu B, Li J, Lei X, et al. 3D-bioprinted functional and biomimetic hydrogel scaffolds incorporated with nanosilicates to promote bone healing in rat calvarial defect model. *Mater Sci Eng C Mater Biol Appl*. 2020;112:110905. doi:10.1016/j.msec.2020.110905
5. Ashammakhi N, Hasan A, Kaarela O, et al. Advancing frontiers in bone bioprinting. *Adv Healthc Mater*. 2019;8(7):e1801048. doi:10.1002/adhm.201801048
6. Byambaa B, Annabi N, Yue K, et al. Bioprinted osteogenic and vasculogenic patterns for engineering 3D bone tissue. *Adv Healthc Mater*. 2017;6(16):10.1002/adhm.201700015. doi:10.1002/adhm.201700015
7. Wang Z, Wang L, Li T, et al. 3D bioprinting in cardiac tissue engineering. *Theranostics*. 2021;11(16):7948-7969. doi:10.7150/thno.61621
8. Di Buduo CA, Lunghi M, Kuzmenko V, et al. Bioprinting soft 3D models of hematopoiesis using natural silk fibroin-based bioink efficiently supports platelet differentiation. *Adv Sci (Weinh)*. 2024;11(18):e2308276. doi:10.1002/advs.202308276
9. Zhang Y, Wang B, Hu J, et al. 3D composite bioprinting for fabrication of artificial biological tissues. *Int J Bioprint*. 2021;7(1):299. doi:10.18063/ijb.v7i1.299
10. Gungor-Ozkerim PS, Inci I, Zhang YS, Khademhosseini A, Dokmeci MR. Bioinks for 3D bioprinting: an overview. *Biomater Sci*. 2018;6(5):915-946. doi:10.1039/c7bm00765e
11. Ma W, Lu H, Xiao Y, Wu C. Advancing organoid development with 3D bioprinting. *OR*. 2025;1(1):025040004. doi:10.36922/or025040004
12. Song MJ, Quinn R, Nguyen E, et al. Bioprinted 3D outer retina barrier uncovers RPE-dependent choroidal phenotype in advanced macular degeneration. *Nat Methods*. 2023;20(1):149-161. doi:10.1038/s41592-022-01701-1
13. Göckler T, Haase S, Kempter X, et al. Tuning superfast curing thiol-norbornene-functionalized gelatin hydrogels for 3D bioprinting. *Adv Healthc Mater*. 2021;10(14):e2100206. doi:10.1002/adhm.202100206
14. Zhang YS, Arneri A, Bersini S, et al. Bioprinting 3D microfibrous scaffolds for engineering endothelialized myocardium and heart-on-a-chip. *Biomaterials*. 2016;110:45-59. doi:10.1016/j.biomaterials.2016.09.003
15. Li M, Gao L, Zhao L, Zou T, Xu H. Toward the next generation of vascularized human neural organoids. *Med Res Rev*. 2023;43(1):31-54. doi:10.1002/med.21922
16. Ning L, Gil CJ, Hwang B, et al. Biomechanical factors in three-dimensional tissue bioprinting. *Appl Phys Rev*. 2020;7(4):041319. doi:10.1063/5.0023206
17. Burdick JA, Chung C, Jia X, Randolph MA, Langer R. Controlled degradation and mechanical behavior of photopolymerized hyaluronic acid networks. *Biomacromolecules*. 2005;6(1):386-391. doi:10.1021/bm049508a
18. Bendtsen ST, Quinnell SP, Wei M. Development of a novel alginate-polyvinyl alcohol-hydroxyapatite hydrogel for 3D

bioprinting bone tissue engineered scaffolds. *J Biomed Mater Res A*. 2017;105(5):1457-1468. doi:10.1002/jbm.a.36036

19. Lian L, Zhou C, Tang G, et al. Uniaxial and coaxial vertical embedded extrusion bioprinting. *Adv Healthc Mater*. 2022;11(9):e2102411. doi:10.1002/adhm.202102411
20. Zeng X, Meng Z, He J, et al. Embedded bioprinting for designer 3D tissue constructs with complex structural organization. *Acta Biomater*. 2022;140:1-22. doi:10.1016/j.actbio.2021.11.048
21. Horváth L, Umehara Y, Jud C, Blank F, Petri-Fink A, Rothen-Rutishauser B. Engineering an in vitro air-blood barrier by 3D bioprinting. *Sci Rep*. 2015;5:7974. doi:10.1038/srep07974
22. Duraj-Thatte AM, Manjula-Basavanna A, Rutledge J, et al. Programmable microbial ink for 3D printing of living materials produced from genetically engineered protein nanofibers. *Nat Commun*. 2021;12(1):6600. doi:10.1038/s41467-021-26791-x
23. Liu X, Yuk H, Lin S, et al. 3D printing of living responsive materials and devices. *Adv Mater*. 2018;30(4):e1704821. doi:10.1002/adma.201704821
24. Naghieh S, Chen X. Printability-a key issue in extrusion-based bioprinting. *J Pharm Anal*. 2021;11(5):564-579. doi:10.1016/j.jpha.2021.02.001
25. Li X, Liu B, Pei B, et al. Inkjet bioprinting of biomaterials. *Chem Rev*. 2020;120(19):10793-10833. doi:10.1021/acs.chemrev.0c00008
26. Zhao L, Lee VK, Yoo SS, Dai G, Intes X. The integration of 3-D cell printing and mesoscopic fluorescence molecular tomography of vascular constructs within thick hydrogel scaffolds. *Biomaterials*. 2012;33(21):5325-5332. doi:10.1016/j.biomaterials.2012.04.004
27. Kim W, Lee Y, Kang D, Kwak T, Lee HR, Jung S. 3D inkjet-bioprinted lung-on-a-chip. *ACS Biomater Sci Eng*. 2023;9(5):2806-2815. doi:10.1021/acsbiomaterials.3c00089
28. Liu J, Shahriar M, Xu H, Xu C. Cell-laden bioink circulation-assisted inkjet-based bioprinting to mitigate cell sedimentation and aggregation. *Biofabrication*. 2022; 14(4):025007. doi:10.1088/1758-5090/ac8fb7
29. Zhang P, Wang H, Wang P, et al. Lightweight 3D bioprinting with point by point photocuring. *Bioact Mater*. 2021;6(5):1402-1412. doi:10.1016/j.bioactmat.2020.10.023
30. Zhu D, Zhu Y, Chen Y, et al. Three-dimensional covalent organic frameworks with pto and mhq-z topologies based on tri- and tetratopic linkers. *Nat Commun*. 2023;14(1):2865. doi:10.1038/s41467-023-38538-x
31. Lee GW, Chandrasekharan A, Roy S, et al. 3D bioprinting of stromal cells-laden artificial cornea based on visible light-crosslinkable bioinks forming multilength networks. *Biofabrication*. 2024;16(3):035002. doi:10.1088/1758-5090/ad35eb
32. Garciamendez-Mijares CE, Aguilar FJ, Hernandez P, et al. Design considerations for digital light processing bioprinters. *Appl Phys Rev*. 2024;11(3):031314. doi:10.1063/5.0187558
33. de Armentia SL, Fernández-Villamarín S, Ballesteros Y, Del Real JC, Dunne N, Paz E. 3D printing of a graphene-modified photopolymer using stereolithography for biomedical applications: a study of the polymerization reaction. *Int J Bioprint*. 2022;8(1):503. doi:10.18063/ijb.v8i1.503
34. Shi H, Li Y, Xu K, Yin J. Advantages of photo-curable collagen-based cell-laden bioinks compared to methacrylated gelatin (GelMA) in digital light processing (DLP) and extrusion bioprinting. *Mater Today Bio*. 2023;23:100799. doi:10.1016/j.mtbio.2023.100799
35. Tien J, Dance YW. Microfluidic biomaterials. *Adv Healthc Mater*. 2021;10(4):e2001028. doi:10.1002/adhm.202001028
36. Achille C, Parra-Cabrera C, Dochy R, et al. 3D printing of monolithic capillarity-driven microfluidic devices for diagnostics. *Adv Mater*. 2021;33(25):e2008712. doi:10.1002/adma.202008712
37. Xie R, Zheng W, Guan L, Ai Y, Liang Q. Engineering of hydrogel materials with perfusable microchannels for building vascularized tissues. *Small*. 2020;16(15):e1902838. doi:10.1002/smll.201902838
38. Ding X, Yu Y, Shang L, Zhao Y. Histidine-triggered GO hybrid hydrogels for microfluidic 3D printing. *ACS Nano*. 2022;16(11):19533-19542. doi:10.1021/acsnano.2c09850
39. Dai B, Zhang L, Zhao C, et al. Biomimetic apposition compound eye fabricated using microfluidic-assisted 3D printing. *Nat Commun*. 2021;12(1):6458. doi:10.1038/s41467-021-26606-z
40. Wang D, Maharjan S, Kuang X, et al. Microfluidic bioprinting of tough hydrogel-based vascular conduits for functional blood vessels. *Sci Adv*. 2022;8(43):eabq6900. doi:10.1126/sciadv.abq6900
41. Jiang S, Zhao H, Zhang W, et al. An automated organoid platform with inter-organoid homogeneity and inter-patient heterogeneity. *Cell Rep Med*. 2020;1(9):100161. doi:10.1016/j.xcrm.2020.100161
42. Tiwari AP, Thorat ND, Pricl S, Patil RM, Rohiwal S, Townley H. Bioink: a 3D-bioprinting tool for anticancer drug discovery and cancer management. *Drug Discov Today*. 2021;26(7):1574-1590. doi:10.1016/j.drudis.2021.03.010

43. Zhang H, Wang Y, Zheng Z, et al. Strategies for improving the 3D printability of decellularized extracellular matrix bioink. *Theranostics*. 2023;13(8):2562-2587. doi:10.7150/thno.81785

44. Liu Q, Yang J, Wang Y, et al. Direct 3D bioprinting of tough and antifatigue cell-laden constructs enabled by a self-healing hydrogel bioink. *Biomacromolecules*. 2023;24(6):2549-2562. doi:10.1021/acs.biomac.3c00057

45. Cheng QP, Hsu SH. A self-healing hydrogel and injectable cryogel of gelatin methacryloyl-polyurethane double network for 3D printing. *Acta Biomater*. 2023;164:124-138. doi:10.1016/j.actbio.2023.04.023

46. Muthukrishnan L. Imminent antimicrobial bioink deploying cellulose, alginate, EPS and synthetic polymers for 3D bioprinting of tissue constructs. *Carbohydr Polym*. 2021;260:117774. doi:10.1016/j.carbpol.2021.117774

47. Antich C, de Vicente J, Jiménez G, et al. Bio-inspired hydrogel composed of hyaluronic acid and alginate as a potential bioink for 3D bioprinting of articular cartilage engineering constructs. *Acta Biomater*. 2020;106:114-123. doi:10.1016/j.actbio.2020.01.046

48. Hafeez S, Aldana AA, Duimel H, et al. Molecular tuning of a benzene-1,3,5-tricarboxamide supramolecular fibrous hydrogel enables control over viscoelasticity and creates tunable ECM-mimetic hydrogels and bioinks. *Adv Mater*. 2023;35(24):e2207053. doi:10.1002/adma.202207053

49. Zhou X, Yu X, You T, et al. 3D printing-based hydrogel dressings for wound healing. *Adv Sci (Weinh)*. 2024;11(47):e2404580. doi:10.1002/advs.202404580

50. Shah M, Maroof A, Gikas P, et al. Dual neutralisation of IL-17F and IL-17A with bimekizumab blocks inflammation-driven osteogenic differentiation of human periosteal cells. *RMD Open*. 2020;6(2):e001306. doi:10.1136/rmdopen-2020-001306

51. Wang J, Wu Y, Li G, et al. Engineering large-scale self-mineralizing bone organoids with bone matrix-inspired hydroxyapatite hybrid bioinks. *Adv Mater*. 2024;36(30):e2309875. doi:10.1002/adma.202309875

52. Sanchez AA, Teixeira FC, Casademunt P, Beeren I, Moroni L, Mota C. Enhanced osteogenic differentiation in hyaluronic acid methacrylate (HAMA) matrix: a comparative study of hPDC and hBMSC spheroids for bone tissue engineering. *Biofabrication*. 2025;17(2):025013. doi:10.1088/1758-5090/adb2e6

53. Hall GN, Fan Y, Viellerobe B, et al. Laser-assisted bioprinting of targeted cartilaginous spheroids for high density bottom-up tissue engineering. *Biofabrication*. 2024;16(4):045029. doi:10.1088/1758-5090/ad6e1a

54. Saravanou SF, Ioannidis K, Dimopoulos A, et al. Dually crosslinked injectable alginate-based graft copolymer thermoresponsive hydrogels as 3D printing bioinks for cell spheroid growth and release. *Carbohydr Polym*. 2023;312:120790. doi:10.1016/j.carbpol.2023.120790

55. Wang F, Qian H, Kong L, et al. Accelerated bone regeneration by astragaloside IV through stimulating the coupling of osteogenesis and angiogenesis. *Int J Biol Sci*. 2021;17(7):1821-1836. doi:10.7150/ijbs.57681

56. Mao L, Xia L, Chang J, et al. The synergistic effects of Sr and Si bioactive ions on osteogenesis, osteoclastogenesis and angiogenesis for osteoporotic bone regeneration. *Acta Biomater*. 2017;61:217-232. doi:10.1016/j.actbio.2017.08.015

57. Bai CW, Tian B, Zhang MC, et al. Targeting NAMPT-OPA1 for treatment of senile osteoporosis. *Aging Cell*. 2025;24(3):e14400. doi:10.1111/acel.14400

58. Guo Y, Chi X, Wang Y, et al. Mitochondria transfer enhances proliferation, migration, and osteogenic differentiation of bone marrow mesenchymal stem cell and promotes bone defect healing. *Stem Cell Res Ther*. 2020;11(1):245. doi:10.1186/s13287-020-01704-9

59. Cui Y, Guo Y, Kong L, et al. A bone-targeted engineered exosome platform delivering siRNA to treat osteoporosis. *Bioact Mater*. 2022;10:207-221. doi:10.1016/j.bioactmat.2021.09.015

60. Lamandé SR, Ng ES, Cameron TL, et al. Modeling human skeletal development using human pluripotent stem cells. *Proc Natl Acad Sci U S A*. 2023;120(19):e2211510120. doi:10.1073/pnas.2211510120

61. Okano H, Morimoto S. iPSC-based disease modeling and drug discovery in cardinal neurodegenerative disorders. *Cell Stem Cell*. 2022;29(2):189-208. doi:10.1016/j.stem.2022.01.007

62. Nguyen VT, Canciani B, Cirillo F, Anastasia L, Peretti GM, Mangiavini L. Effect of chemically induced hypoxia on osteogenic and angiogenic differentiation of bone marrow mesenchymal stem cells and human umbilical vein endothelial cells in direct coculture. *Cells*. 2020; 9(3):757. doi:10.3390/cells9030757

63. Quintard C, Tubbs E, Jonsson G, et al. A microfluidic platform integrating functional vascularized organoids-on-chip. *Nat Commun*. 2024;15(1):1452. doi: 10.1038/s41467-024-45710-4

64. Homan KA, Gupta N, Kroll KT, et al. Flow-enhanced vascularization and maturation of kidney organoids in vitro. *Nat Methods*. 2019;16(3):255-262. doi: 10.1038/s41592-019-0325-y

65. Yoon SJ, Kim SH, Choi JW, Chun HJ, Yang DH. Guided cortical and cancellous bone formation using a minimally invasive technique of BMSC- and BMP-2-laden visible light-cured carboxymethyl chitosan hydrogels. *Int J Biol Macromol*. 2023;227:641-653. doi:10.1016/j.ijbiomac.2022.12.137

66. Wang J, Zhu Q, Cao D, et al. Bone marrow-derived IGF-1 orchestrates maintenance and regeneration of the adult skeleton. *Proc Natl Acad Sci U S A*. 2023;120(1):e2203779120. doi:10.1073/pnas.2203779120

67. Koffi KA, Doublier S, Ricort JM, Babajko S, Nassif A, Isaac J. The role of GH/IGF axis in dento-alveolar complex from development to aging and therapeutics: a narrative review. *Cells*. 2021;10(5):1181. doi:10.3390/cells10051181

68. Song IW, Nagamani SC, Nguyen D, et al. Targeting TGF-β for treatment of osteogenesis imperfecta. *J Clin Invest*. 2022;132(7):e152571. doi:10.1172/jci152571

69. Fitzpatrick V, Martín-Moldes Z, Deck A, et al. Functionalized 3D-printed silk-hydroxyapatite scaffolds for enhanced bone regeneration with innervation and vascularization. *Biomaterials*. 2021;276:120995. doi:10.1016/j.biomaterials.2021.120995

70. He Q, Yang J, Pan Z, et al. Biochanin A protects against iron overload associated knee osteoarthritis via regulating iron levels and NRF2/System xc-/GPX4 axis. *Biomed Pharmacother*. 2023;157:113915. doi:10.1016/j.biopha.2022.113915

71. Mohanakrishnan V, Sivaraj KK, Jeong HW, et al. Specialized post-arterial capillaries facilitate adult bone remodelling. *Nat Cell Biol*. 2024;26(12):2020-2034. doi:10.1038/s41556-024-01545-1

72. Park Y, Cheong E, Kwak JG, Carpenter R, Shim JH, Lee J. Trabecular bone organoid model for studying the regulation of localized bone remodeling. *Sci Adv*. 2021;7(4): eabd6495. doi:10.1126/sciadv.abd6495

73. Bai L, Song P, Su J. Bioactive elements manipulate bone regeneration. *Biomater Transl*. 2023;4(4):248-269. doi:10.12336/biomatertransl.2023.04.005

74. Yao Y, Wei G, Deng L, Cui W. Visualizable and lubricating hydrogel microspheres via NanoPOSS for cartilage regeneration. *Adv Sci (Weinh)*. 2023;10(15):e2207438. doi:10.1002/advs.202207438

75. Shen C, Wang J, Li G, et al. Boosting cartilage repair with silk fibroin-DNA hydrogel-based cartilage organoid precursor. *Bioact Mater*. 2024;35:429-444. doi:10.1016/j.bioactmat.2024.02.016

76. Dönges L, Damle A, Mainardi A, et al. Engineered human osteoarthritic cartilage organoids. *Biomaterials*. 2024;308:122549. doi:10.1016/j.biomaterials.2024.122549

77. Wang XH, Liu N, Zhang H, Yin ZS, Zha ZG. From cells to organs: progress and potential in cartilaginous organoids research. *J Transl Med*. 2023;21(1):926. doi:10.1186/s12967-023-04591-9

78. Zhang L, Tang H, Xiahou Z, et al. Solid multifunctional granular bioink for constructing chondroid basing on stem cell spheroids and chondrocytes. *Biofabrication*. 2022;14(3):035003. doi:10.1088/1758-5090/ac63ee

79. Wang M, Li W, Mille LS, et al. Digital light processing based bioprinting with composable gradients. *Adv Mater*. 2022;34(1):e2107038. doi:10.1002/adma.202107038

80. Comazzetto S, Shen B, Morrison SJ. Niches that regulate stem cells and hematopoiesis in adult bone marrow. *Dev Cell*. 2021;56(13):1848-1860. doi:10.1016/j.devcel.2021.05.018

81. Frenz-Wiessner S, Fairley SD, Buser M, et al. Generation of complex bone marrow organoids from human induced pluripotent stem cells. *Nat Methods*. 2024;21(5):868-881. doi:10.1038/s41592-024-02172-2

82. Xie C, Liang R, Ye J, et al. High-efficient engineering of osteo-callus organoids for rapid bone regeneration within one month. *Biomaterials*. 2022;288:121741. doi:10.1016/j.biomaterials.2022.121741

83. Chae S, Lee SS, Choi YJ, et al. 3D cell-printing of biocompatible and functional meniscus constructs using meniscus-derived bioink. *Biomaterials*. 2021;267:120466. doi:10.1016/j.biomaterials.2020.120466

84. Zhao T, Liu Y, Wu Y, Zhao M, Zhao Y. Controllable and biocompatible 3D bioprinting technology for microorganisms: fundamental, environmental applications and challenges. *Biotechnol Adv*. 2023;69:108243. doi:10.1016/j.biotechadv.2023.108243

85. He H, Li D, Lin Z, et al. Temperature-programmable and enzymatically solidifiable gelatin-based bioinks enable facile extrusion bioprinting. *Biofabrication*. 2020;12(4):045003. doi:10.1088/1758-5090/ab9906

86. Yu GT, Zhu WX, Zhao YY, et al. 3D-printed bioink loading with stem cells and cellular vesicles for periodontitis-derived bone defect repair. *Biofabrication*. 2024;16(2):025007. doi:10.1088/1758-5090/ad2081

87. Schwab A, Levato R, D'Este M, Piluso S, Eglin D, Malda J. Printability and shape fidelity of bioinks in 3D bioprinting. *Chem Rev*. 2020;120(19):11028-11055. doi:10.1021/acs.chemrev.0c00084

88. Li J, Moeinzadeh S, Kim C, et al. Development and systematic characterization of GelMA/alginate/PEGDMA/xanthan gum hydrogel bioink system for extrusion bioprinting. *Biomaterials*. 2023;293:121969. doi:10.1016/j.biomaterials.2022.121969

89. Hu T, Cui X, Zhu M, et al. 3D-printable supramolecular hydrogels with shear-thinning property: fabricating strength tunable bioink via dual crosslinking. *Bioact Mater*. 2020;5(4):808-818. doi:10.1016/j.bioactmat.2020.06.001

90. Gillispie GJ, Copus J, Uzun-Per M, et al. The correlation between rheological properties and extrusion-based printability in bioink artifact quantification. *Mater Des*. 2023;233:112237. doi:10.1016/j.matdes.2023.112237

91. Garcia-Cruz MR, Postma A, Frith JE, Meagher L. Printability and bio-functionality of a shear thinning methacrylated xanthan-gelatin composite bioink. *Biofabrication*. 2021;13(3):035023. doi:10.1088/1758-5090/abec2d

92. De Moor L, Smet J, Plovyt M, et al. Engineering microvasculature by 3D bioprinting of prevascularized spheroids in photo-crosslinkable gelatin. *Biofabrication*. 2021;13(4):045021. doi:10.1088/1758-5090/ac24de

93. Kang SW, Mueller J. Multiscale 3D printing via active nozzle size and shape control. *Sci Adv*. 2024;10(23):eadn7772. doi:10.1126/sciadv.adn7772

94. Kilian D, Holtzhausen S, Groh W, et al. 3D extrusion printing of density gradients by variation of sinusoidal printing paths for tissue engineering and beyond. *Acta Biomater*. 2023;158:308-323. doi:10.1016/j.actbio.2022.12.038

95. Farsheed AC, Thomas AJ, Pogostin BH, Hartgerink JD. 3D printing of self-assembling nanofibrous multidomain peptide hydrogels. *Adv Mater*. 2023;35(11):e2210378. doi:10.1002/adma.202210378

96. Niu R, Xin Q, Xu E, Yao S, Chen M, Liu D. Nanostarch-stimulated cell adhesion in 3D bioprinted hydrogel scaffolds for cell cultured meat. *ACS Appl Mater Interfaces*. 2024;16(18):23015-23026. doi:10.1021/acsami.4c03585

97. Huang Y, Zhang Z, Bi F, et al. Personalized 3D-printed scaffolds with multiple bioactivities for bioroot regeneration. *Adv Healthc Mater*. 2023;12(28):e2300625. doi:10.1002/adhm.202300625

98. Liang Q, Ma Y, Yao X, Wei W. Advanced 3D-printing bioinks for articular cartilage repair. *Int J Bioprint*. 2022; 8(3):511. doi:10.18063/ijb.v8i3.511

99. Lian L, Xie M, Luo Z, et al. Rapid volumetric bioprinting of decellularized extracellular matrix bioinks. *Adv Mater*. 2024;36(34):e2304846. doi:10.1002/adma.202304846

100. Mao J, Sun J, Wang L, Liu X, Bi J. Flexible and high-strength bioactive glass fiber membrane for bone regeneration with the aid of alkoxysilane sol spinnability. *Mater Today Bio*. 2024;28:101224. doi:10.1016/j.mtbio.2024.101224

101. Zhao D, Saiding Q, Li Y, Tang Y, Cui W. Bone organoids: recent advances and future challenges. *Adv Healthc Mater*. 2024;13(5):e2302088. doi:10.1002/adhm.202302088

102. Ding Z, Yan Z, Yuan X, et al. Apoptotic extracellular vesicles derived from hypoxia-preconditioned mesenchymal stem cells within a modified gelatine hydrogel promote osteochondral regeneration by enhancing stem cell activity and regulating immunity. *J Nanobiotechnology*. 2024;22(1):74. doi:10.1186/s12951-024-02333-7

103. Wu X, Hu Y, Sheng S, et al. DNA-based hydrogels for bone regeneration: a promising tool for bone organoids. *Mater Today Bio*. 2025;31:101502. doi:10.1016/j.mtbio.2025.101502

104. Liu X, Zhang Q, Cao Y, et al. An injectable hydrogel composing anti-inflammatory and osteogenic therapy toward bone erosions microenvironment remodeling in rheumatoid arthritis. *Adv Healthc Mater*. 2024;13(22):e2304668. doi:10.1002/adhm.202304668

105. Kim JH, Kim K, Kim I, Seong S, Koh JT, Kim N. Stanniocalcin 1 and 1,25-dihydroxyvitamin D(3) cooperatively regulate bone mineralization by osteoblasts. *Exp Mol Med*. 2024;56(9):1991-2001. doi:10.1038/s12276-024-01302-2

106. Osi AR, Zhang H, Chen J, et al. Three-dimensional-printable thermo/photo-cross-linked methacrylated chitosan-gelatin hydrogel composites for tissue engineering. *ACS Appl Mater Interfaces*. 2021;13(19):22902-22913. doi:10.1021/acsami.1c01321

107. Batoon L, Koh AJ, Millard SM, et al. Induction of osteoblast apoptosis stimulates macrophage efferocytosis and paradoxical bone formation. *Bone Res*. 2024;12(1):43. doi:10.1038/s41413-024-00341-9

108. Wang L, You X, Zhang L, Zhang C, Zou W. Mechanical regulation of bone remodeling. *Bone Res*. 2022; 10(1):16. doi:10.1038/s41413-022-00190-4

109. Iordachescu A, Hughes EAB, Joseph S, Hill EJ, Grover LM, Metcalfe AD. Trabecular bone organoids: a micron-scale 'humanised' prototype designed to study the effects of microgravity and degeneration. *NPJ Microgravity*. 2021;7(1):17. doi:10.1038/s41526-021-00146-8

110. Ju Y, Hu Y, Yang P, Xie X, Fang B. Extracellular vesicle-loaded hydrogels for tissue repair and regeneration. *Mater Today Bio*. 2023;18:100522. doi:10.1016/j.mtbio.2022.100522

111. Laschke MW, Später T, Menger MD. Microvascular fragments: more than just natural vascularization units. *Trends Biotechnol*. 2021;39(1):24-33. doi:10.1016/j.tibtech.2020.06.001

112. Li Z, Wang H, Li K, et al. Combining "waste utilization" and "tissue to tissue" strategies to accelerate vascularization for bone repair. *J Orthop Translat*. 2024;47:132-143. doi:10.1016/j.jot.2024.04.002

113. Candiello J, Grandhi TSP, Goh SK, et al. 3D heterogeneous islet organoid generation from human embryonic stem cells using a novel engineered hydrogel platform. *Biomaterials*. 2018;177:27-39. doi:10.1016/j.biomaterials.2018.05.031

114. Gao Q, Wang J, Zhang H, Wang J, Jing Y, Su J. Organoid vascularization: strategies and applications. *Adv Healthc Mater*. 2025;14(20):e2500301. doi:10.1002/adhm.202500301

115. Li C, An N, Song Q, et al. Enhancing organoid culture: harnessing the potential of decellularized extracellular matrix hydrogels for mimicking microenvironments. *J Biomed Sci*. 2024;31(1):96. doi:10.1186/s12929-024-01086-7

116. Zhang J, Griesbach J, Ganeyev M, et al. Long-term mechanical loading is required for the formation of 3D bioprinted functional osteocyte bone organoids. *Biofabrication*. 2022;14(3):035018. doi:10.1088/1758-5090/ac73b9

117. Dong B, Hiasa M, Higa Y, et al. Osteoblast/osteocyte-derived interleukin-11 regulates osteogenesis and systemic adipogenesis. *Nat Commun*. 2022;13(1):7194. doi:10.1038/s41467-022-34869-3

118. Yang B, Li Z, Yang Z, et al. Recapitulating hypoxic metabolism in cartilaginous organoids via adaptive cell-matrix interactions enhances histone lactylation and cartilage regeneration. *Nat Commun*. 2025;16(1):2711. doi:10.1038/s41467-025-57779-6

119. Hossain Rakin R, Kumar H, Rajeev A, et al. Tunable metacrylated hyaluronic acid-based hybrid bioinks for stereolithography 3D bioprinting. *Biofabrication*. 2021;13(4):044109. doi:10.1088/1758-5090/ac25cb

120. Wang Z, Wang Y, Yan J, et al. Pharmaceutical electrospinning and 3D printing scaffold design for bone regeneration. *Adv Drug Deliv Rev*. 2021;174:504-534. doi:10.1016/j.addr.2021.05.007

121. Rouwkema J, Rivron NC, van Blitterswijk CA. Vascularization in tissue engineering. *Trends Biotechnol*. 2008;26(8):434-41. doi:10.1016/j.tibtech.2008.04.009

122. Fang Y, Guo Y, Wu B, et al. Expanding embedded 3D bioprinting capability for engineering complex organs with freeform vascular networks. *Adv Mater*. 2023;35(22):e2205082. doi:10.1002/adma.202205082

123. Zhao M, Wang S, Zuo A, et al. HIF-1α/JMJD1A signaling regulates inflammation and oxidative stress following hyperglycemia and hypoxia-induced vascular cell injury. *Cell Mol Biol Lett*. 2021;26(1):40. doi:10.1186/s11658-021-00283-8

124. Zhai Y, Schilling K, Wang T, et al. Spatiotemporal blood vessel specification at the osteogenesis and angiogenesis interface of biomimetic nanofiber-enabled bone tissue engineering. *Biomaterials*. 2021;276:121041. doi:10.1016/j.biomaterials.2021.121041

125. Chandel S, Kumaragurubaran R, Giri H, Dixit M. Isolation and culture of human umbilical vein endothelial cells (HUVECs). *Methods Mol Biol*. 2024;2711:147-162. doi:10.1007/978-1-0716-3429-5_12

126. Ostrovidov S, Salehi S, Costantini M, et al. 3D bioprinting in skeletal muscle tissue engineering. *Small*. 2019;15(24):e1805530. doi:10.1002/smll.201805530

127. Li Y, Cheng S, Wen H, et al. Coaxial 3D printing of hierarchical structured hydrogel scaffolds for on-demand repair of spinal cord injury. *Acta Biomater*. 2023;168:400-415. doi:10.1016/j.actbio.2023.07.020

ACCSCIENCE PUBLISHING

International Journal of Bioprinting

REVIEW ARTICLE

Advances in decellularized extracellular matrix bioinks for regenerative medicine applications

Jugal Kishore Bupesh Raja[1,2], Giselle Y. Díaz[3], Fynn S. Owen La Boucan[4], Madeleine A. Perry[3], Sravya Tekumalla[3,5]*, Tharaka Srinatha Dunuwilla[6], Venkatagiri Krishnamoorthy Bupesh Raja[7], and Stephanie M. Willerth[3,5,7,8,9,10]*

[1]Faculty of Medicine, Georgian National University SEU, Tbilisi, Georgia.

[2]Laboratory of Neuron Ultrastructure and Nanoarchitecture, Ivane Beritashvili Center of Experimental Biomedicine, Tbilisi, Georgia

[3]Department of Mechanical Engineering, Faculty of Engineering and Computer Science, University of Victoria, Victoria, British Columbia, Canada

[4]Department of Biology, Faculty of Science, University of Victoria, Victoria, British Columbia, Canada

[5]Center for Advanced Materials and Technology, University of Victoria, Victoria, British Columbia, Canada

[6]Department of Medicine, International Medical School, Alte University, Tbilisi, Georgia

[7]Department of Automobile Engineering, School of Mechanical, Sathyabama Institute of Science and Technology, Chennai, Tamil Nadu, India

[8]Division of Medical Sciences, University of Victoria, Victoria, British Columbia, Canada

[9]Axolotl Biosciences, Victoria, British Columbia, Canada

[10]School of Biomedical Engineering, Faculty of Applied Science, University of British Columbia, Vancouver, British Columbia, Canada

(This article belongs to the *Special Issue: Advances in 3D Bioprinting*)

***Corresponding authors:**
Stephanie M. Willerth (willerth@uvic.ca)

Sravya Tekumalla (stekumalla@uvic.ca)

Citation: Raja JKB, Díaz GY, Owen La Boucan FS, *et al.* Advances in decellularized extracellular matrix bioinks for regenerative medicine applications. *Int J Bioprint.* 2025;11(5):23-45. doi: 10.36922/IJB025210205

Received: May 20, 2025
Revised: June 25, 2025
Accepted: July 7, 2025
Published Online: July 9, 2025

Copyright: © 2025 Author(s). This is an Open Access article distributed under the terms of the Creative Commons Attribution License, permitting distribution, and reproduction in any medium, provided the original work is properly cited.

Publisher's Note: AccScience Publishing remains neutral with regard to jurisdictional claims in published maps and institutional affiliations.

Abstract

Organ transplantation serves as a critical life-saving intervention. However, the persistent global shortage of donor organs continues to result in high mortality rates. This pressing clinical challenge has fueled the search for alternative therapeutic strategies. Among these strategies, three-dimensional (3D) bioprinting has emerged as a transformative technology capable of fabricating complex tissue constructs using bioinks composed of living cells and supportive biomaterials. Notably, recent advancements have highlighted the incorporation of decellularized extracellular matrix (dECM) as a bioactive component, significantly enhancing biocompatibility, structural integrity, cellular support, and the formation and maturation of vascular networks. In this review, we detail the pivotal role of the ECM as a dynamic reservoir of biochemical signals and mechanical cues that regulate cellular behavior through mechanotransduction. These processes guide essential functions including gene expression, tissue development, and remodeling, thereby ensuring tissue-specific mechanical properties such as elasticity and tensile strength. We highlight how dECM-based bioinks can retain the native structural and molecular features of the ECM, making them ideal for replicating physiologically relevant microenvironments. Representative studies demonstrate the successful application of dECM bioinks in engineering complex *in vitro* 3D tissue models. Furthermore, we address current challenges in tissue engineering, including the standardization of bioink formulations, the refinement of decellularization techniques, and the enhancement of the mechanical and architectural properties of scaffolds. Finally, we explore emerging solutions—such as artificial intelligence-guided optimization, *in situ* bioprinting, and

the development of patient-specific bioinks—as promising avenues to overcome current limitations and drive the clinical translation of 3D-bioprinted tissues.

Keywords: Decellularized extracellular matrix; Decellularized extracellular matrix-based bioinks; Regenerative medicine; Three-dimensional bioprinting; Tissue regeneration; Vascularization

1. Introduction

Organ transplantation has become a definitive treatment for end-stage organ or tissue failure,[1] significantly improving patients' quality of life and preventing death.[2] However, access to transplantation remains a major challenge.[3] In 2022, approximately 3777 individuals in Canada were on the transplant waiting list, while in the United States, this number exceeded 103,000 by 2024.[4,5] Each year, hundreds of patients die while waiting for an organ to become available.[6] Consequently, there is an urgent need to explore new avenues to address this critical supply issue.

Three-dimensional (3D) bioprinting is an emergent technology capable of replacing or restoring dysfunctional tissues and organs, and represents a key advancement in the field of regenerative medicine.[7,8] In cases of organ failure, regenerative medicine aims to restore healthy bodily function by implanting tissues that have been engineered through 3D bioprinting in the laboratory.[9] This technique can reduce the risk of organ rejection[10] by using patient-derived induced pluripotent stem cells (iPSCs) for tissue engineering.[11,12] Since its development, regenerative medicine has emerged as a promising field for treating organ failure[9] and addressing other medical challenges, including the development of disease models for drug testing[13,14] and the treatment for autoimmune disorders,[15] such as type 1 diabetes,[16] Crohn's disease,[17] and rheumatoid arthritis.[18,19]

The technique of 3D bioprinting fabricates tissue constructs through the layer-by-layer deposition of cells within printable biomaterials.[20] These printable biological materials, termed "bioinks," consist of cell formulations compatible with automated biofabrication systems. Bioinks may incorporate biologically active components and supportive biomaterials, providing essential properties including structural support, controlled biodegradability, biocompatibility, and minimal immunogenicity.[21,22]

Researchers are currently developing novel bioinks by incorporating biological components such as decellularized extracellular matrices (dECM) to better recapitulate native tissue characteristics. The decellularization process removes cellular components from native tissues while preserving the ECM-rich non-immunogenic scaffold architecture. Depending on the specific decellularization method used, these scaffolds can retain natural vascular templates along with biological cues that support cell differentiation. Additionally, these mixtures could maintain native tissue architecture, including critical mechanical properties such as strength and stiffness, while simultaneously promoting vasculogenesis during the reseeding process.[23] The biological compatibility between seeded cells and the ECM scaffold remains paramount, as it directly enables the cellular adhesion, proliferation, and migration necessary for forming a functional endothelial lining along vascular structures.[24]

Thus, dECM-derived materials represent a promising strategy for optimizing bioink formulations and producing more physiologically relevant scaffolds.[25] These advanced scaffolds simultaneously enhance key biophysical properties, including stiffness and viscoelasticity, to better match native tissue mechanics, while preserving crucial biochemical components that support tissue growth, functionality, and regeneration. Importantly, most dECM preparations naturally contain angiogenic factors that actively promote vascularization following transplantation.[26] This review explores the use of dECM materials to enhance bioink formulations in combination with various 3D bioprinting techniques. Additionally, it examines how dECM scaffolds can create an optimal microenvironment to promote vascularization and enable functional tissue regeneration.

2. Three-dimensional bioprinting techniques for vascularized scaffolds

The application of cutting-edge material design and precise manufacturing processes can create vascularized structures for tissue engineering. The process of vascularization is vital for the survival of tissues, as it enables the transportation of oxygen, nutrients, and waste products. However, replicating the intricate shape and layered structure of natural vascular systems remains challenging. To address this issue, several 3D printing methods have been used to make structures with chosen structure details, clarity, and material mix (Figure 1). These techniques include extrusion-based

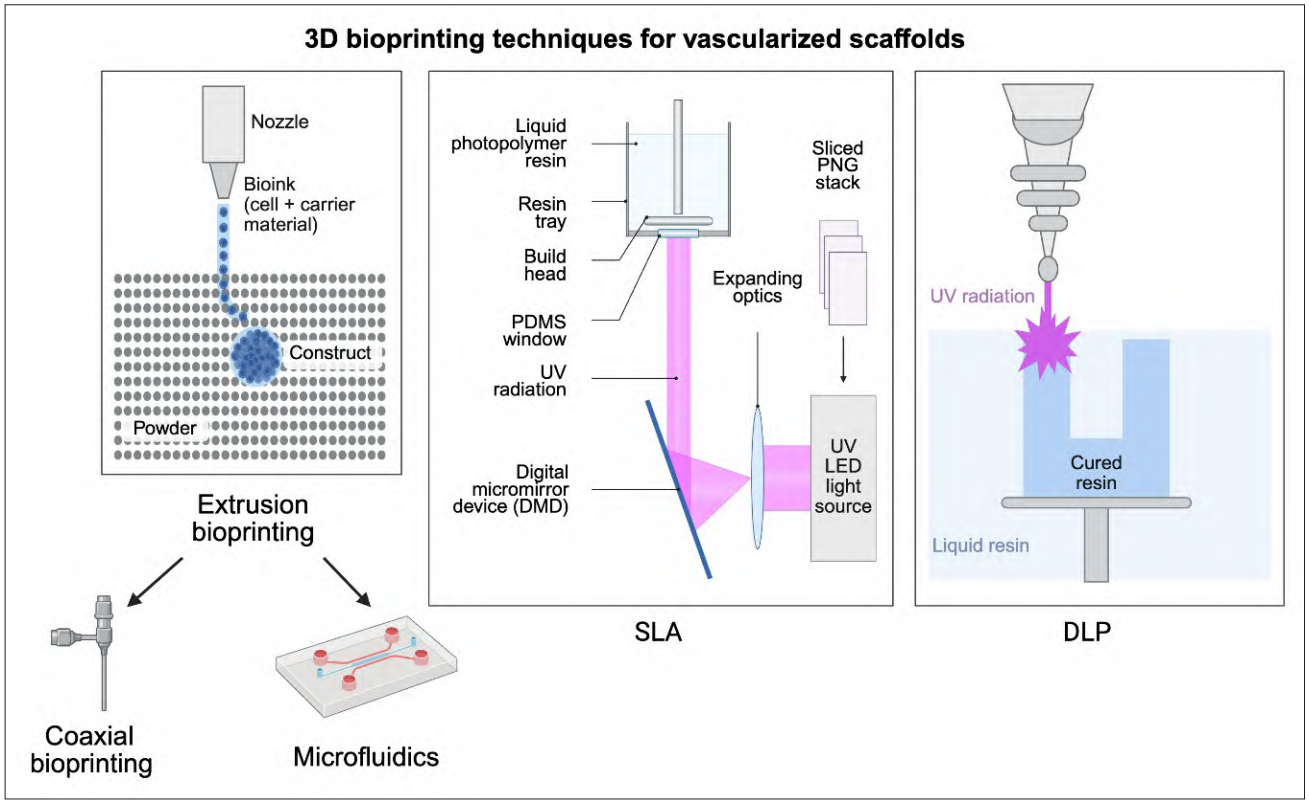


Figure 1. Overview of 3D bioprinting techniques for fabricating vascularized scaffolds. This schematic illustrates key bioprinting modalities. Extrusion-based bioprinting enables layer-by-layer deposition of cell-laden bioinks into sacrificial or coaxial geometries for vascular channel formation. DLP and SLA employ photopolymerization of light-sensitive resins using projected or scanned UV light for high-resolution fabrication of complex vascular structures. Created in BioRender. Willerth, S. (2025). https://BioRender.com/27bauwd. Abbreviations: 3D, three-dimensional; DLP, digital light processing; LED, light-emitting diode; PDMS, polydimethylsiloxane; SLA, stereolithography; UV, ultraviolet.

printing, stereolithography (SLA), digital light processing (DLP), coaxial printing, sacrificial printing, microfluidic printing, and multi-material ways (Table 1). By integrating dECM bioinks into each of these techniques, their biological significance can be improved. dECM provides native biochemical and mechanical signals that stimulate the development of new blood vessels and promote tissue regeneration. By combining these bioprinting techniques with bioactive bioinks, it becomes feasible to create vascularized constructs that closely resemble the intricate structure and functionality of natural tissues.

Sections 2.1–2.4 describe each 3D bioprinting technique in more detail, along with their advantages and limitations. Comparisons between techniques are summarized in Table 1, including defining quantitative parameters such as resolution, cell viability, tolerance, and throughput. **Section 2.5** provides a brief overview of new and emerging 3D bioprinting techniques.

2.1. Extrusion-based bioprinting

Extrusion-based bioprinting, a frequently employed technique for tissue engineering, is able to handle diverse biomaterials, including high-viscosity hydrogels, bioinks with cells, and composite materials.[29] This technique delivers bioink through a nozzle, driven by pneumatic, mechanical, or piston-powered pressure. It enables an accurate and step-by-step creation of complex 3D structures. Its compatibility with dECM bioinks—which are derived from tissues like adipose, cartilage, and cardiac tissues—makes it particularly appealing for creating vascularized tissue constructs. dECM bioinks provide specific biochemical signals and support cell differentiation, while their adaptable rheological properties allow precise printing of cells with compatibility and accuracy.[39,40] Notably, extrusion-based bioprinting has been employed to successfully create vascularized adipose and cardiac patches, aiding in the organization of endothelial cells and the formation of tubules.[40]

While extrusion-based bioprinting provides scalability and versatility, it faces challenges in terms of resolution, affecting the precise alignment of fibers and the ability to control microarchitecture for the creation of vascular networks.[41] Furthermore, shear stress during extrusion can

Table 1. A comprehensive overview of three-dimensional bioprinting techniques using decellularized extracellular matrix bioinks in regenerative medicine

Bioprinting technique	Advantages	Limitations	Typical applications	Quantitative parameters	References
Extrusion-based bioprinting	Widely used due to its simplicity, cost-effectiveness, and ability to print high-viscosity bioinks, including decellularized extracellular matrix. It supports the creation of large, cell-laden constructs with good mechanical properties	Lower resolution; shear stress during the printing process negatively affects cells	Commonly used for fabricating bone, cartilage, and skin tissues. It is particularly effective in creating vascularized structures when combined with coaxial bioprinting	Resolution: ~50–200 μm; cell viability: 40–80%; shear tolerance: low; throughput: medium (slow filament deposition)	[27–30]
Inkjet bioprinting	Offers high resolution and speed, suitable for low-viscosity bioinks. It allows precise placement of cells and bioactive molecules	Limited to low-viscosity bioinks; has the potential for nozzle clogging	Ideal for creating skin and cartilage tissues, and for applications requiring high cell viability and precise patterning, such as drug testing models	Resolution: ~20–100 μm; cell viability: ~90%; shear tolerance: low/moderate; throughput: high (up to ~10,000 droplets/s)	[28,31–33]
Laser-assisted bioprinting	Provides high resolution and cell viability, as it minimizes mechanical stress on cells. It is suitable for printing complex structures with high precision	Expensive equipment; potential thermal damage to cells	Used in skin tissue engineering and for creating intricate vascular networks, as well as in applications requiring high precision, such as neural tissue engineering	Resolution: ~20 μm or better; cell viability: >95%; shear tolerance: high; throughput: Medium (droplet-by-droplet)	[28,31–33]
Digital light processing and stereolithography	·Both techniques use light to cure photosensitive bioinks, offering high resolution and smooth surface finishes. They are suitable for creating complex geometries	Potential ultraviolet damage to cells; limited to photopolymerizable bioinks; potential cytotoxicity from photoinitiators	Effective in fabricating bone and dental tissues, where precision and surface quality are critical	Resolution: ~1–200 μm (often tens of μm); cell viability: >90%; shear tolerance: high; throughput: high (fast layer-by-layer)	[28,34,35]
Coaxial bioprinting	A subtype of extrusion-based bioprinting, it allows the creation of hollow structures and vascular networks by printing concentric layers of bioinks	Complex setup; limited to specific bioink combinations	Particularly useful for vascular tissue engineering and creating constructs with integrated vascular channels	Resolution: ~200 μm (core–shell fiber diameter); cell viability: ~80–90%; shear tolerance: moderate; throughput: medium	[36,37]
Sacrificial bioprinting	Involves printing a sacrificial material that is later removed to create hollow structures or channels. It is useful for creating complex internal geometries	Additional steps for material removal; potential structural instability post-removal	Used in creating vascularized tissues and complex organ models, such as liver and kidney constructs	Resolution: ~400–550 μm (hollow-channel diameter); cell viability: ~80–90%; shear tolerance: moderate; throughput: medium	[34,35,38]
Microfluidic bioprinting	·Allows precise control over the microenvironment and cell distribution, enabling the creation of highly detailed tissue constructs	Complex device fabrication; limited scalability	Suitable for creating organ-on-a-chip models and for applications requiring precise control over cell placement and microenvironment, such as cancer research	Resolution: ~10–250 μm; cell viability: ~85–95%; shear tolerance: low; throughput: medium	[34–36]

negatively impact cell viability, and the resulting constructs may have inadequate porosity and mechanical strength.[41] Innovative approaches like coaxial extrusion—which allows the creation of perfusable vascular channels by extruding bioinks and crosslinking agents simultaneously—have been developed to tackle these problems.[42] Additionally, sacrificial bioinks such as Pluronic F127 can be used to create temporary structures that can be removed post-printing, leaving behind perfusable channels.[41] These methods also improve the alignment of collagen fibers, enhancing cell proliferation and tissue integration.[41] Additionally, various crosslinking methods, such as ultraviolet-assisted or chemical crosslinking, are commonly used to improve the mechanical strength and stability of the printed material. Selecting an appropriate bioprinting strategy is critical for optimizing fiber orientation, porosity, stiffness, and vascular architecture to meet specific tissue engineering goals.[29,43,44]

2.1.1. Coaxial bioprinting

Coaxial bioprinting has attracted considerable attention due to its ability to produce hollow, tubular structures that closely mimic the natural structure of blood vessels.[45] It provides the ability to manipulate vessel geometry, lumen size, and wall thickness with precision. This technique utilizes concentric nozzles to simultaneously inject core and sheath bioinks, enabling the creation of perfusable vascular conduits (Figure 2). The bioink usually contains endothelial cells along with proangiogenic factors, while the secondary component provides structural support or acts as a sacrificial material. Alginate and calcium chloride have been extensively employed in coaxial bioprinting due to their quick ionic crosslinking and compatibility with biological systems.[41,46] dECM-derived bioinks have been combined with coaxial printing to promote endothelial cell adhesion, migration, and vessel formation, with studies demonstrating enhanced tubulogenesis and vascular endothelial growth factor receptor 2 (VEGFR2) expression.[47] Nevertheless, recreating the intricate branching structures of natural blood vessels and replicating their long-term mechanical stability pose significant challenges.[48] Sacrificial bioprinting is frequently employed to generate vascular channels by depositing temporary materials that are subsequently removed to form hollow conduits. Materials like DNA hydrogels, gelatin microparticles, and carbohydrate glass have been utilized to construct perfusable networks.[49,50] dECM bioinks are commonly used to enclose these sacrificial structures, providing biochemical signals that promote endothelial cell adhesion and the formation of a vascular network.[51]

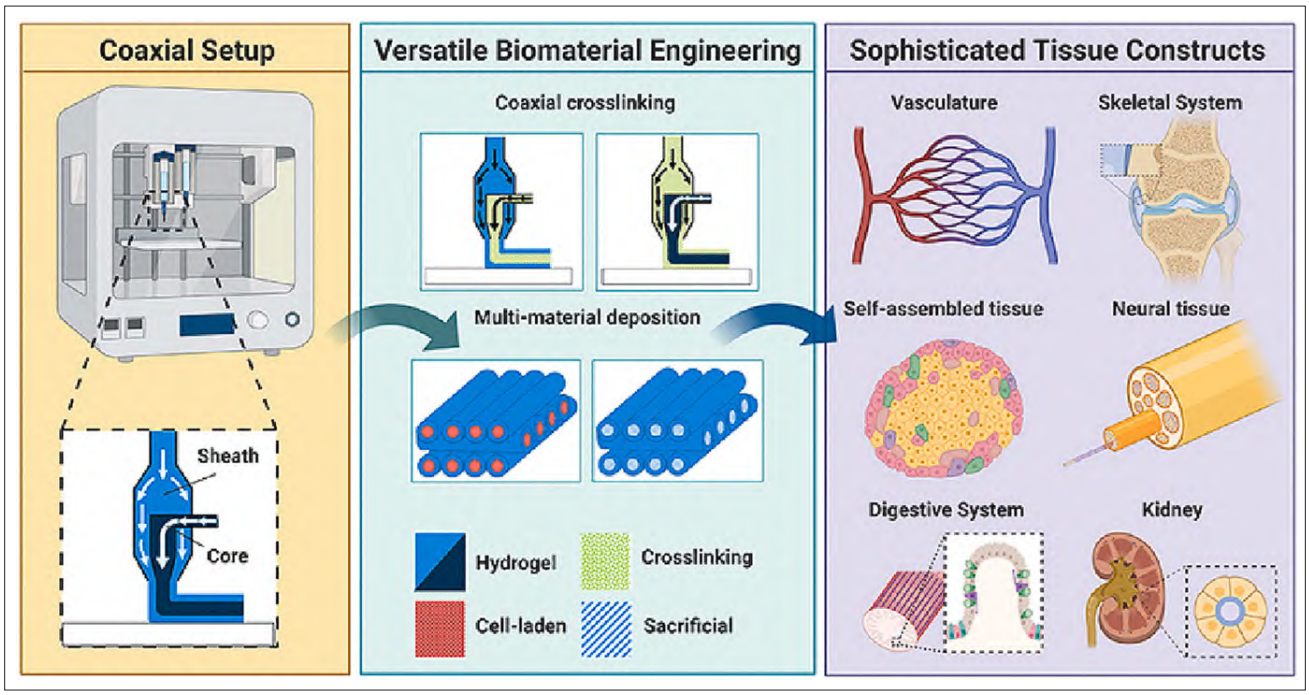


Figure 2. Schematic representation of coaxial bioprinting for tissue engineering applications. The diagram illustrates a coaxial bioprinting setup enabling core–sheath extrusion, followed by versatile biomaterial engineering strategies such as coaxial crosslinking and multi-material deposition. This approach facilitates the fabrication of sophisticated tissue constructs, including vasculature, skeletal, neural, digestive, and renal tissues. Reprinted with permission from Kjar *et al.*[52] Copyright © Elsevier 2020.

2.1.2. Microfluidic bioprinting

Decellularized ECM bioprinting, when combined with microfluidic and organ-on-a-chip technologies, offers a powerful platform for advanced drug testing and disease modeling. Microfluidic bioprinting utilizes microfluidic platforms to fabricate structures with intricate capillary-like features, achieving high precision in their design. These devices enable the accurate handling of bioinks and growth factors, facilitating the creation of complex vascular networks.[36] Incorporation of dECM bioinks into microfluidic systems has been shown to stimulate angiogenesis and promote the growth of endothelial cells,[53] enhancing the biological relevance of *in vitro* tissue models. Furthermore, dECM-based constructs integrated with organ-on-a-chip platforms can replicate both the mechanical and biochemical cues of native tissues, making them highly suitable for simulating physiological and pathological conditions in a controlled setting. This synergy enhances the fidelity of models used for studying disease progression and screening drug responses. However, microfluidic bioprinting still faces key obstacles related to scalability, efficiency, and consistency,[54] which must be addressed for broader adoption in clinical and pharmaceutical research.

2.2. Stereolithography and digital light processing

SLA and DLP are light-based bioprinting techniques that employ photopolymerization to create intricate 3D structures with high resolution. These techniques have become valuable tools for generating microvascular networks due to their high precision and ability to create complex shapes. SLA can achieve resolutions as fine as 5–50 μm,[55] while advanced DLP systems can reach 0.6–30 μm.[56] In SLA, a focused laser beam selectively polymerizes photosensitive bioinks layer by layer, while DLP employs a digital light projector to cure entire layers simultaneously.[57,58] Both techniques have been employed to generate vascularized scaffolds by incorporating endothelial cells into photopolymerizable hydrogels. dECM-based bioinks, such as cardiac-derived dECM hydrogels, have been incorporated into SLA systems to support endothelial cell adhesion, proliferation, and tubulogenesis.[39,40] The main benefit of SLA and DLP is their capability to create detailed and precise 3D models with complex vascular systems. Nevertheless, the restricted range of photopolymerizable bioinks and the potential cytotoxicity of photoinitiators present substantial obstacles.[58,59] Ongoing efforts are centered around creating biocompatible photoinitiators and hybrid bioinks that combine dECM with synthetic polymers to improve printability and functionality.

2.3. Sacrificial bioprinting

Sacrificial bioprinting is commonly used to produce vascular channels by depositing temporary materials that are later eliminated to create hollow conduits. Materials like DNA hydrogels, gelatin microparticles, and carbohydrate glass have been utilized to construct perfusable networks.[49,50] dECM bioinks are frequently employed to enclose these sacrificial structures, offering biochemical signals that facilitate endothelial cell adhesion and the development of a vascular network.[51] Sacrificial bioprinting allows the creation of complex vascular networks, but challenges persist in maintaining channel patency, mechanical stability, and immune compatibility.[50,60]

2.4. Multi-material bioprinting

Multi-material bioprinting merges different bioinks to create tissues with complex structures, consisting of various materials.[61] This method combines bioinks with synthetic and nanostructured materials to create tissues with unique biochemical and mechanical characteristics.[62,63] Advanced bioinks that react to external factors have been created to improve blood vessel growth and facilitate dynamic tissue changes.[31] Although multi-material bioprinting holds great promise, there are still obstacles to overcome, such as ensuring compatibility between different bioinks, optimizing mechanical properties, and establishing standardized processes.[64,65] The combination of 3D bioprinting technologies and dECM bioinks signifies a groundbreaking approach to engineering vascularized tissues. Each bioprinting technique presents unique benefits and obstacles, emphasizing the necessity for hybrid systems that integrate the strengths of multiple approaches. Future studies should concentrate on refining bioink compositions, creating biocompatible photoinitiators, and improving vascularization techniques to enhance the performance and practical application of engineered tissues.

2.5. Emerging innovations in three-dimensional bioprinting

Recent advances in 3D bioprinting include a wave of transformative technologies that address limitations in resolution, cell viability, and structural complexity. One exciting development is the Freeform Reversible Embedding of Suspended Hydrogels method, which allows printing of soft, liquid-like bioinks within a yield-stress bath, preserving construct fidelity and resolution while supporting anatomically accurate structures.[45,66] Similarly, liquid-in-liquid bioprinting also utilizes a bath to ensure electrostatic stabilization. The deposition of high-cell-density bioinks in the granular bath has resulted in cell proportions exceeding 90% v/v.[67]

There are also newly emerging techniques that are specifically tailored to create vascularized tissue models. For example, suspension-based bioprinting techniques, such as suspension bath-based 3D bioprinting, utilize starch hydrogel baths to create vascularized, multicellular constructs with smooth, removal-free support structures.[68] Similarly, infiltration-induced suspension bioprinting employs hyaluronic acid's shear-thinning and self-healing properties to fine-tune scaffold microarchitecture and mechanical strength while maintaining high-resolution endothelial cell patterning.[69] In addition, sacrificial bioprinting enables the fabrication of perfusable, tubular structures by serving as transient supports in soft matrix printing.[70] Sequential printing in reversible ink template is another new technique that uses biphasic microgel-based ink as both medium and bioink to build complex tissues with perfusable vasculature, including cardiac organoids.[71]

In addition, certain techniques that enable the construction of multi-layered tissue models, which are especially important when trying to replicate the complexity of human organs, are currently being developed. For example, multi-material bioprinting enables co-deposition of diverse bioinks containing different cell types to recreate native tissue heterogeneity with spatial precision.[72] In addition, volumetric bioprinting surpasses traditional layer-by-layer constraints by rapidly forming centimeter-scale structures via photopolymerization.[73] Microfluidic-assisted bioprinting provides control over microarchitecture through hierarchical bioink patterning.[74] Lastly, programmable granular hydrogel inks, with tunable porosity and stimuli-responsiveness, are paving the way for advanced four-dimensional bioprinting that enables the alteration of the bioink's mechanical properties during tissue maturation *in vitro* or following implantation *in vivo*.[75]

These emerging technologies have enabled the creation of skin models, vascular tissues, and organoids with increased fidelity and functionality, significantly advancing applications in regenerative medicine and personalized therapy.[33,76] Future efforts will aim to address scalability, material limitations, and regulatory challenges, while integration with artificial intelligence and bioinformatics promises to optimize design, printing parameters, and translational potential.[77,78]

3. The role of decellularized extracellular bioinks in vascularization

3.1. Structural and functional properties of native extracellular matrix and its role in vascularization

The ECM plays a central role in regulating cellular behavior and tissue development, extending far beyond its structural function. Composed of proteins, glycoproteins, and proteoglycans, the ECM modulates angiogenic signaling by sequestering growth factors and guiding cell communication within the native microenvironment.[79–81] This intricate regulatory capacity is largely enabled by the ECM's fundamental yet adaptable architecture, which typically comprises two interconnected compartments: the interstitial matrix and the basement membrane. While these compartments serve as common organizational principles, their specific molecular composition and structural arrangement are tailored to meet the unique functional demands of each tissue.[82] For instance, the interstitial matrix forms the primary structural scaffold of tissues, composed of collagen, elastin, and adhesive glycoproteins like fibronectin that enable cell adhesion, migration, and mechanical integrity. On the other hand, the vascular basement membrane—a dense sheet underlying endothelial cells—primarily contains laminin and collagen IV, both of which regulate cell anchorage and vascular barrier function.[83,84] Crucially, both compartments contain glycosaminoglycans and heparan sulfate proteoglycans, which stabilize growth factors and ensure precise spatiotemporal control over angiogenic signaling and endothelial morphogenesis.[83]

The ECM composition is continuously remodeled through a feedback loop between mechanical and biochemical signals. Cells sense and respond to matrix stiffness and external stresses via surface receptors such as integrins, ion channels, and primary cilia, activating mechanotransduction pathways.[85] These cues activate intracellular signaling cascades that influence gene expression and drive ECM remodeling.[86] This dynamic reciprocity maintains tissue-specific mechanical properties, such as elasticity and tensile strength, which are essential for function.[87]

The interplay between cells and their matrix environment gives rise to ECM specializations tailored to distinct tissue needs. For instance, in cartilage, the mechanical environment dictates chondrocyte behavior and ECM synthesis, with collagen types, elastin, and small leucine-rich proteoglycans shaping tissue stiffness and flexibility, distinguishing hyaline, elastic, and fibrocartilage, and influencing their respective load-bearing capacities.[88,89] Similarly, the skin's ECM exhibits a multi-layered complexity, where laminin-332, collagen IV, and collagen VII anchor the epidermis to the dermis via the basement membrane.[90] Fibroblasts further contribute to fibrillin-rich microfibrils and elastic fibers, while crosslinking enzymes like lysyl oxidases and small leucine-rich proteoglycans reinforce collagen organization—properties vital for skin elasticity and resilience.[91]

The ECM's tissue-specific adaptations extend to various other tissues. Bone, for example, is a mineralized connective tissue composed primarily of collagen I, hydroxyapatite, and proteoglycans such as decorin and biglycan, which support mineralization and biomechanical strength.[89] Moreover, the diverse functional roles shaped by ECM organization and composition are exemplified by the cornea, whose transparency relies on the precise alignment of collagen fibrils and the presence of anti-angiogenic molecules, such as thrombospondins and matrix metalloproteinases, which are essential for preventing vision-impairing vascularization.[92]

This structural diversity is particularly evident in vascular tissues, where ECM cues directly orchestrate angiogenesis. For example, the interaction between integrins (e.g., αvβ3 and αvβ5) and growth factor receptors modulates receptor tyrosine kinase activity, such as that of VEGFR.[93] Upon ligand binding, VEGFR2 triggers downstream signaling pathways that drive angiogenesis and endothelial cell organization into vascular structures.[94] These finely tuned interactions demonstrate how ECM composition and structure regulate vascularization at the molecular level.

Preserving the ECM's biochemical and mechanical cues is vital for directing cellular responses involved in tissue development and remodeling. As a central reservoir of bioactive molecules, the ECM orchestrates mechanotransduction and signaling pathways that regulate gene expression and morphogenesis.[85] dECM, which can retain native structural and molecular features, has therefore emerged as a promising bioink component for recapitulating vascularization in engineered tissues.[23]

3.2. Decellularized extracellular matrix as a bioactive bioink biomaterial to promote vascularization

Decellularized ECM has emerged as a promising biomaterial for regenerative therapies, with several formulations already approved by the Food and Drug Administration.[95] Despite differences in decellularization methods, their shared goal is to eliminate cellular and immunogenic components while preserving the native ECM's structural and biochemical properties. The resulting matrices retain essential components—such as collagen, fibronectin, laminin, glycosaminoglycans, and growth factors—that support tissue-specific cellular functions.[24] These retained cues are particularly critical for promoting angiogenesis, positioning dECM as a promising element in the development of biomaterials aimed at supporting vascular network formation.

A critical challenge in engineering functional tissues is the limited diffusion of oxygen and nutrients within the created 3D structures. In living organisms, cells must reside within a short distance (typically 100–200 μm) of capillaries to ensure adequate supply; beyond this range, they suffer from hypoxia and necrosis.[96,97] Therefore, a crucial goal in tissue engineering is promoting the formation of robust, functional vascular networks throughout engineered scaffolds. One approach involves the growth and formation of new blood vessels from existing ones, known as angiogenesis.[98] Achieving this vascularization requires a two-pronged approach: first, the strategic delivery of angiogenic factors to stimulate blood vessel growth, and second, the effective recruitment and support of endothelial cells, such as human umbilical vein endothelial cells, which exhibit a strong capacity to form vascular structures within environments that mimic natural ECM environments.[99] Furthermore, for these engineered tissues to successfully integrate and function long-term within a host, the biomaterials used must possess a balanced set of properties, including biocompatibility, low immunogenicity, and controlled biodegradation, allowing effective tissue remodeling and seamless integration.[100]

In addition to enhancing regenerative outcomes, dECM biomaterials must recapitulate the biochemical and biophysical features of native ECM. Mechanical properties such as stiffness and viscoelasticity, along with microstructural features like topography, influence how cells sense and respond to their environment. These physical cues regulate critical cellular processes—including migration, proliferation, and morphogenesis—by modulating intracellular signaling through integrin and other mechanotransduction pathways.[101] Incorporating these properties into dECM-based bioinks ensures that the scaffold not only supports vascular network formation but also provides a dynamic microenvironment conducive to tissue regeneration.

3.3. Decellularized extracellular matrix-based bioink formulation

Both the source tissue and the decellularization protocol must be carefully selected for preparing dECM, as they significantly influence the biochemical composition, structural integrity, and immunogenic profile of the final material.[102] dECM can be derived from three main sources: cell-derived matrices, animal tissues, and human tissues. Cell-derived matrix is produced *in vitro* from cultured cells and offers a controllable and reproducible matrix rich in signaling molecules; however, it often lacks the mechanical robustness of native tissue and has limited scalability.[103,104] Animal-derived dECMs, such as porcine bladder and heart, bovine tendons, goat lung and

kidney, or rat liver and lungs, are widely used due to their availability and structural similarity to human tissues. Nonetheless, they present potential challenges, including immunogenicity, cross-species disease transmission, and batch variability.[103,104] Human-derived dECMs, obtained from cadaveric tissues, diseased or discarded organs, or from tissue banks, offer a superior physiological relevance and lower immunological risk, making them particularly valuable in applications related to organ repair and transplantation. However, their availability is limited and subject to strict ethical and regulatory oversight.[103] The selection of the source should therefore align with the intended clinical application, especially in contexts like organ transplantation, where immunocompatibility and structural fidelity are paramount.

Decellularization is equally important as the source of the material, removing all cellular and immunogenic material while preserving the native ECM's 3D architecture, biochemical complexity, and mechanical strength. Decellularization strategies encompass physical methods (e.g., freeze–thaw cycles, agitation, hydrostatic pressure), chemical agents (e.g., detergents, acids, bases), and enzymatic treatments (e.g., nucleases and proteases), often applied in combination to maximize efficacy while minimizing damage to bioactive components.[102,105,106] In contrast to the often more intensive protocols required for decellularizing animal and human tissues with their cellularly dense structure, cell-derived matrices—owing to their relatively less compact and *in vitro*-assembled structure—typically necessitate gentler decellularization procedures. These milder approaches often exclude harsh mechanical disruption, such as crushing, potentially leading to better preservation of the ECM's delicate ultrastructure and molecular composition.[107] Effectiveness is typically assessed through metrics such as residual DNA content, ultrastructural analysis, mechanical property retention, and preservation of key ECM constituents like collagen, fibronectin, laminin, and glycosaminoglycans.[40] Inadequate decellularization can result in immune rejection, while overexposure to harsh treatments can compromise the matrix's biological function.[108]

Once decellularized, dECM-based biomaterials can be processed into either powdered or hydrogel form, each suitable for different biofabrication applications. In their research, Mesquita *et al.*[109] followed a protocol in which decellularized animal tissue was lyophilized, cryomilled, and sieved, yielding powdered particles with sizes ranging from 45–1000 μm. Alternatively, dECM can be solubilized through pepsin digestion, neutralized to promote self-assembly, and then induced to form a hydrogel through incubation at 37°C.[110] These processing endpoints are particularly valuable for bioink development as they preserve the native ECM architecture, a crucial factor for successful tissue regeneration. Figure 3 highlights the different processes used to formulate dECM-based bioink.

Preserving the native ECM architecture is crucial for using dECM in biofabrication, particularly in 3D bioprinting. When properly processed, dECM retains essential biochemical and mechanical signals that promote cell adhesion, proliferation, differentiation, and angiogenesis, which are key for regenerating functional tissues. However, native dECM often lacks the mechanical robustness and printability required for clinical-scale constructs.[40] To address this, researchers have developed composite bioinks that integrate dECM with reinforcing materials to improve rheological properties, extrusion stability, and cellular mechanosensing. These enhancements are vital not only for structural fidelity (mechanical strength) but also for creating a microenvironment conducive to vascular development.[111] Shin *et al.*[112] demonstrated this approach using a bioink comprising porcine cardiac dECM, Laponite-XLG nanoclay, and poly(ethylene glycol)-diacrylate. This formulation achieved enhanced printability and mechanical properties matching both healthy (~5–15 kPa) and fibrotic cardiac tissue (~30–100 kPa), while maintaining cell viability and functionality.[112] Similarly, Alibeigian *et al.*[114] addressed dECM limitations by combining calcium phosphate cement with bone-derived dECM hydrogel. Subcutaneous implantation in rats showed no toxicity or inflammatory responses, with radiographic and computed tomography analyses demonstrating superior bone formation in dECM/calcium phosphate cement-hydrogel and mesenchymal stem cells-incorporated groups compared to controls.[113,114] Figure 4 highlights some of the diverse tissue origins of dECMs used in various tissue engineering applications.

3.4. Decellularized extracellular matrix-based bioinks: advancing vascularization and tissue regeneration in 3D bioprinting

Decellularized ECM can enhance vascularization and tissue regeneration when incorporated into bioinks. For example, You *et al.*[115] developed a liver dECM-gelatin-alginate scaffold that promoted osteogenic differentiation of rat bone mesenchymal stem cells. *In vivo* studies using a calvarial defect model revealed enhanced vascularization and bone regeneration.[115] Martinez *et al.*[116] similarly showcased dECM's potential through reproductive tissue-mimicking hydrogels combining ovarian, oviductal, and endometrial dECM with 1% alginate. These scaffolds maintained viability of multiple cell types and supported microvascularization without supplemental growth factors, highlighting dECM's inherent bioactivity.[116] Additionally,

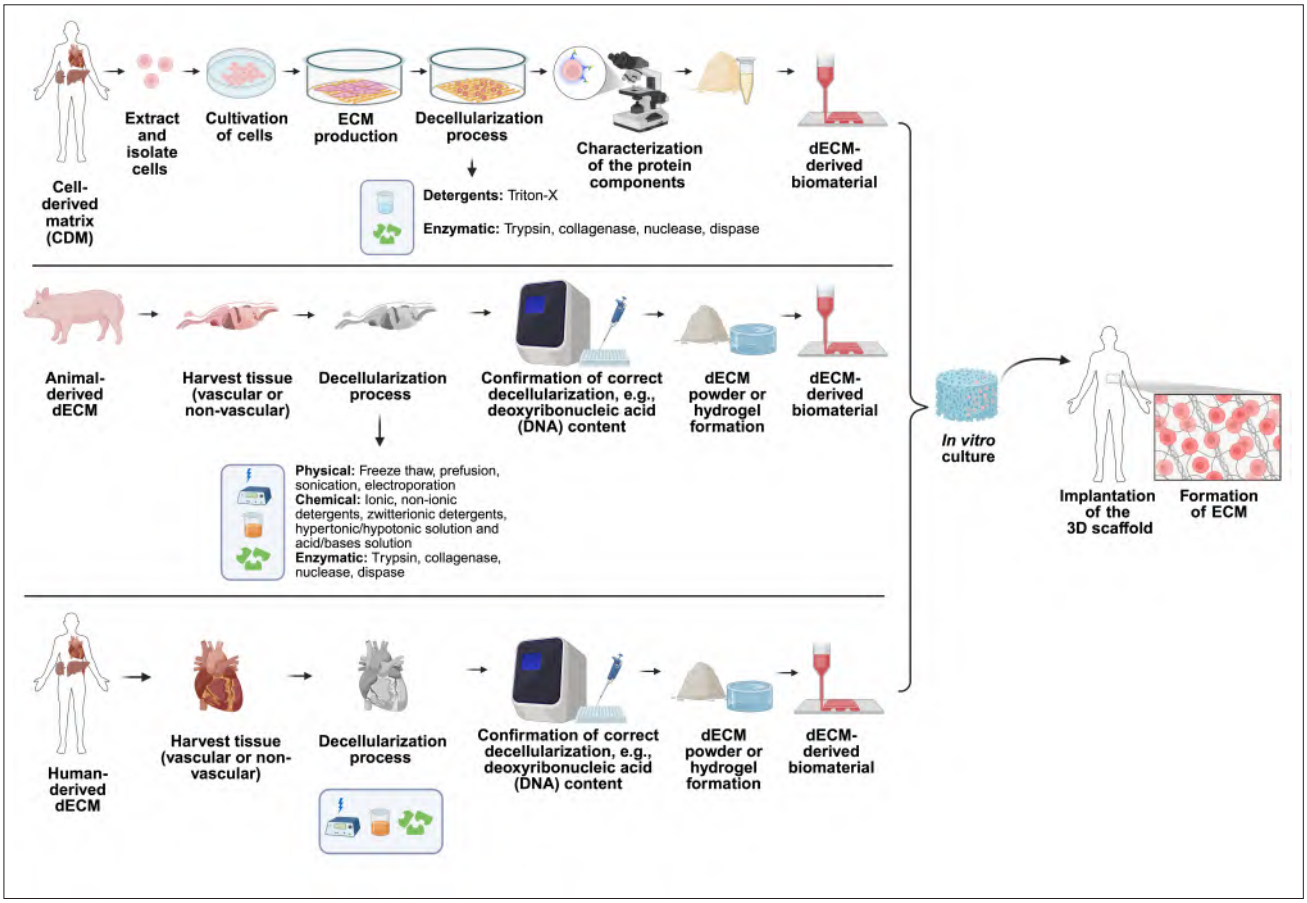


Figure 3. Decellularized extracellular matrix (dECM)-based bioink formulation. The schematic figure shows the key steps in preparing dECM-based bioink from different tissue sources (cell-derived, animal-derived, or human-derived). The process involves decellularization using physical, chemical, or enzymatic methods to remove cellular material while preserving ECM composition and structure, followed by processing into either powdered form (via lyophilization, cryomilling, and sieving) or hydrogel form (via pepsin digestion, neutralization, and thermal gelation). The resulting bioink retains native ECM components (e.g., collagen, fibronectin, glycosaminoglycans) and can be used for tissue engineering applications. Created in BioRender. Willerth, S. (2025). https://BioRender.com/hs597ud.

Kim *et al.*[61] developed a bioink from pancreatic dECM to replicate *in vivo* pancreatic tissue for islet transplantation as a treatment for type 1 diabetes mellitus. The inclusion of human umbilical vein endothelial cells in the bioink promoted vascularization and reduced necrosis in the 3D cultured islets. These results demonstrate the potential of dECM to provide a supportive microenvironment for pancreatic cells, offering promise for pancreatic regeneration and improved islet transplantation outcomes. These studies collectively demonstrate the potential of dECM-based bioinks in supporting tissue-specific cell functions, promoting vascularization, and ultimately improving tissue regeneration across a range of tissue engineering-based applications.

The development of dECM-based bioinks marks an advancement in 3D bioprinting, as they uniquely integrate native biochemical signaling with tunable mechanical properties. However, achieving functional vascularization requires more than an optimized bioink formulation. It also requires precise control over 3D bioprinting parameters to engineer scaffolds with biologically relevant structural features. Key printing considerations, including resolution, pore architecture, and fibrin alignment, must be systematically optimized to facilitate essential physiological processes such as nutrient diffusion, cell migration, and angiogenic sprouting.[103] For example, the combination of dECM with human smooth muscle cells and endothelial cells could be used to create capillary-like networks within the scaffold, which would be critical for ensuring the long-term viability of implanted tissues. This approach builds on previous studies that have shown that dECM's properties support cell attachment, migration, and proliferation—all of which are crucial for successful vascularization.[116] Moreover, using dECM from different tissues, such as cardiac or liver tissue, can be tailored to support specific

tissue types, enhancing the scaffold's ability to replicate the physiological microenvironment of the engineered tissue (Figure 4). Adding this level of vascular support could significantly improve the long-term functionality and tissue regeneration capabilities of 3D-bioprinted constructs, especially when designing scaffolds for complex tissue engineering applications such as wound healing or organ regeneration. By integrating cell assembly strategies with dECM scaffolds, these engineered tissues can achieve advanced levels of vasculature, mimicking the hierarchical architecture of native blood vessels.

4. Challenges in three-dimensional bioprinting vascularized scaffolds with decellularized extracellular matrix bioinks

The advancement of 3D bioprinting technologies and dECM-based bioinks has significantly enhanced the development of vascularized tissue constructs. Despite their biomimetic advantages, dECM-based bioinks face several challenges that hinder their widespread use in tissue engineering and regenerative medicine. Key limitations include poor mechanical properties, difficulties in vascular network maturation, immunogenicity concerns, and scalability issues—all of which pose barriers to clinical translation. Additionally, optimizing bioink rheology, crosslinking kinetics, and printing temperature is critical to ensure scaffolds can accurately replicate native vascular ECM organization. These interdependent factors highlight the need for a synergistic approach, combining advanced material design with precision fabrication techniques to achieve successful vascularization strategies.

4.1. Printability and mechanical properties

The printability of dECM bioinks is influenced by rheological properties, crosslinking mechanisms,

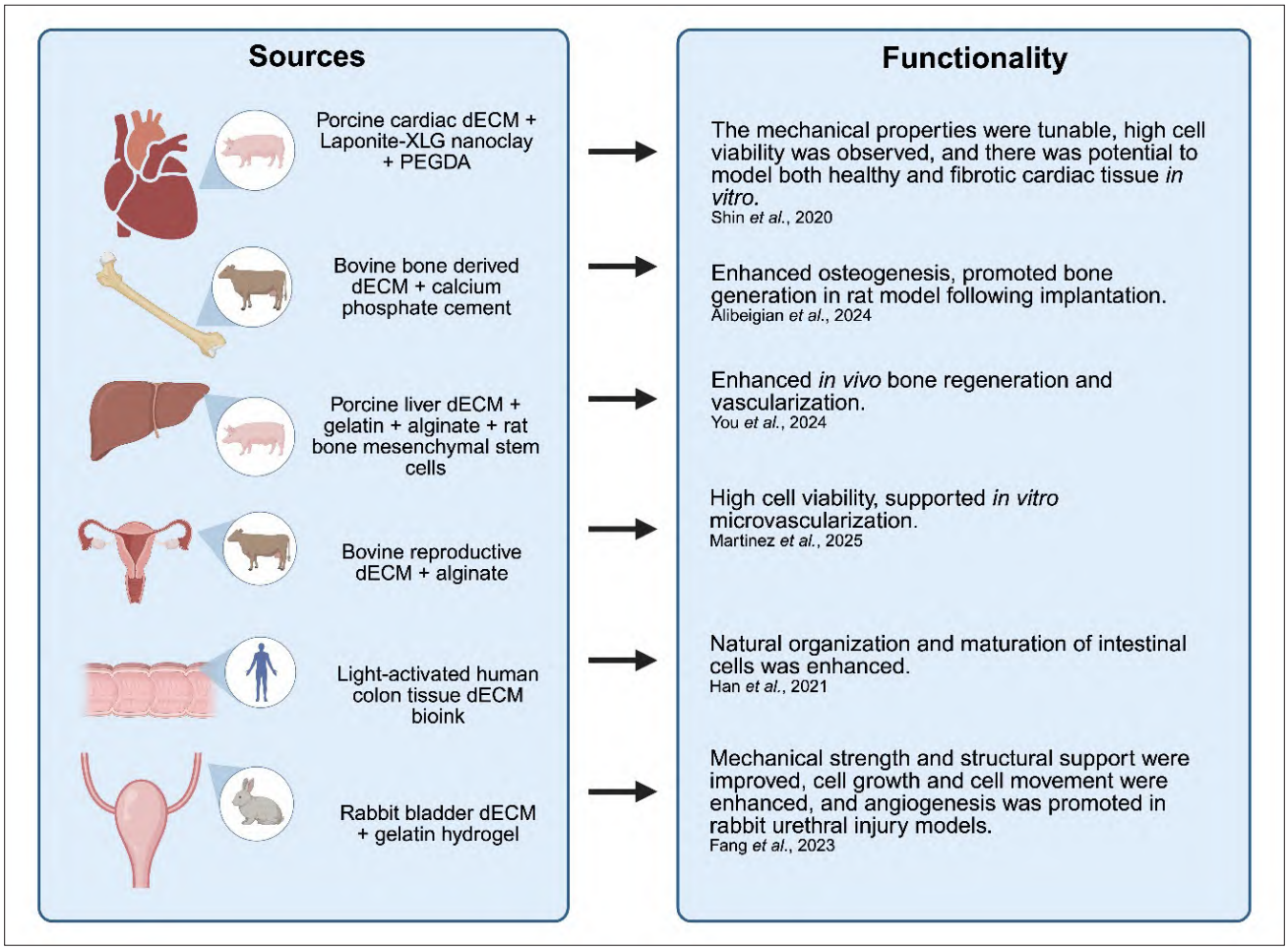


Figure 4. Overview of decellularized extracellular matrix (dECM)-based bioinks and their applications in tissue engineering. Applications for dECM bioinks may span cardiovascular, skeletal, hepatic, reproductive, intestinal, and urinary systems, highlighting its diverse benefits, including tunable mechanical properties, enhanced vascularization, cell viability, and structural support. The studies included in the figure validate these functionalities in both *in vivo* and *in vitro* models. Created in BioRender. Willerth, S. (2025). https://BioRender.com/mmkf47d

and extrusion parameters. All of these factors govern the structural integrity and resolution of bioprinted constructs.[117] However, dECM bioinks lack intrinsic mechanical strength, making it difficult to fabricate scaffolds with high shape fidelity and long-term stability.[117,118] The loss of structural proteins during decellularization results in weak gelation kinetics, leading to deformation or collapse of printed structures, particularly in complex vascular architectures.[118]

To improve printability, researchers have explored dual crosslinking mechanisms that incorporate photo-crosslinking and thermal gelation, thereby enhancing mechanical properties while preserving bioactivity.[118] Additionally, rheological tuning through the incorporation of reinforcing agents and viscosity modifiers has been investigated to optimize the flow behavior and shear-thinning properties of dECM bioinks.[119] However, balancing mechanical reinforcement with biological functionality remains a critical challenge, as excessive crosslinking or material modifications can compromise cell viability and ECM bioactivity.

4.2. Vascular network maturation

Vascularization is essential for the functionality and longevity of bioprinted tissues, yet generating hierarchically organized, perfusable vascular networks remains a major hurdle. dECM bioinks, while rich in angiogenic factors and ECM-based biochemical cues, lack the mechanical stability necessary for sustained vascular lumen formation and perfusability.[117,120] As a result, bioprinted vasculature often exhibits premature collapse, limited branching complexity, or poor endothelialization, limiting its functionality *in vivo*.[47,121] Efforts to enhance vascular maturation have focused on coaxial bioprinting and sacrificial templating approaches, which enable the fabrication of hollow, perfusable vascular conduits with tunable lumen sizes and wall thicknesses.[121,122] Furthermore, the incorporation of endothelial cells, pericytes, and angiogenic growth factors within dECM bioinks has been explored to promote endothelial sprouting and vessel stabilization.[118] Notably, Shiwarski *et al.*[45] demonstrated that combining photocurable, cell-laden hydrogels with high-resolution DLP bioprinting enables the fabrication of perfusable vascular networks with improved mechanical fidelity and biological relevance. However, even with these advancements, functional integration with host vasculature remains a significant challenge, requiring precise biochemical and mechanical signaling to achieve successful anastomosis and long-term viability.

4.3. Immunogenicity and standardization

Although dECM bioinks are derived from native ECMs, they are not entirely free from immunogenic concerns. Residual cellular debris, nucleic acids, and immunogenic proteins from the decellularization process can elicit inflammatory responses and graft rejection when introduced into a biological system.[51,119] Immunogenicity is further exacerbated by batch-to-batch variability, which results from differences in tissue sources, decellularization protocols, and processing conditions, ultimately impacting the reproducibility and safety of dECM bioinks.[123]

The source of the antigen, whether it comes from an animal or a human, has a significant impact on its ability to trigger an immune response. Animal-derived dECM, such as porcine or bovine, often contains species-specific antigens, such as α-gal epitopes, which can cause strong immune reactions in humans, resulting in inflammation and potential graft rejection. In contrast, human-sourced dECM lacks these foreign antigens, which reduces the risk of immune rejection and improves biocompatibility. For instance, research has demonstrated that ECM from humans has a substantial impact on reducing the risk of immune rejection when it comes to xenogenic ECM, such as the response to α-gal epitopes. Consequently, while animal-derived dECM has benefits in terms of availability and scalability, human-derived dECM is commonly chosen for clinical applications where immunogenicity is a significant concern.[124]

The lack of standardized procedures for the generation of dECM represents another major challenge.[95,125] Standardizing dECM production is impeded by wide variation in tissue properties and decellularization outcomes. For instance, a protocol optimized for porcine hearts required extended sodium dodecyl sulfate treatment and additional steps to process human hearts, yet still resulted in markedly different levels of cellular residues among human donors.[95] Likewise, applying a single detergent regimen to five human livers yielded five distinct scaffold outcomes (with only one liver completely devoid of cells).[126] Moreover, if dECM is improperly decellularized, residual immunogenic material may further complicate standardization. Donor-specific antigens, including DNA fragments and human leukocyte antigen/major histocompatibility complex molecules, can provoke host immune responses if not eliminated, but methods harsh enough to remove them often concurrently strip away essential bioactive ECM components.[95]

Standardization of bioink processing and bioprinting protocols is critical for addressing current inconsistencies and ensuring the clinical feasibility of dECM-based constructs. Recent research has focused heavily on optimizing decellularization techniques to minimize immunogenic components while preserving bioactive ECM components.[117] Furthermore, the implementation

of biochemical assays, biocompatibility testing, and quality control measures are also essential in establishing standardized manufacturing and regulatory guidelines.[119,123]

4.4. Scalability and clinical translation

Despite promising advancements in 3D bioprinting and dECM bioink development, scaling up the fabrication process for clinically relevant tissue constructs remains a significant challenge. Current bioprinting platforms are primarily optimized for small-scale constructs, and achieving large-scale, vascularized tissues suitable for implantation requires improvements in bioink stability, tissue perfusion, and automated fabrication techniques.[119,123] The inherent biological variability of dECM bioinks further complicates scalability, as maintaining consistent composition and mechanical properties across batches is difficult. From a regulatory standpoint, clinical translation of bioprinted tissues requires extensive preclinical validation, safety assessments, and compliance with Good Manufacturing Practices. Unlike synthetic biomaterials, dECM-based scaffolds must demonstrate long-term biocompatibility, functional integration, and reproducibility across multiple production cycles to receive regulatory approval.[123]

Real-world commercial products such as CorMatrix® ECM (used in cardiovascular and soft tissue repair) and MatriStem® UBM (a urinary bladder matrix used in wound healing and hernia repair) exemplify how dECM-based materials have successfully navigated some of these translational hurdles. These products, derived from porcine tissues and processed under rigorously standardized conditions, highlight the clinical viability of dECM scaffolds and reinforce the importance of quality control, reproducibility, and long-term safety. Several ongoing clinical trials (e.g., NCT04023254 investigating dECM hydrogel for myocardial infarction repair) further illustrate the potential of these materials in regenerative therapies.

Current efforts are directed toward developing standardized decellularization methods, optimizing biofabrication workflows, and incorporating real-time quality control measures to ensure the scalability and regulatory compliance of dECM-based bioprinted tissues. Ensuring the long-term stability of dECM-based scaffolds—defined by the retention of native matrix architecture, mechanical integrity, and bioactivity during extended implantation—is essential for successful clinical translation. Strategies such as incorporating polymer-dECM composite bioinks and applying post-fabrication crosslinking have been developed to enhance scaffold durability. For example, fibrinogen-dECM hybrid hydrogels have demonstrated improved mechanical modulus and extended structural stability compared to pure dECM gels.[24] Moreover, careful optimization of decellularization protocols, such as minimizing enzymatic degradation from agents like trypsin, helps preserve critical ECM components and mechanical strength.[103] To ensure quality and monitor scaffold behavior over time, advanced imaging modalities are being integrated as non-destructive, real-time analytical tools. High-resolution microscopy techniques such as scanning and transmission electron microscopy are used to confirm the preservation of scaffold microarchitecture post-implantation.[127] In parallel, non-invasive, *in vivo* imaging platforms—including optical coherence tomography, multiphoton microscopy, and ultrasound—are being employed to longitudinally track scaffold degradation, tissue maturation, and host integration. Functional imaging methods such as magnetic resonance imaging and photoacoustic imaging further enable dynamic assessment of vascular perfusion, metabolic activity, and cellular functionality within the developing constructs.[24,127]

4.5. Regulatory and ethical considerations

Decellularized ECM can pose significant risks and ethical concerns when introduced back into the human body due to its bioactive nature. In 2001, a clinical trial using Synergraft® decellularized porcine heart valves passed regulations and gained approval in Europe. However, it was later understood that the valves were insufficiently decellularized, and upon implantation, they resulted in the death of three out of four patients due to immunotoxicity.[128] This case study highlights the importance of thorough regulation and testing prior to the implantation of dECM products.

The introduction of implantable 3D-bioprinted dECM products to the market is currently regulated by both national and international organizations. The International Organization for Standardization (ISO) introduced the ISO 10993 standard for the biological evaluation of medical devices.[121] The ISO 10993 comprises a series of frameworks and tests to assess the safety of medical devices that come in contact with the human body, including tests for immunotoxicity, sensitivity, degradability, and implantation studies. The framework has been incorporated into pre-existing policies by the European Union's European Medical Devices Regulation (MDR), Health Canada's MDR, and the United States' Food and Drug Administration.[129] These regulatory bodies ensure that new medical devices demonstrate safety across applicable ISO 10993 standards by requiring that manufacturers submit extensive biocompatibility data and undergo chemical characterization testing. Independent of the ISO 10993, the Food and Drug Administration and European and Canadian MDR also possess their own safety regulations and requirements, including a

risk-based classification system for new products and post-market tracking.[130–132] Many other countries also use the ISO 10993 as a policy guideline for medical devices, including China's National Medical Products Association, India's Central Drugs Standard Control Organization, and Japan's Pharmaceuticals and Medical Devices Agency. In summary, fulfilling the rigorous evaluation requirements of ISO 10993 is a time-intensive and expensive process, but it is a necessary safeguard to ensure human safety.

In addition to regulatory considerations, there are also multiple ethical considerations that must be taken into account when considering the development of 3D-bioprinted dECM tissues. Firstly, the tissue source for dECM poses significant ethical challenges. dECM has three main sources; however, human-derived dECM is the most beneficial for clinical applications. The most common human dECM sources include cadaveric tissues, diseased, and discarded organs, and must therefore adhere to guidelines surrounding informed consent, confidentiality, and bias minimization.[133] Some researchers are also advocating for the ability of donors to choose how their tissues are used over the long term[134] to better address ethical concerns surrounding human tissue usage. Secondly, the source of the cells needed for recellularization of the dECM construct also poses ethical challenges. iPSCs are a promising avenue to reseed dECM, as they can be derived from pre-established human cell lines and have a reduced risk of immunotoxicity.[127] However, the most significant drawback of iPSCs' use in 3D-bioprinted constructs is the risk of tumor formation.[135] Significant advancements have been made in recent years, with studies successfully reseeding iPSCs into dECM scaffolds while avoiding tumor formation.[136–138] Despite this, tumorigenesis still remains a pressing ethical challenge in iPSC research.[139] While recellularization of dECM is generally considered to be a beneficial process,[127] another growing area of research is the use of dECM scaffolds that are not reseeded with cells.[125] This process involves implanting a cell-free scaffold into the body and recruiting cells from the surrounding tissue. This technique has demonstrated wide success in the cases of skin (AlloDerm® [BioHorizons], Oasis® [Smith & Nephew]), tendon and ligament (GraftJacket® [Wright Medical], Allopatch HD™ [MTF Sports Medicine]), and repair and regeneration.[103,125,127] However, recellularized dECM constructs are preferred when manufacturing multilayered, thick, or complex organ models, where recruiting a sufficient number of endogenous cells would be a challenge.[125]

Lastly, the general risks associated with 3D-printed dECM implantable constructs, such as immune responses,[140] dislodgement, and migration of the implants,[141] must also be considered from an ethical standpoint. Ethical guidelines for 3D-printed tissues are primarily provided by national organizations and at institutional levels; however, certain prominent international organizations, such as the United Nations Educational, Scientific, and Cultural Organization's International Bioethics Committee and the European Molecular Biology Laboratory Ethics Board, also play important roles. At a national level, the risks associated with dECM 3D-printed implantable constructs are evaluated by the Institutional Review Boards in the United States, the Research Ethics Board in Canada, and in Europe, by the Independent Ethics Committee, and through general guidelines created by the European Commission. These ethics boards carefully review each proposed technology and weigh the benefit versus the potential harm caused, monitor ongoing projects, and ensure informed consent and the protection of vulnerable populations in research.[142–144] However, rapid advancements in the fields of tissue engineering and regenerative medicine have led some researchers to propose a specialized ethics framework to ensure that all technological advancements in the field are guided through careful consideration of their societal implications.[141] For example, one specific area of ethical concern is ensuring that tissue engineering technology is made accessible to all members of the population, regardless of differing socioeconomic status.[141,145]

In summary, the incorporation of dECM into regenerative medicine technologies introduces unique ethical challenges, including the dECM tissue source, the source of cells used during recellularization, and the risks associated with implantable constructs. Well-established regulatory and ethical organizations at both international and national levels currently dictate the development of 3D-bioprinted dECM products. However, ethical challenges persist and will continue to grow as the field rapidly develops.

4.6. Summary of challenges

Although 3D bioprinting with dECM bioinks shows great potential for vascularized tissue engineering, several obstacles must be overcome to enable its widespread use in clinical settings and large-scale applications. Future research should focus on improving the printability and mechanical stability of 3D-printed objects by refining crosslinking strategies and rheological properties. This will improve shape accuracy and structural strength. In addition to promoting the growth of vascular networks, it is crucial to focus on improving their stability and functionality. This can be achieved by developing advanced techniques that allow the creation of interconnected and functional vascular systems that can seamlessly integrate with the existing vasculature. Furthermore, minimizing immunogenicity and variability is crucial, and this can

be accomplished by refining decellularization protocols and implementing standardized quality control measures to guarantee consistent results across different batches. Ultimately, overcoming scalability and regulatory hurdles will necessitate the creation of efficient, automated bioprinting platforms and strict adherence to clinical safety protocols. By successfully addressing these obstacles, bioinks and 3D bioprinting technologies can play a crucial role in creating functional, vascularized tissues for regenerative medicine and organ transplantation.

5. Future perspectives

The rapid advancements in bioink design and bioprinting are revolutionizing tissue engineering and regenerative medicine. Future research is expected to focus on developing hybrid bioinks that enhance both biological functionality and mechanical properties, smart bioinks capable of controlled biomolecule release, *in situ* bioprinting for direct tissue repair, artificial intelligence-driven biofabrication optimization, and patient-specific bioinks for personalized regenerative therapies. These innovations aim to overcome current limitations in bioprintability, vascularization, and clinical translation, paving the way for more effective and scalable tissue engineering solutions.

5.1. Advanced bioink design

The development of hybrid bioinks that integrate dECM with synthetic polymers is a promising strategy for enhancing both bioactivity and structural integrity. dECM provides essential biochemical cues that support cell adhesion, proliferation, and differentiation, mimicking native ECM. However, its inherent weak mechanical properties and limited printability necessitate the incorporation of synthetic polymers such as poly(ethylene glycol) diacrylate, gelatin methacryloyl, and nanocellulose, which enhance viscosity, shear-thinning behavior, and crosslinking efficiency.[117,123] Recent advances in modular bioinks, where dECM microgels are incorporated within composite hydrogels, have demonstrated improved post-printing cell viability and tissue-specific functionality.[20] Additionally, the integration of nanomaterials, such as carbon nanotubes and graphene oxide, has been explored to enhance mechanical strength and electrical conductivity, particularly for applications in neural tissue engineering and biosensing.[146,147] Tissue-specific dECM bioinks further refine this approach by providing biologically relevant microenvironments tailored to specific organ systems, such as liver, cartilage, and cardiac tissues, improving their regenerative potential.[119]

5.2. Smart bioinks

The emergence of smart bioinks introduces new opportunities for controlled biomolecule delivery and enhanced tissue functionality. Stimuli-responsive bioinks, designed to release growth factors or other bioactive molecules in response to environmental cues, offer precise spatiotemporal control over tissue development.[148] An important application of smart bioinks is the controlled release of angiogenic factors, such as VEGF, which plays a crucial role in promoting vascularization within bioprinted constructs.[149] Aptamer-based bioinks have demonstrated the ability to sequester and release VEGF in response to specific triggers, guiding endothelial cells in forming hierarchical vascular networks. Furthermore, bioinks incorporating pH-sensitive polymers enable VEGF release in response to the slightly acidic microenvironment of regenerating tissues, optimizing localized angiogenesis.[150,151] Other innovations include bioinks embedded with extracellular vesicles or liposomes that deliver microRNAs involved in angiogenesis regulation, allowing sustained modulation of gene expression in encapsulated cells.[151] These smart bioinks hold significant potential for improving vascular integration, reducing ischemic tissue loss, and enhancing overall tissue maturation in complex bioprinted constructs.

5.3. *In situ* bioprinting

In situ bioprinting represents a transformative approach to tissue engineering by enabling direct deposition of bioinks at the site of injury, eliminating the need for pre-fabricated scaffolds and reducing the time required for tissue maturation. This technology is particularly beneficial for treating large-scale tissue defects, burn wounds, and cartilage injuries, where immediate bioprinting at the injury site enhances integration with host tissues.[119,152] The development of portable and robotic bioprinting systems has significantly improved the precision and feasibility of *in situ* bioprinting, allowing real-time adjustments based on anatomical variations and patient-specific needs. These systems often incorporate advanced imaging techniques, such as optical coherence tomography and real-time ultrasound, to ensure accurate deposition of bioinks within complex tissue geometries.[152] Additionally, patient-specific dECM bioinks used in conjunction with *in situ* bioprinting further enhance tissue integration by providing a biomaterial that closely matches the patient's native ECM composition.[123] As *in situ* bioprinting technology continues to advance, its applications are expected to expand into regenerative therapies for musculoskeletal, cardiovascular, and dermal tissue repair.

5.4. Integration with artificial intelligence and machine learning

Artificial intelligence and machine learning are increasingly transforming bioprinting by optimizing bioink formulations and printing parameters with greater precision and efficiency.[153] Artificial intelligence-

driven models utilize large datasets to predict key bioink properties—such as rheology, printability, and mechanical stability—minimizing trial-and-error experimentation and enhancing reproducibility.[24,46] Notably, Bayesian optimization techniques have enabled the fine-tuning of bioink compositions, ensuring optimal viscosity and crosslinking behavior tailored to specific applications.[24,154] Neural network-based models have also emerged to evaluate cell viability under varying printing conditions, allowing real-time adjustments that support high post-printing cell survival.[155] Furthermore, artificial intelligence-integrated bioprinting platforms now offer real-time feedback and error correction, dynamically adjusting parameters to improve construct fidelity and mechanical integrity.[46,156] Alongside these technological innovations, materials science is also advancing rapidly, particularly in the development of personalized bioinks that enhance tissue compatibility.

5.5. Personalized medicine

The use of patient-specific dECM bioinks is revolutionizing personalized regenerative medicine by enabling the creation of biologically relevant, immune-compatible tissue constructs. Unlike traditional bioinks, which rely on allogeneic or xenogeneic ECM sources, patient-specific dECM bioinks are derived from the individual's own tissues, ensuring a tailored biochemical and biomechanical environment that promotes better tissue integration and function.[123,147] These bioinks offer significant advantages in reducing immune rejection, enhancing cell–matrix interactions, and improving overall regenerative outcomes. Additionally, the mechanical and structural properties of patient-specific dECM bioinks can be customized to match the requirements of specific tissue types, such as increased stiffness for bone regeneration or enhanced elasticity for soft tissue repair.[117,147] The combination of patient-specific dECM bioinks with *in situ* bioprinting has demonstrated great promise in clinical applications, particularly in reconstructive surgery, chronic wound healing, and cardiovascular tissue engineering.[119,152] As the field progresses, personalized biofabrication approaches are expected to become a cornerstone of precision medicine, offering tailored regenerative solutions for a wide range of patient-specific needs.

6. Conclusion

This review highlights the importance of ECM as a dynamic reservoir of biochemical and mechanical cues that regulate cellular behavior through mechanotransduction. These processes play a fundamental role in guiding tissue function by influencing gene expression, cell adhesion, proliferation, migration, and maturation. We also address the ongoing challenges in 3D tissue bioprinting, particularly the difficulty in generating vascularized networks that ensure the compatibility and functionality of bioprinted constructs for transplantation. dECM-based biomaterials have emerged as promising candidates due to their ability to preserve the native structural and molecular characteristics of ECM, thereby enhancing vascular network formation and tissue integration. However, several hurdles remain. These include the standardization of decellularization protocols and dECM sources to minimize immunogenic responses, as well as the development of optimized bioink formulations that improve the mechanical stability of 3D scaffolds while preserving the biological cues necessary for cellular support and tissue maturation. Emerging technologies and strategies such as artificial intelligence, machine learning, *in situ* bioprinting, and personalized medicine offer promising strategies to address these limitations by enabling more precise optimization of bioprinting parameters and reducing immune-related complications.

Acknowledgments

ChatGPT by OpenAI was used to improve text grammar and clarity.

Funding

This study was supported by the NSERC Discovery grant program (No. RGPIN-2017-04044), the NSERC Alliance grant program (No. 590667-2023), the NSERC CREATE training grant in 3D Printing Technology and Materials (No. 565179-2022), the CIHR Project grant program (No. 460840), and the B.C. Ministry of Forests, New Frontiers in Research Fund, Transformation Grant, "Mend the Gap" (No. NFRFT-2020-00238), and the Nanotherapeutics cluster at the University of Victoria.

Conflict of interest

Dr. Willerth is the C.E.O. and co-founder of Axolotl Biosciences, a biotechnology company that sells novel bioinks. The rest of the authors declare they have no competing interests.

Author contributions

Conceptualization: Jugal Kishore B, Giselle Y. Díaz, Sravya Tekumalla, Stephanie M. Willerth

Writing – original draft: Jugal Kishore B, Giselle Y. Díaz, Fynn S. Owen La Boucan, Madeleine A. Perry

Writing – review & editing: All authors

Ethics approval and consent to participate

Not applicable.

Consent for publication

Not applicable.

Availability of data

Not applicable.

References

1. Grinyo JM. Why is organ transplantation clinically important? *Cold Spring Harb Perspect Med*. 2013;3(6): a014985-a014985. doi:10.1101/cshperspect.a014985
2. Jiménez Oliver K. Overview of organ donation. *Mex J Med Res*. 2023;11(21):55-63. doi:10.29057/mjmr.v11i21.10007
3. Girlanda R. Deceased organ donation for transplantation: challenges and opportunities. *WJT*. 2016;6(3):451. doi:10.5500/wjt.v6.i3.451
4. Health Canada. Government of Canada Highlights Key Progress in Support of Organ Donation and Transplantation. Published September 15, 2023. Accessed May 02, 2025. https://www.canada.ca/en/health-canada/news/2023/09/government-of-canada-highlights-key-progress- insupport-of-organ-donation-and-transplantation.html.
5. Health Resources and Services Administration. Organ Donor Statistics: Patients on the Waiting List by Organ. Published on September 15, 2024. Accessed May 02, 2025. https://www.organdonor.gov/learn/organ-donation-statistics#fig1
6. Norris S. Organ Donation and Transplantation in Canada: Statistics, Trends and International Comparisons. (Background Paper No. 2020-28-E). Parliamentary Information and Research Service, Library of Parliament; Ottawa, ON; Published April 01, 2020. Accessed May 02, 2025.
7. Jamee R, Araf Y, Naser IB, Promon SK. The promising rise of bioprinting in revolutionalizing medical science: advances and possibilities. *Regen Ther.* 2021;18(1):133-145. doi:10.1016/j.reth.2021.05.006
8. Kim JJ, Hou L, Huang NF. Vascularization of threedimensional engineered tissues for regenerative medicine applications. *Acta Biomater.* 2016;41:17-26. doi:10.1016/j.actbio.2016.06.001
9. Vyas D, Udyawar D. A review on current state of art of bioprinting. In: Kumar LJ, Pandey PM, Wimpenny DI, eds. *3D Printing and Additive Manufacturing Technologies.* Singapore: Springer. 2019;195-201. doi:10.1007/978-981-13-0305-0_17
10. Shi Y, Inoue H, Wu JC, Yamanaka S. Induced pluripotent stem cell technology: a decade of progress. *Nat. Rev. Drug Discov*. 2017;16(2):115-130. doi:10.1038/nrd.2016.245
11. Takahashi K, Yamanaka S. Induction of pluripotent stem cells from mouse embryonic and adult fibroblast cultures by defined factors. Cell. 2006;126(4):663-676. doi:10.1016/j.cell.2006.07.024
12. Takahashi K, Tanabe K, Ohnuki M, *et al.* Induction of pluripotent stem cells from adult human fibroblasts by defined factors. *Cell*. 2007;131(5):861-872. doi:10.1016/j.cell.2007.11.019
13. Mallya D, Gadre MA, Varadharajan S, Vasanthan KS. 3D bioprinting for the construction of drug testing modelsdevelopment strategies and regulatory concerns. Front. *Bioeng Biotechnol.* 2025;13:1457872. doi:10.3389/fbioe.2025.1457872
14. Van Berlo D, Nguyen VVT, Gkouzioti V, Leineweber K, Verhaar MC, Van Balkom BWM. Stem cells, organoids, and organ-on-a-chip models for personalized in vitro drug testing. *Curr Opin Toxicol*. 2021;28:7-14. doi:10.1016/j.cotox.2021.08.006
15. Van Berlo D, Nguyen VVT, Gkouzioti V, Leineweber K, Verhaar MC, Van Balkom BWM. Stem cells, organoids, and organ-on-a-chip models for personalized in vitro drug testing. UK & USA: Academic Press, as an imprint for Elsevier Inc. 2021. *Curr Opin Toxicol.* 2021;28:7-14. doi:10.1016/B978-0-12-822229-4.00001-2
16. Wang S, Du Y, Zhang B, *et al.* Transplantation of chemically induced pluripotent stem-cell-derived islets under abdominal anterior rectus sheath in a type 1 diabetes patient. *Cell*. 2024;187(22):6152-6164.e18. doi:10.1016/j.cell.2024.09.004
17. Okamoto R, Mizutani T, Shimizu H. Development and application of regenerative medicine in inflammatory bowel disease. *Digestion*. 2023;104(1):24-29. doi:10.1159/000527423
18. Shimizu Y, Ntege EH, Azuma C, *et al.* Management of rheumatoid arthritis: possibilities and challenges of mesenchymal stromal/stem cell-based therapies. *Cells*. 2023;12(14):1905. doi:10.3390/cells12141905
19. Babaahmadi M, Tayebi B, Gholipour NM, *et al.* Rheumatoid arthritis: the old issue, the new therapeutic approach. *Stem Cell Res Ther*. 2023;14(1):268. doi:10.1186/s13287-023-03473-7
20. Chen XB, Fazel Anvari-Yazdi A, Duan X, *et al.* Biomaterials/bioinks and extrusion bioprinting. *Bioact Mater.* 2023;28:511-536. doi:10.1016/j.bioactmat.2023.06.006
21. Groll J, Burdick JA, Cho DW, *et al.* A definition of bioinks and their distinction from biomaterial inks. *Biofabrication*. 2018;11(1):013001. doi:10.1088/1758-5090/aaec52
22. Wang X, Chan V, Corridon PR. Decellularized blood vessel development: current state-of-the-art and future directions. *Front Bioeng Biotechnol.* 2022;10:951644.

doi:10.1007/s12668-018-0525-4

23. Wang X, Chan V, Corridon PR. Decellularized blood vessel development: current state-of-the-art and future directions. *Front Bioeng Biotechnol*. 2022;10:951644. doi:10.3389/fbioe.2022.951644

24. Xu P, Kankala RK, Wang S, Chen A. Decellularized extracellular matrix-based composite scaffolds for tissue engineering and regenerative medicine. *Regen Biomat*. 2024;11:rbad107. doi:10.1093/rb/rbad107

25. Dzobo K, Motaung KSCM, Adesida A. Recent trends in decellularized extracellular matrix bioinks for 3D printing: an updated review. *IJMS*. 2019;20(18):4628. doi:10.3390/ijms20184628

26. Lee J, Lee S, Kim B, *et al.* Paintable decellularized-ecm hydrogel for preventing cardiac tissue damage. *Adv Sci*. 2024;11(21):2307353. doi:10.1002/advs.202307353

27. You S, Xiang Y, Hwang HH, *et al.* High cell density and high-resolution 3D bioprinting for fabricating vascularized tissues. *Sci Adv*. 2023;9(8):eade7923. doi:10.1126/sciadv.ade7923

28. Li J, Chen M, Fan X, Zhou H. Recent advances in bioprinting techniques: approaches, applications and future prospects. *J Transl Med*. 2016;14(1):271. doi:10.1186/s12967-016-1028-0

29. Rossi A, Pescara T, Gambelli AM, *et al.* Biomaterials for extrusion-based bioprinting and biomedical applications. *Front Bioeng Biotechnol.* 2024;12:1393641. doi:10.3389/fbioe.2024.1393641

30. Jiang T, Munguia-Lopez JG, Flores-Torres S, Kort-Mascort J, Kinsella JM. Extrusion bioprinting of soft materials: an emerging technique for biological model fabrication. *Appl Phys Rev*. 2019;6(1):011310. doi:10.1063/1.5059393

31. Cho DW, Kim BS, Jang J, Gao G, Han W, Singh NK. 3D bioprinting techniques. In: *3D Bioprinting*. Switzerland: Springer International Publishing; 2019:25-29. doi:10.1007/978-3-030-32222-9_4

32. Mesbah Z, Subramaniam D, Mariapen H, *et al.* Current applications and future potential of 3d bioprinting in tissue engineering. *JMEDITEC*. 2024;3(2):132-138. doi:10.11113/jmeditec.v3.66

33. Yüksel F. Advanced 3D bioprinting techniques for regenerative medicine: exploring applications in tissue engineering and personalized therapeutics. *NFLSAI*. 2024;8(1):71. doi:10.62802/xa2ak830

34. Arumugam P, Kaarthikeyan G, Eswaramoorthy R. Three-Dimensional Bioprinting: The Ultimate Pinnacle of Tissue *Engg Cureus.* 2024;16(4):e58029. doi:10.7759/cureus.58029

35. Loukelis K, Koutsomarkos N, Mikos AG, Chatzinikolaidou M. Advances in 3D bioprinting for regenerative medicine applications. *Regen Biomater.* 2024;11:rbae033. doi:10.1093/rb/rbae033

36. Chand R, Kamei K ichiro, Vijayavenkataraman S. Advances in microfluidic bioprinting for multi-material multi-cellular tissue constructs. *Cell Eng Connect*. 2025;1(1):1. doi:10.69709/CellEngC.2024.111335

37. Shyam Mohan T, Datta P, Nesaei S, Ozbolat V, Ozbolat IT. 3D coaxial bioprinting: process mechanisms, bioinks and applications. *Prog Biomed Eng*. 2022;4(2):022003. doi:10.1088/2516-1091/ac631c

38. Miri AK, Mostafavi E, Khorsandi D, Hu SK, Malpica M, Khademhosseini A. Bioprinters for organs-on-chips. *Biofabrication*. 2019;11(4):042002. doi:10.1088/1758-5090/ab2798

39. Pati F, Jang J, Ha DH, *et al.* Printing three-dimensional tissue analogues with decellularized extracellular matrix bioink. *Nat Commun*. 2014;5(1):3935. doi:10.1038/ncomms4935

40. Kim MK, Jeong W, Lee SM, Kim JB, Jin S, Kang HW. Decellularized extracellular matrix-based bio-ink with enhanced 3D printability and mechanical properties. *Biofabrication*. 2020;12(2):025003. doi:10.1088/1758-5090/ab5d80

41. Ahmad A, Kim SJ, Jeong YJ, *et al.* Coaxial bioprinting of a stentable and endothelialized human coronary artery-sized *in vitro* model. *J Mater Chem B*. 2024;12(35): 8633-8646. doi:10.1039/D4TB00601A

42. Shan J, Kong Z, Wang X. Formation of stable vascular networks by 3d coaxial printing and schiff-based reaction. *Gels*. 2024;10(6):366. doi:10.3390/gels10060366

43. Gharraei R, Bergstrom DJ, Chen X. Extrusion bioprinting from a fluid mechanics perspective. *Int J Bioprint.* 2024;10(6):114-153. doi:10.36922/ijb.3973

44. Chirianni F, Vairo G, Marino M. Influence of extruder geometry and bio-ink type in extrusion-based bioprinting via an in silico design tool. *Meccanica*. 2024;59(8): 1285-1299. doi:10.1007/s11012-024-01862-7

45. Shiwarski DJ, Hudson AR, Tashman JW, *et al.* 3D bioprinting of collagen-based high-resolution internally perfusable scaffolds for engineering fully biologic tissue systems. *Sci Adv*. 2025;11(17):eadu5905. doi:10.1126/sciadv.adu5905

46. Sun J, Gong Y, Xu M, Chen H, Shao H, Zhou R. Coaxial 3D bioprinting process research and performance tests on vascular scaffolds. *Micromachines*. 2024;15(4):463. doi:10.3390/mi15040463

47. Heidari F, Saadatmand M, Simorgh S. Directly coaxial bioprinting of 3D vascularized tissue using novel bioink based on decellularized human amniotic membrane. *Int J Biol Macromol.* 2023;253 (Pt4):127041. doi:10.1016/j.ijbiomac.2023.127041

48. Stankey PP, Kroll KT, Ainscough AJ, *et al.* Embedding Biomimetic Vascular Networks via Coaxial Sacrificial Writing into Functional Tissue. *Adv Mater.* 2024;36(36):e2401528. doi:10.1002/adma.202401528

49. Shi W, Zhang Z, Wang X. The prospect of hepatic decellularized extracellular matrix as a bioink for liver 3D bioprinting. *Biomolecules*. 2024;14(8):1019. doi:10.3390/biom14081019

50. Brassard JA, Dharmaraj SS, Orimi HE, *et al.* Iterative sacrificial 3D printing and polymer casting to create complex vascular grafts and multi-compartment bioartificial organs. 2024. doi:10.1101/2024.09.29.615298

51. Klak M, Rachalewski M, Filip A, Dobrzański T, Berman A, Wszoła M. Bioprinting of perfusable, biocompatible vessel-like channels with dECM-based bioinks and living cells. *Bioengineering*. 2024;11(5):439. doi:10.3390/bioengineering11050439

52. Kjar A, McFarland B, Mecham K, Harward N, Huang Y. Engineering of tissue constructs using coaxial bioprinting. *Bioact Mater*. 2021;6(2):460-471. doi:10.1016/j.bioactmat.2020.08.020

53. Kafili G, Kabir H, Jalali Kandeloos A, *et al.* Recent advances in soluble decellularized extracellular matrix for heart tissue engineering and organ modeling. *J Biomater Appl*. 2023;38(5):577-604. doi:10.1177/08853282231207216

54. Miao X, Chen T, Lang Z, *et al.* Design, fabrication, and application of bioengineering vascular networks based on microfluidic strategies. *J Mater Chem B*. 2025;13(4):1252-1269. doi:10.1039/D4TB02047B

55. Herzog J, Franke L, Lai Y, Gomez Rossi P, Sachtleben J, Weuster-Botz D. 3D bioprinting of microorganisms: principles and applications. *Bioproc Biosyst Eng*. 2024;47(4):443-461. doi:10.1007/s00449-023-02965-3

56. Jeong YG, Yoo JJ, Lee SJ, Kim MS. 3D digital light process bioprinting: Cutting-edge platforms for resolution of organ fabrication. *Mater Today Bio.* 2024;29:101284. doi:10.1016/j.mtbio.2024.101284

57. Lim KS, Galarraga JH, Cui X, Lindberg GCJ, Burdick JA, Woodfield TBF. Fundamentals and applications of photo-cross-linking in bioprinting. *Chem Rev*. 2020;120(19):10662-10694. doi:10.1021/acs.chemrev.9b00812

58. Mamo HB, Adamiak M, Kunwar A. 3D printed biomedical devices and their applications: A review on state-of-the-art technologies, existing challenges, and future perspectives. *J Mech Behav Biomed Mater.* 2023;143:105930. doi:10.1016/j.jmbbm.2023.105930

59. Gugulothu SB, Chatterjee K. Visible Light-based 4D-bioprinted tissue scaffold. *ACS Macro Lett*. 2023;12(4):494-502. doi:10.1021/acsmacrolett.3c00036

60. Malkani S, Prado O, Stevens KR. Sacrificial templating for accelerating clinical translation of engineered organs. *ACS Biomater Sci Eng*. 2025;11(1):1-12. doi:10.1021/acsbiomaterials.4c01824

61. Kim J, Shim IK, Hwang DG, *et al.* 3D cell printing of islet-laden pancreatic tissue-derived extracellular matrix bioink constructs for enhancing pancreatic functions. *J Mater Chem B*. 2019;7(10):1773-1781. doi:10.1039/C8TB02787K

62. Han D, Lee H. Recent advances in multi-material additive manufacturing: methods and applications. *Curr Opin Chem Eng.* 2020;28:158-166. doi:10.1016/j.coche.2020.03.004

63. Korkeamäki JT, Rashad A, Ojansivu M, *et al.* Systematic development and bioprinting of novel nanostructured multi-material bioinks for bone tissue engineering. *Biofabrication*. 2025;17(2):025005. doi:10.1088/1758-5090/ada63b

64. Jeon O, Park H, Leach JK, Alsberg E. Biofabrication of engineered tissues by 3D bioprinting of tissue specific high cell-density bioinks. *Mater Today.* 2025:S1369702125001294. doi:10.1016/j.mattod.2025.03.021

65. Rasouli R, Sweeney C, Frampton JP. Heterogeneous and composite bioinks for 3d-bioprinting of complex tissue. *Biomed Mater Devices*. 2024;2(1):108-126. doi:10.1007/s44174-024-00171-7

66. Wu CA, Zhu Y, Venkatesh A, Stark CJ, Lee SH, Woo YJ. Optimization of freeform reversible embedding of suspended hydrogel microspheres for substantially improved three-dimensional bioprinting capabilities. *Tissue Eng Part C Methods*. 2023;29(3):85-94. doi:10.1089/ten.tec.2022.0214

67. Jiang J, Yuan C, Zhang X, *et al.* 3D bioprinting of liquid high-cell-proportion bioinks in liquid granular bath. *Adv Mater*. 2024;36(49):2412127. doi:10.1002/adma.202412127

68. Li S, Li J, Xu J, *et al.* Removal-free and multicellular suspension bath-based 3D bioprinting. *Adv Mater*. 2024;36(48):2406891. doi:10.1002/adma.202406891

69. Wang C, Honiball JR, Lin J, *et al.* Infiltration from suspension systems enables effective modulation of 3D

scaffold properties in suspension bioprinting. *ACS Appl Mater Interfaces*. 2022;14(24):27575-27588. doi:10.1021/acsami.2c04163

70. Liu S, Wang T, Li S, Wang X. Application status of sacrificial biomaterials in 3D bioprinting. *Polymers*. 2022;14(11):2182. doi:10.3390/polym14112182

71. Fang Y, Guo Y, Wu B, *et al.* Expanding embedded 3D bioprinting capability for engineering complex organs with freeform vascular networks. *Adv Mater*. 2023;35(22):2205082. doi:10.1002/adma.202205082

72. Ravanbakhsh H, Karamzadeh V, Bao G, Mongeau L, Juncker D, Zhang YS. Emerging technologies in multi-material bioprinting. *Adv Mater*. 2021;33(49):2104730. doi:10.1002/adma.202104730

73. Jing S, Lian L, Hou Y, *et al.* Advances in volumetric bioprinting. *Biofabrication*. 2024;16(1):012004. doi:10.1088/1758-5090/ad0978

74. Mohammadi S, Cidonio G. Unravelling hierarchical patterning of biomaterial inks with 3D microfluidic-assisted spinning: a paradigm shift in bioprinting technologies. *Front Biomater Sci.* 2023;2:1279061. doi:10.3389/fbiom.2023.1279061

75. Ribeiro LS, Gaspar VM, Sobreiro-Almeida R, Camargo ER, Mano JF. Programmable granular hydrogel inks for 3D bioprinting applications. *Adv Mater Technol*. 2023;8(16):2300209. doi:10.1002/admt.202300209

76. Mirshafiei M, Rashedi H, Yazdian F, Rahdar A, Baino F. Advancements in tissue and organ 3D bioprinting: current techniques, applications, and future perspectives. *Mater Des.* 2024;240:112853. doi:10.1016/j.matdes.2024.112853

77. Liu S, Chen Y, Wang Z, *et al.* The cutting-edge progress in bioprinting for biomedicine: principles, applications, and future perspectives. *MedComm*. 2024;5(10):e753. doi:10.1002/mco2.753

78. Zoghi S. Advancements in tissue engineering: a review of bioprinting techniques, scaffolds, and bioinks. *Biomed Eng Comput Biol.* 2024;15:11795972241288099. doi:10.1177/11795972241288099

79. Theocharis AD, Skandalis SS, Gialeli C, Karamanos NK. Extracellular matrix structure. *Adv Drug Deliv Rev.* 2016;97:4-27. doi:10.1016/j.addr.2015.11.001

80. Marchand M, Monnot C, Muller L, Germain S. Extracellular matrix scaffolding in angiogenesis and capillary homeostasis. *Semin Cell Dev Biol.* 2019;89:147-156. doi:10.1016/j.semcdb.2018.08.007

81. Briquez PS, Clegg LE, Martino MM, Gabhann FM, Hubbell JA. Design principles for therapeutic angiogenic materials. *Nat Rev Mater*. 2016;1(1):15006. doi:10.1038/natrevmats.2015.6

82. Crossley RM, Johnson S, Tsingos E, *et al.* Modeling the extracellular matrix in cell migration and morphogenesis: a guide for the curious biologist. *Front Cell Dev Biol.* 2024;12:1354132. doi:10.3389/fcell.2024.1354132

83. Libby JR, Royce H, Walker SR, Li L. The role of extracellular matrix in angiogenesis: beyond adhesion and structure. *Biomater Biosys.* 2024;15:100097. doi:10.1016/j.bbiosy.2024.100097

84. Payne LB, Zhao H, James CC, *et al.* The pericyte microenvironment during vascular development. *Microcirculation*. 2019;26(8):e12554. doi:10.1111/micc.12554

85. Gilbert SJ, Blain EJ. Cartilage mechanobiology: how chondrocytes respond to mechanical load. In: *Mechanobiology in Health and Disease*. UK & USA: Academic Press, as an imprint for Elsevier Inc. 2018; 2018:99-126. doi:10.1016/B978-0-12-812952-4.00004-0

86. Hastings JF, Skhinas JN, Fey D, Croucher DR, Cox TR. The extracellular matrix as a key regulator of intracellular signalling networks. *Br J Pharmacol*. 2019;176(1):82-92. doi:10.1111/bph.14195

87. Saraswathibhatla A, Indana D, Chaudhuri O. Cell–extracellular matrix mechanotransduction in 3D. *Nat Rev Mol Cell Biol*. 2023;24(7):495-516. doi:10.1038/s41580-023-00583-1

88. Akkiraju H, Nohe A. Role of chondrocytes in cartilage formation, progression of osteoarthritis and cartilage regeneration. *JDB*. 2015;3(4):177-192. doi:10.3390/jdb3040177

89. Karamanos NK, Theocharis AD, Piperigkou Z, *et al.* A guide to the composition and functions of the extracellular matrix. *FEBS J*. 2021;288(24):6850-6912. doi:10.1111/febs.15776

90. Nyström A, Bruckner-Tuderman L. Matrix molecules and skin biology. *Semin Cell Dev Biol.* 2019;89:136-146. doi:10.1016/j.semcdb.2018.07.025

91. Rucker RB, Murray J. Cross-linking amino acids in collagen and elastin 1. *Am J Clin Nutr*. 1978;31(7):1221-1236. doi:10.1093/ajcn/31.7.1221

92. Barbariga M, Vallone F, Mosca E, *et al.* The role of extracellular matrix in mouse and human corneal neovascularization. *Sci Rep*. 2019;9(1):14272. doi:10.1038/s41598-019-50718-8

93. Silva R, D'Amico G, Hodivala-Dilke KM, Reynolds LE. Integrins: the keys to unlocking angiogenesis. *ATVB*. 2008;28(10):1703-1713. doi:10.1161/ATVBAHA.108.172015

94. Sottile J. Regulation of angiogenesis by extracellular matrix. *Biochim Biophys Acta (BBA) — Rev Cancer*. 2004;1654(1):13-22. doi:10.1016/j.bbcan.2003.07.002

95. Tan YH, Helms HR, Nakayama KH. Decellularization strategies for regenerating cardiac and skeletal muscle tissues. *Front Bioeng Biotechnol.* 2022;10:831300. doi:10.3389/fbioe.2022.831300

96. Grainger SJ, Putnam AJ. Assessing the permeability of engineered capillary networks in a 3D culture. *PLoS One*. 2011;6(7):e22086. doi:10.1371/journal.pone.0022086

97. Kang B, Shin J, Park HJ, *et al.* High-resolution acoustophoretic 3D cell patterning to construct functional collateral cylindroids for ischemia therapy. *Nat Commun*. 2018;9(1):5402. doi:10.1038/s41467-018-07823-5

98. Rouwkema J, Rivron NC, Van Blitterswijk CA. Vascularization in tissue engineering. *Trends Biotechnol*. 2008;26(8):434-441. doi:10.1016/j.tibtech.2008.04.009

99. Le HT, Phan HL, Lenshof A, *et al.* Ultrasound standing wave spatial patterning of human umbilical vein endothelial cells for 3D micro-vascular networks formation. *Biofabrication*. 2024;16(1):015009. doi:10.1088/1758-5090/ad03be

100. Todros S, Todesco M, Bagno A. Biomaterials and their biomedical applications: from replacement to regeneration. *Processes*. 2021;9(11):1949. doi:10.3390/pr9111949

101. Kretschmer M, Rüdiger D, Zahler S. Mechanical aspects of angiogenesis. *Cancers*. 2021;13(19):4987. doi:10.3390/cancers13194987

102. Mir TA, Nakamura M, Sakai S, *et al.* Mammalian-specific decellularized matrices derived bioink for bioengineering of liver tissue analogues: a review. *IJB*. 2023;9(3):714. doi:10.18063/ijb.714

103. Zhang W, Du A, Liu S, Lv M, Chen S. Research progress in decellularized extracellular matrix-derived hydrogels. *Regen Ther.* 2021;18:88-96. doi:10.1016/j.reth.2021.04.002

104. Tottey S, Johnson SA, Crapo PM, *et al.* The effect of source animal age upon extracellular matrix scaffold properties. *Biomaterials*. 2011;32(1):128-136. doi:10.1016/j.biomaterials.2010.09.006

105. Liu Z, Zhu J, Li Z, Liu H, Fu C. Biomaterial scaffolds regulate macrophage activity to accelerate bone regeneration. Front *Bioeng Biotechnol.* 2023;11:1140393. doi:10.3389/fbioe.2023.1140393

106. Kort-Mascort J, Flores-Torres S, Peza-Chavez O, *et al.* Decellularized ECM hydrogels: prior use considerations, applications, and opportunities in tissue engineering and biofabrication. *Biomater Sci*. 2023;11(2):400-431. doi:10.1039/D2BM01273A

107. Zhu W, Cao L, Song C, Pang Z, Jiang H, Guo C. Cell-derived decellularized extracellular matrix scaffolds for articular cartilage repair. *Int J Artif Organs*. 2021;44(4):269-281. doi:10.1177/0391398820953866

108. Kasravi M, Ahmadi A, Babajani A, *et al.* Immunogenicity of decellularized extracellular matrix scaffolds: a bottleneck in tissue engineering and regenerative medicine. *Biomater Res*. 2023;27(1):10. doi:10.1186/s40824-023-00348-z

109. Mesquita FCP, Morrissey J, Monnerat G, Domont GB, Nogueira FCS, Hochman-Mendez C. Decellularized extracellular matrix powder accelerates metabolic maturation at early stages of cardiac differentiation in human induced pluripotent stem cell-derived cardiomyocytes. *Cells Tissues Organs*. 2023;212(1):32-44. doi:10.1159/000521580

110. Amirazad H, Dadashpour M, Zarghami N. Application of decellularized bone matrix as a bioscaffold in bone tissue engineering. *J Biol Eng*. 2022;16(1):1. doi:10.1186/s13036-021-00282-5

111. Sasikumar S, Chameettachal S, Cromer B, Pati F, Kingshott P. Decellularized extracellular matrix hydrogels—cell behavior as a function of matrix stiffness. *Curr Opin Biomed Eng.* 2019;10:123-133. doi:10.1016/j.cobme.2019.05.002

112. Shin YJ, Shafranek RT, Tsui JH, Walcott J, Nelson A, Kim DH. 3D bioprinting of mechanically tuned bioinks derived from cardiac decellularized extracellular matrix. *Acta Biomaterialia.* 2021;119:75-88. doi:10.1016/j.actbio.2020.11.006

113. Lian L, Xie M, Luo Z, *et al.* Rapid volumetric bioprinting of decellularized extracellular matrix bioinks. *Adv Mater*. 2024;36(34):2304846. doi:10.1002/adma.202304846

114. Alibeigian Y, Kalantari N, Ebrahimi Sadrabadi A, *et al.* Incorporation of calcium phosphate cement into decellularized extracellular matrix enhances its bone regenerative properties. *Colloids Surfs B Biointerfaces.* 2024;244:114175. doi:10.1016/j.colsurfb.2024.114175

115. You P, Sun H, Chen H, *et al.* Composite bioink incorporating cell-laden liver decellularized extracellular matrix for bioprinting of scaffolds for bone tissue engineering. *Biomater Adv.* 2024;165:214017. doi:10.1016/j.bioadv.2024.214017

116. Ribes Martinez E, Franko Y, Franko R, *et al.* Developing and characterising bovine decellularized extracellular matrix hydrogels to biofabricate female reproductive tissues. *Acta Biomater.* 2025;196:152-170. doi:10.1016/j.actbio.2025.03.009

117. Zhang H, Wang Y, Zheng Z, *et al.* Strategies for improving the 3D printability of decellularized extracellular matrix bioink. *Theranostics*. 2023;13(8):2562-2587. doi:10.7150/thno.81785

118. Yeleswarapu S, Dash A, Chameettachal S, Pati F. 3D bioprinting of tissue constructs employing dual crosslinking

of decellularized extracellular matrix hydrogel. *Biomater Adv.* 2023;152:213494.
doi:10.1016/j.bioadv.2023.213494

119. Chae S, Cho DW. Three-dimensional bioprinting with decellularized extracellular matrix-based bioinks in translational regenerative medicine. *MRS Bull.* 2022;47(1):70-79.
doi:10.1557/s43577-021-00260-8

120. Makode S, Maurya S, Niknam SA, *et al.* Three dimensional (bio)printing of blood vessels: from vascularized tissues to functional arteries. *Biofabrication*. 2024;16(2):022005.
doi:10.1088/1758-5090/ad22ed

121. Dikyol C, Altunbek M, Koc B. Embedded multimaterial bioprinting platform for biofabrication of biomimetic vascular structures. *J Mater Res*. 2021;36(19):3851-3864.
doi:10.1557/s43578-021-00254-x

122. Attalla R, Puersten E, Jain N, Selvaganapathy PR. 3D bioprinting of heterogeneous bi- and tri-layered hollow channels within gel scaffolds using scalable multi-axial microfluidic extrusion nozzle. *Biofabrication*. 2018;11(1):015012.
doi:10.1088/1758-5090/aaf7c7

123. Elomaa L, Almalla A, Keshi E, Hillebrandt KH, Sauer IM, Weinhart M. Rise of tissue- and species-specific 3D bioprinting based on decellularized extracellular matrix-derived bioinks and bioresins. *Biomater Biosyst.* 2023;12:100084.
doi:10.1016/j.bbiosy.2023.100084

124. Guo X, Liu B, Zhang Y, *et al.* Decellularized extracellular matrix for organoid and engineered organ culture. *J Tissue Eng.* 2024;15:20417314241300386.
doi:10.1177/20417314241300386

125. Zhang X, Chen X, Hong H, Hu R, Liu J, Liu C. Decellularized extracellular matrix scaffolds: recent trends and emerging strategies in tissue engineering. *Bioact Mater.* 2022;10:15-31.
doi:10.1016/j.bioactmat.2021.09.014

126. Mattei G, Magliaro C, Pirone A, Ahluwalia A. Decellularized human liver is too heterogeneous for designing a generic extracellular matrix mimic hepatic scaffold. *Artif Organs*. 2017;41(12):E347-E355.
doi:10.1111/aor.12925

127. Neishabouri A, Soltani Khaboushan A, Daghigh F, Kajbafzadeh AM, Majidi Zolbin M. Decellularization in tissue engineering and regenerative medicine: evaluation, modification, and application methods. *Front Bioeng Biotechnol.* 2022;10:805299.
doi:10.3389/fbioe.2022.805299

128. Simon P. Early failure of the tissue engineered porcine heart valve SYNERGRAFT™ in pediatric patients. *Eur J Cardiothorac Surg*. 2003;23(6):1002-1006.
doi:10.1016/S1010-7940(03)00094-0

129. Kanďárová H, Pôbiš P. The "Big Three" in biocompatibility testing of medical devices: implementation of alternatives to animal experimentation—are we there yet? *Front Toxicol.* 2024;5:1337468.
doi:10.3389/ftox.2023.1337468

130. Health Canada. Guidance on the Risk-based Classification System for Non-In Vitro Diagnostic Devices (non-IVDDs). Published June 12, 2015. Accessed June 21, 2025.
https://www.canada.ca/en/health-canada/services/drugshealth-products/medical-devices/application-information/guidance-documents/guidance-document-guidance-riskbased-classification-system-non-vitro-diagnostic.html.

131. United States Food and Drug Administration. Regulatory Controls. Published March 27, 2018. Accessed June 21, 2025.
https://www.fda.gov/medical-devices/overview-device-regulation/regulatory-controls#:~:text=Federal%20law%20(Federal%20Food%2C%20Drug,classification%20regulation%20for%20that%20device.

132. Medical Device Coordination Group. MDCG 2021–24 Guidance on Classification of Medical Devices. Published October 2021. Accessed June 21, 2025.
https://health.ec.europa.eu/document/download/cbb19821-a517-4e13-bf87-fdc6ddd1782e_en?filename=mdcg_2021-24_en.pdf

133. Grizzle WE. Issues in the use of human tissues to support precision medicine. *J Health Care Poor Underserved*. 2019;30(4S):66-78.
doi:10.1353/hpu.2019.0117

134. Lensink MA, Jongsma KR, Boers SN, Bredenoord AL. Better governance starts with better words: why responsible human tissue research demands a change of language. *BMC Med Ethics*. 2022;23(1):90.
doi:10.1186/s12910-022-00823-7

135. Zhong C, Liu M, Pan X, Zhu H. Tumorigenicity risk of iPSCs *in vivo* : nip it in the bud. *Precis Clin Med*. 2022;5(1):pbac004.
doi:10.1093/pcmedi/pbac004

136. Gilpin SE, Ren X, Okamoto T, *et al.* Enhanced lung epithelial specification of human induced pluripotent stem cells on decellularized lung matrix. *Ann Thorac Surg*. 2014;98(5):1721-1729.
doi:10.1016/j.athoracsur.2014.05.080

137. Guyette JP, Charest JM, Mills RW, *et al.* Bioengineering human myocardium on native extracellular matrix. *Circ Res*. 2016;118(1):56-72.
doi:10.1161/CIRCRESAHA.115.306874

138. Wan J, Huang Y, Zhou P, *et al.* Culture of iPSCs derived pancreatic β -like cells in vitro using decellularized pancreatic scaffolds: a preliminary trial. *BioMed Res Int.* 2017;2017:1-14.
doi:10.1155/2017/4276928

139. Yamanaka S. Pluripotent stem cell-based cell therapy—promise and challenges. *Cell Stem Cell*. 2020;27(4):523-531.
doi:10.1016/j.stem.2020.09.014

140. Bebiano LB, Presa R, Silva IV, Oliveira AL, Costa JB, Pereira RF. Design and bioprinting of decellularized extracellular matrix-based bioinks for skin tissue engineering. *J 3D Print Med*. 2023;7(4):3DP15. doi:10.2217/3dp-2023-0011

141. Vermeulen N, Haddow G, Seymour T, Faulkner-Jones A, Shu W. 3D bioprint me: a socioethical view of bioprinting human organs and tissues. *J Med Ethics*. 2017; 43(9):618-624. doi:10.1136/medethics-2015-103347

142. Government of Canada. Research Ethics Board: Overview of the Health Canada and Public Health Agency of Canada *REB*. Published April 5, 2024. Accessed June 21, 2025. https://www.canada.ca/en/health-canada/services/science-research/science-advice-decision-making/research-ethics-board.html

143. Grady C. Institutional review boards: purpose and challenges. *Chest*. 2015;148(5):1148-1155. doi:10.1378/chest.15-0706

144. European Commission. The Independent Ethical Committee. (n.d.). Accessed June 21, 2025. https://commission.europa.eu/about/service-standards-and-principles/ethics-and-good-administration/commissioners-and-ethics/independent-ethical-committee_en

145. Ricci G, Gibelli F, Sirignano A. Three-dimensional bioprinting of human organs and tissues: bioethical and medico-legal implications examined through a scoping review. *Bioengineering*. 2023;10(9):1052. doi:10.3390/bioengineering10091052

146. Chandra DK, Reis RL, Kundu SC, Kumar A, Mahapatra C. Nanomaterials-based hybrid bioink platforms in advancing 3D bioprinting technologies for regenerative medicine. *ACS Biomater Sci Eng*. 2024;10(7):4145-4174. doi:10.1021/acsbiomaterials.4c00166

147. Wan H, Xiang J, Mao G, Pan S, Li B, Lu Y. Recent advances in the application of 3D-printing bioinks based on decellularized extracellular matrix in tissue engineering. *ACS Omega*. 2024;9(23):24219-24235. doi:10.1021/acsomega.4c02847

148. Amirthalingam S, Rajendran AK, Moon YG, Hwang NS. Stimuli-responsive dynamic hydrogels: design, properties and tissue engineering applications. *Mater Horiz*. 2023;10(9):3325-3350. doi:10.1039/D3MH00399J

149. Rana MM, De La Hoz Siegler H. Evolution of hybrid hydrogels: next-generation biomaterials for drug delivery and tissue engineering. *Gels*. 2024;10(4):216. doi:10.3390/gels10040216

150. Dwijaksara NLB, Andromeda S, Rahmaning Gusti AW, Siswanto PA, Lestari Devi NLPM, Sri Arnita NP. Innovations in bioink materials and 3D bioprinting for precision tissue engineering. *Metta*. 2024;4(3):101-118. doi:10.37329/metta.v4i3.3520

151. Elkhoury K, Chen M, Koçak P, *et al.* Hybrid extracellular vesicles-liposome incorporated advanced bioink to deliver microRNA. *Biofabrication*. 2022;14(4):045008. doi:10.1088/1758-5090/ac8621

152. Quint JP, Mollocana-Lara E, Samandari M, Shin SR, Sinha I, Tamayol A. A robotic arm with open-source reconstructive workflow for *in vivo* bioprinting of patient-specific scaffolds. *Appl Phys Rev*. 2024;11(4):041402. doi:10.1063/5.0197123

153. Da Silva VA, Sharma R, Shteinberg E, *et al.* Machine learning approaches to 3D models for drug screening. *Biomed Mater Dev*. 2024;2(2):695-720. doi:10.1007/s44174-023-00142-4

154. Limon SM, Quigley C, Sarah R, Habib A. Advancing scaffold porosity through a machine learning framework in extrusion based 3D bioprinting. *Front Mater.* 2024; 10:1337485. doi:10.3389/fmats.2023.1337485

155. Mohammadrezaei D, Podina L, Silva JD, Kohandel M. Cell viability prediction and optimization in extrusion-based bioprinting via neural network-based Bayesian optimization models. *Biofabrication*. 2024;16(2):025016. doi:10.1088/1758-5090/ad17cf

156. Freeman S, Calabro S, Williams R, Jin S, Ye K. Bioink formulation and machine learning-empowered bioprinting optimization. *Front Bioeng Biotechnol.* 2022;10:913579. doi:10.3389/fbioe.2022.913579

ACCSCIENCE PUBLISHING

International Journal of Bioprinting

REVIEW ARTICLE

Bioprinting strategies for skeletal muscle regeneration: Advances in bioinks, technologies, and functional reconstruction

Xiaoguang Liu[1,2†], Miaomiao Xu[3,4†], Huiguo Wang[1,2], and Lin Zhu[1,5*]

[1]Department of Exercise Physiology, College of Sports and Health, Guangzhou Sport University, Guangzhou, Guangdong, China

[2]Key Laboratory of Exercise and Youth Physical Fitness, Research Center for Innovative Development of Sports and Healthcare Integration, Guangzhou Sport University, Guangzhou, Guangdong, China

[3]Department of Social Sports, College of Physical Education, Guangdong University of Education, Guangzhou, Guangdong, China

[4]Department of Sports Medicine, School of Physical Education and Health, Guangzhou University of Chinese Medicine, Guangzhou, Guangdong, China

[5]Department of Sports Training, Innovative Research Center for Sports Science in the Guangdong-Hong Kong-Macao Greater Bay Area, Guangzhou Sport University, Guangzhou, Guangdong, China

Abstract

Volumetric muscle loss (VML) presents a significant clinical challenge because the intrinsic regenerative capacity of skeletal muscle is insufficient to repair extensive defects, and current therapeutic strategies remain inadequate. Bioprinting has emerged as a transformative approach, enabling the spatially controlled deposition of cells, biomaterials, and biochemical cues to create functional, biomimetic muscle tissues. This review offers a comprehensive overview of recent advancements in bioink development, bioprinting technologies, and functional reconstruction strategies for skeletal muscle regeneration. Bioinks derived from natural, synthetic, and composite materials are examined in terms of their effectiveness in supporting myogenesis, promoting cellular alignment, and facilitating neurovascular integration. We compare key bioprinting techniques—including extrusion-based, inkjet, and laser-assisted printing—highlighting their respective strengths and limitations in achieving structural fidelity and multicellular complexity. Emerging technologies such as coaxial and microfluidic-assisted printing are also discussed for their potential to fabricate aligned, anisotropic muscle constructs with hierarchical architectures. Functional outcomes are synthesized from *in vitro* assays (e.g., contractility, gene expression) and *in vivo* studies using VML models, with a focus on vascularization, innervation, and force restoration. Despite significant progress, substantial challenges remain in achieving complete neurovascular integration, long-term functionality, and clinical scalability. Moving forward, future efforts should emphasize the development of dynamic, bioresponsive materials, integration with electrical and mechanical stimulation, and the establishment of standardized preclinical protocols. By bridging material innovation, structural design, and biological functionality, bioprinting holds great promise for next-generation, clinically relevant skeletal muscle regeneration.

Keywords: 3D bioprinting; Hydrogel bioinks; Muscle tissue engineering; Myogenesis; Regenerative medicine

†These authors contributed equally to this work.

***Corresponding author:**
Lin Zhu (11251@gzsport.edu.cn)

Citation: Liu X, Xu M, Wang H, Zhu L. Bioprinting strategies for skeletal muscle regeneration: Advances in bioinks, technologies, and functional reconstruction. *Int J Bioprint*. 2025;11(5):46-67. doi: 10.36922/IJB025300306

Received: July 25, 2025
Revised: August 7, 2025
Accepted: August 18, 2025
Published online: August 19, 2025

Copyright: © 2025 Author(s). This is an Open Access article distributed under the terms of the Creative Commons Attribution License, permitting distribution, and reproduction in any medium, provided the original work is properly cited.

Publisher's Note: AccScience Publishing remains neutral with regard to jurisdictional claims in published maps and institutional affiliations.

1. Introduction

Skeletal muscle is a highly regenerative tissue that relies on tissue-resident stem cells to repair damage after injury.[1–3] However, its intrinsic self-repair capacity becomes insufficient in the case of extensive damage, as observed in volumetric muscle loss (VML), which involves the loss of more than 20% of muscle mass.[4,5] Skeletal muscle injuries, especially VML, therefore represent a significant clinical challenge due to the limited regenerative capacity of adult muscle tissue when large-scale defects occur.[6,7] These injuries can result from trauma, tumor resection, congenital abnormalities, or degenerative diseases such as muscular dystrophies.[8–10] Traditional treatment approaches—including autologous muscle grafts, physical therapy, and pharmacological interventions—often lead to suboptimal outcomes, such as fibrosis, incomplete functional recovery, and donor site complications.[11–15] Therefore, there is a pressing need for bioengineered solutions that can restore both the structure and function of damaged skeletal muscle.

Bioprinting has emerged as a powerful technology in regenerative medicine by enabling the precise spatial deposition of cells, biomaterials, and biochemical signals to fabricate three-dimensional (3D), biomimetic tissue constructs.[16–18] In the context of skeletal muscle, successful regeneration requires not only the recreation of aligned, contractile myofibers but also the establishment of vascular and neural networks to ensure tissue viability and physiological functionality.[19–24]

However, despite growing interest and technological progress, several critical gaps remain unaddressed. Many existing studies report limited long-term contractile function, insufficient neurovascular integration, and poor scalability of printed constructs.[25–29] The lack of standardized bioink formulations that simultaneously support mechanical integrity, myogenic differentiation, and cellular viability also hinders reproducibility and clinical translation.[30,31] Moreover, functional evaluation metrics vary widely across studies, making cross-comparison and validation challenging.[32,33]

To address these limitations, this review offers a comprehensive and structured synthesis of recent advances in bioprinting strategies for skeletal muscle regeneration, with a unique focus on three interdependent pillars: (i) bioink development, (ii) bioprinting technologies, and (iii) functional reconstruction. Unlike previous reviews that emphasize materials or methods in isolation, this work integrates biological requirements, engineering innovations, and translational benchmarks into a cohesive framework. Finally, we propose future directions and design principles for developing next-generation muscle constructs with clinically relevant performance.

2. Methodology

This systematic review was conducted using a transparent, rigorous, and reproducible approach to ensure comprehensive coverage of recent studies on bioprinting strategies for skeletal muscle regeneration.

Relevant literature was retrieved from five major electronic databases: PubMed, Web of Science, Scopus, Embase, and Google Scholar, covering the period from January 1, 2020, to May 31, 2025. The search strategy combined Medical Subject Headings (MeSH) and free-text keywords related to bioprinting, skeletal muscle, regeneration, VML, bioinks, angiogenesis, and myogenesis. Where possible, searches were restricted to titles and abstracts, and only peer-reviewed, English-language publications were included.

The initial search yielded 528 records, distributed as follows: PubMed (n = 94), Web of Science (n = 82), Scopus (n = 88), Embase (n = 96), and Google Scholar (n = 168). After removing 128 duplicates, 400 unique articles remained for screening.

The inclusion criteria were as follows: (i) written in English and published in peer-reviewed journals; (ii) described original experimental studies or systematic/comprehensive reviews; (iii) focused explicitly on bioprinting approaches for skeletal muscle regeneration; and (iv) reported functional evaluations, either *in vitro* (e.g., contractility, myogenic differentiation markers) or *in vivo* (e.g., force generation, vascular integration). Studies were excluded if they: (i) did not pertain specifically to skeletal muscle (n = 38); (ii) lacked functional assessment of the bioprinted constructs (n = 50); (iii) did not involve bioprinting-specific methodologies (n = 37); or (iv) were not peer-reviewed, including conference abstracts and preprints (n = 31).

All articles were screened independently by two reviewers in a three-stage process: title, abstract, and full-text review. Any disagreements were resolved through discussion or adjudication by a third reviewer. The entire review process adhered to the Preferred Reporting Items for Systematic Reviews and Meta-Analyses guidelines. The detailed selection process is summarized in Figure 1.

To enable transparent cross-study comparisons, we systematically extracted and organized core methodological parameters from each included study into Table S1. Specifically, five key items were documented per study: (i) experimental design (e.g., rat VML model, *in vitro* aligned 3D constructs, neuromuscular junction models);

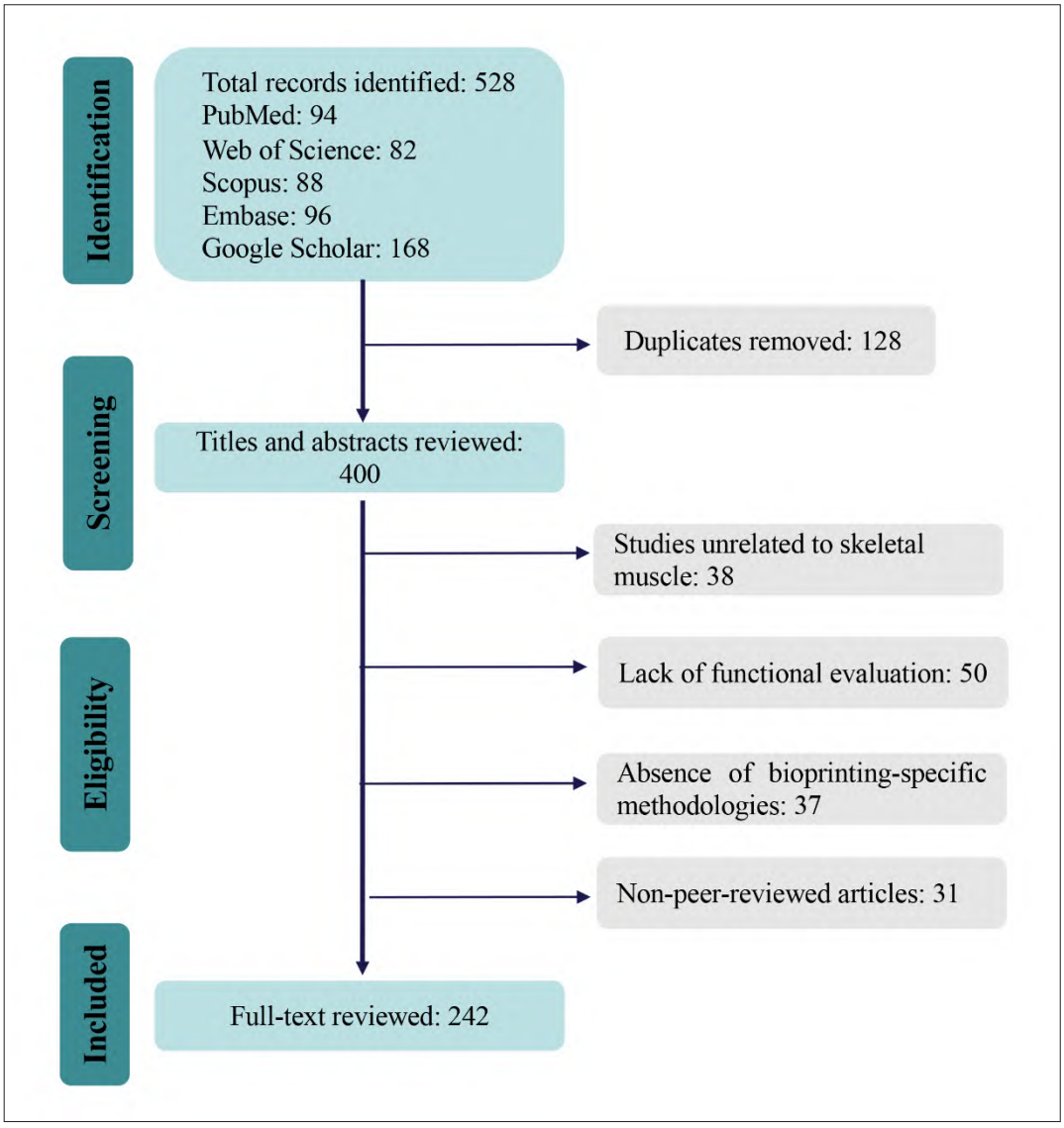


Figure 1. Preferred Reporting Items for Systematic Reviews and Meta-Analyses flow diagram illustrating the identification, screening, eligibility assessment, and inclusion of studies.

(ii) primary scaffold or bioink formulation; (iii) species or cell line used; (iv) reported outcome metrics such as tetanic force, viability, vascularization, calcium transients, or neuromuscular junction formation; and (v) a reference ID (Ref_No) corresponding to our main reference list. Among the included studies, collagen/ extracellular matrix (ECM)-based hydrogels were the most common materials (33%), followed by gelatin methacrylate (GelMA) composites (21%). Rodent models remained the dominant *in vivo* systems, with rats and mice representing 28% and 17% of studies, respectively, while 26% employed human-derived cells for *in vitro* applications. Functional evaluations were distributed across five principal readouts: contractile force (46%), viability or metabolic activity (38%), vascularization (24%), electrophysiology or calcium imaging (19%), and neuromuscular junction formation (12%). This structured extraction enabled consistent cross-study synthesis and highlighted current trends in the design and evaluation of bioprinted skeletal muscle constructs.

3. Structural and biological foundations of skeletal muscle regeneration

Skeletal muscle exhibits a highly organized and hierarchical structure that is essential for its contractile and metabolic functions.[34,35] It consists of parallel arrays of multinucleated myofibers, embedded within an ECM and

enclosed by connective tissue layers.[36] This architecture enables directional force transmission and mechanical stability.[37,38] Surrounding the muscle fibers is a dense network of blood vessels and peripheral nerves, which are critical for oxygen and nutrient delivery, as well as neuromuscular coordination.[39–41] The anisotropic and compartmentalized nature of skeletal muscle presents unique design requirements that must be recapitulated in tissue-engineered constructs.[42]

Endogenous skeletal muscle regeneration is a tightly regulated, multistep process involving both resident and recruited cell populations.[13,43,44] Upon injury, an initial inflammatory phase activates quiescent satellite cells—the primary muscle stem cells—which then proliferate, differentiate, and fuse to form new myotubes.[1,3,45–47] Concurrently, macrophages coordinate tissue clearance and remodeling, while vascular endothelial cells initiate angiogenic processes to re-establish perfusion.[43,44,48–50] Motor neurons gradually reconnect with regenerating fibers to restore neuromuscular junctions and functional innervation.[51,52] This dynamic interplay among myogenic, vascular, and neural elements underscores the integrated nature of functional muscle repair (Figure 2).

4. Engineering strategies: design principles and bioink optimization

4.1. Design requirements for functional muscle constructs

The complexity of skeletal muscle regeneration defines a rigorous set of criteria for tissue engineering.[53,54] Foremost

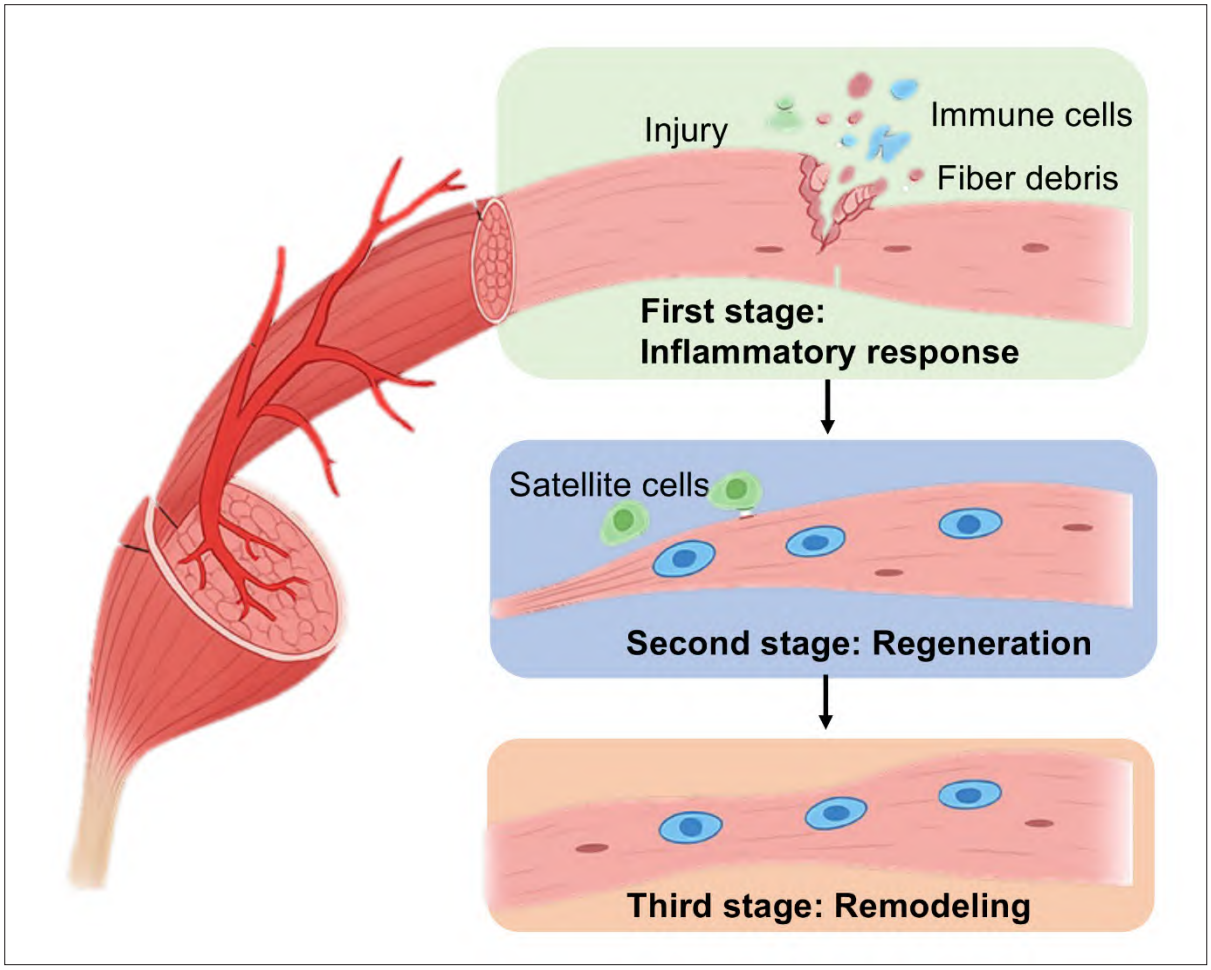


Figure 2. Schematic illustration of native skeletal muscle structure and regenerative phases. This figure depicts the multistep process of skeletal muscle regeneration following injury. On the left, the architecture of native skeletal muscle is shown, including aligned muscle fibers, motor neurons, and surrounding capillaries. The first stage illustrates the inflammatory response, with immune cells clearing debris from damaged fibers. The second stage represents satellite cell activation, proliferation, and differentiation into new myogenic cells. The third stage demonstrates tissue remodeling and regeneration, during which new muscle fibers mature and re-establish functional architecture. This integrated process highlights the dynamic interplay between myogenic, vascular, and neural components essential for muscle repair.

is the recreation of aligned, contractile myofibers capable of generating directional force, necessitating control over cellular orientation and myotube maturation.[55] Equally important is the establishment of a perfusable vascular network to ensure long-term tissue viability, particularly in constructs exceeding the diffusion limit.[56,57] Reinnervation is essential for restoring physiological control, as neuromuscular junctions enable stimulus-responsive contraction.[58,59] In addition, mechanical properties must approximate native muscle elasticity to support load-bearing functionality.[60,61] These multidimensional requirements highlight the need for integrative approaches that combine biological fidelity with structural and mechanical optimization.

The complex architecture and function of skeletal muscle demand bioprinting strategies with high spatial and compositional precision.[19,62] Conventional scaffold-based approaches fail to replicate the anisotropic structure and cellular heterogeneity of native muscle.[63,64] In contrast, bioprinting enables the fabrication of constructs with programmable architecture, controlled cell alignment, and multi-lineage distribution.[65]

To fulfill biological requirements, bioinks must: (i) support myogenic differentiation; (ii) promote cellular alignment; (iii) facilitate vascularization and innervation; and (iv) maintain print fidelity and mechanical integrity.[19,21,23,66–70] Emerging techniques such as coaxial extrusion and microfluidic-assisted printing offer new avenues for producing biomimetic muscle tissues with improved structural and functional fidelity.[71,72] These considerations inform the rational design of next-generation bioprinted muscle constructs, as elaborated in the following sections.

4.2. Bioink formulation and material strategies

The development of bioinks is central to advancing skeletal muscle bioprinting, as it directly influences printability, biocompatibility, cellular behavior, and tissue maturation.[66,73] Muscle-specific bioinks must achieve not only high-resolution patterning but also recreate the biochemical and mechanical cues essential for myogenesis, vascularization, and innervation.[19,23,74,75] Recent studies have focused on tailoring bioink formulations through variations in material origin, tuning of mechanical properties, incorporation of biological factors, and the integration of functional enhancers to improve construct performance.[76,77]

Natural biomaterials such as GelMA, collagen, fibrin, and decellularized extracellular matrix (dECM) have been widely used due to their intrinsic bioactivity and ability to support myogenic differentiation.[78–82] GelMA, for instance, offers tunable stiffness and excellent printability, while retaining bioactive motifs that promote myoblast adhesion and proliferation.[83] Collagen and fibrin closely mimic the native ECM, supporting myotube formation and initial alignment.[84]

Decellularized skeletal muscle-derived ECM provides an even more tissue-specific biochemical milieu, including preserved muscle-specific growth factors and ECM proteins.[85] However, these materials often suffer from low mechanical integrity, rapid degradation, and batch-to-batch variability, limiting their applicability in load-bearing muscle constructs.[86]

Regulatory and manufacturing hurdles remain significant for dECM-based bioinks. Because dECM is procured from animal or human tissues, each batch carries inherent donor-to-donor variability in biochemical composition, residual DNA, and mechanical properties, which can translate into inconsistent cell-fate outcomes after printing.[87] Lot-to-lot testing, therefore, must extend beyond sterility and endotoxin assays to include quantitative proteomics, glycosaminoglycan content, and rheological fingerprints.[88] From a regulatory standpoint, the United States Food and Drug Administration (FDA) typically considers cell-laden dECM constructs as combination products and applies both medical device (21 CFR 820) and biologics (21 CFR 1271) requirements, whereas the European Medicines Agency (EMA) classifies them as advanced-therapy medicinal products (ATMPs) that must satisfy Good Manufacturing Practice (GMP) Annex 1 and ISO 22442 for animal-derived materials. These frameworks mandate traceable sourcing, validated decellularization/viral inactivation, and release criteria that demonstrate batch equivalence in safety, sterility, and functional potency. Meeting such standards at scale remains challenging, particularly when kilogram-scale dECM is required for large human grafts. Emerging solutions include: (i) pooled donor lots combined with statistical process control; (ii) in-line Raman or Fourier transform infrared spectroscopy for real-time compositional monitoring; and (iii) hybrid bioinks that blend dECM with synthetic polymers to buffer mechanical variability while retaining bioactivity.[89]

Synthetic polymers such as polycaprolactone (PCL), polyethylene glycol diacrylate (PEGDA), and polylactic acid offer superior mechanical properties and slower degradation kinetics.[90–92] These materials can provide structural scaffolding for large-volume muscle defects and allow for complex construct shaping during printing.[93]

Nevertheless, synthetic bioinks are generally biologically inert, requiring surface modification (e.g., RGD peptide grafting, plasma treatment) or blending with bioactive components to promote cell adhesion and

differentiation.[94–97] Furthermore, their high stiffness may hinder myotube elongation and reduce cell viability unless carefully tuned.[67]

To overcome the inherent limitations of single-component bioinks, composite systems that integrate both natural and synthetic polymers have been extensively developed.[97–101] These formulations combine the bioactivity of natural materials with the mechanical strength of synthetic polymers, facilitating improved structural integrity while maintaining cellular compatibility and functionality.[101–103] Representative combinations, such as GelMA with PCL or fibrin with PCL, demonstrate enhanced stability under physiological conditions alongside support for tissue-specific cellular processes.[104–107] Similarly, PEGDA blended with collagen improves shape fidelity without sacrificing biocompatibility.[108,109]

These composite systems can be further optimized through tailored crosslinking methods, tunable stiffness, and spatial gradient structuring to address region-specific functional demands within engineered muscle tissue.[110,111] Softer matrix regions may be designed to promote myofiber alignment and maturation, while stiffer domains can serve as anchorage sites or load-bearing compartments, thereby enabling the construction of physiologically relevant muscle architectures.[112]

4.3. Smart bioinks and translational considerations

Incorporating bioactive molecules into bioinks has emerged as a key strategy to enhance muscle regeneration.[113,114] For instance, insulin-like growth factor-1 (IGF-1) accelerates myogenic differentiation, vascular endothelial growth factor promotes angiogenesis, and nerve growth factor supports reinnervation.[115–118] Simultaneously, nanomaterials such as gold nanoparticles, graphene oxide, and carbon nanotubes have been explored to improve electrical conductivity, cellular alignment, and mechanical reinforcement.[119–124] These additives can facilitate neuromuscular signal transmission and promote the maturation of engineered myotubes.[125,126] More recently, electrically conductive hydrogels incorporating materials such as polypyrrole or poly(3,4-ethylenedioxyt hiophene):polystyrene sulfonate have shown promise in enabling stimulus-responsive behavior, which is essential for restoring muscle contractile function.[127,128]

The field is witnessing a shift toward 4D bioinks, which undergo dynamic changes in response to stimuli such as temperature, pH, enzymes, or electrical input.[80,129,130] Such smart bioinks can simulate the adaptive behavior of native muscle, enabling constructs to respond to mechanical loading or neural cues in a physiologically relevant manner.[19,131,132] Additionally, advances in microfluidic-based mixing, multi-phase emulsions, and shear-thinning formulations are enabling the generation of heterogeneous bioinks capable of spatial patterning, gradient generation, and multi-cell co-printing—crucial for recapitulating the compartmentalized structure of skeletal muscle.[71,133–137] A comparative summary of representative bioinks, along with their advantages and limitations, is provided in Table 1.

While substantial progress has been made in developing muscle-specific bioinks, key challenges remain.[139] These include improving long-term stability, vascular permeability, and standardization for reproducibility.[23,74] Future efforts should focus on developing modular, tunable

Table 1. Summary of representative bioinks used in skeletal muscle bioprinting

Bioink type	Advantages	Limitations	References
Natural (GelMA, collagen, fibrin, dECM)	High bioactivity; promotes myogenesis; tissue-specific signals	Poor mechanical strength; variability; fast degradation	[31,79]
Synthetic (PCL, PEGDA, PLA)	Strong mechanical properties; slow degradation	Low bioactivity; needs modification; may reduce viability	[91,92]
Composite (GelMA + PCL, PEGDA + Collagen)	Combines bioactivity and mechanical strength; tunable	Complex preparation; potential crosslinking issues	[99,103]
Biofunctional (with IGF-1, VEGF, NGF)	Enhances differentiation, angiogenesis, and innervation	Dose control; short half-life; potential toxicity	[115,138]
Nanomaterial-enhanced (CNTs, GO, AuNPs)	Improves conductivity, alignment, mechanical reinforcement	Stability; dispersibility; possible immune reactions	[121,124]
4D/stimuli-responsive	Dynamic response to stimuli; mimics physiological behavior	Immature technology; complex fabrication	[130,131]

Abbreviations: AuNPs, gold nanoparticles; CNTs, carbon nanotubes; dECM, decellularized extracellular matrix; GelMA, gelatin methacrylate; GO, graphene oxide; IGF-1, insulin-like growth factor-1; NGF, nerve growth factor; PCL, polycaprolactone; PEGDA, polyethylene glycol diacrylate; PLA, polylactic acid; VEGF, vascular endothelial growth factor.

bioink libraries that can be tailored to patient-specific needs and integrated with real-time monitoring systems for adaptive printing.

Combining biological complexity, mechanical integrity, and functional responsiveness in a single bioink platform will be critical to advancing the clinical translation of skeletal muscle bioprinting.[20,26]

5. Bioprinting strategies, functional validation, and future directions

The fabrication of functional skeletal muscle tissue requires bioprinting approaches capable of replicating its complex anisotropic architecture, multicellular composition, and dynamic responsiveness.[20,110,140] Different bioprinting modalities offer varying degrees of spatial control, resolution, and material compatibility. This section systematically reviews both conventional and emerging bioprinting technologies, with a focus on their applicability to muscle tissue engineering.[141,142] Figure 3 illustrates a representative workflow of skeletal muscle bioprinting, encompassing cell selection, bioink preparation, construct fabrication, and post-printing maturation.

5.1. Bioprinting platforms and construct design

Bioprinting of skeletal muscle constructs leverages several key platforms, each offering unique advantages and limitations. Among them, extrusion-based bioprinting is the most widely adopted, enabling the deposition of high-viscosity, cell-laden bioinks that support fiber alignment—essential for restoring contractility—despite challenges related to resolution and cell shear stress.[71,140,143–150] Inkjet bioprinting provides high precision and rapid droplet-based patterning, making it suitable for growth factor distribution or single-cell placement; however, it is limited by ink viscosity and potential thermal or mechanical stress on cells.[151–159] Laser-assisted bioprinting, particularly laser-induced forward transfer, offers excellent resolution and cell viability for microscale patterning of neural or vascular cells, though it remains costly and technically demanding.[160–163] Emerging platforms such as coaxial extrusion and microfluidic-assisted bioprinting have expanded the design space by enabling spatially organized, perfusable structures and real-time control of bioink composition, providing new opportunities for muscle tissue engineering.[110,164–169] Digital light processing bioprinting employs photopolymerization via patterned

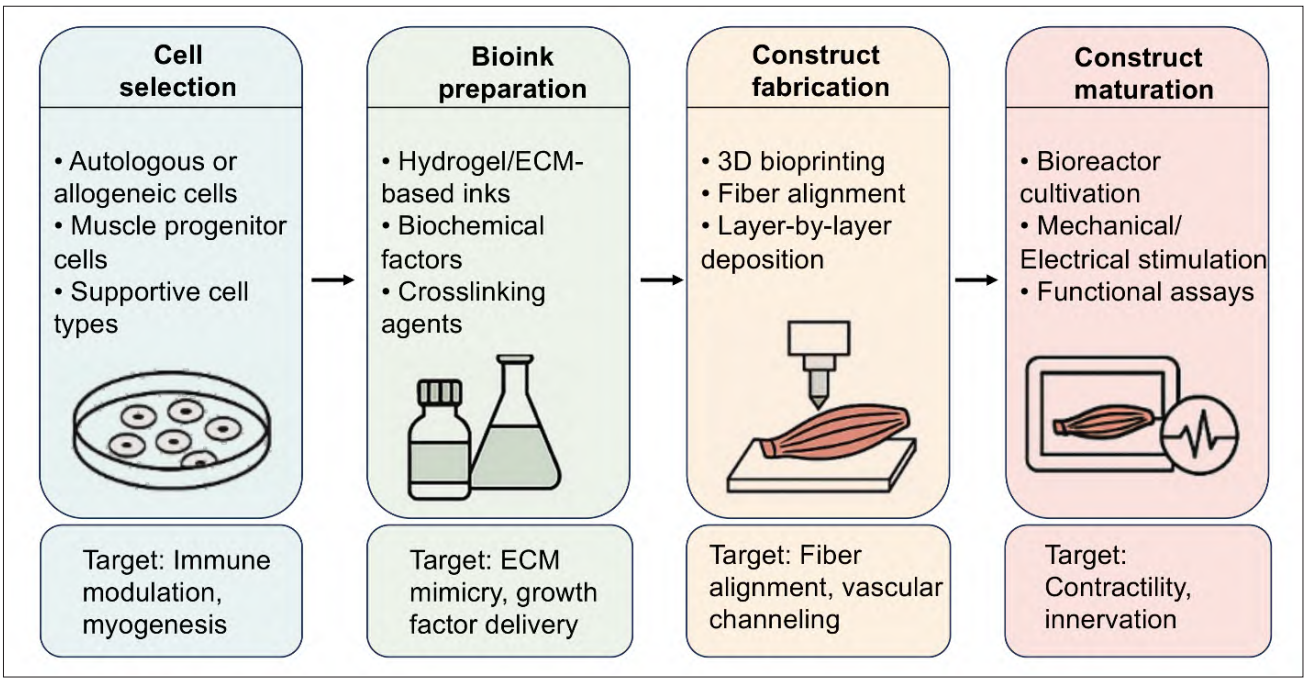


Figure 3. Workflow of skeletal muscle bioprinting, from cell selection to construct maturation. The process includes four key stages: (i) Cell selection—autologous or allogeneic cells, including muscle progenitor and supportive cell types; (ii) Bioink preparation—hydrogel/ extracellular matrix (ECM)-based inks supplemented with biochemical cues and crosslinking agents to mimic the native muscle microenvironment; (iii) Construct fabrication—3D bioprinting (e.g., extrusion-based) to enable fiber alignment and layer-by-layer deposition; (iv) Construct maturation—bioreactor culture, mechanical/ electrical stimulation, and functional assays to promote tissue development and contractility. Each stage is annotated with corresponding biological targets—such as immune modulation, myogenesis, ECM mimicry, fiber alignment, and functional restoration—to emphasize the alignment between engineering strategies and regenerative outcomes.

light exposure, supporting rapid fabrication of high-resolution, multilayered constructs when paired with suitable photo-crosslinkable bioinks.[170,171] These advanced modalities collectively enhance spatial resolution, cell viability, and structural complexity, enabling the creation of muscle tissues with improved biomimetic features.[172] To better contextualize the strengths and limitations of each bioprinting platform, Table 2 provides a comparative overview of key parameters relevant to skeletal muscle tissue engineering applications.

Achieving physiological function in engineered skeletal muscle constructs requires not only structural accuracy but also cellular alignment and maturation.[138,177] Multiple strategies have been implemented to guide fiber orientation and promote myogenic differentiation post-printing.[76,178] The application of electrical or magnetic fields has been shown to direct cytoskeletal alignment and enhance the expression of myogenic genes.[179,180] Topographical patterning through microgrooved substrates or surface templating can guide cell alignment by providing physical cues that mimic the native ECM architecture.[181] Additionally, dynamic culture in bioreactors—applying cyclic mechanical stretching or electrical stimulation—significantly improves sarcomere organization, contractile function, and metabolic activity in engineered muscle tissues.[182] These adjunctive techniques are often integrated during the post-printing phase and are critical for transforming printed constructs into physiologically responsive muscle analogs.

To facilitate clinical translation, muscle constructs must be scalable, vascularizable, and compatible with host integration.[183] Key design considerations include the incorporation of perfusable microchannels or sacrificial templates to overcome diffusion limitations in thick tissues, as well as the spatial organization of myogenic, endothelial, and neural cells to replicate the hierarchical structure of native muscle.[19,56]

Moreover, the selected printing modality must align with downstream processing requirements such as in situ bioprinting, bioreactor conditioning, or integration with wearable bioelectronics.[184–186] Regulatory considerations, including batch consistency, sterilizability, and manufacturing scalability, must also be addressed early in the design process.[187,188] Through the integration of advanced bioprinting platforms and biologically informed design strategies, skeletal muscle constructs can increasingly approach clinical-grade complexity and functionality.

A critical step in validating engineered skeletal muscle constructs is the rigorous assessment of their biological functionality.[189] Both *in vitro* and *in vivo* evaluations are essential to determine the myogenic potential, integration capability, and regenerative efficacy of bioprinted tissues.[19,59,138] The following sections review current

Table 2. Comparative analysis of bioprinting technologies for skeletal muscle engineering

Bioprinting Technology	Spatial resolution (μm)	Post-print cell viability (%)	Bioink compatibility	Advantages	Limitations	References
Extrusion-based	~ 100–400 (typical); best 105 ± 9	No significant effect	High-viscosity, cell-laden inks	Widely used; supports cell-laden viscous inks; good for fiber alignment	Low resolution; potential cell shear stress	140,158,143,145,148
Inkjet-based	20–50	85–98	Low-viscosity, low-cell-density	High precision; low cost; ideal for growth factor or cell patterning	Not suitable for viscous or dense inks	153,156,157
Laser-assisted	<10	90–100	Moderate viscosity, specialized formulation	High resolution and cell viability; precise droplet placement	High cost and complexity; limited ink options	160,161,173
Coaxial extrusion	~100	≥80	Multi-material, core–shell inks	Enables aligned fiber and vessel-like channels; supports multi-phase structures	Complex nozzle setup; scalability challenges	174,165,164
Microfluidic-assisted	50–100	85–95	Gradient or multi-cell bioinks	Fine control of mixing and gradients; spatial patterning	Requires precise flow control; complex setup	167–169,175
Digital light processing	10–50	80–93	Photocrosslinkable bioinks	High speed and resolution; enables complex shape fabrication	Limited bioink options; potential phototoxicity	176

methodologies for functional testing and summarize key outcomes from preclinical models.

5.2. *In vitro* evaluation of engineered muscle

In vitro testing provides initial insights into the viability, differentiation, and contractile behavior of printed muscle constructs.[20,177,190,191] To evaluate post-printing cytocompatibility, cell viability is commonly assessed via live/dead staining, metabolic activity assays such as 3-(4,5-dimethylthiazol-2-yl)-2,5-diphenyltetrazolium bromide or Alamar Blue, and proliferation marker analysis.[192–194]

Myogenic differentiation is evaluated through the expression of lineage-specific markers such as myoblast determination protein 1, myogenin, and myosin heavy chain, using techniques like quantitative polymerase chain reaction, immunofluorescence, and western blotting.[195,196] Alignment and fusion of myoblasts into multinucleated myotubes are considered indicative of successful myogenic maturation.[177]

Functional assessment includes calcium imaging to detect intracellular calcium transients associated with contraction, as well as force generation analysis via electrical stimulation.[177,197,198] These assays provide important indicators of sarcomere formation, excitation–contraction coupling, and overall muscle construct performance at the cellular level.

In addition to assessing regenerative potential, 3D-bioprinted skeletal muscle is now deployed as a human, disease-relevant test-bed. When muscle progenitors isolated from Duchenne muscular dystrophy patients are printed into aligned, contractile bundles, the tissues faithfully reproduce sarcolemmal fragility, reduced twitch force, impaired myotube maturation, and profibrotic extracellular-matrix deposition—hallmarks of the *in vivo* pathology.[199,200] These patient-specific constructs furnish a scalable alternative to animal models for high-throughput screening. "Myobundles" engineered from healthy adult cells hypertrophy in response to IGF-1, yet atrophy after glucocorticoid exposure, mirroring clinical drug responses, while the same platform has recently revealed taxane-induced myotoxicity mechanisms.[201,202] Integrating stretchable piezoresistive hydrogel networks or optogenetic actuators enables non-invasive, real-time monitoring of force generation, calcium transients, and fatigue during pharmacological challenges, further expanding analytical throughput.[203,204] In parallel, Loi *et al.*[205] have designed a bioprinting-integrated cyclic-stretch bioreactor that markedly enhances myogenic maturation of printed constructs. By uniting structural fidelity, patient specificity, and dynamic biosensing, bioprinted skeletal muscle platforms are rapidly maturing into versatile tools for mechanistic discovery and translational drug development.

5.3. *In vivo* validation and translational considerations

Preclinical validation of bioprinted skeletal muscle constructs predominantly relies on VML models, most commonly established in rodents.[198,206] These models involve the surgical excision of a critical volume of muscle tissue that cannot regenerate spontaneously, thereby simulating clinical scenarios such as trauma or tumor resection.[207–209]

Implanted constructs are evaluated for their capacity to integrate with host tissue, restore morphology, and re-establish vascular and neural connections.[59,210] Histological staining, such as hematoxylin and eosin, Masson's trichrome, and immunolabeling of endothelial and neural markers, is used to assess structural integration, fibrosis, and cell fate.[183,211] Functional recovery is measured through a combination of force output testing, typically via *in situ* or *ex vivo* muscle contractility assays, and behavioral metrics such as gait analysis, limb drag, or treadmill performance.[212–215] Electrophysiological testing is also employed to assess neuromuscular junction formation and stimulus-responsive contraction.[206,216] While these models provide crucial data, inter-study variability in defect size, implantation methods, evaluation timelines, and functional benchmarks remains a challenge for reproducibility and translational extrapolation.[14,115,217,218]

Recent studies have reported encouraging results in which bioprinted constructs incorporating aligned myotubes, vascular endothelial cells, and neurogenic components have achieved partial restoration of muscle structure and function. Constructs with hierarchical alignment and prevascularization show improved integration and a reduced fibrotic response.[138,210,219,220] Despite these advancements, complete functional restoration equivalent to native muscle remains elusive. Challenges include insufficient long-term innervation, limited mechanical strength, immune responses in immunocompetent models, and a lack of contractile endurance over time.[12,221–223] Additionally, the absence of standardized protocols for assessing recovery makes cross-study comparisons difficult.[224]

To address these limitations, emerging research is focusing on dynamic *in vitro* maturation platforms, humanized animal models, and long-term follow-up protocols that better emulate clinical scenarios.[225] Furthermore, integration with biosensors and real-time monitoring tools is expected to enhance functional readouts and accelerate clinical readiness.[226] Recent advances in large-animal studies further enhance

translational relevance. For example, bioprinted skeletal muscle constructs larger than 3 cm^3, implanted in rabbits and mini-pigs, have restored 55–70% of tetanic force and demonstrated macroscopically evident vascular and neuromuscular integration.[227,228] In parallel, perfused human muscle slices and patient-derived myobundles have maintained contractile and electrophysiological function for more than 28 days *in vitro*, providing medium-throughput platforms for drug screening and personalized therapy evaluation.[229] Collectively, these two tiers of validation—large-animal functional recovery and human-relevant *in vitro* analytics—align with ISO 10993-6 and ASTM F3224 guidelines, thereby reducing translational risk and meeting key regulatory expectations for first-in-human applications.

6. Future directions and translational outlook

6.1. Multi-tissue integration for physiological fidelity

Bioprinting has significantly advanced our ability to engineer biomimetic skeletal muscle tissues; however, several formidable challenges continue to constrain clinical translation. Current constructs, while demonstrating partial functional restoration in preclinical models, often fail to achieve comprehensive neurovascular integration, sustained mechanical and contractile performance, and long-term tissue remodeling under physiological conditions.[28,230,231] In addition, variability in cell sources, bioink compositions, and assessment protocols hinders cross-study comparability and reproducibility.

From a technical perspective, scale-up manufacturing remains a critical bottleneck.[232] Translating microscale constructs into clinically relevant dimensions demands novel strategies to ensure structural fidelity, cell viability, and mass transport in thicker tissues.[19,20] Moreover, standardized functional benchmarks—including force generation, fatigue resistance, and neuromuscular responsiveness—are urgently needed to facilitate regulatory approval and interlaboratory validation.[205]

6.2. High-throughput functional analytics and artificial intelligence

Emerging technologies are reshaping the landscape of muscle bioprinting. Four-dimensional (4D; time-responsive) bioprinting, which enables time-responsive structural transformations, holds promise for generating constructs capable of dynamic adaptation to biomechanical and biochemical cues *in vivo*—mimicking developmental myogenesis or injury-induced remodeling.[205] Simultaneously, artificial intelligence (AI) and machine learning are revolutionizing design and optimization, offering predictive tools for bioink formulation, anisotropic print path design, and functional outcome modeling.[233,234] Coupled with high-throughput pipelines, AI-guided systems can reduce empirical iterations and accelerate progress toward clinically viable constructs.[235,236] Figure 4 illustrates an integrated, future-oriented muscle bioprinting system that incorporates these emerging components into a unified pipeline.

Integration with bioelectronic and rehabilitation interfaces marks another promising direction. Implantable sensors, neuromuscular stimulators, and stretchable electrodes can establish closed-loop feedback systems to enhance post-implantation adaptation, monitor inflammation, and track host–graft interactions in real time.[237,238] Looking ahead, next-generation muscle bioprinting platforms will likely converge on modular, patient-specific solutions integrating smart biomaterials, autologous or gene-edited cells, and tunable microenvironments.[239] These platforms must not only replicate muscle structure but also support immune compatibility, long-term remodeling, and adaptive rehabilitation.[20] To achieve clinical translation, the field must shift toward standardized, scalable, and regulatory-compliant protocols, enabled by close collaboration across materials science, bioengineering, and clinical disciplines.[188]

6.3. Clinical translation: trials, regulation, and scalability

Despite preclinical success, no skeletal muscle bioprinting trial has yet been initiated in a clinical setting; a recent scoping review found only 11 registered bioprinting studies worldwide, all targeting other tissues.[240] In most jurisdictions, printed, cell-laden muscle grafts will be regulated as combination products (FDA: Technical Considerations for Additive Manufactured Medical Devices, 2021) or as ATMPs (EMA: Regulation (EC) No. 1394/2007 on ATMPs), demanding rigorous demonstration of safety, potency, and manufacturing consistency. Key scalability bottlenecks—including kilogram-scale cell sourcing, perfusable vascular/neuronal networks, closed-loop GMP bioprinting, and cost-effective bioink standardization—remain unresolved.[188] Addressing these intertwined clinical, regulatory, and manufacturing challenges will be critical for moving bioprinted skeletal-muscle constructs from bench to bedside.

7. Conclusion

Bioprinting has rapidly evolved into a transformative strategy for skeletal muscle regeneration, enabling the precise construction of spatially organized, biologically functional, and structurally aligned muscle tissues. Recent

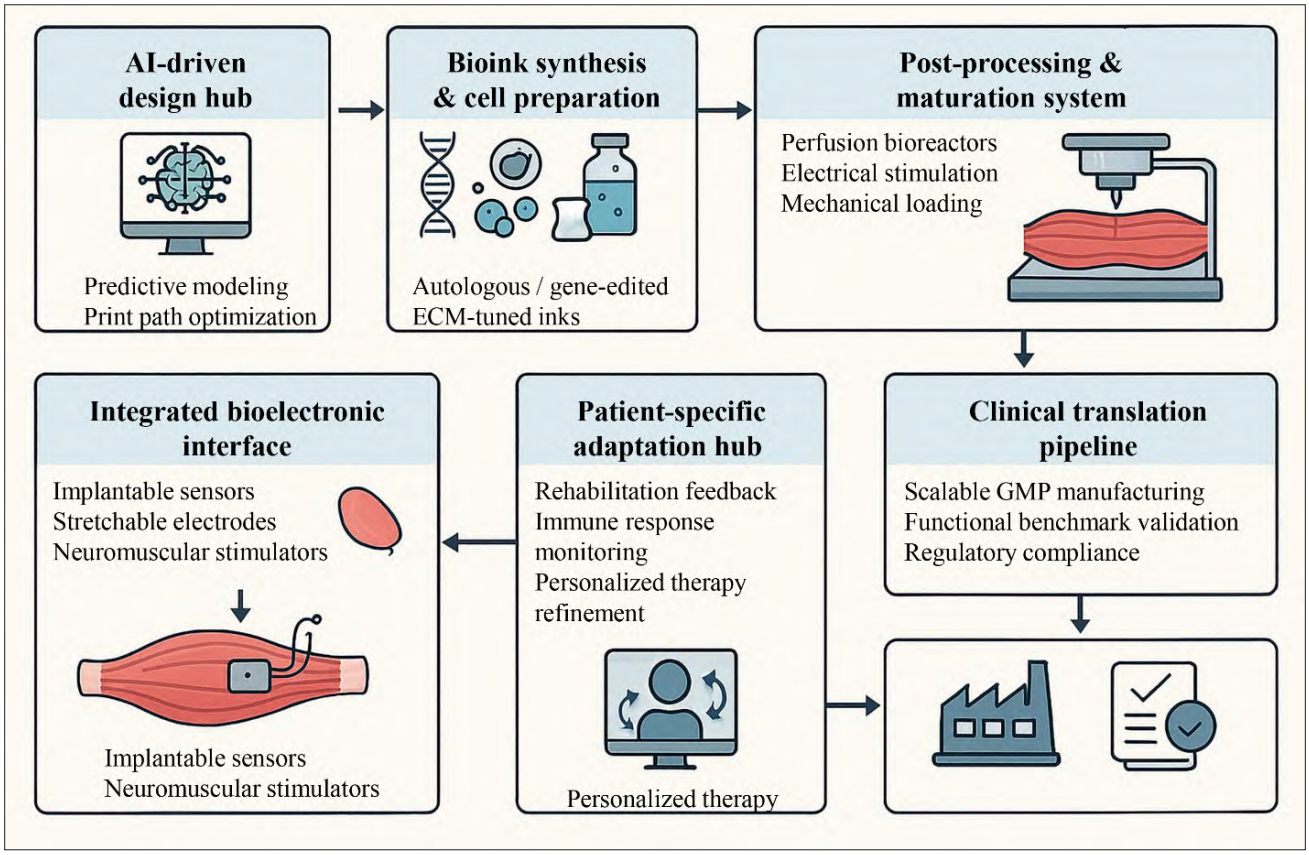


Figure 4. Conceptual illustration of an integrated future-oriented muscle bioprinting system. The diagram outlines a modular workflow integrating AI-guided design, smart bioink and cell preparation, 3D/4D bioprinting, and post-printing maturation. Key components include bioelectronic interfaces for real-time monitoring, patient-specific adaptation hubs, and a clinical translation pipeline supporting scalable, regulatory-compliant manufacturing. This system highlights the convergence of emerging technologies toward personalized, functional skeletal muscle regeneration. Abbreviations: AI, artificial intelligence; ECM, extracellular matrix; GMP, good manufacturing practice.

advances in biomaterials science, cellular engineering, and printing technologies have significantly enhanced the fidelity and functionality of engineered muscle constructs. However, several substantial challenges remain, particularly the achievement of full neurovascular integration, functional restoration comparable to native tissues, and the development of scalable manufacturing processes for clinical application. These challenges highlight the need for standardized evaluation protocols, robust bioink formulations, and interdisciplinary design principles that integrate biology, mechanics, and architecture. Future research must focus on developing dynamic, bioresponsive systems capable not only of replicating structural anisotropy but also of interacting with host physiology in a feedback-responsive manner. The integration of 4D bioprinting, machine learning-based optimization, and electromechanical stimulation technologies will be critical for advancing personalized and adaptive muscle repair strategies. By aligning material innovation with clinical needs, skeletal muscle bioprinting is poised for clinical translation. Continued cross-disciplinary collaboration will be essential in transforming current proof-of-concept studies into standardized, regulatory-compliant, and patient-specific therapies, ultimately revolutionizing the field of musculoskeletal regenerative medicine.

Acknowledgments

None.

Funding

This work was supported by the New type of Regular Higher Education Institutions Think Tanks in Guangdong Province (grant number: 2024TSZK017 to LZ); the National Natural Science Foundation of China (grant number: 32300964 to XL); the Guangdong Basic and Applied Basic Research Foundation (grant number: 2022A1515111105 to XL); the Guangdong Provincial Sports Bureau 2024–2025 Science and Technology

Innovation and Sports Culture Development Research Project (grant number: GDSS2024N010 to MX), and the 2025 First-Class Discipline Capacity Enhancement Project in Sports Science ("Guben" Program), Guangzhou University of Chinese Medicine (No. 7 to MX).

Conflict of interest

The authors declare they have no competing interests.

Author contributions

Conceptualization: Xiaoguang Liu, Miaomiao Xu
Data curation: Xiaoguang Liu, Miaomiao Xu
Formal analysis: Miaomiao Xu
Funding acquisition: Xiaoguang Liu, Lin Zhu, Miaomiao Xu
Investigation: Huiguo Wang, Lin Zhu
Methodology: Xiaoguang Liu
Visualization: Huiguo Wang
Writing–original draft: Miaomiao Xu
Writing–review & editing: Xiaoguang Liu, Huiguo Wang

Ethics approval and consent to participate

Not applicable.

Consent for publication

Not applicable.

Availability of data

Not applicable.

References

1. Relaix F, Bencze M, Borok MJ, *et al*. Perspectives on skeletal muscle stem cells. *Nat Commun*. 2021;12(1):692. doi: 10.1038/s41467-020-20760-6
2. Judson RN, Rossi FMV. Towards stem cell therapies for skeletal muscle repair. *NJP Regen Med*. 2020;5(1):10. doi: 10.1038/s41536-020-0094-3
3. Sousa-Victor P, García-Prat L, Muñoz-Cánoves P. Control of satellite cell function in muscle regeneration and its disruption in ageing. *Nat Rev Mol Cell Bio*. 2022;23(3):204-226. doi: 10.1038/s41580-021-00421-2
4. Qi L, Zhang F, Wang K, *et al*. Advancements in skeletal muscle tissue engineering: Strategies for repair and regeneration of skeletal muscle beyond self-repair. *Regen Biomater*. 2025;12:rbaf050. doi: 10.1093/rb/rbaf050
5. Maimaiti D, Ge X, Wang C, *et al*. Extracellular matrix-mimicking cryogels composed of methacrylated fucoidan enhance vascularized skeletal muscle regeneration following volumetric muscle loss. *Int J Biol Macromol*. 2024;283:137122. doi: 10.1016/j.ijbiomac.2024.137122
6. Sonaye SY, Sikder P. Bioengineered constructs as a tissue engineering-based therapy for volumetric muscle loss. *Tissue Eng Part B Rev*. 2025. doi: 10.1089/ten.teb.2025.0017
7. Cai CW, Grey JA, Hubmacher D, Han WM. Biomaterial-based regenerative strategies for volumetric muscle loss: challenges and solutions. *Adv Wound Care*. 2025;14(3):159-175. doi: 10.1089/wound.2024.0079
8. Edouard P, Reurink G, Mackey AL, *et al*. Traumatic muscle injury. *Nat Rev Dis Primers*. 2023;9(1):56. doi: 10.1038/s41572-023-00469-8
9. SantAnna JPC, Pedrinelli A, Hernandez AJ, Fernandes TL. Muscle injury: pathophysiology, diagnosis, and treatment. *Rev Bras Ortop*. 2022;57(1):1-13. doi: 10.1055/s-0041-1731417
10. Topaloğlu H, Poorshiri B. The congenital muscular dystrophies. *Ann Child Neurol Soc*. 2024;2(1):27-39. doi: 10.1002/cns3.20050
11. Ostojic M, Indelli PF, Lovrekovic B, *et al*. Graft selection in anterior cruciate ligament reconstruction: a comprehensive review of current trends. *Medicina*. 2024;60(12):2090. doi: 10.3390/medicina60122090
12. Gahlawat S, Oruc D, Paul N, *et al*. Tissue engineered 3D constructs for volumetric muscle loss. *Ann Biomed Eng*. 2024;52(9):2325-2347. doi: 10.1007/s10439-024-03541-w
13. Boyer O, Butler-Browne G, Chinoy H, *et al*. Myogenic cell transplantation in genetic and acquired diseases of skeletal muscle. *Front Genet*. 2021;12. doi: 10.3389/fgene.2021.702547
14. Liu H, Cheema U, Player DJ. Photobiomodulation therapy (PBMT) in skeletal muscle regeneration: a comprehensive review of mechanisms, clinical applications, and future directions. *Photodiagn Photodyn*. 2025;53:104634. doi: 10.1016/j.pdpdt.2025.104634
15. de Sire A, Marotta N, Lippi L, *et al*. Pharmacological treatment for acute traumatic musculoskeletal pain in athletes. *Medicina*. 2021;57(11):1208. doi: 10.3390/medicina57111208
16. Wei Q, An Y, Zhao X, Li M, Zhang J. Three-dimensional bioprinting of tissue-engineered skin: biomaterials, fabrication techniques, challenging difficulties, and future directions: a review. *Int J Biol Macromol*. 2024;266:131281. doi: 10.1016/j.ijbiomac.2024.131281
17. Saini G, Segaran N, Mayer JL, Saini A, Albadawi H, Oklu R. Applications of 3D bioprinting in tissue engineering and regenerative medicine. *J Clin Med*. 2021;10(21):4966. doi: 10.3390/jcm10214966

18. Jain P, Kathuria H, Dubey N. Advances in 3D bioprinting of tissues/organs for regenerative medicine and *in-vitro* models. *Biomaterials*. 2022;287:121639. doi: 10.1016/j.biomaterials.2022.121639

19. Samandari M, Quint J, Rodríguez-delaRosa A, Sinha I, Pourquié O, Tamayol A. Bioinks and bioprinting strategies for skeletal muscle tissue engineering. *Adv Mater*. 2022;34(12):2105883. doi: 10.1002/adma.202105883

20. Sabetkish S, Currie P, Meagher L. Recent trends in 3D bioprinting technology for skeletal muscle regeneration. *Acta Biomater*. 2024;181:46-66. doi: 10.1016/j.actbio.2024.04.038

21. Lee H, Kim W, Lee J, *et al*. Self-aligned myofibers in 3D bioprinted extracellular matrix-based construct accelerate skeletal muscle function restoration. *Appl Phys Rev*. 2021;8(2):021405. doi: 10.1063/5.0039639

22. Sicherer ST, Haque N, Parikh Y, Grasman JM. Current methodologies for inducing aligned myofibers in tissue constructs for skeletal muscle tissue regeneration. *Adv Wound Care*. 2025;14(2):114-131. doi: 10.1089/wound.2024.0111

23. Zhang H, Wu C. 3D printing of biomaterials for vascularized and innervated tissue regeneration. *Int J Bioprinting*. 2023;9(3):706. doi: 10.18063/ijb.706

24. Thangadurai M, Ajith A, Budharaju H, Sethuraman S, Sundaramurthi D. Advances in electrospinning and 3D bioprinting strategies to enhance functional regeneration of skeletal muscle tissue. *Biomater Adv*. 2022;142:213135. doi: 10.1016/j.bioadv.2022.213135

25. Miramini S, Fegan KL, Green NC, Espino DM, Zhang L, Thomas-Seale LEJ. The status and challenges of replicating the mechanical properties of connective tissues using additive manufacturing. *J Mech Behav Biomed*. 2020;103:103544. doi: 10.1016/j.jmbbm.2019.103544

26. García-Lizarribar A, Villasante A, Lopez-Martin JA, *et al*. 3D bioprinted functional skeletal muscle models have potential applications for studies of muscle wasting in cancer cachexia. *Biomater Adv*. 2023;150:213426. doi: 10.1016/j.bioadv.2023.213426

27. Alave Reyes-Furrer A, De Andrade S, Bachmann D, *et al*. Matrigel 3D bioprinting of contractile human skeletal muscle models recapitulating exercise and pharmacological responses. *Commun Biol*. 2021;4(1):1183. doi: 10.1038/s42003-021-02691-0

28. Mancuso S, Bhalerao A, Cucullo L. Advances and challenges of bioassembly strategies in neurovascular in vitro modeling: an overview of current technologies with a focus on three-dimensional bioprinting. *Int J Mol Sci*. 2024;25(20):11000. doi: 10.3390/ijms252011000

29. Lee SJ, Jeong W, Atala A. 3D bioprinting for engineered tissue constructs and patient-specific models: current progress and prospects in clinical applications. *Adv Mater*. 2024;36(49):e2408032. doi: 10.1002/adma.202408032

30. Mathur V, Agarwal P, Kasturi M, Srinivasan V, Seetharam RN, Vasanthan KS. Innovative bioinks for 3D bioprinting: exploring technological potential and regulatory challenges. *J Tissue Eng*. 2025;16:20417314241308022. doi: 10.1177/20417314241308022

31. Liu H, Xing F, Yu P, *et al*. Biomimetic fabrication bioprinting strategies based on decellularized extracellular matrix for musculoskeletal tissue regeneration: current status and future perspectives. *Mater Des*. 2024;243:113072. doi: 10.1016/j.matdes.2024.113072

32. Chu J, Lu M, Pfeifer CG, Alt V, Docheva D. Rebuilding tendons: a concise review on the potential of dermal fibroblasts. *Cells-basel*. 2020;9(9):2047. doi: 10.3390/cells9092047

33. Stocco TD, Zhang T, Dimitrov E, *et al*. Carbon nanomaterial-based hydrogels as scaffolds in tissue engineering: a comprehensive review. *Int J Nanomed*. 2023;18:6153-6183. doi: 10.2147/IJN.S436867

34. Brooks SV, Guzman SD, Ruiz LP. Skeletal muscle structure, physiology, and function. *Handb Clin Neurol*. 2023;195:3-16. doi: 10.1016/b978-0-323-98818-6.00013-3

35. Feng LT, Chen ZN, Bian H. Skeletal muscle: molecular structure, myogenesis, biological functions, and diseases. *MedComm*. 2024;5(7):e649. doi: 10.1002/mco2.649

36. Roy BC, Bruce HL. Contribution of intramuscular connective tissue and its structural components on meat tenderness-revisited: a review. *Crit Rev Food Sci*. 2024;64(25):9280-9310. doi: 10.1080/10408398.2023.2211671

37. Sunadome K, Erickson AG, Kah D, *et al*. Directionality of developing skeletal muscles is set by mechanical forces. *Nat Commun*. 2023;14(1):3060. doi: 10.1038/s41467-023-38647-7

38. Wohlgemuth RP, Brashear SE, Smith LR. Alignment, cross linking, and beyond: a collagen architect's guide to the skeletal muscle extracellular matrix. *Am J Physiol Cell Physiol*. 2023;325(4):C1017-C1030. doi: 10.1152/ajpcell.00287.2023

39. Kim W, Kim G. Bioprinting 3D muscle tissue supplemented with endothelial-spheroids for neuromuscular junction model. *Appl Phys Rev*. 2023;10(3):031410. doi: 10.1063/5.0152924

40. Rudolf R, Kettelhut IC, Navegantes LCC. Sympathetic innervation in skeletal muscle and its role at the neuromuscular junction. *J Muscle Res Cell Motil*. 2024;45(2):79-86. doi: 10.1007/s10974-024-09665-9

41. Poole DC, Kano Y, Koga S, Musch TI. August krogh: muscle capillary function and oxygen delivery. *Comp Biochem Physiol A Mol Integr Physiol*. 2021;253:110852. doi: 10.1016/j.cbpa.2020.110852

42. Mondrinos MJ, Alisafaei F, Yi AY, *et al*. Surface-directed engineering of tissue anisotropy in microphysiological models of musculoskeletal tissue. *Sci Adv*. 2021;7(11):eabe9446. doi: 10.1126/sciadv.abe9446

43. Ferrara PJ, Yee EM, Petrocelli JJ, *et al*. Macrophage immunomodulation accelerates skeletal muscle functional recovery in aged mice following disuse atrophy. *J Appl Physiol*. 2022;133(4):919-931. doi: 10.1152/japplphysiol.00374.2022

44. Wirth G, Juusola G, Tarvainen S, Laakkonen JP, Korpisalo P, Ylä-Herttuala S. Capillary dynamics regulate post-ischemic muscle damage and regeneration in experimental hindlimb ischemia. *Cells Basel*. 2023;12(16):2060. doi: 10.3390/cells12162060

45. Pajalunga D, Crescenzi M. Restoring the cell cycle and proliferation competence in terminally differentiated skeletal muscle myotubes. *Cells Basel*. 2021;10(10):2753. doi: 10.3390/cells10102753

46. Fukada S ichiro, Higashimoto T, Kaneshige A. Differences in muscle satellite cell dynamics during muscle hypertrophy and regeneration. *Skelet Muscle*. 2022;12(1):17. doi: 10.1186/s13395-022-00300-0

47. Andre AB, Rees KP, O'Connor S, *et al*. Single cell analysis reveals satellite cell heterogeneity for proinflammatory chemokine expression. *Front Cell Dev Biol*. 2023;11. doi: 10.3389/fcell.2023.1084068

48. Zhong T, Gao N, Niu H, *et al*. Targeted delivery of engineered extracellular vesicles to simultaneously promote vascularization and muscle regeneration in ischemic limbs. *J Control Release*. 2025;384:113938. doi: 10.1016/j.jconrel.2025.113938

49. Wang X, Zhou L. The many roles of macrophages in skeletal muscle injury and repair. *Front Cell Dev Biol*. 2022;10. doi: 10.3389/fcell.2022.952249

50. Wang X, Zhou L. The multifaceted role of macrophages in homeostatic and injured skeletal muscle. *Front Immunol*. 2023;14. doi: 10.3389/fimmu.2023.1274816

51. Zelada D, Bermedo-García F, Collao N, Henríquez JP. Motor function recovery: Deciphering a regenerative niche at the neuromuscular synapse. *Biol Rev*. 2021;96(2):752-766. doi: 10.1111/brv.12675

52. Guzman SD, Brooks SV. Skeletal muscle innervation: reactive oxygen species as regulators of neuromuscular junction dynamics and motor unit remodeling. *Free Radical Bio Med*. 2025;230:58-65. doi: 10.1016/j.freeradbiomed.2025.01.053

53. Cordelle MZ, Snelling SJB, Mouthuy PA. Skeletal muscle tissue engineering: from tissue regeneration to biorobotics. *Cyborg Bionic Syst*. 2025;6:0279. doi: 10.34133/cbsystems.0279

54. Langridge B, Griffin M, Butler PE. Regenerative medicine for skeletal muscle loss: a review of current tissue engineering approaches. *J Mater Sci-mater M*. 2021;32(1):15. doi: 10.1007/s10856-020-06476-5

55. Xing J, Liu N, Xu N, Chen W, Xing D. Engineering complex anisotropic scaffolds beyond simply uniaxial alignment for tissue engineering. *Adv Funct Mater*. 2022;32(15):2110676. doi: 10.1002/adfm.202110676

56. Filippi M, Yasa O, Giachino J, *et al*. Perfusable biohybrid designs for bioprinted skeletal muscle tissue. *Adv Healthc Mater*. 2023;12(18):2300151. doi: 10.1002/adhm.202300151

57. Shiwarski DJ, Hudson AR, Tashman JW, *et al*. 3D bioprinting of collagen-based high-resolution internally perfusable scaffolds for engineering fully biologic tissue systems. *Sci Adv*. 2025;11(17):eadu5905. doi: 10.1126/sciadv.adu5905

58. Gordon T. Peripheral nerve regeneration and muscle reinnervation. *Int J Mol Sci*. 2020;21(22):8652. doi: 10.3390/ijms21228652

59. Kim JH, Kim I, Seol YJ, *et al*. Neural cell integration into 3D bioprinted skeletal muscle constructs accelerates restoration of muscle function. *Nat Commun*. 2020;11(1):1025. doi: 10.1038/s41467-020-14930-9

60. Christensen KW, Turner J, Coughenour K, *et al*. Assembled cell-decorated collagen (AC-DC) fiber bioprinted implants with musculoskeletal tissue properties promote functional recovery in volumetric muscle loss. *Adv Healthc Mater*. 2022;11(3):2101357. doi: 10.1002/adhm.202101357

61. Park W, Gao G, Cho DW. Tissue-specific decellularized extracellular matrix bioinks for musculoskeletal tissue regeneration and modeling using 3D bioprinting technology. *Int J Mol Sci*. 2021;22(15):7837. doi: 10.3390/ijms22157837

62. Cakal SD, Radeke C, Alcala JF, *et al*. A simple and scalable 3D printing methodology for generating aligned and extended human and murine skeletal muscle tissues. *Biomed Mater*. 2022;17(4):045013. doi: 10.1088/1748-605X/ac6b71

63. Volpi M, Paradiso A, Costantini M, Święszkowski W. Hydrogel-based fiber biofabrication techniques for skeletal muscle tissue engineering. *ACS Biomater Sci Eng*. 2022;8(2):379-405. doi: 10.1021/acsbiomaterials.1c01145

64. Baiguera S, Del Gaudio C, Di Nardo P, Manzari V, Carotenuto F, Teodori L. 3D printing decellularized extracellular matrix

to design biomimetic scaffolds for skeletal muscle tissue engineering. *BioMed Res Int*. 2020;2020(1):2689701. doi: 10.1155/2020/2689701

65. Bertassoni LE. Bioprinting of complex multicellular organs with advanced functionality—recent progress and challenges ahead. *Adv Mater*. 2022;34(3):2101321. doi: 10.1002/adma.202101321

66. Zhuang P, An J, Chua CK, Tan LP. Bioprinting of 3D in vitro skeletal muscle models: a review. *Mater Des*. 2020;193:108794. doi: 10.1016/j.matdes.2020.108794

67. Ronzoni FL, Aliberti F, Scocozza F, *et al*. Myoblast 3D bioprinting to burst in vitro skeletal muscle differentiation. *J Tissue Eng Regen Med*. 2022;16(5):484-495. doi: 10.1002/term.3293

68. Kim WJ, Kim GH. 3D bioprinting of functional cell-laden bioinks and its application for cell-alignment and maturation. *Appl Mater Today*. 2020;19:100588. doi: 10.1016/j.apmt.2020.100588

69. Gilbert-Honick J, Grayson W. Vascularized and innervated skeletal muscle tissue engineering. *Adv Healthc Mater*. 2020;9(1):1900626. doi: 10.1002/adhm.201900626

70. Blake C, Massey O, Boyd-Moss M, *et al*. Replace and repair: biomimetic bioprinting for effective muscle engineering. *APL Bioeng*. 2021;5(3):031502. doi: 10.1063/5.0040764

71. Davoodi E, Sarikhani E, Montazerian H, *et al*. Extrusion and microfluidic-based bioprinting to fabricate biomimetic tissues and organs. *Adv Mater Technol*. 2020;5(8):1901044. doi: 10.1002/admt.201901044

72. Abrishamkar A, Nilghaz A, Saadatmand M, Naeimirad M, deMello AJ. Microfluidic-assisted fiber production: potentials, limitations, and prospects. *Biomicrofluidics*. 2022;16(6):061504. doi: 10.1063/5.0129108

73. Adhikari J, Roy A, Das A, *et al*. Effects of processing parameters of 3D bioprinting on the cellular activity of bioinks. *Macromol Biosci*. 2021;21(1):2000179. doi: 10.1002/mabi.202000179

74. Ngan CGY, Quigley A, Williams RJ, *et al*. Matured myofibers in bioprinted constructs with in vivo vascularization and innervation. *Gels Basel*. 2021;7(4):171. doi: 10.3390/gels7040171

75. Kang MS, Lee SH, Park WJ, Lee JE, Kim B, Han DW. Advanced techniques for skeletal muscle tissue engineering and regeneration. *Bioengineering*. 2020;7(3):99. doi: 10.3390/bioengineering7030099

76. Lee S, Kim W, Kim G. Efficient myogenic activities achieved through blade-casting-assisted bioprinting of aligned myoblasts laden in collagen bioink. *Biomacromolecules*. 2023;24(11):5219-5229. doi: 10.1021/acs.biomac.3c00749

77. Xiaorui L, Fuyin Z, Xudong W, *et al*. Biomaterial inks for extrusion-based 3D bioprinting: Property, classification, modification, and selection. *Int J Bioprinting*. 2022;9(2):649. doi: 10.18063/ijb.v9i2.649

78. Smoak MM, Hogan KJ, Grande-Allen KJ, Mikos AG. Bioinspired electrospun dECM scaffolds guide cell growth and control the formation of myotubes. *Sci Adv*. 2021;7(20):eabg4123. doi: 10.1126/sciadv.abg4123

79. Hwangbo H, Lee H, Jin EJ, *et al*. Bio-printing of aligned GelMa-based cell-laden structure for muscle tissue regeneration. *Bioact Mater*. 2022;8(1):57-70. doi: 10.1016/j.bioactmat.2021.06.031

80. Yang GH, Kim W, Kim J, Kim G. A skeleton muscle model using GelMA-based cell-aligned bioink processed with an electric-field assisted 3D/4D bioprinting. *Theranostics*. 2021;11(1):48-63. doi: 10.7150/thno.50794

81. Kim D, Hwangbo H, Kim G. Engineered myoblast-laden collagen filaments fabricated using a submerged bioprinting process to obtain efficient myogenic activities. *Biomacromolecules*. 2021;22(12):5042-5051. doi: 10.1021/acs.biomac.1c01006

82. Li S, Dan X, Chen H, *et al*. Developing fibrin-based biomaterials/scaffolds in tissue engineering. *Bioact Mater*. 2024;40:597-623. doi: 10.1016/j.bioactmat.2024.08.006

83. Xuan Z, Peng Q, Larsen T, *et al*. Tailoring hydrogel composition and stiffness to control smooth muscle cell differentiation in bioprinted constructs. *Tissue Eng Regen Med*. 2023;20(2):199-212. doi: 10.1007/s13770-022-00500-1

84. Lou H, Lu H, Zhang S, *et al*. Highly aligned myotubes formation of piscine satellite cells in 3D fibrin hydrogels of cultured meat. *Int J Biol Macromol*. 2024;282:136879. doi: 10.1016/j.ijbiomac.2024.136879

85. Liu J, Song Q, Yin W, *et al*. Bioactive scaffolds for tissue engineering: a review of decellularized extracellular matrix applications and innovations. *Exploration*. 2025;5(1):20230078. doi: 10.1002/EXP.20230078

86. Askari M, Naniz MA, Kouhi M, Saberi A, Zolfagharian A, Bodaghi M. Recent progress in extrusion 3D bioprinting of hydrogel biomaterials for tissue regeneration: a comprehensive review with focus on advanced fabrication techniques. *Biomater Sci*. 2021;9(3):535-573. doi: 10.1039/D0BM00973C

87. Saldin LT, Cramer MC, Velankar SS, White LJ, Badylak SF. Extracellular matrix hydrogels from decellularized tissues: structure and function. *Acta Biomater*. 2017;49(1):1-15. doi: 10.1016/j.actbio.2016.11.068

88. Zhang H, Wang Y, Zheng Z, *et al*. Strategies for improving the 3D printability of decellularized extracellular matrix bioink. *Theranostics*. 2023;13(8):2562-2587. doi: 10.7150/thno.81785

89. Marzi J, Fuhrmann E, Brauchle E, *et al*. Non-invasive three-dimensional cell analysis in bioinks by Raman imaging. *ACS Appl Mater Interfaces*. 2022;14(27):30455-30465. doi: 10.1021/acsami.1c24463

90. Kalva SN, Zakaria Y, Velasquez CA, Koç M. Tailoring the mechanical and degradation properties of 3DP PLA/PCL scaffolds for biomedical applications. *Rev Adv Mater Sci*. 2025;64(1):12. doi: 10.1515/rams-2025-0098

91. Dias JR, Sousa A, Augusto A, Bártolo PJ, Granja PL. Electrospun polycaprolactone (PCL) degradation: an in vitro and in vivo study. *Polymers Basel*. 2022;14(16):3397. doi: 10.3390/polym14163397

92. Hakim Khalili M, Zhang R, Wilson S, Goel S, Impey SA, Aria AI. Additive manufacturing and physicomechanical characteristics of PEGDA hydrogels: recent advances and perspective for tissue engineering. *Polymers Basel*. 2023;15(10):2341. doi: 10.3390/polym15102341

93. Yuan Z, Bai X, Li S, *et al*. Multimaterial and multidimensional bioprinting in regenerative medicine: advances, limitations, and future directions. *Adv Healthc Mater*. 2025 14(18):e2500475. doi: 10.1002/adhm.202500475

94. Sung TC, Wang T, Liu Q, *et al*. Cell-binding peptides on the material surface guide stem cell fate of adhesion, proliferation and differentiation. *J Mater Chem B*. 2023; 11(7):1389-1415. doi: 10.1039/D2TB02601E

95. Cámara-Torres M, Sinha R, Scopece P, *et al*. Tuning cell behavior on 3D scaffolds fabricated by atmospheric plasma-assisted additive manufacturing. *ACS Appl Mater Interfaces*. 2021;13(3):3631-3644. doi: 10.1021/acsami.0c19687

96. Péter B, Boldizsár I, Kovács GM, *et al*. Natural compounds as target biomolecules in cellular adhesion and migration: from biomolecular stimulation to label-free discovery and bioactivity-based isolation. *Biomedicines*. 2021;9(12):1781. doi: 10.3390/biomedicines9121781

97. Bramhe P, Rarokar N, Kumbhalkar R, Saoji S, Khedekar P. Natural and synthetic polymeric hydrogel: a bioink for 3D bioprinting of tissue models. *J Drug Deliv Sci Technol*. 2024;101:106204. doi: 10.1016/j.jddst.2024.106204

98. Khoeini R, Nosrati H, Akbarzadeh A, *et al*. Natural and synthetic bioinks for 3D bioprinting. *Adv NanoBiomed Res*. 2021;1(8):2000097. doi: 10.1002/anbr.202000097

99. Kumar S, Tharayil A, Thomas S. 3D bioprinting of nature-inspired hydrogel inks based on synthetic polymers. *ACS Appl Polym Mater*. 2021;3(8):3685-3701. doi: 10.1021/acsapm.1c00567

100. Fatimi A, Okoro OV, Podstawczyk D, Siminska-Stanny J, Shavandi A. Natural hydrogel-based bio-inks for 3D bioprinting in tissue engineering: a review. *Gels Basel*. 2022;8(3):179. doi: 10.3390/gels8030179

101. Kumar S. Synthetic polymer-derived single-network inks/bioinks for extrusion-based 3D printing towards bioapplications. *Mater Adv*. 2021;2(21):6928-6941. doi: 10.1039/D1MA00525A

102. Satchanska G, Davidova S, Petrov PD. Natural and synthetic polymers for biomedical and environmental applications. *Polymers Basel*. 2024;16(8):1159. doi: 10.3390/polym16081159

103. Reddy MSB, Ponnamma D, Choudhary R, Sadasivuni KK. A comparative review of natural and synthetic biopolymer composite scaffolds. *Polymers Basel*. 2021;13(7):1105. doi: 10.3390/polym13071105

104. Serna JA, Rueda-Gensini L, Céspedes-Valenzuela DN, Cifuentes J, Cruz JC, Muñoz-Camargo C. Recent advances on stimuli-responsive hydrogels based on tissue-derived ECMs and their components: towards improving functionality for tissue engineering and controlled drug delivery. *Polymers Basel*. 2021;13(19):3263. doi: 10.3390/polym13193263

105. Tripathi S, Dash M, Chakraborty R, *et al*. Engineering considerations in the design of tissue specific bioink for 3D bioprinting applications. *Biomater Sci*. 2025;13(1):93-129. doi: 10.1039/D4BM01192A

106. Lee G, Kim YH, Kim D, Lee DH, Bhang SH, Lee K. PCL-fibrin-alginate hydrogel based cell co-culture system for improving angiogenesis and immune modulation in limb ischemia. *Colloid Surface B*. 2025;250:114553. doi: 10.1016/j.colsurfb.2025.114553

107. Grzelak A, Hnydka A, Higuchi J, *et al*. Recent achievements in the development of biomaterials improved with platelet concentrates for soft and hard tissue engineering applications. *Int J Mol Sci*. 2024;25(3):1525. doi: 10.3390/ijms25031525

108. Xiang Y, Gao Y, Cheng Q, *et al*. Recombinant collagen coating 3D printed PEGDA hydrogel tube loading with differentiable BMSCs to repair bile duct injury. *Colloid Surface B*. 2024;241:114064. doi: 10.1016/j.colsurfb.2024.114064

109. Bartholomew K, Mahapatro A. Rheological characterization and print quality studies of gelatin/collagen I/ PEGDA hydrogels. *Int J Polym Mater Polym Biomater*. 2025;74(11):975-986. doi: 10.1080/00914037.2024.2391964

110. Lee J, Lee H, Jin EJ, Ryu D, Kim GH. 3D bioprinting using a new photo-crosslinking method for muscle tissue restoration. *NPJ Regen Med*. 2023;8(1):18. doi: 10.1038/s41536-023-00292-5

111. Altunbek M, Afghah F, Caliskan OS, Yoo JJ, Koc B. Design and bioprinting for tissue interfaces. *Biofabrication*. 2023;15(2):022002. doi: 10.1088/1758-5090/acb73d

112. Heo G, Kim W, Kim G. Comb-assisted 3D bioprinting for highly aligned 3D muscle bioconstructs with enhanced cellular mechanotransduction. *Virtual Phys Prototyp*. 2025;20(1):e2499440. doi: 10.1080/17452759.2025.2499440

113. Zhu Y, Yu X, Liu H, *et al*. Strategies of functionalized GelMA-based bioinks for bone regeneration: recent advances and future perspectives. *Bioact Mater*. 2024;38:346-373. doi: 10.1016/j.bioactmat.2024.04.032

114. Luo W, Zhang H, Wan R, *et al*. Biomaterials-based technologies in skeletal muscle tissue engineering. *Adv Healthc Mater*. 2024;13(18):2304196. doi: 10.1002/adhm.202304196

115. Poerio A, Mashanov V, Lai D, *et al*. Towards innervation of bioengineered muscle constructs: development of a sustained neurotrophic factor delivery and release system. *Bioprinting*. 2022;27:e00220. doi: 10.1016/j.bprint.2022.e00220

116. Sueters J, van Heiningen R, de Vries R, Guler Z, Huirne J, Smit T. Advances in tissue engineering of peripheral nerve and tissue innervation – a systematic review. *J Tissue Eng*. 2025;16:20417314251316918. doi: 10.1177/20417314251316918

117. P. Quint J, Samandari M, Abbasi L, *et al*. Nanoengineered myogenic scaffolds for skeletal muscle tissue engineering. *Nanoscale*. 2022;14(3):797-814. doi: 10.1039/D1NR06143G

118. Quint JP, Mostafavi A, Endo Y, *et al*. In vivo printing of nanoenabled scaffolds for the treatment of skeletal muscle injuries. *Adv Healthc Mater*. 2021;10(10):e2002152. doi: 10.1002/adhm.202002152

119. Huang B. Carbon nanotubes and their polymeric composites: the applications in tissue engineering. *Biomanuf Rev*. 2020;5(1):3. doi: 10.1007/s40898-020-00009-x

120. Kandhola G, Park S, Lim JW, *et al*. Nanomaterial-based scaffolds for tissue engineering applications: a review on graphene, carbon nanotubes and nanocellulose. *Tissue Eng Regen Med*. 2023;20(3):411-433. doi: 10.1007/s13770-023-00530-3

121. Boularaoui S, Shanti A, Lanotte M, *et al*. Nanocomposite conductive bioinks based on low-concentration GelMA and MXene nanosheets/gold nanoparticles providing enhanced printability of functional skeletal muscle tissues. *ACS Biomater Sci Eng*. 2021;7(12):5810-5822. doi: 10.1021/acsbiomaterials.1c01193

122. Ghaziof S, Shojaei S, Mehdikhani M, Khodaei M, Jafari Nodoushan M. Electro-conductive 3D printed polycaprolactone/gold nanoparticles nanocomposite scaffolds for myocardial tissue engineering. *J Mech Behav Biomed*. 2022;132:105271. doi: 10.1016/j.jmbbm.2022.105271

123. Aparicio-Collado JL, García-San-Martín N, Molina-Mateo J, *et al*. Electroactive calcium-alginate/polycaprolactone/reduced graphene oxide nanohybrid hydrogels for skeletal muscle tissue engineering. *Colloid Surface B*. 2022;214:112455. doi: 10.1016/j.colsurfb.2022.112455

124. Jo SB, Erdenebileg U, Dashnyam K, *et al*. Nano-graphene oxide/polyurethane nanofibers: mechanically flexible and myogenic stimulating matrix for skeletal tissue engineering. *J Tissue Eng*. 2020;11:2041731419900424. doi: 10.1177/2041731419900424

125. Han S, Cruz SH, Park S, Shin SR. Nano-biomaterials and advanced fabrication techniques for engineering skeletal muscle tissue constructs in regenerative medicine. *Nano Converg*. 2023;10(1):48. doi: 10.1186/s40580-023-00398-y

126. Jo HJ, Kang MS, Heo HJ, *et al*. Skeletal muscle regeneration with 3D bioprinted hyaluronate/gelatin hydrogels incorporating MXene nanoparticles. *Int J Biol Macromol*. 2024;265:130696. doi: 10.1016/j.ijbiomac.2024.130696

127. Liu L, Wang C, Wu Z, Xing Y. Ultralow-voltage-drivable artificial muscles based on a 3D structure MXene-PEDOT:PSS/AgNWs electrode. *ACS Appl Mater Interfaces*. 2022;14(16):18150-18158. doi: 10.1021/acsami.2c00760

128. Oldroyd P, Oldroyd S, Meng M, *et al*. Stretchable device for simultaneous measurements of contractility and electrophysiology of neuromuscular tissue in the gastrointestinal tract. *Adv Mater*. 2024;36(19):2312735. doi: 10.1002/adma.202312735

129. Nain A, Chakraborty S, Jain N, *et al*. 4D hydrogels: fabrication strategies, stimulation mechanisms, and biomedical applications. *Biomater Sci*. 2024;12(13):3249-3272. doi: 10.1039/D3BM02044D

130. Arif ZU, Khalid MY, Zolfagharian A, Bodaghi M. 4D bioprinting of smart polymers for biomedical applications: Recent progress, challenges, and future perspectives. *React Funct Polym*. 2022;179:105374. doi: 10.1016/j.reactfunctpolym.2022.105374

131. Wang Y, Cui H, Esworthy T, Mei D, Wang Y, Zhang LG. Emerging 4D printing strategies for next-generation

tissue regeneration and medical devices. *Adv Mater*. 2022;34(20):2109198.
doi: 10.1002/adma.202109198

132. Fuentes J, Guix M, Cenev ZM, *et al*. Ferrofluid-based bioink for 3D printed skeletal muscle tissues with enhanced force and magnetic response. *Adv Mater Interfaces*. 2025;12(13):2400824.
doi: 10.1002/admi.202400824

133. Tuftee C, Alsberg E, Ozbolat IT, Rizwan M. Emerging granular hydrogel bioinks to improve biological function in bioprinted constructs. *Trends Biotechnol*. 2024;42(3):339-352.
doi: 10.1016/j.tibtech.2023.09.007

134. Zhang S, Li G, Man J, *et al*. Fabrication of microspheres from high-viscosity bioink using a novel microfluidic-based 3D bioprinting nozzle. *Micromachines Basel*. 2020;11(7):681.
doi: 10.3390/mi11070681

135. Yang J, Zhang X, Xie J, *et al*. Porous mullite ceramics with hierarchical pores constructed via vat photopolymerization of multi-phase pickering emulsion. *Addit Manuf*. 2024;79:103943.
doi: 10.1016/j.addma.2023.103943

136. Tuladhar S, Clark S, Habib A. Tuning shear thinning factors of 3D bio-printable hydrogels using short fiber. *Materials*. 2023;16(2):572.
doi: 10.3390/ma16020572

137. Sánchez-Sánchez R, Rodríguez-Rego JM, Macías-García A, Mendoza-Cerezo L, Díaz-Parralejo A. Relationship between shear-thinning rheological properties of bioinks and bioprinting parameters. *Int J Bioprinting*. 2023;9(2):687.
doi: 10.18063/ijb.687

138. de Barros NR, Darabi MA, Ma X, *et al*. Enhanced maturation of 3D bioprinted skeletal muscle tissue constructs encapsulating soluble factor-releasing microparticles. *Macromol Biosci*. 2023;23(12):e2300276.
doi: 10.1002/mabi.202300276

139. Cho S, Jang J. Recent trends in biofabrication technologies for studying skeletal muscle tissue-related diseases. *Front Bioeng Biotechnol*. 2021;9.
doi: 10.3389/fbioe.2021.782333

140. Fornetti E, De Paolis F, Fuoco C, *et al*. A novel extrusion-based 3D bioprinting system for skeletal muscle tissue engineering. *Biofabrication*. 2023;15(2):025009.
doi: 10.1088/1758-5090/acb573

141. Zhan Y, Jiang W, Liu Z, Wang Z, Guo K, Sun J. Utilizing bioprinting to engineer spatially organized tissues from the bottom-up. *Stem Cell Res Ther*. 2024;15(1):101.
doi: 10.1186/s13287-024-03712-5

142. Zoghi S. Advancements in tissue engineering: a review of bioprinting techniques, scaffolds, and bioinks. *Biomed Eng Comput Biol*. 2024;15:11795972241288099.
doi: 10.1177/11795972241288099

143. Sonaye SY, Ertugral EG, Kothapalli CR, Sikder P. Extrusion 3D (bio)printing of alginate-gelatin-based composite scaffolds for skeletal muscle tissue engineering. *Materials*. 2022;15(22):7945.
doi: 10.3390/ma15227945

144. Malekpour A, Chen X. Printability and cell viability in extrusion-based bioprinting from experimental, computational, and machine learning views. *J Funct Biomater*. 2022;13(2):40.
doi: 10.3390/jfb13020040

145. McCauley PJ, Fromen CA, Bayles AV. Cell viability in extrusion bioprinting: The impact of process parameters, bioink rheology, and cell mechanics. *Rheol Acta*. 2025.
doi: 10.1007/s00397-025-01504-z

146. Betancourt N, Chen X. Review of extrusion-based multi-material bioprinting processes. *Bioprinting*. 2022;25:e00189.
doi: 10.1016/j.bprint.2021.e00189

147. Rossi A, Pescara T, Gambelli AM, *et al*. Biomaterials for extrusion-based bioprinting and biomedical applications. *Front Bioeng Biotechnol*. 2024;12:1393641.
doi: 10.3389/fbioe.2024.1393641

148. Müller SJ, Fabry B, Gekle S. Predicting cell stress and strain during extrusion bioprinting. *Phys Rev Appl*. 2023;19(6):064061.
doi: 10.1103/PhysRevApplied.19.064061

149. Lombardi L, Scalzone A, Ausilio C, Gentile P, Tammaro D. Optimizing nozzle design in extrusion-based 3D bioprinting to minimize mechanical stress and enhance cell viability. *Int J Bioprinting*. 2025:e025190182.
doi: 10.36922/IJB025190182

150. Reina-Romo E, Mandal S, Amorim P, Bloemen V, Ferraris E, Geris L. Towards the experimentally-informed in silico nozzle design optimization for extrusion-based bioprinting of shear-thinning hydrogels. *Front Bioeng Biotechnol*. 2021;9:701778.
doi: 10.3389/fbioe.2021.701778

151. Rasouli R, Sweeney C, Frampton JP. Heterogeneous and composite bioinks for 3D-bioprinting of complex tissue. *Biomed Mater Devices*. 2025;3(1):108-126.
doi: 10.1007/s44174-024-00171-7

152. Budharaju H, Sundaramurthi D, Sethuraman S. Embedded 3D bioprinting – an emerging strategy to fabricate biomimetic & large vascularized tissue constructs. *Bioact Mater*. 2024;32:356-384.
doi: 10.1016/j.bioactmat.2023.10.012

153. Kumar P, Ebbens S, Zhao X. Inkjet printing of mammalian cells – theory and applications. *Bioprinting*. 2021;23:e00157.
doi: 10.1016/j.bprint.2021.e00157

154. Guida L, Cavallaro M, Levi M. Advancements in high-resolution 3D bioprinting: Exploring technological trends, bioinks and achieved resolutions. *Bioprinting*. 2024;44:e00376.
doi: 10.1016/j.bprint.2024.e00376

155. Huang J, Zhou G, Jiang Q, Li L. *In situ* 3D bioprinting: the future of regenerative medicine. *Fundam Res*. 2025. doi: 10.1016/j.fmre.2025.06.004

156. Ng WL, Shkolnikov V. Optimizing cell deposition for inkjet-based bioprinting. *Int J Bioprinting*. 2024;10(2):2135. doi: 10.36922/ijb.2135

157. Cheng C, Williamson EJ, Chiu GTC, Han B. Engineering biomaterials by inkjet printing of hydrogels with functional particulates. *Med-X*. 2024;2(1):9. doi: 10.1007/s44258-024-00024-4

158. Xu HQ, Liu JC, Zhang ZY, Xu CX. A review on cell damage, viability, and functionality during 3D bioprinting. *Mil Med Res* 2022;9(1):70. doi: 10.1186/s40779-022-00429-5

159. Ghosh E, Rego GP, Ghosh RN, *et al*. Advances in in situ bioprinting: a focus on extrusion and inkjet-based bioprinting techniques. *Regen Eng Transl Med*. 2025. doi: 10.1007/s40883-025-00420-1

160. Chang J, Sun X. Laser-induced forward transfer based laser bioprinting in biomedical applications. *Front Bioeng Biotechnol*. 2023;11:1255782. doi: 10.3389/fbioe.2023.1255782

161. Kryou C, Zergioti I. Laser-induced forward transfer on regenerative medicine applications. *Biomed Mater Devices*. 2023;1(1):5-20. doi: 10.1007/s44174-022-00040-1

162. Leberfinger AN, Dinda S, Wu Y, *et al*. Bioprinting functional tissues. *Acta Biomater*. 2019;95(1):32-49. doi: 10.1016/j.actbio.2019.01.009

163. Bosmans C, Ginés Rodriguez N, Karperien M, *et al*. Towards single-cell bioprinting: micropatterning tools for organ-on-chip development. *Trends Biotechnol*. 2024;42(6):739-759. doi: 10.1016/j.tibtech.2023.11.014

164. Sun J, Gong Y, He Y, *et al*. Process optimization for coaxial extrusion-based bioprinting: a comprehensive analysis of material behavior, structural precision, and cell viability. *Addit Manuf*. 2025;100:104682. doi: 10.1016/j.addma.2025.104682

165. Mohan TS, Datta P, Nesaei S, Ozbolat V, Ozbolat IT. 3D coaxial bioprinting: process mechanisms, bioinks and applications. *Prog Biomed Eng (Bristol)*. 2022;4(2):022003. doi: 10.1088/2516-1091/ac631c

166. Eghosasere E, Osasumwen E, Emmanuella O. 3D bioprinting in tissue engineering: Advancements, challenges, and pathways to clinical translation. *JSM Regen Med Bioeng*. 2025;7(1):1-15. doi: 10.47739/2379-0490/1023

167. Volpi M, Paradiso A, Walejewska E, Gargioli C, Costantini M, Swieszkowski W. Automated microfluidics-assisted hydrogel-based wet-spinning for the biofabrication of biomimetic engineered myotendinous junction. *Adv Healthc Mater*. 2024;13(32):e2402075. doi: 10.1002/adhm.202402075

168. Mohammadi S, Cidonio G. Unravelling hierarchical patterning of biomaterial inks with 3D microfluidic-assisted spinning: a paradigm shift in bioprinting technologies. *Front Biomater Sci*. 2023;2:1279061. doi: 10.3389/fbiom.2023.1279061

169. Serpe F, Casciola CM, Ruocco G, Cidonio G, Scognamiglio C. Microfluidic fiber spinning for 3D bioprinting: harnessing microchannels to build macrotissues. *Int J Bioprinting*. 2024;10(1):1404. doi: 10.36922/ijb.1404

170. Hosseinabadi HG, Dogan E, Miri AK, Ionov L. Digital light processing bioprinting advances for micro-tissue models. *ACS Biomater Sci Eng*. 2022;8(4):1381-1395. doi: 10.1021/acsbiomaterials.1c01509

171. Jeong YG, Yoo JJ, Lee SJ, Kim MS. 3D digital light process bioprinting: cutting-edge platforms for resolution of organ fabrication. *Mater Today Bio*. 2024;29:101284. doi: 10.1016/j.mtbio.2024.101284

172. Seo JW, Kim GM, Choi Y, Cha JM, Bae H. Improving printability of digital-light-processing 3D bioprinting via photoabsorber pigment adjustment. *Int J Mol Sci*. 2022;23(10):5428. doi: 10.3390/ijms23105428

173. Karakaidos P, Kryou C, Simigdala N, Klinakis A, Zergioti I. Laser bioprinting of cells using UV and visible wavelengths: a comparative DNA damage study. *Bioengineering*. 2022;9(8):378. doi: 10.3390/bioengineering9080378

174. Silva C, Cortés-Rodriguez CJ, Hazur J, Reakasame S, Boccaccini AR. Rational design of a triple-layered coaxial extruder system: in silico and in vitro evaluations directed toward optimizing cell viability. *Int J Bioprinting*. 2020;6(4):282. doi: 10.18063/ijb.v6i4.282

175. Zhang P, Liu C, Modavi C, Abate A, Chen H. Printhead on a chip: empowering droplet-based bioprinting with microfluidics. *Trends Biotechnol*. 2024;42(3):353-368. doi: 10.1016/j.tibtech.2023.09.001

176. Duong VT, Lin CC. Digital light processing 3D bioprinting of gelatin-norbornene hydrogel for enhanced vascularization. *Macromol Biosci*. 2023;23(12):e2300213. doi: 10.1002/mabi.202300213

177. Cao T, Warren CR. From 2D myotube cultures to 3D engineered skeletal muscle constructs: a comprehensive review of in vitro skeletal muscle models and disease modeling applications. *Cells Basel*. 2025;14(12):882. doi: 10.3390/cells14120882

178. Kim J, Lee H, Lee G, Ryu D, Kim G. Fabrication of fully aligned self-assembled cell-laden collagen filaments for tissue engineering *via* a hybrid bioprinting process. *Bioact Mater*. 2024;36:14-29. doi: 10.1016/j.bioactmat.2024.02.020

179. Hwangbo H, Koo Y, Nacionales F, Kim J, Chae S, Kim GH. Stimulus-assisted in situ bioprinting: advancing direct bench-to-bedside delivery. *Trends Biotechnol*. 2025;43(5):1015-1030. doi: 10.1016/j.tibtech.2024.11.001

180. Hwangbo H, Chae S, Ryu D, Kim G. *In situ* magnetic-field-assisted bioprinting process using magnetorheological bioink to obtain engineered muscle constructs. *Bioact Mater*. 2025;45:417-433. doi: 10.1016/j.bioactmat.2024.11.035

181. Gao H, Xiao J, Wei Y, Wang H, Wan H, Liu S. Regulation of myogenic differentiation by topologically microgrooved surfaces for skeletal muscle tissue engineering. *ACS Omega*. 2021;6(32):20931-20940. doi: 10.1021/acsomega.1c02347

182. Kamal KY, Othman MA, Kim JH, Lawler JM. Bioreactor development for skeletal muscle hypertrophy and atrophy by manipulating uniaxial cyclic strain: proof of concept. *NPJ Microgravity*. 2024;10(1):62. doi: 10.1038/s41526-023-00320-0

183. Borisov V, Gili Sole L, Reid G, *et al*. Upscaled skeletal muscle engineered tissue with in vivo vascularization and innervation potential. *Bioengineering*. 2023;10(7):800. doi: 10.3390/bioengineering10070800

184. Wang X, Dong W, Dong H, *et al*. Bioprinting of wearable sensors, brain-machine interfaces, and exoskeleton robots. *Int J Bioprinting*. 2024;10(6):3590. doi: 10.36922/ijb.3590

185. Singh S, Choudhury D, Yu F, Mironov V, Naing MW. In situ bioprinting - bioprinting from benchside to bedside? *Acta Biomater*. 2020;101(1):14-25. doi: 10.1016/j.actbio.2019.08.045

186. Gorbenko N, Vaccaro JC, Fagan R, *et al*. Perfusion bioreactor conditioning of small-diameter plant-based vascular grafts. *Tissue Eng Regen Med*. 2024;21(8):1189-1201. doi: 10.1007/s13770-024-00670-0

187. Ng WL, An J, Chua CK. Process, material, and regulatory considerations for 3D printed medical devices and tissue constructs. *Engineering*. 2024;36(5):146-166. doi: 10.1016/j.eng.2024.01.028

188. Mladenovska T, Choong PF, Wallace GG, O'Connell CD. The regulatory challenge of 3D bioprinting. *Regen Med*. 2023;18(8):659-674. doi: 10.2217/rme-2022-0194

189. Yoshida A, Baba K, Takahashi H, Nagase K, Shimizu T. One-step fabrication of 3D-aligned human skeletal muscle tissue and measurement of contractile force for preclinical drug testing. *Mater Today Bio*. 2025;31:101456. doi: 10.1016/j.mtbio.2025.101456

190. Gao L, Li L, Wu W, *et al*. 3D-bioprinted in vitro skeletal muscle with pennate fiber architecture to enhance contractile function. *Int J Bioprinting*. 2024;10(6):4371. doi: 10.36922/ijb.4371

191. Carraro E, Rossi L, Maghin E, Canton M, Piccoli M. 3D in vitro models of pathological skeletal muscle: which cells and scaffolds to elect? *Front Bioeng Biotechnol*. 2022;10:941623. doi: 10.3389/fbioe.2022.941623

192. Mazzoldi EL, Gaudenzi G, Ginestra PS, Ceretti E, Giliani SC. Evaluating cells metabolic activity of bioinks for bioprinting: the role of cell-laden hydrogels and 3D printing on cell survival. *Front Bioeng Biotechnol*. 2024;12:1450838. doi: 10.3389/fbioe.2024.1450838

193. Pellegrini E, Desando G, Petretta M, *et al*. A 3D collagen-based bioprinted model to study osteosarcoma invasiveness and drug response. *Polymers*. 2022;14(19):4070. doi: 10.3390/polym14194070

194. Avnet S, Pompo GD, Borciani G, Fischetti T, Graziani G, Baldini N. Advantages and limitations of using cell viability assays for 3D bioprinted constructs. *Biomed Mater*. 2024;19(2):025033. doi: 10.1088/1748-605X/ad2556

195. VanGenderen CA, Granet JA, Filippelli RL, Liu Y, Chang NC. Modulating myogenesis: an optimized in vitro assay to pharmacologically influence primary myoblast differentiation. *Curr Protoc*. 2022;2(9):e565. doi: 10.1002/cpz1.565

196. Mueller C, Trujillo-Miranda M, Maier M, Heath DE, O'Connor AJ, Salehi S. Effects of external stimulators on engineered skeletal muscle tissue maturation. *Adv Mater Interfaces*. 2021;8(1):2001167. doi: 10.1002/admi.202001167

197. Vesga-Castro C, Aldazabal J, Vallejo-Illarramendi A, Paredes J. Contractile force assessment methods for in vitro skeletal muscle tissues. Huang CLH, Zaidi M, eds. *Elife*. 2022;11:e77204. doi: 10.7554/eLife.77204

198. Khodabukus A. Tissue-engineered skeletal muscle models to study muscle function, plasticity, and disease. *Front Physiol*. 2021;12:619710. doi: 10.3389/fphys.2021.619710

199. Ebrahimi M, Lad H, Fusto A, *et al*. De novo revertant fiber formation and therapy testing in a 3D culture model of duchenne muscular dystrophy skeletal muscle. *Acta Biomater*. 2021;132(1):227-244. doi: 10.1016/j.actbio.2021.05.020

200. Tejedera-Villafranca A, Montolio M, Ramón-Azcón J, Fernández-Costa JM. Mimicking sarcolemmal damagein vitro: a contractile 3D model of skeletal muscle for drug testing in duchenne muscular dystrophy. *Biofabrication*. 2023;15(4). doi: 10.1088/1758-5090/acfb3d

201. Torres MJ, Zhang X, Slentz DH, *et al*. Chemotherapeutic drug screening in 3D-bioengineered human myobundles provides insight into taxane-induced myotoxicities. *Iscience*. 2022;25(10):105189. doi: 10.1016/j.isci.2022.105189

202. Madden L, Juhas M, Kraus WE, Truskey GA, Bursac N. Bioengineered human myobundles mimic clinical responses of skeletal muscle to drugs. Wagers AJ, ed. *Elife*. 2015;4:e04885. doi: 10.7554/eLife.04885

203. Raman R, Cvetkovic C, Uzel SGM, *et al*. Optogenetic skeletal muscle-powered adaptive biological machines. *Proc Natl Acad Sci U S A*. 2016;113(13):3497-3502. doi: 10.1073/pnas.1516139113

204. Filippi M, Badolato A, Georgopoulou A, *et al*. Bioprinting of piezoresistive organohydrogel networks for advanced real-time mechanosensing in engineered tissue models. *Trends Biotechnol*. 2025:S0167-7799(25)00212-4. doi: 10.1016/j.tibtech.2025.05.026

205. Loi G, Scocozza F, Benedetti L, *et al*. Design, development, and benchmarking of a bioreactor integrated with 3D bioprinting: application to skeletal muscle regeneration. *Bioprinting*. 2024;42:e00352. doi: 10.1016/j.bprint.2024.e00352

206. Rodriguez Ayala A, Christ G, Griffin D. Cell-scale porosity minimizes foreign body reaction and promotes innervated myofiber formation after volumetric muscle loss. *NPJ Regen Med*. 2025;10(1):12. doi: 10.1038/s41536-025-00395-1

207. Niknezhad SV, Mehrali M, Khorasgani FR, *et al*. Enhancing volumetric muscle loss (VML) recovery in a rat model using super durable hydrogels derived from bacteria. *Bioact Mater*. 2024;38:540-558. doi: 10.1016/j.bioactmat.2024.04.006

208. Zhao N, Huang Y, Cheng X, *et al*. A critical size volumetric muscle loss model in mouse masseter with impaired mastication on nutrition. *Cell Proliferat*. 2024; 57(6):e13610. doi: 10.1111/cpr.13610

209. Whitaker R, Sung S, Tylek T, *et al*. Effects of injury size on local and systemic immune cell dynamics in volumetric muscle loss. *NPJ Regen Med*. 2025;10(1):9. doi: 10.1038/s41536-025-00397-z

210. Fischer EO, Tsukerman A, Machour M, *et al*. Bioprinting perfusable and vascularized skeletal muscle flaps for the treatment of volumetric muscle loss. *Adv Healthc Mater*. 2025;14(13):e2404542. doi: 10.1002/adhm.202404542

211. Yamaoka Y, Chan WI, Seno S, Iwamori K, Fukada SI, Matsuda H. Quantifying the recovery process of skeletal muscle on hematoxylin and eosin stained images via learning from label proportion. *Sci Rep*. 2024; 14(1):27044. doi: 10.1038/s41598-024-78433-z

212. Rana SP, Dey M. Detrended fluctuation analysis of gait cycles: a study of neuromuscular and ground force dynamics. *Sensors Basel*. 2025;25(13):4122. doi: 10.3390/s25134122

213. Hoffman DB, Schifino AG, Cooley MA, *et al*. Low intensity, high frequency vibration training to improve musculoskeletal function in a mouse model of volumetric muscle loss. *J Orthop Res*. 2025;43(3):622-631. doi: 10.1002/jor.26023

214. Johnson D, Tobo C, Au J, *et al*. Combined regenerative rehabilitation improves recovery following volumetric muscle loss injury in a rat model. *J Biomed Mater Res B*. 2024;112(7):e35438. doi: 10.1002/jbm.b.35438

215. Mehrotra P, Jablonski J, Toftegaard J, *et al*. Skeletal muscle reprogramming enhances reinnervation after peripheral nerve injury. *Nat Commun*. 2024;15(1):9218. doi: 10.1038/s41467-024-53276-4

216. Hoffman DB, Raymond-Pope CJ, Pritchard EE, *et al*. Differential evaluation of neuromuscular injuries to understand re-innervation at the neuromuscular junction. *Exp Neurol*. 2024;382(1):114996. doi: 10.1016/j.expneurol.2024.114996

217. Fabre P, Molina T, Larose J, *et al*. Bioactive lipid mediator class switching regulates myogenic cell progression and muscle regeneration. *Nat Commun*. 2025;16(1):5578. doi: 10.1038/s41467-025-60586-8

218. Zhu C, Sklyar K, Karvar M, Endo Y, Sinha I. Scaffold tissue engineering strategies for volumetric muscle loss. *PAR*. 2023;10:58. doi: 10.20517/2347-9264.2022.89

219. Bülow A, Schäfer B, Beier JP. Three-dimensional bioprinting in soft tissue engineering for plastic and reconstructive surgery. *Bioengineering*. 2023;10(10):1232. doi: 10.3390/bioengineering10101232

220. Lee MC, Jodat YA, Endo Y, *et al*. Engineering large-scale hiPSC-derived vessel-integrated muscle-like lattices for enhanced volumetric muscle regeneration. *Trends Biotechnol*. 2024;42(12):1715-1744. doi: 10.1016/j.tibtech.2024.08.001

221. Zhou Z, Liu J, Xiong T, Liu Y, Tuan RS, Li ZA. Engineering innervated musculoskeletal tissues for regenerative orthopedics and disease modeling. *Small*. 2024;20(23):2310614. doi: 10.1002/smll.202310614

222. Sicherer ST, Venkatarama RS, Grasman JM. Recent trends in injury models to study skeletal muscle regeneration and repair. *Bioengineering*. 2020;7(3):76. doi: 10.3390/bioengineering7030076

223. Fakhr MJ, Kavakebian F, Ababzadeh S, Rezapour A. Challenges and advances in peripheral nerve tissue engineering critical factors affecting nerve regeneration. *J Tissue Eng Regen Med*. 2024;1:8868411. doi: 10.1155/2024/8868411

224. Garg K, Brockhouse J, McAndrew CM, *et al*. Regenerative rehabilitation: navigating the gap between preclinical

promises and clinical realities for treating trauma-induced volumetric muscle loss. *J Physiol*. 2025.
doi: 10.1113/JP286551

225. Jo B, Motoi K, Morimoto Y, Takeuchi S. Dynamic and static workout of in vitro skeletal muscle tissue through a weight training device. *Adv Healthc Mater*. 2024.
doi: 10.1002/adhm.202401844

226. Vesga-Castro C, Mosqueira-Martín L, Ubiria-Urkola P, *et al*. Development of an in vitro platform for the analysis of contractile and calcium dynamics in single human myotubes. *Lab Chip*. 2024;24(20):4741-4754.
doi: 10.1039/D3LC00442B

227. Rousseau E, Raman R, Tamir T, *et al*. Actuated tissue engineered muscle grafts restore functional mobility after volumetric muscle loss. *Biomaterials*. 2023;302(1): 122317.
doi: 10.1016/j.biomaterials.2023.122317

228. De Paolis F, Testa S, Guarnaccia G, *et al*. Long-term longitudinal study on swine VML model. *Biol Direct*. 2023;18(1):42.
doi: 10.1186/s13062-023-00399-1

229. Costantini M, Testa S, Fornetti E, *et al*. Biofabricating murine and human myo-substitutes for rapid volumetric muscle loss restoration. *EMBO Mol Med*. 2021;13(3): e12778.
doi: 10.15252/emmm.202012778

230. Humphrey JD. Constrained mixture models of soft tissue growth and remodeling – twenty years after. *J Elasticity*. 2021;145(1):49-75.
doi: 10.1007/s10659-020-09809-1

231. Roche CD, Sharma P, Ashton AW, Jackson C, Xue M, Gentile C. Printability, durability, contractility and vascular network formation in 3D bioprinted cardiac endothelial cells using alginate–gelatin hydrogels. *Front Bioeng Biotechnol*. 2021;9.
doi: 10.3389/fbioe.2021.636257

232. Kamaraj M, Moghimi N, Joshi A, *et al*. Recent advances in handheld and robotic bioprinting approach for tissue engineering. *Adv Mater Technol*. 2025;10(15):2500206.
doi: 10.1002/admt.202500206

233. Freeman S, Calabro S, Williams R, Jin S, Ye K. Bioink formulation and machine learning-empowered bioprinting optimization. *Front Bioeng Biotechnol*. 2022;10.
doi: 10.3389/fbioe.2022.913579

234. Chen H, Liu Y, Balabani S, Hirayama R, Huang J. Machine learning in predicting printable biomaterial formulations for direct ink writing. *Research*. 2023;0197.
doi: 10.34133/research.0197

235. Zhang Z, Zhou X, Fang Y, Xiong Z, Zhang T. AI-driven 3D bioprinting for regenerative medicine: from bench to bedside. *Bioact Mater*. 2025;45:201-230.
doi: 10.1016/j.bioactmat.2024.11.021

236. Kim MH, Singh YP, Celik N, *et al*. High-throughput bioprinting of spheroids for scalable tissue fabrication. *Nat Commun*. 2024;15(1):10083.
doi: 10.1038/s41467-024-54504-7

237. Jung H, Lee H, Shin M, Son D. Adhesive bioelectronics for closed-loop therapy. *Med-X*. 2025;3(1):11.
doi: 10.1007/s44258-025-00055-5

238. Boufidis D, Garg R, Angelopoulos E, Cullen DK, Vitale F. Bio-inspired electronics: Soft, biohybrid, and "living" neural interfaces. *Nat Commun*. 2025;16(1):1861.
doi: 10.1038/s41467-025-57016-0

239. Ploeger H, Gonzalez-Molina J. Designing biomimetic protocells and prototissues as smart biomaterials. *Cell Biomater*. 2025;(in press)
doi: 10.1016/j.celbio.2025.100097

240. Briones Y, Pascua B, Tiangco N, Crisostomo I, Casiguran S, Remenyi R. Assessing the landscape of clinical and observational trials involving bioprinting: a scoping review. *3D Print Med*. 2025;11(1):5.
doi: 10.1186/s41205-025-00253-2

ACCSCIENCE PUBLISHING

International Journal of Bioprinting

REVIEW ARTICLE

Advances in *in vitro* blood–brain barrier models: Integrating bioprinting with microfluidic chips for compound evaluation

Yating Du[1,2], Zezhi Li[2], Xiang Li[2]*, and Jianping Xie[2]*

[1]Beijing Technology and Business University, Beijing 100048, China

[2]Beijing Life Science Academy, Beijing 102209, China

(This article belongs to the *Special Issue: Biofabrication Breakthroughs: Innovation and Application in Bioprinting, Biomaterials, and Organoid*)

Abstract

The blood–brain barrier (BBB), a vital defense interface of the central nervous system, selectively regulates molecular transport into the brain and maintains brain homeostasis. Disruption of BBB integrity contributes to various neurological diseases, making the BBB a key target for therapeutic compounds. However, traditional *in vitro* models struggle to recreate the BBB's complex structure and dynamic functions. Recent advances in microfluidics and three-dimensional bioprinting have enabled the construction of high-fidelity *in vitro* BBB models that recapitulate key aspects of the brain's vascular microenvironment. By integrating principles from materials science, microfabrication, and cell biology, these "BBB-on-a-chip" platforms support physiologically relevant shear stress, cell–cell interactions, and barrier properties, making them powerful tools for compound screening and mechanistic research. This review summarizes the advances in *in vitro* BBB models and the application of bioprinting and microfluidic technology for compound evaluation.

Keywords: Bioprinting; Blood–brain barrier; Compound evaluation; *In vitro* model; Microfluidic chip

***Corresponding authors:**
Xiang Li (lixiang@blsa.com.cn)

Jianping Xie (ztridicp@126.com)

Citation: Du Y, Li Z, Li X, Xie J. Advances in blood–brain barrier *in vitro* models: Integrating bioprinting with microfluidic chips for compound evaluation. *Int J Bioprint.* 2025;11(5):68-97. doi: 10.36922/IJB025270265

Received: July 3, 2025
Revised: July 29, 2025
Accepted: August 8, 2025
Published online: August 15, 2025

Copyright: © 2025 Author(s). This is an Open Access article distributed under the terms of the Creative Commons Attribution License, permitting distribution, and reproduction in any medium, provided the original work is properly cited.

Publisher's Note: AccScience Publishing remains neutral with regard to jurisdictional claims in published maps and institutional affiliations.

1. Introduction

The brain's vascular system stretches approximately 400 miles, with the blood–brain barrier (BBB) serving as a crucial component of the neurovascular unit (NVU) in the central nervous system (CNS). The BBB consists of brain microvascular endothelial cells (BMECs), astrocytes, microglia, pericytes, oligodendrocytes, and neurons, along with tight junction proteins and extracellular matrix (ECM) constituents.[1] Structurally, it comprises a luminal glycocalyx layer (a polysaccharide–protein complex), as well as two different basement membranes: the endothelial (vascular) basement membrane and the parenchymal basement membrane.[2] The glycocalyx is a dynamic, carbohydrate-rich network structure that coats the apical surface of endothelial cells. Composed primarily of glycolipids, glycoproteins, and mucopolysaccharides, it is often referred to as the "cell coat." This layer performs several core functions, including preserving cellular morphology, facilitating signal transduction, and regulating molecular exchange.[2,3] The BBB's barrier properties are primarily attributed to specialized endothelial

cells and are characterized by significantly reduced paracellular permeability. These cells secrete a range of adhesion molecules and tight junction proteins—such as claudin-5, occludin, zonula occludens (ZO; ZO-1, ZO-2, ZO-3), and junctional adhesion molecules—which are anchored to the actin cytoskeleton through cytoplasmic adaptors like cingulin. This protein complex stabilizes intercellular junctions and restricts the diffusion of solutes. Consequently, only a limited subset of molecules, typically those recognized by specific receptors, are permitted to cross the BBB via receptor-mediated endocytosis.[2,4]

Pericytes, which are embedded within the basement membrane, are positioned along the outer surfaces of parenchymal collateral vessels and capillaries, maintaining direct contact with adjacent endothelial cells. They play a vital role in the formation and maintenance of the basement membrane by secreting structural components such as collagen, laminin, and other ECM proteins.[5] In addition to providing mechanical support to blood vessels and regulating vascular tone, pericytes are essential for preserving the integrity of the BBB.[5] Disruption of genes specifically expressed by pericytes significantly compromises BBB function, demonstrating their critical regulatory role.[6] Astrocytes contribute to BBB stability through their end-feet, which envelop the blood vessels and provide physical scaffolding. These end-feet are involved in the regulation of water transport across the BBB, primarily mediated by the aquaporin-4 water channel. Furthermore, molecular interactions between astrocytes and endothelial cells are crucial in modulating the structural and functional integrity of the BBB.[7,8] Neurons are closely associated with astrocytes and rely on oligodendrocytes for axonal insulation. Oligodendrocytes form myelin sheaths around neuronal processes, enhancing electrical conductivity and protecting neural pathways.[2] Microglia, the resident macrophages of the CNS, typically cover distinct, non-overlapping domains but can migrate toward cerebral blood vessels during injury or inflammation. In doing so, they contribute to the maintenance and restoration of BBB integrity under pathological conditions.[2] Figure 1 presents a schematic representation of the major cellular components of the BBB structure.

The integrity of the BBB is vital for preserving brain homeostasis and normal neurological function. By tightly regulating the transport of small molecules and biological agents, the BBB maintains a stable microenvironment within the CNS.[9] Disruption of this barrier has been implicated in a range of neurological diseases, including Alzheimer's disease (AD), multiple sclerosis, stroke, and epilepsy.[10] Increased BBB permeability enables the migration of neurotoxic substances and immune cells into the brain parenchyma via the paracellular pathway, potentially inducing inflammatory responses.[11] Compromised BBB integrity is a hallmark of several pathological conditions. In acute ischemic stroke, both ischemia and reperfusion lead to the excessive generation of reactive oxygen and nitrogen radicals in the microvascular endothelium, resulting in vascular injury and BBB breakdown.[12] In brain tumors, whether primary brain cancers or metastases, BBB permeability is often elevated, facilitating tumor cell invasion into CNS tissues.[13] Sepsis-associated encephalopathy, a serious complication of systemic infection, is characterized by microglial hyperactivation, endothelial barrier dysfunction, and BBB disruption, inducing symptoms ranging from mild cognitive disturbances to severe neurological impairment or coma.[14]

Current *in vitro* models of the BBB primarily consist of two-dimensional (2D) systems, such as conventional dish cultures and Transwell platforms, as well as three-dimensional (3D) models, including spheroids, organoids, and microfluidic chips.[15,16] The emergence of bioprinting introduces new opportunities for advancing these traditional BBB models.[17,18] Bioprinting refers to the fabrication of tissue-like or organoid structures using 3D printing technologies with biological materials, enabling precise spatial control of cellular organization and extracellular architecture.[19] This level of control significantly enhances the functional fidelity and physiological relevance of BBB models, particularly in compound evaluation.[20] Reliable and physiologically representative *in vitro* BBB models are indispensable tools for disease modeling and high-throughput screening of therapeutic compounds targeting the CNS. In recent years, biomimetic BBB-on-a-chip platforms have emerged as accurate and dynamic systems for simulating *in vivo* conditions and evaluating compound permeability and toxicity. This review provides a comprehensive overview of recent advances in BBB *in vitro* modeling, with a particular focus on microfluidic chip-based platforms for compound evaluation. Additionally, we examine the contributions of bioprinting technology to the development of next-generation BBB models and discuss the current challenges and prospects in this evolving field.

2. *In vitro* blood–brain barrier models

In vitro BBB models are essential tools for recapitulating the structure and function of the BBB under controlled laboratory conditions. With continuous advancements in biomedical engineering and tissue modeling, these models have undergone significant evolution. Figure 2 illustrates the development of *in vitro* biomimetic BBB models. The earliest models were simple 2D systems, followed by the introduction of the Transwell model,[21]

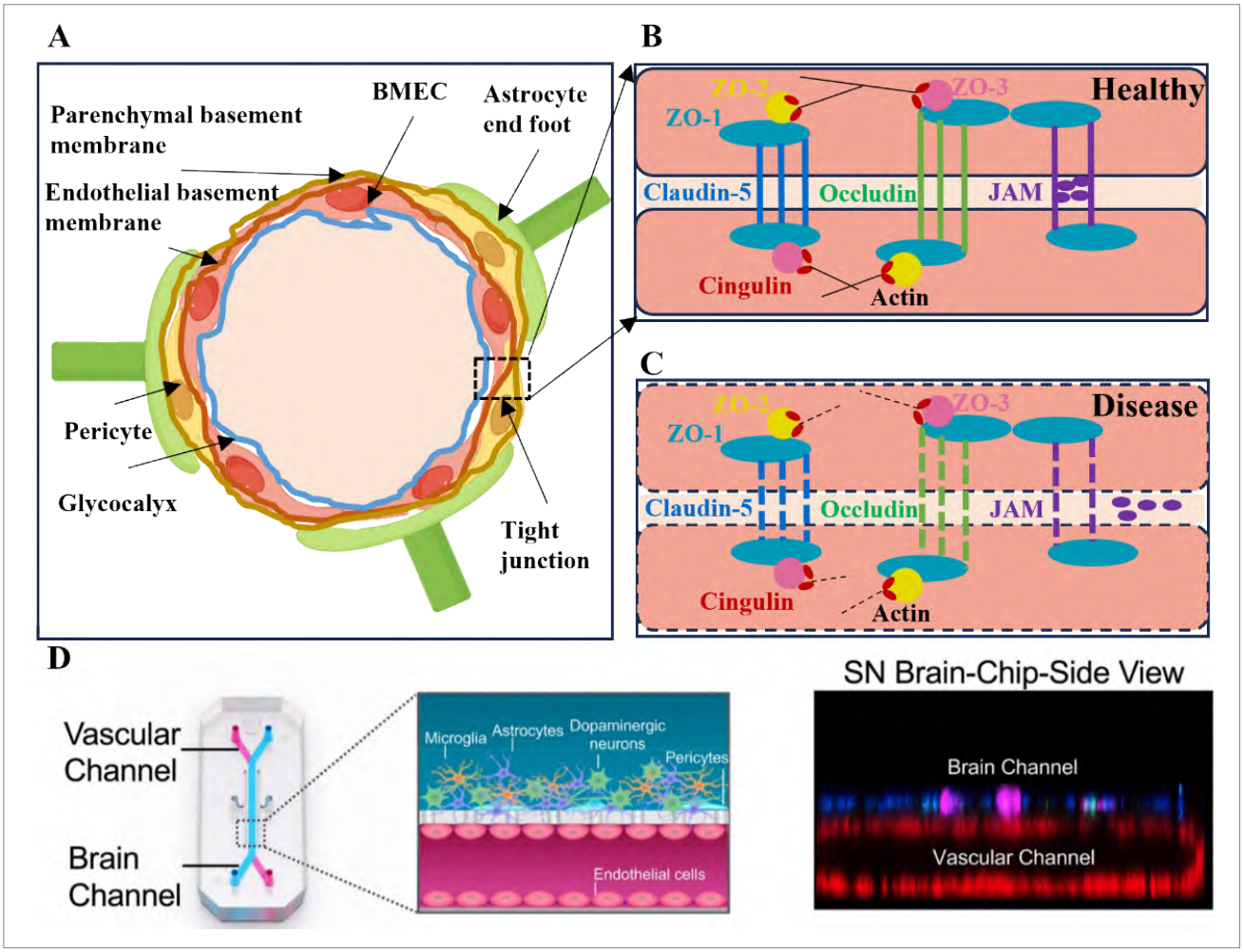


Figure 1. Schematic representation of the primary cellular components of the BBB structure. (A) Cross-sectional schematic of a brain microvessel illustrating the spatial organization of BBB key cellular components. (B) Tight junctions between BMECs under healthy physiological conditions. (C) Disrupted tight junctions in pathological states, contributing to increased BBB permeability. Illustrations (A–C) were modified from Vetter *et al.*[8] (D) Three-dimensional reconstruction of a confocal z-stack showing the organization of BMECs, pericytes, astrocytes, microglia, and neurons in an SN brain-chip model. Image adapted from Pediaditakis *et al.*[16] The selected cell images used in the figure were sourced or adapted from Servier Medical Art via the scifig.bio plugin (version 1.3.2). Abbreviations: BBB, blood–brain barrier; BMEC, brain microvascular endothelial cell; JAM, junction adhesion molecule; SN, substantia nigra; ZO, zonula occludens.

which enabled the co-culture of multiple cell types across a semipermeable membrane. Subsequently, 3D models such as spheroids[22] and organoids[23] were developed, offering improved cellular interactions and structural complexity. Currently, microfluidic chip-based models represent the most advanced form of dynamic 3D BBB models, closely mimicking *in vivo* physiological conditions.[24] As an emerging approach, bioprinting holds considerable promise for addressing the limitations of traditional models,[25] such as the static nature of conventional 3D cultures, particularly when integrated with microfluidic systems.[26] Table 1 summarizes several relevant studies on the development of *in vitro* BBB models, detailing the cell types, the apparatuses, the applications, the advantages, and the limitations associated with each model.

2.1. Two-dimensional model

The Petri dish model, one of the earliest 2D cell culture systems, remains widely used due to its low cost, ease of handling, and suitability for observing and analyzing cellular characteristics. Despite its simplicity, this model has been proven effective in simulating certain structural and functional aspects of the BBB. For instance, in 1986, Audus *et al.*[27] established a monolayer BBB model using bovine BMECs, demonstrating its utility in evaluating the permeability of centrally acting drugs and other substances

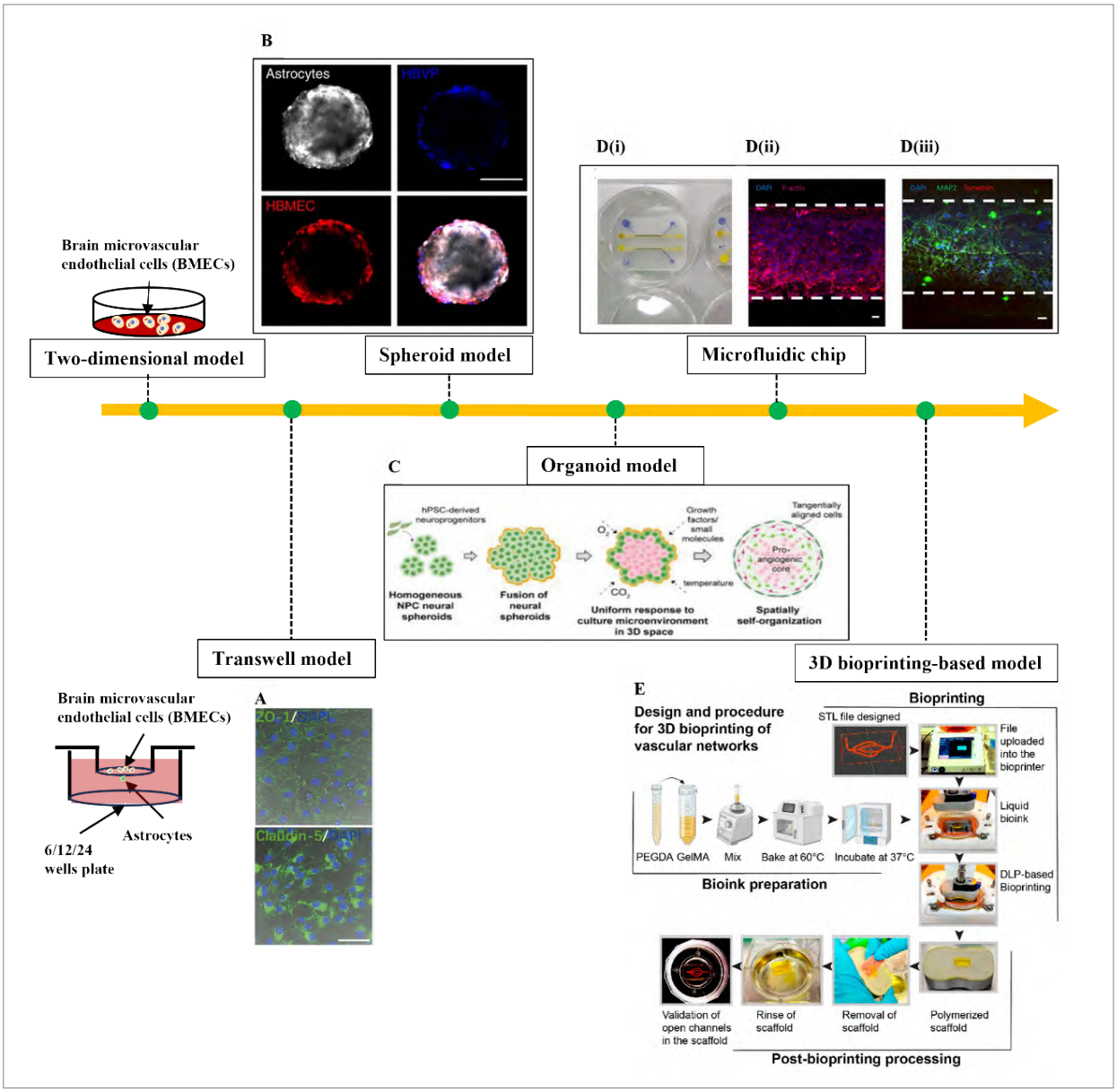


Figure 2. The development of *in vitro* biomimetic BBB models. (A) Representative immunofluorescence staining of tight junction proteins ZO-1 and claudin-5 in cultured brain endothelial cells, demonstrating tight junction formation. Scale bar: 50 μm, magnification: 63×. Image adapted from Li *et al.*[21] (B) Representative confocal images showing the organization of human astrocytes (hAs; white), HBVP (blue), and primary HBMEC (red) when co-cultured to form a spheroid. Scale bar: 100 μm. Image adapted from Cho *et al.*[22] (C) Schematics showing the concept of generating spatially self-organized neural concentroid from hPSC-derived neuroprogenitor cells. Image adapted from Chai *et al.*[23] (D) NVU-on-a-chip microfluidic model. (i) Open-top microfluidic chip integrated into a 6-well plate. The bottom channel (yellow) supports endothelial cell culture, while the open-top channel (blue) enables neuronal differentiation. (ii) Immunofluorescence staining of endothelial cell monoculture in the bottom channel on a polyester membrane showing a confluent monolayer (Blue: nuclei; red: F-actin). Scale bar: 50 μm, magnification: 10×. (iii) Immunostaining of neurons in the top channel showing neuronal markers (Blue: nuclei, green: MAP2, and red: synapsin-1/2). Scale bar: 50 μm, magnification: 10×. Image adapted from Middelkamp *et al.*[24] (E) Schematic representation of the steps for the fabrication of the scaffold with a 3D vascular network. The bioprinting steps include generating a computer-aided design file (STL) of a 3D microvascular network using a computer graphics software tool (i.e., Blender) and uploading it to the bioprinter. Bioinks were prepared by mixing PEGDA and GelMA, heating at 60°C, and then incubating at 37°C. The liquid bioink was then polymerized using DLP bioprinting to form a scaffold with channels. Red food coloring dissolved in PBS was then perfused to validate the integrity of the hollow channels. Image adapted from Don *et al.*[25] Selected cell graphics in this figure were sourced or adapted from Servier Medical Art via the scifig.bio plugin (version 1.3.2). Abbreviations: 3D, three-dimensional; BBB, blood–brain barrier; DLP, digital light-based; GelMA, gelatin methacryloyl; HBMEC, human brain microvascular endothelial cells; HBVP, human brain vascular pericytes; MAP2, microtubule associated protein 2; NVU, neurovascular unit; PBS, phosphate-buffered saline; PEGDA, polyethylene glycol diacrylate; STL, standard tessellation language; ZO, zonula occludens.

Table 1. Studies on the development of *in vitro* blood–brain barrier models

Model	Cell sources	Apparatus	Application	TEER ($\Omega \cdot cm^2$)	Permeability	Duration	Throughput	Advantages	Limitations	Ref.
Two-dimensional model	Bovine BMECs	100 mm petri dish	Drug delivery and metabolism	–	Leucine, propranolol, and sucrose	5 days	–	Low cost, easy to operate, easy to observe and analyze, repeatable	The physiologic environment of the 2D model differs significantly from *in vivo*; imperfect barrier structure and function	[27]
	Bovine BMECs	100 mm petri dish	Model verification	–	Fluorescein-conjugated dextrans	–	–			[28]
	Human BMECs and astrocytes	100 mm petri dish	Compound metabolism	–	Essential polyunsaturated fatty acids: 18:2n–6 and 18:3n–3	6–7 days	–			[29]
Transwell model	Primary cells: BMECs, astrocytes, pericytes, and neurons	12-well Transwell plate	Model verification	10–50	Dexamethasone	10 days	–	Simulates barrier structure and function; representative of the NVU	Limited barrier function, mainly applicable to transport mechanism studies	[31]
	Endothelial cells, astrocytes differentiated from human iPSC	12-well Transwell plate	Model verification	300–2000	70 kDa FITC dextran and lucifer yellow	10 days	–			[34]
	Mouse BMECs, astrocytes	24-well Transwell plate	Sepsis disease modeling	20–600	10 kDa FITC-dextran	24 hours	–			[36]
	b. End3-mouse BECs; rat BMSCs	24-well Transwell plate	Ischemic stroke disease modeling	–	4.4 kDa TRITC-dextran, Evans blue	24 hours	–			[21]
	Mouse BECs (bEnd.3); rat glioblastomas (C6)	24-well Transwell plate	Brain glioma disease modeling	300	–	12 hours	–			[37]
	HCMEC/D3, astrocytes (SC-1800), HBVP	24-well Transwell plate	Model verification	1200	–	24 hours	–			[38]

(Continue)

doi: 10.36922/IJB025270265

Table 1. Studies on the development of *in vitro* blood–brain barrier models

Model	Cell sources	Apparatus	Application	TEER (Ω·cm²)	Permeability	Duration	Throughput	Advantages	Limitations	Ref.
Spheroid model	Primary human cells: astrocytes, pericytes, endothelial cells	ULA 24-well plates	Compound evaluation	–	FITC solution	72–120 hours	–	Simulate barrier structures; combine with Transwell models for drug delivery	Simple cellular composition lacks an accurate barrier function; internal conditions need molecular labeling and further observation	45
	Human primary BECs, primary pericytes, and primary astrocytes	24-well hanging droplet culture plates (HDCPs)	Model verification	–	–	72 hours	–			46
	Human glioma cells (U87, U118, and U251)	24-well Transwell plate	Compound evaluation	–	–	8–10 days	–			47
	bEnd.3 cells, glial cells (SVG-p12), glioblastoma multiforme (GBM8401), T98G cells	24-well Transwell plate	Compound evaluation	–	CC12 (NSC749232)- an anthraquinone tetraheterocyclic homolog with lipophilic structure	48 hours	–			48
Organoid model	Human iPSCs	ULA 96-well plates	Model verification	–	70,000 MW Texas Red dextran	13 days	–	Long-term maintenance (up to 50+ days); valuable for pathology modeling; scalable for high throughput and multi-organ fusion	Lack functional circulation and a dynamic physiological environment	50
	Human iPSCs	ULA 24-well plates	Alzheimer's disease modeling	–	Gamma-secretase inhibitor DAPT, heparin, and heparinase III	71 days	–			51
	Human PSCs	ULA 24-well plates	Alzheimer's disease modeling	–	–	10 days	–			52
	Human ESCs	Micropillar array 24-well plate	Model verification	–	–	70 days	Medium throughput			23
	Human PSCs	ULA 6-well plates	Cerebral cavernous malformation disease modeling	Around 1190.8	–	75 days	–			53
	hiPSC-derived neurons, astrocytes	12-well transparent MEA plates	Alzheimer's disease modeling	–	–	40 days	–			55

(*Continue*)

doi: 10.36922/IJB025270265

Table 1. Studies on the development of *in vitro* blood–brain barrier models

Model	Cell sources	Apparatus	Application	TEER (Ω·cm²)	Permeability	Duration	Throughput	Advantages	Limitations	Ref.
Microfluidic chip model	hiPSC-derived neurons, rat astrocytes, and human endothelial cells	PDMS microfluidic chip	Model verification	–	4 and 20 kDa FITC-dextrans, 0.5 kDa lucifer yellow	14 days	24 individual microfluidic units	Allow study of cell–cell interactions; mimic *in vivo* shear stress with high fidelity; support parallel testing of multiple stimuli	Complicated, costly design and fabrication; electrode-chip integration needs further research; multi-channel errors and cross-contamination	[24]
	Primary mouse BMECs	PDMS microfluidic chip	Model verification	–	–	38 days	–			[61]
	HCMEC/D3 and human astrocytes	PDMS multiplexing chips	Model verification	–	–	3 days	–			[62]
	BMECs (bEnd.3), astrocytes (C8D1A), pericytes (MBVP)	PDMS microfluidic chip	Model verification	220	–	12 hours	–			[63]
3D bioprinting-based model	Human astrocytes, primary human BMECs, and pericytes	Complex 3D vascular network fabricated within a hydrogel, and combined with fluid dynamics	Model development	–	40 kDa dextrans	7 days	–	More closely replicates the cellular structure and multicellular arrangement of microvessels *in vivo*	Biodegradable scaffold materials need to be developed, and more suitable cells need to be selected to improve epithelial barrier properties	[25]
	HAs, HBVPs, and HBMECs	The aqueous two-phase 3D printing (ATPP) model	Model verification	–	10 kDa dextran Texas Red	8 days	–			[69]
	Human brain endothelial cells, pericytes, and astrocytes	3D-printed serpentine channel model	Model verification	–	150 kDa FITC-dextran; ultrasound	9 days	–			[70]
	hiPSCs (IMR90-4) derived BCECs	Chip bioreactor, a membrane chip	Model verification	285–2609	–	168 hours	–			[71]

Abbreviations: 2D, two-dimensional; 3D, three-dimensional; BECs, brain endothelial cells; BMSCs, bone marrow mesenchymal stem cells; DAPT, N-[N-(3,5-difluorophenacetyl)-L-alanyl]-S-phenylglycine t-butyl ester; ESCs, embryonic stem cells; FITC-dextran, fluorescein isothiocyanate-dextran; HA, human astrocytes; HBMECs, human brain microvascular endothelial cells; HBVP, human brain vascular pericytes; HCMEC, human cerebral microvascular endothelial cells; iPSCs, induced pluripotent stem cells; MEA, microelectrode arrays; NVU, neurovascular unit; PDMS, polydimethylsiloxane; PSCs, pluripotent stem cells; ULA, ultra-low attachment.

doi: 10.36922/IJB025270265

(Table 1).[27] Similarly, in 1988, van Bree *et al.*[28] developed a BBB model composed of bovine cerebrovascular cells that formed tight junctions and exhibited transport characteristics consistent with those observed *in vivo* (Table 1).[28] Further advancing the approach, Bernoud *et al.*[29] co-cultured human BMECs with astrocytes in Petri dishes. Their results highlighted the critical role of astrocytes in facilitating fatty acid transport across the BBB (Table 1).[29]

However, simple Petri dish models are inherently limited in their ability to replicate the complex structure and function of the BBB under both physiological and pathological conditions. These models typically rely on monolayer or mixed-cell cultures,[30] which lack the cellular organization and dynamic intercellular signaling necessary to accurately mimic barrier properties and the exchange of soluble factors. As a result, researchers seek to develop more physiologically relevant BBB models that better emulate the *in vivo* microenvironment.

2.2. Transwell model

To address the limitations of conventional Petri dish models, researchers developed the Transwell model, which incorporates a semipermeable polymer membrane. This platform supports the establishment of single-cell or multicellular co-culture systems and enables the spatial organization of key cellular components of the BBB, including BMECs, astrocytes, pericytes, neurons, and microglia. These cells are typically cultured on the apical and basal surfaces of the porous membrane to simulate the anatomical and functional distribution found *in vivo* (Table 1).[31,32] The structural integrity and permeability of Transwell-based BBB models have been validated in multiple studies. The critical parameter for assessing barrier function is trans-epithelial electrical resistance (TEER), which reflects the permeability of the cell layer and the tightness of intercellular junctions. Higher TEER values indicate stronger cell–cell adhesion and reduced paracellular transport.[33] *In vitro* Transwell models of the BBB have been shown to express tight junction markers reliably, and fluctuations in TEER values are indicative of functional barrier properties. For example, Singh *et al.*[34] suggested that the optimal window for conducting transport studies lies between 24 and 72 hours post model establishment (Table 1).[34] Model performance can be enhanced through optimization of several culture parameters, including growth medium composition, membrane material, cell seeding density, and co-culture strategies.[32] Notably, coupling the Transwell platform with adjustable electrospun polyethyleneimine–fibronectin membranes has enabled the development of high-throughput permeability assays, further extending its application in compound screening.[35] The Transwell model has been widely applied in research on neurological diseases such as ischemic stroke and glioma, serving as a valuable tool for investigating disease mechanisms. For instance, Chen *et al.*[36] demonstrated that Maf1 protein significantly suppressed lipopolysaccharide-induced neuroinflammation and neuronal apoptosis in both *in vitro* and *in vivo* models of sepsis-associated encephalopathy (Table 1).[36] Similarly, studies on ischemic stroke have shown that caveolin-1 scaffolding proteins increase BBB permeability, whereas extracellular vesicles derived from mesenchymal stem cells can restore BBB integrity and promote neurological recovery (Table 1).[21] Additionally, the Transwell model has been used to evaluate the targeted delivery of adriamycin to glioma cells, successfully demonstrating the drug's ability to traverse the BBB and localize within tumor tissue (Table 1).[37]

However, static Transwell models are limited in their ability to replicate the dynamic physiological conditions of the *in vivo* environment—such as blood flow, shear stress, and continuous molecular signaling.[38] The absence of these mechanical and biochemical cues can result in altered cellular behavior, including aberrant proliferation and phenotypic drift. Furthermore, the lack of real-time intercellular interactions and soluble factor gradients restricts the model's ability to fully emulate the complex neurovascular microenvironment. In addition, the manual handling required for Transwell assays is time-consuming and labor-intensive, and the system's relatively low throughput poses challenges for scalability in high-throughput screening applications.

2.3. Spheroid model

Advances in materials science and bioengineering have enabled the development of novel biomaterials—such as collagen sponges—for use in constructing 3D spheroid models.[39] The spheroid model, one of the earliest forms of 3D culture, was introduced in the 1970s.[40] In 1977, Schmitz *et al.*[41] reported the spontaneous aggregation of cells into 3D spheroidal structures during *in vitro* culture, marking a foundational step in the development of spheroid modeling.[41] By the late 20th and early 21st centuries, spheroid models gained widespread application in cancer research due to their ability to replicate critical *in vivo* features, including hypoxic microenvironments and drug resistance, which are often absent in traditional 2D cultures.[42,43] More recently, spheroid models have been employed to simulate the human NVU and BBB, offering physiologically relevant platforms for studying brain function and pathology.[44] For example, Sokolova *et al.*[45] developed a multicellular 3D spheroid BBB model using primary human astrocytes, pericytes, and endothelial cells. In this configuration,

astrocytes formed the spheroid core, which was encased by pericytes, while brain endothelial cells constituted the outermost layer—successfully reconstituting a functional BBB structure (Table 1).[45] Similarly, other studies using primary human brain endothelial cells, pericytes, and astrocytes demonstrated the feasibility of assembling multicellular spheroids capable of modeling key BBB features *in vitro* (Table 1).[46]

While spheroid models offer valuable insights, they generally feature simpler cellular compositions and lack the structural and functional complexity of fully differentiated tissues. As a result, spheroid models are often integrated with other platforms—such as Transwell systems—to enhance their applicability for evaluating therapeutic agents, particularly in oncology research. For instance, iguratimod-loaded poly (lactic acid)-glycolic acid nanoparticles demonstrated inhibitory effects on tumor cell migration when tested using a combination of spheroid and Transwell tumor models (Table 1).[47] In another study, a glioblastoma multiforme spheroid model was coupled with a BBB Transwell system to evaluate the therapeutic efficacy of the lipophilic compound CC12 (NSC749232), providing a more comprehensive assessment of drug permeability and antitumor activity across the BBB (Table 1).[48]

2.4. Organoid model

Organoids are 3D culture systems derived from stem cells that differentiate under the influence of specific growth factors. These models can closely mimic the structural and functional characteristics of native organs. Organoids have been widely employed to study human organ development and disease pathogenesis—including that of the brain—due to their ability to recapitulate complex tissue architecture and cellular interactions. In the context of BBB modeling, organoids exhibit promising physiological relevance. Reported TEER values for brain organoid-based BBB models range from 1500 to 8000 $\Omega \cdot cm^2$, which is comparable to the *in vivo* BBB range from approximately 1800 to 2000 $\Omega \cdot cm^2$.[49] Additionally, organoid systems support extended culture durations, making them suitable for long-term studies. For example, Ahn *et al.*[50] successfully maintained a neural-specific vascular network for over 50 days, enabling the reconstruction of BBB-like structures and functions (Table 1).[50]

Organoids also offer the potential for constructing personalized models, making them valuable tools for both disease modeling and therapeutic development. Organoids have been applied to model the pathophysiology of neurodegenerative diseases such as AD. For example, using human induced pluripotent stem cells (hiPSCs), researchers have generated brain organoids to simulate the BBB microenvironment associated with AD. Yan *et al.*[51] demonstrated that BBB organoids derived from AD patients exhibited upregulated expression of pro-inflammatory cytokines—including interleukins and tumor necrosis factor—along with altered ECM protein profiles, providing mechanistic insights into AD pathogenesis (Table 1).[51] Additionally, Huang *et al.*[52] employed cerebrovascular organoids to investigate the role of apolipoprotein E4 in neurons and astrocytes, thereby identifying potential therapeutic targets for neurovascular dysfunction in AD (Table 1).[52] Despite their advantages, conventional brain organoids are typically composed of ectodermal cell types and lack vascular structures, limiting their ability to replicate key physiological aspects of the BBB. To address this limitation, Chai *et al.*[23] incorporated pluripotent stem cell-derived endothelial cells into organoid cultures, promoting vascularization and creating a "vascularized" brain model. This advancement provided a novel *in vitro* approach for studying angiogenesis and vascular involvement in brain disorders (Table 1).[23] Further extending this strategy, Dao *et al.*[53] developed a human BBB assemblage by combining brain and vascular organoids derived from hiPSCs. This model successfully recapitulated anatomical and functional features of cavernous hemangiomas and BBB disruption observed in patients with cerebral cavernous malformations (Table 1).[53] Taken together, organoid models are highly representative of native tissue composition, structure, and function—especially when integrated with co-culture techniques, multi-tissue interactions, biosensing platforms, bioimaging technologies, or histological analysis (Table 1).[54,55]

Despite its many advantages, the organoid model presents several notable limitations. First, the generation of organoids typically requires long incubation periods and a high level of technical expertise, which can pose challenges for widespread adoption. Moreover, variability in organoid structure and function across different batches leads to low reproducibility, thereby limiting their reliability and consistency in experimental research. Another significant drawback is the static nature of organoid models, which hinders their ability to accurately replicate the dynamic physiological conditions of the BBB, such as fluid flow, shear stress, and real-time biochemical signaling. This lack of dynamic interaction reduces the model's fidelity in mimicking *in vivo* neurovascular environments and may restrict its utility in certain applications.

2.5. Microfluidic chip model

The advent of microfluidic technology has opened new avenues for the development of *in vitro* biomimetic BBB models.[56] Traditional static 3D models lack critical physiological features, such as blood flow, shear stress, and dynamic intercellular interactions, which are essential for

accurately simulating the complex *in vivo* microenvironment of the BBB.[56] To address these limitations, Kawakita *et al.*[57] developed dynamic BBB organoid models using microfluidic platforms, aiming to more precisely recreate the human brain microenvironment.[57] Microfluidic BBB models integrate microfluidics, cell culture technology, and in some cases, 3D printing, to construct miniaturized *in vitro* systems that replicate both the structure and function of the BBB. These models enable spatial and temporal control over key cell types, including endothelial cells, pericytes, and astrocytes, which are cultured according to their native anatomical distribution and functional interactions. This approach facilitates the formation of highly biomimetic barrier structures with enhanced physiological relevance.[58] Currently, common types of microfluidic chips for the human brain include compartmentalized chips with microchannel separation, compartmentalized chips with membrane separation, and gradient-inducing chips.[59] For instance, Sonninen *et al.*[60] co-cultured hiPSC-derived endothelial cells and astrocytes on AKITA plates (a commercially available organ-on-a-chip microfluidic platform) and applied a shaking-induced flow of 0.6 dyne/cm^2. Permeability assays and protein expression analyses confirmed the successful construction of a functional microfluidic BBB chip (Table 1).[60] In another study, Middelkamp *et al.*[24] demonstrated that culturing cells in a microfluidic environment induced significant changes in gene expression compared to conventional static plates. Specifically, endothelial cells exhibited reduced proliferation, while neurons and astrocytes showed enhanced adhesion and neuronal maturation (Table 1).[24] These findings highlight the potential of microfluidic chips for disease modeling and compound screening. Furthermore, Jeong *et al.*[61] employed numerical simulations to predict shear stress within microfluidic BBB chip channels. Their results showed that shear stress increased with decreasing channel size and porosity, and the simulation error was maintained within 2.17%, establishing a quantitative framework for optimizing microfluidic organ-on-a-chip systems to more closely replicate *in vivo* physiological conditions (Table 1).[61]

In addition, multichannel microfluidic chips enable the parallel testing of multiple experimental conditions, thereby improving experimental throughput and reproducibility. For example, Zakharova *et al.*[62] developed a polydimethylsiloxane (PDMS)-based chip featuring eight parallel microchannels, allowing simultaneous analysis of permeability under varying conditions. Their study revealed significant differences in permeability coefficients among molecules of different sizes, demonstrating the chip's sensitivity and versatility.[62] In short, biomimetic BBB microfluidic chips represent a transformative platform for the evaluation of BBB-permeable compounds. Their ability to closely mimic physiological conditions, combined with high-throughput and modular design capabilities, makes them highly valuable for both basic neuroscience research and translational drug development.[63]

2.6. Bioprinting-based model

3D bioprinting is an additive manufacturing technology that enables the precise layer-by-layer deposition of biomaterials and living cells under computer-aided design control to construct tissue-like structures.[64] Bioink (the printable formulation) is a key component of this process; it is typically composed of biocompatible hydrogels combined with live cells.[65] The choice of cell types included in the bioink depends on the target tissue. For neural tissue or BBB models, common cell types include astrocytes, pericytes, endothelial cells, and neurons. During the printing process, the bioink is rapidly solidified or crosslinked upon deposition to ensure cell encapsulation and structural stability. Crosslinking can occur through various mechanisms, such as ultraviolet light exposure in the case of photosensitive bioinks, or through the addition of crosslinking agents.[65,66] Bioprinting technologies can be broadly categorized into several types, each with distinct advantages and limitations.[64,67] For example, inkjet bioprinting is suitable for low-viscosity bioinks and offers high-speed printing, but may struggle with cell density and resolution. Extrusion-based bioprinting can accommodate higher-viscosity materials and cell densities but may expose cells to shear stress during printing. Laser-assisted bioprinting provides high resolution and avoids nozzle clogging, but it requires complex and costly optical systems. Regardless of the specific method, all bioprinting techniques construct 3D structures through the sequential deposition and curing of bioink layers based on pre-defined models.[64,65,67]

Traditional 2D cell culture methods are limited in their ability to replicate the 3D architecture and biomechanical cues—such as shear stress—present in the native capillary microenvironment. In contrast, 3D bioprinting offers a promising strategy for constructing physiologically relevant BBB models. This technology enables the spatial organization of multiple cell types—such as endothelial cells, pericytes, and astrocytes—into layered, biomimetic structures that closely resemble the vascular architecture of the blood–brain interface.[68] For example, Dona *et al.*[25] used digital light processing-based 3D bioprinting to construct a human brain microvascular model embedded with primary human astrocytes. The vascular component was formed using human BMECs and pericytes, and continuous perfusion was performed to promote vascular maturation. The

printed model was functionally evaluated for immune-endothelial interactions, permeability, and barrier integrity, demonstrating key BBB characteristics (Table 1).[25] Similarly, Oh *et al.*[69] introduced an aqueous two-phase printing approach to construct a BBB microstructure model in a liquid-phase environment. This technique overcame the limitations associated with air–liquid interface printing and then resulted in improved barrier functionality. The model incorporated three different human cell types: astrocytes, endothelial cells, and vascular pericytes, and enabled precise control over nutrient supply and drug concentrations during experimentation (Table 1).[69] In another study, Royse *et al.*[70] applied stereolithography-based 3D bioprinting to fabricate a BBB model, which is used as a drug screening platform. They printed a cylindrical hydrogel-based vascular network populated with human brain endothelial cells, pericytes, and astrocytes in an anatomically relevant arrangement. The model exhibited proper cell adhesion, expressed tight junction proteins, and was perfused to assess compound transport. Functional assays confirmed the presence of intact barrier properties and expression of key efflux transporters, including P-glycoprotein (P-gp) and breast cancer resistance protein (BCRP), highlighting the model's utility in CNS drug delivery research (Table 1).[70]

Additionally, the integration of 3D bioprinting with microfluidic technology offers a powerful approach for constructing physiologically and dynamically relevant *in vitro* BBB models. This hybrid strategy enables the simulation of fluidic conditions and precise architectural control that closely resemble the *in vivo* microenvironment. For example, Choi *et al.*[71] developed a bioreactor system designed to assess BBB integrity under dynamic flow conditions (Table 1).[71] The bioreactor was fabricated using a combination of 3D printing techniques and PDMS casting, and subsequently evaluated using a hiPSC-derived BBB model over a 7-day culture period. The system successfully supported real-time barrier monitoring and dynamic tissue culture, demonstrating its applicability for advanced BBB modeling studies.[71]

3. Structural and functional characterization of *in vitro* blood–brain barrier models

The structural and functional integrity of *in vitro* BBB models is fundamental to their reliability and relevance. Structural integrity serves as the foundation for functional performance, providing the necessary cellular architecture to support intercellular communication and maintain the physical barrier properties of the model. Conversely, functional integrity reflects the model's ability to preserve physiological homeostasis, regulate selective permeability, and respond appropriately to pathological stimuli. Structural integrity is typically assessed by evaluating cellular morphology and the expression and localization of tight junction proteins, such as claudin-5, occludin, and ZO-1, which are essential for maintaining paracellular barrier function. Functional integrity is commonly evaluated using several key parameters, including TEER, permeability to molecular tracers, and the expression or activity of transporter proteins, such as P-gp and BCRP. Together, these structural and functional assessments are critical for validating the fidelity of BBB models and ensuring their suitability for applications in disease modeling, compound evaluation, and neurovascular research.

3.1. Structural integrity

Structural integrity is a fundamental criterion for evaluating the physiological relevance of *in vitro* BBB models. Fluorescence imaging is commonly employed to visualize cellular morphology, spatial arrangement, and intercellular interactions, allowing researchers to assess whether the architecture of the model mimics that of the *in vivo* BBB. Astrocytes, which reside between capillaries and neurons, play a crucial role in BBB structure by forming a basement membrane surrounding BMECs. These glial cells are essential for maintaining brain homeostasis by regulating the balance of ions, amino acids, neurotransmitters, and water. Serving as a bridge between the vascular and neural systems, astrocytes are key contributors to the integrity and function of the BBB.[7] Ohbuchi *et al.*[72] used fluorescence imaging to examine the structural organization of brain endothelial cells and pericytes within a BBB model. Their findings showed that the cellular arrangement closely resembled *in vivo* conditions and exhibited selective permeability, providing strong evidence for the structural fidelity of the model.[72]

Tight junction proteins and adhesion complexes between endothelial cells play a central role in the formation and maintenance of the BBB. These tight junctions are composed of both transmembrane and intracellular proteins, including zonula occludens (ZO-1, ZO-2, ZO-3), claudin-5, occludin, and junctional adhesion molecules, which are anchored to the actin cytoskeleton via adaptor proteins such as cingulin.[2] The proper assembly of tight junctions is essential for establishing the structural integrity and selective permeability of the BBB. However, tight junction integrity is highly susceptible to disruption under pathological conditions. Studies have shown that diseases such as ischemic stroke,[73] major depressive disorder,[74] and encephalitis[75] can significantly impair the expression and organization of tight junction proteins, compromising BBB function. A variety of analytical

techniques have been used to assess tight junction protein expression and localization in BBB models. These include transmission electron microscopy for ultrastructural analysis,[76] immunofluorescence staining for spatial distribution,[77] western blotting for protein identification and quantification,[78] and quantitative real-time polymerase chain reaction for gene expression analysis.[79] Although maintaining BBB integrity remains a key challenge in the development of *in vitro* models, optimization of critical culture parameters, such as medium composition, cell seeding density, and substrate material, can improve the physiological relevance and structural fidelity of these models.[80]

3.2. Functional integrity

Barrier function is a fundamental characteristic of the BBB and a critical criterion for assessing the validity of *in vitro* BBB models. A functionally competent BBB is essential for protecting the brain by blocking the entry of neurotoxic substances, regulating the selective transport of nutrients, and facilitating the clearance of metabolic waste products.[81] These barrier properties are tightly associated with the presence and organization of tight junction proteins, which form the structural basis for paracellular restriction. TEER measurement is one of the most widely used and reliable methods for evaluating the integrity and permeability of endothelial monolayers in *in vitro* BBB models.[82,83] TEER provides a quantitative, non-invasive, and real-time assessment of tight junction formation and is particularly useful for monitoring intracellular signaling events and barrier dynamics. Although TEER values of *in vitro* models are generally lower than those observed *in vivo* (typically 1800–2000 $\Omega \cdot cm^2$), recent advances have led to significant improvements. For example, Chang *et al.*[63] developed a microfluidic chip-based BBB model with a TEER value of approximately 220 $\Omega \cdot cm^2$ (Table 1).[63] Co-culture systems, particularly those combining endothelial cells with astrocytes, have been shown to markedly enhance barrier function, achieving TEER values as high as 1200 $\Omega \cdot cm^2$ (Table 1).[38] In addition to TEER, the use of permeability assays with hydrophilic tracers is another common approach for evaluating barrier function. Tracers such as fluorescein isothiocyanate-dextran (FITC-dextran), glucose, sucrose, mannitol, fluorescein sodium, and fluorescein yellow are commonly employed due to their low permeability across an intact BBB. These compounds enable the quantification of paracellular leakage and provide complementary evidence of tight junction integrity in microfluidic BBB models.[84,85] Evans blue dye, which binds tightly to serum albumin, is another established tracer for assessing BBB permeability.[86] Under normal physiological conditions, albumin does not cross the BBB. However, the presence of Evans blue-albumin complexes in the brain parenchyma serves as a clear indicator of tight junction disruption and paracellular leakage.[87]

Selective permeability is another hallmark feature of the BBB and a critical functional parameter in evaluating *in vitro* BBB models. Under physiological conditions, large hydrophilic tracers such as FITC-dextran are unable to cross the BBB. However, smaller hydrophilic molecules may traverse the barrier via transcellular or paracellular pathways, with permeability generally decreasing as molecular weight increases, which demonstrates the size-selective permeability of the model.[77] Alterations in permeability often correlate with BBB dysfunction, particularly in pathological states such as ischemic stroke, where endothelial permeability is markedly increased. Therefore, permeability assays that combine exogenous tracers with other functional measurements, such as TEER and immunostaining, can provide valuable insights into the mechanisms of BBB disruption in neurological disorders. For instance, TEER measurements, FITC-dextran permeability assays, and immunofluorescence staining have been widely used to evaluate the BBB integrity of *in vitro* ischemic stroke models.[88] However, assessing selective permeability based solely on non-permeable compounds is insufficient. A more robust evaluation requires testing a range of molecules with varying permeability characteristics and comparing the results to those obtained from Transwell systems or *in vivo* data. For example, Shi *et al.*[77] assessed BBB permeability using three compounds with distinct transport properties: (i) caffeine, a lipophilic small molecule that crosses the BBB via passive diffusion and carrier-mediated transport, (ii) cimetidine, a moderately permeable compound subject to efflux transporter activity, and (iii) adriamycin, a compound that does not cross the BBB. The permeability coefficients obtained from the *in vitro* model closely matched those observed *in vivo*, supporting the model's ability to replicate the physiological barrier properties of the human BBB.[77]

Furthermore, the BBB is characterized by high expression of various functional proteins and transporters that are critical for regulating the selective transport of nutrients and xenobiotics. These include P-gp, BCRP, multidrug resistance-associated proteins, glucose transporters (e.g., glucose transporter 1), and amino acid transporters.[89] These transporters collectively contribute to the homeostatic and protective functions of the BBB by facilitating the uptake of essential molecules and actively excluding potentially harmful compounds. For instance, P-gp plays a key role in limiting the distribution of many CNS drugs by actively effluxing them back into the bloodstream. In *in vitro* BBB models, the functional expression of P-gp has been validated using rhodamine

123—a known P-gp substrate—along with its inhibitor verapamil, which demonstrated the transporter's activity and regulatory capacity.[77] Additionally, Ito *et al.*[90] confirmed the presence and functionality of multiple BBB-specific transporters, including P-gp, BCRP, and other adenosine triphosphate-binding cassette transporters, in their *in vitro* model system. Their results emphasized not only the intercellular barrier properties but also the functional transporter activity necessary for maintaining BBB fidelity and physiological relevance.[90] These transporters are indispensable for preserving the functional integrity of the BBB and are essential parameters for evaluating the accuracy and utility of *in vitro* BBB models in drug screening and neurological research.

3.3. Characterization of the blood–brain barrier model integrating microfluidics and bioprinting

In vitro BBB models that integrate microfluidic technology with bioprinting offer advanced platforms for replicating physiologically and dynamically relevant neurovascular environments. The characterization of such models typically involves a combination of assessments, including cell viability and morphology, barrier permeability, junctional protein expression, receptor-mediated transport, and response to dynamic stimulation. For instance, in the study by Oh *et al.*,[69] cell viability and morphology of endothelial and glial cells within 3D-printed scaffolds were evaluated under flow conditions using viability dyes with confocal laser scanning microscopy.[69] Barrier permeability was commonly assessed by perfusing fluorescent dextrans of various molecular weights through the microchannels, such as 10 kDa Texas Red or 40 kDa FITC-dextran. Real-time monitoring and calculation of apparent permeability coefficients enabled quantification of barrier integrity within the 3D-printed BBB models.[25,69] Notably, Royse *et al.*[70] conducted permeability studies and ultrasound studies through FITC-dextran in a 3D-printed *in vitro* BBB model. Under continuous perfusion, FITC-dextran was used as a tracer while fluorescence imaging was conducted in parallel with ultrasound application. Fluorescence signals were collected through molecular channels in real time, and the permeability coefficient values were calculated to evaluate the effects of mechanical stimuli on barrier permeability.[70] In addition to permeability assessments, immunofluorescence staining of key proteins provided insights into the structural and functional fidelity of the models. Junctional markers such as ZO-1 and claudin 5 (tight junctions), vascular endothelial cadherin (adherens junctions), and efflux transporters, including P-gp and BCRP, were used to verify cell–cell connectivity and transporter expression. Transcytosis receptors, such as the transferrin receptor and low-density lipoprotein receptor-related protein 1, were also analyzed to confirm the presence of receptor-mediated uptake pathways vital for CNS drug delivery.[25,70] Collectively, these characterization strategies demonstrate that the performance and reliability of bioprinting-microfluidic integrated BBB models depend heavily on how well they recapitulate key structural and functional features of the *in vivo* BBB. Therefore, rigorous evaluation against these parameters is essential for validating the model's application in compound evaluation and neurovascular research.

4. Principles of blood–brain barrier chip design

Figure 3 shows the graphical abstract of BBB-on-a-chip construction and application. The development of a BBB microfluidic chip typically involves three key components: material and fabrication, cell sources, and physiological conditions simulation. From early BBB models based on static culture dishes to Transwell-based platforms and, ultimately, dynamic microfluidic chips, the reliability and physiological relevance of *in vitro* BBB models have progressively improved. Recent advances suggest that the integration of 3D bioprinting technology may represent the next frontier in organ-on-chip development, offering greater spatial control and enhanced tissue complexity.[91] Table 2 summarizes the applications of 3D bioprinting for developing organ-on-chip models. The application trajectory of BBB microfluidic chips has evolved over time. Initially, these models were primarily used for validating barrier properties and model fidelity. Subsequently, their use expanded into disease modeling, enabling mechanistic research of neurological disorders under more physiologically relevant conditions. At present, the most prominent application of BBB microfluidic chips is in compound evaluation, particularly for assessing compound permeability, transport mechanisms, and neurotoxicity. This progression highlights the growing utility of BBB-on-a-chip systems as versatile and powerful tools in both basic research and translational biomedical applications.

4.1. Materials and fabrication

The selection of materials for constructing BBB microfluidic chips must balance several critical criteria, including biocompatibility, chemical stability, optical transparency, and compatibility with cell culture. PDMS is the most widely used material due to its favorable properties, such as gas permeability, flexibility, ease of molding, and optical clarity. However, PDMS also presents several limitations, including incompatibility with non-polar organic solvents, high water vapor permeability, hydrophobic surface characteristics, and a strong tendency to adsorb biomolecules, which may interfere with experimental reproducibility and sensitivity.[92] Alternative

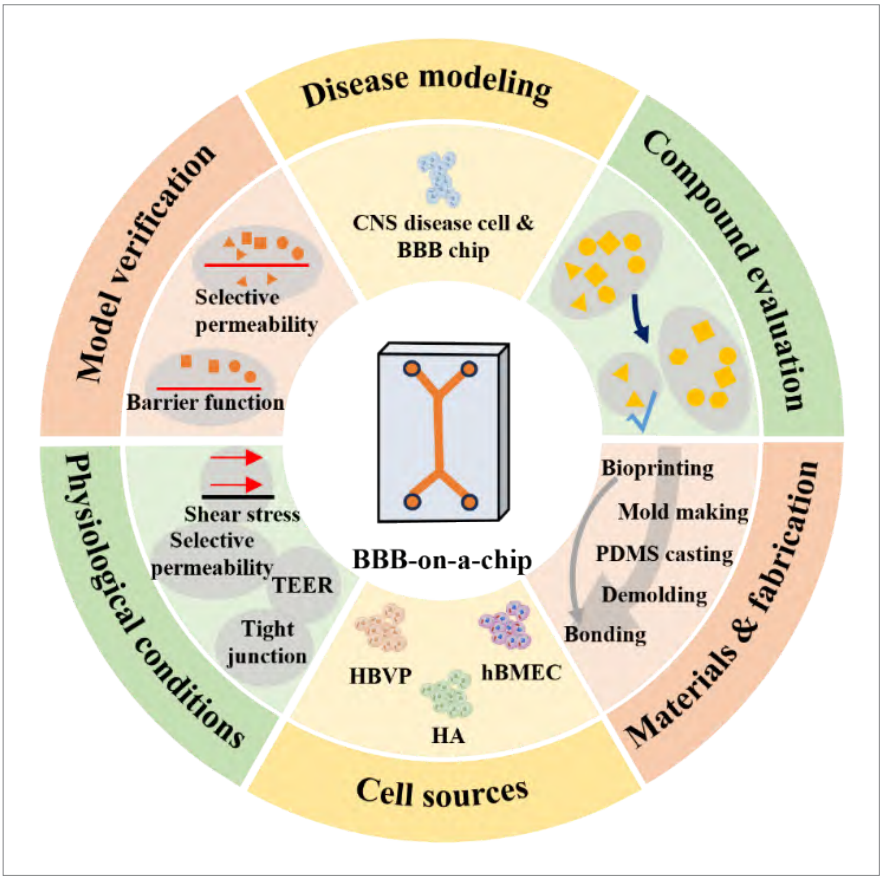


Figure 3. Graphical abstract of BBB-on-a-chip construction and application. The construction of a BBB-on-a-chip system involves three primary components: materials and fabrication, cell sources, and simulation of physiological conditions. The key application areas include model verification, disease modeling, and compound evaluation. Selected cellular elements shown in the figure were sourced or adapted from Servier Medical Art via the scifig.bio plugin (version 1.3.2). Abbreviations: BBB, blood–brain barrier; CNS, central nervous system; HA, human astrocytes; hBMEC, human brain microvascular endothelial cells; HBVP, human brain vascular pericytes; PDMS, polydimethylsiloxane; TEER, transepithelial electrical resistance.

materials have been explored to overcome these limitations. Polymethylmethacrylate has gained attention for its rigidity, optical transparency, low refractive index, and minimal autofluorescence, making it suitable for optical imaging and analytical applications. Polycarbonate membranes are frequently employed as porous interfaces due to their permeability, enabling the simulation of cell–cell interactions and transport across barriers.[93] Polystyrene, a well-established material in traditional cell culture, offers high biocompatibility and supports robust cell adhesion and proliferation.[94] Additionally, fiber-based ECM membranes have shown promise in facilitating cell–cell communication and migration, making them ideal for studies focused on intercellular signaling and barrier remodeling.[95] Despite the availability of alternative materials, PDMS remains the predominant material used in BBB chip fabrication due to its superior mechanical and chemical processing characteristics. While polymethylmethacrylate has been employed in a limited number of studies, approximately 50% of BBB microfluidic models incorporate porous membranes made from various materials to physically separate fluidic channels and mimic basement membranes.[96]

Soft lithography is the most commonly used method for fabricating microfluidic chips, particularly when working with PDMS. This technique involves a series of steps, including photolithography to define microchannel features, mold fabrication, PDMS casting, demolding, and bonding of the PDMS structure to a substrate (e.g., glass or polymer). However, the tendency of PDMS to adsorb biomolecules and its relatively poor long-term structural stability present challenges for durability and reproducibility in extended culture systems.[97]

To address the limitations associated with traditional soft lithography and PDMS-based fabrication, researchers have

Table 2. Applications of three-dimensional bioprinting for developing organ-on-chip models

Organ/Tissue	Cells	Bioprinting technology	Bioink	Fabrication	Apparatus	Finding	Ref.
Blood–brain barrier for neurodegenerative diseases	Neuroblastoma (SH-SY5Y) and glioblastoma (U87) cell; human FPA	Syringe extrusion printhead on a Cellink BIOX 3D bioprinter	Mixtures of hydrogel and cells	Extrusion printing with a syringe printhead on a Cellink BIOX 3D bioprinter	Modular hyaluronan-based hydrogel system	Enhanced interaction of FPA with hyaluronan-based gels	[101]
Blood–brain barrier	Mouse brain endothelial cells (bEnd.3)	Co-printed resins using the EDEN 260V 3D printing system	Vero White PlusFullCure 835 resin, PVA	3D-printed frame, insert microneedles, apply collagen mixture in the square opening, remove microneedles, seed cells in the collagen channel	Engineered brain microvessel array	The disruption of the barrier function of the model and its functional recovery demonstrated its effectiveness	[102]
Blood–brain barrier	Outer: astrocytes (C8-D1A), inner: pericytes (MBVP), endothelial cells (bEnd.3), mouse hippocampal neurons (HT22)	Coaxial extrusion bioprinting with the inner and outer layer nozzle (EFL-BP-6602)	GelMA, GMHA, and LAP, photocurable bioink	Layer-by-layer deposition, followed by UV-induced cross-linking of the photocurable components	Hollow vessel with inner and outer layers	The device exhibits perfusion capacity and barrier function, making it a promising platform for compound evaluation	[103]
Cardiac for thrombosis research	HUVECs, human dermal fibroblasts (CRL-2522, ATCC)	Hydrogel printing, bioprinter (BioBots, Inc.) equipped with a 27G blunt needle	Alginate/GelMA	Bioprinting channels and walls, printing the GelMA scaffold, curing with UV, dissolving the sacrificial layer, and obtaining the final GelMA block	The final construct with hollow channels	A powerful model for studying thrombosis, thrombolysis, and fibrosis, as well as the interactions among different components. It may be extended to other vascularized models	[105]

Abbreviations: BCECs, brain capillary-like endothelial cells; FPA, fetal primary astrocytes; GelMA, gelatin methacrylate; hiPSCs, human induced pluripotent stem cells; HUVECs, human umbilical vein endothelial cells; LAP, lithium phenyl-2,4,6-trimethylbenzoylphosphinate; PDMS, polydimethylsiloxane; PEGDA, poly(ethylene glycol) diacrylate; PVA, poly-vinyl alcohol; UV, ultraviolet

doi: 10.36922/IJB025270265

explored alternative techniques such as laser engraving and 3D printing. Laser engraving involves directing a laser beam onto the material surface to selectively ablate regions and create microfluidic channels. This method is particularly effective for post-processing tasks, such as punching access ports or removing excess material.[98] However, the high cost of laser engraving equipment and the risk of thermal damage to heat-sensitive substrates present notable challenges. The integration of 3D printing technology with microfluidic platform design has opened new avenues for simulating complex biological environments, including multi-organ interactions. This advancement significantly enhances the applicability of microfluidic models in compound evaluation and translational research.[99] For instance, Cenhrang *et al.*[100] incorporated biologically relevant ECM materials, such as collagen, into 3D-printed microfluidic devices to generate high-barrier-function BBB models. The integration of ECM materials with microfluidics provided a physiologically relevant matrix environment, supporting cell–matrix interactions and mimicking the native BBB structure more effectively.[100] Moreover, 3D printing offers substantial advantages in the rapid prototyping and customization of chip components, making it a powerful tool in the construction of BBB-on-a-chip systems. Its flexibility, cost-effectiveness, and ability to fabricate complex geometries position it as a promising approach for next-generation *in vitro* BBB modeling.

In bioprinting, material selection is a critical factor, particularly the choice of bioink. Customizing ECM-mimicking hydrogels that are compatible with astrocytes enables additive biofabrication of advanced CNS tissues and disease models.[101] For example, Matthiesen *et al.*[101] developed a modular hydrogel system based on hyaluronic acid using 3D bioprinting to study interactions among neuroblastoma (SHSY5Y), glioblastoma (U87) cell lines, and human fetal primary astrocytes. They found that bioprinting enhanced astrocyte interactions with the hyaluronan-based matrix, thereby facilitating the development of physiologically relevant CNS disease models (Table 2).[101] Similarly, Kim *et al.*[102] utilized microneedles and 3D-printed frameworks to construct a functional *in vitro* brain microvascular hydrogel model. Mouse brain endothelial cells (bEnd.3) were seeded onto the luminal surface of cylindrical collagen microchannels. This model successfully demonstrated barrier function, which could be disrupted by hypertonic mannitol and subsequently restored—highlighting its suitability for simulating both normal and pathological BBB conditions (Table 2).[102] Wang *et al.*[103] introduced a coaxial extrusion bioprinting technique to fabricate triple-layered tubular blood vessels that mimic the BBB structure. In their model, photopolymerizable bioink was used to form the inner and outer vessel walls, with endothelial cells seeded between two layers. Following crosslinking and removal of uncured materials, the resulting hollow vessel was perfused with culture medium. Functional testing revealed that the bioprinting vessels allowed the passage of small neuroprotective molecules while restricting larger compounds, effectively replicating the selective permeability of the physiological BBB (Table 2).[103] These examples underscore the ability of 3D bioprinting to generate hollow, cell-lined channels with capillary-like properties, including layer-specific architecture, fluid perfusion, and molecular selectivity. Collectively, these advances demonstrate that 3D-bioprinting constructs can successfully recapitulate key structural and functional features of the BBB, such as multi-layered cellular organization, flow dynamics, and selective permeability, which makes them valuable platforms for compound screening and neuropharmacological research.[68]

Bioprinting tissues can be seamlessly integrated into microfluidic organ-on-a-chip platforms to more accurately simulate the dynamic physiological environment of living organs. Microfluidic chips offer precise control over fluid flow and shear stress, which are critical for promoting vascular maturation and enhancing BBB functionality. Notably, shear stress has been shown to strengthen tight junction formation between endothelial cells, thereby improving barrier integrity.[104] One practical approach involves directly bioprinting the tissue construct and coupling it with a perfusion system for dynamic cell culture. For example, Dona *et al.*[25] utilized digital light processing-based 3D bioprinting to fabricate a human brain microvascular model surrounded by embedded astrocytes. Using computer-aided design software, they designed a microvascular scaffold composed of crosslinkable photosensitive bioinks, including polyethylene glycol diacrylate and gelatin methacrylate. The successful formation of perfusable channels was verified by infusing red dye. Human BMECs were then seeded into the channels to achieve endothelialization, and the construct was enclosed with a PDMS cap and cultured under gradually increasing flow rates via perfusion.[25] In another example, Zhang *et al.*[105] applied bioprinting technology to precisely position both cells and matrix materials within a prefabricated microfluidic chip (Table 2).[105] They developed a sacrificial bioprinting method to produce vascularized hydrogels: Pluronic F127 was printed as a sacrificial template and dried before being transferred onto a PDMS substrate. The template was then embedded in gelatin methacrylate, which was crosslinked under ultraviolet light. Following the dissolution of the sacrificial material, a hollow channel network remained. Human umbilical vein endothelial cells were seeded into

these channels and cultured under perfusion to establish a functional endothelialized microvasculature. While this specific model was heart-related, the same fabrication principle can be extended to create bioprinted-BBB systems by embedding NVUs within perfusable scaffolds. Overall, the integration of bioprinting tissues with microfluidic platforms, known as "bioprinting organ-on-a-chip" systems, enables physiological fluid flow, real-time monitoring, and high-throughput experimental capabilities. For BBB modeling, such systems allow the construction of multicellular, flow-responsive barrier structures that closely mimic the architecture and function of the NVU. These next-generation platforms hold significant promise for applications in CNS disease modeling, compound permeability testing, and neuropharmacological compound evaluation.[25,104]

4.2. Cell sources

The choice of cell source is a critical determinant of the physiological relevance, functionality, and reproducibility of *in vitro* BBB models. Among the available options, primary cells offer high fidelity to native tissue, as they retain key phenotypic characteristics, differentiation status, and metabolic activity. Moreover, primary human cells pose a relatively low risk of oncogenic transformation. In dynamic microfluidic cultures, primary cells have been shown to maintain functional activity for several days to over a week, underscoring their growing importance in advanced *in vitro* BBB models.[106]

Immortalized cell lines offer practical advantages such as ease of acquisition, simple handling, and high proliferative capacity, enabling repeated passaging and high-throughput applications. Although they may not fully replicate the properties of native cells, immortalized cell-based BBB models are widely used for evaluating compound permeability and performing large-scale screening assays. For instance, Yang *et al.*[107] co-cultured immortalized human cerebral microvascular endothelial cells (CMECs) with pericytes and astrocytes to assess the permeability of 10 pharmacological agents, including caffeine, carbamazepine, and desipramine. Their results revealed that permeability trends in the *in vitro* model closely mirrored those observed *in vivo*, supporting the model's utility for drug evaluation.[107] Immortalized cell lines are also instrumental in studying the mechanisms underlying neuroimmune responses and neurodegenerative diseases. Ohbuchi *et al.*[72] demonstrated that brain endothelial cells formed microvascular-like structures *in vitro*, while pericytes enhanced barrier integrity. This system effectively modeled BBB dysfunction and immune cell infiltration, providing insights into the pathophysiology of CNS disorders.[72]

hiPSCs, which can differentiate into various cell types, are increasingly utilized in BBB models for disease modeling and compound evaluation, particularly in the context of rare or patient-specific neurological disorders.[96] For example, Ferreira *et al.*[108] developed BBB models using hiPSCs derived from patients with neurodegenerative diseases to enhance understanding of disease mechanisms and support the development of improved therapeutic strategies.[108] Although the combination of hiPSC-derived endothelial cells, pericytes, and astrocytes within fibrin hydrogels has enabled the construction of vascularized chip models, challenges remain. Notably, in some 3D configurations, endothelial cells fail to integrate fully into the hydrogel scaffold, thereby limiting the acquisition of key BBB-like properties such as tight junction formation and selective permeability.[109] In recent years, significant progress has been made in developing human *in vitro* BBB models. This includes the differentiation of NVU cell types from stem cells, improved replication of the native ECM environment, and the application of BBB-on-a-chip platforms to better mimic *in vivo* physiology and function.[108] In summary, hiPSC-based BBB models offer a personalized and scalable approach for investigating individual differences in BBB characteristics, disease phenotypes, and drug responses, thereby holding great promise for both basic research and precision medicine applications.

Another common strategy for constructing physiologically relevant BBB models involves the use of multiple cell types, including a combination of primary cells and hiPSCs. This hybrid approach enables the preservation of specific functional properties inherent to primary cells while leveraging the scalability and patient specificity offered by hiPSC-derived components, thereby enhancing the biological realism and applicability of the model. For example, Noorani *et al.*[84] demonstrated that essential BBB characteristics could be faithfully reproduced by co-culturing hiPSC-derived BMECs with primary human pericytes and astrocytes within a microfluidic chip platform, such as low paracellular permeability, active efflux transporter function, and appropriate osmotic responsiveness.[84] This integrated BBB-on-a-chip model effectively mimicked the structural and functional properties of the human NVU. Such composite models, combining the strengths of both cell sources, not only provide a more physiologically accurate platform but also serve as valuable tools for therapeutic screening and mechanistic studies of brain diseases. As shown in recent work, these hybrid BBB models offer insights into disease pathophysiology and compound transport, supporting their use in preclinical evaluation and personalized medicine.[110]

4.3. Simulation of physiological conditions

The validity of *in vitro* BBB modeling depends on its ability to replicate the physiological structure and dynamic microenvironment of the *in vivo* BBB. Effective BBB models must accurately mimic local microenvironmental conditions, support cellular communication, and simulate organ interactions.[59] BBB microfluidic chips were proven effective in compound screening by replicating endothelial glycocalyx structure and dynamics, which provided effective protection to endothelial cells under shear stress and enhanced transendothelial transport efficiency.[111]

Fluid shear stress is a critical biomechanical regulator of BBB function. It plays a key role in inducing the expression of tight junction proteins by BMECs, thereby enhancing the barrier's selective permeability. This selectivity allows lipid-soluble molecules, such as theophylline, to accumulate outside the lumen, while restricting the passage of hydrophilic or larger compounds like morphine and sucrose, thus preserving BBB integrity.[112] Cucullo *et al.*[113] demonstrated that human BMECs cultured under dynamic flow conditions exhibited permeability profiles closely resembling those of the *in vivo* BBB, even in the absence of astrocytes. Their model achieved a high correlation coefficient (r = 0.93) with *in vivo* data, underscoring the importance of shear stress in maintaining BBB-like function.[113] Physiologically, fluid shear stress is generated by blood flow within cerebral vessels, acting directly on the endothelial surface and subsequently influencing surrounding neurons and glial cells. In the human cerebral vasculature, shear stress ranges from 10–70 dyn/cm^2 in arteries and 2.8–95.5 dyn/cm^2 in capillaries, with an average capillary shear stress typically between 5 and 23 dyn/cm^2.[114] However, several *in vitro* models fall short of reproducing these physiological flow conditions. For instance, models developed by Chim *et al.*[110] and Griep *et al.*[115] produced shear stress values ranging only from 0.01 to 0.06 dyn/cm^2, which are considerably lower than those observed *in vivo* and may be insufficient to induce appropriate endothelial responses.[110,115] Notably, Ceccarelli *et al.*[116] addressed this limitation by employing a dual syringe pump system to drive fluid through a BBB microfluidic chip at a flow rate of 40 μL/min. This setup generated shear stress values of approximately 11–13 dyn/cm^2, successfully replicating physiologically relevant conditions and supporting the development of a more accurate and functional *in vitro* BBB model.[116]

5. Application of blood–brain barrier chips in compound evaluation

In vitro biomimetic BBB chip models offer several significant advantages for compound evaluation and drug development. These models closely replicate the physiological structure and functional characteristics of the native BBB, including selective permeability, active transport of nutrients and neurotransmitters, and barrier responses to various stimuli.[81] This physiological relevance makes BBB chips well-suited for evaluating drug candidates and other bioactive compounds under both normal and pathological conditions. One of the major strengths of microfluidic BBB chips is the ability to dynamically control the cellular microenvironment. Parameters such as shear stress, flow rate, and biochemical gradients can be precisely modulated, enabling more accurate simulation of *in vivo* conditions and allowing compounds to be tested under disease-specific or stress-inducing settings. Importantly, BBB chip models can reduce reliance on traditional animal models, thereby aligning with the principles of the 3Rs (Replacement, Reduction, and Refinement) in ethical research. By minimizing animal usage and circumventing inter-individual variability inherent to animal studies, these models improve data reproducibility while addressing ethical concerns associated with *in vivo* experimentation.[117] In addition, microfluidic platforms support parallelized culture conditions and real-time monitoring, enabling high-throughput screening of a large number of compounds during the early stages of drug discovery. This capability significantly reduces the time and cost associated with conventional drug development pipelines.[118,119] Furthermore, the high degree of standardization and environmental control afforded by BBB chip models reduces the confounding influence of systemic metabolic variability seen in whole animal studies. As a result, these platforms are particularly valuable for mechanistic studies and basic research aimed at elucidating BBB transport, barrier integrity, and cellular interactions under defined conditions.[120] Table 3 summarizes the application of BBB microfluidic chips in compound evaluation.

In vitro biomimetic BBB chips have emerged as a rational and versatile platform for investigating the effects of hazardous compounds on the CNS (Table 3). By integrating microfluidic technologies with advanced cell culture techniques, these chips enable the replication of key structural, functional, and mechanical characteristics of the *in vivo* BBB. For example, Xu *et al.*[121] utilized a microfluidic-based BBB chip to culture cells and tissues in a dynamic environment that closely mimicked the native NVU, enabling reliable assessments of compound permeability, toxicity, and therapeutic efficacy.[121] This platform has proven particularly valuable in preclinical drug development, safety testing, and evaluating the risk of clinical trial failure. Recent studies have demonstrated the effectiveness of BBB chip models in elucidating toxicity mechanisms and supporting compound evaluation.

Table 3. Application of blood–brain barrier microfluidic chips in compound evaluation

Compound name	Compound usage	Chip materials	Chip characteristics	Cell sources	Evaluation parameters	Ref.
Methamphetamine	Neuroactive, used in drug and medicine production	PDMS	Three coupled chips simulate BBB inflow, brain parenchyma, and BBB outflow	Primary human BMECs, pericytes, astrocytes, neurons	BBB permeability increased; immunofluorescence micrographs of cells showed integrity; untargeted metabolomics showed metabolite production altered	[122]
Organic phosphate malathion	Neurotoxic effects, organophosphorus malathion	Two-lane OrganoPlate	3D microfluidic brain-on-a-chip model	Neurons and astrocytes derived from human iPSCs	Confocal imaging of lanes and immunofluorescence images of cells showed integrity; cell viability decreased	[123]
Organophosphate chlorpyrifos (CPF)	Neurotoxic effects, agricultural pesticides	PDMS, PET membrane	Two-chamber device made with three layers separated by a membrane	Primary human BMECs, astrocytes (SVG p12), pericytes	Combined with MS and electrochemical analysis; CPF and primary metabolites distribution; acetylcholine levels increased; microscopy images showed contracted cells	[124]
Citronellol	Neurotoxicity, used in cosmetics, perfumes, and furniture	Not reported	Two parallel microchannels separated by a porous membrane	Human BMECs, pericytes (HBVP), astrocytes (NHA)	Neurotoxic effects sustained; neurochemical alterations; permeation measurement of citronellol	[125]
Sunitinib	Model drugs	PDMS sheets and porous PC membrane	Microfluidic platform connecting two separate microchips	Human CMEC/D3, glioma cells U251	Determination of permeation by MS; cell viability decreased; structural and functional characterization by immunofluorescence imaging	[127]
Caffeine, cimetidine, and coxorubicin	Model drugs	PDMS, silicone sheets, and a sandwiched porous polycarbonate membrane	Three-layer model: lid layer, chamber layer, and media perfusion layer	Human iPSCs-derived brain endothelial cells (IMR90-4), rat primary astrocytes	Shear stress simulation; TEER value measurement; evaluation of permeability coefficients	[99]
Paclitaxel and carboplatin-loaded biomimetic hybrid liposomes	Drugs for the treatment of glioblastoma	Microfluidic devices integrated with 3D printing	Two different T-shaped devices from a 3D-printed, digital-light processing AsigaMax UV (Asiga, Alexandria, Australia) printer, PlasCLEAR resin, resolution of 0.0025 mm	Human glioblastoma U87-MG cells, human CMEC/D3	Hybrid liposomes increased *in vitro* uptake and BBB penetration ability of drugs; tumor cell viability decreased; drug-loaded biomimetic hybrid liposomes increase the efficacy of paclitaxel and carboplatin	[126]

(*Continue*)

Table 3. Application of blood–brain barrier microfluidic chips in compound evaluation

Compound name	Compound usage	Chip materials	Chip characteristics	Cell sources	Evaluation parameters	Ref.
Dexamethasone	Glucocorticosteroid (corticosteroid drug)	PDMS, porous absorbent paper tube	PDMS chips with siphon-driven flow control, flow rate limited by porous absorbent paper tube	Primary rat BECs, pericytes, astrocytes	Immunofluorescence images of cells showed integrity; relative gene expression altered; dextran dye leakage reduced; measurement of TEER value changed; inflammatory activation and treatment	[128]
Nanoparticles-gold nanorods	Gold nanorods-PEG-Ang2/D1 for β-amyloid fibrinolysis	PDMS	BBB organ-on-a-chip with resistive permeability sensor	Human CMEC/D3, hippocampal astrocytes, cerebral perivascular cells	Optical images of cells and fluorescence imaging of tight junction proteins showed integrity; permeability assays of model and compound; cell viability assay	[130]
Nanoparticles-PLGA polymers	Ferulic acid encapsulated PLGA nanoparticles	PDMS	Three parallel microchambers: a central main chamber and two side channels	Immortalized human CMEC/D3), pericytes, astrocytes	Permeability assays of model and compound; cellular internalization of nanoparticle	[131]
Ang2 functionalized lipid cubes loaded with cisplatin and temozolomide	Cisplatin and temozolomide delivery for glioblastoma	PDMS	Microfluid-based BBB-GBM model for drug permeability and cellular uptake	Human CMEC/D3, human glioblastoma U87 cell line	Physicochemical characterization and permeability coefficients measurements of the compound; TEER and transport ratio measurements of the model; confocal imaging of tight junction proteins showed integrity	[132]
Matrine, wogonin, osthole, paeoniflorin, resveratrol, and quercetin	Anti-glioma components in traditional Chinese medicine	PDMS	Chip with four parallel channels	Primary human BMECs, human astrocytes, and human brain vascular pericytes	Immunofluorescence staining of cells showed integrity; TEER values measurements and permeability assay of the chip	[77]

Abbreviations: 3D, three-dimensional; Ang2, angiopoietin-2; BBB, blood–brain barrier; BECs, brain endothelial cells; BMECs, brain microvascular endothelial cells; CMEC, cerebral microvascular endothelial cells; GBM, glioblastoma multiforme; iPSCs, induced pluripotent stem cells; MS, mass spectrometry; PC, polycarbonate; PDMS, polydimethylsiloxane; PEG, polyethylene glycol; PET, polyethylene terephthalate; PLGA, poly(lactic-co-glycolic acid); TEER, transepithelial electrical resistance.

doi: 10.36922/IJB025270265

Maoz *et al.*[122] successfully used a microfluidic BBB chip to simulate the penetration of the psychoactive drug methamphetamine, which comprised primary human BMECs, pericytes, astrocytes, and neurons. Their findings revealed that methamphetamine exposure increased BBB permeability and altered cellular metabolite profiles, highlighting its neurotoxic effects and providing mechanistic insight into drug transport across the NVU (Table 3).[122] Similarly, Liu *et al.*[123] employed a BBB chip model incorporating neurons and astrocytes derived from hiPSCs to assess the neurotoxicity of the organophosphate compound malathion. Confocal imaging, cell viability assays, and enzymatic activity measurements demonstrated a significant reduction in total acetylcholinesterase and butyrylcholinesterase activity, validating the model as a platform for neurotoxicity screening.[123] In addition, combining BBB-on-a-chip systems with targeted mass spectrometry and electrochemical analysis has enabled quantitative assessment of compound exposure. For example, this approach was used to study the neurovascular effects of organophosphate compounds, further supporting the application of BBB chips in toxicology testing (Table 3).[124] Furthermore, citronellol, as a fragrance compound commonly found in cosmetics and personal care products, was shown to cross the BBB and induce neurotoxic effects, including inflammation and apoptosis. This finding highlights the utility of BBB microfluidic models for evaluating consumer product safety and identifying potential CNS hazards.[125] Overall, BBB chip models represent a powerful tool for investigating compound-induced CNS toxicity. Their ability to recapitulate neurovascular physiology, support high-throughput testing, and provide mechanistic insights makes them invaluable for both basic research and translational applications in neurotoxicology.

Biomimetic BBB chips offer considerable advantages in the screening of biologically active compounds, particularly for research related to neurological diseases such as glioma and neuroinflammation (Table 3). These models replicate essential features of the human BBB, enabling precise evaluation of compound transport, efficacy, and barrier disruption in physiologically relevant contexts. The integration of 3D bioprinting technology has further simplified the fabrication of microfluidic BBB models. For instance, Arduino *et al.*[126] utilized 3D bioprinting to develop an *in vitro* BBB microfluidic model, which was used to assess the delivery of paclitaxel and carboplatin encapsulated in liposomes for glioblastoma treatment. The results demonstrated that the liposomal formulations successfully crossed the BBB while retaining therapeutic efficacy, underscoring the utility of the bioprinting platform for brain tumor drug screening (Table 3).[126] Shao *et al.*[127] developed a BBB chip by co-culturing human CMEC/D3 with glioma cells (U251) to study the BBB penetration of sunitinib, a model therapeutic compound. Using electrospray ionization quadrupole time-of-flight mass spectrometry, they quantified drug transport and observed that glioblastoma cells exhibited higher viability in the 3D culture compared to traditional 2D conditions, highlighting the physiological relevance of the microfluidic environment (Table 3).[127] In another study, Wang *et al.*[99] constructed a BBB chip using BMECs differentiated from hiPSCs and primary rat astrocytes. By monitoring TEER and shear stress, they confirmed the functional integrity of the model. Permeability assays for three model drugs (caffeine, cimetidine, and doxorubicin) demonstrated that their transport profiles closely matched *in vivo* data, validating the model for compound screening applications (Table 3).[99] Furthermore, a microfluidic BBB chip was developed by Yu *et al.*[128] to simulate neuroinflammation-induced barrier dysfunction. The model, composed of primary rat brain endothelial cells, pericytes, and astrocytes, showed high expression of cell-type-specific genes, confirming cellular maturity and *in vitro* differentiation. Upon induction of neuroinflammation and treatment with dexamethasone, the chip exhibited measurable therapeutic responses, demonstrating its applicability for validating biologically active compounds in neuroinflammatory disease contexts (Table 3).[128] Together, these studies illustrate the growing utility of BBB-on-a-chip platforms in translational neuroscience, offering a physiologically relevant, high-throughput approach to evaluate compound transport, neurotoxicity, and therapeutic potential in CNS-related diseases.

Based on recent *in vitro* BBB chip studies, nanoparticles have emerged as promising drug delivery vehicles capable of overcoming biological barriers and enabling efficient transport of therapeutic agents across the BBB.[129] These nanoformulations offer targeted delivery, improved drug bioavailability, and enhanced therapeutic outcomes, particularly for CNS disorders. As summarized in Table 3, Palma *et al.*[130] evaluated the permeability of peptide-functionalized gold nanorods using a BBB organ-on-a-chip platform. Their study demonstrated that gold nanorods were able to cross the BBB and degrade β-amyloid aggregates, highlighting their potential for the treatment of AD.[130] In a separate study, ferulic acid-loaded poly(lactic-co-glycolic acid) nanoparticles were shown to traverse the BBB and exert antioxidant effects, suggesting a novel therapeutic strategy for combating oxidative stress-related neurological disorders.[131] For glioblastoma therapy, Cai *et al.*[132] developed lipid-based nanoparticles functionalized with vascular endothelin ligand, angiopoietin-2, and co-loaded with cisplatin

and temozolomide. These nanoparticles successfully penetrated the BBB and enhanced drug accumulation within glioblastoma cells, demonstrating improved therapeutic efficacy compared to free drugs (Table 3).[132] Collectively, these findings underscore the value of BBB chip models in evaluating the transport behavior, targeting efficiency, and therapeutic potential of nanoparticle-based drug delivery systems. Such platforms not only facilitate mechanistic insights but also accelerate the development of advanced nanomedicines for CNS applications.

Natural compounds derived from plants, animals, and microorganisms remain a vital source for the discovery of new therapeutic agents. These substances are often associated with low toxicity and are particularly suitable for the treatment of mild or chronic diseases. However, the quality control of the compounds remains challenging due to variability in raw material sources and environmental factors, along with high production costs.[133] In recent years, there has been growing interest in the potential of traditional Chinese medicine and its active constituents for treating CNS disorders.[134–136] Karthika *et al.*[137] further synthesized evidence regarding the efficacy of various traditional Chinese medicine-derived compounds in the treatment of neurological diseases.[137,138] In this context, *in vitro* BBB chip models offer a valuable platform for elucidating the mechanisms of action of herbal medicines and bridging the gap between modern pharmacology and traditional herbal therapies.[139] For example, Shi *et al.*[77] developed a BBB-glioma microfluidic chip (referred to as the BBB-U251 chip) using a co-culture of primary human BMECs, pericytes, astrocytes, and glioma (U251) cells. The model was validated using immunofluorescence imaging, TEER measurements, and permeability assays with FITC-dextran and model drugs, demonstrating barrier properties closely resembling *in vivo* conditions. This platform was then employed to screen anti-glioma compounds derived from traditional Chinese medicine using high-performance liquid chromatography combined with ultraviolet detection. Active components, such as baicalein and naringenin, were identified for their antitumor properties. Notably, the study also revealed that the presence of an intact BBB significantly limited the effectiveness of these compounds on glioma cells, underscoring the importance of incorporating barrier functions into compound evaluation platforms (Table 3).[77] These findings highlight the utility of BBB microfluidic chip models in advancing the mechanistic understanding and pharmacological screening of traditional Chinese medicines. Such platforms are instrumental in identifying bioactive compounds, evaluating BBB permeability, and supporting the development of novel therapeutics derived from natural products.

6. Perspectives

6.1. Challenges for bioprinting and microfluidic integrated systems

The integration of 3D bioprinting with microfluidic technology offers great promise for developing physiologically relevant *in vitro* BBB models, but also presents a series of unique technical challenges. The shear stress serves as a double-edged sword. Moderate shear stress generated by perfusion enhances tight junction formation and improves BBB integrity,[140] whereas excessive shear stress during the bioprinting process can compromise cell viability, particularly in extrusion-based systems.[141] Nozzle design further complicates the balance between print resolution and cell safety.[142,143] Microfluidic integration introduces additional design complexities. Seamless bonding between the printed scaffold and microfluidic materials must be achieved to ensure sealed fluid flow and maintain optical transparency for real-time imaging. Under continuous perfusion, it is essential to preserve vascular lumen patency and ensure that printed structures can withstand the resulting fluidic pressures without collapsing or delaminating.

Despite the challenges mentioned above, recent advancements have led to the successful development of hybrid platforms that integrate 3D bioprinting with microfluidic technology, enabling the creation of increasingly complex BBB-on-a-chip systems. For example, Xu *et al.*[142] designed a sophisticated human NVU chip using 3D bioprinting to simulate the pediatric brain microenvironment.[144] The model's integrated, automated perfusion system mimics physiological blood flow, while specialized fluidic channels in the brain region facilitate comprehensive metabolite analysis. Another particularly promising area is the development of high-throughput screening platforms. 3D bioprinting offers a scalable and efficient manufacturing method for generating multiplexed vascularized models. For example, Ahmad *et al.*[143] proposed a bioprinting strategy that created six perfusable hollow channels embedded in hydrogel; this multi-channel design supports the parallel evaluation of multiple compounds or concentration gradients.[145] These innovations pave the way for customizable, scalable, and multifunctional *in vitro* brain models.

6.2. The future of biomimetic blood–brain barrier chips

The biomimetic BBB chip is poised to make substantial contributions to the future of compound evaluation and CNS drug development. With ongoing developments in biomaterials science, new ECM-mimicking materials are expected to emerge that better replicate the mechanical and biochemical cues of the native brain microenvironment.[146,147] These materials would enhance cell viability, differentiation,

and functionality, further improving the physiological relevance of *in vitro* BBB models.

Moreover, the integration of biomimetic BBB chips with emerging analytical and sensing technologies represents a critical frontier in next-generation model development. Recent studies have shown that combining metabolomic analysis with microfluidic organ-on-a-chip models enables detailed characterization of metabolic pathway shifts associated with neuroinflammatory damage and BBB integrity loss.[148] Collectively, the integration of biomimetic BBB chips with biosensing,[149] proteomic,[150] and metabolomic technologies is expected to uncover complex interaction networks at the neurovascular interface, delivering predictive insights into compound behavior.

The serial integration of BBB microfluidic chips with other organ-on-a-chip systems presents additional opportunities for comprehensive compound evaluation. For example, Koenig *et al.*[149] developed a closed microfluidic system that interconnected a hiPSC-derived BBB model with cortical brain and hepatospheroid models, all derived from the same donor.[151] Such interconnected systems enable researchers to study compounds in a more holistic context, mimicking systemic circulation and inter-organ interactions. By replicating physiologically relevant inter-organ communication, these platforms represent a promising step toward more predictive preclinical testing and personalized drug development strategies.

7. Conclusion

The biomimetic BBB microfluidic chip represents a powerful and promising platform for replicating the structure and function of the human BBB *in vitro*. Constructed using microfluidic technology, these chips co-culture key neurovascular cell types, such as BMECs, astrocytes, pericytes, and neurons, within a controlled environment that closely mimics the physiological microenvironment of cerebral vasculature and brain tissue. This system enables dynamic simulation of intercellular interactions, shear stress, and nutrient exchange, thereby providing an advanced and physiologically relevant tool for evaluating the permeability of candidate compounds, offering significant advantages over traditional static and animal-based models.[152,153] As a result, biomimetic BBB microfluidic chips hold significant potential for accelerating CNS drug development, reducing reliance on animal testing, and deepening our understanding of neurovascular pathophysiology.

Acknowledgments

Schematic illustrations of cells shown in the graphical abstract or figures were used from or adapted from pictures provided by Servier Medical Art based on the plugin scifig.bio (version 1.3.2), licensed under a Creative Commons Attribution 4.0 Unported License.

Funding

This work was supported by the Beijing Life Science Academy (2024400CB0060) and (2023600CA0080).

Conflict of interest

The authors declare no conflicts of interest.

Author contributions

Conceptualization: Xiang Li, Yating Du
Funding acquisition: Xiang Li
Investigation: Yating Du, Zezhi Li
Supervision: Jianping Xie
Visualization: Yating Du
Writing–original draft: Yating Du
Writing–review & editing: Xiang Li

Ethics approval and consent to participate

Not applicable.

Consent for publication

Not applicable.

Availability of data

Not applicable.

References

1. Floryanzia SD, Nance E. Applications and considerations for microfluidic systems to model the blood–brain barrier. *ACS Appl Bio Mater*. 2023;6(9):3617-3632. doi: 10.1021/acsabm.3c00364

2. Shamul JG, Wang Z, Gong H, *et al*. Meta-analysis of the make-up and properties of in vitro models of the healthy and diseased blood–brain barrier. *Nat Biomed Eng*. 2024;9(4):566-598. doi: 10.1038/s41551-024-01250-2

3. Shi SM, Suh RJ, Shon DJ, *et al*. Glycocalyx dysregulation impairs blood–brain barrier in ageing and disease. *Nature*. 2025;639(8056):985-994. doi: 10.1038/s41586-025-08589-9

4. Sumpio BE, Timothy Riley J, Dardik A, Cells in focus: endothelial cell. *Int J Biochem Cell Biol*. 2002;34(12):1508-1512. doi: 10.1016/S1357-2725(02)00075-4

5. Bonkowski, D, Katyshev V, Balabanov RD, Borisov A, Dore-Duffy P. The CNS microvascular pericyte: pericyte-astrocyte

crosstalk in the regulation of tissue survival. *Fluids Barriers CNS*. 2011;8(1):8.
doi: 10.1186/2045-8118-8-8

6. Candelario-Jalil E, Dijkhuizen RM, Magnus T. Neuroinflammation, stroke, blood-brain barrier dysfunction, and imaging modalities. *Stroke*. 2022;53(5):1473-1486.
doi: 10.1161/strokeaha.122.036946

7. Abbott NJ, Rönnbäck L, Hansson E. Astrocyte–endothelial interactions at the blood–brain barrier. *Nat Rev Neurosci*. 2006;7(1):41-53.
doi: 10.1038/nrn1824

8. Vetter J, Palagi I, Waisman A, Blaeser A. Recent advances in blood-brain barrier-on-a-chip models. *Acta Biomater*. 2025;197:1-28.
doi: 10.1016/j.actbio.2025.03.041

9. Katt ME, Shusta EV. In vitro models of the blood-brain barrier: building in physiological complexity. *Curr Opin Chem Eng*. 2020;30:42-52.
doi: 10.1016/j.coche.2020.07.002

10. Profaci CP, Munji RN, Pulido RS, Daneman R. The blood-brain barrier in health and disease: important unanswered questions. *J Exp Med*. 2020;217(4):e20190062.
doi: 10.1084/jem.20190062

11. Engelhardt B, Ransohoff RM. Capture, crawl, cross: the T cell code to breach the blood–brain barriers. *Trends Immunol*. 2012;33(12):579-589.
doi: 10.1016/j.it.2012.07.004

12. Gursoy-Ozdemir Y, Yemisci M, Dalkara T. Microvascular protection is essential for successful neuroprotection in stroke. *J Neurochem*. 2012;123(s2):2-11.
doi: 10.1111/j.1471-4159.2012.07938.x

13. Nance E, Pun SH, Saigal R, Sellers DL. Drug delivery to the central nervous system. *Nat Rev Mater*. 2022;7(4):314-331.
doi: 10.1038/s41578-021-00394-w

14. Gao Q, Hernandes MS. Sepsis-associated encephalopathy and blood-brain barrier dysfunction. *Inflammation*. 2021;44(6):2143-2150.
doi: 10.1007/s10753-021-01501-3

15. Yin P, Wang X. Progresses in the establishment, evaluation, and application of in vitro blood-brain barrier models. *J Neurosci Res*. 2024;102(6):e25359.
doi: 10.1002/jnr.25359

16. Pediaditakis I, Kodella KR, Manatakis DV, *et al*. Modeling alpha-synuclein pathology in a human brain-chip to assess blood-brain barrier disruption. *Nat Commun*. 2021;12(1):5907.
doi: 10.1038/s41467-021-26066-5

17. Liu X, Li J, Liu S, *et al*. Fabrication of a 3D bioprinting model for posterior capsule opacification using GelMA and PLMA hydrogel-coated resin. *Regenerative Biomaterials*. 2024;11:rbae020.
doi: 10.1093/rb/rbae020

18. Lee, G., Kim, S. J., Park, J. K., Fabrication of a self-assembled and vascularized tumor array via bioprinting on a microfluidic chip. *Lab Chip*. 2023;23(18):4079-4091.
doi: 10.1039/d3lc00275f

19. Dudman, J., Ferreira, A. M., Gentile, P., Wang, X., Dalgarno, K., Microvalve Bioprinting of MSC-Chondrocyte Co-Cultures. *Cells*. 2021;10(12):3329.
doi: 10.3390/cells10123329

20. Rueda-Gensini, L., Serna, J. A., Rubio, D., Orozco, J. C., Bolaños, N. I., Cruz, J. C., Muñoz-Camargo, C., Three-dimensional neuroimmune co-culture system for modeling Parkinson's disease microenvironments in vitro. *Biofabrication*. 2023;15(4).
doi: 10.1088/1758-5090/ace21b

21. Li Y, Liu B, Zhao T, *et al*. Comparative study of extracellular vesicles derived from mesenchymal stem cells and brain endothelial cells attenuating blood-brain barrier permeability via regulating Caveolin-1-dependent ZO-1 and Claudin-5 endocytosis in acute ischemic stroke. *J Nanobiotechnology*. 2023;21(1):70.
doi: 10.1186/s12951-023-01828-z

22. Cho C-F, Wolfe JM, Fadzen CM, *et al*. Blood-brain-barrier spheroids as an in vitro screening platform for brain-penetrating agents. *Nat Commun*. 2017;8(1):15623.
doi: 10.1038/ncomms15623

23. Chai YC, To SK, Simorgh S, *et al*. Spatially self-organized three-dimensional neural concentroid as a novel reductionist humanized model to study neurovascular development. *Adv Sci (Weinh)*. 2024;11(5):e2304421.
doi: 10.1002/advs.202304421

24. Middelkamp HHT, Verboven AHA, De Sá Vivas AG, *et al*. Cell type-specific changes in transcriptomic profiles of endothelial cells, iPSC-derived neurons and astrocytes cultured on microfluidic chips. *Sci Rep*. 2021;11(1):2281.
doi: 10.1038/s41598-021-81933-x

25. Galpayage Dona KNU, Ramirez SH, Andrews AM. A Next-generation 3D tissue-engineered model of the human brain microvasculature to study the blood-brain barrier. *Bioengineering (Basel)*. 2023;10(7):817.
doi: 10.3390/bioengineering10070817

26. Mancuso S, Bhalerao A, Cucullo L. Advances and challenges of bioassembly strategies in neurovascular in vitro modeling: an overview of current technologies with a focus on three-dimensional bioprinting. *Int J Mol Sci*. 2024;25(20):11000.
doi: 10.3390/ijms252011000

27. Audus KL, Borchardt RT. Characterization of an in vitro blood-brain barrier model system for studying drug transport and metabolism. *Pharm Res*. 1986;3(2):81-87.
doi: 10.1023/a:1016337202335

28. van Bree JB, de Boer AG, Danhof M, Ginsel LA, Breimer DD. Characterization of an "in vitro" blood-brain barrier: effects of molecular size and lipophilicity on cerebrovascular

endothelial transport rates of drugs. *J Pharmacol Exp Ther*. 1988;247(3):1233-1239.
doi: 10.1016/S0022-3565(25)13283-7

29. Bernoud N, Fenart L, Bénistant C, *et al*. Astrocytes are mainly responsible for the polyunsaturated fatty acid enrichment in blood-brain barrier endothelial cells in vitro. *J Lipid Res*. 1998;39(9):1816-1824.
doi: 10.1016/S0022-2275(20)32169-6

30. Al-Ahmad AJ. Human-induced pluripotent stem cell-based model of the blood-brain at 10 years: a retrospective on past and current disease models. *Handb Exp Pharmacol*. 2023;281:141-156.
doi: 10.1007/164_2023_645

31. Stone NL, England TJ, O'Sullivan SE. A novel transwell blood brain barrier model using primary human cells. *Front Cell Neurosci*. 2019;13:230.
doi: 10.3389/fncel.2019.00230

32. Qi D, Lin H, Hu B, Wei Y. A review on in vitro model of the blood-brain barrier (BBB) based on hCMEC/D3 cells. *J Control Release*. 2023;358:78-97.
doi: 10.1016/j.jconrel.2023.04.020

33. Xie Y, Ye L, Zhang X, *et al*. Transport of nerve growth factor encapsulated into liposomes across the blood-brain barrier: in vitro and in vivo studies. *J Control Release*. 2005;105(1-2):106-119.
doi: 10.1016/j.jconrel.2005.03.005

34. Singh NR, Gromnicova R, Brachner A, *et al*. A hydrogel model of the human blood-brain barrier using differentiated stem cells. *PLoS One*. 2023;18(4):e0283954.
doi: 10.1371/journal.pone.0283954

35. Schofield C, Sarrigiannidis S, Moran-Horowich A, *et al*. An in vitro model of the blood-brain barrier for the investigation and isolation of the key drivers of barriergenesis. *Adv Healthc Mater*. 2024;13(32):e2303777.
doi: 10.1002/adhm.202303777

36. Chen S, Tang C, Ding H, *et al*. Maf1 ameliorates sepsis-associated encephalopathy by suppressing the NF-kB/NLRP3 inflammasome signaling pathway. *Front Immunol*. 2020;11:594071.
doi: 10.3389/fimmu.2020.594071

37. Wang J, Tang W, Yang M, *et al*. Inflammatory tumor microenvironment responsive neutrophil exosomes-based drug delivery system for targeted glioma therapy. *Biomaterials*. 2021;273:120784.
doi: 10.1016/j.biomaterials.2021.120784

38. Maherally Z, Fillmore HL, Tan SL, *et al*. Real-time acquisition of transendothelial electrical resistance in an all-human, in vitro, 3-dimensional, blood-brain barrier model exemplifies tight-junction integrity. *Faseb J*. 2018;32(1):168-182.
doi: 10.1096/fj.201700162R

39. Jain MK, Chernomorsky A, Silver FH, Berg RA. Material properties of living soft tissue composites. *J Biomed Mater Res*. 1988;22(3 Suppl):311-326.
doi: 10.1002/jbm.820221409

40. Alpert, S. S., Banks, G., The concentration dependence of the hemoglobin mutual diffusion coefficient. *Biophys Chem*. 1976;4(3):287-296.
doi: 10.1016/0301-4622(76)80077-4

41. Schmitz KS, Shaw BR. Hydrodynamic evidence in support of spacer regions in chromatin. *Science*. 1977;197(4304):661-663.
doi: 10.1126/science.877579

42. Wang PY, Youson JH, Drakos TT. Mouse 3T3 cell filtrability correlating with concanavalin A agglutinability. *Biochim Biophys Acta*. 1984;802(3):467-476.
doi: 10.1016/0304-4165(84)90366-0

43. Oelze ML, O'Brien WD, Jr. Application of three scattering models to characterization of solid tumors in mice. *Ultrason Imaging*. 2006;28(2):83-96.
doi: 10.1177/016173460602800202

44. Pérez-López A, Torres-Suárez AI, Martín-Sabroso C, Aparicio-Blanco J. An overview of in vitro 3D models of the blood-brain barrier as a tool to predict the in vivo permeability of nanomedicines. *Adv Drug Deliv Rev*. 2023;196:114816.
doi: 10.1016/j.addr.2023.114816

45. Sokolova V, Nzou G, van der Meer SB, *et al*. Ultrasmall gold nanoparticles (2 nm) can penetrate and enter cell nuclei in an in vitro 3D brain spheroid model. *Acta Biomater*. 2020;111:349-362.
doi: 10.1016/j.actbio.2020.04.023

46. Urich E, Patsch C, Aigner S, Graf M, Iacone R, Freskgård PO. Multicellular self-assembled spheroidal model of the blood brain barrier. *Sci Rep*. 2013;3:1500.
doi: 10.1038/srep01500

47. Younis M, Faming W, Hongyan Z, Mengmeng T, Hang S, Liudi Y. Iguratimod encapsulated PLGA-NPs improves therapeutic outcome in glioma, glioma stem-like cells and temozolomide resistant glioma cells. *Nanomedicine*. 2019;22:102101.
doi: 10.1016/j.nano.2019.102101

48. Huang H-S, Chiang IT, Lawal B, *et al*. A novel isotope-labeled small molecule probe CC12 for anti-glioma via suppressing LYN-mediated progression and activating apoptosis pathways. *Int J Biol Sci*. 2023;19(10):3209-3225.
doi: 10.7150/ijbs.82266

49. Clevers H. Modeling development and disease with organoids. *Cell*. 2016;165(7):1586-1597.
doi: 10.1016/j.cell.2016.05.082

50. Ahn Y, An J-H, Yang H-J, *et al*. Human blood vessel organoids penetrate human cerebral organoids and form a vessel-like system. *Cells*. 2021;10(8):2036.
doi: 10.3390/cells10082036

51. Yan Y, Song L, Bejoy J, *et al*. Modeling neurodegenerative microenvironment using cortical organoids

derived from human stem cells. *Tissue Eng Part A*. 2018;24(13-14):1125-1137.
doi: 10.1089/ten.TEA.2017.0423

52. Huang S, Zhang Z, Cao J, Yu Y, Pei G. Chimeric cerebral organoids reveal the essentials of neuronal and astrocytic APOE4 for Alzheimer's tau pathology. *Signal Transduct Target Ther*. 2022;7(1):176.
doi: 10.1038/s41392-022-01006-x

53. Dao L, You Z, Lu L, *et al*. Modeling blood-brain barrier formation and cerebral cavernous malformations in human PSC-derived organoids. *Cell Stem Cell*. 2024;31(6):818-833.e11.
doi: 10.1016/j.stem.2024.04.019

54. Fang GC, Chen YC, Lu HX, Jin DY. Advances in spheroids and organoids on a chip. *Adv Funct Mater*. 2023;33(19):2215043.
doi: 10.1002/adfm.202215043

55. Chen X, Sun G, Tian E, *et al*. Modeling sporadic alzheimer's disease in human brain organoids under serum exposure. *Adv Sci*. 2021;8(18):e2101462.
doi: 10.1002/advs.202101462

56. Sooriyaarachchi D, Maharubin S, Tan GZ. Fabrication of microtube-embedded chip to mimic blood–brain barrier capillary vessels. In: Stone N, ed. *The Blood-Brain Barrier: Methods and Protocols*. US, New York, NY: Springer; 2022: 241-249.

57. Kawakita S, Mandal K, Mou L, *et al*. Organ-on-a-chip models of the blood-brain barrier: recent advances and future prospects. *Small*. 2022;18(39):e2201401.
doi: 10.1002/smll.202201401

58. Ponmozhi J, Dhinakaran S, Kocsis D, Iván K, Erdő F. Models for barrier understanding in health and disease in lab-on-a-chips. *Tissue Barriers*. 2024;12(2):2221632.
doi: 10.1080/21688370.2023.2221632

59. Nahon DM, Moerkens R, Aydogmus H, *et al*. Standardizing designed and emergent quantitative features in microphysiological systems. *Nat Biomed Eng*. 2024;8(8):941-962.
doi: 10.1038/s41551-024-01236-0

60. Sonninen TM, Peltonen S, Kalvala S, *et al*. From inserts to chips: microfluidic culture and 3D astrocyte co-culture drive functional and transcriptomic changes in hiPSC-derived endothelial cells. *Fluids Barriers CNS*. 2025;22(1):58.
doi: 10.1186/s12987-025-00672-7

61. Jeong S, Seo J-H, Garud KS, Park SW, Lee M-Y. Numerical approach-based simulation to predict cerebrovascular shear stress in a blood-brain barrier organ-on-a-chip. *Biosens Bioelectron*. 2021;183:113197.
doi: 10.1016/j.bios.2021.113197

62. Zakharova M, Palma do Carmo MA, van der Helm MW, *et al*. Multiplexed blood–brain barrier organ-on-chip. *Lab Chip*. 2020;20(17):3132-3143.
doi: 10.1039/d0lc00399a

63. Chang Y, Chen T, Geng S, *et al*. A scenario-adaptive microfluidic chip for constructing in vitro models of biological barriers. *Anal Chem*. 2025;97(7):3816-3821.
doi: 10.1021/acs.analchem.4c06602

64. Wu CA, Zhu Y, Woo YJ. Advances in 3D bioprinting: techniques, applications, and future directions for cardiac tissue engineering. *Bioengineering (Basel)*. 2023;10(7):842.
doi: 10.3390/bioengineering10070842

65. Gungor-Ozkerim PS, Inci I, Zhang YS, Khademhosseini A, Dokmeci MR. Bioinks for 3D bioprinting: an overview. *Biomater Sci*. 2018;6(5):915-946.
doi: 10.1039/c7bm00765e

66. Shi W, Zhang Z, Wang X. The prospect of hepatic decellularized extracellular matrix as a bioink for liver 3D bioprinting. *Biomolecules*. 2024;14(8):1019.
doi: 10.3390/biom14081019

67. Tang M, Rich JN, Chen S. Biomaterials and 3D bioprinting strategies to model glioblastoma and the blood–brain barrier. *Adv Mater*. 2020;33(5):e2004776.
doi: 10.1002/adma.202004776

68. Galpayage Dona KNU, Hale JF, Salako T, *et al*. The use of tissue engineering to fabricate perfusable 3D brain microvessels in vitro. *Front Physiol*. 2021;12:715431.
doi: 10.3389/fphys.2021.715431

69. Oh H, Kang M, Bae E, *et al*. Fabrication of hydrogel microchannels using aqueous two-phase printing for 3D blood brain barrier. *BioChip J*. 2023;17(3):369-383.
doi: 10.1007/s13206-023-00110-6

70. Royse MK, Fowler M, Mai AK, *et al*. Development of a 3D printed perfusable in vitro blood-brain barrier model for use as a scalable screening tool. *Biomater Sci*. 2024;12(17):4363-4375.
doi: 10.1039/d4bm00663a

71. Choi, J., Mathew, S., Oerter, S., Appelt-Menzel, A., Hansmann, J., Schmitz, T., Online measurement system for dynamic flow bioreactors to study barrier integrity of hipsc-based blood–brain barrier in vitro models. *Bioengineering*. 2022;9(1):39.
doi: 10.3390/bioengineering9010039

72. Ohbuchi M, Shibuta M, Tetsuka K, *et al*. Modeling of blood-brain barrier (BBB) dysfunction and immune cell migration using human BBB-on-a-chip for drug discovery research. *Int J Mol Sci*. 2024;25(12):6496.
doi: 10.3390/ijms25126496

73. Sugiyama S, Sasaki T, Tanaka H, *et al*. The tight junction protein occludin modulates blood-brain barrier integrity and neurological function after ischemic stroke in mice. *Sci Rep*. 2023;13(1):2892.
doi: 10.1038/s41598-023-29894-1

74. Dudek KA, Dion-Albert L, Lebel M, *et al*. Molecular adaptations of the blood-brain barrier promote stress resilience vs. depression. *Proc Natl Acad Sci USA*. 2020;117(6):3326-3336.

doi: 10.1073/pnas.1914655117

75. Shu Y, Peng F, Zhao B, *et al*. Transfer of patient's peripheral blood mononuclear cells (PBMCs) disrupts blood-brain barrier and induces anti-NMDAR encephalitis: a study of novel humanized PBMC mouse model. *J Neuroinflammation*. 2023;20(1):164. doi: 10.1186/s12974-023-02844-4

76. Lin L, Bi H, Yang J, *et al*. Pasteurella multocida infection induces blood-brain barrier disruption by decreasing tight junctions and adherens junctions between neighbored brain microvascular endothelial cells. *Vet Res*. 2024;55(1):104. doi: 10.1186/s13567-024-01351-5

77. Shi Y, He X, Wang H, *et al*. Construction of a novel blood brain barrier-glioma microfluidic chip model: applications in the evaluation of permeability and anti-glioma activity of traditional Chinese medicine components. *Talanta*. 2023;253:123971. doi: 10.1016/j.talanta.2022.123971

78. Park JS, Choe K, Khan A, *et al*. Establishing co-culture blood-brain barrier models for different neurodegeneration conditions to understand its effect on BBB integrity. *Int J Mol Sci*. 2023;24(6):5283. doi: 10.3390/ijms24065283

79. Zorkina YA, Volgina NE, Gorlachev GE, *et al*. Effect of γ-irradiation on expression of tight and adherens junction protein mRNA on in vitro blood-brain barrier model. *Bull Exp Biol Med*. 2014;158(1):127-136. doi: 10.1007/s10517-014-2708-5

80. Petrovskaya AV, Barykin EP, Tverskoi AM, *et al*. Blood-brain barrier transwell modeling. *Mol Biol (Mosk)*. 2022;56(6):1086-1094. doi: 10.31857/s0026898422060179

81. Sun P, Hamblin MH, Yin KJ. Non-coding RNAs in the regulation of blood-brain barrier functions in central nervous system disorders. *Fluids Barriers CNS*. 2022;19(1):27. doi: 10.1186/s12987-022-00317-z

82. Eigenmann DE, Xue G, Kim KS, Moses AV, Hamburger M, Oufir M. Comparative study of four immortalized human brain capillary endothelial cell lines, hCMEC/D3, hBMEC, TY10, and BB19, and optimization of culture conditions, for an in vitro blood-brain barrier model for drug permeability studies. *Fluids Barriers CNS*. 2013;10(1):33. doi: 10.1186/2045-8118-10-33

83. Waithe OY, Peng X, Childs EW, Tharakan B. Measurement of transendothelial electrical resistance in blood-brain barrier endothelial cells. *Methods Mol Biol*. 2024;2711:199-203. doi: 10.1007/978-1-0716-3429-5_16

84. Noorani B, Bhalerao A, Raut S, Nozohouri E, Bickel U, Cucullo L. A quasi-physiological microfluidic blood-brain barrier model for brain permeability studies. *Pharmaceutics*. 2021;13(9):1474. doi: 10.3390/pharmaceutics13091474

85. Offeddu GS, Haase K, Gillrie MR, *et al*. An on-chip model of protein paracellular and transcellular permeability in the microcirculation. *Biomaterials*. 2019;212:115-125. doi: 10.1016/j.biomaterials.2019.05.022

86. Kim Y, Lee S, Zhang H, *et al*. CLEC14A deficiency exacerbates neuronal loss by increasing blood-brain barrier permeability and inflammation. *J Neuroinflammation*. 2020;17(1):48. doi: 10.1186/s12974-020-1727-6

87. Waithe OY, Peng X, Childs EW, Tharakan B. Measurement of blood-brain barrier hyperpermeability using evans blue extravasation assay. *Methods Mol Biol*. 2024;2711:177-184. doi: 10.1007/978-1-0716-3429-5_14

88. Ahishali B, Kaya M. Evaluation of blood-brain barrier integrity using vascular permeability markers: evans blue, sodium fluorescein, albumin-alexa fluor conjugates, and horseradish peroxidase. *Methods Mol Biol*. 2021;2367:87-103. doi: 10.1007/7651_2020_316

89. Ozgür B, Puris E, Brachner A, *et al*. Characterization of an iPSC-based barrier model for blood-brain barrier investigations using the SBAD0201 stem cell line. *Fluids Barriers CNS*. 2023;20(1):96. doi: 10.1186/s12987-023-00501-9

90. Ito R, Morio H, Baba T, *et al*. In vitro-in vivo correlation of blood-brain barrier permeability of drugs: a feasibility study towards development of prediction methods for brain drug concentration in humans. *Pharm Res*. 2022;39(7):1575-1586. doi: 10.1007/s11095-022-03189-y

91. Heidari H, Taylor H. Review article: capturing the physiological complexity of the brain's neuro-vascular unit in vitro. *Biomicrofluidics*. 2018;12(5):051502. doi: 10.1063/1.5045126

92. Koch EV, Ledwig V, Bendas S, Reichl S, Dietzel A. Tissue barrier-on-chip: a technology for reproducible practice in drug testing. *Pharmaceutics*. 2022;14(7):1451. doi: 10.3390/pharmaceutics14071451

93. Guan M, Tang S, Chang H, *et al*. Development of alveolar-capillary-exchange (ACE) chip and its application for assessment of PM(2.5)-induced toxicity. *Ecotoxicol Environ Saf*. 2021;223:112601. doi: 10.1016/j.ecoenv.2021.112601

94. Wang Z, Zhang Y, Li Z, Wang H, Li N, Deng Y. Microfluidic brain-on-a-chip: from key technology to system integration and application. *Small*. 2023;19(52):e2304427. doi: 10.1002/smll.202304427

95. Choi B, Choi JW, Jin H, *et al*. Condensed ECM-based nanofilms on highly permeable PET membranes for robust cell-to-cell communications with improved optical clarity. *Biofabrication*. 2021;13(4):045020. doi: 10.1088/1758-5090/ac23ad

96. Alves ADH, Nucci MP, Ennes do Valle NM, *et al*. Current overview of induced pluripotent stem cell-based blood-

brain barrier-on-a-chip. *World J Stem Cells*. 2023;15(6):632-653.
doi: 10.4252/wjsc.v15.i6.632

97. Hosic S, Bindas AJ, Puzan ML, *et al*. Rapid prototyping of multilayer microphysiological systems. *ACS Biomater Sci Eng*. 2021;7(7):2949-2963.
doi: 10.1021/acsbiomaterials.0c00190

98. Pungjunun K, Yakoh A, Chaiyo S, *et al*. Laser engraved microapillary pump paper-based microfluidic device for colorimetric and electrochemical detection of salivary thiocyanate. *Mikrochim Acta*. 2021;188(4):140.
doi: 10.1007/s00604-021-04793-2

99. Wang YI, Abaci HE, Shuler ML. Microfluidic blood-brain barrier model provides in vivo-like barrier properties for drug permeability screening. *Biotechnol Bioeng*. 2017;114(1):184-194.
doi: 10.1002/bit.26045

100. Cenhrang K, Robart L, Castiaux AD, Martin RS. 3D printed devices with integrated collagen scaffolds for cell culture studies including transepithelial/transendothelial electrical resistance (TEER) measurements. *Anal Chim Acta*. 2022;1221:340166.
doi: 10.1016/j.aca.2022.340166

101. Matthiesen I, Jury M, Rasti Boroojeni F, *et al*. Astrocyte 3D culture and bioprinting using peptide functionalized hyaluronan hydrogels. *Sci Technol Adv Mater*. 2023;24(1):2165871.
doi: 10.1080/14686996.2023.2165871

102. Kim JA, Kim HN, Im S-K, Chung S, Kang JY, Choi N. Collagen-based brain microvasculature modelin vitrousing three-dimensional printed template. *Biomicrofluidics*. 2015;9(2):024115.
doi: 10.1063/1.4917508

103. Wang Z, Huang C, Shi Z, *et al*. Coaxial bioprinting of a three-layer vascular structure exhibiting blood-brain barrier function for neuroprotective drug screening. *Colloids Surf B Biointerfaces*. 2025;249:114494.
doi: 10.1016/j.colsurfb.2025.114494

104. Cucullo L, Hossain M, Puvenna V, Marchi N, Janigro D. The role of shear stress in Blood-Brain Barrier endothelial physiology. *BMC Neurosci*. 2011;12:40.
doi: 10.1186/1471-2202-12-40

105. Zhang YS, Davoudi F, Walch P, *et al*. Bioprinted thrombosis-on-a-chip. *Lab Chip*. 2016;16(21):4097-4105.
doi: 10.1039/c6lc00380j

106. Wang R, Zhang H, Li S, *et al*. Current progress ofin vitrovascular models on microfluidic chips. *Biofabrication*. 2025;17(2).
doi: 10.1088/1758-5090/adb182

107. Yang JY, Shin DS, Jeong M, *et al*. Evaluation of drug blood-brain-barrier permeability using a microfluidic chip. *Pharmaceutics*. 2024;16(5):574.
doi: 10.3390/pharmaceutics16050574

108. Ferreira L. What human blood-brain barrier models can tell us about BBB function and drug discovery? *Expert Opin Drug Discov*. 2019;14(11):1113-1123.
doi: 10.1080/17460441.2019.1646722

109. Nahon DM, Vila Cuenca M, van den Hil FE, *et al*. Self-assembling 3D vessel-on-chip model with hiPSC-derived astrocytes. *Stem Cell Reports*. 2024;19(7):946-956.
doi: 10.1016/j.stemcr.2024.05.006

110. Chim SM, Howell K, Kokkosis A, Zambrowicz B, Karalis K, Pavlopoulos E. A human brain-chip for modeling brain pathologies and screening blood-brain barrier crossing therapeutic strategies. *Pharmaceutics*. 2024;16(10):1314.
doi: 10.3390/pharmaceutics16101314

111. Choi JW, Kim K, Mukhambetiyar K, *et al*. Organ-on-a-chip approach for accelerating blood-brain barrier nanoshuttle discovery. *ACS Nano*. 2024;18(22):14388-14402.
doi: 10.1021/acsnano.4c00994

112. Stanness KA, Westrum LE, Fornaciari E, *et al*. Morphological and functional characterization of an in vitro blood-brain barrier model. *Brain Res*. 1997;771(2):329-42.
doi: 10.1016/s0006-8993(97)00829-9

113. Cucullo L, Couraud PO, Weksler B, *et al*. Immortalized human brain endothelial cells and flow-based vascular modeling: a marriage of convenience for rational neurovascular studies. *J Cereb Blood Flow Metab*. 2008;28(2):312-328.
doi: 10.1038/sj.jcbfm.9600525

114. Wang X, Xu B, Xiang M, *et al*. Advances on fluid shear stress regulating blood-brain barrier. *Microvasc Res*. 2020;128:103930.
doi: 10.1016/j.mvr.2019.103930

115. Griep LM, Wolbers F, de Wagenaar B, *et al*. BBB on chip: microfluidic platform to mechanically and biochemically modulate blood-brain barrier function. *Biomed Microdevices*. 2013;15(1):145-150.
doi: 10.1007/s10544-012-9699-7

116. Ceccarelli MC, Lefevre MC, Marino A, *et al*. Real-time monitoring of a 3D blood-brain barrier model maturation and integrity with a sensorized microfluidic device. *Lab Chip*. 2024;24(22):5085-5100.
doi: 10.1039/d4lc00633j

117. Pichler V, Schwingenschlögl-Maisetschläger V, Duman I, *et al*. Bioanalytic hybrid system merging 3-dimensional cell culture and chromatographic precision for unprecedented preclinical insights in molecular imaging. *J Nucl Med*. 2025;66(5):813-816.
doi: 10.2967/jnumed.124.269133

118. Mossburg KJ, Shepherd SJ, Barragan D, *et al*. Towards the clinical translation of a silver sulfide nanoparticle contrast agent: large scale production with a highly parallelized microfluidic chip. *Eur J Nucl Med Mol Imaging*. 2025;52(3):1177-1188.
doi: 10.1007/s00259-024-06967-5

119. Yan X, Liu X, Zhao C, Chen GQ. Applications of synthetic biology in medical and pharmaceutical fields. *Signal Transduct Target Ther*. 2023;8(1):199. doi: 10.1038/s41392-023-01440-5

120. Lu YL, Lin CM, Huang JH. Triplicate dynamic cell culture platform for enhanced reproducibility in anti-cancer drug testing. *ACS Biomater Sci Eng*. 2025;11(2):1222-1231. doi: 10.1021/acsbiomaterials.4c02142

121. Xu H, Li Z, Yu Y, *et al*. A dynamic in vivo-like organotypic blood-brain barrier model to probe metastatic brain tumors. *Sci Rep*. 2016;6(1):36670. doi: 10.1038/srep36670

122. Maoz BM, Herland A, FitzGerald EA, *et al*. A linked organ-on-chip model of the human neurovascular unit reveals the metabolic coupling of endothelial and neuronal cells. *Nat Biotechnol*. 2018;36(9):865-874. doi: 10.1038/nbt.4226

123. Liu L, Koo Y, Russell T, Yun Y. A three-dimensional brain-on-a-chip using human ipsc-derived gabaergic neurons and astrocytes. *Methods Mol Biol*. 2022;2492:117-128. doi: 10.1007/978-1-0716-2289-6_6

124. Miller DR, McClain ES, Dodds JN, *et al*. Chlorpyrifos disrupts acetylcholine metabolism across model blood-brain barrier. *Front Bioeng Biotechnol*. 2021;9:622175. doi: 10.3389/fbioe.2021.622175

125. Kim SS, Kim S, Kim Y, *et al*. Neurotoxic effects of citronellol induced by the conversion of kynurenine to 3-hydroxykynurenine. *J Hazard Mater*. 2025;486:136965. doi: 10.1016/j.jhazmat.2024.136965

126. Arduino I, Di Fonte R, Sommonte F, *et al*. Fabrication of biomimetic hybrid liposomes via microfluidic technology: homotypic targeting and antitumor efficacy studies in glioma cells. *Int J Nanomed*. 2024;19:13217-13233. doi: 10.2147/ijn.S489872

127. Shao X, Gao D, Chen Y, *et al*. Development of a blood-brain barrier model in a membrane-based microchip for characterization of drug permeability and cytotoxicity for drug screening. *Anal Chim Acta*. 2016;934:186-193. doi: 10.1016/j.aca.2016.06.028

128. Yu F, Kumar NDOS, Foo LC, Ng SH, Hunziker W, Choudhury D. A pump-free tricellular blood–brain barrier on-a-chip model to understand barrier property and evaluate drug response. *Biotechnol Bioeng*. 2020;117(4): 1127-1136. doi: 10.1002/bit.27260

129. Mitchell MJ, Billingsley MM, Haley RM, Wechsler ME, Peppas NA, Langer R. Engineering precision nanoparticles for drug delivery. *Nat Rev Drug Discov*. 2020;20(2):101-124. doi: 10.1038/s41573-020-0090-8

130. Palma-Florez S, López-Canosa A, Moralez-Zavala F, *et al*. BBB-on-a-chip with integrated micro-TEER for permeability evaluation of multi-functionalized gold nanorods against Alzheimer's disease. *Journal of Nanobiotechnology*. 2023;21(1):115. doi: 10.1186/s12951-023-01798-2

131. Garcia L, Palma-Florez S, Espinosa V, *et al*. Ferulic acid-loaded polymeric nanoparticles prepared from nano-emulsion templates facilitate internalisation across the blood–brain barrier in model membranes. *Nanoscale*. 2023;15(17):7929-7944. doi: 10.1039/d2nr07256d

132. Cai X, Refaat A, Gan P-Y, *et al*. Angiopep-2-Functionalized Lipid Cubosomes for Blood–Brain Barrier Crossing and Glioblastoma Treatment. *ACS Applied Materials & Interfaces*. 2024;16(10):12161-12174. doi: 10.1021/acsami.3c14709

133. Heard, S. C., Wu, G., Winter, J. M., Antifungal natural products. *Curr Opin Biotechnol*. 2021;69(232-241. doi: 10.1016/j.copbio.2021.02.001

134. Shan L, Fan Y, Yuanchun C, *et al*. Sanhua Tang protects against ischemic stroke by preventing blood-brain barrier injury: a network pharmacology and experiments. *J Tradit Chin Med*. 2024;44(4):794-803. doi: 10.19852/j.cnki.jtcm.20240515.001

135. Liu G, Liang Y, Xu M, *et al*. Protective mechanism of Erigeron breviscapus injection on blood-brain barrier injury induced by cerebral ischemia in rats. *Sci Rep*. 2021;11(1):18451. doi: 10.1038/s41598-021-97908-x

136. Zhang Y, Shen L, Xie J, *et al*. Pushen capsule treatment promotes functional recovery after ischemic stroke. *Phytomedicine*. 2023;111(154664. doi: 10.1016/j.phymed.2023.154664

137. Karthika C, Najda A, Klepacka J, *et al*. Involvement of resveratrol against brain cancer: a combination strategy with a pharmaceutical approach. *Molecules*. 2022;27(14):4663. doi: 10.3390/molecules27144663

138. Liu Y, Yang G, Cui W, Zhang Y, Liang X. Regulatory mechanisms of tetramethylpyrazine on central nervous system diseases: a review. *Front Pharmacol*. 2022;13:948600. doi: 10.3389/fphar.2022.948600

139. Ru J, Li P, Wang J, *et al*. TCMSP: a database of systems pharmacology for drug discovery from herbal medicines. *J Cheminform*. 2014;6:13. doi: 10.1186/1758-2946-6-13

140. Meena M, Vandormael R, De Laere M, *et al*. A microfluidic in vitro three-dimensional dynamic model of the blood–brain barrier to study the transmigration of immune cells. *Brain Sci*. 2022;12(10):1293. doi: 10.3390/brainsci12101293

141. Malekpour A, Chen X. Printability and cell viability in extrusion-based bioprinting from experimental, computational, and machine learning views. *J Funct Biomater*. 2022;13(2):40. doi: 10.3390/jfb13020040

142. Billiet T, Gevaert E, De Schryver T, Cornelissen M, Dubruel P. The 3D printing of gelatin methacrylamide cell-laden tissue-engineered constructs with high cell viability. *Biomaterials*. 2014;35(1):49-62.
doi: 10.1016/j.biomaterials.2013.09.078

143. Naghieh S, Karamooz-Ravari MR, Sarker MD, Karki E, Chen X. Influence of crosslinking on the mechanical behavior of 3D printed alginate scaffolds: Experimental and numerical approaches. *J Mech Behav Biomed Mater*. 2018;80:111-118.
doi: 10.1016/j.jmbbm.2018.01.034

144. Xu Y, Kong D, Zhang T, Xiong Z, Sun W. A parallel multilayered neurovascular unit-on-a-chip for modeling neurovascular microenvironment and screening chemotherapeutic drugs. *Int J Bioprint*. 2024;10(3):1684.
doi: 10.36922/ijb.1684

145. Ahmad A, Zobaida Akter M, Kim SY, Choi YJ, Yi HG. High-throughput bioprinting method for modeling vascular permeability in standard six-well plates with size and pattern flexibility. *J Vis Exp*. 2024;210.
doi: 10.3791/66676

146. Mou L, Mandal K, Mecwan MM, *et al*. Integrated biosensors for monitoring microphysiological systems. *Lab Chip*. 2022;22(20):3801-3816.
doi: 10.1039/d2lc00262k

147. Gnatowski P, Ansariaghmiuni M, Piłat E, *et al*. Hydrogel membranes in organ-on-a-chip devices: a review. *Colloids Surf B Biointerfaces*. 2025;251:114591.
doi: 10.1016/j.colsurfb.2025.114591

148. Brown JA, Codreanu SG, Shi M, *et al*. Metabolic consequences of inflammatory disruption of the blood-brain barrier in an organ-on-chip model of the human neurovascular unit. *J Neuroinflammation*. 2016;13(1):306.
doi: 10.1186/s12974-016-0760-y

149. Su S-H, Song Y, Stephens A, *et al*. A tissue chip with integrated digital immunosensors: In situ brain endothelial barrier cytokine secretion monitoring. *Biosens Bioelectron*. 2023;224:115030.
doi: 10.1016/j.bios.2022.115030

150. Feng Y, Chen C-S, Ho J, *et al*. High-throughput chip assay for investigating *Escherichia coli* interaction with the blood–brain barrier using microbial and human proteome microarrays (dual-microarray technology). *Anal Chem*. 2018;90(18):10958-10966.
doi: 10.1021/acs.analchem.8b02513

151. Koenig L, Ramme AP, Faust D, *et al*. A human stem cell-derived brain-liver chip for assessing blood-brain-barrier permeation of pharmaceutical drugs. *Cells*. 2022;11(20):3295.
doi: 10.3390/cells11203295

152. Ahn SI, Kim Y. Human blood–brain barrier on a chip: featuring unique multicellular cooperation in pathophysiology. *Trends Biotechnol*. 2021;39(8):749-752.
doi: 10.1016/j.tibtech.2021.01.010

153. Oddo A, Peng B, Tong Z, *et al*. Advances in microfluidic blood-brain barrier (BBB) models. *Trends Biotechnol*. 2019;37(12):1295-1314.
doi: 10.1016/j.tibtech.2019.04.006

ACCSCIENCE PUBLISHING

International Journal of Bioprinting

REVIEW ARTICLE

A multidisciplinary review on footwear 3D printing: From biomechanics to therapeutics

Kijung Kim[1†], Hyunji Kim[2†], Wonjae Hwang[3,4,5], Yoonseo Choi[1], Keewon Kim[3,4*], Jooeun Ahn[2,6*], and Howon Lee[1*]

[1]Department of Mechanical Engineering, Institute of Advanced Machines and Design, Seoul National University, Seoul, Republic of Korea

[2]Department of Physical Education, Seoul National University, Seoul, Republic of Korea

[3]Department of Rehabilitation Medicine, Seoul National University Hospital, Seoul, Republic of Korea

[4]Department of Rehabilitation Medicine, Seoul National University College of Medicine, Seoul, Republic of Korea

[5]Department of Rehabilitation Medicine, The Armed Forces Daejeon Hospital, Daejeon, Republic of Korea

[6]Institute of Sport Science, Seoul National University, Seoul, Republic of Korea

Abstract

Advancements in three-dimensional (3D) printing have expanded design freedom across various fields, including footwear. Driven by recent progress in biomechanics, footwear has increasingly adopted complex structural designs to meet diverse functional demands, ranging from personal activity to competitive athletics and medical rehabilitation. Accordingly, the role of 3D printing in footwear development has become increasingly significant. This review categorizes the functions of footwear into protection, performance enhancement, and therapeutic applications, and systematically explores the impact of 3D printing on each of these primary functions. 3D printing technology enables the fabrication of complex but mechanically efficient structures, while the 3D scanning method facilitates the application of optimal, personalized designs tailored to individual biomechanics, which significantly impact all three functional areas of footwear. Such design advantages offered by 3D printing have been demonstrated across various fields, with both commercial and academic examples presented to support these findings. This review highlights interdisciplinary insights from biomechanics, ergonomics, and clinical studies to discuss the current status, limitations, and future potential of 3D-printed footwear. We conclude that continuous advancements in design methodology, material science, and printing technology will accelerate the adoption of 3D printing in next-generation footwear.

Keywords: 3D printing; 3D printed shoes; Footwear; Foot protection; Running efficiency; Foot orthotics

[†]These authors contributed equally to this work.

***Corresponding authors:**
Howon Lee
(howon.lee@snu.ac.kr)

Jooeun Ahn
(ahnjooeun@snu.ac.kr)

Keewon Kim
(keien1@snu.ac.kr)

Citation: Kim K, Kim H, Hwang W, *et al.* A multidisciplinary review on footwear 3D printing: From biomechanics to therapeutics. *Int J Bioprint.* 2025;11(5):98-121. doi: 10.36922/IJB025210204

Received: May 19, 2025
Revised: June 25, 2025
Accepted: July 7, 2025
Published online: August 14, 2025

Copyright: © 2025 Author(s). This is an Open Access article distributed under the terms of the Creative Commons Attribution License, permitting distribution, and reproduction in any medium, provided the original work is properly cited.

Publisher's Note: AccScience Publishing remains neutral with regard to jurisdictional claims in published maps and institutional affiliations.

1. Introduction

Footwear is an essential component of daily life, playing a crucial role in various physical activities. Traditionally, footwear has been designed to protect the foot from

external hazards by providing structural support and impact absorption, thereby minimizing the risk of injuries during movement. This protective function is a fundamental aspect of conventional shoes and also an essential factor in orthotic devices, which assist individuals with specific medical conditions. However, modern footwear designs have advanced beyond basic protective functions, incorporating advanced features such as athletic performance enhancement and even therapeutic approaches.[1] As such, footwear has significantly expanded its application areas from everyday life to specialized fields, ranging from high-performance sports equipment to medical rehabilitation tools. As the functions of footwear have evolved, footwear designs have become increasingly complex to meet diverse needs of users, prompting the incorporation of innovative manufacturing techniques. In recent years, additive manufacturing, commonly known as three-dimensional (3D) printing technology, has emerged as a transformative approach in footwear manufacturing, enabling unprecedented design freedom and facilitating intricate structural designs to fulfill advanced functional requirements.

To fully exploit the potential of 3D printed footwear, it is essential to first understand the basic and advanced functions that modern footwear can offer. Footwear serves three primary functions: foot protection, performance enhancement, and therapeutic application. First, foot protection has always been a fundamental function of footwear, not only shielding the foot from external impacts but also preventing foot disorders caused by excessive strain and repetitive motion. Footwear helps alleviate fatigue during standing,[2-4] enhances stability during walking,[1,5–7] and ultimately reduces injury risk and improves comfort during full gait cycle. The second footwear function is performance enhancement. Key factors that influence gait performance include shoe weight,[8–10] compression elasticity,[11,12] longitudinal bending stiffness,[13–17] and proper supporting.[18,19] These factors can influence athletic performance by improving joint motion control, optimizing load distribution, and providing enhanced cushioning and support[20] for various physical activities. Lastly, the use of footwear as therapeutic aids is on the rise. Orthotic footwear is widely used for medical use. It can be categorized as foot orthosis, ankle–foot orthosis, insoles, or other shoe modifications. These orthoses have been used in the treatment of various adverse foot conditions, including flat feet,[21–26] plantar fasciitis,[27–31] diabetic foot,[32–38] and even above-foot disease like knee osteoarthritis.[39–42] By modifying pressure distribution on the feet and improving the movement of the ankle and foot unit, orthosis can reduce pain and enhance physical function. As footwear continues to evolve its functions, there is a growing interest in footwear design for improved functionality or personal customization. However, conventional footwear manufacturing relies on mass production techniques such as molding or casting, restricting the ability to create highly customized footwear tailored to unique foot structures and biomechanical needs of individual. This limitation on design freedom drives the demand for innovative manufacturing technologies, such as 3D printing.

3D printing offers unique advantages over traditional manufacturing methods. 3D printing enables direct fabrication of computer-aided design (CAD) into physical objects through layer-by-layer manner, allowing facile fabrication of complex structures. As the demand for diverse functions continues to grow, design of footwear has become increasingly complex. Therefore, manufacturing industry has revolutionized its production process by embracing 3D printing technology. This shift allows footwear manufacturing to overcome the limitations of traditional manufacturing methods and achieve unparalleled range of design options, opening a new pathway to the production of footwear with intricate but highly functional designs. The ability to design complex structures through 3D printing has contributed to improved foot protection, enhanced gait performance, and patient-specific therapeutic treatment, by incorporating features such as enhanced cushioning,[43] adaptive support,[25,44–46] and customized fit[31,47–49] that were previously unattainable with conventional manufacturing methods. Furthermore, employment of 3D scanning technology simplifies the customization process by rapid measurement and detailed feature capture, thereby facilitating the production of personalized footwear,[36,44,47,50–52] as shown in Figure 1.

Many recent publications have demonstrated the effectiveness of 3D printing in footwear manufacturing by highlighting its capability to create complex geometries and facilitate personalized design. Despite such advances, most 3D-printed footwear designs are still based on traditional design principles merely replicating conventional footwear structures, thus limiting the full potential of additive manufacturing. Therefore, rather than merely applying 3D printing to existing footwear designs, there is a growing demand for new design strategies that can fully utilize the capabilities of 3D printing for next-generation footwear. Given the multifaceted aspects of footwear functions, this review aims to achieve this goal by providing insights into footwear design from an interdisciplinary perspective, incorporating ergonomic, biomechanical, and therapeutic considerations. Then, we discuss various design advantages and unique characteristics of additive manufacturing, highlighting the strength of 3D printing

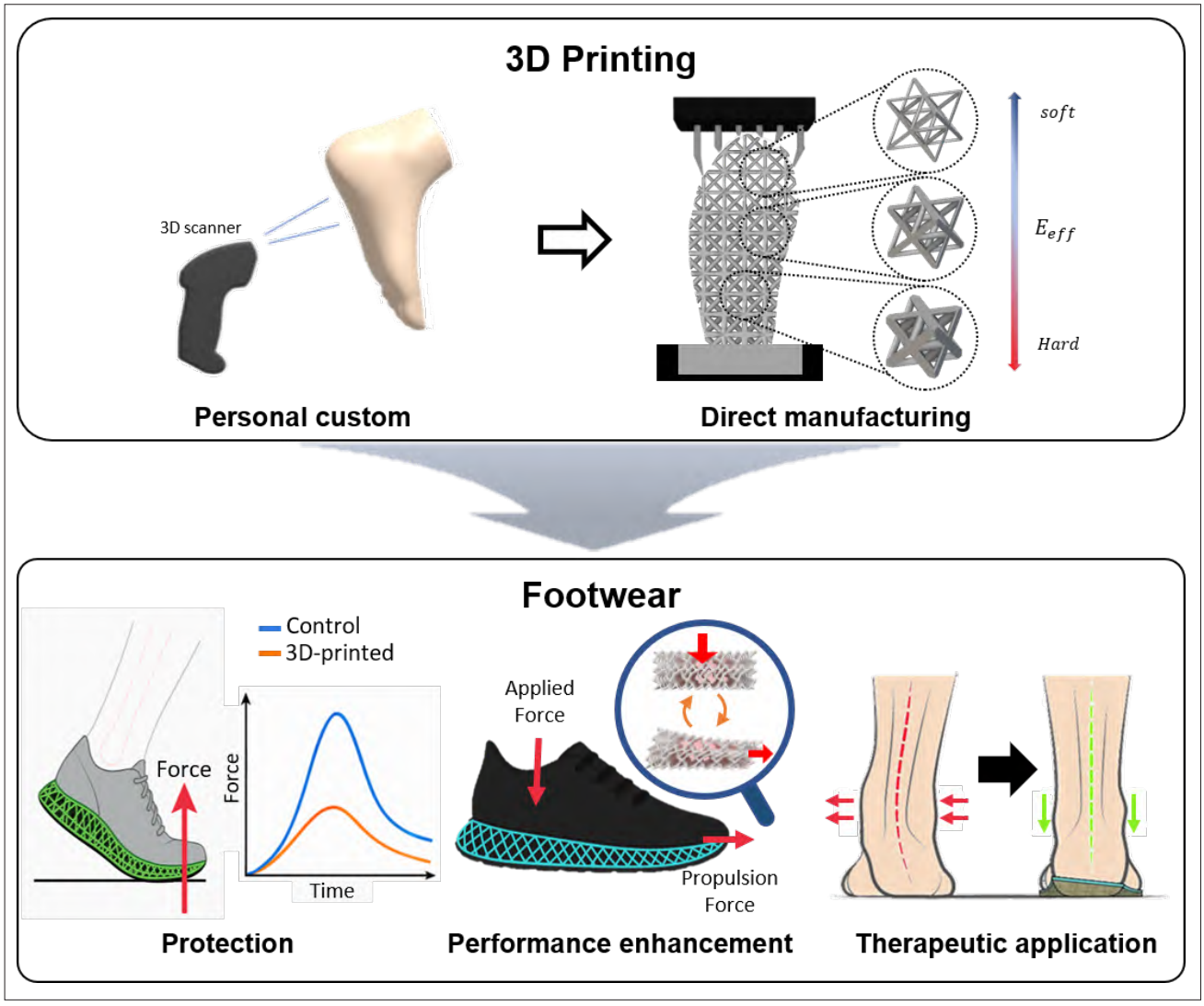


Figure 1. Overview of footwear, orthoses, and 3D printing

as an emerging manufacturing technology for footwear. Finally, we briefly address current limitations and future potential of 3D-printed footwear, suggesting diverse research directions for further exploration of additive manufacturing in footwear design.

2. Consideration of footwear function

Traditional footwear typically consists of two major components: the upper and the sole, with the sole further subdivided into three parts: insole, midsole, and outsole. While the upper plays a crucial role in fit and comfort, most footwear research has focused on the sole, which interacts with the plantar surface of the foot and the ground.[6,53] This section examines three key functional aspects to consider when manufacturing 3D-printed footwear. First, we discuss 'protection', the most basic and traditional function of footwear, exploring how 3D-printied midsole materials and outsole thickness can contribute to foot safety and injury prevention. Next, we focus on 'performance enhancement', a core element in modern footwear industry, analyzing how 3D-printed sole properties and contours can enhance energy return and mechanical efficiency during athletic activities. Finally, we examine 'clinical application' investigating how 3D-printed insoles and orthosis, with their capacity for precise geometric customization, can address specific pathologies and biomechanical abnormalities. Through these three perspectives, we aim to provide a comprehensive understanding of the current state and future possibilities of 3D-printed footwear technology.

2.1. Protection

Historically serving as physical safeguard for the feet, footwear has evolved from primitive coverings to technologically advanced systems that protect foot biomechanics.[54] During gait, the foot performs three mechanical functions: the heel absorbs shock at initial contact, the midfoot arch stabilizes body weight (BW) transfer from heel to toe, and the forefoot acts as a lever arm for effective propulsion.[55–57] Footwear has to support these functions to reduce injury risks and provide comfort.[58] This section categorizes the protective functions into three aspects: impact distribution and absorption, structural support and stability, and individual fit and customization. It reviews representative applications in each domain (Figure 2), with particular focus on how these principles can be applied and extended through 3D printing technologies.

2.1.1 Impact distribution and absorption

Footwear mitigates mechanical loading by redistributing impact forces across the foot. While walking and standing generate relatively low ground reaction forces (GRFs) (approximately 1.0–1.2 BW), long exposure can cause fatigue, swelling, low-back pain, and foot problems like plantar fasciitis and blisters.[2] Prolonged stress can impair balance due to reduced sensory feedback and muscle fatigue.[3,4] Footwear with effective cushioning, thicker soles, and rocker profiles (Figure 2A) helps to alleviate localized pressure and fatigue.[2,43,59–62]

In running, GRFs reach 2–3 BW, potentially elevating the risk for running-related injuries.[1,5–7] The midsole technologies target shock attenuation, with maximalist (or heavily cushioned) footwears exemplifying the approach through increased stack height (Figure 2B; Hoka One One Clifton 2) and compliant foams (Figure 2C).[12,53,63,64] However, evidence supporting these assumptions remains inconclusive. Some studies question whether cushioning effectively reduces impact loading or injury risk, and suggest that excessive cushioning may even reduce proprioceptive feedback, potentially increasing injury risk in other ways.[65,66]

Optimal cushioning is highly individual-dependent, influenced by body mass index, foot morphology, and running patterns. Recent trends emphasize personalized cushioning through strategic midsole tuning rather than a one-size-fits-all approach.[1,67] In this context, lattice structures in shoe soles using 3D printing have emerged as a promising solution. Their geometry can be precisely engineered to manipulate stiffness and pressure distribution under dynamic loading[68–71] (Figure 2D). Moreover, 3D-printed design offers significantly greater room in structural configuration than traditional dual-density footwear, which typically relies on layering different materials.[72] Advanced 3D-printed geometries—such as variable-density lattices (Figure 2D), directional spring structures (Figure 2E), honeycomb configurations (Figure 2F), and spiral supports (Figure 2G)—enable modulation of cushioning and plantar pressure redistribution within a single continuous structure.[72–74]

In summary, impact protection in footwear design should be viewed not only as a function of material properties but also as a matter of geometric customization. 3D printing enables region-specific modulation of compliance and damping, allowing designers to address diverse biomechanical demands through individualized structural solutions. Through 3D printing, region-specific compliance and force attenuation can be finely modulated to address the biomechanical needs of diverse users.

2.1.2 Structural support and stability

Foot stability and injury prevention are influenced by midsole and insole geometry, outsole traction, and upper fit. As soles became thicker and more compliant in the 1970s, stability trade-offs emerged.[53] Thicker midsoles raise the center of mass and increase leverage at the subtalar joint, reducing lateral ankle stability.[67] In response to these stability concerns, footwear developers in the 1990s introduced various motion-control features—such as medial posts, heel flares, firm heel counters—to mitigate excessive rearfoot motion (Figure 2H).[1,5,6,53,54,58,75] Firm heel counters (Figure 2H) function to cradle the rearfoot and limit rearfoot eversion, which is particularly critical for individuals with excessive pronation or medial instability. Footwear have been reported to be effective in pathologic conditions such as flexible flatfoot, where controlling excessive pronation and medial collapse is crucial. However, evidence on their efficacy in injury prevention remains inconclusive under physiologic conditions, due to individual differences in foot structure, gait patterns, and biomechanics.[6,65]

Outsole traction is a critical component of stability; insufficient grip may lead to slipping, while excessive grip can result in torque-related injuries such as tears in anterior cruciate ligament and ankle strains,[76] highlighting the need for an optimal balance. Tread patterns (Figure 2I) vary in depth and type, with deeper patterned treads providing greater traction for activities requiring higher grip such as trail running.[54,77,78] Optimal outsole design must balance slip resistance and safe rotational freedom for different sports and surfaces.

The shoe's upper (the enclosing material and lacing system) serves as the interface between foot and shoe,

playing a vital role in stability, fit and breathability. Inadequate toe box fit can lead to friction injuries (*e.g.*, blisters, bunions), while excessive looseness compromises stability.[7,63,79] Modern designs use adaptive uppers (*e.g.*, BOA® lacing (Figure 2J), knit fabrics (Figure 2K), overlays) to enhance fit while maintaining flexibility.[80–83] Although research on upper fit's direct impact on injury rates remains limited, it is widely acknowledged as essential for structural support, particularly in sports involving rapid directional changes.[63,84]

From a 3D printing perspective, these findings highlight opportunities for integrating heterogeneous stiffness profiles and upper-midsole interactions within a single print. Customized heel counters, arch bridges, or lateral supports could be embedded directly into the midsole geometry, enabling targeted reinforcement without compromising comfort. Such designs open the door to patient-specific pronation control and stability optimization.

2.1.3. Individual fit and customization, and smart footwear

As discussed in **Sections 2.1.1** and **2.1.2**, no universal "ideal shoe" exists for preventing injuries, as effectiveness varies across individuals based on foot shape, biomechanics, past injury history, and activity patterns.[6,7,20,65,79,85–93] Instead of

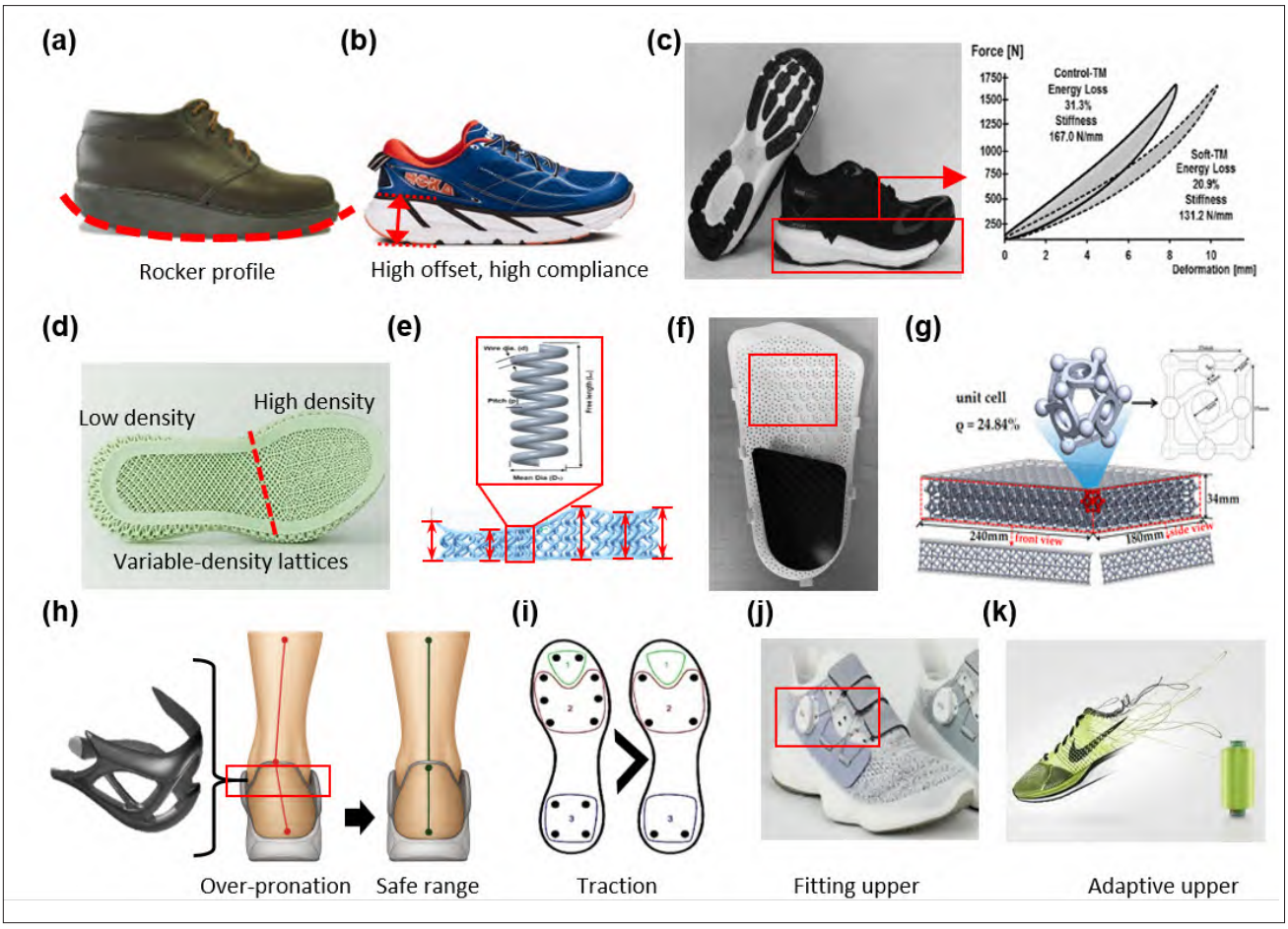


Figure 2. Representative design features and technologies for protective functions in footwear. (A) Rocker-profiled sole forward roll-over. Adapted with permission from ref.[2] Copyright © 2016 Elsevier. (B) Maximalist running shoe with enhanced cushioning. Adapted with permission from ref.[64] Copyright © 2021 Taylor & Francis. (C) Running shoe providing foam cushioning. Adapted with permission from ref.[12] Copyright © 2014 Taylor & Francis. (D) 3D-printed lattice with region-specific compliance. Adapted from ref.[71] (E) Helical lattice for zonal stiffness variation. Adapted with permission from ref.[72] Copyright © 2020 Springer Nature. (F) Honeycomb unit-cell for midsole lattices. Adapted with permission from ref.[73] Copyright © 2021 Elsevier. (G) Spiral topology of midsole lattices with directional shock absorption. Reproduced from ref.[74] (H) CAD-modeled heel counter for rearfoot stability. Adapted with permission from ref.[75] Copyright © 2009 Taylor & Francis. (I) Outsole patterns for traction. Adapted from ref.[78] (J) BOA® lacing system for adjustable foot lockdown. Adapted with permission from ref.[82] Copyright © 2023 Taylor & Francis. (K) Stretchable Flyknit upper. Reproduced from ref.[83] Abbreviation: CAD, computer-aided design.

prescribing a single correct shoe type, the focus has shifted to modular and customizable designs that allow for fine-tuned adjustments. 3D printing plays a key role in this shift, offering capabilities for individualized fabrication of midsoles, insoles, and uppers tailored to specific anatomical and biomechanical profiles.[69,94–96]

Recent advances have extended this customization potential to smart footwear by enabling the direct integration of embedded sensors in 3D-printed footwear. For example, one study presented a sensor-integrated insole that facilitates iterative redesign and fabrication by capturing gait and pressure data to inform personal biomechanical data.[97] Another study demonstrated real-time pressure sensing and wireless data streaming during walking, suggesting the potential of responsive, sensor-integrated footwear in real-world settings.[98] Currently, sensor-integrated footwear systems are limited to relatively simple measurements compared to conventional sensor platforms. However, with advances in 3D printing and sensor technologies, more complex sensing functions—such as advanced gait analysis and real-time impact feedback—may become achievable. These capabilities could be further enhanced through the future integration of AI-driven sensing and data interpretation frameworks. If such advancements are realized, sensor-integrated footwear may eventually replace traditional foot pressure sensors and significantly enhance therapeutic applications by enabling more responsive and adaptive interventions. Furthermore, the ability to directly acquire digitized sensor data from the footwear itself offers new opportunities for producing improved customized insoles.[97] If future research enables the effective coupling of this sensor data with footwear design, potentially through AI-driven methods, it could accelerate the development of next-generation smart footwear tailored to individual biomechanical requirements.

2.2. Performance enhancement

Footwear contributes not only to protecting lower extremities but also to enhancing biomechanical efficiency. Gait motion can be categorized into walking and running, but biomechanical performance is particularly relevant to running and high-intensity movements.[18,19,99] Therefore, this section will focus on various footwear designs for improving running performance. Performance-related benefits of footwear include reducing metabolic cost, improving running economy (RE), and optimizing force transmission.[100,101] Among these, RE is one of the most commonly used indicators for comparing different footwear properties.[102,103] RE refers to the amount of oxygen consumption at a given submaximal speed, and better RE indicates a lower metabolic cost for the same pace or workload, allowing the runner to go faster or farther for the same physiological capacity.[104] Footwear contributes to performance through multiple mechanisms. In this section, we reorganize previous categories into three key factors: mass and propulsion efficiency, push-off mechanics and energy efficiency, and fit and force transmission. Then, we discuss how each factor can be leveraged through 3D printing technologies (Figure 3).

2.2.1. Mass and propulsion efficiency

Shoe mass plays a critical role in performance, particularly during cyclic lower-limb movements like running. Research suggest that reducing shoe mass by 100 g leads to approximately 1% improvement in RE.[8] This effect is attributed to decreased moment of inertia, lowering leg swing cost, which can account for up to 20% of the total running energy expenditure.[9,10] Consequently, modern racing shoes prioritize minimal weight to enhance efficiency.

3D printing enables targeted ultra-lightweight through process-level innovation and structural design. For instance, On Running's Cloudboom Strike LS applies LightSpray™ technology (Figure 3A)—a one-step, robotic spray-deposition method that forms a seamless 30 g upper without stitching or adhesives.[96] Additionally, engineered hollow-core midsoles, such as in Under Armour's Architech shoe or On Running's Cloudmonster Hyper (Figure 3B) demonstrate how lightweight design can preserve cushioning through internal voids.[105,106]

2.2.2. Push-off mechanics and energy efficiency

Midsole thickness, elasticity, and material composition significantly influence performance.[11] Responsive midsoles, made from elastic materials, such as ethylene-vinyl acetate (EVA) foam or specialized cushioning technologies, provide energy return for efficient push-off.[12] The curves in Figure 3C illustrate how midsole materials differ in compliance (amount of deformation, upper trace in each curve) and resilience (efficiency of energy return, lower trace[104]). The area between the loading and unloading curves indicates energy loss, while the area under the unloading curve reflects the elastic energy returned. High-rebound foams, such as thermoplastic polyurethane (TPU) (adidas Boost™) and Pebax® foams (Figure 3C), introduced in the 2010s, offered greater energy return and lower density than classic EVA, contributing to about 1% RE improvement.[104,107] Thicker foam also increases effective leg length and stride length, enhancing RE.[99]

The incorporation of carbon fiber plates in the midsole increases longitudinal bending stiffness (Figure 3D)[13,14,104] It can enhance push-off efficiency by limiting metatarsal-phalangeal joint movement and increasing the mechanical

advantage of the GRF lever arm.[14–16] This is beneficial because less bending at the toes means less energy lost to stretching and recoiling those joints.[14,15] Among other factors, increasing longitudinal bending stiffness is evaluated as one of the most powerful factors that improves RE.[14,100,101] The introduction of super shoes in 2017, combining ultralight Pebax® foam and carbon-fiber plates, reduced the energetic cost of running by 4%, translating to 2–4% faster race times.[14,16,101] However, optimal stiffness varies across individual's characteristics and running speed, and excessive stiffness can be counterproductive (Figure 3D).[13,14,17,108]

3D printing offers a platform for precise control over energy return and bending behavior through geometric customization. Previously discussed lattice and variable-stiffness designs (Figure 2D–G) can be engineered within a single midsole to meet individualized performance needs. Furthermore, the technology allows designers to engineer lattice structures that can be deformed to redirect vertical impact forces into forward-propulsive components.[109,110] For instance, Adidas' 4DFWD's directional lattice structures (Figure 3E[69]) demonstrate how 3D-printed geometry can actively redirect forces to improve propulsive efficiency.

2.2.3. Fit and force transmission

Footwear fit and traction directly influence biomechanical efficiency by affecting the coupling between the foot and the ground. A secure, personalized fit minimizes internal foot-shoe motion and enhances comfort, thereby reducing energy wasted on compensatory muscle activation.[18,19]

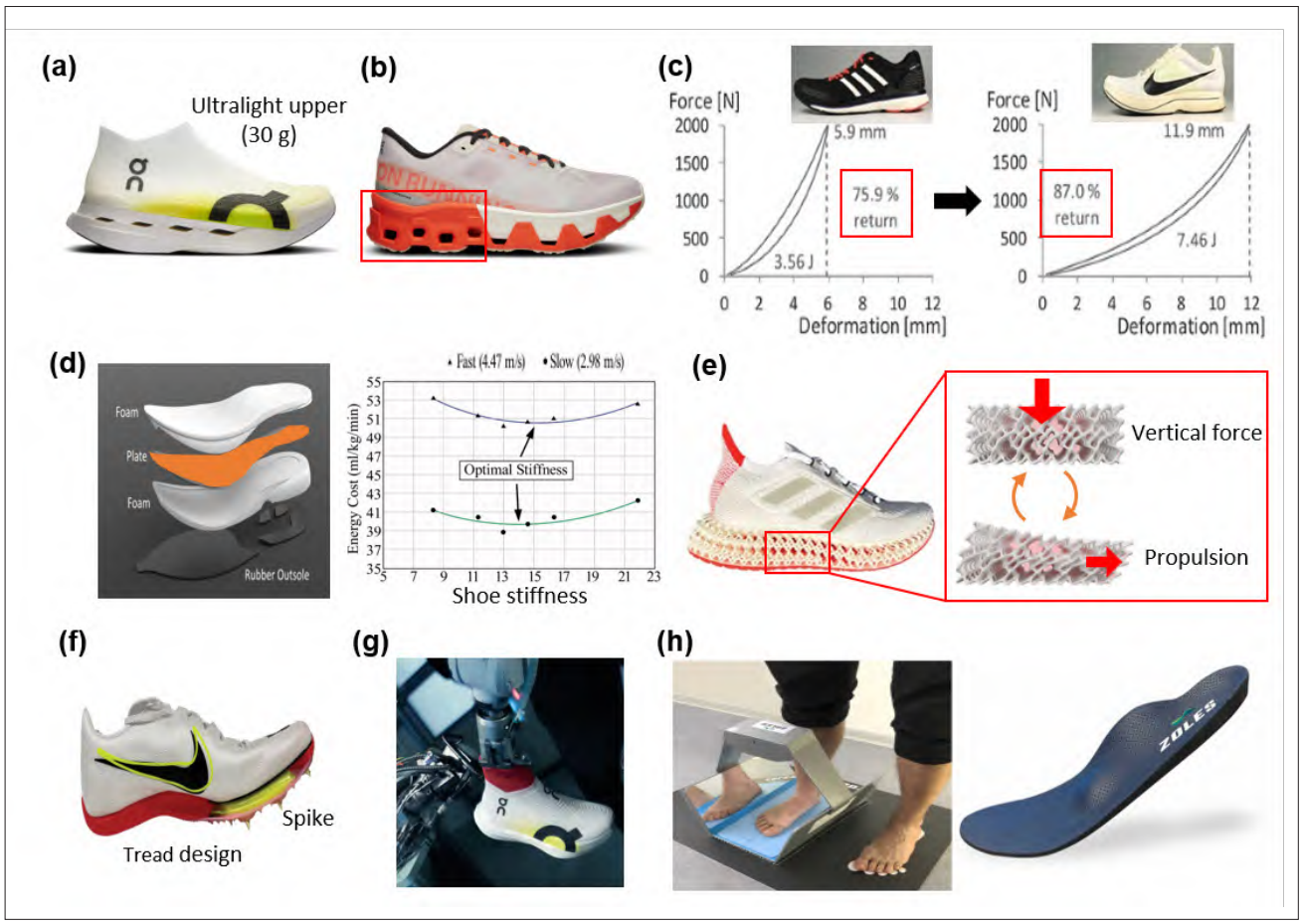


Figure 3. Representative footwear technologies and 3D printing applications for performance enhancement. (A) Light footwear with ultralight upper. Reproduced with permission from ref.[96] Copyright © 2025 On AG. (B) Light footwear with hollow midsole lattice. Reproduced with permission from ref.[106] Copyright © 2025 On AG. (C) Mechanical comparison of low- and high-rebound midsoles. Adapted from ref.[104] (D) Longitudinal bending stiffness: carbon-fiber plate schematic (left; adapted from ref.[104]) and optimal stiffness curve showing minimized oxygen cost (right; reproduced with permission from ref.[108] Copyright © 2020 Taylor & Francis). (E) Anisotropic midsole lattice promoting forward shear deformation. Adapted with permission from ref.[69] Copyright © 2022 Taylor & Francis. (F) Track spike with integrated carbon plate for propulsion. Adapted with permission from ref.[99] Copyright © 2022 Taylor & Francis. (G) Spray deposition technology for ultralight, form-fitting uppers. Reproduced with permission from ref.[96] Copyright © 2025 On AG. (H) Personalized 3D-printed insoles based on foot scans. Reproduced from ref.[113]

Likewise, outsole traction governs how effectively applied force is transmitted into forward motion. Both aspects are crucial for improving RE, especially under high-intensity or multi-directional loading.

Upper materials and systems have evolved to balance lockdown and compliance. Technologies such as BOA® systems (Figure 2J) and knit meshes (Figure 2K) conform to individual foot morphology while maintaining structural security.[82,83] Research demonstrated that runners consumed 0.7% less oxygen when wearing the shoes, which they rated as the most comfortable and well-fitted,[107] indicating that perceived comfort aligns with reduced metabolic cost.

Outsole compounds and tread geometries further affect energy efficiency. Insufficient grip can lead to compensatory muscle activation and increased oxygen cost, while excessive grip may increase torque-related injuries.[99] Advanced footwear technologies, including specialized 'super spikes (Figure 3F)', now feature lightweight carbon rubber, tuned spike placement, and tread patterns to improve grip on track surfaces,[111] contributing to recent record-breaking track performances.[99]

3D printing expands the design space across these domains by enabling precise control over geometry and material properties.[14] Technologies such as Nike's Flyprint™ and On's LightSpray™ (Figure 3G) exemplify how 3D printing enables ultralight, form-fitting uppers with seamless support and adaptive lockdown.[81,96,112] These designs eliminate conventional stitching and lacing, offering precision fit and minimized distraction—especially beneficial under race-day conditions.[110,112] Personalized insoles fabricated from foot scans and plantar pressure data (Figure 3H[113]), as demonstrated in both research workflows[113] and commercial services like those offered by ASICS.[114] Such designs can contribute to improving perceived comfort and gait stability, especially in individuals with foot deformities like flat feet or arthritis.[24,25] Additionally, outsole traction patterns can be directionally optimized through additive manufacturing, which allows data-driven personalization of outsole geometry based on gait asymmetries or sport-specific ground interactions. Together, these advances illustrate how 3D printing supports integrated, performance-driven customization across upper, midsole, insole, and outsole components.

2.3. Clinical applications

Specialized therapeutic footwear and orthotic interventions play a critical role in managing various foot disorders by redistributing plantar pressure, reducing impact force, and correcting deformities. Clinical applications represent one of the earliest domains where customized footwear approaches were introduced, with skilled orthopedic shoemakers crafting personalized solutions for individuals with specific needs. The most representative foot disorders treated by footwear modification are flat feet, plantar fasciitis, and diabetic foot. Additionally, footwear modifications are also prescribed for conditions affecting areas above the foot, such as knee osteoarthritis and leg length discrepancy. In this section, we review both foot disorders and above-foot disorders, considering the potential for 3D printing technology to address these clinical needs (**Figure 4**).

2.3.1. Clinical applications for foot disorders

Flat feet are primarily caused by ligamentous laxity or dysfunction of the tibialis posterior muscle, leading to foot deformities such as a lowered medial longitudinal arch, rearfoot eversion, and forefoot abduction.[21,22] Although various insoles are used to correct flat feet, no standardized form exists. The most representative designs involve inverting the rearfoot, providing medial arch support using fill or flange, and a forefoot post (Figure 4A)[23,26,28,115] These modifications are designed to control foot pronation, reduce GRF, and redistribute midfoot pressure.[24] The evidence supporting insole effectiveness for flat feet remains limited. A systematic review of 13 studies found moderate to good evidence for improvements in physical function, but insufficient evidence for reductions in pain, foot kinetics, and rearfoot kinematics.[23] This gap stems primarily from the scarcity of well-designed randomized controlled trials examining specific design elements and their correlation with clinical outcomes. Conducting such trials is particularly challenging due to differences in foot structure between individuals, making it difficult to standardize treatment protocols and assess outcomes consistently.

Plantar fasciitis is characterized as chronic injury at the origin of the plantar fascia, which commonly manifests as a painful heel. The primary pathogenesis involves cumulative strain at the plantar fascia insertion, exacerbated by various mechanical factors including flat feet, high-arched feet, reduced ankle dorsiflexion range of motion, and deficits in ankle plantar flexor or toe flexor strength.[27] The most commonly studied orthotic device for the treatment of plantar fasciitis is the heel pad or cup, which can be made by either of silicone, nylon, rubber, or polypropylene (Figure 4B).[29,30] These are frequently prescribed in combination with foot orthoses that support the medial longitudinal arch. The main purpose is to redistribute plantar pressure to reduce pressure beneath the painful heel and enhance the mechanical efficacy of plantar fascia.[27,31]

Diabetic foot, affecting approximately 15% of the diabetic population, is a common complication primarily caused by peripheral neuropathy that impairs the feet's sensory, motor, and autonomic nerve functions.[33] Sensory neuropathy results in loss of protective sensation, motor neuropathy leads to muscle atrophy and foot deformities, and autonomic neuropathy leads to dry skin and altered microcirculation. Excessive foot pressure due to limited joint mobility and deformities further increases the risk of tissue breakdown and ulcers.[116]

Orthotic interventions for diabetic foot management can be broadly classified into preventive and therapeutic applications. Preventively, customized footwear and inserts are essential to protect patients with reduced sensation from unnoticed injuries and excessive pressure.[33] Therapeutically, strategies vary according to clinical stage. During the early stage of diabetic foot management, movement is typically limited to prevent weight bearing on the injured area. However, when mobility is necessary, assistive devices such as walker boots or customized ankle–foot orthoses (Figure 4C[38]) can be utilized. After the wound has been treated, therapeutic footwear, including in-depth shoes with accommodative inserts or triple-layer molded orthoses are commonly recommended for ongoing pressure management,[34] often with external shoe modifications such as rocker soles.[35] Despite strong clinical recommendations, current evidence supporting their efficacy remains limited,[37] highlighting the need for more rigorous clinical research. This challenge is further compounded by the considerable variability in

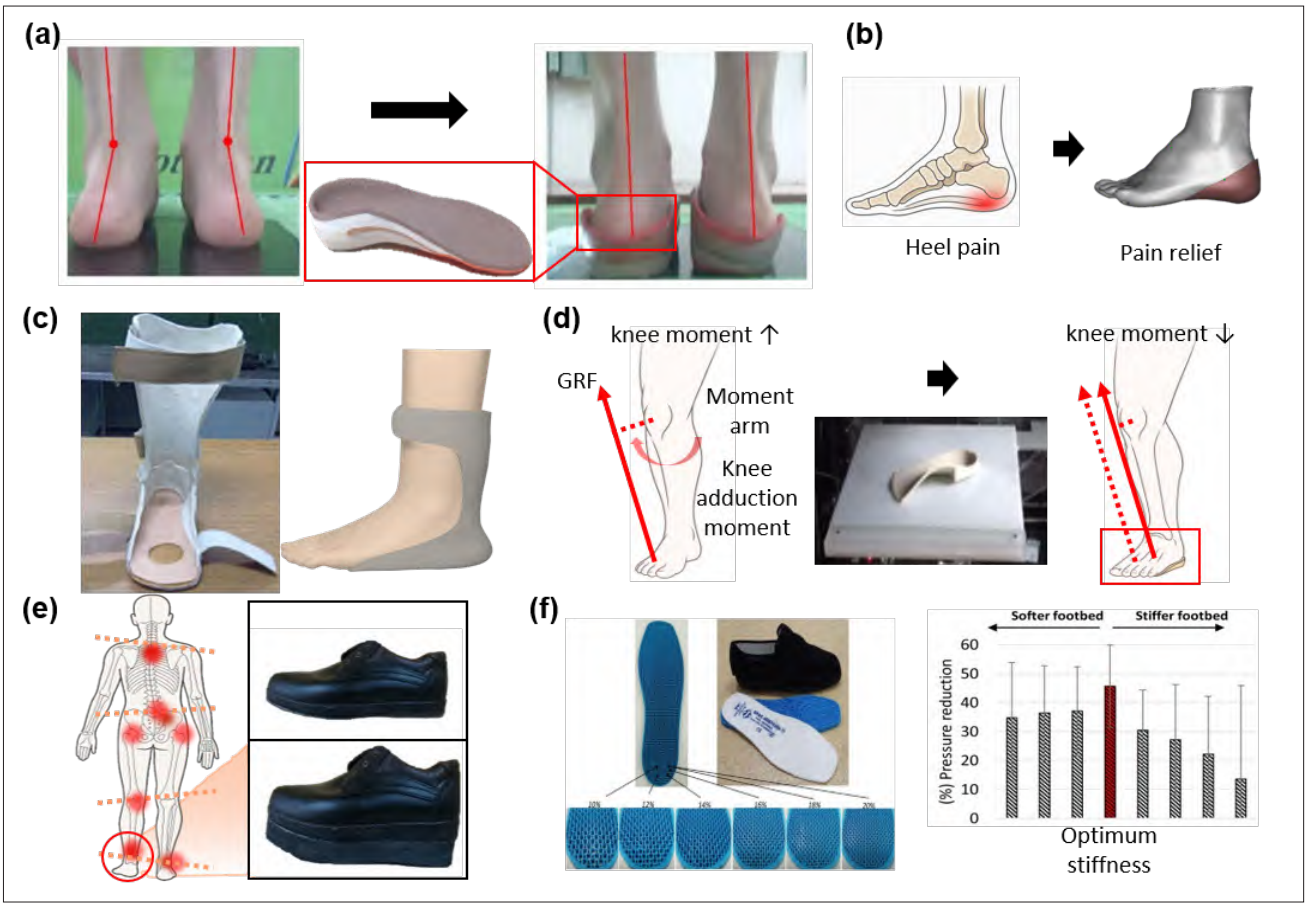


Figure 4. Clinical applications of footwear and orthotic devices enabled by 3D printing. (A) 3D-printed insoles for rearfoot inversion and medial arch support in flat feet. Adapted with permission from ref.[26] Copyright © 2020 Elsevier and ref.[115] Copyright © 2022 Springer Nature. (B) Heel cup to relieve heel strain and redistributes pressure in plantar fasciitis. Adapted from ref.[29] (C) Ankle–foot orthoses for pressure offloading in diabetic foot. Adapted with permission from ref.[38] Copyright © 2014 Diabetes Technology Society. (D) A 3D-printed lateral wedge insole to reduce knee adduction moment in knee osteoarthritis. Adapted with permission from ref.[41] Copyright © IMechE 2017. (E) Insole and outsole modifications for postural alignment in scoliosis and leg length discrepancy. Adapted with permission from ref.[120] Copyright © 2022 Elsevier. (F) A 3D-printed porous insole with region-specific stiffness for plantar pressure reduction (left) and optimal stiffness (right). Reproduced with permission from ref.[121] Copyright © 2020 Elsevier. Abbreviation: GRF, ground reaction force.

lesion location and severity among patients, necessitating personalized assistive device match with individual needs. 3D printing technology is able to address this issue by enabling efficient customization of orthoses and footwear, providing targeted pressure relief and structural support tailored to each patient's specific condition.

2.3.2. Clinical applications for above-foot disorders

Shoe modifications can be used to treat not only foot disorders but also disorders occurring above the foot, such as medial knee osteoarthritis, scoliosis, and leg length discrepancy. In knee osteoarthritis, the medial compartment is more preferentially degenerated than the lateral compartment, causing the malalignment of knee joint, or genu varum (bow-legged deformity).[40] Lateral wedge insoles (Figure 4D) are prescribed to shift the center of pressure laterally, thereby reducing the knee adduction moment.[40-42,117] Meta-analyses have confirmed their effectiveness in pain reduction,[40] with significant reductions in both external knee adduction moment and knee adduction angular impulse in individuals with this condition.[39]

For patients with scoliosis and leg length discrepancy, various shoe modifications offer therapeutic benefits. These include heel pads, outsole modifications, and heel lift insoles (Figure 4E). Such interventions aim to improve spinal deformity, enhance static balance, and compensate for leg length discrepancy and its associated biomechanical consequences.[118–120]

2.3.3. Role of 3D printing in clinical applications

In clinical footwear, patient-specific intervention is essential, and 3D printing offers key advantages over conventional methods by significantly reducing cost, weight, and production time. Using individual foot scans and plantar pressure maps, 3D printing allows for the fabrication of precision orthoses tailored to anatomical and functional needs. For example, insoles with graded stiffness or geometry-optimized arch supports have been shown to improve gait stability and comfort in patients with flat feet or arthritis (Figure 4A and B).[24,26,30] In diabetic foot, 3D-printed ankle–foot orthoses and custom rocker soles can deliver targeted offloading, while also accommodating complex deformities that evolve over time (Figure 4C). Additionally, porous insoles manufactured via 3D printing have demonstrated effectiveness in redistributing plantar pressure by adjusting regional stiffness based on pressure data (Figure 4F).[121] For above-foot disorders such as medial knee osteoarthritis, the ability to digitally model and print lateral wedge insoles or corrective lifts allows for better alignment control with reduced material bulk (Figure 4D).[41] These attributes position 3D printing as a transformative tool in clinical footwear design, capable of delivering scalable, personalized, and evidence-informed interventions.

3. Integration of 3D printing technology into footwear manufacturing

The design and manufacturing of footwear have continuously evolved to meet the functional demands of protection, performance enhancement, and therapeutic application. Traditional footwear manufacturing has undergone significant transition, from craftsmanship-based manufacturing to mechanized mass-production. However, the reliance on molding and casting limits the design complexity of footwear, and multi-step assembly still requires human involvement. These constraints hinder the development of highly optimized footwear designs that could enhance biomechanical functionality.

Additive manufacturing, commonly known as 3D printing, has revolutionized the footwear industry by providing an unprecedented level of design freedom.[122,123] Unlike conventional methods, 3D printing enables the direct fabrication of digitally modeled structures, which are too intricate to be manufactured using traditional techniques. This approach allows for the creation of highly optimized geometries to enhance performance by integrating metamaterial structures, gradient stiffness change, and adaptive cushioning.[44,124] Avoiding the need for physical molds in the manufacturing process has also enabled rapid prototyping. This approach is particularly effective for personalized shoes, which traditionally require labor-intensive and time-consuming tasks due to customization process (Figure 5A).[44,50] Customization plays a crucial role in protection and therapeutic applications, as footwear must accommodate unique foot structures and biomechanical needs to prevent injuries and support medical treatments. Several recent studies have explored the application of 3D printing and 3D scanning in accommodating these individual variables and developing customized footwear solutions to treat foot disorders (Figure 5B).[36,44,47]

Beyond improvements in footwear functions, 3D printing also offers significant advantages in streamlining the manufacturing process and reducing production time, particularly for small-batch, customized production. While traditional manufacturing remains faster for mass production, 3D printing accelerates personalized product development by enabling direct fabrication from digital models, often informed by 3D scanning of user-specific anatomy data. In addition, the elimination of molds and tooling streamlines the prototyping process, allowing for faster transitions from design to physical

product. For example, it has been reported that the total product development cycle for footwear, including design, testing, and production, which typically takes 15–18 months in conventional manufacturing, was shortened by approximately 40% when 3D printing was employed.[125] These advantages have driven major footwear companies such as Adidas, New Balance, and Nike to form partnerships with 3D printing enterprises. As a result of these collaborations, several commercially available 3D-printed footwear models, such as Adidas' 4DFWD™ series and New Balance's TripleCell™, have been introduced to the market. This progress demonstrates the viability and potential of additive manufacturing and reflects the growing role of the technology in the footwear industry.

In this section, we provide comprehensive overview of the design advantages, fabrication method, and current applications of 3D-printed footwear.

3.1. Design advantages of 3D-printed footwear

3D printing provides significant design advantages, such as the freedom to fabricate complex geometries, precise structural control, and simplified manufacturing processes. Among these advantages, one notable approach is the monolithic design, which is created by directly fabricating footwear without the need for assembly between different materials. This approach eliminates seams, resulting in a more durable and sustainable product that avoids structural weaknesses typically associated with multi-material interfaces (Figure 5C).[126,127] Therefore, footwear fabricated with a monolithic design provides enhanced foot protection by minimizing stress concentrations and reducing the likelihood of material failure under repetitive loading conditions. It has been especially beneficial for orthotic insoles, optimizing their production and long-term durability for clinical applications.[46,48,49,128,129] Lastly, a simplified manufacturing process improves sustainability by reducing material waste and production time.

Mechanical metamaterials are one of the most representative structures that highlight the design advantages of 3D printing, which cannot be fabricated through traditional manufacturing methods. These complex artificial porous structures can enhance the performance efficiency of physical activities by leveraging their lightweight properties[130] and adaptive stiffness control.[44] Unlike traditional materials, which require material modifications to adjust stiffness, metamaterials enable precise stiffness control solely through structural design (Figure 5D).[34] This characteristic allows footwear to have variable stiffness options, making it an ideal candidate for both high-performance and therapeutic applications. For instance, sports footwear brands such as Adidas and Carbon 3D, incorporate bow-tied shape lattice midsoles that convert vertical pressure into horizontal force to improve running performance.[69] Additionally, custom insoles with porous structure have been developed for diabetic foot treatment, aiming to prevent ulcers by reducing localized pressure points through gradient stiffness variation (Figure 5E).[44,45]

The convergence of 3D printing and scanning technologies can significantly impact the design of personalized footwear. While 3D scanning-based personalized footwear serves various functions, it is particularly crucial in therapeutic applications. This approach digitalizes the orthosis manufacturing process for clinical applications, reducing production time and eliminating labor-intensive procedures which were conventionally performed exclusively by licensed orthotists.[44,48,50] These conventional methods typically involve using foam impression boxes or plaster casting, where physical contact is unavoidable and may alter the natural posture of the foot. In contrast, 3D scanning offers a contactless and accurate measurement of anatomical details without distortion. Furthermore, acquired scan data can be customized through CAD modeling to optimize pressure distribution, arch support, and motion control (Figure 5F and G).[29,46] This process enables precise customization and adaptation to the individual's specific requirements. For instance, direct scanning of the posterior ankle and legs is utilized in designing ankle–foot orthoses,[50–52,129,131,132] and when direct foot scanning is challenging, scanning foam impression boxes serves as an effective alternative.[25,44,47] Additionally, force plate measurements on plantar pressure distribution are often combined with 3D scanning data, to design orthotic insoles that provide optimal support and alleviate high pressure.[25,46]

3.2. 3D printing methods and materials

Despite extensive research on 3D printing driven by its design advantages, the range of available materials remains limited. Within the realm of footwear production, elastomeric materials are conventionally used to manufacture the sole component because of their properties, such as shock absorption and enhanced user comfort. However, the range of elastomers available for 3D printing is relatively limited, compared to rigid materials. Various 3D printing techniques, such as fused deposition modeling (FDM), selective laser sintering (SLS), and vat polymerization, have been employed in footwear fabrication (Figure 6A).[133]

FDM is one of the most commonly used 3D printing methods due to its cost-effectiveness and simplicity. In FDM, filament is melted and deposited through a nozzle onto a partially constructed 3D structure. TPU, polylactic

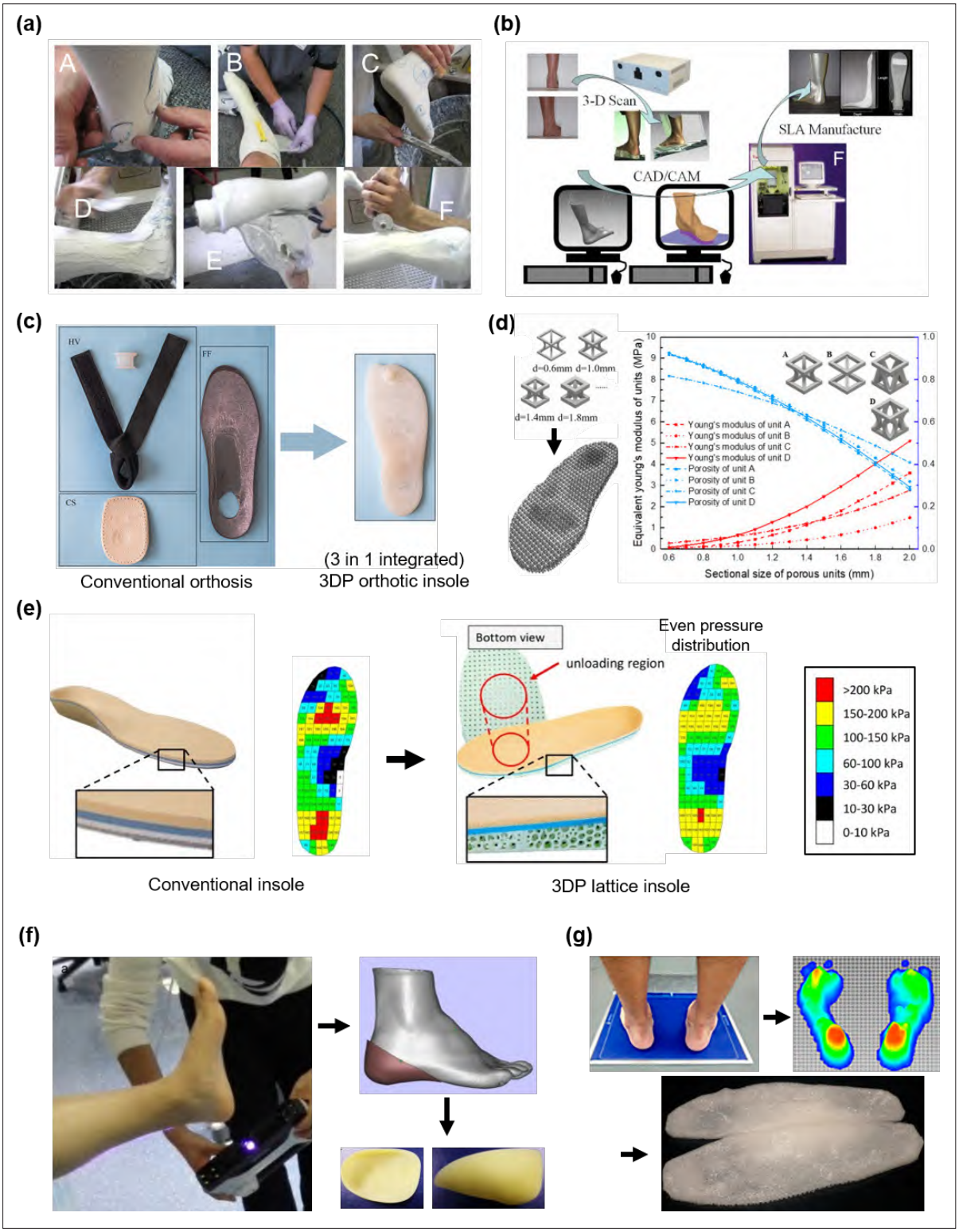


Figure 5. Design advantage of 3D-printed footwear. (A, B) Comparison of footwear manufacturing methods, and (C–G) design advantage. (A) Conventional orthosis manufacturing. Reproduced from ref.[50] (B) 3D-printed footwear manufacturing. Reproduced from ref.[50] (C) Monolithic design. Reproduced with permission from ref.[127] Copyright © IMechE 2021. (D, E) Insole with lattice structure. Adapted with permission from ref.[34] Copyright © 2019 Elsevier and ref.[44] Copyright © 2022 Elsevier. (F, G) 3D scanning and manufacturing. Adapted from refs.[29,46] Abbreviations: 3DP, 3D-printed; CAD/CAM, computer-aided design/computer-aided manufacturing; SLA, stereolithography.

acid, and acrylonitrile butadiene styrene are generally used materials for fabricating orthoses (Figure 6B and C).[25,46,122,123]

SLS is a technology that uses a high-power laser to selectively sinter powder particles into a solid object. Ankle–foot orthoses have been fabricated using SLS due to their complexity and cost-effectiveness (Figure 6D).[51,131,134] In order to minimize energy dissipation during walking, ankle–foot orthoses are typically fabricated using materials like Nylon, which are rigid but offer limited flexibility. Foot orthoses printed by SLS with such materials have been validated through actual walking and mechanical failure tests (Figure 6E).[52,135]

Vat photopolymerization, which includes stereolithography (SLA) and digital light processing (DLP), solidifies liquid resin by selectively curing it with a light source, such as a laser or digital projector. These methods offer high resolution, making them suitable for producing intricate and detailed designs. Photopolymer resins used in SLA and DLP offer a range of material properties, including flexibility, toughness, and biocompatibility.[136] These materials are ideal for the production of metamaterial shoes; consequently, they have been widely adopted in academic research focusing on stiffness control (Figure 6F),[137] and commercial footwear products incorporating metamaterials, including New Balance TripleCell, Asics Actibreeze, and Adidas 4DFWD (Figure 6G).[69,138] These shoes utilize highly elastic resins, such as the Rebound and Elastomeric polyurethane (EPU) resin series. These tough and high-stretchable materials, based on polyurethane acrylate, are well-suited for lattice structures incorporated in both shoes.

3.3. Applications of 3D-printed footwear

The use of 3D printing technology has revolutionized the footwear industry by enabling the production of customized and innovative designs that were previously impossible to manufacture using traditional methods. Major footwear companies such as Adidas, New Balance, and Nike have collaborated with 3D printing companies to develop footwear to optimize athletic performance. Adidas and New Balance have integrated 3D-printed lattice midsoles into their running shoes, aiming to enhance energy return, shock absorption, and responsiveness (Figure 3E–G).[139] Nike and Raise3D took a different approach by using 3D printing to fabricate the shoe upper (Figure 7A),[140,141] which is typically made from woven fabric. The 3D-printed upper allows enhanced flexibility and breathability without compromising durability by adding dynamic interconnection between warp and weft. Beyond midsoles and uppers, FitMyFoot, a Canadian start-up, offers custom 3D-printed insoles and sandals using 3D scanning.[143] ASICS has also adopted a unique approach of fully 3D-printing sandals, designed for recovery and relaxation (Figure 7B). Many other companies, including Columbia and Dior, have also showcased 3D-printed shoes, highlighting the growing trend of 3D printing in the footwear industry. Recent studies have also demonstrated the long-term durability and performance of 3D-printed footwear. For example, one study conducted a fatigue test involving 700,000 loading cycles on 3D-printed footwear made from polyurethane, which is equivalent to several months of regular walking, and no permanent deformation or material hardness change was observed.[143] In another case, midsoles made from conventional EVA showed a noticeable decline in performance after 100,000 heel strikes, whereas 3D-printed midsoles retained their mechanical properties even after 1,000,000 heel strikes.[144] These examples demonstrate the verified durability of 3D-printed footwear and indicate its promising potential for future development.

In the field of medical applications, a number of studies have been conducted with 3D-printed custom insoles and foot orthoses. One prevalent foot disorder is flat feet, and several studies have been conducted to address the issue using 3D printing.[25,46,47,127,145] These studies have explored the control of factors, including arch support height, stiffness, or wedge height, to redistribute plantar pressure or improve foot kinetics. Similarly, 3D printing has also been employed in the treatment of plantar fasciitis. Orthotic insoles[29] and Foot orthosis[31] were designed and fabricated using 3D scanning and 3D printing (Figure 7C and D). These custom-made orthotic insoles have been effective in reducing the load on midfoot during walking and jogging, alleviating direct load from the plantar fascia. Additionally, by increasing the longitudinal arch angle, they help maintain the natural curvature of the foot arch. These results show similar efficacy for reducing pain and distributing pressure. Compared to traditional devices, 3D-printed foot orthoses have demonstrated effectiveness in supporting arch and provide less movement of the plantar flexor muscle, resulting in lower tensile strain in the plantar fascia. In the case of diabetic feet, 3D-printed insoles have been studied to provide plantar pressure offloading.[34,36,44,45,146] These insoles aim to reduce pressure on specific areas of the foot to prevent complications associated with diabetes. Several studies have demonstrated that increasing the foot contact area to reduce peak contact pressure or incorporating porous structures which provide a gradient stiffness to effectively distribute pressure. Beyond insoles and foot orthoses, customized ankle–foot orthoses and insoles have been extensively studied and developed using 3D scanning. While many 3D-printed ankle–foot orthoses follow designs of conventional fabrication methods, some

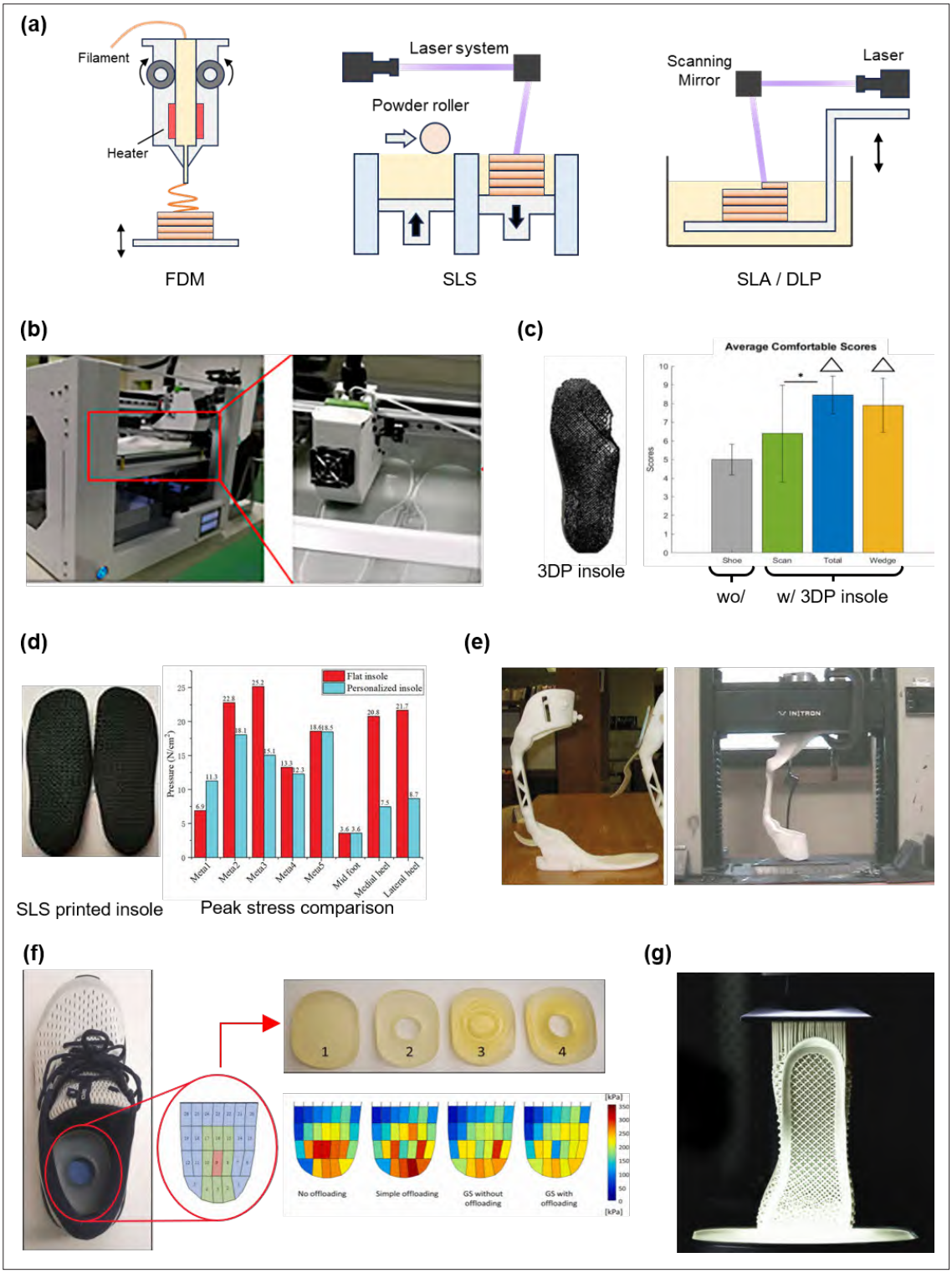


Figure 6. Fabrication methods of 3D-printed footwear. (A) 3D printing methods used to fabricate footwear. Reproduced from ref.[133] (B) FDM printer manufacturing shoe insole. Adapted from ref.[46] (C) 3D-printed insole using the FDM method. Adapted from ref.[25] (D, E) 3D-printed foot orthosis using the SLS method. Adapted with permission from ref.[134] Copyright © 2020 Taylor & Francis and ref. [52] Copyright © 2008 IEEE. (F) Heel cup manufacturing by the SLA method. Adapted with permission from ref.[137] Copyright © 2023 Elsevier. (G) Insole printing using the SLA method. Reproduced with permission from ref.[138] Copyright © 2020, Nature. Abbreviations: 3DP, 3D-printed; DLP, digital light processing; FDM, fused deposition modeling; SLA, stereolithography; SLS, selective laser sintering.

studies have demonstrated the potential of 3D printing's design freedom by creating an ankle–foot orthosis with has adjustable stiffness in the sagittal plane, enabling a more adaptable and patient-specific orthotic solution.[51,132,147]

In summary for athletic and clinical aspects, several studies have examined the efficacy of 3D printed footwear and found promising results. However, despite advancements in 3D-printed footwear, some researches also report that efficacy remains insufficient due to lack of comprehensive scientific evaluations. Systematic reviews on 3D-printed insoles have yielded mixed results, with some studies reporting significant improvements in pressure distribution and biomechanical performance, while others found no major differences compared to traditional footwear.[24] Therefore, further research is required to establish comprehensive performance metrics

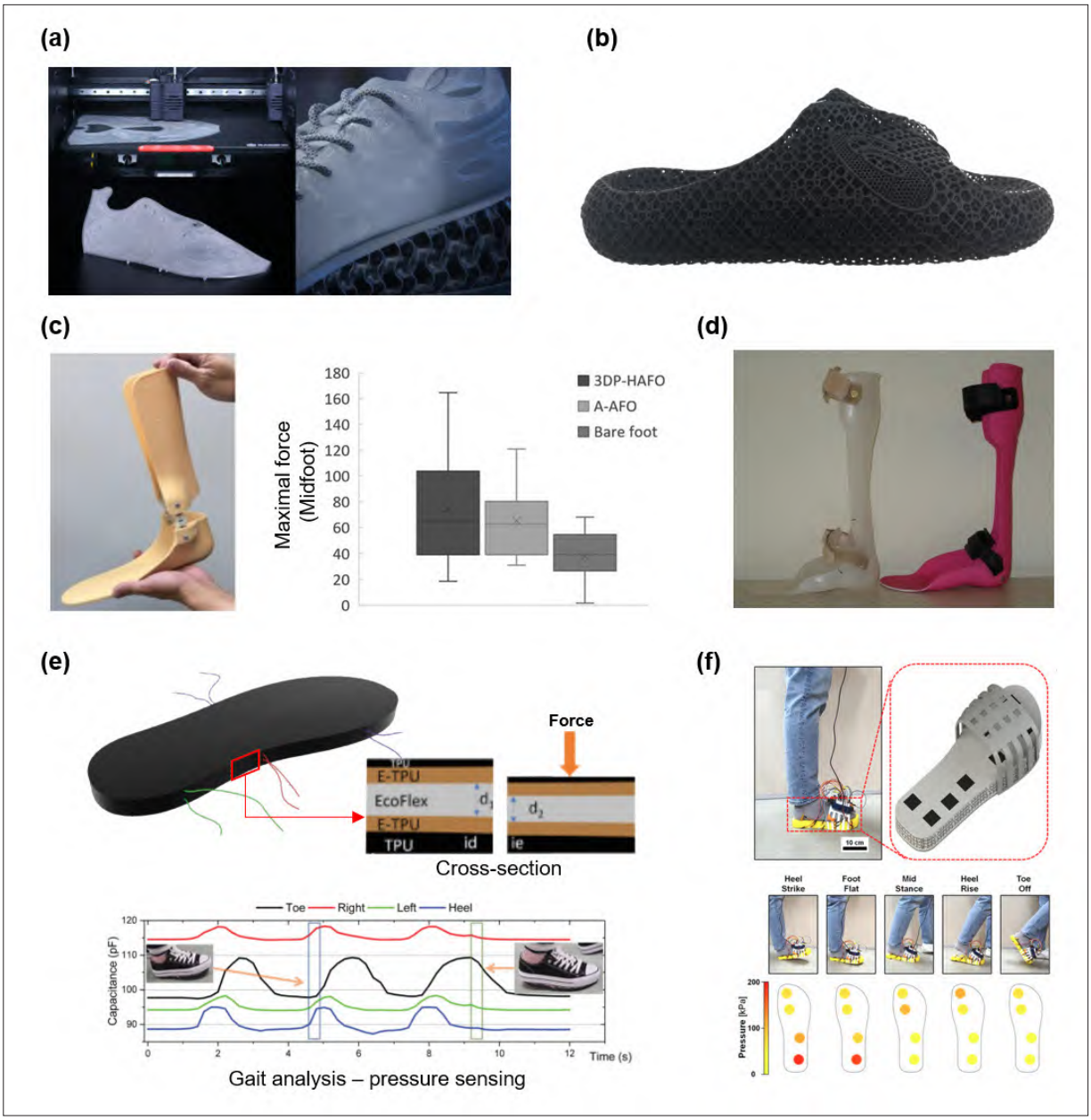


Figure 7. Applications of 3D-printed footwear. (A) Shoe upper fabricated with 3D printing. Reproduced with permission from ref.[141] Copyright © 2025 Raise3D Technologies, Inc. (B) Commercial footwear fabricated with 3D-printed insole. (C, D) 3D-printed medical orthosis. Reproduced with permission from ref.[147] Copyright © 2022 Elsevier and ref.[51] Copyright © 2013, © International Society for Prosthetics and Orthotics 2013. (E, F) 3D-printed smart footwear – pressure sensor-integrated footwear. Adapted from ref.[98] Copyright © 2023 Wiley-VCH GmbH and adapted with permission from ref.[148]

and validate the effectiveness of 3D-printed footwear modifications compared to traditional ones.

Beyond conventional applications such as performance enhancement and therapeutic application, 3D printing enables novel functionalities that were previously unattainable with traditional shoe manufacturing. First, 3D-printed insoles can act as pressure sensors, providing plantar pressure measurement capabilities of up to 300 kPa without saturation (Figure 7E and F).[98,148] These smart insoles provide real-time biomechanical feedback, offering potential applications in rehabilitation and gait analysis. Additionally, recent developments on foot pressure data suggest that data can be used to dynamically adjust stiffness within a 3D-printed shoe midsole, optimizing it to improve an individual's overall comfort level.[124] This advancement opens the door for real-time footwear adaptation, which could be particularly beneficial for individuals with biomechanical asymmetries or mobility impairments. In sum, the integration of sensing and customization capabilities into 3D-printed footwear opens up new possibilities for various applications.

4. Current limitations and future directions

While 3D printing offers unique advantages in footwear production, several limitations remain that must be resolved for broader adoption. First, further studies are needed to explore novel 3D footwear designs with enhanced performance that would be difficult to achieve without the use of 3D printing. Even though 3D printing offers high design freedom and precise personal customization, determining the optimal design for each footwear function remains a challenge. Current 3D-printed footwear designs focus more on replicating the design of conventional footwear, rather than fully exploiting the potential of 3D printing for enhanced footwear functions. This highlights the need for further research to identify optimal geometries that can effectively enhance the functions of footwear while maximizing the capabilities of 3D printing.[24,69] Another challenge involves the limited material selection suitable for 3D-printed footwear. Footwear requires materials with low viscoelasticity to ensure rapid recovery after deformation caused by stepping, providing smooth movement between stride transitions. Previous research and commercial applications employ materials such as EPU or rebound resins to meet this requirement,[69] but the variety of materials suitable for 3D-printed footwear remains limited. This feature is closely related to another limitation, namely, relatively high unit cost and low production throughput of 3D printing. Conventional manufacturing has benefited from decades of process optimization and highly efficient mass-production systems, which significantly reduce unit cost and production time for manufacturing. In contrast, 3D printing remains limited in terms of available materials and is mostly applied to small-scale production only, which results in comparatively higher unit costs.[149] These limitations pose challenges to the widespread adoption of 3D-printed footwear in industrial applications. Nevertheless, by the ongoing development of printing processes and materials, recent studies suggest that some 3D-printed footwear products may achieve cost levels comparable to those of traditionally manufactured ones, highlighting their growing economic viability.[149] In addition, some reports have shown that the advantages of 3D-printed footwear in customization and rapid prototyping can significantly accelerate the total product development cycle, including the design and testing process, by eliminating the need for tooling, molds, or die-specific hardware.[125,150] Furthermore, the additive nature of the process reduces material waste, supporting its potential for more sustainable manufacturing. For example, Nike's Flyknit uses 3D printing to fabricate shoe upper, eliminating the need for cutting and stitching. This approach has been reported to reduce waste by as much as 66%, while also lowering labor costs.[151] Based on these factors, we believe that the economic feasibility and environmental sustainability of 3D-printed footwear can be sufficiently realized in the future.

Despite several limitations, 3D printing technology holds great potential to revolutionize the way footwear is designed and manufactured. To fully utilize this potential, continued research and development efforts are essential to optimize footwear design methodologies, diversify material options, and boost manufacturing productivity. We expect that continuous advancements in 3D printing technology will drive innovation in design methodologies, material diversification, and manufacturing scalability, thereby promoting wider adoption of 3D-printed footwear with improved comfort, enhanced performance, and increased personalization.[138]

5. Conclusion

3D printing has garnered significant attention as an innovative manufacturing approach for footwear, due to its capability to fabricate complex shapes, which is impossible to achieve through traditional methods.[122] Given the multifaceted nature of footwear functions, optimal design of 3D-printed footwear requires a holistic approach considering ergonomic, biomechanical, and clinical aspects, along with the advantages and limitations of 3D printing. In this review, we have categorized the functions of footwear into three sections: protection, performance enhancement, and therapeutic applications. In terms of protection, footwear supports gait motions by impact absorption and structural support, and individual

fit. 3D printing contributes a protective function through monolithic manufacturing and customization capabilities.[44,48] The second function, performance enhancement, focuses on improving motion efficiency and reducing energy expenditure. A key enabler of this function is adaptive stiffness control using mechanical metamaterials, which can be fabricated through 3D printing.[69,104] Finally, therapeutic applications such as medical orthoses play a significant role in managing various foot disorders. Here, both customization and stiffness control enabled by 3D printing technology significantly improve clinical footwear applications.[49,127] Additionally, various manufacturing methods and application fields of 3D printing are presented. This review expands on previous research by systematically integrating interdisciplinary perspectives, such as biomechanical, ergonomic, and therapeutic viewpoints, thus providing a comprehensive understanding of the capabilities and applications of additive manufacturing in footwear.

Glossary

- **Laxity**: Looseness or reduced tension in ligaments, often leading to instability.
- **Tibialis posterior**: A key muscle that supports the foot arch and prevents flatfoot deformity.
- **Pronation**: The inward roll of the foot during walking or running; excessive pronation is linked to various injuries.
- **Plantar fasciitis/fascia**: The fascia is the fibrous band under the foot; plantar fasciitis refers to its painful inflammation, often near the heel.
- **Dorsiflexion**: The motion of lifting the foot upward at the ankle, important for normal gait.
- **Osteoarthritis**: A degenerative joint disease that causes pain and stiffness, often in the knees.
- **Scoliosis**: A condition involving lateral curvature of the spine.
- **Diabetic foot**: A complication from diabetes involving nerve damage and poor circulation in the feet, increasing ulcer risk.
- **Ankle–foot orthosis**: A brace supporting the ankle and foot, often custom-molded for deformities or neuromuscular deficits.

Acknowledgments

None.

Funding

This work was supported by Seoul National University Research Grant in 2021. The authors also acknowledge the financial support from the National Research Foundation of Korea (NRF) Grants funded by the Korean Government (MSIT) (RS-2022-NR070098, RS-2023-00208052, and RS-2023-00218543).

Conflict of interest

The authors have no conflicts of interest to declare.

Author contributions

Conceptualization: Howon Lee, Jooeun Ahn, Keewon Kim
Visualization: Kijung Kim, Hyunji Kim
Writing–original draft: Kijung Kim, Hyunji Kim, Wonjae Hwang, Yoonseo Choi
Writing–review & editing: Howon Lee, Jooeun Ahn, Keewon Kim

Ethics approval and consent to participate

Not applicable.

Consent for publication

Not applicable.

Availability of data

Not applicable.

References

1. Nigg BM, Baltich J, Hoerzer S, Enders H. Running shoes and running injuries: mythbusting and a proposal for two new paradigms: 'preferred movement path' and 'comfort filter'. *Br J Sports Med*. 2015;49(20):1290. doi: 10.1136/bjsports-2015-095054
2. Karimi Z, Allahyari T, Azghani MR, Khalkhali H. Influence of unstable footwear on lower leg muscle activity, volume change and subjective discomfort during prolonged standing. *Appl Ergon*. 2016;53(partA):95-102. doi: 10.1016/j.apergo.2015.09.003
3. MacKinnon CD. Sensorimotor anatomy of gait, balance, and falls. *Handb Clin Neurol*. 2018;159:3-26. doi: 10.1016/b978-0-444-63916-5.00001-x
4. Petersen E, Zech A, Hamacher D. Walking barefoot vs. with minimalist footwear - influence on gait in younger and older adults. *BMC Geriatr*. 2020;20(1):88. doi: 10.1186/s12877-020-1486-3
5. Nigg B, Mohr M, Nigg S. Muscle tuning and preferred movement path – a paradigm shift. *Curr Issues Sport Sci*. 2017;2:1-12. doi: 10.15203/CISS_2017.007

6. Nigg BM, Nigg S, Hoitz F, *et al*. Highlighting the present state of biomechanics in shoe research (2000–2023). *Footwear Sci*. 2023;15(2):133-143. doi: 10.1080/19424280.2023.2209044
7. Ceyssens L, Vanelderen R, Barton C, Malliaras P, Dingenen B. Biomechanical risk factors associated with running-related injuries: a systematic review. *Sports Med*. 2019;49(7):1095-1115. doi: 10.1007/s40279-019-01110-z
8. Franz J, Wierzbinski C, Kram R. Metabolic cost of running barefoot versus shod: is lighter better? *Med Sci Sports Exerc*. 2012;44(8):1519-1525. doi: 10.1249/MSS.0b013e3182514a88
9. Marsh RL, Ellerby DJ, Carr JA, Henry HT, Buchanan CI. Partitioning the energetics of walking and running: swinging the limbs is expensive. *Science*. 2004;303(5654):80-83. doi: 10.1126/science.1090704
10. Perl DP, Daoud AI, Lieberman DE. Effects of footwear and strike type on running economy. *Med Sci Sports Exerc*. 2012;44(7):1335-1343. doi: 10.1249/MSS.0b013e318247989e
11. Tung KD, Franz JR, Kram R. A test of the metabolic cost of cushioning hypothesis during unshod and shod running. *Med Sci Sports Exerc*. 2014;46(2):324-329. doi: 10.1249/MSS.0b013e3182a63b81
12. Worobets J, Wannop JW, Tomaras E, Stefanyshyn D. Softer and more resilient running shoe cushioning properties enhance running economy. *Footwear Sci*. 2014;6(3):147-153. doi: 10.1080/19424280.2014.918184
13. Oh K, Park S. The bending stiffness of shoes is beneficial to running energetics if it does not disturb the natural MTP joint flexion. *J Biomech*. 2017;53:127-135. doi: 10.1016/j.jbiomech.2017.01.014
14. Ortega JA, Healey LA, Swinnen W, Hoogkamer W. Energetics and biomechanics of running footwear with increased longitudinal bending stiffness: a narrative review. *Sports Med*. 2021;51(5):873-894. doi: 10.1007/s40279-020-01406-5
15. Willwacher S, König M, Braunstein B, Goldmann JP, Brüggemann GP. The gearing function of running shoe longitudinal bending stiffness. *Gait Posture*. 2014;40(3):386-90. doi: 10.1016/j.gaitpost.2014.05.005
16. Cigoja S, Asmussen MJ, Firminger CR, Fletcher JR, Edwards WB, Nigg BM. The effects of increased midsole bending stiffness of sport shoes on muscle-tendon unit shortening and shortening velocity: a randomised crossover trial in recreational male runners. *Sports Med Open*. 2020;6(1):9. doi: 10.1186/s40798-020-0241-9
17. Chollet M, Michelet S, Horvais N, Pavailler S, Giandolini M. Individual physiological responses to changes in shoe bending stiffness: a cluster analysis study on 96 runners. *Eur J Appl Physiol*. 2023;123(1):169-177. doi: 10.1007/s00421-022-05060-9
18. Girard O, Morin JB, Ryu JH, Van Alsenoy K. Custom foot orthoses improve performance, but do not modify the biomechanical manifestation of fatigue, during repeated treadmill sprints. *Eur J Appl Physiol*. 2020;120(9):2037-2045. doi: 10.1007/s00421-020-04427-0
19. Van Alsenoy K, Ryu JH, Girard O. The effect of EVA and TPU custom foot orthoses on running economy, running mechanics, and comfort. *Front Sports Act Living*. 2019;1:34. doi: 10.3389/fspor.2019.00034
20. Cheng J, Zeng Q, Lai J, Zhang X. Effects of arch support doses on the center of pressure and pressure distribution of running using statistical parametric mapping. *Front Bioeng Biotechnol*. 2022;10:1051747. doi: 10.3389/fbioe.2022.1051747
21. Harris EJ. The natural history and pathophysiology of flexible flatfoot. *Clin Podiatr Med Surg*. 2010;27(1):1-23. doi: 10.1016/j.cpm.2009.09.002
22. Banwell HA, Mackintosh S, Thewlis D. Foot orthoses for adults with flexible pes planus: a systematic review. *J Foot Ankle Res*. 2014;7(1):1-18. doi: 10.1186/1757-1146-7-23
23. Dars S, Uden H, Banwell HA, Kumar S. The effectiveness of non-surgical intervention (foot orthoses) for paediatric flexible pes planus: a systematic review: update. *PloS One*. 2018;13(2):e0193060. doi: 10.1371/journal.pone.0193060
24. Daryabor A, Kobayashi T, Saeedi H, Lyons SM, Maeda N, Naimi SS. Effect of 3D printed insoles for people with flatfeet: a systematic review. *Assist Technol*. 2022;35(2):169-179. doi: 10.1080/10400435.2022.2105438
25. Hsu C-Y, Wang C-S, Lin K-W, Chien M-J, Wei S-H, Chen C-S. Biomechanical analysis of the flatfoot with different 3D-printed insoles on the lower extremities. *Bioengineering*. 2022;9(10):563. doi: 10.3390/bioengineering9100563
26. Choi JY, Lee DJ, Kim SJ, Suh JS. Does the long-term use of medial arch support insole induce the radiographic structural changes for pediatric flexible flat foot? — A prospective comparative study. *Foot Ankle Surg*. 2020;26(4):449-456. doi: 10.1016/j.fas.2019.05.017
27. Lee SY, McKeon P, Hertel J. Does the use of orthoses improve self-reported pain and function measures in patients with plantar fasciitis? A meta-analysis. *Phys Ther Sport*. 2009;10(1):12-18. doi: 10.1016/j.ptsp.2008.09.002
28. Banwell HA, Mackintosh S, Thewlis D, Landorf KB. Consensus-based recommendations of Australian

podiatrists for the prescription of foot orthoses for symptomatic flexible pes planus in adults. *J Foot Ankle Res*. 2014;7(1):1-13.
doi: 10.1186/s13047-014-0049-2

29. Li L, Yang L, Yu F, *et al*. 3D printing individualized heel cup for improving the self-reported pain of plantar fasciitis. *J Transl Med*. 2018;16:167.
doi: 10.1186/s12967-018-1547-y

30. Pfeffer G, Bacchetti P, Deland J, *et al*. Comparison of custom and prefabricated orthoses in the initial treatment of proximal plantar fasciitis. *Foot Ankle Int*. 1999;20(4):214-221.
doi: 10.1177/107110079902000402

31. Ho M, Nguyen J, Heales L, Stanton R, Kong PW, Kean C. The biomechanical effects of 3D printed and traditionally made foot orthoses in individuals with unilateral plantar fasciopathy and flat feet. *Gait Posture*. 2022;96:257-264.
doi: 10.1016/j.gaitpost.2022.06.006

32. Singh N, Armstrong DG, Lipsky BA. Preventing foot ulcers in patients with diabetes. *Jama*. 2005;293(2):217-228.
doi: 10.1001/jama.293.2.217

33. Katoulis E, Boulton A, Raptis S. The role of diabetic neuropathy and high plantar pressures in the pathogenesis of foot ulceration. *Horm Metab Res*. 1996;28(04):159-164.
doi: 10.1055/s-2007-979152

34. Tang L, Wang L, Bao W, Zhu S, Li D, Liu C. Functional gradient structural design of customized diabetic insoles. *J Mech Behav Biomed Mater*. 2019;94:279-287.
doi: 10.1016/j.jmbbm.2019.03.003

35. Janisse D, Janisse E. Pedorthic management of the diabetic foot. *Prosthet Orthot Int*. 2015;39(1):40-47.
doi: 10.1177/0309364614535233

36. Telfer S, Woodburn J, Collier A, Cavanagh P. Virtually optimized insoles for offloading the diabetic foot: a randomized crossover study. *J Biomech*. 2017;60:157-161.
doi: 10.1016/j.jbiomech.2017.06.028

37. Bus SA, Lavery LA, Monteiro-Soares M, *et al*. Guidelines on the prevention of foot ulcers in persons with diabetes (IWGDF 2019 update). *Diabetes Metab Res Rev*. 2020;36:e3269.
doi: 10.1002/dmrr.3269

38. Chakraborty PP, Ray S, Biswas D, *et al*. A comparative study between total contact cast and pressure-relieving ankle foot orthosis in diabetic neuropathic foot ulcers. *J Diabetes Sci Technol*. 2014;9(2):302-308.
doi: 10.1177/1932296814560788

39. Hinman RS, Bowles KA, Metcalf BB, Wrigley TV, Bennell KL. Lateral wedge insoles for medial knee osteoarthritis: effects on lower limb frontal plane biomechanics. *Clin Biomech*. 2012;27(1):27-33.
doi: 10.1016/j.clinbiomech.2011.07.010

40. Parkes MJ, Maricar N, Lunt M, *et al*. Lateral wedge insoles as a conservative treatment for pain in patients with medial knee osteoarthritis: a meta-analysis. *Jama*. 2013;310(7):722-730.
doi: 10.1001/jama.2013.243229

41. Allan R, Woodburn J, Telfer S, Abbott M, Steultjens MP. Knee joint kinetics in response to multiple three-dimensional printed, customised foot orthoses for the treatment of medial compartment knee osteoarthritis. *Proc Inst Mech Eng H J Eng Med*. 2017;231(6):487-498.
doi: 10.1177/0954411917691318

42. Mannisi M, Dell'Isola A, Andersen MS, Woodburn J. Effect of lateral wedged insoles on the knee internal contact forces in medial knee osteoarthritis. *Gait Posture*. 2019;68:443-448.
doi: 10.1016/j.gaitpost.2018.12.030

43. Jin H, Xu R, Wang S, Wang J. Use of 3D-printed heel support insoles based on arch lift improves foot pressure distribution in healthy people. *Med Sci Monit*. 2019;25:7175-7181.
doi: 10.12659/msm.918763

44. Hudak YF, Li J-S, Cullum S, *et al*. A novel workflow to fabricate a patient-specific 3D printed accommodative foot orthosis with personalized latticed metamaterial. *Med Eng Phys*. 2022;104:103802.
doi: 10.1016/j.medengphy.2022.103802

45. Ma Z, Lin J, Xu X, *et al*. Design and 3D printing of adjustable modulus porous structures for customized diabetic foot insoles. *Int J Lightweight Mater Manuf*. 2019;2(1):57-63.
doi: 10.1016/j.ijlmm.2018.10.003

46. Jiang Y, Wang D, Ying J, Chu P, Qian Y, Chen W. Design and preliminary validation of individual customized insole for adults with flexible flatfeet based on the plantar pressure redistribution. *Sensors*. 2021;21(5):1780.
doi: 10.3390/s21051780

47. Cheng K-W, Peng Y, Chen TL-W, *et al*. A three-dimensional printed foot orthosis for flexible flatfoot: an exploratory biomechanical study on arch support reinforcement and undercut. *Materials*. 2021;14(18):5297.
doi: 10.3390/ma14185297

48. Surmen K, Ortes F, Arslan YZ. Design and production of subject specific insole using reverse engineering and 3D printing technology. *Int J Eng Sci Invent*. 2016;5(12):11-15.
doi: 10.6084/m9.figshare.19729495

49. Peker A, Aydin L, Kucuk S, *et al*. Additive manufacturing and biomechanical validation of a patient-specific diabetic insole. *Polym Adv Technol*. 2020;31(5):988-996.
doi: 10.1002/pat.4832

50. Mavroidis C, Ranky RG, Sivak ML, *et al*. Patient specific ankle–foot orthoses using rapid prototyping. *J Neuroeng Rehabil*. 2011;8(1):1-11.
doi: 10.1186/1743-0003-8-1

51. Creylman V, Muraru L, Pallari J, Vertommen H, Peeraer L. Gait assessment during the initial fitting of customized

selective laser sintering ankle foot orthoses in subjects with drop foot. *Prosthet Orthot Int*. 2013;37(2):132-138. doi: 10.1177/0309364612451269

52. Faustini MC, Neptune RR, Crawford RH, Stanhope SJ. Manufacture of passive dynamic ankle–foot orthoses using selective laser sintering. *IEEE Trans Biomed Eng*. 2008;55(2):784-790. doi: 10.1109/TBME.2007.912638
53. Hamill J, Bates BT. Biomechanics and footwear research 1970–2000. *Footwear Sci*. 2023;15(2):123-131. doi: 10.1080/19424280.2023.2209045
54. Werd MB, Knight EL, Langer PR. *Athletic Footwear and Orthoses in Sports Medicine*. New York, USA: Springer; 2010.
55. Hicks JH. The mechanics of the foot. II. The plantar aponeurosis and the arch. *J Anat*. 1954;88(1):25-30.
56. Stolwijk NM, Koenraadt KLM, Louwerens JWK, Grim D, Duysens J, Keijsers NLW. Foot lengthening and shortening during gait: a parameter to investigate foot function? *Gait Posture*. 2014;39(2):773-777. doi: 10.1016/j.gaitpost.2013.10.014
57. McKeon PO, Hertel J, Bramble D, Davis I. The foot core system: a new paradigm for understanding intrinsic foot muscle function. *Br J Sports Med*. 2015;49(5):290-290. doi: 10.1136/bjsports-2013-092690
58. Gil-Calvo M, Jimenez-Perez I, Priego-Quesada JI, Lucas-Cuevas ÁG, Pérez-Soriano P. Effect of custom-made and prefabricated foot orthoses on kinematic parameters during an intense prolonged run. *PLoS One*. 2020;15(3):e0230877. doi: 10.1371/journal.pone.0230877
59. Stewart L, Gibson JNA, Thomson CE. In-shoe pressure distribution in "unstable" (MBT) shoes and flat-bottomed training shoes: a comparative study. *Gait Posture*. 2007;25(4):648-651. doi: 10.1016/j.gaitpost.2006.06.012
60. Hutchins S, Bowker P, Geary N, Richards J. The biomechanics and clinical efficacy of footwear adapted with rocker profiles—evidence in the literature. *Foot*. 2009;19(3):165-170. doi: 10.1016/j.foot.2009.01.001
61. Zhang X, Li B, Hu K, Wan Q, Ding Y, Vanwanseele B. Adding an arch support to a heel lift improves stability and comfort during gait. *Gait Posture*. 2017;58:94-97. doi: 10.1016/j.gaitpost.2017.07.110
62. Chen W-M, Lee S-J, Lee PVS. Plantar pressure relief under the metatarsal heads – therapeutic insole design using three-dimensional finite element model of the foot. *J Biomech*. 2015;48(4):659-665. doi: 10.1016/j.jbiomech.2014.12.043
63. Agresta C, Giacomazzi C, Harrast M, Zendler J. Running injury paradigms and their influence on footwear design features and runner assessment methods: a focused review to advance evidence-based practice for running medicine clinicians. *Front Sports Act Living*. 2022;4:815675. doi: 10.3389/fspor.2022.815675
64. Stoneham R, Barry G, Saxby L, Waters L, Wilkinson M. Differences in stride length and lower limb moments of recreational runners during over-ground running while barefoot, in minimalist and in maximalist running shoes. *Footwear Sci*. 2021;13(2):133-141. doi: 10.1080/19424280.2021.1878285
65. Richards CE, Magin PJ, Callister R. Is your prescription of distance running shoes evidence-based? *Br J Sports Med*. 2009;43(3):159-62. doi: 10.1136/bjsm.2008.046680
66. Robbins S, Waked E. Foot position awareness: the effect of footwear on instability, excessive impact, and ankle spraining. *Crit Rev Phys Rehabil Med*. 1997;9(1):53-74. doi: 10.1615/CritRevPhysRehabilMed.v9.i1.30
67. Mai P, Robertz L, Robbin J, *et al*. Towards functionally individualised designed footwear recommendation for overuse injury prevention: a scoping review. *BMC Sports Sci Med Rehabil*. 2023;15(1):152. doi: 10.1186/s13102-023-00760-x
68. Mohammadi MM, Nourani A. Testing the effects of footwear on biomechanics of human body: a review. *Heliyon*. 2025. doi: 10.1016/j.heliyon.2025;11(4):e42870
69. Clermont C, Barrons ZB, Esposito M, *et al*. The influence of midsole shear on running economy and smoothness with a 3D-printed midsole. *Sports Biomech*. 2023;22(3):410-421. doi: 10.1080/14763141.2022.2029936
70. Carbon3d. *Carbon Lattice Innovation — The Adidas Story*. https://www.carbon3d.com/resources/whitepaper/the-adidas-story. Accessed March 21, 2025.
71. Paoletti I, Ceccon L. The evolution of 3D printing in AEC: from experimental to consolidated techniques. In: Cvetković D, ed. *3D Printing*. London, UK: IntechOpen; 2018.
72. Ali M, Nazir A, Jeng J-Y. Mechanical performance of additive manufactured shoe midsole designed using variable-dimension helical springs. *Int J Adv Manuf Technol*. 2020;111:3273-3292. doi: 10.1007/s00170-020-06227-4
73. Desmyttere G, Hajizadeh M, Bleau J, Leteneur S, Begon M. Anti-pronator components are essential to effectively alter lower-limb kinematics and kinetics in individuals with flexible flatfeet. *Clin Biomech*. 2021;86:105390. doi: 10.1016/j.clinbiomech.2021.105390
74. Zhou Q, Niu W, Yick K-L, Gu B, Sun Y. Numerical simulation of the effect of different footwear midsole structures on plantar pressure distribution and bone stress in obese and healthy children. *Bioengineering*. 2023;10(11):1306. doi: 10.3390/bioengineering10111306

75. Nishiwaki T, Nonogawa M. Topological optimization of heel counter for footwear stability. *Footwear Sci*. 2009;1(sup1): 107-109.
doi: 10.1080/19424280903063531

76. Hemler SL, Pliner EM, Redfern MS, Haight JM, Beschorner KE. Effects of natural shoe wear on traction performance: a longitudinal study. *Footwear Sci*. 2022;14(1):1-12.
doi: 10.1080/19424280.2021.1994022

77. Medicine TAAoPS. *Footwear—Running Shoes*. https://www.aapsm.org/runshoe.html. Accessed March 21, 2025.

78. Keshvari B, Lehoang L, Senner V. Investigating the effect of outsole configurations on rotational and translational traction using a mechanical prosthetic foot. *Sports Eng*. 2023;26(1):43.
doi: 10.1007/s12283-023-00436-2

79. Willwacher S, Kurz M, Robbin J, *et al*. Running-related biomechanical risk factors for overuse injuries in distance runners: a systematic review considering injury specificity and the potentials for future research. *Sports Med*. 2022;52(8):1863-1877.
doi: 10.1007/s40279-022-01666-3

80. BOA Technology. *Redefining the Future of Fit*. https://www.boafit.com/en-us/innovation#:~:text=BOA%C2%AE%20delivers%20fit%20solutions,an%20athlete%20and%20their%20equipment. Accessed March 12, 2025.

81. Knitting Industry. *Flat Knitting: Nike Launches Next Generation 3D Flyknit*. https://www.knittingindustry.com/nike-launches-next-generation-3d-flyknit/. Accessed March 12, 2025.

82. Luftglass AR, Feeney DF, Queen RM. The effect of upper panel stiffness on biomechanical performance in athletic footwear. *Footwear Sci*. 2023;15(3):193-202.
doi: 10.1080/19424280.2023.2184874

83. Moorhouse D, Moorhouse D. Sustainable design: circular economy in fashion and textiles. *Des J* 2017;20(suppl 1):S1948-S1959.
doi: 10.1080/14606925.2017.1352713

84. Menz HB, Bonanno DR. Footwear comfort: a systematic search and narrative synthesis of the literature. *J Foot Ankle Res*. 2021;14:63.
doi: 10.1186/s13047-021-00500-9

85. Munteanu SE, Scott LA, Bonanno DR, *et al*. Effectiveness of customised foot orthoses for Achilles tendinopathy: a randomised controlled trial. *Br J Sports Med*. 2015;49(15):989-94.
doi: 10.1136/bjsports-2014-093845

86. Kayll SA, Hinman RS, Bryant AL, Bennell KL, Rowe PL, Paterson KL. Do biomechanical foot-based interventions reduce patellofemoral joint loads in adults with and without patellofemoral pain or osteoarthritis? A systematic review and meta-analysis. *Br J Sports Med*. 2023; 57(13):872-881.
doi: 10.1136/bjsports-2022-106542

87. Dillon S, Burke A, Whyte EF, O'Connor S, Gore S, Moran KA. Running towards injury? A prospective investigation of factors associated with running injuries. *PLoS One*. 2023;18(8):e0288814.
doi: 10.1371/journal.pone.0288814

88. Stearne SM, Alderson JA, Green BA, Donnelly CJ, Rubenson J. Joint kinetics in rearfoot versus forefoot running: implications of switching technique. *Med Sci Sports Exerc*. 2014;46(8):1578-1587.
doi: 10.1249/mss.0000000000000254

89. James LNA, Richard WW, Christopher N, Daniel RB, Christian JB. Infographic. Running myth: switching to a non-rearfoot strike reduces injury risk and improves running economy. *Br J Sports Med*. 2021;55(3):175.
doi: 10.1136/bjsports-2020-102262

90. Chhikara K, Sidhu SS, Gupta S, Saharawat S, Kataria C, Chanda A. Development and effectiveness testing of a novel 3d-printed multi-material orthosis in nurses with plantar foot pain. *Prosthesis*. 2023;5(1):73-87.
doi: 10.3390/prosthesis5010006

91. Rodrigues P, Chang R, TenBroek T, Hamill J. Medially posted insoles consistently influence foot pronation in runners with and without anterior knee pain. *Gait Posture*. 2013;37(4):526-531.
doi: 10.1016/j.gaitpost.2012.09.027

92. Willwacher S, Weir G. The future of footwear biomechanics research. 2023;15(2):145-154.
doi: 10.1080/19424280.2023.2199011

93. Kathryn M, Peter B, Andrew RC, Thomas GM, Bill V. Foot orthoses and gait: a systematic review and meta-analysis of literature pertaining to potential mechanisms. *Br J Sports Med*. 2010;44(14):1035.
doi: 10.1136/bjsm.2009.066977

94. News. S. *Adidas Combines Two Next-Gen Innovations With The 4DFWD STRUNG*. https://sneakernews.com/2024/07/04/adidas-4dfwd-strung-id8893-release-date/. Accessed March 21, 2025.

95. Asics. *Asics and Dassault System to Offer On-Demand Insoles Personalized for Individual Foot Shape*. https://corp.asics.com/en/press/article/2024-07-25. Accessed March 12, 2025.

96. On AG. Swiss Sportswear Brand On Unveils LightSpray™: a new High Performance Upper technology crafted by a Revolutionary single step Manufacturing Process. Accessed August 12, 2025. https://press.on-running.com/swiss-sportswear-brand-on-unveils-lightspray-a-new-high-performance-upper-technology-crafted-by-a-revolutionary-single-step-manufacturing-process-rvo865

97. Binelli MR, van Dommelen R, Nagel Y, *et al*. Digital manufacturing of personalised footwear with embedded sensors. *Sci Rep*. 2023;13(1):1962. doi: 10.1038/s41598-023-29261-0

98. Kim H-G, Hajra S, Lee H, Kim N, Kim HJ. Additively manufactured mechanical metamaterial-based pressure sensor with tunable sensing properties for stance and motion analysis. *Adv Eng Mater*. 2023;25(14):2201499. doi: 10.1002/adem.202201499

99. Hébert-Losier K, Pamment M. Advancements in running shoe technology and their effects on running economy and performance – a current concepts overview. *Sports Biomech*. 2023;22(3):335-350. doi: 10.1080/14763141.2022.2110512

100. Nigg BM, Cigoja S, Nigg SR. Effects of running shoe construction on performance in long distance running. *Footwear Sci*. 2020;12(3):133-138. doi: 10.1080/19424280.2020.1778799

101. Hoogkamer W, Kipp S, Kram R. The biomechanics of competitive male runners in three marathon racing shoes: a randomized crossover study. *Sports Med*. 2019;49(1):133-143. doi: 10.1007/s40279-018-1024-z

102. Foster C, Lucia A. Running economy. *Sports Med*. 2007;37(4):316-319. doi: 10.2165/00007256-200737040-00011

103. Barnes KR, Kilding AE. Running economy: measurement, norms, and determining factors. *Sports Med Open*. 2015;1(1):8. doi: 10.1186/s40798-015-0007-y

104. Hoogkamer W, Kipp S, Frank JH, Farina EM, Luo G, Kram R. A comparison of the energetic cost of running in marathon racing shoes. *Sports Med*. 2018;48(4):1009-1019. doi: 10.1007/s40279-017-0811-2

105. Grunewald SJ. Under Armour Unveils a New 3D Printed Training Shoe Designed with Autodesk Software. *3Dprint.com*. Accessed March 12, 2025 https://3dprint.com/123064/under-armour-3d-printed-shoe/

106. On. *Cloudmonster Hyper*. https://press.on-running.com/cloudmonster-hyper. Accessed 2025.

107. Fletcher JR, MacIntosh BR. Running economy from a muscle energetics perspective. *Front Physiol*. 2017;8:433. doi: 10.3389/fphys.2017.00433

108. McLeod AR, Bruening D, Johnson AW, Ward J, Hunter I. Improving running economy through altered shoe bending stiffness across speeds. *Footwear Sci*. 2020;12(2):79-89. doi: 10.1080/19424280.2020.1734870

109. Adidas. *Futurecraft 4D Running Shoe*. https://www.adidas.com/us/futurecraft-4d. Accessed March 12, 2025.

110. Avery S. *Decathlon Unveils New Sports Shoe in Collaboration with HP and Lonati*. https://www.3dnatives.com/en/decathlon-new-sports-shoe-1506234/. Accessed March 12, 2025.

111. Worobets J, Wannop JW. Influence of basketball shoe mass, outsole traction, and forefoot bending stiffness on three athletic movements. *Sports Biomech*. 2015;14(3):351-360. doi: 10.1080/14763141.2015.1084031

112. Nike. *The Future of 3D*. https://www.nike.com/launch/t/vaporfly-elite-flyprint-future-3d. Accessed March 21, 2025.

113. Ibrahim S, Djurtoft C, Mellor R, Thorborg K, Lysdal FG. The effectiveness of customised 3D-printed insoles on perceived pain, comfort, and completion time among frequent Park Runners: study protocol for a pragmatic randomised controlled trial (The ZOLES RCT). *Foot*. 2024;58:102068. doi: 10.1016/j.foot.2024.102068

114. P. M. ASICS works with Dassault Systems on 3D printed shoes. *3Dnatives*. Accessed June 12, 2025 https://www.3dnatives.com/en/asics-works-with-dassault-systems-on-3d-printed-shoes-310720244/

115. Li J, Yang Z, Rai S, *et al*. Effect of insoles treatment on school-age children with symptomatic flexible flatfoot: a 2-year follow-up study. *Indian J Orthop*. 2022;56(11):1985-1991. doi: 10.1007/s43465-022-00698-1

116. Frykberg RG, Lavery LA, Pham H, Harvey C, Harkless L, Veves A. Role of neuropathy and high foot pressures in diabetic foot ulceration. *Diabetes Care*. 1998;21(10):1714-1719. doi: 10.2337/diacare.21.10.1714

117. Alshawabka AZ, Liu A, Tyson SF, Jones RK. The use of a lateral wedge insole to reduce knee loading when ascending and descending stairs in medial knee osteoarthritis patients. *Clin Biomech*. 2014;29(6):650-656. doi: 10.1016/j.clinbiomech.2014.04.011

118. Wang B, Sun Y, Guo X, *et al*. The efficacy of 3D personalized insoles in moderate adolescent idiopathic scoliosis: a randomized controlled trial. *BMC Musculoskelet Disord*. 2022;23(1):983. doi: 10.1186/s12891-022-05952-z

119. Wang K, Lu C, Ye R, *et al*. Research and development of 3D printing orthotic insoles and preliminary treatment of leg length discrepancy patients. *Technol Health Care*. 2020;28(6):615-624. doi: 10.3233/THC-202170

120. Tirtashi FH, Eslami M, Taghipour M. Effect of shoe insole on the dynamics of lower extremities in individuals with leg length discrepancy during walking. *J Bodyw Mov Ther*. 2022;31:51-56. doi: 10.1016/j.jbmt.2022.03.006

121. Chatzistergos PE, Gatt A, Formosa C, Farrugia K, Chockalingam N. Optimised cushioning in diabetic

footwear can significantly enhance their capacity to reduce plantar pressure. *Gait Posture*. 2020;79:244-250. doi: 10.1016/j.gaitpost.2020.05.009

122. Chen RK, Jin Y-a, Wensman J, Shih A. Additive manufacturing of custom orthoses and prostheses—a review. *Addit Manuf*. 2016;12(Part A):77-89. doi: 10.1016/j.addma.2016.04.002

123. Silva R, Veloso A, Alves N, Fernandes C, Morouço P. A review of additive manufacturing studies for producing customized ankle–foot orthoses. *Bioengineering*. 2022;9(6):249. doi: 10.3390/bioengineering9060249

124. Teixeira R, Coelho C, Oliveira J, *et al*. Towards customized footwear with improved comfort. *Materials*. 2021;14(7):1738. doi: 10.3390/ma14071738

125. Cheng A. How Adidas Plans To Bring 3D Printing To The Masses. Forbes. https://www.forbes.com/sites/andriacheng/2018/05/22/with-adidas-3d-printing-may- finally-see-its-mass-retail-potential/

126. Boër CR, Dulio S. *Mass Customization and Footwear*. London, UK: Springer; 2007.

127. Yildiz K, Medetalibeyoglu F, Kaymaz I, Ulusoy GR. Triad of foot deformities and its conservative treatment: with a 3D customized insole. *Proc Inst Mech Eng H J Eng Med*. 2021;235(7):780-791. doi: 10.1177/09544119211006528

128. Lin K-W, Chou L-W, Su Y-T, Wei S-H, Chen C-S. Biomechanical effect of 3D-printed foot orthoses in patients with knee osteoarthritis. *Appl Sci*. 2021;11(9):4200. doi: 10.3390/app11094200

129. Cha YH, Lee KH, Ryu HJ, *et al*. Ankle-foot orthosis made by 3D printing technique and automated design software. *Appl Bionics Biomech*. 2017;2017(1):9610468. doi: 10.1155/2017/9610468

130. Zheng XY, Lee H, Weisgraber TH, *et al*. Ultralight, ultrastiff mechanical metamaterials. *Science*. 2014;344(6190):1373-1377. doi: 10.1126/science.1252291

131. Schrank ES, Stanhope SJ. Dimensional accuracy of ankle–foot orthoses constructed by rapid customization and manufacturing framework. *J Rehabil Res Dev*. 2011;48(1):31-42. doi: 10.1682/jrrd.2009.12.0195

132. Telfer S, Pallari J, Munguia J, Dalgarno K, McGeough M, Woodburn J. Embracing additive manufacture: implications for foot and ankle orthosis design. *BMC Musculoskelet Disord*. 2012;13(1):1-9. doi: 10.1186/1471-2474-13-84

133. Son J-h, Kim H, Choi Y, Lee H. 3D printed energy devices: generation, conversion, and storage. *Microsyst Nanoeng*. 2024;10(1):93. doi: 10.1038/s41378-024-00708-2

134. Li J, Shu W, Yang Y, Yan R. Parametric modeling and performance analysis of a personalized insole based on 3D scanning and selective laser sintering. *Int J Comput Integr Manuf*. 2020;33(9):936-945. doi: 10.1080/0951192X.2020.1815849

135. Pallari J, Dalgarno K, Munguia J, *et al*. Design and additive fabrication of foot and ankle–foot orthoses. *21st Annual International Solid Freeform Fabrication Symposium — An Additive Manufacturing Conference*, SFF 2010; 2010

136. Pagac M, Hajnys J, Ma Q-P, *et al*. A review of vat photopolymerization technology: materials, applications, challenges, and future trends of 3D printing. *Polymers*. 2021;13(4):598. doi: 10.3390/polym13040598

137. Shaulian H, Gefen A, Biton H, Wolf A. Graded stiffness offloading insoles better redistribute heel plantar pressure to protect the diabetic neuropathic foot. *Gait Posture*. 2023;101:28-34. doi: 10.1016/j.gaitpost.2023.01.013

138. Zastrow M. 3D printing gets bigger, faster and stronger. *Nature News Feature*. doi: 10.1038/d41586-020-00271-6. Accessed April 25, 2025.

139. Corcoran-tadd F, Arias C, Perilla AN, Padovani M, inventors; Google Patents, assignee. Footwear with 3-D Printed Midsole. United States Patent 11,786,008. 2023.

140. Chris. 'Next-Generation Flyknit' — revolutionary all-new nike flyprint technology revealed. *Footy Headline*. https://www.footyheadlines.com/2018/04/revolutionary-all-new-nike-flyprint.html. Accessed March 31, 2025.

141. Raise3D. *3D-Printed Shoe Uppers: Efficient Small Batch Manufacturing and Improved Prototyping*. https://www.raise3d.com/case/3d-printed-shoe-uppers-efficient-small-batch-manufacturing-and-improved-prototyping/. Accessed June 12, 2025.

142. Hargovan SM, Bewza EL, Lawson CM, *et al*, inventors; Google Patents, assignee. Generating of 3D-printed custom wearables. United States Patent 10,564,628. 2020.

143. Iacob MC, Popescu D, Petcu D, Marinescu R. Assessment of the flexural fatigue performance of 3D-printed foot orthoses made from different thermoplastic polyurethanes. *Appl Sci*. 2023;13(22):12149. doi: 10.3390/app132212149

144. LuxCreo. *Footwear Manufacturing Industry Analysis: Evaluating the Impact of 3D Printing*. https://luxcreo.com/footwear-manufacturing-industry-analysis-evaluating-the-impact-of-3d-printing-lc/?utm_source=chatgpt.com. Accessed June 12, 2025.

145. Xu R, Wang Z, Ren Z, *et al*. Comparative study of the effects of customized 3D printed insole and prefabricated insole on plantar pressure and comfort in patients with symptomatic flatfoot. *Med Sci Monit Int Med J Exp Clin Res*. 2019;25:3510. doi: 10.12659/MSM.916975

146. Chen T, Tian M, Wang X. A Novel Porous Structural Design of the Orthotic Insole for Diabetic Foot. *International Conference on Computer, Control and Robotics (ICCCR)*. 2021:188-192

147. Fu JC-M, Chen Y-J, Li C-F, Hsiao Y-H, Chen C-H. The effect of three dimensional printing hinged ankle foot orthosis for equinovarus control in stroke patients. *Clin Biomech*. 2022;94:105622.
doi: 10.1016/j.clinbiomech.2022.105622

148. Ntagios M, Dahiya R. 3d printed soft and flexible insole with intrinsic pressure sensing capability. *IEEE Sens J*. 2022; 23(20):23995–24003.
doi: 10.1109/JSEN.2022.3179233

149. Hoeffner S. 3D printing of foot orthoses: clinical feasibility and cost-benefit analyses. *Lower Extremity Review*. https://lermagazine.com/cover_story/3d-printing-of-foot-orthoses-clinical-feasibility-and-cost-benefit-analyses. Accessed June 12, 2025.

150. Kantaros A, Drosos C, Papoutsidakis M, Pallis E, Ganetsos T. The role of 3D printing in advancing automated manufacturing systems: opportunities and challenges. *Automation*. 2025;6(2):21.
doi: 10.3390/automation6020021

151. Cui TZ, Raji RK, Han JL, Chen Y. Application of 3D printing technology in footwear design and manufacture—a review of developing trends. *Text Leather Rev*. 2024; 7:1304-1321.
doi: 10.31881/TLR.2024.151

ACCSCIENCE PUBLISHING

International Journal of Bioprinting

REVIEW ARTICLE

From cells to organs: Technical challenges of two-photon polymerization in biomedical engineering

Yanzhe Fu[1,2,3,4,5†], Mingming Huang[6†], Jiayong Wei[7], Xiang Ding[5], Bosong Yu[8], Jiebo Li[1,2,3,4,*], Jianmin Han[9*], Lizhen Wang[1,2,3,4*], and Yubo Fan[1,2,3,4*]

[1]Key Laboratory of Biomechanics and Mechanobiology, Ministry of Education, Beihang University, Beijing, China

[2]Key Laboratory of Innovation and Transformation of Advanced Medical Devices, Ministry of Industry and Information Technology, Beihang University, Beijing, China

[3]National Medical Innovation Platform for Industry–Education Integration in Advanced Medical Devices, Beihang University, Beijing, China

[4]School of Biological Science and Medical Engineering, Beihang University, Beijing, China

[5]Center for Medical Metrology, National Institute of Metrology, Beijing, China

[6]Department of Dental Materials, Peking University School and Hospital of Stomatology, Beijing, China

[7]Industrial Science and Engineering Technology Laboratory, Hangzhou International Innovation Institute, Beihang University, Hangzhou, Zhejiang, China

[8]School of Instrumentation and Optoelectronic Engineering, Beihang University, Beijing, China

[9]Department of Prosthetics, Tianjin Medical University School and Hospital of Stomatology, Tianjin, China

[10]Tianjin Key Laboratory of Oral Soft and Hard Tissues Restoration and Regeneration, Tianjin, China

(This article belongs to the *Special Issue*: *Three-Dimensional (3D) Bioprinting for Tissue Engineering and Food Printing*)

Abstract

Nanomanufacturing technology is crucial in advancing sophisticated biomedical devices, biochips, tissue engineering, and advanced biomedical materials. Two-photon polymerization (TPP) offers nanoscale fabrication precision, eliminates the need for masks, and allows the creation of arbitrary three-dimensional structures, providing technical advantages unparalleled by traditional methods. Applying TPP technology in the biomedical field presents new challenges related to materials and systems. Although there has been significant discussion regarding biomaterials, comparatively little attention has been given to the limitations of manufacturing systems for biomedical functional devices. Commercial TPP systems predominantly rely on point-by-point scanning for fabrication, which leads to low throughput. From a biomedical perspective, the goal is to achieve manufacturing precision at the single-cell level while scaling production throughput to the organ level. Advancements in precision and throughput are critical to expanding the applications of TPP in biomedical engineering. This review introduces the fundamental principles of TPP and summarizes recent advancements in TPP applications within tissue engineering, medical devices, and microfluidics. It then delves into the technological progress of TPP in recent years, focusing on aspects such as system design, manufacturing processes, and fabrication principles. The review highlights advancements in areas including the kinetics of light–matter interactions and the development of

[†]These authors contributed equally to this work.

***Corresponding authors:**
Jiebo Li (jiebo39@buaa.edu.cn)

Jianmin Han (hanjm@tmu.edu.cn)

Lizhen Wang (lizhenwang@buaa.edu.cn)

Yubo Fan (yubofan@buaa.edu.cn)

Citation: Fu Y, Huang M, Wei J, *et al.* From cells to organs: Technical challenges of two-photon polymerization in biomedical engineering. *Int J Bioprint*. 2025;11(5):122-153. doi: 10.36922/IJB025280281

Received: July 11, 2025
Revised: August 5, 2025
Accepted: August 13, 2025
Published online: August 20, 2025

Copyright: © 2025 Author(s). This is an Open Access article distributed under the terms of the Creative Commons Attribution License, permitting distribution, and reproduction in any medium, provided the original work is properly cited.

Publisher's Note: AccScience Publishing remains neutral with regard to jurisdictional claims in published maps and institutional affiliations.

cutting-edge techniques such as spatiotemporal focusing. Finally, it discusses future development directions of TPP technology in biomedical applications.

Keywords: Biomedical functional devices; Kinetics; Spatiotemporal focusing; Tissue engineering; Two-photon polymerization

1. Introduction

High-precision manufacturing technology plays a vital role in advancing the biomedical field. Fabricating structures at the micro- and nanoscale facilitates the analysis of interactions between cells and their environment at the single-cell level, enhancing our understanding of various physiological processes under microenvironmental influences.[1] Moreover, developing micro and nanoscale implantable medical devices can minimize trauma to patients, enable more precise imaging and treatment targeting specific disease sites, and improve patient compliance.[2] Additionally, by mimicking the structure of biological tissues and analyzing the macroscopic property changes induced by microstructures, these technologies advance the development of biomimetic materials.[3]

Contemporary micro- and nano-manufacturing technologies include ultraviolet lithography, electron beam lithography, nanoimprint lithography, projection micro stereolithography, and laser direct writing. While ultraviolet and electron beam lithography offer high precision, they face challenges in crafting complex three-dimensional (3D) structures. Nanoimprint lithography excels in precision and efficiency but requires specific molds, which limits its adaptability to unique scenarios. Projection micro stereolithography achieves micrometer-scale precision in 3D structure fabrication, but it has yet to achieve single-cell precision, particularly in hydrogels. Laser direct writing, which requires minimal environmental control, does not need masks, and can create 3D structures, possesses an irreplaceable advantage in fabricating specialized micro and nanoscale structures.

Laser direct writing based on linear absorption can achieve sub-micron precision, yet it is restricted by the diffraction limit, which makes manufacturing features smaller than the wavelength challenging. Two-photon polymerization (TPP), utilizing the nonlinear absorption of materials with femtosecond lasers, can overcome the diffraction limit and significantly enhance structural precision.[4] However, as precision increases, the efficiency of this technique decreases significantly, thereby limiting its further development in the biomedical field.

Numerous excellent reviews have delved into TPP bioprinting, exploring domains including polymers, biodegradable materials, and hydrogels.[5–7] In addition to material-focused discussions, technological advancements play a crucial role in driving the biomedical applications of TPP. This review is prompted by the demand for biomedical applications and aims to provide a comprehensive discussion on the development trends of TPP. As shown in Figure 1, this paper explores TPP, explaining its fundamental principles and outlining its current applications in biomedical engineering, particularly in tissue engineering scaffolds, medical devices, and microfluidic chips. It analyzes the limitations of current mainstream techniques for enhancing the efficiency and precision of TPP and concludes by summarizing the technological advancements and forecasting future trends and potential applications.

2. The principle of two-photon polymerization

TPP is a 3D micro/nano-fabrication technique that employs a femtosecond laser. Femtosecond laser pulses possess an ultrashort duration, on the order of femtoseconds (1 fs = 10^{-15} s), allowing for extremely high peak powers at equivalent average power compared to a continuous laser. The high peak power enables a wide range of physical and chemical processes during material interactions. The nonlinear interactions between femtosecond lasers and materials facilitate the ultra-precise manufacturing of challenging materials and complex micro/nano structures.

In conventional photopolymerization, a single photon absorbed by a dye, initiator, or photosensitizer generates free radicals or cations, thereby triggering monomer polymerization. Conversely, TPP requires simultaneous absorption of two photons to induce the polymerization reaction. The single-photon absorption cross-section is around $\sigma_1=10^{-18}\sim10^{-17}$ cm^2, whereas the two-photon absorption cross-section is approximately $\sigma_2=10^{-50}\sim10^{-46}$ cm^4, indicating that polymerization can occur solely in regions with sufficiently high light intensity.[8] Figure 2A illustrates the single-photon absorption process, in which fluorescence is excited throughout the dye region. In contrast, the two-photon absorption process confines fluorescence signals to the laser focus, where the photon density is sufficiently high. This selective excitation of

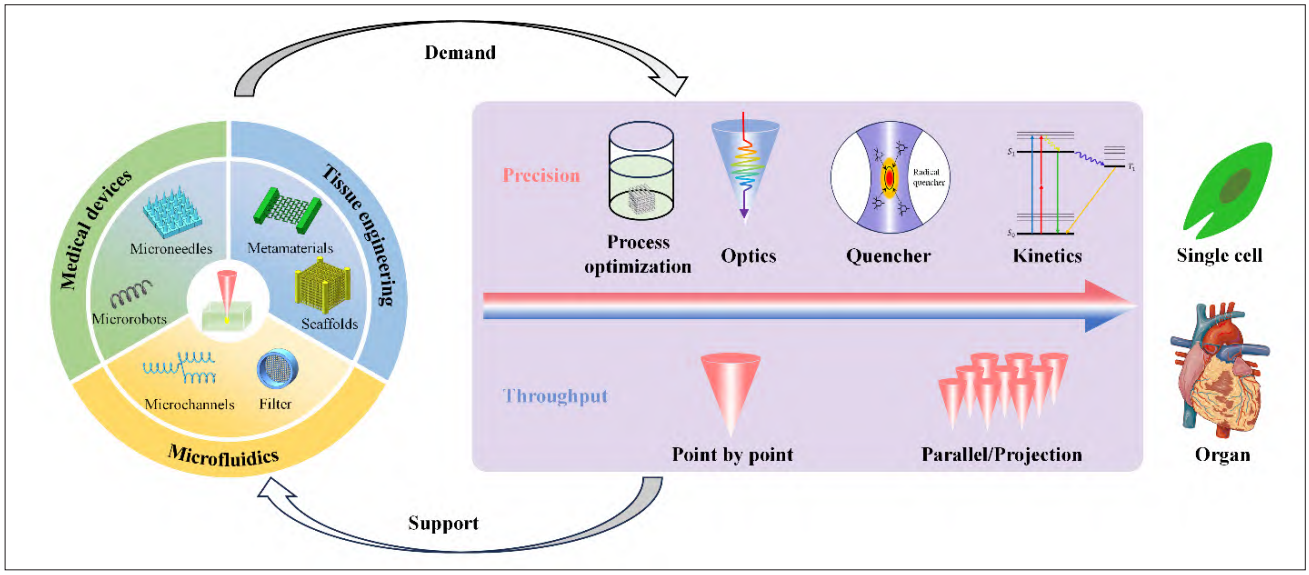


Figure 1. The relationship between biomedical applications and the evolutionary trends of two-photon polymerization. The heart image was adapted from Servier Medical Art.

chemical reactions via two-photon absorption within a transparent medium enables the fabrication of authentic 3D structures. The interaction between light and matter during 3D printing is illustrated in Figure 2B.[9] In the ground-state initiator molecule (S_0), electrons in the highest occupied molecular orbital typically exist as a pair with opposite spins. Upon photon absorption, one of these electrons acquires energy and transitions to the lowest unoccupied molecular orbital, forming an excited singlet state (S_1). Variations in the power of femtosecond laser pulses and photoresist systems yield distinct nonlinear interactions.[10,11] The excited initiator molecules may return to S_0 via spontaneous or stimulated fluorescence, undergo excited-state absorption to higher energy levels,

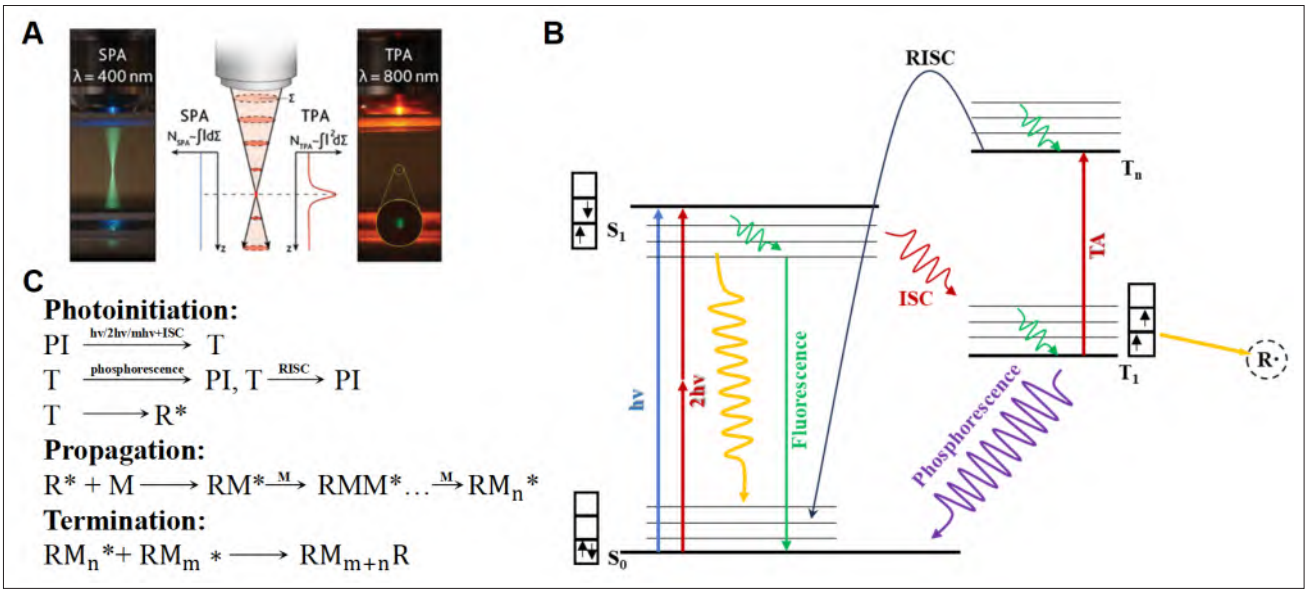


Figure 2. Schematic illustration of the principle of TPP. (A) The differences between SPA and TPA. Adapted with permission from ref.[12] Copyright © 2025 Wiley. (B) Energy level diagram of light–matter interaction during the three-dimensional printing process. (C) The process of the TPP reaction, where PI is the photoinitiator, RM is the monomer radical, *M* is a monomer, and M_n is a polymeric chain of *n* monomers. Abbreviations: ISC, intersystem crossing; RISC, reverse intersystem crossing; SPA, single-photon absorption; TPP, two-photon polymerization; TPA, two-photon absorption.

or transition to a triplet state (T_1) through intersystem crossing (ISC). During the ISC from S_1 to T_1, the spin of the excited electron undergoes inversion. This spin inversion leads to the excited electron's spin aligning parallel to its paired ground-state electron, yielding a parallel spin configuration. Molecules in the triplet state can return to the ground state through phosphorescence, undergo triplet-state absorption to higher energy levels followed by reverse ISC, or directly generate free radicals (R*). Furthermore, triplet-state absorption may result in the formation of higher-level free radicals.

The TPP process consists of three primary steps: chain initiation, chain growth, and chain termination, as illustrated in Figure 2C. Photoinitiator molecules in the ground state (PI) within the photoresist generate free radicals (R*) through a series of dynamic processes. These free radicals then react with monomers or oligomers (M), resulting in monomer radicals (RM*). These radicals propagate via a chain reaction to form (RMn*). The chain reaction is terminated when two monomer radicals meet.

In 1997, Maruo *et al.*[13] pioneered the application of TPP for the fabrication of 3D structures, successfully creating helical architectures in three dimensions.[13] In 2001, the research team employed a femtosecond laser to fabricate a "micro-bull" measuring 10 μm in length and 7 μm in height, thereby establishing a seminal milestone within the domain of TPP. This work represented a groundbreaking advancement by surpassing the optical diffraction limit, achieving a processing resolution of 120 nm, significantly exceeding the diffraction limit of 460 nm, thereby indicating the progressive maturation of TPP.[4]

3. The application of two-photon polymerization in biomedical engineering

TPP provides new possibilities for biomedical engineering research and applications, including tissue engineering, medical devices, and biochips. In biomedical applications, the biocompatibility of materials must also be taken into consideration. Commonly used photoinitiators are typically lipophilic, whereas biocompatible materials such as hydrogels require water-soluble photoinitiators, posing significant challenges for the application of TPP. Some of these aspects have been addressed in previous reviews[5] and will not be elaborated further in this paper.

3.1. Tissue engineering

In 1993, Robert Langer[14] defined tissue engineering as a modern science that is an interdisciplinary field that applies the principles of life sciences and engineering to the development of biological substitutes that restore, maintain, or improve tissue function.[14]. In the past 30 years, tissue engineering has achieved rapid progress. It plays a significant role in healing bone and cartilage defects, skin burns, nervous system injuries, corneal replacement, and cosmetic surgery. Tissue engineering technology generates the organization by adding suitable cells and materials to specific scaffolds. Most cells other than blood cells exist within the extracellular matrix (ECM). Ideally, for a specific organization, the best 3D scaffolds are its original ECM. However, the native ECM has diverse functions, complex compositions, and dynamic changes; to build such an environment *in vitro* is extremely challenging.[15] When fabricating scaffolds, even if the functions of ECM cannot be completely mimicked, it is necessary to mimic the functions of ECM, including good biocompatibility, bioactivity, and mechanical properties. The ideal 3D scaffold should possess a porous structure, network connection, and uniform pore size to facilitate cell migration and invasion.

At present, various techniques have been used to fabricate tissue engineering scaffolds, such as spinning,[16] thermally induced phase separation,[17] solvent casting/particle leaching,[18] and membrane laminating.[19] However, these techniques fail to precisely control the structure, pore size, and network of scaffolds. With the advent of 3D printing, it has become possible to fabricate scaffolds with controllable structures and sizes.[20] Compared to other methods, optical printing not only has higher precision, but can also be applied to different materials, including polymers, metals, and ceramics, and can meet the requirements of different application scenarios, which has been widely concerned. Currently, primary optical printing methods in tissue scaffolds fabrication are TPP, stereolithography apparatus, selective laser melting, and light-curing material jetting/extrusion.[21,22] The size of a typical cell is generally within the micron range, and to ensure that interactions between cells and their microenvironment are not compromised, the scale of the scaffold structure must closely match the cell size. This necessitates manufacturing precision within the range of 0.1–10 μm. Among all the above 3D fabrication technologies, only TPP can achieve the fabricated feature size below 1 μm; therefore, TPP is of great value for tissue engineering and regenerative medicine.[20,23,24] At present, engineering scaffolds manufactured based on TPP have been used in the culture of many cell systems.

In 2007, Ovsianikov and coworkers[25] successfully created 3D scaffolds with the TPP technique using commercially available photoresist SU8 and ORMOCER®, demonstrating their ability to support cell growth.[25] In 2010, Klein *et al.*[26] utilized the 3D scaffold fabricated by TPP to analyze the stress change during cell growth, demonstrated that the beam in

contact with the cell was bent and stretched during a single contraction cycle of the cardiomyocyte, and tested its deflection (Figure 3A).[26] In 2011, this group combined TPP with composite materials to obtain two-component 3D scaffolds with distinct mechanical and protein-binding properties, achieving full control over the formation of cell adhesion sites and cell shape in three dimensions (Figure 3B).[27] In 2017, Ricci *et al.*[28] fabricated tightly packed tissue engineering scaffolds and demonstrated the culture results of human bone marrow mesenchymal stem cells with 88% surface coverage.[28] In the same year, Turunen *et al.*[29] fabricated a tubular microtower-based 3D platform featuring intraluminal guidance cues and wall openings via TPP for culturing human pluripotent stem cell-derived neuronal cells.[29] Tissue scaffolds fabricated by TPP can influence cell culture not only through structural design but also by dynamically altering the mechanical properties of the microenvironment. In 2017, Lemma *et al.*[30] exploited an innovative polymeric scaffold based on TPP, featuring cage-like structures and cylindric stent-like micro-scaffolds fabricated with varying Young's moduli and stiffness gradients. These scaffolds allowed precise control of 3D microenvironmental stiffness to study cancer cell invasiveness and analyze how external mechanical properties influence cellular behavior (Figure 3C).[30] In 2018, Tudor *et al.*[31] achieved the creation of soft, stimulus-responsive 3D structures using crosslinked poly(ionic liquid)s through TPP. These structures exhibit properties such as swelling, temperature response (known as the four-dimensional effect), and programmed movement.[31] Marino *et al.*[32] innovatively fabricated a 1:1 real-scale biomimetic and biohybrid blood–brain barrier model by TPP. The system co-cultured endothelial and glioblastoma cells on biomimetic microtubes inspired by the brain capillaries, demonstrating mature tight junctions. Combined with mathematical optimization of fluid

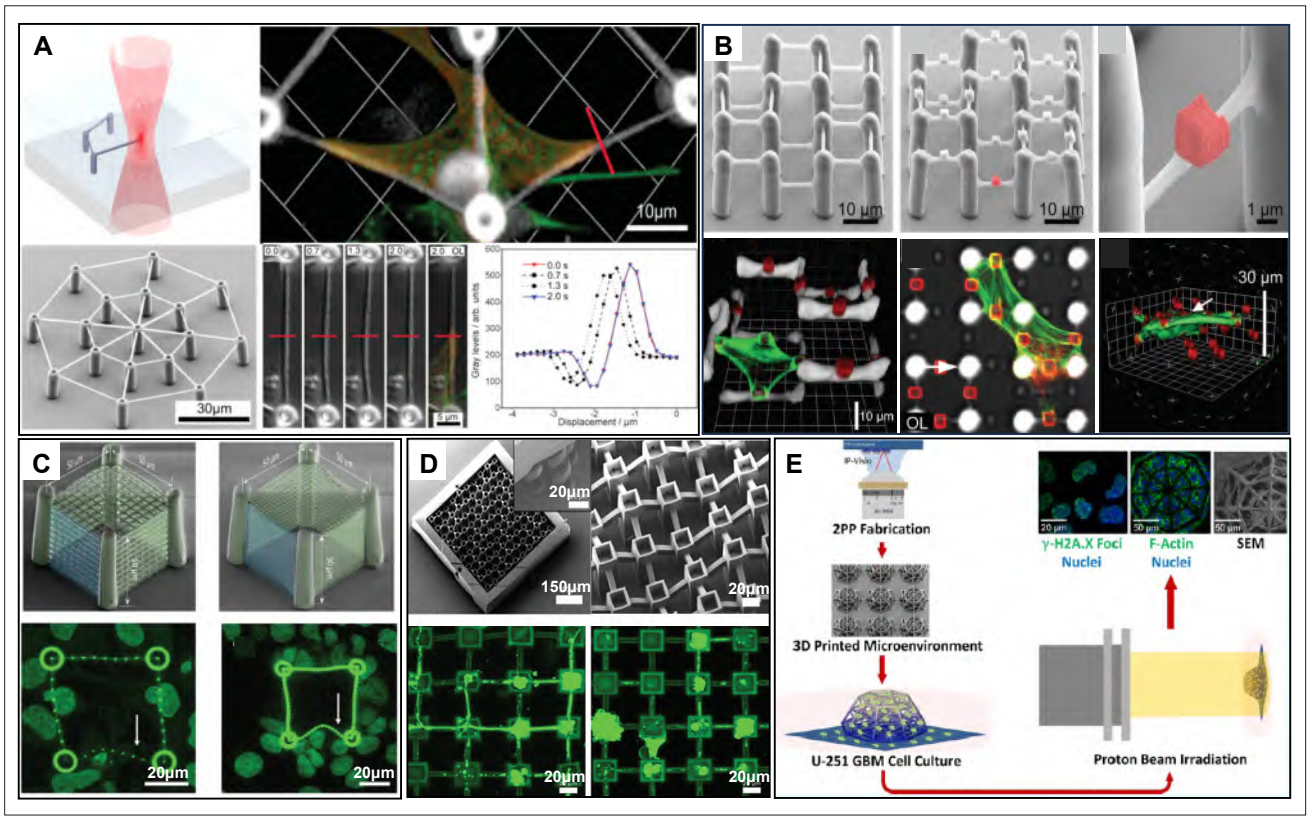


Figure 3. Tissue engineering scaffolds fabricated using two-photon polymerization. (A) Three-dimensional (3D) scaffolds utilized to analyze the stress change during a single contraction cycle of the cardiomyocyte. Scale bars: 5, 10, and 30 μm. Reproduced with permission from Klein *et al.*[26] Copyright © 2010, Wiley. (B) Two-component 3D scaffolds with distinct mechanical and protein-binding properties. Scale bars: 1, 10, and 30 μm. Reproduced with permission from Klein *et al.*[27] Copyright © 2011, Wiley. (C) 3D scaffolds with different Young's modulus and stiffness gradients to study cancer cell invasiveness. Scale bar: 20 μm. Reproduced with permission from Lemma *et al.*[30] Copyright © 2017, Wiley. (D) 3D neuronal scaffolds to culture neurons *in vitro*. Scale bars: 20 and 150 μm. Reproduced with permission from Fendler *et al.*[33] Copyright © 2019, Wiley. (E) Research on assessing the effects of proton beam therapy on 3D glioblastoma cell networks. Reproduced with permission from Akolawala *et al.*[34]

dynamics, this system offers a referenceable *in vitro* model for investigating the delivery of nanomaterial/drug across the blood–brain barrier.[32] Given that low-density neuronal cultures *in vitro* are useful for studying neurons at the cellular level, in 2019, researchers used direct laser writing via TPP to fabricate tailor-made 3D culturing substrates. These substrates consisted of pillars with different heights connected through freestanding microtubes with quadratic cross sections (Figure 3D).[33] The truly 3D neuronal networks built in the work combined site-specific chemical-guiding adhesion with topological limitation of potential neurite growth paths to determine predefined pathways as well as guidance paths for controlled axon and dendrite outgrowth. In 2022, Akolawala *et al.*[34] designed 3D scaffolds inspired by the geometry of brain blood vessels to be cultured with U-251 glioblastoma cells and assess their response to proton radiation (Figure 3E).[34] In 2022, Rengaraj *et al.*[35] combined a microscale 3D scaffold to engineer a microscale niche for pancreatic tumor cells fabricated via TPP with a bioactive layer-by-layer film coating. The functionalized scaffold successfully supported 3D tumor-like tissue culture for up to 20 days and revealed significant context-specific cell responses, confirming its potential to simulate the early microenvironment of metastasis and provide a controllable *in vitro* model to study pancreatic cancer mechanisms and drug screening.[35] In 2022, Costa *et al.*[36] optimized 3D woodpile microscaffolds from different photosensitive polymers (IP-S and SZ2080) and hydrogel (PEGDA 700) using TPP and coated them with fibronectin to investigate the behavior of bone marrow mesenchymal stem cells. These scaffolds maintained stemness and supported co-culture with HeLa cells, offering a novel biomimetic platform for modeling bone marrow niches, studying hematological disorders (e.g., leukemia), and advancing drug screening applications.[36]

Currently, tissue engineering scaffolds manufactured using TPP have been successfully applied to various cell lines, including neurons derived from human induced pluripotent stem cells, pancreatic cell lines, and bone marrow mesenchymal stem cells. In tissue engineering, the development of TPP technology has shown a trend of shifting from structure-oriented to function-oriented approaches. Early studies primarily focused on constructing precise 3D cellular microenvironments to enable passive cell growth. With continuous advancements in materials science and manufacturing technologies, current research has begun regulating cell morphology and exploring the impact of microenvironment on cellular behavior. However, during this developmental process, the throughput limitations of TPP manufacturing have constrained the ability to construct highly complex microenvironments. Additionally, beyond existing polymer materials, developing relatively soft hydrogel materials that better facilitate cell adhesion, extension, and growth imposes higher requirements on the light–matter interaction in TPP. If manufacturing throughput can be effectively improved, it could potentially extend single-cell scale regulation capabilities to organ-level applications. Notably, some parallel manufacturing technologies have already provided preliminary implementation pathways for this vision. The deep integration of micro/nano manufacturing techniques with biological 3D printing technology holds promise for catalyzing entirely new paradigms in tissue engineering manufacturing.

3.2. Medical devices

TPP has unlocked new possibilities for medical device fabrication, enabling the creation of micro and nanoscale devices that facilitate minimally invasive, precision medicine—such as microneedles, endoscopes, and micro/nano robots.

Advances in genetic engineering and proteomics technology have introduced protein- and nucleic acid-based therapies for cancer and other chronic diseases. However, many of the pharmacologic agents are not suitable for oral or transdermal use, as the liver, kidney, and other organs may metabolize them. Therefore, intravenous injection can improve drug absorption in the human body, while the traditional hypodermic needles are less suitable for extended delivery, causing pain and trauma at the injection site and requiring professional administration. Microneedles, as a minimally invasive drug delivery method, possess a needle size of 300–400 μm, which can avoid pain to the patient and reduce bruising to the injection site.[37] Hollow microneedles can enable slow release of medicine over a longer period through diffusion- or pressure-driven transport. Compared to solitary needles, arrays of microneedles can provide injection or extraction over a wider area and at higher rates. In 2007, Ovsianikov *et al.*[38] created 3D hollow microneedle arrays with complex geometries using TPP, which demonstrated the applicability of TPP on large-area fabrication of microneedles and the possibility of using TPP for portable medical devices.[38] In addition to drug delivery, microneedles also hold great promise for vaccine injection. The use of microneedles can avoid medical waste generated by traditional subcutaneous and intramuscular injections and reduce the risk of infection caused by reusing syringes.[39] In 2017, Rad *et al.*[40] combined hollow microneedles with open microfluidic channels to fabricate novel microneedle arrays for subcutaneous fluid sampling and drug delivery,

demonstrating that TPP is more flexible in fabricating micro/nano devices (Figure 4A).[40] In 2020, Balmert *et al.*[41] used TPP to produce master molds of microneedle arrays to generate dissolving undercut microneedle arrays for multicomponent cutaneous vaccination, and showed that this drug delivery technology can elicit potent antigen-specific cellular and humoral immune responses through the skin.[41]

Endoscopes can provide diagnostic images of hollow organs at high resolution to assist clinicians in diagnosing and intervening. However, commonly used endoscopes have difficulty imaging small luminal or delicate organs due to the limitations of the traditional fabrication method of endoscopes. In 2020, researchers used TPP to 3D print 125-μm-diameter micro-optics directly onto a single-mode optical fiber (Figure 4B).[42] This is by far the smallest freeform 3D imaging probe and the smallest aberration-corrected intravascular probe reported, with a diameter of 0.457 mm including the catheter sheath, and is able to image atherosclerotic human and mouse arteries.

Moreover, TPP can be applied to create micro/nanorobots for drug delivery, thrombolytic procedures, and assisted reproduction.[43,44] Unlike traditional robots, micro/nanorobots are limited by their minute size, which restricts the integration of complex computational, actuation, sensing, functional, and communication units. Instead, their motion relies predominantly on energy conversion mechanisms and interactions within their microenvironment.[45] The propulsion modes of micro/nanorobots include ultrasonic, chemical, and magnetic propulsion modes.[46–49] Among the various propulsion methods, magnetic field actuation has been extensively employed due to its non-contact operation, safety profile, and precise controllability. Poor sperm motility is one of the main causes of male infertility.[50] In 2015, Medina-Sanchez *et al.*[51] fabricated polymer microhelices using TPP with soft-magnetic nickel–titanium bilayer coatings, which

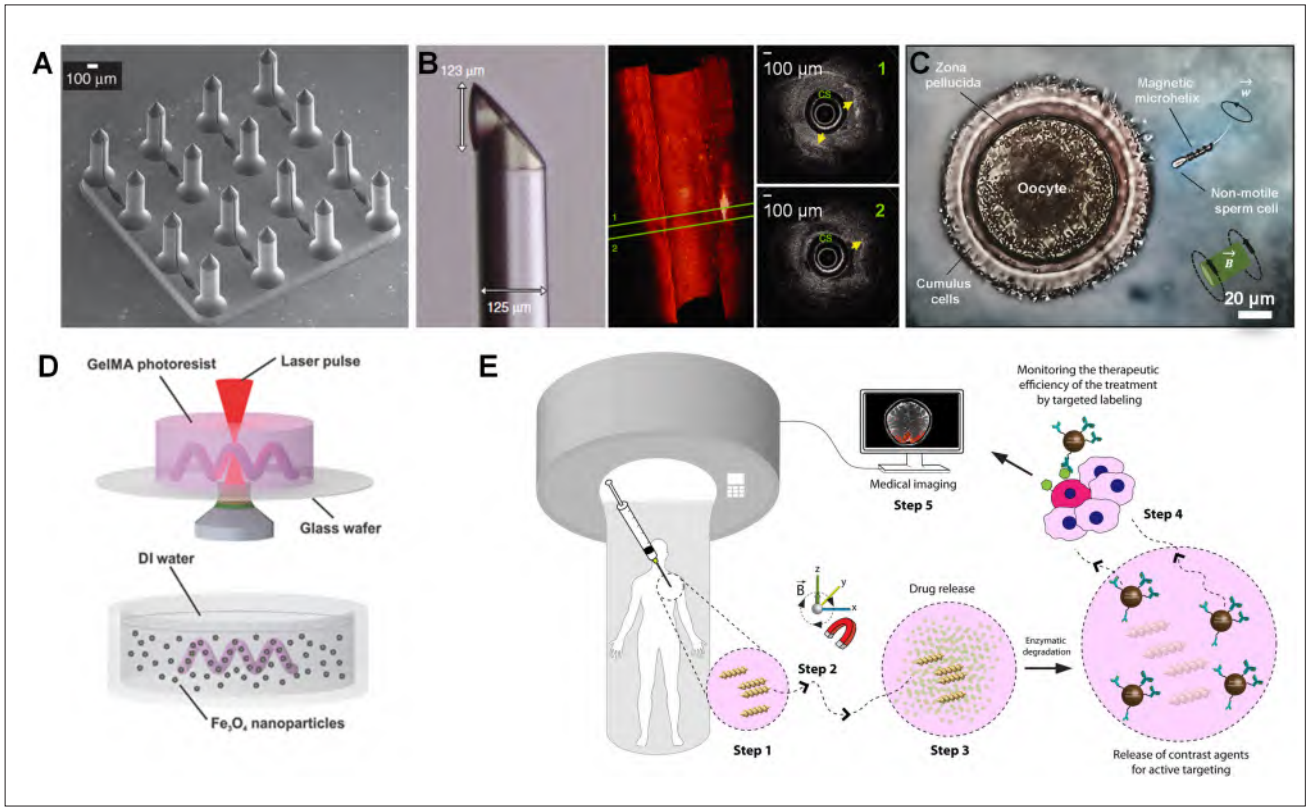


Figure 4. Implantable and interventional medical devices fabricated using two-photon polymerization. (A) Hollow microneedles with open microfluidic channels. Scale bar: 100 μm. Reproduced with permission from Rad *et al.*[40] (B) Micro-optics directly printed onto the single-mode optical fiber. Scale bars: 100 μm. Reproduced with permission from Li *et al.*[42] (C) Sperm carrying micromotors assisted fertilization. Scale bar: 20 μm. Reproduced with permission from Medina-Sanchez *et al.*[51] Copyright © 2016, American Chemical Society. (D) Enzymatically biodegradable soft helical microswimmers. Reproduced with permission from Wang *et al.*[53] Copyright © 2018, Wiley. (E) Biodegradable microswimmer for drug delivery and release. Reproduced with permission from Ceylan *et al.*[54]

showed controllable 3D motion (Figure 4C).[51] Through the rotating magnetic fields generated by Helmholtz coils, microhelices can capture, transport, and release single live sperm cells under physiological conditions. Moreover, sperm cells can be successfully delivered to the oocyte cell wall, which presents the potential of this novel technique toward assisted reproduction. In 2023, Fan *et al.*[52] developed a magnetic fiber robot with integrated terminal functionality, offering a flexible and innovative solution for integrating and assembling distal functional components. This development has considerable potential to advance the miniaturization and functional capabilities of interventional medical robots.[52] Beyond structural design, biocompatibility represents a fundamental consideration for micro/nanorobots. In 2018, Wang *et al.*[53] utilized P2CK as an initiator to fabricate biodegradable micro/nanorobots from gelatin methacryloyl-based materials (Figure 4D).[53] In 2019, Ceylan *et al.*[54] demonstrated precise drug delivery via the controlled degradation of biodegradable microrobots (Figure 4E).[54]

3.3. Microfluidics

Beyond direct fabrication of 3D microfluidic structures, TPP can be applied for the realization of microscale 3D structures printed inside the microchannels, including the nozzle, mixer, filter, and capillary pump, which can expand the diversity and flexibility of microfluidic chips.[55–57]

The number of circulating tumor cells is closely correlated with the lethal potential of the tumor. In 2019, Jiménez-Zenteno *et al.*[57] created a 3D stealthy intravascular microdevice with the aid of TPP, engineered as a hollow circular cylinder with a holey membrane at the downstream end-wall, adapted to the physical capture of circulating tumor cells in the venous blood flow *in vivo*.[57] Biosensors can be fabricated through processing micro/nanoscale 3D structures in the microchannels. In 2020, Lao *et al.*[58] exploited the tendency of delicate micro/nanostructures to collapse during solvent development due to existing capillary forces. They manufactured 3D nanogap-enabled plasmonic structures by combining supercritical drying, noble metal coating, and switchable capillary-force-driven self-assembly of TPP-fabricated micropillars.[58] The nanogap-enabled microfluidic device integrated in microchannels, together with the electromagnetic enhancement, showed great potential for surface-enhanced Raman spectroscopy sensing research. Poorly soluble drugs struggle to elicit effects through oral or parenteral administration, but using lipid nanoparticles as a carrier enabled the drugs to achieve sufficient bioavailability. Microfluidic systems can effectively control the particle size distribution and mixing scheme of nanoparticles. However, there is a risk of particle-containing fluids deposition on the surface of microchannels, which limits the repeatability and stability of long-term continuous processing during practical use. In 2021, Erfle *et al.*[59] created a coaxial lamination mixer using TPP with a unique 3D design to address challenges in the manufacturing process of drug nanoparticles, which can eliminate contact of the organic phase with the channel walls, avoid particle deposition, mix organic and aqueous phases efficiently, and reduce

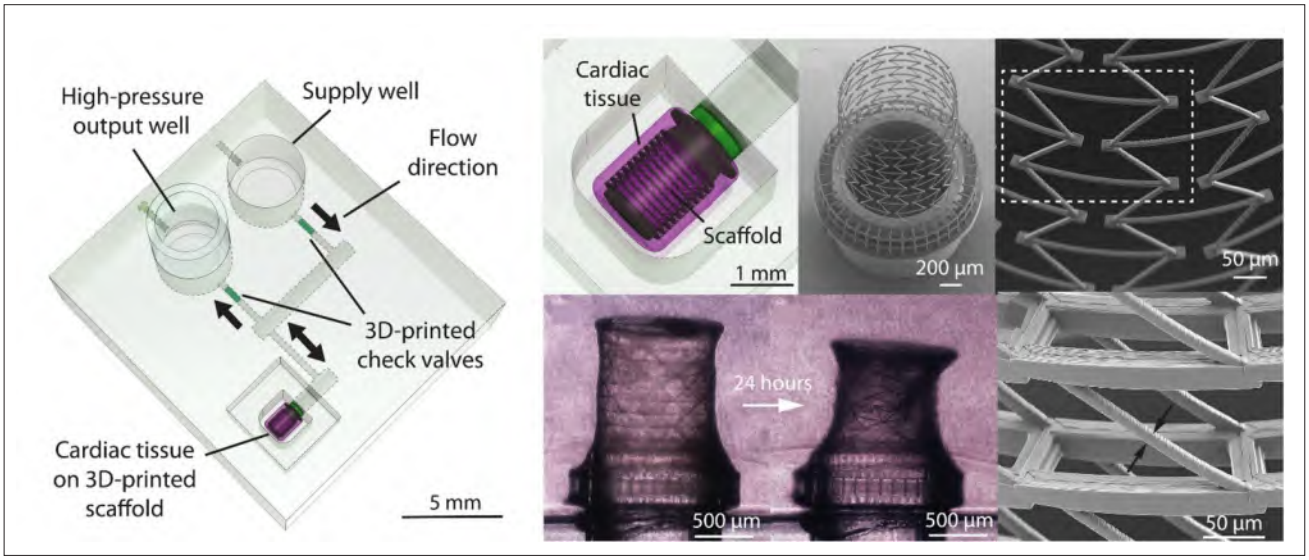


Figure 5. Heart-on-chip system via two-photon polymerization. Scale bars: 1 mm, 5 mm, 50 μm, 100 μm, and 500 μm. Reproduced with permission from Michas *et al.*[60] Copyright © 2022, AAAS Wiley. Abbreviation: 3D, three-dimensional.

fouling, proving the feasibility of this approach in high-throughput monodisperse drug carrier nanoparticles production.[59] In 2022, Michas *et al.*[60] developed a novel heart-on-chip system via TPP (Figure 5). The platform utilized a nanoscale metamaterial scaffold to guide human induced pluripotent stem cells-derived cardiomyocytes into contractile ventricular chambers, integrated with fabricated microfluidic valves for unidirectional flow, achieving the first complete pressure-volume loop *in vitro*. This work overcomes limitations in constructing functionally ordered microstructures for organ chips, providing a vital tool for cardiac biomechanics, drug screening, and disease modeling.[60]

TPP serves as a powerful tool in the biomedical field; however, its manufacturing throughput limits its further development. Precision and efficiency are mutually constrained because the size of a single voxel in TPP is approximately 200 nm, resulting in extremely low efficiency when manufacturing large-scale devices. Assuming a scanning speed of 5 mm/s, fabricating a 1 mm^2 area would take 1×10^3 s. For a 1 mm^3 area with an axial dimension of 500 nm and no voxel overlap, this process would require 2×10^6 s, or approximately 23 days. Moreover, the need to maintain the femtosecond laser in a stable working condition, regulate water content in materials, or preserve cell viability throughout this process imposes significant environmental demands. Therefore, manufacturing efficiency in TPP represents a significant limitation to its further development in the biomedical field. Furthermore, enhancing the precision of TPP could significantly facilitate the observation and study of cellular processes at the single-cell level. Optimizing TPP in terms of precision and efficiency assists in the fabrication of multiscale, hierarchically organized biological structures, which have significant implications for the biomedical field. Researchers have conducted extensive studies to improve the throughput and precision of TPP.

4. Two-photon polymerization throughput enhancement

4.1. Single-focus serial scanning

As illustrated in Figure 6, the mainstream writing methods currently include point-by-point scanning using a translation stage or piezoelectric stage, as well as scanning with a galvo mirror. Additionally, resonant mirrors combined with rapid shutters (such as Pockels cells) are also employed for scanning. During the construction of optical pathways, relay lens groups are carefully selected and configured to achieve the desired spot size and field of view. These approaches can be further categorized into raster scanning and vector scanning.[12]

Manufacturing via TPP typically employs stepper motors or piezoelectric stages to enable precise sample movement. However, due to the inherent inertia of these stages, they are restricted to scanning speeds ranging roughly from 0.1 to 30 mm/s.[61] The use of galvanometer scanners can increase these speeds to several tens or hundreds of millimeter per second; however, this is still insufficient to meet the efficiency requirements for the mass production of most devices. With the advent of novel scanning technologies, researchers have utilized commercial resonant galvanometer mirrors, achieving scanning speeds of up to 8 kHz and an extraordinary 8000

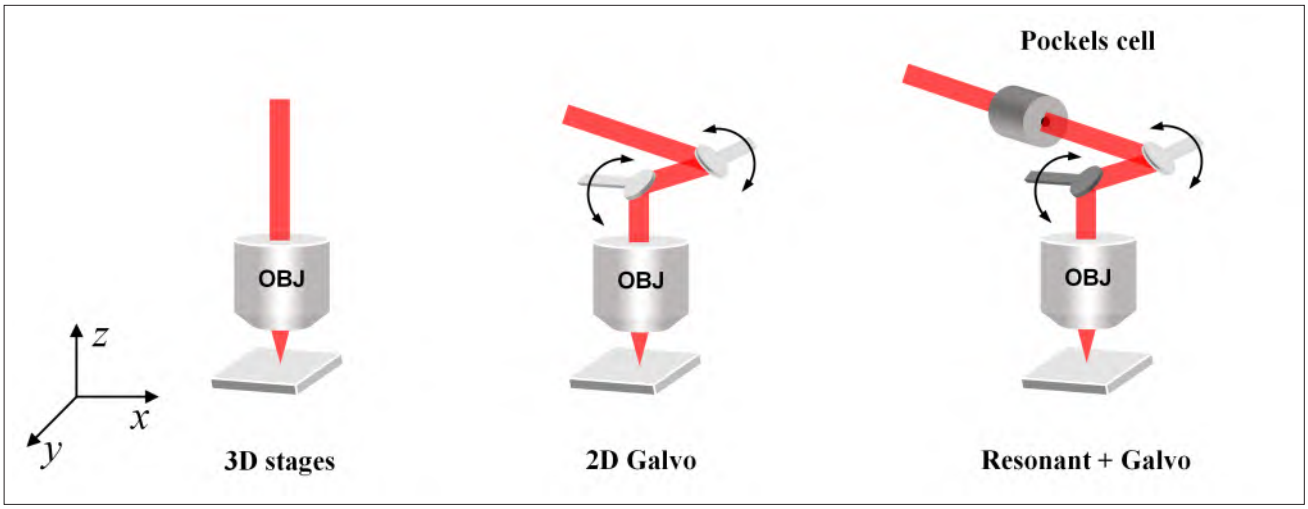


Figure 6. Common scanning methods in two-photon polymerization systems. Created by the authors with Microsoft PowerPoint. Abbreviations: 2D, two-dimensional; 3D, three-dimensional; OBJ, objective.

mm/s, representing the fastest processing throughput for serial scanning known to date.[61] Resonant mirrors, with their high-frequency operation, enable even faster scanning speeds, requiring integration with high-speed shutters to control energy modulation, thereby achieving a raster scanning effect.

4.2. Parallel fabrication

4.2.1. Static multi-foci or light field

To enhance efficiency, optical devices can be employed to generate multiple foci, enabling high-speed fabrication when combined with the scanning method described in Figure 6.

The scanning speed of serial methods is often constrained by the capabilities of scanning devices, whereas parallel devices such as micro lens array (MLA), diffractive optical elements (DOE), and meta-lens facilitate high-efficiency, multi-focus parallel processing, thereby offering the potential for significantly enhanced processing throughput.[62–65] In 2005, Kato's team[66] first introduced a parallel multi-focus printing method using MLA with 41×41 lenses in a 10×10 mm^2 area, achieving simultaneous printing of over 200 points.[66] However, combining the microlens array with a galvanometer to increase manufacturing speed inevitably resulted in aberrations from large-angle incident light.[67] In 2007, Dong *et al.*[68] utilized DOE and a galvanometer to fabricate complex 3D structures, significantly enhancing manufacturing efficiency. Nonetheless, the dispersion and pulse broadening introduced by the optical components reduced the efficiency of two-photon absorption. There is a contradictory relationship between focus size, energy, distribution uniformity, and the number of focal points—more focal points result in lower focus energy, larger laser spots, poorer uniformity, and reduced resolution in direct writing. In 2020, Hahn *et al.*[69] proposed a rapid multi-focus 3D printing method using an acousto-optic modulator instead of a shutter and employing prisms and dispersion-compensating prisms to offset pulse broadening caused by optical components, ensuring the efficiency of two-photon absorption and achieving a printing rate of over 10 million voxels per second.[69] In 2024, the team combined DOE and MLA to optimize dispersion and uniformity, achieving a manufacturing speed of over 10^8 voxels per second (Figure 7).[70]

TPP is fundamentally a photochemical process wherein the spatial distribution of light dictates the polymerization. Compared to point-by-point scanning, light field modulation techniques offer additional dimensions of control for TPP. In 2006, Ježek *et al.*[71] utilized conical lenses to generate Bessel beams, thereby achieving rapid printing of hollow cylindrical structures.[71] In 2012, researchers in Lithuania analyzed the differences among laser direct writing, vortex light, and holographic lithography for fabricating microtubes. Compared to laser direct writing, holographic lithography increased efficiency four hundredfold, and vortex light five hundredfold.[72] In 2014, the team from the University of Science and Technology of China rapidly fabricated arrays of cylindrical tubes using Fresnel lenses.[73] That same year, Zhang's research team[74] employed orbital angular momentum beams to fabricate double-helical 3D microstructures, thereby demonstrating optical chirality.[74] In addition to the advancements mentioned above, the advancement of light field modulation techniques, including Bessel beams, Airy beams, Mathieu beams, and emerging

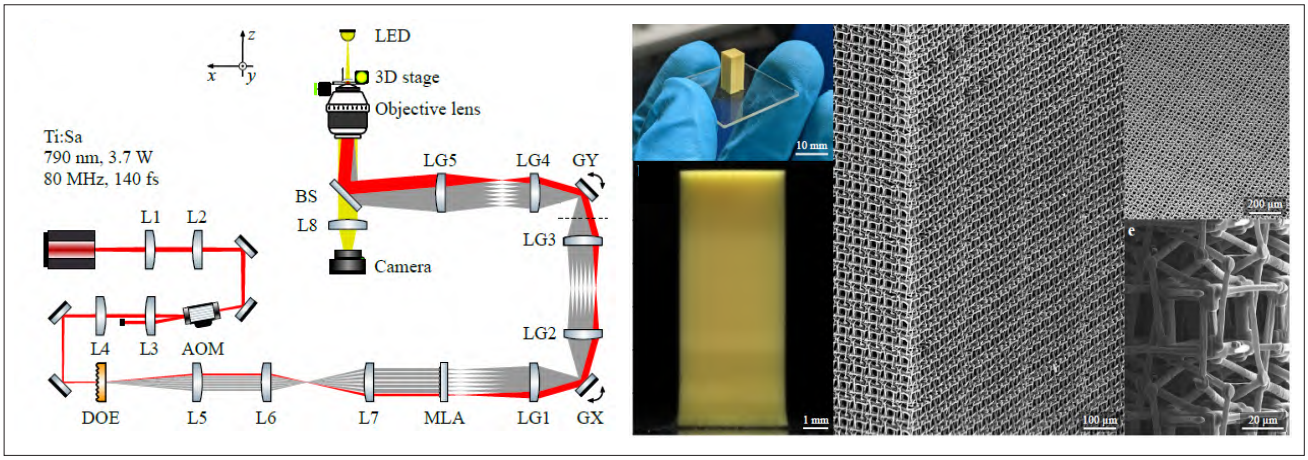


Figure 7. Multi-focal scanning based on a DOE and an MLA. Scale bars: 1 mm, 10 mm, 20 μm, and 200 μm. Reproduced with permission from Kiefer *et al.*[70] Abbreviations: 3D, three-dimensional; DOE, diffractive optical element; LED, light-emitting diode; MLA, micro lens array.

holographic technologies, has the potential to enable novel opportunities in micro-nano fabrication.[75–78]

4.2.2. Dynamic multi-foci or pattern exposure

In addition to static multi-focus, dynamic multi-focus or dynamic masking can be utilized to achieve more flexible fabrication, enabling greater versatility in structural manufacturing. The digital micromirror device (DMD) and liquid crystal spatial light modulator (LC-SLM) represent the two most widely utilized types of spatial light modulators, and Figure 8 illustrates their basic configurations within optical systems. Figure 8A illustrates the application of an LC-SLM for computational holography, Figure 8B demonstrates pattern projection through a 4-f system using a DMD, and Figure 8C illustrates binary holography with a DMD, utilizing a grating to compensate for the dispersion introduced by the DMD.

Parallel TPP based on beam-splitting devices has effectively enhanced efficiency, but still faces challenges in achieving precise control and remains confined to the production of periodic structures. SLM allows for greater flexibility in loading holograms and more precise manipulation of the light field. In 2007, Kelemen *et al.*[79] harnessed an LC-SLM to generate multiple foci, demonstrating the adaptability of programmable devices in creating multiple focal points.[79] Further optimization of the holograms improved the uniformity of the multi-foci, facilitating the fabrication of micro-nano optical devices and photonic crystal structures.[80] In 2024, Zhang's team[81] optimized focal point uniformity by suppressing zero-order spots and using a grayscale modulation strategy, reaching a peak printing rate of 1.49×10^8 voxels per second (Figure 9A).[81] Beyond generating multiple foci, different holograms loaded onto the SLM can enable scanning capabilities without requiring mechanical platform movement. In 2017, Yang *et al.*[82] introduced a fabrication strategy using non-diffractive superimposed Bessel beams. By adjusting the order of the superimposed Bessel light fields, they were able to control the number of foci generated. The complex 3D structures were fabricated by dynamically controlling the focal pattern.[82] In 2020, Manousidaki *et al.*[83] proposed a method for generating 3D holograms, which, by loading various holograms, enables the spatial movement of foci without mechanical platform motion, achieving efficiencies approximately 20 times greater than point-by-point scanning methods.[83] In 2022, Zhang *et al.*[84] successfully fabricated 3D structures through predesigned holograms integrated with lens phase modulation, eliminating the need for any movable components during the construction process (Figure 9B).[84]

DMDs function as innovative intensity control elements, offering a distinct advantage over LC-SLM. By rapidly flipping surface mirrors, they achieve binary modulation between "on" and "off" states, thus offering higher refresh rates.[85] The employment of grayscale holography has enabled efficient light field control, which is now successfully applied in areas such as beam shaping, pulse shaping, and two-photon microscopic imaging.[86–89]

In 2019, Geng *et al.*[90] developed a high-speed TPP system with multi-foci capabilities using Lee holography.

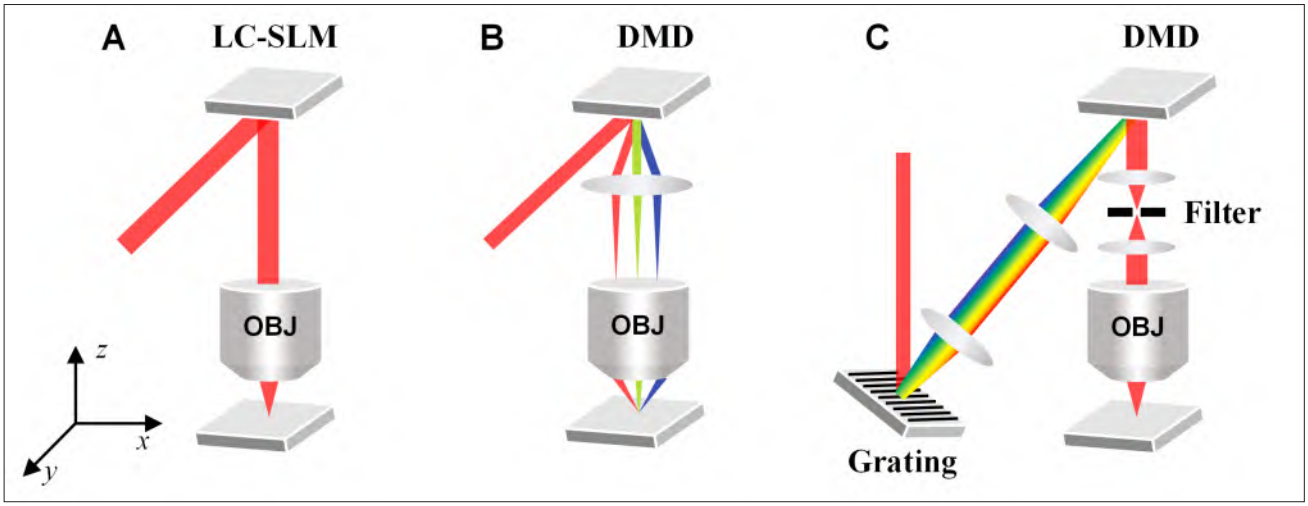


Figure 8. Dynamic modulation by spatial light modulators. (A) Computational holography utilizing LC-SLM. (B) Projection by DMD. (C) Binary holography implemented by DMD. Created by the authors with Microsoft PowerPoint. Abbreviations: DMD, digital micromirror device; LC-SLM, liquid crystal spatial light modulator; OBJ, objective.

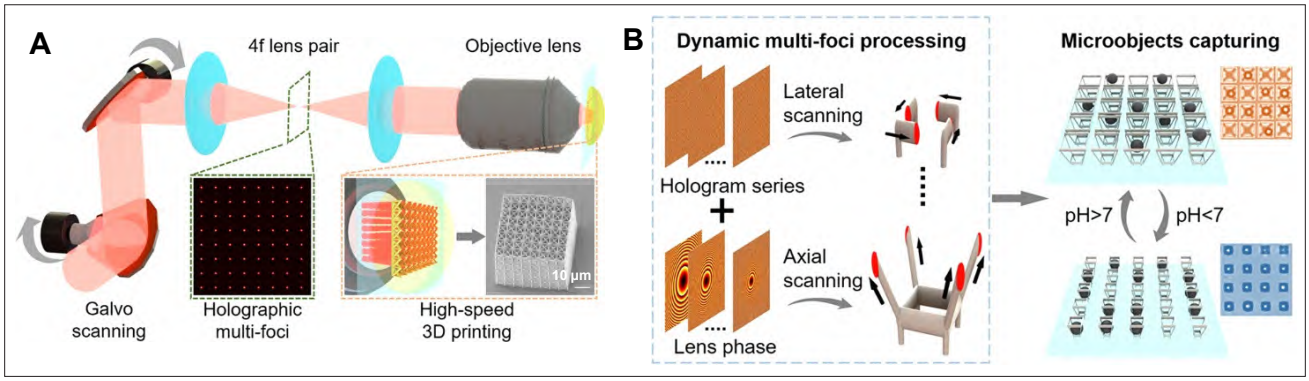


Figure 9. Multi-foci generated via spatial light modulators. (A) High-throughput two-photon polymerization enabled by holographic multi-foci high-speed scanning. Reproduced with permission from Zhang *et al.*[81] Copyright © 2024, American Chemical Society. (B) Microarchitectures fabricated by dynamic holographically shifted femtosecond multi-foci. Reproduced with permission from Zhang *et al.*[84] Copyright © 2022, American Chemical Society.

This system facilitated synchronous scanning that printed up to several foci, with a refresh rate of 22.7 kHz and a resolution of approximately 500 nm.[90] By 2023, this team had advanced to synchronously printing up to 2000 foci, achieving speeds of 2,000,000 voxels/s, and by analyzing polymerization dynamics, they reached a maximum resolution of 90 nm (Figure 10A).[91] In 2024, Jiao *et al.*[92] utilized a DMD as a digital mask, integrating an acousto-optic deflector with spatial light switching. The acousto-optic deflector driven by a non-linear swept signal significantly reduced the wavefront aberration. This approach not only achieved a printing rate of 7.6×10^7 voxels/s but also facilitated the fabrication of non-periodic structures (Figure 10B).[92]

The multi-foci parallel approach can significantly enhance throughput. The increase in laser power provides a basis for enabling patterned exposure through SLM. In 2014, Yang *et al.*[93] utilized an LC-SLM to generate large-format holographic patterns for the manufacture of specific patterns in a single exposure.[93] However, due to optical speckle noise, the printed surfaces lacked smoothness. That same year, the team introduced a multiple exposure technique that significantly improved the uniformity of the processed structures' surfaces, applying it to create high-quality DOE.[94] Although the multiple exposure method enhanced uniformity to some extent, it required the continuous loading of computed holograms to average out noise, thus reducing the throughput of the technique. In 2016, Zhang *et al.*[95] developed the mixed-region amplitude freedom holographic algorithm, which dramatically enhanced the quality of hologram generation, enabling high-quality single-exposure print formations. Fabricating masks with various patterns and projecting these designs through an optical system enables high-throughput manufacturing.[96–98] With the advancement of projection technology, DMD now enables the creation of adjustable 3D structures.[99,100] Beyond serving as a projection tool, DMD also functions as a dispersion element. By modulating the spatial chirp of a femtosecond laser pulse, the DMD confines a narrow pulse width exclusively to the sample locations, achieving synchronized spatio-temporal focusing. This method achieves an impressive lateral feature size of 140 nm and axial feature size of 170 nm, alongside high throughput in 3D micro-nano fabrication.[101,102] However, during the patterned exposure process, fluctuations in photochemical reaction intensities resulted in more proximity effects compared to point-by-point scanning methods, thus requiring an extended and meticulous process optimization.

5. High precision of two-photon polymerization

5.1. Processing parameters

The process parameters of TPP significantly influence fabrication precision. Figure 11 illustrates the typical workflow of TPP, encompassing direct writing, development, and drying. Adjusting these parameters can yield varying effects on the structures fabricated.

The feature size formed by TPP is influenced by both the optical diffraction limit and the threshold of polymer cross-linking. By regulating the light flux, the precision of the feature size can be improved, particularly when the scanning speed is high or the pulse energy is low. Moreover, when the spacing between two sets of cured structures is sufficiently small, re-polymerization occurs, resulting in finer lines. In 2007, Tan *et al.*[103] achieved line widths of less than 25 nm, merely 1/50 of the excitation wavelength, by modulating the light flux and increasing the scanning speed. By controlling the spacing between

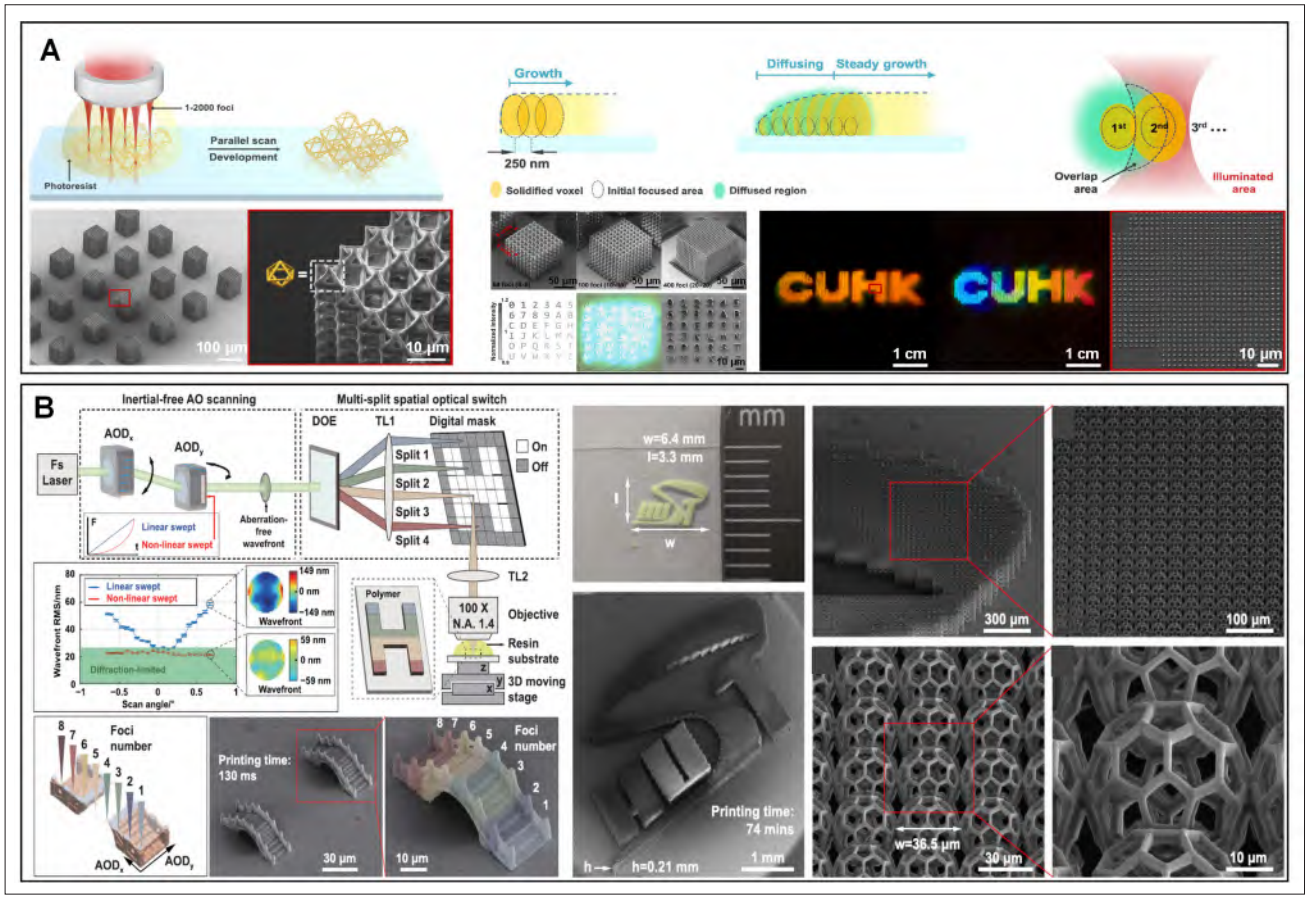


Figure 10. Employing a digital micromirror device for multi-foci parallel methods. (A) Efficient three-dimensional manufacturing facilitated by integrating polymerization dynamics. Scale bars: 1 cm, 10 μm, 50 μm, and 100 μm. Reproduced with permission from Ouyang *et al.*[91] (B) High-speed manufacturing through acousto-optic scanning integrated with spatial switching. Scale bars: 1 mm, 10 μm, 30 μm, and 300 μm. Reproduced with permission from Jiao *et al.*[92]

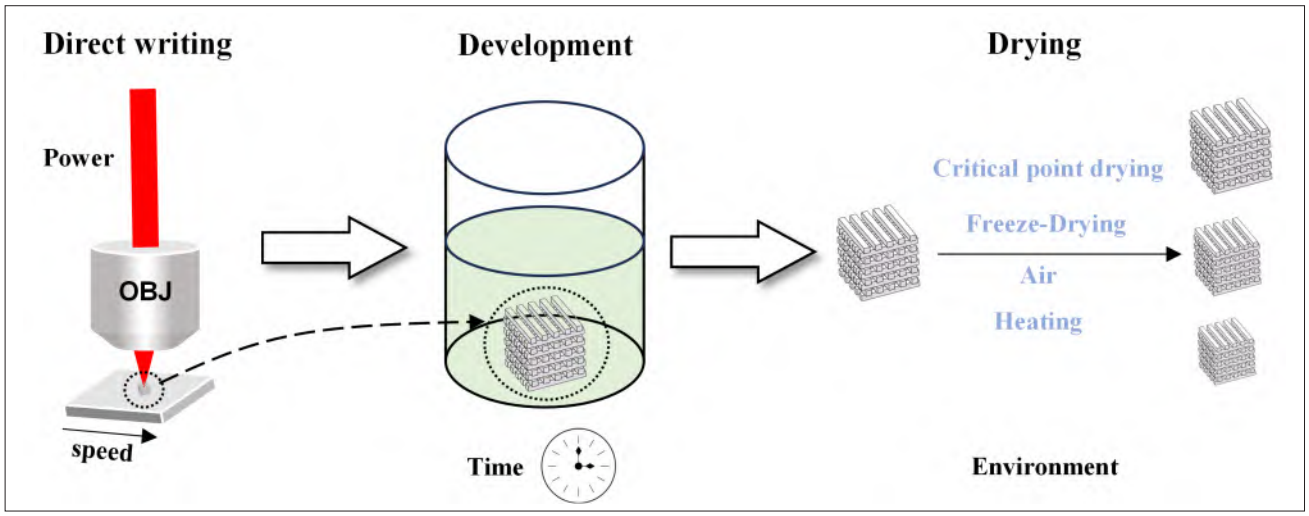


Figure 11. The workflow of two-point polymerization. Created by the authors with Microsoft PowerPoint. Abbreviation: OBJ, objective.

two sets of structures to induce re-polymerization, they achieved feature sizes of approximately 15 nm.[103]

However, solely controlling the laser dose also presents certain limitations. Firstly, the overall degree of cross-linking is low due to the reduced density of free radicals in the cross-linked regions, leading to weak structures that are prone to deformation during development and are insufficient to support 3D structures.[104] Secondly, this method does not reduce the spacing between lines. Although the feature size of a single line can be very small, free radicals persist around the lines. These free radicals are insufficient for monomer cross-linking, but when high-density patterns are inscribed, the residual free radicals accumulate, resulting in unintended structures.[105]

During the post-processing phase, the developer solution dissolves partially uncrosslinked structures, thereby reducing the feature size of the sample. The degree of cross-linking in TPP is typically below 75%, as demonstrated by Raman spectroscopy and Fourier transform infrared spectroscopy.[106–109] In this process, development time plays a crucial role. Insufficient time can result in residual ink remaining on the structure, while excessive time can compromise the structural integrity. Thus, the development duration must be carefully tailored to align with the properties of various ink types. In the drying process, capillary forces induce deformation in regions that lack sufficient strength to support the overall structure.[110] Additionally, certain materials, such as glass, necessitate the incorporation of nanoparticles into the photoresist for printing. The solid content of these nanoparticles in the photoresist is comparatively low. During the subsequent sintering process, the printed structures experience further shrinkage, resulting in an additional reduction in overall dimensions.[111]

In 2009, Maruo *et al.*[112] analyzed the overall structural shrinkage resulting from drying in air compared to that achieved with a critical point dryer.[112] Ovsianikov *et al.*[113] investigated the modifications in the photonic crystal bandgap under varying shrinkage ratios, indicating that shrinkage may be employed to enhance overall manufacturing precision.[113] In 2019, Liu *et al.*[114] introduced a heat-shrinking method to produce 3D-printed photonic crystals, achieving sub-100-nm features with a full range of colors (Figure 12).[114]

5.2. Optical systems

The optical system is crucial for the precision of the manufacturing systems. This section introduces several

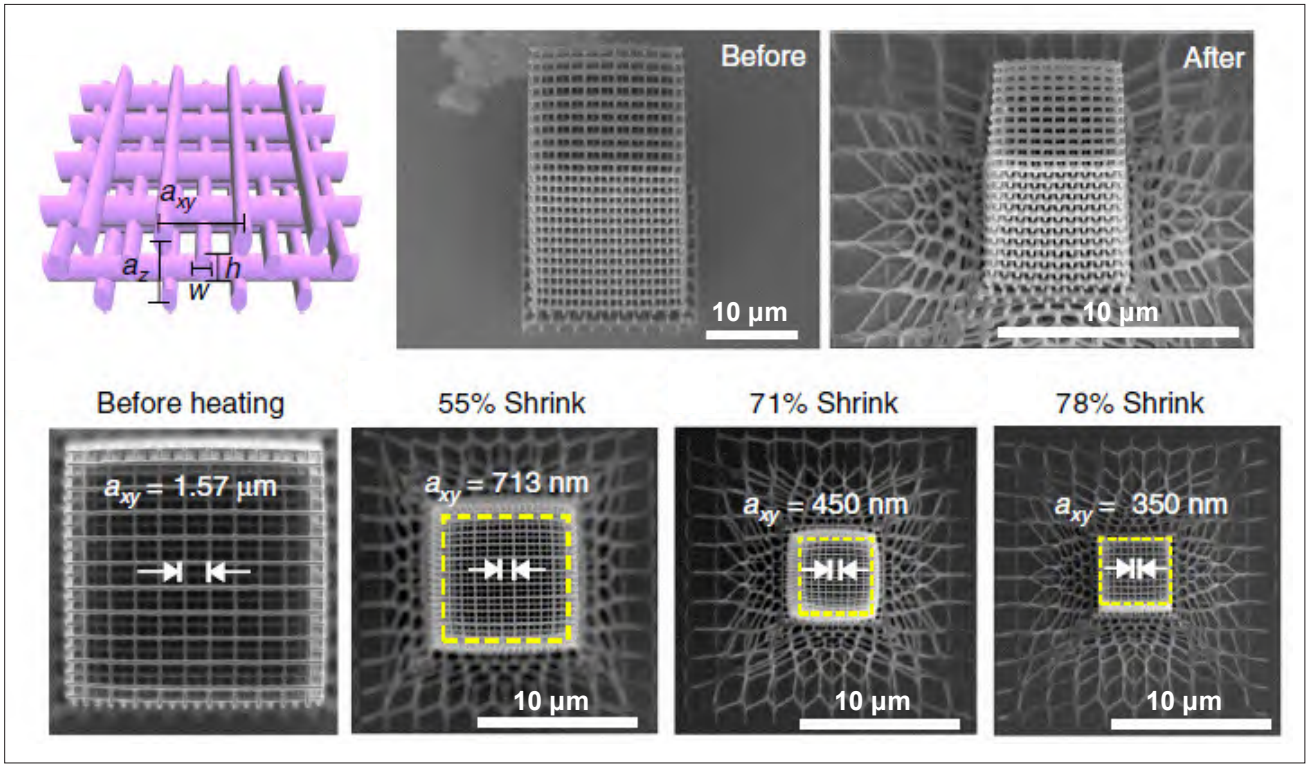


Figure 12. Variations in shrinkage after heating for different times. Scale bar: 10 μm. Reproduced with permission from Liu *et al.*[114]

methods to enhance precision based on optical imaging principles, as illustrated in Figure 13. These include reducing the wavelength, optimizing wavefront utilization (4Pi), and utilizing the properties of ultrafast lasers (spatiotemporal focusing).

According to the Rayleigh criterion, the diffraction limit of an optical system is defined by $\sigma = 0.61\lambda/\mathrm{NA}$, where λ represents the laser wavelength, and NA denotes the numerical aperture of the objective lens. Under fixed conditions for the objective lens, reducing the excitation light wavelength effectively diminishes the spot size, thereby enhancing resolution. Typically, the excitation wavelength of commonly used initiators in TPP is approximately 780 nm. Haske *et al.*[115] employed E,E-1,4-bis[4-(di-*n*-butylamino)styryl]-2,5-dimethoxybenzene as the initiator, exhibiting a two-photon absorption cross-section of 200 GM at 520 nm. By decreasing the wavelength, precision was significantly improved, ultimately achieving a linewidth of approximately 65 nm.[115] In 2022, Liu *et al.*[116] fabricated planar structures with a minimal feature size of 32 nm using DMD with an excitation wavelength of 400 nm.[116]

In super-resolution imaging, lateral resolution is typically enhanced, while axial resolution is approximately 2.5 times lower. Achieving isotropic resolution remains a significant scientific challenge. Generally, imaging with a single lens covers only half of the spherical wavefront; if the optical system could collect the other half behind the focal plane, the system's point spread function (PSF) would retain its spherical shape due to restored symmetry.[117] In 1992, Hell and colleagues[118] invented the 4Pi microscope using two opposing objective lenses, nearly capturing the entire 4Pi steradian angle.[118] The properties of micro/nanostructures fabricated using TPP are closely related to the smallest feature size of the voxel. Enhanced axial precision would improve the structural color exhibited by fabricated photonic crystals. In 2019, Tičkūnas *et al.*[119] proposed a TPP method based on 4Pi microscopy, significantly enhancing axial precision.[119] Using a 1030 nm laser, they achieved feature sizes of 200 nm laterally and 150 nm axially, resulting in nearly isotropic voxel features. Additionally, periodic layered structures can be directly fabricated using interference fringes formed in the axial direction.

In TPP fabrication, a voxel is the smallest unit. Its shape is directly related to the optical system's PSF. In single-photon absorption systems, the axial dimension of the PSF is typically about twice that of the lateral dimension. In contrast, femtosecond lasers offer richer temporal and frequency information than continuous lasers. This information can be utilized to effectively improve axial resolution. The product of the pulse width (τ_p) in the time domain and the spectral bandwidth ($\Delta\nu$) of a laser pulse, known as the time-bandwidth product, exceeds a specific constant κ, denoted by $\Delta\nu \cdot \tau_p \geq \kappa$. In 1985, Strickland and Mourou[120] proposed the chirped pulse amplification technique, which involves temporally stretching femtosecond pulses by separating the different

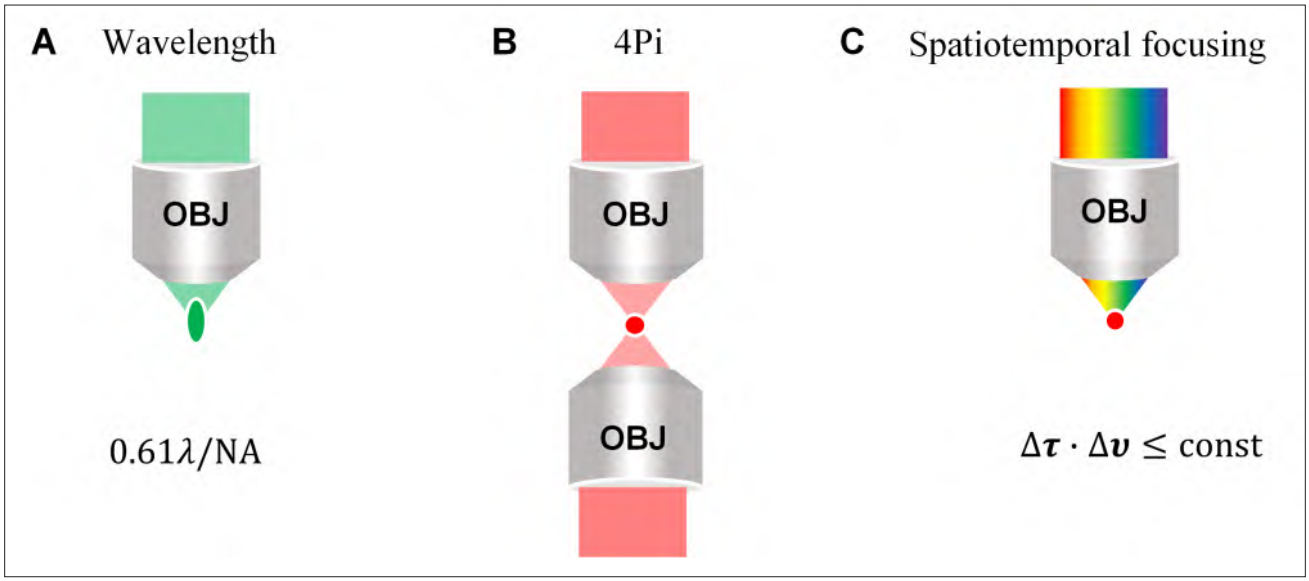


Figure 13. The enhancement of precision in two-photon polymerization through optical principles. (A) Reducing the wavelength of the laser. (B) Employing a 4Pi printing system. (C) Utilizing a spatiotemporal focusing system. Created by the authors with Microsoft PowerPoint. Abbreviation: OBJ, objective.

frequency components, thereby reducing peak power. After amplification, the pulses are then compressed. This technique was awarded the Nobel Prize in Physics in 2018. It fully exploits the temporal, spatial, and frequency characteristics of femtosecond pulses and has been widely applied in femtosecond laser-based technologies.

In two-photon imaging, the signal-to-noise ratio deteriorates with increased penetration depth. In 2005, Zhu's team[121] proposed a spatiotemporal focusing method. By broadening the femtosecond pulses with a grating to form spatial chirps and employing a 4f system during transmission, different frequency components converge at the focal point. Due to the time-bandwidth product, the peak power is insufficient to generate two-photon fluorescence signals after forming spatial chirps. However, at the focal point, the pulse width is minimized, achieving the focused pulse width necessary for effective two-photon fluorescence.[121] This method improves the PSF aspect ratio and enhances the axial precision of nonlinear optical systems. It has found broad applications in isotropic processing, two-photon imaging, and femtosecond laser filamentation.[122–125]

In 2010, an MIT research team utilized a mask and spatiotemporal focusing for high-throughput 3D printing. However, this method was confined to the fabrication of specific structures.[126] In 2012, Li *et al.*[127] used a DMD as a digital mask combined with spatiotemporal focusing for TPP (Figure 14A).[127] This approach entails a complex optical path due to the necessity of coupling the DMD with grating devices. In 2014, the team synchronized the DMD as a projection element and grating, achieving spatial light modulation and spatial chirp.[99] Despite this advancement, large-area manufacturing with DMD continued to encounter issues of inhomogeneous energy distribution and low structural precision. In 2017, Gu *et al.*[128] achieved uniform laser ablation using a beam homogenizer with spatiotemporal focusing, which resulted in a surface roughness not exceeding 96 nm.[128] By 2018, this system was applied to metal 3D printing.[129] In 2019, it enabled the rapid fabrication of nanoscale precision 3D structures, achieving up to 140 nm horizontal and 170 nm axial feature size, and improving manufacturing efficiency by more than three orders of magnitude compared to traditional point-by-point scanning methods.[101] In 2021, Somers' team[102] demonstrated the feasibility of this system for efficient large-scale micro- and nano-manufacturing (Figure 14B).[102] By 2022, Han's team[130] expanded this technology's precision using expansion microscopy, employing hydrogels as templates to assemble materials such as metals, two-dimensional materials, oxides, semiconductors, polymers, biological materials, and molecular crystals, achieving resolutions ranging from 20 to 200 nm in two-dimensional and 3D structures.[130]

This technology harnesses the temporal and spatial characteristics of femtosecond lasers, significantly enhancing precision and efficiency. It offers a novel technical direction for manufacturing cross-scale devices using TPP. However, due to the shift in processing paradigms, the fabrication of complex structures still necessitates substantial effort.[69,131–135]

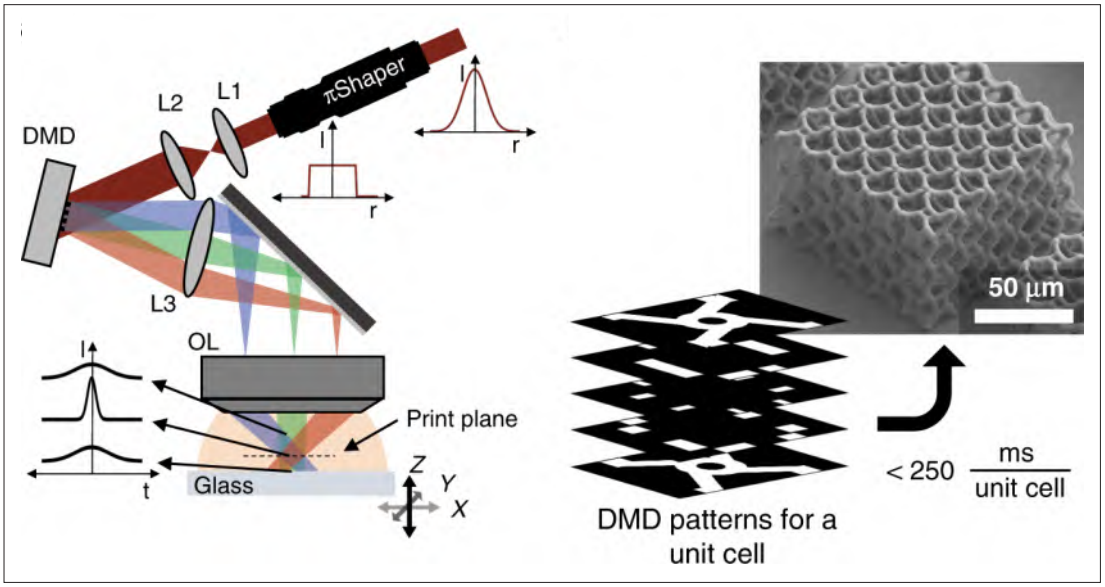


Figure 14. Spatiotemporal focusing in two-photon polymerization for the fabrication of metamaterials. Scale bar: 50 μm. Reproduced with permission from Somers *et al.*[102] Abbreviation: DMD, digital micromirror device.

5.3 Light–matter interactions

The TPP process involves both the optical system and the complex interactions between the laser and matter. By modulating the excited-state dynamics of the reaction system or modulating the interactions between ink components with light of varying wavelengths, it is possible to achieve higher precision in micro-nanostructure fabrication.

Hell[136] pioneered far-field super-resolution technology, specifically stimulated emission depletion (STED) microscopy. This technique utilizes the principle of reversible saturable optical linear fluorescence transition, which involves molecules that can reversibly switch between at least two states.[136] In 2014, this technique received the Nobel Prize in Chemistry, underscoring its significance. The process begins with exciting molecules to the excited state (λ_{exc}). If another beam (λ_{SE}) is applied before fluorescence emission, the excited molecules return to the ground state via stimulated emission, thereby reducing the rate of radiative transition. When both beams are coupled as Gaussian light, no signal is detected. However, when the excitation light is Gaussian and the depletion light is a vortex beam formed by a phase plate, their coupling effectively erases the PSF. This method has achieved a resolution of up to 2.4 nm, further highlighting its potential.[137] The mechanism and basic setup of STED are depicted in Figure 15.[138] Currently, methods that enhance precision through light–matter interactions are mainly inspired by STED technology. However, in their specific implementation, TPP and imaging techniques exhibit significant distinctions.

5.3.1. Kinetics

The kinetics, encompassing stimulated emission, electron transfer, triplet absorption, and photoisomerization, have been utilized in TPP. STED-assisted TPP was initially inspired by STED. By analyzing the excitation spectrum of the photoinitiator and selecting a wavelength close to its fluorescence spectrum for depletion, manufacturing precision is enhanced.[139] Unlike imaging techniques that prioritize the fluorescence quantum yield of fluorescent molecules—seeking the highest possible yield to minimize photobleaching and phototoxicity—TPP is inherently a photochemical reaction. It features a low fluorescence yield and a high ISC rate, allowing the photoinitiator molecules to participate more efficiently in chemical reactions. However, adapting STED from microscopy to lithography presents significant challenges to the material system.

The suppression of single-photon and TPP,[104,140] significantly promoted the application of STED in super-resolution lithography. However, the material systems still face limitations in fabricating complex 3D structures, including a slow response time and irreversible processes.[141] In 2010, Fischer *et al.*[139] introduced a photoresist based on the photoinitiator 2-isopropylthioxanthone (ITX), achieving results similar to stimulated emission depletion.[139] In 2011, using the same experimental setup, the group employed 7-diethylamino-3-thenoylcoumarin (DETC) as a photoinitiator to fabricate visible light photonic crystals, demonstrating the system's ultra-high resolution.[142] Compared to the reference, the region in the cloak exhibited invisibility under circular polarization illumination. In fact, beyond the expected stimulated emission pathway, when excited state molecules are exposed to depletion light, some excited state absorption or triplet state absorption may occur, which can increase polymerization probability, reduce depletion efficiency, and limit high-resolution performance.[143]

Photoresists for stimulated emission must possess a large oscillator strength for the S_0–S_1 transition, long excited state lifetimes, and high fluorescence quantum yields. A pump-probe experiment comparing ITX and DETC revealed that DETC exhibits a stronger

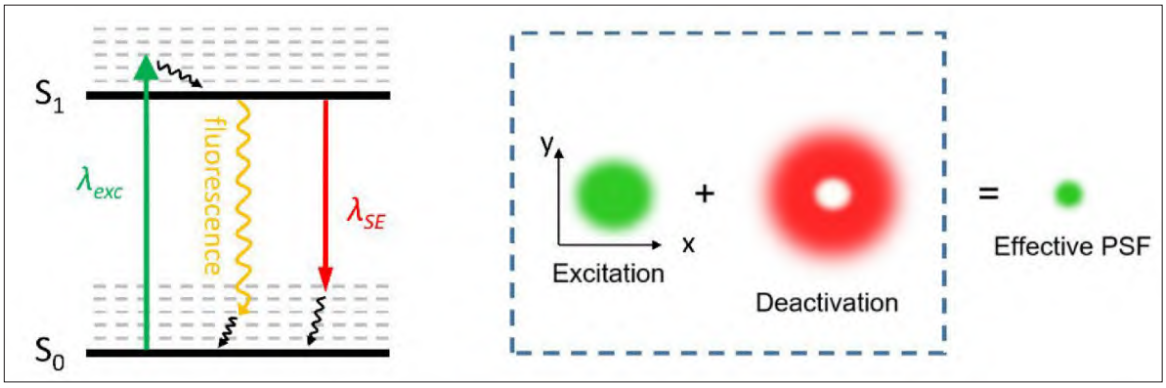


Figure 15. The Jablonski diagram and structural schematic of stimulated emission depletion microscopy. Reproduced with permission from Liaros and Fourkas.[138] Abbreviation: PSF, point spread function.

stimulated emission effect compared to its excited state absorption, making it more suitable as a photoinitiator for the stimulated emission mechanism.[144] Although ITX can achieve suppression in dual-color systems, it is not primarily driven by the stimulated emission process. DETC remains the leading photoinitiator supporting the stimulated emission suppression mechanism.[145] In 2013, Wollhofen *et al.* achieved a feature size of 55 nm and a resolution of 120 nm using DETC.[145] In 2015, Fischer *et al.* explored the mechanisms in STED-enhanced direct laser writing.[146]

With the advancement of this system, interest in enhancing the throughput of stimulated emission TPP has increased. In 2022, Zhu *et al.*[147] proposed a parallel peripheral-photoinhibition method by independently controlling the two polarization components of a light beam. They increased throughput while ensuring a minimum feature size of less than 40 nm (Figure 16).[147] To prevent the chromatic aberration of conventional multicolor inhibition lithography, they also developed single-color photoinhibition systems.[148,149]

The dual-color suppression method based on stimulated emission offers process reversibility. Additionally, the short fluorescence lifetime allows completion of this process within a nanosecond timescale, making it highly promising for high-throughput manufacturing.[150] However, given the short fluorescence lifetime, the stimulated emission rate must exceed the spontaneous emission rate, which demands high intensity for the depletion light, thereby increasing the method's cost and complexity.[151] The exploration of long-lived intermediate states to expand this approach warrants in-depth investigation.

The DETC inhibition mechanisms have been investigated in numerous studies. Fischer *et al.*[150] employed the pump-probe technique to analyze the efficacy of inhibition at various temporal delays. If the inhibition mechanism of DETC relies solely on stimulated emission, the inhibition timescale correlates with the molecule's inherent fluorescence lifetime, typically a few nanoseconds. Experimental findings revealed significant inhibition effects within nanoseconds post-pulse, which subsequently diminished. Furthermore, experiments indicated inhibition occurring before the excitation pulse, suggesting a residual impact from the previous pulse. This suggests that DETC's inhibition mechanism involves pathways additional to stimulated emission. In 2012, Harke *et al.*[152] explored the dynamics of super-resolution lithography polymerization, using a 642 nm laser that surpasses the fluorescence spectral range of ITX and DETC, discussing the possibility of ISC induced by triplet state absorption.[152] In these experiments, significant inhibition effects were observed even when the delay between the inhibition and excitation lights (800 ns for ITX and 5 μs for DETC) far exceeded the fluorescence lifetimes (0.1 ns–4 ns). To further analyze the triplet state processes, Harke *et al.*[153] conducted transient absorption studies on ITX and DETC, showing enhanced absorption rates over a prolonged duration at specific wavelengths. ITX absorbs at 630 nm, while DETC absorbs across a spectrum from visible to near-infrared.

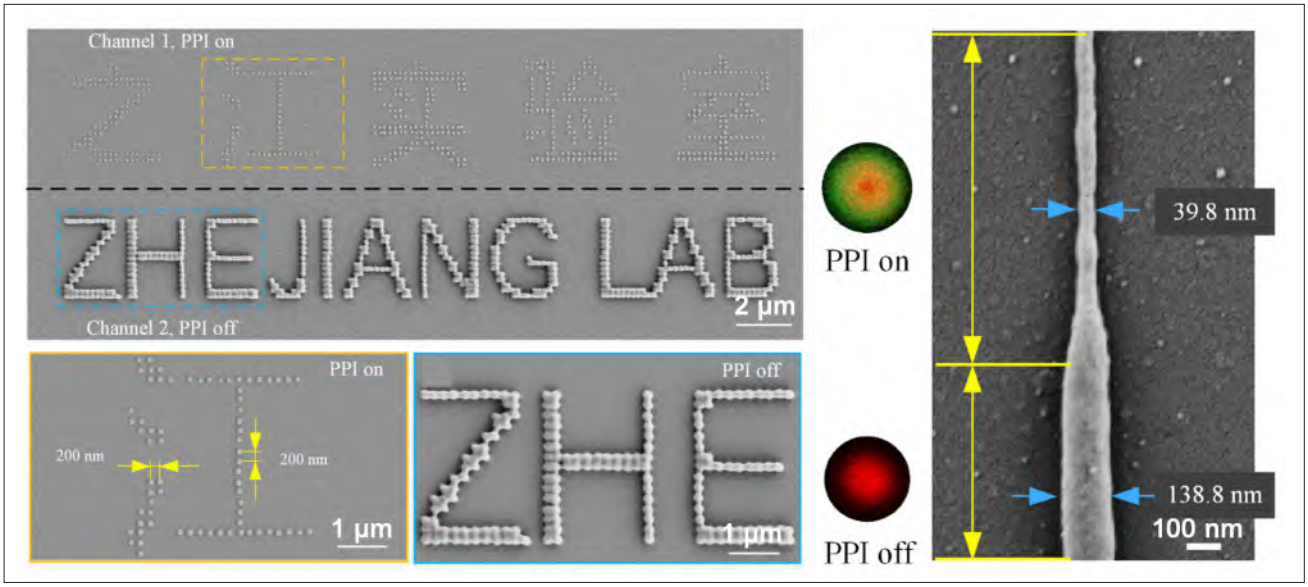


Figure 16. Enhancing two-photon polymerization precision through stimulated emission depletion microscopy. Scale bars: 1 μm, 2 μm, and 100 nm. Reproduced with permission from Zhu *et al.*[147]

Additionally, the discrete Fourier transform was utilized to calculate the triplet state absorption spectra of ITX and DETC, with the results aligning well with experimentally obtained photo-induced absorption spectra.[153] Thiel *et al.*[154] also successfully integrated the triplet state absorption in fabricating dual-band polarizers using a dip-in mode. Somers' team conducted a systematic study on DETC, examining the effects of co-initiators and various temporal delays, and confirming triplet state inhibition under an 808 nm laser (Figure 17).[155]

In 2009, Li *et al.*[140] first introduced the resolution augmentation through photoinduced deactivation (RAPID) technique for super-resolution lithography using a single-color light.[140] As dye molecules typically exhibit fluorescent lifetimes on the order of nanoseconds, subsequent studies have shown that the inhibitory time scale of this material system exceeds 13 ns, indicating that stimulated emission alone cannot account for this process. In 2011, Stocker and coworkers[156] proposed a self-inhibiting mechanism. In conventional photoresist systems, the degree of polymerization correlates directly with the laser dose; the slower the scanning speed, the greater the accumulation of light, and thus, the larger the polymer dimensions. However, an increased scanning speed paradoxically led to wider line widths, a phenomenon that classical excited-state dynamics models could not explain. To explain this process, they posited the solvent-stabilized electrons mechanism. After excitation to the excited state, the initiator undergoes ISC to the triplet state. Subsequently, molecules in the triplet state are converted into solvent-stabilized electrons and free radical cations, both of which can facilitate polymerization over extended periods. However, upon irradiation with an additional 800 nm light, the solvent-stabilized electrons and free radical cations recombine, resulting in the regeneration of the photoinitiator within photoresists based on the RAPID system. The method, owing to the extended lifetime of intermediate states, requires lower light power, thus enabling effective inhibition with relatively low-power continuous-wave lasers.

In two-color schemes, residual, partially cross-linked areas can persist if the suppression is not absolute, resulting in less than 100% effectiveness. These areas, though insufficient to reach the polymerization threshold, may overlap when constructing dense structures, leading to unwanted cross-linking. During the two-color suppression process, the excited state molecules influenced by the excitation light follow various pathways. The inhibition light suppresses some of these pathways, and when the inhibition light is strong, some non-suppressed pathways may be enhanced, ultimately compromising the suppression effect.[146] Decoupling the processes of polymerization and cross-linking can mitigate this issue and enhance resolution.[157] In 2018, Liaros *et al.*[157] proposed a three-color suppression scheme. Initially, using an 800 nm femtosecond laser, the material was pre-activated without directly inducing cross-linking. Similarly, illumination with a 445 nm continuous laser alone did

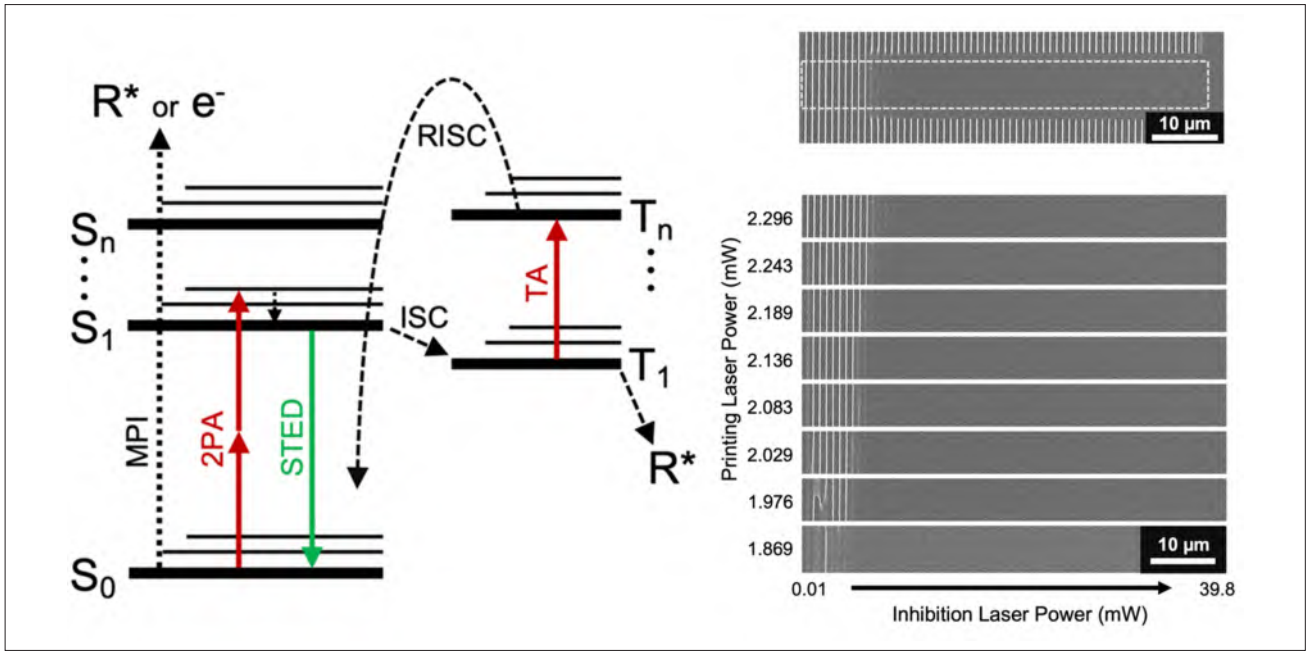


Figure 17. Experimental results of triplet state inhibition with DETC. Scale bar: 10 μm. Reproduced with permission from Somers *et al.*[155] Abbreviations: DETC, 7-diethylamino-3-thenoylcoumarin; ISC, intersystem crossing; RISC, reverse intersystem crossing; STED, stimulated emission depletion.

not lead to cross-linking. Cross-linking occurred only when both beams were applied simultaneously. A third beam was then introduced for inhibition. This process, by decoupling inhibition and cross-linking, significantly enhanced feature precision.

Photochromic materials provide a method to directly modulate either the transparency or the availability of monomers to light. Mueller *et al.*[158] proposed a super-resolution lithography technique using photoinduced isomerization. In 2017, they developed their method based on the cis-trans photoisomerization of intermediate photoenol species derived from α-methylbenzyl. In the presence of active enes, the E-enol undergoes a Diels–Alder reaction to form stable products. The short-lived Z-enol reverts to the original compound through a rapid reverse hydrogen transfer. By irradiating with 440 nm light, the E-enol is photoisomerized to Z-enol, inhibiting the formation of cyclic products and achieving a linewidth of 60 nm and resolution of 100 nm (Figure 18A).[158] In 2019, the team introduced a photoresist based on a methacrylic copolymer, with side chains composed of photochromic spirothiopyran moieties capable of forming crosslinks via supramolecular interactions between chromophores, achieving feature sizes as small as 31.2 nm (Figure 18B).[159] The variation in line thickness depicted in Figure 18 reflects the fabrication precision under two laser writing conditions: excitation light alone and the addition of quenching light.

5.3.2. Interactions among matter

In addition to regulating the behavior of individual components, light–matter interactions can also be employed to modulate the interaction between components. This approach can alter a material's light absorption properties and govern interactions between two kinds of molecules or between a molecule and the excited state of another type of molecule, ultimately achieving enhanced precision.

In 2009, Andrew and colleagues[160] utilized photochromic materials to achieve super-resolution lithography.[160] In their study, a layer of photochromic film, with two modes capable of absorbing either UV or visible light, was applied to the surface of a photoresist. Exposure to a specific light source toggled these molecules between an "OPEN" state, which absorbs ultraviolet light, and a "CLOSED" state, which absorbs visible light. This dynamic adjustment of the film's transparency to ultraviolet light narrowed the spatial distribution of ultraviolet exposure, enabling the etching of sub-wavelength-scale patterns. However, the method was limited by its relatively slow switching times and a finite number of adjustable cycles. The method of photoisomerization has broadened the dimensions of super-resolution lithography. However, challenges such as a slow photochromic response, low direct-write efficiency, and limited switching cycles persist. Enhancing the processing throughput of this system continues to be a significant area of research.

The mechanism of photoinhibition employs two distinct photonic pathways with different spatial distributions and wavelengths to initiate varied chemical reactions. One pathway promotes photopolymerization, while the other generates substances that lead to polymerization quenching. This photonic control of chemical reactions effectively suppresses the production of free radicals, thereby significantly enhancing the spatial resolution of printing. In 2009, Scott *et al.*[104] pioneered this technique, achieving processing precision beyond the diffraction limit. By shaping the inhibition light into a "doughnut" mode and overlaying it with the excitation light, they achieved lines as fine as 65 nm. However, the monomers used in the work polymerized slowly, and the

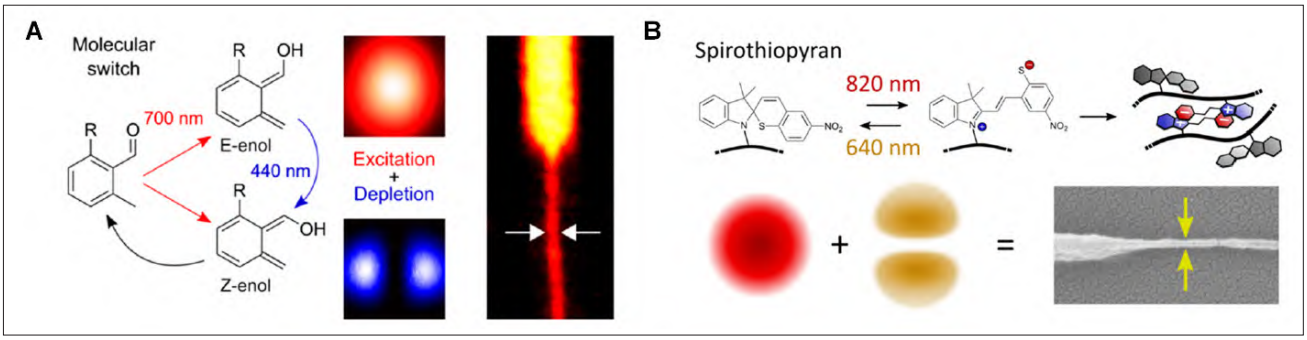


Figure 18. Enhancing two-photon polymerization precision through photoisomerization inhibition. (A) Achieving super-resolution through cis-trans isomerization of photoisomerization molecules. Reproduced with permission from Mueller *et al.*[158] Copyright © 2017, American Chemical Society. (B) Regulating crosslinking of photoisomerization molecules. Reproduced with permission from Müller *et al.*[159] Copyright © 2019, American Chemical Society.

cured modulus was relatively low, potentially leading to unforeseen precision loss. In 2011, Cao's team[161] employed BPE 100 photoresist, which boasts higher photosensitivity and modulus, to form voxels as small as 40 nm within an exposure time of 400 ms.[161] These studies were all based on single-photon absorption. In 2013, based on this system, Gan and coworkers[162] developed a method of TPP photoinduced dissipative inhibition. A lateral feature size of 9 nm is achieved by controlling the laser dose (Figure 19).[162] This technique requires relatively low power for the inhibition light, typically only at the milliwatt level, but its mechanism dictates an irreversibility that somewhat limits the development of this method.

A quencher, which is a traditional component in TPP inks, primarily inhibits radical diffusion and, as a result, improves precision. In 2024, Guan *et al.*[163] conducted an in-depth study on the relationship between initiators and quenchers, which revealed that 2,2,6,6-tetramethyl-4-piperidyl-1-oxyl efficiently quenches the excited state of DETC. They proposed a novel manufacturing approach based on the mutual suppression of light and matter, achieving an impressive precision of 30 nm, as illustrated in Figure 20.[163] The voxel sizes and throughputs have been extensively summarized in some articles.[70,81] Improved precision and higher throughput remain key trends in TPP. The performance and details of different TPP technologies are summarized in Figure 21 and Table 1.

Some techniques are very inspiring and show great feature sizes; however, they do not demonstrate the ability to fabricate 3D structures. Although these technologies are typically realized using polymer resins, they still face certain limitations before being fully applicable to biomedical fields. Biomedical materials such as gelatin methacryloyl and hyaluronic acid often require high biocompatibility or softness. Nevertheless, these technologies, as versatile platforms, offer promising new possibilities for biofabrication.

6. Conclusion

This paper provides a comprehensive overview of TPP in biomedical applications and explores advancements in TPP. Although TPP is a powerful micro-nanofabrication technique, its applications in biomedical engineering are still limited. In tissue engineering, constructing a 3D cell growth environment *in vitro* poses significant challenges in terms of manufacturing accuracy, material strength, and biocompatibility. Possible photodamage, along with the toxicity of substances in partially crosslinked materials, can significantly impact cell growth. Even if a micro-nano device exhibits good properties at the cellular level, for complex multi-level structures such as biological systems, cellular-level performance is difficult to directly guide macroscopic properties, thus necessitating higher manufacturing throughput. Taking human dental enamel as an example, this naturally occurring biomaterial, renowned for its exceptional hardness, stiffness, and toughness, provides valuable insights into the development of new medical materials and technologies. Dental enamel exemplifies a typical layered, multi-level structure; its primary components are hydroxyapatite nanowires (30–50 nm) tightly organized into enamel rods (4–6 μm), with the overall dimensions extending to the millimeter

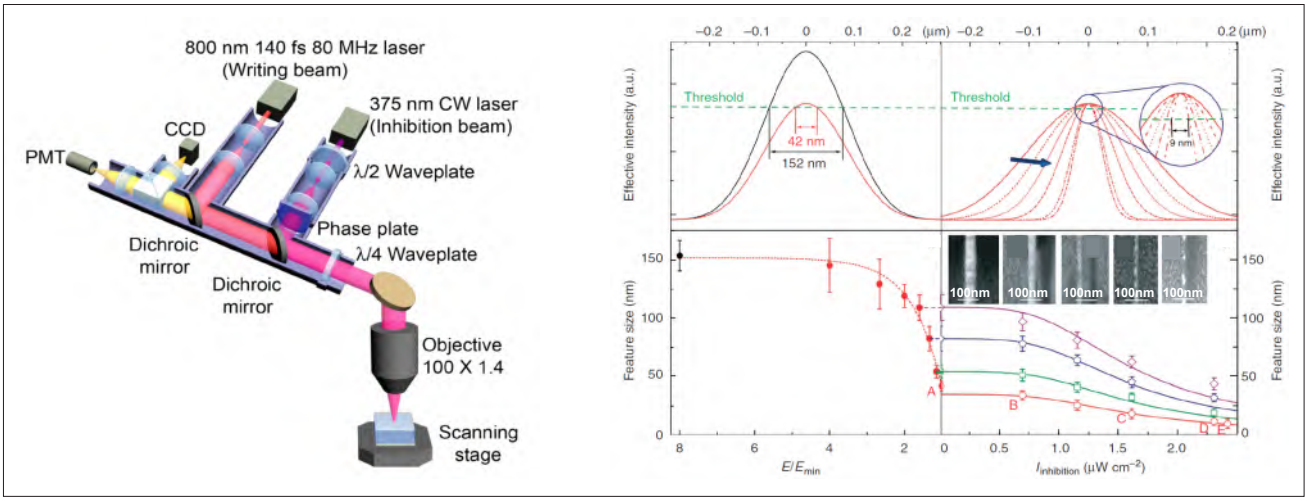


Figure 19. Enhancing the precision of two-photon polymerization through a photoinhibitor. Reproduced with permission from Gan *et al.*[162] Copyright © 2013, Springer Nature.

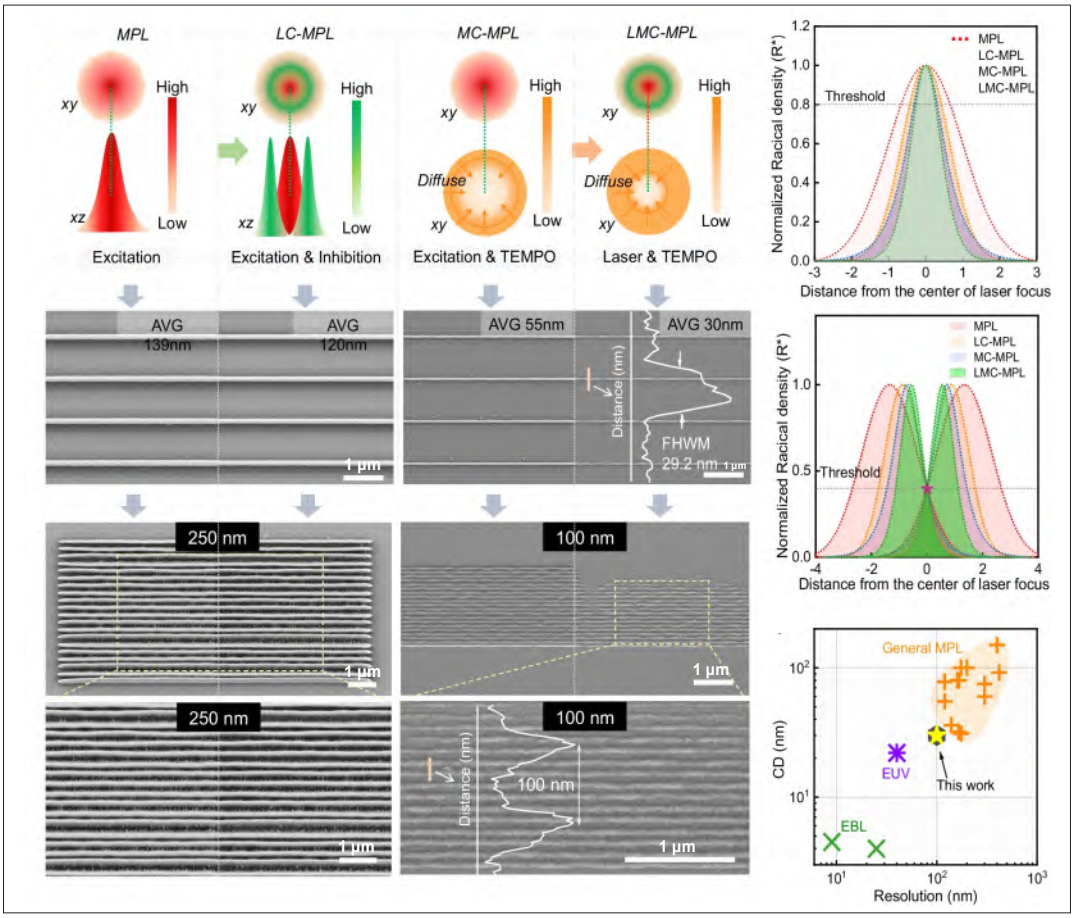


Figure 20. Light and matter co-confined multi-photon lithography. Scale bar: 1 μm. Reproduced with permission from Guan *et al.*[163] Abbreviations: EBL, E-beam lithography; EUV, extreme ultraviolet lithography; LC, light-confined; LMC, light and matter co-confined; MC, matter-confined; MPL, multi-photon lithography; TEMPO, 2,2,6,6-tetramethyl-4-piperidyl-1-oxyl

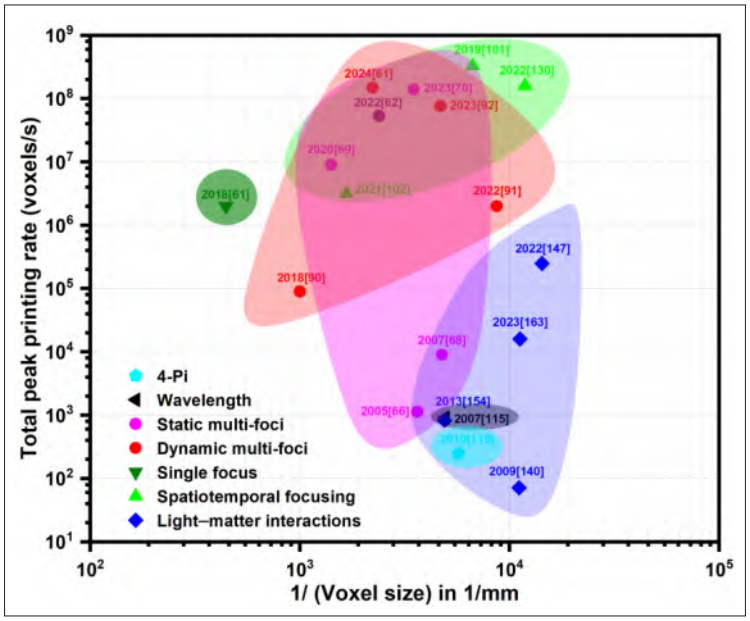


Figure 21. Comparison of various technologies based on their printing rate and voxel size. Created by the authors using Origin and Microsoft PowerPoint.

Table 1. Summary of two-photon polymerization efficiency and precision

Parameter		Approach	Feature size	Resolution	Speed	3D	Wavelength	Year	Ref
Efficiency	Serial scanning	Resonant-galvo mirror	1–4 μm (xy) 2 μm (z)	–	2×10^6 voxels/s	Yes	780 nm fs	2019	[61]
	Multi-foci	MLA	250 nm (xy)	–	1.13×10^3 voxels/s	Yes	799 nm fs	2005	[66]
		DOE + Galvo	120 nm (xy)	–	9×10^3 voxels/s	Yes	780 nm fs	2007	[68]
		DMD	500 nm (xy) 1500 nm (z)	–	9×10^4 voxels/s	Yes	800 nm fs	2019	[90]
		AOM + DOE + Galvo	406 nm (xy) 1010 nm (z)	–	9×10^6 voxels/s	Yes	790 nm fs	2020	[69]
		DMD	90 nm (xy) 141 nm (z)	–	2×10^6 voxels/s	Yes	800 nm fs	2023	[91]
		DMD	163 nm (xy) 263 nm (z)	220 nm (xy)	7.6×10^7 voxels/s	Yes	517 nm fs	2023	[92]
		DOE + MLA + Galvo	245 nm (xy) 328 nm (z)	–	1.4×10^8 voxels/s	Yes	790 nm fs	2024	[70]
		SLM + Galvo	215 nm (xy) 686 nm (z)	–	1.49×10^8 voxels/s	Yes	1,030 nm fs	2024	[81]
	Pattern	Projection	650 nm (xy) 10 μm (z)	–	1,000 patterns/s	No	800 nm fs	2013	[100]
		Computational holography	350 nm (xy)	–	200 patterns/s	No	800 nm fs	2016	[95]
	Light field	Bessel beam	Tube	–	2.5 structures/s	Yes	800 nm fs	2014	[73]
		OAM beam	Double-helix	–	10 sturctures/s	Yes	800 nm fs	2014	[74]
Precision	Processing Parameters	Laser dose	25 nm (xy)	–	700 μm/s	No	780 nm fs	2007	[103]
		Shrinkage	100 nm (xy)	–	200 μm/s	Yes	780 nm fs	2009	[113]
	Optical system	Wavelength	65 nm (xy) 340 nm (z)	500 nm (xy)	60 μm/s	Yes	520 nm fs	2007	[115]
			32 nm (xy)	165 nm (xy)	1 pattern/s	No	400 nm fs	2021	[116]
		4Pi	200 nm (xy) 150 nm (z)	–	50 μm/s	Yes	1030 nm fs	2020	[119]
		Spatiotemporal focusing	130–140 nm (xy) 170 nm (z)	–	3.33×10^8 voxels/s	Yes	800 nm fs	2019	[101]
			200 nm (xy) 1 um (z)	7 μm (z)	3.2×10^6 voxels/s	Yes	800 nm fs	2021	[102]
			20–200 nm (xy) 148.4 nm (z)	–	1.6×10^8 voxels/s	Yes	800 nm fs	2022	[130]

(Continue)

Table 1. Summary of two-photon polymerization efficiency and precision

Parameter		Approach	Feature size	Resolution	Speed	3D	Wavelength	Year	Ref
Precision	Laser-matter interaction	Photoinduced deactivation	40 nm (z)	–	10 μm/s	Yes	800 nm fs excitation 800 nm cw depletion	2009	[140]
		Stimulated emission depletion	–	175 nm (xy)	100 μm/s	No	810 nm fs excitation 532 nm cw depletion	2011	[143]
			40 nm (xy)	140 nm (xy)	1 mm/s	Yes	780 nm fs excitation 532 nm cw depletion	2022	[148]
			30 nm (xy) 148 nm (z)	100 nm (xy)	500 μm/s	Yes	525 nm fs excitation 532 nm ps depletion	2024	[163]
		Triplet state absorption	120 nm (xy) 288 nm (z)	525 nm (xy) 495 nm (z)	100 μm/s	Yes	780 nm fs excitation 639 nm cw depletion	2013	[154]
		Photoinhibitors	9 nm (xy)	52 nm (xy)	160 μm/s	No	800 nm fs excitation 375 nm cw depletion	2013	[162]
		Photoisomerization	60 nm (xy)	100 nm (xy)	10 μm/s	No	700 nm fs excitation 440 nm cw depletion	2017	[158]
			31.2 nm (xy)	175 nm (xy)	100 μm/s	Yes	820 nm fs excitation 640 nm cw depletion	2019	[159]
		Three-color strategy	101 nm (xy)	–	20–80 μm/s	No	800 nm fs preactivation 445 nm cw activation 800 nm cw deactivation	2018	[157]

Abbreviations: 3D, three-dimensional; AOM, acousto-optic modulator; DOE, diffractive optical element; DMD, digital micromirror device; MLA, micro lens array; OAM, orbital angular momentum of light; SLM, spatial light modulator.

scale.[3] Achieving a fully biomimetic, multi-level ordered structure requires exceedingly high precision, resolution, and throughput from manufacturing technologies. Current methods, while achieving high precision, often struggle to maintain adequate physical, mechanical, and optical properties. Furthermore, limited by proximity effects, replicating the naturally densely packed structure is challenging. To overcome these obstacles, efforts can include, but should not be restricted to, the following strategies.

Optically, advanced optical measurement technology can be integrated with TPP to enable high-precision manufacturing and facilitate real-time feedback. Some technologies, such as two-photon fluorescence imaging, optical coherence tomography, optical diffraction tomography, STED, 4Pi, and expansion microscopy, have been incorporated into the process.[119,127,130,140,164,165] Moreover, certain approaches involving polar coordinates and volumetric additive manufacturing also hold promising potential in TPP.[166,167] TPP devices share structural similarities with many imaging systems. Imaging technology primarily focuses on information extraction. Optical signals contain multidimensional information, including time, space, frequency, and polarization. It enables the observation of the dynamic processes of the micro-robots and facilitates an understanding of the principles governing their motion.[168] Furthermore, new light–material interaction mechanisms are also necessary to broaden the range of material applications.

Chemically, a more comprehensive analysis of the properties of photoresists is required, encompassing both their steady-state and transient behaviors. Besides the nonlinearity induced by the femtosecond laser, higher-order nonlinear effects during the chemical reactions initiated by different photoinitiators necessitate diverse analytical techniques. Steady-state methods like Fourier transform infrared spectroscopy, Raman, and coherent anti-Stokes Raman scattering spectroscopy analyze polymerization process and kinetics, while time-resolved scattering and transient absorption spectroscopy examine transient phenomena.[10,153] Additionally, kinetic models of different photoresist systems enable precise manufacturing predictions through multi-physical field coupling models using new computational methods.[163] For instance, COMSOL models reaction kinetics, MATLAB assesses the impact of various kinetic processes, and molecular dynamics analyzes experimentally challenging scenarios.[109,169,170]

From a materials perspective, broadening the range of functional materials and designing high-performance photoinitiators remain critical objectives. To address diverse applications, researchers have proposed various strategies. For instance, coating polymer surfaces with nickel and titanium enhances magnetic control and biocompatibility of these devices, depositing metals on polymer surfaces enhances the electric field for biosensing, and integrating silica nanospheres within polymers creates highly transparent glass structures. Moreover, exploring visible-light photoinitiators offers potential to further reduce phototoxicity and enable the application of TPP in bioprinting.

In summary, TPP technology holds significant research and practical value across multiple domains. By exploring its primary development directions and technical features, this paper underscores its indispensable role in biomedicine. As throughput and efficiency improve, TPP will increasingly impact the fabrication of advanced interventional medical devices, single-cell interaction studies, organ-on-chip research, and the development of hierarchical materials.

Acknowledgments

We acknowledge support by Beijing Advanced Innovation Center for Biomedical Engineering.

Funding

This study was funded National Natural Science Foundation of China (92477111, 22073003), Beijing Natural Science Foundation (L232109), Fundamental Research Funds for the Central Universities (YWF-22-K101).

Conflict of interest

Jiebo Li is a Guest Editor of this special issue, but was not in any way involved in the editorial and peer-review process conducted for this paper, directly or indirectly. Separately, other authors declared that they have no known competing financial interests or personal relationships that could have influenced the work reported in this paper.

Author contributions

Conceptualization: Yanzhe Fu, Bosong Yu
Visualization: Yanzhe Fu, Mingming Huang, Jiayong Wei
Writing-original draft: Yanzhe Fu, Mingming Huang, Jiebo Li
Writing–review & editing: Xiang Ding, Jiebo Li, Jianmin Han, Lizhen Wang, Yubo Fan

Ethics approval and consent to participate

Not applicable.

Consent for publication

Not applicable.

Availability of data

Not applicable.

References

1. Khademhosseini A, Langer R. Microengineered hydrogels for tissue engineering. *Biomaterials*. 2007;28(34):5087-5092. doi: 10.1016/j.biomaterials.2007.07.021.
2. Asadollahbaik A, Thiele S, Weber K, *et al*. Highly efficient dual-fiber optical trapping with 3D printed diffractive fresnel lenses. *ACS Photonics*. 2020;7(1):88-97. doi: 10.1021/acsphotonics.9b01024.
3. Zhao H, Liu S. Liu S, Wei Y, *et al*. Multiscale engineered artificial tooth enamel. *Science*. 2022;375 (6580):551-556. doi: 10.1126/science.abj3343
4. Kawata S, Sun H-B, Tanaka T, *et al*. Finer features for functional microdevices. *Nature*. 2001;412(6848):697-698. doi: 10.1038/35089130.
5. Greant C, Van Durme B, Van Hoorick J, *et al*. Multiphoton lithography as a promising tool for biomedical applications. *Adv Funct Mater*. 2023;33(39):202212641. doi: 10.1002/adfm.202212641.
6. Arslan A, Steiger W, Roose P, *et al*. Polymer architecture as key to unprecedented high-resolution 3D-printing performance: the case of biodegradable hexa-functional telechelic urethane-based poly-ε-caprolactone. *Mater Today*. 2021;44:25-39. doi: 10.1016/j.mattod.2020.10.005.
7. Song J, Michas C, Chen CS, *et al*. From simple to architecturally complex hydrogel scaffolds for cell and tissue engineering applications: opportunities presented by two-photon polymerization. *Adv Healthc Mater*. 2020;9(1):e1901217. doi: 10.1002/adhm.201901217.
8. Zipfel WR, Williams RM, Webb WW. Nonlinear magic: multiphoton microscopy in the biosciences. *Nat Biotechnol*. 2003;21(11):1369-1377. doi: 10.1038/nbt899.
9. Somers P, Münchinger A, Maruo S, *et al*. The physics of 3D printing with light. *Nat Rev Phys*. 2023;6:99-113. doi: 10.1038/s42254-023-00671-3.
10. Mueller JB, Fischer J, Mayer F, *et al*. Polymerization kinetics in three-dimensional direct laser writing. *Adv Mater*. 2014;26(38):6566-6571. doi: 10.1002/adma.201402366.
11. Fischer J, Mueller JB, Kaschke J, *et al*. Three-dimensional multi-photon direct laser writing with variable repetition rate. *Opt Express*. 2013;21(22):26244-26260. doi: 10.1364/OE.21.026244.
12. Balena A, Bianco M, Pisanello F, *et al*. Recent advances on high-speed and holographic two-photon direct laser writing. *Adv Funct Mater*. 2023;33(39). doi: 10.1002/adfm.202211773.
13. Maruo S, Nakamura O, Kawata S. Three-dimensional microfabrication with two-photon-absorbed photopolymerization. *Opt Lett*. 1997;22(2):132-134. doi: 10.1364/OL.22.000132.
14. Langer R, Vacanti JP. Tissue engineering. *Science*. 1993;260(5110):920-926. doi: 10.1126/science.8493529.
15. Chan BP, Leong KW. Scaffolding in tissue engineering: general approaches and tissue-specific considerations. *Eur Spine J*. 2008;17(4):467-479. doi: 10.1007/s00586-008-0745-3.
16. Chung S, Ingle NP, Montero GA, *et al*. Bioresorbable elastomeric vascular tissue engineering scaffolds via melt spinning and electrospinning. *Acta Biomater*. 2010;6(6):1958-1967. doi: 10.1016/j.actbio.2009.12.007.
17. Liu X, Ma PX. Phase separation, pore structure, and properties of nanofibrous gelatin scaffolds. *Biomaterials*. 2009;30(25):4094-4103. doi: 10.1016/j.biomaterials.2009.04.024.
18. Sin D, Miao X, Liu G, *et al*. Polyurethane (PU) scaffolds prepared by solvent casting/particulate leaching (SCPL) combined with centrifugation. *Mater Sci Eng C*. 2010;30(1):78-85. doi: 10.1016/j.msec.2009.09.002.
19. Amensag S, McFetridge PS. Tuning scaffold mechanics by laminating native extracellular matrix membranes and effects on early cellular remodeling. *J Biomed Mater Res A*. 2014;102(5):1325-1333. doi: 10.1002/jbm.a.34791.
20. Li X, Lu W, Xu X, *et al*. Advanced optical methods and materials for fabricating 3D tissue scaffolds. *Light Adv Manuf*. 2022;3(3):1. doi: 10.37188/lam.2022.026.
21. Lee J-Y, An J, Chua CK. Fundamentals and applications of 3D printing for novel materials. *Appl Mater Today*. 2017;7:120-133. doi: 10.1016/j.apmt.2017.02.004.
22. Chia HN, Wu BM. Recent advances in 3D printing of biomaterials. *J Biol Eng*. 2015;9(1):4. doi: 10.1186/s13036-015-0001-4.
23. Zandrini T, Shan O, Parodi V, *et al*. Multi-foci laser microfabrication of 3D polymeric scaffolds for stem cell expansion in regenerative medicine. *Sci Rep*. 2019;9(1):11761. doi: 10.1038/s41598-019-48080-w.
24. Torgersen J, Qin X-H, Li Z, *et al*. Hydrogels for two-photon polymerization: a toolbox for mimicking the extracellular matrix. *Adv Funct Mater*. 2013;23(36):4542-4554. doi: 10.1002/adfm.201203880.

25. Ovsianikov A, Schlie S, Ngezahayo A, *et al*. Two-photon polymerization technique for microfabrication of CAD-designed 3D scaffolds from commercially available photosensitive materials. *J Tissue Eng Regen Med*. 2007;1(6):443-449.
doi: 10.1002/term.57.

26. Klein F, Striebel T, Fischer J, *et al*. Elastic fully three-dimensional microstructure scaffolds for cell force measurements. *Adv Mater*. 2010;22(8):868-871.
doi: 10.1002/adma.200902515.

27. Klein F, Richter B, Striebel T, *et al*. Two-component polymer scaffolds for controlled three-dimensional cell culture. *Adv Mater*. 2011;23(11):1341-1345.
doi: 10.1002/adma.201004060.

28. Ricci D, Nava MM, Zandrini T, *et al*. Scaling-up techniques for the nanofabrication of cell culture substrates via two-photon polymerization for industrial-scale expansion of stem cells. *Materials*. 2017;10(1):66.
doi: 10.3390/ma10010066.

29. Turunen S, Joki T, Hiltunen ML, *et al*. Direct laser writing of tubular microtowers for 3D culture of human pluripotent stem cell-derived neuronal cells. *ACS Appl Mater Interfaces*. 2017;9(31):25717-25730.
doi: 10.1021/acsami.7b05536.

30. Lemma ED, Spagnolo B, Rizzi F, *et al*. Microenvironmental stiffness of 3D polymeric structures to study invasive rates of cancer cells. *Adv Healthc Mater*. 2017;6(22):1700888.
doi: 10.1002/adhm.201700888.

31. Tudor A, Delaney C, Zhang H, *et al*. Fabrication of soft, stimulus-responsive structures with sub-micron resolution via two-photon polymerization of poly(ionic liquid)s. *Mater Today*. 2018;21(8):807-816.
doi: 10.1016/j.mattod.2018.07.017.

32. Marino A, Tricinci O, Battaglini M, *et al*. A 3D real-scale, biomimetic, and biohybrid model of the blood-brain barrier fabricated through two-photon lithography. *Small*. 2018;14(6).
doi: 10.1002/smll.201702959.

33. Fendler C, Denker C, Harberts J, *et al*. Microscaffolds by direct laser writing for neurite guidance leading to tailor-made neuronal networks. *Adv Biosyst*. 2019;3(5):1800329.
doi: 10.1002/adbi.201800329.

34. Akolawala Q, Rovituso M, Versteeg HH, *et al*. Evaluation of proton-induced DNA damage in 3D-engineered glioblastoma microenvironments. *ACS Appl Mater Interfaces*. 2022;14(18):20778-20789.
doi: 10.1021/acsami.2c03706.

35. Rengaraj A, Bosc L, Machillot P, *et al*. Engineering of a microscale niche for pancreatic tumor cells using bioactive film coatings combined with 3D-architectured scaffolds. *ACS Appl Mater Interfaces*. 2022;14(11):13107-13121.
doi: 10.1021/acsami.2c01747.

36. Costa BNL, Adao RMR, Maibohm C, *et al*. Cellular interaction of bone marrow mesenchymal stem cells with polymer and hydrogel 3D microscaffold templates. *ACS Appl Mater Interfaces*. 2022;14(11):13013-13024.
doi: 10.1021/acsami.1c23442.

37. Kaushik S, Hord AH, Denson DD, *et al*. Lack of pain associated with microfabricated microneedles. *Anesth. Analg*. 2001;92(2):502-504.
doi: 10.1213/00000539-200102000-00041.

38. Ovsianikov A, Chichkov B, Mente P, *et al*. Two photon polymerization of polymer–ceramic hybrid materials for transdermal drug delivery. *Int J Appl Ceram Technol*. 2007;4(1):22-29.
doi: 10.1111/j.1744-7402.2007.02115.x.

39. Prausnitz MR, Langer R, Transdermal drug delivery. *Nat Biotechnol*. 2008;26(11):1261-1268.
doi: 10.1038/nbt.1504.

40. Faraji Rad Z, Nordon RE, Anthony CJ, *et al*. High-fidelity replication of thermoplastic microneedles with open microfluidic channels. *Microsyst Nanoeng*. 2017;3(1):17034.
doi: 10.1038/micronano.2017.34.

41. Balmert SC, Carey CD, Falo GD, *et al*. Dissolving undercut microneedle arrays for multicomponent cutaneous vaccination. *J Controlled Release*. 2020;317:336-346.
doi: 10.1016/j.jconrel.2019.11.023.

42. Li J, Thiele S, Quirk BC, *et al*. Ultrathin monolithic 3D printed optical coherence tomography endoscopy for preclinical and clinical use. *Light Sci Appl*. 2020;9(1):124.
doi: 10.1038/s41377-020-00365-w.

43. Lee S, Kim JY, Kim J, *et al*. A needle-type microrobot for targeted drug delivery by affixing to a microtissue. *Adv Healthc Mater*. 2020;9(7):e1901697.
doi: 10.1002/adhm.201901697.

44. Yang T, Si T, Wu Y, *et al*. Breaking the limitation of laminar flow in thrombolytic therapy with reconfigurable vortex-like nanobot swarms. *Angew Chem Int Ed*. 2025;64(17):e202425189.
doi: 10.1002/anie.202425189.

45. Wrede P, Remlova E, Chen Y, *et al*. Synergistic integration of materials in medical microrobots for advanced imaging and actuation. *Nat Rev Mater*. 2025.
doi: 10.1038/s41578-025-00811-4.

46. Ren L, Nama N, McNeill JM, *et al*. 3D steerable, acoustically powered microswimmers for single-particle manipulation. *Sci Adv*. 2019;5(10):eaax3084.
doi: 10.1126/sciadv.aax3084.

47. Li D, Liu Y, Yang Y, *et al*. A fast and powerful swimming microrobot with a serrated tail enhanced propulsion interface. *Nanoscale*. 2018;10(42):19673-19677.
doi: 10.1039/c8nr04907f.

48. Huang T-Y, Huang H-W, Jin DD, *et al*. Four-dimensional micro-building blocks. *Sci Adv*. 2020;6(3):eaav8219.

doi: 10.1126/sciadv.aav8219.

49. Han H, Ma X, Deng W, *et al*. Imaging-guided bioresorbable acoustic hydrogel microrobots. *Sci Robot*. 2024;9(97):eadp3593. doi: 10.1126/scirobotics.adp3593.

50. Papanikolaou EG, D'Haeseleer E, Verheyen G, *et al*. Live birth rate is significantly higher after blastocyst transfer than after cleavage-stage embryo transfer when at least four embryos are available on day 3 of embryo culture. A randomized prospective study. *Hum. Reprod*. 2005;20(11):3198-203. doi: 10.1093/humrep/dei217.

51. Medina-Sanchez M, Schwarz L, Meyer AK, *et al*. Cellular cargo delivery: toward assisted fertilization by sperm-carrying micromotors. *Nano Lett*. 2016;16(1):555-561. doi: 10.1021/acs.nanolett.5b04221.

52. Fan J, Ren S, Han B, *et al*. Magnetic fiber robots with multiscale functional structures at the distal end. *Adv Funct Mater*. 2023;34(12). doi: 10.1002/adfm.202309424.

53. Wang X, Qin XH, Hu C, *et al*. 3D printed enzymatically biodegradable soft helical microswimmers. *Adv Funct Mater*. 2018;28(45):1804107. doi: 10.1002/adfm.201804107.

54. Ceylan H, Yasa IC, Yasa O, *et al*. 3D-printed biodegradable microswimmer for theranostic cargo delivery and release. *ACS Nano*. 2019;13(3):3353-3362. doi: 10.1021/acsnano.8b09233.

55. Oellers M, Lucklum F, Vellekoop MJ. On-chip mixing of liquids with swap structures written by two-photon polymerization. *Microfluid Nanofluidics*. 2019;24(1):4. doi: 10.1007/s10404-019-2309-8.

56. Lölsberg J, Linkhorst J, Cinar A, *et al*. 3D nanofabrication inside rapid prototyped microfluidic channels showcased by wet-spinning of single micrometre fibres. *Lab Chip*. 2018;18(9):1341-1348. doi: 10.1039/C7LC01366C.

57. Jiménez-Zenteno AK, Estève A, Cayron H, *et al*. A novel 3D microdevice for the in vivo capture of cancer-associated cells. *Med Devices Sens*. 2019;2(5–6):e10056. doi: 10.1002/mds3.10056.

58. Lao Z, Zheng Y, Dai Y, *et al*. Nanogap plasmonic structures fabricated by switchable capillary-force driven self-assembly for localized sensing of anticancer medicines with microfluidic SERS. *Adv Funct Mater*. 2020;30(15): 1909467. doi: 10.1002/adfm.201909467.

59. Erfle P, Riewe J, Bunjes H, *et al*. Goodbye fouling: a unique coaxial lamination mixer (CLM) enabled by two-photon polymerization for the stable production of monodisperse drug carrier nanoparticles. *Lab Chip*. 2021;21(11): 2178-2193. doi: 10.1039/D1LC00047K.

60. Michas C, Karakan MÇ, Nautiyal P, *et al*. Engineering a living cardiac pump on a chip using high-precision fabrication. *Sci Adv*. 2022;8(16):eabm3791. doi: 10.1126/sciadv.abm3791.

61. Pearre BW, Michas C, Tsang JM, *et al*. Fast micron-scale 3D printing with a resonant-scanning two-photon microscope. *Addit Manuf*. 2019;30:100887. doi: 10.1016/j.addma.2019.100887.

62. Kuroiwa Y, Takeshima N, Narita Y, *et al*. Arbitrary micropatterning method in femtosecond laser microprocessing using diffractive optical elements. *Opt Express*. 2004;12(9):1908-1915. doi: 10.1364/OPEX.12.001908.

63. Hasegawa S, Hayasaki Y, Nishida N. Holographic femtosecond laser processing with multiplexed phase Fresnel lenses. *Opt Lett*. 2006;31(11):1705-1707. doi: 10.1364/OL.31.001705.

64. Yamaji M, Kawashima H, Suzuki Ji, *et al*. Three dimensional micromachining inside a transparent material by single pulse femtosecond laser through a hologram. *Appl Phys Lett*. 2008;93(4):041116. doi: 10.1063/1.2965451.

65. Wang X, Fan X, Liu Y, *et al*. 3D nanolithography via holographic multi-focus metalens. *Laser Photonics Rev*. 2024;18(11). doi: 10.1002/lpor.202400181.

66. Kato J-i, Takeyasu N, Adachi Y, *et al*. Multiple-spot parallel processing for laser micronanofabrication. *Appl Phys Lett*. 2005;86(4):044102. doi: 10.1063/1.1855404.

67. Jesacher A, Booth MJ. Parallel direct laser writing in three dimensions with spatially dependent aberration correction. *Opt Express*. 2010;18(20):21090-21099. doi: 10.1364/OE.18.021090.

68. Dong X-Z, Zhao Z-S, Duan X-M. Micronanofabrication of assembled three-dimensional microstructures by designable multiple beams multiphoton processing. *Appl Phys Lett*. 2007;91(12):124103. doi: 10.1063/1.2789661.

69. Hahn V, Kiefer P, Frenzel T, *et al*. Rapid assembly of small materials building blocks (voxels) into large functional 3D metamaterials. *Adv Funct Mater*. 2020;30(26):1907795. doi: 10.1002/adfm.201907795.

70. Kiefer P, Hahn V, Kalt S, *et al*. A multi-photon (7 × 7)-focus 3D laser printer based on a 3D-printed diffractive optical element and a 3D-printed multi-lens array. *Light Adv Manuf*. 2024;4(1):28-41. doi: 10.37188/lam.2024.003.

71. Ježek J, Čižmár T, Neděla V, *et al*. Formation of long and thin polymer fiber using nondiffracting beam. *Opt Express*. 2006;14(19):8506-8515. doi: 10.1364/OE.14.008506.

72. Stankevicius E, Gertus T, Rutkauskas M, *et al*. Fabrication of micro-tube arrays in photopolymer SZ2080 by using three different methods of a direct laser polymerization technique. *J Micromech Microeng*. 2012;22(6):065022. doi: 10.1088/0960-1317/22/6/065022.

73. Zhang C, Hu Y, Li J, *et al*. A rapid two-photon fabrication of tube array using an annular Fresnel lens. *Opt Express*. 2014;22(4):3983-3990. doi: 10.1364/OE.22.003983.

74. Zhang S-J, Li Y, Liu Z-P, *et al*. Two-photon polymerization of a three dimensional structure using beams with orbital angular momentum. *Appl Phys Lett*. 2014;105(6):061101. doi: 10.1063/1.4893007.

75. Pan D, Liu S, Ji S, *et al*. Efficient fabrication of a high-aspect-ratio AFM tip by one-step exposure of a long focal depth holographic femtosecond axilens beam. *Opt Lett*. 2020;45(4):897-900. doi: 10.1364/OL.384249.

76. Wang C, Rao R, Cai Z, *et al*. Microclaw array fabricated by single exposure of femtosecond airy beam and self-assembly for regulating cell migratory plasticity. *ACS Nano*. 2023;17(10):9025-9038. doi: 10.1021/acsnano.2c11577.

77. Wang C, Yang L, Hu Y, *et al*. Femtosecond Mathieu beams for rapid controllable fabrication of complex microcages and application in trapping microobjects. *ACS Nano*. 2019;13(4):4667-4676. doi: 10.1021/acsnano.9b00893.

78. Dorrah AH, Bordoloi P, de Angelis VS, *et al*. Light sheets for continuous-depth holography and three-dimensional volumetric displays. *Nat Photonics*. 2023;17(5):427-434. doi: 10.1038/s41566-023-01188-y.

79. Kelemen L, Valkai S, Ormos P. Parallel photopolymerisation with complex light patterns generated by diffractive optical elements. *Opt Express*. 2007;15(22):14488-14497. doi: 10.1364/OE.15.014488.

80. Yang L, El-Tamer A, Hinze U, *et al*. Parallel direct laser writing of micro-optical and photonic structures using spatial light modulator. *Opt Lasers Eng*. 2015;70:26-32. doi: 10.1016/j.optlaseng.2015.02.006.

81. Zhang L, Wang C, Zhang C, *et al*. High-throughput two-photon 3D printing enabled by holographic multi-foci high-speed scanning. *Nano Lett*. 2024;24(8):2671-2679. doi: 10.1021/acs.nanolett.4c00505.

82. Yang L, Qian D, Xin C, *et al*. Two-photon polymerization of microstructures by a non-diffraction multifoci pattern generated from a superposed Bessel beam. *Opt Lett*. 2017;42(4):743-746. doi: 10.1364/OL.42.000743.

83. Manousidaki M, Papazoglou DG, Farsari M, *et al*. 3D holographic light shaping for advanced multiphoton polymerization. *Opt Lett*. 2020;45(1):85-88. doi: 10.1364/OL.45.000085.

84. Zhang L, Liu B, Wang C, *et al*. Functional shape-morphing microarchitectures fabricated by dynamic holographically shifted femtosecond multifoci. *Nano Lett*. 2022;22(13):5277-5286. doi: 10.1021/acs.nanolett.2c01178.

85. Dudley D, Duncan W, Slaughter J. Emerging digital micromirror device (DMD) applications. Proceedings of SPIE; 2003:4985. doi: 10.1117/12.480761.

86. Cheng J, Gu C, Zhang D, *et al*. High-speed femtosecond laser beam shaping based on binary holography using a digital micromirror device. *Opt Lett*. 2015;40(21):4875-4878. doi: 10.1364/OL.40.004875.

87. Cheng J, Gu C, Zhang D, *et al*. Ultrafast axial scanning for two-photon microscopy via a digital micromirror device and binary holography. *Opt Lett*. 2016;41(7):1451-1454. doi: 10.1364/OL.41.001451.

88. Gu C, Zhang D, Chang Y, *et al*. Digital micromirror device-based ultrafast pulse shaping for femtosecond laser. *Opt Lett*. 2015;40(12):2870-2873. doi: 10.1364/OL.40.002870.

89. Geng Q, Gu C, Cheng J, *et al*. Digital micromirror device-based two-photon microscopy for three-dimensional and random-access imaging. *Optica*. 2017;4(6):674-677. doi: 10.1364/OPTICA.4.000674.

90. Geng Q, Wang D, Chen P, *et al*. Ultrafast multi-focus 3-D nano-fabrication based on two-photon polymerization. *Nat Commun*. 2019;10(1):2179. doi: 10.1038/s41467-019-10249-2.

91. Ouyang W, Xu X, Lu W, *et al*. Ultrafast 3D nanofabrication via digital holography. *Nat Commun*. 2023;14(1):1716. doi: 10.1038/s41467-023-37163-y.

92. Jiao BJ, Chen F, Liu Y, *et al*. Acousto-optic scanning spatial-switching multiphoton lithography. *Int J Extreme Manuf*. 2023;5(3):035008. doi: 10.1088/2631-7990/ace0a7.

93. Yang L, Li J, Hu Y, *et al*. Projection two-photon polymerization using a spatial light modulator. *Opt Commun*. 2014;331:82-86. doi: 10.1016/j.optcom.2014.05.051.

94. Zhang C, Hu Y, Li J, *et al*. An improved multi-exposure approach for high quality holographic femtosecond laser patterning. *Appl Phys Lett*. 2014;105(22):221104. doi: 10.1063/1.4902925.

95. Zhang C, Hu Y, Du W, *et al*. Optimized holographic femtosecond laser patterning method towards rapid integration of high-quality functional devices in microchannels. *Sci Rep*. 2016;6(1):33281. doi: 10.1038/srep33281.

96. Kaehr B, Shear JB. Multiphoton fabrication of chemically responsive protein hydrogels for microactuation. *Proc Natl Acad Sci*. 2008;105(26):8850-8854. doi: 10.1073/pnas.0709571105.

97. Kaehr B, Shear JB. Mask-directed multiphoton lithography. *J Am Chem Soc*. 2007;129(7):1904-1905. doi: 10.1021/ja068390y.

98. Kaehr B, Shear JB. High-throughput design of microfluidics based on directed bacterial motility. *Lab Chip*. 2009;9(18):2632-2637. doi: 10.1039/B908119D.

99. Yih J-N, Hu YY, Sie YD, *et al*. Temporal focusing-based multiphoton excitation microscopy via digital micromirror device. *Opt Lett*. 2014;39(11):3134-3137. doi: 10.1364/OL.39.003134.

100. Mills B, Grant-Jacob JA, Feinaeugle M, *et al*. Single-pulse multiphoton polymerization of complex structures using a digital multimirror device. *Opt Express*. 2013;21(12):14853-14858. doi: 10.1364/OE.21.014853.

101. Saha SK, Wang D, Nguyen VH, *et al*. Scalable submicrometer additive manufacturing. *Science*. 2019;366(6461): 105-109. doi: 10.1126/science.aax8760.

102. Somers P, Liang Z, Johnson JE, *et al*. Rapid, continuous projection multi-photon 3D printing enabled by spatiotemporal focusing of femtosecond pulses. *Light Sci Appl*. 2021;10(1):199. doi: 10.1038/s41377-021-00645-z.

103. Tan D, Li Y, Qi F, *et al*. Reduction in feature size of two-photon polymerization using SCR500. *Appl Phys Lett*. 2007;90(7):071106. doi: 10.1063/1.2535504.

104. Scott TF, Kowalski BA, Sullivan AC, *et al*. Two-color single-photon photoinitiation and photoinhibition for subdiffraction photolithography. *Science*. 2009;324(5929):913-917. doi: 10.1126/science.1167610.

105. Fischer J, Wegener M. Three-dimensional optical laser lithography beyond the diffraction limit. *Laser Photonics Rev*. 2013;7(1):22-44. doi: 10.1002/lpor.201100046.

106. Baldacchini T, Zimmerley M, Kuo CH, *et al*. Characterization of microstructures fabricated by two-photon polymerization using coherent anti-stokes Raman scattering microscopy. *J Phys Chem B*. 2009;113(38):12663-12668. doi: 10.1021/jp9058998.

107. Cicha K, Li Z, Stadlmann K, *et al*. Evaluation of 3D structures fabricated with two-photon-photopolymerization by using FTIR spectroscopy. *J Appl Phys*. 2011;110(6):064911. doi: 10.1063/1.3639304.

108. Jiang LJ, Zhou YS, Xiong W, *et al*. Two-photon polymerization: investigation of chemical and mechanical properties of resins using Raman microspectroscopy. *Opt Lett*. 2014;39(10):3034-3037. doi: 10.1364/OL.39.003034.

109. Sedghamiz E, Liu M, Wenzel W. Challenges and limits of mechanical stability in 3D direct laser writing. *Nat Commun*. 2022;13(1):2115. doi: 10.1038/s41467-022-29749-9.

110. Li Y, Qi FJ, Yang HH, *et al*. Nonuniform shrinkage and stretching of polymerized nanostructures fabricated by two-photon photopolymerization. *Nanotechnology*. 2008;19(5):055303. doi: 10.1088/0957-4484/19/05/055303.

111. Wen X, Zhang B, Wang W, *et al*. 3D-printed silica with nanoscale resolution. *Nat Mater*. 2021;20(11): 1506-1511. doi: 10.1038/s41563-021-01111-2.

112. Maruo S, Hasegawa T, Yoshimura N. Single-anchor support and supercritical CO2 drying enable high-precision microfabrication of three-dimensional structures. *Opt Express*. 2009;17(23):20945-20951. doi: 10.1364/OE.17.020945.

113. Ovsianikov A, Shizhou X, Farsari M, *et al*. Shrinkage of microstructures produced by two-photon polymerization of Zr-based hybrid photosensitive materials. *Opt Express*. 2009;17(4):2143-2148. doi: 10.1364/OE.17.002143.

114. Liu Y, Wang H, Ho J, *et al*. Structural color three-dimensional printing by shrinking photonic crystals. *Nat Commun*. 2019;10(1):4340. doi: 10.1038/s41467-019-12360-w.

115. Haske W, Chen VW, Hales JM, *et al*. 65 nm feature sizes using visible wavelength 3-D multiphoton lithography. *Opt Express*. 2007;15(6):3426-3436. doi: 10.1364/OE.15.003426.

116. Liu YH, Zhao YY, Jin F, *et al*. Lambda/12 super resolution achieved in maskless optical projection nanolithography for efficient cross-scale patterning. *Nano Lett*. 2021;21(9):3915-3921. doi: 10.1021/acs.nanolett.1c00559.

117. Hao X, Li Y, Fu S, *et al*. Review of 4Pi fluorescence nanoscopy. *Engineering*. 2022;11:146-153. doi: 10.1016/j.eng.2020.07.028.

118. Hell S, Stelzer EHK. Properties of a 4Pi confocal fluorescence microscope. *J Opt Soc Am A*. 1992;9(12):2159-2166. doi: 10.1364/JOSAA.9.002159.

119. Tičkūnas T, Paipulas D, Purlys V. 4Pi multiphoton polymerization. *Appl Phys Lett*. 2020;116(3):031101. doi: 10.1063/1.5128786.

120. Strickland D, Mourou G. Compression of amplified chirped optical pulses. *Opt Commun*. 1985;55(6):447-449. doi: 10.1016/0030-4018(85)90151-8.

121. Zhu G, Howe Jv, Durst M, *et al*. Simultaneous spatial and temporal focusing of femtosecond pulses. *Opt Express*. 2005;13(6):2153-2159. doi: 10.1364/OPEX.13.002153.

122. Papagiakoumou E, de Sars V, Oron D, *et al*. Patterned two-photon illumination by spatiotemporal shaping of ultrashort pulses. *Opt Express*. 2008;16(26):22039-22047. doi: 10.1364/OE.16.022039.

123. He F, Xu H, Cheng Y, *et al*. Fabrication of microfluidic channels with a circular cross section using spatiotemporally focused femtosecond laser pulses. *Opt Lett*. 2010;35(7):1106-1108. doi: 10.1364/OL.35.001106.

124. Vitek DN, Adams DE, Johnson A, *et al*. Temporally focused femtosecond laser pulses for low numerical aperture micromachining through optically transparent materials. *Opt Express*. 2010;18(17):18086-18094. doi: 10.1364/OE.18.018086.

125. Chu W, Tan Y, Wang P, *et al*. Centimeter-height 3D printing with femtosecond laser two-photon polymerization. *Adv Mater Technol*. 2018;3(5):1700396. doi: 10.1002/admt.201700396.

126. Kim D, So PTC. High-throughput three-dimensional lithographic microfabrication. *Opt Lett*. 2010;35(10):1602-1604. doi: 10.1364/ol.35.001602.

127. Li YC, Cheng LC, Chang CY, *et al*. Fast multiphoton microfabrication of freeform polymer microstructures by spatiotemporal focusing and patterned excitation. *Opt Express*. 2012;20(17):19030-19038. doi: 10.1364/oe.20.019030.

128. Gu C, Zhang D, Wang D, *et al*. Parallel femtosecond laser light sheet micro-manufacturing based on temporal focusing. *Precis Eng*. 2017;50:198-203. doi: 10.1016/j.precisioneng.2017.05.006.

129. Wang D, Wen C, Chang Y, *et al*. Ultrafast laser-enabled 3D metal printing: a solution to fabricate arbitrary submicron metal structures. *Precis. Eng*. 2018;52:106-111. doi: 10.1016/j.precisioneng.2017.11.015.

130. Han F, Gu S, Klimas A, *et al*. Three-dimensional nanofabrication via ultrafast laser patterning and kinetically regulated material assembly. *Science*. 2022;378(6626):1325-1331. doi: 10.1126/science.abm8420.

131. Saha SK, Chen S-C. Comment on "Rapid Assembly of Small Materials Building Blocks (Voxels) into Large Functional 3D Metamaterials". *Adv Funct Mater*. 2020;30(30):2001060. doi: 10.1002/adfm.202001060.

132. Kim H, Pingali R, Saha SK. Rapid printing of nanoporous 3D structures by overcoming the proximity effects in projection two-photon lithography. *Virtual Phys Prototyp*. 2023;18(1):e2230979. doi: 10.1080/17452759.2023.2230979.

133. Johnson JE, Jamil IR, Pan L, *et al*. Bayesian optimization with Gaussian-process-based active machine learning for improvement of geometric accuracy in projection multi-photon 3D printing. *Light Sci Appl*. 2025;14(1):56. doi: 10.1038/s41377-024-01707-8.

134. Fu Y, Wang B, Wei J, *et al*. Single-step and parallel high-speed fabrication for Au micro-/nanostructures. *Opt Lett*. 2024;49(21):6001-6004. doi: 10.1364/ol.539524.

135. Fu Y, Li N, Ding X, *et al*. Medium-assisted scalable printing of LIPSS via femtosecond laser projection manufacturing. *Opt Lett*. 2025;50(3):844-847. doi.: 10.1364/OL.549389.

136. Hell SW. Far-field optical nanoscopy. *Science*. 2007;316(5828):1153-1158. doi: 10.1126/science.1137395.

137. Wildanger D, Patton BR, Schill H, *et al*. Solid immersion facilitates fluorescence microscopy with nanometer resolution and sub-ångström emitter localization. *Adv Mater*. 2012;24(44):OP309-OP313. doi: 10.1002/adma.201203033.

138. Liaros N, Fourkas JT. Ten years of two-color photolithography. Invited. *Opt Mater Express*. 2019;9(7):3006. doi: 10.1364/ome.9.003006.

139. Fischer J, von Freymann G, Wegener M. The materials challenge in diffraction-unlimited direct-laser-writing optical lithography. *Adv Mater*. 2010;22(32):3578-3582. doi: 10.1002/adma.201000892.

140. Li L, Gattass RR, Gershgoren E, *et al*. Achieving λ/20 resolution by one-color initiation and deactivation of polymerization. *Science*. 2009;324(5929):910-913. doi: 10.1126/science.1168996.

141. He M, Zhang Z, Cao C, *et al*. 3D sub-diffraction printing by multicolor photoinhibition lithography: from optics to chemistry. *Laser Photonics Rev*. 2022;16(2):2100229. doi: 10.1002/lpor.202100229.

142. Fischer J, Ergin T, Wegener M. Three-dimensional polarization-independent visible-frequency carpet invisibility cloak. *Opt Lett*. 2011;36(11):2059-2061. doi: 10.1364/ol.36.002059.

143. Fischer J, Wegener M. Three-dimensional direct laser writing inspired by stimulated-emission-depletion microscopy. Invited. *Opt Mater Express*. 2011;1(4):614-624. doi: 10.1364/OME.1.000614.

144. Wolf TJA, Fischer J, Wegener M, *et al*. Pump-probe spectroscopy on photoinitiators for stimulated-emission-depletion optical lithography. *Opt Lett*. 2011;36(16):3188-3190. doi: 10.1364/OL.36.003188.

145. Wollhofen R, Katzmann J, Hrelescu C, *et al*. 120 nm resolution and 55 nm structure size in STED-lithography. *Opt Express*. 2013;21(9):10831-10840. doi: 10.1364/OE.21.010831.

146. Fischer J, Mueller JB, Quick AS, *et al*. Exploring the mechanisms in STED-enhanced direct laser writing. *Adv. Opt. Mater.* 2015;3(2):221-232. doi: 10.1002/adom.201400413.

147. Zhu D, Xu L, Ding C, *et al*. Direct laser writing breaking diffraction barrier based on two-focus parallel peripheral-photoinhibition lithography. *Adv Photonics*. 2022;4(6):066002. doi: 10.1117/1.AP.4.6.066002.

148. He M, Zhang Z, Cao C, *et al*. Single-color peripheral photoinhibition lithography of nanophotonic structures. *PhotoniX*. 2022;3(1):25. doi: 10.1186/s43074-022-00072-2.

149. Ding C, Liu X, Liu Q, *et al*. Subdiffraction 3D nanolithography by two-photon two-step absorption and photoinhibition. *Laser Photonics Rev*. 2023;18(3):2300645. doi: 10.1002/lpor.202300645.

150. Fischer J, Wegener M. Ultrafast polymerization inhibition by stimulated emission depletion for three-dimensional nanolithography. *Adv Mater*. 2012;24(10):OP65-OP69. doi: 10.1002/adma.201103758.

151. Donnert G, Keller J, Medda R, *et al*. Macromolecular-scale resolution in biological fluorescence microscopy. *Proc Natl Acad Sci*. 2006;103(31):11440-11445. doi: 10.1073/pnas.0604965103.

152. Harke B, Bianchini P, Brandi F, *et al*. Photopolymerization inhibition dynamics for sub-diffraction direct laser writing lithography. *Chemphyschem*. 2012;13(6):1429-1434. doi: 10.1002/cphc.201200006.

153. Harke B, Dallari W, Grancini G, *et al*. Polymerization inhibition by triplet state absorption for nanoscale lithography. *Adv Mater*. 2013;25(6):904-909. doi: 10.1002/adma.201204141.

154. Thiel M, Ott J, Radke A, *et al*. Dip-in depletion optical lithography of three-dimensional chiral polarizers. *Opt Lett*. 2013,38(20):4252-4255. doi: 10.1364/OL.38.004252.

155. Somers P, Liang Z, Chi T, *et al*. Photo-activated polymerization inhibition process in photoinitiator systems for high-throughput 3D nanoprinting. *Nanophotonics*. 2023;12(8):1571-1580. doi: 10.1515/nanoph-2022-0611.

156. Stocker MP, Li L, Gattass RR, *et al*. Multiphoton photoresists giving nanoscale resolution that is inversely dependent on exposure time. *Nat Chem*. 2011;3(3):223-227. doi: 10.1038/nchem.965.

157. Liaros N, Tomova Z, Razo SAG, *et al*. The state of the art in multicolor visible photolithography. *Proceedings Novel Patterning Technologies*. 2018;10584:26-32, doi: 10.1117/12.2297653

158. Mueller P, Zieger MM, Richter B, *et al*. Molecular switch for sub-diffraction laser lithography by photoenol intermediate-state cis-trans isomerization. *ACS Nano*. 2017;11(6):6396-6403. doi: 10.1021/acsnano.7b02820.

159. Müller P, Müller R, Hammer L, *et al*. STED-inspired laser lithography based on photoswitchable spirothiopyran moieties. *Chem Mater*. 2019;31(6):1966-1972. doi: 10.1021/acs.chemmater.8b04696.

160. Andrew TL, Tsai HY, Menon R. Confining light to deep subwavelength dimensions to enable optical nanopatterning. *Science*. 2009;324(5929):917-921. doi: 10.1126/science.1167704.

161. Cao Y, Gan Z, Jia B, *et al*. High-photosensitive resin for super-resolution direct-laser-writing based on photoinhibited polymerization. *Opt Express*. 2011;19(20):19486-19494. doi: 10.1364/OE.19.019486.

162. Gan Z, Cao Y, Evans RA, *et al*. Three-dimensional deep sub-diffraction optical beam lithography with 9 nm feature size. *Nat Commun*. 2013;4(1):2061. doi: 10.1038/ncomms3061.

163. Guan L, Cao C, Liu X, *et al*. Light and matter co-confined multi-photon lithography. *Nat Commun*. 2024;15(1):2387. doi: 10.1038/s41467-024-46743-5.

164. Zvagelsky R, Mayer F, Beutel D, *et al*. Towards in-situ diagnostics of multi-photon 3D laser printing using optical coherence tomography. *Light Adv Manuf*. 2022;3(3):1. doi: 10.37188/lam.2022.039.

165. He Y, Shao Q, Chen S-C, *et al*. Characterization of two-photon photopolymerization fabrication using high-speed optical diffraction tomography. *Addit Manuf*. 2022;60:103293. doi: 10.1016/j.addma.2022.103293.

166. Wang H, Liu S, Yin X, *et al*. Polar-coordinate line-projection light-curing continuous 3D printing for tubular structures. *Int J Extreme Manuf*. 2024;6(4):045004. doi: 10.1088/2631-7990/ad3c7f.

167. Wang H, Gao F, Shi Y, *et al*. Sparse-view irradiation processing volumetric additive manufacturing. *Int J Extreme Manuf*. 2025;7(6):065001. doi: 10.1088/2631-7990/adebbf.

168. Hu N, Ding L, Wang A, *et al*. Comprehensive modeling of corkscrew motion in micro-/nano-robots with general helical structures. *Nat Commun*. 2024;15(1):7399. doi: 10.1038/s41467-024-51518-z

169. Johnson JE, Chen Y, Xu X. Model for polymerization and self-deactivation in two-photon nanolithography. *Opt Express*. 2022;30(15):26824. doi: 10.1364/oe.461969.

170. Pingali R, Saha SK. Reaction-diffusion modeling of photopolymerization during femtosecond projection two-photon lithography. *J Manuf Sci Eng*. 2021;144(2):021011. doi: 10.1115/1.4051830.

ACCSCIENCE PUBLISHING

International Journal of Bioprinting

RESEARCH ARTICLE

Three-dimensional-printed hydrogel scaffolds with neuregulin-1 sustained-release microspheres for enhanced dedifferentiation and myelin regeneration in peripheral nerve injury

Guanhua Zhang[1†], Enpeng Song[2†], Peng Yu[1†], Jie Wei[3], Yaqiong Wang[4*], Jie Liu[5*], and Hou Bo[2*]

[1]Department of Cerebrovascular Surgery, The Third Affiliated Hospital of Sun Yat-sen University, Guangzhou, Guangdong, China

[2]Department of Neurosurgery, Lingnan Hospital, The Third Affiliated Hospital of Sun Yat-sen University, Guangzhou, Guangdong, China

[3]Department of Pediatrics, School of Pediatrics, Guangzhou Medical University, Guangzhou, Guangdong, China

[4]Department of Electron Microscopy, Zhongshan School of Medicine, Sun Yat-sen University, Guangzhou, Guangdong, China

[5]Department of Neurosurgery, Hezhou People's Hospital, Guangxi, China

[†]These authors contributed equally to this work.

***Corresponding authors:**
Yaqiong Wang
(wangyaq2@mail.sysu.edu.cn)

Jie Liu
(liuj616@163.com)

Hou Bo
(houb@mail.sysu.edu.cn)

Citation: Zhang G, Song E, Yu P, *et al.* Three-dimensional-printed hydrogel scaffolds with neuregulin-1 sustained-release microspheres for enhanced dedifferentiation and myelin regeneration in peripheral nerve injury. *Int J Bioprint.* 2025;11(5):154-177. doi: 10.36922/IJB025170168

Received: April 26, 2025
1st revised: May 31, 2025
2nd revised: June 11, 2025
Accepted: June 16, 2025
Published Online: June 16, 2025

Copyright: © 2025 Author(s). This is an Open Access article distributed under the terms of the Creative Commons Attribution License, permitting distribution, and reproduction in any medium, provided the original work is properly cited.

Publisher's Note: AccScience Publishing remains neutral with regard to jurisdictional claims in published maps and institutional affiliations.

Abstract

Remyelination is critical for functional recovery following peripheral nerve injury. Although autologous Schwann cell transplantation promotes effective myelin repair, its clinical translation remains limited due to donor scarcity and associated morbidity. Bone marrow-derived Schwann-like cells (B-dSCs) offer a promising alternative; however, their limited dedifferentiation capacity significantly constrains therapeutic outcomes. Neuregulin-1 (NRG1), a key axonal signal, effectively induces Schwann cell dedifferentiation but requires precise, sustained delivery to exert optimal effects. Here, we developed a three-dimensional (3D)-printed hydrogel scaffold incorporating NRG1-loaded sustained-release microspheres to achieve localized, prolonged NRG1 delivery. *In vitro* studies demonstrated that NRG1 significantly enhanced the dedifferentiation and remyelination capacity of B-dSCs in a dorsal root ganglion co-culture system. Mechanistically, NRG1 promoted dedifferentiation by activating the c-Jun N-terminal kinase (JNK) signaling pathway—a pivotal regulator of Schwann cell plasticity. Pharmacological inhibition of JNK markedly suppressed NRG1-induced dedifferentiation and downregulated myelin-associated gene expression, confirming pathway specificity. Furthermore, the 3D-printed scaffold effectively maintained uniform NRG1 distribution, facilitating enhanced axonal regeneration and improved myelin integrity. Collectively, these findings highlight the essential role of JNK signaling in NRG1-driven Schwann cell dedifferentiation and underscore the therapeutic promise of combining sustained-release systems with engineered cell therapies to advance peripheral nerve repair.

Keywords: C-Jun N-terminal kinase pathway; Dedifferentiation; Neuregulin-1; Peripheral nerve injury; Schwann cells; Sustained-release microspheres

1. Introduction

Peripheral nerve injury (PNI) is a major global health issue, and successful remyelination is critical for functional nerve repair.[1,2] Autologous Schwann cell (ASC) transplantation has shown considerable promise in enhancing myelin regeneration[3,4]; however, harvesting ASCs from functional nerves often leads to significant donor-site morbidity.[5] To address this challenge, Schwann-like cells derived from bone marrow mesenchymal stem cells (BMSCs), termed bone marrow-derived Schwann-like cells (B-dSCs), have emerged as a promising alternative.[6] Although these cells share key functional properties with ASCs and are more accessible, our previous studies identified a critical limitation: B-dSCs exhibit insufficient dedifferentiation capacity, leading to suboptimal *in vivo* myelination compared to ASCs.[7] Therefore, strategies to enhance B-dSC dedifferentiation are urgently needed to fully harness their therapeutic potential.

Dedifferentiation refers to the phenotypic reversion of Schwann cells to a "repair" state in response to injury-induced signals following PNI.[8,9] This transition is characterized by cytoskeletal remodeling, the adoption of bipolar or multipolar morphologies, and the reacquisition of high motility and neurotrophic factor secretion.[10] Given that dedifferentiation is essential for initiating remyelination, impaired dedifferentiation significantly hampers nerve regeneration.[11,12] Current strategies aimed at promoting Schwann cell dedifferentiation include chemical stimulation, gene editing, and the use of bioactive molecules such as tumor necrosis factor (TNF), interleukins (ILs), and neuregulin-1 (NRG1).[13–15] However, chemical and genetic approaches often lack specificity or raise safety concerns, while TNF and ILs primarily activate inflammatory or apoptotic pathways, potentially causing adverse effects.[16–21]

In contrast, NRG1, an endogenous nervous system protein, offers excellent biocompatibility and a strong affinity for Schwann cells.[22,23] After nerve injury, NRG1 critically orchestrates Schwann cell dedifferentiation via activation of the mitogen-activated protein kinase signaling pathways, notably through the v-erb-b2 avian erythroblastic leukemia viral oncogene homolog 2/3 receptors, leading to downstream activation of c-Jun N-terminal kinase (JNK), a central regulator of Schwann cell plasticity.[24–26] Activation of JNK promotes Schwann cell transition into the repair phenotype by inhibiting myelin-related gene expression and upregulating dedifferentiation markers such as c-Jun.[27] *In vivo*, inhibition of the JNK pathway impairs the formation of repair Schwann cells, emphasizing the indispensable role of JNK signaling in demyelination-regeneration cycles.[28] Thus, sustained NRG1 delivery presents a promising mechanism to overcome intrinsic dedifferentiation limitations of B-dSCs through persistent JNK pathway activation.

Nevertheless, the protracted nature of nerve regeneration and the anatomical complexity necessitate sustained and localized delivery of NRG1 at the injury site. Current delivery strategies—including subcutaneous injections, engineered cell therapies, and biomaterial-based protein release—often fail to maintain optimal NRG1 concentrations over extended periods.[29–31] Although hydrogels and other biomaterials are widely used, they generally provide limited sustained-release capabilities.[32–35] Additionally, due to its inherent water solubility, NRG1 is prone to diffusion, enzymatic degradation, and rapid clearance.[36,37] In previous work, we encapsulated NRG1 within sustained-release microspheres (NRG1-SRMs) to prolong its release and improve stability.[38] However, traditional hydrogel matrices lack sufficient structural constraints, resulting in microsphere sedimentation and uneven NRG1 distribution.[39]

To address this limitation, we developed a composite gelatin/sodium alginate hydrogel system. Gelatin provides favorable biocompatibility and cell adhesion properties, while sodium alginate contributes mechanical stability and mild gelation capability. This material combination is ideally suited for precise three-dimensional (3D) printing, allowing for controlled scaffold architecture and uniform microsphere integration. Our previous work confirmed this hydrogel's capability for sustained bioactive factor release and tissue regeneration.[7]

Building upon this composite system, we utilized advanced 3D printing technology to fabricate highly organized, grid-like scaffolds composed of interconnected hydrogel fibers. This structural design allows for the physical entrapment of NRG1-SRMs within individual hydrogel fibers, effectively preventing microsphere aggregation and ensuring homogeneous NRG1 distribution throughout the scaffold.

In summary, this study investigates the hypothesis that embedding NRG1-SRMs within 3D-printed composite hydrogel scaffolds enhances B-dSC dedifferentiation and improves their *in vivo* myelination efficacy. Our findings offer novel mechanistic insights and propose advanced biomaterial strategies for improving therapeutic outcomes in peripheral nerve repair.

2. Materials and methods

2.1. Animals

Newborn Sprague–Dawley rats (3–5 days old; n=21) were used for the isolation of BMSCs, while adult female

Sprague–Dawley rats (weighing 180–200 g; *n*=90) were used to establish the PNI model and to isolate ASCs. All animals were housed under a 12-h light/dark cycle with *ad libitum* access to food and water and were acclimatized for at least 7 days prior to experimentation. The animals were obtained from the Laboratory Animal Center of the Sun Yat-sen University School of Medicine. All experimental procedures were approved by the Institutional Animal Care and Use Committee (IACUC) of Sun Yat-sen University and conducted in accordance with the Guide for the Care and Use of Laboratory Animals issued by the Chinese Institute of Health.

2.2. Preparation of neuregulin-1-loaded sustained-release microspheres

To prepare NRG1-SRMs, NRG1 (R1866r, EIAab Science, China), dextran (molecular weight 67 kDa; Sigma-Aldrich, USA), and polyethylene glycol (PEG; molecular weight 8000; Sigma-Aldrich, USA) were mixed at a mass ratio of 1:5:50. The mixture was stirred for 1 min and subsequently stored at −80°C for 12 h. It was then subjected to vacuum freeze-drying. The resulting lyophilized powder was washed with dichloromethane (Sigma-Aldrich, USA) and centrifuged. The supernatant, containing PEG, was collected, and the solvent was evaporated to obtain NRG1-loaded dextran microspheres.

These microspheres were suspended in 15% polylactic-co-glycolic acid (PLGA) dissolved in dichloromethane and subsequently emulsified in an aqueous solution containing 1% polyvinyl alcohol and 5% sodium chloride. The protein–dextran–PLGA emulsion was then solidified, hardened, freeze-dried, and stored for subsequent use as SRMs.

2.3. Evaluation of neuregulin-1-loaded sustained-release microspheres

2.3.1. Particle size distribution

The particle size distribution of NRG1-SRMs was measured using a laser diffraction particle size analyzer (LS-909, OMEC Instruments, China). Approximately 10 mg of dried microspheres were dispersed and analyzed in a quartz cuvette.

2.3.2. Encapsulation efficiency

To assess encapsulation efficiency, 10 mg of microspheres were dissolved in 10 mL of dichloromethane and centrifuged at 10,000 rpm for 5 min. The supernatant containing PLGA was discarded, and the NRG1-loaded core was resuspended in phosphate-buffered saline (PBS). The concentration of NRG1 was quantified using an enzyme-linked immunosorbent assay (ELISA) kit (RDR-NRG1-Ra-96T, Reddot Biotech, Canada). Encapsulation efficiency was calculated using the following formula:

$$\text{Encapsulation efficiency (\%)} = (Wa/Wt) \times 100 \quad \text{(I)}$$

where *Wa* is the actual weight of NRG1, and *Wt* is the theoretical loading. Each experiment was repeated five times.

2.3.3. In vitro release of neuregulin-1-loaded sustained-release microspheres

For *in vitro* release studies, 10 mg of NRG1-SRMs were suspended in 1 mL of PBS and incubated at 37°C under continuous agitation. At 2-day intervals, the entire volume of PBS was collected and replaced with an equal volume of fresh buffer. The concentration of NRG1 in the collected supernatants was quantified using an ELISA kit (KL-NRG1-Mu, KALANG, China). Each experiment was performed in quintuplicate.

2.3.4. Preparation of three dimensional-printed neuregulin-1 microsphere hydrogel scaffolds

To fabricate the 3D scaffolds, NRG1-SRMs were mixed with 20% gelatin and 4% sodium alginate at a volume ratio of 2:1:1 and maintained at 37°C. The resulting mixture was loaded into a 1 mL syringe equipped with a 100 μm nozzle. Extrusion and scanning speeds were set at 0.1 mL/s and 2.5 mm/s, respectively. The printing process was conducted at 25°C to generate cylindrical, grid-like scaffolds. Following fabrication, the scaffolds were immersed in 10% (w/v) calcium chloride at 5°C for 5 min to induce crosslinking. The excess solution was removed, and the scaffolds were rinsed thoroughly and stored in sterile PBS for subsequent use.

2.3.5. Cell compatibility evaluation

For cell viability testing, cells were embedded directly within the hydrogel scaffold by mixing at a density of 1×10^6 cells/mL prior to 3D printing. The cell–hydrogel mixture was then printed to fabricate cell-laden scaffolds. Cell viability within the scaffold was assessed using the Live/Dead cell imaging kit (R37601, Invitrogen, Thermo Fisher Scientific, USA). The 3D-printed scaffold was incubated in calcein AM (2 μM) and propidium iodide (PI; 8 μM) at 20–25°C for 15 min and examined under a laser scanning microscope (LSM880 with Fast Airyscan; ZEISS, Germany). The results were analyzed using Image-Pro Plus (IPP) 6.0 software (Media Cybernetic Inc., USA).

2.3.6. Scanning electron microscopy

Samples were fixed in glutaraldehyde for 6 h, followed by dehydration through a graded ethanol series. Subsequently, the samples were immersed in acetone for 15 min to

eliminate residual ethanol and then transferred to isoamyl acetate for 15 min to replace the acetone. Critical point drying was performed for 4 h using a Hitachi apparatus (Japan). The dried specimens were then sputter-coated with gold and examined using a Quanta 200 scanning electron microscope (FEI, USA).

2.4. Cell culture

2.4.1. Acquisition, culture, and neuregulin-1-loaded sustained-release microsphere treatment of bone marrow-derived Schwann-like cells

To isolate B-dSCs, femurs from neonatal rats were harvested under sterile conditions and flushed 15–20 times with α-minimum essential medium (α-MEM; Gibco, USA) containing 10% fetal bovine serum (FBS; Gibco, USA) and penicillin/streptomycin (50 U/mL and 50 mg/mL, respectively). The cell suspension was filtered through a 200-mesh sieve and cultured at 37°C. After 12 h, the medium was refreshed to remove non-adherent cells. Thereafter, media were changed every 3–4 days.

Third-passage BMSCs were induced to differentiate into Schwann-like cells using a stepwise protocol. Cells were suspended at 1×10^5 cells/mL in a mixed induction medium (1:1 Dulbecco's modified eagle medium [DMEM]/F12 and neurobasal medium) supplemented with basic fibroblast growth factor (bFGF; 40 ng/mL), epidermal growth factor (20 ng/mL), and B27 (2%). Neurospheres formed after 3 weeks were transferred to poly-L-lysine-coated flasks and cultured in basal medium supplemented with 10% FBS, forskolin (5 mM), platelet-derived growth factor with two A subunits (5 ng/mL), bFGF (10 ng/mL), and β-heregulin (200 ng/mL). The resulting B-dSCs were further cultured in DMEM/F12 with 10% FBS. Cells were seeded with NRG1-SRMs (1×10^5 cells per well) in 12-well plates, and the medium was replaced after 36 h. Successful differentiation of BMSCs into Schwann-like cells (B-dSCs) was confirmed by immunofluorescence staining for Schwann cell-specific markers S-100 and glial fibrillary acidic protein (GFAP) (Figure A1A and A1B). Additionally, the efficacy of this differentiation protocol was verified in our previously published study.[7]

2.4.2. Acquisition, culture, and neuregulin-1-loaded sustained-release microsphere treatment of autologous Schwann cells

To isolate ASCs, 0.5 cm segments of the radial nerve were excised and enzymatically digested with 0.05% collagenase. The digested tissue was triturated and filtered. Cells were cultured in DMEM/F12 with 10% FBS in a humidified 10% carbon dioxide incubator. Fibroblasts were removed using cytosine arabinoside and G418. bFGF was added to promote Schwann cell proliferation. Schwann cells were identified by vimentin staining. For treatment, 1×10^5 ASCs were co-incubated with NRG1-SRMs in 12-well plates, and the medium was replaced after 36 h.

2.4.3. Targeted inhibition of c-Jun N-terminal kinase pathway in bone marrow-derived Schwann-like cells

B-dSCs (1×10^5/mL) were seeded in 24-well plates and cultured for 24 h at 37°C. Cells were then treated with SP600125 (a JNK inhibitor; Sigma, USA) in complete medium. Lysates were collected using radioimmunoprecipitation assay (RIPA) buffer containing sodium dodecyl sulfate (SDS) and protease inhibitors. Protein concentrations were measured by Bradford assay, and JNK phosphorylation was assessed by Western blotting to confirm pathway inhibition.

2.4.4. Construction of bone marrow-derived Schwann-like cells/Schwann cells–dorsal root ganglion co-culture model

Dorsal root ganglia (DRG) were harvested from an 8-week-old Sprague–Dawley rat. DRG neurons were seeded onto 12 × 12 mm square glass coverslips pre-coated with 0.2% poly-L-lysine (P875130-25mg, Macklin, China) and placed in six-well culture plates. The neurons were maintained in neurobasal medium supplemented with B27, 0.08% glucose, nerve growth factor (NGF; 50 ng/mL), and 5-fluorodeoxyuridine (15 μM; Sigma-Aldrich, USA) to inhibit the proliferation of non-neuronal cells. Once DRG axons extended to the edges of the coverslips, Schwann cells were seeded at a density of 1.5×10^5 cells per coverslip and cultured in MEM supplemented with 10% FBS, 0.08% glucose, and 50 ng/mL NGF. After 7 days, the culture medium was switched to a myelination-inducing medium containing MEM, 10% FBS, 0.08% glucose, 50 ng/mL NGF, and 50 μg/mL ascorbic acid.

2.5. Evaluation of cell morphology and migration ability

2.5.1. Immunofluorescence staining

Cells were fixed with cold methanol for 25 min, blocked with 5% normal goat serum and 0.3% Triton X-100, and incubated overnight with S-100 antibody (1:800; Sigma, USA). After PBS washes, cells were incubated with an Alexa Fluor 492-conjugated secondary antibody (1:100; Servicebio, China) and counterstained with 4',6-diamidino-2-phenylindole (DAPI). Samples were mounted and visualized using a Nikon E800 fluorescence microscope.

2.5.2. Observation of cell morphology under a light microscope

Cell morphology was observed and recorded 24h after seeding using a Nikon E800 microscope.

2.5.3. Scratch assay

A sterile 10μL pipette tip was used to create a linear scratch across confluent cell monolayers in 24-well plates. After washing with PBS to remove cellular debris, fresh culture medium was added. Images were captured at 0 and 48h post-scratch. The initial scratch width was consistently maintained at approximately 500μm across all groups to ensure experimental comparability. The wound closure area was quantified using IPP software (Media Cybernetic Inc., USA), and the cell migration rate was calculated accordingly.

2.5.4. Transwell migration assay

Migration was assessed using BD BioCoat inserts (6.5mm diameter, 8μm pore size). Cells (1.5×10^5 per well) were seeded into the upper chamber with medium, and complete medium containing uridine triphosphate was added to the lower chamber as a chemoattractant. After 24h, migrated cells were fixed with ethanol, stained with crystal violet, and counted under a light microscope.

2.6. Evaluation of the dorsal root ganglion–Schwann cells/bone marrow-derived Schwann-like cells co-culture system

2.6.1. Immunofluorescence staining

Samples were permeabilized, blocked, and sequentially incubated with myelin basic protein (MBP; 1:800; Abcam, UK) and neurofilament heavy (NF200; 1:2000; Sigma, USA) primary antibodies. After washing, secondary antibodies (Alexa Fluor 594 and 488) were applied. Nuclei were counterstained with DAPI. Images were captured using a Nikon E800 microscope.

2.6.2. Western blot

Protein lysates were prepared from co-culture systems using RIPA buffer. After SDS-polyacrylamide gel electrophoresis and membrane transfer, blots were blocked and incubated overnight with primary antibodies against early growth response protein 2 (Krox-20; 1:1000; Abcam, UK), myelin-associated glycoprotein (MAG; 1:1000; GB11260-100, Servicebio, China), neurotrophin receptor (p75; 1:1400; GB115462-100, Servicebio, China), GFAP (1:1500; GB15100-100, Servicebio, China), glial-derived neurotrophic factor (GDNF; 1:1200; GB11403-100, Servicebio, China), phosphorylated JNK (1:300; GB15018-100, Servicebio, China), and JNK (1:1000; GB114321-100, Servicebio, China). Horseradish peroxidase-conjugated secondary antibodies (1:1000; Sigma, USA) were applied, and signals were detected using enhanced chemiluminescence. Quantification was performed using ImageJ (National Institutes of Health, USA).

2.7. Construction of peripheral nerve injury rat model and *in vivo* evaluation

2.7.1. Construction of peripheral nerve injury rat model

Rats were anesthetized with atropine (15mg/kg) and xylazine (1mg/kg), followed by 3% isoflurane. A 1cm segment of the sciatic nerve was resected and bridged using silicone tubes (length: 1.2cm; inner diameter: 2mm; wall thickness: 0.2mm; see Figure 5B) containing different scaffold compositions: PBS, NRG1-SRMs, B-dSCs, or both. Sham-operated animals received skin incisions without nerve transection. In groups involving cell transplantation, cells were embedded within the 3D-printed hydrogel scaffolds prior to implantation. Each group comprised six rats.

2.7.2. In vivo neuregulin-1 release and hydrogel scaffold degradation assessment

Scaffolds were implanted subcutaneously, and tissue samples were collected on days 1, 3, 7, 14, and 28. NRG1 expression was assessed by immunofluorescence using a rabbit anti-NRG1 primary antibody (1:200; Abcam, UK) followed by Alexa Fluor 594-conjugated secondary antibody (1:500). NRG1 itself does not exhibit autofluorescence. Three rats per group per time point were used for analysis. The fluorescent signal intensity of NRG1 was quantified using integrated optical density (OD) measurements to generate release curves.

To evaluate the structural integrity and degradation profile of the 3D-printed hydrogel scaffold *in vivo*, scaffolds were subcutaneously implanted in rats and harvested at 10, 20, and 30 days post-implantation. Due to the high water content and fragile structure of the hydrogel, conventional paraffin or cryosection embedding was not feasible. Instead, the explanted scaffolds were gently rinsed in PBS and embedded in 2% agarose at room temperature. The embedded samples were sectioned into 100 μm-thick slices using a vibrating microtome (Leica VT1000S, Germany). Sections were stained with hematoxylin and eosin (H&E) to visualize internal scaffold morphology and degradation over time.

2.7.3. Green fluorescent protein tracing of bone marrow-derived Schwann-like cells

Green fluorescent protein (GFP)-labeled B-dSCs were implanted within the scaffolds. Tissue sections were collected on day 3 for p75 immunostaining and on week 4 for MBP immunostaining. Fluorescence images were acquired using a Nikon fluorescence microscope and analyzed using ImageJ software.

2.7.4. Immunofluorescence staining

Fresh nerve graft specimens were harvested and cryosectioned at a thickness of 5–10μm. Tissue sections were incubated overnight at 4°C with primary antibodies against NF200 (1:2000; Sigma-Aldrich, USA) and MBP (1:800; Abcam, UK). Following PBS washes, Alexa Fluor 488- and 594-conjugated secondary antibodies were applied for 1h at room temperature. Fluorescence images were acquired using a Nikon fluorescence microscope (Digital Sight US-U2, Japan) equipped with a high-resolution digital camera. Quantitative analysis was performed using IPP software (Media Cybernetics Inc., USA).

2.7.5. Transmission electron microscopy

A 4-week observation period was selected to assess early-stage nerve regeneration and myelin sheath formation. Previous studies have indicated that early remyelination and initial axonal regeneration can be effectively evaluated at this stage.[7] Future studies with longer observation periods will further evaluate complete functional recovery. Nerve grafts were collected at 4 weeks post-surgery. After removal of surrounding adipose and vascular tissues, nerves were fixed in 2.5% glutaraldehyde at 4°C for 6h and washed in PBS (pH 7.2). Samples were then post-fixed in 1% osmium tetroxide, dehydrated through a graded acetone series, and embedded in Poly/Bed 812 resin (Ted Pella, USA). Polymerization was carried out at 60°C for 48h. Ultrathin sections (60–80nm) were cut using a Leica EM UC7 ultramicrotome and mounted onto 200-mesh formvar-coated copper grids. Sections were stained with uranyl acetate and lead citrate and then examined using a FEI Tecnai Spirit G2 Transmission Electron Microscope (TEM).

Six TEM sections and six toluidine blue-stained sections were prepared per group. Myelin thickness, axon diameter, the number of myelinated fibers, and the G-ratio[40] (**Equation II**; axon diameter divided by fiber diameter) were calculated using IPP software.

$$\text{G-ratio} = AD/(AD+MT) \quad \text{(II)}$$

where AD is axon diameter, and MT is myelin sheath thickness. All G-ratio assessments were performed by a pathologist blinded to the experimental groups.

2.7.6. Muscle wet weight and histological analysis

Following euthanasia, bilateral gastrocnemius muscles were harvested, and wet weights were measured using a precision electronic scale. The relative muscle weight was calculated as:

$$\text{Relative weight (\%)} = (\text{experimental side/control side}) \times 100 \quad \text{(III)}$$

Muscle tissues were fixed in 4% paraformaldehyde overnight, dehydrated, and embedded in paraffin. Cross-sections (5μm) were prepared and stained with Masson's trichrome. Muscle fiber morphology and area were visualized using a Nikon fluorescence microscope (Digital Sight US-U2, Nikon, Japan).

2.7.7. Neuromuscular junction synapse fluorescence staining

Frozen transverse sections (5–10μm) of the mid-belly gastrocnemius were prepared. Sections were incubated overnight at 4°C with primary antibodies against NF200 (1:1000; Servicebio, China) and synaptophysin (1:1000; Servicebio, China). After PBS washes, Alexa Fluor 594- and 488-conjugated secondary antibodies were applied at room temperature for 2h. Following final washes, images were acquired using a Nikon fluorescence microscope and quantified using IPP software.

2.7.8. Sciatic nerve functional index

Three rats from each group were randomly selected, and gait parameters were recorded at week 0, 1, 2, 3, and 4 post-surgery. Measurements included experimental paw length (EPL), toe spread (ETS), and intermediary toe spread (EIT), along with the corresponding values for the contralateral side (NPL, NTS, NIT). The sciatic nerve functional index (SFI) was calculated using the formula:

$$\text{SFI} = -38.3*(\text{EPL} - \text{NPL})/\text{NPL} + 109.5 \times (\text{ETS} - \text{NTS})/\text{NTS} + 13.3 \times (\text{EIT} - \text{NIT})/\text{NIT} - 8.8 \quad \text{(IV)}$$

2.7.9. Electrophysiological testing

At 4 weeks post-surgery, electrophysiological recordings were conducted using an RM6240 multi-channel signal acquisition system (Chengdu Instrument Factory, China). Under pentobarbital anesthesia (45mg/kg), the sciatic nerve graft site was re-exposed. A stimulating electrode was placed 0.5cm proximal to the graft site, and a recording electrode was inserted into the triceps surae muscle. Stimulation parameters were: 1–2 mA current, 0.1 ms pulse duration, and 1.0 Hz frequency. Compound muscle action potential amplitude (AP), latency (LT), and conduction velocity (CV) were recorded and analyzed.

2.7.10. Magnetic resonance imaging

At 4 weeks post-surgery, rats were anesthetized and scanned using a Bruker PharmaScan 70/16 Ultra-Shielded Magnetic Resonance Imaging (MRI) system (Germany). High-resolution T2-weighted sagittal images

were acquired, focusing on the sciatic nerve region. Signal intensity and structural continuity at the injury site were evaluated to assess nerve regeneration.

2.7.11. Statistical analysis

Data are presented as mean ± standard deviation. Statistical comparisons between groups were performed using one-way analysis of variance (ANOVA) followed by Tukey's multiple comparison test. A significance threshold of $\alpha = 0.05$ was applied. All statistical analyses were conducted using GraphPad Prism 9.0 software (GraphPad Software, USA).

3. Results

3.1. Characterization and evaluation of three-dimensional-printed hydrogel scaffolds with neuregulin-1 sustained-release microspheres

3.1.1. Morphological characterization, encapsulation efficiency (neuregulin-1 ELISA kit), particle size distribution, and in vitro release profile

(a) **Particle size distribution of NRG1-loaded SRMs** Scanning electron microscopy revealed that NRG1-SRMs were spherical with slightly rough surface textures and displayed good dispersion without noticeable aggregation (Figure 1A-a1). The microspheres demonstrated a relatively uniform size distribution, with an average diameter of 19.4 ± 4.3μm (Figure 1A-a1 and 1C).

(b) **Morphological evaluation of 3D-printed hydrogel** *scaffolds*Using sodium alginate as the primary component, we successfully fabricated multilayered, grid-like 3D-printed scaffolds (Figure 1B). SEM analysis revealed scaffold fibers with an average diameter of approximately 80 μm and an interconnected porous architecture with pore sizes around 120 μm (Figure 1A-a4). The NRG1-SRMs were uniformly distributed across the scaffold surface (Figure 1A-a2 and 1A-a3), appearing as hemispherical protrusions (~20μm in diameter), without compromising scaffold structural integrity.

(c) **Encapsulation efficiency of NRG1-loaded SRMs** Encapsulation efficiency, determined using an NRG1 ELISA kit, was 84 ± 4.3% (w/w).

(d) **In vitro release profile of NRG1-loaded SRM** Enzyme-linked immunosorbent assay-based analysis demonstrated continuous NRG1 release over 30 days. On day 30, cumulative release from the 3D-printed hydrogel scaffolds reached 88.7 ± 1.2%, compared to 36.3 ± 1.2% from non-printed hydrogels (Figure 1D).

3.1.2. Cell compatibility test

Live/dead staining showed a significantly higher cell survival rate in 3D-printed scaffolds (87.2 ± 1.3%) compared to non-printed hydrogels (73.8 ± 3.7%) (Figure 1F), confirming the scaffold system's excellent cytocompatibility.

3.1.3. In vivo release of NRG1-loaded sustained-release microspheres

3D-printed scaffolds were implanted subcutaneously, and NRG1 fluorescence was assessed on days 0, 3, 7, 14, 21, and 28 (n=3). Fluorescence intensity gradually decreased over time, with a relative OD of 0.77 ± 0.05 on day 3 and 0.26 ± 0.03 on day 28 (Figure 1G and H), indicating sustained *in vivo* release.

3.1.4. Distribution of neuregulin-1-loaded sustained-release microspheres in non-printed and three-dimensional-printed hydrogels

In non-printed hydrogels, microspheres showed sedimentation, with significantly higher density in the lower layer (15.0 ± 2.5/18,000μm^2) compared to the upper layer (4.4 ± 1.1/18,000μm^2; $p < 0.01$). In contrast, 3D-printed scaffolds demonstrated uniform distribution across both layers (upper: 16.8 ± 2.6; lower: 16.0 ± 2.8) (Figure 1I and J).

3.2. Dorsal root ganglion and autologous Schwann cells/bone marrow-derived Schwann-like cells co-culture

NRG1 significantly enhanced the myelination ability of B-dSCs in a DRG co-culture system. This effect is mediated via the JNK signaling pathway, as shown by increased myelin-associated protein expression, which is reversed upon JNK inhibition.

3.2.1. Quantification of neurofilament length and myelination via immunofluorescence staining

To assess neurofilament outgrowth and myelination, five DRG neurons were randomly selected from each co-culture group for analysis (Figure 2A, green; Table 1). Fluorescence co-localization analysis revealed a strong spatial overlap between MBP and NF200 in the N+B group, indicating enhanced myelination of B-dSCs upon NRG1 treatment (Figure 2B).

Quantification of neurite extension length (Figure 2C) showed that both the N+A group (202.60 ± 8.55μm) and N+B group (202.60 ± 7.94μm) had significantly longer neurites than the ASC group (157.60 ± 6.80μm) and B-dSC group (45.00 ± 6.23μm) ($p < 0.05$).

For myelination analysis, five immunofluorescence images per group were used to quantify MBP fluorescence intensity (Figure 2A, red; Figure 2D). The N+A (1.06 ± 0.19) and N+B (1.00 ± 0.26) groups showed

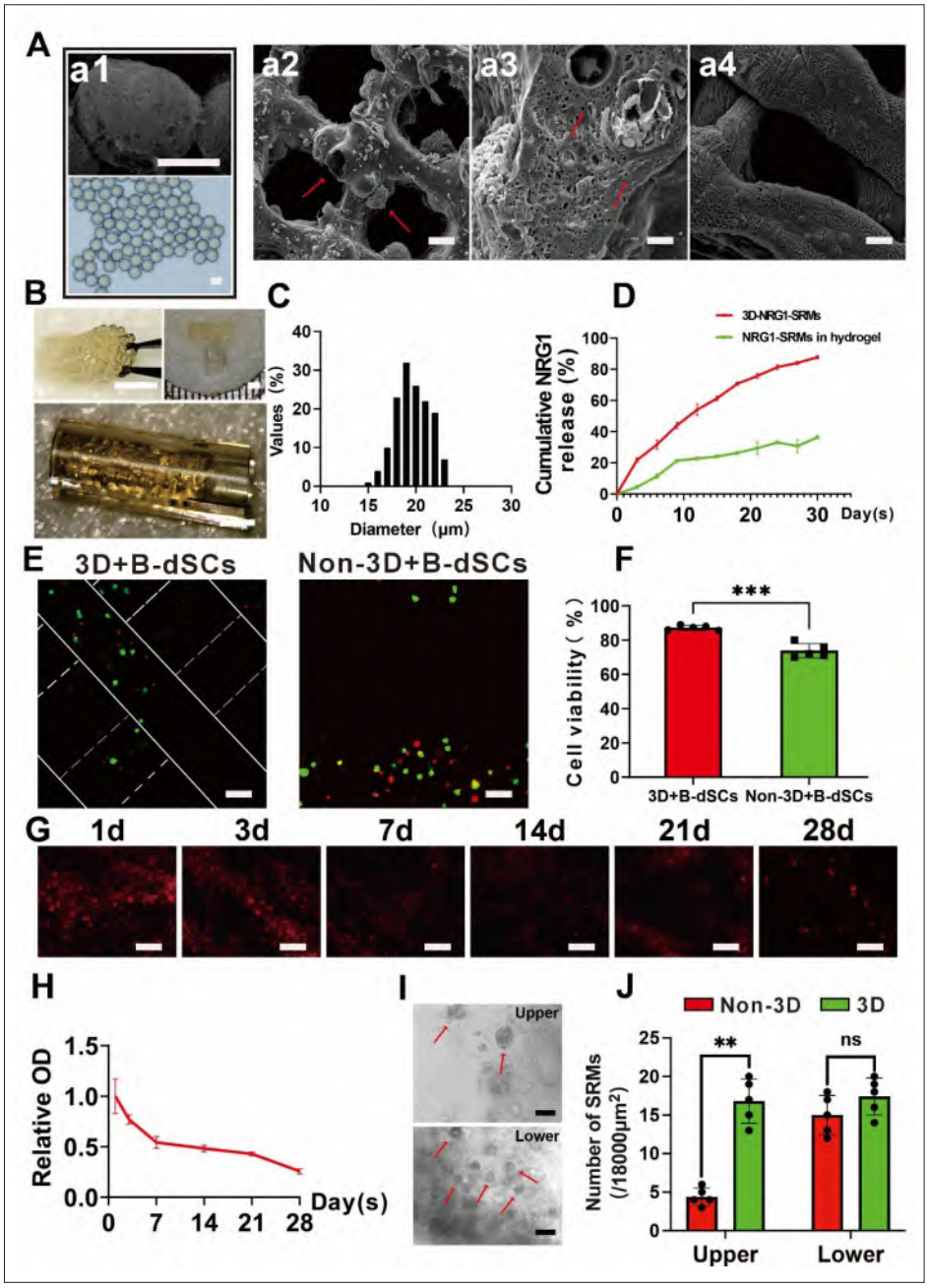


Figure 1. Preparation and characterization of three-dimensional-printed hydrogel scaffolds with neuregulin-1 sustained-release microspheres (3D-NRG1-SRMs). (A) Scanning electron microscopy and microscopic images showing the morphology of (a1) NRG1-SRMs, (a2, a3) 3D-NRG1-SRMs, and (a4) 3D-printed hydrogel scaffolds without NRG1-SRMs. Red arrows indicate the NRG1-SRMs in the scaffold. (B) Photographs showing the 3D-printed hydrogel scaffold before implantation. The scaffold was inserted into a silicone tube (inner diameter: 2.5 mm), demonstrating dimensional compatibility. The scaffold diameter was approximately 2 mm and its length 10 mm, allowing tight yet feasible insertion into the conduit. (C) Particle size distribution of NRG1-SRMs, showing an average diameter of 19.4 ± 4.3 μm. (D) In vitro release profiles of NRG1-SRMs in 3D-printed and non-3D printed hydrogels, demonstrating sustained NRG1 release over 30 days. (E) Live/dead staining of bone marrow-derived Schwann-like cells (B-dSCs) in 3D-printed and non-3D-printed hydrogels. (F) Quantification of the proportion of live cells in (E), indicating higher cell viability in 3D-printed hydrogels. (G) Subcutaneous NRG1 fluorescence staining over 28 days, illustrating the gradual release of NRG1 from the microspheres. (H) Quantitative analysis of NRG1 release from 3D-NRG1-SRMs in vivo. (I) Light microscopy images comparing the distribution of NRG1-SRMs in the upper and lower layers of non-3D printed hydrogels. Red arrows indicate the NRG1-SRMs in the hydrogel. (J) Quantification of NRG1-SRMs distribution in 3D-printed and non-3D-printed hydrogels, showing more uniform distribution in 3D-printed hydrogels. Statistical significance was determined using non-parametric t-tests. Scale bars: a1 = 10 μm; a2 and a4 = 30 μm; a3 = 15 μm; B = 2 mm; E and G = 50 μm; I = 30 μm. Magnifications: a1 = 2500×; a2 and a4 = 1000×; a3 = 1500×; B = 1×; E and G = 100×; I = 400×.

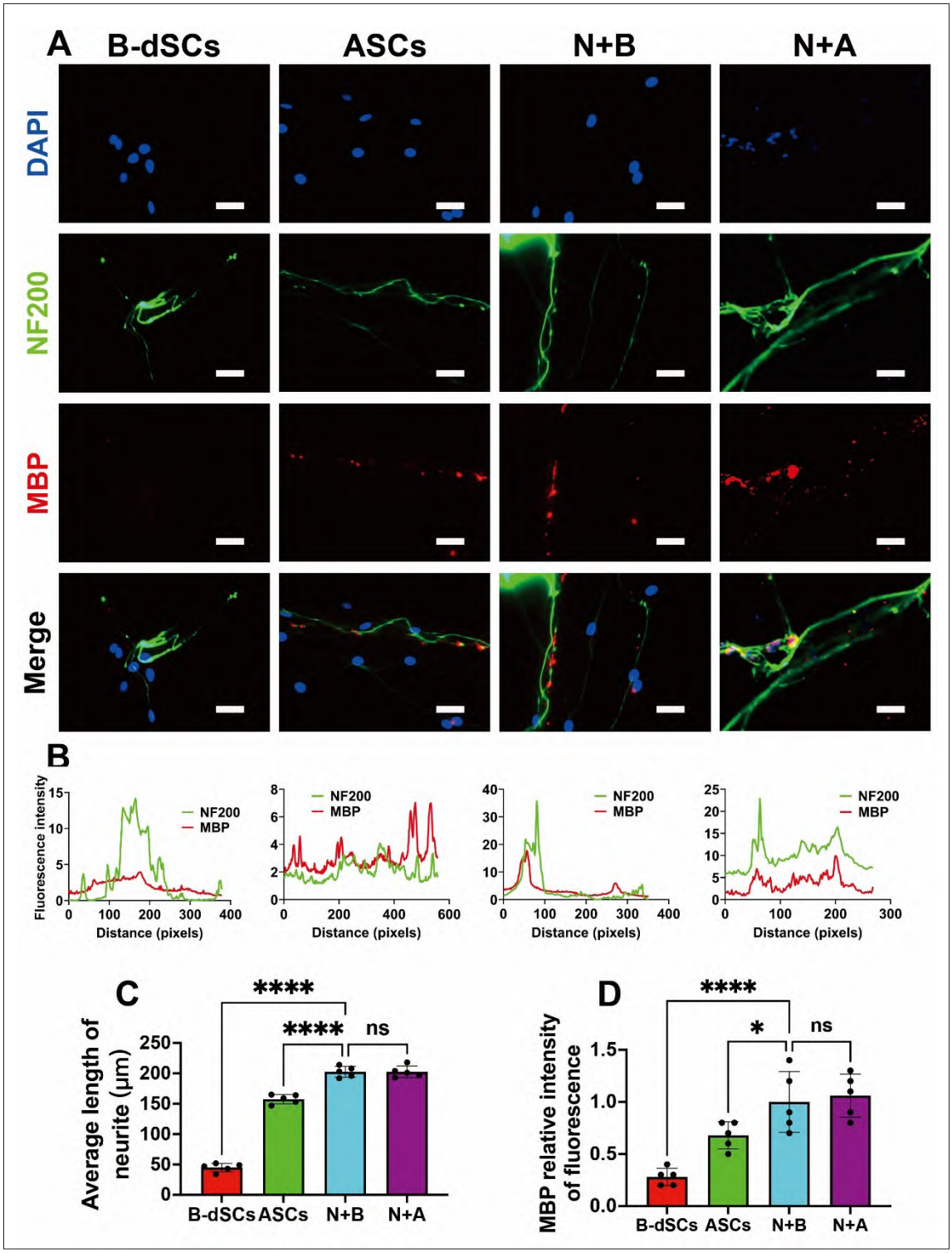


Figure 2. Immunofluorescence analysis of B-dSC/ASC and DRG neuron co-culture. (A) Co-staining of axons (NF200, green) and myelin sheaths (MBP, red) in the co-culture system. (B) Immunofluorescence co-localization of NF200 and MBP, showing poor co-localization in the B-dSCs group. (C) Quantification of axon length, revealing significantly longer neurites in the NRG1-treated groups. (D) Quantification of relative myelin expression, indicating higher MBP expression in the NRG1-treated groups. Statistical significance was determined using one-way analysis of variance with Tukey's post hoc test. $^{*}p < 0.05$, $^{****}p < 0.0001$, $^{ns}p > 0.05$. Scale bar = 40 μm; magnification = 400×. *Notes*: N+A: (NRG1 + ASCs) + DRG co-culture; N+B: (NRG1 + B-dSCs) + DRG co-culture. Abbreviations: ASC, autologous Schwann cell; B-dSC, bone marrow-derived Schwann-like cell; DRG, dorsal root ganglion; MBP, myelin basic protein; NF200, neurofilament heavy; NRG1, neuregulin-1.

Table 1. Co-culture groups and corresponding treatment methods

Group (n=3)	Treatment method
(1) B-dSCs	B-dSCs + DRG co-culture
(2) ASCs	ASCs + DRG co-culture
(3) N+B	(NRG1 + B-dSCs) + DRG co-culture
(4) N+A	(NRG1 + ASCs) + DRG co-culture
(5) N+B+I	(SP600125 + NRG1+B-dSCs) + DRG co-culture

Abbreviations: ASCs, autologous Schwann cells; B-dSC, bone marrow-derived Schwann-like cells; DRG, dorsal root ganglion; NRG1, neuregulin-1.

markedly higher MBP levels than the ASC (0.68 ± 0.12) and B-dSC (0.28 ± 0.07) groups ($p < 0.05$).

3.2.2. Western blot analysis of myelin-related transcription factors and protein expression

Western blot analysis was conducted to assess the expression of key transcription factors and myelin-associated proteins in the DRG co-culture system. The relative expression of Krox-20, a pivotal transcription factor for myelin formation, was significantly upregulated in the N+B group (1.41 ± 0.11) compared to the ASC (1.05 ± 0.04) and B-dSC (0.91 ± 0.15) groups but remained lower than in the N+A group (1.81 ± 0.05) (Figure 3A).

Similarly, the expression of the MAG followed the same trend. The N+B group exhibited a relative MAG expression level of 1.55 ± 0.07, which was higher than that observed in the ASCs group (1.09 ± 0.05) and the B-dSCs group (0.88 ± 0.03), but slightly lower than in the N+A group (1.64 ± 0.26) (Figure 3C and D).

These results indicate that treatment with NRG1 significantly enhances the myelination potential of B-dSCs, though the response remains somewhat inferior to that of native ASCs under the same conditions. Nonetheless, the NRG1-induced improvement in B-dSC function highlights its potential for regenerative applications in PNI.

3.2.3. Validation of c-Jun N-terminal kinase pathway inhibition in the dorsal root ganglion–bone marrow-derived Schwann-like cell co-culture system

To verify whether the JNK signaling pathway mediates the effects of NRG1 on B-dSC dedifferentiation and myelination, we introduced SP600125, a selective JNK inhibitor, into the DRG–B-dSCs co-culture system treated with NRG1-SRMs (Figure 3B). Western blot analysis showed that the expression of phosphorylated JNK in the inhibitor group (NRG1 + SP600125 + B-dSCs) was significantly decreased compared to the NRG1 + B-dSCs group (Figure 3E and F), confirming effective suppression of the JNK pathway.

Subsequently, we assessed downstream functional markers. In the presence of SP600125, the protein expression levels of Krox-20 (0.71 ± 0.06), p75 (0.72 ± 0.03), MAG (0.90 ± 0.11), GFAP (0.86 ± 0.05), and GDNF (0.85 ± 0.03) were significantly reduced compared to the NRG1 + B-dSCs group (Krox-20: 1.41 ± 0.11; p75: 1.18 ± 0.04; MAG: 1.55 ± 0.07; GFAP: 1.35 ± 0.02; GDNF: 1.49 ± 0.03), all $p < 0.05$.

These findings suggest that NRG1 enhances B-dSCs dedifferentiation and myelination, in part through activation of the JNK signaling pathway. Inhibition of JNK reverses these effects, indicating its essential regulatory role in NRG1-mediated functional enhancement of B-dSCs.

3.3. Comparison of Schwann cell and bone marrow-derived Schwann-like cell morphology and migration ability before and after neuregulin-1 induction

To further characterize the effects of NRG1 on B-dSC function, we evaluated their morphological features and migratory capacity under both two-dimensional (2D) and 3D conditions. These experiments revealed that NRG1 significantly promotes morphological maturation and enhances motility of B-dSCs, thereby improving their functional resemblance to native Schwann cells.

3.3.1. Morphological changes in Schwann cells and bone marrow-derived Schwann-like cells before and after neuregulin-1 induction

At 24 h post-seeding, all cells adhered well to the culture surface. Microscopic examination revealed distinct morphological differences among the groups (Table 2). In the N+B group, 72.1 ± 3.1% of cells exhibited a bipolar or multipolar spindle-shaped morphology, comparable to the N+A group (76.9 ± 2.5%). These proportions were significantly higher than those observed in the untreated B-dSC group (20.4 ± 3.0%) and the ASC group (34.1 ± 3.6%) (Figure 4A and D). These findings indicate that NRG1 stimulation induces a morphological transition in B-dSCs toward a Schwann cell-like phenotype, supporting their enhanced structural maturation.

3.3.2. Changes in Schwann cells and bone marrow-derived Schwann-like cell migration ability before and after neuregulin-1 induction under two-dimensional conditions (scratch assay)

To assess cell motility in a 2D environment, a scratch assay was performed. No significant differences were observed in initial scratch widths among groups, confirming consistent experimental conditions across all comparisons (initial scratch width ~500 μm). After 48 h, the migration rate in the N+B group reached 61.4 ± 3.2%, which was similar to that in the N+A group (72.8 ± 3.4%) and significantly

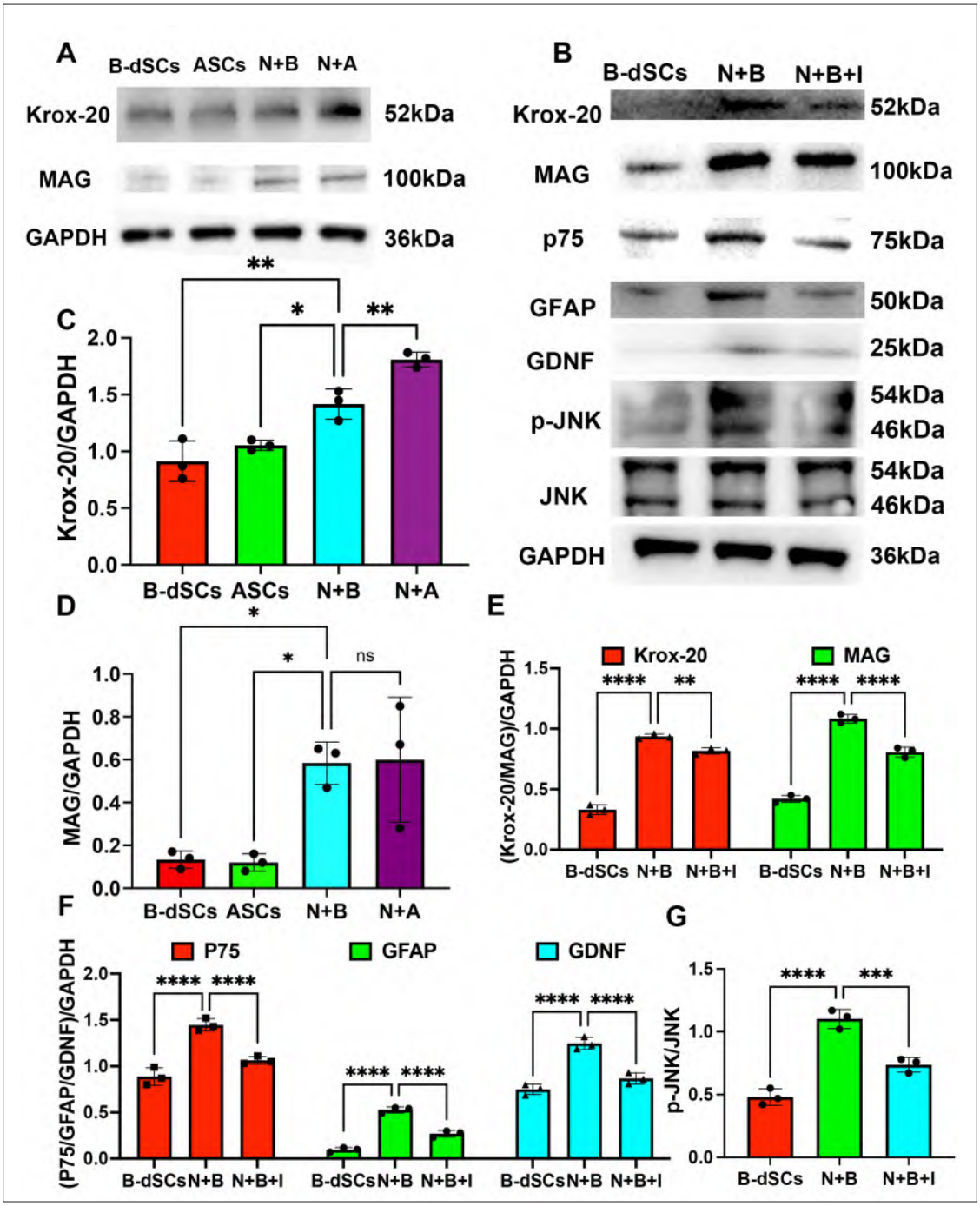


Figure 3. Western blot analysis of protein expression in the (B-dSC/ASC and DRG neuron co-culture system. (A) Western blot bands showing the expression of Krox-20 and MAG before and after NRG1 treatment in the co-culture system. (B) Western blot bands of myelin-related proteins (Krox-20, MAG), dedifferentiation markers (p75, GFAP, GDNF), and JNK pathway proteins (p-JNK, JNK) in the B-dSCs group, N+B group, and N+B+I group. (C, D) Quantification of Krox-20 and MAG expression levels before and after NRG1 treatment in the co-culture system. (E) Quantification of Krox-20 and MAG expression levels in B-dSCs, B-dSCs + NRG1 (N+B), and B-dSCs + NRG1 + SP600125 (N+B+I) co-cultured with DRG neurons. (F) Quantification of p75, GFAP, and GDNF expression in B-dSCs, B-dSCs + NRG1, and B-dSCs + NRG1 + SP600125 co-cultured with DRG neurons. (G) Quantification of p-JNK/JNK expression in B-dSCs, B-dSCs + NRG1 (N+B), and B-dSCs + NRG1 + SP600125 (N+B+I) co-cultured with DRG neurons. Statistical analysis was performed using one-way analysis of variance with Tukey's post hoc test. $^{*}p < 0.05$, $^{**}p < 0.01$, $^{***}p < 0.001$, $^{****}p < 0.0001$, $^{ns}p > 0.05$. Abbreviations: ASCs, autologous Schwann cells; B-dSCs, bone marrow-derived Schwann-like cells; GAPDH, glyceraldehyde 3-phosphate dehydrogenase; GDNF, glial-derived neurotrophic factor; GFAP, glial fibrillary acidic protein; JNK, C-Jun N-terminal kinase; Krox-20, early growth response protein 2; MAG, myelin-associated glycoprotein; NRG1, neuregulin-1; p75, neurotrophin receptor; p-JNK, phosphorylated JNK.

Table 2. *In vitro* cell culture groups and treatment methods

Group	Treatment method
(1) B-dSCs	B-dSCs treated with PBS
(2) ASCs	ASCs treated with PBS
(3) N+B	B-dSCs treated with NRG1
(4) N+A	ASCs treated with NRG1

Abbreviations: ASC, autologous Schwann cell; B-dSC, bone marrow-derived Schwann-like cell; NRG1, neuregulin-1; PBS, phosphate-buffered saline.

higher than in the B-dSC (31.6 ± 2.9%) and ASC (21.2 ± 2.8%) groups (Figure 4B and E). The migration rate was calculated using the formula:

$$\text{Migration (\%)} = (\text{Initial scratch width} - \text{Final scratch width})/\text{Initial scratch width} \times 100\% \quad (V)$$

These results indicate that NRG1 enhances the 2D migratory capacity of B-dSCs, comparable to native Schwann cells.

3.3.3. Changes in Schwann cells and bone marrow-derived Schwann-like cell migration ability before and after neuregulin-1 induction under three-dimensional conditions (transwell assay)

Cell migration was further evaluated under 3D conditions using a transwell assay. The relative number of cells that migrated through the membrane in the N+B group (1.0 ± 0.3) was similar to that in the N+A group (1.3 ± 0.2) and significantly higher than in the B-dSC (0.7 ± 0.1) and ASC (0.3 ± 0.1) groups (Figure 4C and F). These findings confirm that NRG1 promotes both 2D and 3D migratory capabilities in B-dSCs, aligning their behavior more closely with that of native Schwann cells.

3.4. Evaluation of *in vivo* gel scaffold degradation, myelin regeneration, and nerve function

Section 3.4 examines the sustained release behavior and biological activity of NRG1-SRMs. Results demonstrated that NRG1-SRMs released bioactive NRG1 in a controlled manner over 28 days, maintaining sufficient activity to support B-dSC viability and function. The grouping of animals used in the *in vivo* studies is summarized in Table 3.

3.4.1. In vivo fluorescence tracing of bone marrow-derived Schwann-like cells and gel scaffold degradation

To evaluate the *in vivo* fate and functional status of B-dSCs, we conducted fluorescence co-localization analysis at early and late stages post-transplantation (Figure 5A). GFP-labeled B-dSCs were found to co-express p75—a marker of early Schwann cell dedifferentiation—indicating successful phenotypic reversion in the repair microenvironment (Figure 5D). At later stages, GFP-positive cells also co-localized with MBP, a key myelin structural protein, suggesting that the transplanted B-dSCs not only survived *in vivo* but also contributed directly to remyelination (Figure 5D–F). *In vivo* degradation of the hydrogel scaffold (without NRG1-SRMs) was assessed by H&E staining of agarose-embedded sections collected at 10, 20, and 30 days after subcutaneous implantation. As shown in Figure 5B and C, the hydrogel exhibited a well-defined porous structure at day 10, which became progressively fragmented and less defined by days 20 and 30, indicating gradual degradation of the scaffold matrix. These results confirm the scaffold's ability to provide initial support while allowing for time-dependent resorption.

3.4.2. Immunofluorescence analysis of nerve and myelin regeneration

To quantify myelin regeneration, immunofluorescence staining for MBP was performed on sciatic nerve sections 4 weeks after injury. The relative MBP fluorescence intensity in the N+B group (0.80 ± 0.03) was comparable to that in the Sham group (1.00 ± 0.11), and significantly higher than in the PNI (0.11 ± 0.03), B-dSCs (0.51 ± 0.05), and NRG1-only (0.34 ± 0.05) groups ($p < 0.0001$) (Figure 6A and C). These findings confirm that combined treatment with NRG1 and B-dSCs yields superior myelin regeneration relative to either component alone.

3.4.3. Myelinated nerve fibers and large-diameter axons in regenerated nerves

The proportion of myelinated nerve fibers in the regenerated sciatic nerve was 71.3 ± 7.1% in the N+B group, closely approximating the Sham group (78.7 ± 4.1%), and significantly greater than in the PNI (14.3 ± 2.5%), B-dSCs (22.3 ± 2.5%), and NRG1 (35.7 ± 2.5%) groups ($p < 0.0001$) (Figure 6B and D).

Analysis of axon caliber revealed that the proportion of large-diameter axons (>2μm) in the N+B group (36.7 ± 1.5%) was slightly lower than that in the Sham group

Table 3. *In vivo* experimental groups and treatment methods

Group (*n*=6)	Treatment method
(1) PNI	PBS treatment
(2) NRG1	3D-NRG1-SRMs
(3) B-dSCs	3D scaffold (without NRG1-SRMs) + B-dSCs
(4) NRG1+B	3D-NRG1-SRMs + B-dSCs
(5) Sham	Sham operation

Abbreviations: B-dSCs, bone marrow-derived Schwann-like cells; NRG1-SRM, neuregulin-1-loaded sustained-release microspheres; PBS, phosphate-buffered saline; PNI, peripheral nerve injury; 3D, three-dimensional.

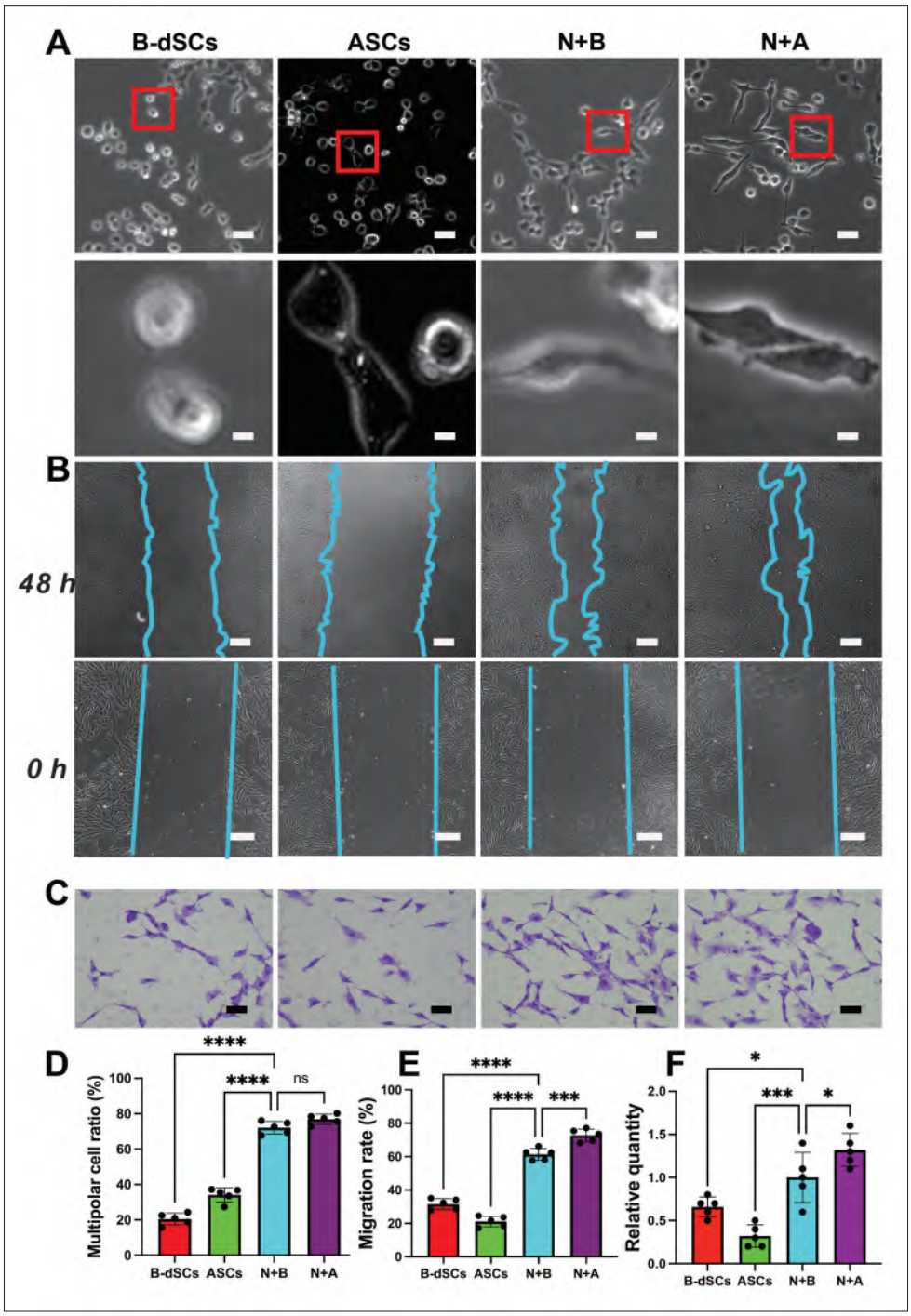


Figure 4. Morphology and motility of B-dSCs/ASCs before and after NRG1 treatment. (A) Light microscopy images of B-dSCs/ASCs before and after NRG1 treatment, including corresponding magnified views of the areas indicated by red boxes. (B) Two-dimensional motility of B-dSCs/ASCs assessed via scratch assay before and after NRG1 treatment. (C) Three-dimensional motility of B-dSCs/ASCs assessed via transwell assay before and after NRG1 treatment. (D) Quantification of the proportion of multipolar cells, demonstrating increased multipolarity following NRG1 treatment. (E) Quantification of cell migration rates in the scratch assay, showing enhanced migration in NRG1-treated groups. (F) Quantification of cell motility in the transwell assay, indicating increased motility in the NRG1-treated groups. Statistical analysis was performed using one-way analysis of variance with Tukey's post hoc test. $^{*}p < 0.05$, $^{***}p < 0.001$, $^{****}p < 0.0001$, $^{ns}p > 0.05$. Scale bars: (A upper) and (C) = 40 μm; (A lower) = 5 μm; (B upper) = 80 μm; (B lower) = 100 μm. Magnifications: (A upper) and (C) = 400×; (A lower) = 1000×; (B upper) = 40×; (B lower) = 100×. *Notes*: N+A: (NRG1 + ASCs) + DRG co-culture; N+B: (NRG1 + B-dSCs) + DRG co-culture. Abbreviations: ASC, autologous Schwann cell; B-dSC, bone marrow-derived Schwann-like cell; DRG, dorsal root ganglion; NRG1, neuregulin-1.

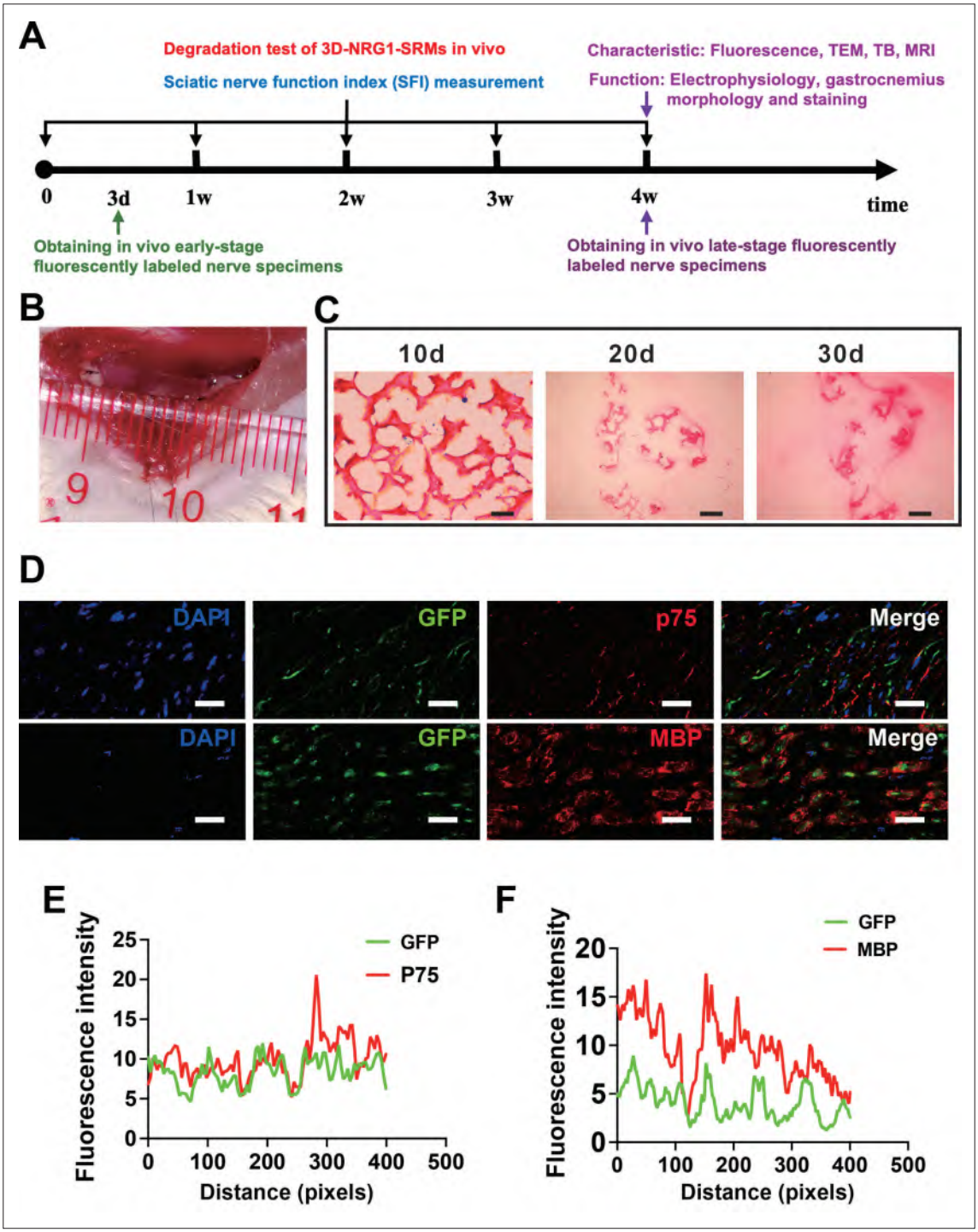


Figure 5. *In vivo* detection timeline and fluorescence tracing of bone marrow-derived Schwann-like cells (B-dSCs). (A) Schematic timeline for tissue collection and assessment following the establishment of peripheral nerve injury model. (B) Macroscopic intraoperative photograph showing the three-dimensional (3D)-printed hydrogel scaffold bridging the transected sciatic nerve ends within a silicone tube (inner diameter: 2.5 mm). A ruler is included for reference. (C) Hematoxylin and eosin staining of scaffold sections were collected from subcutaneous implantation sites at 10, 20, and 30 days (d), respectively. Progressive degradation of the porous hydrogel structure was observed over time. (D, E) Co-localization of GFP-labeled B-dSCs with p75 and MBP indicates their early dedifferentiation and subsequent myelination *in vivo*. Scale bars: (B) = 5 mm; (C) = 100 μm; (D) = 50 μm. Magnifications: (C) = 100×; (D) = 100×. Abbreviations: DAPI, 4',6-diamidino-2-phenylindole; GFP, green fluorescence protein; MBP, myelin basic protein; MRI, magnetic resonance imaging; NRG1-SRMs, neuregulin-1-loaded sustained-release microspheres; p75, neurotrophin receptor; TEM, transmission electron microscopy; TB, toluidine blue.

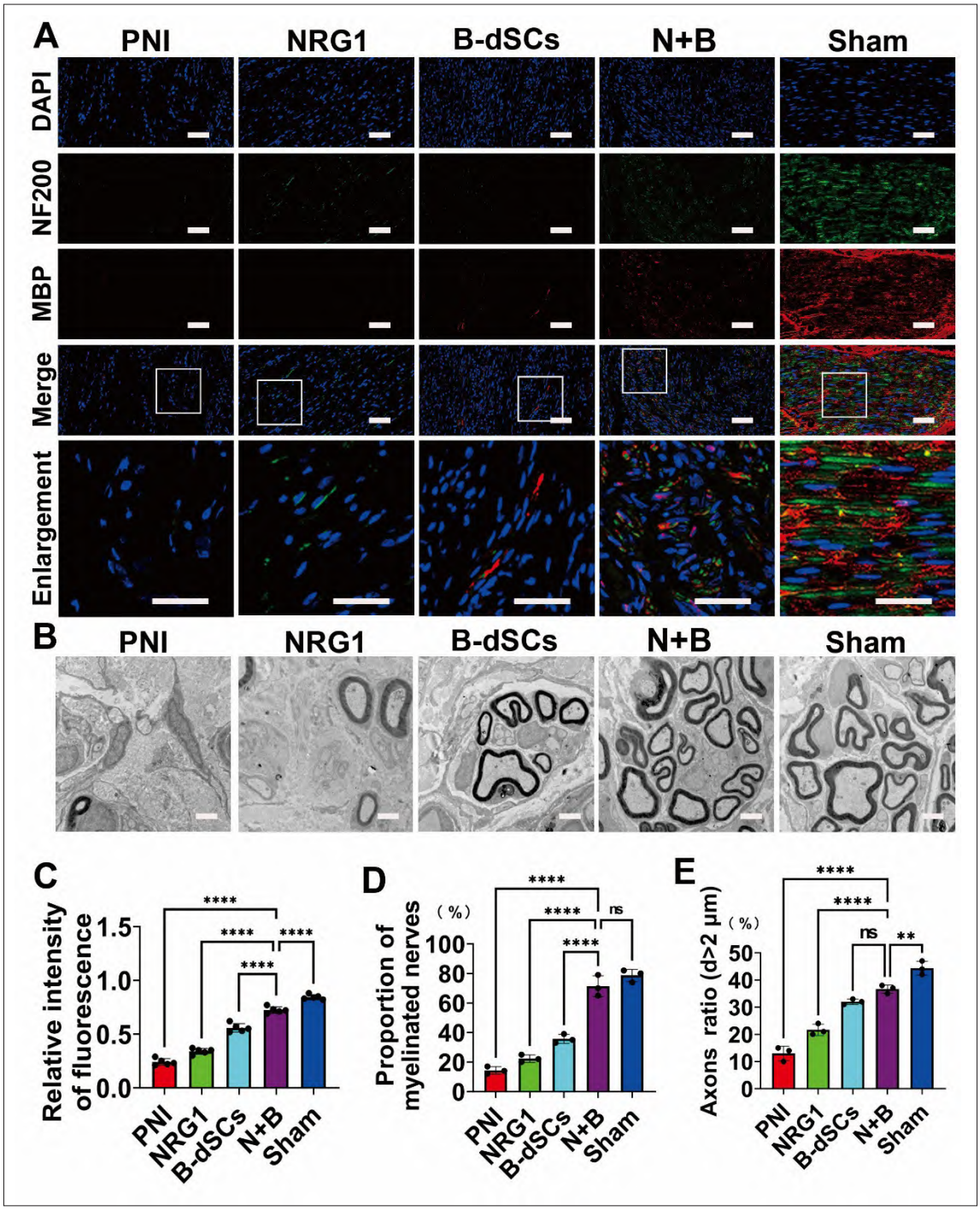


Figure 6. *In vivo* nerve regeneration and quantification of myelinated nerves and large-diameter axons. (A) Immunofluorescence staining of regenerated axons (NF200) and myelin sheaths (MBP) in sciatic nerve sections. (B) TEM images of nerve cross-sections at the distal end. (C) Quantification of relative MBP fluorescence intensity in (A), showing greater myelination in the N+B group. (D) Quantification of the proportion of myelinated nerve fibers in (A), indicating a higher proportion in the N+B group. (E) Quantification of the proportion of large-diameter axons (> 2 μm) in (A), showing enhanced axonal regeneration in the N+B group. Statistical analysis was performed using one-way analysis of variance with Tukey's post hoc test. $^{**}p < 0.01$, $^{***}p < 0.001$, $^{****}p < 0.0001$, $^{ns}p > 0.05$. Scale bars: (A) = 40 μm; (B) = 2 μm. Magnifications: (A) = 100×; (B) = 400×. *Note*: N+B: (NRG1 + B-dSCs) + dorsal root ganglion co-culture. Abbreviations: B-dSCs, bone marrow-derived Schwann-like cells; DAPI, 4',6-diamidino-2-phenylindole; MBP, myelin basic protein; NF200, neurofilament heavy; NRG1, neuregulin-1; PNI, peripheral nerve injury; TEM, transmission electron microscopy.

(44.3 ± 2.5%), but markedly higher than in the PNI (13.0 ± 2.6%), B-dSC (32.0 ± 2.1%), and NRG1 (21.7 ± 2.1%) groups (Figure 6B and E). These results indicate that combined NRG1 and B-dSC treatment not only promotes myelination but also supports axonal maturation and regeneration.

3.4.4. Myelin sheath thickness and G-ratio in regenerated nerves

TEM was employed to assess the structural maturity of regenerated myelin. The average myelin sheath thickness in the N+B group was 0.72 ± 0.03μm, which is slightly lower than that of the Sham group (0.84 ± 0.03μm), but significantly greater than in the PNI (0.23 ± 0.02μm), B-dSC (0.54 ± 0.03μm), and NRG1-only (0.33 ± 0.03μm) groups ($p < 0.001$) (Figure 7A and E). These results demonstrate that combined NRG1 and B-dSC treatment markedly enhances remyelination, achieving near-physiological myelin thickness.

The G-ratio (axon diameter/fiber diameter), a well-established indicator of myelin compactness, was analyzed separately for large- and small-diameter axons. For large-diameter axons (>2μm), the G-ratio in the N+B group (0.56 ± 0.05) approached the optimal physiological range (~0.6) and was comparable to that in the Sham group (0.67 ± 0.06). In contrast, the G-ratios in the B-dSCs (0.37 ± 0.05), NRG1-only (0.73 ± 0.04), and PNI (0.86 ± 0.06) groups deviated significantly from the ideal range (Figure 7B), indicating impaired remyelination or axonal degeneration.

For small-diameter axons, G-ratio values remained relatively consistent across all groups and aligned with the physiological norm: Sham (0.61 ± 0.09), N+B (0.59 ± 0.08), B-dSCs (0.59 ± 0.10), NRG1 (0.59 ± 0.09), and PNI (0.58 ± 0.07) (Figure 7C). Collectively, these findings suggest that NRG1-SRMs combined with B-dSCs not only enhance myelin thickness but also restore the structural integrity of large-caliber axons, thereby supporting improved functional recovery (Figure 7D and E).

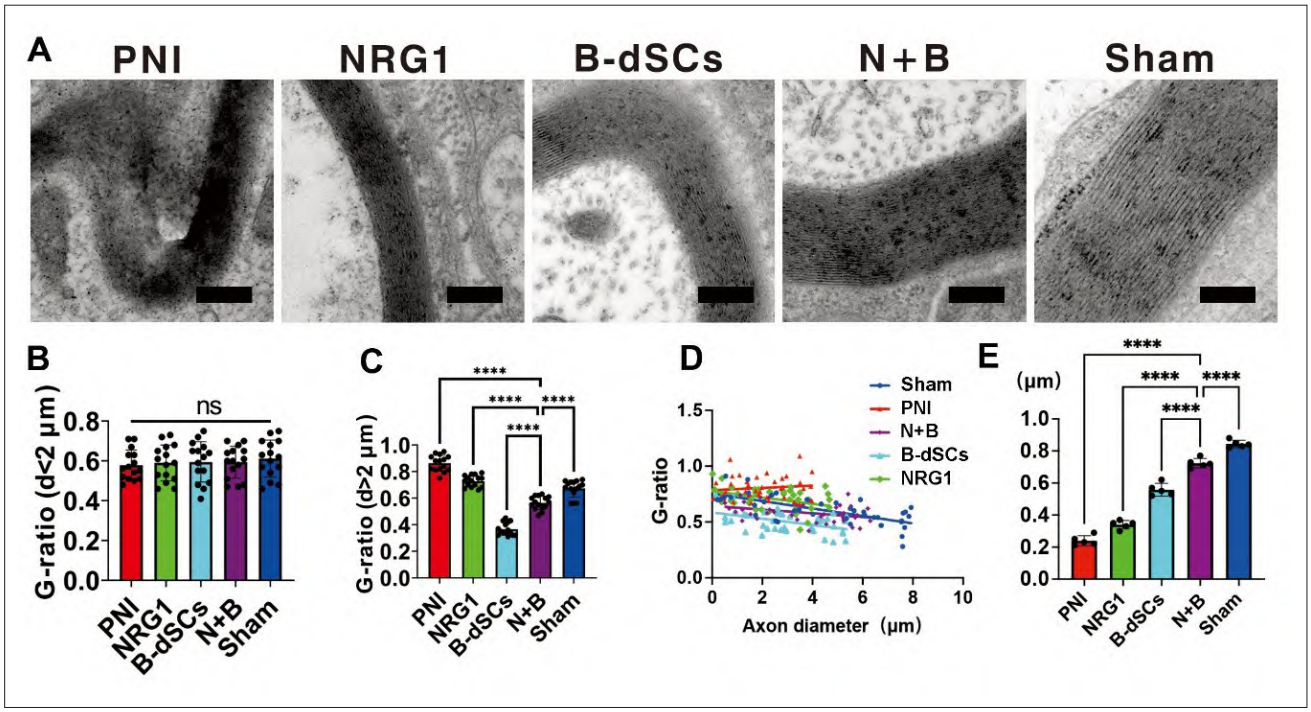


Figure 7. Myelin sheath thickness and G-ratio in regenerated nerves. (A) Transmission electron microscopy images of regenerated myelin sheaths, showing differences in thickness across groups. (B) Quantification of G-ratio for large-diameter axons (>2 μm), demonstrating optimal myelination in the N+B group. (C) Quantification of G-ratio for small-diameter axons (<2 μm), showing consistent ratios across all groups. (D) Scatter plot and fitted curves for the G-ratio in each group, highlighting the relationship between axon diameter and myelination. (E) Quantification of regenerated myelin sheath thickness, indicating significantly thicker myelin in the N+B group compared to others. $^{****}p < 0.0001$, $^{ns}p > 0.05$. One-way ANOVA with Tukey's post hoc test. Scale bar (A) = 200 nm; Magnification: (A) = 15,000×. *Note*: N+B: (NRG1 + B-dSCs) + dorsal root ganglion co-culture. Abbreviations: B-dSCs, bone marrow-derived Schwann-like cells; d, diameter; NRG1, neuregulin-1; PNI, peripheral nerve injury.

3.4.5. Gastrocnemius muscle wet weight and muscle fiber atrophy

At 4 weeks post-surgery, gastrocnemius muscles from both hindlimbs were harvested for wet weight measurement (Figure 8A). Relative muscle weight was calculated as:

$$\text{Relative weight (\%)} = (\text{Experimental side}/\text{Normal side}) \times 100 \quad \text{(VI)}$$

In the Sham group, no obvious difference was observed between the two limbs. In contrast, the injured muscle in the NRG1+B group was slightly reduced in size, while more severe atrophy was evident in the PNI, B-dSCs, and NRG1 groups. Quantitatively, the relative muscle weight in the N+B group (80.32 ± 3.48%) was significantly lower than in the Sham group (98.92 ± 0.37%) but notably higher than in the PNI (28.46 ± 1.32%), B-dSC (50.64 ± 4.33%), and NRG1 (51.08 ± 4.05%) groups ($p < 0.0001$) (Figure 8D).

Histological analysis using Masson's trichrome staining revealed the average cross-sectional area of muscle fibers (Figure 8B): Sham (1428.4 ± 42.81 μm^2), N+B (1205 ± 48.29 μm^2), B-dSCs (812.4 ± 36.21 μm^2), NRG1 (832.2 ± 54.55 μm^2), and PNI (539 ± 28.11 μm^2). Muscle atrophy in the N+B group was moderate and significantly improved compared to the other injury groups ($p < 0.0001$) (Figure 8E).

3.4.6. Neuromuscular junction synapse fluorescence staining

To evaluate neuromuscular reinnervation, immunofluorescence staining of neuromuscular junctions (NMJs) was performed on gastrocnemius muscle sections. The density of NMJs in the N+B group (29.6 ± 4.2 per 120,000 μm^2) was significantly lower than in the Sham group (50.4 ± 3.0), but markedly higher than in the PNI (2.6 ± 1.8), B-dSC (7.4 ± 3.0), and NRG1 (7.4 ± 1.1) groups (Figure 8C and F). These results indicate enhanced NMJ preservation and reinnervation in the N+B group.

3.4.7. Dynamic monitoring of sciatic nerve function index after surgery

The SFI was used to dynamically evaluate locomotor recovery over 4 weeks. SFI remained near 0 in the Sham group, indicating normal function, while the PNI group showed persistently low SFI values (~ −100), reflecting complete functional loss.

In the first postoperative week, all groups except the Sham group exhibited a sharp decline in SFI. From weeks 2 to 4, functional recovery in the N+B group accelerated significantly compared to the NRG1 and B-dSC groups, which showed moderate improvement, whereas the PNI group showed no meaningful recovery (Figures A1C and 8G).

3.4.8. Electrophysiology

Electrophysiological recordings were conducted to assess functional myelin integrity via CV, LT, and compound muscle action potential amplitude. 4 weeks after surgery, the N+B group exhibited superior neural function (CV: 104 ± 3m/s; LT: 6.0 ± 0.4ms; AP: 2.41 ± 0.14mV) compared to the PNI (CV: 13 ± 3m/s; LT: 12.8 ± 0.8ms; AP: 0.79 ± 0.08mV), NRG1 (CV: 53 ± 6m/s; LT: 10.9 ± 0.7ms; AP: 1.45 ± 0.05mV), and B-dSC (CV: 63 ± 6m/s; LT: 9.0 ± 0.7ms; AP: 1.78 ± 0.05mV) groups.

While still slightly inferior to the Sham group (CV: 115 ± 5m/s; LT: 3.3 ± 0.2ms; AP: 2.88 ± 0.07mV), the NRG1+B group demonstrated robust electrophysiological recovery ($p < 0.05$) (Figure 8H–J).

3.4.9. Sciatic nerve magnetic resonance imaging

T2-weighted MRI was employed to visualize structural recovery. In the PNI group, the injury site appeared as a hypointense gap ("black void") on the nerve pathway. In contrast, the N+B and other treated groups showed filling of the injury region with regenerated nerve tissue. However, the signal intensity remained slightly lower than that of native nerve tissue, indicating ongoing remodeling (Figure 8K).

4. Discussion

Dedifferentiation is a crucial prerequisite for myelin regeneration and nerve repair following PNI.[8,41] The limited dedifferentiation capacity of B-dSCs restricts their potential to effectively replace ASCs in PNI repair.[7] To enhance the dedifferentiation of B-dSCs and improve their myelination capabilities *in vivo*, we applied NRG1, a widely recognized inducer of Schwann cell dedifferentiation, to a B-dSC and DRG neuron co-culture system. Our observations revealed an upregulation in the expression of both dedifferentiation markers and myelin markers, suggesting that NRG1 can drive B-dSCs into a dedifferentiation-myelin regeneration phase. This finding implies that NRG1 may enhance the myelination ability of B-dSCs by promoting their dedifferentiation, although further *in vivo* studies are required to validate this.

Given that transection-type PNIs necessitate prolonged recovery periods and extensive regeneration distances, it is essential to employ a suitable delivery carrier capable of bridging nerve stumps while providing sustained and localized release of NRG1. Although hydrogels and other biomaterials have been widely employed as NRG1 delivery vehicles *in vivo*,[42,43] they generally fail to maintain therapeutic concentrations of NRG1 over

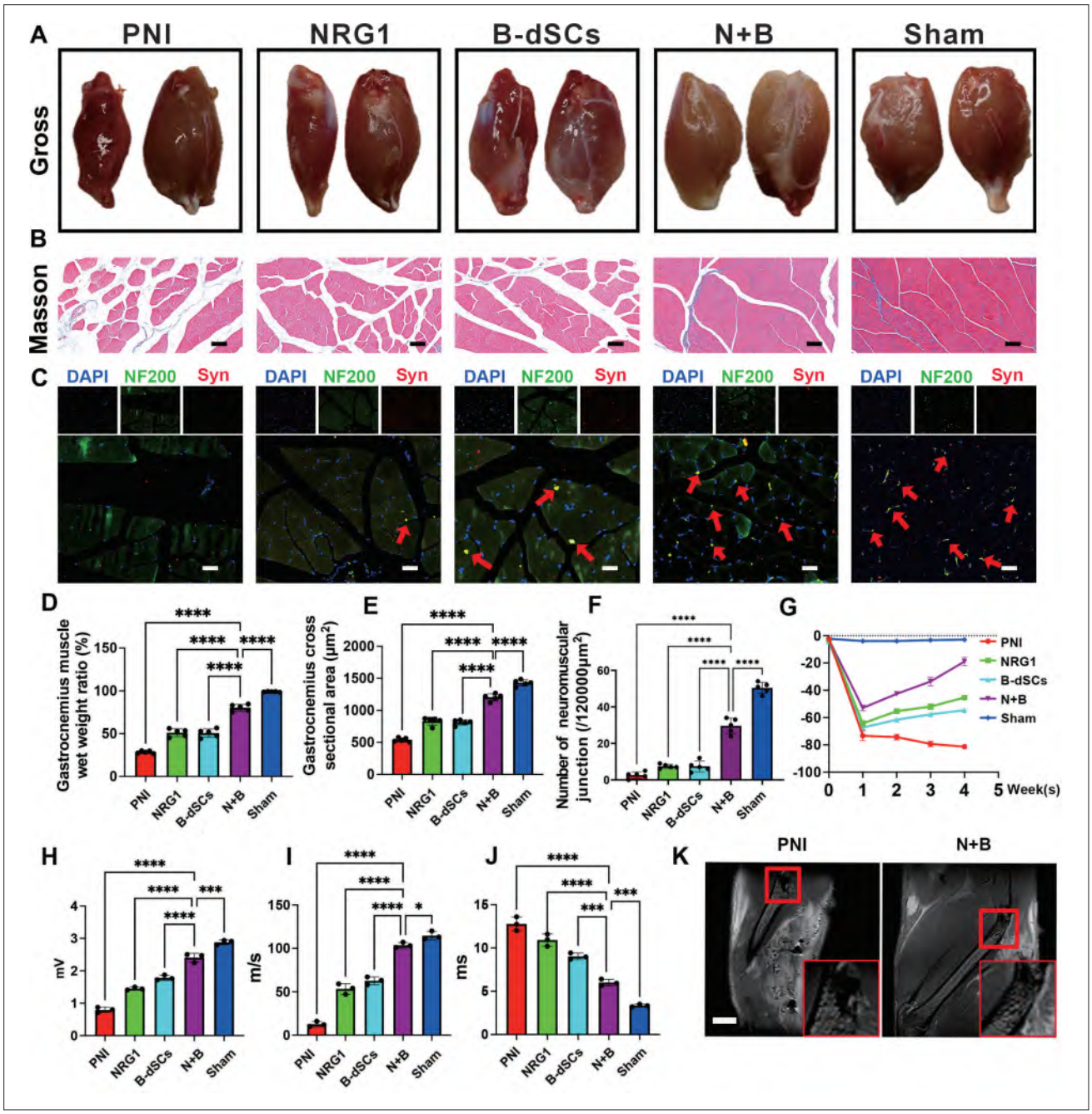


Figure 8. Assessments related to regenerated nerve function. (A) Gross images of the gastrocnemius muscle, comparing the injured side (left) with the normal side (right). (B) Masson staining of gastrocnemius muscle cross-sections, revealing differences in muscle fiber density. (C) Fluorescence staining of neurofilaments (green) and synapses (red) in gastrocnemius muscle sections, indicating neuromuscular junction density. Red arrows point to synapses in muscle tissue. (D) Quantification of the relative wet weight of the gastrocnemius muscle, showing less atrophy in the N+B group. (E) Quantification of gastrocnemius muscle cross-sectional area, indicating reduced muscle atrophy in the N+B group. (F) Quantification of neuromuscular junction density in the gastrocnemius muscle, showing higher density in the N+B group. (G) Quantification of the SFI, demonstrating faster functional recovery in the N+B group. (H) Quantification of the regenerated nerve electrical signal, showing greater signal strength in the N+B group. (I) Quantification of conduction velocity of the regenerated nerve electrical signal, with improved conduction in the N+B group. (J) Quantification of latency of the regenerated nerve electrical signal, indicating faster signal transmission in the N+B group. (K) Magnetic resonance images of nerve repair, highlighting the extent of structural recovery in the N+B group. Red boxes show corresponding magnified views. $^{*}p < 0.05$; $^{***}p < 0.001$; $^{****}p < 0.0001$. One-way analysis of variance with Tukey's post hoc test. Scale bars: (B) = 30 μm; (C) = 50 μm. Magnifications: (B) = 200×; (C) = 100×. *Note*: N+B: (NRG1 + B-dSCs) + dorsal root ganglion co-culture. Abbreviations: B-dSCs, bone marrow-derived Schwann-like cells; DAPI, 4',6-diamidino-2-phenylindole; NF200, neurofilament heavy; NRG1, neuregulin-1; PNI, peripheral nerve injury; SFI, sciatic nerve function index; Syn, synaptophysin.

extended periods. While SRMs can prolong NRG1 release, traditional hydrogel matrices embedding these microspheres often lack structural constraints, leading to microsphere sedimentation and aggregation due to gravity, and thus creating uneven distributions (Figure 1I). This unevenness results in significant local variations in NRG1 concentration.

To address this challenge, we utilized advanced 3D-printing technology to fabricate highly interconnected, grid-like hydrogel scaffolds that effectively confine NRG1-SRMs within the hydrogel fibers. This architectural design minimized microsphere mobility and prevented sedimentation, maintaining a uniform distribution of NRG1 after printing and ensuring stable local concentrations.

In vivo experiments demonstrated that NRG1 initiated robust axonal regeneration, markedly increasing the number of small-diameter axons. Concurrently, the hydrogel scaffold facilitated axonal growth through its intrinsic porous structure. Furthermore, 3D printing significantly increased the hydrogel's surface area, enabling NRG1 to diffuse effectively into scaffold pores and maintain optimal concentrations around regenerating axons, thereby promoting extensive axonal elongation and regeneration.

In vivo fluorescence tracing of B-dSCs embedded within 3D-NRG1-SRM scaffolds confirmed early-stage expression of dedifferentiation-associated proteins induced by NRG1 treatment. *In vitro* experiments corroborated these findings, demonstrating that NRG1 induced B-dSCs to adopt a bipolar spindle-shaped morphology and significantly enhanced cell motility, indicating effective dedifferentiation. Enhanced motility enabled dedifferentiated B-dSCs to rapidly migrate toward regenerating axons, forming tube-like structures analogous to bands of Büngner that guide axonal growth. Following axonal regeneration, the superior remodeling capabilities of dedifferentiated B-dSCs facilitated radial sorting and subsequent myelin sheath formation around axons. Notably, the initiation of radial sorting depends on axonal diameter, with dedifferentiated B-dSCs preferentially myelinating larger-diameter axons while bundling smaller axons into Remak fibers.[44] Without dedifferentiated B-dSCs, NRG1 alone increased axon numbers, but these were predominantly small-diameter axons exhibiting sparse myelination. Conversely, introducing dedifferentiated B-dSCs substantially increased axon diameter, prompting B-dSC-mediated radial sorting and robust myelination rather than Remak fiber formation. These results suggest that enhanced myelination primarily arises indirectly through dedifferentiated B-dSC-induced increases in axonal diameter, rather than direct NRG1 action alone. This finding further emphasizes the importance of integrating supportive seed cells to achieve effective myelin regeneration post-PNI.

Mechanistically, the dedifferentiation process of B-dSCs appears closely linked to the JNK signaling pathway, which is critically involved in Schwann cell dedifferentiation.[26,45] Activation of the JNK pathway promotes the expression of dedifferentiation-associated proteins, induces morphological changes, and enhances Schwann cell motility.[46] Our findings indicate significant JNK pathway activation in dedifferentiated B-dSCs following NRG1 treatment, while pharmacological inhibition of JNK markedly suppressed NRG1-induced dedifferentiation and myelin gene expression. These results suggest that NRG1 facilitates the myelination capability of B-dSCs by activating the JNK signaling cascade, thereby altering the biological and functional properties of these cells.

Moreover, we observed that insufficient myelination correlated with reduced NMJ formation and subsequent muscle atrophy, possibly due to disrupted nerve impulse conduction, leaving muscles in disuse. Interestingly, despite relatively better axon regeneration, the NRG1-alone group exhibited poor electrophysiological recovery and pronounced muscle atrophy. This finding highlights that intact myelination, in addition to axonal regeneration, is critical for maintaining functional neuromuscular connectivity. MRI further supported the beneficial effects of dedifferentiated B-dSCs in nerve structural restoration and prevention of muscle atrophy, providing valuable insights for future clinical translation.

5. Conclusion

NRG1 effectively promotes B-dSC dedifferentiation, significantly enhancing their myelination capacity *in vivo*. The spatial precision afforded by 3D-printing technology, combined with the sustained-release properties of microspheres, ensures stable, prolonged, and homogeneous NRG1 delivery. Together, this integrated biomaterial and biological approach offers a promising therapeutic strategy for promoting nerve and myelin regeneration following PNI.

Acknowledgments

None.

Funding

This research was supported by the National Natural Science Foundation of China (Grant No. 82201785), the Guangdong Basic and Applied Basic Research Foundation (supported by the Medical Scientific Research Foundation of Guangdong Province, China, Grant No. 20241120250;

A2025267), the Provincial Enterprise Joint Fund—General Project (Grant No. 2022A1515220046), Guangzhou City-University (Institute)-Enterprise Joint Funding Project (Grant No. SL2023A03J00448) as well as Science and Technology Projects in Guangzhou and the City-University (Institute) Enterprise Joint Funded Project (Grant Nos. 202201020633; 2024A03J0277).

Conflict of interest

The authors declare no potential conflicts of interest with respect to the research, authorship, and/or publication of this article.

Author contributions

Conceptualization: Bo Hou, Guanhua Zhang
Formal analysis: Bo Hou, Enpeng Song
Investigation: Bo Hou, Enpeng Song, Peng Yu, Jie Wei
Methodology: Bo Hou, Jie Liu
Writing–original draft: Guanhua Zhang
Writing–review & editing: Guanhua Zhang, Yaqiong Wang, Jie Liu

Ethics approval and consent to participate

All experimental procedures were approved by the Institutional Animal Care and Use Committee (IACUC) of Sun Yat-sen University (approval number SYSU-IACUC-2023-000125; [11/30/2023]) and conducted in accordance with the Guide for the Care and Use of Laboratory Animals issued by the Chinese Institute of Health.

Consent for publication

Not applicable.

Availability of data

The datasets generated and analyzed during the current study are available from the corresponding author upon reasonable request.

References

1. Zhang Y, Yi D, Hong Q, et al. Platelet-rich plasma-derived exosomes boost mesenchymal stem cells to promote peripheral nerve regeneration. *J Control Release*. 2024;367(2):265-282.
doi: 10.1016/j.jconrel.2024.01.043.

2. Dai Y, Lu T, Li L, et al. Electrospun composite PLLA-PPSB nanofiber nerve conduits for peripheral nerve defects repair and regeneration. *Adv Healthc Mater*. 2024;13(10):e2303539.
doi: 10.1002/adhm.202303539.

3. Rodríguez FJ, Verdú E, Ceballos D, Navarro X. Nerve guides seeded with autologous schwann cells improve nerve regeneration. *Exp Neurol*. 2000;161(2):571-584.
doi: 10.1006/exnr.1999.7315.

4. Bachelin C, Lachapelle F, Girard C, et al. Efficient myelin repair in the macaque spinal cord by autologous grafts of Schwann cells. *Brain*. 2005;128(3):540-549.
doi: 10.1093/brain/awh406.

5. Sun X, Zhu Y, Yin HY, et al. Differentiation of adipose-derived stem cells into Schwann cell-like cells through intermittent induction: potential advantage of cellular transient memory function. *Stem Cell Res Ther*. 2018;9:133.
doi: 10.1186/s13287-018-0884-3.

6. Wei C, Guo Y, Ci Z, Li M, Zhang Y, Zhou Y. Advances of Schwann cells in peripheral nerve regeneration: from mechanism to cell therapy. *Biomed Pharmacother*. 2024;175:116645.
doi: 10.1016/j.biopha.2024.116645.

7. Hou B, Ye Z, Ji W, et al. Comparison of the effects of BMSC-derived Schwann cells and autologous Schwann cells on remyelination using a rat sciatic nerve defect model. *Int J Biol Sci*. 2018;14(14):1910-1922.
doi: 10.7150/ijbs.26765.

8. Li R, Li D, Wu C, et al. Nerve growth factor activates autophagy in Schwann cells to enhance myelin debris clearance and to expedite nerve regeneration. *Theranostics*. 2020;10(4):1649-1677.
doi: 10.7150/thno.40919.

9. Kataria H, Alizadeh A, Karimi-Abdolrezaee S. Neuregulin-1/ErbB network: an emerging modulator of nervous system injury and repair. *Prog Neurobiol*. 2019;180:101643.
doi: 10.1016/j.pneurobio.2019.101643.

10. Soto J, Monje PV. Axon contact-driven Schwann cell dedifferentiation. *Glia*. 2017;65(6):864-882.
doi: 10.1002/glia.23131.

11. Li X, Zhang T, Li C, et al. Electrical stimulation accelerates Wallerian degeneration and promotes nerve regeneration after sciatic nerve injury. *Glia*. 2023;71(4):758-774.
doi: 10.1002/glia.24309.

12. Stoll G, Müller HW. Nerve injury, axonal degeneration and neural regeneration: basic insights. *Brain Pathol*. 1999;9(2):313-325.
doi: 10.1111/j.1750-3639.1999.tb00229.x.

13. Ding Z, Dai C, Shan W, et al. TNF-α up-regulates Nanog by activating NF-κB pathway to induce primary rat spinal cord astrocytes dedifferentiation. *Life Sci*. 2021;287:120126.
doi: 10.1016/j.lfs.2021.120126.

14. Boerboom A, Reusch C, Pieltain A, Chariot A, Franzen R. KIAA1199: a novel regulator of MEK/ERK-induced Schwann cell dedifferentiation. *Glia*. 2017;65(10):1682-1696.
doi: 10.1002/glia.23188.

15. Honorati MC, Cattini L, Facchini A. IL-17, IL-1beta and TNF-alpha stimulate VEGF production by dedifferentiated chondrocytes. *Osteoarthritis Cartilage*. 2004;12(8):683-691. doi: 10.1016/j.joca.2004.05.009.

16. Dinarello CA. Proinflammatory cytokines. *Chest*. 2000;118(2):503-508. doi: 10.1378/chest.118.2.503.

17. Jayaraman T, Paget A, Shin YS, et al. TNF-alpha-mediated inflammation in cerebral aneurysms: a potential link to growth and rupture. *Vasc Health Risk Manag*. 2008;4:805-817. doi: 10.2147/vhrm.s2700.

18. Zhou Y, Xu Z, Liu Z. Role of IL-33-ST2 pathway in regulating inflammation: current evidence and future perspectives. *J Transl Med*. 2023;21:902. doi: 10.1186/s12967-023-04782-4.

19. Min B, Kim D, Feige MJ. IL-30(†) (IL-27A): a familiar stranger in immunity, inflammation, and cancer. *Exp Mol Med*. 2021;53:823-834. doi: 10.1038/s12276-021-00630-x.

20. Wang P, Qian H, Xiao M, Lv J. Role of signal transduction pathways in IL-1β-induced apoptosis: pathological and therapeutic aspects. *Immun Inflamm Dis*. 2023;11(5):e762. doi: 10.1002/iid3.762.

21. Kang R, Li R, Dai P, Li Z, Li Y, Li C. Deoxynivalenol induced apoptosis and inflammation of IPEC-J2 cells by promoting ROS production. *Environ Pollut*. 2019;251:689-698. doi: 10.1016/j.envpol.2019.05.026.

22. Newbern J, Birchmeier C. Nrg1/ErbB signaling networks in Schwann cell development and myelination. *Semin Cell Dev Biol*. 2010;21(8-9):922-928. doi: 10.1016/j.semcdb.2010.08.008.

23. Birchmeier C. ErbB receptors and the development of the nervous system. *Exp Cell Res*. 2009;315(4):611-618. doi: 10.1016/j.yexcr.2008.10.035.

24. Boerboom A, Dion V, Chariot A, Franzen R. Molecular mechanisms involved in Schwann cell plasticity. *Front Mol Neurosci*. 2017;10:38. doi: 10.3389/fnmol.2017.00038.

25. Fornasari BE, El Soury M, Nato G, et al. Fibroblasts colonizing nerve conduits express high levels of soluble neuregulin1, a factor promoting schwann cell dedifferentiation. *Cells*. 2020;9(6):1366. doi: 10.3390/cells9061366.

26. Monje PV, Soto J, Bacallao K, Wood PM. Schwann cell dedifferentiation is independent of mitogenic signaling and uncoupled to proliferation: role of cAMP and JNK in the maintenance of the differentiated state. *J Biol Chem*. 2010;285(42):31024-31036. doi: 10.1074/jbc.M110.116970.

27. Kong L, Hassinan CW, Gerstner F, et al. Boosting neuregulin 1 type-III expression hastens SMA motor axon maturation. *Acta Neuropathol Commun*. 2023;11:53. doi: 10.1186/s40478-023-01551-8.

28. Michailov GV, Sereda MW, Brinkmann BG, et al. Axonal neuregulin-1 regulates myelin sheath thickness. *Science*. 2004;304(5671):700-703. doi: 10.1126/science.1095862.

29. Kim H, Park H, Lee SJ. Effective method for drug injection into subcutaneous tissue. *Sci Rep*. 2017;7:9613. doi: 10.1038/s41598-017-10110-w.

30. Yin PT, Han E, Lee KB. Engineering stem cells for biomedical applications. *Adv Healthc Mater*. 2016;5(1):10-55. doi: 10.1002/adhm.201400842.

31. Liu L, Wannemuehler MJ, Narasimhan B. Biomaterial nanocarrier-driven mechanisms to modulate anti-tumor immunity. *Curr Opin Biomed Eng*. 2021;20:100322. doi: 10.1016/j.cobme.2021.100322.

32. Gutierrez AM, Frazar EM, Klaus MVX, Paul P, Hilt JZ. Hydrogels and hydrogel nanocomposites: enhancing healthcare through human and environmental treatment. *Adv Healthc Mater*. 2022;11(2):e2101820. doi: 10.1002/adhm.202101820.

33. Qian Y, Lu S, Meng J, Chen W, Li J. Thermo-responsive hydrogels coupled with photothermal agents for biomedical applications. *Macromol Biosci*. 2023;23(3):e2300214. doi: 10.1002/mabi.202300214.

34. Gu D, O'Connor AJ, Qiao GHG, Ladewig K. Hydrogels with smart systems for delivery of hydrophobic drugs. *Expert Opin Drug Deliv*. 2017;14(8):879-895. doi: 10.1080/17425247.2017.1245290.

35. Asadi N, Alizadeh E, Salehi R, Khalandi B, Davaran S, Akbarzadeh A. Nanocomposite hydrogels for cartilage tissue engineering: a review. *Artif Cells Nanomed Biotechnol*. 2018;46(6):465-471. doi: 10.1080/21691401.2017.1345924.

36. Buonanno A, Fischbach GD. Neuregulin and ErbB receptor signaling pathways in the nervous system. *Curr Opin Neurobiol*. 2001;11(2):287-296. doi: 10.1016/s0959-4388(00)00210-5.

37. Jorissen RN, Walker F, Pouliot N, Garrett TPJ, Ward CW, Burgess AW. Epidermal growth factor receptor: mechanisms of activation and signalling. *Exp Cell Res*. 2003; 284(1):31-53. doi: 10.1016/s0014-4827(02)00098-8.

38. Wen J, Hou B, Lin W, et al. 3D-printed hydrogel scaffold-loaded granulocyte colony-stimulating factor sustained-release microspheres and their effect on endometrial regeneration. *Biomater Sci*. 2022;10(12):3346-3358. doi: 10.1039/d2bm00109h.

39. Griffith LG, Naughton G. Tissue engineering—current challenges and expanding opportunities. *Science*. 2002;295(5557):1009-1014. doi: 10.1126/science.1069210.

40. Fraher JP. Myelin-axon relationships in the rat phrenic nerve: longitudinal variation and lateral asymmetry. *J Comp Neurol*. 1992;323(3):551-557.
doi: 10.1002/cne.903230407.

41. Su Q, Nasser MI, He J, et al. Engineered schwann cell-based therapies for injury peripheral nerve reconstruction. *Front Cell Neurosci*. 2022;16:865266.
doi: 10.3389/fncel.2022.865266.

42. Hui T, Wang C, Yu L, Zhou C, Qiu M. Phosphorene hydrogel conduits as "neurotrophin reservoirs" for promoting regeneration of peripheral nerves. *J Mater Chem B*. 2023;11(18):3808-3815.
doi: 10.1039/d3tb00340j.

43. Yasui G, Yamamoto Y, Shichinohe R, et al. Neuregulin-1 released by biodegradable gelatin hydrogels can accelerate facial nerve regeneration and functional recovery of traumatic facial nerve palsy. *J Plast Reconstr Aesthet Surg*. 2016;69(2):328-334.
doi: 10.1016/j.bjps.2015.10.037.

44. Jung N, Park S, Choi Y, et al. Tonsil-derived mesenchymal stem cells differentiate into a Schwann cell phenotype and promote peripheral nerve regeneration. *Int J Mol Sci*. 2016;17(11):1867.
doi: 10.3390/ijms17111867.

45. Shin YK, Jang SY, Park JY, et al. The neuregulin-Rac-MKK7 pathway regulates antagonistic c-jun/Krox20 expression in Schwann cell dedifferentiation. *Glia*. 2013;61(5):892-904.
doi: 10.1002/glia.22482.

46. Kaempchen K, Mielke K, Utermark T, Langmesser S, Hanemann CO. Upregulation of the Rac1/JNK signaling pathway in primary human schwannoma cells. *Hum Mol Genet*. 2003;12(10):1211-1221.
doi: 10.1093/hmg/ddg146.

Appendix

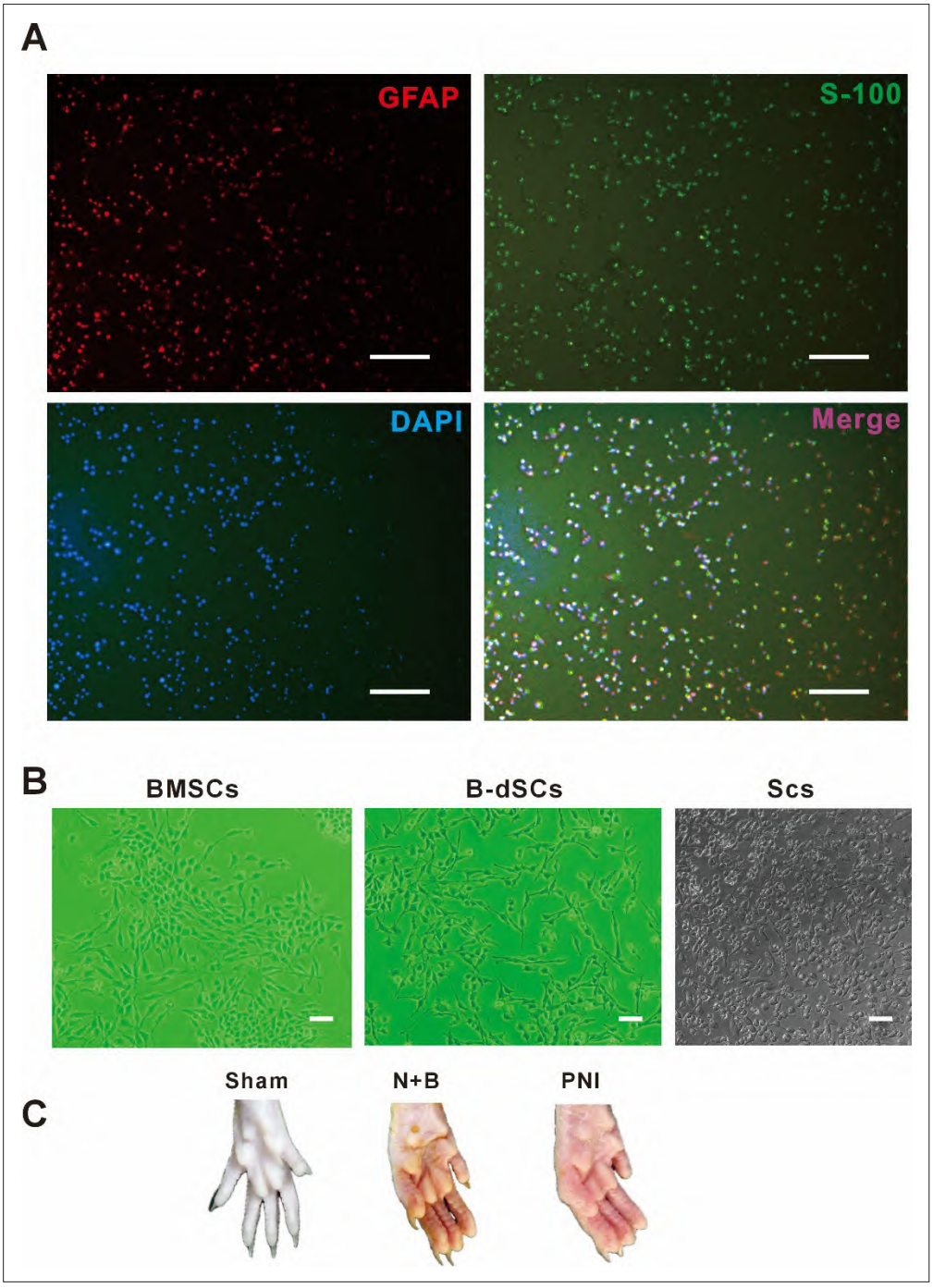


Figure A1. Characterization of B-dSCs and schematic images of rat hindlimbs at 4 weeks post-surgery. (A) Most B-dSCs positively expressed Schwann cell-specific markers, including S-100 and GFAP. (B) Compared to normal BMSCs, the induced B-dSCs displayed a disorganized cellular arrangement and a spindle-shaped morphology with elongated processes, resembling SCs. (C) Compared to the severe muscle atrophy and toenail loss in the PNI group, the N+B group showed only mild atrophy. Scale bars: (A) = 50 μm; (B) = 100 μm. **Magnifications:** (A) = **100**×; (B) = **100**×. *Note*: **N+B: (NRG1 + B-dSCs) + dorsal root ganglion co-culture.** Abbreviations: B-dSC, bone marrow-derived Schwann-like cell; BMSCs, bone marrow mesenchymal stem cells; DAPI, 4',6-diamidino-2-phenylindole; GFAP, glial fibrillary acidic protein; NRG1, neuregulin-1; PNI, peripheral nerve injury; SCs, Schwann cells.

Raw image file

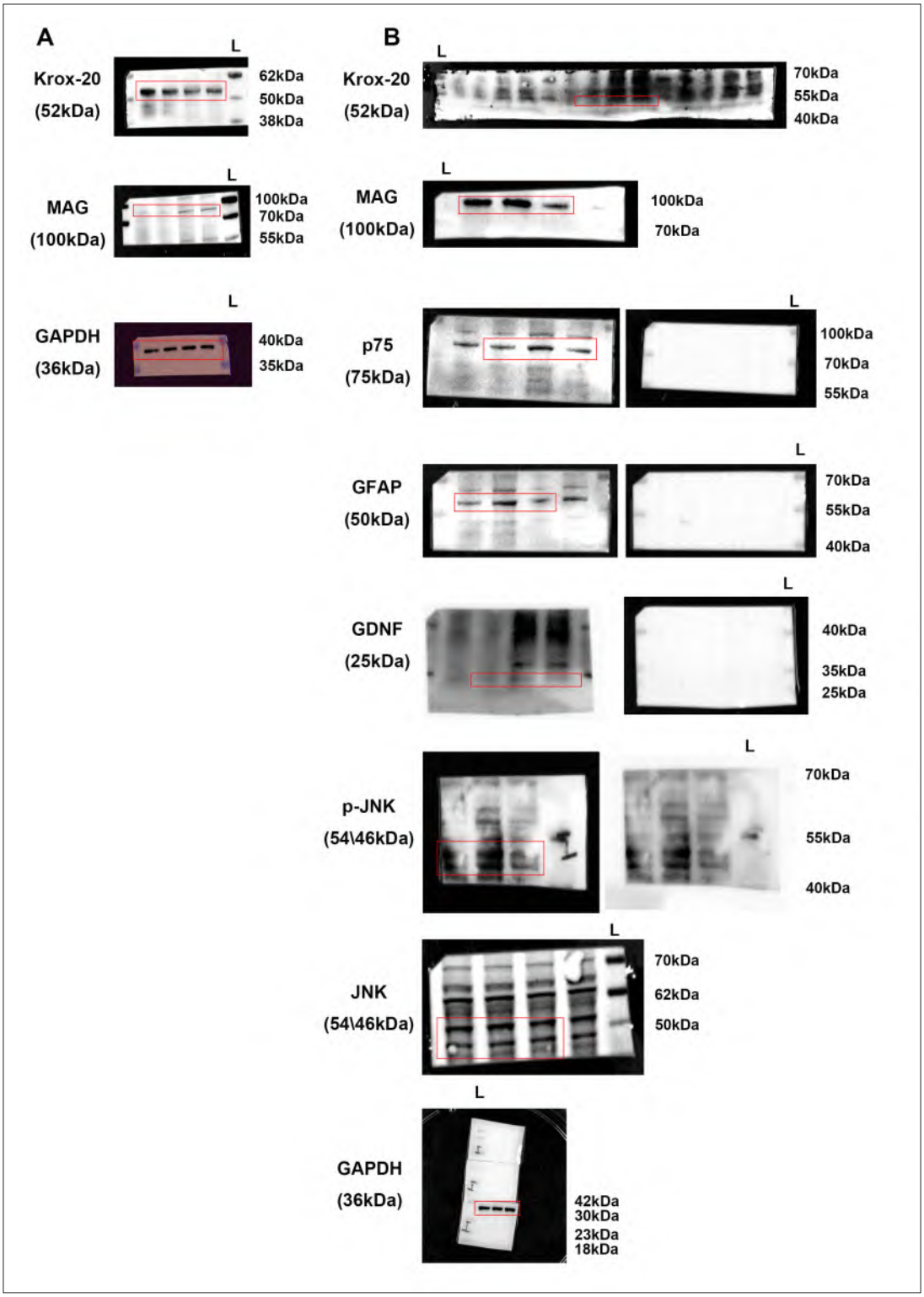


Figure R1. Raw images for Western blotting results in **Figure 3**. (A) Raw images for **Figure 3A**; (B) Raw images for **Figure 3B**.

ACCSCIENCE PUBLISHING

International Journal of Bioprinting

RESEARCH ARTICLE

3D-bioprinted placenta-on-a-chip platform for modeling the human maternal–fetal barrier

Yazhi Sun[1†], Henry H. Hwang[1†], Chandana Tekkatte[2,3†], Scott A. Lindsay[2,3], Anelizze Castro-Martinez[2,3], Claire Yu[1], Isabella Saldana[2,3], Xuanyi Ma[1], Omar Farah[3,4], Mana M. Parast[3,4], Louise C. Laurent[2,3*], and Shaochen Chen[1*]

[1]Department of Chemical and Nano Engineering, University of California San Diego, San Diego, CA, United States of America

[2]Department of Obstetrics, Gynecology, and Reproductive Sciences, University of California San Diego, San Diego, CA, United States of America

[3]Sanford Consortium for Regenerative Medicine, University of California San Diego, San Diego, CA, United States of America

[4]Department of Pathology, University of California San Diego, San Diego, CA, United States of America

Abstract

The placenta plays a vital role in pregnancy by regulating selective exchange between the maternal and fetal circulations and producing essential hormonal signals. In this study, we present an *in vitro* placenta-on-a-chip platform that leverages 3D bioprinting to replicate the structural and functional features of the human placental barrier. This microengineered system utilizes digital light processing-based 3D bioprinting to fabricate the microfluidic mold and construct 3D encapsulated cell cultures within a biomimetic hydrogel scaffold, enabling co-culture of three human cell types, including two derived from primary placental tissue. The system demonstrated excellent cell viability, high metabolic activity, placental hormone secretion, and native-like selective barrier transport properties. This system offers a versatile platform for experimental perturbations to explore mechanisms of normal placental function and identify contributors to placental dysfunction.

Keywords: Bioprinting; Microfluidics; Microphysiological system; Organ-on-a-chip; Placenta; Trophoblast stem cells

1. Introduction

The human placenta acts as a vital interface mediating the exchange of nutrients, gases, and waste products between the maternal and fetal compartments, while also producing key hormones essential for maintaining pregnancy. It plays a crucial role in fetal health, not only in supporting fetal growth and development but also serving as a barrier to exogenous factors, such as environmental pollutants, pharmaceutical compounds, and pathogens. Notably, about 90% of women take at least one medication during their pregnancy,[1,2] underscoring the urgent need for placental models that can be used to evaluate whether and how these new medications can cross over into the fetal circulation.

†These authors contributed equally to this work.

***Corresponding authors:**
Louise C. Laurent (llaurent@ucsd.edu)

Shaochen Chen (shc064@ucsd.edu)

Citation: Sun Y, Hwang HH, Tekkatte C, *et al*. 3D-bioprinted placenta-on-a-chip platform for modeling the human maternal–fetal barrier. *Int J Bioprint*. 2025;11(5):178-196. doi: 10.36922/IJB025270262

Received: July 2, 2025
Revised: July 22, 2025
Accepted: July 28, 2025
Published Online: July 28, 2025

Copyright: © 2025 Author(s). This is an Open Access article distributed under the terms of the Creative Commons Attribution License, permitting distribution and reproduction in any medium, provided the original work is properly cited.

Publisher's Note: AccScience Publishing remains neutral with regard to jurisdictional claims in published maps and institutional affiliations.

The functional units of the human placenta are the chorionic villi—finger-like structures that extend from the fetal tissue into the maternal blood space, allowing close contact between fetal capillaries and maternal blood (Figure 1A). Chorionic villi serve as the primary interface for gas and nutrient exchange between the maternal and fetal circulations. Each villus consists of an outer layer of syncytiotrophoblast (STB) and an interior filled with stromal connective tissue, resident stromal cells, and a variably distributed network of fetal capillaries. The villi are bathed in maternal blood within the intervillous space, allowing direct contact between maternal blood and the STB surface. This close proximity to the fetal capillaries facilitates efficient exchange of gases, nutrients, and waste products between the maternal and fetal circulations.

Several existing strategies have been developed to study placental function, but each has important limitations. For example, 2D cell culture models fail to replicate the complex interactions between different cell types and the influence of blood flow present in the placenta. *Ex vivo* perfusion of the human placenta preserves the complex tissue architecture, but often lacks accurate representation of the *in vivo* flow environment, and is hampered by low throughput, donor variability, and scarcity.[3–5] Animal models, while useful for *in vivo* studies, have limited relevance to human physiology due to cross-species differences in placental morphology and cellular composition.[6,7] Studies involving pregnant women are constrained by ethical, safety, and logistical concerns. In contrast, *in vitro* microfluidic and microphysiological systems offer key advantages, including standardized fabrication, the ability to mimic tissue architecture and support long-term culture, physiological relevance, and precise experimental control.[8]

Recent *in vitro* microfluidic models have sought to recapitulate the physiological and functional aspects of these structures. To simulate the fetal-maternal interface, many studies employ synthetic porous membranes,[9,10] such as commercial Transwell inserts (Corning), or natural materials like vitrified collagen and Matrigel,[11,12] which serve to separate the two compartments, with cells seeded accordingly. While these studies demonstrated some placental functions, such as drug transport, the placental cells used were often immortalized lines derived from cancerous placental cells ("choriocarcinomas"), resulting in behavior and expression profiles markedly different from healthy placental cells.[13] Advanced microfluidics-based platforms have also been used as a more intricate and dynamic approach to model the multi-cellular interactions in the placental villus. Some of these systems incorporated primary or induced pluripotent stem cell-derived placental cells; however, they generally relied on monolayer cell seeding, rather than mimicking the 3D *in vivo* architecture.[14–16] One recent study utilized trophoblast organoids to establish a 3D culture, but the spherical organoids did not fully cover the interface and lacked the inclusion of other relevant cell types and intercellular interactions.[17] Moreover, a major challenge in recapitulating human placental physiology with microfluidics is the enclosed chamber design, which complicates patterning multiple cell types into organized structures that mimic native placental architecture. Although sequential perfusion of different cell types into chambers is possible, the resulting 2D cultures fail to reproduce the 3D *in vivo* environment. Thus, an *in vitro* system that mimics the 3D structure and functionality of the human chorionic villus remains to be developed with primary cells for investigation of drug transport across this barrier in the setting of normal pregnancy and disease.

Currently, most placenta-on-a-chip platforms require photolithography for microfluidic device fabrication, which is time-consuming, labor-intensive, and dependent on expensive cleanroom infrastructure.[18–20] In contrast, digital light processing (DLP)-based 3D printing offers a rapid, cost-effective, and mask-free alternative for fabricating microfluidic molds with high spatial resolution. By projecting patterned light onto photopolymerizable materials, DLP 3D printing enables the precise creation of high-resolution geometries directly from digital designs, thereby streamlining the microfabrication process for the master molds. In addition, it has also been widely adopted in 3D cell culture and tissue engineering, where it supports the fabrication of cell-laden hydrogels and organ-on-a-chip platforms with tunable architecture and mechanical properties.[21,22] Its versatility makes DLP 3D printing an ideal tool for developing physiologically relevant *in vitro* models.

In this study, we present a novel human placenta-on-a-chip (hPOC) microfluidic system featuring primary placental cell tri-coculture within a "hybrid" open/closed microfluidic design (Figure 1B–D). The device contains dual compartments separated by a porous membrane that provides structural support for both the maternal compartment and fetal capillaries. This configuration recapitulates the spatial organization of the chorionic villus. On the maternal side, primary human trophoblast stem cells (hTSCs) are cultured on the membrane-facing surface, with placenta-derived stromal fibroblasts (PDSFs) embedded in a methacrylated gelatin (GelMA) layer beneath them by DLP bioprinting. On the fetal side, primary human umbilical vein endothelial cells (HUVECs) are seeded on the underside of the membrane and maintained under continuous perfusion to simulate dynamic fetal circulation.

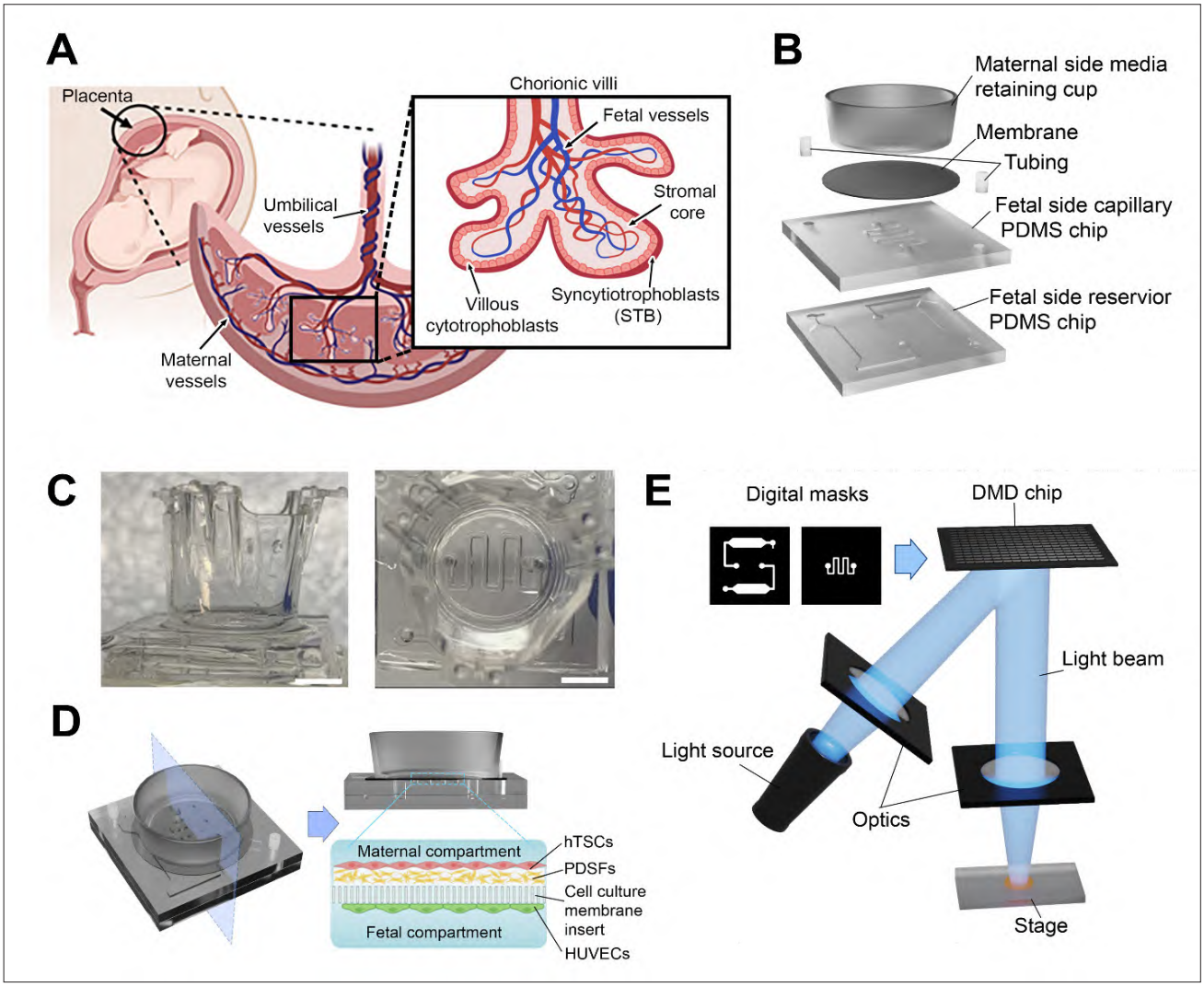


Figure 1. Schematic of the human placenta and the hPOC design. (A) Illustration of the human placenta, featuring the chorionic villi, which mediate nutrient and gas exchange at the maternal-fetal interface. (B) Exploded view of the hPOC device components, highlighting the porous membrane that separates the maternal and fetal compartments. (C) Side view (C, left) and top view (C, right) of the assembled hPOC device. Scale bar: 5 mm. (D) Cross-sectional schematic of the assembled hPOC device, displaying the multi-layered cellular architecture that recapitulates key features of the placental barrier. (E) Schematic of DLP bioprinting. Digital masks are projected via a DMD onto the sample stage, selectively solidifying the polymer precursor to create patterned structures. Abbreviations: DLP, digital light processing; DMD, digital mirror device; hPOC, human placenta-on-a-chip; hTSCs, human trophoblast stem cells; HUVECs, human umbilical vein endothelial cells; PDMS, polydimethylsiloxane; PDSFs, placenta-derived stromal fibroblasts.

We employed DLP 3D printing (Figure 1E) to fabricate the master molds of the microfluidic chambers for polydimethylsiloxane (PDMS) casting. This enabled assembly of the hPOC device with an open media-retaining cup and enclosed microfluidic channels. After extensive optimization of cell attachment and viability of the primary placental cell types on 3D-printed hydrogel scaffolds with varying stiffness, we identified optimal stiffness, culture, and flow conditions for device assembly. The three cell types were systematically seeded into the 3D tri-coculture model to test functional transport properties. Our results demonstrated that the hPOC device produces placental hormones and mimics key placental barrier and transport functions, suggesting utility in applications such as drug/nutrient transport. To the best of our knowledge, this open/closed microfluidic design is the first system incorporating primary placenta-derived cells alongside primary endothelial cells in a tri-coculture configuration. This setup offers the capability to support both genetic and environmental manipulations, providing a versatile platform for future studies of human placental transport and function.

2. Materials and methods

2.1. hPOC device fabrication

The microfluidic architecture was designed using computer-aided design software (AutoCAD, Autodesk, USA). The photocrosslinkable hydrogel, poly(ethylene glycol) diacrylate (PEGDA; molecular weight [MW]: 250 Da) and the photoinitiator phenyl bis(2,4,6-trimethylbenzoyl) phosphine oxide (trade name: Irgacure-819, BASF) were obtained from Sigma Aldrich (USA). The polymer precursor consisted of PEGDA 250 and 1% (w/v) Irgacure-819.

An in-house DLP 3D printer was utilized to fabricate positive master molds for both the microfluidic fetal capillary compartment and fluid reservoirs. After printing, the molds were rinsed with isopropanol to remove any uncrosslinked PEGDA, which would otherwise inhibit the crosslinking of PDMS.

PDMS was prepared by mixing the curing agent and base monomer at a 1:10 mass ratio, poured over the master molds, degassed, and cured overnight at 80°C. Once cured, the PDMS chips containing the fetal capillary and fluidic reservoir features were demolded, cut, and ported. The fluidic reservoir component was bonded to a glass slide using oxygen plasma treatment, and the fetal capillary component was aligned and affixed atop the reservoir using a thin layer of PDMS glue.

To form the membrane separating the fetal and maternal compartments, a commercially available cell culture insert membrane (polyethylene terephthalate with 3 μm pores, cellQART, Germany) was used. A 1:1 mixture of toluene and standard-mix PDMS was spin-coated onto a glass slide (60 s, 1500 rpm) to serve as an adhesive, after which the fetal side of the partially assembled device was gently stamped onto the spin-coated slide, ensuring coating of the negative spaces without obstructing channel patency.

The membrane was aligned and placed atop the fetal capillary compartment and cured for 10 min at 80°C. Finally, the retaining cup from the cell culture insert was bonded atop the membrane using additional PDMS, completing the maternal compartment of the hPOC device.

2.2. Cell culture

2.2.1. Primary placenta-derived stromal fibroblasts

The current study involving human-sourced tissues used in biomedical research was approved by the Institutional Review Board at the University of California San Diego (IRB #181917). Following written informed consent from donors, third-trimester placentas (gestational age: 36–38 weeks) from uncomplicated pregnancies were collected and transported to the laboratory on ice within 1 h of delivery.

Primary PDSFs were isolated from placental chorionic villi using the explant culture method, as previously described by Igura et al.[23] Briefly, the basal and chorionic plates were excised using sterile surgical scissors and discarded to eliminate maternal cell contamination. Lobes of placental villi were then dissected, carefully avoiding large blood vessels, and rinsed thoroughly in sterile phosphate-buffered saline (PBS) to remove maternal blood. Villus chunks were placed in a petri dish containing pre-warmed Dulbecco's Modified Eagle Medium (DMEM)-high glucose medium and dissected into 7–10 mm explants.

A total of 10 explants were transferred to a 10 cm tissue culture-treated dish and allowed to adhere by drying at room temperature for 1 h. Once firmly attached, 15 mL of pre-warmed growth medium (DMEM-high glucose supplemented with 10% fetal bovine serum (FBS) and 1% penicillin–streptomycin) was gently added to the side of each dish to avoid dislodging the explants. Cultures were maintained in a humidified incubator at 37°C and 5% CO_2 under normoxic conditions for up to 4 weeks. During this time, PDSFs migrated out of the cut surfaces of the explants. Growth medium was replenished every 3–4 days (Figure S1). Migrated cells were harvested using 0.05% trypsin-EDTA solution (3 min at 37°C), expanded in culture, and cryopreserved in liquid nitrogen for future use. All encapsulated cells used in this study were within 12 population doublings (approximately four to six passages).

2.2.2. Human trophoblast stem cells

We used a hTSC line (1049) that was established from early gestation (gestational age: 6–8 weeks) placentas, as previously described by Okae et al.[24] The use of early gestation placental tissues in this study was approved by the Institutional Review Board of the University of California, San Diego (IRB #172111). Written informed consent was obtained from all donors. Cells were routinely maintained on tissue culture plates coated with 5 μg/mL collagen-IV (C0543-1VL, Sigma-Aldrich, USA) in iCTB medium,[25] modified from the medium used by Okae et al.[24] hTSC media, consisting of Advanced DMEM/F12 supplemented with 1× N2 and 1× B27 supplements, 2 mM glutamine, 150 μM 1-thioglycerol, 0.05% of 30% BSA solution, and 1× Knockout Serum Replacement (KSR). The medium was further supplemented with 2 μM CHIR99021, 500 nM A83-01, 1 μM SB431542, 5 μM Y-27632, 0.8 mM valproic acid sodium salt, 100 ng/mL FGF2, 50 ng/mL EGF, 20 ng/mL Noggin, and 50 ng/mL HGF.

To induce differentiation into multinucleated STB, hTSCs were switched to STB differentiation medium, as per the protocol by Okae et al.,[24] composed of DMEM/F12 (without HEPES), supplemented with 1× ITS-X, 3.2% KSR, 1% of 30% BSA solution, 0.1 mM beta-mercaptoethanol,

2.5 μM Y27632, and 2 μM forskolin. For the tri-coculture experiments, primary hTSCs between passages 35 and 40 were used for syncytialization.

2.2.3. Human umbilical vein endothelial cells

HUVECs were obtained from the American Type Culture Collection (USA) and expanded in standard 2D culture using EGM-2 endothelial cell growth medium supplemented with 2% FBS and vascular endothelial growth factor (Lonza, USA). Prior to seeding into the microfluidic device, HUVECs were cultured under these conditions to ensure optimal cell health and expansion. HUVECs used for the tri-coculture experiments were between passages 3 and 5.

During static culture within the device, media were manually replenished daily. Once perfusion was initiated, continuous media flow was maintained to support endothelial maturation and viability.

2.3. Tri-coculture assembly and functional characterization

2.3.1. Sequential cell seeding and culture timeline

Prior to cell culture, both the fetal and maternal compartments of the device were incubated at 37°C overnight with a solution containing 5 μg/mL rat tail collagen type I (354236, Corning, USA) and a 1:25 dilution of bovine plasma-derived fibronectin (F1141, Sigma-Aldrich, USA) in 1× DPBS to promote cellular attachment.

On day 0, a PDSF layer was established in the maternal compartment using a GelMA-based bioink. GelMA was synthesized as previously described[26] and used at 7.5% (v/v) in 1× DPBS. The photoinitiator lithium phenyl-2,4,6-trimethylbenzoylphosphinate (LAP, Tokyo Chemistry Industry, Japan) was added at 0.6% (v/v). DiD (Vybrant™, Thermo Fisher, USA)-stained PDSFs were encapsulated within the GelMA bioink at a density of 75,000 cells/mL and carefully layered onto the membrane "floor" of the maternal compartment using PDMS spacers (125 μm thick) to constrain hydrogel thickness. The construct was crosslinked using UV light from the DLP 3D printer. After polymerization, the PDMS spacers were carefully removed, leaving the GelMA-encapsulated PDSF layer intact and adhered to the membrane.

On day 1, green fluorescent protein (GFP)-expressing HUVECs were seeded into the fetal compartment at a density of approximately 8×10^6 cells/mL and statically cultured for 3 days. Media in the fetal compartment were replenished daily through the reservoir.

On day 4, approximately 500,000 red fluorescent protein (RFP)-expressing hTSCs were suspension-seeded into the maternal compartment atop the PDSF-encapsulated GelMA layer. Gravity-assisted sedimentation facilitated their attachment. hTSCs were cultured in iCTB media for 24 h.

On day 5, the media in the maternal compartment were switched to STB differentiation media. On the same day, perfusion of the fetal compartment was initiated using a peristaltic pump (PeriWave Micro, CorSolutions, USA) at a volumetric flow rate of 3.5 μL/min. This perfusion continued for 3 days, and the media outflow was collected every 24 h. Maternal supernatant was also collected daily, and media in the maternal compartment were replaced with fresh STB differentiation media.

On day 8, after 3 days of syncytialization and perfusion, assays to assess placental barrier formation and function—including cell viability, fluorescent molecule transport, and imaging—were performed.

2.3.2. Mechanical measurement of GelMA constructs

Cylindrical GelMA hydrogel samples (1 mm diameter × 1 mm height) were bioprinted using the designated light exposure parameters. The Young's modulus was measured using a Microtester system (CellScale, USA). Samples were compressed to 20% strain using a cantilever with a platen tip at a rate of 8 μm/s, held for 2 s, then allowed to recover. Strain and force were recorded, and the Young's modulus was calculated using a custom MATLAB script.

2.3.3. LIVE/DEAD™ staining

Cell viability was assessed using the LIVE/DEAD® Viability/Cytotoxicity Kit (Invitrogen, USA), which employs calcein AM (2 μM, 1:2000 dilution) to label live cells green and propidium iodide (4 μM, 1:500 dilution) to stain dead cells red. Cells were incubated with the dye mixture in serum-free media for 30 min at 37°C and 5% CO_2. Following incubation, cultures were washed with fresh media to eliminate excess dye and imaged using a Leica DMI6000B fluorescence microscope (Leica Microsystems, Germany).

2.3.4. XTT viability assay

Cell metabolic activity was quantified using the CyQUANT XTT Cell Viability Assay Kit (Invitrogen, USA). A working solution was prepared by mixing 5 mL of XTT labeling reagent with 0.1 mL of the electron-coupling reagent. The solution was added to both maternal and fetal compartments to a final XTT concentration of 0.3 mg/mL. Supernatant samples were collected every 15 min for 3 h, and absorbance was measured using a microplate reader (Tecan Infinite 200 Pro, Tecan Trading AG, Switzerland) at 450 nm with a reference wavelength of 650 nm.

2.3.5. Quantification of placenta-specific hormones via ELISA

Supernatant samples collected daily from the maternal and fetal compartments following hTSC seeding were analyzed for placenta-specific hormone secretion using enzyme-linked immunosorbent assays (ELISAs), following the manufacturer's protocols for each kit. Estradiol levels were measured using the Estradiol Human ELISA Kit (KAQ0621, Thermo Scientific, USA). Human placental lactogen (hPL) was quantified using the Human CSH1 Placental Lactogen Sandwich ELISA Kit (LS-F16356, LSBio, USA). Beta subunit human chorionic gonadotropin (hCGβ) was assessed using the Human Chorionic Gonadotropin ELISA Kit (HC251F, Calbiotech, USA). Progesterone was measured using the Progesterone Competitive ELISA Kit (EIAP4C21, Invitrogen, USA).

2.3.6. Imaging and morphological characterization

An upright fluorescence microscope with a motorized stage (Leica DMI6000B, Leica Microsystems, Germany) and stage-top cell culture incubator (Tokai Hit INU, Tokai Hit, USA) was used for live imaging of the tri-coculture system during the first 24 h of perfusion. Fluorescent tile scans (5×) were acquired at defined time points across multiple channels and stitched into mosaic images using the onboard LAS-X software (Leica, Germany). For 3D imaging, a ZEISS LSM 880 Confocal with FAST Airyscan (ZEISS, Germany) was used to capture Z-stacks of the PDSF-encapsulated GelMA hydrogels and the materno-fetal barrier in the tri-coculture model, which were processed into maximum projections using ZEISS Airyscan Software or 3D reconstructions using Imaris (Oxford Instruments, UK).

2.4. Assessment of barrier integrity and molecular permeability

2.4.1. Sodium fluorescein permeability

Sodium fluorescein salt (Na-F; Sigma-Aldrich, USA) was used as a tracer molecule to assess passive permeability across the placental barrier. A working solution of Na-F (40 ng/mL; 100 nM) was introduced to the maternal compartment. After 24 h, samples were collected from the fetal compartment and analyzed using a microplate reader (Tecan Infinite 200 Pro, Tecan Trading AG, Switzerland) with excitation at 485 nm and emission at 528 nm. The assay was performed on four types of devices: Type 1 was an acellular device; Type 2 included an acellular GelMA layer; Type 3 incorporated HUVECs on the fetal side; and Type 4 represented the full tri-coculture system. The concentration of 40 ng/mL was selected based on preliminary experiments, which demonstrated that higher concentrations, such as 2 μg/mL, resulted in excessive nonspecific staining of the polyethylene terephthalate (PET) membrane.

2.4.2. FITC-conjugated dextran permeability

FITC-conjugated dextran (FITC-dextran) was introduced into the maternal compartment at a concentration of 1 mg/mL in STB media. After 24 h, samples from the fetal compartment were collected and analyzed using a microplate reader (Tecan Infinite 200 Pro, Tecan Trading AG, Switzerland) with excitation at 490 nm and emission at 520 nm. The assay was performed on four types of devices: Type 1 was an acellular device; Type 2 included an acellular GelMA layer; Type 3 incorporated HUVECs on the fetal side; and Type 4 represented the full tri-coculture system.

2.4.3. Glucose transport

To assess glucose transfer across the tri-coculture model, media containing glucose (STB media in the maternal compartment and EGM-2 media in the fetal compartment) were used. The maternal and fetal compartments initially contained approximately 300 mg/dL and 100 mg/dL glucose, respectively. Samples were collected from both compartments at defined time points and analyzed using a commercial glucose monitoring system (GlucCELL, Chemglass Life Sciences, USA). These measurements were conducted in both tri-coculture devices and control devices containing acellular membranes to assess baseline permeability.

2.5. Statistical analysis

All data are presented as mean ± standard deviation, unless otherwise noted. Statistical analyses and graphical representations were performed using GraphPad Prism software (GraphPad Software, USA). Paired *t*-tests were used to assess differences between the fetal and maternal sides in Figure 4. One-way analysis of variance (ANOVA) was used to assess differences among multiple groups for other figures. Statistical significance was defined as $^{*}p < 0.05$, $^{**}p < 0.01$, $^{***}p < 0.001$, and $^{****}p < 0.0001$.

3. Results

3.1. Fabrication of the hPOC device

Figure 1B displays the schematic of the hPOC device design, and Figure S2 features the cross-sectional view. The hPOC device was constructed through a multi-step process: to model the fetal capillary compartment, a serpentine microchannel (500 μm diameter) was fabricated using DLP 3D printing. Two digital masks were projected onto a PEGDA resin to create a mold directly on glass coverslips. PDMS was then cast onto this mold to form the fetal capillary chip, which was adhered to the underside of a porous membrane with the serpentine pattern facing upward. Four access ports were punched in the PDMS to

allow for media inflow, outflow, and connection to the fetal media reservoir. A separate reservoir chip was then aligned and bonded to the fetal capillary chip, and tubing was inserted into two diagonal ports to enable perfusion. On the maternal side, a plastic reservoir cup was affixed atop the porous membrane using a thin layer of PDMS glue to complete the assembly. This configuration supports static culture, with culture media retained within the cup. In contrast, the fetal side supports dynamic culture through continuous media perfusion: media is introduced via the inlet tubing, flows through the reservoir layer, and is directed into the fetal capillary compartment.

The hPOC device incorporates two primary placenta-derived cell lines—hTSCs and PDSFs—along with HUVECs derived from the human umbilical vein endothelium, to represent key structural components of the human placental villus (Figure 1A and D). In the maternal compartment, PDSFs are first encapsulated in a 125 μm GelMA layer on top of the porous membrane, followed by seeding of hTSCs, which are induced to differentiate to STB (hTSC–STB), mimicking the native arrangement of trophoblasts overlaying the stromal core. On the fetal side, HUVECs are seeded onto the inner surface of the serpentine microchannel beneath the membrane, representing the fetal capillary endothelium. While the perfusable fetal compartment enables dynamic culture with continuous media flow, an initial period of static culture is necessary to promote HUVEC adhesion. During this period of static culture, the reservoir permits sufficient passive diffusion to support cell viability. Our novel multi-layer design enables interaction between the maternal and fetal compartments through an engineered placental barrier comprised of hTSC–STB, PDSFs, a porous membrane, and HUVECs, with transport driven by gravity and diffusion. Additionally, the design recapitulates the physiological relationship between maternal and fetal blood spaces: a larger maternal surface area and fine fetal capillary channels mimic the natural arrangement in which maternal blood in the intervillous space surrounds the chorionic villi, offering greater exchange surface area and blood volume relative to the fetal capillary network within each villus.

3.2. Optimization of cell culture in the maternal compartment

To optimize the maternal compartment, we first established culture conditions for PDSFs encapsulated in a 125 μm-thick GelMA slab. This thickness approximates the physiological thickness of the stromal layer in the human placenta and enables adequate nutrient diffusion to support the 3D culture of PDSFs. The growth and morphology of PDSFs are influenced by the stiffness of the surrounding matrix. Utilizing DLP bioprinting, we are able to tune the bulk stiffness of the hydrogel network by adjusting the light exposure,[21] achieving stiffnesses ranging from ~1.5 to ~30 kPa (Figure S3). We assessed the viability of PDSFs encapsulated in GelMA at stiffness levels of ~1.5, ~7, and ~18 kPa (Figure 2A). PDSFs maintained high viability across this range of stiffness; however, we selected the GelMA stiffness of ~18 kPa for subsequent experiments based on cellular morphology, as cells exhibited more pronounced elongated processes characteristic of fibroblasts at this higher stiffness level.

We then assessed the viability, morphology, and growth of hTSCs as a function of GelMA stiffness. Figure 2B presents hTSCs cultured on printed GelMA scaffolds spanning the same stiffness range used for PDSF encapsulation. Live/dead viability staining and fluorescence imaging demonstrated excellent viability and typical hTSC morphology across the range of stiffness, including the previously identified optimal stiffness of ~18 kPa.

During gestation, the placenta undergoes significant structural remodeling, including the syncytialization of cytotrophoblasts (CTB), forming large, multinucleated STB on the maternal side of the chorionic villi.[27] This transformation is a defining feature of the placental barrier and is widely regarded as essential to replicate in any *in vitro* chorionic villus model.[28] In many such models, syncytialization of mononuclear CTB-like cells (such as those from the BeWo choriocarcinoma cell line) is induced by treatment with forskolin, which elevates intracellular cyclic adenosine monophosphate (cAMP) levels. The rise in cAMP activates protein kinase A and other downstream signaling molecules that regulate the expression of proteins and enzymes involved in cell-cell adhesion and membrane fusion, driving the formation of STBs.[29] To induce syncytialization, hTSCs seeded on ~18 kPa GelMA scaffolds were cultured in forskolin-containing media. After 72 h, the cells were stained with wheat germ agglutinin to evaluate cell borders and DAPI to mark nuclei, revealing complete coverage of the culture surface and a high degree of syncytialization (Figure 2C). The ability of the GelMA scaffold to support a high density of hTSC growth and syncytialization is critically important, as these are essential to mimicking the integrity of the placental barrier.

3.3. Optimization of HUVEC culture in the fetal compartment

We optimized the culture conditions for HUVECs in the microchannels of the fetal compartment. While hTSCs could adhere readily to the GelMA surface on the maternal side due to intrinsic cell-binding motifs in GelMA,[30] seeding HUVECs on the fetal side was

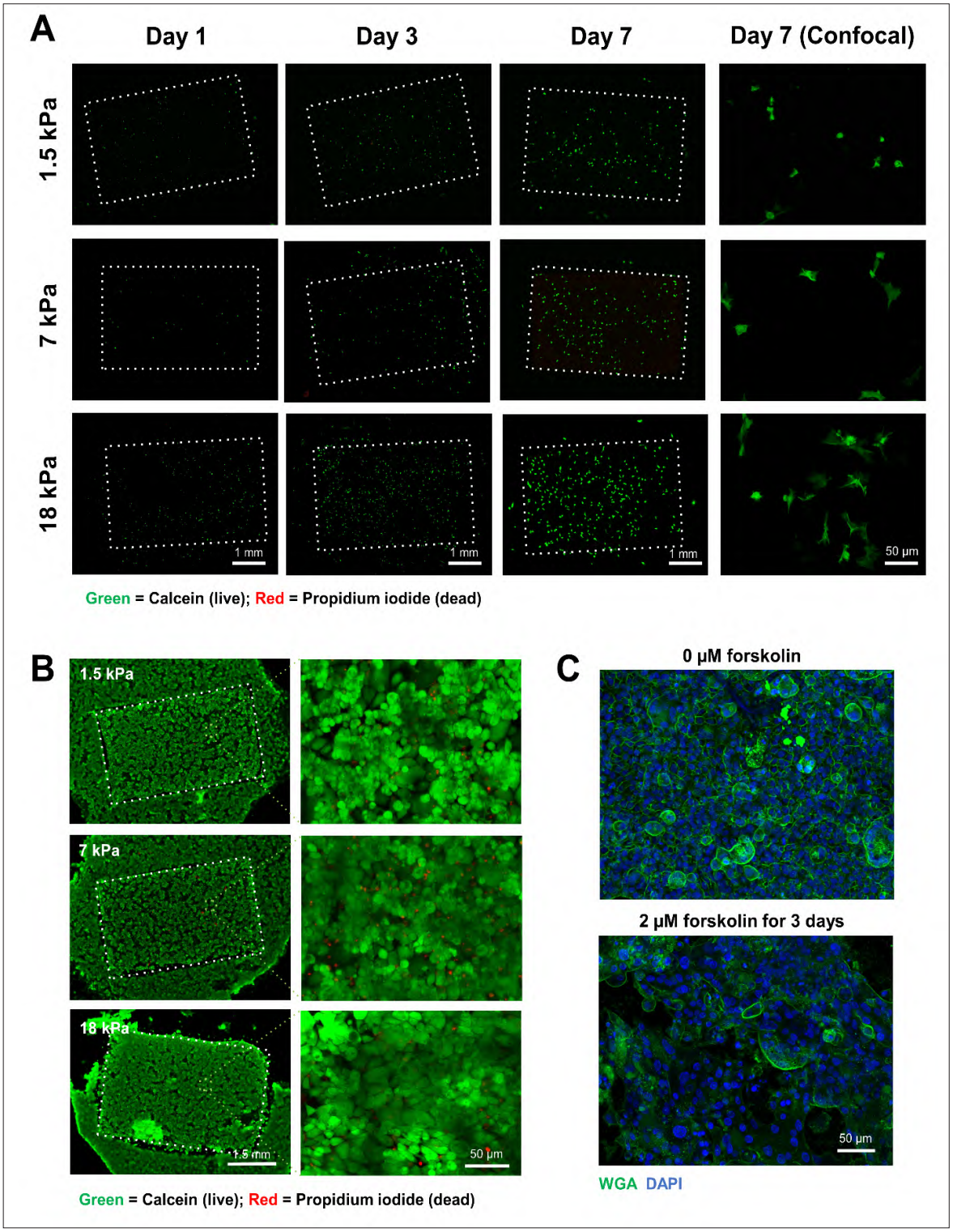


Figure 2. Optimization of cell culture conditions in the maternal compartment. (A) Live/dead staining of placental-derived stromal fibroblasts (PDSFs) encapsulated in methacrylated gelatin (GelMA) hydrogels and cultured over 7 days. (B) Live/dead staining of human trophoblast stem cells (hTSCs) cultured atop 3D-printed GelMA scaffolds for 7 days. (C) Confocal microscopy images of hTSCs stained with wheat germ agglutinin (WGA, cell membrane) and DAPI (nuclei): cells cultured in standard media (C, top) and cells treated with forskolin-containing media for 3 days to induce syncytialization (C, bottom). Scale bars: 1.5 mm (B, left); 1.0 mm (A, far-left, left-middle, right-middle); 50 μm (A, far-right; B, right; C).

more challenging. The synthetic cell culture insert lacks natural extracellular matrix (ECM) ligands and does not inherently support effective cell adhesion. To enhance attachment, both maternal and fetal compartments were pre-treated with bovine plasma-derived fibronectin and collagen-I for overnight incubation prior to HUVEC seeding, consequently promoting cell adhesion within the microchannels and on the fetal-side membrane surface. We then inverted the hPOC device, seeded HUVECs at a density of 1×10^6 cells/mL on the fetal side membrane through the channel, and incubated the device for 1 h to allow for cell adhesion. The devices were then returned to an upright position and connected to the media-filled reservoir. In an initial experiment, we examined HUVEC viability inside the 500 μm-wide microchannels in static culture over the course of 72 h using live/dead staining (Figure 3A), with daily imaging. While a slight increase in dead cells was observed over the 3 days of static culture (Figure 3A**, inset**), the vast majority of HUVECs remained viable at the end of the experiment.

In the second experiment, we used GFP-labeled HUVECs for the main co-culture experiments to facilitate monitoring of HUVEC morphology under perfusion and quantified cell circularity and area over time. As displayed in Figure 3B, GFP-HUVECs exhibited a rounded, highly circular morphology immediately post-seeding, indicative of seeding stress. A day after static culture in the microchannels, the cells spread out and exhibited increased area as they flattened, while maintaining the characteristic "cobblestone" morphology typically observed in static culture. After 1 day of perfusion culture, GFP-HUVECs began to adopt a more elongated, striated morphology, reflecting their response to shear forces within the microchannel. Quantitative image analysis confirmed these observations: by day 2, HUVEC circularity markedly decreased while cell area increased (Figure 3C and D), consistent with the morphological transition induced by perfusion.

3.4. Tri-coculture assembly of maternal and fetal compartments

The assembly of the complete tri-coculture device was carefully designed to allow sufficient time for cell adhesion, proliferation, and functionality of the placental barrier (Figure 4A). The three cell types (PDSFs, GFP-HUVECs, and RFP-labeled hTSCs) were seeded according to a staggered timeline (Figure 4A) to ensure that optimal cell viability, cell density, and functionality were achieved.

Following the previously optimized conditions for each cell type, we began the tri-coculture assembly with DLP 3D bioprinting of the GelMA-encapsulated PDSFs on day 0. On the following day, GFP-HUVECs were seeded into the fetal compartment with care to avoid drying the PDSF-containing GelMA layer in the maternal compartment. After incubation, the device was returned to its upright orientation; fresh PDSF growth media was introduced into the maternal compartment, and the reservoir with HUVEC growth media was connected to the fetal compartment. The system was maintained under static culture for 3 days to allow for initial cell proliferation and stabilization. On day 3, the PDSF-encapsulated GelMA layer in the maternal chamber was coated with collagen and fibronectin to prepare the surface for hTSC seeding the following day. On day 4, RFP-hTSCs were seeded in the maternal compartment and maintained in iCTB media for 24 h. On day 5, perfusion was initiated for the GFP-HUVECs in the fetal compartment, using a peristaltic pump to deliver media at a flow rate of 3.5 μL/min. At this point (day 5), the media in the maternal compartment were replaced with forskolin-containing STB differentiation medium to induce the differentiation of hTSCs into STB, which continued for 3 days. Figure 4B features a fluorescence image of the tri-coculture system on day 6, *i.e.*, 24 h after syncytialization was initiated on the maternal side and overnight media perfusion began in the fetal microchannels. On day 8, the tri-coculture system was considered mature and ready for downstream viability and barrier function assays. 3D confocal microscopy reconstruction (Figure 4C) confirmed the layered architecture of our placental barrier model, revealing a dense, differentiated RFP-expressing STB layer overlaying the GelMA-encapsulated DiD-labeled PDSFs, while GFP-expressing HUVECs were clearly visible on the fetal side. Confocal images indicate good morphology across all cell types, with the STBs forming a compact layer on the GelMA surface (Figure S4).

3.5. Functional characterization of the tri-coculture model

Given the presence of three distinct cell types co-cultured within the same system, we were not able to measure the metabolic activity of each cell type individually. However, we assessed metabolic activity at the compartment level by comparing the maternal and fetal sides of the hPOC device. We used a commercially available colorimetric cell metabolic activity assay, CyQUANT Cell Proliferation Kit XTT Assay (Invitrogen, USA), which relies on the mitochondrial enzymes of live cells to convert the yellow XTT dye to an orange-colored compound called formazan. The absorbance of XTT increased over time in both compartments, albeit at a lower rate in the fetal compartment, potentially reflecting a lower overall cell number compared to the maternal compartment and the lower metabolic activity of endothelial cells compared to the highly metabolically active trophoblasts in the maternal compartment (Figure S5).

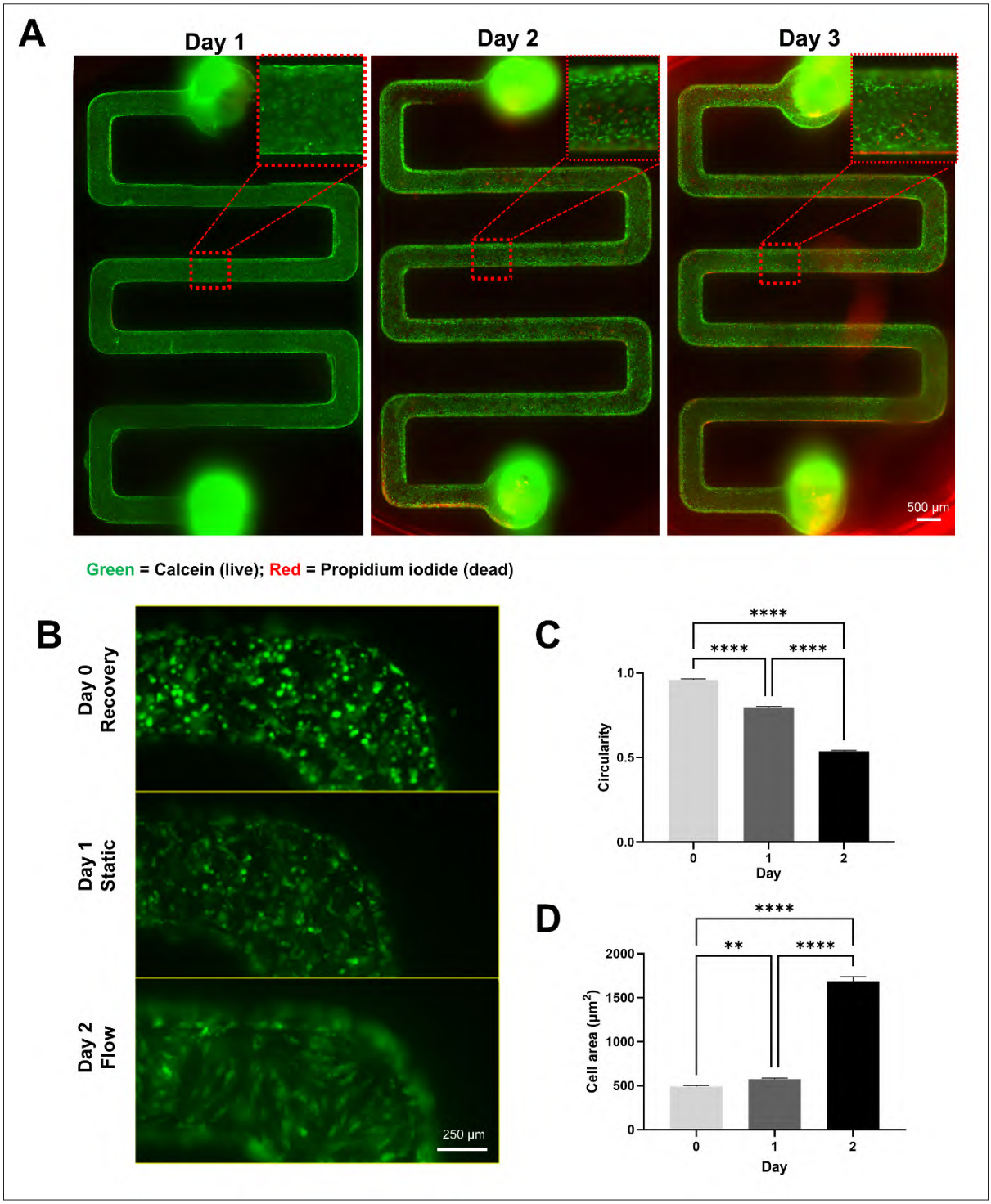


Figure 3. Optimization of HUVEC culture in the fetal compartment. (A) Live/dead staining of HUVECs seeded into microchannels (width: 500 µm) over 3 days of static culture, displaying high cell viability. (B) Morphological progression of GFP-HUVECs within the microchannels: cells exhibited a rounded morphology upon seeding, transitioned to a characteristic "cobblestone" appearance after 1 day of static culture, and adopted an elongated, striated morphology after 1 day of perfusion culture. (C) Quantification of GFP-HUVEC circularity reveals a significant decrease over the 2-day culture period (n = 3). Error bars indicate the SEM. (D) Cell area significantly increased following transition from static to dynamic (perfused) culture conditions (n = 3). Error bars indicate SEM. $^{**}p < 0.01$; $^{****}p < 0.0001$. Scale bars: 500 µm (A); 250 µm (B). Abbreviations: GFP, green fluorescent protein; HUVEC, human umbilical vein endothelial cells; SEM, standard error of the mean.

In the placenta, STB secretes several key hormones, including hCGβ, progesterone, estradiol, and hPL. To evaluate the functionality of the STB layer in our tri-coculture hPOC model, we collected media from both the maternal and fetal compartments every 24 h, starting on day 4 immediately after hTSC seeding, and assessed hormone levels using ELISA (Figure 4D–G).

Estradiol, a key steroid hormone involved in promoting trophoblast proliferation and differentiation into STBs,[31] was detected at high concentrations in the maternal compartment of the hPOC model as early as 1 day after the addition of forskolin, with levels remaining stable at ~20 ng/mL over the subsequent 3 days (Figure 4D). Similar to *in vivo* findings, where estradiol is also detected in the fetal circulation,[32] the spent media in the fetal compartment contained nearly 12 ng/mL estradiol 1 day after induction of syncytialization, with concentrations progressively increasing over the consecutive days.

hPL is a protein hormone secreted by the STB that plays key roles in regulating maternal metabolism and supporting fetal growth and development.[33] In our 3D hPOC model, hPL levels rose sharply in the maternal compartment 48 h after forskolin addition (*i.e.*, 3 days after hTSC seeding), but remained ~10-fold lower in the fetal compartment (Figure 4E).

hCGβ is a peptide hormone produced by the STB that reaches the fetal circulation primarily through passive diffusion.[34] In our tri-coculture model, the hCGβ concentration in the maternal compartment increased progressively each day following hTSC seeding, ranging from 6 to 15 μg/mL (Figure 4F). In contrast, hCGβ levels in the fetal compartment remained >100-fold lower, remaining below 200 ng/mL, consistent with limited diffusion across the placental barrier (Figure 4F).

Finally, progesterone is a steroid hormone with multiple roles in the maintenance of pregnancy, and it is typically found at markedly higher concentrations in the maternal circulation compared to the fetal circulation.[35] In our hPOC model, progesterone was detectable in the maternal compartment starting 1 day after hTSC seeding (Figure 4G), whereas levels in the fetal compartment remained below the assay's detection limit.

3.6. Evaluation of placental barrier integrity

To assess barrier integrity, we designed four configurations of the hPOC device for diffusion assays (Figure 5A). Type 1 was an acellular device; Type 2 included an acellular GelMA layer; Type 3 incorporated HUVECs on the fetal side; and Type 4 represented the full tri-coculture system on day 8, featuring the complete placental barrier.

To evaluate placental barrier function against passive diffusion, we used Na-F salt, a small-molecule fluorescent tracer (MW 376.3 g/mol) that is commonly employed to assess membrane permeability, including in blood-brain barrier models.[36] Due to its low MW and comparable size to sucrose (342.3 g/mol), Na-F serves as a representative probe for passive diffusion.[37,38] Na-F was introduced into the maternal compartment on day 8 of tri-coculture, and media samples from the fetal compartment were collected after 24 h (Figure 5B). A progressive decrease in fetal Na-F concentration was observed from Type 1 through Type 4 devices, with the full tri-coculture model (Type 4) exhibiting the lowest levels. These findings highlight the cumulative contribution of each component of the hPOC to the system's resistance to passive transfer of small, charged molecules.

To assess the barrier's ability to restrict the diffusion of large molecules, we used FITC-dextran, a high-MW, neutral fluorescent tracer. FITC-dextran-containing culture media were added to the maternal compartment on day 8 of the tri-coculture, and media from the fetal compartment were collected after 24 h. Among the four device configurations, the Type 4 tri-coculture model exhibited the lowest FITC-dextran level in the fetal compartment (Figure 5C), indicating superior resistance to large molecule penetration. We note that the difference between the Type 1 and Type 4 devices was approximately threefold for Na-F and 1.5-fold for FITC-dextran, demonstrating that the hPOC model is more effective at limiting diffusion of small, charged molecules than large, neutral molecules.

We also investigated the contributions of the acellular and cellular components of the hPOC device to active transport. In the placenta, glucose transport is primarily mediated by the GLUT1 transporter, a member of the glucose transporter (GLUT) family. To assess glucose dynamics in our model, we used physiologic glucose concentrations in both maternal and fetal compartments and monitored glucose levels in both compartments over time in the Type 1 and Type 4 devices. In the acellular device, the glucose concentration gradually decreased on the maternal side and correspondingly increased in the fetal side (Figure 5D), consistent with passive diffusion from a compartment with a higher concentration to one with a lower concentration. In contrast, in the tri-coculture system, maternal glucose concentration decreased dramatically within 1 h after the media was refreshed on both sides, while fetal glucose concentration increased gradually (**Figure 5E**). We postulate that the rapid decline in glucose concentration in the maternal compartment was

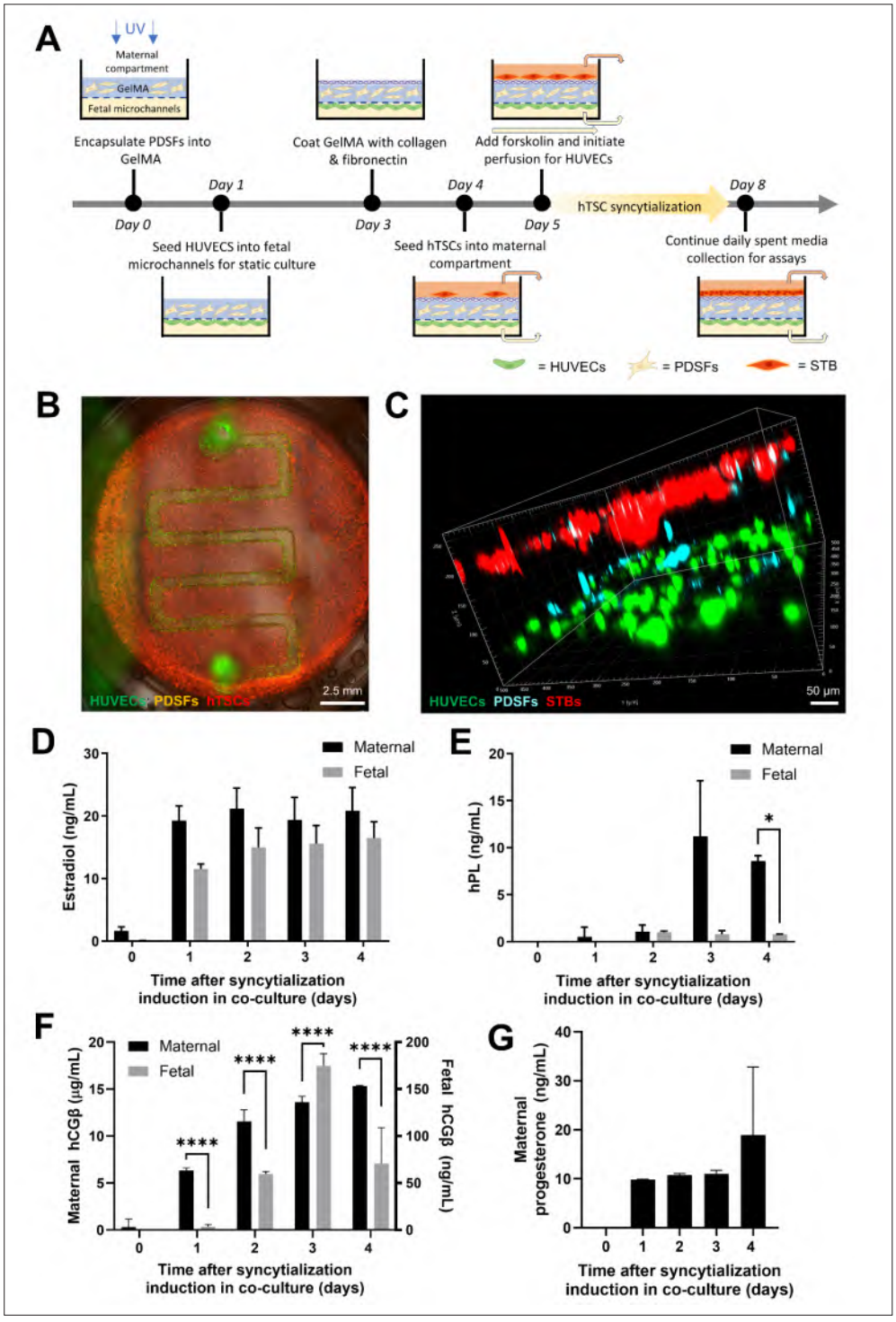


Figure 4. Assembly and functional characterization of the hPOC device. (A) Schematic timeline of assembling the tri-coculture placental model. (B) Composite fluorescence image of the tri-coculture model on day 6 (after 1 day of perfusion culture), featuring GFP-expressing HUVECs (green), DiD-labeled PDSFs (yellow), and RFP-expressing hTSCs (red). (C) 3D confocal reconstruction of the placental barrier on day 8 of tri-coculture, displaying the layered organization of STB, PDSFs, and HUVECs. (D–G) Hormone secretion assays measuring estradiol (D), hPL (E), hCGβ (F), and progesterone (G) levels over 4 days of forskolin treatment to induce syncytialization. Error bars indicate standard deviation of the mean ($n = 3$). Scale bars: 2.5 mm (B); 50 µm (C). *$p < 0.05$; ****$p < 0.0001$. Abbreviations: GelMA, methacrylated gelatin; GFP, green fluorescent protein; hPOC, human placenta-on-a-chip; hTSCs, human trophoblast stem cells; HUVECs, human umbilical vein endothelial cells; PDSFs, placenta-derived stromal fibroblasts; RFP, red fluorescent protein; STB, syncytiotrophoblast; hPL, human placental lactogen; hCGβ, beta subunit human chorionic gonadotropin.

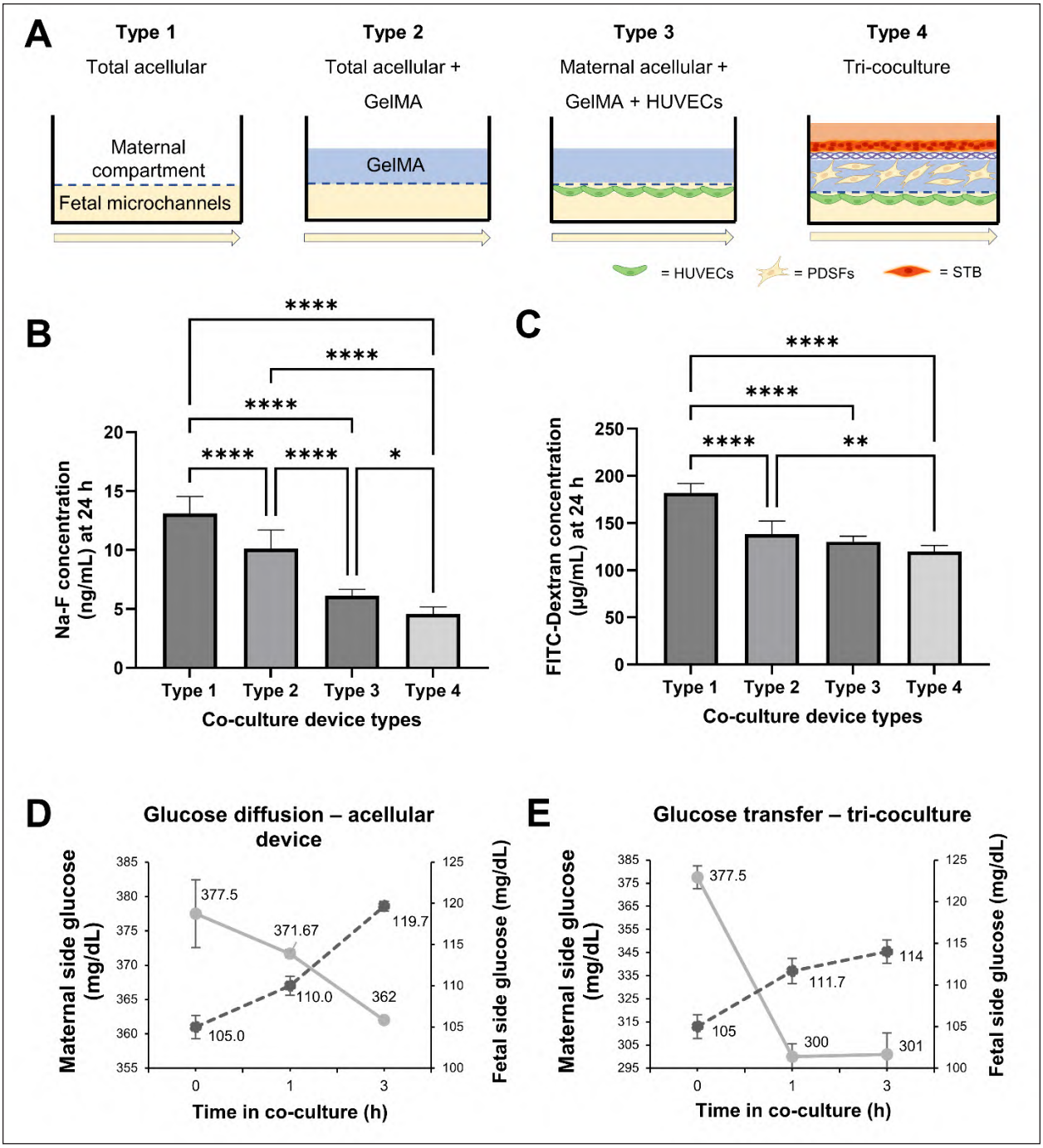


Figure 5. Assessment of placental barrier integrity in the hPOC model. (A) Schematic representation of the four hPOC devices used for barrier assays: Type 1 (fully acellular), Type 2 (acellular with GelMA layer), Type 3 (acellular GelMA layer on the maternal side; HUVECs on the fetal side), and Type 4 (full tri-coculture with GelMA-encapsulated PDSFs, STB, and HUVECs). (B) Sodium fluorescein (Na-F) penetration across the barrier displayed progressively lower fetal concentrations from Type 1 to Type 4, with the lowest leakage observed in the full tri-coculture system. Error bars indicate SD of the mean (n = 3). (C) FITC-dextran penetration was similarly reduced in the Type 4 device, indicating the model's ability to restrict the transport of large molecules. Error bars indicate SD of the mean (n = 3). (D) In the acellular device type, maternal glucose levels decreased gradually while fetal glucose increased over time, consistent with passive diffusion. (E) In the tri-coculture system, maternal glucose concentration dropped sharply within the first hour, suggesting high metabolic consumption by the STB layer; a corresponding but modest increase was observed on the fetal side. Error bars indicate SD of the mean (n = 3). *p < 0.05; **p < 0.01; ****p < 0.0001. Abbreviations: GelMA, methacrylated gelatin; hPOC, human placenta-on-a-chip; HUVECs, human umbilical vein endothelial cells; PDSFs, placenta-derived stromal fibroblasts; SD, standard deviation; STB, syncytiotrophoblast.

likely due to high metabolic consumption by STB, which is present at high cell density in the maternal compartment.

4. Discussion

In this study, we developed a hybrid open/closed microfluidic platform that enables both 3D cell encapsulation and 2D surface seeding. On the maternal side, we achieved 3D encapsulation of PDSFs and 2D seeding of hTSCs, while the fetal side mimics perfusable capillaries, where HUVECs are cultured to model the fetal endothelium. Compared to previous placenta-on-a-chip models that rely primarily on 2D cell seeding,[15,18,20,28] our design offers enhanced flexibility for recapitulating the complex 3D architecture of chorionic villi in the human placenta. To achieve precise structural control, we utilized DLP 3D printing to fabricate a multi-layered microfluidic device with customizable geometries and integrated features. Notably, the fetal-side channel was engineered with tunable dimensions to accommodate varying experimental requirements, highlighting the system's versatility. Beyond placental modeling, the modular and customizable nature of our platform renders it broadly applicable to other *in vitro* barrier models, including gut, lung, and blood–brain barrier systems, where spatial organization and compartment-specific cell interactions are critical.

The results from our tri-coculture hPOC device offer important insights into cellular interactions and barrier function that closely mimic the *in vivo* placental environment. All three cell types in the model exhibited excellent viability throughout the experimental timeline. All three primary cell types in the model maintained excellent viability throughout the 8-day culture period. Achieving this level of cellular performance required systematic optimization of multiple parameters to support the distinct requirements of each cell type. Specifically, we finetuned the substrate stiffness, coatings, and embedding methods to establish a stable and functional tri-culture system. Among these, the GelMA layer—which encapsulates PDSFs and supports hTSC seeding—was a key focus. We tested multiple stiffness levels and selected 18 kPa as the optimal stiffness based on cell viability, morphology, and structural integrity during culture. Although the reported stiffness of native placental tissue varies widely depending on anatomical region and measurement method, with values ranging from sub-kPa to as high as 30 kPa, we selected a range of GelMA stiffnesses spanning this spectrum to identify the optimal condition for cell performance.[19,39,40] Based on assessments of cell viability, morphology, and structural integrity, we chose 18 kPa as the final stiffness. This value not only falls within the broader physiological range but also supports robust growth and function of both PDSFs and hTSCs in our *in vitro* microfluidic setting. During the optimization of hTSC and HUVEC seeding, we found that surface coating with fibronectin and collagen was essential for promoting robust cell adhesion. In future iterations of the model, additional ECM components, such as fibronectin and laminin, could also be incorporated into the GelMA layer to further enhance cell viability, morphology, and function. On the fetal side, the flow rate of 3.5 μL/min was selected based on the channel size and the need for cell proliferation. While this rate generates wall shear stress lower than the 10 dyn/cm² observed in fetal capillaries *in vivo*,[41] it is closer to other placenta-on-a-chip models, which typically apply 0.5–2.5 μL/min to maintain cell viability, preserve barrier function, and prevent flow-induced damage.[20,42–44] This flow rate supports endothelial cell alignment and nutrient exchange while preserving the structural and functional integrity of the tri-culture model over extended culture periods. The metabolic activity assay demonstrated higher activity in the maternal compartment, likely due to the higher cell density and metabolic activity of hTSCs/STB relative to HUVECs on the fetal side.

In regard to placental hormone secretion, all four tested hormones were readily detected in the hPOC model. The observation that estradiol concentration was only slightly lower in the fetal compartment compared to the maternal compartment suggests that it is either secreted by both the apical and basal sides of the STB or secreted apically and readily transferred from the maternal to the fetal compartment. In contrast, the markedly lower levels of hPL, hCGβ, and progesterone in the fetal compartment suggest selective secretion of these hormones by the apical side of the STB, with limited transport across the placental barrier. Notably, we observed a plateau in maternal hCGβ levels over time, which aligns with the well-documented decline in hCGβ production as pregnancy advances.[45] The transient decrease in fetal hCGβ concentration on day 4 may reflect the progressive maturation of the fetomaternal barrier, potentially making it less permissive to hormone diffusion as syncytialization stabilizes. Although this interpretation remains speculative, it is consistent with the overall trend of functional barrier maturation observed throughout the 8-day culture period. These findings highlight the potential of the hPOC system to serve as a platform for future studies aimed at elucidating the mechanisms of placental hormone secretion and transport.

The diffusion assays using Na-F and FITC-dextran highlight the effectiveness of the tri-coculture model in recapitulating the selective permeability of the human

placental barrier. The progressive decrease in Na-F penetration across device types—from fully acellular to the tri-coculture system—demonstrates the critical role of cellular components in reinforcing barrier integrity against passive diffusion of small, charged molecules. Similarly, the marked reduction in FITC-dextran permeability in the tri-coculture device confirms the model's resistance to the passage of large, neutral molecules. Taken together, these findings validate the physiological relevance of the hPOC model and support its future application in pharmacological and toxicological studies of placental transport.

Physiological rates of glucose transfer across the human placenta over a 2 h period, as measured in *ex vivo* perfusion studies, range from 26.5 to 38.3%.[42,46] This transport is primarily mediated by the GLUT1 receptor on the STB and involves active, facilitated diffusion mechanisms.[47] In our hPOC model, glucose concentration in the fetal compartment increased similarly over time in both the acellular and tri-coculture systems. However, in the maternal compartment, the glucose concentration fell more rapidly and to a greater extent in the tri-coculture model, which we attribute to glucose consumption by the STB. The similarity in fetal glucose concentrations between the two systems (acellular and tri-coculture) limits our ability to distinguish whether the maternal-to-fetal compartment glucose transfer in the tri-coculture system is mediated by passive, facilitated, or active transport. Future studies are warranted to address this issue, potentially through the use of real-time glucose monitoring or by introducing a non-metabolizable glucose analog—such as 3-O-methyl-D-glucose—which is transported via GLUT1 but not metabolized, thereby enabling direct assessment of transcellular transport independent of cellular consumption.

Our hPOC model is designed to recapitulate key placental functions within a tractable experimental window. Therefore, we intentionally accelerated hTSC differentiation into STBs to enable functional assessment of hormone secretion and barrier function within an 8-day timeframe. In contrast to traditional placental explant cultures, which are often difficult to maintain beyond a few days due to declining viability and function,[4,48] our platform remained structurally intact and functionally active for at least 8 days, which is comparable to the culture durations reported for other placenta-on-a-chip systems.[43,49,50]

Overall, our study advances the understanding of placental barrier function and establishes a robust and modular platform for testing and developing therapeutic strategies relevant to pregnancy. While the hPOC device successfully recapitulates key structural and functional features of the human placenta, *in vitro* models inevitably face challenges in fully mimicking the complexity of the *in vivo* environment. Continued refinements in cell culture conditions, barrier composition, and transport dynamics will be critical to further improving the physiological relevance of the system.

Future studies should expand barrier integrity assessments by incorporating biologically relevant molecules or drugs beyond glucose. For example, insulin—an essential hormone for fetal growth—represents a particularly relevant candidate to test in conjunction with glucose to evaluate hormone-specific transport behavior. Likewise, evaluating the selective translocation of immunoglobulins could further validate the model's fidelity. Immunoglobulin G (IgG) is known to cross the placenta via FcRn-mediated transport in STB cells, whereas immunoglobulin M (IgM) does not.[51] Demonstrating the differential transport of IgG and IgM within the hPOC system would be a strong indicator of its physiological accuracy. In addition, future improvements to the model could include incorporating fetal Hofbauer cells into the stromal compartment and adjusting the distance between the maternal and fetal compartments—as well as modifying the trophoblast compartment—to better mimic the structure and transport characteristics of chorionic villi at distinct stages of gestation. In addition to assessing molecular transport across the platform, molecular profiling techniques, such as transcriptomic and metabolomic analyses, could be employed to comprehensively evaluate the physiological relevance of the model. It is worth noting that in our hPOC system, hTSCs are derived from early gestation, whereas PDSFs are isolated from the third-trimester placentas, resulting in a gestational age mismatch between the two cell types. While this approach is common due to the accessibility and stability of these cell sources, it may not fully capture the stage-specific cellular interactions of the native placenta. Protocols for deriving hTSCs from mid- to late-gestation placental tissues[24,25,52] could enable the development of gestational age-matched models that more accurately reflect the physiological state of the placenta at specific stages. Incorporating such advances into future versions of our model may enhance its relevance for studying stage-specific placental functions.

Further testing and optimization of this model will have important implications for the development of physiologically relevant *in vitro* models for understanding placental function. These advances will support deeper mechanistic studies of placental function, facilitate the assessment of environmental and pharmaceutical exposures during pregnancy, and enable safer therapeutic development for maternal-fetal health.

5. Conclusion

In this study, we have developed a biomimetic, microfluidic, tri-coculture 3D transport model that recapitulates key features of the human placenta. This model incorporates two primary placental tissue-derived cell types—hTSCs differentiated to STB facing the maternal compartment and PDSFs within a 3D stromal matrix—alongside HUVECs, a well-established endothelial model used to represent the fetal-facing vasculature. The microfluidic device's open-top design enables modular assembly of the maternal compartment—featuring a 2D layer of differentiated hTSCs layered atop a stiffness-tuned, GelMA-encapsulated 3D PDSF scaffold—while the closed fetal microchannel compartment supports perfusion flow and HUVEC seeding.

Our results demonstrate that the device sustains a viable tri-coculture system over multiple days, supports perfusion, and satisfies a critical requirement for *in vitro* placenta models: the formation of a functional, syncytialized layer of trophoblast that creates the tight barrier essential for proper placental function. Barrier formation was confirmed via microscopy, and functional validation was achieved through a variety of hormone secretion profiling and molecular transport assays.

This platform offers a robust and physiologically relevant system for studying placental transport in both normal and diseased conditions. Its modularity and cell-type specificity also provide opportunities to investigate genetic and environmental perturbations to better understand placental physiology and pathophysiology.

Acknowledgments

Figures 1A, 1D, 4A, and 5A partly feature schematics that were generated using BioRender (biorender.com) under an academic license. Additional customized schematics were added to the BioRender-generated images to complete the figures.

Funding

This work was supported in part by grants from the National Institutes of Health (NIH) to S.C., L.L., and M.P. (R21HD100132) and the National Science Foundation (NSF) to S.C. (2135720). The UCSD School of Medicine Microscopy Core facility was supported by the NIH grant P30 NS047101.

Conflict of interest

The authors declare no competing interests.

Author contributions

Conceptualization: Henry H. Hwang, Chandana Tekkatte, Louise C. Laurent, Shaochen Chen

Data curation: Yazhi Sun, Henry H. Hwang, Chandana Tekkatte, Scott A. Lindsay

Formal analysis: Yazhi Sun, Henry H. Hwang, Chandana Tekkatte, Scott A. Lindsay

Funding acquisition: Mana M. Parast, Louise C. Laurent, Shaochen Chen

Investigation: Yazhi Sun, Henry H. Hwang, Chandana Tekkatte, Scott A. Lindsay, Anelizze Castro-Martinez, Claire Yu, Isabella Saldana, Xuanyi Ma, Omar Farah

Methodology: Yazhi Sun, Henry H. Hwang, Chandana Tekkatte, Scott A. Lindsay, Anelizze Castro-Martinez, Claire Yu, Isabella Saldana, Xuanyi Ma, Omar Farah

Project administration: Louise C. Laurent, Shaochen Chen

Resources: Mana M. Parast, Louise C. Laurent, Shaochen Chen

Supervision: Louise C. Laurent, Shaochen Chen

Visualization: Yazhi Sun, Henry H. Hwang, Chandana Tekkatte, Scott A. Lindsay

Writing–original draft: Yazhi Sun, Henry H. Hwang, Chandana Tekkatte, Scott A. Lindsay,

Writing–review & editing: Mana M. Parast, Louise C. Laurent, Shaochen Chen

Ethics approval and consent to participate

The current study involving human-sourced tissues used in biomedical research was approved by the Institutional Review Board at the University of California San Diego (IRB #181917).

Consent for publication

Written informed consent was obtained from the donors to publish the data.

Availability of data

The data that support the findings of this study are available from the corresponding authors upon reasonable request.

References

1. Mitchell AA, Gilboa SM, Werler MM, Kelley KE, Louik C, Hernández-Díaz S. Medication use during pregnancy, with particular focus on prescription drugs: 1976–2008. *Am J Obstetr Gynecol.* 2011;205(1):51.e1-51.e8. doi: 10.1016/j.ajog.2011.02.029

2. Wesley BD, Sewell CA, Chang CY, Hatfield KP, Nguyen CP. Prescription medications for use in pregnancy–perspective from the US Food and Drug Administration. *Am J Obstetr Gynecol.* 2021;225(1):21-32.

doi: 10.1016/j.ajog.2021.02.032

3. Zubizarreta ME, Xiao S. Bioengineering models of female reproduction. *Bio Des Manuf*. 2020;3(3):237. doi: 10.1007/s42242-020-00082-8

4. Zabel RR, Favaro RR, Groten T, Brownbill P, Jones S. Ex vivo perfusion of the human placenta to investigate pregnancy pathologies. *Placenta*. 2022;130:1-8. doi: 10.1016/j.placenta.2022.10.006

5. Glättli SC, Elzinga FA, van der Bijl W, et al. Variability in perfusion conditions and set-up parameters used in *ex vivo* human placenta models: a literature review. *Placenta*. 2024;157:37-49. doi: 10.1016/j.placenta.2024.03.007

6. Carter AM. Animal models of human placentation – a review. *Placenta*. 2007;28:S41-S47. doi: 10.1016/j.placenta.2006.11.002

7. Carter AM. Evolution of placental hormones: implications for animal models. *Front Endocrinol*. 2022;13:891927. doi: 10.3389/fendo.2022.891927

8. Sood A, Kumar A, Gupta VK, Kim CM, Han SS. Translational nanomedicines across human reproductive organs modeling on microfluidic chips: state-of-the-art and future prospects. *ACS Biomater Sci Eng*. 2023;9(1):62-84. doi: 10.1021/acsbiomaterials.2c01080

9. Pu Y, Gingrich J, Veiga-Lopez A. A 3-dimensional microfluidic platform for modeling human extravillous trophoblast invasion and toxicological screening. *Lab Chip*. 2021;21(3):546-557. doi: 10.1039/D0LC01013H

10. Heaton SJ, Eady JJ, Parker ML, et al. The use of BeWo cells as an in vitro model for placental iron transport. *Am J Physiol Cell Physiol*. 2008;295(5):C1445-C1453. doi: 10.1152/ajpcell.00286.2008

11. Park JY, Mani S, Clair G, et al. A microphysiological model of human trophoblast invasion during implantation. *Nat Commun*. 2022;13(1):1252. doi: 10.1038/s41467-022-28663-4

12. Hori T, Okae H, Shibata S, et al. Trophoblast stem cell-based organoid models of the human placental barrier. *Nat Commun*. 2024;15(1):962. doi: 10.1038/s41467-024-45279-y

13. Kallol S, Moser-Haessig R, Ontsouka CE, Albrecht C. Comparative expression patterns of selected membrane transporters in differentiated BeWo and human primary trophoblast cells. *Placenta*. 2018;72-73:48-52. doi: 10.1016/j.placenta.2018.10.008

14. Cao R, Wang Y, Liu J, Rong L, Qin J. Self-assembled human placental model from trophoblast stem cells in a dynamic organ-on-a-chip system. *Cell Prolif*. 2023;56(5):e13469. doi: 10.1111/cpr.13469

15. Cao R, Guo Y, Liu J, et al. Assessment of nanotoxicity in a human placenta-on-a-chip from trophoblast stem cells. *Ecotoxicol Environ Saf*. 2024;285:117051. doi: 10.1016/j.ecoenv.2024.117051

16. Lermant A, Rabussier G, Davidson L, Lanz HL, Murdoch CE. Protocol for a placenta-on-a-chip model using trophoblasts differentiated from human induced pluripotent stem cells. *STAR Protoc*. 2024;5(1):102879. doi: 10.1016/j.xpro.2024.102879

17. Wang Y, Guo Y, Wang P, et al. An engineered human placental organoid microphysiological system in a vascular niche to model viral infection. *Commun Biol*. 2025;8(1):669. doi: 10.1038/s42003-025-08057-0

18. Pemathilaka RL, Caplin JD, Aykar SS, *et al*. Placenta-on-a-Chip: In Vitro Study of Caffeine Transport across Placental Barrier Using Liquid Chromatography Mass Spectrometry. *Global Challenges*. 2019;3(3):1800112. doi: 10.1002/gch2.201800112

19. Ma Z, Sagrillo-Fagundes L, Mok S, Vaillancourt C, Moraes C. Mechanobiological regulation of placental trophoblast fusion and function through extracellular matrix rigidity. *Sci Rep*. 2020;10(1):5837. doi: 10.1038/s41598-020-62659-8

20. Lee JS, Romero R, Han YM, et al. Placenta-on-a-chip: a novel platform to study the biology of the human placenta. *J Matern Fetal Neonatal Med*. 2016;29(7):1046-1054. doi: 10.3109/14767058.2015.1038518

21. Ma X, Yu C, Wang P, et al. Rapid 3D bioprinting of decellularized extracellular matrix with regionally varied mechanical properties and biomimetic microarchitecture. *Biomaterials*. 2018;185:310-321. doi: 10.1016/j.biomaterials.2018.09.026

22. Pyo SH, Wang P, Hwang HH, Zhu W, Warner J, Chen S. Continuous optical 3D printing of green aliphatic polyurethanes. *ACS Appl Mater Interfaces*. 2017;9(1):836-844. doi: 10.1021/acsami.6b12500

23. Igura K, Zhang X, Takahashi K, Mitsuru A, Yamaguchi S, Takahashi TA. Isolation and characterization of mesenchymal progenitor cells from chorionic villi of human placenta. *Cytotherapy*. 2004;6(6):543-553. doi: 10.1080/14653240410005366-1

24. Okae H, Toh H, Sato T, et al. Derivation of human trophoblast stem cells. *Cell Stem Cell*. 2018;22(1):50-63.e6. doi: 10.1016/j.stem.2017.11.004

25. Bai T, Peng CY, Aneas I, et al. Establishment of human induced trophoblast stem-like cells from term villous cytotrophoblasts. *Stem Cell Res*. 2021;56:102507. doi: 10.1016/j.scr.2021.102507

26. Zhu W, Qu X, Zhu J, et al. Direct 3D bioprinting of prevascularized tissue constructs with complex microarchitecture. *Biomaterials*. 2017;124:106-115.

doi: 10.1016/j.biomaterials.2017.01.042

27. Teasdale F. Gestational changes in the functional structure of the human placenta in relation to fetal growth: a morphometric study. *Am J Obstetr Gynecol*. 1980;137(5):560-568.
doi: 10.1016/0002-9378(80)90696-1

28. Blundell C, Yi YS, Ma L, et al. Placental drug transport-on-a-chip: a microengineered in vitro model of transporter-mediated drug efflux in the human placental barrier. *Adv Healthc Mater*. 2018;7(2):1700786.
doi: 10.1002/adhm.201700786

29. Wice B, Menton D, Geuze H, Schwartz AL. Modulators of cyclic AMP metabolism induce syncytiotrophoblast formation *in vitro*. *Exp Cell Res*. 1990;186(2):306-316.
doi: 10.1016/0014-4827(90)90310-7

30. Das S, Jegadeesan JT, Basu B. Gelatin methacryloyl (GelMA)-based biomaterial inks: process science for 3D/4D printing and current status. *Biomacromolecules*. 2024;25(4):2156-2221.
doi: 10.1021/acs.biomac.3c01271.

31. Tang C, Jin M, Ma B, et al. RGS2 promotes estradiol biosynthesis by trophoblasts during human pregnancy. *Exp Mol Med*. 2023;55(1):240-252.
doi: 10.1038/s12276-023-00927-z

32. Shutt DA, Smith ID, Shearman RP. Oestrone, oestradiol-17beta and oestriol levels in human foetal plasma during gestation and at term. *J Endocrinol*. 1974;60(2):333-341.
doi: 10.1677/joe.0.0600333

33. Johnson MS, Jackson DL, Schust DJ. Endocrinology of pregnancy. In: Skinner MK, ed. *Encyclopedia of Reproduction (Second Edition)*. Academic Press, Cambridge, MA, USA.; 2018:469-476.
doi: 10.1016/B978-0-12-801238-3.64672-X

34. Malek A, Sager R, Schneider H. Transport of proteins across the human placenta. *Am J Reprod Immunol*. 1998;40(5):347-351.
doi: 10.1111/j.1600-0897.1998.tb00064.x

35. Tal R, Taylor HS. Endocrinology of pregnancy. In: Feingold KR, Ahmed SF, Anawalt B, Blackman MR, Boyce A, Chrousos G, et al., eds. *Endotext*. MDText.com, Inc., South Dartmouth, MA, USA.; 2000.
http://www.ncbi.nlm.nih.gov/books/NBK278962/. Accessed May 15, 2025.

36. Kozler P, Pokorný J. Altered blood-brain barrier permeability and its effect on the distribution of Evans blue and sodium fluorescein in the rat brain applied by intracarotid injection. *Physiol Res*. 2003;52(5):607-14.
doi: 10.33549/physiolres.930289

37. Wevers NR, Nair AL, Fowke TM, et al. Modeling ischemic stroke in a triculture neurovascular unit on-a-chip. *Fluids Barriers CNS*. 2021;18(1):59.
doi: 10.1186/s12987-021-00294-9

38. Schaffenrath J, Huang SF, Wyss T, Delorenzi M, Keller A. Characterization of the blood–brain barrier in genetically diverse laboratory mouse strains. *Fluids Barriers CNS*. 2021;18(1):34.
doi: 10.1186/s12987-021-00269-w

39. Zambuto SG, Clancy KBH, Harley BAC. A gelatin hydrogel to study endometrial angiogenesis and trophoblast invasion. *Interface Focus*. 2019;9(5):20190016.
doi: 10.1098/rsfs.2019.0016

40. Kılıç F, Kayadibi Y, Yüksel MA, *et al*. Shear wave elastography of placenta: in vivo quantitation of placental elasticity in preeclampsia. *Diagn Interv Radiol*. 2015; 21(3):202-207.
doi: 10.5152/dir.2014.14338

41. Tarbell JM. Shear stress and the endothelial transport barrier. *Cardiovasc Res*. 2010;87(2):320-330.
doi: 10.1093/cvr/cvq146

42. Blundell C, Tess ER, Schanzer ASR, *et al*. A microphysiological model of the human placental barrier. *Lab Chip*. 2016;16(16):3065-3073.
doi: 10.1039/C6LC00259E

43. Boos JA, Misun PM, Brunoldi G, et al. Microfluidic co-culture platform to recapitulate the maternal–placental–embryonic axis. *Adv Biol*. 2021;5(8):2100609.
doi: 10.1002/adbi.202100609

44. Bhide A, Aboo A, Sawant M, Majumder A, Paul D, Modi D. Placenta on chip: a modern approach to probe feto-maternal interface. In: Mohanan PV, ed. *Microfluidics and Multi Organs on Chip*. Springer Nature, Singapore.; 2022:359-380.
doi: 10.1007/978-981-19-1379-2_16

45. Cole LA. Biological functions of hCG and hCG-related molecules. *Reprod Biol Endocrinol*. 2010;8(1):102.
doi: 10.1186/1477-7827-8-102

46. Brandes JM, Tavoloni N, Potter BJ, Sarkozi L, Shepard MD, Berk PD. A new recycling technique for human placental cotyledon perfusion: Application to studies of the fetomaternal transfer of glucose, inulin, and antipyrine. *Am J Obstetr Gynecol*. 1983;146(7):800-806.
doi: 10.1016/0002-9378(83)91081-5

47. Hahn T, Barth S, Weiss U, Mosgoeller W, Desoye G. Sustained hyperglycemia in vitro down-regulates the GLUT1 glucose transport system of cultured human term placental trophoblast: a mechanism to protect fetal development? *FASEB J*. 1998;12(12):1221-1231.
doi: 10.1096/fasebj.12.12.1221

48. Brownbill P, Sebire N, McGillick EV, Ellery S, Murthi P. Ex vivo dual perfusion of the human placenta: disease simulation, therapeutic pharmacokinetics and analysis of off-target effects. In: Murthi P, Vaillancourt C, eds. *Preeclampsia: Methods and Protocols*. Springer, New York, NY, USA.; 2018:173-189.

doi: 10.1007/978-1-4939-7498-6_14

49. Kouthouridis S, Saha P, Ludlow M, N. Truong BY, Zhang B. Late-stage placental barrier model for transport studies of prescription drugs during pregnancy. *Lab Chip*. 2025;25(13):3168-3184.
doi: 10.1039/D5LC00075K

50. Rabussier G, Bünter I, Bouwhuis J, et al. Healthy and diseased placental barrier on-a-chip models suitable for standardized studies. *Acta Biomater*. 2023;164:363-376.
doi: 10.1016/j.actbio.2023.04.033

51. Palmeira P, Quinello C, Silveira-Lessa AL, Zago CA, Carneiro-Sampaio M. IgG placental transfer in healthy and pathological pregnancies. *J Immunol Res*. 2012;2012(1):985646.
doi: 10.1155/2012/985646

52. Karakis V, Britt JW, Jabeen M, San Miguel A, Rao BM. Derivation of human trophoblast stem cells from placentas at birth. *J Biol Chem*. 2025;301(6):108505.
doi: 10.1016/j.jbc.2025.108505

ACCSCIENCE PUBLISHING

International Journal of Bioprinting

RESEARCH ARTICLE

Macro–micro analysis of the physical and biological properties of 3D-printed hydroxyapatite/β-tricalcium phosphate scaffolds with varying polyvinyl alcohol concentrations

Zhitao Yin[1], Yutong Chen[1,2], Guang Yang[1], Shuaishuai Wang[3], Bingbing Wang[1,4], Yue Zhao[1], Xujing Zhang[1]*, and Yan Xu[1]*

[1]College of Mechanical Engineering, Xinjiang University, Urumqi, Xinjiang, China

[2]Department of Mechanical Engineering, College of Design and Engineering, National University of Singapore, Singapore, Singapore

[3]College of Mechanical Engineering, Dalian University of Technology, Dalian, Liaoning, China

[4]College of Aviation Academy, Changji University, Changji, Xinjiang, China

(This article belongs to the *Special Issue*: *Future Bioprinting—Celebrating the 10th Anniversary of the International Journal of Bioprinting*)

Abstract

The concentration of the binder is a key factor affecting the quality of 3D-printed bone scaffolds. In this study, a macro–micro analysis was conducted to evaluate the effects of varying concentrations of polyvinyl alcohol (PVA) aqueous solution on the physical and biological properties of hydroxyapatite/β-tricalcium phosphate bone scaffolds. Both molecular dynamics (MD) simulations and experimental approaches were employed. The MD simulations analyzed microscopic interactions between PVA and ceramic powders by assessing changes in chain length at different concentrations. Experimentally, slurries containing 5–15% wt% PVA were characterized in terms of solid content, zeta potential, and extrusion rheology. Bone scaffolds were fabricated via 3D printing followed by freeze-drying, and their porosity, mechanical properties, dimensional shrinkage, and swelling behavior were examined. *In vitro* tests were conducted to assess biological performance. The results indicated that hydrogen and ionic bonding between PVA and ceramic powders were the primary mechanisms of adhesion. Increased chain length led to higher Cauchy pressure, thereby enhancing the mechanical properties of the material. Higher PVA concentrations produced slurries with increased solid content and shear-thinning capabilities, improving printability. The resulting bone scaffolds exhibited higher mechanical properties and shrinkage during drying but showed reduced porosity and swelling capability. *In vitro* experiments revealed that increasing PVA concentration decreased both the porosity and ion concentration of the bone scaffolds, thereby reducing their bioactivity. These findings provide a theoretical basis for optimizing binder concentration in 3D-printed bone scaffolds by linking slurry characteristics to scaffold performance.

Keywords: Biological properties; Extrusion rheology; Freeze-drying; Mechanical properties; Molecular dynamics simulation

***Corresponding authors:**
Xujing Zhang
(007099@xju.edu.cn)

Yan Xu
(xuyan2018@xju.edu.cn)

Citation: Yin Z, Chen Y, Yang G, *et al*. Macro–micro analysis of the physical and biological properties of 3D-printed hydroxyapatite/β-tricalcium phosphate scaffolds with varying polyvinyl alcohol concentrations. *Int J Bioprint*. 2025;11(5)197-216. doi: 10.36922/IJB025280274

Received: May 20, 2025
Revised: July 8, 2025
Accepted: July 14, 2025
Published online: July 14, 2025

Copyright: © 2025 Author(s). This is an Open Access article distributed under the terms of the Creative Commons Attribution License, permitting distribution, and reproduction in any medium, provided the original work is properly cited.

Publisher's Note: AccScience Publishing remains neutral with regard to jurisdictional claims in published maps and institutional affiliations.

1. Introduction

Bone defects often result from trauma, infections, and tumors.[1–5] Although bone tissue possesses an inherent capacity for repair and regeneration, this capacity is typically limited to small-scale injuries. When a defect involves more than 50% of the bone structure or the missing segment exceeds 2 cm, bone grafting or replacement surgery is typically required for effective repair.[6] Notably, ~4 million people worldwide undergo bone grafting procedures each year.[7] However, bone defect surgeries face limitations related to donor sources and graft preparation techniques. Autologous bone grafting, regarded as the gold standard, is constrained by the limited availability of donor bone and the risk of secondary injury to the patient.[8]

In recent years, the use of 3D printing technology to fabricate bone tissue engineering scaffolds for patient-specific implants has gained significant attention.[9] The success of surgical implantation depends largely on the customization and quality of the bone implant. Among various 3D printing methods, direct ink writing—an extrusion-based method—offers flexibility in print pattern design, facilitating the fabrication of complex structures.[10] This technique is particularly well-suited for producing intricate designs and imposes relatively few constraints on the printable materials, provided that the ink exhibits suitable viscoelastic properties.[11–13] Bioceramics are commonly used in direct ink writing,[13–16] with calcium phosphate-based bioceramics and their composites being extensively studied for their biocompatibility and stability.[17] Hydroxyapatite (HA) and β-tricalcium phosphate (β-TCP) are among the most widely used phosphate-based bioceramics.[18] HA is known for its excellent biocompatibility and osteoconductivity, promoting osseointegration and osteoblast recruitment at bone defect sites.[19] In contrast, β-TCP is fully degradable *in vivo* through cell-mediated resorption.[20] However, both HA and β-TCP suffer from high brittleness and low mechanical strength.[21] To address these limitations, polymers are often incorporated into ceramic composites to enhance mechanical performance. Polyvinyl alcohol (PVA), a water-soluble synthetic polymer, is frequently used in this context due to its favorable mechanical strength, degradability, and biocompatibility. PVA has been extensively applied in biomedical applications and is often combined with HA and β-TCP for scaffold fabrication.[22–27]

The interactions between binder and powder materials occur at the microscale and are often difficult to study in-depth using conventional experimental methods. Molecular dynamics (MD) simulations have emerged as a powerful tool for exploring interfacial interactions between inorganic fillers and polymer matrices.[28] MD simulations have consistently demonstrated remarkable capabilities in analyzing structure formation,[29] structural alterations,[30] and intermolecular interactions[31] at the nanoscale.

Consequently, in this study, the properties of bone scaffolds composed of HA and β-TCP as powder materials, along with varying concentrations of PVA solutions as binders, were comprehensively investigated through a combination of microscopic and macroscopic experiments. The bonding characteristics of PVA, both intrinsic and in interaction with the ceramic powders, as well as the variation in fundamental material properties, were elucidated using MD simulations. These simulations provided insights into the nature of interfacial forces between the binder and ceramic powders, as well as the intermolecular forces among PVA chains. Changes in slurry viscosity with varying PVA concentrations were analyzed by correlating zeta potential and solid content data. Scaffold porosity and mechanical properties were examined from both micro-morphological and intermolecular force perspectives. Additionally, drying shrinkage and swelling behavior were characterized, and the biological properties of the bone scaffolds were assessed through *in vitro* simulation experiments.

2. Molecular dynamics simulations

2.1. Molecular modeling

2.1.1. Binder modeling

The solubility parameter, which reflects the cohesive energy density and compatibility of polymer materials, increases with the number of monomer units and eventually stabilizes. A stable solubility parameter is generally considered an indicator of molecular chain suitability for MD studies. In this study, eight PVA molecular chain models with different degrees of polymerization (n = 5, 10, 15, 20, 25, 30, 35, 40) were constructed. After geometric and annealing optimization to identify low-energy conformations, MD simulations were performed at a temperature of 298 K. The annealing temperature ranged from 298 to 598 K over 50 cycles. The COMPASS II force field was used, along with the Andersen thermostat and Berendsen barostat. The density was set at 1.29 g/cm³. The MD procedure consisted of 500 ps of dynamic relaxation under the conical (NVT) ensemble, followed by 500 ps of dynamic equilibrium under the microcanonical (NVE) ensemble. Based on this, the solubility parameter was calculated. The results (Figure 1D) indicate that the solubility parameter stabilizes when the molecular chain reaches approximately 20 repeating units. Therefore, for subsequent comparative simulations involving varying concentrations of aqueous PVA solutions, two

representative chain lengths—corresponding to 94 and 114 repeating units—were selected.

2.1.2. Powder material modeling

Hydroxyapatite and β-tricalcium phosphate are anisotropic materials. In this study, the Bravais–Friedel–Donnay–Harker (BFDH) method was used to uniformly select the most easily exposed crystalline facets to construct supercells for MD simulations. According to the BFDH law, crystal planes with larger interplanar spacings (higher d_{hkl} values) grow more slowly and are therefore more likely to be retained during crystal growth, resulting in a larger exposed surface area. The calculated parameters listed in Table 1 (HA) and Table 2 (β-TCP) indicate that the (100) plane of HA and the (001) plane of β-TCP possess the largest d_{hkl} values, consistent with this rule. Consequently, these planes were selected as the basis for constructing the crystal models.

2.2. Interaction modeling between powder material and polyvinyl alcohol

To investigate the interactions between HA/β-TCP hybrid powders and PVA, a molecular interaction model was constructed (Figure 1A). The truncation radius was set to 18.5 Å to ensure computational accuracy. A 1:1 ratio of HA to β-TCP was employed, with a total molecular molarity of 336. The unit cell parameters for both HA and β-TCP were set as: a = 38.056 Å, b = 38.056 Å, c = 87.642602 Å, and $\alpha = \beta = \gamma = 90°$.

Geometry and annealing optimizations were performed on the PVA molecular chains to construct a binder model composed of 10 PVA chains, minimizing the energy of the model. The final simulation model consisted of a layered structure: β-TCP on the top, PVA in the middle, and HA at the bottom, with a vacuum layer of 30 Å introduced above the structure (Figure 1B). MD simulations were performed in three main steps:

(i) NVT ensemble simulation (500 ps) to release residual stress in the system;

(ii) isothermal–isobaric (NPT) ensemble simulation (P = 1 bar, 500 ps) to approximate the system's equilibrium density (Figure 1E);

(iii) Final NVT ensemble simulation (500 ps) to generate an equilibrium conformation for analysis.

After the 1500 ps simulation, both the conformation of the system (Figure 1C) and its energy (Figure 1F) had changed. The final 50 ps of the trajectory file was used for interaction analysis.

3. Material preparation and characterization

3.1. Experiments

3.1.1. Materials

Rat primary bone marrow mesenchymal stem cells (BMSCs) (RAT-iCell-s018) were purchased from Cyagen Biotechnology Co., Ltd (China). PVA was purchased from Boaotoda Technology Co., Ltd (China). HA (40 nm, 96% purity) and β-TCP (500–15,000 nm, 96% purity) were both purchased from Aipure Nanomaterials Co., Ltd. (China). Ultrapure water was prepared in-house.

Fetal bovine serum was purchased from Xiao Peng Biological Technology Co., Ltd (China). Dulbecco's Modified Eagle Medium, High Glucose (DMEM/HIGH), Dulbecco's Modified Eagle Medium/Nutrient Mixture F-12 (DMEM/F12), penicillin, streptomycin, trypsin, phosphate-buffered saline (PBS), and simulated body fluid (SBF) were purchased from Zhongsheng Aobang Biological Technology Co., Ltd. (China). PBS was purchased from Thermo Fisher Scientific (United States of America). Cell Counting Kit-8 (CCK-8), 4',6-diamidino-2-phenylindole (DAPI), and ascorbic acid were purchased from Lanjieke

Table 1. Parameters of hydroxyapatite crystal planes calculated using the Bravais–Friedel–Donnay–Harker method

h k l	d_{hkl} (Å)	Distance (Å)	Total facet area (Å²)	Total facet area (%)
(1 0 0)	16.479	6.068	605.899	25.020
(0 1 0)	9.514	10.511	349.816	14.445
(0 0 1)	6.939	14.411	255.137	10.535

Table 2. Parameters of β-tricalcium phosphate crystal planes calculated using the Bravais–Friedel–Donnay–Harker method

h k l	d_{hkl} (Å)	Distance (Å)	Total facet area (Å²)	Total facet area (%)
(0 0 1)	18.69	5.350	837.176	28.285
(1 0 0)	9.097	10.993	407.483	13.767
(0 1 0)	5.252	19.040	235.260	7.948

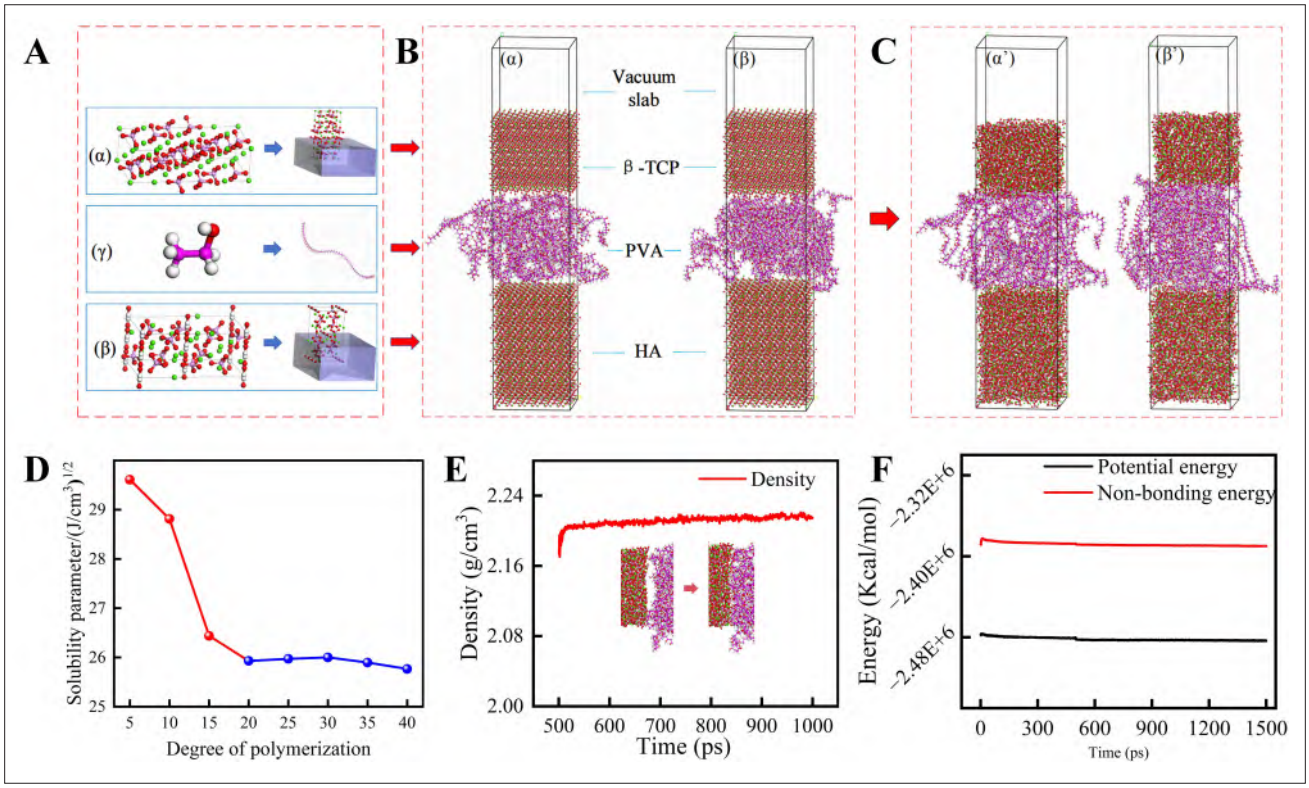


Figure 1. Establishment and simulation workflow. (A) Preparation of material. (B) Preparation of interaction models. (C) Morphology of the simulated system after molecular dynamics simulation. (D) Solubility parameters of PVA at different degrees of polymerization. (E) Density profile of the simulation models as a function of NPT simulation time. (F) Potential energy variation of the simulation models over the total MD simulation time. Abbreviations: β-TCP, β-tricalcium phosphate; C, carbon; Ca, calcium; H, hydrogen; HA, hydroxyapatite; O, oxygen; P, phosphorus; PVA, polyvinyl alcohol.

Technology Co., Ltd (China). The nitro blue tetrazolium (BCIP/NBT) alkaline phosphatase color development kit and alkaline phosphatase (ALP) assay kit were purchased from Biyuntian Institute of Biotechnology (China). Alizarin Red S (ARS) staining solution was purchased from Yuanqi Biotechnology Co., Ltd (China). Glycerol phosphate was purchased from Yuanye Biotechnology Co., Ltd (China). Dexamethasone was purchased from Cybikang Biotechnology Co., Ltd (China). Insulin-like growth factor I (IGF-I) and insulin-like growth factor II (IGF-II) were purchased from Novoprotein Technology Co., Ltd (China).

The normal culture medium consisted of 89% DMEM/F12, 10% fetal bovine serum, and 1% antibiotics. The osteogenic culture medium consisted of the normal culture medium supplemented with 50 μm ascorbic acid, 10 mM glycerol phosphate, 100 nM dexamethasone, 11 nM IGF-I, and 22 nM IGF-II.

3.1.2. Preparation of aqueous adhesive solutions

As an example, a 5 wt% PVA solution was prepared by dissolving 5 g of PVA particles in 95 g of ultrapure water. The mixture was heated and stirred in a sealed vessel at 90°C for 2 h, then allowed to cool to room temperature. Using the same procedure, PVA aqueous solutions with concentrations from 6% to 15% were also prepared. Each solution was designated as C5, C6, C7, ..., C13, C14, C15, corresponding to its respective concentration.

3.1.3. Preparation of mechanical test specimens, annular scaffolds, and cross-mesh scaffolds

The procedures for specimen and scaffold preparation are as follows:

(i) Preparation of mechanical test specimens: HA and β-TCP powders were homogeneously mixed at a mass ratio of 1.5:1. An aqueous PVA solution, with a volume 1.5 times the total mass of the powder mixture, was added and thoroughly mixed to form a uniform slurry. The slurry was poured into cylindrical molds and frozen at −20°C for 12 h, followed by freeze-drying for 24 h. Finally, the dried samples were sanded and shaped into cylindrical mechanical test specimens with a diameter of 10 mm and a height of 12 mm.

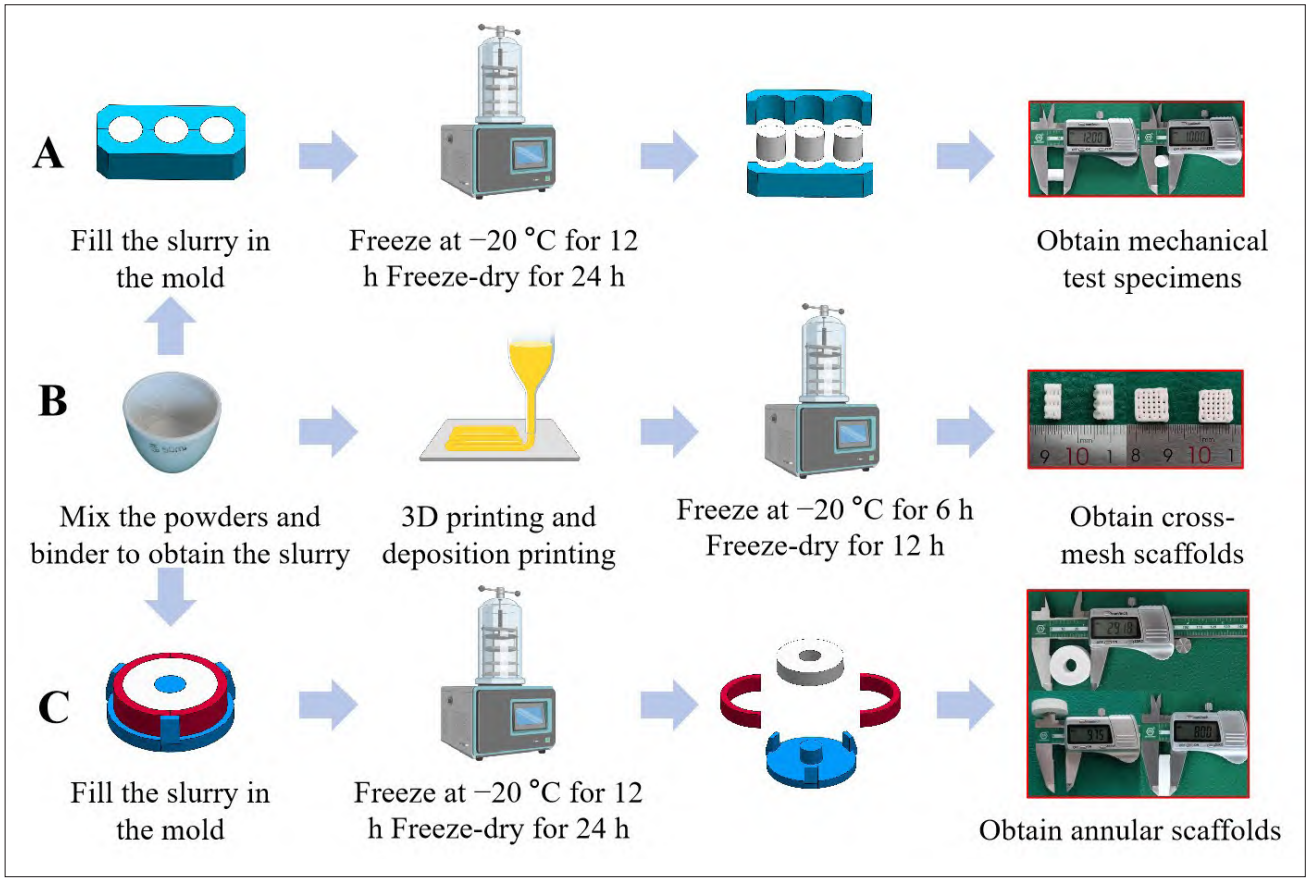


Figure 2. Preparation procedures for experimental materials: (A) mechanical test specimen, (B) cross-mesh scaffold, and (C) annular scaffold.

(ii) Preparation of annular scaffolds: The prepared slurry was carefully poured into specifically designed annular molds. Subsequently, the samples were frozen at −20°C for 12 h and subsequently freeze-dried for 24 h. The resulting annular scaffolds had an outer diameter of 30 mm, an inner diameter of 10 mm, and a height of 8 mm.

(iii) Preparation of cross-mesh scaffold: To achieve suitable viscosity for 3D printing, slurries with concentrations of C9 and C13 were selected. Scaffolds were printed using a custom-built 3D printer, with extrusion performed at room temperature and the deposition platform maintained at −10°C. After printing, the scaffolds were frozen at −20°C for 6 h and then freeze-dried for 12 h. The post-processing steps were consistent with those used for the mechanical test specimens (see Figure 2).

3.2. Slurry and scaffold performance testing

3.2.1. Zeta potential measurement of the slurry

A total of 100 mg of slurry was diluted to 100 g with deionized water and dispersed by ultrasonication for 20 min. After resting, the supernatant was collected and its zeta potential was measured using a laser particle size analyzer (ZEN3690, Malvern Instruments, United Kingdom).

3.2.2. Calculation of solid content and water content

Based on the slurry mixing ratios, the solid content and water content of slurries prepared with varying PVA concentrations were calculated using **Equations (I)** and (**II**):

$$Solid\ content\left(\%\right)=\frac{c\times1.5+1}{2.5}\times100 \quad \text{(I)}$$

$$Water\ Content\left(\%\right)=1-solid\ content \quad \text{(II)}$$

where C is the mass fraction of the PVA aqueous solution.

3.2.3. Shear thinning behavior of the slurry

Eleven PVA aqueous slurry systems, ranging in concentrations from 5% to 15%, were evaluated for their

fluid properties using a rheometer (MCR 302, Anton-Paar, Austria). Measurements were conducted at 25°C using a linear sweep mode with 40 data acquisition points.

3.2.4. Scaffold porosity measurement

Scaffold porosity was measured using the Archimedes drainage method. Each prepared scaffold block was weighed to determine its dry mass (m_1). The sample was then partially immersed in anhydrous ethanol, and its mass after air exclusion was recorded as m_2. Subsequently, the sample was fully submerged in anhydrous ethanol, and its mass was recorded as m_3. The sample was then transferred to a freeze-dryer, where the pressure was maintained below 5000 Pa (but not lower than 2000 Pa, to prevent ethanol boiling). A vacuum was applied until all air bubbles were discharged. The sample was kept under vacuum for an additional 20 min. After removal, the scaffold was gently blotted with ethanol-moistened, dust-free cloths to remove surface ethanol without applying pressure. The final mass was recorded as m_4. Each group consisted of six specimens. Porosity was calculated using **Equation (III)**:

$$P = \frac{m_4 - m_1}{m_3 - m_2} \quad \text{(III)}$$

3.2.5. Scaffold compression testing

The compressive strength of the scaffolds was tested using an electronic universal testing machine (RWT10, Shenzhen Reger Instruments Co., Ltd, China) at room temperature. The test was conducted at a crosshead speed of 1 mm/min, and each measurement was repeated at least three times.

3.2.6. Shrinkage and swelling behavior of scaffolds

Shrinkage and swelling behavior were evaluated using deformation specimens prepared with different PVA concentrations. The initial outer diameter (d_1), height (h_1), and mass (m_5) of each specimen were recorded. The specimens were immersed in deionized water, ensuring they did not contact the inner walls of the container.

Subsequent measurements of outer diameter (d_2), height (h_2), and mass (m_6) were taken at various time points: 0.5, 1, 3, 6, 12, 24, 48, ..., 312, and 336 h. The following equations were used to calculate dimensional shrinkage and swelling:

Outer diameter shrinkage: $n_1 = \frac{30 - d_1}{30}$ (IV)

Height shrinkage: $n_2 = \frac{8 - h_1}{8}$ (V)

Swelling ratio: $s = \frac{m_6 - m_5}{m_5}$ (VI)

Height change rate during swelling: $n_3 = \frac{h_2 - h_1}{h_1}$ (VII)

Outer diameter change rate during swelling:

$$n_3 = \frac{d_2 - d_1}{d_1} \quad \text{(VIII)}$$

3.2.7. Biological characterization of scaffolds

3.2.7.1. In vitro biodegradability

Scaffolds were immersed in PBS at a ratio of 1 g of scaffold to 50 mL of PBS and sealed in PVA tubes. The PBS was refreshed every 7 days. These tubes were placed in a water-bath shaker (SHA-B, Bona Technology Co., Ltd, China) maintained at 37°C with a reciprocating oscillation speed of 100 rpm. At 7-day intervals, one group of scaffolds (three parallel samples per group) was removed for testing. The pH of the PBS was measured for each group. After removal, the scaffolds were freeze-dried and weighed. The average mass of the three samples was recorded as m_{10}. These scaffolds were not returned to the shaker. The percentage mass loss was calculated using **Equation (IX)**:

$$Weight(\%) = \left(\frac{m_9 - m_{10}}{m_9} \right) \times 100 \quad \text{(IX)}$$

3.2.7.2. In vitro simulated mineralization

The initial mass m_{11} of each freeze-dried scaffold was recorded. SBF was added at a ratio of 1 g of scaffold to 20 mL of SBF, and the mixture was sealed in PVA tubes. The setup was identical to that used for the biodegradation experiments, with incubation in a thermostatic water-bath shaker at 37 °C and 100 rpm.

The SBF solution was not replaced during the immersion period. Samples were collected at 1, 3, 5, 7, 14, **21, and 28** days. The pH of the solution was measured at each time point: 1, 3, 5, 7, 14, 21, and 28 days. At each interval, a small volume of the supernatant was collected to analyze calcium (Ca) and phosphorus (P) ion concentrations. An equal volume of fresh SBF was added to maintain a constant volume.

3.2.7.3. Cell culture and cytotoxicity assessment of bone marrow stem cells

Bone marrow stem cells (BMSCs) are adult stem cells with multidirectional differentiation potential and are widely present in the bone marrow. BMSCs were selected to evaluate the biological properties of scaffolds.

Rat primary BMSCs were cultured in DMEM supplemented with 10% fetal bovine serum and 1% penicillin–streptomycin in a humidified incubator containing 5% CO_2. Cells in the exponential growth phase were used for experiments. Twenty-four hours prior to the experiment, the cell suspension was treated with trypsin, and the cell concentration was adjusted to 8×10^4 cells/mL. Cells were seeded in 96-well culture plates at approximately 8×10^3 cells per well.

Scaffolds from groups C9 and C13 were selected for analysis. After autoclaving, one bone scaffold was incubated in 2 mL of osteogenic medium for 48 h. Subsequently, the same bone scaffold was incubated in 4 mL of osteogenic medium for an additional 48 h. The immersion solutions were collected from both incubations, combined, and diluted with osteogenic medium at a ratio of 1:4 to serve as the experimental group's culture medium. The resulting medium was sterilized by filtrating through a 0.22 μm membrane filter before use.

Cells were divided into three groups:

- Blank group: cultured in standard growth medium
- Model group: cultured in osteogenic medium
- Sample group: cultured in the experimental group medium (scaffold-derived)

After 24 h of initial culture, the experimental media were applied to the corresponding groups. The culture medium was refreshed every 2 days. On days 1 and 7, the medium was replaced with 100 μL of a mixture containing 10% CCK-8 in DMEM and incubated at 37°C for 2 h. Absorbance was measured at 450 nm using a multifunctional microplate reader (MK-3, Thermo, France) at 450 nm. Cell viability was calculated using the following equation:

$$Cell\,viability\,(\%) = \frac{OD_1 - OD_2}{OD_3 - OD_2} \times 100 \quad (X)$$

where OD_1, optical density the sample group; OD_2, optical density of the blank group; OD_3, optical density of the model group.

3.2.7.4. Proliferation, adhesion, and osteogenic differentiation of bone marrow stem cells

After autoclaving, the scaffolds were placed into 24-well plates. Each well was seeded with approximately 1.6×10^5 cells, and the culture medium was changed every 2 days. Experiments were carried out at specific time points, as described below:

- Cell morphology: After 1 and 7 days of culture, the morphology of cells on the scaffolds was observed using scanning electron microscopy (SEM; Sigma 300, Zeiss, Germany). Cells were then stained with phalloidin–TRITC (300 tests, cat. no. 40734ES75, Yeasen Biotechnology [Shanghai] Co., Ltd.) and DAPI solution after medium removal, and cytoskeletal and nuclear structures were visualized using a laser scanning confocal microscope (LSM 710, Carl Zeiss, Germany).
- ALP staining: After 7 and 14 days of culture, samples were stained with BCIP/NBT solution. Staining results were observed using a laser confocal microscope laser scanning confocal microscope (LSM 710, Carl Zeiss, Germany).
- ARS staining: After 21 days of culture, scaffolds were stained with AR solution. The absorbance of the supernatant was measured at 560 nm, and mineralization was further assessed by observing stained samples under a laser confocal microscope (LSM 710, Carl Zeiss, Germany).

3.3. Statistical analysis

All data are expressed as mean ± standard deviation. Statistical significance was considered at $p < 0.05$ (significance levels: ns: $p \geq 0.05$ [not significant], $^*p < 0.05$, $^{**}p < 0.01$, $^{***}p < 0.001$, and $^{****}p < 0.0001$). All results were confirmed by at least three independent experimental replicates.

4. Results and discussion

4.1. Bonding and mechanical properties in simulation models

The radial distribution function (RDF) and relative concentration distribution function are powerful tools for quantifying interactions between polymers and powder materials. In the RDF analysis, ionic and hydrogen (H) bonds are typically observed at distances up to 3.5 Å; strong van der Waals interactions occur between 3.5 and 5 Å, while weak van der Waals forces dominate beyond 5 Å.[32] As shown in Figure 3A and B, P and oxygen (O) atoms in HA and β-TCP form hydrogen bonds with H in PVA, whereas Ca and O atoms form ionic bonds. Figure 3C illustrates that O and H atoms within PVA exhibit

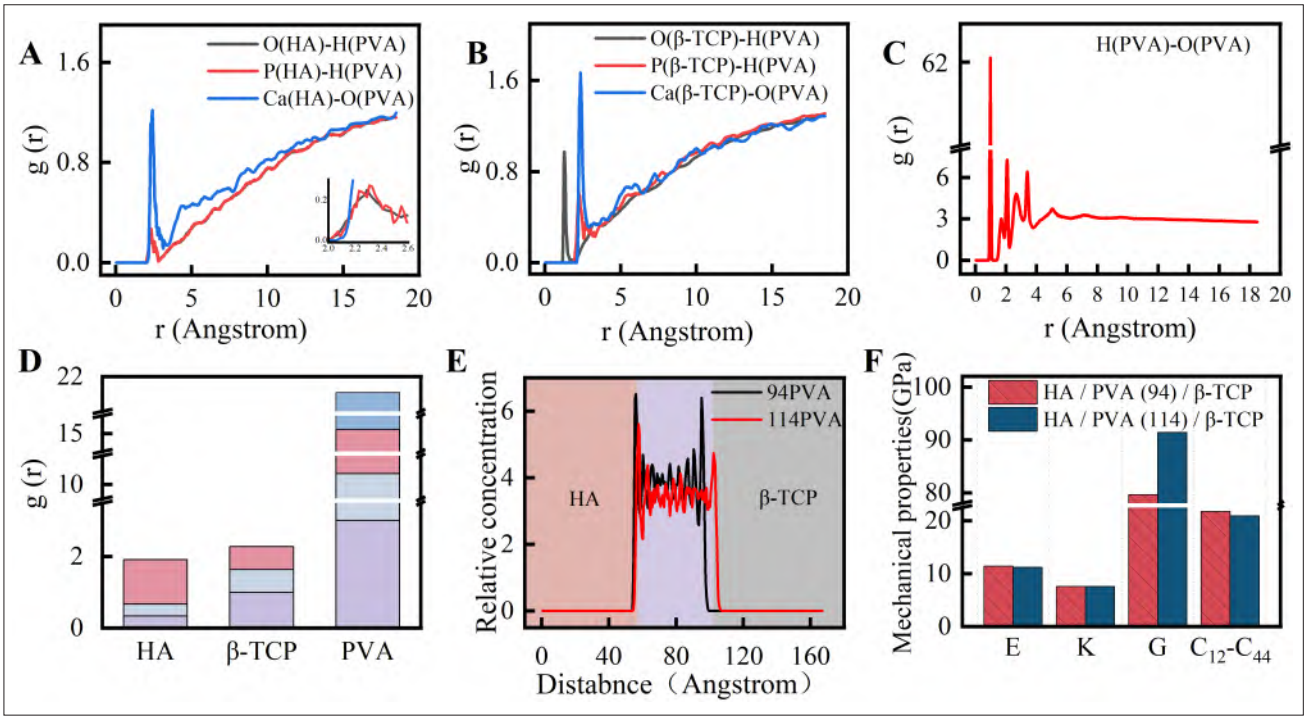


Figure 3. Radial distribution function (RDF), relative concentration distribution functions, and mechanical properties of interface systems: (A) RDF between hydroxyapatite (HA) and polyvinyl alcohol (PVA) (O element in PVA). (B) RDF between β-tricalcium phosphate (β-TCP) and PVA; (C) RDF between PVA and PVA; (D) summed RDF interface peaks; (E) relative concentration distribution functions of PVA. (F) Young's modulus (*E*), bulk modulus (*K*), shear modulus (*G*), and Cauchy pressure (C12–C44). Abbreviations: Ca, calcium; O, oxygen; P, phosphorus.

peaks at multiple distances: the first peak corresponds to hydroxyl covalent bonds within the PVA chain, the final peak represents van der Waals interactions, and the intermediate peaks indicate hydrogen bonding.

Molecular interactions in the system are a combination of various bonding types. Compared to H bonding, van der Waals forces contribute less to overall interaction strength. As shown in Figure 3D, the cumulative RDF peak intensity for PVA–PVA H and ionic bonding is significantly higher than that for interactions between PVA and either HA or β-TCP, suggesting that intermolecular interactions among PVA chains are stronger than those between PVA and ceramic particles.

In this study, the C backbone of PVA was employed to represent the entire PVA molecule. Figure 3E illustrates that the concentration of PVA C chains near β-TCP and HA particles is higher than in the central region containing only PVA. This observation indicates strong adhesive interactions between PVA and the particulate materials. Combined with the RDF results in Figure 3D, although internal PVA interactions are stronger in total magnitude, the interaction between PVA and the ceramic powders has a greater influence on the spatial distribution of PVA C chains. This finding suggests that internal PVA interactions should be considered as vector sums rather than simple scalar additions.

Young's modulus (*E*) is a key indicator of material stiffness, reflecting its resistance to elastic deformation. Shear modulus (*G*) is defined as the ratio of shear stress to shear strain and characterizes a material's resistance to shear deformation. Cauchy pressure (C12–C44) is an important indicator of plasticity, brittleness, and bonding characteristics. The mechanical performance of a material depends on a combination of these properties. Generally, higher values of *E*, *G*, and C12–C44 indicate better mechanical performance of bone scaffolds. As shown in Figure 3F, simulation results demonstrate that the *E*, bulk modulus, and C12–C44 values for PVA with 114 repetition units are highly comparable to those for PVA with 94 repetition units. However, the *G* value is noticeably higher in the 114-unit PVA, indicating improved shear resistance. This finding indicates that increasing the PVA chain length improves material hardness, thereby increasing the overall strength of the scaffold.

4.2. Experimental results

4.2.1. Characterization of slurries

Slurries with proper viscosity and excellent shear-thinning properties are critical for successful scaffold fabrication via printing. As shown in Figure 4C, increasing the concentration of PVA aqueous solution results in higher slurry viscosity and improved shear-thinning behavior. Zeta potential and solid content are important factors affecting slurry performance. According to Figure 4A, the zeta potential remains relatively unchanged across different PVA concentrations. In general, solid content is positively correlated with slurry viscosity (Figure 4B). Higher PVA concentrations lead to increased solid content and enhanced chain entanglement, which makes the slurry more resistant to deformation. As a result, the slurry exhibits greater viscosity and shear-thinning capability. These rheological properties are essential for maintaining the shape fidelity of bone scaffolds during the printing process. The superior shaping effect of slurry prepared with 13% PVA compared to that with 7% (Figure 4D) underscores the significance of optimizing binder concentration in the printing and preparation of bone scaffolds.

4.2.2. Characterization of scaffold features

4.2.2.1. Analysis of adhesive effect

Binders function by encapsulating powder particles and forming crosslinked polymer chains that stabilize the scaffold structure. To evaluate bonding efficiency, we analyzed the scaffolds' microscopic morphology. As shown in Figure 5, PVA encapsulates the powder particles and forms interconnecting networks, thereby supporting structural integrity and ensuring effective scaffold performance.

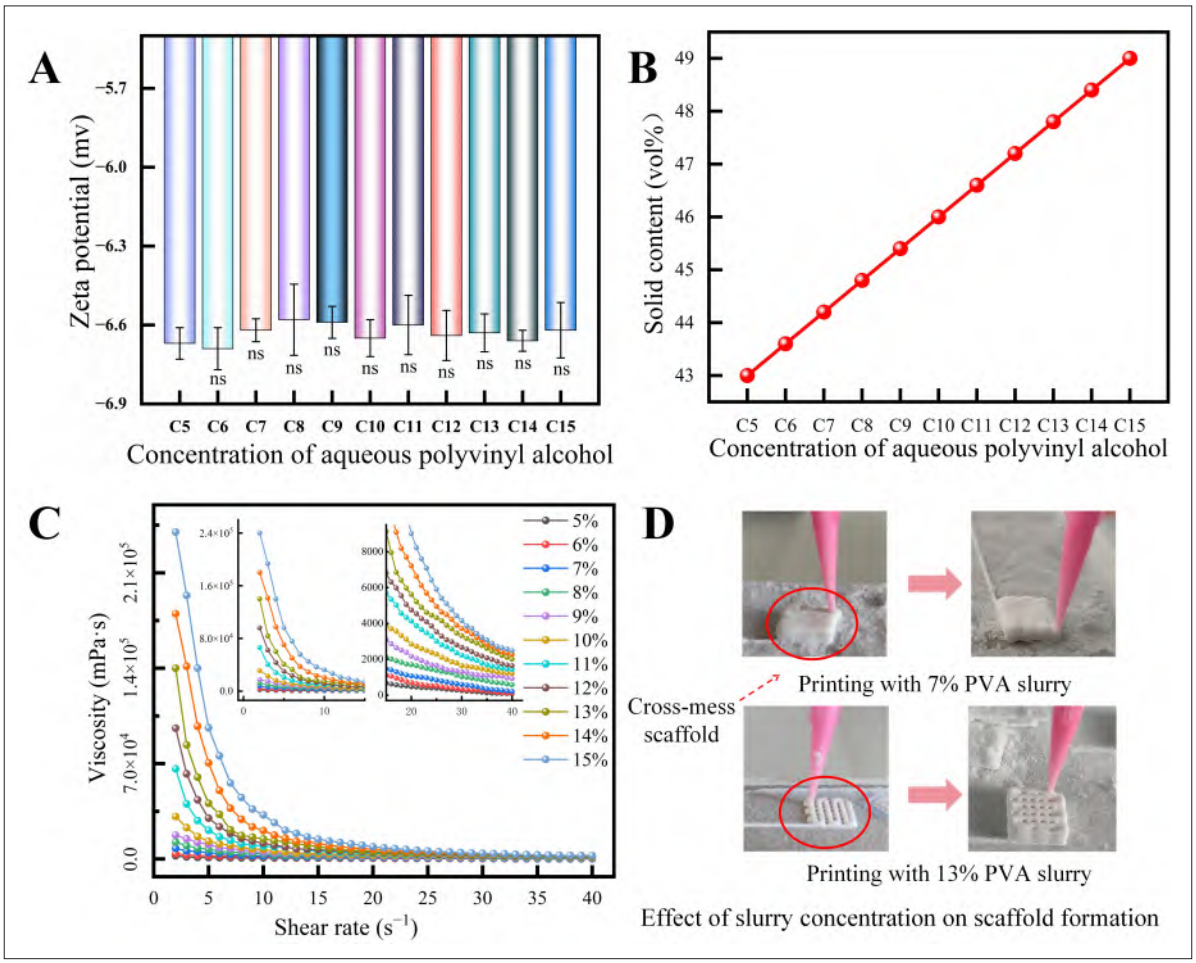


Figure 4. Characterization of slurries with varying polyvinyl alcohol (PVA) concentrations: (A) zeta potential, (B) solid content, (C) Shear viscosity, and (D) print quality. Note: ns: $p \geq 0.05$.

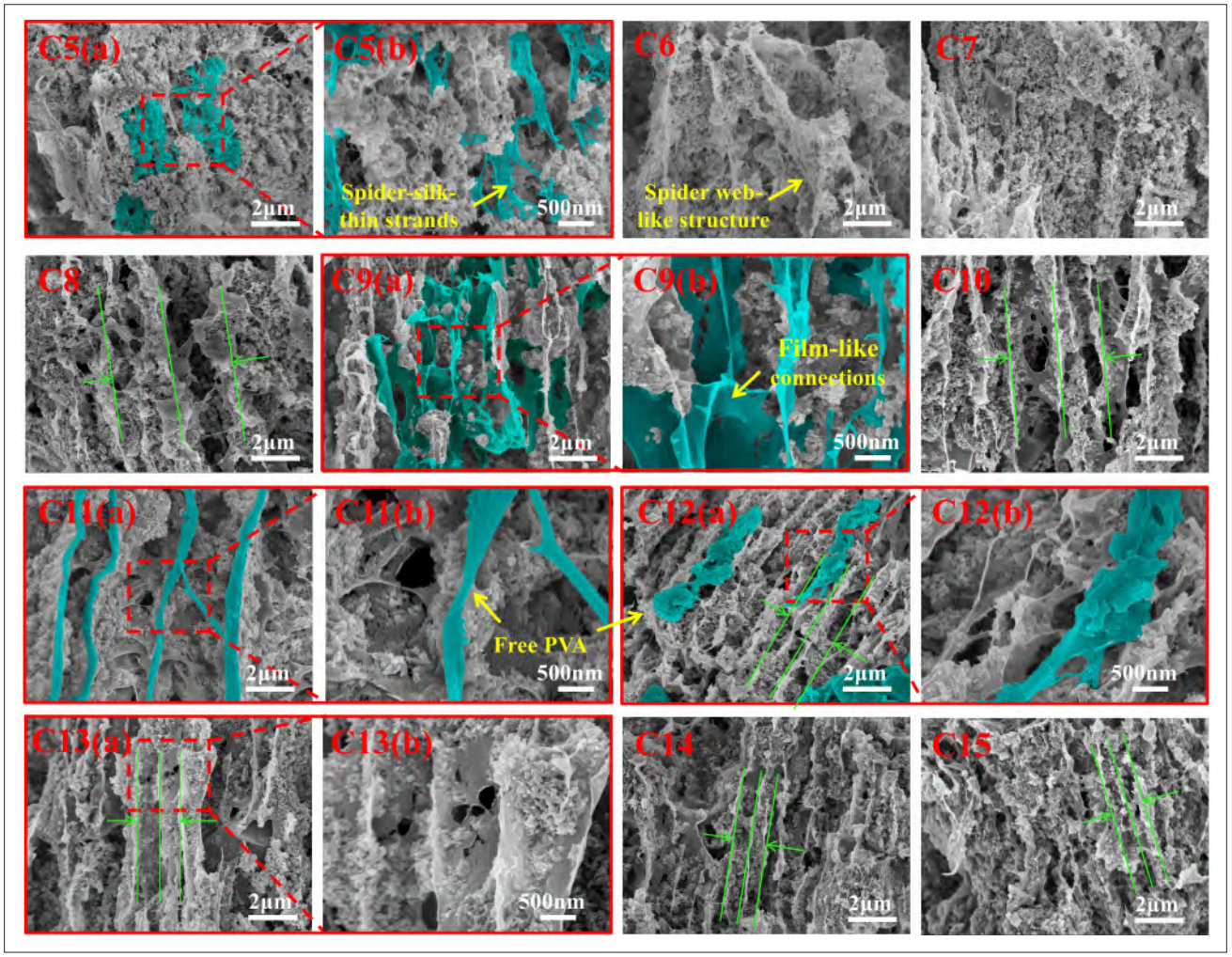


Figure 5. The bonding effect within scaffolds under varying concentrations of polyvinyl alcohol (PVA) aqueous solution. Green-lined structures denote polyvinyl alcohol aggregate morphology. Scale bars: 2 μm; magnification: 10,000×.

At PVA concentrations below 8%, the connections between powder particles appeared weak and fragmented, leading to greater dispersion and reduced structural integrity. As PVA concentration increased, these connections transitioned progressively from thin, spider silk-like strands (Figure 5-C5) to spider web-like structures (Figure 5-C6, -C7), and eventually to continuous membranes (Figure 5-C8). At low PVA concentrations, fewer PVA chains were available for crosslinking, resulting in fewer crosslinking points. Consequently, upon drying, the remaining PVA molecules formed only fragile and fragmented connections. At a PVA concentration of 9%, film-like connections between powder particles became more continuous (Figure 5-C9). With further increases in concentration, the powders exhibited a bar-like bonding morphology, attributed to enhanced intermolecular binding caused by the greater PVA content. This increase in binder facilitated tighter aggregation and stronger bonding structure (Figure 5-C10). At even higher concentrations, the internal scaffold structure began to exhibit free-form agglomerates of unencapsulated powder and striated clusters of sticky PVA (Figure 5-C11, -C12). Although higher binder concentrations increase the number of potential crosslinking sites, excess PVA may remain unbound, leading to overlapping and aggregation. Thus, achieving an optimal binder concentration is crucial to ensuring complete encapsulation and effective particle adhesion. With continued increases in PVA concentration, a uniform strip-block bonding structure gradually emerged. This block structure became increasingly uniform and compact across samples (Figures 5-C8, -C10, -C13, -C14, -C15), ultimately resulting in improved adhesive performance.

4.2.2.2. Scaffold porosity

Porosity plays a crucial role in the performance of scaffolds used for grafting, as it facilitates cell adhesion, proliferation, nutrient exchange, and the removal of metabolic waste. During the freeze-drying process, scaffold porosity is primarily influenced by the water content of the slurry. As PVA concentration increases, the water content of the solution decreases accordingly. As shown in Figure 6, experimental results confirmed that scaffold porosity decreases with increasing PVA concentration. However, while the water content of a 15% PVA aqueous solution is ~51% and that of a 5% solution is ~57%—a difference of only ~6%—the resulting porosity difference in the prepared slurry is ~70%. This finding indicates that water content alone is not the sole factor influencing scaffold porosity. For example, at 5% PVA concentration, the measured porosity exceeded theoretical estimates. This discrepancy can be attributed to residual anhydrous ethanol on the scaffold surface during measurement, which was erroneously included in the porosity calculation, leading to overestimation. A similar measurement error was also observed at 15% PVA concentration. However, even in this case, the porosity was significantly lower than the water content of the slurry. This discrepancy can be attributed to scaffold shrinkage during the drying process, which further reduces porosity. A detailed explanation of this shrinkage phenomenon is provided in **Section 4.2.2.4**.

4.2.2.3. Mechanical properties

Mechanical properties are crucial for assessing the performance of bone scaffolds. As shown in Figure 7, the compressive strength of scaffolds increased with PVA concentration. Scaffolds fabricated using a 15% PVA aqueous solution achieved a compressive strength of 35.7 MPa, whereas those prepared with a 5% PVA aqueous solution reached only 2.1 MPa. This pronounced difference clearly demonstrates the critical role of PVA concentration in determining the mechanical properties of scaffolds. As PVA concentration increases, the water content in the slurry decreases, leading to a significant reduction in porosity. This increase in porosity effectively enhances the mechanical properties of the bone scaffold. Furthermore, the increased PVA content strengthens intermolecular interactions, enhancing internal bonding and making the scaffold structure more compact and stable. However, these interactions also intensify scaffold shrinkage during drying, further reducing porosity. These combined

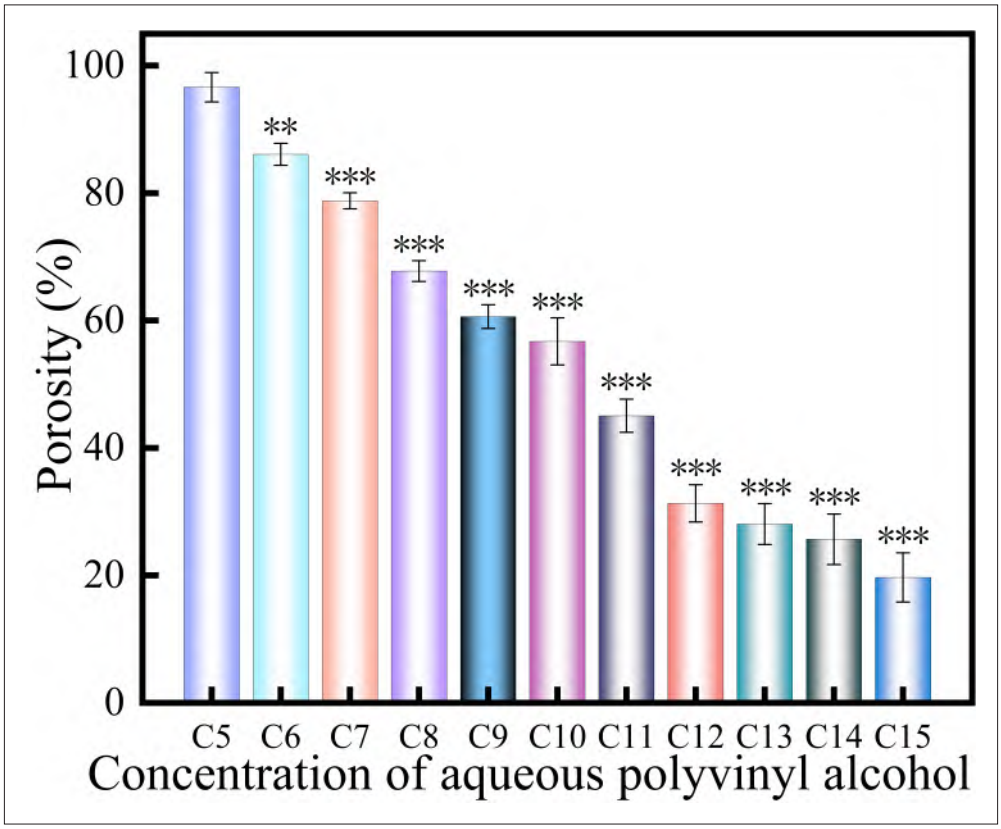


Figure 6. Porosity of scaffolds prepared with different concentrations of polyvinyl alcohol aqueous solution. Notes: $^{**}p < 0.01$; $^{***}p < 0.001$.

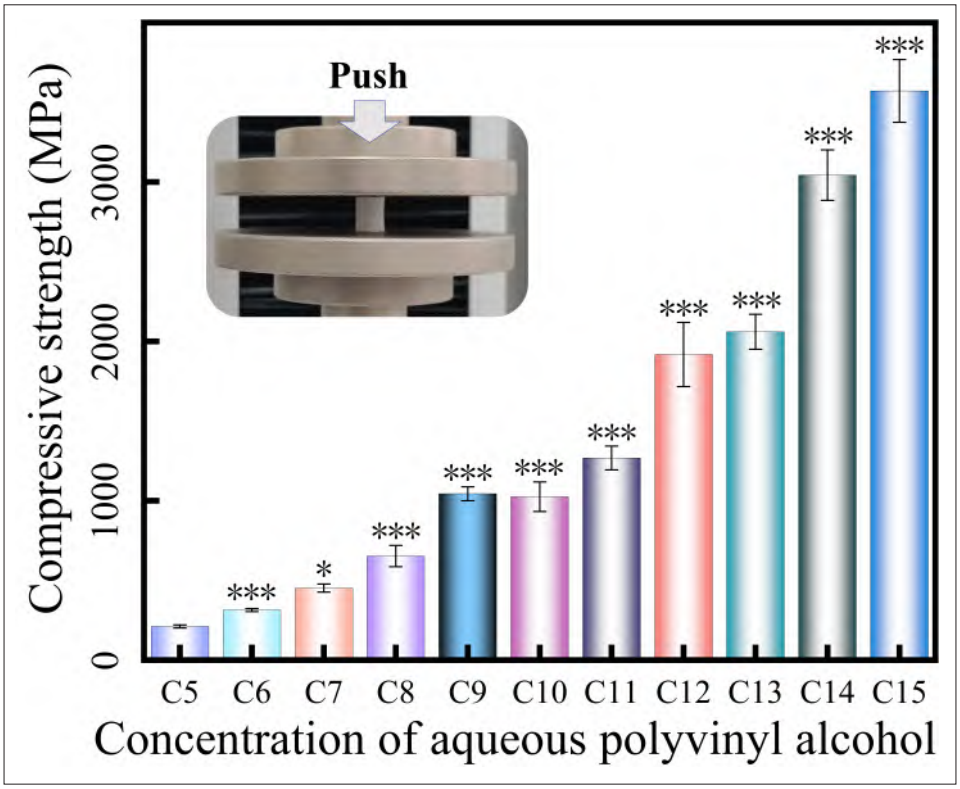


Figure 7. Compressive strength of scaffolds prepared with different concentrations of polyvinyl alcohol aqueous solution. Notes: $^{*}p < 0.05$; $^{**}p < 0.01$; $^{***}p < 0.001$.

effects—decreased porosity, enhanced molecular bonding, and increased shrinkage—synergistically contribute to the significant improvement in the mechanical properties of bone scaffolds.

4.2.2.4. Shrinkage

In this study, scaffolds exhibited varying degrees of shrinkage after drying, with shrinkage becoming more pronounced as the PVA concentration increased. To further investigate this effect, the size of the bone scaffold samples was increased to amplify the absolute deformation. The actual dimensions of the scaffolds after freeze-drying were compared with the predetermined dimensions to calculate the extent of shrinkage (Figure 8A). The results revealed that scaffold shrinkage increased with PVA concentration, while the rates of change in thickness and outer diameter remained consistent (Figure 8B). At a PVA concentration of 5%, scaffolds exhibited 2% shrinkage. In contrast, at 15% PVA concentration, the external dimensions shrank by approximately 14%. Notably, when the PVA mass fraction reached 9%, the dry scaffold surface started to exhibit visible concave deformation (see Figure 8A-A1).

Typically, lower solid content in a slurry leads to greater shrinkage. However, based on the trend observed in solid content with increasing PVA concentration (Figure 4D), solid content was not the primary driver of scaffold shrinkage or shape deformation in this study. Instead, shrinkage was primarily attributed to the curling and entanglement of PVA chains during water sublimation. These polymer chain movements drew powder particles together, and as crosslinking density increased, intermolecular interactions strengthened, leading to greater macroscopic contraction of the scaffold structure. This conclusion is further supported by SEM observations and porosity data. Additionally, MD simulation results indicated significant interactions among PVA molecules (Figure 3D). Although the net effect of these interactions should be considered in terms of vector forces, the inter-PVA bonding during drying likely contributed to scaffold deformation by mobilizing adjacent powder particles.

4.2.2.5. Swelling rate

Scaffolds were evaluated for their swelling characteristics and dimensional changes upon immersion. The results indicated that scaffolds fabricated with lower PVA concentrations achieved swelling equilibrium more quickly (Figure 9A) and exhibited greater maximum swelling ratios (Figure 9B). Specifically, scaffolds fabricated using a 5% PVA aqueous solution reached swelling equilibrium

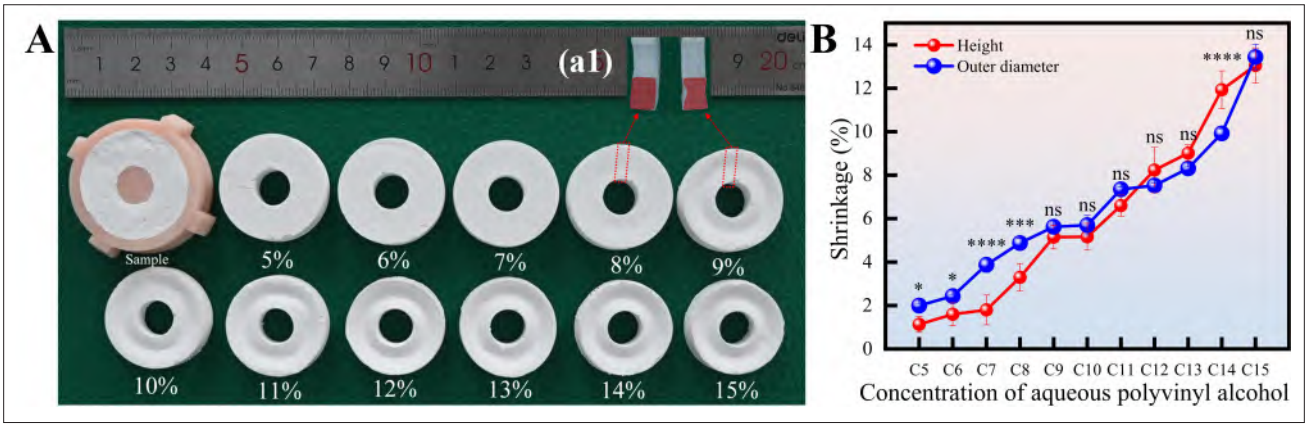


Figure 8. Drying shrinkage characteristics of annular scaffolds: (A) scaffold appearance after drying; (B) dimensional change rates for scaffolds. Notes: ns: $p \geq 0.05$; *$p < 0.05$; **$p < 0.01$; ***$p < 0.001$; ****$p < < 0.0001$.

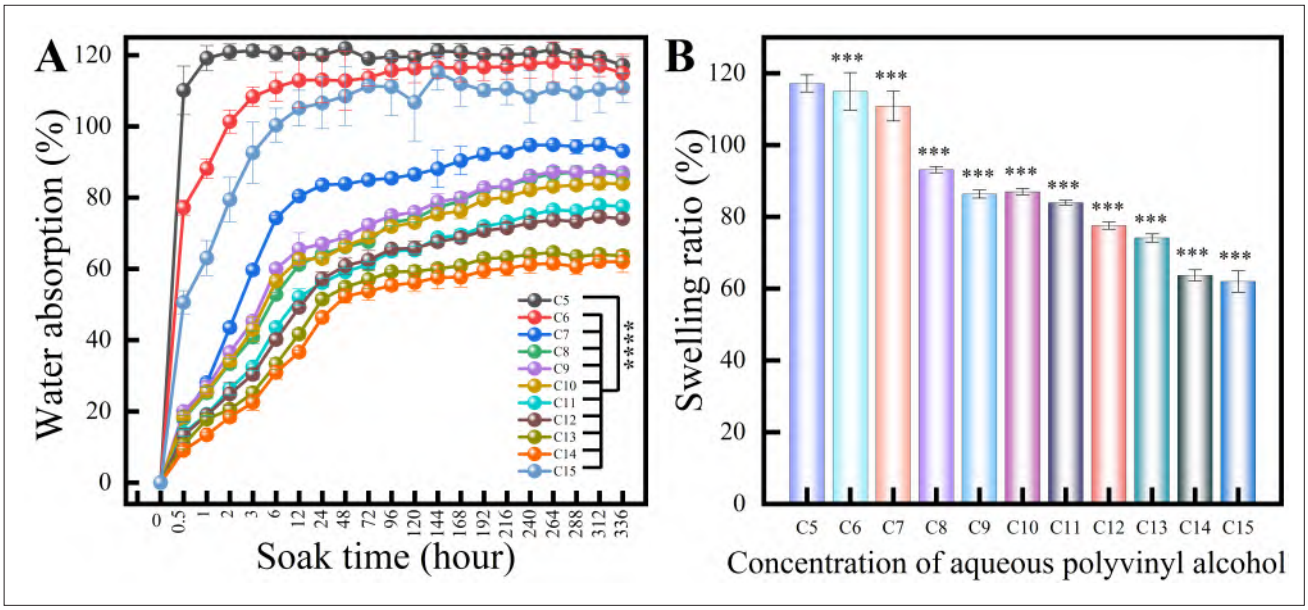


Figure 9. Swelling characteristics of annular scaffolds: (A) water absorption over time; (B) maximum swelling ratio of scaffolds. Notes: *$p < 0.05$; **$p < 0.01$; ***$p < 0.001$; ****$p < 0.0001$.

after 1.5 h of immersion, with no significant changes thereafter. In contrast, scaffolds prepared with a 15% PVA aqueous solution required up to 48 h of immersion to approach equilibrium, with the swelling rate continuing to rise over time. Two main factors influenced scaffold swelling behavior are as follows: (i) porosity and (ii) the internal space available for water absorption owing to the curling of PVA chains. At lower PVA concentrations, the bone scaffolds exhibited higher porosity, which promoted water absorption. Additionally, the lower crosslinking density of PVA chains allowed water to penetrate and diffuse more easily, thereby accelerating the swelling process.

4.2.2.6. Dimensional changes

As shown in Figure 10, after 336 h of soaking, the bone scaffolds maintained their annular structure and demonstrated excellent dimensional stability. Initially, scaffolds fabricated with lower PVA concentrations showed a decrease in size due to softening and shrinkage. As the PVA concentration increased, this dimensional reduction became less pronounced and eventually reversed, with some scaffolds exhibiting a slight expansion. Dimensional changes in the scaffolds were governed by the following two competing mechanisms: hydrophilic swelling and softening-induced shrinkage. At lower

binder concentrations, while scaffold dissolution was more pronounced, the high porosity also led to enhanced softening and shrinkage, resulting in a net reduction in size. In contrast, at higher PVA concentrations, reduced porosity, and a denser internal structure limited softening and shrinkage effects. Although increased crosslinking limited swelling, the polymer chains still retained some intrinsic swelling capacity. Once the swelling from

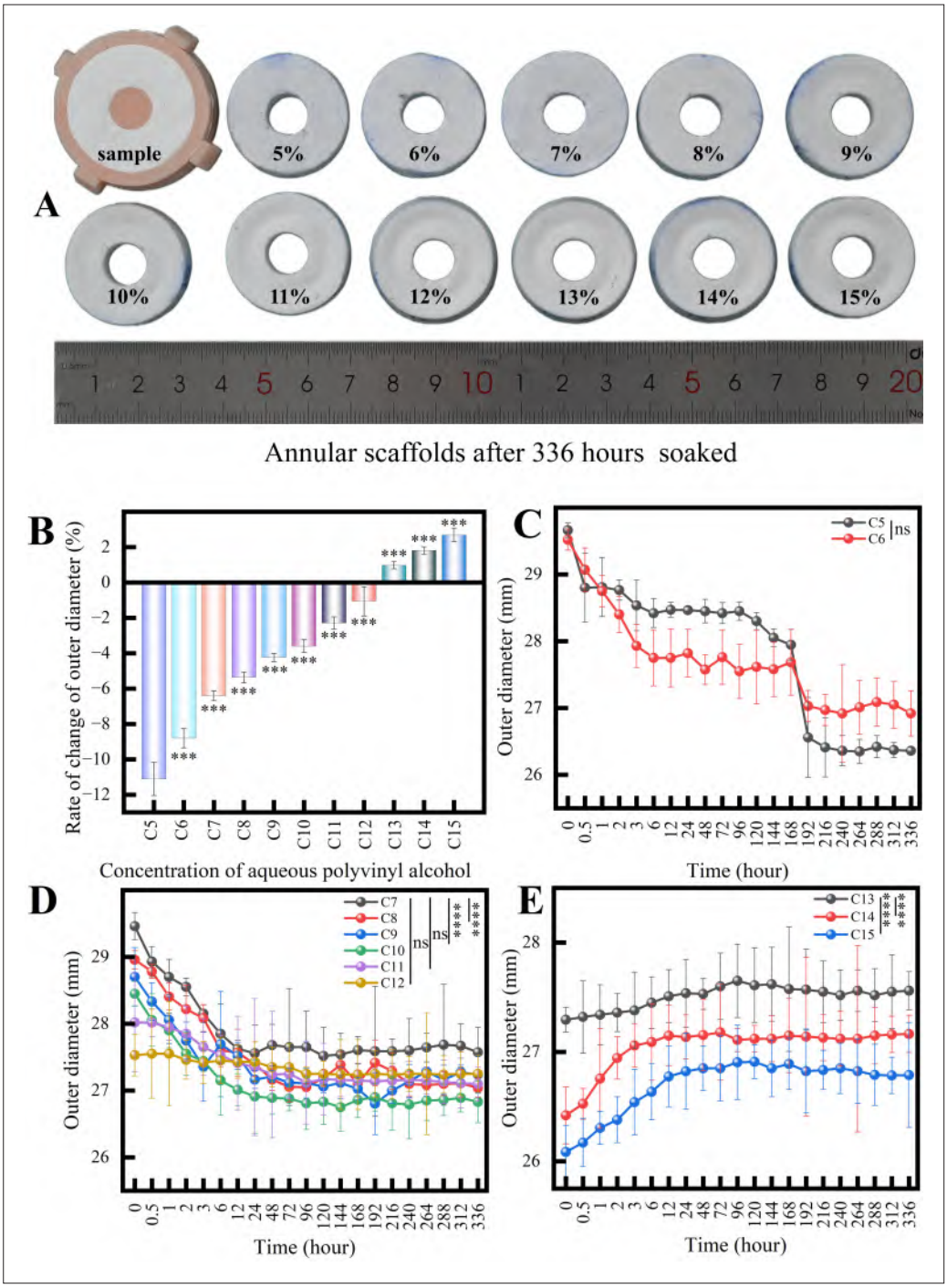


Figure 10. Dimensional changes in annular scaffolds after 336 h of soaking. (A) Appearance of annular scaffolds after 336 h of soaking; (B) outer diameter change rate; (C) variation in external diameter of C5 and C6 scaffolds; (D) variation in external diameter of C7 to C12 scaffolds; (e) variation in external diameter of C13–C15 scaffolds. Notes: ns: $p \geq 0.05$; *$p < 0.05$; **$p < 0.01$; ***$p < 0.001$; ****$p < 0.0001$.

polymer lysis exceeded the shrinkage from softening and contraction, a net expansion was observed.

Interestingly, scaffolds fabricated with 5% and 6% PVA concentrations exhibited a sudden size reduction at 312 h (Figure 10B). This phenomenon was likely attributed to prolonged immersion, during which PVA molecules began dissolving into the surrounding water and entering the dissolution phase, leading to structural collapse and a further decrease in scaffold size. A similar phenomenon was observed in scaffolds with higher PVA concentrations; however, their more compact structure prevented noticeable changes in external dimensions.

4.2.3. In vitro evaluation of the biological performance of the scaffolds

4.2.3.1. In vitro biodegradation and simulated mineralization

The degradation rate of bone scaffold materials significantly impacts their effectiveness for bone repair. Four scaffold groups—C9, C11, C13, and C15—were fabricated from corresponding slurries and tested at cross-mesh constructs. As illustrated in Figure 11A, scaffold mass loss increased with immersion time, and the degradation rate was inversely proportional to the PVA concentration. During degradation, the pH of the medium initially decreased, then increased, and eventually stabilized. Once stabilized,

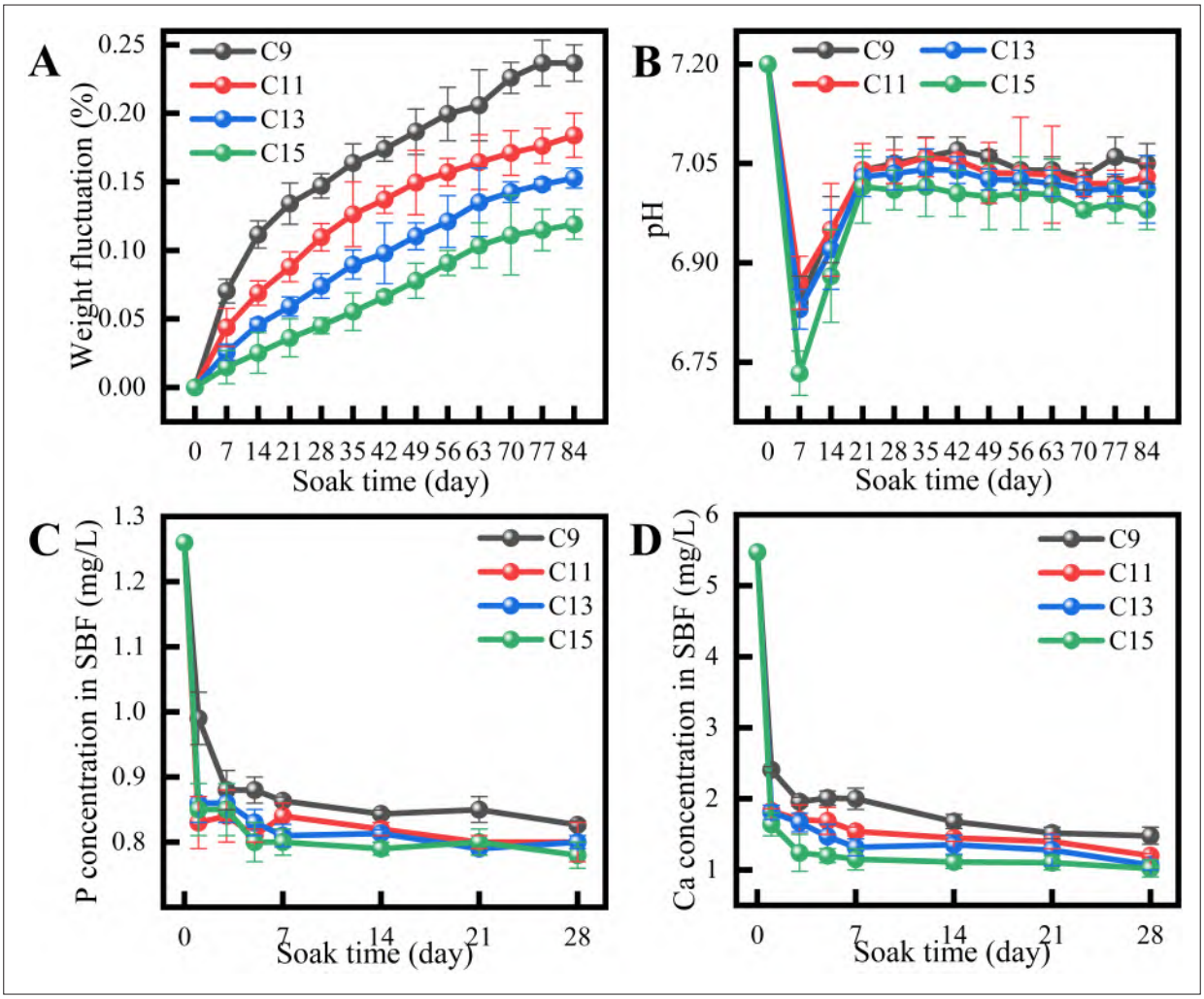


Figure 11. Biodegradation performance, pH values, and ion release concentrations of scaffolds immersed in phosphate-buffered saline (PBS) at various time points. (A) Mass loss of scaffolds at different immersion times in PBS. (B) pH changes at different immersion times in PBS. (C) Phosphate (P) ion concentration in simulated body fluid (SBF). (D) Calcium (Ca) ion concentration in SBF. Notes: ns: $p \geq 0.05$; *$p < 0.05$; **$p < 0.01$; ***$p < 0.001$; ****$p < 0.0001$.

the pH followed the order: C9 < C11 < C13 < C15 (Figure 11B). We hypothesize that scaffold degradation is closely related to porosity. Higher porosity increases the contact surface area between the bone scaffold and the surrounding SBF, facilitating faster degradation. Consequently, scaffolds with higher PVA concentrations—characterized by lower porosity—undergo slower degradation. The pH shift in SBF is associated with both scaffold degradation and mineralization. Initially, degradation releases PO_4^{3-} and other acid ions, while hydrolysis produces OH^-, leading to a temporary pH rise. Over time, mineralization processes (e.g., formation of HA from Ca^{2+} and PO_4^{3-}) consume OH^- and lower the pH. The initial drop in pH is likely due to an imbalance between degradation and mineralization rates. As these rates equilibrate, the pH stabilizes. Ultimately, lower PVA concentration scaffolds degrade faster, releasing more Ca^{2+} and PO_4^{3-} into the SBF (Figure 11C and D), accelerating mineralization and leading to a lower final pH.

4.2.3.2. Biocompatibility

C9 and C13 cross-mesh scaffolds were selected for comparative analysis of cell proliferation and biotoxicity. As illustrated in Figure 12A, CCK-8 assay results revealed that the cell viability of BMSCs for both scaffold groups exceeded 90%, demonstrating excellent biocompatibility. After 1 day of culture, no significant difference was observed between groups. However, by day 7, the cell proliferation rate was significantly higher in the C9 group (corresponds to P4 group) compared to the C13

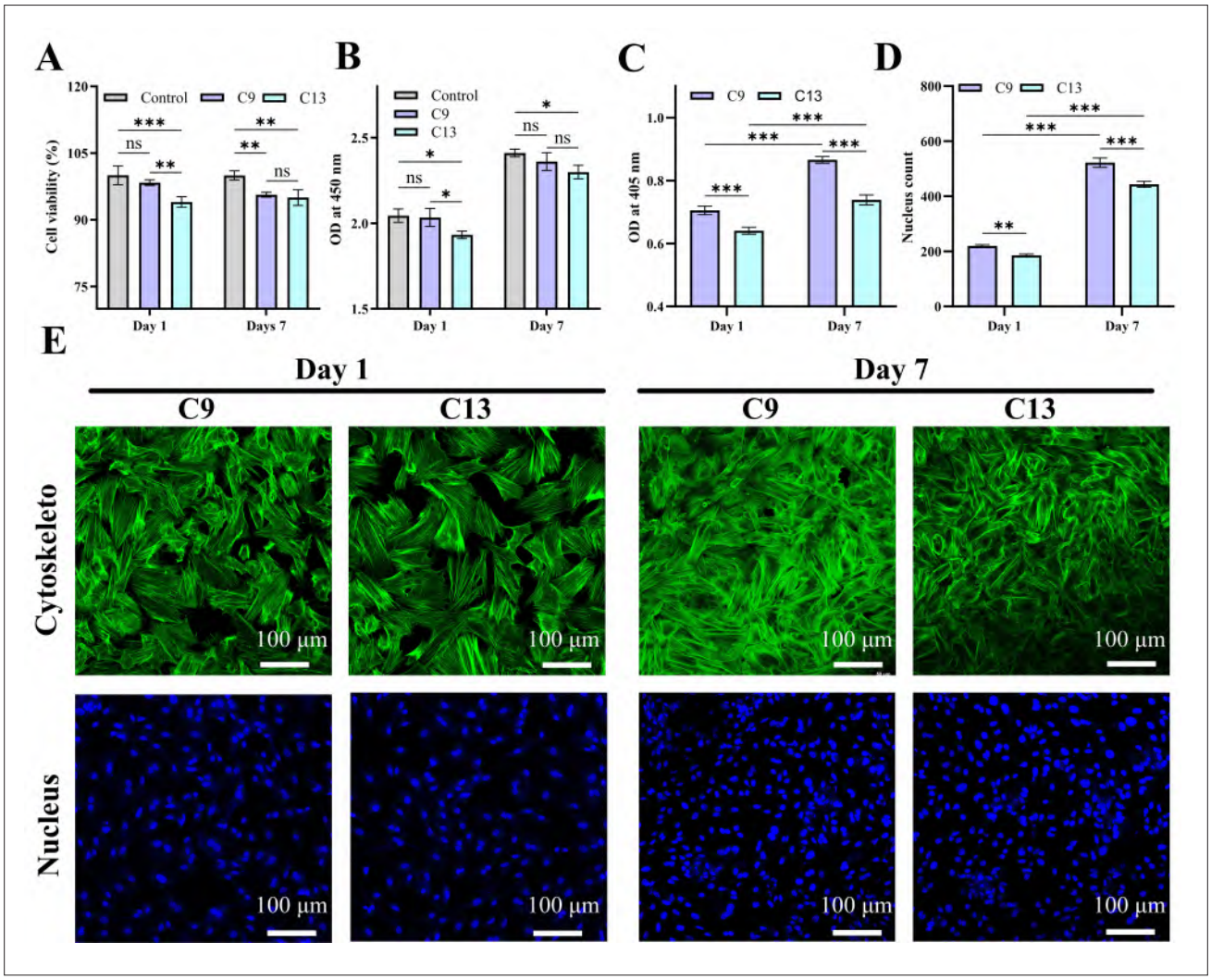


Figure 12. Assessment of cell viability at different culture times. (A) CCK-8 assay results for cell viability. (B) Optical density (OD) values from the CCK8 assay. (C) OD values of cytoskeleton staining. (D) Nucleus count. (E) Immunofluorescence images of the cytoskeleton and nuclei. Scale bars: 100 μm; magnification: 200×. Notes: ns: $p \geq 0.05$; *$p < 0.05$; **$p < 0.01$; ***$p < 0.001$.

group—(corresponds to P0 group), a trend that was consistent with increased fluorescence intensity (Figure 12B). This enhanced proliferation can be attributed to higher concentrations of Ca^{2+} and PO_4^{3-} ions in the P4 scaffold immersion system, which supported the growth and proliferation of rat BMSCs. Immunofluorescence images of the cytoskeleton and nuclei further confirmed strong cell viability (Figure 12E). Quantitative analyses of the cytoskeleton and nuclear staining (Figure 12C and D) revealed that rat BMSCs cultured on C9 scaffolds exhibited superior viability compared to those on C13.

As shown in Figure 13, rat BMSCs adhered well to both scaffold groups, with cell density increasing over time. On both day 1 and 7, rat BMSCs cultured on C9 scaffolds exhibited a larger spreading area, more pseudopodia, and—on day 7—a denser and more uniform distribution compared to those on C13 scaffolds. This trend was in line with the CCK8 results. The observed difference is attributed to scaffold porosity. Higher porosity provides a larger surface area and more adhesion sites, facilitating greater cell attachment. The C9 scaffolds, with their higher porosity, offered more favorable conditions for rat BMSC adhesion. In addition, increased porosity and swelling capacity improve nutrient diffusion and waste removal, further promoting cell adhesion and growth. These factors likely explain the enhanced adhesion observed in the C9 group compared to C13.

4.2.3.3. Cell osteogenic differentiation

Alizarin Red staining revealed greater calcium nodule deposition in rat BMSCs cultured on C13 scaffolds compared to those on C9 (Figure 14B and E), suggesting stronger mineralization capacity. As shown in Figure 14A, ALP staining intensity in both C9 and C13 groups increased after 7 and 14 days, relative to the model group, indicating scaffold-induced osteogenic differentiation. Notably, rat BMSCs on C9 scaffolds exhibited deeper and more intense ALP staining, reflecting higher ALP activity and stronger osteogenic potential. This was confirmed by quantitative fluorescence analyses (Figure 14C and D). Meanwhile, AR staining results for C13 scaffolds (Figure 14B and E) indicated enhanced calcium nodule deposition, suggesting superior osteogenic potential compared to C9.

5. Conclusion

In this study, HA/β-TCP bone scaffolds were fabricated using varying concentrations of PVA aqueous solutions and shaped via freeze-drying. Combined with MD simulations, both the microscopic and macroscopic property changes of the scaffolds were analyzed, and their biological performance was experimentally verified. The following conclusions were drawn:

- MD simulation results demonstrated that H bonding and ionic interactions are the primary mechanisms underlying PVA adhesion, leading to chain entanglement. An increase in *G* corresponded with enhanced intrinsic mechanical properties of the material.
- The influence of PVA concentration on both the slurry and bone scaffold properties is primarily governed by changes in the degree of PVA chain

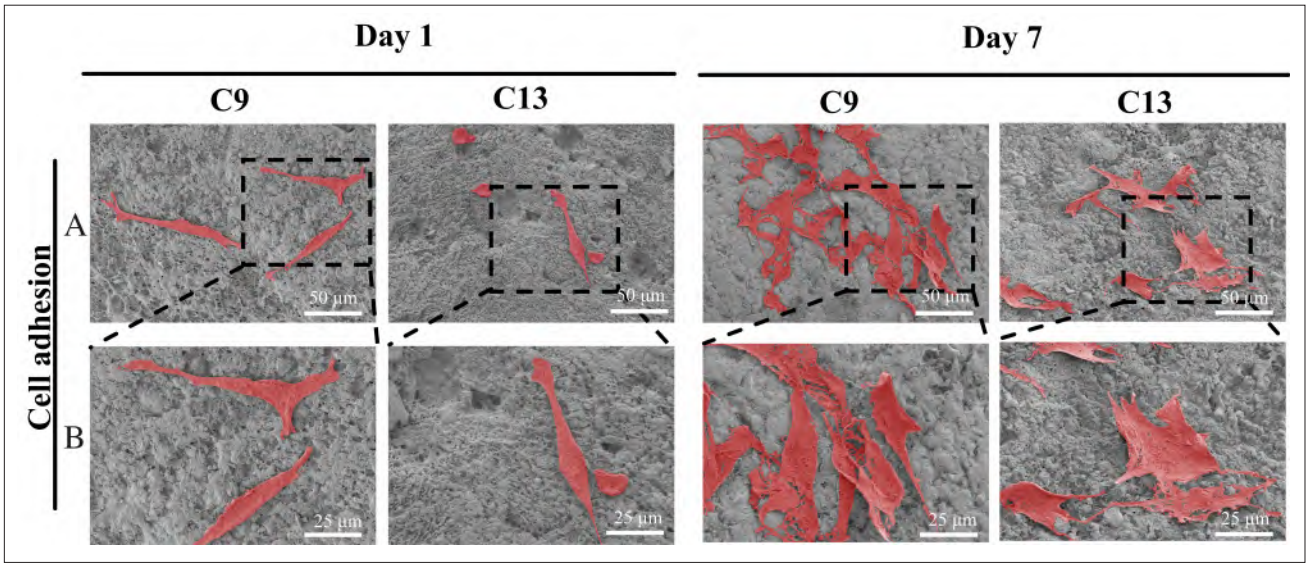


Figure 13. Cell adhesion on bone scaffolds: (A) scanning electron microscopic (SEM) images of cell adhesion on the scaffold surface. Scale bars: 50 μm; magnification: 500×; (B) SEM images showing adhesion of cells within scaffold macropores. Scale bars: 25 μm; magnification: 1000×.

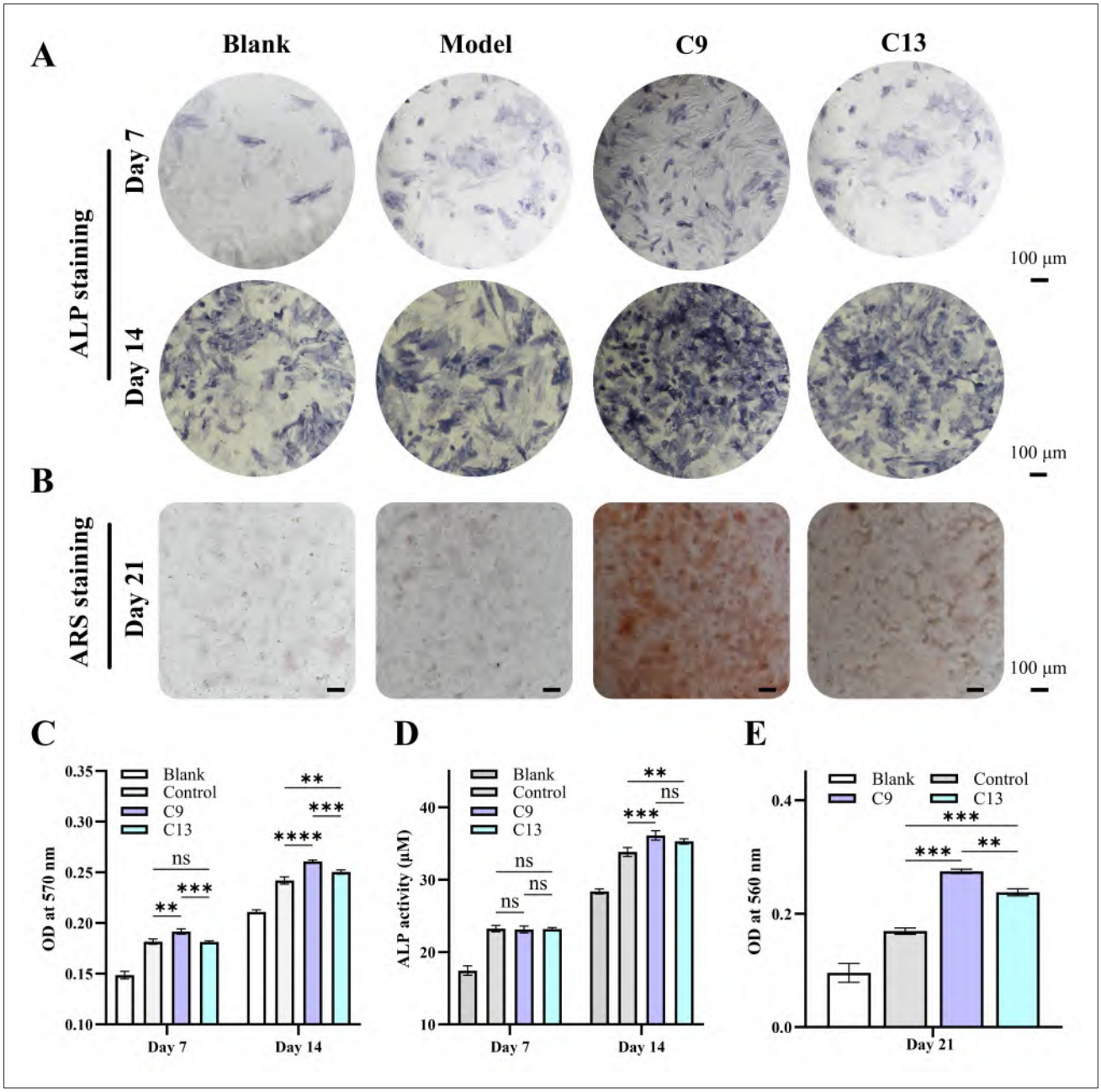


Figure 14. Osteogenic differentiation and mineralization of rat bone marrow mesenchymal stem cells *in vitro* at different time points. (A) Alkaline phosphatase (ALP) staining. (B) Alizarin Red S (ARS)" staining. (C) Optical density (OD) of ALP. (D) Quantitative analysis of ALP activity. (E) Optical density of AR. Scale bars: 100 μm; magnification: 100×. Notes: ns: $p \geq 0.05$; *$p < 0.05$; **$p < 0.01$; ***$p < 0.001$; ****$p < 0.0001$.

crosslinking and slurry solid content. These factors increase slurry viscosity and shear-thinning behavior, thereby improving printability. A higher degree of crosslinking results in more pronounced shrinkage during drying, affecting scaffold dimensional accuracy. Swelling experiments showed that while scaffolds fabricated with higher PVA concentrations had lower porosity and exhibited greater deformation, they demonstrated better dimensional stability during immersion. Improvements in porosity and intrinsic mechanical properties contributed to enhanced scaffold strength. According to MD simulation results, enhanced base material properties also accounted for improvements in scaffold mechanical performance.

Bone scaffolds prepared with lower PVA concentrations exhibited superior biological performance. Their higher porosity accelerated scaffold degradation, releasing greater amounts of Ca^{2+} and PO_4^{3-}, which promoted cell proliferation. Increased porosity also facilitated mass transfer, provided more adhesion sites, and supported better cell attachment and proliferation, along with enhanced biomineralization capacity.

In summary, adjusting PVA concentration allows for the modulation of porosity, mechanical properties, and degradation rate in bone scaffolds. This tunability enables the customization of bone scaffolds for various healing durations and defect types. Furthermore, improving scaffold dimensional precision can enhance production efficiency and reduce manufacturing costs, thereby lowering treatment expenses and enabling scalable production of bone scaffolds.

Acknowledgments

All molecular dynamics calculations using Materials Studio were performed at the Supercomputing Center of Dalian University of Technology.

Funding

This work was supported by the National Natural Science Foundation of China (grant no.: 52365053).

Conflict of interest

The authors declare they have no competing interests.

Author contributions

Conceptualization: Zhitao Yin, Yan Xu, Xujing Zhang
Formal analysis: Zhitao Yin, Yutong Chen
Investigation: Zhitao Yin
Methodology: Zhitao Yin, Yutong Chen
Writing–original draft: Zhitao Yin
Writing–review & editing: Guang Yang, Shuaishuai Wang, Bingbing Wang, Yue Zhao

Ethics approval and consent to participate

Not applicable.

Consent for publication

Not applicable.

Availability of data

The data that used during this study are available from the corresponding author upon reasonable request.

References

1. Thurzo A, Gálfiová P, Nováková Z, et al. Fabrication and in vitro characterization of novel hydroxyapatite scaffolds 3-D printed using polyvinyl alcohol as a thermoplastic binder. *Int J Mol Sci*. 2022;23(23):14870.
doi: 10.3390/ijms232314870

2. Wascher DC, Bulthuis L. Extremity trauma: field management of sports injuries. *Curr Rev Musculoskelet Med*. 2014;7(4):387-393.
doi: 10.1007/s12178-014-9242-y

3. Xu C, Kang Y, Guan S, Dong X, Jiang D, Qi M. Iron-based metal–organic framework as a dual cooperative release system for enhanced vascularization and bone regeneration. *Chinese Chem Lett*. 2023;34:107825.
doi: 10.1016/j.cclet.2022.107825

4. Huang K, Liu G, Gu Z, Wu J. Tofu as excellent scaffolds for potential bone regeneration. *Chinese Chem Lett*. 2020;31:3190-3194.
doi: 10.1016/j.cclet.2020.07.002

5. Shi W, Jiang Y, Wu T, Zhang Y, Li T. Advancements in drug-loaded hydrogel systems for bone defect repair. *Regen Ther*. 2024;25:174-185.
doi: 10.1016/j.reth.2023.12.010

6. Mauffrey C, Barlow BT, Smith W. Management of segmental bone defects. *J Am Acad Orthop Surg*. 2015;23(3):143-153.
doi: 10.5435/JAAOS-D-14-00018

7. Faour O, Dimitriou R, Cousins CA, Giannoudis PV. The use of bone graft substitutes in large cancellous voids: any specific needs? *Injury*. 2011;42(Suppl 2):S87-S90.
doi: 10.1016/j.injury.2011.06.020

8. Yang DH, Nah H, Lee D, et al. A review on gold nanoparticles as an innovative therapeutic cue in bone tissue engineering: prospects and future clinical applications. *Mater Today Bio*. 2024;26:101016.
doi: 10.1016/j.mtbio.2024.101016

9. Kelly CN, Miller AT, Hollister SJ, Guldberg RE, Gall K. Design and structure–function characterization of 3-D printed synthetic porous biomaterials for tissue engineering. *Adv Healthcare Mater*. 2018;7(1):1701095.
doi: 10.1002/adhm.201701095

10. Baniasadi H, Abidnejad R, Fazeli M, et al. Innovations in hydrogel-based manufacturing: a comprehensive review of direct ink writing technique for biomedical applications. *Adv Colloid Interface Sci*. 2024;324:103095.
doi: 10.1016/j.cis.2024.103095

11. Murab S, Gupta A, Włodarczyk-Biegun MK, et al. Alginate-based hydrogel inks for 3-D bioprinting of engineered orthopedic tissues. *Carbohydr Polym*. 2022;296:119964.
doi: 10.1016/j.carbpol.2022.119964

12. Li L, Lin Q, Tang M, Duncan AJ, Ke C. Advanced polymer designs for direct-ink-write 3-D printing. *Chem – Eur J*. 2019;25(47):10768-10781.
doi: 10.1002/chem.201900975

13. Kumar A, Matari IAI, Han SS. 3-D printable carboxylated cellulose nanocrystal-reinforced hydrogel inks for tissue engineering. *Biofabrication*. 2020;12(2):025029.
doi: 10.1088/1758-5090/ab736e

14. Haring AP, Thompson EG, Tong Y, et al. Process- and bio-inspired hydrogels for 3-D bioprinting of soft free-standing neural and glial tissues. *Biofabrication*. 2019;11(2):025009.
doi: 10.1088/1758-5090/ab02c9

15. Fu Q, Saiz E, Tomsia AP. Direct ink writing of highly porous and strong glass scaffolds for load-bearing bone defects repair and regeneration. *Acta Biomater*. 2011;7(10):3547-3554.
doi: 10.1016/j.actbio.2011.06.030

16. Jiang P, Yan C, Guo Y, *et al*. Direct ink writing with high-strength and swelling-resistant biocompatible physically crosslinked hydrogels. *Biomater Sci*. 2019;7(5):1805-1814.
doi: 10.1039/C9BM00081J

17. Ingwersen L-C, Ahlhelm M, Schwarzer-Fischer E, et al. Characterization of the osteogenic differentiation capacity of human bone cells on hybrid β-TCP/ZrO_2 structures. *Mater Design*. 2024;238:112687.
doi: 10.1016/j.matdes.2024.112687

18. Agrawal V, Sinha M. A review on carrier systems for bone morphogenetic protein-2. *J Biomed Mater Res B Appl Biomater*. 2017;105(4):904-925.
doi: 10.1002/jbm.b.33599

19. Lima DB, de Souza MAA, de Lima GG, et al. Injectable bone substitute based on chitosan with polyethylene glycol polymeric solution and biphasic calcium phosphate microspheres. *Carbohydr Polym*. 2020;245:116575.
doi: 10.1016/j.carbpol.2020.116575

20. Shakir M, Jolly R, Khan AA, et al. Resole-based chitosan/nano-hydroxyapatite nanoensemble for effective bone tissue engineering. *Carbohydr Polym*. 2018;179:317-327.
doi: 10.1016/j.carbpol.2017.09.103

21. Yang Y, Yang S, Wang Y, et al. Anti-infective efficacy, cytocompatibility and biocompatibility of a 3-D-printed osteoconductive composite scaffold functionalized with quaternized chitosan. *Acta Biomater*. 2016;46:112-128.
doi: 10.1016/j.actbio.2016.09.035

22. Anjaneyulu U, Priyadarshini B, Nirmala Grace A, Vijayalakshmi U. Fabrication and characterization of Ag doped hydroxyapatite–polyvinyl alcohol composite nanofibers and its in vitro biological evaluations for bone tissue engineering applications. *J Sol-Gel Sci Technol*. 2017;81(3):750-761.
doi: 10.1007/s10971-016-4243-5

23. Nie L, Chen D, Suo J, et al. Physicochemical characterization and biocompatibility in vitro of biphasic calcium phosphate/polyvinyl alcohol scaffolds prepared by freeze-drying method for bone tissue engineering applications. *Colloids Surf B Biointerfaces*. 2012;100:169-176.
doi: 10.1016/j.colsurfb.2012.04.046

24. Bendtsen ST, Quinnell SP, Wei M. Development of a novel alginate-polyvinyl alcohol-hydroxyapatite hydrogel for 3-D bioprinting bone tissue engineered scaffolds. *J Biomed Mater Res A*. 2017;105(6):1457-1468.
doi: 10.1002/jbm.a.36036

25. Ba Linh NT, Lee KH, Lee BT. Functional nanofiber mat of polyvinyl alcohol/gelatin containing nanoparticles of biphasic calcium phosphate for bone regeneration in rat calvaria defects. *J Biomed Mater Res A*. 2013;101(9):2412-2423.
doi: 10.1002/jbm.a.34533

26. Poursamar SA, Azami M, Mozafari M. Controllable synthesis and characterization of porous polyvinyl alcohol/hydroxyapatite nanocomposite scaffolds via an in situ colloidal technique. *Colloids Surf B Biointerfaces*. 2011;84(2):310-316.
doi: 10.1016/j.colsurfb.2011.01.015

27. Nie L, Deng Y, Li P, Hou R, Shavandi A, Yang S. Hydroxyethyl chitosan-reinforced polyvinyl alcohol/biphasic calcium phosphate hydrogels for bone regeneration. *ACS Omega*. 2020;5(18):10948-10957.
doi: 10.1021/acsomega.0c00727

28. Wei Q, Wang Y, Li X, Yang M, Chai W, Wang K. Study the bonding mechanism of binders on hydroxyapatite surface and mechanical properties for 3-DP fabrication bone scaffolds. *J Mech Behav Biomed Mater*. 2016;57:190-200.
doi: 10.1016/j.jmbbm.2015.12.007

29. Li Z, Lu H, Deng Y, Rao S, Huang X, Zhang Q. Advances in molecular dynamics simulation on heterogeneous nucleation of gas hydrate. *Funct Mater Lett*. 2021;14(1):2130010.
doi: 10.1142/S1793604721300103

30. Zhang L. Understanding the radiation resistance mechanisms of nanocrystalline metals from atomistic simulation. *Metals*. 2021;11(12):1875.
doi: 10.3390/met11111875

31. Róg T, Girych M, Bunker A. Mechanistic understanding from molecular dynamics in pharmaceutical research 2: lipid membrane in drug design. *Pharmaceuticals*. 2021;14(10):1062.
doi: 10.3390/ph14101062

32. Wei Q, Zhang Y, Wang Y, et al. Study of the effects of water content and temperature on polyacrylamide/polyvinyl alcohol interpenetrating network hydrogel performance by a molecular dynamics method. *e-Polymers*. 2015;15(1):301-309.
doi: 10.1515/epoly-2015-0087

ACCSCIENCE PUBLISHING

International Journal of Bioprinting

RESEARCH ARTICLE

Inkjet bioprinting of NE-4C neural progenitor cells with enhanced neuronal differentiation via retinoic acid treatment

Xinda Li[1,2†], Xiaolei Guo[3,4†], Jinzhou Feng[1], Lihua Chen[1], Huan Xiong[1], Ruxiang Xu[1*], and Tao Xu[1,2,5*]

[1]Department of Neurosurgery, Sichuan Provincial People's Hospital, University of Electronic Science and Technology of China, Chengdu, Sichuan, China

[2]Department of Mechanical Engineering, School of Mechanical Engineering, Tsinghua University, Beijing, China

[3]Center for Medical Device Evaluation, National Medical Products Administration, Beijing, China

[4]State Key Laboratory of Tribology, Department of Mechanical Engineering, School of Mechanical Engineering, Tsinghua University, Beijing, China

[5]Center for Bio-intelligent Manufacturing and Living Matter Bioprinting, Research Institute of Tsinghua University in Shenzhen, Tsinghua University, Shenzhen, Guangdong, China

Abstract

During inkjet bioprinting, cells are subjected to direct shear stress as they pass through the nozzles, causing reversible deformation of the cell membranes and potentially triggering subcellular changes, such as activation of molecular pathways, leading to beneficial outcomes. In this study, neural progenitor NE-4C cells were printed through 30μm thermal inkjet nozzles. Compared to manually pipetted cells (control group), bioprinted cells (inkjet group) exhibited several distinct changes, such as reduced cell proliferation during the first four days after bioprinting, increased tolerance to high-concentration retinoic acid, and significantly elevated expression of the early neuronal marker class III β-tubulin, indicating enhanced neuronal differentiation. Furthermore, RNA sequencing and enrichment analysis further revealed upregulation of cell metabolism pathways in the bioprinted group. Collectively, these findings suggest that inkjet bioprinting may be a promising strategy to accelerate neural tissue formation, warranting further studies.

Keywords: Inkjet bioprinting; Neural differentiation; Neural progenitor cells

†These authors contributed equally to this work.

***Corresponding authors:**
Tao Xu
(xut@tsinghua-sz.org)

Ruxiang Xu
(xuruxiang1123@uestc.edu.cn)

Citation: Li X, Guo X, Feng J, *et al*. Inkjet bioprinting of NE-4C neural progenitor cells with enhanced neuronal differentiation via retinoic acid treatment. *Int J Bioprint.* 2025;11(5):217-230. doi: 10.36922/IJB025260245

Received: June 24, 2025
Revised: July 22, 2025
Accepted: July 25, 2025
Published Online: July 25, 2025

Copyright: © 2025 Author(s). This is an Open Access article distributed under the terms of the Creative Commons Attribution License, permitting distribution, and reproduction in any medium, provided the original work is properly cited.

Publisher's Note: AccScience Publishing remains neutral with regard to jurisdictional claims in published maps and institutional affiliations.

1. Introduction

Inkjet bioprinting possesses exceptional capability to deliver biological components and form high-resolution patterns in a sterile, economical, and high-throughput manner.[1,2] To date, inkjet bioprinting has evolved as a powerful tool for tissue engineering and regenerative medicine, enabling the fabrication of biomaterial scaffolds,[3-5] biomolecule gradients[6-8] and cell patterns.[9-15] Consequently, inkjet bioprinting has been regarded as one of the mainstream bioprinting strategies.[16,17] Moreover, it is feasible to print living cells with minimal damage using this approach.[18-20] Generally, inkjet bioprinting

operates via a drop-on-demand (DOD) mechanism, generating droplets containing only one or a few cells.[21-22] Due to this inherent feature, inkjet bioprinting confers practical value in cell isolation, single-cell analysis, and cell cryopreservation.[23-26]

During inkjet bioprinting, cells pass through narrow, cell-sized orifices and are therefore subjected to velocity-induced shear stress, which can cause temporary disruption of the cell membrane. Leveraging this phenomenon, Xu *et al.*[27] successfully transfected pmax green fluorescent protein plasmids into living porcine aortic endothelial cells by bioprinting a cell plasmid suspension with a thermal inkjet printer.[27] Cui *et al.*[28] further demonstrated the existence of ≈105Å transient pores on cell membranes during thermal inkjet bioprinting.[28] Sohrabi *et al.*[29] performed numerical simulation and found that the areal strain could generate multiple pores on the cell membrane during inkjet bioprinting without compromising overall cell viability.[29] This conclusion is consistent with experimental results, supporting the notion that membrane disruption caused by inkjet bioprinting may be beneficial.

Inkjet printing could facilitate neural tissue formation by depositing macromolecule patterns or fabricating electrode arrays to regulate stem cell fate.[7,30,31] Moreover, neural cells could be directly deposited to form neural tissue with inkjet bioprinting.[32,33] For instance, Tse *et al.*[32] printed neuronal analog NG108-15 cells with a piezoelectric inkjet system and found that the inkjet-printed neuronal cells expressed longer neurites at earlier stages compared to manually pipetted cells. This phenomenon may result from the piezoelectric effect, shear stress, or a combination of both applied directly to the cells.[32] These results indicate that the close contact between cells and nozzles could directly affect cellular behavior. Solis *et al.*[34] printed human microvascular endothelial cells with a thermal inkjet system. Compared with manually pipetted cells, printed endothelial cells showed elongated morphology and significant overexpression of several angiogenesis cytokines.[34] However, how inkjet bioprinting influences cellular behavior remains unclear, and further experimental evidence is needed.[35] Therefore, exploring neural cell behavior during inkjet bioprinting remains of great significance.

NE-4C is a p53-deficient immortalized neuroectodermal progenitor cell line derived from cerebral vesicles of E9-12 mouse embryos. It has been reported that NE-4C cells maintain stable karyotypes and exhibit neural differentiation both *in vitro* and *in vivo*.[36,37] The neural differentiation of NE-4C could also be triggered by all-trans retinoic acid (RA) at appropriate concentrations.[37,38] In this study, NE-4C cells were printed using a thermal inkjet printer (Figure 1). Since RA

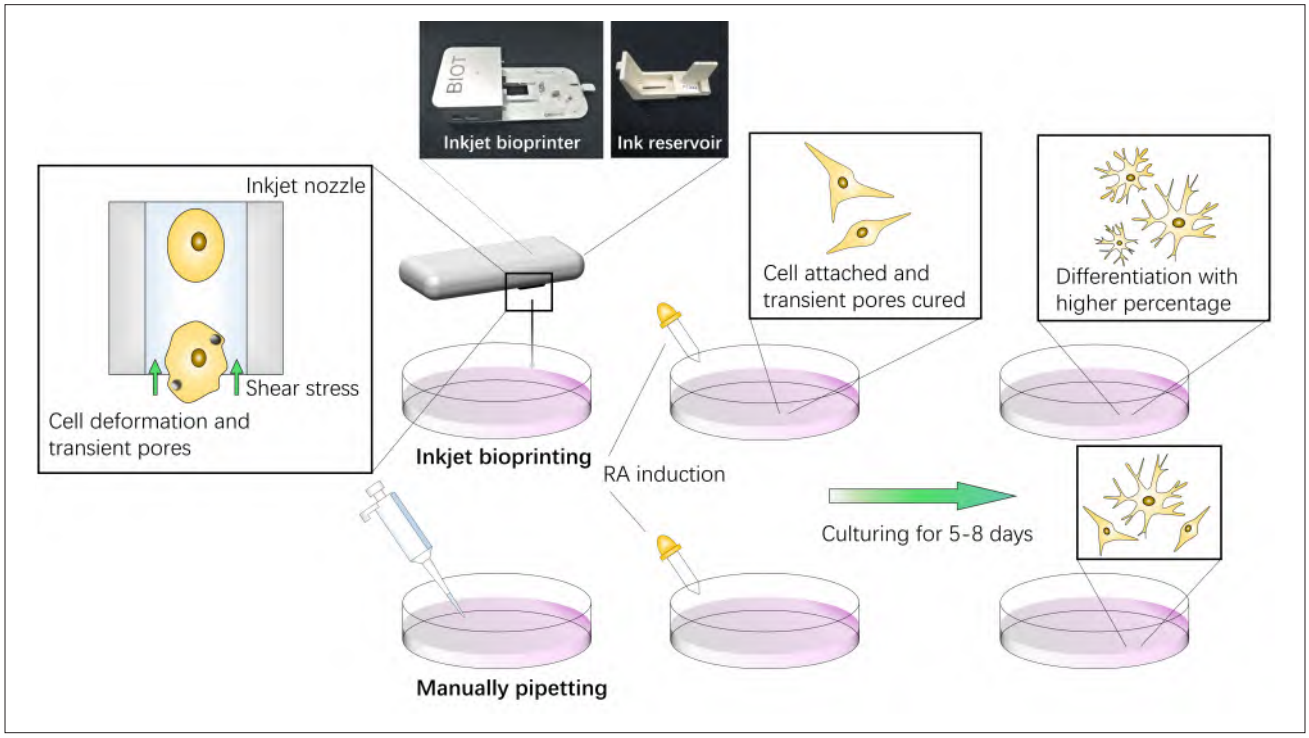


Figure 1. Schematic view of the experimental design. Abbreviation: RA: Retinoic acid.

receptors (RARs) and retinoid X receptors (RXRs) are located in the nucleus,[39,40] we hypothesized that thermal inkjet printing could facilitate RA transfer by creating transient pores on cell membranes. We first demonstrated the formation of transient pores on NE-4C cell membranes via calcein-acetoxymethyl (AM)/propidium iodide (PI) staining. RA treatment was applied immediately after inkjet printing for 48 hours. Nestin and class III β-tubulin (TuJ1) immunostaining were performed on days 5 and 8 post-RA treatment to detect the differentiation profiles of inkjet-bioprinted versus manually pipetted NE-4C cells. Furthermore, the cell counting kit-8 (CCK-8) assay showed that inkjet-printed NE-4C cells exhibited higher viability at high RA concentrations (10^{-5} to 10^{-4}M). Finally, RNA sequencing (RNA-seq) was performed at day 3 post-printing to evaluate differences in gene expression between inkjet-printed and manually pipetted NE-4C cells.

2. Materials and methods

2.1. Cell culture

NE-4C cell line (ATCC, CRL-2925™) was provided by the Stem Cell Bank, Chinese Academy of Sciences. The cells were cultured in minimum essential medium (MEM; 11090081, Gibco, United States) supplemented with 10% fetal bovine serum (10099141, Gibco, United States), 1% GlutaMAX™ (35050, Gibco, United States), and 1% non-essential acids (11140, Gibco, United States) at 37° in 5% carbon dioxide.

2.2. Inkjet bioprinting

The equipment used in this experiment was a self-developed thermal inkjet cell printer (BioT Athena) kindly provided by Shanghai Industrial μTechnology Research Institute (Figure 1). Before printing, NE-4C cells were digested and resuspended in 3% sodium chloride solution, serving as the bioink. Then, 100μL of bioink was loaded into the ink reservoir of the printhead. The printing voltage was maintained at a constant 10.8 V. During printing, each of the 325 printing nozzles was set to fire between 1,000 to 5,000 times. A 6-cm culture dish containing 1 to 2 mL MEM was placed below the printhead to collect the ejected droplets as biopaper.

2.3. Membrane integrity evaluation

Calcein-AM/PI staining was performed to evaluate the membrane integrity after inkjet bioprinting. As previously reported, PI could penetrate living-cell membranes exhibiting transient pores larger than approximately 16 Å.[28] Briefly, cells were cultured in MEM for at least an hour to ensure full attachment to the Petri dishes. The culture medium was then removed, and 1–2 mL of staining solution containing 2 μM calcein-AM and 8 μM PI was added. After incubation for 10 minutes, the Petri dishes were washed with phosphate buffer saline. Cells stained red or green were counted under a fluorescence microscope (Nikon Eclipse Ti2-u, Japan).

2.4. Cell proliferation evaluation

Alamar Blue assay was performed to depict NE-4C proliferation profile after inkjet bioprinting. Briefly, NE-4C cells were bioprinted into a 6-well plate with 1×10^4 cells in each well. Meanwhile, an equal density of cells was manually pipetted into the wells as the control group. On days 1, 4, 7, and 10 after bioprinting, 3 mL of Alamar Blue (Yeasen Biotechnology, China) working solution (1 Alamar Blue: 9 MEM) was added to each well and incubated for three hours. Optical density (OD) values were obtained on the microplate reader at wavelengths of 570 and 600 nm. For data presentation, all OD values were normalized to those on day 1.

2.5. NE-4C differentiation and cell counting kit-8 assay

As previously reported, NE-4C is an RA-inducible cell line that is insensitive to conventional neural differentiation factors such as basic fibroblast growth factor and epidermal growth factor.[37] Generally, a 48-hour RA treatment is sufficient to induce NE-4C differentiation into neurons or astrocytes.[36,37] Therefore, RA treatment was applied here to explore whether inkjet bioprinting affects NE-4C differentiation. All-trans RA (R2625, Sigma-Aldrich, United States) was dissolved in dimethyl sulfoxide at 10^{-1} mol/L as a stock solution and stored at−20° before use. Thermal-inkjet-printed NE-4C cells were set as the experimental group, and manually pipetted cells served as the control group.

For the CCK-8 cytotoxic assay, cells from each group were seeded in a 96-well plate at a density of 2×10^3 cells in each well. During induction, NE-4C cells were incubated in supplemented MEM with RA at concentrations of 0, 10^{-6}, 10^{-5}, and 10^{-4} mol/L for 48 hours. No extra growth factors were added throughout the process. After induction, the culture medium was carefully removed, and the CCK-8 assay was performed following the manufacturer's instructions. Briefly, 100 μL of CCK-8 (CK04, Dojindo Laboratories, Japan) working solution was added to each well and incubated for two hours. OD values were obtained on a microplate reader at a wavelength of 450 nm.

2.6. Immunofluorescence staining

According to the literature, NE-4C cells exhibit neuronal characteristics 3–4 days after RA induction.[36,37] Immunostaining with neural stem cell marker Nestin and early neuron marker TuJ1 was performed on days 5 and 8 post-RA treatment. Briefly, NE-4C cells in the experimental

and control groups were seeded in a 24-well plate and underwent RA treatment for 48 hours as described in **Section 2.4**. Subsequently, the cells were maintained in supplemented MEM without additional treatment. At each time point for immunostaining, the culture medium was removed, and 3 mL of 2.5% glutaraldehyde was added to each well for 30 minutes. Following fixation, blocking solution (Keygen Biotech, China) was added for another 30 minutes. Anti-Nestin (ab11306, Abcam, United Kingdom) and anti-βIII tubulin (ab18207, Abcam, United Kingdom) primary antibodies were diluted in the manufacturer-supplied diluent to the recommended concentrations. Then, 500 µL of the primary antibody solutions were added to each well and incubated overnight at 4˚C. On the following day, samples were incubated in secondary antibody solution (diluted in secondary antibody diluent) for an hour. Finally, 4',6-diamidino-2-phenylindole solution was added for 10 minutes, and fluorescent images were taken under a fluorescence microscope. Moreover, anti-Notch1 (ab52627, Abcam, United Kingdom) immunostaining was performed on NE-4C cells without RA treatment at day 4 after inkjet bioprinting, following the same procedure described above.

2.7. RNA sequencing

As previously reported, thermal inkjet bioprinting can influence cellular gene expression through heat shock or other relevant mechanical factors.[34] Therefore, RNA sequencing was performed to compare the transcriptomic profiles of the inkjet-printed cells and the control group. Briefly, at day 3 after bioprinting, NE-4C cells from the inkjet group and the control group were harvested and stored at 80°. The samples were then sent for sequencing and analysis. The RNA sequencing and sequencing data analysis were performed by Novogene Co., Ltd. (China).

2.8. Statistical analysis

Two-way analysis of variance was used to compare means across multiple groups with three replicates for each. Paired Student's *t*-test was used to compare means across single groups with five replicates. Statistical significance was determined at $^{*}p < 0.05$, $^{**}p < 0.01$, and $^{***}p < 0.001$. Data analysis was performed using GraphPad Prism 5 software.

3. Results

3.1. Number of cell-containing droplets

In the pre-experiment, bioinks with cell concentrations of 2 ×1 0^6/mL, 5 × 10^6/mL, and 1 ×10^7/mL were printed on empty culture dishes. The number of cell-containing droplets was recorded under a microscope. The number of cell-containing droplets for these three different concentrations is listed in Table 1. The results are consistent with a previous study, reporting that the cell-containing droplet percentage increased with cell concentration.[21] However, among the cell-containing droplets, the proportion of droplets containing a single cell may decrease as cell concentration continues to increase, due to a higher frequency of droplets containing more than one cell. Therefore, the bioink with a cell concentration of 5 × 10^6/mL was selected for further experiments for a higher frequency of single-cell-containing droplets.

3.2. Permeability variation of NE-4C membranes during inkjet printing

As previously reported, transient pores may form during thermal inkjet bioprinting due to the combined effects of thermal heat and mechanical stress. PI could penetrate cells through the transient pores (>16Å) on cell membranes.[28] In this experiment, calcein-AM/PI staining was performed at one hour and one day after bioprinting. Manually pipetted NE-4C cells served as the control group. NE-4C cells with green or red fluorescence were counted under a fluorescence microscope. An hour after printing, a portion of the cells in view were stained green while others were stained red (Figure 2). A total of 61 cells were observed, of which 35 were stained green while 25 cells were stained red, indicating that around 42.62% of the cells exhibited transient pores one hour after bioprinting. One day after bioprinting, all attached cells in view were stained green, as dead cells had detached (Figure 2B). In contrast, all manually pipetted cells were stained green at one hour after bioprinting (Figure 2C).

Table 1. Number of cell-containing droplets under different cell concentrations

Cell concentration (/mL)	Total number of droplets (N)	Number of cell-containing droplets (N_1)	Number of single-cell-containing droplets (N_2)	Percentage of cell-containing droplets (N_1/N)	Percentage of single-cell-containing droplets (N_2/N_1)
2×10^6	162	12	11	7.41%	91.67%
5×10^6	135	35	27	25.93%	77.14%
1×10^7	136	40	26	29.41%	65%

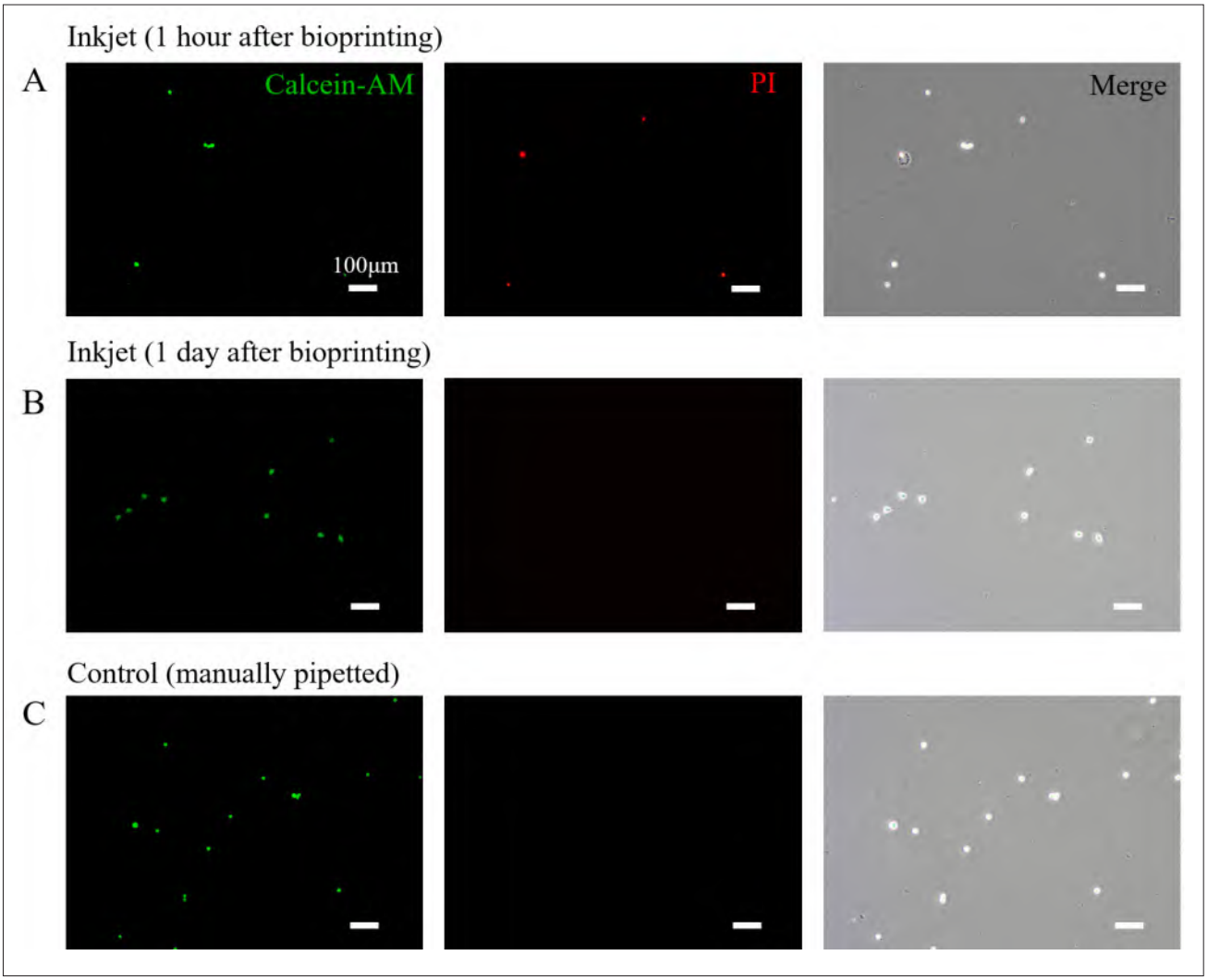


Figure 2. Calcein-acetoxymethyl (AM)/propidium iodide (PI) staining of NE-4C cells after inkjet printing. (A) Fluorescent images of NE-4C cells one hour after bioprinting, and (B) one day after printing. (C) Manually pipetted NE-4C cells. Scale bar: 100 μm, magnification: 100×.

3.3. NE-4C proliferation profile after inkjet printing

Inkjet-bioprinted and manually pipetted NE-4C cells were cultured at the same initial density for microscopic evaluation. A difference in the proliferation rate emerged at day 4 after bioprinting, with NE-4C cells in the control group showing a larger increment. By day 7, prominent cell propagation was observed in the inkjet group, while cells in the control group had nearly reached confluence. NE-4C cells in the inkjet group reached confluence at day 10, and clusters formed on the surface of the cell layer in the control group (Figure 3A & B). Results of the Alamar Blue assay are shown in Figure 3C and D. As depicted, the general tendency is similar to that observed under a microscope. Cells in the inkjet group showed minimal proliferation during the initial four days, followed by persistent multiplication until day 10. On the contrary, cells in the control group proliferated rapidly during the initial four days and gradually reached confluence, which dampened their multiplication from day 4 to day 10 (Figure 3C & D).

3.4. Differentiated induction of inkjet-printed NE-4C with retinoic acid

3.4.1. Cytotoxicity measurement post-retinoic acid treatment

All-trans RA with three different concentrations was used to treat inkjet-bioprinted or manually pipetted NE-4C cells for neural differentiation. CCK-8 assay was performed to measure the cytotoxicity after 48 hours of RA treatment. Briefly, at RA concentration of 10^{-6}M, the inkjet group sustained a relative viability of 0.88±0.02 while the control

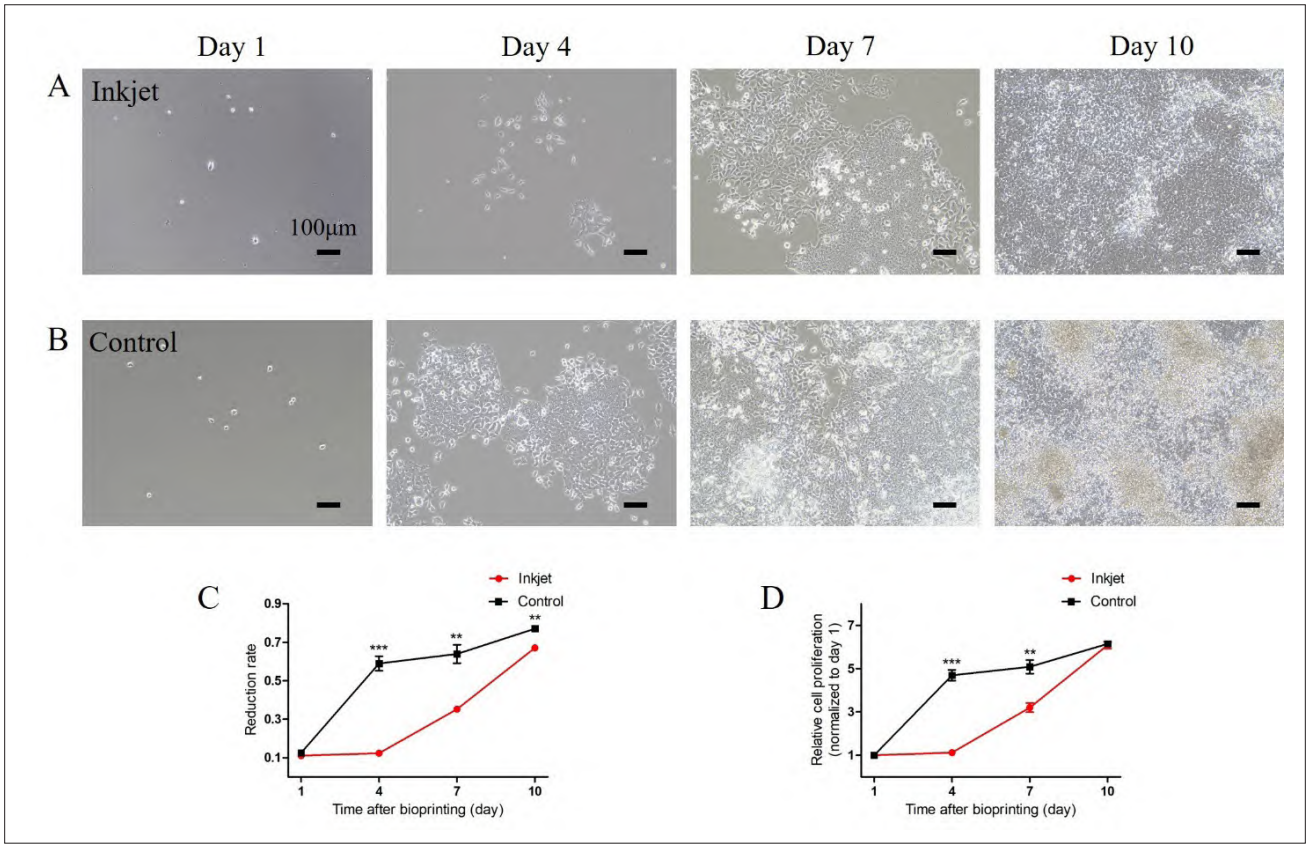


Figure 3. Microscopy images and proliferation profiles of inkjet-printed (inkjet) and manually pipetted (control) NE-4C cells from day 1 to day 10 post-printing. (A) Microscopy images of inkjet-printed NE-4C cells from day 1 to day 10. Scale bar: 100 μm, magnification: 100×. (B) Microscopy images of manually pipetted NE-4C cells. Scale bar: 100 μm, magnification: 100×. (C) The reduction rate of Alamar Blue stain on each corresponding day. (D) Relative proliferation rate by normalizing all values to day 1. Statistical significance determined at $^{**}p<0.01$, $^{***}p<0.001$.

group only achieved a relative viability of 0.46±0.12. At an RA concentration of 10^{-5}M, the relative viability of the inkjet group and the control group was 0.84±0.14 and 0.44±0.17, respectively. Furthermore, for both groups, complete cell death occurred at an RA concentration of 10^{-4}M (Figure 4). These results indicate that inkjet-bioprinted NE-4C cells presented higher viability at RA concentrations ranging from 10^{-6}M to 10^{-5}M.

3.4.2. NE-4C differentiation post-retinoic acid treatment

NE-4C cells are derived from cerebral vesicles. As reported, Notch1 is a key regulator for neural stem cell maintenance, and inhibition of Notch1 signaling could lead to eventual depletion of hippocampal neural stem cells.[41] Therefore, prior to RA treatment, Notch1 immunostaining was performed at day 4 post-bioprinting to evaluate the stemness of NE-4C following inkjet bioprinting. The results are shown in Figure 5. NE-4C cells in both groups were Notch1-positive, with similar fluorescence intensity, indicating that the differentiation capability of NE-4C cells was not affected by inkjet bioprinting.

After 48 hours of RA treatment at a concentration of 10^{-6}M, immunofluorescence staining of neural progenitor cell marker Nestin and neuron marker TuJ1 was performed on Day 5. The results are presented in Figure 6. In both groups, most NE-4C cells were Nestin-positive and showed morphological changes, including neurite sprouting, which distinguished them from undifferentiated NE-4C cells (Figure 6A & B). A portion of cells in both groups were TuJ1-positive, indicating the initiation of neural differentiation (Figure 6A & B). The average fluorescence intensities of Nestin and TuJ1 were measured with Image J (version ImageJ 1.53t). For Nestin, the average fluorescence intensities for the inkjet and control groups were 58.17±6.32 and 50.23±10.60, respectively (n=5). For TuJ1, the average fluorescence intensities for the inkjet and control groups were 86.09±13.98 and 75.93±7.15, respectively (n=5). No statistical significance was observed between these two groups for both markers (Figure 6C & D).

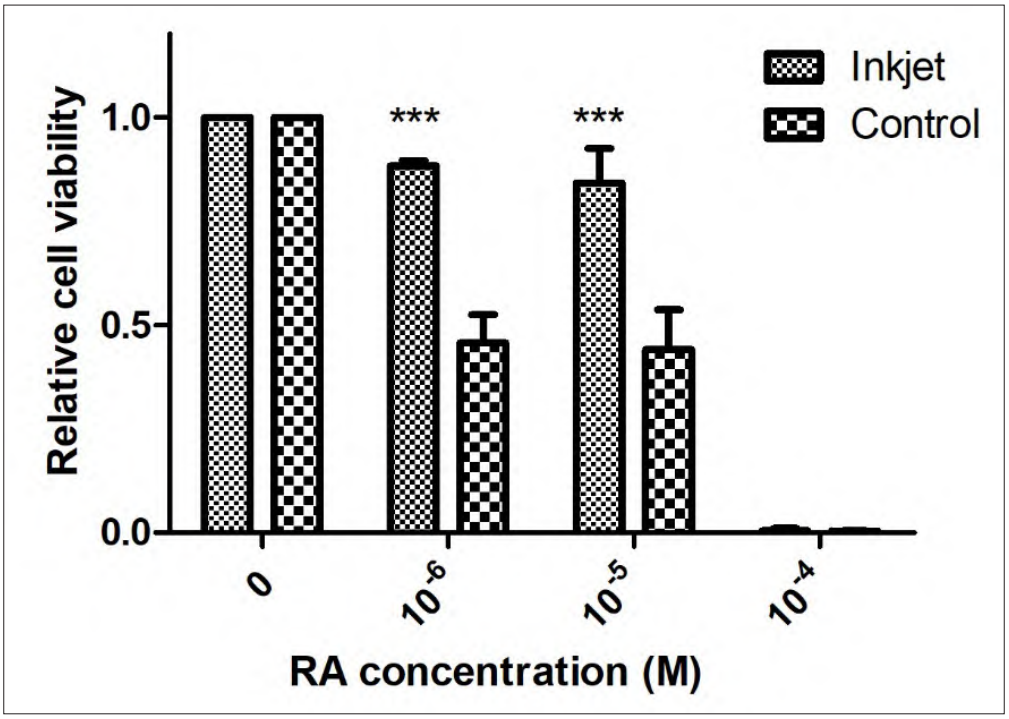


Figure 4. Retinoic acid (RA) susceptibility of inkjet-printed (inkjet) and manually pipetted (control) NE-4C cells. Statistical significance determined at ***p<0.001.

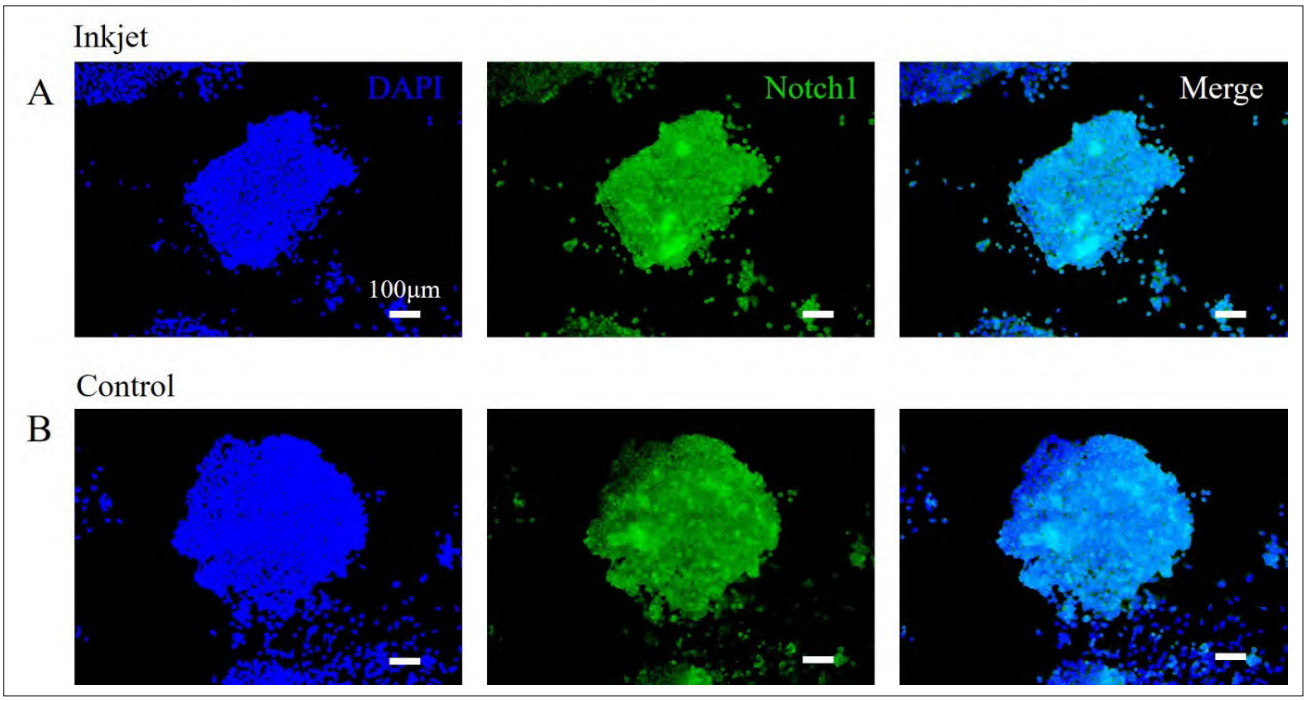


Figure 5. Notch1 immunofluorescence staining of inkjet-printed (inkjet) and manually pipetted (control) NE-4C cells at day four after printing. (A) Fluorescent images of Notch1 for the inkjet group. (B) Fluorescent images of Notch1 for the control group. Scale bar: 100 μm, magnification: 100×. Abbreviation: DAPI: 4',6-diamidino-2-phenylindole.

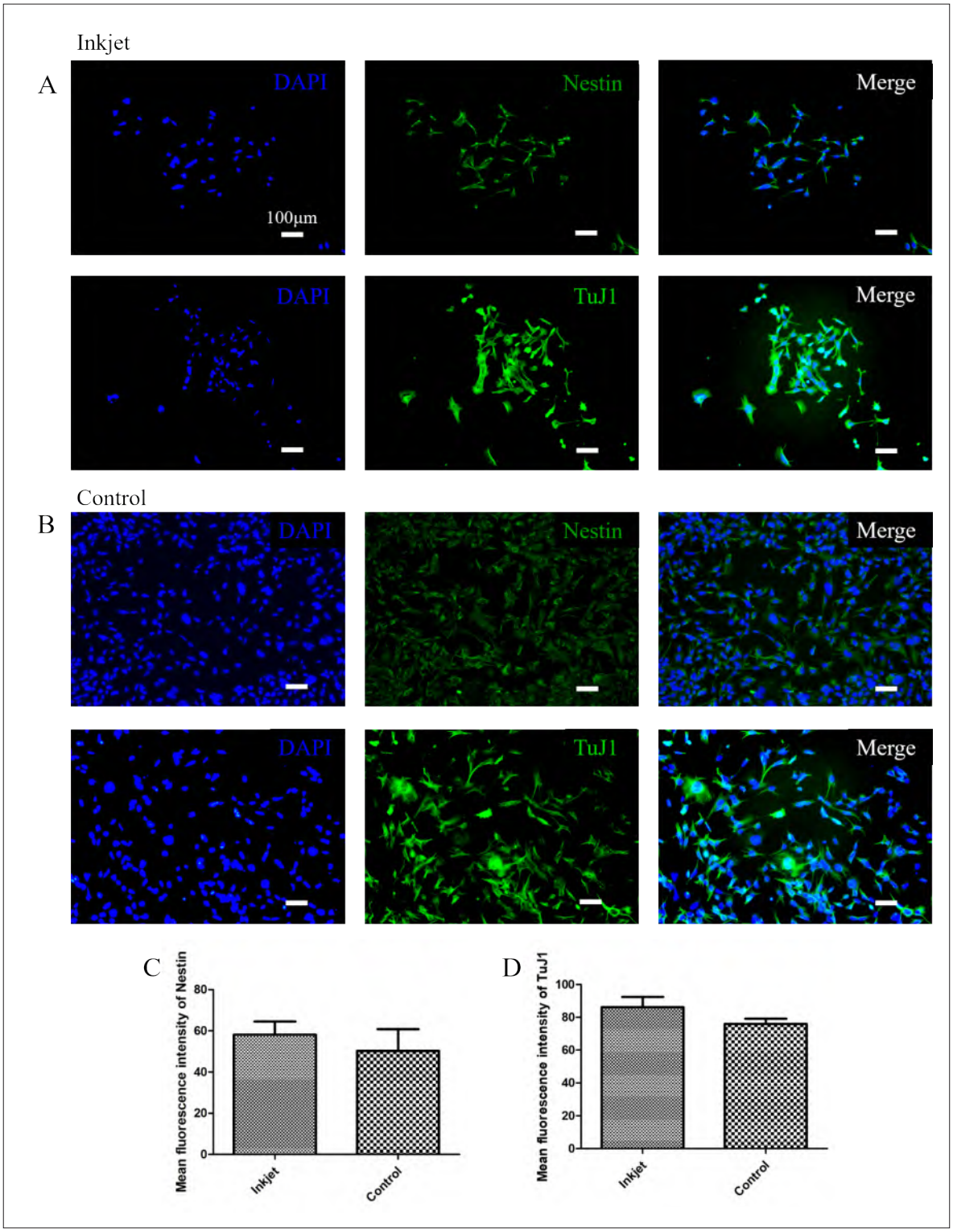


Figure 6. Nestin and TuJ1 immunofluorescence staining of inkjet-printed (inkjet) and manually pipetted (control) NE-4C cells at day five after retinoic acid treatment. (A) Fluorescent images of Nestin and TuJ1 for the inkjet group. Scale bar: 100 μm, magnification: 100×. (B) Fluorescent images of Nestin and TuJ1 for the control group. Scale bar: 100 μm, magnification: 100×. (C) Average fluorescence intensity of Nestin. (D) Average fluorescence intensity of TuJ1. Abbreviations: DAPI: 4',6-diamidino-2-phenylindole, TuJ1: Class III β-tubulin.

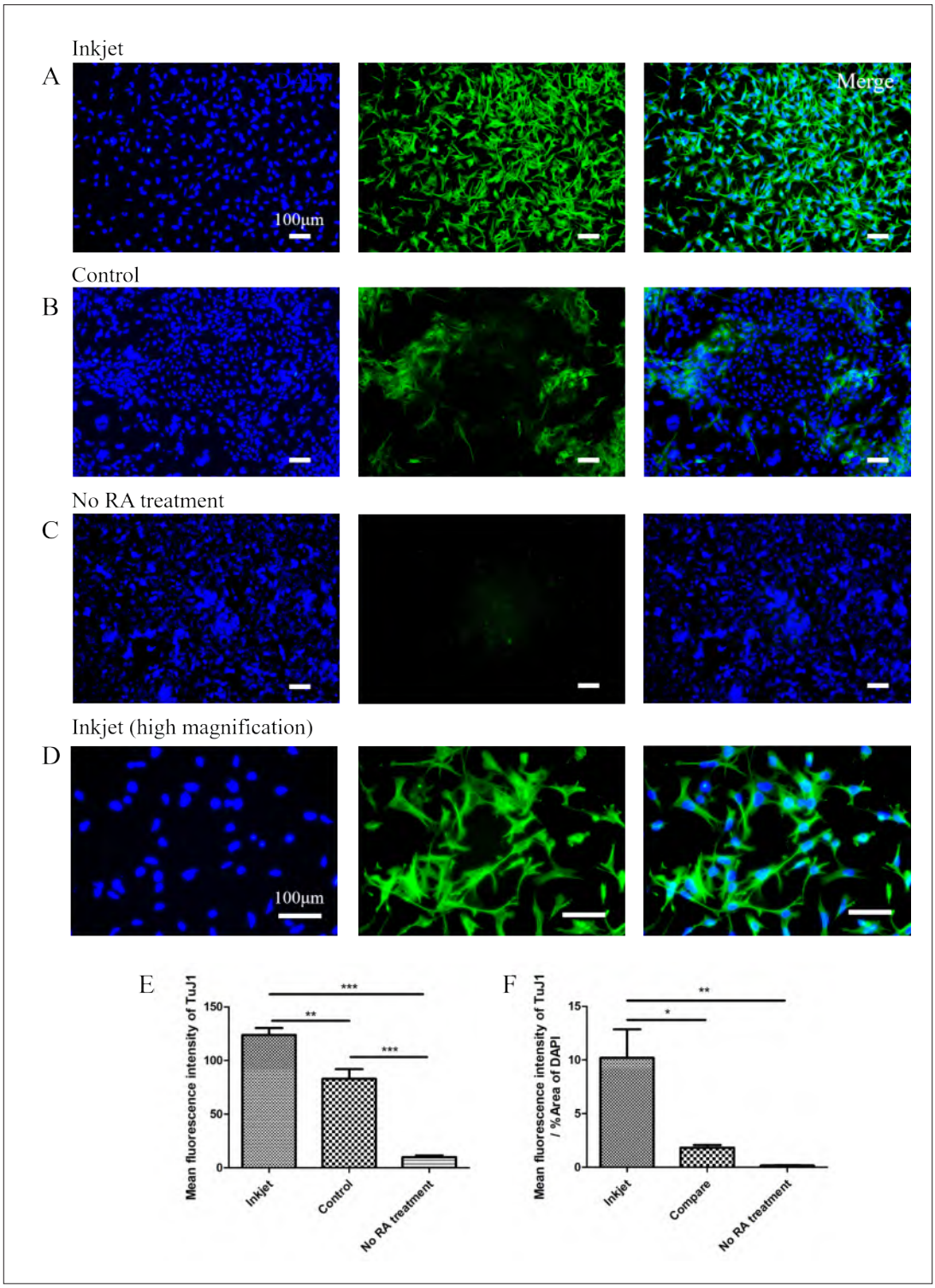


Figure 7. TuJ1 immunofluorescence staining of inkjet-printed (inkjet) and manually pipetted (control) NE-4C cells at day 8 after retinoic acid (RA) treatment. (A) Fluorescent images of TuJ1 for the inkjet and control groups. Scale bar: 100 μm, magnification: 100×. (B) Fluorescent images of TuJ1 for the control group. Scale bar: 100 μm, magnification: 100×. (C) Fluorescent images of TuJ1 for the no RA treatment group. Scale bar: 100 μm, magnification: 100×. (D) Fluorescent images of high magnification for the inkjet group. Scale bar: 100 μm, magnification: 200×. (E) Average fluorescence intensity of TuJ1. (F) The ratio of average fluorescence intensity and area of DAPI. Statistical significance determined at $^{*}p<0.05$, $^{**}p<0.01$, $^{***}p<0.001$. Abbreviation: DAPI: 4',6-diamidino-2-phenylindole, TuJ1: Class III β-tubulin.

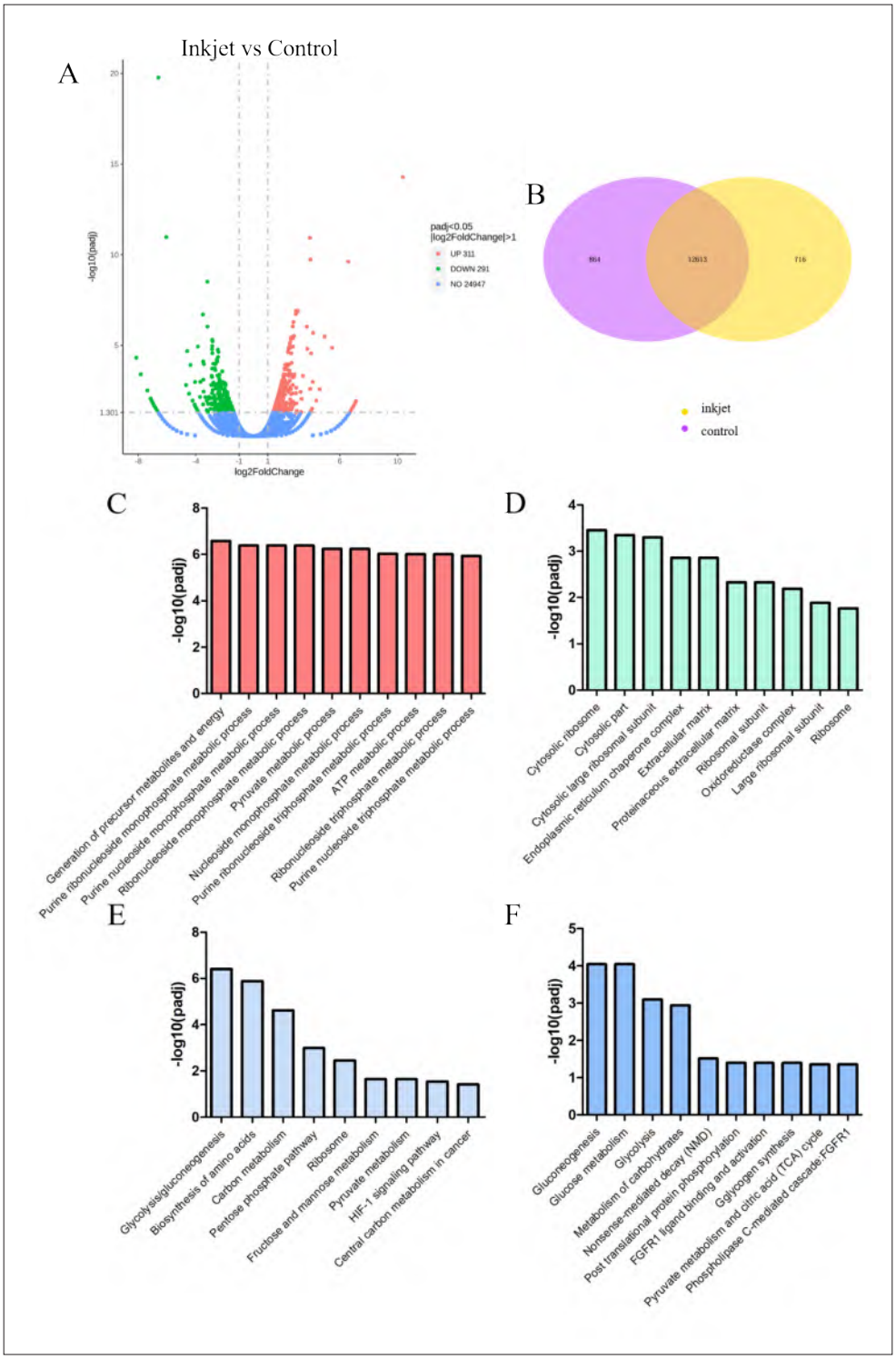


Figure 8. Results of RNA sequencing analysis of inkjet-printed (inkjet) and manually pipetted (control) on day 3 after printing. (A) The volcano plot of differential expression between the inkjet and control groups. (B) The Venn diagram. (C & D) Most significantly upregulated pathways for Gene Ontology enrichment analysis in terms of biological process and cellular component. (E) Most significantly upregulated pathways for Kyoto Encyclopedia of Genes and Genomes enrichment analysis. (F) Most significantly upregulated pathways for Reactome enrichment analysis. Abbreviation: padj: Adjusted *p*-value.

On day 8 after RA treatment, most of the cells in the inkjet group were TuJ1-positive, exhibiting further morphological changes compared to day 5 (Figure 7A & D). In contrast, a portion of cells in the control group were TuJ1-positive, with higher fluorescence intensity observed primarily in clustered cells (Figure 7B). Moreover, cells without RA treatment displayed minimal fluorescence intensity (Figure 7C). The average TuJ1 fluorescence intensities for the inkjet group, the control group, and the no RA treatment group were 123.82±14.52, 83.06±19.94, and 9.97±3.10, respectively (Figure 7E). Furthermore, the ratio of fluorescence intensity to the area of 4',6-diamidino-2-phenylindole staining was calculated to estimate differentiation efficiency. The values were 10.20±5.95 for the inkjet group, 1.84±0.51 for the control group, and 0.16±0.04 for the no RA treatment group (Figure 7F). Both measurements showed statistically significant differences between groups.

3.5. Difference in gene expression of NE-4C post-inkjet printing

After three days of culture, the inkjet-printed and manually pipetted (control) NE-4C cells were subjected to RNA-seq to assess differences in gene expression. As presented in Figure 8A, compared to the manually pipetted NE-4C cells, 311 genes were significantly upregulated and 291 genes downregulated in the inkjet group, indicating that inkjet bioprinting modulates gene expression in NE-4C cells. The Venn diagram further revealed 716 unique differential genes in the inkjet group, while 12,613 differential genes were common in both groups (Figure 8B). Gene Oncology (GO), Kyoto Encyclopedia of Genes and Genomes (KEGG), and Reactome enrichment analyses were performed to identify upregulated gene sets in inkjet-bioprinted NE-4C cells. In the GO biological process category, pathways related to cell metabolism were found to be significantly upregulated after inkjet bioprinting, including the generation of precursor metabolites and energy, pyruvate metabolic process, and adenosine triphosphate metabolic process (Figure 8C). In the GO cellular component category, ribosome-related pathways were significantly upregulated, including cytosolic ribosome, large ribosome subunit, and ribosome (Figure 8D). KEGG and Reactome analyses identified gluconeogenesis, biosynthesis of amino acids, and carbon metabolism-related pathways as being most significantly upregulated (Figure 8D & E). In summary, inkjet-bioprinted NE-4C cells exhibited an enhanced metabolic profile during the initial culture.

4. Discussion

In this study, NE-4C cells were directly printed into a culture dish containing culture medium using a thermal inkjet printhead. This method has previously been demonstrated to be feasible for creating cell patterns with high viability.[42] During inkjet bioprinting, the average number of cells in each ejected droplet depends on the nozzle diameter and cell concentration.[21,22] Here, a uniform NE-4C suspension with optimized cell concentration was used to increase the percentage of single-cell-containing droplets. This procedure ensured that most cells passed through the nozzle orifice under similar shear stress. Calcein-AM/PI staining was performed one hour post-bioprinting, at which point complete cell attachment had taken place. Under these conditions, 42.62% NE-4C were PI-positive, indicating the formation of transient pores on cell membranes that persisted for at least one hour. Considering that some pores likely resealed within this period, the actual percentage of cells with transient pores immediately after bioprinting may be higher than 42.62%.[43] Meanwhile, nearly all NE-4C were PI-negative and calcein-AM-positive one day after bioprinting, indicating that these transient pores were fully repaired. Given that the molecular weight of RA (300.44) is lower than that of PI (668.39), it is rational to hypothesize that RA would easily enter NE-4C through these transient pores.

During the initial four days after inkjet printing, a slower proliferation rate was found in inkjet-bioprinted NE-4C cells compared to manually pipetted cells, despite equal initial cell seeding densities. In a previous research, NG108-15 neuronal cells bioprinted using a 60 μm piezoelectric inkjet nozzle failed to exhibit significant proliferation slowdown during the initial incubation period.[32] In this study, a 30 μm nozzle was used, likely subjecting NE-4C cells to greater shear stress. A portion of NE-4C cells were found to be proliferating-inert while remaining attached to culture dishes and calcein-AM positive. Meanwhile, numerous cell clusters formed in the control group, whereas cells remained scattered in the inkjet group on day 4 post-bioprinting. Therefore, we infer that fewer proliferatively active NE-4C cells were present in the inkjet group, leading to a delayed proliferating peak.

Exposure to RA concentrations above 10^{-6}M has been reported to be cytotoxic to carcinoma cells, and the recommended RA concentration for neural differentiation of NE-4C cells is 10^{-9}–10^{-6}M.[37,38] In this study, we performed RA treatment immediately after inkjet printing and found that inkjet-bioprinted NE-4C cells exposed to 10^{-6} and 10^{-5}M RA exhibited 1.91 times higher viability than manually pipetted NE-4C cells (Figure 4). It has been reported that NE-4C cells, upon reaching confluency, localize to the top of the basal layer.[36] According to the proliferating profile, it is clear that inkjet-bioprinted NE-4C would reach confluency later than the control group. Therefore, we consider that cells emerging from the basal

layer were more sensitive to RA and prone to detachment at higher RA concentrations (10^{-5}M). Moreover, at RA concentrations of 10^{-4}M, the culture environment becomes excessively cytotoxic. Additionally, the inkjet group exhibited a higher percentage of TuJ1-positive cells at day 8 after a 48-hour RA treatment, indicating an enhanced tendency toward neuronal differentiation. Although RA treatment was performed immediately after inkjet printing, NE-4C cells undergo multiple mitotic cycles during the advanced stages of neural differentiation.[37] Neuronal fate decisions occur in randomly distributed, scattered cells governed by short-distance effects within local cell assemblies, which continue proliferating.[37] This phenomenon was observed in the control group, where randomly localized expressed TuJ1 at day 8 post-RA treatment. Since RA is needed to commit proliferating cells into neuronal progenitors, we believed the transient pores caused by inkjet bioprinting facilitated enhanced RA uptake during the initial treatment. Moreover, prolonged culture time (~4 weeks) is necessary for early neurons to mature and develop into neurons with various morphological patterns, during which antimitotic treatment should be applied.[37] Future studies are needed to provide stronger evidence evaluating the percentage of mature neurons produced by inkjet-bioprinted NE-4C cells.

NE-4C cells were collected on day 3 post-bioprinting for RNA-seq to evaluate gene expression differences between the inkjet and the control groups. GO, KEGG, and Reactome enrichment analyses revealed a higher level of cell metabolism in the inkjet group at this time point. In the biological process category, pathways related to nucleoside, pyruvate, and adenosine triphosphate metabolic processes were significantly upregulated. In the cellular component category, pathways related to ribosome biogenesis and components of the extracellular matrix were significantly upregulated. KEGG and Reactome analyses collectively suggested the upregulation of glucose and amino acid metabolic pathways. Taken together, these findings suggest that at day 3 post-bioprinting, a higher percentage of inkjet-printed NE-4C cells may be in the G1 or G2 phases of the cell cycle, during which the synthesis of amino acids and ribosomes is elevated to support cell growth and preparation for division. This deduction aligns with the observation that inkjet-printed NE-4C cells did not exhibit exponential proliferation during the initial 4-day culture period.

Shear stress during inkjet bioprinting is usually considered a detrimental effect. To mitigate cell damage, inkjet bioprinters often employ larger nozzle diameters (80–100 μm).[32,33] In this study, cell loss was observed due to the narrower nozzle used. However, previous research also found that shear stress is beneficial for gene transfection or specific cellular pathway activation.[27,34] We also found that NE-4C cells exhibited a stronger differentiation tendency under RA treatment following inkjet printing. This phenomenon might be partially attributed to transient pores induced in the cells during printing, facilitating RA molecule entry. However, additional pathway-related mechanisms likely contribute, warranting further investigation. Unlike hydrogel-encapsulated cell printing methods such as extrusion-based or laser-assisted printing, inkjet printing exerts direct influence on individual cells during droplet ejection. We believed that this nozzle-cell interaction represents a valuable avenue for further exploration.

5. Conclusion

In this study, NE-4C cells, a p53-deficient immortalized neuroectodermal progenitor cell line, were bioprinted for the first time using a 30 μm inkjet nozzle. Approximately 42.62% of cells exhibited transient pores an hour after printing. All transient pores were repaired within a day, and all attached cells remained viable. Following inkjet bioprinting, NE-4C cells demonstrated increased resistance to RA at concentrations ranging from 10^{-6} to 10^{-5}M. Furthermore, inkjet-bioprinted NE-4C cells showed a higher level of TuJ1 expression on day 8 after RA treatment, indicating a stronger differentiation tendency. Additionally, RNA-seq analysis suggested that pathways related to cell metabolism were upregulated in inkjet-bioprinted NE-4C cells. Collectively, these results indicate that inkjet bioprinting could modulate NE-4C cell behavior and may represent a promising strategy for subcellular manipulation of neural progenitor cells.

Acknowledgments

None.

Funding

This research is supported by the National Natural Science Foundation of China (Grant No.52075285), the Applied Basic Research Project of Sichuan Province (Grant No.2021YJ0563), and the Natural Science Foundation of Sichuan Province (Grant No. 2023NSFSC0851).

Conflict of interest

The authors declare they have no competing interests.

Author contributions

Conceptualization: Xinda Li, Ruxiang Xu, Tao Xu
Formal analysis: Xinda Li, Huan Xiong
Investigation: Xinda Li, Xiaolei Guo

Methodology: Xinda Li, Jinzhou Feng, Lihua Chen
Writing–original draft: Xinda Li, Xiaolei Guo
Writing–review & editing: Xinda Li, Ruxiang Xu, Tao Xu

Ethics approval and consent to participate

Not applicable.

Consent for publication

Not applicable.

Availability of data

Data will be made available upon request to the corresponding author.

References

1. Saunders RE, Derby B. Inkjet printing biomaterials for tissue engineering: bioprinting. *Int Mater Rev*. 2014;59(8):430-448. doi: 10.1179/1743280414Y.0000000040.
2. Gudapati H, Dey M, Ozbolat I. A comprehensive review on droplet-based bioprinting: Past, present and future. *Biomaterials*. 2016;102:20-42. doi: 10.1016/j.biomaterials.2016.06.012.
3. Yeong WY, Chua C.K, Leong KF *et al*. Indirect fabrication of collagen scaffold based on inkjet printing technique. *Rapid Prototyping J*. 2006;12(4):229-237. doi: 10.1108/13552540610682741.
4. Zhang C, Wen X, Vyavahare NR, Boland T. Synthesis and characterization of biodegradable elastomeric polyurethane scaffolds fabricated by the inkjet technique. *Biomaterials*. 2008;29(28):3781-3791. doi: 10.1016/j.biomaterials.2008.06.009.
5. Inzana JA, Olvera D, Fuller SM, *et al*. 3D printing of composite calcium phosphate and collagen scaffolds for bone regeneration. *Biomaterials*. 2014;35(13): 4026-4034. doi: 10.1016/j.biomaterials.2014.01.064.
6. Campbell PG, Miller ED, Fisher GW, Walker LM, Weiss LE. Engineered spatial patterns of FGF-2 immobilized on fibrin direct cell organization. *Biomaterials*. 2005;26(33): 6762-6770. doi: 10.1016/j.biomaterials.2005.04.032.
7. Ilkhanizadeh S, Teixeira AI, Hermanson O, *et al*. Inkjet printing of macromolecules on hydrogels to steer neural stem cell differentiation. *Biomaterials*. 2007;28(27):3936-3943. doi: 10.1016/j.biomaterials.2007.05.018.
8. Miller ED, Li K, Kanade T Weiss LE, Walker LM, Campbell PG. Spatially directed guidance of stem cell population migration by immobilized patterns of growth factors. *Biomaterials*. 2011;32(11):2775-2785. doi: 10.1016/j.biomaterials.2010.12.005.
9. Xu T, Petridou S, Lee EH, *et al*. Construction of high-density bacterial colony arrays and patterns by the ink-jet method. *Biotechnol Bioeng*. 2004;85(1):29-33. doi: 10.1002/bit.10768.
10. Merrin J, Leibler S, Chuang JS. Printing multistrain bacterial patterns with a piezoelectric inkjet printer. *PLoS One*. 2007;2(7):e663. doi: 10.1371/journal.pone.0000663.
11. Yamazoe H, Tanabe T. Cell micropatterning on an albumin-based substrate using an inkjet printing technique. *J Biomed Mater Res A*. 2009;91(4):1202-1209. doi: 10.1002/jbm.a.32312.
12. Arai K, Iwanaga S, Toda H, Genci C, Nishiyama Y, Nakamura M. Three-dimensional inkjet biofabrication based on designed images. *Biofabrication*. 2011;3(3):034113. doi: 10.1088/1758-5082/3/3/034113.
13. Xu C, Chai W, Huang Y, Markwald RR. Scaffold-free inkjet printing of three-dimensional zigzag cellular tubes. *Biotechnol Bioeng*. 2012;109(12):3152-3160. doi: 10.1002/bit.24591.
14. Xu T, Zhao W, Zhu JM, Albanna MZ, Yoo JJ, Atala, A. Complex heterogeneous tissue constructs containing multiple cell types prepared by inkjet printing technology. *Biomaterials*. 2013;34(1):130-139. doi: 10.1016/j.biomaterials.2012.09.035.
15. Christensen K, Xu C, Chai W, Zhang Z, Fu J, Huang, Y. Freeform inkjet printing of cellular structures with bifurcations. *Biotechnol Bioeng*. 2015;112(5):1047-1055. doi: 10.1002/bit.25501.
16. Li X, Liu B, Pei B, *et al*. Inkjet Bioprinting of Biomaterials. *Chem Rev*. 2020 14;120(19):10793-10833. doi: 10.1021/acs.chem rev.0c00008.
17. Murphy SV, Atala A. 3D bioprinting of tissues and organs. *Nat Biotechnol*. 2014;32(8):773-785. doi: 10.1038/nbt.2958.
18. Xu T, Jin J, Gregory C, Hickman JJ, Boland T. Inkjet printing of viable mammalian cells. *Biomaterials*. 2005;26(1): 93-99. doi: 10.1016/j.biomaterials.2004.04.011.
19. Saunders RE, Gough JE, Derby B. Delivery of human fibroblast cells by piezoelectric drop-on-demand inkjet printing. *Biomaterials*. 2008;29(2):193-203. doi: 10.1016/j.biomaterials.2007.09.032.
20. Nakamura M, Kobayashi A, Takagi F, *et al*. Biocompatible inkjet printing technique for designed seeding of individual living cells. *Tissue Eng*. 2005;11(11-12):1658-1666. doi: 10.1089/ten.2005.11.1658.
21. Xu T, Kincaid H, Atala A, Yoo JJ. High-throughput production of single-cell microparticles using an inkjet printing technology. *J Manuf Sci E*. 2008;130(2):021017. doi: 10.1115/1.2903064.

22. Kim YK, Park JA, Yoon WH, Kim J, Jung, S. Drop-on-demand inkjet-based cell printing with 30-μm nozzle diameter for cell-level accuracy. *Biomicrofluidics*. 2016 30;10(6):064110. doi: 10.1063/1.4968845.

23. Stumpf F, Schoendube J, Gross A, *et al*. Single-cell PCR of genomic DNA enabled by automated single-cell printing for cell isolation. *Biosens Bioelectron*. 2015;69:301-306. doi: 10.1016/j.bios.2015.03.008.

24. Chen F, Lin L, Zhang J, He Z, Uchiyama K, Lin, J.M. Single-Cell Analysis Using Drop-on-Demand Inkjet Printing and Probe Electrospray Ionization Mass Spectrometry. *Anal Chem*. 2016;88(8):4354-4360. doi: 10.1021/acs.analchem.5b04749.

25. Dou R, Saunders RE, Mohamet L, Ward CM, Derby, B. High throughput cryopreservation of cells by rapid freezing of sub-μl drops using inkjet printing--cryoprinting. *Lab Chip*. 2015;15(17):3503-3513. doi: 10.1039/c5lc00674k.

26. Akiyama Y, Shinose M, Watanabe H, Yamada S, Kanda Y. Cryoprotectant-free cryopreservation of mammalian cells by superflash freezing. *Proc Natl Acad Sci USA*. 2019;116(16):7738-7743. doi: 10.1073/pnas.1808645116.

27. Xu T, Rohozinski J, Zhao W, Moorefield EC, Atala A, Yoo JJ. Inkjet-mediated gene transfection into living cells combined with targeted delivery. *Tissue Eng Part A*. 2009;15(1):95-101. doi: 10.1089/ten.tea.2008.0095.

28. Cui X, Dean D, Ruggeri ZM, Boland T. Cell damage evaluation of thermal inkjet printed Chinese hamster ovary cells. *Biotechnol Bioeng*. 2010;106(6):963-969. doi: 10.1002/bit.22762.

29. Sohrabi S, Liu Y. Modeling thermal inkjet and cell printing process using modified pseudopotential and thermal lattice Boltzmann methods. *Phys Rev E*. 2018;97(3-1):033105. doi: 10.1103/PhysRevE.97.033105.

30. Das SR, Uz M, Ding S, *et al*. Electrical differentiation of mesenchymal stem cells into Schwann-Cell-Like phenotypes using inkjet-printed graphene circuits. *Adv Healthc Mater*. 2017;6(7):1601087. doi: 10.1002/adhm.201601087.

31. Zips S, Huang B, Hotte S, *et al*. Aerosol Jet-Printed High-Aspect ratio Micro-Needle electrode arrays applied for human cerebral organoids and 3D neurospheroid networks. *ACS Appl Mater Interfaces*. 2023;15(30):35950-35961. doi: 10.1021/acsami.3c06210.

32. Tse C, Whiteley R, Yu T, *et al*. Inkjet printing Schwann cells and neuronal analogue NG108-15 cells. *Biofabrication*. 2016;8(1):015017. doi: 10.1088/1758-5090/8/1/015017.

33. Lorber B, Hsiao WK, Hutchings, IM, Martin KR. Adult rat retinal ganglion cells and glia can be printed by piezoelectric inkjet printing. *Biofabrication*. 2014;6(1):015001. doi: 10.1088/1758-5082/6/1/015001.

34. Solis LH, Ayala Y, Portillo S, Varela-Ramirez A, Aguilera R, Boland, T. Thermal inkjet bioprinting triggers the activation of the VEGF pathway in human microvascular endothelial cells in vitro. *Biofabrication*. 2019;11(4):045005. doi: 10.1088/1758-5090/ab25f9.

35. Yumoto M, Hemmi N, Sato N, *et al*. Evaluation of the effects of cell-dispensing using an inkjet-based bioprinter on cell integrity by RNA-seq analysis. *Sci Rep*. 2020;10(1):7158. doi: 10.1038/s41598-020-64193-z.

36. Schlett K, Herberth B, Madarász E. In vitro pattern formation during neurogenesis in neuroectodermal progenitor cells immortalized by p53-deficiency. *Int J Dev Neurosci*. 1997;15(6):795-804. doi: 10.1016/s0736-5748(97)00015-4.

37. Schlett K, Madarász E. Retinoic acid induced neural differentiation in a neuroectodermal cell line immortalized by p53 deficiency. *J Neurosci Res*. 1997;47(4):405-415.

38. Strickland S, Mahdavi V. The induction of differentiation in teratocarcinoma stem cells by retinoic acid. *Cell*. 1978;15(2):393-403. doi: 10.1016/0092-8674(78)90008-9.

39. Maden, M. Retinoic acid in the development, regeneration and maintenance of the nervous system. *Nat Rev Neurosci*. 2007;8(10):755-765. doi: 10.1038/nrn2212.

40. Napoli JL. Interactions of retinoid binding proteins and enzymes in retinoid metabolism. *Biochim Biophys Acta*. 1999;1440(2-3):139-162. doi: 10.1016/s1388-1981(99)00117-1.

41. Ables JL, Decarolis NA, Johnson MA, *et al*. Notch1 is required for maintenance of the reservoir of adult hippocampal stem cells. *J Neurosci*. 2010;30(31):10484-10492. doi: 10.1523/JNEUROSCI.4721-09.2010.

43. Park JA, Yoon S, Kwon J, *et al*. Freeform micropatterning of living cells into cell culture medium using direct inkjet printing. *Sci Rep*. 2017;7(1):14610. doi: 10.1038/s41598-017-14726-w.

43. Barui S, Saunders RE, Naskar S, Basu B, Derby B. Acoustic poration and dynamic healing of mammalian cell membranes during inkjet printing. *ACS Biomater Sci Eng*. 2020;6(1):749-757. doi: 10.1021/acsbiomaterials.9b01635.

ACCSCIENCE PUBLISHING

International Journal of Bioprinting

RESEARCH ARTICLE

Multi-material bioprinting using a helical mixer for fabricating fibers with controlled composition

Reza Gharraei[1], Donald J. Bergstrom[2], and Xiongbiao Chen[1,2]*

[1]Division of Biomedical Engineering, College of Engineering, University of Saskatchewan, Saskatoon, Saskatchewan, Canada

[2]Department of Mechanical Engineering, College of Engineering, University of Saskatchewan, Saskatoon, Saskatchewan, Canada

(This article belongs to the *Special Issue*: *Bioprinting for Tissue Engineering and Modeling*)

Abstract

Multi-material bioprinting is a promising technique for fabricating complex, heterogeneous constructs with tailored mechanical and biological properties for tissue engineering applications. Recently, the use of a helical static mixer in bioprinting has shown feasibility for producing fibers from multiple biomaterials. However, the underlying mechanisms of transient stream mixing and the control of composition gradients during the printing process remain insufficiently understood. This study investigates biomaterial mixing with the objective of improving the spatial resolution of composition gradients along the longitudinal axis of printed fibers. Computational fluid dynamics (CFD) simulations were utilized to investigate the flow and mixing behavior of precursor streams, and the insights obtained were used to redesign the bioprinting head for improved performance. Rheological studies were performed to characterize the flow behavior of the biomaterials. The results were used, in conjunction with CFD, to examine the mixing performance and to estimate the transition time—defined as the delay between flow rate changes at the inlets and the corresponding change in fiber composition. Our results demonstrate that the redesigned bioprinting head achieved complete mixing of biomaterials and that transition time can be effectively regulated or reduced by preemptively adjusting inlet flow rates. This advancement enhanced the spatial resolution of composition gradients by 17–30%, as confirmed through a case study presented in this article. Additionally, adjustments to the toolpath further improved gradient resolution. Overall, this study elucidates key principles underlying multi-material bioprinting and provides strategies for improving bioprinting head design to achieve finer spatial control of composition gradients.

Keywords: 3D bioprinting; Computational fluid dynamics; Flow behavior; Multi-material bioprinting; Tissue engineering

***Corresponding author:**
Xiongbiao Chen
(xbc719@mail.usask.ca)

Citation: Gharraei R, Bergstrom DJ, Chen X. Multi-material bioprinting using a helical mixer for fabricating fibers with controlled composition. *Int J Bioprint*. 2025;11(5):231-265. doi: 10.36922/IJB025140119

Received: April 2, 2025
1st revised: June 8, 2025
2nd revised: June 27, 2025
Accepted: July 1, 2025
Published Online: July 1, 2025

Copyright: © 2025 Author(s). This is an Open Access article distributed under the terms of the Creative Commons Attribution License, permitting distribution, and reproduction in any medium, provided the original work is properly cited.

Publisher's Note: AccScience Publishing remains neutral with regard to jurisdictional claims in published maps and institutional affiliations.

1. Introduction

Three-dimensional (3D) bioprinting has attracted significant attention for the fabrication of constructs and scaffolds in tissue engineering. This technology allows for the production of constructs with customized internal architectures, mechanical and biological properties, and the incorporation of bioactive agents such as drugs and

growth factors, all aimed at mimicking the structure and composition of native tissues.[1–4] Native tissues are inherently heterogeneous, composed of diverse material and cell types organized into complex architectures that support specific biological functions. Successfully replicating this complexity requires reproducing both the compositional and structural heterogeneity, which in turn demands the integration of multiple biomaterials and various cell types during the bioprinting process.[5–7] Multi-material bioprinting is an emerging technique that facilitates the printing of multiple biomaterials and cell types, as well as the control of compositional gradients within the printed constructs. This approach markedly enhances the capacity to replicate the heterogeneous structure of native tissues.[6,8–11] Various techniques have been adopted to achieve multi-material bioprinting, such as the use of multiple dispensing heads,[12–16] selector valves,[17–19] and/or microfluidic systems.[19,20] One such method involves a multi-material printing head equipped with a microfluidic mixing system, which can extrude a single fiber composed of a controlled gradient of biomaterials along its length. Despite its promise, microfluidic bioprinting faces several limitations. The narrow flow paths inherent to microfluidic channels can generate high shear stresses that may compromise cell viability during extrusion.[4,21,22] As an alternative, mixing strategies involving static mixers—particularly helical static mixers—have gained popularity due to their simple geometry and effective mixing performance.[23,24] Alternating twisted helical elements facilitate stream mixing via chaotic advection, which is the most efficient mechanism for mixing in creeping flows characterized by extremely low Reynolds number, where inertial forces are negligible and mixing is achieved through vortex generation.[25,26]

Although the use of a helical mixer has been demonstrated to be feasible for printing multi-material fibers,[26–29] many aspects remain unexplored, particularly regarding the mixing behavior of multiple flow streams and their influence on bioprinting performance. In a multi-material bioprinting head, precise manipulation of biomaterial flow rates at the inlets is essential for controlling the composition of the outflow stream along the longitudinal axis. This control enables the printing of scaffolds with controlled property gradients that mimic the heterogeneous structure of natural tissues. However, due to the internal volume between the inlets and the outlet of the print head, changes in precursor flow rates at the inlets do not immediately result in corresponding changes in fiber composition at the outlet. This delay is referred to as the transition time (t_t). Notably, the transition time is a dynamic parameter that depends on the internal biomaterial volume of the print head, the initial composition of the flow, and the targeted composition in the printed fiber. Figure 1 illustrates two major challenges encountered during compositional transitions in multi-material bioprinting. During the transition phase, the deposited fiber contains varying fractions of the precursor materials, gradually shifting from the initial to the intended composition (Figure 1A). Therefore, minimizing the transition time is crucial for improving the spatial resolution of property gradients in printed fibers. Furthermore, if the precursor streams are not well mixed during this phase, streaky patterns may emerge in the printed fiber[10,17] (Figure 1B). These streaks can result in weak points along the fiber,

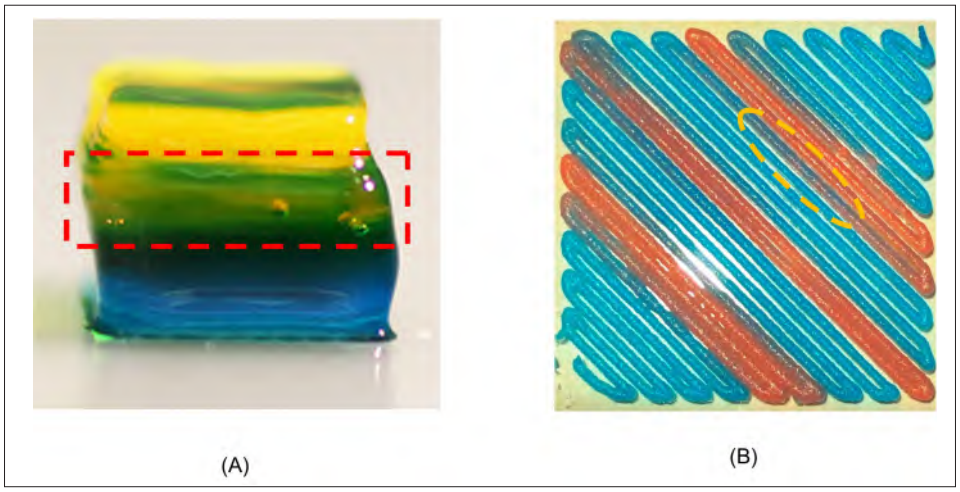


Figure 1. Composition changes in multi-material scaffolds. (A) Transition region with variable composition in a printed multi-material construct. Reprinted with permission from Ref.[10] Copyright © 2016 WILEY-VCH Verlag GmbH & Co. KGaA, Weinheim. (B) Streaky fiber pattern resulting from incomplete mixing during composition change.[17]

especially at locations with abrupt compositional changes, increasing the risk of mechanical failure.

This issue can be addressed by improving the mixing efficiency of the multi-material print head during its transient operation. A precise and comprehensive understanding of the flow and mixing processes enables refinement of inlet flow rate control, thereby improving composition modulation throughout the multi-material bioprinting process. Unfortunately, the dynamics of compositional transition and associated problems (such as the formation of streaky patterns) have not been thoroughly investigated and elucidated in the literature, largely due to the complexity of the system and challenges related to experimental observation. In this context, computational fluid dynamics (CFD) modeling has recently emerged as a powerful and promising approach.[30–32] CFD employs numerical methods to solve the partial differential equations governing fluid flow and mass transport, providing comprehensive insights into phenomena such as velocity distribution, pressure fields, shear stress, and mass fraction evolution. CFD has been extensively used to predict the performance of extrusion-based bioprinting systems, including conventional and coaxial print heads, under varying operational conditions such as different extrusion pressures and printing speeds.[30,33–36] It has also been applied to evaluate the performance of helical mixers, particularly in predicting the striated internal structure of fibers generated by chaotic flows—referred to as chaotic printing.[37,38]

Studies have shown that CFD simulations of biomaterials mixing in multi-material bioprinting heads equipped with helical mixers can elucidate velocity and shear stress distributions in cylindrical and conical nozzle geometries, providing valuable insights for optimizing bioprinting performance.[39] Other studies have reported that CFD can assist in the design optimization of multi-material bioprinting heads.[40] For instance, it was found that increasing the inclination angle of helical mixing elements elevates shear stress, and that these simulated shear stresses correlate with cell viability outcomes from live/dead assays using alginate-based bioinks containing MC3T3-E1 mouse embryonic osteoblasts. It is important to note, however, that the aforementioned studies were performed under steady-state flow conditions, focusing primarily on the impact of print head and mixer geometry on shear stress distribution and mixing performance. These studies did not consider transitional flow conditions, as encountered during compositional changes in multi-material bioprinting. As such, the literature remains limited in its exploration of transient precursor mixing, the dynamics of transition time, and the potential structural and biological issues associated with gradient-based multi-material bioprinting.

This paper presents a study on the multi-material bioprinting process using a helical mixer to print fibers with controlled compositional gradients. CFD was utilized to investigate the flow and mixing behavior of precursor streams within a multi-material bioprinting head, and the CFD simulation results were used to inform the design of a bioprinting head optimized for improved performance. Unlike previous studies,[30,33–39] the present work explicitly considers the effect of biomaterial volume within the bioprinting head and reveals its influence on the transition dynamics during changes in fiber composition.[30,39] The flow behavior of the biomaterials and their mixture at different temperatures was characterized using a parallel plate rheometer. A composition- and temperature-dependent model was developed to represent their rheological behavior accurately. Furthermore, mathematical equations were derived to relate the inlet stream compositions and flow rates to the resulting fiber composition in the multi-material bioprinting process. The designed bioprinting head was evaluated using two distinct biomaterials, and transition times for composition changes in the printed fibers were calculated based on CFD simulation results. In addition to demonstrating the successful operation of the modified print head for producing composition gradients, the CFD simulations revealed that a predictable portion of the transition time can be eliminated by preemptively adjusting the inlet flow rates. This approach significantly enhances the spatial resolution of compositional gradients, demonstrating its value for multi-material bioprinting. Moreover, by linking the apparent viscosity of the biomaterial mixture at the nozzle outlet to the CFD-predicted transition time, this study proposes strategies to further improve the spatial resolution of composition through adjustments in the bioprinting toolpath.

2. Materials and methods

2.1. Multi-material bioprinting head

Figure 2A and B illustrates the flow geometry of the initial design for a multi-material bioprinting head equipped with a helical mixer and two inlets. The overall geometry resembles that of a T-mixer with a circular cross-section, featuring a helical static mixer to enhance mixing efficiency. This configuration is similar to the basic layouts of multi-material heads reported in previous studies, albeit with certain modifications.[26–28] The tapered and chamfered nozzle geometries were adapted from GA27 Luer lock nozzles, as specified in technical data provided by Nordson-EFD (Nordson, United States of America [USA]).[41] The cylindrical T-shaped body of the head, designed to be compatible with Nordson's Luer lock fittings, was modeled using SOLIDWORKS (Dassault Systèmes, France) computer-aided design (CAD) software.

The geometry of the helical mixing elements was based on the Series 190 spiral mixers available from Nordson-EFD (Nordson, USA). As shown in Figure 2C, the helical static mixer consists of alternating clockwise and counterclockwise 180° twisted plates arranged axially. The leading edge of each element is positioned at a right angle to the trailing edge of the preceding one. These elements were mounted onto a 0.9 mm diameter rod for installation inside the print head. The 3D geometries of the T-shaped head body, the helical mixer, and the printing nozzle were assembled in SOLIDWORKS to construct a complete model of the multi-material bioprinting head. The assembly process in SOLIDWORKS was adjusted to match the geometric and dimensional constraints of real-world components.

Once the head geometry was finalized, ANSYS SpaceClaim software (Ansys, USA) was employed to extract the internal fluid domain (flow geometry) by subtracting

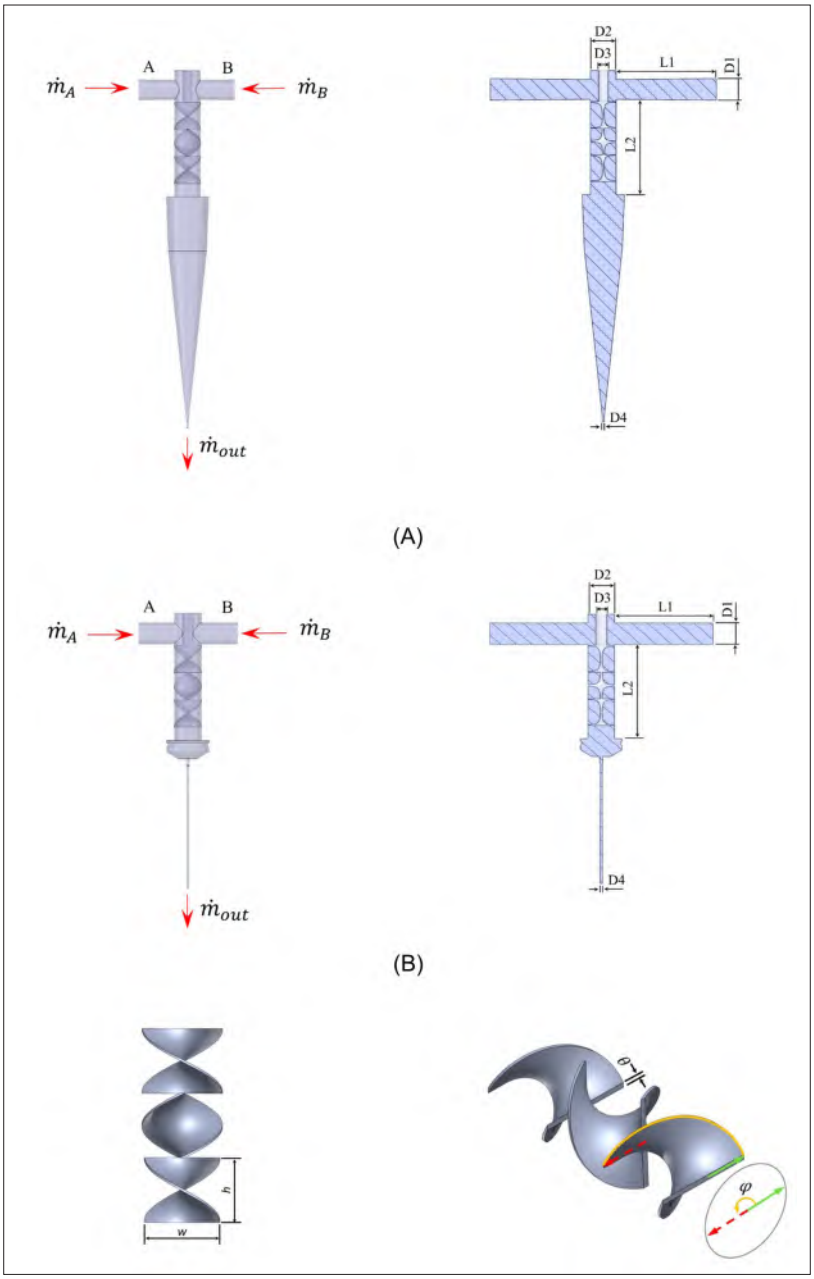


Figure 2. Fluid domain geometry inside the multi-material head with helical mixer connected to (A) a tapered nozzle and (B) a chamfered nozzle. Fluid volume (left); symmetry plane section with dimensions (right). (C) Geometry of the helical mixer (solid body): front view (left) and isometric view (right).

the solid parts from the 3D model. The resulting continuous internal volume was defined as the fluid flow domain for simulation purposes. The dimensional specifications of the fluid domain and the helical mixer elements are presented in Tables 1 and 2, respectively.

The dimensions of the printed head components in this initial design are fully compatible with the helical mixers and Nordson-EFD's Luer lock nozzles. However, these nozzles were not designed for applications involving variable compositions or gradient printing. As a result, they retain a considerable internal volume of fluid, which contributes to delays in transitioning fiber composition during bioprinting.

The composition of the printed fiber corresponds directly to the composition of the outflow stream, which is controlled by the compositions and flow rates of the biomaterials introduced at the two inlets. Assuming that the average velocity of the outflow stream is equal to the printing speed,[42] and that the total flow rate and composition remain constant during a given operational mode, then any increase in flow rate at one inlet must be offset by a corresponding decrease at the other. This reciprocal adjustment alters the composition of the printed fiber while maintaining a constant total flow rate.

On the other hand, the flow inside the bioprinting head is characterized by creeping flow with an extremely low Reynolds number, indicating minimal natural mixing. The alternating twist of the helical mixing elements creates a striated structure within the flow by dividing the stream into two sub-streams, which are then radially redistributed and recombined in an alternating pattern. This process induces chaotic advection, the most efficient mixing mechanism at low Reynolds numbers.[25] Therefore, sufficient space should be allocated within the print head to accommodate a static mixer that enhances biomaterial mixing through chaotic advection. This requirement presents a significant design challenge when developing a multi-material print head intended to control fiber composition with minimal transition time.

For the mixing of two streams using helical mixers, the number of striations in the cross-section increases exponentially, given by[43]:

$$s = 2^n \tag{I}$$

where s is the number of striations and n is the number of mixing elements. The average striation thickness is:

$$\delta = \frac{d_p}{s} \tag{II}$$

where d_p denotes the diameter of the flow passage.[25] This striation effect significantly reduces the mixing length and, consequently, the mixing time.[25] The mixing time can be approximated by:

$$t_{mix} = \frac{d_p^2}{Ds^2} \tag{III}$$

The mixing time becomes comparable to the residence time of the flow within the head, which is given by:

Table 1. G1ometrical characteristics of multi-material heads with various nozzles and helical mixers (all dimensions[a] in millimeter)

Nozzle type	Mixer diameter	D1	D2	D3	D4	L1	L2
Tapered	3.18	2.0	3.18	0.9	0.2	10.0	8.8
	2.36	2.0	2.36	0.9	0.2	10.0	8.8
Chamfered	3.18	2.0	3.18	0.9	0.2	10.0	9.7
	2.36	2.0	2.36	0.9	0.2	10.0	9.7
Conical	2.36	2.0	2.36	0.9	0.2	10.0	7.4
	1.8	1.6	1.8	0.6	0.2	10.0	7.4

[a]Dimensions based on the geometry of nozzles, mixers, and connection of parts in SOLIDWORK assemblies (except for the 1.8 mm conical nozzle that has a customized geometry).

Table 2. Geometrical characteristics of Series 190 spiral mixers from Nordson[41] (all dimensions in millimeter)

Diameter (w)[a]	Element length (h)	Element thickness (θ)	Twist angle (φ)
3.18	2.75	0.62	180°
2.36	2.46	0.4	180°

Note: aAs a customized geometry, 1.8 mm helical mixers have the same geometrical characteristics as the 2.36 mm ones, except for the smaller diameter.

$$t_{res} = \frac{\ell}{u_m} \quad \text{(IV)}$$

where D, ℓ, and u_m denote the diffusion coefficient, flow passage length, and average flow velocity, respectively.

2.2. Dependencies between inlet and outlet flow conditions

During steady-state operation of the multi-material print head, two aqueous streams enter from inlets A and B with mass flow rates $\dot{m}_A$ and $\dot{m}_B$, respectively. The combined stream exits through the nozzle with a total mass flow rate $\dot{m}_{out}$ (see Figure 2). To ensure smooth fiber deposition with a consistent diameter—assumed equal to the nozzle outlet diameter and neglecting swelling effects—the average velocity is taken to match the print head movement speed V during printing[42]:

$$\dot{m}_{out} = \frac{\pi d^2 \rho V}{4} \quad \text{(V)}$$

where ρ is the fluid density. By the principle of mass conservation:

$$\dot{m}_{out} = \dot{m}_A + \dot{m}_B \quad \text{(VI)}$$

Assume the inlet streams consist of aqueous solutions of biomaterials C1 and C2, with mass fractions $Y_{C1,A}$ and $Y_{C2,B}$ at inlets A and B, respectively. The outflow will then contain mass fractions $Y_{C1,out}$ and $Y_{C2,out}$. The concentration ratio of precursors at the outlet, denoted ψ, is defined as:

$$\psi = \frac{Y_{C1,out}}{Y_{C2,out}} \quad \text{(VII)}$$

For a given printing condition, this concentration ratio represents the composition of the printed fiber. To simplify composition control, a reference operation is defined in which the two inlet streams are mixed in a 1:1 ratio:

$$\dot{m}_{A,ref} = \dot{m}_{B,ref} = \frac{\dot{m}_{out}}{2} \quad \text{(VIII)}$$

By applying mass conservation for individual components and through some mathematical operations and rearranging (Appendix A), the following reference relationships are obtained:

$$\psi_{ref} = \frac{Y_{C1,A}}{Y_{C2,B}} \quad \text{(IX)}$$

and:

$$Y_{C1,out,ref} = \frac{\psi_{ref}}{2\left(\psi_{ref}+1\right)}\left(Y_{C1,A} + Y_{C2,B}\right) \quad \text{(X)}$$

$$Y_{C2,out,ref} = \frac{1}{2\left(\psi_{ref}+1\right)}\left(Y_{C1,A} + Y_{C2,B}\right) \quad \text{(XI)}$$

For printability considerations, it is essential to maintain a constant total outflow rate throughout the process. To relate the composition of the outflow stream to the reference case, flow ratios α and β are introduced:

$$\alpha = \frac{Y_{C1,out}}{Y_{C1,out,ref}} = \frac{\dot{m}_{C1,out}}{\dot{m}_{C1,out,ref}} = \frac{\dot{m}_A}{\dot{m}_{A,ref}} \quad \text{(XII)}$$

$$\beta = \frac{Y_{C2,out}}{Y_{C2,out,ref}} = \frac{\dot{m}_{C2,out}}{\dot{m}_{C2,out,ref}} = \frac{\dot{m}_B}{\dot{m}_{B,ref}} \quad \text{(XIII)}$$

These relations describe how the inlet flow rates are scaled relative to their reference values. Notably, α and β satisfy:

$$\alpha + \beta = 2 \quad \text{(XIV)}$$

They can also be expressed in terms of concentration ratios:

$$\alpha = \frac{2\psi}{\psi + \psi_{ref}}, \quad \beta = \frac{2\psi_{ref}}{\psi + \psi_{ref}} \quad \text{(XV)}$$

These relations show that α can be used as a control parameter to adjust the biomaterial flow rates at the inlets to achieve the intended composition ψ at the printed fiber. Appendix A provides detailed steps for deriving the equations listed in this section. **Equations VII, XII, XIV, and XV** are the key governing relationships for controlling printed fiber composition by manipulating the mass flow rates at the two inlets. By adjusting these parameters, the multi-material print head can produce fibers with a controlled longitudinal gradient in composition. Given the known precursor compositions at the inlets ($Y_{C1,A}$, $Y_{C2,B}$)

and the printing speed, the intended ψ can be achieved by appropriately adjusting the α value. The algorithm for this adjustment will be discussed in the following sections.

Any change in the inlet flow rates initiates a transient flow regime, triggered by the application of step-function inputs at both inlets. A new steady-state condition is established after a transition period, which is required for the complete change in the composition of the outflow.

2.3. Preparation of biomaterials

Medium-viscosity sodium alginate salt derived from brown algae (CAS no. 9005-38-3) and medium-viscosity sodium carboxymethylcellulose (CMC) salt (CAS no. 9004-32-4) were procured from Sigma-Aldrich (USA). Aqueous solutions at specified concentrations (mass fractions) were prepared by first blending the dry powders in desired mass ratios, followed by dissolution in Milli-Q water. After preparation, the solutions were allowed to stand undisturbed for 6 h to relieve any residual stresses and to eliminate bubbles that may have formed during the mixing process.

2.4. Rheology

All rheological measurements were performed using a Discovery HR-20 Rheometer (TA Instruments, USA) with 60 mm parallel plates, under controlled temperatures ranging from 10 to 40°C. Samples were gently loaded onto the bottom plate using a spatula, and the upper plate was lowered slowly to prevent disruption of the fluid structure. The samples were then allowed to rest for 10 min prior to testing. Flow curves were obtained by applying shear rates ranging from 0.01 to 1000 s^{-1}.

The apparent viscosity η is defined using a generalized form of the viscosity law, which relates the shear stress tensor ($\overline{\overline{\tau}}$) to the strain rate tensor ($\overline{\overline{\dot{\gamma}}}$) as follows[44]:

$$\overline{\overline{\tau}} = \eta \overline{\overline{\dot{\gamma}}} \tag{XVI}$$

For a Newtonian fluid, η is the constant dynamic viscosity. However, for non-Newtonian fluids, η varies with the strain rate.

Several time-independent mathematical models describe the flow behavior of non-Newtonian biomaterials by expressing apparent viscosity as a function of shear rate. The model that best fit the steady shear behavior of the tested fluids was selected using TRIOS software (TA Instruments, USA), which analyzes rheological data acquired from the rheometer.

In addition to steady shear tests, oscillatory shear tests were conducted on alginate and CMC aqueous solutions at different temperatures to determine the storage (G′) and loss moduli (G′), thereby characterizing the rheological behavior of the solutions. However, due to the limited ability of current mathematical viscoelastic models to accurately describe the flow behavior of mixtures (as discussed in **Section 3.1**), the rheological investigation primarily focused on steady shear rheology.

Results from steady shear tests on alginate, CMC, and alginate–CMC aqueous solutions—with various mass fractions and tested across multiple temperatures—were used to develop a composition- and temperature-dependent non-Newtonian viscosity model. This model captures how the mixture's flow behavior evolves during mixing inside the print head. The experiments followed a design matrix generated in Minitab (Minitab LLC, USA) for a design of experiments (DOE) at 25°C, covering alginate–CMC mixtures with alginate mass fractions ranging from 0 to 4% and CMC from 0 to 1%. To examine temperature dependency, a second DOE was generated, covering the temperature range of 10–40°C. All tests were performed in triplicate, and concentrations are presented as mass fractions.

To relate the apparent viscosity of alginate–CMC solutions to the mass fraction of the biomaterials, composition-dependent equations were fitted to the parameters of the selected non-Newtonian model. Data analysis was performed using OriginPRO 2021b (OriginLab, USA). Surface equations were fitted using alginate and CMC mass fractions as independent variables and the non-Newtonian model parameters as dependent variables. Temperature dependence was incorporated by fitting Arrhenius-type equations to the temperature-dependent apparent viscosity data for various compositions.

2.5. Governing equations and numerical methods

Assuming incompressible flow, the governing equations for biomaterial flow are expressed as follows[45]:

Continuity equation:

$$\frac{\partial \rho}{\partial t} + \nabla . \rho \vec{U} = 0 \tag{XVII}$$

Momentum transport equation:

$$\frac{D\left(\rho \vec{U}\right)}{Dt} = -\nabla \mathrm{p} + \nabla . \overline{\overline{\tau}} + \rho \vec{g} \tag{XVIII}$$

where $\frac{D}{Dt}$ is the material derivative, $\vec{U}$ is the fluid velocity vector, $\vec{g}$ is the gravitational acceleration vector,

and p and ρ denote the pressure and density of the fluid, respectively.

The mixing of biomaterials is modeled by solving the convection–diffusion transport equation for each component, assuming no chemical reactions or phase changes[45]:

$$\frac{D(\rho Y_i)}{Dt} = -\nabla . \vec{J}_i \quad \text{(XIX)}$$

where the diffusion flux is given by:

$$\vec{J}_i = -\rho D_i \nabla Y_i \quad \text{(XX)}$$

Here, Y_i is the mass fraction of i component, and D_i is its diffusion coefficient in the mixture. The diffusion coefficients of alginate and CMC in aqueous solutions at 25°C were taken as 0.78×10^{-9} m^2/s and 0.49×10^{-9} m^2/s, respectively.[46,47]

The governing equations, along with appropriate boundary conditions and flow behavior models, were solved using the finite-volume CFD software ANSYS Fluent 2021-R1 (ANSYS, USA). Polyhedral meshes were generated using ANSYS Fluent Meshing, with local mesh refinement around small geometric features (e.g., the thickness of the helical mixer elements). Mass flow inlet boundary conditions specifying the component mass fractions were applied at the inlets, while a pressure outlet boundary condition with ambient pressure was set at the outlet of the multi-material bioprinting head. Additionally, a no-slip condition with a zero-gradient condition for mass fractions was applied on all solid walls. All simulations employed a pressure-based solver with the SIMPLEC algorithm for pressure–velocity coupling and the QUICK scheme for spatial discretization of the momentum and component transport equations. Grid independence was verified for all cases by examining the axial velocity profile at the outlet boundary.

To calculate the apparent viscosity of alginate, CMC, and their ternary mixtures, user-defined functions (UDFs) were written and interpreted to the Fluent solver. These UDFs calculated the parameters of the composition-dependent viscosity model (at 25°C) and updated the apparent viscosity distribution within the flow domain after each step of the numerical solution.

2.6. Validation

While CFD is a powerful tool for analyzing fluid flow and mixing, it is important to validate the validity of the numerical results by comparing them with experimental data for simplified flow scenarios that share similar physics and geometry with the original problem. Given that the intended multi-material bioprinting process involves fluid flow and mixing through a helical static mixer and a nozzle, validation was performed using both experimental results and empirical correlations related to flow and mixing in helical mixers,[24,48–53] as well as extrusion through a tapered nozzle. Figure B1 (Appendix B) shows the geometry of the fluid domain used to simulate flow and mixing through a helical mixer with a diameter of 3.18 mm. Table 2 provides the geometrical specifications of the helical mixer employed in the CFD simulations. The mixer was positioned 300 mm downstream from the inlet and 200 mm upstream of the outlet of a pipe with the same diameter.

Experimental studies reported in the literature primarily focus on the flow and mixing of Newtonian and power-law non-Newtonian fluids in helical mixers.[24,48–53] The power-law model, one of the simplest non-Newtonian fluid models, describes the relationship between shear stress and shear rate in a simple shear flow as follows[44]:

$$\tau = K\dot{\gamma}^n \quad \text{(XXI)}$$

where K and n are the consistency coefficient and power-law index, respectively. The apparent viscosity is defined as:

$$\eta = K\bar{\dot{\gamma}}^{n-1} \quad \text{(XXII)}$$

where $\bar{\dot{\gamma}}$ denotes the magnitude of the shear rate. This formulation allows the generalized viscosity law (**Equation XVI**) to be applied to power-law fluids.

Table 3 lists the physical and rheological properties of the Newtonian and non-Newtonian fluids considered for validation of flow and mixing in the helical mixers.[48,54] For all cases, mass flow inlet and pressure outlet boundary conditions were applied at the respective boundaries, while all solid walls were treated with a no-slip condition.

Given the role of stress distribution and the striated flow patterns generated by the helical mixer in promoting mixing, validating CFD results against a hydrodynamic parameter such as the friction factor is crucial. The friction factor calculated from the CFD results for both Newtonian and non-Newtonian fluids was compared against empirical correlations from the literature to assess the accuracy of the numerical simulation. For Newtonian fluids, the Reynolds number and Fanning friction factor are calculated as[44]:

$$Re = \frac{\rho d u_m}{\eta} \quad \text{(XXIII)}$$

$$f = \frac{d\Delta P}{2L\rho u_m^{\ 2}} \quad \text{(XXIV)}$$

where u_m is the average velocity, and d and L are the diameter of the pipe (and mixer) and the length over which the pressure loss is measured, respectively. For power-law fluids, most researchers use a generalized form of these definitions for helical mixer flow[48,52]:

$$Re_{gen} = \frac{d^n u_m^{\ 2-n} \rho}{K\varepsilon^{2-n}\left[\left(3n+1\right)/4n\right]^n 8^{n-1}} \quad \text{(XXV)}$$

$$f = \frac{d\Delta P}{2L\rho u_m^{\ 2}}\varepsilon^2 \quad \text{(XXVI)}$$

Here, ε is the void fraction of the static mixer, set to 0.9 based on the mixer geometry.

Several criteria exist to measure mixing homogeneity,[43,55,56] with the mixing index (MI) being the most commonly used parameter for evaluating homogeneity in a flow cross-section. It is calculated as follows[55,56]:

$$MI = 1 - \sqrt{\frac{\sigma_Y^2}{\sigma_{max}^2}} \quad \text{(XXVII)}$$

$$\sigma_Y = \sqrt{\frac{1}{m}\sum_{j=1}^{m}\left(Y_j - \bar{Y}\right)^2} \quad \text{(XXVIII)}$$

where σ_Y denotes the standard deviation of the mass fraction at a cross-section, σ_{max} is the maximum standard deviation when no mixing occurs,[56] Y_j is the mass fraction at point j, $\bar{Y}$ is the mass fraction in a homogeneous mixture, and m is the number of sampling points. A mixture is generally considered homogeneous when MI exceeds 0.95.[24,43] For the mixing of identical fluid streams, mass flow inlets were applied at both entry points, and a pressure outlet boundary condition was assigned at the outlet. All solid walls were considered as no-slip boundaries. The experimental results of Alloca[23] were used to validate numerical results for mixing. The geometry used was the same as in Figure B1 (Appendix B), except for the inclusion of a secondary stream inlet located along the pipe's centerline. The number of mixing elements varied from 8 to 12. The physical properties of the primary and secondary streams were identical to those listed for the Newtonian fluid in Table 3, and the secondary flow rate was 10% of the primary flow rate.

In order to validate the numerical simulation results for predicting the flow of non-Newtonian biomaterials through a nozzle, experimental tests were performed using the GESIM Bioscaffolder (GESIM Bioinstruments and Microfluidics, Germany). Flow rates of 3 and 4% alginate aqueous solutions were measured as they passed through a GA27 tapered nozzle connected to a 10 mL syringe (Nordson-EFD, USA), driven by various upstream pneumatic pressures.

The geometry used in the simulations was generated by extracting the fluid domain geometry from a solid assembly model created in SOLIDWORKS, which combined the geometries of the 10 mL syringe and the GA27 Luer lock tapered nozzle. The CAD models were adapted from files available on the Nordson website (https://www.3dcontentcentral.com/parts/supplier/EFD,-Inc/71022.aspx).[57] The fluid domain was extracted from the solid assembly file using SpaceClaim. Figure 3 illustrates the geometry of the fluid domain used in the numerical simulations of alginate solution flow through the syringe and tapered nozzle. Given the axisymmetric geometry of the fluid domain, only one quarter of the domain—bounded by two symmetry planes—was modeled in the simulations. Boundary conditions included a pressure inlet at the liquid–gas interface inside the syringe, a pressure outlet at the nozzle outlet, no-slip conditions on all solid walls, and symmetry boundary conditions on the symmetry planes.

During the experimental measurements, the flow rate was measured by weighing the amount of fluid

Table 3. Physical and rheological properties of Newtonian and non-Newtonian fluids used in computational fluid dynamics validation[48,54]

Fluid	Density (kg/m³)	Dynamic viscosity (Pa·s)	Consistency coefficient (Pa·sⁿ)	Power-law index
Newtonian fluid	997	0.001	–	–
Non-Newtonian fluid	1000	–	2.44	0.550

dispensed from the nozzle over a specified time interval. As the GESIM Bioscaffolder employs pneumatic pressure to extrude biomaterials, there are inherent delays at the start and end of flow due to the compressibility of the nitrogen gas. To minimize the effect of these delays, the measurement duration was chosen to be sufficiently long, thereby effectively reducing the effect of pressure ramping on the average flow rate. The results were reported as the average of five measurements conducted at a consistent pneumatic driving pressure. After each measurement, the syringe was refilled to minimize the impact of fluid column height reduction. The average height of the liquid column before and after each test was used to determine the volume of biomaterial within the syringe's fluid domain.

2.7. Improving the geometry of the multi-material head based on computational fluid dynamics simulations

The initial geometry of the multi-material head, shown in Figure 2, was designed to be compatible with tapered and chamfered nozzles and helical static mixers, all commercially available from Nordson. The geometric and dimensional constraints for assembling the mixing elements, Luer lock fitting, and nozzles were adapted from Nordson's specifications.[41,57] Two mixing elements with diameters of 2.36 and 3.18 mm were fitted inside the cylindrical body of the multi-material head, which serves as the mixing chamber. The internal diameter of the Luer lock fitting was adjusted to match the diameter of the selected mixer.

CFD simulations were performed to analyze the flow and mixing of two identical 4% alginate streams, designated as alginate-A and alginate-B, within the bioprinting head. Evaluating mixing efficiency using fluids with identical properties is a common approach in numerical and experimental studies to simplify the problem and isolate the effectiveness of the mixing method,[23,53] avoiding complications originating from differences in rheological and diffusive behavior. To further simplify the analysis, both alginate-A and alginate-B were treated as pure fluids, with alginate-A modeled as a passive tracer.[53,58,59] This approach leads to the solution of **Equation XIX**, which governs the mixing of the passive tracer (alginate-A) with alginate-B. The boundary conditions for **Equation XIX** were defined as follows: a mass fraction of 1 at inlet A, 0 at inlet B, and zero-gradient conditions on the solid walls and at the outlet. Solving **Equation XIX** yields the distribution of alginate-A within the flow field, with values ranging from 0 (100% alginate-B) to 1 (100% alginate-A). A value of 1 represents 100% alginate-A (0% alginate-B), and a value of 0 represents 0% alginate-A (100% alginate-B). A value of 0.5 indicates complete mixing, corresponding to a 1:1 mixture. This method provides a clear visualization of the mixing process within the flow field and is specifically

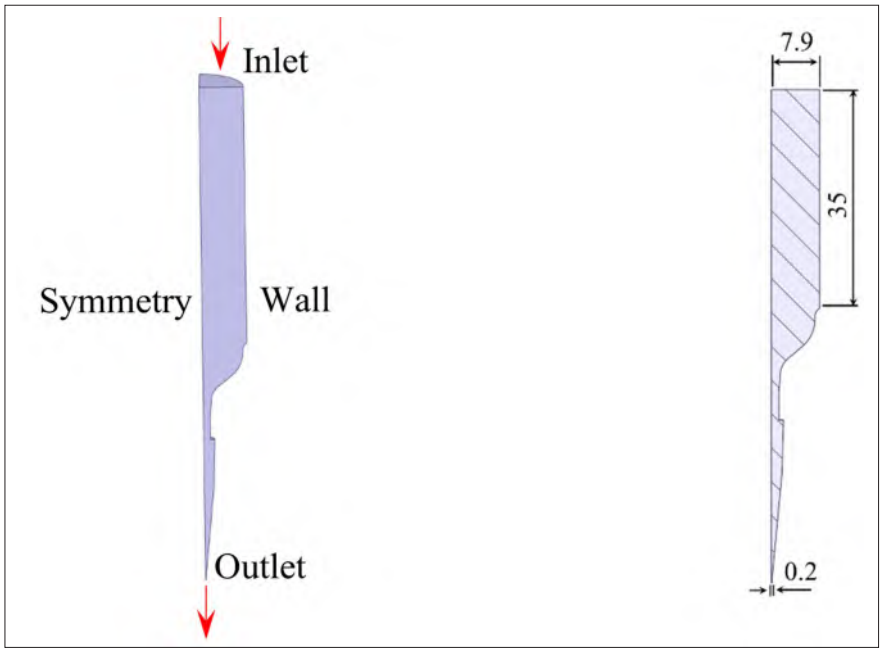


Figure 3. Fluid domain geometry (quarter view) for a GA27 tapered nozzle connected to a 10 mL syringe (left); symmetry plane section with dimensions (right). All dimensions are in millimeter.

applicable to the mixing of two chemically and physically identical solutions.

The results of the simulations were used to examine and refine the initial design of the multi-material head, allowing the identification of optimal geometries and dimensions. After implementing design improvements, the modified geometry was reconstructed in SOLIDWORKS, and the corresponding fluid domain was prepared for further CFD simulations, following the procedure described in **Section 2.1**.

To evaluate the modified design under realistic operating conditions, simulations were performed using a mixture of 4% alginate and 1% CMC aqueous solutions. Alginate–CMC ternary aqueous solutions are widely used in bioprinting and drug delivery applications[60–62] due to their favorable mechanical properties following $CaCl_2$-induced crosslinking. Additionally, CMC enhances cell migration and attachment in fabricated constructs.[62,63] Due to the differing properties of alginate and CMC solutions, **Equation XIX** was solved using the actual mass fraction values of both components. To focus on enhancing the spatial resolution of the composition gradient in multi-material bioprinting, simulations were conducted under the assumption that all printing parameters (e.g., speed, crosslinking, and stage temperature) were properly optimized, ensuring sufficient printability across all intended alginate–CMC compositions. This allowed the study to isolate and examine the flow and mixing dynamics associated with composition transitions, without the confounding effects of material-specific printability constraints. The simulation results also provided crucial insights for designing the flow control system and tool path strategies required for precise, compositional graded printing.

3. Results and discussion

3.1. Flow behavior

Figure 4 presents the results of steady and oscillatory shear rheological tests for 3 and 4% alginate and 1% CMC solutions at various temperatures. The apparent viscosity η is defined by **Equation XVI**. The variation in apparent viscosity shown in Figure 4A and B highlights the shear-thinning behavior of these solutions and the reduction in apparent viscosity with increasing temperature. Meanwhile, G′ and G″ presented in Figure 4C demonstrate the viscoelastic behavior of both alginate and CMC solutions across different temperatures, consistent with findings reported in previous studies.[64,65] However, due to the challenges associated with mathematically modeling viscoelastic behavior, there is currently no model that can accurately describe the rheology of viscoelastic fluids during the mixing process. As a result, time-independent models based on steady shear behavior are typically used in CFD simulations for mixing viscoelastic fluid streams. Accordingly, this study employed time-independent models derived from steady shear test results to simulate the flow and mixing of alginate and CMC aqueous solutions.

Among the various mathematical models evaluated for fitting the steady shear test results, the Cross model[66] was found to provide the best fit, based on goodness-of-fit analysis performed using TRIOS software. For both alginate and CMC solutions, the Cross model achieved a high correlation ($R^2 > 0.99$). The Cross model is a time-independent formulation that describes the apparent viscosity of shear-thinning fluids over a wide range of shear rate[66]:

$$\frac{\eta-\eta_\infty}{\eta_0-\eta_\infty}=\frac{1}{1+k\dot{\gamma}^n} \quad \text{(XXIX)}$$

where k and n are fitting parameters (with $n < 1$), and and η_∞ represent the limiting viscosities at low and high shear rates, respectively. Here, η_0 corresponds to the zero-shear viscosity, typically observed in t η_0 he plateau region at low shear rates, while η_∞, usually a very small value, is treated as a fitting parameter.

Table 4 lists the Cross model fitting parameters for the alginate and CMC solutions at 25°C, along with their densities, which were determined by weighing a known volume of fluid. Previous studies on the rheology of alginate and CMC aqueous solutions have also demonstrated that their flow behavior aligns well with the Cross model.[64,65] Furthermore, steady shear tests conducted on alginate solutions (0.1–4%), CMC solutions (0.1–1%), and alginate–CMC mixtures with various mass fractions confirmed the compatibility of their flow behavior with the Cross model.

Using OriginPRO software, surface fitting was performed to express the Cross model parameters as functions of alginate and CMC mass fractions. The resulting empirical relationships for the composition-dependent Cross model parameters are as follows:

$$\eta_{0,mix}=\Big(2551670.7\ Y_{alg}^{\ 3.34}+\exp\big(407.7\ Y_{CMC}\big)+\Big(256292.29+\exp\big(300.28\ Y_{alg}\big)\Big)\ Y_{alg}Y_{CMC}\Big)\ H_{\eta_0} \quad \text{(XXX)}$$

$$k_{mix}=\Big(21.11Y_{alg}^{\ 1.66}+450941.4\ Y_{CMC}^{\ 2.408}\exp\big(-285.98\ Y_{alg}\big)+2395.91\ Y_{alg}Y_{alg}\Big)H_k \quad \text{(XXXI)}$$

$$n_{mix}=3.74\ Y_{alg}+2025.66\ Y_{CMC}^{\ 2}-25\ Y_{CMC}-254.5\ Y_{alg}\ Y_{CMC}+0.6877 \quad \text{(XXXII)}$$

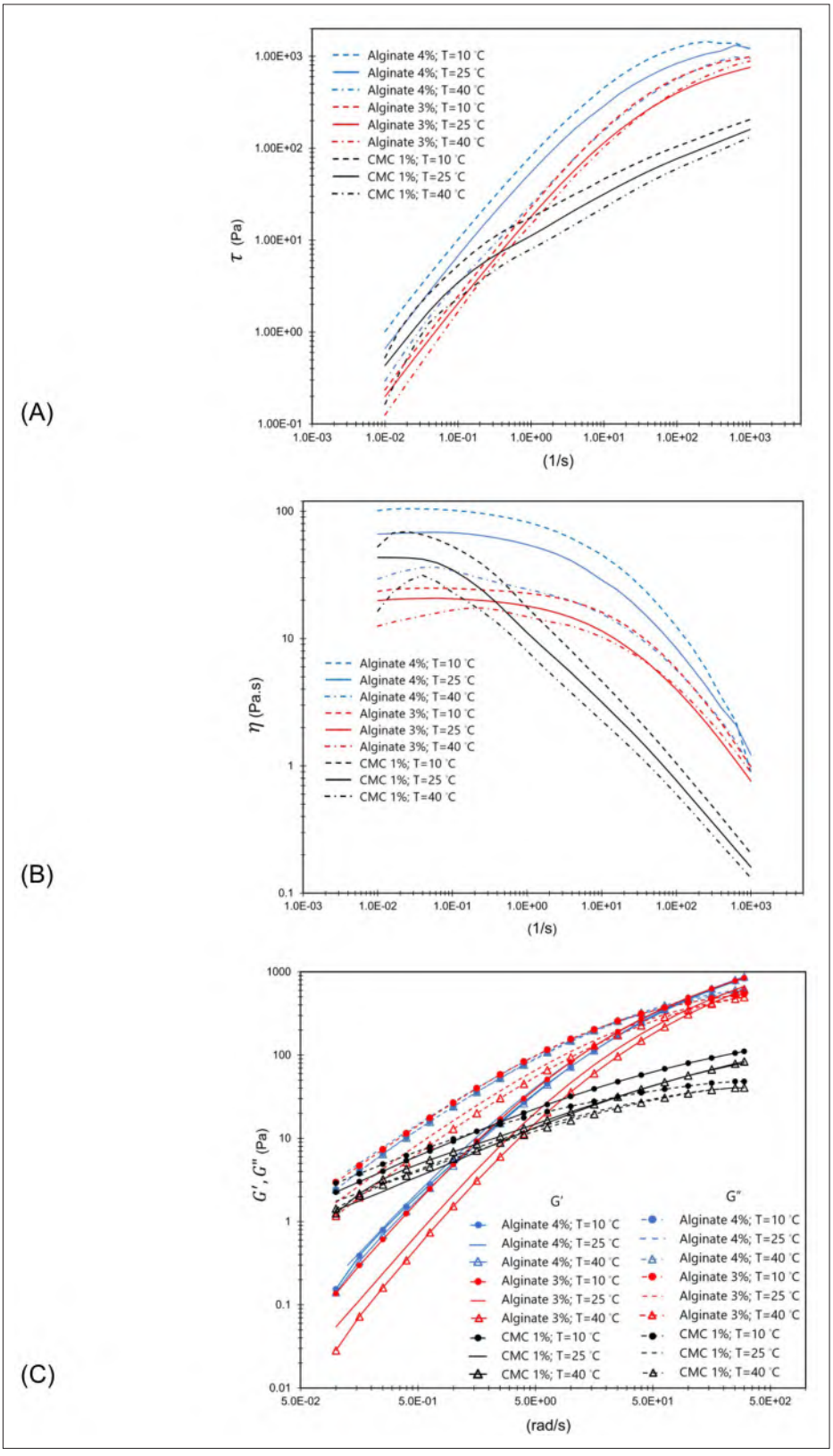


Figure 4. Rheological behavior of biomaterials. (A) Flow behavior, (B) apparent viscosity, and (C) loss (G′) and storage (G″) moduli for 3% alginate, 4% alginate, and carboxymethylcellulose (CMC) 1% aqueous solutions.

where Y_{alg} and Y_{CMC} are the mass fractions of alginate and CMC, respectively, with the valid range $Y_{alg} \leq 0.04$ and $Y_{CMC} \leq 0.01$. The high-shear viscosity ($\eta_{\infty, mix}$) was negligible for all solutions and was omitted from the expressions. The R^2 values for the surface fits were 0.98, 0.97, and 0.93 for $\eta_{0,mix}$, K_{mix}, *and* n_{mix} respectively, indicating excellent agreement with the experimental data.

H_{η_0} and H_k in **Equations XXX and XXXI** are temperature correction functions used to adjust the values of η_0 and k for temperatures other than 25°C. Surface fitting of steady shear test results for alginate–CMC aqueous solutions across a temperature range of 10–40°C resulted in the following Arrhenius-type viscosity correction functions[67,68]:

$$H_{\eta_0} = \exp\left[\frac{E_{\eta_0}}{\mathcal{R}}\left(\frac{1}{T} - \frac{1}{298.15}\right)\right] \quad \text{(XXXIII)}$$

$$H_k = \exp\left[\frac{E_k}{\mathcal{R}}\left(\frac{1}{T} - \frac{1}{298.15}\right)\right] \quad \text{(XXXIV)}$$

where $\mathcal{R} = 8.314$ J/mol·K is the universal gas constant, T is the absolute temperature in Kelvin (K), and E_{η_0} and E_k E_k are the activation energies (in J/mol), both dependent on composition:

$$E_{\eta_0} = \frac{-29590 Y_{alg} + 18205\ Y_{CMC} - 34343 Y_{alg}\ Y_{CMC}}{1 - 2.951 Y_{alg} - 317.70\ Y_{CMC}} \quad \text{(XXXV)}$$

$$E_k = \frac{-307790 Y_{alg} + 170810\ Y_{CMC} - 579870 Y_{alg}\ Y_{CMC}}{1 - 188.83 Y_{alg} + 180.80\ Y_{CMC}} \quad \text{(XXXVI)}$$

3.2. Valuation of numerical results

Figure 5 presents the validation of the numerical simulations for flow through the helical mixer. This figure compares the numerically predicted friction factor f with values calculated from various empirical correlations available in the literature.[24,48–52] Figure 5A and B shows that the numerical results for the Newtonian fluids are in good agreement with the correlations proposed by Cybulski and Werner[49] and Shah and Kale.[48] For non-Newtonian fluid flow, the predicted friction factor closely matches the data reported by Xu et al.[52]

Figure 5C compares the simulation results with experimental data from Alloca[23] for the mixing of two fluid streams through helical mixers with varying numbers of elements, denoted by different L/d values (the ratio of the total mixer length L to the diameter d). This comparison demonstrates strong agreement between the numerical results and experimental data of Alloca.[23] Since no experimental studies have been reported on the flow and mixing of non-Newtonian Cross fluids in helical mixers, validation was carried out using results from experimental studies on Newtonian and power-law non-Newtonian fluids. The Cross model transitions to the Newtonian model as $k \to 0$, and behaves like a power-law fluid when $\eta_\infty \ll \eta \ll \eta_0$,[44,66] which covers a wide range of shear rates typically encountered in helical mixers. Consequently, validation of CFD simulations using existing data on Newtonian and power-law fluids provides an insightful assessment of the reliability of the CFD results for Cross fluids.

Figure 6 compares the numerically predicted flow rates of 3 and 4% alginate solutions through a syringe and nozzle under various upstream pneumatic pressures. Error bars represent uncertainties in flow rate measurements, calculated using the Moffat method.[69] The GESIM Bioscaffolder utilizes pressure regulators with an accuracy of 0.6% of full scale or better, within a pressure range of 0–900 kPa. Its solenoid valves also feature a response time of 25 ms or less. The agreement between experimental and simulation results confirms the accuracy of the numerical model in predicting the flow of a Cross fluid through a nozzle.

Given the demonstrated accuracy of the numerical simulations in predicting flow and mixing in both helical mixers and nozzles, it can be concluded that the CFD approach is reliable for analyzing the flow and mixing of biomaterials within a multi-material bioprinting head equipped with a helical mixer.

Table 4. Density and cross model fitting parameters for alginate and carboxymethylcellulose (CMC) aqueous solutions at T = 25°C

Fluid	ρ (kg/m³)	η_0 (Pa·s)	η_∞ (Pa·s)	k (s)	n
Alginate 3%	998.3	20.52	9.18E-6	0.067	0.770
Alginate 4%	998.7	55.23	4.62E-15	0.095	0.85
CMC 1%	1000	54.8	1.95E-17	6.6	0.66

3.3. Improving the multi-material head geometry based on computational fluid dynamics simulation results

As discussed above, an improved design of the multi-material head should ensure not only high MI but also low shear stress levels and reduced internal volume—factors critical for maintaining cell viability and achieving high spatial resolution in controlled composition gradient multi-material bioprinting. To evaluate performance, the mixing of two 4% alginate solutions was considered as a test case for examining the performance of multi-material heads with different geometric parameters. Figure 7 demonstrates the impact of the number of mixing elements (N) on the MI at the outlet of the multi-material head, for the flow and mixing of two 4% alginate streams (alginate-A and alginate-B). The inlet flow rates were equal, and the average outlet velocity was set to 10 mm/s, consistent with the printing speed. All MI values in Figure 7 exceed 0.95, suggesting that as few as two mixing elements are sufficient to mix two 4% alginate streams within a multi-material head equipped with a chamfered or tapered nozzle. However, as shown in Figure 8, the distribution of the mass fraction indicates that mixing is not complete after the second element; instead, the mixing process continues as the fluid flows through the nozzle.

Table 5 compares the estimated mixing time and residence time for the mixing of 4% alginate solutions using two and three 2.36 mm mixing elements. The results indicate that with two elements, the required mixing time exceeds the residence time for flow through the mixing elements. This suggests that the fluid streams are not thoroughly mixed immediately after the second element, and the remaining mixing is completed inside the nozzle, as shown in Figure 8. According to **Equation III**, the flow through the nozzle needle accelerates mixing due to its extremely small diameter, which enhances the breakdown of striations. When three elements are used, the mixing time closely matches the residence time, resulting in well-mixed streams by the trailing edge of the third element.

Comparing the MI values for 3.18 and 2.36 mm mixing elements in Figure 7 shows that the 2.36 mm elements yield better mixing performance, primarily due to the thinner striations they generate.[28] In addition, the 2.36 mm elements require a smaller internal volume within the head. The maximum shear stress for configurations with three mixing elements of either size, combined with a tapered nozzle, remains nearly constant at 1.45 kPa. However, when a chamfered nozzle is used, this value increases to 2.9 kPa for both mixer sizes. Given that the 2.36 mm elements provide superior mixing and produce similar maximum shear stress levels compared to the 3.18 mm elements, they are the preferred choice for the modified design. Chamfered nozzles, due to their small diameter and high length-to-diameter ratio, facilitate efficient mixing of extremely thin striations and offer a smaller internal volume (as illustrated in Figure 2). However, they also generate significantly higher shear stress than tapered nozzles. As a result, chamfered nozzles were not selected for the improved design of the multi-material head due to potential negative effects on cell viability.

Despite their popularity, tapered nozzles are not ideal for controlled-gradient multi-material bioprinting because they retain a relatively large internal volume, which increases the response time of the head to changes in inlet flow rates. To strike a balance between the small internal volume and high shear stress of chamfered nozzles and the larger internal volume and lower shear stress of tapered nozzles, a simple conical nozzle geometry was considered for the improved multi-material head. Figure 9 illustrates the fluid domain geometry of the multi-material head equipped with a threaded conical nozzle. The nozzle dimensions are provided in Table 1. Unlike tapered nozzles, which have a profile with two distinct cone angles, the conical nozzle consists of a single cone connected to a needle. In contrast to the Luer lock connection used in the initial design, the threaded connection offers greater flexibility in sizing the head.

Due to the space required for Luer lock fittings and the internal geometry of the bioprinting nozzles, the L2 length (as shown in Figure 2) cannot be reduced below 8.8 mm for tapered nozzles or 9.7 mm for chamfered nozzles. This means that even with a single mixing element, the L2 length remains unchanged. In contrast, a customized conical nozzle with a threaded connection does not require additional fitting length, allowing the L2 length in Figure 9 to be equal to the length of the helical mixer installed within the head. While the modified design employs custom components with fewer limitations on size and fittings, its overall geometry and dimensions remain within the range of high-precision nozzles and fittings commercially produced by GESIM and Nordson.

Figure 10 displays the shear stress distribution on the symmetry plane for three different head geometries equipped with tapered, chamfered, and conical nozzles. The results indicate that the maximum shear stress within the helical mixer is less than 5% of the peak value observed at the contraction region of the printing nozzle. This confirms that the mixing elements do not significantly contribute to the maximum shear stress, and that the nozzle shape

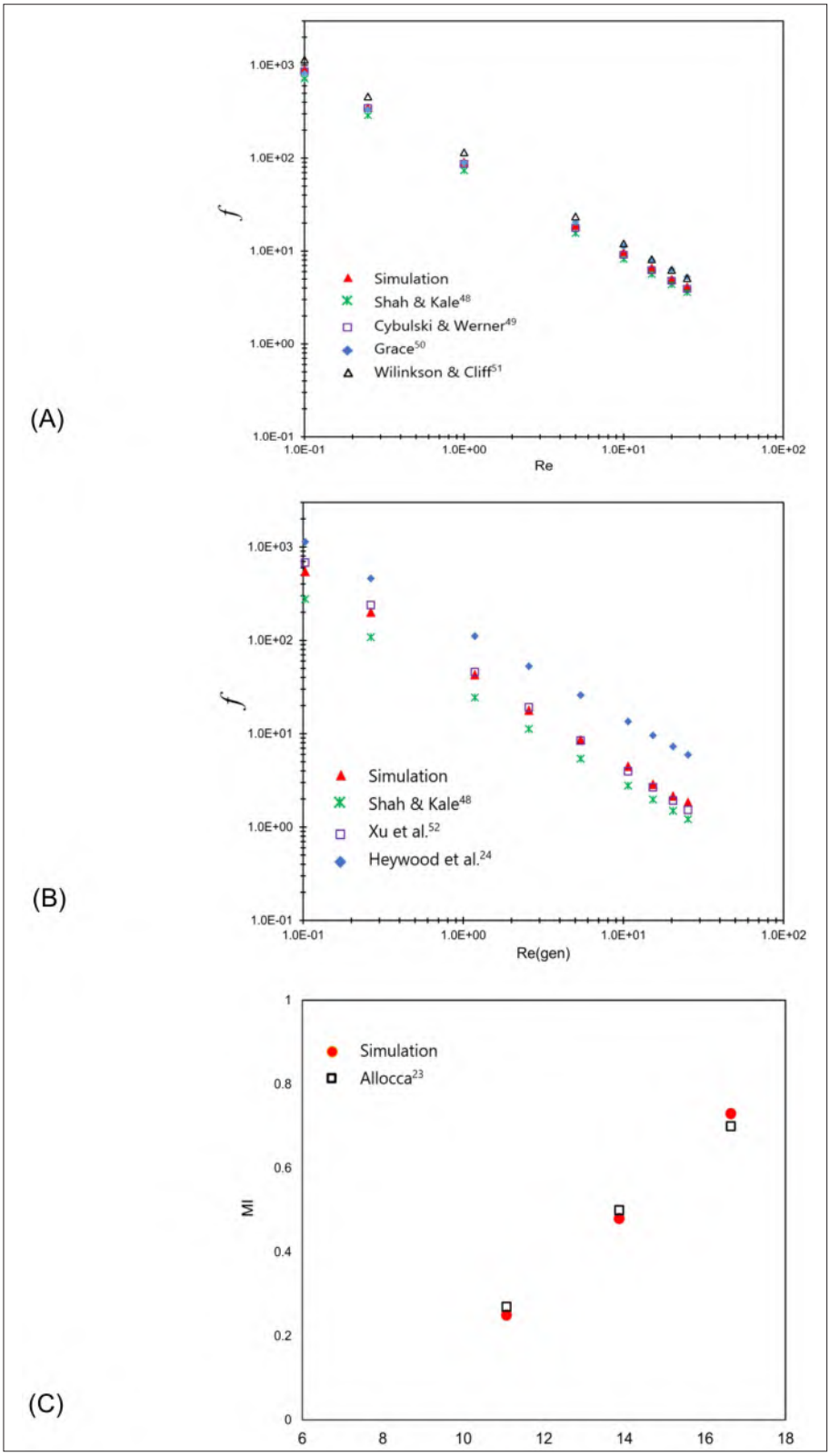


Figure 5. Validation of computational fluid dynamics (CFD) results: Comparison of friction factor predicted by numerical simulations and empirical correlations for (A) Newtonian fluid, (B) for non-Newtonian fluid, and (C) comparison of the mixing index predicted by CFD with the experimental results of Alloca.[23]

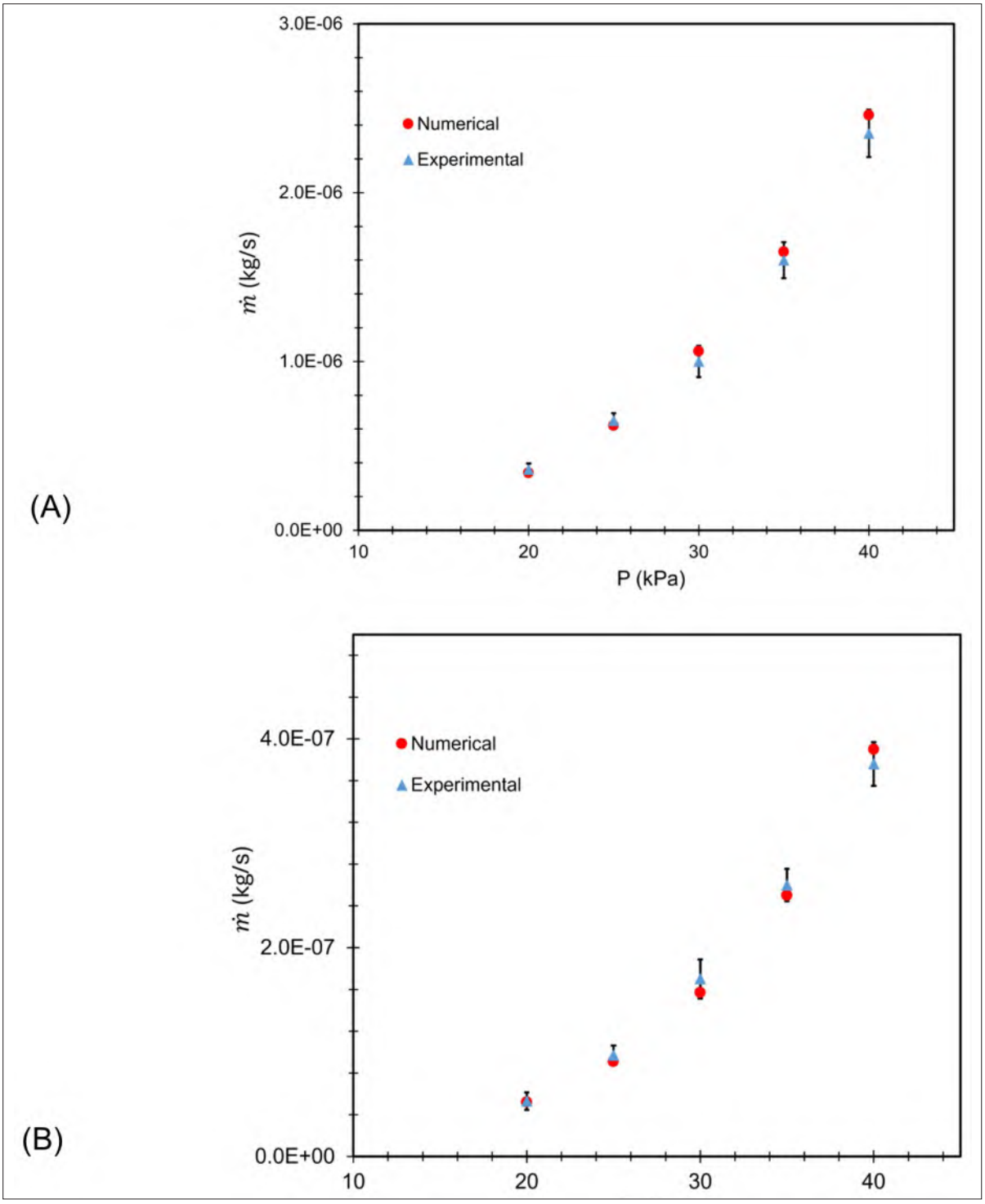


Figure 6. Validation of computational fluid dynamics (CFD) results: Comparison of flow rate predicted by CFD and experimental measurements for the flow of (A) 3% alginate and (B) 4% alginate solutions driven by various upstream pressures.

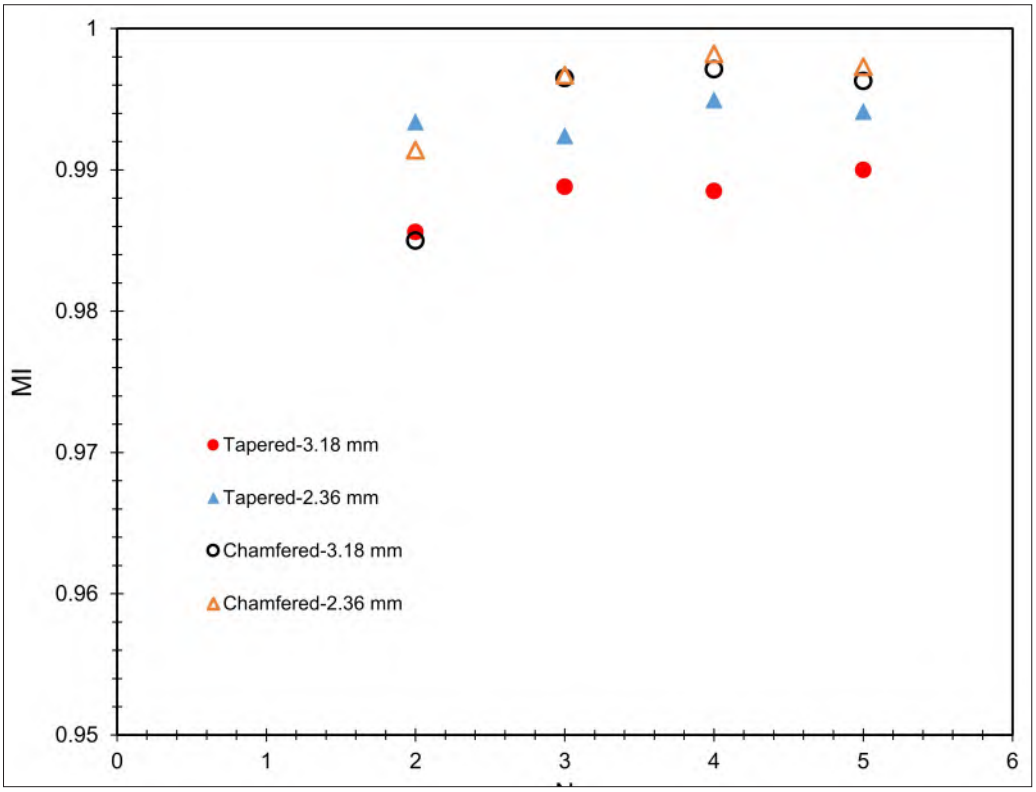


Figure 7. Variation of mixing index (MI) with the number of mixing elements for designs with tapered and chamfered nozzles of different diameters.

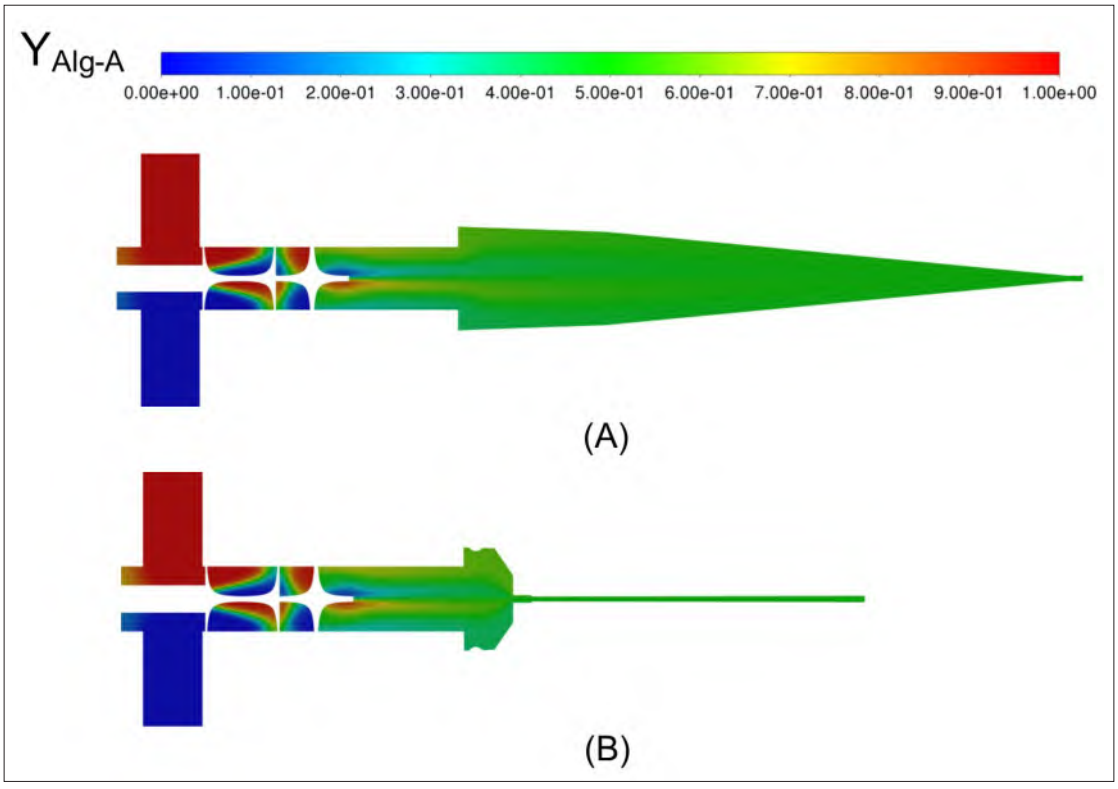


Figure 8. Distribution of alginate-A inside the heads with (A) tapered and (B) chamfered nozzles. Contours are shown on the middle plane of the geometry.

Table 5. Estimated mixing and residence times for 4% alginate solutions through helical mixers (based on Section 2.1)

Number of elements	t_{mix} (s)	t_{res} (s)
2	446.3	68.5
3	111.6	102.8

primarily determines the level of process-induced forces that may affect cell viability during bioprinting.

The distribution of alginate-A inside the multi-material heads, shown in Figure 11, supports the estimations made in Table 3. It demonstrates that the mixing process is almost complete immediately after the third mixing element, with no additional length inside the nozzle required to achieve homogeneity. In other words, with three mixing elements, the influence of nozzle geometry on mixing is minimal. However, the nozzle geometry still affects both the maximum shear stress and the internal volume of the head. As a custom geometry, the conical nozzle is not subject to the size limitations of standard Luer tapered and chamfered nozzles and can be fabricated in arbitrary dimensions. Nevertheless, to avoid excessively narrow flow passages—which would compromise the meso-scale advantage of the multi-material head over micro-scale systems—conical nozzles with outlet diameters of 2.36 and 1.8 mm were selected as candidates for the modified geometry.

Figure 12A compares the MI values for combinations of three mixing elements with 2.36 and 1.8 mm conical nozzles, each with various length-to-diameter ratios ($\frac{l}{d}$). The results show that all tested length-to-diameter ratios yield a homogeneous mixture at the outlet. Once complete mixing is achieved by the three helical elements, the conical nozzle geometry has little effect on the MI. Therefore, MI alone is insufficient for determining the optimal length-to-diameter ratio of the conical nozzle.

Figure 12B and C compares the internal volume ($\mathbb{V}_{head}$) and the maximum shear stress for different nozzle configurations, respectively. Figure 12B shows that changes in the length-to-diameter ratio have only a minor impact on the internal volume. In contrast, Figure 12C shows that the maximum shear stress decreases significantly for $\frac{l}{d} \leq 1.5$, and then levels off for both sizes of mixing elements. Based on the insights from Figure 12A–C, it can be concluded that a head equipped with three 1.8 mm mixing elements and a conical nozzle with $\frac{l}{d} = 1.5$ effectively mixes two 4% alginate streams while maintaining relatively small internal volume and a maximum shear stress comparable to that of a tapered nozzle—currently considered the most favorable option for preserving cell viability. Accordingly, this configuration was chosen as the optimized head geometry for printing biomaterials with properties similar to 4% alginate.

Various criteria have been proposed in the literature[22,70,71] to predict the effect of process-induced forces on cell viability. While cell viability depends on multiple factors, examining the shear stress distribution during the flow of 4% alginate—which is highly viscous and less ideal for cell-laden bioprinting—can help guarantee that shear stress remains within a tolerable range for lower-viscosity biomaterials, such as 2.5 or 3% alginate solutions, which are more suitable for encapsulating cells. The maximum shear stress values shown in Figure 12C are significantly lower than the critical thresholds reported in the literature for potential cell damage, such as for Rat L929 or RAMEC cell lines.[22,70] Therefore, the improved multi-material head geometry is expected to support good cell viability during extrusion. Nevertheless, cell viability is influenced by several factors, such as stress magnitude and duration, cell type, and the physical properties of the biomaterial, and must be evaluated experimentally.[22,70,71] Accordingly, laboratory-based investigations are necessary to draw reliable conclusions about cell viability during and after multi-material extrusion.

While the improvements to the multi-material head were based on numerical simulations involving the mixing of two 4% alginate streams, experimental evaluation of its performance in bioprinting other materials is necessary to assess its broader applicability and limitations. As a case study, multi-material bioprinting using alginate and CMC solutions was conducted to evaluate the performance of the modified head in controlled composition gradient printing.

3.4. Multi-material bioprinting of alginate and carboxymethylcellulose solutions

Mixing 4% alginate and 1% CMC solutions at different ratios was considered a practical case to examine the performance of the modified multi-material head for on-the-fly mixing in controlled-gradient bioprinting. The fiber composition at the outlet is controlled by manipulating the inlet flow rates of the biomaterials, which determine the precursor mixing ratio. This manipulation is achieved by adjusting the α value, which defines the mass flow rates at the inlets according to **Equations XV, XIV, XIII, and XII**. For the mixing of 4% alginate and 1% CMC solutions, the reference parameters are:

$$\psi_{ref} = 4,\ \alpha_{ref} = 1,\ \beta_{ref} = 1 \qquad \text{(XXXVII)}$$

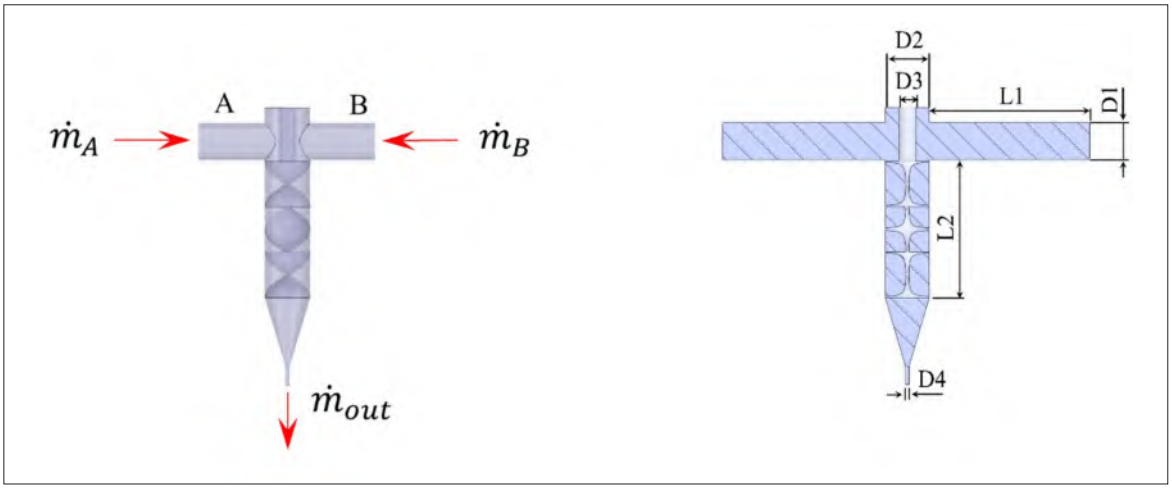


Figure 9. Fluid domain geometry inside the multi-material head with helical mixer connected to a conical nozzle. Fluid domain (left); symmetry plane section with dimensions (right).

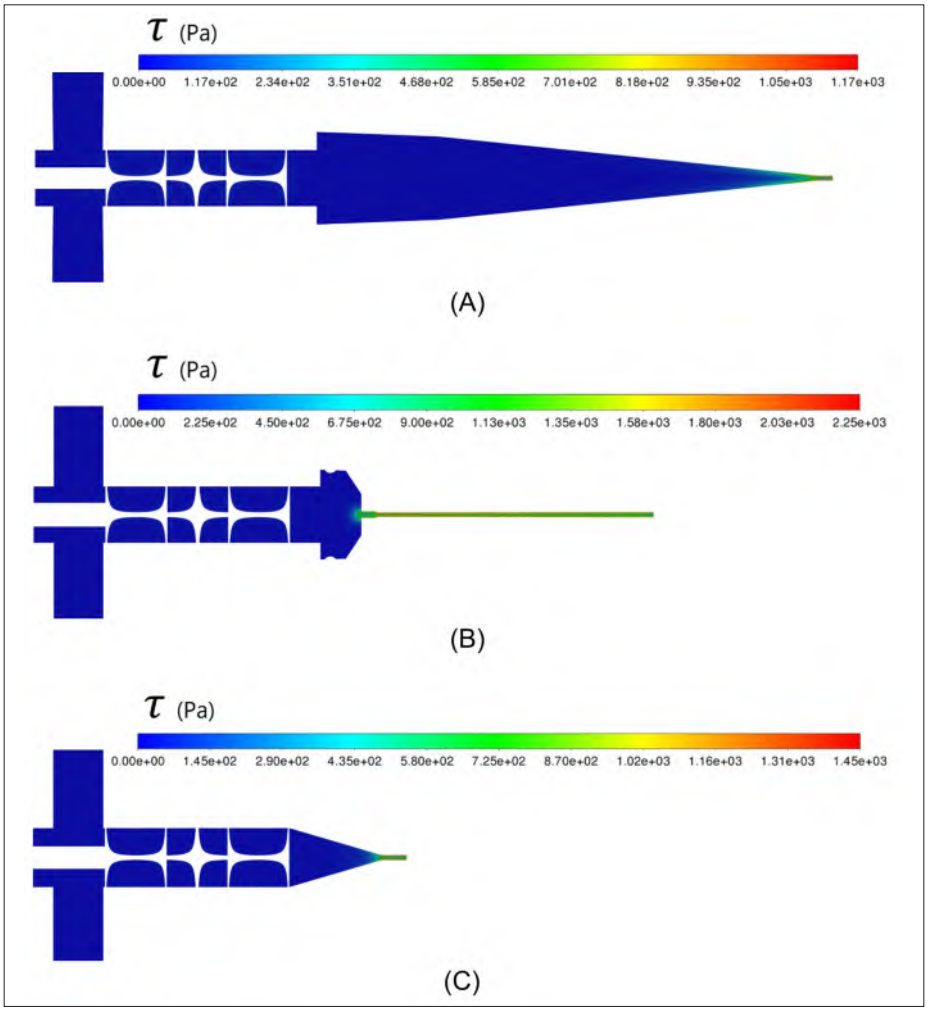


Figure 10. Shear stress distribution for (A) tapered, (B) chamfered, and (C) conical nozzles with d = 2.36 mm. Contours shown on the symmetry plane.

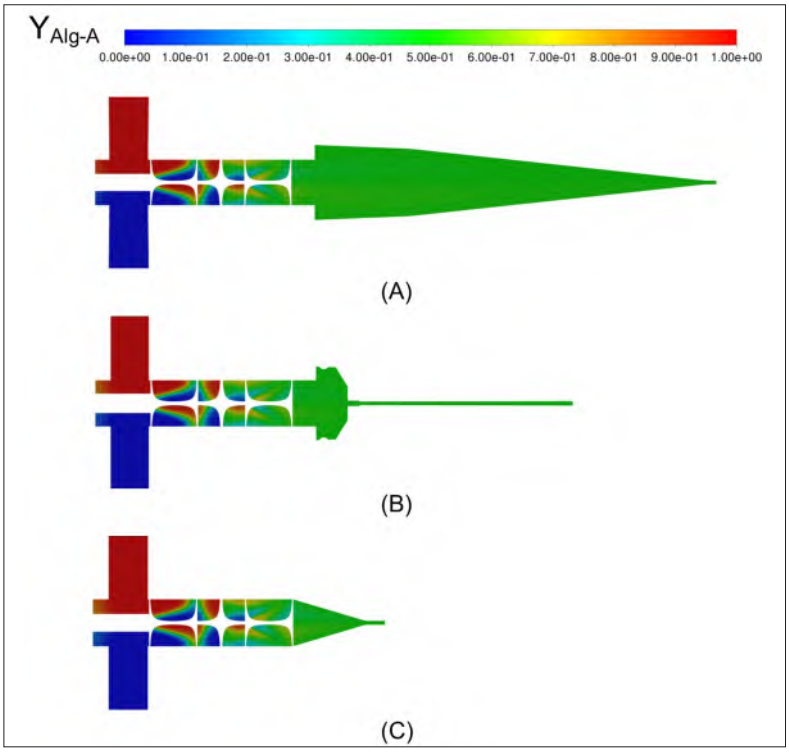


Figure 11. Distribution of alginate-A mass fraction inside the heads with (A) tapered, (B) chamfered, and (C) conical nozzles. Contours shown on the symmetry plane.

Figure 13 illustrates the distribution of alginate and CMC mass fractions inside the head for three different mixing scenarios, each with a distinct α value. The figure qualitatively demonstrates the capability of a multi-material head equipped with helical mixers to combine two biomaterials with different flow rates. Figure 14 provides a more quantitative assessment by comparing MI values across various α values and printing speeds. The results confirm the head's ability to achieve adequate mixing of 4% alginate and 1% CMC solutions over a wide range of ratios, even at a relatively high printing speed of 10 mm/s, which is significant for multi-material bioprinting.[26,72] As expected, slower printing speeds result in lower total flow rates and longer residence times, which facilitate mixing. Therefore, reducing the printing speed to 5 mm/s improves mixing for all tested conditions. Figure 14 also shows improved mixing performance for $\alpha > 1$, representing compositions with higher alginate content. This observation is consistent with previous findings by Jaffer and Wood[73] and Regner et al.,[74] who studied the mixing of Newtonian fluids with varying viscosities using helical mixers and Lightnin Series 45 mixers. While these mixers differ slightly in geometry, their functionality is comparable to that of helical mixers.

One particularly interesting operational mode for a multi-material bioprinting head is the ability to generate controlled composition gradients within a scaffold—essential for creating zonal heterogeneity. As previously discussed, the key factor in controlled composition gradient printing is the transition time required to fully shift from one composition to another at the outlet.

To evaluate this, numerical simulations of unsteady mixing and extrusion were conducted for various composition transitions relative to the reference case (i.e., various α values). Figure 15 illustrates the temporal variation of the normalized concentration ratio, $\frac{\psi}{\psi_{ref}}$, for transitions from $\alpha = 1$ to other values at printing speeds of 10 and 5 mm/s. Time is normalized by the sweep time (t_s), defined as the time to displace the internal volume of the head with the total flow rate (or outlet flow rate):

$$t_s = \frac{\mathbb{V}_{head}}{Q_{out}} \quad \text{(XXXVIII)}$$

Surprisingly, despite the differences in precursor velocities and mixture viscosities, the first deviation from the initial composition consistently occurs at the same interval (t_0), approximately 20–25% of the sweep

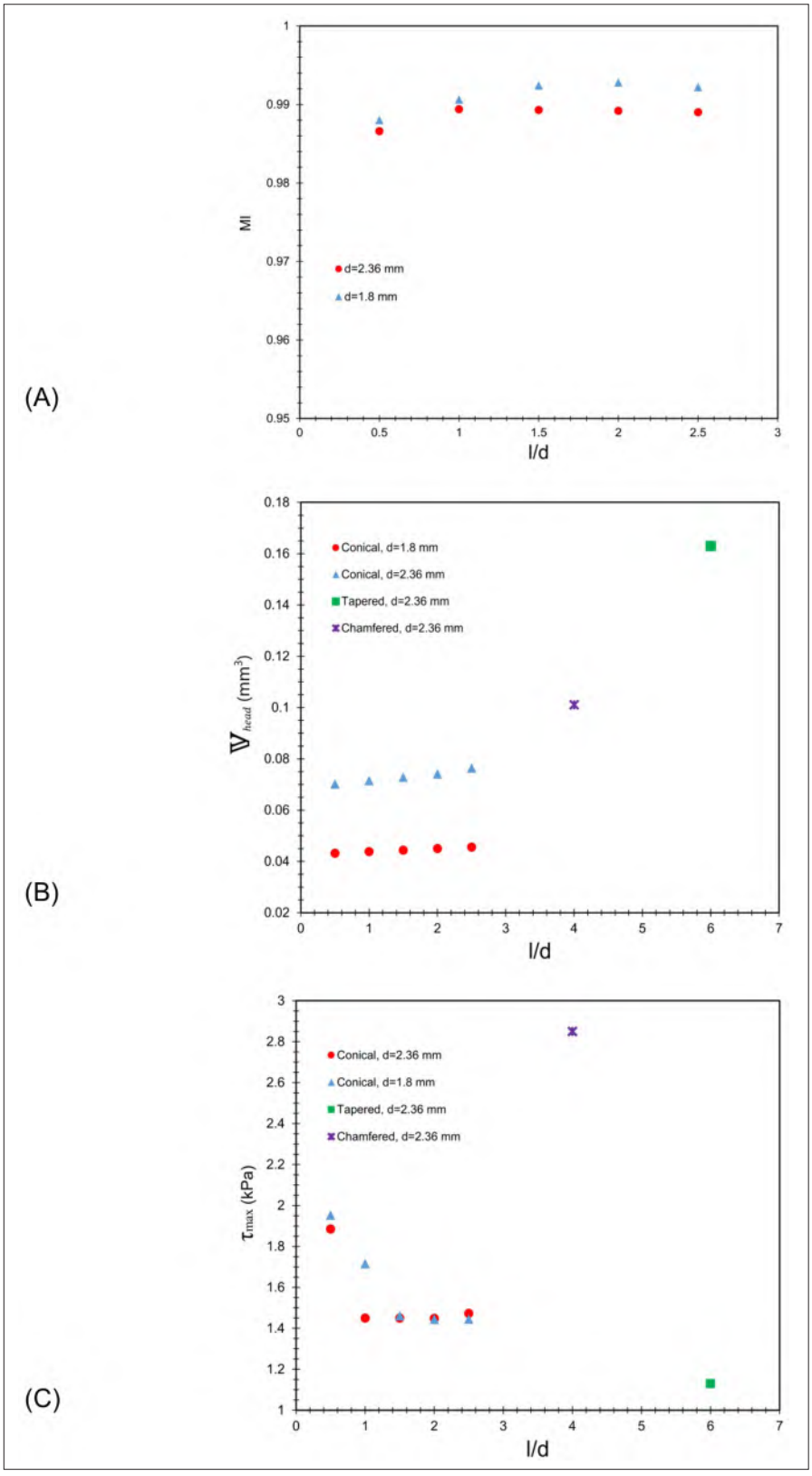


Figure 12. Effect of conical nozzle length-to-diameter ratio (l/d) on key parameters affecting performance in multi-material bioprinting with composition gradients. (A) Mixing index (MI), (B) internal volume, and (C) maximum shear stress.

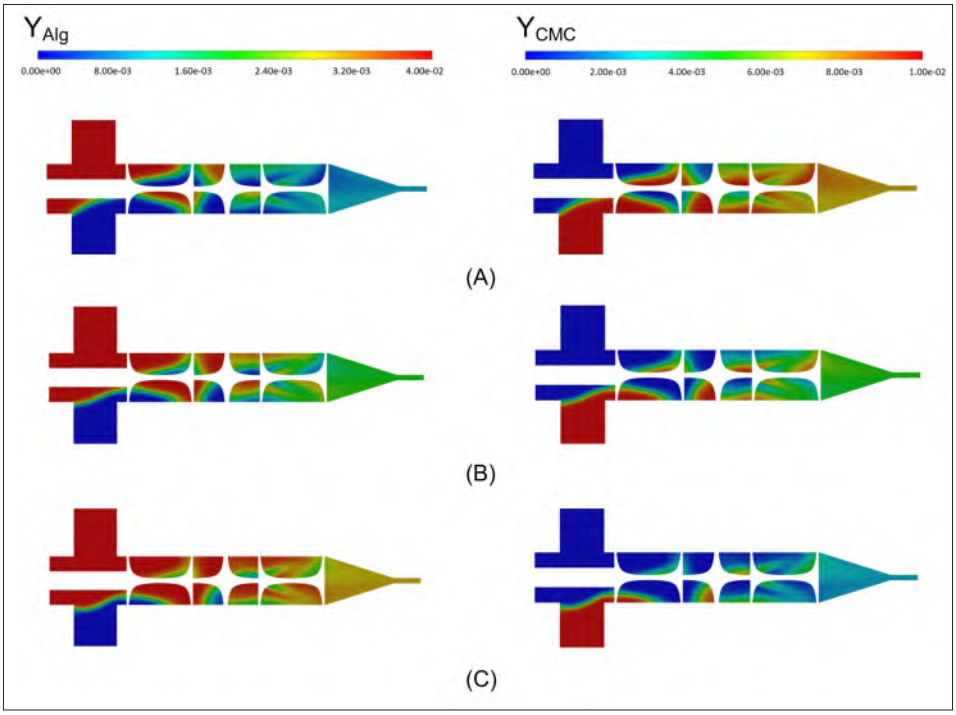


Figure 13. Distribution of mass fractions of (left) alginate and (right) carboxymethylcellulose during multi-material bioprinting for (A) α = 0.5, (B) α = 1, (C) α = 1.5.

time. Since this initial delay is predictable, its effect on composition control can be eliminated by advancing the inlet flow rate changes by t_0. However, the overall transition time for composition change is longer and varies across different mixing scenarios. Figure 16 shows the variation in MI for cases corresponding to Figure 15. The initial delay is clearly visible, followed by a dip in MI, with a minimum occurring 35–50% of the sweep time. This minimum homogeneity point is important for toolpath design, as significant drops in MI (especially below 0.95) may lead to precursor separation and the formation of streaky fibers (Figure 1). For applications requiring high structural integrity, this point should be carefully considered—particularly if it occurs at a scaffold surface, where it may compromise mechanical performance under shear or frictional stress. Following the minimum, MI increases monotonically until it reaches a steady-state value. For the 5mm/s printing speed cases shown in Figures 15 and 16, the initial delay again occurs around 20–25% of the sweep time, and the minimum homogeneity point arises at a similar sweep time fraction as in the 10 mm/s case. However, due to the longer residence time at 5 mm/s, the outflow stream becomes more thoroughly mixed, rendering the minimum homogeneity point less critical. Figures 15B and 16B illustrate changes in ψ and MI for reverse transitions, i.e., from different α values back to α = 1. Compared to Figures 15A and 16A, these represent reciprocal composition changes between high and low alginate or CMC concentrations, which may occur during controlled-gradient multi-material bioprinting. Notably, the initial delay remains consistent across all reverse cases, just as it does in the forward transitions. The minimum homogeneity point also occurs within a similar sweep time range.

The transition time for a composition change can be calculated based on either the MI or the outlet concentration ratio (ψ). However, as shown in Figure 16, most cases—except for the transition from α = 1→0.5 with V = 10 mm/s—remain within the fully mixed region (MI > 0.95), where the MI threshold is insufficient to define transition time. Therefore, transition time was instead calculated based on the outlet concentration ratio ψ, adopting a 5% deviation from the final (target) value as criterion. Figure 17 reports the transition times for various composition changes. The results show that transition times are almost identical for both forward and reverse transitions when $\alpha \geq 1$. However, for $\alpha \leq 1$, transitions toward higher alginate content (i.e., $\alpha \rightarrow 1$) have shorter transition times compared to the reverse direction (i.e., $1 \rightarrow \alpha$).

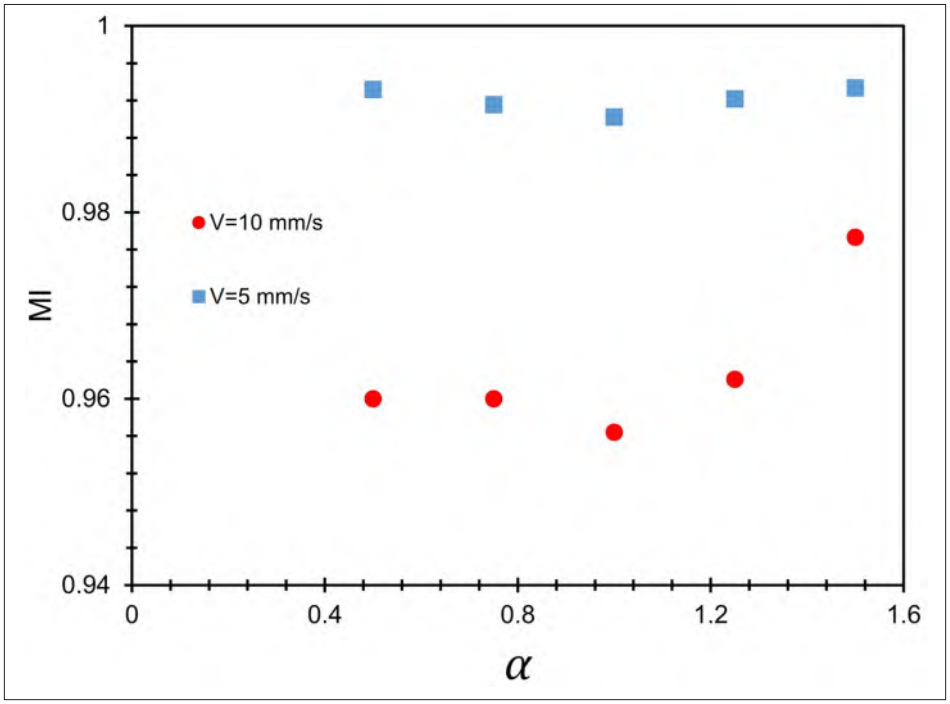


Figure 14. Variation of mixing index (MI) with alginate flow ratio (α) under different printing speeds.

Using a particle tracking method, Regner et al.[74] defined separate residence times for each component of a mixture and showed that, during transient flow, the more viscous precursor exhibits a longer residence time compared to the less viscous one. Moreover, this residence time difference increases with the viscosity ratio of the two precursors. Neglecting surface tension effects and assuming equal shear stress across the interface between the precursor streams, the stream with lower apparent viscosity experiences a higher shear rate, leading to greater stretching and the formation of thinner striations. This enhances mixing within the helical mixer, as previously explained by Jaffer and Wood[73] in the context of Newtonian fluid mixing. For the shear-thinning biomaterials used in the current study, a higher shear rate in the low-viscosity CMC stream further reduces its apparent viscosity, promoting even more stretching on that side of the interface. Additionally, increasing the flow rate of the more viscous precursor (alginate) while maintaining the same total flow rate increases the velocity and shear rate differences at the interface. This leads to finer striations of the lower-viscosity precursor (CMC) and thus better mixing. Since transition time is determined based on reaching the target composition (ψ), improved mixing translates into a shorter transition time.

The effective shear rate for flow inside a helical mixer can be estimated as[43]:

$$\dot{\gamma}_{eff} = \frac{112\ Q}{\pi\ d^3} \qquad \text{(XXXIX)}$$

This effective shear rate is used to calculate the characteristic apparent viscosity of each biomaterial solution (via **Equation XXIX**) and of the mixture (using **Equations XXX–XXXII**) inside the printing head with a helical mixer. Figure 18 presents the apparent viscosity of various alginate–CMC solutions under effective shear rates corresponding to printing speeds of 10 and 5 mm/s. An increase in ψ reflects a higher alginate concentration in the printed fiber and also a higher α value (see **Equation XV**). As shown in Figure 18, higher ψ or α values are associated with alginate–CMC solutions with higher apparent viscosity. Accordingly, the results in Figures 14–17 suggest improved mixing performance for outlet mixtures with higher apparent viscosity. In practical terms, adjusting the toolpath in controlled-gradient multi-material bioprinting to follow a positive viscosity gradient can shorten the transition time. This holds true when increasing the mass fraction of one precursor (i.e., increasing α or β) results in a noticeable increase in the apparent viscosity of the mixture within the effective shear rate range, as shown in Figure 18. However, printing along a positive viscosity gradient may deform lower scaffold layers or cause mechanical failure. Therefore, appropriate

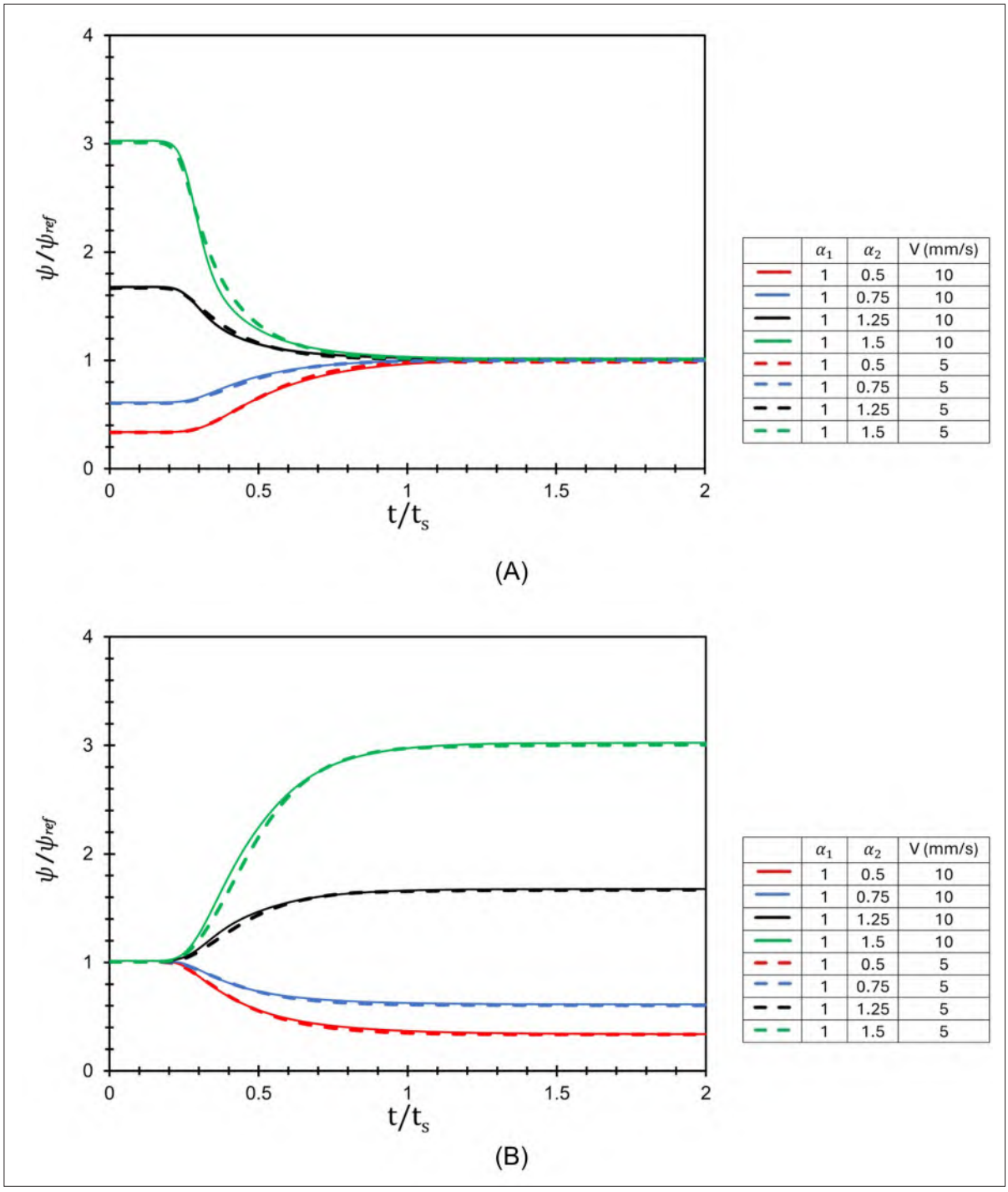


Figure 15. Temporal variation of normalized concentration ratio for various composition changes: (A) $\alpha_1 \rightarrow \alpha_2$, (B) $\alpha_2 \rightarrow \alpha_1$.

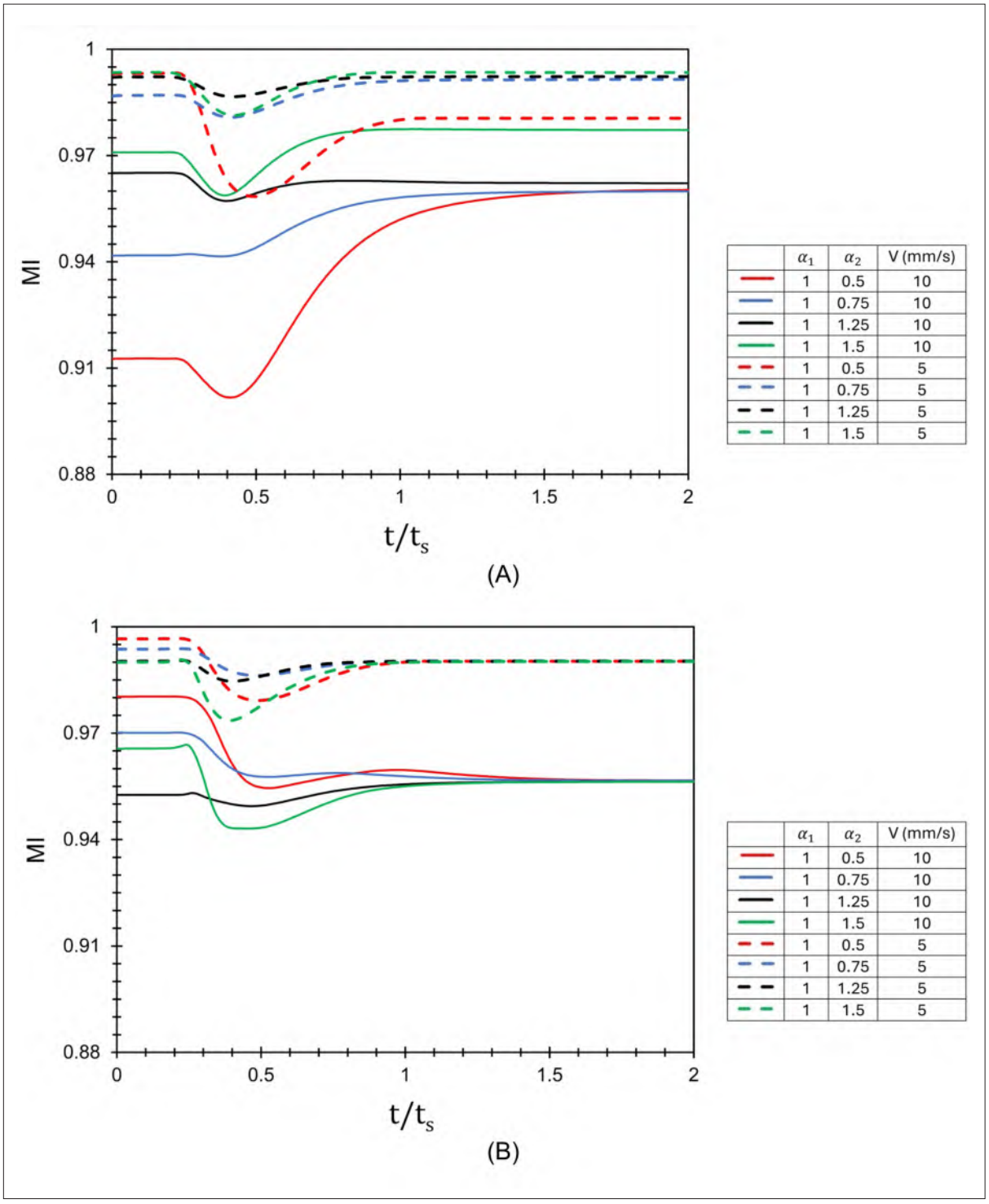


Figure 16. Temporal variation of mixing index (MI) for composition changes: (A) $\alpha_1 \rightarrow \alpha_2$, (B) $\alpha_2 \rightarrow \alpha_1$.

crosslinking of the lower layers is required to maintain the structural integrity of the scaffold.

As an extreme test case, the head was examined for a composition change from α = 0.5 to α = 1.5, and vice versa, representing a significant change in composition (between ψ = 1.33 and ψ = 12). Figure 19A and B illustrates the corresponding outflow stream composition and MI from CFD simulations. The initial delay and minimum homogeneity points are almost identical to those observed in Figures 15 and 16, confirming that these characteristics are independent of the initial and target compositions. The transition times for α = 0.5 → 1.5 and its reverse case are shown in Figure 17, alongside other scenarios. Comparing these results confirms that transitions toward higher-viscosity compositions result in shorter transition times.

The transition times shown in Figure 17 can be further reduced by advancing the flow rate changes based on the initial delay (t_0). When transition time is multiplied by the printing speed, it yields the transition length, representing the spatial resolution of the printer for printing fibers with composition gradients (neglecting the delay in mechanical and electrical control systems). To highlight the improvement in spatial resolution, Table 6 presents the relative change in spatial resolution (transition length) resulting from advancing the inlet flow rate changes by $t_0 = 0.2t_s$. The table shows a 17–30% improvement in the spatial resolution of the composition gradient. The smallest improvement occurs in the extreme case with a negative viscosity gradient ($\alpha = 1.5 \rightarrow 0.5$), while the largest improvements are observed for moderate composition changes in the $\alpha \geq 1$ range ($\alpha = 1 \leftrightarrows 1.25$).

Comparing the normalized transition time values for various composition changes in Figure 17—and considering the overall insights from the computational results—it can be concluded that adjusting the overall print direction toward a higher fraction of the more viscous precursor can improve the spatial resolution of controlled composition gradient printing. To ensure precise control over fiber composition and to improve the spatial resolution of composition gradients in multi-material bioprinting, the following steps are recommended:

(i) If increasing the mass fraction of one precursor effectively enhances the apparent viscosity of the mixture (calculated based on effective strain rate from **Equation XXXIX**), and if printability considerations (i.e., structural integrity) allow, adjust the printing direction in the toolpath to produce a predominantly positive gradient in apparent viscosity along the fiber.

(ii) Calculate ψ_{ref} using **Equation IX**, based on the mass fractions of the precursors.

(iii) Select a suitable printing speed, then calculate the reference inlet flow rates using **Equations V and VIII**. Calculate the corresponding reference mass

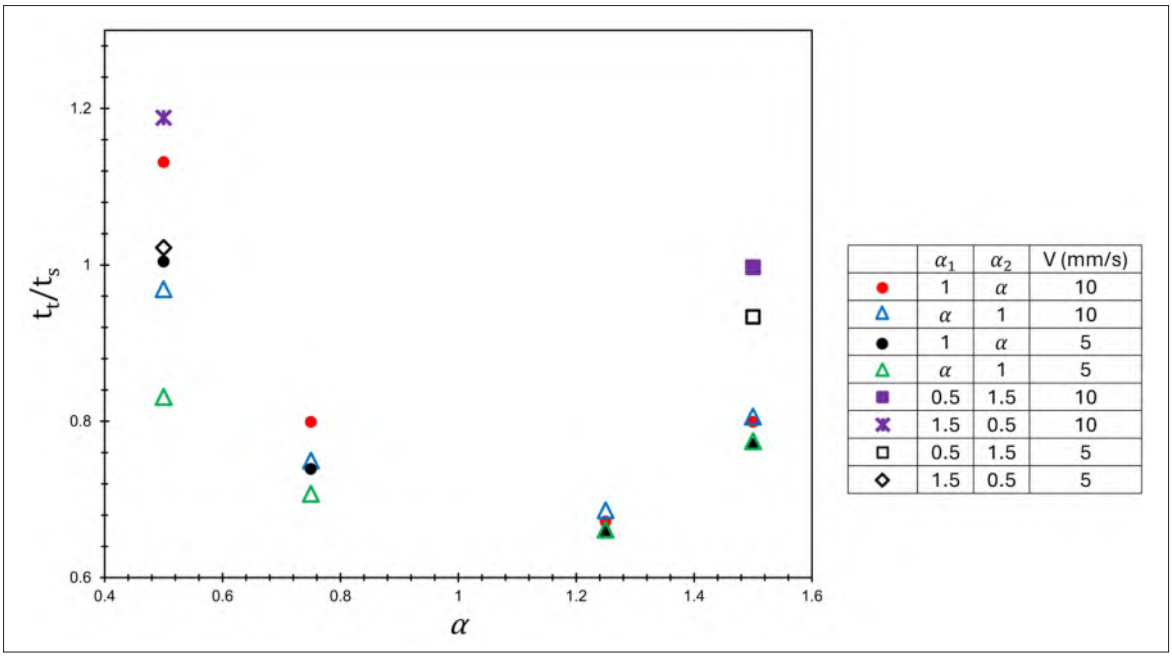


Figure 17. Variation of normalized transition time for different composition changes.

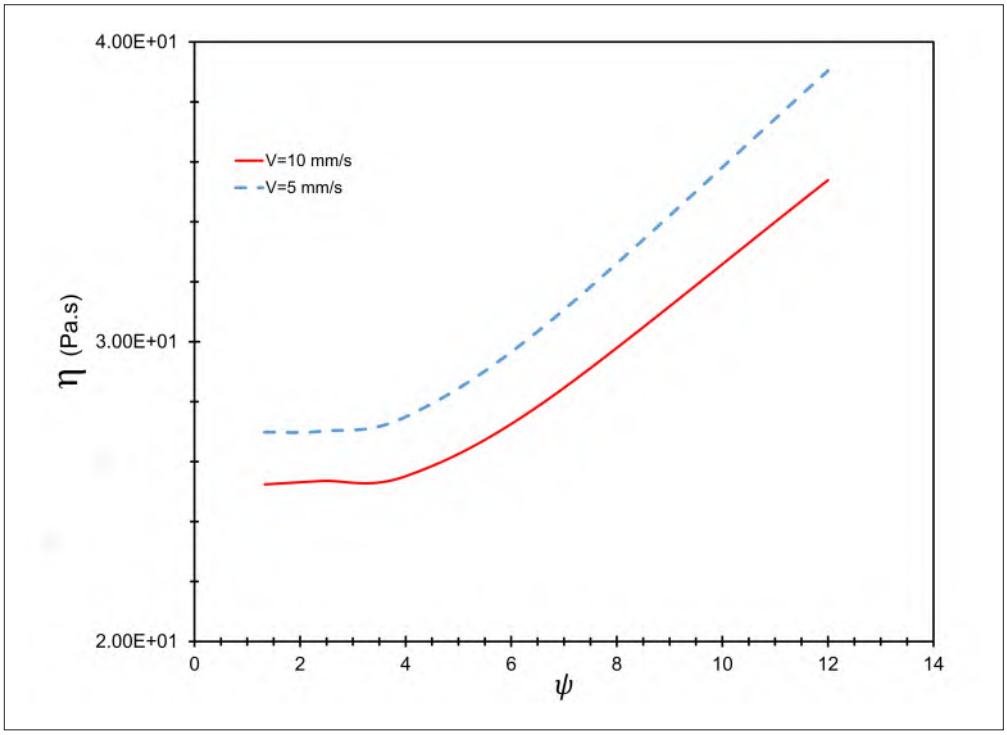


Figure 18. Apparent viscosity of alginate–carboxymethylcellulose solutions with various concentration ratios under effective shear rates corresponding to different printing speeds.

fractions at the outflow stream using **Equations X and XI**.

(iv) If the reference composition, characterized by ψ_{ref}, differs from the intended fiber composition, calculate the required α and β using **Equation XV** to achieve the target concentration ratio (ψ) at the outflow. Then, calculate the corresponding inlet flow rates using **Equations XII and XIII**.

(v) During the printing process, dynamically adjust the fiber composition by updating α and β, which determines the inlet mass flow rates based on **Equations XII and XIII**.

(vi) Advance each change in α and β by the delay time t_0, as predicted by CFD simulations, to improve the spatial resolution of the resulting composition gradient.

For multi-material bioprinting with precursors other than alginate–CMC, the initial delay time may differ from the range identified in this study (0.2–0.25 t_s) and should be determined based on CFD simulations tailored to the specific precursors.

If there is flexibility in selecting the mass fractions at the inlets, using precursor streams with smaller differences in apparent viscosity (calculated at the effective shear rate) can facilitate more efficient mixing in the helical mixer.[74] Additionally, when consecutive changes in fiber composition are required, careful selection of inlet mass fractions can help set a reference point near the midpoint of the overall composition range, thereby preventing large, abrupt changes in composition. For example, if the overall composition range falls ψ = 6–12, selecting a reference point at ψ = 9—the midpoint—can lead to shorter transition delays and better control over the composition gradient within the printed scaffold. This is because the selected reference point results in moderate mass fractions at the inlet (determined using **Equations XII–XV**), which in turn require minimal adjustments to achieve the full range of intended composition change during printing.

The applicability of the analyses presented in this study relies on the prior assumption that all intended compositions are printable under appropriate printing conditions, as established in **Section 2.7**. However, in real-world applications involving diverse biomaterials—many of which exhibit viscoelastic and thixotropic behavior—the stress history during mixing can influence both printability and cell viability,[75,76] potentially resulting in discrepancies between experimental outcomes and the computational simulations and analyses presented in this study.

Table 6. Relative improvement in spatial resolution of the composition gradient when advancing flow rate changes by $t_0 = 0.2t_s$

α_1	α_2	Relative improvement $\left(\frac{\Delta \ell_t}{\ell_t}\right)$			
		V = 10 mm/s		V = 5 mm/s	
		$\alpha_1 \rightarrow \alpha_2$	$\alpha_2 \rightarrow \alpha_1$	$\alpha_1 \rightarrow \alpha_2$	$\alpha_2 \rightarrow \alpha_1$
1	0.5	0.18	0.21	0.20	0.24
1	0.75	0.25	0.27	0.27	0.28
1	1.25	0.30	0.29	0.30	0.30
1	1.5	0.25	0.25	0.26	0.26
0.5	1.5	0.20	0.17	0.21	0.19

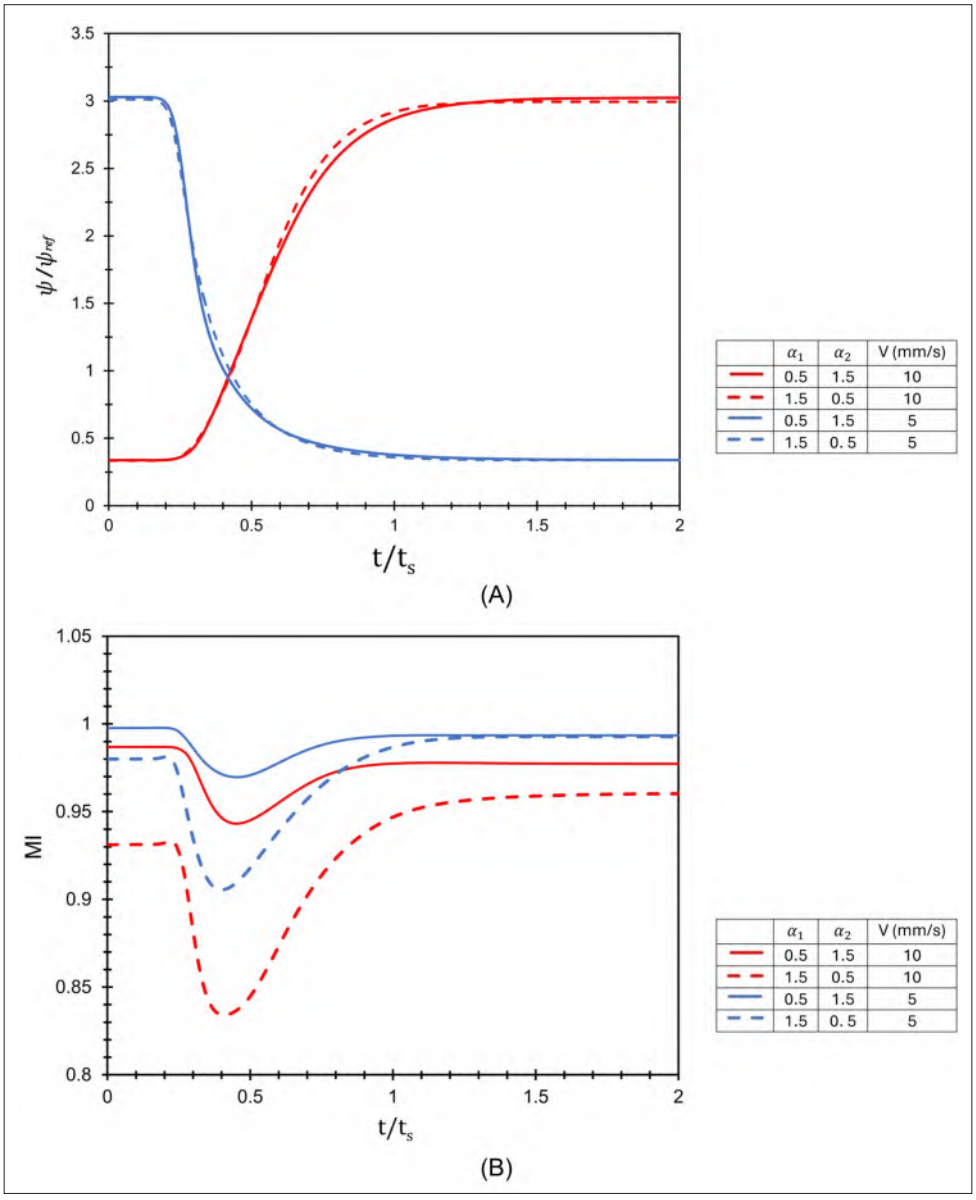


Figure 19. Temporal variation of (A) normalized concentration ratio and (B) mixing index (MI) for extreme composition changes.

Moreover, the computational and mathematical models used in this study do not account for complex cell–biomaterial interactions during mixing within the print head or during the crosslinking process after fiber deposition. Therefore, the performance of the designed multi-material bioprinting head should be experimentally validated. This involves fabricating the designed head, integrating it into a bioprinting system, printing multi-material fibers, and assessing both printability and cell viability in the printed constructs.

4. Conclusion

Multi-material bioprinting with controlled composition gradients is a promising approach for accurately replicating the heterogeneous structures of native tissues in printed constructs. Despite its potential, comprehensive studies on the performance of printing heads equipped with helical static mixers for this application remain limited. This study aimed to address this gap by investigating biomaterial mixing and exploring design modifications and flow control strategies to enhance the spatial resolution of composition gradients. CFD simulations served as the primary tool for this investigation and were validated against experimental data. Based on these validated simulations, a multi-material bioprinting head with a helical mixer was designed. The CFD results revealed the effects of various geometrical parameters on mixing performance, process-induced forces, and internal volume.

A mathematical framework was developed to describe the characteristic parameters governing the outflow conditions during composition changes. While the head geometry was optimized using numerical simulation involving two 4% alginate aqueous solutions, further evaluation using alginate–CMC aqueous mixtures demonstrated the head's capability to print fibers with controlled composition gradients. A composition- and temperature-dependent Cross non-Newtonian viscosity model was fitted to rheological test data of various alginate–CMC aqueous solutions to relate their apparent viscosity to precursor mass fractions across a range of temperatures. Although the numerical simulations of multi-material bioprinting addressed alginate–CMC systems, the insights gained are broadly applicable to the design and operation of multi-material heads for gradient-based bioprinting.

Numerical results for mixing 4% alginate and 1% CMC aqueous solutions demonstrated that the transition time for composition changes includes an initial delay of about 20–25% of the sweep time. A streaky pattern with reduced homogeneity may appear in the printed fiber for 35–50% of the sweep time. Lower printing speeds can mitigate this issue by increasing residence time and promoting more thorough mixing. Based on numerical results covering a wide range of fiber composition changes, an algorithm was developed to improve control over composition gradients in multi-material bioprinting by reducing transition time. Specifically, for bioprinting with 4% alginate and 1% CMC aqueous solutions, combining the modified head geometry with an adjustment of inlet flow rate timing (to account for the initial delay) resulted in a 17–30% improvement in the spatial resolution of composition gradients. Additionally, designing the toolpath to follow a positive gradient in apparent viscosity further improved gradient resolution.

While real-world multi-material bioprinting involves diverse biomaterials with varying properties, CFD simulations offer valuable insights into processes involving controlled composition gradients. In practical applications, CFD can predict outcomes such as MIs, transition times, and flow dynamics, guiding adjustments to enhance spatial resolution along the fiber. However, the actual performance of the bioprinting head should be validated experimentally. This requires fabricating the prototype, integrating it into a bioprinting system, and assessing both printability and cell viability in the printed constructs.

Acknowledgments

The authors extend their appreciation to the GESIM company for sharing the technical datasheets of the GESIM Bioscaffolder.

Funding

This work was supported by the University of Saskatchewan Dean's Scholarship and the Devolved Scholarship from the Department of Mechanical Engineering for the first author, and by the Natural Sciences and Engineering Research Council (NSERC) funds (Grant numbers: RGPIN 06396-2019, RGPIN 04981-2022) for the co-authors.

Conflict of interest

Xiongbiao Chen serves as the Editorial Board Member of the journal, but did not in any way involve in the editorial and peer-review process conducted for this paper, directly or indirectly. Other authors declare they have no competing interests.

Author contributions

Conceptualization: All authors
Formal analysis: Reza Gharraei
Funding acquisition: Xiongbiao Chen, Donald J. Bergstrom

Investigation: Reza Gharraei
Methodology: Reza Gharraei
Validation: Reza Gharraei
Supervision: Xiongbiao Chen, Donald J. Bergstrom
Writing–original draft: Reza Gharraei
Writing–review & editing: All authors

Ethics approval and consent to participate

Not applicable.

Consent for publication

Not applicable.

Availability of data

Data is available from the corresponding author upon reasonable request.

References

1. Ozbolat IT, Moncal KK, Gudapati H. Evaluation of bioprinter technologies. *Addit Manuf*. 2017;13:179-200. doi: 10.1016/j.addma.2016.10.003
2. Levato R, Jungst T, Scheuring RG, Blunk T, Groll J, Malda J. From shape to function: the next step in bioprinting. *Adv Mater*. 2020;32(12):1906423. doi: 10.1002/adma.201906423
3. Rutz AL, Hyland KE, Jakus AE, Burghardt WR, Shah RN. A multimaterial bioink method for 3D printing tunable, cell-compatible hydrogels. *Adv Mater*. 2015;27(9):1607-1614. doi: 10.1002/adma.201405076
4. Chen XB, Fazel Anvari-Yazdi A, Duan X, et al. Biomaterials/bioinks and extrusion bioprinting. *Bioact Mater*. 2023;28:511-536. doi: 10.1016/j.bioactmat.2023.06.006
5. Sodupe-Ortega E, Sanz-Garcia A, Pernia-Espinoza A, Escobedo-Lucea C. Accurate calibration in multi-material 3D bioprinting for tissue engineering. *Materials*. 2018;11(8):1402. doi: 10.3390/ma11081402
6. Betancourt N, Chen X. Review of extrusion-based multi-material bioprinting processes. *Bioprinting*. 2022;25:e00189. doi: 10.1016/j.bprint.2021.e00189
7. Wei Q, Zhou J, An Y, Li M, Zhang J, Yang S. Modification, 3D printing process and application of sodium alginate based hydrogels in soft tissue engineering: a review. *Int J Biol Macromol*. 2023;232:123450. doi: 10.1016/j.ijbiomac.2023.123450
8. Kang HW, Lee SJ, Ko IK, Kengla C, Yoo JJ, Atala A. A 3D bioprinting system to produce human-scale tissue constructs with structural integrity. *Nat Biotechnol*. 2016;34(3):312-319. doi: 10.1038/nbt.3413
9. Ozbolat IT, Hospodiuk M. Current advances and future perspectives in extrusion-based bioprinting. *Biomaterials*. 2016;76:321-343. doi: 10.1016/j.biomaterials.2015.10.076
10. Liu W, Zhang YS, Heinrich MA, et al. Rapid continuous multimaterial extrusion bioprinting. *Adv Mater*. 2017;29(3):1604630. doi: 10.1002/adma.201604630
11. Wei Q, An Y, Zhao X, Li M, Zhang J. Three-dimensional bioprinting of tissue-engineered skin: Biomaterials, fabrication techniques, challenging difficulties, and future directions: a review. *Int J Biol Macromol*. 2024;266(1):131281. doi: 10.1016/j.ijbiomac.2024.131281
12. Tirella A, De Maria C, Criscenti G, Vozzi G, Ahluwalia A. The PAM 2 system: a multilevel approach for fabrication of complex three-dimensional microstructures. *Rapid Prototyp J*. 2012;18(4): 299-307. doi: 10.1108/13552541211231725
13. Ning L, Sun H, Lelong T, et al. 3D bioprinting of scaffolds with living Schwann cells for potential nerve tissue engineering applications. *Biofabrication*. 2018;10(3): 035014. doi: 10.1088/1758-5090/aacd30
14. Sarker Md, Izadifar M, Schreyer D, Chen X. Influence of ionic crosslinkers (Ca^{2+} /Ba^{2+} /Zn^{2+}) on the mechanical and biological properties of 3D bioplotted hydrogel scaffolds. *J Biomater Sci Polym Ed*. 2018;29(10):1126-1154. doi: 10.1080/09205063.2018.1433420
15. Naghieh S, Karamooz-Ravari MR, Sarker M, Karki E, Chen X. Influence of crosslinking on the mechanical behavior of 3D printed alginate scaffolds: experimental and numerical approaches. *J Mech Behav Biomed Mater*. 2018;80:111-118. doi: 10.1016/j.jmbbm.2018.01.034
16. Izadifar Z, Chang T, Kulyk W, Chen X, Eames BF. Analyzing biological performance of 3D-printed, cell-impregnated hybrid constructs for cartilage tissue engineering. *Tissue Eng Part C Methods*. 2016;22(3):173-188. doi: 10.1089/ten.tec.2015.0307
17. Cameron T, Naseri E, MacCallum B, Ahmadi A. Development of a disposable single-nozzle printhead for 3D bioprinting of continuous multi-material constructs. *Micromachines (Basel)*. 2020;11(5):459. doi: 10.3390/MI11050459
18. Snyder J, Son AR, Hamid Q, Wu H, Sun W. Hetero-cellular prototyping by synchronized multi-material bioprinting for rotary cell culture system. *Biofabrication*. 2016;8(1):015002. doi: 10.1088/1758-5090/8/1/015002
19. Ashammakhi N, Ahadian S, Xu C, et al. Bioinks and bioprinting technologies to make heterogeneous and biomimetic tissue constructs. *Mater Today Bio*. 2019;1:100008. doi: 10.1016/j.mtbio.2019.100008

20. Colosi C, Shin SR, Manoharan V, et al. Microfluidic bioprinting of heterogeneous 3D tissue constructs using low-viscosity bioink. *Adv Mater*. 2016;28(4):677-684. doi: 10.1002/adma.201503310

21. du Chatinier DN, Figler KP, Agrawal P, Liu W, Zhang YS. The potential of microfluidics-enhanced extrusion bioprinting. *Biomicrofluidics*. 2021;15(4):041304. doi: 10.1063/5.0033280

22. Blaeser A, Duarte Campos DF, Puster U, Richtering W, Stevens MM, Fischer H. Controlling shear stress in 3D bioprinting is a key factor to balance printing resolution and stem cell integrity. *Adv Healthc Mater*. 2016;5(3):326-333. doi: 10.1002/adhm.201500677

23. Alloca PT. Mixing efficiency of static mixing units in laminar flow. *Fiber Prod*. 1982;10(1):12-19.

24. Heywood NI, Viney LJ, Stewart IW. Mixing efficiencies and energy requirements of various motionless mixer designs for laminar mixing applications. In: *Institution of Chemical Engineers Symposium Series*. 1984;89:147-176. doi: 10.1016/b978-0-85295-171-2.50013-x

25. Ober TJ, Foresti D, Lewis JA. Active mixing of complex fluids at the microscale. *Proceedings of the National Academy of Sciences of the United States of America*. 2015;112(40):12293-12298. doi: 10.1073/pnas.1509224112

26. Chávez-Madero C, de León-Derby MD, Samandari M, et al. Using chaotic advection for facile high-throughput fabrication of ordered multilayer micro- and nanostructures: continuous chaotic printing. *Biofabrication*. 2020;12(3):035023. doi: 10.1088/1758-5090/ab84cc

27. Puertas-Bartolomé M, Włodarczyk-Biegun MK, del Campo A, Vázquez-Lasa B, San Román J. 3D printing of a reactive hydrogel bio-ink using a static mixing tool. *Polymers (Basel)*. 2020;12(9):1986. doi: 10.3390/polym12091986

28. Giachini PAGS, Gupta SS, Wang W, et al. Additive manufacturing of cellulose-based materials with continuous, multidirectional stiffness gradients. *Sci Adv*. 2020;6(8):eaay0929. doi: 10.1126/sciadv.aay0929

29. Kuzucu M, Vera G, Beaumont M, et al. Extrusion-based 3D bioprinting of gradients of stiffness, cell density, and immobilized peptide using thermogelling hydrogels. *ACS Biomater Sci Eng*. 2021;7(6):2192-2197. doi: 10.1021/acsbiomaterials.1c00183

30. Chand R, Muhire BS, Vijayavenkataraman S. Computational fluid dynamics assessment of the effect of bioprinting parameters in extrusion bioprinting. *Int J Bioprint*. 2022;8(2):545. doi: 10.18063/ijb.v8i2.545

31. Lee S, Son M, Lee J, et al. Computational fluid dynamics analysis and empirical evaluation of carboxymethylcellulose/alginate 3D bioprinting inks for screw-based microextrusion. *Polymers (Basel)*. 2024;16(8):1137. doi: 10.3390/polym16081137

32. Fareez UNM, Naqvi SAA, Mahmud M, Temirel M. Computational fluid dynamics (CFD) analysis of bioprinting. *Adv Healthc Mater*. 2024;13(20):2400643. doi: 10.1002/adhm.202400643

33. Martanto W, Baisch SM, Costner EA, Prausnitz MR, Smith MK. Fluid dynamics in conically tapered microneedles. *AIChE J*. 2005;51(6):1599-1607. doi: 10.1002/aic.10424

34. Liravi F, Darleux R, Toyserkani E. Additive manufacturing of 3D structures with non-Newtonian highly viscous fluids: finite element modeling and experimental validation. *Addit Manuf*. 2017;13:113-123. doi: 10.1016/j.addma.2016.10.008

35. Li Y, Liu Y, Jiang C, Li S, Liang G, Hu Q. A reactor-like spinneret used in 3D printing alginate hollow fiber: a numerical study of morphological evolution. *Soft Matter*. 2016;12(8):2392-2399. doi: 10.1039/c5sm02733k

36. Li S, Liu Y, Li Y, Zhang Y, Hu Q. Computational and experimental investigations of the mechanisms used by coaxial fluids to fabricate hollow hydrogel fibers. *Chem Eng Process Process Intensif*. 2015;95:98-104. doi: 10.1016/j.cep.2015.05.018

37. Samandari M, Alipanah F, Majidzadeh-A K, Alvarez MM, Trujillo-de Santiago G, Tamayol A. Controlling cellular organization in bioprinting through designed 3D microcompartmentalization. *Appl Phys Rev*. 2021;8(2):021404. doi: 10.1063/5.0040732

38. Ceballos-González CF, Bolívar-Monsalve EJ, Quevedo-Moreno DA, et al. Plug-and-play multimaterial chaotic printing/bioprinting to produce radial and axial micropatterns in hydrogel filaments. *Adv Mater Technol*. 2023;8(17):2202208. doi: 10.1002/admt.202202208

39. Ates G, Bartolo P. Computational fluid dynamics for the optimization of internal bioprinting parameters and mixing conditions. *Int J Bioprint*. 2023;9(6):0219. doi: 10.36922/ijb.0219

40. Wei Q, An Y, Zhao X, Li M, Zhang J, Cui N. Optimal design of multi-biomaterials mixed extrusion nozzle for 3D bioprinting considering cell activity. *Virtual Phys Prototyp*. 2025;20(1):e2438897. doi: 10.1080/17452759.2024.2438897

41. *Series 190 disposable plastic spiral bayonet mixer.* v111424, Nordson-EFD, 2024:2.

42. Chen DXB. *Extrusion Bioprinting of Scaffolds for Tissue Engineering Applications*. 1st ed. Springer Nature; 2019. doi: 10.1007/978-3-030-03460-3

43. Paul EL, Atiemo-Obeng VA, Kresta SM, eds. *Handbook of Industrial Mixing*. New Jersey, NJ: John Wiley & Sons; 2003. doi: 10.1002/0471451452
doi: 10.1002/0471451452

44. Chahabra RP, Richardson JF. *Non-Newtonian Flow and Applied Rheology, Engineering Applications*. 2nd ed. Oxford, UK: Butterworth-Heinemann; 2008. doi: 10.1016/B978-0-7506-8532-0.X0001-7

45. White FM. *Viscous Fluid Flow*. Boston, MA, Mcgraw Hill; 2006.

46. Ribeiro ACF, Fabela I, Sobral AJFN, et al. Diffusion of sodium alginate in aqueous solutions at T=298.15K. *J Chem Thermodyn*. 2014;74:263-268. doi: 10.1016/j.jct.2014.02.014

47. Paradies HH, Wagner D, Fischer WR. Multicomponent diffusion of sodium alginate solutions with added salt. II. Charged vs. uncharged system. *Berichte der Bunsengesellschaft für physikalische Chemie*. 1996;100(8):1299-1307. doi: 10.1002/bbpc.19961000806

48. Shah NF, Kale DD. Pressure drop for laminar flow of non-Newtonian fluids in static mixers. *Chem Eng Sci*. 1991;46(8):2159-2161. doi: 10.1016/0009-2509(91)80175-X

49. Cybulski, A. and Werner K. Static mixers—criteria for applications and selection. *Int J Chem Eng*. 1986;26:171-180.

50. Grace HP. Dispersion phenomena in high viscosity immiscible fluid systems and application of static mixers as dispersion devices in such systems. *Chem Eng Commun*. 1982;14(3-6):225-277. doi: 10.1080/00986448208911047

51. Wilkinson WL, Cliff MJ. An investigation into the performance of a static inline-mixer. In: *Second European Conference on Mixing*. 1977:A2.15-A2.29.

52. Xu G, Feng L, Li Y, Wang K. Pressure drop of pseudo-plastic fluids in static mixers. *Chin J Chem Eng*. 1997;5:93-96.

53. Nyande BW, Thomas MK, Lakerveld R. CFD analysis of a kenics static mixer with a low pressure drop under laminar flow conditions. *Ind Eng Chem Res*. 2021;60(14):5264-5277. doi: 10.1021/acs.iecr.1c00135

54. White F. *Fluid Mechanics*. 9th ed. New York, NY: Mc GrawHill; 2021.

55. Feng X, Ren Y, Hou L, et al. Tri-fluid mixing in a microchannel for nanoparticle synthesis. *Lab Chip*. 2019;19(17):2936-2946. doi: 10.1039/C9LC00425D

56. Viktorov V, Mahmud MR, Visconte C. Numerical study of fluid mixing at different inlet flow-rate ratios in tear-drop and chain micromixers compared to a new H-C passive micromixer. *Eng Appl Comput Fluid Mech*. 2016;10(1):182-192. doi: 10.1080/19942060.2016.1140075

57. 3D content central, Nordson-EFD. https://www.3dcontentcentral.com/parts/supplier/EFD,-Inc.aspx, access July 24,2025.

58. Jiang X, Yang N, Wang R. Effect of aspect ratio on the mixing performance in the kenics static mixer. *Processes*. 2021;9(3):464. doi: 10.3390/pr9030464

59. Fatima U, Shakaib M, Memon I. Analysis of mass transfer performance of micromixer device with varying confluence angle using CFD. *Chem Pap*. 2020;74(4):1267-1279. doi: 10.1007/s11696-019-00975-8

60. Kim MS, Park SJ, Gu BK, Kim CH. Ionically crosslinked alginate–carboxymethyl cellulose beads for the delivery of protein therapeutics. *Appl Surf Sci*. 2012;262:28-33. doi: 10.1016/j.apsusc.2012.01.010

61. Agarwal T, Narayana SNGH, Pal K, Pramanik K, Giri S, Banerjee I. Calcium alginate-carboxymethyl cellulose beads for colon-targeted drug delivery. *Int J Biol Macromol*. 2015;75:409-417. doi: 10.1016/j.ijbiomac.2014.12.052

62. Habib A, Sathish V, Mallik S, Khoda B. 3D printability of alginate-carboxymethyl cellulose hydrogel. *Materials*. 2018;11(3):454. doi: 10.3390/ma11030454

63. Garrett Q, Simmons PA, Xu S, et al. Carboxymethylcellulose binds to human corneal epithelial cells and is a modulator of corneal epithelial wound healing. *Invest Opthalmol Vis Sci*. 2007;48(4):1559. doi: 10.1167/iovs.06-0848

64. Benchabane A, Bekkour K. Rheological properties of carboxymethyl cellulose (CMC) solutions. *Colloid Polym Sci*. 2008;286(10):1173-1180. doi: 10.1007/s00396-008-1882-2

65. Ma J, Lin Y, Chen X, Zhao B, Zhang J. Flow behavior, thixotropy and dynamical viscoelasticity of sodium alginate aqueous solutions. *Food Hydrocoll*. 2014; 38:119-128. doi: 10.1016/j.foodhyd.2013.11.016

66. Cross MM. Rheology of non-Newtonian fluids: a new flow equation for pseudoplastic systems. *J Colloid Sci*. 1965;20(5):417-437. doi: 10.1016/0095-8522(65)90022-X

67. Messaâdi A, Dhouibi N, Hamda H, et al. A new equation relating the viscosity arrhenius temperature and the activation energy for some newtonian classical solvents. *J Chem*. 2015;2015:1-12. doi: 10.1155/2015/163262

68. Toth G, Nagy D, Bata A, Belina K. Determination of polymer melts flow-activation energy a function of wide range shear rate. *J Phys Conf Ser*. 2018;1045:012040. doi: 10.1088/1742-6596/1045/1/012040

69. Moffat RJ. Describing the uncertainties in experimental results. *Exp Therm Fluid Sci*. 1988;1(1):3-17.
doi: 10.1016/0894-1777(88)90043-X

70. Nair K, Gandhi M, Khalil S, et al. Characterization of cell viability during bioprinting processes. *Biotechnol J*. 2009;4(8):1168-1177.
doi: 10.1002/biot.200900004

71. Ning L, Betancourt N, Schreyer DJ, Chen X. Characterization of cell damage and proliferative ability during and after bioprinting. *ACS Biomater Sci Eng*. 2018;4(11): 3906-3918.
doi: 10.1021/acsbiomaterials.8b00714

72. Miri AK, Mirzaee I, Hassan S, et al. Effective bioprinting resolution in tissue model fabrication. *Lab Chip*. 2019;19(11):2019-2037.
doi: 10.1039/C8LC01037D

73. Jaffer SA, Wood PE. Quantification of laminar mixing in the kenics static mixer: An experimental study. *Can J Chem Eng*. 1998;76(3):516-521.
doi: 10.1002/cjce.5450760323

74. Regner M, Östergren K, Trägårdh C. Influence of viscosity ratio on the mixing process in a static mixer: numerical study. *Ind Eng Chem Res*. 2008;47(9):3030-3036.
doi: 10.1021/ie0708071

75. Cui R, Li S, Li T, et al. Natural polymer derived hydrogel bioink with enhanced thixotropy improves printability and cellular preservation in 3D bioprinting. *J Mater Chem B*. 2023;11(17):3907-3918.
doi: 10.1039/D2TB02786K

76. Maillard M, Fournier S, García-Tuñón E, Courtial EJ. Advances and obstacles to unify the concept of "printability" in ceramics direct ink writing. *Open Ceram*. 2025;23:100808.
doi: 10.1016/j.oceram.2025.100808

APPENDIX

Appendix A

Derivation of the equations describing the dependencies between inlet and outlet flow conditions

Mass conservation:

$$\dot{m}_{out} = \dot{m}_A + \dot{m}_B \tag{A-I}$$

Assuming the inlet streams as aqueous solutions of biomaterials C_1 and C_2, with mass fractions $Y_{C1,A}$ and $Y_{C2,B}$ at the inlets A and B, respectively:

$$\dot{m}_A = \dot{m}_{C1,A} + \dot{m}_{w,A} = Y_{C1,A}\ m_A + Y_{w,A}\ \dot{m}_A \tag{A-II}$$

and

$$\dot{m}_B = \dot{m}_{C2,B} + \dot{m}_{w,B} = Y_{C2,B}\ \dot{m}_B + Y_{w,B}\ \dot{m}_B \tag{A-III}$$

where $Y_{w,A}$, $Y_{w,B}$ are mass fractions of water for inlet streams at A and B, respectively. The compositions of inlet streams remain consistent during the printing task.

Substituting **Equations A-II and A-III** in **Equation A-I**:

$$\dot{m}_{out} = \dot{m}_{C1,A} + \dot{m}_{C2,B} + \dot{m}_{w,A} + \dot{m}_{w,B} \tag{A-IV}$$

For steady operation, as components C_1 and C_2 are feeding solely from inlet A and inlet B, respectively:

$$\begin{aligned} &\dot{m}_{C1,out} = \dot{m}_{C1,A};\ \dot{m}_{C2,out} = \dot{m}_{C2,B};\\ &\dot{m}_{w,out} = \dot{m}_{w,A} + \dot{m}_{w,B} \end{aligned} \tag{A-V}$$

By substitution in **Equation A-IV** and rearranging:

$$Y_{C1,out} + Y_{C2,out} = \frac{\dot{m}_A}{\dot{m}_A + \dot{m}_B} Y_{C1,A} + \frac{\dot{m}_B}{\dot{m}_A + \dot{m}_B} Y_{C2,B} \tag{A-VI}$$

The concentration ratio of precursors at the outlet (ψ) is defined as:

$$\psi = \frac{Y_{C1,out}}{Y_{C2,out}} \tag{A-VII}$$

Reference condition:

$$\dot{m}_{A,ref} = \dot{m}_{B,ref} = \frac{\dot{m}_{out}}{2} \tag{A-VIII}$$

Regarding **Equations A-V and A-VIII**, for the reference case:

$$\psi_{ref} = \frac{Y_{C1,A}}{Y_{C2,B}} \tag{A-IX}$$

Substituting **Equations A-VIII and A-IX** in **Equation A-VI** for the reference case and rearranging:

$$Y_{C1,out,ref} = \frac{\psi_{ref}}{2\left(\psi_{ref}+1\right)}\left(Y_{C1,A} + Y_{C2,B}\right) \tag{A-X}$$

$$Y_{C2,out,ref} = \frac{1}{2\left(\psi_{ref}+1\right)}\left(Y_{C1,A} + Y_{C2,B}\right) \tag{A-XI}$$

Defining flow ratios of precursors, α and β:

$$\alpha = \frac{Y_{C1,out}}{Y_{C1,out,ref}} = \frac{\dot{m}_{C1,out}}{\dot{m}_{C1,out,ref}} = \frac{\dot{m}_A}{\dot{m}_{A,ref}} \tag{A-XII}$$

$$\beta = \frac{Y_{C2,out}}{Y_{C2,out,ref}} = \frac{\dot{m}_{C2,out}}{\dot{m}_{C2,out,ref}} = \frac{\dot{m}_B}{\dot{m}_{B,ref}} \tag{A-XIII}$$

From **Equations A-12, A-13, and A-1**:

$$\frac{\alpha \dot{m}_{A,ref}}{\dot{m}_{out}} + \frac{\beta \dot{m}_{B,ref}}{\dot{m}_{out}} = 1 \tag{A-XIV}$$

Substituting from **Equation A-VIII** leads to:

$$\alpha + \beta = 2 \tag{A-XV}$$

Using **Equations A-VII and A-IX**:

$$\frac{Y_{C1,out}}{Y_{C1,out,ref}} + \frac{\psi_{ref}}{\psi}\frac{Y_{C1,out}}{Y_{C1,out,ref}} = 2 \tag{A-XVI}$$

or

$$\alpha = \frac{2\psi}{\psi + \psi_{ref}},\ \beta = \frac{2\psi_{ref}}{\psi + \psi_{ref}} \tag{A-XVII}$$

Appendix B

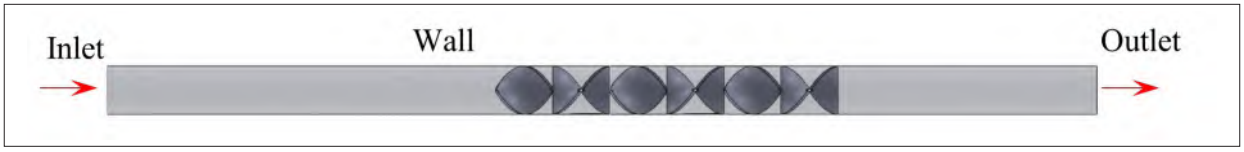


Figure B1. The geometry of the fluid domain for simulation of flow and mixing through a helical mixer inside a pipe (the mixer volume is extracted).

ACCSCIENCE PUBLISHING

International Journal of Bioprinting

RESEARCH ARTICLE

Low-concentration GOQD-functionalized Ti6Al4V scaffolds enhance osteogenesis and angiogenesis for vascularized bone regeneration

Duoling Xu[1,2†], Song Yang[3†], Chao Wang[4†], Shujun Li[5], Wentao Hou[5], Jie Wu[1,2], Leyi Liu[1,2], Dongsheng Yu[1,2], Huancai Lin[1,2*], and Wei Zhao[1,2*]

[1]Hospital of Stomatology, Guanghua School of Stomatology, Sun Yat-sen University, Guangzhou, Guangdong, China

[2]Guangdong Provincial Key Laboratory of Stomatology, Sun Yat-sen University, Guangzhou, Guangdong, China

[3]Fujian Key Laboratory of Oral Diseases, Fujian Provincial Engineering Research Center of Oral Biomaterial and Stomatological Key Laboratory of Fujian College and University, Department of Prosthodontics, School and Hospital of Stomatology, Fujian Medical University, Fuzhou, Fujian, China

[4]Departments of Oral Biology, College of Dentistry, University of Illinois Chicago, Chicago, IL, United States of America

[5]Institute of Metal Research, Chinese Academy of Sciences, Shenyang, Liaoning, China

[†]These authors contributed equally to this work.

***Corresponding authors:**
Huancai Lin
(linhc@mail.sysu.edu.cn)

Wei Zhao
(zhaowei3@mail.sysu.edu.cn)

Citation: Xu D, Yang S, Wang C, *et al*. Low-concentration GOQD-functionalized Ti6Al4V scaffolds enhance osteogenesis and angiogenesis for vascularized bone regeneration. *Int J Bioprint*. 2025;11(5):266-283. doi: 10.36922/IJB025290286

Received: June 15, 2025
1st revised: July 14, 2025
2nd revised: July 31, 2025
Accepted: July 31, 2025
Published online: July 31, 2025

Copyright: © 2025 Author(s). This is an Open Access article distributed under the terms of the Creative Commons Attribution License, permitting distribution and reproduction in any medium, provided the original work is properly cited.

Publisher's Note: AccScience Publishing remains neutral with regard to jurisdictional claims in published maps and institutional affiliations.

Abstract

Graphene oxide quantum dots (GOQDs) possess excellent biocompatibility and have demonstrated potential to enhance osteogenesis and angiogenesis. The objective of this work was to construct Ti6Al4V porous scaffolds modified with different GOQD concentrations and investigate their influence on osteogenesis and angiogenesis. Porous Ti6Al4V scaffolds were coated with GOQDs at concentrations of 0.1, 1, and 10 μg/mL. The proliferation and adhesion of bone marrow mesenchymal stem cells (BMSCs) and human umbilical vein endothelial cells (HUVECs) on these scaffolds were evaluated using CCK-8 assay, immunofluorescence staining, and real time-polymerase chain reaction (RT-PCR). *In vivo* bone regeneration and angiogenesis were assessed through micro-computed tomography imaging and tissue section staining analysis. The results demonstrated successful deposition of GOQDs and the presence of characteristic functional groups. *In vitro* assays demonstrated that scaffolds coated with 0.1 μg/mL GOQDs significantly promoted the osteogenic/angiogenic differentiation of BMSCs and HUVECs. *In vivo* experiments revealed that the 0.1 μg/mL GOQDs-coated scaffold (GQ@TC4) significantly enhanced bone formation and vascularization after 12 weeks. These findings suggest that Ti6Al4V biomimetic porous scaffolds functionalized with an optimal concentration (0.1 μg/mL) of GOQDs can effectively promote both osteogenesis and angiogenesis, offering a promising strategy for bone defect repair.

Keywords: Bone marrow mesenchymal stem cells; Graphene oxide quantum dots; Human umbilical vein endothelial cells; Ti6Al4V biomimetic porous scaffolds; Vascularized bone regeneration

1. Introduction

Bone defects resulting from tumors, infections, trauma, and congenital deformities are common in oral and maxillofacial surgery. Achieving efficient and predictable bone regeneration remains a major clinical challenge.[1] Currently, vascularized autografts or allografts are widely used for bone defect repair. However, their application is limited by donor site availability, associated complications, and delayed bone healing. Moreover, systemic conditions, such as diabetes and local inflammation, can significantly impair the regenerative capacity of bone tissue.[2,3]

An ideal bone graft substitute should meet the following criteria: mechanical properties compatible with native bone (*e.g.*, high strength and appropriate elastic modulus) to provide structural support and biomechanical stimulation; excellent osteogenic and angiogenic capabilities to facilitate vascularized bone regeneration; and superior interfacial compatibility to promote implant–host bone integration. To date, no single material fully meets the requirements for repairing large-scale bone defects.

Ti6Al4V alloy scaffolds have been widely utilized in orthopedics and maxillofacial surgery.[4–7] However, their bioinert surfaces tend to form fibrous interfaces with surrounding bone tissue, compromising osseointegration.[8] Furthermore, the elastic modulus of Ti6Al4V greatly exceeds that of native bone, which may lead to stress shielding effects, implant instability, and eventual failure.[9,10]

Studies have demonstrated that introducing porous architecture into Ti6Al4V scaffolds can effectively reduce their bulk elastic modulus and significantly enhance the adhesion, proliferation, and differentiation of osteoblasts by optimizing pore parameters, such as pore size, porosity, and irregularity.[11,12] Among these, trabecular bone-mimicking irregular porous structures exhibit superior biological performance due to their closer resemblance to the microarchitecture of native bone.[13,14] For instance, Kapat *et al.*[14] reported that an irregular foam scaffold with 70% porosity significantly enhanced osteogenic potential. Our prior study also demonstrated that irregular porous scaffolds with an average pore size of 525 μm effectively enhanced both osteogenesis and angiogenesis.[15–17] Similarly, Jung *et al.*[18,19] have systematically optimized pore geometry and structural characteristics of porous titanium scaffolds to enhance osteoconductivity and mechanical properties, offering valuable insights for scaffold design. However, despite the improved mechanical performance and cellular response afforded by porosity, the intrinsic bioinertness of Ti6Al4V still limits its ability to induce vascularized bone regeneration, necessitating further surface functionalization.

Surface modification of titanium scaffolds includes both physical and chemical approaches, such as coating, electrochemical treatment, and chemical vapor deposition.[20,21] Among these, functional coating by spraying is an efficient physical strategy using materials like metal nanoparticles, hydroxyapatite, or graphene derivatives.[22–24] Graphene coatings have been verified to enhance the bioactivity of titanium-based scaffolds, improve the osteogenic differentiation of bone marrow mesenchymal stem cells (BMSCs), and reduce immune rejection and inflammation.[25] Graphite oxide quantum dots (GOQDs), a graphene derivative, exhibit quantum size effects and good water dispersibility, along with lower cytotoxicity and superior biocompatibility compared to conventional GO.[26,27] Our previous work confirmed that GOQDs significantly promote the proliferation and osteogenic differentiation of both deciduous dental pulp stem cells and mesenchymal stem cells.[28,29] Furthermore, the biological activity of GOQDs is dose-dependent. While low concentrations are beneficial for maintaining cell viability and enhancing osteogenic differentiation, concentrations exceeding 10 μg/mL have been reported to inhibit cell proliferation.[30,31] Given our earlier results indicating that 0.1 and 1 μg/mL GOQDs enhance BMSC behavior,[32] these concentrations were selected as low-dose groups, with 10 μg/mL serving as the high-dose reference in this study.

Based on this foundation, we hypothesize that constructing an optimal concentration of GOQDs coating on biomimetic trabecular porous Ti6Al4V scaffolds can synergistically enhance mechanical compatibility and biofunctionality, providing both structural support and osteogenic/angiogenic stimulation. Therefore, this study aims to functionalize biomimetic porous Ti6Al4V scaffolds with low-concentration GOQDs, assess their effects through co-culture with BMSCs and human umbilical vein endothelial cells (HUVECs), and validate the osteogenic and angiogenic efficacy via *in vivo* experiments. The results are expected to provide new insights and theoretical guidance for the design of advanced bone graft substitutes and promote their clinical translation.

2. Materials and methods

2.1. Preparation of GOQD-modified biomimetic scaffolds

The GOQD stock solution (1 mg/mL) (Nanjing XFNANO Materials, China) was ultrasonicated to achieve homogeneous dispersion and then diluted with deionized water. The final concentrations of GOQDs (0.1, 1, and 10 μg/mL) were prepared for subsequent experiments. Ti6Al4V biomimetic porous scaffolds with an actual pore size of 525 μm were printed using an electron beam melting

(EBM) system (A1, ARCAM, Sweden), as previously reported.[16] For *in vitro* studies, the scaffolds were 10 mm in diameter and 2 mm in thickness; for *in vivo* studies, the scaffolds measured 5 mm in diameter and 8 mm in thickness (Figure 1A). The spray-coating method was used to prepare GOQD coatings with different concentrations on the surface of Ti6Al4V biomimetic porous scaffolds. Four experimental groups were established: (i) control: untreated Ti6Al4V porous scaffolds; (ii) GQ0.1@TC4: Ti6Al4V scaffolds coated with 0.1 μg/mL GOQD solution; (iii) GQ1@TC4: Ti6Al4V scaffolds coated with 1 μg/mL GOQD solution; and (iv) GQ10@TC4: Ti6Al4V scaffolds coated with 10 μg/mL GOQD solution.

Ti6Al4V porous scaffolds with an actual pore size of 525 μm were selected and cleaned three times with anhydrous ethanol to remove surface dust and grease. The scaffolds were then dried and subjected to plasma treatment to enhance surface hydrophilicity and coating adhesion. After treatment, the scaffolds were placed on a 100°C heating platform, and the pre-prepared GOQD solutions (0.1, 1, and 10 μg/mL) were uniformly sprayed onto the scaffold surfaces using a spray gun. As the solvent evaporated, a uniform GOQD coating was formed. Finally, the coated scaffolds were baked in a 100°C oven for 2–3 h to obtain GOQD-modified Ti6Al4V porous scaffolds (Figure 1A).

2.2. GOQD-modified biomimetic scaffold characterization

X-ray powder diffraction (XRD) was carried out using a Supernova diffractometer (Japan) to determine the phase composition of the samples. The scanning was performed over a 2θ range of 5°–80°, employing Cu Kα radiation (λ = 1.5411 Å) as the source. X-ray photoelectron spectroscopy (XPS) (Nexsa, Thermo Fisher Scientific, USA) was utilized to assess the surface elemental composition of the samples. Fourier transform infrared spectroscopy (FTIR) (Nicolet NXR 9650, Thermo Fisher Scientific, USA) was used to detect the functional groups present in the GOQDs, with spectra recorded in the range of 500–4000 cm^{-1}.

2.3. Effect of modified biomimetic scaffold extracts on the proliferation of BMSCs and HUVECs

2.3.1. Preparation of GOQD-modified biomimetic scaffold conditioned medium

BMSCs were extracted from Sprague–Dawley rats. Upon reaching approximately 80% confluency, the cells were collected by treatment with 0.25% trypsin-EDTA (Gibco, USA). The BMSCs (passage 3) were used for further experiments. HUVECs were purchased from ScienCell™ Research Laboratories (USA). The culture conditions for HUVECs were maintained similarly to those applied for BMSCs.

For the preparation of conditioned medium, BMSCs or HUVECs were seeded onto the scaffolds and incubated in their respective complete media for 72 h. After incubation, the supernatant was collected and then stored at 4°C until it was used for subsequent experiments.

2.3.2. Effect of GOQD-modified biomimetic scaffold extracts on the proliferation of BMSCs

At predetermined time points, cell proliferation and viability were assessed accordingly. The cell proliferation rate in each group was evaluated using Cell Counting Kit-8 (CCK8) (Dojindo, Japan). Cells were incubated with medium containing 10% (v/v) CCK-8 reagent (Dojindo Laboratories, Japan) for 60 min in the dark. Subsequently, the absorbance at 450 nm was detected using a microplate reader (Bio-Tek, UK) to assess cell proliferation.

The cells were treated with a working solution containing calcein AM and ethidium homodimer-1 (Invitrogen, USA). After incubation for 30 min at 37°C, fluorescence signals were tested using a confocal laser scanning microscope (LSM780, Zeiss, Germany).

The samples were incubated with phalloidin (Solarbio, China) for 30 min at 37°C to stain the F-actin cytoskeleton. The nuclear staining was carried out using 4′,6-diamidino-2-phenylindole (Solarbio, China).

2.3.3. Effect of GOQD-modified biomimetic scaffold extracts on the proliferation of HUVECs

HUVECs at passage 3 were cultured in complete Dulbecco's Modified Eagle's Medium (DMEM) for 2 days prior to treatment. The medium was subsequently replaced with conditioned medium derived from the GOQD-modified scaffold groups. CCK-8 assay and immunofluorescence staining were performed as described in **Section 2.3.2**.

2.3.4. Effect of GOQD-modified biomimetic scaffold extracts on the angiogenic potential of HUVECs

HUVECs were digested with trypsin, centrifuged, and resuspended in complete DMEM. HUVECs were divided into four experimental groups: control, GQ0.1@TC4, GQ1@TC4, and GQ10@TC4. When cell monolayers reached approximately 80% confluence, a linear wound was created using a 1000 μL pipette tip held perpendicular to the plate surface. The migration area was then quantified using ImageJ software to assess wound closure efficiency.

Cell migration was evaluated using a Transwell system (8 μm pore size, Corning, USA). A total of 3×10^4 HUVECs suspended in serum-free medium were added to the upper chamber, while 750 μL of complete F-12K medium (without antibiotics) was placed in the lower chamber as

a chemoattractant. The migrated cells were then imaged using an inverted microscope and quantitatively analyzed with ImageJ software.

The capacity of HUVECs to form capillary-like structures was assessed using a Matrigel-based tube formation assay. A 96-well plate was precooled on ice, and 50 μL of Matrigel (Corning, USA) was added to each well. HUVECs, pretreated with the scaffold extracts for 24 h, were then collected, counted, and seeded onto the solidified Matrigel. After 24 h of incubation, tube formation was observed. The total tube length and branch points were analyzed using ImageJ software.

2.4. Effects of GOQD-modified biomimetic scaffolds on cell adhesion and osteogenic/angiogenic differentiation of BMSCs and HUVECs

2.4.1. Effects of GOQD-modified biomimetic scaffolds on the adhesion and osteogenic differentiation of BMSCs

The morphological characteristics and adhesion of BMSCs on GOQD-modified biomimetic scaffolds were observed using scanning electron microscopy (SEM) (Nexsa, Thermo Fisher Scientific, USA). To evaluate the osteogenic differentiation potential of BMSCs, the expression levels of osteogenesis-related genes (*Runx2*, *Bmp2*, *Ocn*, and *Alp*) were analyzed by real time-polymerase chain reaction (RT-PCR) after culture on GOQD-modified biomimetic scaffolds. The primer sequences used are listed in **Table S1**.

2.4.2. Effects of GOQD-modified biomimetic scaffolds on the adhesion and angiogenic differentiation of HUVECs

The morphology and adhesion behavior of HUVECs on GOQD-modified biomimetic scaffolds were assessed using SEM. To assess the angiogenic potential of HUVECs, the vascular endothelial growth factor (VEGF) and hypoxia-inducible factor 1-alpha (HIF-1α) were detected by RT-PCR, following culture on GOQD-modified scaffolds. The primer sequences are listed in **Table S2**.

2.5. *In vivo* evaluation of osteogenic and angiogenic performance of GOQD-modified biomimetic scaffolds

In vivo experiments were conducted using 12 adult male New Zealand white rabbits (weighing 2.5–3.0 kg each). The animal procedures strictly adhered to relevant ethical guidelines and were approved by the Institutional Animal Care and Use Committee of Sun Yat-sen University (Approval No. SYSU-IACUC-2019-000169).

Two types of porous biomimetic scaffolds (diameter: 5 mm; height: 8 mm) were implanted into the femoral condyles of rabbits. Group 1 (control) consisted of Ti6Al4V scaffolds with a solid core and an irregular porous outer surface with a pore size of approximately 525 μm. Group 2 (GQ@TC4) was composed of the same Ti6Al4V scaffold, with the surface coated with GOQDs at the optimal concentration previously identified in **Sections 2.2 and 2.3** for promoting osteogenesis and angiogenesis.

After 3 months of implantation, bone regeneration and neovascularization around the scaffolds were assessed using micro-computed tomography (micro-CT), histological analysis, and immunohistochemical staining.

2.6. Statistical analysis

All data are presented as mean ± standard deviation. To ensure the reliability of the statistical results, sample sizes were determined based on previous studies and pilot experiments to achieve a statistical power greater than 80% at a significance level of 0.05. The normality of the data was assessed using the Shapiro–Wilk test. For comparisons among multiple groups, one-way analysis of variance was performed, followed by Tukey's Honestly Significant Difference test as a post hoc analysis to identify specific group differences. A p-value <0.05 was considered statistically significant. All experiments were conducted in triplicate or more.

3. Results

3.1. GOQD-modified biomimetic scaffold surface characterization

To evaluate the effects of GOQDs at different concentrations, biomimetic porous Ti6Al4V scaffolds were coated with GOQDs at 0, 0.1, 1, and 10 μg/mL. These four groups were designated as control, GQ0.1@TC4, GQ1@TC4, and GQ10@TC4, respectively. After conducting the *in vitro* experiments, the optimal GOQDs concentration was selected for subsequent *in vivo* evaluation. For the animal study, Ti6Al4V scaffolds without GOQD coating and those coated with the optimal concentration of GOQDs were designated as control and GOQDs@TC4, respectively. The fabricated scaffold samples are displayed in Figure 1A.

Figure 1B presents the XRD patterns of the GQ0.1@TC4, GQ1@TC4, and GQ10@TC4 scaffolds. All samples exhibited distinct diffraction peaks at 2θ values of 35.2°, 38.3°, 40.5°, 54.3°, 63.1°, and 72.2°, which correspond to characteristic peaks of Ti6Al4V. Additionally, a prominent diffraction peak was observed at 2θ = 10.2° in the GQ10@TC4 group, indicating the successful incorporation of GOQDs on the scaffold surface. No extraneous peaks were detected in the XRD spectra, suggesting the absence of impurities introduced during fabrication.

The XPS analysis (Figure 1C and D) confirmed the presence of characteristic peaks for C1s, O1s, and

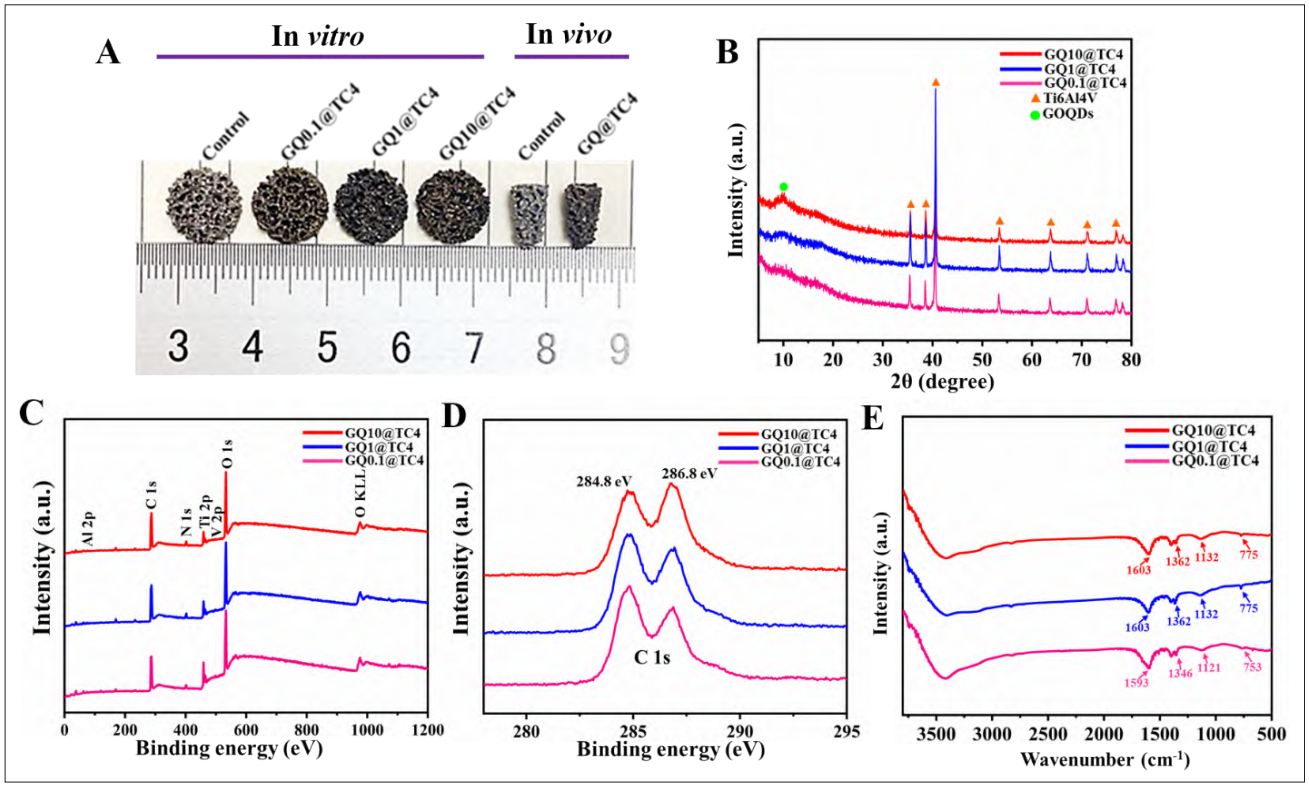


Figure 1. Surface characteristics of the biomimetic porous Ti6Al4V scaffolds. (A) Biomimetic porous scaffolds fabricated by EBM for *in vitro* and *in vivo* experiments. (B) XRD patterns of the biomimetic porous Ti6Al4V scaffolds. (C) XPS survey spectra of scaffolds modified with different concentrations of GOQDs. (D) High-resolution XPS spectra of the C1s region on the scaffold surfaces. (E) FTIR spectra of the biomimetic porous Ti6Al4V scaffolds. Abbreviations: EBM, electron beam melted; FTIR, Fourier transform infrared spectroscopy; XPS, X-ray photoelectron spectroscopy; XRD, X-ray powder diffraction.

Ti2p elements, further validating the successful surface modification with GOQDs. The incorporation of GOQDs altered the surface chemical composition of Ti6Al4V, which may contribute to enhanced biocompatibility.

FTIR results (Figure 1E) demonstrated typical absorption bands in the range of 1100–1600 cm^{-1} that correspond to C=O stretching vibrations, as well as a broad O–H stretching peak around 3450 cm^{-1}. These findings confirm the successful attachment of GOQDs onto the Ti6Al4V scaffold surface. The increased presence of hydroxyl, carbonyl, and conjugated double bond groups introduced by GOQDs may enhance the surface bioactivity and improve cellular interactions.

3.2. Effects of GOQD-modified biomimetic scaffold extracts on the proliferation of BMSCs and HUVECs

3.2.1. Effects on BMSC proliferation

According to the Raman spectra of the GQ0.1@TC4 scaffolds before and after immersion in culture medium for 2 weeks in the preliminary experiment of this study (Figure S1), GOQDs were still coating on the TC4 surface, indicating good stability of the GOQDs coating on the biomimetic scaffold and supporting its suitability for subsequent cell experiments. The proliferation results of BMSCs cultured with scaffold extracts are displayed in Figure 2C. Within the concentration range of 0.1–10 μg/mL, BMSC proliferation decreased with increasing GOQD concentration. Notably, the GQ0.1@TC4 group exhibited significantly higher proliferation at days 1, 3, 5, and 7 compared to the other groups ($p < 0.001$).

Live/dead staining results are presented in Figure 2A. As the GOQD concentration increased, the number of viable BMSCs decreased. Both GQ0.1@TC4 and GQ1@TC4 groups displayed a relatively high number of live cells, with GQ0.1@TC4 demonstrating the highest cell viability and strongest fluorescence intensity.

Immunofluorescence staining results are presented in Figure 2B. A gradual decline in BMSC number was observed with increasing GOQD concentrations. The GQ0.1@TC4 group had the highest cell count with regular, spindle-shaped morphology. In contrast, the GQ10@

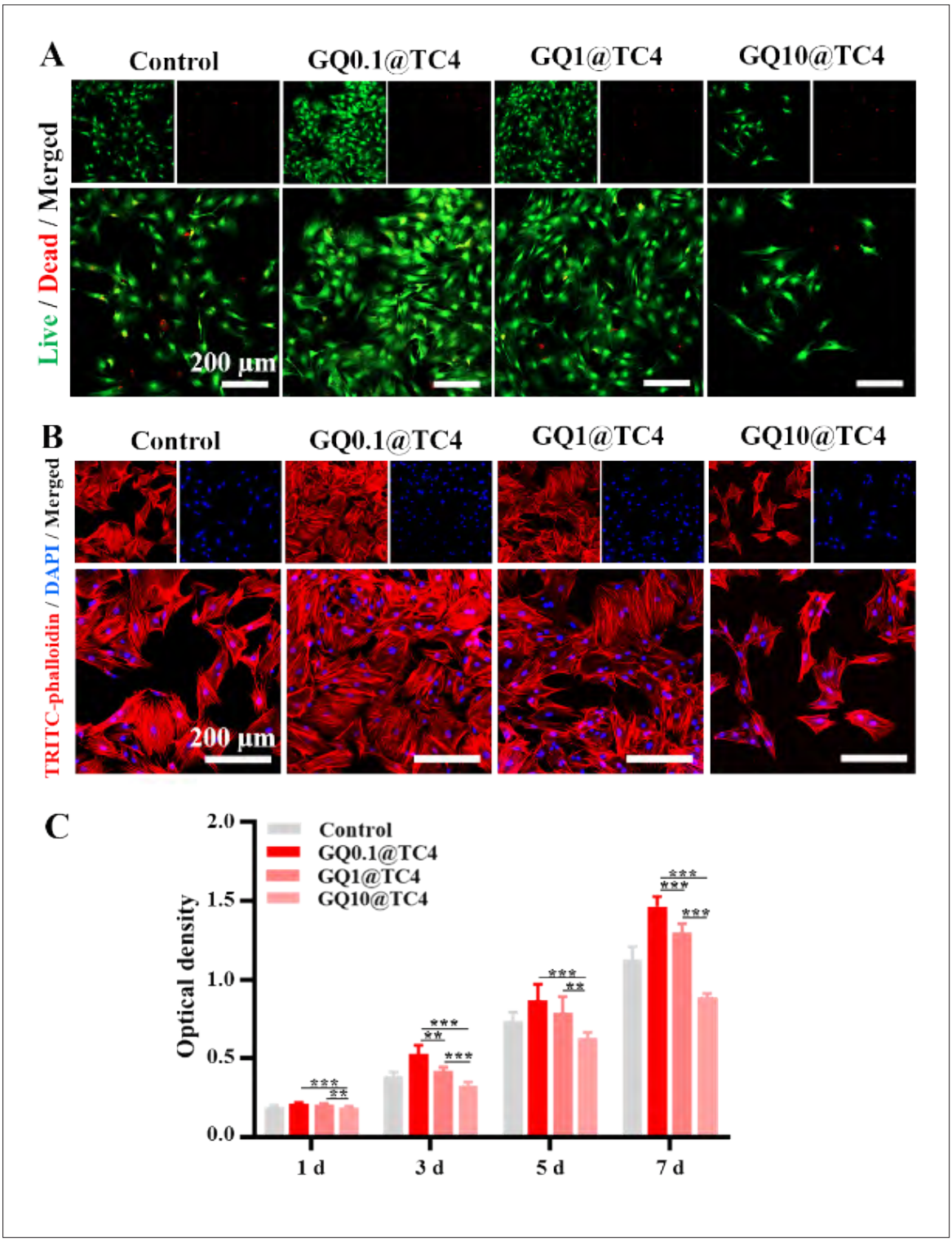


Figure 2. Effects of GOQD-modified biomimetic scaffold extracts on BMSC proliferation. (A) Confocal laser scanning microscopy images of live/dead staining of BMSCs co-cultured with extracts from four groups of titanium alloy scaffolds. (B) Confocal images of immunofluorescence staining, featuring the cytoskeletal morphology of BMSCs after 3 days of co-culture; the red stain indicates F-actin filaments, while the blue stain indicates nuclei. (C) Proliferation of BMSCs co-cultured with extracts from the four scaffold groups for 1, 3, 5, and 7 days, assessed by the CCK-8 assay. ($n = 3$; $^{**}p < 0.01$ and $^{***}p < 0.001$, compared to the control). Scale bars: 200 μm (A and B). Abbreviations: BMSC, bone marrow mesenchymal stem cells; GOQD, graphite oxide quantum dots.

TC4 group displayed the fewest cells, with shrunken and irregular cytoskeletal structures.

3.2.2. Effects on HUVEC proliferation

The proliferation results of HUVECs cultured with scaffold extracts are presented in Figure 3C. Similar to BMSCs, HUVEC proliferation declined with increasing GOQD concentration. The GQ0.1@TC4 group demonstrated significantly higher proliferation at days 1, 3, 5, and 7 compared to other groups ($p < 0.001$).

Immunofluorescence staining (Figure 3A) revealed a decrease in HUVEC number with increasing GOQD concentration. The GQ0.1@TC4 group had the highest number of HUVECs, predominantly exhibiting an oval morphology and well-organized cytoskeletal structures.

As displayed in Figure 3B and D, after 24 h of treatment with scaffold extracts, the GQ0.1@TC4 group exhibited significantly enhanced migration of HUVECs compared to the GQ1@TC4 and GQ10@TC4 groups ($p < 0.05$). The wound area in the GQ0.1@TC4 group was nearly completely closed within 24 h. After 24 h of treatment, the number of HUVECs migrating through the Transwell membrane was higher in the GQ0.1@TC4 group (635 ± 59) compared to the GQ1@TC4 (428 ± 47) and GQ10@TC4 (149 ± 56) groups ($p < 0.05$) (Figure 4A and C). As presented in Figure 4B and D, after 24 h of extract treatment, HUVECs in the GQ0.1@TC4 group formed significantly longer tube-like structures than those in the GQ1@TC4 and GQ10@TC4 groups ($p < 0.05$). The total tube length in the GQ0.1@TC4 group (2867 ± 49 μm) was approximately three times that of the GQ10@TC4 group (1054 ± 55 μm). Consistently, in our preliminary experiment, co-culturing different GQ@TC4 groups with human bone marrow mesenchymal stem cells (HMSCs) yielded nearly identical results (Figure S2), further confirming the superior pro-migratoryand pro-angiogenic effects of the GQ0.1@TC4 group.

3.3. Effects of GOQD-modified biomimetic scaffolds on BMSC/HUVEC adhesion and osteogenic/angiogenic differentiation

3.3.1. Effects of GOQD-modified scaffolds on BMSC adhesion and osteogenic differentiation

The SEM images featured in Figure 5A indicate that BMSCs adhered to the scaffold surface and exhibited elongated spindle-like morphology. After 7 days of co-culture with biomimetic porous scaffolds modified with varying concentrations of GOQDs, the number of adherent BMSCs decreased with increasing GOQD concentration. Among all groups, the GQ0.1@TC4 group demonstrated the highest degree of cell adhesion on the scaffold surface.

The RT-PCR analysis (Figure 5C) revealed that after 7 days of co-culture, the expression levels of osteogenic-related genes (*Bmp2*, *Ocn*, and *Alp*) were significantly higher in the GQ0.1@TC4 group compared to the GQ1@TC4 and GQ10@TC4 groups ($p < 0.05$), indicating enhanced osteogenic differentiation.

3.3.2. Effects of GOQD-modified scaffolds on HUVEC adhesion and angiogenic differentiation

The SEM images presented in Figure 5B indicate that HUVECs adhered to the scaffold surface in both scattered and clustered formations. After 7 days of co-culture, the GQ0.1@TC4 group exhibited the greatest number of adherent cells, with cells forming confluent layers and overlapping in some regions, compared to the other groups.

The RT-PCR results (Figure 5D) demonstrated that the mRNA expression levels of angiogenesis-related genes (*VEGF* and *HIF1A*) were significantly higher in the GQ0.1@TC4 group than in the GQ1@TC4 and GQ10@TC4 groups ($p < 0.05$), suggesting that low-concentration GOQD modification promotes angiogenic differentiation of HUVECs.

3.4. *In vivo* osteogenic and angiogenic evaluation of GOQD-functionalized biomimetic scaffolds

Based on *in vitro* osteogenesis and angiogenesis experiments conducted using both extract and co-culture methods, the GQ0.1@TC4 group exhibited the most favorable outcomes in promoting BMSC adhesion, proliferation, and differentiation, as well as the strongest pro-angiogenic effects on HUVECs. Therefore, the GQ0.1@TC4 scaffold was selected for subsequent *in vivo* studies. To evaluate its osteogenic and angiogenic capacity *in vivo*, a comparative analysis was performed between the GQ0.1@TC4 scaffold and a biomimetic scaffold without GOQD modification using micro-CT, histological staining, and immunohistochemistry. In this section, the scaffold without GOQDs is referred to as the control, while the Ti6Al4V scaffold coated with 0.1 μg/mL GOQDs is denoted as GQ@TC4.

3.4.1. Micro-CT analysis

The micro-CT results (Figure 6A) revealed that at 4 weeks post-implantation in rabbit femurs, more bone tissue had formed around the GQ@TC4 scaffolds, and the gaps between the scaffold and cortical bone were significantly reduced. The bone volume fraction (BV/TV) of the GQ@TC4 group reached 4.85 ± 1.08% (Figure 6B). By week 12, the bone coverage on the scaffold surface had notably increased compared to week 4. The GQ@TC4 scaffolds demonstrated close integration with surrounding cortical bone, with a higher proportion of newly formed yellow-colored bone tissue. The BV/TV in the GQ@TC4 group

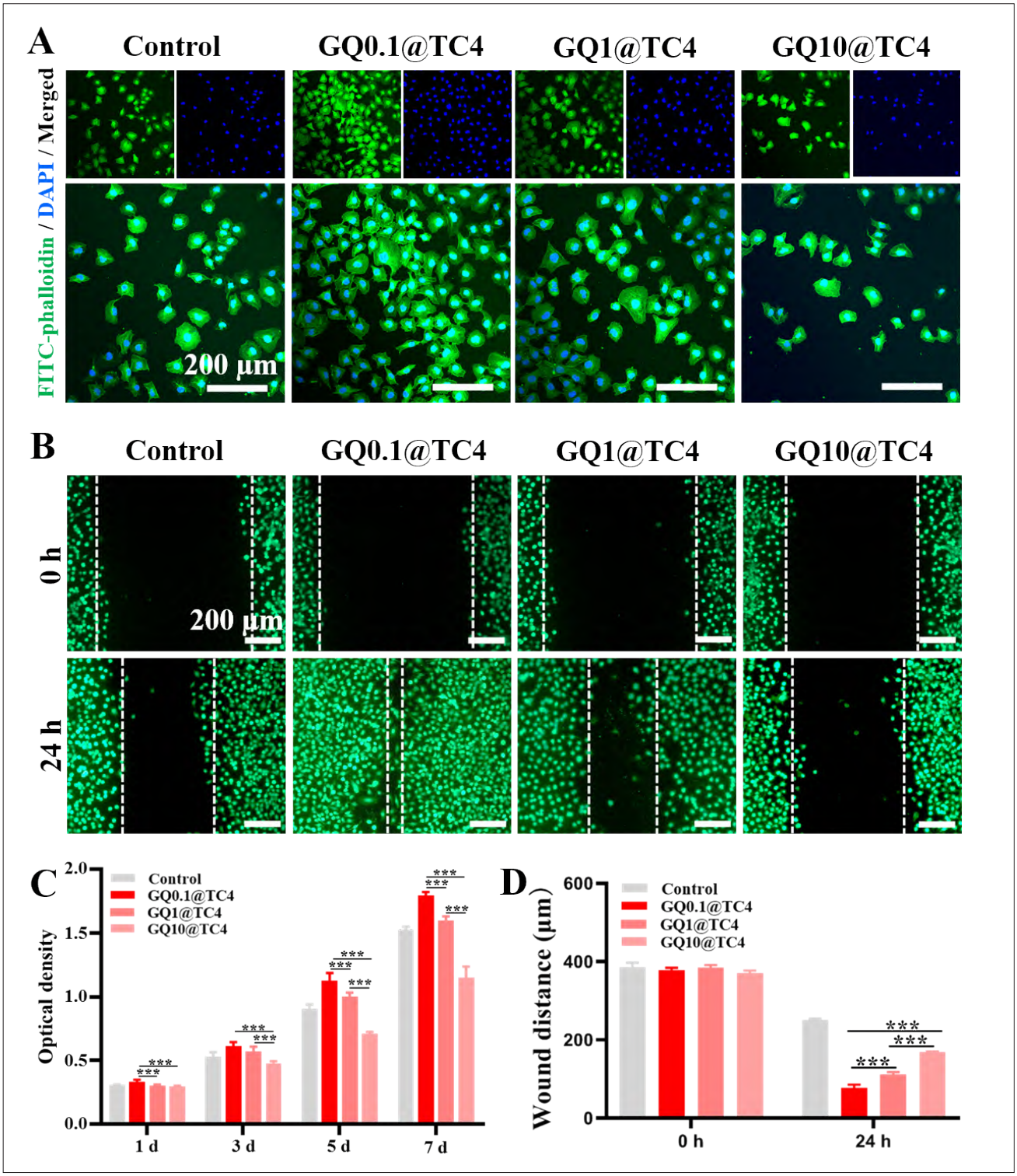


Figure 3. Effects of GOQD-modified biomimetic scaffold extracts on HUVEC proliferation and angiogenic capacity. (A) Confocal laser scanning microscopy images of immunofluorescence staining, displaying HUVEC morphology after co-culture with extracts from four groups of titanium alloy scaffolds for 3 days; the green stain indicates F-actin filaments, while the blue stain indicates nuclei. (B) Fluorescence images of scratch assays, indicating HUVEC migration at 0 and 24 h after treatment with the four scaffold extracts. (C) Proliferation of HUVECs co-cultured with the scaffold extracts for 1, 3, 5, and 7 days, assessed using the CCK-8 assay. (D) Quantitative bar graph of HUVEC migration distances. $n = 3$; ***$p < 0.001$ compared to the control. Scale bars: 200 μm (A and C). Abbreviations: GOQD, graphite oxide quantum dots; HUVEC, human umbilical vein endothelial cells.

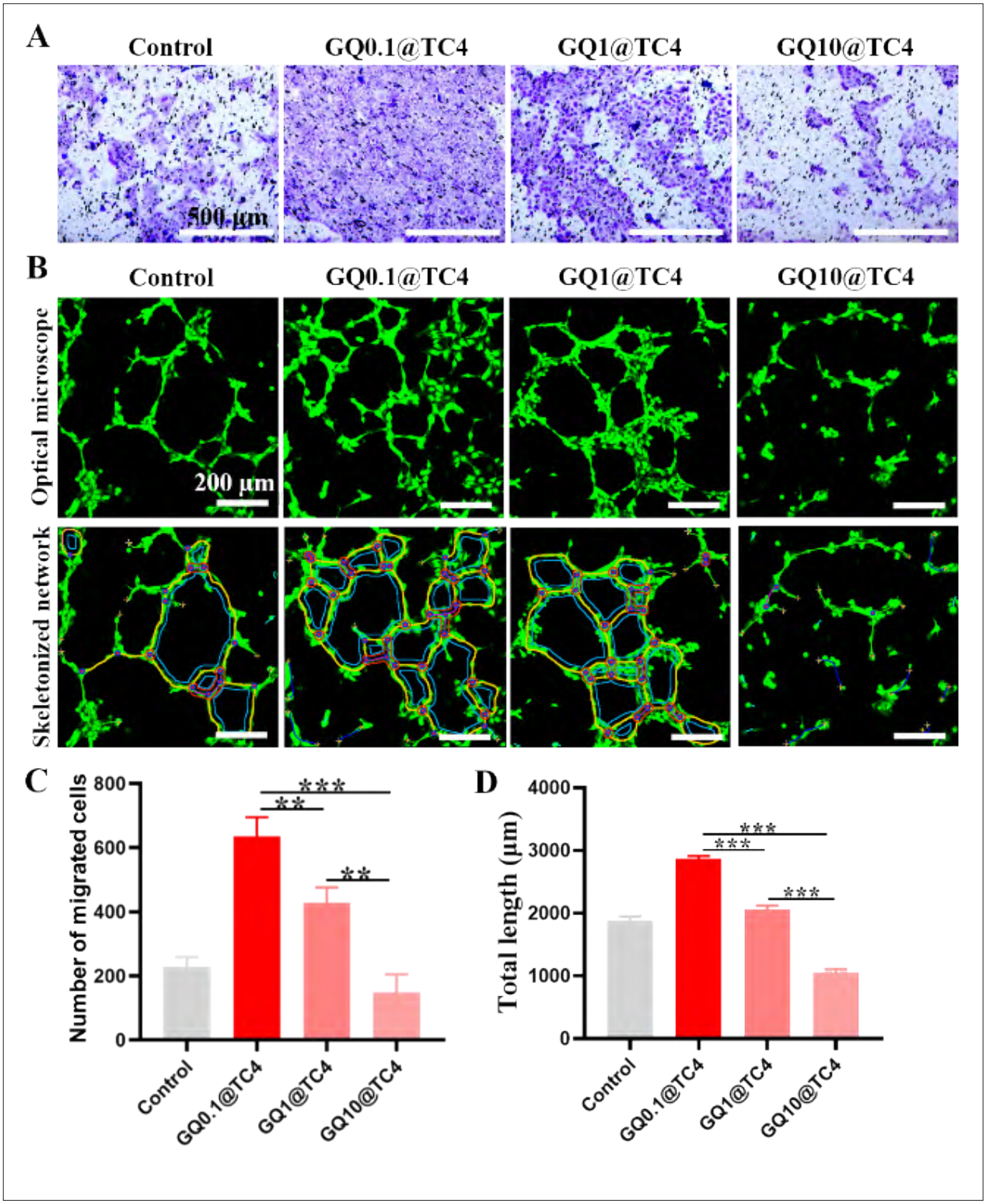


Figure 4. Transwell migration and tube formation assays of HUVECs after 24 h treatment with scaffold extract from the four groups. (A) Representative images of migrated HUVECs stained after the Transwell assay. (B) Fluorescence microscopy images displaying tube formation by HUVECs after treatment with different scaffold extracts. (C) Quantitative analysis of the number of HUVECs that migrated through the membrane. (D) Quantification of total tube length formed by HUVECs. $n = 3$; $^{**}p < 0.01$ and $^{***}p < 0.001$, compared to the control. Scale bars: 500 μm (A); 200 μm (C). Abbreviation: HUVEC, human umbilical vein endothelial cells.

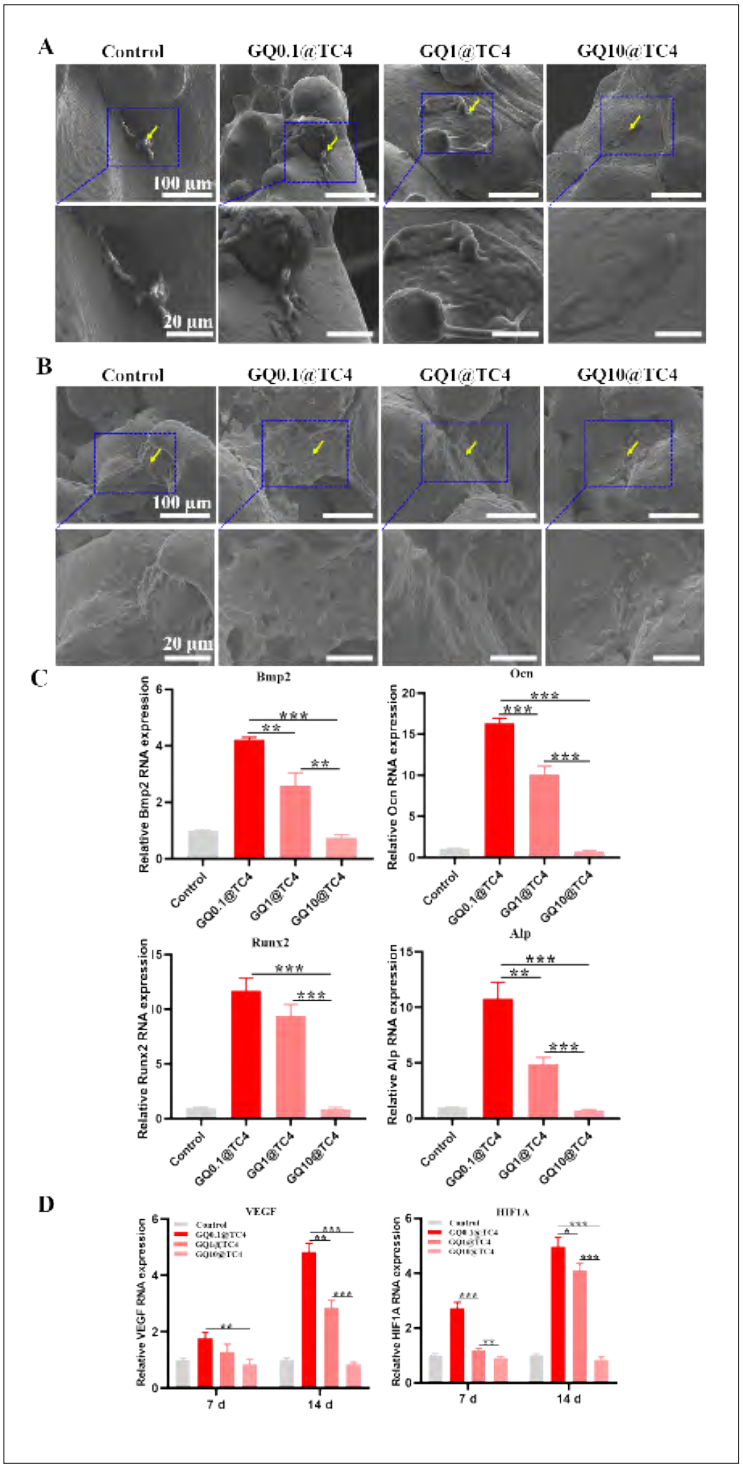


Figure 5. Cell adhesion and morphology on the surface of GOQD-modified biomimetic scaffolds observed by SEM, and RT-PCR analysis of osteogenic and angiogenic gene expression. (A) SEM images displaying cell adhesion on the scaffolds after 7 days of culture. Yellow arrows indicate BMSCs adhering and growing on the scaffold surface. (B) SEM images displaying HUVECs adhered to the scaffold surface after 7 days of culture. Yellow arrows indicate attached HUVECs. (C) RT-PCR analysis of osteogenic gene expression (*Bmp2*, *Ocn*, *Runx2*, and *Alp*) in BMSCs cultured on the four groups of Ti6Al4V scaffolds. (D) RT-PCR analysis of angiogenesis-related gene expression (*VEGF* and *HIF1A*) in HUVECs cultured on the four groups of scaffolds. $n = 3$; $^{**}p < 0.01$ and $^{***}p < 0.001$, compared to the control. Scale bars: 100 μm (A and C, top); 20 μm (A and C, bottom). Abbreviations: BMSCs, bone marrow mesenchymal stem cells; HUVECs, human umbilical vein endothelial cells; RT-PCR, real time-polymerase chain reaction; SEM, scanning electron microscope.

reached 43.29 ± 3.26%, significantly higher than that in the control group ($p < 0.05$).

3.4.2. Histological observation

Hematoxylin and eosin (H&E) staining (Figure 6C) revealed the formation of small areas of red-stained bone tissue around the GQ@TC4 scaffolds at week 4 (yellow arrows in Figure 6C). The BV/TV was 3.60 ± 0.68%. By week 12, new bone formation on the scaffold increased markedly, with the GQ@TC4 group exhibiting a BV/TV of 16.72 ± 1.07%, significantly greater than that of the control group ($p < 0.05$) (Figure 6D).

Modified Masson's trichrome staining (Figure 6E) further confirmed these findings. At week 4, limited new bone tissue was observed at the interface between the GQ@TC4 scaffold and host bone (yellow arrows in Figures 6C and E), with a BV/TV of 6.13 ± 0.85%. At week 12, extensive new bone formation was evident, with the newly formed tissue connecting across the scaffold. The BV/TV reached 10.37 ± 1.13% in the GQ@TC4 group, significantly higher than that in the control group ($p < 0.05$) (Figure 6F).

CD31 immunohistochemical staining was used to assess neovascularization. CD31-positive endothelial cells formed round or oval yellow to brown ring-like structures representing vascular lumens (Figure 6G). At week 4, only a few vessels were observed in the control group, while significantly more blood vessels of various diameters were present in the GQ@TC4 group. At week 12, the GQ@TC4 scaffolds exhibited a larger number and diameter of vascular lumens compared to the control group, with statistically significant differences ($p < 0.05$) (Figure 6H).

4. Discussion

Owing to their favorable properties in promoting osteogenesis and angiogenesis, GOQDs have attracted great attention in the fields of orthopedic implants and dental prosthetics.[33,34] As a derivative of graphene oxide (GO), GOQDs have demonstrated promising osteoinductive potential in both *in vitro* and *in vivo* studies.[35,36] However, differences in oxygen content and particle size during GOQD synthesis result in variations in their physicochemical properties. Previous studies have demonstrated that parameters such as the oxygen content, diameter, and thickness of graphene-based materials significantly influence their osteoinductive capabilities.[37–39]

Based on the findings in our previous study,[16] Ti6Al4V scaffolds with irregular porous structures and an average pore size of 525 μm effectively promoted BMSC osteogenic differentiation. In combination with our previous research,[32] which identified the optimal GOQD concentration (0.1 μg/mL) for enhancing BMSC proliferation and differentiation, this study focused on coating Ti6Al4V scaffolds (pore size: 525 μm) with three concentrations of GOQDs. Furthermore, *in vivo* experiments were conducted to assess the scaffolds' capacities for bone and vascular regeneration under appropriate GOQD loading concentration.

As a surface modification strategy for metallic implants, GOQD coating is considered a safe and effective approach.[40] Variations in GOQDs' characteristics, such as particle size and chemical composition, can alter the physicochemical properties of the implant material, including its structure and morphology.[41] In this study, the XRD results (Figure 1B) revealed the presence of characteristic peaks for both Ti6Al4V and GOQDs without any additional impurity peaks, indicating that the coating process did not introduce contaminants. Specifically, Ti6Al4V exhibited a characteristic peak near $2\theta = 40°$, corresponding to the (110) plane, while GOQDs exhibited a peak at $2\theta \approx 10°$, corresponding to the (001) plane. Notably, the intensity of the Ti6Al4V peak varied with increasing GOQD concentration, which may be attributed to lattice structure alterations induced by the GOQD coating. These findings confirm the successful deposition of GOQDs onto the Ti6Al4V scaffold surface and validate the purity and integrity of the composite structure.

As presented in Figure 1C and D, survey spectra and high-resolution C1s spectra demonstrated clear peaks corresponding to C1s, O1s, and Ti2p. With increasing GOQD concentration, the Ti2p signal intensity gradually decreased, suggesting that the GOQDs coating partially covered the Ti6Al4V surface, thereby reducing the detectable Ti element signal. These results confirm the successful and dose-dependent loading of GOQDs on the Ti6Al4V scaffolds. Moreover, the XPS findings are consistent with previous literature reports,[42] further supporting the conclusion that GOQD coating modifies the surface elemental composition and distribution of Ti6Al4V implants.

Following the coating of Ti6Al4V scaffolds with varying concentrations of GOQDs, the FTIR spectra (Figure 1E) revealed characteristic peaks in the range of 1100–1600 cm^{-1} corresponding to C=O stretching vibrations, and a broad O–H absorption band near 3450 cm^{-1}. These findings indicate the successful incorporation of GOQDs onto the Ti6Al4V scaffold surface. Moreover, the presence of GOQDs increased the surface content of hydroxyl, carbonyl, and unsaturated double bond functional groups on the Ti6Al4V scaffolds, potentially enhancing their biocompatibility. This enhancement is likely due to chemical interactions between oxygen-containing functional groups

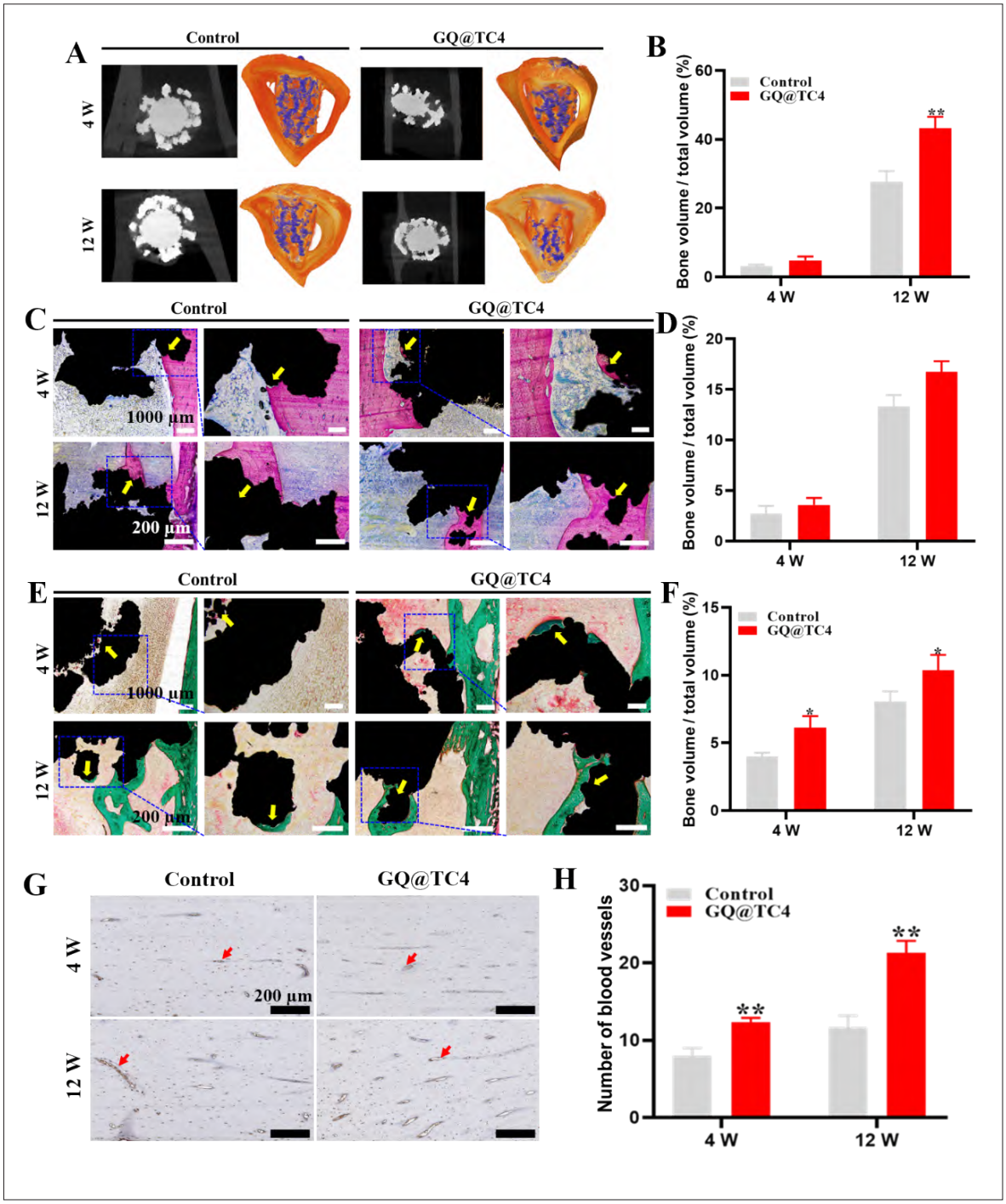


Figure 6. *In vivo* evaluation of osteogenic and angiogenic performance of the scaffolds. (A) 3D-reconstructed micro-CT images of scaffolds implanted in rabbit femurs for 4 and 12 weeks (W); the blue color indicates the Ti6Al4V scaffold, while the yellow color represents newly formed bone tissue. (B) BV/TV of different scaffolds based on micro-CT analysis. (C) H&E staining images of undecalcified sections at weeks 4 and 12 post-implantation; the red area indicates bone tissue, the black area represents the Ti6Al4V scaffold, and the yellow arrows indicate newly formed bone. (D) Quantitative analysis of BV/TV from H&E-stained sections. (E) Masson's trichrome staining images of undecalcified sections at weeks 4 and 12 post-implantation; the green area represents bone tissue, the black area represents the Ti6Al4V scaffold, and the yellow arrows indicate newly formed bone. (F) Quantitative analysis of BV/TV from Masson-stained sections. (G) Immunohistochemical images of CD31 staining at weeks 4 and 12 post-implantation, with red arrows indicating newly formed blood vessels. (H) Quantitative comparison of microvessel density among different scaffold groups. $n = 3$; $^{*}p < 0.05$ and $^{**}p < 0.01$, compared to the control. Scale bars: 1000 μm (C and E, top); 200 μm (C and E, bottom); 200 μm G. Abbreviations: BV/TV, bone volume/total volume; CT, computed tomography; H&E, hematoxylin and eosin.

on the GOQDs and the native surface functionalities of the Ti6Al4V scaffold, resulting in enriched surface chemistry.

In the context of bone repair materials, *in vitro* biological performance evaluation serves as a critical step in understanding the material–cell interactions that mimic *in vivo* bone regeneration processes. Bone scaffolds not only provide a mechanical and spatial framework for cellular adhesion, migration, proliferation, and differentiation, but also actively modulate the local microenvironment and intercellular signaling, thereby triggering a cascade of osteogenic events essential for effective bone regeneration. Thus, *in vitro* studies of biological responses are indispensable for guiding the rational design, optimization, and application of bone regenerative materials.

Upon implantation, bone repair scaffolds release bioactive components into the surrounding milieu, influencing cellular behavior through dynamic interactions with resident cells. To simulate this process, we prepared extract solutions from GOQD-functionalized porous scaffolds using complete culture medium and subsequently co-cultured these extracts with BMSCs and HUVECs.

Previous studies have demonstrated that graphene and its derivatives promote BMSC proliferation and differentiation.[31,43] Our earlier work also confirmed that GOQDs possess a strong capacity to enhance BMSC activity.[32] However, the impact of GOQD-coated titanium alloy scaffolds at different concentrations on cellular behavior remained unclear. In this study, extract solutions derived from scaffolds coated with varying concentrations of GOQDs were used to treat BMSCs, and cell proliferation was assessed using CCK-8 assays (Figure 2C). The results indicated that BMSC proliferation decreased progressively with increasing GOQD concentration. Notably, the GQ0.1@TC4 group consistently exhibited the highest proliferation rates on days 1, 3, 5, and 7 compared to the other groups. These findings indicate that while low concentrations of GOQDs can enhance BMSC proliferation, 0.1 μg/mL GOQDs (GQ0.1@TC4 group) offer the most favorable outcome, highlighting the importance of optimizing GOQD dosage for maximizing bioactivity.

The promotion of BMSC proliferation and differentiation by bone repair materials is fundamentally dependent on the initial adhesion and spreading of BMSCs on the material surface, which subsequently triggers proliferation, migration, and osteogenic differentiation. The composition and surface morphology of the substrate materials were reported to influence cellular adhesion properties.[44,45] In this study, SEM observations (Figure 5A) revealed that the number of adherent cells on scaffolds decreased as the concentration of GOQDs increased. Among all groups, the GQ0.1@TC4 scaffold displayed the highest number of adherent BMSCs. This phenomenon might have been attributed to the elevated production of reactive oxygen species (ROS) induced by higher concentrations of GOQDs, which may have damaged cell structures and impaired adhesion.[46] Previous studies have reported that excessive internalization of GOQDs can lead to elevated intracellular ROS generation, mitochondrial dysfunction, and apoptosis in stem cells and endothelial cells.[47] These ROS-mediated effects are dose-dependent and are known to compromise scaffold biocompatibility and long-term safety.

Cell adhesion on material surfaces is known to be affected by the local microenvironment. Over time, cells gradually spread and form stable attachments to the scaffold via cytoskeletal proteins. These proteins not only help maintain cellular morphology but also mediate interactions with surrounding cells and materials, thereby facilitating biological signal transmission.[48] Studies have demonstrated that the chemical composition and microtopography of biomaterials could directly affect cell spreading behavior.[49] Immunofluorescence staining further implies that within the GOQD concentration range of 0.1–10 μg/mL, an inverse relationship is observed between GOQD concentration and BMSC number. The GQ0.1@TC4 group exhibited the highest BMSC count with consistently well-organized cytoskeletal structures, whereas in the GQ10@TC4 group, fewer cells were observed with noticeably shrunken cytoskeletons. These results indicated that scaffolds coated with 0.1 μg/mL GOQD more effectively promoted BMSC adhesion. A plausible mechanism could be that low concentrations of GOQDs upregulated actin expression, which facilitated transmembrane signal transduction and enhanced cell adhesion.[42,50]

Furthermore, for RT-PCR analysis, cells were harvested directly from the scaffold to better reflect the proliferation and differentiation status of adherent cells. RT-PCR results revealed that after 7 days of co-culture, the expression levels of *Bmp2*, *Ocn*, and *Alp* genes were significantly higher in the GQ0.1@TC4 group compared to the GQ1@TC4 and GQ10@TC4 groups ($p < 0.05$), indicating enhanced osteogenic differentiation. This effect may have resulted from more effective activation of membrane receptors by low-concentration GOQDs, thereby promoting stem cell proliferation and osteogenic differentiation.[50]

To assess the effect of GOQD-functionalized scaffold extracts on HUVEC proliferation, CCK-8 assays were conducted on days 1, 3, 5, and 7 after treatment. The results indicated a dose-dependent decline in HUVEC proliferation as GOQD concentration increased. The GQ0.1@TC4 group consistently displayed significantly

greater proliferation than the other groups at all time points ($p < 0.001$).

To evaluate the pro-angiogenic effects of different GOQD concentrations, a scratch assay was performed. After 24 h, nearly complete scratch closure was observed in the GQ0.1@TC4 group, significantly faster than that of the GQ1@TC4 and GQ10@TC4 groups ($p < 0.05$). In addition, the Transwell migration assay indicated that after 24 h, the GQ0.1@TC4 group exhibited the highest number of migrated cells (635 ± 59), suggesting superior migratory capacity. Tube formation assays further demonstrated that HUVECs treated with GQ0.1@TC4 extract formed significantly longer tubular structures compared to the GQ1@TC4 and GQ10@TC4 groups ($p < 0.05$). These results were consistent with previous reports, which have reported that increasing concentrations of GO and its derivatives negatively affects the angiogenic potential of HUVECs, suppressing capillary-like structure formation in a dose-dependent manner.[51,52]

The enhanced vascularization observed with 0.1 μg/mL GOQDs might have been attributed to the moderate mechanical stress imposed on HUVECs by low concentrations of GOQDs. This stress may have induced the remodeling of actin cytoskeleton into lamellipodia and filopodia, which are involved in cell membrane protrusion, extracellular matrix adhesion, and cytoplasmic contraction—all critical processes for cell migration and angiogenesis.[53,54] HIF-1α and VEGF are two critical RNA transcripts involved in the regulation of angiogenesis. HIF-1α, a transcription factor, is known to promote angiogenesis under hypoxic conditions by enhancing the transcription of VEGF.[55] VEGF functions as a key pro-angiogenic factor and signaling RNA essential for vascular development.[56]

To investigate the *in vivo* osteogenic and early angiogenic potential of the GOQD-functionalized biomimetic scaffold, a femoral defect model was established in New Zealand white rabbits. The study aimed to evaluate the scaffold's capacity to support bone formation and early-stage vascularization *in vivo*. Micro-CT analysis revealed that 12 weeks after implantation, the GQ@TC4 scaffolds featured close integration with the adjacent cortical bone, with a substantial amount of newly formed yellow bone tissue covering the scaffold surface. The BV/TV reached 43.29 ± 3.26%, suggesting that the 0.1 μg/mL GOQDs-coated scaffold effectively promoted new bone formation. These findings indicated that low concentrations of GOQDs enhanced the osteogenic performance of titanium alloy scaffolds *in vivo*. Histological analysis using H&E staining and Masson's trichrome staining corroborated the micro-CT results. At 12 weeks post-implantation, a notable increase in newly formed bone tissue was observed surrounding the GQ@TC4 scaffolds, accompanied by a significant increase in bone volume. The ability of scaffold materials to promote new bone formation after implantation is closely associated with their capacity to stimulate neovascularization. A greater number of newly formed blood vessels typically contributes to more efficient and effective bone regeneration.[57] In this study, CD31 immunohistochemical staining further confirmed enhanced vascularization. At week 12 following implantation, the GQ@TC4 group exhibited a significantly greater number of vascular lumens with relatively larger diameters compared to the control group, and the intergroup difference was statistically significant ($p < 0.05$). These results suggested that scaffolds loaded with a specific concentration of GOQDs could promote bone tissue formation by enhancing neovascularization.

Although our study demonstrated favorable short-term biocompatibility and therapeutic efficacy of GOQD-coated scaffolds, the long-term biosafety profile of GOQDs remains insufficiently characterized. The degradation kinetics of GOQDs *in vivo* remain unclear. Unlike traditional biodegradable polymers, GOQDs may undergo incomplete enzymatic or oxidative degradation, generating intermediate species whose bioactivity or toxicity is not well-defined. Furthermore, the biodistribution and clearance mechanisms remain speculative in the absence of long-term *in vivo* tracking studies. Without such data, it is difficult to predict how GOQDs behave over extended periods or after repeated implantation. To ensure safe clinical translation, future studies should incorporate long-term *in vivo* imaging, quantitative organ-level distribution assays, and immunohistochemical analysis to determine potential inflammatory responses, nanoparticle persistence, or off-target effects. Although GOQDs are known to exhibit size-dependent quantum effects, the current coating strategy primarily utilizes their surface chemical functionality rather than their intrinsic quantum properties. Future studies should explore whether the nanoscale quantum effects of GOQDs contribute directly to the biological outcomes observed. Additionally, while standard physicochemical techniques, such as XRD, XPS, and FTIR, confirmed the successful deposition of GOQDs, comprehensive characterization of the coating properties—including structural morphology, long-term stability, and quantum dot-specific features—was not fully performed. These analyses are crucial for a deeper understanding of the coating's functionality and will be essential for future optimization and translational application.

5. Conclusion

This study systematically investigated the effects of GOQDs at varying concentrations (0, 0.1, 1, and 10 μg/mL) on the

proliferation and osteogenic differentiation of BMSCs, as well as on the proliferation and angiogenic differentiation of HUVECs. The results demonstrated that 0.1 μg/mL GOQDs most effectively promoted the proliferation and functional differentiation of both cell types. Furthermore, Ti6Al4V scaffolds coated with 0.1 μg/mL GOQDs significantly enhanced *in vivo* bone and vascular tissue formation. These findings provide a theoretical basis for the application of GOQD-functionalized biomimetic porous scaffolds in the repair of bone defects.

Acknowledgments

None.

Funding

This research was supported by the National Natural Sciences Foundation of China (No. 81974146), the Guangdong Natural Sciences Foundation (No. 2023A1515012554), the Fujian Key Laboratory of Oral Diseases, School and Hospital of Stomatology, Fujian Medical University (Grant No. 2023SZ-B01), and the International Postdoctoral Exchange Fellowship Program 2023 by the Human Resources and Social Security Department of Guangdong Province.

Conflict of interest

The authors declare that they have no known competing financial interests or personal relationships that could have appeared to influence the work reported in this article.

Author contributions

Conceptualization: Duoling Xu, Chao Wang, Dongsheng Yu, Huancai Lin, Wei Zhao
Data curation: Duoling Xu, Chao Wang, Song Yang
Formal analysis: Shujun Li, Wentao Hou, Huancai Lin, Wei Zhao
Funding acquisition: Wei Zhao, Duoling Xu, Chao Wang
Investigation: Duoling Xu, Chao Wang, Song Yang, Jie Wu, Leyi Liu
Methodology: Shujun Li, Wentao Hou
Supervision: Huancai Lin, Wei Zhao
Writing – original draft: Duoling Xu, Chao Wang, Song Yang, Jie Wu, Leyi Liu
Writing – review & editing: Dongsheng Yu, Huancai Lin, Wei Zhao

Ethics approval and consent to participate

All animal procedures strictly adhered to relevant ethical guidelines and were approved by the Institutional Animal Care and Use Committee of Sun Yat-sen University (Approval No. SYSU-IACUC-2019-000169). The study was conducted in strict adherence to the ethical principles outlined by the National Institutes of Health (NIH) regarding the care and utilization of laboratory animals.

Consent for publication

Not applicable.

Availability of data

The data that support the findings of this study are available from the corresponding authors upon reasonable request.

References

1. Ding Q, Cui J, Shen H, *et al*. Advances of nanomaterial applications in oral and maxillofacial tissue regeneration and disease treatment. *Wiley Interdiscip Rev Nanomed Nanobiotechnol*. 2020;13(2):e1669.
doi: 10.1002/wnan.1669

2. Liang Y, Li M, Yang Y, Qiao L, Xu H, Guo B. pH/glucose dual responsive metformin release hydrogel dressings with adhesion and self-healing via dual-dynamic bonding for athletic diabetic foot wound healing. *ACS Nano*. 2022;16(2):3194-3207.
doi: 10.1021/acsnano.1c11040

3. Li B, Shu R, Dai W, *et al*. Bioheterojunction-engineered polyetheretherketone implants with diabetic infectious micromilieu twin-engine powered disinfection for boosted osteogenicity. *Small*. 2022;18(45):e2203619.
doi: 10.1002/smll.202203619

4. Jang HJ, Kang MS, Jang J, *et al*. Harnessing 3D printed highly porous Ti-6Al-4V scaffolds coated with graphene oxide to promote osteogenesis. *Biomater Sci*. 2024;12(21): 5491-5503.
doi: 10.1039/d4bm00970c

5. Xiao F, Ye JH, Huang CX, *et al*. Gradient gyroid Ti6Al4V scaffolds with TiO(2) surface modification: promising approach for large bone defect repair. *Biomater Adv*. 2024;161:213899.
doi: 10.1016/j.bioadv.2024.213899

6. Zarei M, Hasanzadeh Azar M, Sayedain SS, *et al*. Material extrusion additive manufacturing of poly(lactic acid)/ Ti6Al4V@calcium phosphate core-shell nanocomposite scaffolds for bone tissue applications. *Int J Biol Macromol*. 024;255:128040.
doi: 10.1016/j.ijbiomac.2023.128040

7. Zhang X, Guan S, Qiu J, *et al*. Atomic layer deposition of tantalum oxide films on 3D-printed Ti6al4v scaffolds with enhanced osteogenic property for orthopedic implants. *ACS Biomater Sci Eng*. 2023;9(7):4197-4207.
doi: 10.1021/acsbiomaterials.3c00217

8. Shah NJ, Hyder MN, Moskowitz JS, *et al*. Surface-mediated bone tissue morphogenesis from tunable nanolayered implant coatings. *Sci Transl Med*. 2013;5(191):191ra83. doi: 10.1126/scitranslmed.3005576

9. Shum JM, Gadomski BC, Tredinnick SJ, *et al*. Enhanced bone formation in locally-optimised, low-stiffness additive manufactured titanium implants: an in silico and in vivo tibial advancement study. *Acta Biomater*. 2023;156:202-213. doi: 10.1016/j.actbio.2022.04.006

10. Abaricia JO, Farzad N, Heath TJ, Simmons J, Morandini L, Olivares-Navarrete R. Control of innate immune response by biomaterial surface topography, energy, and stiffness. *Acta Biomater*. 2021;133:58-73. doi: 10.1016/j.actbio.2021.04.021

11. Ching HA, Choudhury D, Nine MJ, Abu Osman NA. Effects of surface coating on reducing friction and wear of orthopaedic implants. *Sci Technol Adv Mater*. 2014;15(1):014402. doi: 10.1088/1468-6996/15/1/014402

12. Mediero A, Frenkel SR, Wilder T, He W, Mazumder A, Cronstein BN. Adenosine A2A receptor activation prevents wear particle-induced osteolysis. *Sci Transl Med*. 2012;4(135):135ra65. doi: 10.1126/scitranslmed.3003393

13. Dinoro J, Maher M, Talebian S, *et al*. Sulfated polysaccharide-based scaffolds for orthopaedic tissue engineering. *Biomaterials*. 2019;214:119214. doi: 10.1016/j.biomaterials.2019.05.025

14. Kapat K, Srivas PK, Rameshbabu AP, *et al*. Influence of porosity and pore-size distribution in Ti(6)Al(4) V foam on physicomechanical properties, osteogenesis, and quantitative validation of bone ingrowth by micro-computed tomography. *ACS Appl Mater Interfaces*. 2017;9(45):39235-39248. doi: 10.1021/acsami.7b13960

15. Wang C, Xu D, Li S, *et al*. Effect of pore size on the physicochemical properties and osteogenesis of ti6al4v porous scaffolds with bionic structure. *ACS Omega*. 2020;5(44):28684-28692. doi: 10.1021/acsomega.0c03824

16. Wang C, Xu D, Lin L, *et al*. Large-pore-size Ti6Al4V scaffolds with different pore structures for vascularized bone regeneration. *Mater Sci Eng C Mater Biol Appl*. 1;131:112499. doi: 10.1016/j.msec.2021.112499

17. Wang C, Wu J, Liu L, *et al*. Improving osteoinduction and osteogenesis of ti6al4v alloy porous scaffold by regulating the pore structure. *Front Chem*. 2023;11:1190630. doi: 10.3389/fchem.2023.1190630

18. Lee H, Lee MK, Han G, *et al*. Customizable design of multiple-biomolecule delivery platform for enhanced osteogenic responses via 'tailored assembly system'. *Bio Des Manuf*. 2022;5(3):451-464. doi: 10.1007/s42242-022-00190-7

19. Lee MK, Lee H, Park C, *et al*. Accelerated biodegradation of iron-based implants via tantalum-implanted surface nanostructures. *Bioact Mater*. 2022;9:239-250. doi: 10.1016/j.bioactmat.2021.07.003

20. Deshmukh S, Chand A, Ghorpade R. Bio-mechanical analysis of porous Ti-6Al-4V scaffold: a comprehensive review on unit cell structures in orthopaedic application. *Biomed Phys Eng Express*. 2024;10(6):062003. doi: 10.1088/2057-1976/ad8202

21. Unsworth T. Proceedings of the Institution of Mechanical Engineers Part H. *Proc Inst Mech Eng H*. 2008;222(7):i. doi: 10.1177/095441190822200701

22. Awonusi BO, Li H, Yin Z, Zhao J, Yang K, Li J. Surface modification of Zn-Cu Alloy with heparin nanoparticles for urinary implant applications. *ACS Appl Bio Mater*. 2024;7(3):1748-1762. doi: 10.1021/acsabm.3c01177

23. Ehlert M, Radtke A, Bartmanski M, Piszczek P. Evaluation of the cathodic electrodeposition effectiveness of the hydroxyapatite layer used in surface modification of Ti6Al4V-based biomaterials. *Materials (Basel)*. 2022;15(19):6925. doi: 10.3390/ma15196925

24. Teixeira-Santos R, Belo S, Vieira R, Mergulhao FJM, Gomes LC. Graphene-based composites for biomedical applications: surface modification for enhanced antimicrobial activity and biocompatibility. *Biomolecules*. 2023;13(11):1571. doi: 10.3390/biom13111571

25. Kang MS, Jeong SJ, Lee SH, *et al*. Reduced graphene oxide coating enhances osteogenic differentiation of human mesenchymal stem cells on Ti surfaces. *Biomater Res*. 2021;25(1):4. doi: 10.1186/s40824-021-00205-x

26. Li P, Di Stasio F, Eda G, *et al*. Luminescent properties of a water-soluble conjugated polymer incorporating graphene-oxide quantum dots. *Chemphyschem*. 2015;16(6):1258-1262. doi: 10.1002/cphc.201402744

27. Liu G, Zhang K, Ma K, Care A, Hutchinson MR, Goldys EM. Graphene quantum dot-based "switch-on" nanosensors for intracellular cytokine monitoring. *Nanoscale*. 2017;9(15):4934-4943. doi: 10.1039/c6nr09381g

28. Yang X, Zhao Q, Chen Y, *et al*. Effects of graphene oxide and graphene oxide quantum dots on the osteogenic differentiation of stem cells from human exfoliated deciduous teeth. *Artif Cells Nanomed Biotechnol*. 2019;47(1):822-832. doi: 10.1080/21691401.2019.1576706

29. Lin L, Zheng Y, Wang C, Li P, Xu D, Zhao W. Concentration-dependent cellular uptake of graphene oxide quantum dots promotes the odontoblastic differentiation of dental pulp cells via the AMPK/mTOR pathway. *ACS Omega*. 2023;8(6):5393-5405. doi: 10.1021/acsomega.2c06508

30. Liao TT, Deng QY, Wu BJ, *et al*. Dose-dependent cytotoxicity evaluation of graphite nanoparticles for diamond-like carbon film application on artificial joints. *Biomed Mater*. 2017;12(1):015018. doi: 10.1088/1748-605X/aa52ca

31. Qiu J, Li D, Mou X, *et al*. Effects of graphene quantum dots on the self-renewal and differentiation of mesenchymal stem cells. *Adv Healthc Mater*. 2016;5(6):702-710. doi: 10.1002/adhm.201500770

32. Xu D, Wang C, Wu J, *et al*. Effects of low-concentration graphene oxide quantum dots on improving the proliferation and differentiation ability of bone marrow mesenchymal stem cells through the Wnt/beta-catenin signaling pathway. *ACS Omega*. 2022;7(16):13546-13556. doi: 10.1021/acsomega.1c06892

33. Xie H, Cao T, Rodriguez-Lozano FJ, Luong-Van EK, Rosa V. Graphene for the development of the next-generation of biocomposites for dental and medical applications. *Dental Mater*. 2017;33(7):765-774. doi: 10.1016/j.dental.2017.04.008

34. Pruna A, Cembrero J, Pullini D, Mocioiu AM, Busquets-Mataix D. Effect of reduced graphene oxide on photocatalytic properties of electrodeposited ZnO. *Appl Phys A Mater*. 2017;123(12):792. doi: 10.1007/s00339-017-1424-1

35. Yan X, An N, Zhang Z, *et al*. Graphene oxide quantum dots-preactivated dental pulp stem cells/GelMA facilitates mitophagy-regulated bone regeneration. *Int J Nanomed*. 2024;19:10107-10128. doi: 10.2147/IJN.S480979

36. An N, Yan X, Qiu Q, *et al*. Human periodontal ligament stem cell sheets activated by graphene oxide quantum dots repair periodontal bone defects by promoting mitochondrial dynamics dependent osteogenic differentiation. *J Nanobiotechnol*. 2024;22(1):133. doi: 10.1186/s12951-024-02422-7

37. Jia ZJ, Shi YY, Xiong P, *et al*. From solution to biointerface: graphene self-assemblies of varying lateral sizes and surface properties for biofilm control and osteodifferentiation. *ACS Appl Mater Inter*. 2016;8(27):17151-17165. doi: 10.1021/acsami.6b05198

38. Kang ES, Song I, Kim DS, *et al*. Size-dependent effects of graphene oxide on the osteogenesis of human adipose-derived mesenchymal stem cells. *Colloid Surface B*. 2018;169:20-29. doi: 10.1016/j.colsurfb.2018.04.053

39. Li XJ, Lin KL, Wang ZL. Enhanced growth and osteogenic differentiation of MC3T3-E1 cells on Ti6Al4V alloys modified with reduced graphene oxide. *Rsc Adv*. 2017;7(24):14430-14437. doi: 10.1039/c6ra25832h

40. Li D, Dai D, Wang J, Zhang C. Honeycomb bionic graphene oxide quantum dot/layered double hydroxide composite nanocoating promotes osteoporotic bone regeneration via activating mitophagy. *Small*. 2024;20(50):e2403907. doi: 10.1002/smll.202403907

41. Ha HD, Jang MH, Liu F, Cho YH, Seo TS. Upconversion photoluminescent metal ion sensors via two photon absorption in graphene oxide quantum dots. *Carbon*. 2015;81:367-375. doi: 10.1016/j.carbon.2014.09.069

42. Qiu JJ, Geng H, Wang DH, *et al*. Layer-number dependent antibacterial and osteogenic behaviors of graphene oxide electrophoretic deposited on titanium. *ACS Appl Mater Inter*. 2017;9(14):12253-12263. doi: 10.1021/acsami.7b00314

43. Chen X, Sun Z, Peng X, *et al*. Graphene oxide/black phosphorus functionalized collagen scaffolds with enhanced near-infrared controlled in situ biomineralization for promoting infectious bone defect repair through PI3K/Akt pathway. *ACS Appl Mater Interfaces*. 2024;16(38):50369-50388. doi: 10.1021/acsami.4c10284

44. Kiroshka VV, Petrova VA, Chernyakov DD, *et al*. Influence of chitosan-chitin nanofiber composites on cytoskeleton structure and the proliferation of rat bone marrow stromal cells. *J Mater Sci Mater M*. 2017;28(1):21. doi: 10.1007/s10856-016-5822-2

45. Xue DT, Chen EM, Zhong HM, *et al*. Immunomodulatory properties of graphene oxide for osteogenesis and angiogenesis. *Int J Nanomed*. 2018;13:5799-5810. doi: 10.2147/Ijn.S170305

46. Zhou J, Zhao L. Multifunction Sr, Co and F co-doped microporous coating on titanium of antibacterial, angiogenic and osteogenic activities. *Sci Rep*. 2016;6:29069. doi: 10.1038/srep29069

47. Jiang X, Chen X, Li Q, *et al*. Synergistic effects of polydopamine-coated reduced graphene oxide on osteogenesis and anti-inflammation in periodontitis. *J Mater Sci Mater Med*. 2025;36(1):51. doi: 10.1007/s10856-025-06905-3

48. Ma R, Tang SC, Tan HL, *et al*. Preparation, characterization, and in vitro osteoblast functions of a nano-hydroxyapatite/polyetheretherketone biocomposite as orthopedic implant material. *Int J Nanomed*. 2014;9:3949-3961. doi: 10.2147/Ijn.S67358

49. Sankar D, Shalumon KT, Chennazhi KP, Menon D, Jayakumar R. Surface plasma treatment of poly(caprolactone) micro, nano, and multiscale fibrous scaffolds for enhanced osteoconductivity. *Tissue Eng Pt A*. 2014;20(11-12):1689-1702. doi: 10.1089/ten.tea.2013.0569

50. Park JB, Ahn JY, Yang WS, *et al*. Stacked graphene with nanoscale wrinkles supports osteogenic differentiation of human adipose-derived stromal cells. *2D Mater*. 2021;8(2):025034. doi: 10.1088/2053-1583/abe105

51. Lamalice L, Le Boeuf F, Huot J. Endothelial cell migration during angiogenesis. *Circ Res*. 2007;100(6):782-794. doi: 10.1161/01.RES.0000259593.07661.1e

52. Wang Q, Chen MC, Schafer NP, *et al*. Assemblies of calcium/calmodulin-dependent kinase II with actin and their dynamic regulation by calmodulin in dendritic spines. *Proc Natl Acad Sci U S A*. 2019;116(38): 18937-18942. doi: 10.1073/pnas.1911452116

53. Cota Teixeira S, Silva Lopes D, Santos da Silva M, *et al*. Pentachloropseudilin impairs angiogenesis by disrupting the actin cytoskeleton, integrin trafficking and the cell cycle. *Chembiochem*. 2019;20(18):2390-2401. doi: 10.1002/cbic.201900203

54. Yadunandanan Nair N, Samuel V, Ramesh L, Marib A, David DT, Sundararaman A. Actin cytoskeleton in angiogenesis. *Biol Open*. 2022;11(12):bio058899. doi: 10.1242/bio.058899

55. Nakayama M, Nakayama A, van Lessen M, *et al*. Spatial regulation of VEGF receptor endocytosis in angiogenesis. *Nat Cell Biol*. 2013;15(3):249-260. doi: 10.1038/ncb2679

56. Soker S, Machado M, Atala A. Systems for therapeutic angiogenesis in tissue engineering. *World J Urol*. 2000;18(1):10-18. doi: 10.1007/Pl00007070

57. Liu WC, Chen SH, Zheng LZ, Qin L. Angiogenesis assays for the evaluation of angiogenic properties of orthopaedic biomaterials-a general review. *Adv Healthc Mater*. 2017;6(5):1600434. doi: 10.1002/adhm.201600434

ACCSCIENCE PUBLISHING

International Journal of Bioprinting

RESEARCH ARTICLE

Preparation and biocompatibility of 3D-printed partially degradable Ta–Mg interpenetrating composites

Jingchao Xu[1], Yanru Zhang[1]*, Shuixian Guo[1], Yue Yang[1], and Jinwei Yu[2]

[1]School of Medicine, Henan Polytechnic University, Jiaozuo, China

[2]Third Department of Orthopedics, First Affiliated Hospital, Henan Polytechnic University, Jiaozuo, Henan, China

(This article belongs to the *Special Issue*: *3D Printing for Advancing Orthopedic Applications*)

Abstract

The treatment of large-area bone defects has the risk of poor healing, and the development of implantable materials with mechanical adaptability, biological activity, and degradability is a clinical challenge. In this study, we prepared a 3D-printed porous tantalum (Ta) scaffold with an elastic modulus comparable to human bone, combined with biologically active magnesium (Mg) using a pressure-free impregnation process. We then conducted a comprehensive evaluation of the material's characteristics, mechanical properties, degradation process, and its impact on MC3T3 cells. Scanning Electron Microscope (SEM) and Energy Dispersive X-ray Spectrometer (EDS) results indicated that the composite scaffold consisted of Ta and Mg phases. Through compression testing, the Ta–Mg composite scaffold displayed higher strength compared to porous Ta scaffolds. *In vitro* experiments revealed good biological activity of the composite material. The degradation results demonstrated that the Mg concentration within the composite material was favorable for cell growth, while the Ta scaffold maintained the integrity of the substrate throughout the degradation process. Likewise, *in vivo* results revealed that the Ta–Mg composite scaffold has stronger biological activity. Taken together, the excellent *in vitro* and *ex vivo* osteogenic properties and favorable degradation characteristics suggest that the Ta–Mg composite could provide new strategies and methods for developing next-generation customizable bone repair implant materials.

Keywords: 3D printing; Ta–Mg composite; Localized degradation; Biological activity; Osteogenesis

***Corresponding author:**
Yanru Zhang (zyr@hpu.edu.cn)

Citation: Xu J, Zhang Y, Guo S, Yang Y, Yu J. Preparation and biocompatibility of 3D-printed partially degradable Ta-Mg interpenetrating composite. *Int J Bioprint*. 2025;11(5):284-300. doi: 10.36922/IJB025290287

Received: July 14, 2025
Revised: August 7, 2025
Accepted: August 11, 2025
Published online: August 11, 2025

Copyright: © 2025 Author(s). This is an Open Access article distributed under the terms of the Creative Commons Attribution License, permitting distribution and reproduction in any medium, provided the original work is properly cited.

Publisher's Note: AccScience Publishing remains neutral with regard to jurisdictional claims in published maps and institutional affiliations.

1. Introduction

Natural bone exhibits remarkable strength, elasticity, and a degree of self-healing capacity following injury. However, the body's innate regenerative capabilities are often insufficient to address large bone defects.[1–3] In recent years, the growing aging population, along with increasing incidence of tumors, traffic accidents, and sports injuries, has led to an increase in large bone defect cases. Therefore, developing effective biomaterials for the treatment of bone defects has become an urgent challenge in orthopedic clinical practice.[4] Ideal bone tissue biomaterials should possess the following characteristics: (i) excellent

biocompatibility, (ii) mechanical strength matching that of bone tissue, and (iii) good osteogenic activity.[5–7] Tantalum (Ta) has excellent biocompatibility, corrosion resistance, and plastic deformation ability. Owing to the inert oxide layer formed on its surface, Ta can promote stable osseointegration, making it suitable as a bone filling and fixation material.[8–10] Although Ta has been widely used in clinical practice, its elastic modulus (183 GPa) is significantly higher than that of natural bone (0.1–30 GPa), which can induce stress shielding. Consequently, this causes the implant to bear higher stress, leading to disuse atrophy of the regenerated bone.[7,11,12] Although studies have reported that surface modification can promote the proliferation and differentiation of osteoblasts, the inherently high elastic modulus of Ta remains at a relatively high level.[13–15] Therefore, designing and manufacturing Ta implants with a lower elastic modulus and higher surface bioactivity to meet clinical needs is particularly important. 3D printing supports personalized design, allowing for a perfect match between complex defects and anatomical structures.[9,16,17] By optimizing material porosity and pre-designing the material structure, the elastic modulus of 3D-printed Ta implants can be significantly reduced to match that of bone tissue. Likewise, the delicate porous scaffold structure facilitates the endogenous growth of bone tissue, promoting ideal bone-implant integration.

Magnesium (Mg) and its alloys, renowned for their excellent biocompatibility, degradability, and moderate mechanical properties, are regarded as revolutionary biodegradable metal materials in the field of orthopedics.[18–20] Furthermore, Mg possesses good bone-inducing properties. Studies have demonstrated that Mg ions play a crucial role in promoting new bone formation. Zhang *et al.*[21] investigated the osteogenic mechanism of Mg and found that Mg ions stimulate periosteal sensory nerve endings to release more neurotransmitters, primarily calcitonin gene-related peptide (CGRP), which promotes osteogenic differentiation of periosteal stem cells. Therefore, Mg exerts its bone-inducing characteristics through this pathway to accelerate fracture healing, making it an ideal bone repair material. However, the rapid degradation of Mg-based bone repair materials in the human body remains a major obstacle to clinical application.[22,23] As biodegradable implants, their degradation rate must match the healing process of bone tissue.[24,25] This process typically includes an initial inflammatory phase (3–7 days), a repair phase (approximately 3–4 months), and a subsequent remodeling phase (several months to years). Therefore, the implant must maintain structural integrity for at least 12 weeks. However, as Mg alloys gradually degrade in the body, their mechanical strength rapidly diminishes, making them insufficient to provide adequate mechanical support for load-bearing bones during the critical healing period, especially the repair phase.[26,27]

Based on the above advantages and challenges, the synergistic combination of Ta and Mg represents a promising new approach to developing high-performance orthopedic biomaterials. In this study, a 3D porous Ta scaffold was fabricated using selective laser melting (SLM) 3D printing technology. Subsequently, pure Mg was incorporated into the porous scaffold through a pressureless infiltration method to obtain the Ta-Mg composite material. Functionally, this composite material has the potential to serve as a partially biodegradable implant material, combining mechanical durability and bioactivity. This study aims to demonstrate the potential of the Ta–Mg composite as a biodegradable biomaterial by examining its mechanical properties, corrosion behavior, *in vitro* cell compatibility, and *in vivo* biocompatibility.

2. Materials and methods

2.1. Preparation of porous Ta scaffolds

A 3D model with a diamond structure was created using Solidworks 21 3D modeling software (Dassault Systèmes, United States of America [USA]). The scaffold model consists of a 3 × 3 × 3 cubic unit structure, with each unit cell measuring 3.33 × 3.33 × 3.33 mm^3.[28] The model was sliced into a 30-μm-single layer thickness using commercial Materialise Magics 21.0 software (Materialise, Belgium). A selective laser melting (SLM) printer (ZRapid Tech, China) was used to fabricate the porous Ta scaffold. The printing material used was pure Ta powder (Arcam AB, Sweden) with a nearly spherical shape and a diameter of 15–53 μm. The entire printing process was conducted under an atmosphere of high-purity argon gas (>99.99%). The specific parameters were as follows: laser scanning speed of 250 mm/s; laser power of 300 W; scan spacing of 75 μm; beam offset of 0.015 mm; laser beam trajectory length of 5 mm; layer thickness of 30 μm; and laser energy density (Ev) of 241.54 J/mm^3. Post-processing included pneumatic sandblasting surface treatment with Ta powder of 50–150 μm and air pressure of 0.2–0.7 MPa for 10 min. This was followed by inspection, where the porous Ta scaffold was freely dropped from a height of ≥200 mm onto a hard wooden surface covered with white paper three times consecutively; the scaffold passed the inspection if no powder fell onto the white paper. After that, the scaffold was washed with anhydrous ethanol using ultrasonic cleaning (power: 200 W; frequency: 40 kHz; duration: 20 min) and then dried before use.

2.2. Preparation of Ta–Mg composites

In a SRYL-2300/9 vertical graphite resistance furnace (Jvjing Instrument, China), high-purity Mg melt

(purity: > 99.99%) was incorporated into the porous Ta scaffold via pressureless infiltration. The treated porous Ta scaffold was placed at the bottom of the resistance furnace, and pure Mg was placed on top of the scaffold. Under a high-purity argon atmosphere, the scaffold was heated at a rate of 10 °C/min to 800 °C, held for 10 min, and then cooled in the furnace. Subsequently, the Ta–Mg composite was cut into the following two sample specifications using wire cutting technology: (i) cylinders (Φ 10 × 2 mm) for *in vitro* experiments and (ii) cylinders (Φ 3 × 5 mm) for *in vivo* experiments and mechanical tests. After gradient mechanical grinding (800#–2000# silicon carbide sandpaper), the samples were washed with anhydrous ethanol using ultrasonic cleaning, followed by blow-drying treatment.

2.3. Characterization of Ta–Mg composites

The Ta–Mg composite was fixed onto the sample stage using conductive adhesive and placed into the sample chamber of a scanning electron microscope (SEM; HITACHI SU8100, Hitachi High-Tech, Japan). SEM imaging was conducted at an acceleration voltage of 20 kV. Adjustments were made to height, brightness, contrast, and sharpness, and images were captured at different positions and magnifications. Energy-dispersive X-ray spectroscopy (EDS; Oxford ULTIMMAX 100, Oxford Instruments, United Kingdom) measurements were performed using an Oxford-type spectrometer equipped with a microscope to analyze the structural morphology, elemental composition, content of the sample surface, and thickness of the reaction layer.

2.4. Immersion test and extract preparation

In the Ta-Mg composite system, Mg acts as the sacrificial anode, while Ta is cathodically protected. The corrosion products of Mg are mainly $Mg(OH)_2$ and H_2, where the $Mg(OH)_2$ passivation film can temporarily inhibit further corrosion of the Mg substrate in an alkaline environment. However, the stability of this passivation film is significantly reduced in a physiological environment containing ions, such as Cl^- and SO_4^{2-}, gradually transforming into soluble $MgCl_2$ and further mineralizing into $Mg_3(PO_4)_2$ and HA deposition layers. This transformation process may be a key mechanism for the stabilization of solution pH in immersion tests.[37,38] Notably, the hydrogen generated by the non-homogeneous corrosion of Mg can create localized stress concentrations within the Ta skeleton, particularly in enclosed pore areas, potentially leading to microcracks and ultimately structural failure. Esen *et al.*[38] have reported that Ti6Al4V-Mg composites prepared using powder metallurgy methods exhibit a significant reduction in the structural integrity of the titanium (Ti) skeleton after just one day of immersion. The primary failure mechanism is attributed to the stress induced by hydrogen pressure accumulation exceeding the yield strength of the Ti phase. In contrast, Yang *et al.*[39] have effectively dispersed hydrogen-induced stress and maintained the integrity of the Ti skeleton by constructing a 3D interpenetrating network structure that utilizes the stress transfer effect between the Mg/Ti bi-continuous phases. Based on this, the present study employed a similar 3D interpenetrating structure design for the Ta-Mg system. Compared to Ti, Ta not only exhibits higher mechanical strength and chemical inertness but also forms a dense passivation film of Ta_2O5 *in vivo*, which can act as a hydrogen barrier at room temperature to inhibit hydrogen permeation, thereby demonstrating superior structural stability during long-term bone integration.[40,41]

2.5. Mechanical test

Pure Mg (Φ 3 × 5 mm^2), porous Ta scaffolds, and Ta–Mg composites (including a 7-day degradation group) that were ultrasonically cleaned with anhydrous ethanol for 15 min were subjected to quasi-static uniaxial compression tests at a strain rate of 10^{-3}/s using the IIC-MST-100 universal testing machine (Zhongji Testing, China) at room temperature. Displacement–load curves were obtained using an extensometer, and the compressive strength (σc), elastic modulus (E), and variations in plastic deformation behavior were determined for each sample group.

2.6. Extraction and culture of MC3T3

The extraction of mouse embryonic osteoblasts (MC3T3) was performed with reference to the literature.[29] Newborn Sprague-Dawley suckling mice (≤48 h) were euthanized by cervical dislocation and sterilized by soaking in 75% ethanol for 10 min. The cranial bones were aseptically separated, and the periosteum and connective tissue were removed. The bones were then cut into 0.5 × 0.5 cm^2 bone chips and rinsed with phosphate-buffered saline (PBS; Thermo Fisher Scientific, China). The bone chips were digested sequentially with 0.25% trypsin (Biosharp, China) for 10 min and 2 mg/mL collagenase A (Beyotime, China) at 37 °C for 30 min, followed by additional incubation at 37 °C with 5% CO_2 complete α-MEM medium containing 10% FBS and 1% PS for 60 min. The cells were collected by centrifugation (800–2000 × g) and resuspended in α-MEM complete medium (Thermo Fisher Scientific, China) containing 10% FBS and 1% PS (HyClone, China). The cells were then seeded into culture flasks and incubated at 37°C with 5% CO_2. The medium was completely replaced every 2 days. After the cells reached 80%–90% confluence, they were passaged with 0.25% trypsin, and the third-passage cells were used for subsequent experiments.

2.7. Cytotoxicity and proliferation experiments

The Cell Counting Kit-8 (CCK-8; Beyotime, China) was used to evaluate the biocompatibility of the material extract. The experimental groups were divided into Ta–Mg composite extract and pure Mg extract, while the control group used standard α-MEM culture medium. MC3T3 cells were seeded into 96-well plates at a density of 3×10^3 cells/well and pre-cultured for 24 h at 37 °C with 5% CO_2 to achieve complete adherence. After discarding the original medium and washing twice with PBS, 100 μL of the corresponding extract was added to each well. After culturing for 1, 2, and 3 days, respectively, the original medium was removed and washed twice with PBS, followed by the addition of 100 μL α-MEM containing 10% CCK-8 solution. Subsequently, the plates were incubated at 37°C in the dark for 2 h. The absorbance at a wavelength of 450 nm was measured using a multimode microplate reader (Multiskan FC, Thermo Fisher Scientific, China). Each group was subjected to three independent measurements, and the data are expressed as mean ± standard deviation.

2.8. Cellular morphology staining experiment

The dual fluorescence labeling method was employed to assess the effect of the material extract on the cytoskeleton of MC3T3-E1 cells.[30] The cell suspension was inoculated into a 24-well plate (1×10^4 cells/well) and co-cultured with Ta–Mg composite extract and pure Mg extract for 6 and 24 h, respectively. Subsequently, the cells were washed three times with PBS and permeabilized with 0.1% Triton X-100 (Biosharp, China) for 10 min at room temperature and in the dark. The cells were then stained with TRITC-Phalloidin (Biosharp, China) for actin for 30 min and DAPI (1 μg/mL, Beyotime, China) for nuclear staining for 2 min, with all steps performed in the dark. Images were acquired using a confocal fluorescence microscope (IX73, Olympus, Japan).

2.9. Alkaline phosphatase activity detection

Alkaline phosphatase (ALP) activity was assessed using the Alkaline Phosphatase Activity Assay Kit (Biosharp, China). Third-passage MC3T3 cells were seeded in a 12-well cell culture plate (1×10^5 cells/well) and pre-cultured at 37°C with 5% CO_2 for 24 h to achieve at least 80% confluence. The original medium was then replaced with the prepared extract solution. The extract was replaced every 48 h. The cultures were terminated at 24 and 168 h post-intervention. The cells were then washed three times with pre-cooled PBS, and RIPA lysis buffer (containing 1% protease inhibitor) was added. The cells were lysed on ice for 30 min, followed by centrifugation at 12,000 × *g* for 10 min to collect the supernatant. The supernatant was then incubated with pNPP substrate at 37°C in the dark for 30 min. The absorbance at 405 nm was measured using a full-wavelength microplate reader (Multiskan FC, Thermo Fisher, China).

2.10. Establishment of the rabbit implantation model

The animal experiments were approved by the Animal Ethics Research Committee of Henan Polytechnic University (approval ID: HPULLSC2025-034) and adhered to the Declaration of Helsinki. Adult male New Zealand rabbits (2.5 ± 0.3 kg; $n = 5$) were selected for the bone defect repair models, with preoperative intravenous injection of 3% pentobarbital sodium (30 mg/kg) via the ear margin and a supplementary injection of 1% lidocaine hydrochloride (1 mg/kg) at the surgical site. The surgical area was disinfected three times with alternating applications of 5% povidone-iodine and 75% ethanol. A 3 cm longitudinal incision was made in the middle segment of both femurs to expose the periosteum, and a cavity with a diameter of 3 mm and a depth of 5 mm was drilled perpendicular to the femoral axis using a high-speed drill. Ta–Mg composite and porous Ta scaffolds, both with a diameter of 3 mm and a height of 5 mm, were implanted into the bilateral defect sites. After sealing the medullary cavity, the muscle and epidermis were sutured in layers. Post-surgery, the wounds were covered with surgical dressings, and penicillin (50,000 U) was injected for three consecutive days. The rabbits were euthanized at Weeks 1 and 4 by intravenous injection of an overdose of pentobarbital sodium (≥ 150 mg/kg) via the ear vein.

2.11. Histological staining

Ex vivo bone samples were fixed in 4% paraformaldehyde (PFA; Sigma Aldrich, USA) for 48 h, followed by dehydration through a graded ethanol series (70%–100%). The samples were then embedded in polymethyl methacrylate (PMMA) and vacuum-cured at 38 °C for 72 h. Coarse sections (150 μm) were prepared using an EXAKT E302 diamond saw and subsequently ground and polished to a final thickness of 10 μm for analysis. To systematically characterize the morphological features of the newborn bone tissue, a double-staining strategy was employed, utilizing Masson's trichrome staining and hematoxylin and eosin (H&E) staining, followed by microscopic imaging.

2.12. Statistical analysis

Statistical analyses were performed using SPSS (version 19.0, IBM, USA). Experimental data are presented as mean ± standard deviation. Two-way analysis of variance (ANOVA) was used for comparisons between two groups, and one-way ANOVA was used for single-group data. Statistical significance was set at $p < 0.05$.

3. Results and discussion

3.1. Structure and characterization of Ta–Mg composites

Both Mg and Ta are key materials in orthopedic implants, characterized by degradability and bioinertness, respectively.[31–33] These metals exhibit significant physical differences; Mg has a melting point of 650°C, while Ta has a melting point of 3017°C. Both metals possess low solubility, providing ideal conditions for melt infiltration composite technology.[34] In this study, porous Ta scaffolds with a diamond structure were successfully fabricated using SLM technology, featuring a lattice unit side length of 3.33 mm, a pore size of 738.3 ± 64.6 μm, and porosity

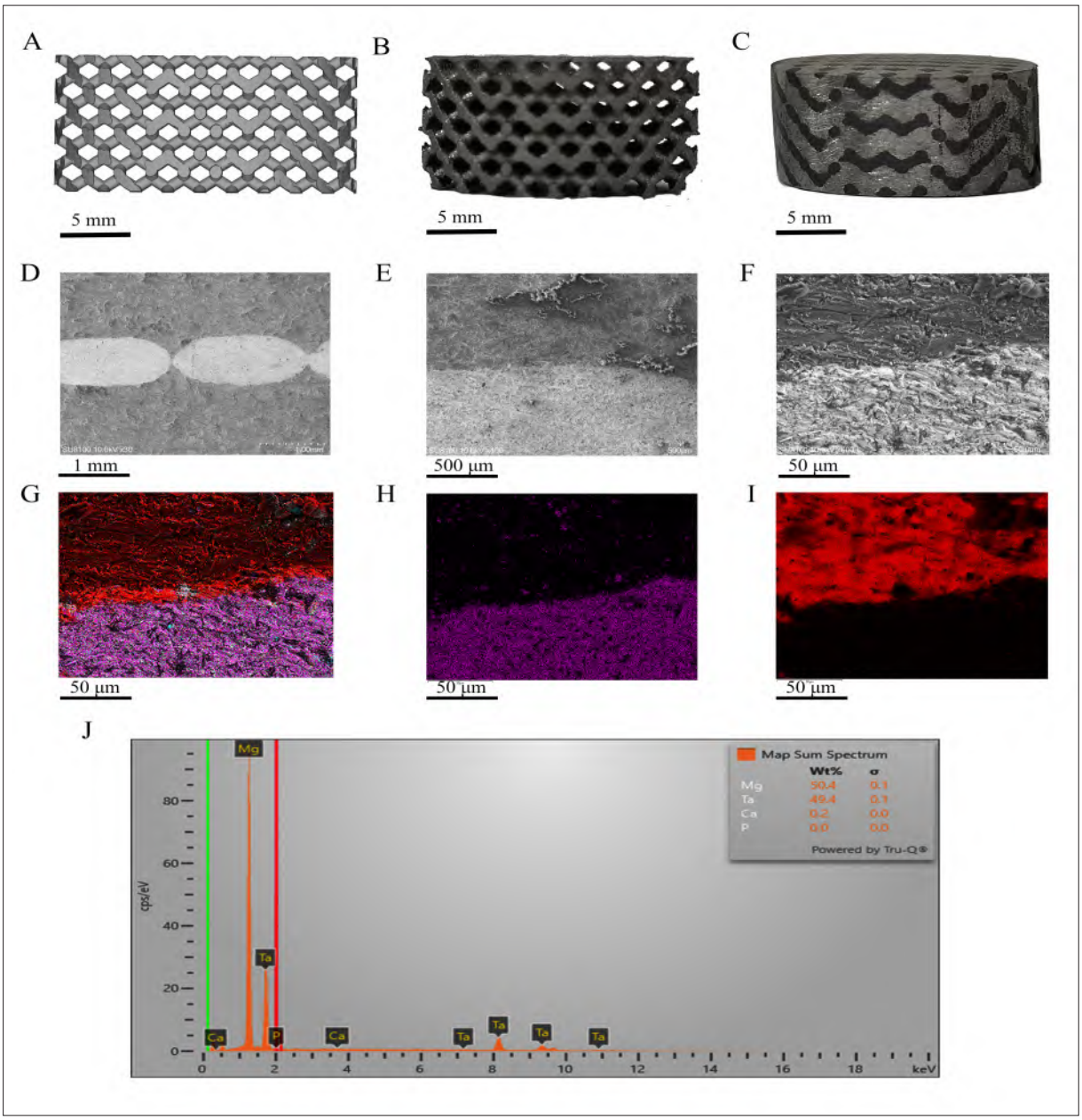


Figure 1. Macroscopic and microscopic characterization of Ta–Mg composites. (A–C) Progressive hierarchy of the porous Ta scaffold model (A), porous Ta scaffold (B), and Ta–Mg composite (C). (D–F) Scanning electron microscopy (SEM) images of the composite scaffold at different magnifications: 10.0 kV ×30 (D), 10.0 kV ×100 (E), 10.0 kV ×600 (F). (G–I) Representative energy dispersive spectroscopy (EDS) images of the composite scaffold: Ta–Mg (G), Ta (H), and Mg (I). (J and K) EDS spectra and corresponding quantitative representation. Scale bars: 5 mm (A–C); 1 mm (D); 500 μm (E); 50 μm (F); 50 μm (G); 50 μm (H and I).

of 70%. On this basis, the pressureless infiltration process was employed to precisely incorporate Mg melt into the pores of the Ta scaffold, thereby forming a dense Ta–Mg composite. Figure 1 presents the macroscopic and microscopic characterizations of the Ta–Mg composite. Microstructural analysis (Figure 1D–F) revealed that the composite surface exhibits a smooth morphology, with no structural defects such as pores or cracks. This indicates that after the Mg melt infiltrates into the Ta scaffold and subsequently solidifies, the Ta–Mg composite becomes highly dense. EDS analysis (Figure 1G–J) confirms that the material is primarily composed of Ta and Mg, with a clear and tight interface between the two phases. The element distribution exhibits a gradient transition, with Ta and Mg forming a continuous and interconnected 3D interpenetrating network structure. Likewise, the reaction layer thickness of the Ta–Mg composite was measured to be 9.56 ± 0.66 μm (Figure S1, Table S1), suggesting significant diffusion reactions between the two metals during melt infiltration processing.

Inspired by the layered and ordered "brick-and-mortar" structure of natural pearls, this study manufactured Ta–Mg composites by incorporating molten Mg. The porous regions within the 3D interpenetrating network structure are interconnected, facilitating the exchange of nutrients and the growth of new tissues, thereby enhancing the bonding strength between the host and the implant.[16] Based on the significant difference in elastic modulus between the Ta and Mg phases, a biomimetic brick-and-mortar structure was formed. This structure promotes effective stress transfer, delocalizes damage, and prevents cracking, resulting in higher strength and ductility compared to composites with discrete materials.[36]

3.2. Immersion test

Figure 2 displays the *in vitro* degradation behavior of pure Mg and Ta–Mg composites, including changes in pH, weight, and macroscopic morphology of the two materials. Figure 2A presents the changes in the macroscopic morphology of the Ta–Mg composite over time. The Ta–Mg composite exhibits typical corrosion characteristics during the degradation period. In the first

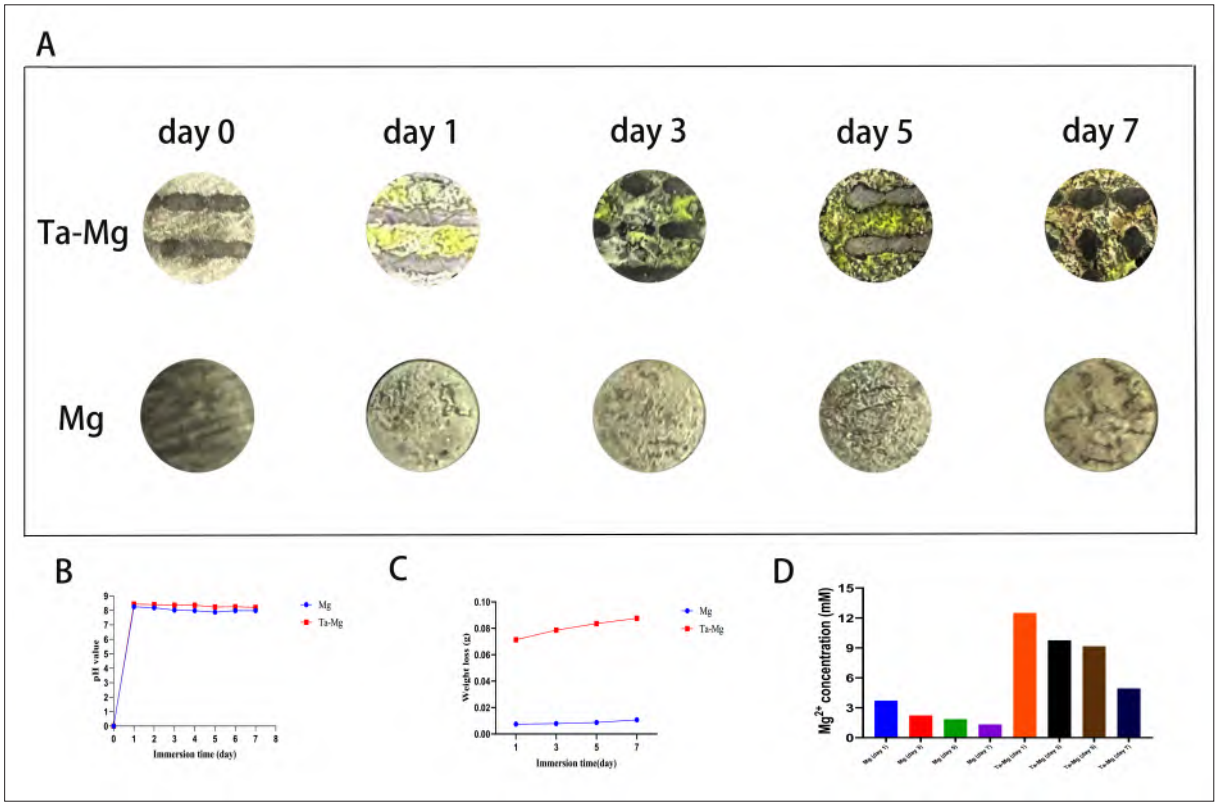


Figure 2. Macroscopic characterization and degradation parameters of Ta Mg composite materials and pure magnesium degradation process (corrosion behavior over time, pH evolution, weight loss, and Mg^{2+} release). (A) Macroscopic corrosion surfaces of the Ta–Mg composite and pure Mg scaffolds over time. (B) Changes in pH of the Ta–Mg composite and pure Mg scaffolds during the degradation period. (C) Weight loss of the Ta–Mg composite and pure Mg scaffolds. (D) Mg^{2+} release from the Ta–Mg composite and pure Mg scaffolds over the degradation period. Magnification: ×1(A).

24 h, corrosion preferentially occurs along the interface between the Ta and Mg phases, forming radial corrosion grooves. After 3 days of corrosion, the corrosion extends from the interface toward the center of the Mg phase, forming a honeycomb-like corrosion morphology. Notably, the corrosion propagation rate of the composite is significantly higher than that of pure Mg, which is closely related to the galvanic corrosion effect between the two phases, with a potential difference of 3.87 V. The pH of the extract solutions from both groups reached their peaks within the first 24 h (Figure 2B). The pH of the Ta–Mg composite group was higher than that of the pure Mg group from Days 1 to 7, maintaining a higher alkalinity throughout the entire experimental period. As indicated in Figure 2C, the cumulative weight loss rate of the Ta–Mg composite reached 33.7% at Day 7, significantly higher than that of pure Mg at 12.1%. Similar to the pH results, the Ta–Mg composite experienced the greatest weight loss within the first 24 h, followed by a gradual decrease in its degradation rate.

Figure 2D presents the changes in Mg^{2+} concentration over the degradation period. The Ta–Mg (Day 1) group and the pure Mg (Day 1) group reported the highest Mg^{2+} concentrations, with the maximum concentration reaching 12.5 mM for the composite and 3.7 mM for the pure Mg. As the immersion time extended, the Mg^{2+} concentrations in both the pure Mg group and the Ta–Mg group gradually decreased, exhibiting a similar trend. This finding aligns with the expected results, as the degradation outcomes of the Ta–Mg composite and control groups were compared over the experimental period.

Figure 3 features the microstructure of the Ta–Mg composite. After removing the corrosion products, the Ta matrix maintains structural integrity, while the Mg phase exhibits selective corrosion characteristics. Within the first 24 h of corrosion, corrosion grooves formed at the interface between the Ta and Mg phases. As the immersion time extends to 7 days, the Mg phase develops a typical pitting corrosion morphology.

Figure 4 displays the EDS results of the Ta–Mg composite after immersion for 1 and 7 days. It can be observed that after Day 1 of degradation (Figure 4A, B), Ca, P, and O are evenly distributed in both phases. This is attributed to the preferential degradation of the Mg phase, leading to a rapid increase in pH to 8.4. The oversaturation of Ca^{2+} and PO_4^{3-} in the culture medium results in the formation of amorphous calcium phosphate (ACP). However, due to the high surface roughness of the Mg matrix, ACP randomly deposits on the surfaces of both phases. The enrichment of O is related to the formation of a

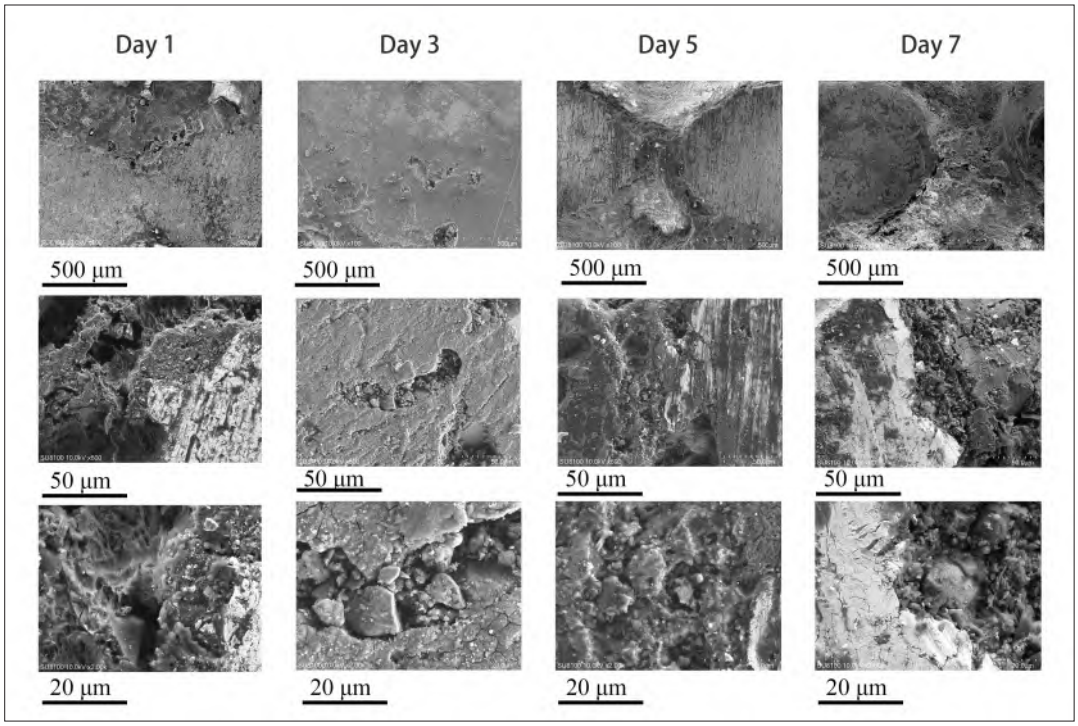


Figure 3. Micromorphology of the Ta–Mg composite scaffold after 1, 3, 5, and 7 days of degradation. Magnification from top to bottom: 10.0 kV ×100, 10.0 kV ×600, 10.0 kV ×2000. Scale bars from top to bottom: 500, 50, and 20 μm.

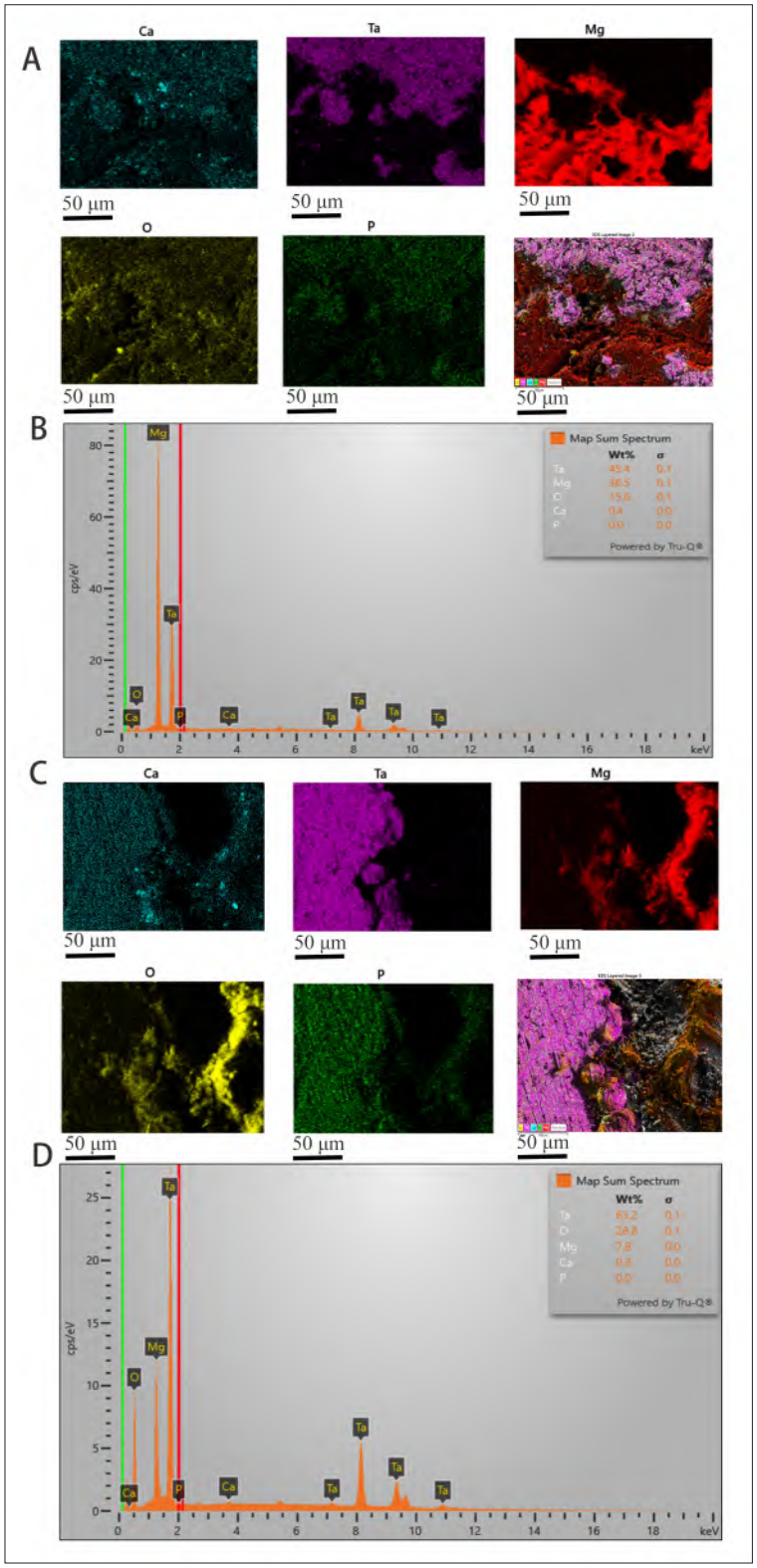


Figure 4. EDS elemental analysis of the degradation process of Ta–Mg composites: comparison of degradation characteristics between Day 1 and Day 7. (A) Elemental distribution of Ta, Mg, Ca, O, and P in the Ta–Mg composite after 1 day of degradation. (B) Elemental content of the Ta–Mg composite after 1 day of degradation. (C) Elemental distribution of Ta, Mg, Ca, O, and P in the Ta–Mg composite after 7 days of degradation. (D) Elemental content of the Ta–Mg composite after 7 days of degradation. Scale bar: 50 μm (A and C).

$Mg(OH)_2$ passivation layer on the surface of the Mg phase and the oxidation to form Ta_2O_5 on the surface of the Ta phase. In the later stages of degradation (Figure 4C, D), Ca, P, and O become concentrated on the Ta phase. This is associated with the potential difference between the two phases, where the Ta phase serves as a cathode, facilitating the migration of PO_4^{3-} and forming a locally high-concentration area. Ca^{2+}, through electrostatic adsorption, co-deposits with PO_4^{3-} on the surface of the Ta phase, forming crystalline hydroxyapatite (HA). As displayed by the EDS area scan (Figure 4C), Mg content decreases in the edges of the corrosion pits, confirming the infiltration of corrosive media. Notably, no significant corrosion damage is observed on the surface of the Ta phase, and its elemental composition remains stable, indicating that the Ta matrix exhibits good chemical inertness throughout the experimental period.

In the Ta–Mg composite system, Mg acts as the sacrificial anode, while Ta is cathodically protected. The corrosion products of Mg are mainly $Mg(OH)_2$ and H_2, where the $Mg(OH)_2$ passivation film can temporarily inhibit further corrosion of the Mg substrate in an alkaline environment. However, the stability of this passivation film is significantly reduced in a physiological environment containing ions, such as Cl^- and SO_4^{2-}, gradually transforming into soluble $MgCl_2$ and further mineralizing into $Mg_3(PO_4)_2$ and HA deposition layers. This transformation process may be a key mechanism for the stabilization of solution pH in immersion tests.[37,38] Notably, the hydrogen generated by the non-homogeneous corrosion of Mg can create localized stress concentrations within the Ta skeleton, particularly in enclosed pore areas, potentially leading to microcracks and ultimately structural failure. Wen *et al.*[38] have reported that Ti6Al4V–Mg composites prepared using powder metallurgy methods exhibit a significant reduction in the structural integrity of the titanium (Ti) skeleton after just 1 day of immersion. The primary failure mechanism is attributed to the stress induced by hydrogen pressure accumulation exceeding the yield strength of the Ti phase. In contrast, Esen *et al.*[39] have effectively dispersed hydrogen-induced stress and maintained the integrity of the Ti skeleton by constructing a 3D interpenetrating network structure that utilizes the stress transfer effect between the Mg/Ti bi-continuous phases. Based on this, the present study employed a similar 3D interpenetrating structure design for the Ta–Mg system. Compared to Ti, Ta not only exhibits higher mechanical strength and chemical inertness but also forms a dense passivation film of Ta_2O_5 *in vivo*, which can act as a hydrogen barrier at room temperature to inhibit hydrogen permeation, thereby demonstrating superior structural stability during long-term bone integration.[41]

3.3. Mechanical properties of Ta–Mg composites at room temperature

Figure 5 presents a comparison of the room-temperature compressive stress–strain curves of pure Mg, porous Ta, and Ta–Mg composite scaffolds, as well as the Ta–Mg composite scaffold after 7 days of degradation, along with the quantification of elastic moduli and yield strength for each group. As displayed in Figure 5A, the mechanical properties of porous Ta (tantalum) scaffolds are completely different from traditional Ta implants; i.e., the calculated elastic modulus of the porous Ta scaffold is 1.12 GPa. As illustrated in Figure 5B, the highest compressive strength of the prepared porous Ta is 137.54 MPa, with a yield strength of 84.47 MPa. The elastic modulus of the Ta–Mg composite is 3.67 GPa, which falls between the elastic moduli of cortical bone and trabecular bone. An elastic modulus similar to that of human bone can effectively reduce the occurrence of stress shielding, thereby achieving long-term bone integration capability.[35] Notably, Ta–Mg elastic modulus after 7 days of degradation is 1.36 GPa, comparable to that of the porous Ta scaffold. As featured in Figure 5C, the Ta–Mg composite exhibits unique mechanical response characteristics after initial yielding, with stress steadily increasing from approximately 152 MPa to a peak of 252 MPa, followed by the formation of a stress plateau accompanied by a slight decrease. Before degradation, the stress–strain curve of the Ta–Mg composite aligns with that of porous Ta up to a strain of 4.3%, after which it follows a trend similar to pure Mg. This result indicates that when the strain surpasses the brittleness of Ta, the stress is primarily concentrated in the Mg matrix. The Mg matrix dominates the composite material, which is related to the porosity of porous Ta. Notably, under the same strain conditions, the Ta–Mg composite demonstrates a significantly higher load-bearing stress compared to porous Ta scaffolds.

After 7 days of *in vitro* degradation, the overall mechanical properties of the Ta–Mg composite displayed a decreasing trend, likely due to the disruption of the continuous Mg phase in the network structure. However, the stress of the degraded material remained comparable to that of the original porous Ta scaffold, indicating that the Ta matrix effectively maintained structural integrity throughout the degradation process without significant attenuation of the mechanical properties. To further elucidate the structure–mechanical property relationship of the Ta–Mg composite, we assessed its micromorphological features using SEM, revealing that the Mg phase formed a 3D interpenetrating network structure within the Ta skeleton, with microcracks observed at the interface between the two phases (Figure 5D). This unique configuration provides a

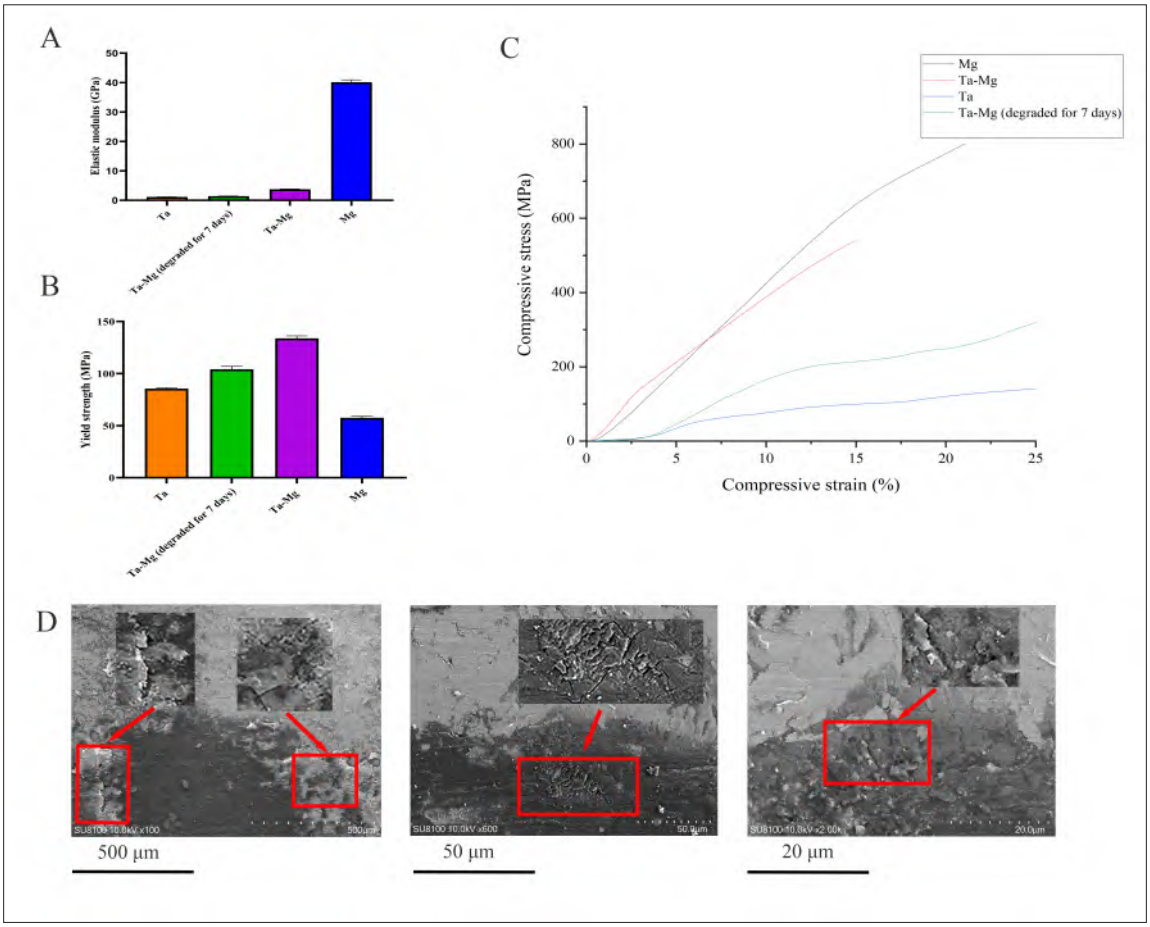


Figure 5. Mechanical properties of Ta–Mg composites and porous Ta scaffolds under room temperature compression and their microstructure characterization after degradation. (A) Elastic modulus of the Ta–Mg composite, pure Mg, and porous Ta scaffolds, along with the Ta–Mg composite scaffold after 7 days of degradation under room temperature compression (n = 3). (B) Yield strength of the Ta–Mg composite, pure Mg, and porous Ta scaffolds, along with the Ta–Mg composite scaffold after 7 days of degradation under room temperature compression (n = 3). (C) Stress–strain curves of the Ta–Mg composite, pure Mg, and porous Ta scaffolds, along with the Ta–Mg composite scaffold after 7 days of degradation under room temperature compression. (D) Microscopic characterization of the Ta–Mg composite after compression. 10.0 kV ×100 (left); 10.0 kV ×600 (middle); 10.0 kV ×2000 (right). Scale bars: 500, 50, 20 μm (D); 500, 50, 20 μm (D, inset).

microstructural basis for validating the mechanical behavior of the Ta–Mg composite.

3.4. Biocompatibility *in vitro*

3.4.1. Cell viability

Biocompatibility evaluation of biodegradable orthopedic implant materials requires particular attention to their degradation behavior in the physiological environment and the impact of their degradation products. According to Gao *et al.*,[42] there is a significant difference in the degradation rate of Mg between *in vitro* and *in vivo* conditions, with the *in vitro* degradation rate typically being 2–4 times faster than that of *in vivo*. This suggests that a reasonable concentration conversion system needs to be established for *in vitro* experiments. Based on the recommended dilution range of 6–10 times for cell toxicity evaluation of extract solutions proposed by Wang *et al.*,[43] a sixfold diluted extract solution was used in the present study to control the Mg^{2+} concentration within a physiologically relevant range. The effects of Ta–Mg composites and pure Mg on the morphology, proliferation, and ALP activity of MC3T3 pre-osteoblastic cells were systematically evaluated.

This study systematically evaluated the effects of pure Mg and Ta–Mg composites on the proliferative activity of MC3T3 pre-osteoblasts using CCK-8. As displayed in Figure 6A, cells in both material groups exhibited good proliferation trends over the 3-day culture period, characterized by a continuous increase in optical density (OD450) values with prolonged culture time. Notably, the OD value of the Ta–Mg group after 3 days of culture

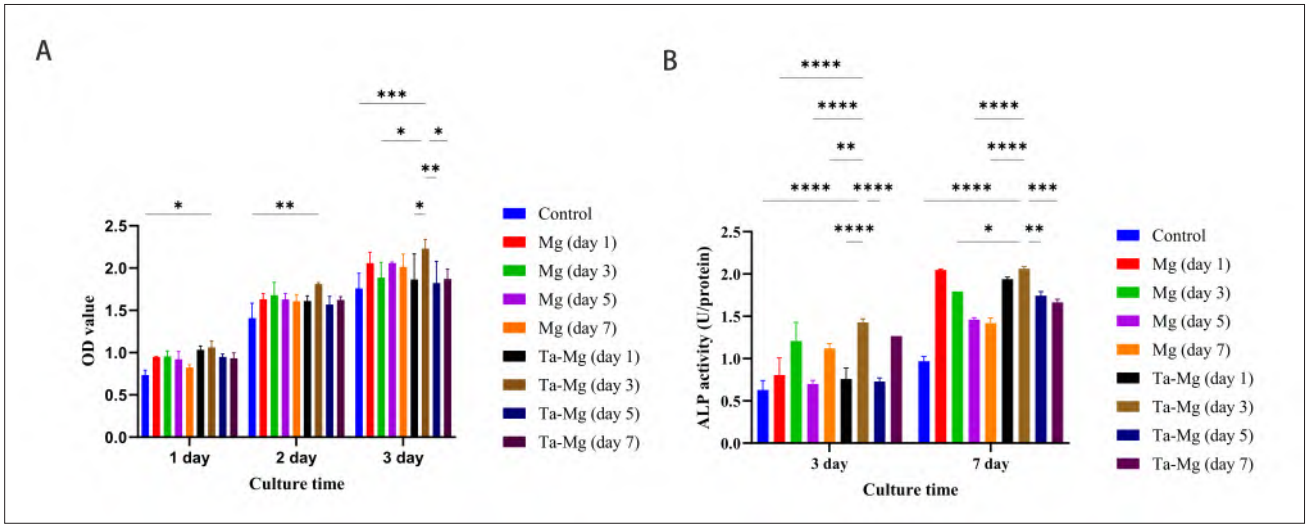


Figure 6. Evaluation of the cytocompatibility and osteogenic activity of Ta–Mg Composite Material and pure Mg degradation products. (A) Optical density (OD) of MC3T3-E1 cells cultured with extracts of degraded Ta–Mg composite and pure Mg scaffolds over 3 days. (B) Alkaline phosphatase (ALP) produced by MC3T3-E1 cells cultured with degraded scaffold extracts for 3 and 7 days. *$p < 0.05$, **$p < 0.01$, ***$p < 0.001$, ****$p < 0.0001$; $n = 3$.

(9.75 mM) was significantly higher than that of the pure Mg and control groups ($p < 0.05$), indicating the enhanced proliferative capacity of the Ta–Mg composite. This finding correlated with the Mg^{2+} concentration in the Ta–Mg group at Day 3 (9.75 mM). Our results corroborated the study by Nie *et al.*,[44] who reported that 10 mM Mg^{2+} can promote osteogenic function by enhancing integrin-mediated cell adhesion and cytoskeletal remodeling; the Mg^{2+} concentration in the Ta–Mg (Day 3) group in the present study was close to the reported concentration range (5–10 mM). The Mg^{2+} concentration in the Ta–Mg (Day 1) group reached 12.5 mM, and its OD value was lower than that of the pure Mg group and other Ta–Mg groups during the 3-day culture period. This is consistent with the findings by Zhang *et al.*,[45] who reported that Mg^{2+} can significantly enhance osteoblast activity within the concentration range of 4–10 mM; at medium to high concentrations (10–20 mM), inhibitory effects begin to emerge; and at high concentrations (>20 mM), Mg^{2+} inhibits osteoblast activity. This phenomenon is related to multiple factors. At low concentrations, Mg^{2+} upregulates the expression of Runx2 and ALP through the TRPM7/PI3K signaling pathway, thereby significantly enhancing the osteogenic activity of human osteoblasts. However, at high concentrations, Mg^{2+} competitively occupies Ca channels, reducing intracellular Ca^{2+} concentrations, which disrupts Ca-mediated mineralization. Additionally, excessive chelation of Mg^{2+} with ATP inhibits mitochondrial function. Likewise, high concentrations of Mg^{2+} significantly downregulate p-Akt expression, blocking survival signals and inhibiting proliferation and differentiation.[46–48] In this study, the Mg^{2+} concentration of the Ta–Mg composite was within 4.9–12.5 mM and gradually stabilized over the degradation period, indicating its promotive effect on osteoblast activity.

3.4.2. ALP activity

The differentiation capacity of MC3T3 cells is often used to characterize the maturation of osteoblasts and can be assessed through ALP activity detection. ALP, a key enzyme regulating bone formation, is highly expressed in the early stages of bone development and is recognized as an early marker of osteoblast differentiation.[45] As displayed in Figure 6B, over the 7-day culture period, Mg-containing samples exhibited a promotive effect on ALP activity. The ALP level in both the Ta–Mg composite and pure Mg groups was significantly higher than that in the control group at the two detection time points ($p < 0.05$), confirming that Mg enrichment has a positive effect on osteogenic differentiation.

On Day 3, ALP activity in the Ta–Mg composite group was significantly higher than that in the pure Mg and control groups, indicating that the composite possesses superior osteogenic properties. The higher ALP activity observed in the pure Mg group compared to the Ta–Mg group on Day 1 could be attributed to the excessively high Mg^{2+} release (12.5 mM) during the early stage in the Ta–Mg group. Studies have demonstrated that an appropriate amount of Mg^{2+} (6–10 mmol/L) can significantly enhance the ALP activity of osteoblasts, but excessively high Mg^{2+} concentrations may be toxic to cells.[27,38,41] Mg^{2+}, the main cofactor of ALP, stabilizes the enzyme conformation and promotes the hydrolysis of substrate phosphate

bonds by binding to the metal site in the active center of ALP. At medium to high concentrations (>10 mM), Mg^{2+} competitively occupies the metal-binding sites of ALP, interfering with the catalytic function of Zn^{2+} and decreasing enzyme activity.[49] At the molecular level, low concentrations of Mg^{2+} upregulate osteogenic genes, such as *RUNX2*, by activating the Wnt/β-catenin pathway, indirectly enhancing ALP expression. Conversely, medium to high physiological concentrations of Mg^{2+} (>10 mM) inhibit the PI3K/Akt pathway, blocking osteogenic differentiation and decreasing ALP synthesis.[44,45,50,51] In this study, the Mg^{2+} release rate of the Ta–Mg composite gradually slowed down over the culture period, maintaining its concentration within an appropriate range. Therefore, ALP activity in the Ta–Mg composite group at subsequent time points was superior to that in the pure Mg group, indicating a more stable and sustained promotion of osteogenic differentiation.

3.4.3. Cell morphological staining

Figure 7 displays the distribution of the F-actin cytoskeleton network within cells, characterized using Rhodamine-labeled phalloidin and DAPI dual fluorescent staining techniques. After 6 h of culture, cells in both the pure Mg and Ta–Mg composite groups exhibited a typical spindle-shaped morphology with a relatively low number of filamentous pseudopodia. When the culture period was extended to 24 h, cells in the Ta–Mg composite group gradually developed highly extended fibrous structures, exhibiting a clear network of F-actin stress fibers

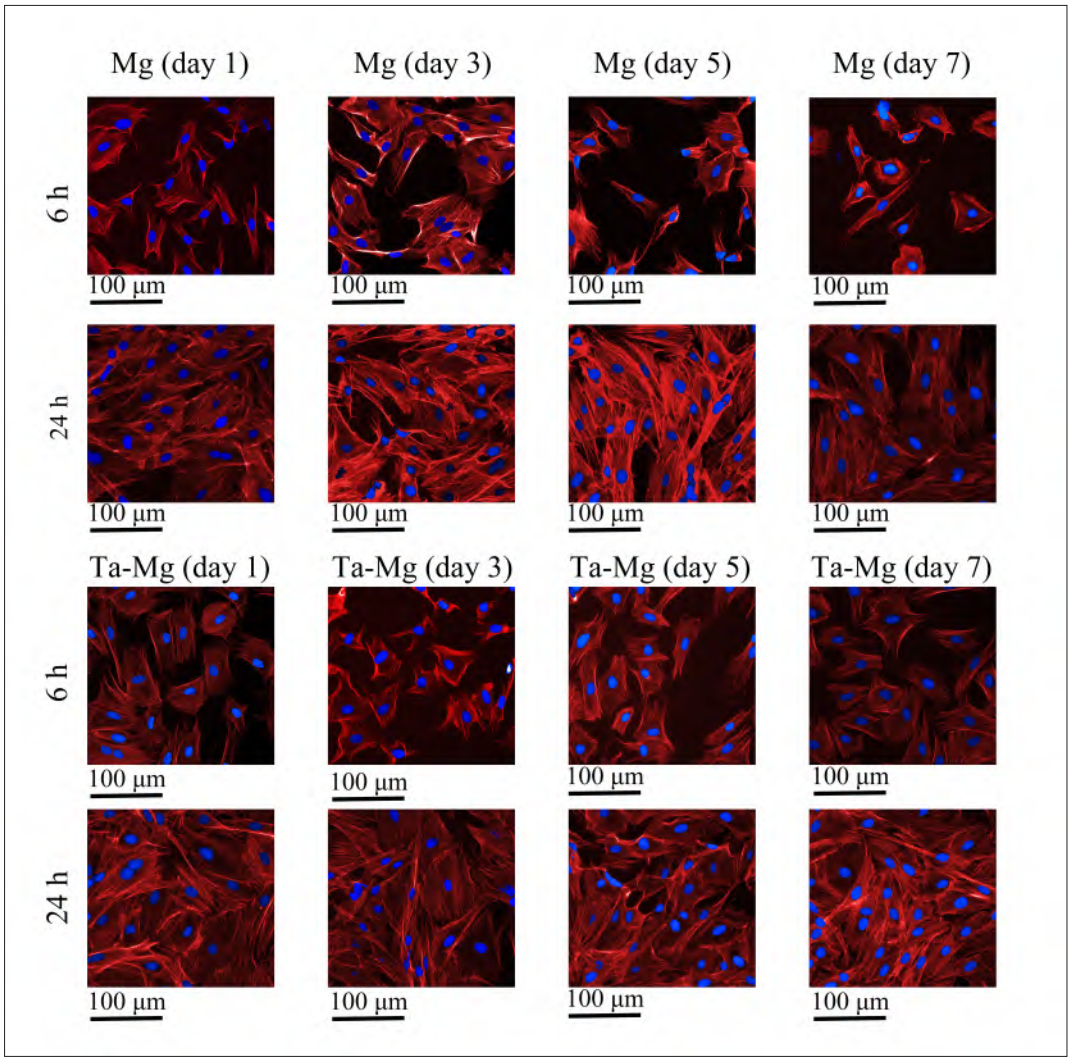


Figure 7. Morphological staining of MC3T3-E1 cells cultured with extracts of Ta–Mg composite and pure Mg scaffolds for 6 and 24 h over 7 days. Scale bars: 100 μm.

accompanied by abundant filamentous and lamellipodial structures. Compared to the pure Mg group, the Ta–Mg composite group demonstrated significantly increased cell spreading area, indicating superior initial adhesion behavior of MC3T3-E1 cells on its surface. This phenomenon can also be attributed to the Mg^{2+} concentration, further supporting the excellent performance of Ta–Mg composites in promoting cell differentiation, enhancing osteogenic activity, and mineralization capacity.

Additionally, Mg^{2+} promotes osteoblast proliferation, migration, adhesion, and osteogenic activity while inhibiting osteoblast apoptosis through the TRPM/PI3K signaling pathway. Mg^{2+} also participates in the PI3K/Akt signaling pathway via the ion channel-kinase protein TRPM7.[44] According to Maier *et al.*,[52] Mg^{2+} has a significant impact on the overall structure of actin filament bundles; at low concentrations (2–12 mM), the addition of Mg^{2+} changes the elasticity of the actin network. These findings suggest that a concentration of approximately 10 mM Mg^{2+} is optimal for facilitating implant integration with surrounding tissues.

3.5. Biocompatibility *in vivo*

Figure 8 presents the histological evaluation of Ta–Mg composite and porous Ta scaffolds through H&E and Masson's staining, aiming to assess their osseointegration and osteogenic capacity. At Week 1, we observed new bone growth surrounding the Mg phase (in red) in the Ta–Mg composite group (Figure 8A). With the degradation of the Mg phase, purple staining appeared in the degraded area, indicating the presence of bone cells. Although mineralized new bone was also observed in the porous Ta group, cell infiltration was more evident, and the cell distribution was denser in the Ta–Mg composite group, suggesting a greater capacity to attract and attach cells. At Week 4, the Ta–Mg composite scaffold exhibited significant corrosion grooves. Notably, mild inflammation (red arrow) was observed in the porous Ta group. The results of Masson's trichrome staining are featured in Figure 8B, revealing substantial extracellular matrix deposition around the implants in all groups at Week 1. The extracellular matrix deposition in the Ta–Mg composite group was significantly greater than that in the porous Ta group, indicating its effectiveness in inducing collagen fiber formation in the early stage. At

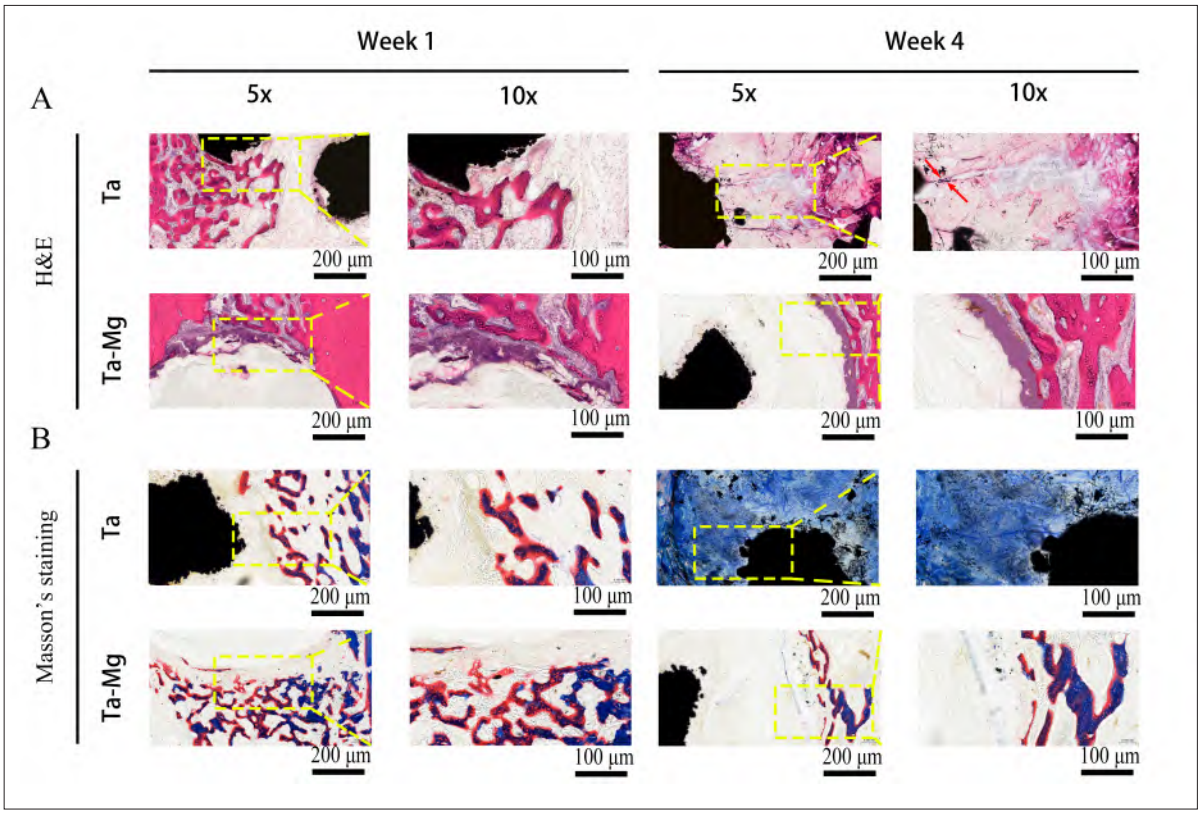


Figure 8. Histological analysis of *in vivo* animal experiments on porous Ta and Ta–Mg composite scaffolds. (A) Representative images of hematoxylin and eosin (H&E) staining of porous Ta and Ta–Mg composite scaffolds at Weeks 1 and 4. (B) Representative images of Masson's staining of porous Ta and Ta–Mg composite scaffolds at Weeks 1 and 4. The black areas represent the Ta phase, while the white spaces between the black areas and the tissue represent the Mg phase. The area marked with a red arrow is the inflammatory region. Scale bars: 200 μm (magnification: 5×); 100 μm (magnification: 10×).

Week 4, collagen fibers (in blue) in the porous Ta group appeared fragmented and distributed in a discontinuous ring around the porous Ta scaffold, likely attributed to inflammatory cell infiltration. In contrast, the Ta–Mg composite group displayed an interspersed area (red and blue), typical of connective tissue structure. These findings demonstrate the superior osteogenic activity of the Ta–Mg composite.

As this study primarily focused on the biocompatibility and activity of Ta–Mg composites, the implant duration was relatively short, limiting the ability to detect differences between groups. Extending the implant duration in future studies may help minimize such deviations. In comparison with the *in vitro* experiments, the degradation rate of Mg-based materials is significantly slower *in vivo*, consistent with the findings of Wang *et al.*[38] Likewise, Ma *et al.*[53] incorporated Mg onto the surface of Ta scaffolds using the Polydopamine (PDA) coating method, resulting in enhanced osseointegration and vascularization. The study also reported that 20 mM Mg^{2+} achieved the greatest osseointegration and vascularization during long-term bone integration.

Overall, the *in vivo* experiments have demonstrated that Ta–Mg composites possess stronger bioactivity than the other scaffolds, consistent with *in vitro* results, suggesting significant advantages in early bone repair. However, osseointegration capability arises from the combined effects of bioactivity, adaptive mechanical properties, and spatial structure, warranting more in-depth and comprehensive research to explore its mechanisms.

4. Conclusion

In this study, we combined additive manufacturing technology with pressureless infiltration to fabricate Ta–Mg composites with a 3D interpenetrating network structure. The composite was obtained through pressureless infiltration of Mg into the porous Ta scaffold. Mechanical assessments indicated that the composite possesses a compressive modulus and strength conducive to bone tissue ingrowth, and its bone–implant interface bonding strength significantly surpasses that of human cortical bone. *In vitro* and *in vivo* results confirmed the composite's excellent biocompatibility and osteogenic activity, validating its vast potential for application in load-bearing bone defect repair.

Acknowledgments

None.

Funding

This work was supported by the Horizontal Research Project of Henan Polytechnic University (grant no. 12200442). The funding source had no involvement in the study design; collection, analysis, and interpretation of data; article preparation; or the decision to submit the article for publication.

Conflict of interest

The authors declare they have no competing interests.

Author contributions

Conceptualization: Jingchao Xu
Data curation: Jingchao Xu, Shuixian Guo
Formal analysis: Jingchao Xu, Shuixian Guo
Funding acquisition: Yanru Zhang
Investigation: Jingchao Xu
Methodology: Jingchao Xu
Project administration: Jingchao Xu
Resources: Yanru Zhang, Yue Yang
Supervision: Yanru Zhang, Jingwei Yu
Writing–original draft: Jingchao Xu
Writing–review & editing: Yanru Zhang

Ethics approval and consent to participate

This study was reviewed and approved by the Medical Ethics Committee of Henan Polytechnic University (approval ID: HPULLSC2025-034. For animal experiments, the protocol complied with the ARRIVE 2.0 guidelines and was conducted in accordance with the National Standard GB/T 35892-2018 "Laboratory animal – Guidelines for ethical review of animal welfare." All surgical interventions were performed under sodium pentobarbital anesthesia, and every effort was made to minimize animal suffering.

Consent for publication

Not applicable

Availability of data

Data supporting the findings of this study are available from the corresponding author upon reasonable request.

References

1. Salhotra A, Shah HN, Levi B, Longaker MT. Mechanisms of bone development and repair. *Nat Rev Mol Cell Biol.* 2020;21(11):696-711.
doi: 10.1038/s41580-020-00279-w

2. Loi F, Córdova LA, Pajarin en J, Lin T, Yao Z, Goodman SB. Inflammation, fracture and bone repair. *Bone.* 2016;86:119-130.
doi: 10.1016/j.bone.2016.02.020

3. Robinson PG, Gray AC, Cooper C, *et al.* Autologous bone grafting. *Oper Tech Sports Med.* 2020;28(4):150780.
doi: 10.1016/j.otsm.2020.150780

4. Seo Y, Wang ZJ. Measurement and evaluation of specific absorption rate and temperature elevation caused by an artificial hip joint during MRI scanning. *Sci Rep.* 2021;11(1):1134.
doi: 10.1038/s41598-020-80828-7

5. Qu H, Fu H, Han Z, Sun Y. Biomaterials for bone tissue engineering scaffolds: a review. *RSC Adv.* 2019;9(45):26252-26262.
doi: 10.1039/c9ra05214c

6. Chen C, Lin C, Wang Q, *et al.* α-hemihydrate calcium sulfate/octacalcium phosphate combined with sodium hyaluronate promotes bone marrow-derived mesenchymal stem cell osteogenesis in vitro and in vivo. *Drug Des Devel Ther.* 2018;12:3269-3287.
doi: 10.2147/DDDT.S173289

7. Bandyopadhyay A, De A, Bose S. Improving biocompatibility for next generation of metallic implants. *Prog Mater Sci.* 2023;133:101053.
doi: 10.1016/j.pmatsci.2022.101053

8. Carraro F, Bagno A. Tantalum as trabecular metal for endosseous implantable applications. *Biomimetics.* 2023;8(1):49.
doi: 10.3390/biomimetics8010049

9. Zhu W, Ma X, Gou M, Mei D, Zhang K, Chen S. 3D printing of functional biomaterials for tissue engineering. *Curr Opin Biotechnol.* 2016;40:103-112.
doi: 10.1016/j.copbio.2016.03.014

10. Li J, Wang C, Huang Y, Luo J. Materials evolution of bone plates for internal fixation of bone fractures: a review. *J Mater Sci Technol.* 2020;36:190-208.
doi: 10.1016/j.jmst.2019.07.024

11. Al-Tamimi AA, Totonchi A, Garcia-Gonzalez D, Harrysson OLA, Redondo J, Malakhov K. Stress analysis in a bone fracture fixed with topology-optimised plates. *Biomech Model Mechanobiol.* 2020;19:693-699.
doi: 10.1007/s10237-019-01240-3

12. Klingebiel S, Gosheger G, Nottrott M, *et al.* Periprosthetic stress shielding of the humerus after reconstruction with modular shoulder megaprostheses in patients with sarcoma. *J Clin Med.* 2021;10(15):3424.
doi: 10.3390/jcm10153424

13. Uslu E, Kucuk A, Yetmez M, Ozkan S, Celik E. Fabrication and cellular interactions of nanoporous tantalum oxide. *J Biomed Mater Res B Appl Biomater.* 2020;108(7): 2743-2753.
doi: 10.1002/jbm.b.34604

14. Wang X, Li L, Fu W, *et al.* Advances in surface modification of tantalum and porous tantalum for rapid osseointegration: a thematic review. *Front Bioeng Biotechnol.* 2022; 10:983695.
doi: 10.3389/fbio.2022.983695

15. Liu DC, Chen J, Li D, *et al.* Micro-arc oxidation coating containing phosphorus on tantalum substrates prepared by micro-arc oxidation. *J Test Eval.* 2021;49(6):4662-4670.
doi: 10.1520/JTE20200647

16. Wang H, Su K, Su L, Liang P, Ji P. Comparison of 3D-printed porous tantalum and titanium scaffolds on osteointegration and osteogenesis. *Mater Sci Eng C.* 2019;104:109908.
doi: 10.1016/j.msec.2019.109908

17. Liu T, Wang J, Zhu L, *et al.* Biofunctionalization of 3D printed porous tantalum using a vancomycin–carboxymethyl chitosan composite coating to improve osteogenesis and antibiofilm properties. *ACS Appl Mater Interfaces.* 2022;14(37):41764-41778.
doi: 10.1021/acsami.2c11715

18. Fan L, Guo R, Zhang X, *et al.* Metallic materials for bone repair. *Adv Healthc Mater.* 2024;13(3):2302132.
doi: 10.1016/j.jmrt.2025.05.069

19. Zhi P, Li Y, Yuan J, *et al.* Advances in the study of magnesium alloys and their use in bone implant material. *Metals.* 2022;12(9):1500.
doi: 10.3390/met12091500

20. He M, Wu P, Tang Y, *et al.* Review on magnesium and magnesium-based alloys as biomaterials for bone immobilization. *J Mater Res Technol.* 2023;23:4396-4419.
doi: 10.1016/j.jmrt.2023.02.037

21. Zhang Y, Xu J, Ruan YC, *et al.* Implant-derived magnesium induces local neuronal production of CGRP to improve bone-fracture healing in rats. *Nat Med.* 2016;22(10):1160-1169.
doi: 10.1038/nm.4162

22. Song J, Atrens A, Wu Y, *et al.* Latest research advances on magnesium and magnesium alloys worldwide. *J Magnes Alloy.* 2020;8(1):1-41.
doi: 10.1016/j.jma.2020.02.003

23. Pelczyńska M, Moszak M, Bogdański P. The role of magnesium in the pathogenesis of metabolic disorders. *Nutrients.* 2022;14(9):1714.
doi: 10.3390/nu14091714

24. Fattah-Alhosseini A, Kowalski D, Zakeri M, *et al.* Performance of PEO/polymer coatings on the biodegradability, antibacterial effect and biocompatibility of Mg-based materials. *J Funct Biomater.* 2022;13(4):267.
doi: 10.3390/jfb13040267

25. Kim KW, Padalhin A. Application of photobiomodulation therapy in the recovery of a fracture model in different countries: a concise review. *Med Lasers Eng Basic Res Clin Appl.* 2022;11(4):201-207.
doi: 10.25289/ml.22.055

26. Xue D, Yun Y, Yong Han E. In vivo and in vitro degradation behavior of magnesium alloys as biomaterials. *J Mater Sci Technol.* 2012;28(3):261-267.
doi: 10.1016/S1005-0302(12)60051-6.

27. Luo Y, Wu Y, Zhu W, *et al*. Update on the research and development of magnesium-based biodegradable implants and their clinical translation in orthopaedics. *Biomater Transl.* 2021;2(3):188-201.
doi: 10.12336/biomatertransl.2021.03.003

28. Zhang M, Wang Y, Zhang J, *et al*. 3D printed Mg-NiTi interpenetrating-phase composites with high strength, damping capacity, and energy absorption efficiency. *Sci Adv.* 2020;6(19):eaba5581.
doi: 10.1126/sciadv.aba5581

29. Ecarot-Charrier B, Glimcher MJ, Lian J, *et al*. Osteoblasts isolated from mouse calvaria initiate matrix mineralization in culture. *J Cell Biol.* 1983;96(3):639-643.
doi: 10.1083/jcb.96.3.639

30. Liu J, Wang L, Chen X, *et al*. Effects of allogeneic bone substitute configurations on cell adhesion process in vitro. *Orthop Surg.* 2023;15(2):579-590.
doi: 10.1111/os.13395

31. Atrens A, Song G, Cao F, *et al*. Review of Mg alloy corrosion rates. *J Magnes Alloy.* 2020;8(4):989-998.
doi: 10.1016/j.jma.2020.08.002

32. Wauthle R, van der Stok J, Yavari SA, *et al*. Additively manufactured porous tantalum implants. *Acta Biomater.* 2015;14:217-225.
doi: 10.1016/j.actbio.2014.12.003

33. Shan Z, Qu H, Jia Y, *et al*. Development of degradable magnesium-based metal implants and their function in promoting bone metabolism: a review. *J Orthop Transl.* 2022;36:184-193.
doi: 10.1016/j.jot.2022.09.013

34. Blake AH, Cáceres CH. Solid-solution hardening and softening in Mg–Zn alloys. *Mater Sci Eng A.* 2008;483–484:161-163.
doi: 10.1016/j.msea.2006.10.205

35. Bandyopadhyay A, Mitra I, Shivaram A, Dasgupta N, Bose S. Direct comparison of additively manufactured porous titanium and tantalum implants towards in vivo osseointegration. *Addit Manuf.* 2019;28:259-266.
doi: 10.1016/j.addma.2019.04.025

36. Curto M, Schiavone G, Zappone B, *et al*. Multi-material 3D printed composites inspired by nacre: a hard/soft mechanical interplay. *Sci Rep.* 2025;15(1):6728.
doi: 10.1038/s41598-025-91080-2

37. Ning C, Zhou Y, Zhou X, *et al*. Influence of surrounding cations on the surface degradation of magnesium alloy implants under a compressive pressure. *Langmuir.* 2015;31(50):13561-13570.
doi: 10.1021/acs.langmuir.5b03699

38. Wen Y, Guo X, Zhang Y, *et al*. Improving in vitro and in vivo corrosion resistance and biocompatibility of Mg–1Zn–1Sn alloys by microalloying with Sr. *Bioact Mater.* 2021;6(12):4654-4669.
doi: 10.1016/j.bioactmat.2021.04.043

39. Esen Z, Kaya AA, Gülmez T, *et al*. Corrosion behaviours of Ti6Al4V-Mg/Mg-alloy composites. *Corros Sci.* 2020;166:108470.
doi: 10.1016/j.corsci.2020.108470

40. Yang X, Wu H, Xu J, *et al*. Biodegradability and cytocompatibility of 3D-printed Mg-Ti interpenetrating phase composites. *Front Bioeng Biotechnol.* 2022;10:891632.
doi: 10.3389/fbioe.2022.891632

41. Kim S. Hydrogen gas sensors using a thin Ta2O5 dielectric film. *J Korean Phys Soc.* 2014;65(11):1749-1753.
doi: 10.3938/jkps.65.1749

42. Gao J, Su Y, Qin Y. Calcium phosphate coatings enhance biocompatibility and degradation resistance of magnesium alloy: correlating in vitro and in vivo studies. *Bioact Mater.* 2021;6(5):1223-1229.
doi: 10.1016/j.bioactmat.2020.10.024

43. Wang J, Witte F, Xi T, *et al*. Recommendation for modifying current cytotoxicity testing standards for biodegradable magnesium-based materials. *Acta Biomater.* 2015;21:237-249.
doi: 10.1016/j.actbio.2015.04.011

44. Nie X, Chen W, Zhu Y, *et al*. Effect of magnesium ions/Type I collagen promote the biological behavior of osteoblasts and its mechanism. *Regen Biomater.* 2020;7(1):53-61.
doi: 10.1093/rb/rbz033

45. Zhang X, Xu L, Zhong C, *et al*. Ion channel functional protein kinase TRPM7 regulates Mg ions to promote the osteoinduction of human osteoblast via PI3K pathway: in vitro simulation of the bone-repairing effect of Mg-based alloy implant. *Acta Biomater.* 2017;63:369-382.
doi: 10.1016/j.actbio.2017.08.051

46. Maradze D, Seitz JM, Goldman J, Drelich J, Goldman R. High magnesium corrosion rate has an effect on osteoclast and mesenchymal stem cell role during bone remodelling. *Sci Rep.* 2018;8(1):10003.
doi: 10.1038/s41598-018-28476-w

47. Zheng LZ, Wang JL, Xu JK, *et al*. Magnesium and vitamin C supplementation attenuates steroid-associated osteonecrosis in a rat model. *Biomaterials.* 2020;238:119828.
doi: 10.1016/j.biomaterials.2020.119828

48. Wu X, Li S, Huang Y, *et al*. Laser powder bed fusion of biodegradable magnesium alloys: process, microstructure and properties. *Int J Extrem Manuf.* 2024;7(2):022007.
doi: 10.1088/2631-7990/ad967e

49. Hung HC, Chang GG. Differentiation of the slow-binding

mechanism for magnesium ion activation and zinc ion inhibition of human placental alkaline phosphatase. *Protein Sci.* 2001;10(1):34-45.
doi: 10.1110/ps.35201

50. Vimalraj S. Alkaline phosphatase: structure, expression and its function in bone mineralization. *Gene.* 2020;754: 144855.
doi: 10.1016/j.gene.2020.144855

51. Zhang J, Li Y, Chen Z, *et al*. Molecular mechanism of magnesium ion promoting bone regeneration. *Chin J Tissue Eng Res.* 2022;26(33):5384-5390.
doi: 10.12307/2022.779

52. Maier T, Haraszti T. Reversibility and viscoelastic properties of micropillar supported and oriented magnesium bundled f-actin. *PLoS One.* 2015;10(8):e0136432.
doi: 10.1371/journal.pone.0136432

53. Ma L, Wang X, Zhao N, *et al*. Immobilizing magnesium ions on 3D printed porous tantalum scaffolds with polydopamine for improved vascularization and osteogenesis. *Mater Sci Eng C.* 2020;117:111303.
doi: 10.1016/j.msec.2020.111303

ACCSCIENCE PUBLISHING

International Journal of Bioprinting

RESEARCH ARTICLE

3D-printable alginate-MoS_2-AgNW hydrogel bioink for dual-mode wearable capacitive biosensors

Suraj Shinde[1†], Kang Hyeon Kim[1,2†], Omkar Pawar[3], Omkar A. Patil[3], Sooman Lim[3], and Han Eol Lee[1,2,4*]

[1]Division of Advanced Materials Engineering, Jeonbuk National University, Jeonju-si, Jeonbuk State, South Korea

[2]Division of Electronics and Information Engineering, Jeonbuk National University, Jeonju-si, Jeonbuk State, South Korea

[3]Department of Flexible and Printable Electronics, LANL-JBNU Engineering Institute, Jeonbuk National University, Jeonju, South Korea

[4]Department of JBNU-KIST Industry-Academia Convergence Research, Jeonbuk National University, Jeonju-si, Jeonbuk State, South Korea

(This article belongs to the *Special Issue: 3D-Printed Biomedical Devices*)

Abstract

The advancement of bioinks capable of enabling multifunctional, skin-conformal sensing platforms is essential for the next generation of wearable health monitoring systems. In this study, we present a 3D-printed, dual-mode biosensor fabricated using a composite hydrogel ink comprising sodium alginate, exfoliated molybdenum disulfide nanosheets (MoS_2NSs), silver nanowires (AgNWs), and Ca^{2+} crosslinkers. This bioink enables reliable extrusion-based printing on flexible substrates, forming wearable, conductive, and mechanically robust sensor architectures. The resulting soft sensor exhibits high-sensitivity capacitive touch sensing with fast response times and excellent mechanical repeatability under dynamic loading conditions. Furthermore, the device allows for real-time monitoring of sweat rate in response to constant humidity and perspiration levels. The synergistic integration of 2D MoS_2NSs and 1D AgNWs significantly improves electrical conductivity and mechanical durability, without compromising printability or hydration compatibility. The demonstrated dual-sensing functionality and scalable fabrication strategy underscore the potential of this platform for low-cost, customizable applications in wearable healthcare, fitness tracking, and human-machine interfaces.

Keywords: 3D bioprinting; Alginate hydrogel; Capacitive touch sensing; Sweat rate monitoring; Flexible sensors; Skin-interfaced devices

1. Introduction

Recent advances in wearable electronics have enabled the development of skin-conformal, soft sensors capable of real-time physiological monitoring, offering transformative potential in personalized healthcare and human-machine interfaces.[1-4] Among the various biosensing modalities, simultaneous monitoring of tactile stimuli[5, 6]

†These authors contributed equally to this work

***Corresponding author:**
Han Eol Lee
(haneol@jbnu.ac.kr)

Citation: Shinde S, Kim KH, Pawar O Patil OA Lim S, Lee HE. 3D-printable alginate-MoS_2-AgNWs hydrogel bioink for dual-mode wearable capacitive biosensors. *Int J Bioprint*. 2025;11(5):301-314. doi: 10.36922/IJB025290295

Received: July 18, 2025
Revised: August 14, 2025
Accepted: August 22, 2025
Published online: August 25, 2025

Copyright: © 2025 Author(s). This is an Open Access article distributed under the terms of the Creative Commons Attribution License, permitting distribution, and reproduction in any medium, provided the original work is properly cited.

Publisher's Note: AccScience Publishing remains neutral with regard to jurisdictional claims in published maps and institutional affiliations.

and sweat secretion[7, 8] at the skin's surface provides critical insights into an individual's hydration status, psychological stress levels, and physical activity.[9-11] To realize these functions in epidermal devices, sensors must meet specific requirements—including mechanical flexibility, biocompatibility, and stable signal transduction—under conditions of repeated mechanical deformation and prolonged skin contact.[12-14]

Hydrogel-based sensors have emerged as attractive platforms for skin-integrated electronics due to their high water content, intrinsic softness, and tunable mechanical properties.[15-17] Alginate, a naturally derived polysaccharide extracted from brown algae, is widely utilized in biomedical applications owing to its biocompatibility, gel-forming capability via divalent ion crosslinking, and excellent water retention properties.[18-21] These features make alginate a promising matrix material for soft hydrogel-based biosensors. However, the intrinsically insulating nature of alginate limits its application in electrically active devices, necessitating the incorporation of conductive nanomaterials to impart electronic functionality.[22,23] To overcome this limitation, recent research has explored the integration of conductive polymers, 1D and 2D nanomaterials, ionic compounds, liquid metals within hydrogel matrices to develop multifunctional and conductive composites, such as Poly(2,3-dihydrothieno-1,4-dioxin)-poly(styrenesulfonate) (PEDOT:PSS), metal nanoparticles, graphene oxide (GO), and carbon nanotubes (CNTs).[24] The integration of 1D and 2D nanomaterials and hydrogel matrices demonstrated great advances, such as an uncomplicated synthesis process, high electrical performance, mechanical reinforcement, flexibility, and biocompatibility.[25-28] However, hydrogel matrices dispersed with metal particles, conductive polymers, ionic compounds, and liquid metals presented disadvantages in various fields, such as degradation of mechanical strength, conductivity, toughness, deformability, and stability in a complex environment, which deteriorate their practical application as wearable devices.[29-31] Molybdenum disulfide (MoS_2), a prototypical 2D transition metal dichalcogenide (TMD), exhibits tunable semiconducting behavior, large specific surface area, and notable environmental stability.[32,33] When exfoliated into ultrathin nanosheets (NSs), MoS_2 enhances electronic coupling and provides capacitive characteristics within polymeric matrices. MoS_2 was also spotlighted as a humidity sensor with high sensitivity due to the presence of inherent defects. However, the pristine MoS_2 is not appropriate for a hydrogel filler with a monolithic sensor due to its low conductive properties.[34-36] Complementing this, silver nanowires (AgNWs) serve as highly conductive 1D fillers that create percolating networks for efficient charge transport, even under mechanical deformation.[37] Notably, both MoS_2NSs and AgNWs display favorable biocompatibility: MoS_2 exhibits low cytotoxicity and chemical stability, while AgNWs confer additional antibacterial functionality, mitigating the risk of microbial activity and skin irritation during prolonged use.[38-44] Despite significant advancements in nanocomposite hydrogel systems, most existing studies have focused on single-function sensors, and few have reported a single printable bioink formulation capable of supporting multimodal biosensing performance, such as both touch detection and hydration monitoring. In the case of the MoS_2 and AgNW, only a few studies have reported on a hydrogel, even a non-sensing application such as flame retardancy, wound healing patch, and flexible heater.[45-47] This limitation has constrained the development of versatile, skin-compatible platforms for integrated physiological assessment.

In this study, we report a printable nanocomposite ink composed of sodium alginate, MoS_2NSs, AgNWs, and Ca^{2+}, designed for extrusion-based 3D bioprinting. The combinations of MoS_2NSs and AgNWs featured enhanced conductive and carrier dynamics in the monolithic electrode-sensor system. The resulting nanocomposite bioink exhibits excellent rheological and structural properties for extrusion-based 3D printing on flexible substrates, while achieving high electrical conductivity and biocompatibility. Calcium-induced crosslinking reinforces the mechanical integrity of the alginate network and preserves hydration, which is critical for both skin comfort and ionic conduction. Using this printable bioink and a custom-designed bioprinting apparatus, we fabricated soft, flexible biosensors capable of dual-mode sensing: capacitive touch detection and real-time sweat rate monitoring. The printed devices demonstrate stable performance after bending and tensile strain, and maintain sensitivity in both ambient and on-body environments. The capacitive haptic sensor array displayed a capacitance difference at 10-8 mm from the sensor to the bare hand, indicating the high sensitivity of the system as a touch sensor. The integration of multifunctionality, high sensitivity, mechanical robustness, and printability highlights the potential of nanocomposite hydrogel materials for next-generation soft electronic devices.

2. Materials and methods

2.1. Materials

Sodium alginate, calcium chloride ($CaCl_2$), bulk MoS_2 powder, sodium chloride (NaCl), AgNWs in ethanol suspension (diameter: ~40 nm; length: ~30 μm), styrene-ethylene-butylene-styrene (SEBS), phosphate-buffered saline (PBS), and toluene were purchased from Sigma-

Aldrich (USA). All reagents were used as received without further purification.

2.2. Preparation of exfoliated MoS_2 nanosheets

The MoS_2NSs were synthesized via a liquid-phase exfoliation method.[48] Briefly, 100 mg of bulk MoS_2 powder was dispersed in 100 mL of an ethanol/deionized (DI) water mixture (volume ratio: 40:50 v/v). The suspension was sonicated in a bath sonicator (Branson Ultrasonics, United States of America [USA]) for 12 h at room temperature. Following sonication, the dispersion was centrifuged at 4000 rpm for 30 min (5810 R, Eppendorf, Germany) to remove unexfoliated particles. The supernatant containing few-layer MoS_2 nanosheets was collected and stored at 4°C for subsequent use.

2.3. Fabrication of alginate/MoS_2NS/AgNW composite ink

A 2 wt% sodium alginate solution was prepared by dissolving alginate in DI water under continuous overhead stirring at 600 rpm for 3 h until a clear, homogeneous gel was obtained. Exfoliated MoS_2NSs were added at varying concentrations (2, 3, and 4 wt% relative to alginate mass), followed by the addition of 0.1 wt% AgNWs. The mixture was further homogenized using magnetic stirring for 1 h to achieve a uniform composite ink. The final ink formulation was denoted as AAM.

2.4. 3D printing of soft sensor array

The AAM ink was transferred into a 5 mL syringe barrel equipped with a 26-gauge nozzle (inner diameter: 210 μm). Extrusion-based 3D printing was conducted using a custom-built bioprinter (Dr. INVIVO 4D6, ROKIT Healthcare, South Korea) with a pneumatic pressure of 700 kPa and a printing speed of 1 mm/s. The sensor patterns were deposited on flexible SEBS substrates (thickness: 200 μm) affixed to a heated bed maintained at 40°C. Sensor geometries were designed using Autodesk 3ds Max 2024 and sliced with Dr. INVIVO Slicer (ROKIT Healthcare, South Korea). Printed structures were crosslinked post-printing by immersion in 10 mM $CaCl_2$ solution for 30 min, followed by rinsing with DI water to remove unbound calcium ions.

2.5. Material characterization

Morphological features were characterized using field-emission scanning electron microscopy (FE-SEM; Hitachi S-4800, Japan) equipped with energy-dispersive X-ray spectroscopy (EDS) for elemental mapping. Raman spectroscopy (Horiba, Japan) was performed using a 532 nm excitation laser to analyze the structural properties of the AAM composite. Thermogravimetric analysis (TGA) was conducted using a TGA Q550 system (TA Instruments, USA) in a nitrogen atmosphere from room temperature to 500°C at a heating rate of 10°C/min.

2.6. Electrical and sensing performance evaluation

Sheet resistance measurements were carried out using a standard four-point probe setup (Keithley, USA). Capacitive touch sensing performance was evaluated via a customized setup where a human finger applied periodic touch stimuli (~10 kPa), while the electrical signals were recorded using an impedance analyzer (Keysight E4990A, USA). To assess moisture sensitivity, humidity-controlled tests were performed in an environmental chamber with relative humidity (RH) at 60%. For on-skin measurements, the sensor was attached to the volar forearm and operated under natural skin conditions (surface temperature ≈ 35°C) for up to 8 h while monitoring capacitive touch and sweat rate signals.

2.7. Statistical analysis

All experiments were conducted in triplicate unless otherwise indicated. Data are expressed as mean ± standard deviation. Statistical analyses and graphical visualizations were performed using OriginPro 2025 (OriginLab Corporation, USA) and MATLAB R2022b (MathWorks, USA).

3. Results and discussion

3.1. Fabrication of AAM-based conductive sensor array

The fabrication process of the alginate-based sensor array incorporating MoS_2NSs and AgNWs is schematically illustrated in **Figure 1**. Bulk MoS_2 powder was exfoliated via sonication in an ethanol/water solvent mixture to yield few-layer MoS_2NSs. The NSs and AgNWs were then homogeneously dispersed in a sodium alginate solution to formulate a printable, hydrogel-based conductive ink (**Figure 1a**). This composite ink was extruded using a syringe-assisted 3D bioprinter onto flexible SEBS substrates in a predefined sensor array geometry (**Figure 1b**). The inset in **Figure 1b** confirms stable extrusion through a 260 μm nozzle and high printing fidelity at the microscale. Post-printing, the structures were immersed in a 10 mM $CaCl_2$ bath, enabling ionic crosslinking of the alginate matrix and improving mechanical robustness. The resulting device consisted of a 10 × 10 array of 5 × 5 mm square sensor pads arranged with 7 mm spacing, forming a soft, conformal surface suitable for skin integration (**Figure 1c**).

3.2. Morphological and structural characterization

Figure 2a presents the morphological, structural, and compositional analysis of the AAM composite. The field-emission SEM image reveals the surface topology of the printed hydrogel film, exhibiting a continuous

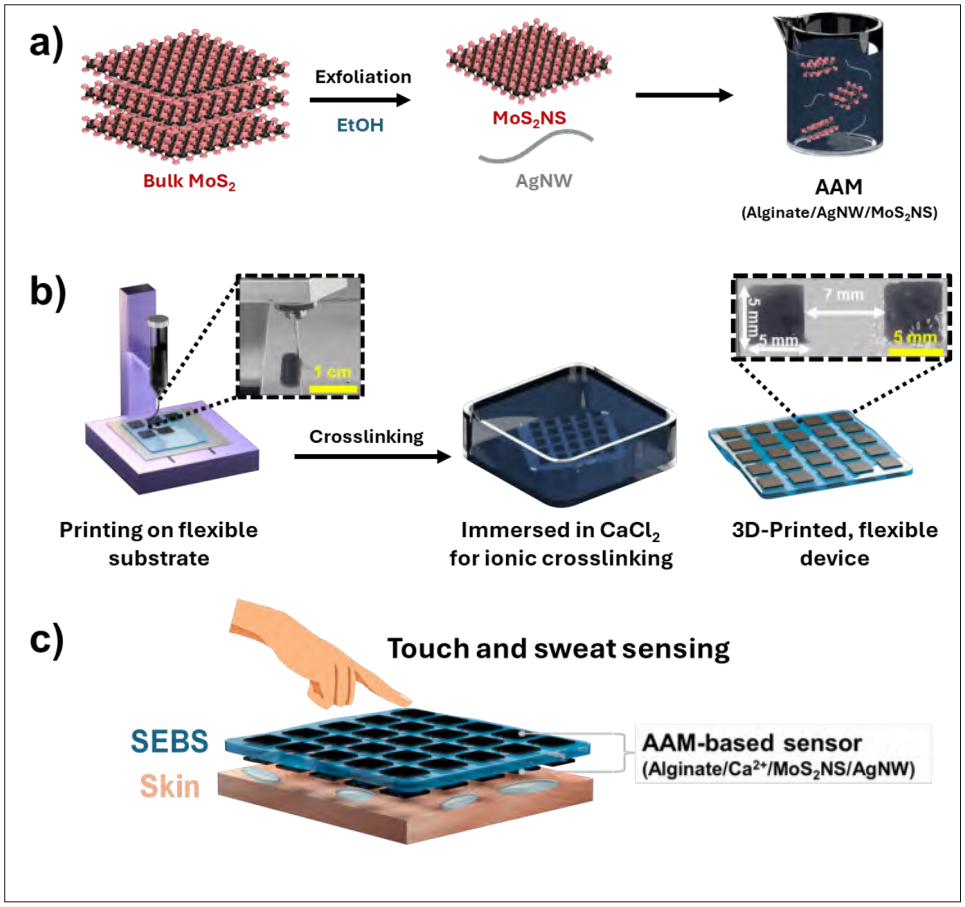


Figure 1. AAM-based sensor fabrication and sensing. (a) Schematic fabrication processes of AAM-based bioink. (b) 3D printing of AAM bioink on flexible SEBS substrate, and final crosslinking process. Optical images of printed sensor arrays (5 × 5 mm pads, 7 mm spacing) on flexible SEBS. (c) 3D illustration of dual-mode wearable capacitive biosensors with touch and sweat sensing. Abbreviations: AAM (Alginate-AgNWs-MoS_2NS), AgNW (silver nanowire), MoS_2NS (Molybdenum disulfide nanosheet) .

polymeric network embedded with nanoscale features. The magnified view confirms the incorporation of exfoliated MoS_2 nanosheets and interconnected AgNWs uniformly dispersed within the alginate matrix, forming a conductive percolation pathway. Additional high-resolution SEM images of the individual MoS_2NSs and AgNWs are provided in **Figure S1**, further validating their representative morphology and dispersion quality prior to composite formulation. **Figure 2b** displays an SEM image of the crosslinked AAM composite, which demonstrates a dense and integrated microstructure with uniformly distributed nanofillers. Elemental mapping via energy-dispersive X-ray spectroscopy (EDS) confirms the successful incorporation of all key constituent elements of Mo, S, Ag, Na, Ca, and Cl, corresponding to the AAM composition. **Figure 2c** presents the Raman spectra of the composite inks, highlighting characteristic vibrational features of MoS_2 within the hydrogel matrix. Both alginate/MoS_2NS and alginate/MoS_2NS/AgNW formulations exhibit two prominent peaks corresponding to the $E_{12}g$ (~383 cm^{-1}) and A_1g (~410 cm^{-1}) modes of MoS_2, indicative of in-plane and out-of-plane phonon vibrations, respectively. Notably, the AgNW-integrated composite (blue curve) exhibits an enhanced Raman signal intensity, suggesting improved NS dispersion and interfacial interactions between MoS_2 and the embedded AgNW network. These findings support the formation of a homogeneous, hybrid conductive matrix suitable for next-generation sensing applications. The TGA analysis was conducted to assess the thermal stability and decomposition behavior of the AAM ink and its individual components, MoS_2NSs and AgNWs, as displayed in **Figure 2d**. The TGA profile of MoS_2NSs demonstrates excellent thermal stability with negligible weight loss up to 500°C, confirming its inert behavior under the specified conditions. Similarly, AgNWs exhibit minimal mass change throughout the temperature range, reflecting their

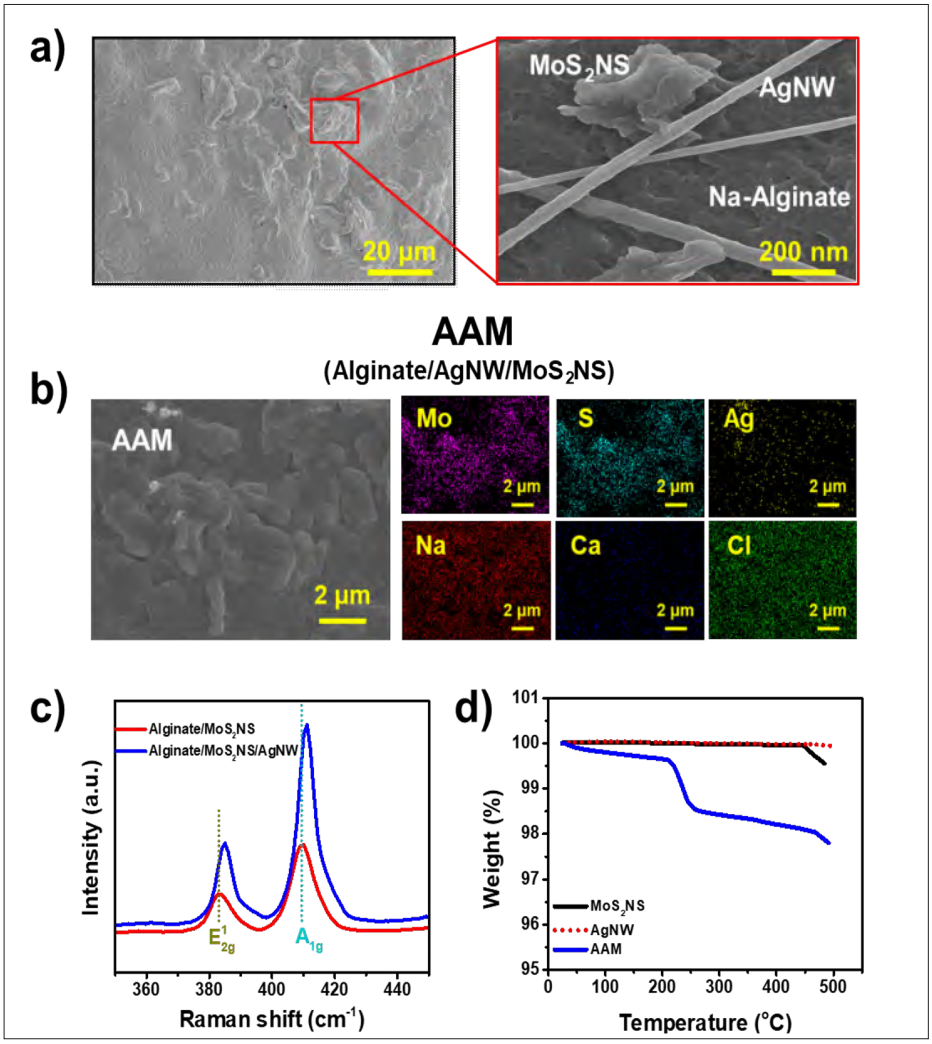


Figure 2. Material analysis of AAM component (a) SEM image of AAM composite, showing uniform distribution of nanoscale fillers. (b) EDS mapping images of Mo, S, Ag, Na, Ca, and Cl within the printed AAM matrix. (c) Raman spectra of Alginate/MoS_2NS and Alginate/MoS_2NS/AgNW inks, showing enhanced signal intensity and peak definition upon AgNW inclusion. (d) TGA results of MoS_2NS, AgNW, and AAM. Abbreviations: AAM (Alginate-AgNWs-MoS_2NS), AgNW (silver nanowire), MoS_2NS (Molybdenum disulfide nanosheet)

intrinsic high thermal stability and oxidation resistance at moderate temperatures. In contrast, the AAM composite exhibits a multistep decomposition profile. An initial minor mass loss below 150°C is attributed to the evaporation of absorbed moisture. A significant weight reduction between ~200°C and 300°C corresponds to thermal degradation of the alginate matrix via glycosidic bond cleavage and the release of volatile products. Above 300°C, a gradual mass loss occurs, likely associated with decomposition of residual carbonaceous species originating from alginate. The remaining mass beyond 500°C predominantly corresponds to inorganic residues, including MoS_2NSs and AgNWs. Collectively, these results confirm the enhanced thermal stability of the AAM composite due to the incorporation of thermally resilient MoS_2 and AgNW nanofillers and validate the material's structural integrity for practical and environmental applications in wearable electronics.

3.3. Influence of MoS_2NS/AgNW content on rheology, printability, and conductivity

Figure 3 presents the influence of conductive filler concentration on the electrical and rheological properties of the alginate-based composite inks. To minimize the deterioration of the mechanical properties of a hydrogel, nanomaterials within the hydrogel have to be minimally dispersed.[29] As displayed in Figure 3a, the electrical conductivity of the composites markedly increases with higher nanofiller loadings, particularly for the alginate/MoS_2NS/AgNW formulation. Notably, the inclusion of AgNWs into the MoS_2NS matrix results in a pronounced

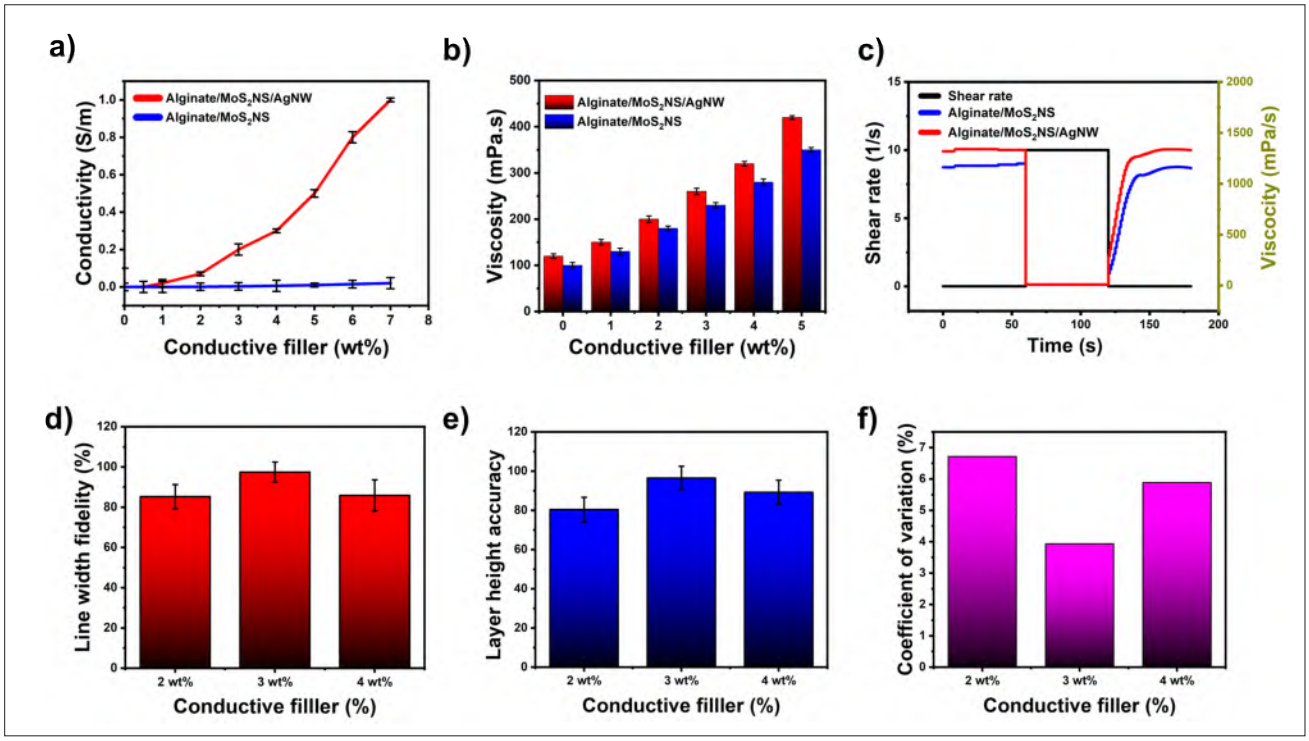


Figure 3. Electrical and rheological analysis and 3D printing optimization of AAM (a) Electrical conductivity of bioink according to nanofiller contents, demonstrating synergistic improvement with MoS_2NS and AgNW co-loading. (b) Viscosity profile of bioinks with increasing MoS_2NS/AgNW. (c) Shear-thinning behavior of both composite formulations. (d) Line width fidelity (%). (e) Layer height accuracy (%). (f) Extrusion stability over 180 s continuous printing. The replicates for error bar is (a,b) $n = 5$, (d,e) $n = 3$. Abbreviations:AAM (Alginate-AgNWs-MoS_2NS), AgNW (silver nanowire), MoS_2NS (Molybdenum disulfide nanosheet)

enhancement in conductivity, especially beyond 2 wt%, reaching values approaching 1 S/m at 7 wt%. In contrast, composites containing only MoS_2NSs exhibit minimal improvement, underscoring the synergistic effect of combining 2D MoS_2NSs with 1D AgNWs to form an efficient percolated conductive network. The results indicate AgNW rapidly improved the conductivity of alginate/MoS_2NS with the additional lower ratio of materials than MoS_2NS to prevent the unequal dispersion of nanomaterials (**Table 1**). The viscosity profiles presented in **Figure 3b** indicate a progressive increase in viscosity with increasing filler concentration for both composite types. The AgNW-integrated inks consistently exhibit slightly higher viscosities across all concentrations, which is attributed to enhanced mechanical entanglement and improved interfacial interactions within the hybrid network. Further rheological analysis under applied shear reveals that both formulations demonstrate characteristic shear-thinning behavior, a desirable feature for extrusion-based 3D printing (**Figure 3c**). The alginate/MoS_2NS/AgNW formulation maintains a higher viscosity across all shear rates, reflecting stronger internal network interactions facilitated by the presence of AgNWs. Importantly, both ink systems exhibit good structural recovery after shear removal, confirming their suitability for precise, layer-by-layer deposition during printing. **Figure S2** displays optical microscopy images of printed lines fabricated using inks with different filler concentrations (2, 3, and 4 wt%). The 3 wt% formulation produces the most uniform and well-defined printed features, representing an optimal balance between flow stability and spatial resolution. At 2 wt%, the printed lines appear weakly defined and underdeveloped, while at 4 wt%, irregular extrusion and occasional nozzle clogging are observed. These defects are attributed to excessive filler content, which negatively impacts the ink's flowability and extrusion consistency. Taken together, these results illustrate the critical importance of optimizing nanofiller concentrations to achieve stable printability, reliable electrical performance, and appropriate rheological behavior. To quantitatively evaluate the printability of the composite inks, three printing quality metrics were assessed: line width fidelity, layer height accuracy, and extrusion stability. The line width fidelity, defined as the ratio of the measured to the designed width, was measured for inks containing 2, 3, and 4 wt% MoS_2NS/AgNWs. The optimal formulation (3 wt% MoS_2NS/AgNWs) achieved a

Table 1. Comparison of conductive hydrogel with different fillers

Study	Filler material	Matrix	Conductivity (S/cm)	Fracture energy (kJ/m²)	Printability (line width fidelity %)	Ref.
Li *et al.*	Polyaniline (PANI)	Polyacrylamide (PAAm) hydrogel	0.12	15.8	~90%	[25]
Yu *et al.*	PEDOT:PSS	Poly(vinyl alcohol) (PVA) hydrogel	0.093	12.4	~95%	[26]
Van Tam *et al.*	Phosphorus-doped graphene QDs + graphene	Alginate hydrogel	0.85	9.6	~92%	[28]
Shinde *et al.*	MoS_2NS and AgNWs	Alginate hydrogel	0.01	27.55	98.3%	This work

Abbreviations: AgNW (silver nanowire), MoS_2NS (Molybdenum disulfide nanosheet), PAAm (Polyacrylamide), PANI (Polyaniline), PEDOT:PSS (Poly(2,3-dihydrothieno-1,4-dioxin)-poly(styrenesulfonate)), PVA (Poly(vinyl alcohol))

fidelity of 98.3 ± 3.1%, significantly higher than 2 wt% (91.7 ± 6.4%) and 4 wt% (88.2 ± 9.5%) formulations (**Figure 3d**). Layer height accuracy followed a similar trend, with 3 wt% MoS_2NS/AgNWs producing heights within 98.7 ± 4.2% of the designed 150 μm, indicating excellent vertical stacking precision (**Figure 3e**). Extrusion stability was monitored by measuring instantaneous line width over a 180 s continuous print. The coefficient of variation (CV) for the 3 wt% formulation was only 3.9%, compared to 4.6% for 2 wt% and 5.1% for 4 wt%, confirming minimal fluctuation in extrusion flow. These results quantitatively validate the superior print fidelity, structural resolution, and extrusion consistency of the optimized bioink, aligning with the high-resolution features observed in **Figure 3f**. This optimized hydrogel ink enables high-resolution patterning, consistent extrusion, and superior electrical functionality, making it an excellent candidate for our capacitive biosensor.

3.4. Mechanical properties of AAM composite

Figure 4 illustrates the mechanical performance of the AAM composite under both tensile and cyclic loading conditions. As presented in **Figure 4a**, photographic images of the printed hydrogel specimen demonstrate its high flexibility and stretchability when subjected to uniaxial elongation, transitioning smoothly from a relaxed to an extended state. This behavior confirms the excellent mechanical compliance of the material, which is essential for integration into wearable sensor platforms. The tensile stress–strain curves presented in **Figure 4b** indicate that both alginate/MoS_2NS and alginate/MoS_2NS/AgNW composites undergo similar elastic deformation up to approximately 10%. The incorporation of AgNWs yields a modest but consistent increase in mechanical strength, suggesting that AgNWs contribute incrementally to mechanical reinforcement without significantly compromising the innate extensibility of the hydrogel matrix (**Table 1**). **Figure 4c** displays the results of cyclic tensile testing, performed to assess the mechanical durability of the composites under repeated mechanical stress. Over 20 consecutive loading/unloading cycles, both formulations retain their stress-bearing capabilities, with the AgNW-reinforced AAM sample consistently exhibiting higher stress levels than its MoS_2-only counterpart. This indicates improved mechanical resilience and fatigue resistance conferred by the hybrid nanofiller network, featuring an essential characteristic for reliable operation in dynamic, body-mounted environments. The effect of crosslinking density on mechanical stiffness is investigated in **Figure 4d**, where increasing concentrations of $CaCl_2$ solution produced a nearly linear increase in compressive stress. This observation confirms that the ionic crosslinking facilitated by Ca^{2+} can be employed to modulate the mechanical properties of the hydrogel systematically. Such tunability provides a versatile strategy for tailoring the composite's softness or rigidity depending on the specific application or anatomical site of deployment.[48] Collectively, these findings validate that the AAM hydrogel composite exhibits robust mechanical integrity, high deformability, and enhanced toughness. The combined effects of 1D/2D nanofiller reinforcement and controllable ionic crosslinking provide a favorable mechanical profile, establishing the AAM composite as a promising candidate material for flexible and skin-compatible biosensing devices.

3.5. Capacitive touch sensing performance

The capacitive sensing performance of the AAM-based sensor was systematically evaluated under varying mechanical loading and proximity conditions, as presented in **Figure 5**. As displayed in **Figure 5a**, a progressive increase in capacitance was observed with increasing applied normal force ranging from 1 to 10 N, confirming the pressure-sensitive nature of the sensor. The touch sensitivity of the AAM-based sensor was determined from the slope of the normalized capacitance change (ΔC/

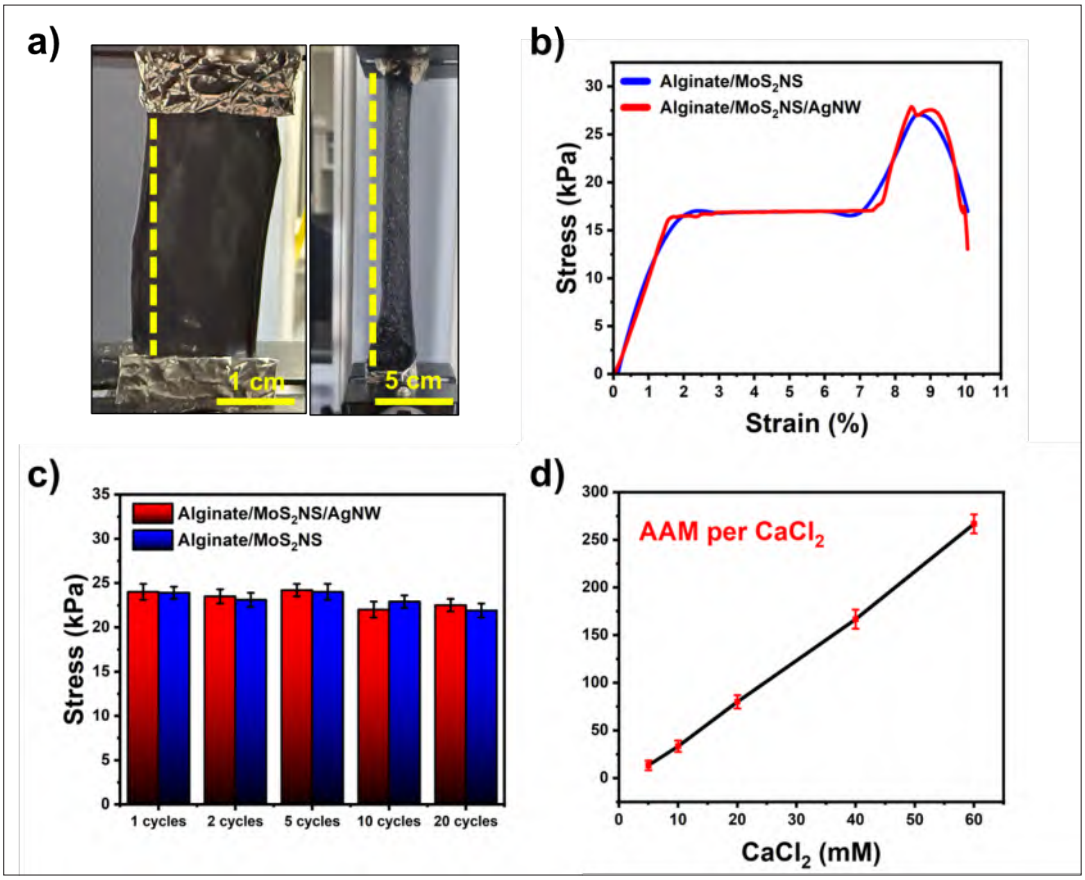


Figure 4. Mechanical properties of AAM-based hydrogel. (a) Optical images of AAM composite, featuring mechanical flexibility and elongation capability. (b) Tensile stress-strain profiles of alginate/MoS_2NS and AAM composites. (c) Cyclic tensile testing results over 20 loading/unloading cycles confirm mechanical durability ($n = 5$). (d) Compressive strength as a function of $CaCl_2$ concentration, featuring tunability of hydrogel stiffness through crosslinker variation ($n = 5$). AAM (Alginate-AgNWs-MoS_2NS), AgNW (silver nanowire), MoS_2NS (Molybdenum disulfide nanosheet)

C_0) versus applied pressure in the low-pressure range (10–50 kPa, corresponding to 1–5 N in **Figure 5a**). The calculated value was ≈ 0.15 kPa^{-1}, which is comparable to or higher than those reported for similar hydrogel-based capacitive sensors.[49] Repetitive finger-touch experiments were conducted to assess signal stability and repeatability under dynamic input conditions. As illustrated in **Figure 5b**, distinct and reproducible capacitive peaks were consistently generated over multiple touch-release cycles. Each mechanical stimulus resulted in a sharp increase in capacitance followed by rapid signal recovery upon unloading, indicating high temporal resolution and signal fidelity. This behavior is attributed to the elastic recoverability of the alginate hydrogel matrix and the robustness of the embedded MoS_2NS/AgNW conductive network. To further assess proximity sensing capability, controlled finger approaches were performed at varying distances (9–10, 7–5, and 4–2 mm) from the sensor surface. As displayed in **Figure 5c**, a gradual increase in capacitance was recorded as the distance decreased, culminating in a sharp peak upon direct contact. These results validate the sensor's efficacy in near-field proximity detection, enabling pre-contact recognition for potential human-machine interface applications. Spatial pressure distribution mapping was demonstrated using a 5 × 5 electrode array configuration (**Figure 5d**). The corresponding heatmap reflects localized capacitance changes across the array when mechanical pressure was selectively applied. Each coloured cell represents the capacitive response of a specific electrode pair subjected to pressure input. The gradient from blue to red denotes increasing signal magnitude, with electrodes at positions (1,1) and (2,1) exhibiting notably higher capacitance values. These elevated readings indicate focused mechanical stimulus in the lower-left region, further confirming the system's spatial resolution. Collectively, these findings demonstrate that the AAM-based capacitive sensor is capable of both pressure and proximity detection with high spatial and temporal

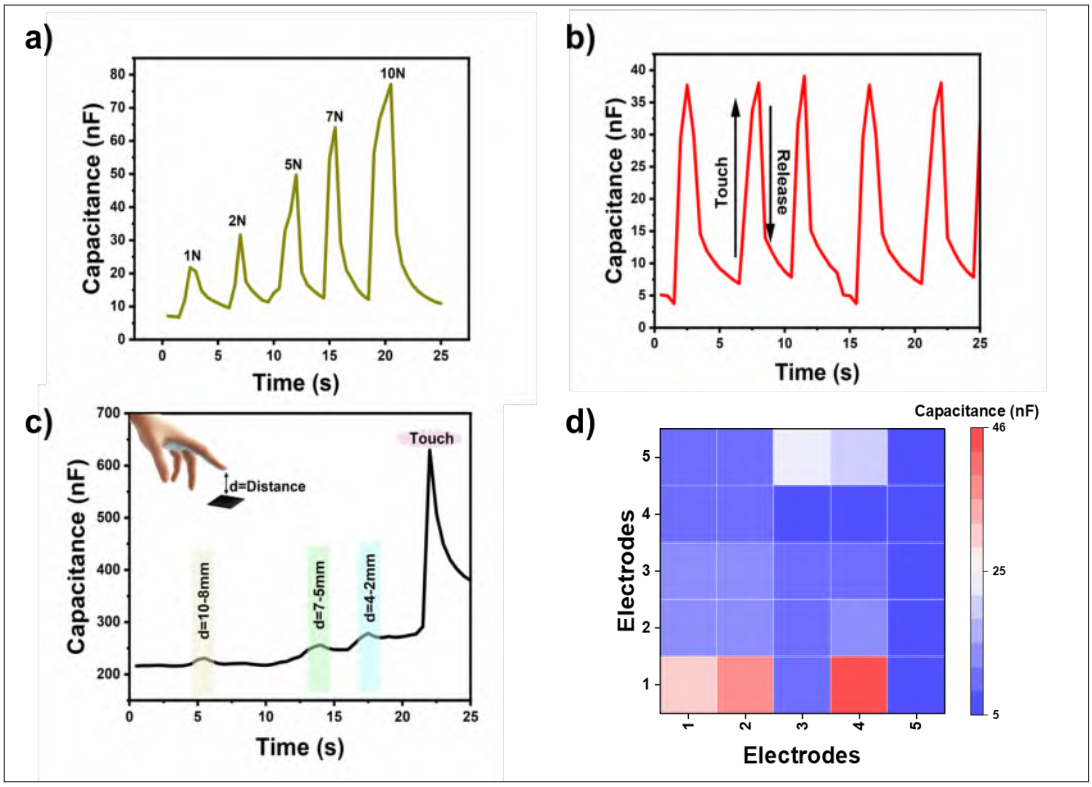


Figure 5. Pressure sensing performance of AAM-based sensor (a) Capacitance response of AAM sensor under increasing finger-applied forces (1–10 N). (b) Repetitive touch cycles display high signal fidelity and recovery. (c) Capacitance variation with proximity sensing (2–10 mm). (d) Heatmap generated by a 5 × 5 sensor array for spatial mapping, demonstrating multiple high-resolution touch localizations.

resolution. The integrated functionality renders the system highly applicable for use in wearable touch sensors and pressure-mapping technologies, where reliable detection of dynamic and localized stimuli is essential.

3.6. Hydration and sweat rate sensing

Sweat absorption into the hydrogel leads to a modification of its dielectric constant due to the presence of the aqueous phase. The electrolyte species present in sweat, including Na^+, Cl^-, and K^+, further accelerate the capacitance changes. This acceleration arises from the enhancement of ionic transport mechanisms provided by MoS_2NS to amplify the electrical response of the hydrogel-based sensor.[50-52] The capacitive response of the printed AAM sensor was investigated under varying sweat flow rates to evaluate its sensitivity to perspiration-related stimuli (**Figure 6**). In **Figure 6a**, the normalized capacitance change ($\Delta C/C_0$) exhibited a clear increasing trend with rising artificial sweat flow rates, ranging from 1.0 to 4.0 μL/min. This progressive signal enhancement indicates improved surface interaction between absorbed moisture and the conductive hydrogel interface under elevated moisture flux. The observed increase in signal amplitude and slope suggests that higher flow rates promote more effective electrolyte–electrode interactions and facilitate ion transport within the capacitive sensing interface. Specifically, the response amplitude increased from approximately 40% at a flow rate of 1.0 μL/min to over 130% at 4.0 μL/min, demonstrating the sensor's high sensitivity to variations in fluid dynamics. The corresponding response factor (K) (**Figure 6b**) displayed a near-linear correlation with sweat speed, confirming the sensor's quantitative responsiveness to dynamic hydration levels. The upward trend in K values is attributed to enhanced dielectric interactions at the hydrogel-moisture interface, facilitated by the porous and highly hydrophilic structure of the composite matrix. Further evaluation of electrolyte specificity was performed by comparing sensor responses to deionized water, artificial sweat, and NaCl solutions with varying ionic strengths (1, 10, and 100 mM), as depicted in **Figure 6c**. The resulting capacitance responses remained consistent across the different electrolyte types and concentrations, indicating that the sensor's humidity detection mechanism is governed predominantly by moisture content rather than ionic conductivity. This ionic insensitivity is advantageous for wearable monitoring, where sweat composition may fluctuate significantly over

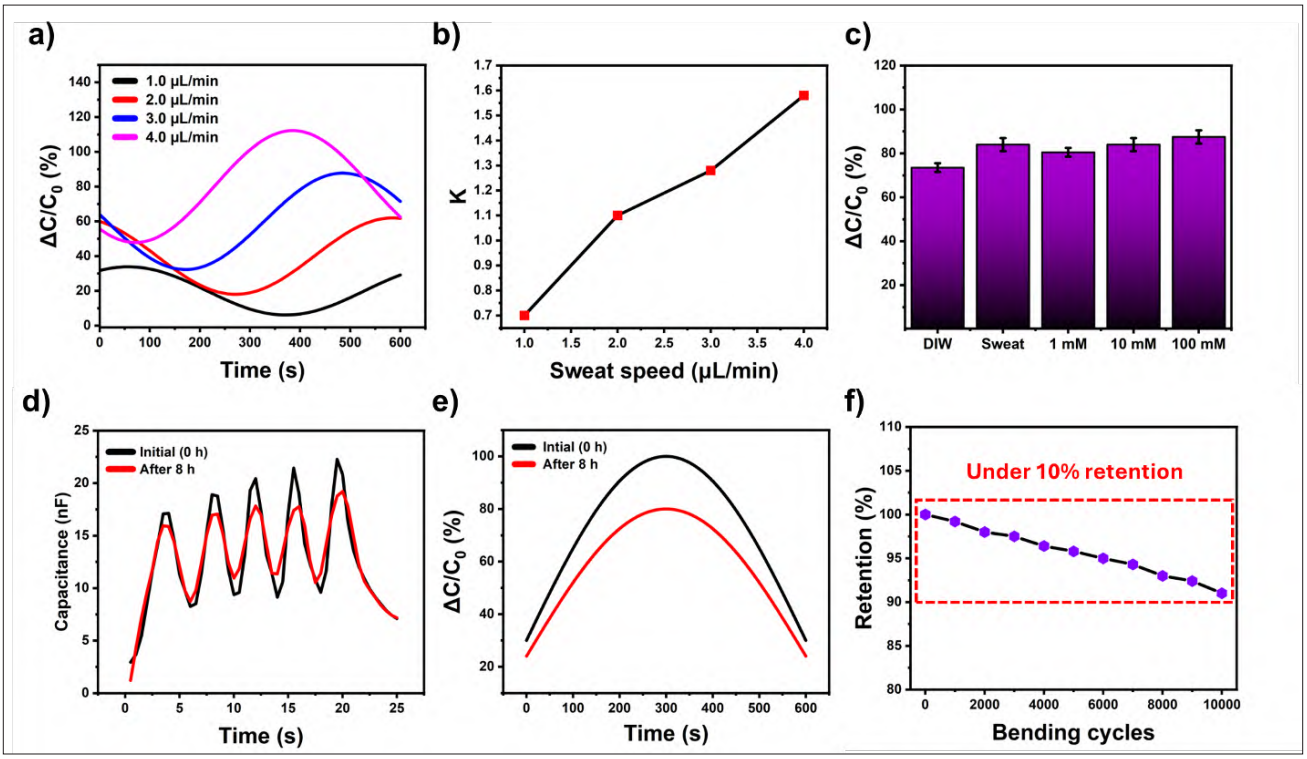


Figure 6. Sweat ion sensing results of AAM-based sensor. (a) Normalized capacitance change ($\Delta C/C_0$) with increasing artificial sweat rates (1.0–4.0 μL/min). (b) Response factor (K) as a function of sweat rate, displaying near-linear behavior. (c) Comparison of capacitance response in DI water, artificial sweat, and NaCl solutions of varying concentration, confirming moisture-dominant sensitivity (n = 5). (d) Capacitance variation over time during real-time wearable testing. The black line represents the initial capacitive response, while the red line indicates performance after 8 h of continuous wear. (e) Normalized capacitance change ($\Delta C/C_0$) over time under constant human sweat flow rate (3.0 μL/min), comparing initial state and after 8 h of on-skin wear. (f) Cyclic bending retention curve showing less than 10% degradation after 10000 cycles.

time due to physiological and environmental factors. Altogether, these results demonstrate that the AAM sensor is capable of real-time sweat rate monitoring with stable, reversible capacitive output.

3.7. Long-term stability and on-skin performance

To verify the applicability of the AAM-based dual-mode biosensor under realistic wearable conditions, extended-duration tests were conducted. For on-skin performance evaluation, the sensor was attached to the forearm and worn continuously during daily activities for over 8 h. During the 8 h continuous on-skin test, the device operated at a constant skin temperature (~35°C). Despite this thermal exposure, baseline signals remained stable, and the device displayed only moderate amplitude reduction (~33%), confirming minimal performance drift at physiological temperatures (**Figure 6d**). Long-term sweat rate monitoring stability was also examined under a constant sweat flow rate (3.0 μL/min) for 8 h. The normalized capacitance change ($\Delta C/C_0$) decreased by ~20%, yet the waveform shape and periodicity remained consistent (**Figure 6e**), confirming robust hydration sensing performance during extended operation.

Additionally, mechanical durability under repetitive deformation was assessed by cyclic bending tests (radius ≈ 5 mm) up to 10000 cycles. The device retained ~90% of its initial signal response after the full cycle count (**Figure 6f**), indicating that the percolated MoS_2-AgNW conductive network within the alginate matrix remains stable under prolonged dynamic loading. Collectively, these findings demonstrate that the AAM-based biosensor maintains functional stability and durability in dynamic, skin-mounted environments, underscoring its potential for practical wearable healthcare and human-machine interface applications.

4. Conclusion

In this study, we developed and demonstrated a 3D-printed, dual-mode wearable biosensor based on a nanocomposite hydrogel ink composed of sodium alginate, exfoliated MoS_2NSs, AgNWs, and Ca^{2+} as ionic crosslinkers. The

composite ink exhibited excellent rheological properties suitable for extrusion-based printing and enabled the fabrication of soft, skin-conformal sensor arrays with high structural fidelity on flexible SEBS substrates. Comprehensive morphological and spectroscopic analyses confirmed the uniform dispersion of MoS_2NSs and AgNWs within the alginate matrix, forming a robust, percolating conductive network. The synergistic combination of 2D-MoS_2 and 1D-Ag nanowires led to enhanced electrical conductivity, carrier dynamics, and mechanical stability, while maintaining the hydrophilic and biocompatible nature of the hydrogel scaffold. The optimized formulation with 3 wt% MoS_2NS/AgNW provided the best balance between printability, conductivity, and viscoelastic control. The resulting AAM sensors demonstrated reliable capacitive performance in response to both mechanical and hydration stimuli. The device exhibited pressure-sensitive and proximity-dependent capacitance changes, with high spatial and temporal resolution in a 5 × 5 electrode array configuration. Moreover, the sensor exhibited strong responsiveness to varying sweat flow rates, with signal intensity increasing proportionally with moisture flux, and remained functionally robust across a wide range of ionic concentrations.

The capacitive haptic sensor array demonstrated a capacitance difference of 10-8 mm from the sensor to the bare hand, highlighting the high sensitivity of the system as a touch sensor. This confirms that the capacitive sensing mechanism is primarily driven by hydration level rather than ion concentration, making it highly suitable for wearable sweat monitoring. Overall, the proposed AAM-based sensor platform offers a low-cost, scalable solution for dual-mode biosensing in healthcare, fitness tracking, and human-machine interface applications. This dual-functional sensor platform offers broad application potential in healthcare monitoring for hydration and stress levels, fitness tracking, prosthetics, and interactive wearable systems requiring simultaneous mechanical and perspiration sensing.

Acknowledgments

This work was supported by the National University Development Project at Jeonbuk National University in 2024.

Funding

Not applicable

Conflict of interest

The authors declare no conflicts of interest.

Author contributions

Conceptualization: Suraj Shinde
Data curation: Suraj Shinde, Omkar A. Patil
Formal analysis: Omkar Pawar
Funding acquisition: Han Eol Lee
Investigation: Han Eol Lee
Methodology: Suraj Shinde, Sooman Lim, Han Eol Lee
Resources: Suraj Shinde, Kang Hyeon Kim, Omkar Pawar
Supervision: Han Eol Lee
Validation: Kang Hyeon Kim, Han Eol Lee
Visualization: Kang Hyeon Kim
Writing–original draft: Suraj Shinde
Writing–review & editing: Han Eol Lee

Ethics approval and consent to participate

Not applicable

Consent for publication

Not applicable.

Availability of data

The authors confirm that the data supporting the findings of this study are available within the article and its Supplementary File. Raw data that support the findings of this study are available from the corresponding author, upon reasonable request.

References

1. Che Ab Rahman A, Lee B-J,Lim S. Optimizing polymethyl methacrylate (PMMA)-based stretchable microneedle arrays by vat photopolymerization for efficient drug loading. *Additive Manufacturing*. 2024;94:104472. doi: j.addma.2024.104472

2. Bae L K,Choi M K. Deformable Heat-Dissipation Materials for Smart E-Skin. *J Korean Inst Electr Electron Mater Eng*. 2025;38(1):21-32. doi: 10.4313/JKEM.2025.38.1.3

3. Jeong S, Hwang Y S, *et al.* Formation of Metal Mesh Electrodes via Laser Plasmonic Annealing of Metal Nanoparticles for Application in Flexible Touch Sensors. *J Korean Inst Electr Electron Mater Eng*. 2024;37(2):223-229. doi: 10.4313/JKEM.2024.37.2.15

4. Park J-C. Influence of Al Content on the Resonant Characteristics of Al-Mo Thin Film-Based SAW Devices. *Trans Electr Electron Mater*. 2025;38(1):65-71. doi: 10.4313/JKEM.2025.38.1.8

5. Khan F, Mubashir T, Ahmed K, Shahoor M, Mateen A, Lee S N,Ahmed T. Fabrication and Characterization of Carbon Nanotubes-Based Pressure Nanosensors: A Study

on Piezoresistive Behavior. *Trans Electr Electron Mater*. 2023;24(6):518-527.
doi: 10.1007/s42341-023-00472-6

6. Pawar O Y,Lim S. 3D-Printed piezoelectric nanogenerator with aligned graphitic carbon nitrate nanosheets for enhancing piezoelectric performance. *J Colloid Interface Sci*. 2024;654(Pt B):868-877.
doi: 10.1016/j.jcis.2023.10.105

7. Kim J H, Joe D J,Lee H E. Sweat-permeable electronic skin with a pattern of eyes for body temperature monitoring. *Micro Nano Syst Lett*. 2023;11(1):7
doi: 10.1186/s40486-023-00170-1

8. Shinde S, Kim K H, Park S Y, Kim J H, Kim J, Joe D J,Lee H E. Wearable sweat-sensing patches for non-invasive and continuous health tracking. *Sens Actuators Rep*. 2025;9:100265.
doi: 10.1016/j.snr.2024.100265

9. Son J, Bae G Y, *et al.* Cactus-Spine-Inspired Sweat-Collecting Patch for Fast and Continuous Monitoring of Sweat. *Adv Mater*. 2021;33(40):e2102740.
doi: 10.1002/adma.202102740.

10. Liang H R, Zhu M J, *et al.* Sweat-Enhanced Self-Adhesive Double-Network Hydrogel for Dynamic Skin Electrophysiology. *Acs Materials Letters*. 2024;6(11):4922-4931.
doi: 10.1021/acsmaterialslett.4c01748

11. Lyzwinski L, Elgendi M, Shokurov A V, Cuthbert T J, Ahmadizadeh C,Menon C. Opportunities and challenges for sweat-based monitoring of metabolic syndrome via wearable technologies. *Commun Eng-London*. 2023;2(1):48.
doi: 10.1038/s44172-023-00097-w

12. Yeon H, Lee H, *et al.* Long-term reliable physical health monitoring by sweat pore-inspired perforated electronic skins. *Sci Adv*. 2021;7(27):eabg8459
doi: 10.1126/sciadv.abg8459

13. Kim J H, Kim H, Jeong C K,Lee H E. 3D-Porous Structured Piezoelectric Strain Sensors Based on PVDF Nanocomposites. *J Sens Sci Technol*. 2022;31(5):307-311.
doi: 10.46670/jsst.2022.31.5.307.

14. Liu Y, Liu J, *et al.* Soft and elastic hydrogel-based microelectronics for localized low-voltage neuromodulation. *Nat Biomed Eng*. 2019;3(1):58-68.
doi: 10.1038/s41551-018-0335-6

15. Zhou P C, Zhang Z M, Mo F,Wang Y. A Review of Functional Hydrogels for Flexible Chemical Sensors. *Adv Sensor Res*. 2024;3(3):2300021.
doi: 10.1002/adsr.202300021

16. Shinde S, Patil O A, *et al.* Wearable sweat glucose monitoring patches enabled by double network hydrogel-MoS2/PEDOT: PSS nanocomposite. *Microchem J*. 2025;215:114309.
doi: 10.1016/j.microc.2025.114309

17. Morozkina S, Strekalovskaya U, Vanina A, Snetkov P, Krasichkov A, Polyakova V,Uspenskaya M. The Fabrication of Alginate-Carboxymethyl Cellulose-Based Composites and Drug Release Profiles. *Polymers (Basel)*. 2022;14(17):3604.
doi: 10.3390/polym14173604.

18. Jia J, Richards D J, *et al.* Engineering alginate as bioink for bioprinting. *Acta Biomater*. 2014;10(10):4323-4331.
doi: 10.1016/j.actbio.2014.06.034

19. Zhang W, Kuss M, Yan Y,Shi W. Dynamic Alginate Hydrogel as an Antioxidative Bioink for Bioprinting. *Gels*. 2023;9(4):312.
doi: 10.3390/gels9040312

20. Salesa B, Llorens-Gamez M,Serrano-Aroca A. Study of 1D and 2D Carbon Nanomaterial in Alginate Films. *Nanomaterials (Basel)*. 2020;10(2):206.
doi: 10.3390/nano10020206

21. Zhang Y, Li S, *et al.* Highly conductive and tough polyacrylamide/sodium alginate hydrogel with uniformly distributed polypyrrole nanospheres for wearable strain sensors. *Carbohydr Polym*. 2023;315:120953.
doi: 10.1016/j.carbpol.2023.120953

22. Huang J, Chen G, *et al.* Ultrafast and facile construction of programmable, multidimensional wrinkled-patterned polyacrylamide/sodium alginate hydrogels for human skin-like tactile perception. *Carbohydr Polym*. 2023;319:121196.
doi: 10.1016/j.carbpol.2023.121196

23. Shinde S,Lee H E. Wearable Strain Sensors via Tough and Conductive Hydrogel-Based MoS (2) Composites for Real-Time Motion Tracking. *ACS Omega*. 2025;10(23):25102-25110.
doi: 10.1021/acsomega.5c03752

24. Choudhury S, Deepak D, Bhattacharya G, McLaughlign J,Roy S S. MoS-Polyaniline Based Flexible Electrochemical Biosensor: Toward pH Monitoring in Human Sweat. *Macromol Mater Eng*. 2023;308(8):2300007.
doi: 10.1002/mame.202300007

25. Li L, Ai Z, Wu J, Lin Z, Huang M, Gao Y,Bai H. A robust polyaniline hydrogel electrode enables superior rate capability at ultrahigh mass loadings. *Nat Commun*. 2024;15(1):6591.
doi: 10.1038/s41467-024-50831-x

26. Yu J, Wan R, *et al.* 3D Printing of Robust High-Performance Conducting Polymer Hydrogel-Based Electrical Bioadhesive Interface for Soft Bioelectronics. *Small*. 2024;20(19):e2308778.
doi: 10.1002/smll.202308778

27. Lu Y Y, Yang G, *et al.* Stretchable graphene-hydrogel interfaces for wearable and implantable bioelectronics. *Nature Electronics*. 2023;7(1):51-65.
doi: 10.1038/s41928-023-01091-y

28. Van Tam T, Chandra Bhamu K, Jae Kim M, Gu Kang S, Suk Chung J, Hyun Hur S,Mook Choi W. Engineering

phosphorous doped graphene quantum dots decorated on graphene hydrogel as effective photocatalyst and high-current density electrocatalyst for seawater splitting. *Chem Eng J*. 2024;480:148190.
doi: 10.1016/j.cej.2023.148190

29. Peng Q Y, Chen J S, *et al.* Recent advances in designing conductive hydrogels for flexible electronics. *Infomat*. 2020;2(5):843-865.
doi: 10.1002/inf2.12113

30. Fan Q, Zhang K, *et al.* Molecular Weight Tailored Hydrogen Bonding Networks in PVA/PEDOT: PSS: Decoupling the Conductivity-Flexibility Trade-Off for Robust Epidermal EMG Monitoring. *ACS Appl Mater Interfaces*. 2025;17(29):42278-42292.
doi: 10.1021/acsami.5c08001

31. Lo L W, Zhao J, Wan H, Wang Y, Chakrabartty S,Wang C. An Inkjet-Printed PEDOT:PSS-Based Stretchable Conductor for Wearable Health Monitoring Device Applications. *ACS Appl Mater Interfaces*. 2021;13(18):21693-21702.
doi: 10.1021/acsami.1c00537

32. Er E,Ates A K. Design of an electrochemical sensing platform based on MoS2-PEDOT:PSS nanocomposite for the detection of epirubicin in biological samples. *Microchem J*. 2023;189:108534.
doi: 10.1016/j.microc.2023.108534

33. Zhao C, Deng B, Chen G C, Lei B, Hua H, Peng H L,Yan Z M. Large-area chemical vapor deposition-grown monolayer graphene-wrapped silver nanowires for broad-spectrum and robust antimicrobial coating. *Nano Res*. 2016;9(4): 963-973.
doi: 10.1007/s12274-016-0984-2

34. Li P, Zhang D,Wu Z. Flexible MoS2 sensor arrays for high performance label-free ion sensing. *Sensors and Actuators A: Physical*. 2019;286:51-58.
doi: 10.1016/j.sna.2018.12.026

35. Kinnamon D, Ghanta R, Lin K-C, Muthukumar S,Prasad S. Portable biosensor for monitoring cortisol in low-volume perspired human sweat. *Sci Rep*. 2017;7(1):13312.
doi: 10.1038/s41598-017-13684-7

36. Shalini V, Harish S, Ikeda H, Hayakawa Y, Archana J,Navaneethan M. Investigating the effect of defect states and to enhance the electrical conductivity of p-type Vanadium-doped MoS2 for wearable thermoelectric application. *Journal of Alloys and Compounds*. 2023;960:170317.
doi: 10.1016/j.jallcom.2023.170317

37. Sha R,Bhattacharyya T K. MoS-based nanosensors in biomedical and environmental monitoring applications. *Electrochim Acta*. 2020;349:136370.
doi: 10.1016/j.electacta.2020.136370

38. Lee H G,Lee G. The Change of IV Characteristics by Gate Voltage Stress on Few Atomic Layered MoS 2 Field Effect Transistors. *J Korean Inst Electr Electron Mater Eng*. 2018;31(3):135-140.
doi: 10.4313/JKEM.2018.31.3.135

39. Sharma R, Kumar A, *et al.* Liquid Phase Exfoliation and Characterization of Few Layer MoS and WS Nanosheets as Channel Material in Field Effect Transistor. *Trans Electr Electron Mater*. 2023;24(2):140-148.
doi: 10.1007/s42341-023-00429-9

40. Choi S, Han S I, *et al.* Highly conductive, stretchable and biocompatible Ag-Au core-sheath nanowire composite for wearable and implantable bioelectronics. *Nat Nanotechnol*. 2018;13(11):1048-1056.
doi: 10.1038/s41565-018-0226-8

41. Ahn Y, Lee H, Lee D,Lee Y. Highly conductive and flexible silver nanowire-based microelectrodes on biocompatible hydrogel. *ACS Appl Mater Interfaces*. 2014;6(21):18401-18407.
doi: 10.1021/am504462f

42. Appel J H, Li D O, Podlevsky J D, Debnath A, Green A A, Wang Q H,Chae J. Low Cytotoxicity and Genotoxicity of Two-Dimensional MoS(2) and WS(2). *ACS Biomater Sci Eng*. 2016;2(3):361-367.
doi: 10.1021/acsbiomaterials.5b00467

43. Kaur J, Singh M, *et al.* Biological interactions of biocompatible and water-dispersed MoS(2) nanosheets with bacteria and human cells. *Sci Rep*. 2018;8(1):16386.
doi: 10.1038/s41598-018-34679-y

44. Mondal S, Kim S J,Choi C G. Honeycomb-like MoS(2) Nanotube Array-Based Wearable Sensors for Noninvasive Detection of Human Skin Moisture. *ACS Appl Mater Interfaces*. 2020;12(14):17029-17038.
doi: 10.1021/acsami.9b22915

45. Liu Y, Liu D, Xue Y, Sun H, Zhan X, Sun L,Kang K. How Advanced are Conductive Nanocomposite Hydrogels for Repairing and Monitoring Myocardial Infarction? *Int J Nanomedicine*. 2025;20(null):6777-6812.
doi: 10.2147/IJN.S503445

46. Chang C, Guan X, Lin J, Nie H, Zhou X, Xie X,Ye Y. MoS(2) Decorated Silver Nanowire-Reduced Graphene Oxide Aerogel Micro-Particle for Thermally Conductive Polymer Composites with Enhanced Flame Retardancy. *Macromol Rapid Commun*. 2022;43(18):e2200026.
doi: 10.1002/marc.202200026

47. Choi S G, Seok H J, Kim J, Kang J,Kim H K. Transparent and flexible passivation of MoS(2)/Ag nanowire with sputtered polytetrafluoroethylene film for high performance flexible heaters. *Sci Rep*. 2022;12(1):6010.
doi: 10.1038/s41598-022-09813-6

48. Zhou H W, Yang N, *et al.* Effects of CaCl, HCl, acetic acid or citric acid on dynamic mechanical performances and physicochemical properties of sodium alginate edible films. *Food Packaging Shelf*. 2022;34:100935.
doi: 10.1016/j.fpsl.2022.100935

49. Tai Y, Mulle M, Aguilar Ventura I,Lubineau G. A highly sensitive, low-cost, wearable pressure sensor based on

conductive hydrogel spheres. *Nanoscale*. 2015;7(35): 14766-14773.
doi: 10.1039/c5nr03155a

50. Wang C, Wang H, *et al.* On-skin paintable biogel for long-term high-fidelity electroencephalogram recording. *Sci Adv*. 2022;8(20):eabo1396.
doi: 10.1126/sciadv.abo1396

51. Zhang Z, Yang J, *et al.* A 10-micrometer-thick nanomesh-reinforced gas-permeable hydrogel skin sensor for long-term electrophysiological monitoring. *Sci Adv*. 2024;10(2):eadj5389.
doi: 10.1126/sciadv.adj5389

52. Qiao X, Cai Y, Kong Z, Xu Z,Luo X. A Wearable Electrochemical Sensor Based on Anti-Fouling and Self-Healing Polypeptide Complex Hydrogels for Sweat Monitoring. *ACS Sens*. 2023;8(7): 2834-2842.
doi: 10.1021/acssensors.3c00778

ACCSCIENCE PUBLISHING

International Journal of Bioprinting

RESEARCH ARTICLE

Pyridinium-based acrylate additives for multifunctional 3D-printable photosensitive resins with antibacterial, antistatic, and high-strength properties

Qiaoling Zhang[1†], Tongyi Wu[1†], Taojun Lin[1], Xiangqin Ding[1], Zhiwei Zhang[1], Jianqing Liang[1], Rong Li[1], Xiaomin Zhang[2*], Guoqiao Lai[1*], and Qiu Chen[1*]

[1]College of Material, Chemistry, and Chemical Engineering, Hangzhou Normal University, Hangzhou, Zhejiang, China

[2]Zhejiang Xunshi Technology Co., Ltd., Shaoxing, Zhejiang, China

Abstract

The increasing demand for biomaterial safety in precision medical device manufacturing and electronic packaging highlights the critical need for the rapid development of 3D-printable photosensitive resins that offer high mechanical strength, durable antibacterial effectiveness, and consistent antistatic properties. Traditional approaches involving multiple additives often result in poor compatibility, low success rates in 3D printing, compromised functionality or mechanical properties, and insufficient functional stability and longevity. To address this challenge, we introduce a new category of pyridinium-based acrylate photosensitive additives. By adjusting the quantity of pyridinium functional groups within a single additive, we have successfully achieved multifunctionalization of the 3D printing resin. The findings indicated that the pyridinium-based acrylate additive endows the 3D-printed photosensitive resin with exceptional antibacterial efficacy (>99.99% against *Escherichia coli* and *Staphylococcus aureus*), strong antistatic performance (resistance: 10^9 Ω), and high tensile strength (40.86 MPa). Furthermore, the resin demonstrated enduring and consistent antibacterial and antistatic properties. The study suggests that the novel pyridinium-based acrylate photosensitive additive can achieve a breakthrough in enhancing multifunctional 3D printing resin performance.

Keywords: Antibacterial; Antistatic; Photosensitive resin; Pyridine-based acrylic ester; UV-light curing 3D printing

†These authors contributed equally to this work

***Corresponding authors:**
Xiaomin Zhang (zhangxiaomin@sprintray.cn)

Guoqiao Lai (20020549@hznu.edu.cn)

Qiu Chen (20070057@hznu.edu.cn)

Citation: Zhang Q, Wu T, Lin T, *et al.* Pyridinium-based acrylate additives for multifunctional 3D-printable photosensitive resins with antibacterial, antistatic, and high-strength properties. *Int J Bioprint.* 2025;11(5):315-332. doi: 10.36922/IJB025280279

Received: July 10, 2025
Revised: August 14, 2025
Accepted: August 22, 2025
Published online: August 25, 2025

Copyright: © 2025 Author(s). This is an Open Access article distributed under the terms of the Creative Commons Attribution License, permitting distribution and reproduction in any medium, provided the original work is properly cited.

Publisher's Note: AccScience Publishing remains neutral with regard to jurisdictional claims in published maps and institutional affiliations.

1. Introduction

Photocuring 3D printing technology has gained widespread application across multiple fields in recent years due to its low energy consumption and high fabrication precision.[1-3] However, the mechanical properties of printed parts, including strength, toughness, and modulus, are often inadequate due to limitations in existing photosensitive resins, restricting their use in demanding production applications.[4-6] Therefore, it is essential

to modify photosensitive resins with functional additives to improve their mechanical performance.[7] Additionally, the polymer surfaces of these printed parts are prone to microbial colonization during storage, transportation, and use, posing biological safety risks. Moreover, the insulating properties of polymeric materials can result in electrostatic accumulation, compromising the dimensional stability and functionality of precision medical and electronic devices.[8–10] To address these challenges, the development of multifunctional modifiers for photosensitive resin systems that can enhance mechanical properties, prevent microbial growth, and reduce static buildup has become a crucial research focus to meet the market demand for high-performance, multifunctional 3D printing materials.

Recently, various pyridinium salts have emerged as multifunctional modifiers with combined antibacterial and antistatic properties.[11] Their antibacterial mechanism primarily relies on a cationic contact-killing effect: the quaternary ammonium cation ($[R_4N]^+$), where R is the substituent in the pyridinium structure, electrostatically binds to negatively charged microbial cell membranes, membrane protein hydrolysates, and other anionic molecules. Simultaneously, their hydrophobic chains penetrate the hydrophobic core of the bacterial membrane, disrupting its structure and denaturing critical proteins (e.g., structural proteins and enzymes), ultimately leading to microbial death.[12,13] Concerning antistatic performance, the quaternary ammonium groups of pyridinium salts interact with negatively charged environmental particles (e.g., dust and ions) to achieve charge neutralization. Additionally, their hygroscopicity promotes the adsorption of water molecules onto the material surface, forming ionic conductive pathways that effectively dissipate static charges.[14,15] However, the current pyridinium-based antibacterial/antistatic agents still encounter practical challenges, including limited chemical reactivity, insufficient thermal stability, and short functional longevity.

The integration of pyridinium salt additives into photopolymerization-based 3D printing systems poses challenges. The limited absorption range of pyridinium salts (<360 nm) impedes their direct initiation of visible-light polymerization. Despite the potential redshift in absorption (375–560 nm) through charge-transfer complex formation with electron donors, this approach adds complexity to the system, leading to compatibility issues, phase separation risks, and necessitates precise polymerization kinetics control.[16,17] Moreover, excessive or inappropriate addition can negatively impact the mechanical properties (e.g., strength and toughness) of the cured material.[18] Therefore, optimizing the molecular structure, loading amount, and compatibility with the resin matrix is crucial to develop pyridinium-modified photosensitive resins with enhanced antibacterial and antistatic properties, as well as targeted mechanical performance. This optimization is essential to strike a balance between multifunctionality, processability, and overall performance of the final printed components.

Building upon this groundwork, we developed a new pyridinium-based acrylate photosensitive additive by incorporating pyridine into the acrylate backbone, followed by quaternization. Through tailored chemical modification of the pyridinium functional groups, we synthesized two acrylate reactive monomers using isophorone diisocyanate (IPDI; a monopyridinium salt functional monomer [IPDI'-PS] and a bis-pyridinium salt functional monomer [IPDI"-PS]) as the primary reactant. These monomers were then blended with reactive diluents, oligomers, and a photoinitiator to create photosensitive resins, which were subsequently photopolymerized using digital light processing (DLP) 3D printing. We systematically assessed the mechanical properties of the printed components and explored the impact of varying the concentration of the pyridinium-based acrylate additives (IPDI'-PS and IPDI"-PS) on the antibacterial and antistatic properties of the prints. Finally, we conducted a comparative evaluation of the overall performance between the 3D-printed photosensitive resins containing IPDI'-PS and those containing IPDI"-PS.

2. Materials and methods

2.1. Materials

Isophorone diisocyanate (IPDI), dibutyl tin dilaurate (DBTDL), 1,3-propanediol (PDO), trimethylolpropane (TMP), 4-aminopyridine (4-AP), iodomethane (CH_3I), 4-acryloyl morpholine (ACMO), cyclotrimethylolpropane acrylate (CTFA), acetonitrile (MeCN), and hydroquinone were procured from Sinopharm Chemical Reagent Co., Ltd. (China). Methyl methacrylate-2-hydroxyethyl ester (HEMA), diphenyl (2,4,6-trimethylbenzoyl) oxime (TPO), and N,N-dimethylformamide (DMF) were obtained from Beijing Warwick Chemical Co., Ltd. (China). *Staphylococcus aureus* and *Escherichia coli* were acquired from Shanghai Macklin Biochemical Co., Ltd. (China).

2.2. Synthesis of the pyridinium-based acrylate photosensitive additive

Monofunctional (IPDI'-PS) and bifunctional (IPDI"-PS) pyridinium salt acrylate reactive monomers were synthesized by reacting IPDI with different alcohols (PDO and TMP), followed by introducing photosensitive unsaturated double bonds via HEMA, and finally end-capping with 4-AP and quaternization. The specific procedure is as follows.

2.2.1. Synthesis of monofunctional pyridinium-based acrylate photosensitive additive (IPDI'-PS)

As displayed in Line 1 of Figure 1, a three-necked flask containing 0.1 mol of PDO, 0.1 g of DBTDL, 0.1 g of hydroquinone, and 50 mL of DMF was placed in an ice–water bath. Subsequently, 0.2 mol of IPDI was added dropwise. After complete addition, the mixture was heated to 35°C and reacted for 3 h, resulting in the formation of the precursor OCN-PDO-NCO. Following this, 0.1 mol of HEMA was added dropwise and allowed to react for 2 h to introduce a photosensitive group successfully. Then, 0.2 mol of 4-AP was added to cap the remaining isocyanate groups (–NCO) in the system. The reaction progress was monitored using Fourier-transform infrared (FTIR) spectroscopy or chemical titration until no detectable –NCO groups were present, indicating complete end-capping and the formation of the intermediate HEMA-PDO-AP. Finally, CH_3I was added for the quaternization of the intermediate. Upon completion of the reaction, the solvent and volatile byproducts were removed under reduced pressure. The crude product was dried under vacuum at 60°C for 12 h, resulting in the production of the IPDI'-PS additive.

2.2.2 Synthesis of the IPDI'-PS additive

As displayed in Line 2 of Figure 1, a three-necked flask was charged with 0.1 mol of TMP, 0.2 g of DBTDL, 0.2 g of hydroquinone, and 50 mL of DMF and placed in an ice–water bath. Subsequently, 0.3 mol of IPDI was added dropwise. The reaction was conducted at 60°C for 3 h, resulting in the formation of the precursor TMP-TriNCO. Subsequently, 0.1 mol of HEMA was added dropwise and allowed to react for 2 h to introduce a photosensitive group. Following this, 0.3 mol of 4-AP was added to end-cap the remaining isocyanate groups (–NCO). The reaction progress was monitored using FTIR spectroscopy or chemical titration until no –NCO groups were detectable, indicating complete end-capping and the formation of the intermediate HEMA-TMP-DiAP. Finally, CH_3I was then added for quaternization of the intermediate. Upon completion of the reaction, the solvent and volatile byproducts were removed under reduced pressure. The crude product was dried under vacuum at 60°C for 12 h, yielding the bis-pyridinium salt functional acrylate reactive monomer (IPDI"-PS).

2.3. Preparation of 3D-printable photosensitive resins

According to the feed ratios specified in Tables 1 and 2, the oligomer (tris(2-hydroxyethyl) isocyanurate triacrylate), the reactive diluents CTFA and ACMO, the pyridinium-based acrylate photosensitive additive (either IPDI'-PS or IPDI"-PS), and the photoinitiator TPO were added sequentially to an opaque container. The formulated 3D-printable photosensitive resin was then mixed uniformly using a mechanical stirrer, followed by sonication to remove air bubbles. Finally, the resin was sealed and stored in light-protected conditions.

2.4. Photopolymerization of 3D-printable photosensitive resins

The 3D printable photosensitive resins were poured into the resin vat of a DLP 3D printer (AccuFab-D1; Hangzhou Shining 3D Tech Co., Ltd., China) for printing. Subsequently, the printed samples were washed with anhydrous ethanol to eliminate surface-uncured resin and subsequently cured in a UV chamber for 5 min (Figure 2a and b).

2.5. Characterization and testing

2.5.1. ^{1}H nuclear magnetic resonance characterization

^{1}H nuclear magnetic resonance (NMR) spectra of the synthesized pyridinium-based acrylate photosensitive additive were recorded on an AVANCE AV 400 MHz spectrometer (Bruker, Germany) using $CDCl_3$ or DMSO-d_6 as the solvent.

2.5.2. Fourier-transform infrared characterization

Fourier-transform infrared (FTIR) spectra of the pyridinium-based acrylate photosensitive additive, the 3D-printable photosensitive resins, and the printed samples were recorded on a Nicolet 5700 spectrometer (Nicolet, United States of America [USA]) in the range of 4000–500 cm^{-1}.

2.5.3. Curing shrinkage testing

The curing shrinkage of the 3D-printable photosensitive resins was measured according to ISO 3521:1997 using an HTY-300SL multifunctional solid–liquid densitometer (Dedu, China). Measurements were performed according to the sample state as follows:

(i) Solid samples: The measurement chamber was filled with deionized water and equilibrated on the balance. The wire basket was immersed. After the bubble disappearance, the balance was tared ("0"). The solid sample was placed on the basket cover. Following the "OK" display, "MEMORY" was pressed. The sample was then fully immersed in water within the basket. After achieving a bubble-free state and "OK" display, "MEMORY" was pressed to record the measurement.

(ii) Liquid samples: The base plate, stand, and hook were positioned on the balance and tared ("0"). The sinker was suspended from the stand's center. After the "OK" display, "MEMORY" was pressed. A beaker containing the liquid photopolymer resin was

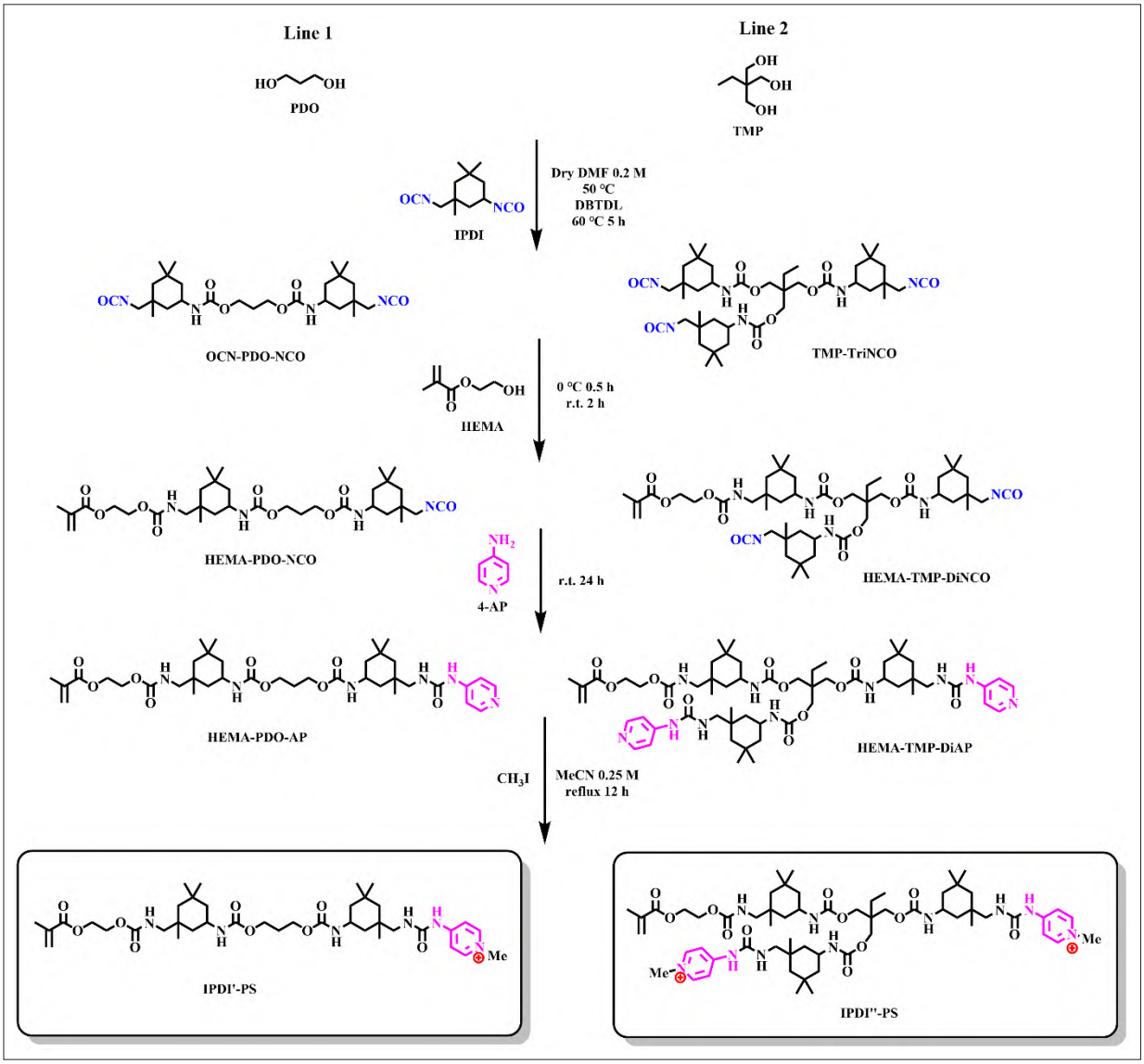


Figure 1. Synthesis of the pyridinium-based acrylate photosensitive additives: IPDI'-PS and IPDI"-PS. Abbreviations: 4-AP, 4-aminopyridine; CH_3I, Iodomethane; DBTDL, dibutyl tin dilaurate; DMF, N,N-dimethylformamide; HEMA, methyl methacrylate-2-hydroxyethyl ester; IPDI'-PS, monopyridine salt functional group photosensitive additive monomer; IPDI"-PS, bipyridine salt functional group photosensitive additive monomer; MeCN, acetonitrile; PDO, 1,3-propanediol; TMP, trimethylolpropane.

Table 1. Formulation of 3D-printable photosensitive resins using IPDI'-PS

Resin	Polyurethane acrylate (wt%)	CTFA (wt%)	ACMO (wt%)	IPDI'-PS (wt%)	TPO (wt%)
PR- IPDI'-PS-1	50	35	24.5	0	0.5
PR- IPDI'-PS-2	50	35	22.5	2	0.5
PR- IPDI'-PS-3	50	35	20.5	4	0.5
PR- IPDI'-PS-4	50	35	18.5	6	0.5
PR- IPDI'-PS-5	50	35	16.5	8	0.5
PR- IPDI'-PS-6	50	35	14.5	10	0.5

Abbreviations: ACMO, 4-acryloyl morpholine; CTFA, cyclotrimethylolpropane acrylate; IPDI'-PS, monopyridine salt functional group photosensitive additive monomer; PR-IPDI'-PS-1, blank control (3D printed photosensitive resin without pyridine salt photosensitive additive); PR-IPDI'-PS-2 to 6, 3D printed photosensitive resins with different contents of monofunctional pyridine salt photosensitive additives; TPO, diphenyl (2,4,6-trimethylbenzoyl) oxime.

positioned beneath the sinker, which was tilted and fully immersed. Following the bubble disappearance at the liquid surface, "MEMORY" was pressed to record the measurement.

Each measurement was repeated three times, and the average value was used to calculate the curing shrinkage according to **Equation (I)**:

$$V_s = \frac{\rho_c - \rho_l}{\rho_c} \times 100\% \quad \text{(I)}$$

where V_s is the curing shrinkage, ρ_l is the density of the liquid photopolymer resin, and ρ_c is the density of the cured 3D-printed material.

2.5.4. Gel content testing

The gel content of the elastomer was measured by solvent extraction before and after thermal curing. Samples, with dimensions of 10 × 10 × 0.65 mm^3, were immersed in toluene at 25°C for 48 h, followed by drying in an oven at 80°C for 24 h. The weights of the original samples (m_0), the swollen samples (m_s), and the dried samples (m_d) were recorded. Additionally, the crosslink density (ν_e) and the average molecular weight of the polymer between the crosslinks (M_c) were calculated by using the Flory–Rehner equation (**Equations II–IV**):

$$\nu_e = \frac{-\left[\ln\left(1 - V_r\right) + V_r + \chi V_r^2\right]}{V_0\left(V_r^{\frac{1}{3}}\right)} \quad \text{(II)}$$

where

$$V_r = \frac{\frac{m_d}{\rho_2}}{\frac{m_d}{\rho_2} + \frac{m_s - m_d}{\rho_1}} \quad \text{(III)}$$

$$M_c = \frac{\rho_2}{\nu_e} \quad \text{(IV)}$$

where V_r denotes the volume fraction of the samples, χ denotes the Flory–Huggins polymer–solvent interaction parameter, and V_0 denotes the molar volume of toluene (106.2 cm^3/mol). The values obtained from this equation were used in the derivation, where ρ_1 (0.865 g/mol) represents the density of the solvent and ρ_2 (1.113 g/mol) represents the density of the polymer.

2.5.5. Hardness testing

Hardness of the 3D-printed specimens was measured according to ISO 868:2003 using an LX-D Shore D durometer (Shanghai Luling Instrument Factory, China). Individual samples (10 × 10 × 5 mm^3) were placed on a rigid, stable horizontal surface. The durometer's presser foot was applied to the sample surface to obtain hardness readings. Five measurements were performed per sample group, and the average value was reported.

2.5.6. Tensile testing

Tensile strength and elongation at break of the 3D-printed specimens were measured according to ISO 527-1:2019 using an AI-7000-MU1 universal testing machine (Gotech Testing Machines Co., Ltd., China) equipped with a 5000 N load cell. Specimens were machined into a dumbbell shape with a gauge section measuring 20 × 4 × 3 mm^3. Five specimens per group were tested, and the average values were reported.

2.5.7. Heat distortion temperature testing

The heat deflection temperature (HDT) of the 3D-printed specimens was measured according to ISO 75 using a GT-HV2000-C3W heat deflection tester (Gotech Testing Machines Co., Ltd., China). Rectangular specimens (100 × 10 × 4 mm^3) were tested in an oil bath with a heating rate of 120°C/h, a deflection limit of 0.34 mm, and an applied

Table 2. Formulation of 3D-printable photosensitive resins using IPDI"-PS

Resin	Polyurethane acrylate (wt%)	CTFA (wt%)	ACMO (wt%)	IPDI"-PS (wt%)	TPO (wt%)
PR- IPDI"-PS-1	50	35	24.5	0	0.5
PR- IPDI"-PS-2	50	35	22.5	2	0.5
PR- IPDI"-PS-3	50	35	20.5	4	0.5
PR- IPDI"-PS-4	50	35	18.5	6	0.5
PR- IPDI"-PS-5	50	35	16.5	8	0.5
PR- IPDI"-PS-6	50	35	14.5	10	0.5

Abbreviations: ACMO, 4-acryloyl morpholine; CTFA, cyclotrimethylolpropane acrylate; IPDI"-PS, bipyridine salt functional group photosensitive additive monomer; PR-IPDI"-PS-1, blank control (3D printed photosensitive resin without pyridine salt photosensitive additive); PR-IPDI"-PS-2 to 6, 3D printed photosensitive resins with different contents of bipyridine salt photosensitive additives; TPO, diphenyl (2,4,6-trimethylbenzoyl) oxime.

stress of 0.455 MPa (66 psi). Three specimens were tested per group, and the average value was reported.

2.5.8. Thermogravimetric analysis

Thermal stability of the 3D-printed specimens was determined using a Q500 thermogravimetric analyzer (TA Instruments, USA). Samples (~5 mg) were loaded into alumina crucibles and heated under a nitrogen atmosphere from 25 to 600°C at a rate of 20°C/min. Thermogravimetric (TG) curves were recorded.

2.5.9. Penetration depth testing

The resin to be tested was placed in a small tank, and the laser power was set to 300 mW. The scanning distance was set to 0.08 mm, and the resin running temperature was set to 25 °C. A series of different scanning times was then set, and a single-layer 20 × 20 mm^2 square sheet was made using the plane scanning method. The thickness of the sheet was measured with a thickness gauge. Subsequently, the square sheet was subjected to a cleaning process involving a mixture of ethanol and isopropanol. Thereafter, the sample was UV-cured, as previously described. Following these steps, the thickness of the sheet was measured once more, and the penetration depth (D_p) was derived in accordance with the Lambert–Beer law using **Equation (V)**:

$$C_d = D_p \times \ln\frac{E}{E_c} \quad \text{(V)}$$

where C_d denotes the depth of cure, E represents the exposure energy, and E_c signifies the critical exposure energy.[19]

2.5.10. Antistatic property testing

Surface resistivity of the 3D-printed specimens was measured in accordance with ISO 3915 using a CXT5015 surface resistivity meter (Xinyang Electronics Co., Ltd., China). This measurement serves as an indicator of antistatic performance, as electrostatic charge generation, accumulation, and dissipation are directly governed by a material's electrical conductivity. Resistivity values were recorded at 1, 14, and 30 days after specimen preparation. Five measurements were performed per time interval, and the average value was calculated.

2.5.11. Antibacterial property testing

Antibacterial activity of the samples was evaluated against *E. coli* and *S. aureus* according to ISO 22196:2007 using the colony counting method.

The test sample was put into a petri dish, and 30 μL of bacterial liquid was added dropwise to the front side of the test sample membrane. A non-toxic and non-resistant polyethylene (PE) film (50 × 50 mm^2) was used to cover the top of the bacterial liquid, and the film was gently pressed to push the bacterial liquid to be in close contact with the sample to ensure that the bacteria were tightly affixed to the surface of the sample. The sample was finally cultivated in a CO_2 thermostatic incubator at 37°C. The test sample was then incubated for 8 h with an LB liquid medium to elute the eluted bacterial liquid. After 8 h of incubation, bacteria on the sample's surface were eluted with LB liquid medium, and the eluted bacterial liquid was collected. The test sample specification was a rectangle of 80 × 80 × 5 mm^3. After incubation, the culture broth and eluate were diluted with sterile water to the appropriate concentration. Then, 30 μL of the broth was pipetted into the LB solid medium, spread evenly with a spreader, and sealed with a sealing film. The solid medium was placed upside down in a CO_2 incubator at 37°C for 24 h, and the number of colonies on the solid medium was counted to calculate the antibacterial rate. The antibacterial rate was calculated using **Equation (VI)**:

$$G = \frac{A - B}{A} \times 100\% \quad \text{(VI)}$$

where G is the antibacterial rate of the sample, A is the colony count of the control group, and B is the colony count of the experimental sample group.

2.5.12. Statistical analysis

All quantitative data are expressed as the mean ± standard deviation from at least three independent experiments ($n \geq 3$). Graphs were generated using OriginPro 2022 software (OriginLab, USA), with error bars representing standard deviation. Statistical significance between groups was determined by one-way analysis of variance (ANOVA) followed by Tukey's post hoc test, with $p < 0.05$ considered statistically significant.

3. Results and discussion

3.1. Synthesis of the photosensitive additives IPDI'-PS and IPDI"-PS

Comparison of the FTIR spectra with those of the raw material IPDI (Figure 2c) revealed identical spectral changes for both the mono-pyridinium salt (IPDI'-PS) and bis-pyridinium salt (IPDI"-PS) systems. The complete disappearance of the characteristic isocyanate (–NCO) peak at 2246 cm^{-1} indicates the full consumption of –NCO groups in IPDI and successful end-capping. Key characteristic peaks corresponding to the formation of urethane bonds via the –NCO/–OH reaction appeared: the C=O stretching vibration at ~1680 cm^{-1}, the strong N–H stretching vibration absorption at ~3313 cm^{-1}, and the characteristic peaks for N–H bending vibration coupled

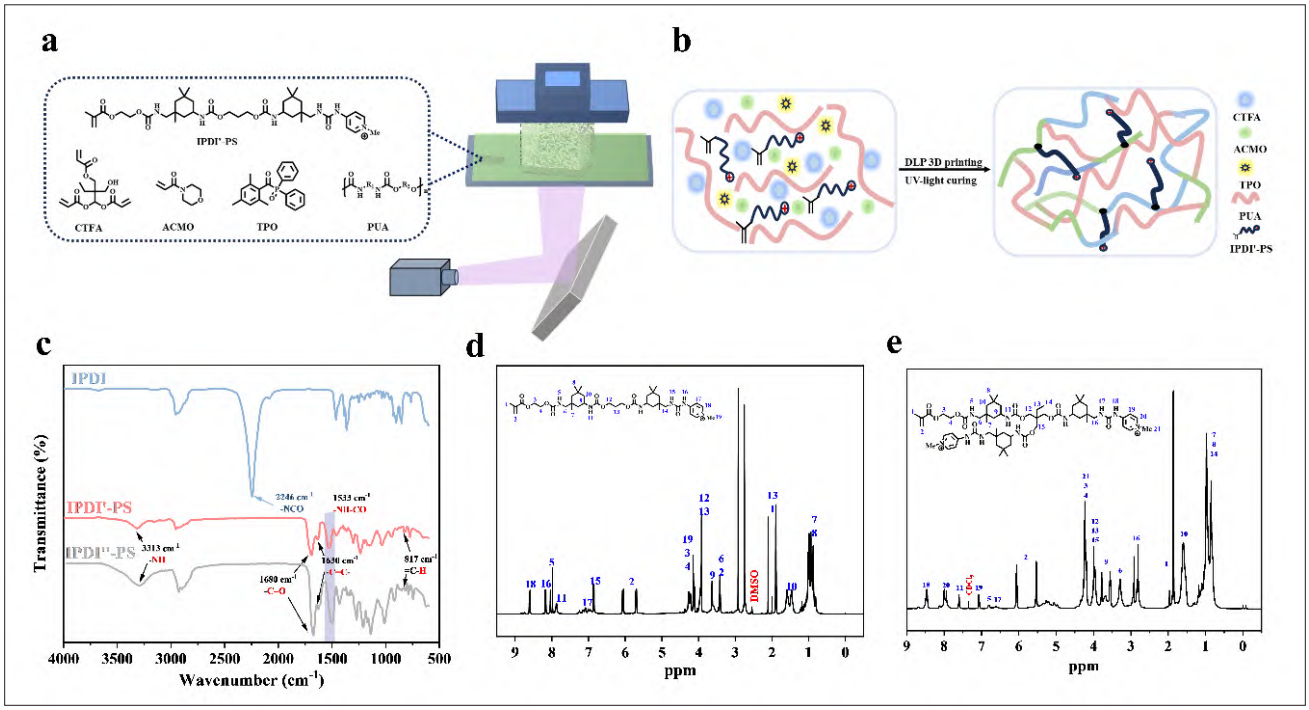


Figure 2. DLP 3D printing and additives characterization. (a) Schematic of DLP 3D printing. (b) UV-curing mechanism of the IPDI'-PS system. (c) FTIR spectra of the pyridinium-based acrylate photosensitive additives IPDI'-PS and IPDI"-PS. (d) ^{1}H NMR spectrum of IPDI'-PS in DMSO-d_6. (e) ^{1}H NMR spectrum of IPDI"-PS in $CDCl_3$. Abbreviations: ACMO, 4-acryloyl morpholine; CTFA, cyclotrimethylolpropane acrylate; DLP, digital light processing; IPDI, isophorone diisocyanate; IPDI'-PS, monopyridine salt functional group photosensitive additive monomer; TPO, diphenyl (2,4,6-trimethylbenzoyl) oxime; PUA, polyurethane acrylate; UV-light, ultraviolet light; ^{1}H NMR, ^{1}H nuclear magnetic resonance.

with C–N stretching vibration at ~1533 cm^{-1}. Furthermore, the emergence of the =C–H bending vibration peak of the alkene group at ~817 cm^{-1} confirms the successful grafting of the photosensitive group. The appearance of these characteristic peaks and their associated functional groups aligned with the expected structures of the target products, IPDI'-PS and IPDI"-PS. The successful synthesis was further confirmed by ^{1}H NMR analysis (Figure 2d and e).

3.2. Double bond conversion, volumetric shrinkage, and penetration depth

The characteristics of the photosensitive resin itself, such as its curability, cure shrinkage, and printing accuracy, play a crucial role in influencing the material performance in DLP 3D printing. Initially, the FTIR spectra (Figure 3a) of the uncured liquid resins were compared with those of samples post-photopolymerization and UV post-curing. The distinctive C=C double bond absorption peak at 1643 cm^{-1} was significantly reduced after photopolymerization, indicating a substantial C=C conversion (>99%) and efficient photocuring. These findings validate that the formulation utilized in this study improved the reactivity and integration of photosensitive components within the curing system, leading to enhanced photoconversion.[20,21] High conversion rates are essential for establishing a dense crosslinked network and achieving optimal material performance.[22]

During photopolymerization-based 3D printing, photosensitive resins transform from liquid monomers to a solid crosslinked network. This process inherently causes significant volume shrinkage due to reduced intermolecular distances.[23] Consequently, cure shrinkage plays a crucial role in determining printing accuracy, dimensional stability, and final part performance. Excessive shrinkage can result in internal stress buildup, warping, and interlayer delamination, significantly affecting the fabrication of high-precision devices.[24] Volumetric shrinkage primarily stems from the shortening of molecular distances during covalent bond formation in C=C double bond polymerization, with its extent determined by the total concentration of C=C bonds and the final conversion within the system.[25–27]

To systematically evaluate the impact of the pyridinium molecular structure on curing shrinkage, we compared the modification effects of IPDI'-PS containing a single pyridinium group and IPDI'-PS containing dual pyridinium groups across the same loading range. Figure 3b illustrates that the addition of photosensitizing

additives with varying pyridinium group numbers effectively reduced cure shrinkage compared to the unmodified resin (control group, 10.81% shrinkage). The reduction in shrinkage was dependent on the molecular structure, displaying a consistent decrease as the additive loading increased. At a 10 wt% loading, shrinkage minimized to 7.20%, marking a significant 33.4% reduction compared with the control. This decrease can be attributed to three main factors. Firstly, as a non-polymerizing component, IPDI'-PS diluted the concentration of polymerizable C=C bonds per unit volume, thereby reducing the total amount of shrinkage-contributing monomers/oligomers. Secondly, FTIR results confirmed a high C=C conversion (>99%), ensuring that the dilution effect translated effectively into reduced shrinkage and improved dimensional accuracy of printed parts. In contrast, the IPDI"-PS photosensitizing additive exhibited a more pronounced effect in suppressing cure shrinkage, which decreased continuously at higher loadings. Notably, even at a low 2 wt% loading, IPDI"-PS exhibited a clear modification effect, reducing shrinkage to 9.61% (an 11.1% reduction). With a 10 wt% loading, shrinkage further decreased to 6.05%, achieving a substantial 44.0% reduction compared to that of the control. The superior efficiency of IPDI"-PS arises from its role as a nonshrinking component that dilutes the C=C bond concentration. Additionally, its dipyridinium salt structure provides higher functionality, potentially altering the ν_e or network architecture upon network participation or influence, thereby further suppressing shrinkage behavior.

Furthermore, the Dp of the photosensitive resins was assessed using a DLP 3D printer to evaluate their suitability for creating intricate structures with high precision and their potential as DLP 3D printing materials.[28] As the curing degree increased, the single-layer cure thickness of the resin also increased. Figure 3c illustrates that the unmodified resin (control) had a Dp value of 0.1776. In contrast, the Dp values of resins modified with either IPDI'-PS or IPDI"-PS progressively decreased with increasing additive loading, consistently falling within an intermediate range between high and low Dp. This suggests that the resins incorporating pyridinium-based acrylate photosensitizing additives can maintain relatively fast printing speeds while enabling the fabrication of complex structures with enhanced resolution.

Collectively, these results demonstrate that the intrinsic properties of the photosensitive resins prepared in this study are compatible with the requirements of DLP 3D printing.

3.3. Thermal properties

To systematically evaluate the impact of the pyridinium group count (IPDI'-PS vs. IPDI"-PS) on the thermal stability of 3D-printed materials, HDT measurements and thermogravimetric analysis (TGA) were conducted. The HDT demonstrated a notable correlation with the loading of pyridinium additives (IPDI'-PS and IPDI"-PS) (Figure 3d).

For the IPDI'-PS system, the HDT increased with additive loading up to 6 wt%, peaking at 43.5°C. This improvement of 1.5°C over the unmodified reference system highlights the positive impact of optimal IPDI'-PS loading on thermal deformation resistance. Beyond 6 wt%, the HDT decreased, which is attributed to the effective participation of IPDI'-PS in the reaction and the optimization of the crosslinked network at optimal loadings. However, excessive loading may lead to pyridinium stacking and poor dispersion, compromising network homogeneity and introducing defects that reduce thermal stability.[29,30] In contrast, the IPDI"-PS system achieved its maximum HDT of 44.6°C (a 2.6°C increase over the control) at a lower loading of only 4 wt%, showcasing superior network densification efficiency at lower concentrations. However, the HDT progressively decreased beyond 4 wt% (41.9°C at 8 wt%; 40.9°C at 10 wt%), indicating that its more flexible molecular structure induces a milder disruption to network integrity. Although IPDI"-PS attained a higher peak HDT (44.6°C vs. 43.5°C) and required a lower optimal loading (4 wt% vs. 6 wt%) compared to IPDI'-PS, it exhibited a greater reduction at excessive loadings (–3.7°C at 10 wt% vs. –2.3°C for IPDI'-PS). This divergence in structure–property relationships stems from variances in pyridinium content and molecular rigidity.[31]

Thermogravimetric analysis (TGA) provided further insights into the thermal decomposition behavior of the materials (Figure 3e and f), specifically focusing on the initial decomposition temperature, defined as the temperature at 5% weight loss (T_D5). For the IPDI'-PS system, T_D5 initially increased and then decreased with higher IPDI'-PS loading. At 2 wt% loading, T_D5 was 158°C, peaking at 168°C at 6 wt% loading and decreasing to 153°C at 10 wt% loading. This suggests that IPDI'-PS effectively improved the thermal decomposition stability within the 6 wt% loading range, consistent with the HDT results. The IPDI"-PS system exhibited a unique trend: T_D5 presented an anomalous increase to 131.8°C at 4 wt% loading. However, at 2, 6, 8, and 10 wt% loadings, the T_D5 values were 113, 116, 115, and 107°C, respectively. These values were significantly lower than the peak observed at 4 wt% and notably below the corresponding T_D5 values of the IPDI'-PS system at equivalent loadings. This indicates that while IPDI"-PS notably raised the decomposition temperature at 4 wt%, its effectiveness in improving T_D5 was limited at other loadings (2, 6, 8, and 10 wt%). Furthermore, even

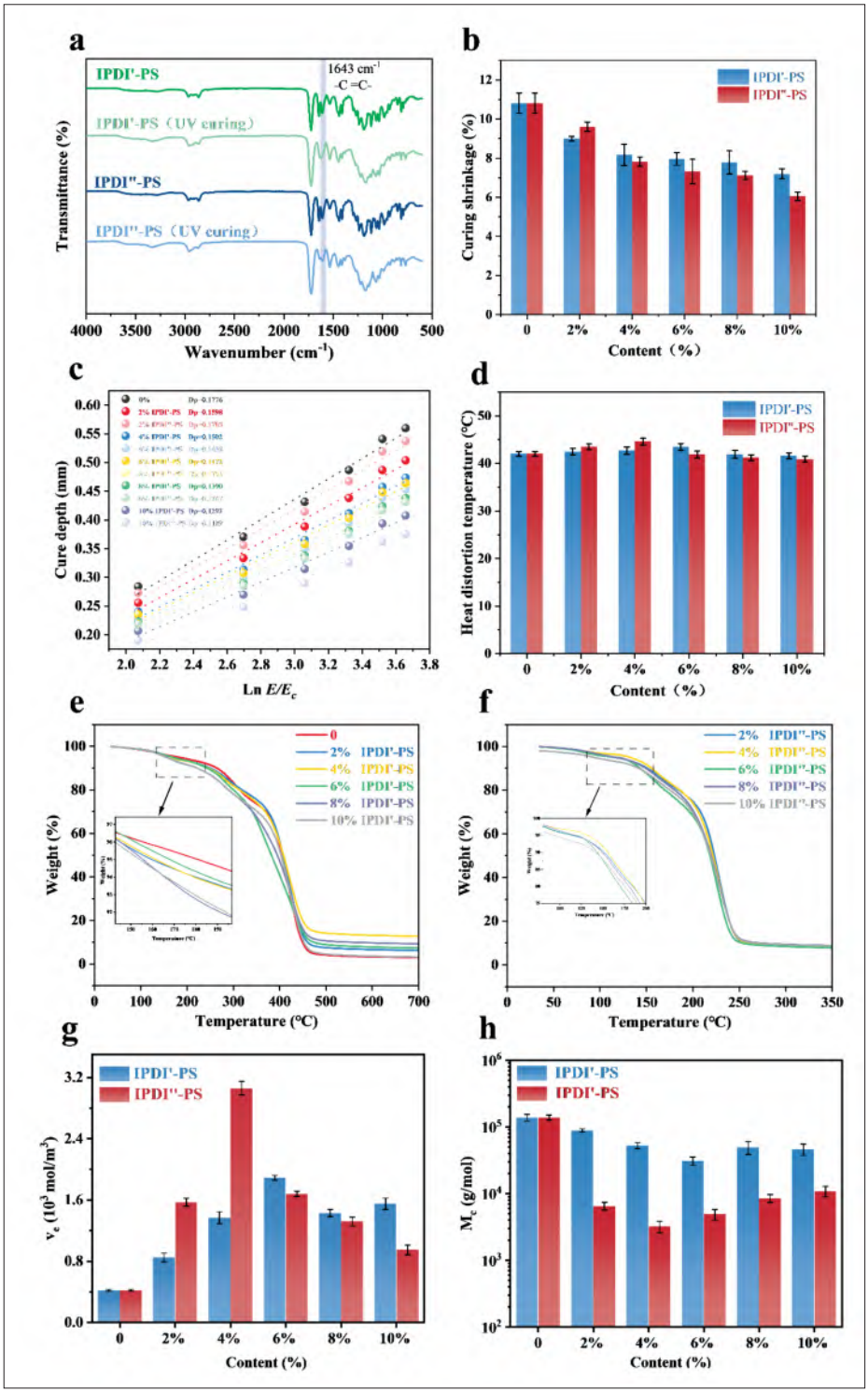


Figure 3. The effect of photosensitive additives on resin properties. (a) FTIR spectra of uncured liquid resins with IPDI'-PS or IPDI"-PS compared to their photocured counterparts. (b) Cure shrinkage of photosensitive resins at different loadings of IPDI'-PS or IPDI"-PS (n = 5). (c) Dp of photosensitive resins at different loadings of IPDI'-PS or IPDI"-PS. (d) HDT of photosensitive resins modified with varying loadings of IPDI'-PS or IPDI"-PS (n = 5). (e) TGA curves of photosensitive resins containing different loadings of IPDI'-PS. (f) TGA curves of IPDI"-PS-modified photosensitive resins at varying additive loadings. (g) Crosslink density (v_e) of photopolymers with varying loadings of IPDI'-PS or IPDI"-PS (n = 5). (h) Average molecular weight between crosslinks (M_c) of photopolymers with varying loadings of IPDI'-PS or IPDI"-PS (n = 5). Abbreviations: IPDI'-PS, 3D printed photosensitive resins of monopyridine salt photosensitive additive; IPDI"-PS, 3D printed photosensitive resins of bipyridine salt photosensitive additive.

the peak T_D5 achieved by IPDI"-PS (131.8°C) was notably lower than that of IPDI'-PS at its optimal loading (168°C). Overall, the TGA data suggested that IPDI'-PS generally performed less effectively than IPDI'-PS in enhancing the long-term thermal stability (resistance to decomposition) of the materials. However, the simultaneous peaks in both HDT and T_D5 for the IPDI"-PS system at 4 wt% confirmed a relatively optimal modification effect at this specific concentration.

Additionally, the v_e and average molecular weight between crosslinks (M_c) of photopolymer resins containing different pyridinium salt additives were determined through swelling tests using the Flory–Rehner equation.[32] For the IPDI'-PS system, v_e initially increased then decreased with increasing additive loading, peaking at 6 wt% (Figure 3g). This trend closely corresponds to the HDT and TGA (T_D5) results, where the maximum v_e coincided with the highest HDT (43.5°C) and T_D5 (168°C). This suggests an optimal crosslink network density at 6 wt%, which effectively restricts polymer chain mobility, enhancing resistance to thermal deformation and decomposition. Excessive loading (> 6 wt%) likely leads to molecular crowding, compromising network homogeneity, and introducing stress concentration points, thereby reducing v_e and diminishing thermal stability (as indicated by decreased HDT and T_D5). The M_c data further support this mechanism (Figure 3h); at 6 wt%, M_c reached its minimum (30,930 g/mol), indicating the shortest chain length between crosslinks and a rigid network structure essential for high thermal stability. Beyond 6 wt%, the significantly increased M_c suggests enlarged crosslink spacing and network degradation, weakening thermal resistance. For IPDI"-PS, the peak v_e (3.06×10^3 mol/m³) was observed at a lower loading (4 wt%) due to the higher crosslinking efficiency per molecule conferred by its rigid pyridinium rings, facilitating rapid network densification (v_e exceeded IPDI'-PS at equivalent concentrations). Beyond 4 wt%, excessively rigid groups induced molecular crowding and phase separation, expanding crosslink spacing and reducing v_e. Similarly, M_c reached its minimum (3215 g/mol) at 4 wt%, confirming ultra-dense network formation. Above this threshold, progressively increasing M_c indicated incremental network disruption from additive aggregation, resulting in a higher peak HDT (44.6 °C) but limited T_D5 improvement.

3.4. Mechanical properties

The mechanical properties of materials significantly impact wear resistance, compressive strength, and long-term dimensional stability, crucial for precision instruments and dental prosthetics. To assess the influence of two photosensitizing additives, IPDI'-PS and IPDI"-PS, on the mechanical properties of 3D-printed photosensitive resins, durometer measurements were conducted to determine sample hardness. Both systems exhibited similar trends (Figure 4a) as follows: hardness increased with higher pyridinium content but displayed saturation behavior beyond specific loadings. The increase was notably slower for IPDI'-PS beyond 8 wt%, while IPDI"-PS reached a plateau after 6 wt%. This observation suggests that pyridinium groups enhance network rigidity through ionic crosslinking, but excessive loading leads to an uneven distribution of crosslinking points due to steric hindrance, resulting in network defects.[33,34] Consequently, optimizing hardness is limited by the material's physical upper limit of v_e, necessitating a balance between molecular rigidity design and network integrity.

Regarding tensile strength, the material exhibited continuous improvement with increasing IPDI'-PS loading. At 10 wt% loading, the tensile strength increased significantly from 30.04 MPa (unmodified control) to 40.86 MPa, representing a 36.02% enhancement (Figure 4b and c). In contrast, the impact of IPDI"-PS loading on tensile strength exhibited an initial rise followed by a decline. A peak tensile strength of 37.96 MPa (26.32% increase over the control) was attained at 6 wt% loading. Beyond this concentration, the strength gradually decreased (Figure 4d and e). Notably, at higher IPDI"-PS loadings (8 and 10 wt%), a significant decrease in solubility within the system was observed, requiring notably extended mechanical stirring and sonication times. This solubility limitation is considered a key factor contributing to the decrease in tensile strength. Overall, IPDI'-PS demonstrated superior and more consistent performance in enhancing the tensile strength of the material (Figure 4f).

Both additives caused a significant decrease in the elongation at break (Figure 4c and e) at low loadings (2 wt%). This decrease is primarily due to the disruption of the native crosslinked structure of the resin by the additive molecules, which restricts molecular chain mobility.[35] However, as the loading increases, their effects diverge noticeably. Specifically, the continuous introduction of IPDI'-PS incorporates flexible chain segments into the system, enhancing molecular chain mobility and leading to a gradual recovery in the elongation at break. In contrast, increasing the IPDI"-PS loading only results in a brief initial increase, followed by a continuous decrease in the elongation at break, demonstrating its inferior effectiveness compared to that of IPDI'-PS in improving material toughness.

3.5. Antibacterial properties

Given the inherent antibacterial properties of pyridinium groups, this study systematically evaluated the antibacterial

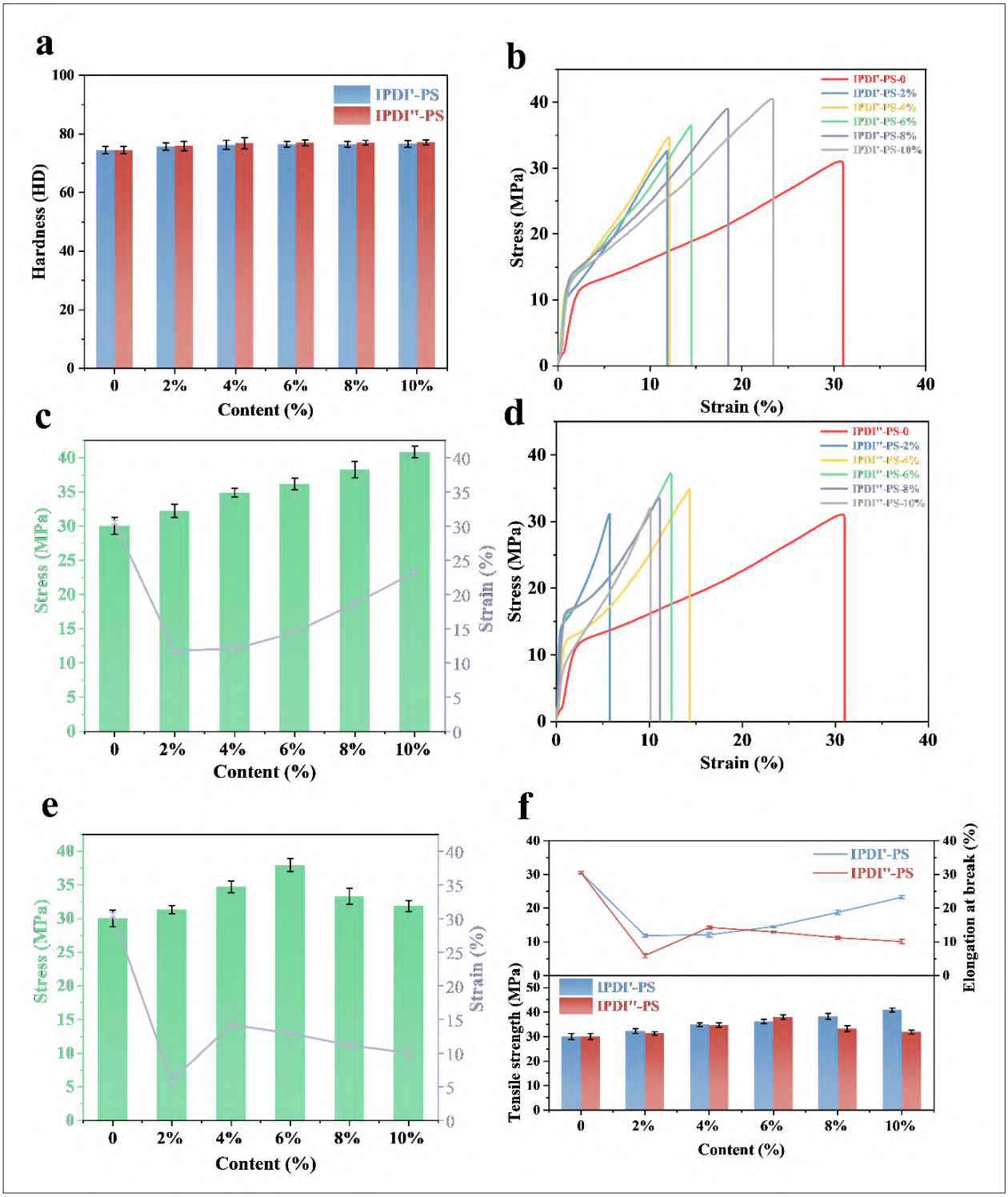


Figure 4. Effect of photosensitive additive content on the material's mechanical properties. (a) Hardness values of 3D-printed materials containing different loadings of IPDI'-PS or IPDI"-PS (n = 5). (b) Stress–strain curves of 3D-printed materials with different IPDI'-PS loadings. (c) Tensile strength and elongation at break of 3D-printed materials modified with IPDI'-PS at different loadings (n = 5). (d) Stress–strain curves of IPDI"-PS-modified 3D-printed materials at varying additive concentrations. (e) Tensile strength versus elongation at break for 3D-printed materials containing IPDI"-PS at different loadings (n = 5). (f) Comparative tensile strength and elongation at break of 3D-printed resin systems incorporating IPDI'-PS or IPDI"-PS at different loadings (n = 5). Abbreviations: IPDI'-PS, 3D printed photosensitive resins of monopyridine salt photosensitive additive; IPDI"-PS, 3D printed photosensitive resins of bipyridine salt photosensitive additive.

efficacy of photosensitizing additives containing pyridinium functional monomers against *S. aureus* and *E. coli* using the colony counting method. The study aimed to assess the enhancement effect on their antibacterial properties of 3D printing materials. The proposed antibacterial mechanism of pyridinium-containing groups is presented in Figure 5a. The results demonstrated that incorporating IPDI'-PS significantly enhanced the antibacterial activity of the resin (Figure 5b). Remarkably, 3D-printed samples containing only 2 wt% IPDI'-PS exhibited pronounced antibacterial effects against both common pathogens. Furthermore, antibacterial efficacy was continuously enhanced with increasing IPDI'-PS loading. Against *S. aureus*, a bactericidal rate of 99% was achieved at a 10 wt% loading. This effect was even more pronounced against *E. coli*, where a bactericidal rate as

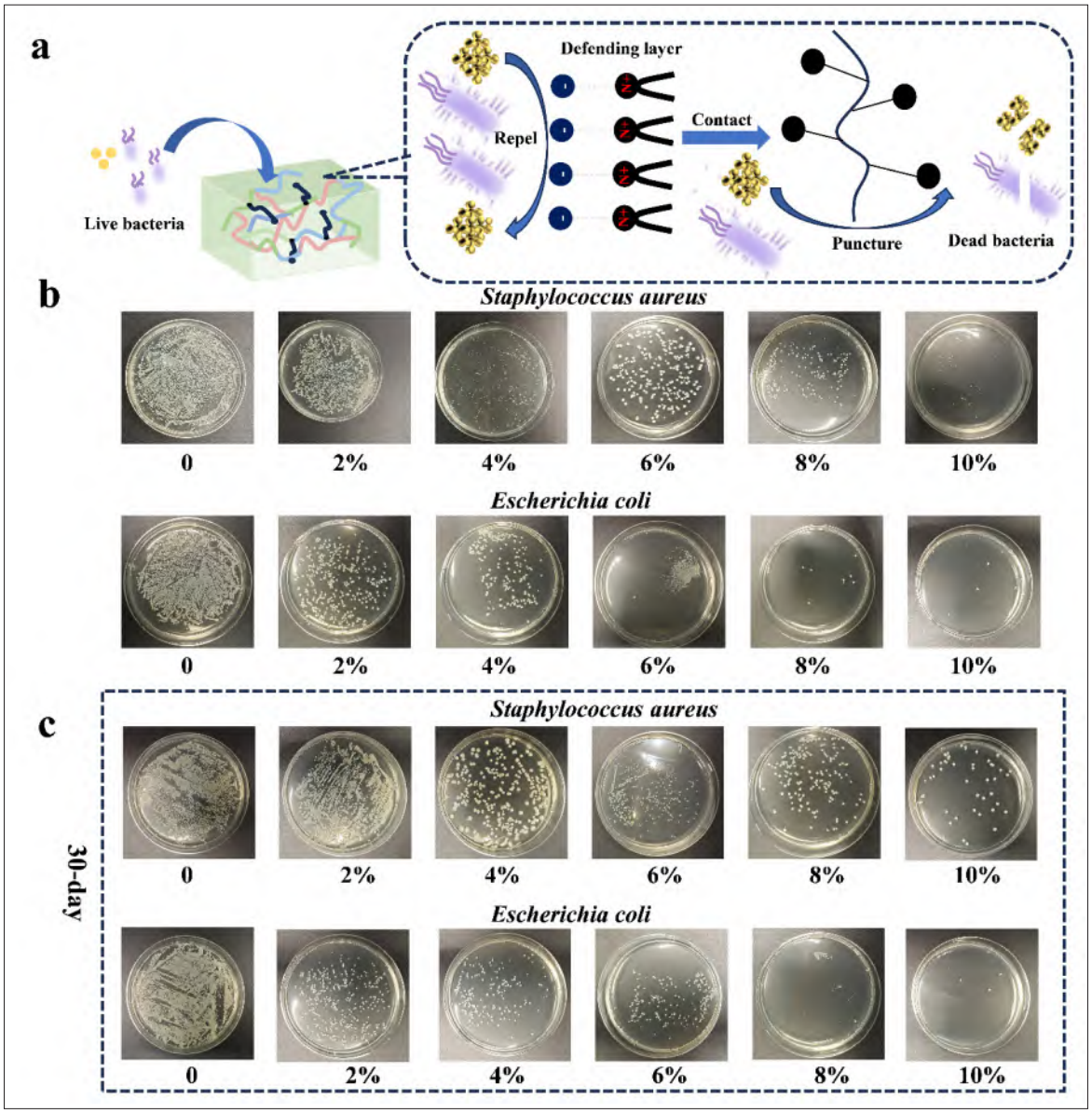


Figure 5. Antibacterial mechanism and evaluation of 3D printed materials. (a) Schematic of the contact-killing antibacterial mechanism of pyridinium-containing photosensitive resin. (b) Antibacterial efficacy of IPDI'-PS-modified 3D-printed materials against *Staphylococcus aureus* and *Escherichia coli* with different additive (IPDI'-PS) loadings. (c) Sustained antibacterial performance against *S. aureus* and *E. coli* after 30-day light-proof storage of IPDI'-PS-modified 3D-printed materials at various concentrations. Abbreviations: IPDI'-PS, 3D printed photosensitive resins of monopyridine salt photosensitive additive.

high as 99.99% was attained with only 8 wt% loading. To assess the durability of the antibacterial performance, the samples were stored under light-proof sealed conditions for 30 days and re-tested (Figure 5c). The results revealed no significant changes in the bactericidal rate in any group. Crucially, samples containing 10 wt% IPDI'-PS maintained a 99% bactericidal rate against *S. aureus*, whereas those with 8 wt% IPDI'-PS retained a high bactericidal rate of 99.99% against *E. coli*, presenting a negligible deviation from the initial values (Figure 6c and d). This confirms the excellent stability and long-term persistence of the synthesized pyridinium-containing molecules within the material matrix, indicating a low susceptibility to deactivation.

Similarly, the photosensitive resin composition containing dual-pyridinium IPDI"-PS demonstrated excellent antibacterial properties against *S. aureus* and *E. coli* (Figure 6a). At an ultralow IPDI"-PS loading of 2 wt%, the composition exhibited significant antibacterial activity, achieving bactericidal rates of 91% against *S. aureus* and 92% against *E. coli*. The antibacterial efficacy further increased continuously with higher IPDI"-PS loadings and plateaued at higher concentrations. For *S. aureus*, a bactericidal rate of 99% was attained at 10 wt% loading, with a diminished enhancement beyond approximately 6 wt%. Against *E. coli*, a bactericidal rate as high as 99.99% was achieved at 10 wt% loading. To evaluate durability, the samples were retested after 30 days of light-proof sealed storage (Figure 6b). The results confirmed that the IPDI"-PS system maintained high antibacterial efficacy; at 2 wt% loading, substantial activity against *S. aureus* persisted, whereas at 10 wt% loading, the bactericidal rates remained consistently high at 99% for *S. aureus* and 99.99% for *E. coli* (Figure 6e and f). Comparative analysis revealed that the IPDI"-PS system significantly outperformed the IPDI'-PS system against both the tested bacteria at equivalent loadings, particularly in the low-loading regime, with a more pronounced antibacterial advantage against *E. coli*. This validates the superiority of pyridinium-containing photosensitizing additives for enhancing the antibacterial performance of 3D printing materials.

3.6. Antistatic properties

Photosensitive resin-based 3D printing materials are susceptible to static charge accumulation during use, leading to printing defects, reduced material lifespan, and safety hazards.[36–38] Therefore, it is crucial to impart efficient and long-lasting antistatic properties to these materials. Pyridinium-based ionic antistatic agents have been extensively researched for their effectiveness, with their performance closely tied to molecular structural features.[39–41] The material's ability to conduct or dissipate charge is directly characterized by surface resistivity (Figure 7a).[42,43] Low resistivity (typically $\leq 10^{11}$ Ω) facilitates rapid charge migration, preventing electrostatic accumulation and providing antistatic properties. In contrast, high resistivity ($\geq 10^{12}$ Ω) encourages charge buildup, increasing electrostatic risks.[44] Therefore, this study systematically assessed the influence of photosensitive compositions containing pyridinium functional monomers with varying group counts on the antistatic performance of 3D-printed materials through surface resistivity measurements. As displayed in Figure 7b and c, the unmodified resin (devoid of pyridinium-based acrylate photosensitizing additives) demonstrated resistivity > 10^{12} Ω, indicating insulating behavior. The addition of any pyridinium-containing photosensitizing additive notably decreased the resistivity, with the reduction magnitude escalating with loading. Moreover, after both systems underwent light-proof storage for 14 and 60 days, followed by resistivity re-measurement, only gradual increases in resistivity were observed. Both systems exhibited consistent antistatic performance over time, affirming their exceptional persistence and low susceptibility to migration or leaching of the synthesized pyridinium-containing molecules.

A significant difference was observed between the following two systems: The IPDI"-PS composition exhibited superior efficiency. The IPDI'-PS system needed an 8 wt% loading to reduce resistivity to 10^{10} Ω (indicating effective antistatic performance), while the IPDI"-PS system achieved resistivity as low as 10^{9} Ω with just a 4 wt% loading—well within the effective electrostatic dissipation range (10^{6}–10^{9} Ω). This performance advantage is attributed to the two PS cationic (N^{+}) groups in the IPDI"-PS structure, which result in a higher charge carrier concentration, thus more effectively facilitating charge migration and dissipation.

4. Conclusion

In this study, we synthesized acrylate photosensitive additives containing either monopyridinium salt groups (IPDI'-PS) or bispyridinium salt groups (IPDI"-PS) using IPDI as the starting material. The synthesis involved chain extension through a reaction with a polyol, followed by HEMA functionalization and subsequent quaternization with 4-AP. These additives were then integrated into a photosensitive resin matrix at 0–10 wt%. The specimens were fabricated using DLP 3D printing. The study aimed to investigate the effects of the number of pyridinium salt groups and additive loading on the thermal and mechanical properties, curing shrinkage, antibacterial activity, and antistatic performance of 3D-printed materials.

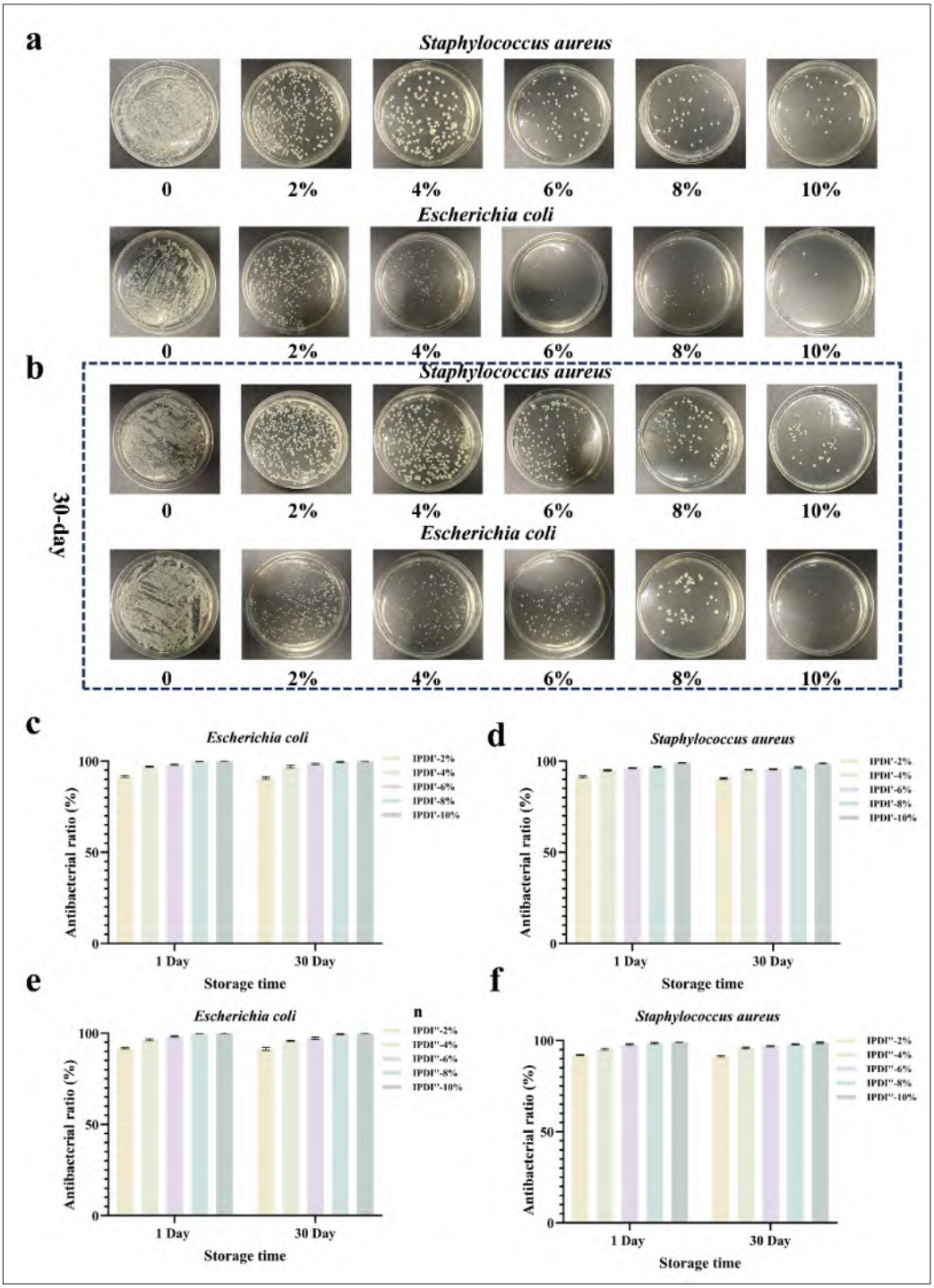


Figure 6. Antibacterial performance testing for 3D printed materials. (a) Antibacterial efficacy of IPDI"-PS-modified 3D-printed materials against *Staphylococcus aureus* and *Escherichia coli* at different additive (IPDI"-PS) loadings. (b) Retained antibacterial performance against *S. aureus* and *E. coli* after 30 days of light-proof storage at varying concentrations of IPDI"-PS-modified 3D-printed materials. (c) Time-dependent antibacterial efficiency against *E. coli* during extended storage of IPDI'-PS-modified 3D-printed materials at different additive (IPDI'-PS) loadings (n = 5). (d) Antibacterial efficiency against *S. aureus* as a function of storage duration for IPDI'-PS-modified 3D-printed materials at varying additive (IPDI'-PS) concentrations (n = 5). (e) Changes in antibacterial activity against *E. coli* over storage time for IPDI"-PS-modified 3D-printed materials at different loadings (n = 5). (f) Storage-time dependence of antibacterial efficacy against *S. aureus* for IPDI"-PS 3D-printed materials at various concentrations (n = 5). Abbreviations: IPDI'-PS, 3D printed photosensitive resins with different contents of monopyridine salt photosensitive additives; IPDI"-PS, 3D printed photosensitive resins with different contents of bipyridine salt photosensitive additives.

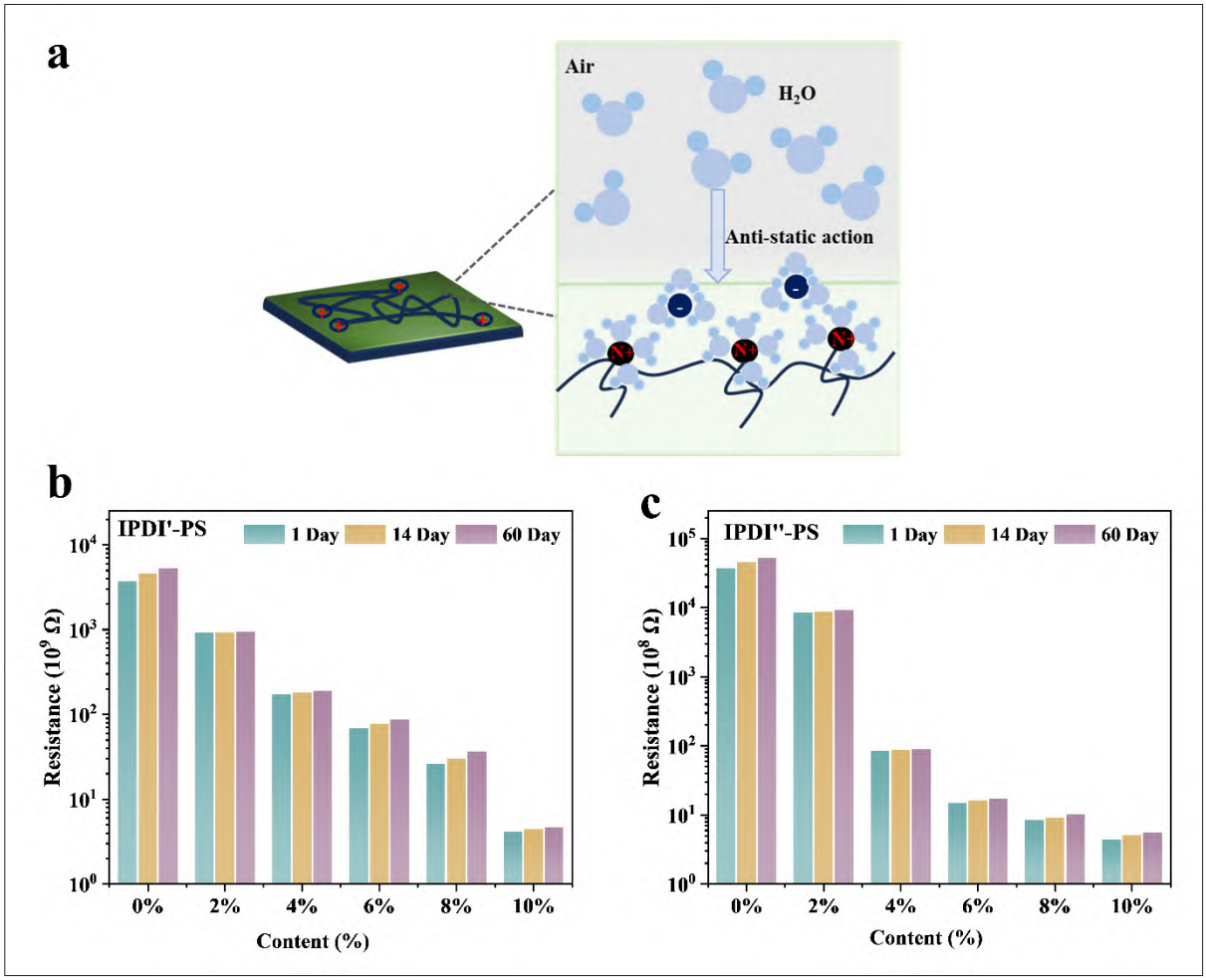


Figure 7. Antistatic mechanism and performance testing of 3D printed materials. (a) Antistatic mechanism of photosensitive resin containing pyridinium salt groups. (b) Resistivity changes in 3D-printed materials with IPDI'-PS at various concentration levels after different storage periods. (c) Resistivity changes in 3D-printed materials with IPDI"-PS at different concentration levels after various storage durations. Abbreviations: IPDI'-PS, 3D printed photosensitive resins of monopyridine salt photosensitive additive; IPDI"-PS, 3D printed photosensitive resins of bipyridine salt photosensitive additive.

The experimental results indicated that the cured materials containing IPDI'-PS within the photosensitive resin demonstrated superior mechanical strength and thermal stability. In contrast, the materials incorporating IPDI"-PS exhibited high antibacterial efficacy, excellent antistatic performance, and low curing shrinkage.

In the IPDI'-PS system, the best combination for overall performance was attained at a 10 wt% additive loading, resulting in a tensile strength of 40.86 MPa (a 36.0% increase compared to the control), a 30.6% increase in elongation at break, and a T_D5 of 168°C.

In the IPDI"-PS system, the ideal composition for overall performance was 4 wt% additive loading, leading to an HDT of 44.6 °C. The volume resistivity decreased to 10^9 Ω, entering the effective antistatic range, with a curing shrinkage as low as 6.05%. Additionally, it exhibited a 99.99% bactericidal rate against *E. coli*.

Compared to the unmodified resin, the IPDI"-PS system, with bis-pyridinium salt groups, exhibited significantly enhanced functional efficiency. It achieved over 91% antibacterial efficacy at a low loading (2 wt%), while the IPDI'-PS system needed 8 wt% for similar efficacy. Furthermore, the IPDI"-PS system required only half the additive loading (50% reduction) for equivalent antistatic performance. The inclusion of pyridinium salt-based acrylate photosensitive additives provided long-term stability to these materials. After 30 days of dark storage, the antibacterial rate remained above 99%, and the resistivity stayed within the original order of magnitude. These enduring antistatic and antibacterial

properties highlight the material's potential, enabling the development of efficient 3D printing resins with a single low-loading additive, offering high mechanical strength and durable antibacterial/antistatic functionality. However, while pyridinium salt-based acrylate photosensitive additives effectively enhance the strength and functionality (e.g., antibacterial/antistatic properties) of 3D-printed photopolymer resins, their low solubility in the resin system raises viscosity, affecting printing reliability and resolution. Furthermore, their poor biocompatibility limits their use in non-implantable scenarios.

Acknowledgments

The authors are grateful to the Key Laboratory of Organosilicon Chemistry and Materials Technology, Ministry of Education, for providing analytical instrument support and Eceshi (www.eceshi.com) for conducting the tests related to liquid photosensitive resin.

Funding

This work was financially supported by Hangzhou Normal University (grant nos. 114095F49123259 and 4095F49123037).

Conflict of interest

The authors declare no conflict of interest.

Author contributions

Conceptualization: Xiaomin Zhang, Guoqiao Lai, Qiu Chen
Formal analysis: Qiaoling Zhang, Zhiwei Zhang, Taojun Lin
Investigation: Qiaoling Zhang, Tongyi Wu, Xiangqin Ding, Rong Li
Methodology: Qiaoling Zhang, Tongyi Wu, Jianqing Liang, Taojun Lin
Visualization: Qiaoling Zhang, Tongyi Wu, Taojun Lin, Xiangqin Ding
Writing–original draft: Qiaoling Zhang, Tongyi Wu, Xiangqin Ding
Writing–review & editing: Xiaomin Zhang, Guoqiao Lai, Qiu Chen

Ethics approval and consent to participate

Not applicable.

Consent for publication

Not applicable.

Availability of data

Experimental data and details of the materials used in the study can be obtained from the corresponding authors upon request.

References

1. Stevens LM, Almada NT, Kim HS, Page ZA. Visible-light-fueled polymerizations for 3D printing. *Accounts Chem Res*. 2025;58(2):250-260.
doi: 10.1021/acs.accounts.4c00680

2. Wu T, Ding X, Yuan K, Liu T, Lai G, Chen Q. Synthesis and characterization of silicon-modified polyurethane acrylate for UV-thermal dual curing in three dimensional printing. *ACS Appl Polym Mater*. 2024;6(14):8585-8597.
doi: 10.1021/acsapm.4c01581

3. Quan H, Zhang T, Xu H, Luo S, Nie J, Zhu X. Photo-curing 3D printing technique and its challenges. *Bioact Mater*. 2020;5(1):110-115.
doi: 10.1016/j.bioactmat.2019.12.003

4. Gao W, Guo Y, Cui J, *et al*. Dual-curing polymer systems for photo-curing 3D printing. *Addit Manuf*. 2024;85:104142.
doi: 10.1016/j.addma.2024.104142

5. Zheng M-Y, Jin Z-B, Ma Z-Z, Gu Z-G, Zhang J. Photo-curable 3D printing of circularly polarized afterglow metal–organic framework monoliths. *Adv Mater*. 2024;36(25):2313749.
doi: 10.1002/adma.202313749

6. He C-F, Sun Y, Liu N, Yu K, Qian Y, He Y. Formation theory and printability of photocurable hydrogel for 3D bioprinting. *Adv Funct Mater*. 2023;33(29):2301209.
doi: 10.1002/adfm.202301209

7. Wu T, Zhang Q, Zhang Z, *et al*. Multiple hydrogen bonded 3D-printed elastomers with enhanced toughening by photothermal dual curing for customizable biomimetic flexible grippers. *Adv Funct Mater*. 2025;e10489.
doi: 10.1002/adfm.202510489

8. Mu X, Bertron T, Dunn C, *et al*. Porous polymeric materials by 3D printing of photocurable resin. *Mater Horiz*. 2017;4(3):442-449.
doi: 10.1039/C7MH00084G

9. Sun X, Chen S, Qu B, *et al*. Light-oriented 3D printing of liquid crystal/photocurable resins and in-situ enhancement of mechanical performance. *Nat Commun*. 2023; 14(1):6586.
doi: 10.1038/s41467-023-42369-1

10. You J-L, Liu IT, Chen Y-H, Balaji R, Tung S-H, Liao Y-C. Adamantane-based low-dielectric-constant photocurable resin for 3D printing electronics. *Addit Manuf*. 2024;82:104047.

doi: 10.1016/j.addma.2024.104047

11. Zhang T, Chen D, Zhang N, *et al*. Self-assembled supramolecular nanofibers integrate pH-responsive drug delivery and antimicrobial for combined cancer therapy. *Chinese Chem Lett*. 2025;111117. doi: 10.1016/j.cclet.2025.111117
12. Zhong G, Deng S, Hong Y, *et al*. AIE-active antibacterial photosensitizer disrupting bacterial structure: multicenter validation against drug-resistant pathogens. *Small Methods*. 2025;9(5):2401663. doi: 10.1002/smtd.202401663
13. Zhu Y, Qin L, Yang M, *et al*. Dual-functional benzotrithiophene-based covalent organic frameworks for photocatalytic detoxification of mustard gas simulants and antibacterial defense. *Small*. 2025;21(12):2412118. doi: 10.1002/smll.202412118
14. Tang X, Yan G, Wang J, *et al*. Self-assembly and antistatic property of ionic liquid crystalline polymers. *Polym Adv Technol*. 2022;33(5):1628-1641. doi: 10.1002/pat.5626
15. Zhuang Y, Tang X, Chang X, *et al*. Self-assembly and antistatic property of poly(styrene sulfonic acid)-based graphene oxide liquid crystal compounds. *Liquid Crystals*. 2022;49(5):731-741. doi: 10.1080/02678292.2021.2006810
16. Ma Q, Buchon L, Magné V, *et al*. Charge transfer complexes (CTCs) with pyridinium salts: toward efficient dual photochemical/thermal initiators and 3D printing applications. *Macromol Rapid Commun*. 2022;43(19):2200314. doi: 10.1002/marc.202200314
17. Goldbach E, Allonas X, Halbardier L, Ley C, Croutxé-Barghorn C. Use of pyridine derivatives as inhibitor/retarding agent for photoinduced cationic polymerization of epoxides. *React Funct Polym*. 2024;200:105922. doi: 10.1016/j.reactfunctpolym.2024.105922
18. Zhou Q, Chen S, Guo X, Zhou C, Jin M. New water-soluble coumarin-ketone-pyridium salts photoinitiators for antibacterial coatings under visible LED photocuring. *Eur Polym J*. 2025;230:113896. doi: 10.1016/j.eurpolymj.2025.113896
19. Wu T, Zhang Q, Xie Z, *et al*. High dispersibility Organosilicon@ZnO-NPs prepared by spray sedimentation method: similar chain extender enhances the strength, antimicrobial, and UV shielding of 3D printing composite materials. *Compos Part B Eng*. 2025;295:112196. doi: 10.1016/j.compositesb.2025.112196
20. Jarach N, Cohen M, Gitt R, Dodiuk H, Kenig S, Magdassi S. Untying the knot: a fully recyclable, solvent-free, wide-spectral photocurable thermoset adhesive. *Adv Mater*. 2025;37:e2502040. doi: 10.1002/adma.202502040
21. Lv Y, Xu Y, Zhang S, *et al*. Rapidly photocurable and strongly adhesive hydrogel-based sealant with good procoagulant activity for lethal hemorrhage control. *Adv Funct Mater*. 2025;e2501904. doi: 10.1002/adfm.202501904
22. Hu P, Xu H, Pan Y, Sang X, Liu R. Upconversion particle-assisted NIR polymerization enables microdomain gradient photopolymerization at inter-particulate length scale. *Nat Commun*. 2023;14(1):3653. doi: 10.1038/s41467-023-39440-2
23. Chen Q, Liu Y, Peng X, *et al*. A novel photosensitive poly(amic acid) for reducing film thickness shrinkage after curing. *Mater Today Commun*. 2025;47:113210. doi: 10.1016/j.mtcomm.2025.113210
24. Ding A, Zhang P, Zhou B, *et al*. Structural design and performance study of a biobased UV/moisture dual-curing coating for UV inadequate curing conditions. *Mater Today Commun*. 2025;44:111863. doi: 10.1016/j.mtcomm.2025.111863
25. Sun G, Wu X, Liu R. A comprehensive investigation of acrylates photopolymerization shrinkage stress from micro and macro perspectives by real time MIR-photo-rheology. *Prog Org Coat*. 2021;155:106229. doi: 10.1016/j.porgcoat.2021.106229
26. Wang J, Li J, Wang X, *et al*. Synthesis and properties of UV-curable polyester acrylate resins from biodegradable poly(l-lactide) and poly(ε-caprolactone). *React Funct Polym*. 2020;155:104695. doi: 10.1016/j.reactfunctpolym.2020.104695
27. Xiao N, Zhang Y, Gao Y, Hu D, Sun F. A dual-functional α-diketone-based disulfide monomer for visible LED photopolymerization: mitigating volumetric shrinkage and triggering polymerization. *Eur Polym J*. 2024;217:113341. doi: 10.1016/j.eurpolymj.2024.113341
28. Zhu G, Liu M, Kou Z, *et al*. Universal approach for developing reprocessable and reprintable plant oil-based resins for digital light processing 3D printing. *Chem Eng J*. 2023;475:146080. doi: 10.1016/j.cej.2023.146080
29. Alhajj M, Liau LS, Al-Fakih AM. Polymer electrolytes for sustainable energy: a minireview on zero-carbon storage and conversion. *ACS Appl Polym Mater*. 2025;7(6):3442-3465. doi: 10.1021/acsapm.4c03958
30. Wang W, Li X, Gao L, *et al*. Thermal cross-linking hole-transport self-assembled monolayers for perovskite solar cells. *ACS Energy Lett*. 2025;10(5):2250-2258.

doi: 10.1021/acsenergylett.5c00457

31. Jamal M, Benkaddour A, Pal L, *et al*. Multi-scale assembly and structure-process-property relationships in nanocellulosic materials. *Prog Mater Sci*. 2025;151:101430. doi: 10.1016/j.pmatsci.2025.101430

32. Richbourg NR, Peppas NA. The swollen polymer network hypothesis: quantitative models of hydrogel swelling, stiffness, and solute transport. *Prog Polym Sci*. 2020;105:101243. doi: 10.1016/j.progpolymsci.2020.101243

33. Huang Y-W, Torkelson JM. Catalyst-free polyhydroxyurethane covalent adaptable networks exhibiting full cross-link density recovery after reprocessing: facilitation by synthesis with well-designed secondary amines. *Macromolecules*. 2025;58(10):5356-5367. doi: 10.1021/acs.macromol.5c00280

34. Mao H-I, Chen Y-Z, Chu R-J, *et al*. Recyclable thermoset-like polyurethanes from renewable epoxidized soybean oil via dynamic ester bond exchange. *J Polym Sci*. 2025;63(11):2379-2390. doi: 10.1002/pol.20250378

35. Zhang Z, Liu G, Wu J, *et al*. High-strength dual-network hydrogels with chain-growth enhancement for multifunctional flexible sensors, triboelectric nanogenerators, and EMI shielding. *Chem Eng J*. 2025;519:165710. doi: 10.1016/j.cej.2025.165710

36. Sun Q, Xu B, Du J, *et al*. Interfacial electrostatic charges promoted chemistry: reactions and mechanisms. *Adv Colloid Interface Sci*. 2025;339:103436. doi: 10.1016/j.cis.2025.103436

37. Koochak P, Lin M, Afzalifar A, *et al*. Self-accelerating drops on silicone-based super liquid-repellent surfaces. *ACS Nano*. 2025;19(25):23105-23119. doi: 10.1021/acsnano.5c04250

38. Nie J, Sun B, Jiao T, *et al*. Biodegradable air filter with electrospun composite nanofibers and cellulose fibers dual network: enhanced electrostatic adsorption, humidity resistance, and extended service life. *J Hazard Mater*. 2025;489:137557. doi: 10.1016/j.jhazmat.2025.137557

39. Sun N, Yi C, Xu C, *et al*. Fabrication of permanent antistatic PMMA copolymer for enhanced antistatic and mechanical properties. *ACS Appl Polym Mater*. 2023;5(7):5537-5543. doi: 10.1021/acsapm.3c00833

40. Ren J, Zheng L, Wang Y, *et al*. Synthesis and characterization of quaternary ammonium based ionic liquids and its antistatic applications for diesel. *Colloids Surf A Physicochem Eng Asp*. 2018;556:239-247. doi: 10.1016/j.colsurfa.2018.08.038

41. Tsurumaki A, Iwata T, Tokuda M, *et al*. Polymerized ionic liquids as durable antistatic agents for polyether-based polyurethanes. *Electrochim Acta*. 2019;308:115-120. doi: 10.1016/j.electacta.2019.04.031

42. Bera M, De B, Gupta KBNVSG, *et al*. A critical review on recent progress in anti-static fiber-reinforced polymer (FRP) composites. *Polym Compos*. 2025;e70078. doi: 10.1002/pc.70078

43. Yousefi E, Dolati A, Najafkhani H. Preparation of robust antistatic waterborne polyurethane coating. *Prog Org Coat*. 2020;139:105450. doi: 10.1016/j.porgcoat.2019.105450

44. Huang Z, Yin L, Hu C, *et al*. Low contact resistivity and long-term thermal stability of Nb0.8Ti0.2FeSb/Ti thermoelectric junction. *J Mater Sci Technol*. 2020;40:113-118. doi: 10.1016/j.jmst.2019.08.046

ACCSCIENCE PUBLISHING

International Journal of Bioprinting

RESEARCH ARTICLE

Dual-nozzle 3D-printed calcium sulfate/polylactic acid scaffold incorporating linezolid microspheres for effective repair of femoral condyle defects in rats

Xiaojie Tang[1,2†], Chenxu Li[1†], Yanan Wang[3†], Hai Huang[2], Tongshuai Xu[2], Shannan Cao[2], Changlin Lv[1], Xiaofan Du[1], Shuqing Chen[1], Wenkang Yang[1], Jiale Shao[1], Yukun Du[1*], and Yongming Xi[1*]

[1]Department of Orthopaedic Surgery, Affiliated Hospital of Qingdao University, Qingdao, Shandong, China

[2]Yantai Affiliated Hospital of Binzhou Medical University, Yantai, Shandong, China

[3]Department of Nuclear Medicine, Xuzhou Central Hospital, Xuzhou, Jiangsu, China

[†]These authors contributed equally to this work.

***Corresponding authors:**
Yongming Xi
(xym700118@163.com)

Yukun Du
(qdfydyk0728@163.com)

Citation: Tang X, Li C, Wang Y, *et al*. Dual-nozzle 3D-printed calcium sulfate/polylactic acid scaffold incorporating linezolid microspheres for effective repair of femoral condyle defects in rats. *Int J Bioprint*. 2025;11(5):333-349. doi: 10.36922/IJB025270069

Received: July 4, 2025
1st revised: August 4, 2025
2nd revised: August 18, 2025
Accepted: August 25, 2025
Published online: August 27, 2025

Copyright: © 2025 Author(s). This is an Open Access article distributed under the terms of the Creative Commons Attribution License, permitting distribution, and reproduction in any medium, provided the original work is properly cited.

Publisher's Note: AccScience Publishing remains neutral with regard to jurisdictional claims in published maps and institutional affiliations.

Abstract

Large, complex bone defects pose a significant clinical challenge. Conventional bone grafting approaches cannot simultaneously achieve tissue regeneration and infection prevention, resulting in impaired healing outcomes and prolonged treatment cycles. Existing therapeutic strategies lack integrated solutions capable of concurrently providing infection prevention and osteogenesis promotion within a single platform. This study developed a novel multifunctional composite scaffold using dual-nozzle three-dimensional printing technology to simultaneously achieve infection prevention and accelerated bone regeneration. Linezolid-loaded polylactic-co-glycolic acid microspheres (LMS) were uniformly dispersed within the pores of calcium sulfate/polylactic acid (CS/PLA) scaffolds to successfully construct the composite scaffold. *In vitro* characterization revealed uniform distribution of microspheres within the scaffold pores, with the fabricated CS/PLA-LMS demonstrating excellent biocompatibility and mechanical properties, achieving an elastic modulus of 87 MPa. Furthermore, the composite scaffold effectively inhibited *Staphylococcus aureus* activity *in vitro*. *In vivo* rat femoral condyle defect model revealed that the composite scaffold significantly enhanced bone formation compared to blank controls. Additionally, bone volume fraction increased by 3.2 times, and trabecular spacing decreased by 50%, with mechanistic analysis indicating activation of the phosphoinositide 3-kinase-protein kinase B signaling pathway. The integrated design successfully prevented infection-related complications while promoting robust osteogenesis, offering a clinically relevant solution for treating complex bone defects where infection prevention and regenerative capacity are primary therapeutic concerns.

Keywords: Bone defect repair, Dual-nozzle three-dimensional printing, Calcium sulfate, Linezolid microspheres

1. Introduction

Bone defect refers to the loss or damage of bone tissue caused by trauma, infection, tumor resection, or other etiologies, representing a common clinical issue in orthopedics.[1] The repair and regeneration of bone defects constitute a complex biological process. Although bone tissue possesses intrinsic self-healing capacity, this natural mechanism often proves insufficient in cases of extensive or critical-sized defects, necessitating the use of bone grafts to facilitate regeneration.[2,3] Over two million bone grafting procedures are performed globally each year, making it the second most common type of tissue transplantation after blood transfusion.[4,5] While autologous and allogeneic bone grafts are considered the gold standard for bone defect repair,[4–6] these materials have certain limitations.[7] Autologous bone grafts yield good results but may cause complications, pain, increased blood loss, and limited availability of graft material.[8,9] Allogeneic bone grafts avoid issues related to the donor site but may face challenges such as immune rejection or poor biocompatibility.[10–12] Furthermore, infection poses a significant challenge in the treatment of bone defects.[13] Bacteria can proliferate at the defect site, releasing toxins and inflammatory mediators that damage bone tissue and blood vessels, hindering regeneration.[5,10] Infected bone defects are also prone to a range of complications, including chronic osteomyelitis, bone necrosis, and arthritis.[14] These complications not only complicate treatment but may also lead to permanent functional impairment and disability. Therefore, effectively preventing and controlling infection to accelerate the repair of bone defects is crucial in clinical practice.[15,16]

Emerging materials and technologies for bone defect repair exhibit significant developmental potential.[17] Three-dimensional (3D) printing technology utilizes bioinks and customized implants to create complex, personalized bone substitutes.[18–20] Among these, fused deposition modeling is the most common technique, enabling precise control over the internal porosity, pore size, and interconnected structure of biomaterials.[21] Polylactic acid (PLA), a medical polymer synthesized from lactic acid, features a stable chemical structure, excellent plasticity, and mechanical properties.[22] Additionally, PLA can undergo controlled degradation without producing toxic byproducts.[23,24] The United States Food and Drug Administration approved its biomedical applications in the 1970s, and it remains widely used in this field.[25] Calcium sulfate (CS), tricalcium phosphate, and hydroxyapatite are typical bone-filling materials.[26] Among them, CS is widely used clinically as a filling support material for compressive fractures due to its good tolerance, excellent absorbability, and dual role in inhibiting fibrous tissue proliferation while promoting bone regeneration.[27–29] Furthermore, polylactic-co-glycolic acid (PLGA) microspheres demonstrate numerous advantages in drug delivery for bone repair. Firstly, they enable efficient drug delivery, ensuring effective concentrations at the lesion site and significantly enhancing therapeutic outcomes. Secondly, PLGA microspheres can function as sustained-release systems, precisely controlling the drug release rate, prolonging the biological activity of the drug in the body, and reducing the frequency of administration.[30–32] Additionally, PLGA microspheres exhibit excellent biocompatibility and biodegradability.

The current study developed a 3D-printed CS/PLA composite scaffold incorporating linezolid (LN)-loaded microspheres (LMS), which combines the properties of infection prevention and bone defect repair. Initially, PLGA copolymer microspheres containing LN were prepared to achieve controlled and sustained drug release. Then, utilizing dual-nozzle 3D printing technology, a porous CS/PLA scaffold was created, which enabled consistent LMS integration within the scaffold pores. A comprehensive evaluation was conducted on the composite scaffold's structural morphology, mechanical properties, *in vitro* drug release profile, and antibacterial activity. Finally, transcriptomic analyses alongside *in vitro* and *in vivo* experiments demonstrated the scaffold's superior osteogenic capabilities, mediated via the phosphoinositide 3-kinase (PI3K)-protein kinase B (Akt) signaling pathway. This engineered bone material not only surpasses natural cancellous bone in mechanical performance but also demonstrates outstanding biocompatibility, minimizing the risk of immune rejection. Furthermore, incorporating LMS into the material enables sustained and stable drug release to surrounding tissues, effectively preventing and controlling infections, thus accelerating bone tissue regeneration and repair (Figure 1). The development of this multifunctional material provides a novel method and means to treat bone defects and prevent implant infection, potentially improving patients' speed of recovery and quality of life.

2. Materials and methods

2.1. Materials

Linezolid was purchased from Beijing Epson Technology Co., Ltd. (China). Phosphate-buffered saline (PBS), minimum essential medium alpha (α-MEM), trypsin-ethylenediaminetetraacetic acid solution, and cell counting kit-8 (CCK-8) were obtained from Gibco (America). Fetal

bovine serum (FBS) was sourced from Wisent (China). PLGA was acquired from Shanghai Yuanye Bio-Technology Co., Ltd., China, while polyvinyl alcohol was purchased from Acros Organics (Belgium). Dichloromethane (DCM) was purchased from Sinopharm Group (China), and PLA was purchased from Acmec Biochemical Co., Ltd. (China). Sodium alginate (SA) and CS were obtained from Aladdin Industrial Corporation (China).

2.2. Preparation of linezolid-loaded microspheres

This study employed the solvent evaporation method of double emulsion (W/O/W) to prepare drug microspheres. A certain amount of LN was dissolved in 1 mL of purified water to form the internal aqueous phase. A defined amount of PLGA was dissolved in 9 mL of DCM, and 200 μL of 1% Tween-80 was added and mixed to form the oil phase. The internal aqueous phase was then added dropwise into the oil phase, followed by emulsification using an ultrasonic cell disruptor (Ningbo Scientz Biotechnology Co., Ltd, China) under an ice bath for 10 min (200 W, 7 s on/3 s off), resulting in a stable milky primary emulsion. This primary emulsion was then slowly and evenly introduced into 40 mL of polyvinyl alcohol solution (external aqueous phase) under continuous stirring for 4 h to allow complete evaporation of DCM. The resulting double emulsion was left to stand for an hour until the microspheres had fully precipitated. The microspheres were then transferred to centrifuge tubes, washed twice with distilled water, and centrifuged twice. After pre-freezing at −80°C for 4 h, the microspheres were freeze-dried under vacuum for 12 h to obtain the final LMS.[33]

2.3. Characterization of linezolid-loaded microspheres

The Marvel 3000 particle size analyzer from Malvern Instruments (United Kingdom) was used to measure the microspheres' particle sizes. Moreover, a scanning electron microscope (EVO/LS15, Carl Zeiss, Germany) was used to examine the micro-morphology of the microspheres.

2.4. Construction of linezolid standard curve

Using an electronic balance, 25 mg of LN was measured and dissolved in 50 mL of PBS buffer solution. This solution was transferred to a 50 mL volumetric flask to prepare a stock solution of 0.5 mg/mL LN. A dilution concentration of 200, 100, 50, 25, 12.5, 6.25, and 3.125 μg/mL was then obtained by diluting 4, 2, 1, 0.5, 0.25, 0.125, and 0.0625 mL of the stock solution with 10 mL of PBS. The optical density (OD) values at 280 nm for each concentration were measured using a ultraviolet spectrophotometer (Beijing Purkinje General Instrument Co., Ltd. China), and a standard curve of LN in PBS buffer was generated.

2.5. *In vitro* release test of linezolid-loaded microspheres

To evaluate the *in vitro* release profile of LN, 100 mg of LMS and 100 mg of standard LN were suspended in 50 mL of PBS and incubated in a constant-temperature shaker (Changzhou Runhua Electric Appliances Co., Ltd. China) at 37°C and 100 rpm. Each day, 4 mL of the solution was sampled for analysis, and an equal volume of fresh PBS was added to maintain consistent conditions. The absorbance at 280 nm was recorded using a spectrophotometer, and the mean values were employed to calculate the daily and cumulative drug release amounts, as well as the sustained release rate.

2.6. *In vitro* antibacterial test of linezolid-loaded microspheres

The model bacterium used in the antibacterial test was *Staphylococcus aureus* (*S. aureus* [ATCC 25923] courtesy from Binzhou Medical University Affiliated Yantai Hospital). The strain was inoculated into an appropriate volume of sterile liquid medium and cultured overnight at 37°C to prepare a bacterial suspension. The prepared suspension (1.54×10^8 CFU/mL) was spread onto sterile Muller–Hinton agar plates (Jinan Babio Biotechnology Co., Ltd., China). Prior to the antibacterial test, LMS was exposed to ultraviolet light for 10 min to ensure sterilization. LMS was then added to the medium and incubated at 37°C for 24 h. The diameter of the inhibition zone was measured and recorded to determine the degree of bacterial inhibition. In addition, we also tested the antibacterial activity of LMS at Days 3, 7, and 14.

2.7. Preparation of sodium alginate hydrogel carrier

A 2% SA hydrogel was selected as the carrier. Two grams of SA powder were weighed and dissolved in 100 mL of 1% dilute hydrochloric acid solution. The SA powder was stirred continuously at a uniform speed for 8 h until completely dissolved, resulting in a uniform gel-like solution. The SA hydrogel was then prepared.

2.8. Design and preparation of composite scaffolds

A computer-aided design software was used to design the printing model of the CS/PLA scaffold. A dual-nozzle 3D printer was employed to fabricate a scaffold structure with dimensions of $3.5 \times 2.5 \times 0.3$ cm^3, a line width of 300 μm, and a pore size of 500 μm, with adjacent layers printed at a 90° orientation. The mixing ratio of CS powder and PLA powder was based on previous studies, where the powders were blended at a mass ratio of 1:9 before being fed into the hot-melt nozzle.[33] The printing temperature was set between 110 and 130°C, with a printing speed of 12 mm/s. A total of 0.6 g of microspheres was dispersed in 10 mL of

1% SA hydrogel containing 400 μL of Tween-80. The resulting mixture was loaded into a room-temperature nozzle and printed at a speed of 12 mm/s. After printing, the scaffold was placed in a refrigerator (4°C) to dry for 8 h. The control group was printed using only the hot-melt nozzle without including drug-loaded microspheres. The printed scaffold was precisely cut using a 4 mm diameter specialized punch to prepare circular scaffolds with a diameter of 4 mm and a thickness of 3 mm for subsequent use.

2.9. Scanning electron microscopy and energy-dispersive X-ray spectroscopy characterization

The CS/PLA and CS/PLA-LMS scaffolds' overall look and microstructural features were analyzed through scanning electron microscopy (SEM). Elemental analysis of the CS/PLA and CS/PLA-LMS scaffolds was conducted using energy-dispersive X-ray spectroscopy (EDS; Carl Zeiss AG Merlin, Germany) to examine the distribution of elements within the scaffolds.

2.10. Determination of mechanical properties of stent

A universal testing machine (Instron, America) was used to conduct compression tests on three CS/PLA blank scaffolds and three drug-loaded CS/PLA composite scaffolds, with the compression speed set to 5 mm/min. The experimental data from each sample were analyzed to record the maximum stress strength, and stress–strain curves were plotted for both scaffold groups. The elastic modulus and compressive strength for each scaffold group were assessed by finding the slope of the secant line between two points in the 10%–20% strain range.

2.11. Preparation of two groups of scaffold material extracts

Scaffold materials from each group were sliced into 5 × 5 mm^2 squares and sterilized using hydrogen peroxide. The extraction medium, physiological saline, was added at a ratio of 6 cm^2/mL according to the surface area of the samples. To produce scaffold extracts, the scaffolds were incubated at 37°C for 24 h and then stored at 4°C for future use.

2.12. Cell culture

Bone marrow stromal cells (BMSCs) were extracted from 2-week-old Sprague–Dawley rats (n = 3). After cervical dislocation, the tibia and femur were isolated, with the ends of both bones trimmed. The bone marrow cavity was flushed with a syringe, and the suspension was homogenized and cultured in a medium containing 10% FBS, 100 U/mL penicillin, and 100 μg/mL streptomycin at 37°C with 5% carbon dioxide. The culture medium was refreshed every 2 days. BMSCs were utilized for subsequent experiments within five passages. To create the osteogenic differentiation medium, 10 mM glycerol phosphate, 50 μL ascorbic acid, and 100 nM dexamethasone were added to the α-MEM culture medium.

2.13. *In vitro* cytotoxicity and cell proliferation assays of the two groups of scaffold materials

The cytotoxicity and cell proliferation of the scaffold materials were assessed using fluorescein isothiocyanate-phalloidin staining and the CCK-8 assay. An initial density of 25,000 BMSCs per well was seeded in a 24-well plate and incubated overnight at 37°C. The supernatant was then removed, and osteogenic induction medium, with or without 50% extract, was added to the wells. Once the cell confluence reached 70–80%, the cells were washed twice with PBS for 10 min each. They were then fixed with 4% paraformaldehyde for 20 min and washed twice with PBS. Fluorescein isothiocyanate-phalloidin at 5 μg/mL was added for staining at room temperature for 30–60 min, followed by two PBS washes. 4',6-diamidino-2-phenylindole was used to stain the nuclei for 10 min, and the cells were washed twice with PBS again. Excess moisture was removed, and a fluorescence mounting medium was added for observation under a confocal microscope (Leica, America).

After being initially planted at a density of 5000 cells per well in a 96-well plate, the BMSCs were incubated overnight at 37°C. The supernatant was then removed, and osteogenic induction medium, with or without 50% extract, was added to the plate for incubation at 24, 48, and 72 h. After incubation, the supernatant was replaced with 100 μL of serum-free medium containing 10% CCK-8 reagent. Following a 2-h incubation at 37°C, the OD values of each group were measured using a microplate reader, and a bar graph was plotted based on the OD values. Cell viability (%) can be calculated with the formula in **Equation (I)**:

$$\text{Cell viability (\%)} = \frac{OD(\textit{experimental group}) - OD(\textit{blank group})}{OD(\textit{negative control group}) - OD(\textit{blank group})} \times 100\% \quad \text{(I)}$$

2.14. Evaluation of the *in vitro* antibacterial properties of the two scaffold material groups

Using a pre-prepared bacterial suspension (1.54 × 10^8 CFU/mL), bacteria were spread onto sterile Muller–Hinton agar plates. Prior to the antimicrobial test, both groups of scaffolds were exposed to ultraviolet light for 10 min to complete the sterilization process. The scaffolds

were then placed in the medium and incubated at 37°C for 24 h. The extent of bacterial inhibition was determined by measuring and recording the diameter of the inhibition zones. In addition, we also tested the antibacterial activity of CS/PLA-LMS at Days 3, 7, and 14.

2.15. *In vitro* osteogenic potential of the two groups of scaffolds

The influence of scaffolds on the osteogenic differentiation potential of BMSCs was measured with an alkaline phosphatase (ALP) staining kit (P0321S, Beyotime, China). In a 12-well plate, BMSCs were seeded, divided into the blank group, CS/PLA group, and CS/PLA-LMS group, at a density of 1×10^5 cells per well. Following cell adhesion, particular treatments were given to each group, and they were maintained in osteogenic induction medium for 7 days. ALP staining was then performed using the kit, with p-nitrophenyl phosphate serving as the substrate to assess ALP activity in the samples. ALP activity was quantified by assessing the absorbance at 405 nm using the ALP assay kit.

To evaluate the impact of scaffolds on the degree of mineralization of BMSCs, the extracted BMSCs were seeded at a density of 1×10^5 cells per well onto a 12-well plate under the same grouping (blank, CS/PLA, and CS/PLA-LMS). Following cell adhesion, the cells received the designated treatments before being cultivated for 21 days in osteogenic induction medium. Subsequently, the cells were rinsed twice with PBS, fixed with 4% paraformaldehyde for 15 min, and then washed three times with PBS again. They were then stained with Alizarin Red solution (Cyagen Biosciences, China) for 30 min at room temperature. The mineralization level of BMSCs was quantitatively assessed by dissolving the bound Alizarin Red in a 10% cetylpyridinium chloride (Sigma-Aldrich, USA) solution for an hour. The OD of the resulting solution was then measured at 570 nm using a spectrophotometer.

The BMSCs from the designated groups were seeded into a 6-well plate at a density of 2×10^5 cells per well. Following the application of specific treatments, the cells were cultured in osteogenic induction medium for 7 days. The gene expression levels of osteogenic differentiation markers, including Runt-related transcription factor 2 (*Runx2*), osteocalcin (*Ocn*), *Alp*, and collagen I (*Col1a1*), were analyzed using quantitative polymerase chain reaction (qPCR). Total RNA was extracted using Trizol reagent, and then reverse-transcribed into complementary DNA with the PrimeScript RT reagent kit (TaKaRa Biotechnology [Dalian] Co., Ltd. Japan). Gene expression was measured using real-time qPCR (Applied biosystems, America) with SYBR Green Master Mix (Yeasen Biotechnology (Shanghai) Co., Ltd. China). Primer sequences are shown in Table S1, Supporting Information.

Total protein was extracted from BMSCs by lysis in radioimmunoprecipitation assay buffer for protein blot analysis following the same treatments and a 14-day culture period (with non-induced BMSCs serving as the sham group, induced but untreated BMSCs as the control group, and other groups treated with different scaffold extracts). Protein concentration was determined using the bicinchoninic acid protein assay kit (Shanghai Biyuntian Biological Co., Ltd., China). Proteins were then mixed with loading buffer, boiled, and subjected to sodium dodecyl sulfate-polyacrylamide gel electrophoresis before being transferred to a polyvinylidene fluoride membrane. The membrane was blocked for an hour using non-fat milk, followed by the addition of primary antibodies against RUNX2 (1:1000), OCN (1:1000), ALP (1:1000), and *Col1a1* (1:500), and incubated overnight at 4°C. It was then treated with secondary antibodies conjugated with horseradish peroxidase. Protein bands were visualized using an enhanced chemiluminescence kit, and Scion imaging software (version 4.0) captured the images. ImageJ software (version 1.46) was used for quantitative analysis. All antibodies, including the secondary antibodies (goat anti-mouse IgG and goat anti-rabbit IgG), were obtained from Abcam. Transcriptome sequencing was also performed to observe the underlying osteogenic mechanisms.

2.16. Transcriptome sequencing analysis

After 2 weeks of culture, mRNA was extracted from bone-induced BMSC cells treated with CS/PLA-LMS extraction solution using Trizol reagent. Bone-induced BMSC cells without CS/PLA-LMS extraction solution served as the control. RNA sequencing was conducted at Shanghai Berhao Biotechnology Co., Ltd. (China) to determine the mRNA expression profiles across different groups. mRNAs with a $\log_2$ fold change ($\log_2$FC) of ≥1 or ≤−1 and a q-value ≤ 0.05 were considered differentially expressed. To depict the number of differentially expressed mRNAs, a volcano plot was constructed, featuring both upregulated and downregulated transcripts. The gene expression trend was visualized using a heatmap. Gene Ontology (GO) and Kyoto Encyclopedia of Genes and Genomes (KEGG) analyses were performed to identify the enriched signaling pathways of differentially expressed genes. A scatter bubble plot was used to display the top 30 significantly enriched signaling pathways with a p-value of less than 0.05.

2.17. Animal model and surgical procedures

A femoral bone defect model was established in 8-week-old male Sprague–Dawley rats. All animals were acclimated at a supervised animal facility for at least 2 weeks before trials began, during which time their health was monitored every day. Three sets of four rats each were randomly assigned: CS/PLA, CS/PLA-LMS, and control (untreated defect).

The rat femoral condyle defect model was established according to the method reported in the literature.[34,35] Specifically, after shaving the rat's fur and disinfecting with povidone-iodine, a longitudinal incision was made on the lateral side of the patellar ligament to expose the lateral femoral condyle. A 4 mm orthopedic drill was used to create a bone defect with a diameter of 4 mm and a depth of 3 mm. The defect area was then irrigated with saline solution to remove bone debris. Subsequently, scaffolds from different groups were placed into the hole. Finally, the surgical site was washed, sutured, and disinfected. The three groups were the following: the blank control group, the CS/PLA group, and the CS/PLA-LMS group.

At 4- and 8-week postoperative intervals, the animals were euthanized through cervical dislocation. The entire femora were collected by removing the surrounding soft tissues, and major organs such as the heart, liver, spleen, lungs, and kidneys were collected for biosafety assessment. All samples were then fixed with 4% paraformaldehyde.

2.18. Micro-computed tomography evaluation

After fixation, the femoral specimens were scanned using micro-computed tomography (CT; Bruker Skyscan, Belgium). Subsequently, bone volume fraction (BV/TV), trabecular thickness, trabecular number, and trabecular separation were calculated using DataViewer (version 1.5.6.2) and the Comprehensive TeX Archive Network software (version 1.20.8.0). Three-dimensional reconstruction of the femur was performed with CTVox (version 3.3.0).

2.19. Histological analysis and immunofluorescence staining

Following fixation and decalcification, specimens were embedded in paraffin, sectioned into 4 μm slices, and mounted on glass slides. For histological evaluation, sections were stained with hematoxylin and eosin (H&E) and Masson's trichrome to assess tissue morphology and bone regeneration.

For immunofluorescence staining, sections were permeabilized with 0.1% Triton X-100, blocked with 5% bovine serum albumin, and incubated overnight at 4°C with primary antibodies targeting *Col1a1*, OSN, and RUNX2. After washing, sections were incubated with Alexa Fluor 488-conjugated secondary antibodies, and nuclei were counterstained with 4',6-diamidino-2-phenylindole. Fluorescent images were acquired using a digital slide scanner (KFBIO, China) and analyzed quantitatively with ImageJ software (version 1.46).

2.20. Statistical analysis

The statistical program Statistical Package for Social Sciences version 24 was used to analyze the data. All samples were measured in triplicate, unless otherwise indicated, and the findings are shown as mean ± standard deviation. The least significant difference test was used for multiple group comparisons for normally distributed data in the context of a one-way analysis of variance. The threshold for statistical significance was set at $p < 0.05$. GraphPad Prism version 10 was used to construct data-related figures.

3. Results

3.1. Characterization of linezolid-loaded microspheres

The microspheres prepared in this study appeared as a white, fine sandy powder, evenly dispersed and free of clumping (Figure 1A). SEM showed that the microspheres exhibited a regular spherical structure (Figure 1B and C). Particle size analysis of the LMS powder indicated a normal distribution of particle sizes (Figure 1D). The Dv (90) of the LMS sample was measured at 46.2 μm, signifying that 90% of the microspheres had a diameter smaller than 46.2 μm, thereby meeting the anticipated size specifications. The equation for the LN standard curve was determined to be (**Equation II;** Figure 1E):

$$y = 27.568x + 10.176, R^2 = 0.999 \quad \text{(II)}$$

3.2. Sustained release and antibacterial effects of linezolid-loaded microspheres

The drug release curve of LMS over 20 days is illustrated in Figure 1F and G. During the first 3 days, the residual drugs were still present on the microspheres, which led to a sudden release. From Day 4 onward, the residual drugs on the microspheres were completely released, and the drug concentration at this stage was solely attributable to microsphere degradation. A significant release was observed starting from Day 11. By Day 20, the cumulative drug release rate reached 87.53 ± 1.79%. In terms of the clinical application of LN, a consensus among Chinese experts indicates that the trough concentration of LN should be maintained above 2.0 μg/mL to prevent the development of resistance. In this study, LMS exhibited a relatively stable drug release rate starting from Day 4, with an average daily release of approximately 4.8 ± 0.419 μg/mL for 100 mg of microspheres in 50 mL of PBS solution, surpassing the minimum trough concentration recommended for treating complex infections. Furthermore, *in vitro* antibacterial assays demonstrated that 10 mg of LMS (Figure 1H) showed significant antibacterial activity against *S. aureus* ATCC-29213 in agar culture, with an inhibition zone diameter of about 35.33 ± 0.057 mm within 24 h, compared to the blank control microspheres lacking LMS. Notably, the LMS maintained

effective antibacterial activity for up to 14 days (Figure S1A, Supporting Information).

3.3. Preparation and characterization of calcium sulfate/polylactic acid-linezolid-loaded microsphere scaffolds

In this study, the white rectangular solid CS/PLA scaffold was created according to the printing method in Figure S2, Supporting Information. The printing volume was 3.5 × 2.5 × 0.3 cm^3 (Figure 2A). SEM images show a homogeneous distribution of pore diameters with a line width of about 300 μm and pore sizes of around 500 μm (Figure 2E–H). White particles are uniformly distributed within the pores of the CS/PLA-LMS scaffold (Figure 2C). Electron microscopy observations show that multiple microspheres are evenly distributed on the scaffold's surface and internal pores, interconnected by SA hydrogel to prevent them from dislodging (Figure 2I–L). The stress–strain curves for both material groups are presented in Figure 2B and D. The elastic modulus of the CS/PLA scaffold was measured at 67.537 ± 2.867 MPa, while the CS/PLA-LMS scaffold group showed an elastic modulus of 87.563 ± 3.256 MPa. Furthermore, EDS analysis revealed the elemental distribution within the CS/PLA scaffold (Figure 2M).

3.4. *In vitro* biocompatibility and antibacterial ability of calcium sulfate/polylactic acid-linezolid-loaded microsphere scaffolds

This study assessed the cytotoxic effects of scaffold extracts on BMSCs. Both phalloidin-cytoskeleton staining and CCK-8 assays demonstrated that the extracts from both scaffolds were non-toxic to the cells (Figures S3 and S4,

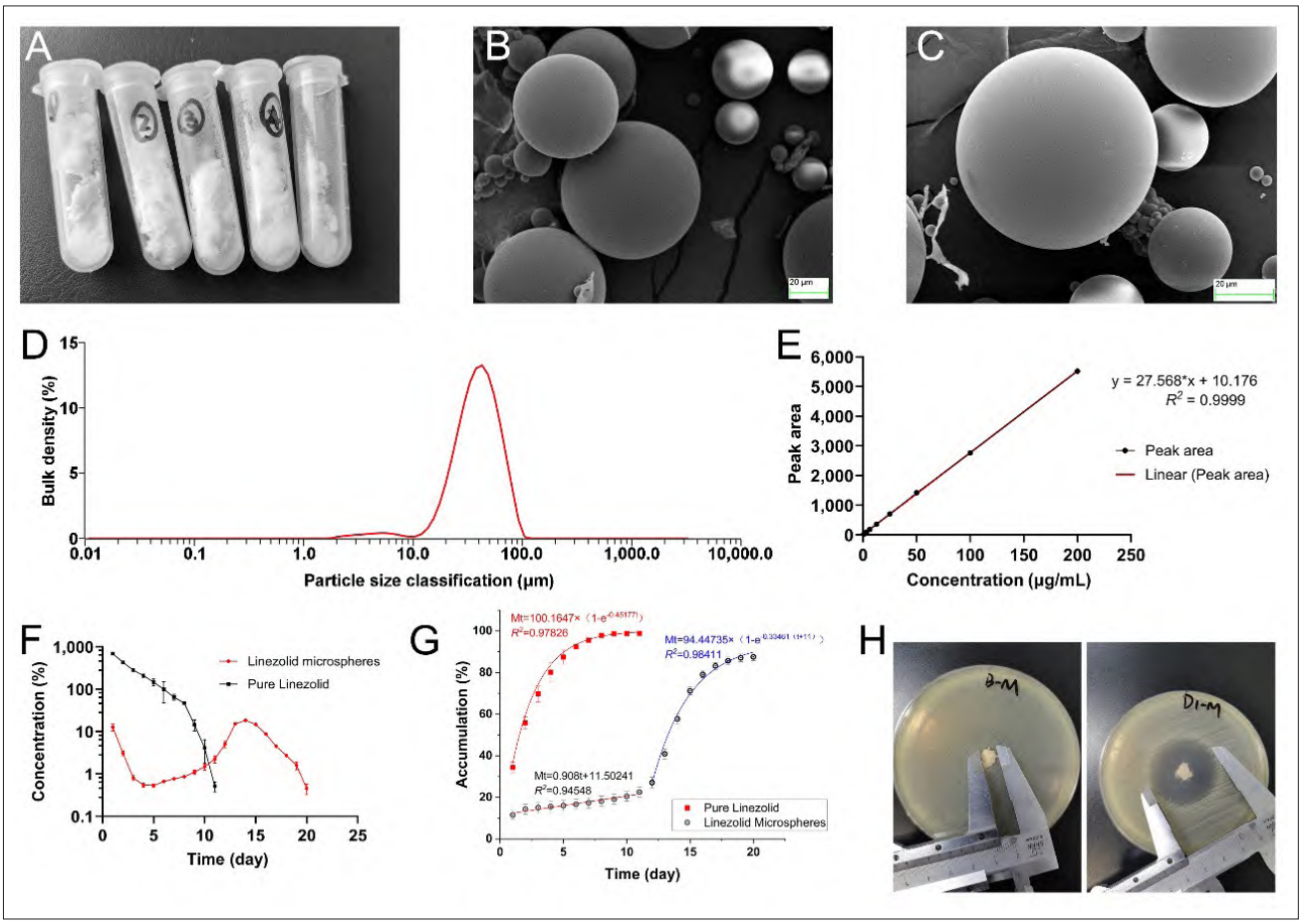


Figure 1. The physical properties and antibacterial capabilities of LMS. (A) Digital photographs of LMS, showing their spherical morphology and uniform size distribution. (B and C) Scanning electron microscopy images of LMS at different magnifications, highlighting their surface structure and texture. Scale bar: 20 μm. (D) Particle size distribution of LMS, indicating the size range and uniformity of the particles. (E) Linezolid (LN) standard curve, used to determine the drug concentration in release studies, demonstrating a linear relationship between concentration and absorbance. (F) Daily *in vitro* release efficiency of LMS, showing the release profile of LN over time under physiological conditions. (G) Cumulative *in vitro* release efficiency of LMS, illustrating the total drug release over a period of time, and demonstrating sustained release characteristics. (H) Antimicrobial properties of LMS *in vitro*, assessed by their ability to inhibit bacterial growth, with a comparison to control groups to highlight their efficacy. Abbreviation: LMS, linezolid-loaded microspheres.

Supporting Information). Additionally, the results of the cell adhesion assay on the composite scaffold demonstrated that cells adhered well to the scaffold surface, showing no significant difference compared to the blank scaffold (Figure 2N and O). We assessed the *in vitro* antibacterial properties of the two scaffold groups. With an inhibition zone diameter of roughly 20.97 ± 0.061 mm after 24 h, the CS/PLA-LMS scaffold demonstrated a noticeably better antibacterial activity against *S. aureus* ATCC-29213 in agar medium compared to the CS/PLA scaffold (Figure 2P). Furthermore, it maintained effective antibacterial activity for up to 14 days (Figure S5B, Supporting Information).

3.5. *In vitro* osteogenesis of calcium sulfate/polylactic acid-linezolid-loaded microsphere scaffolds

On Day 7 of osteogenic induction, BMSCs co-cultured with scaffold extracts were subjected to ALP staining and quantitative analysis to evaluate their osteogenic differentiation potential (Figure 3A and B). The results demonstrated that while both the CS/PLA and CS/PLA-LMS scaffold groups exhibited higher staining intensity compared to the control group, no statistically significant difference was observed between the two scaffold groups. To further investigate mineralization characteristics,

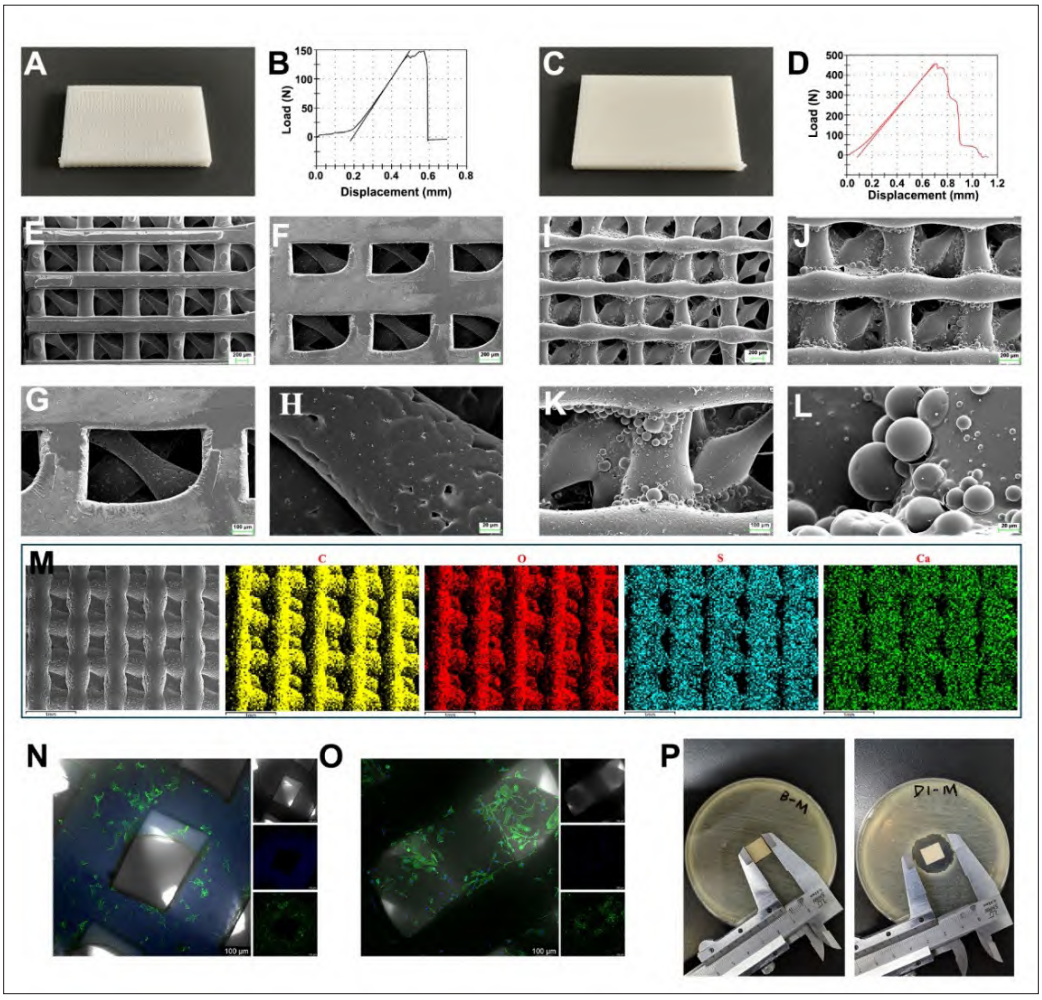


Figure 2. The physical properties and *in vitro* antibacterial capabilities of the composite scaffolds. (A and C) Digital photographs of the CS/PLA and CS/PLA-LMS scaffolds, showing their overall structure, with LMS incorporated into the composite scaffold. (B and D) Compressive stress–strain curves for the CS/PLA and CS/PLA-LMS scaffolds, illustrating their mechanical properties; the CS/PLA-LMS scaffold exhibits higher load-bearing capacity. (E–H) SEM images of the CS/PLA scaffold at various magnifications, showing its porous structure and surface features. Scale bars: 20, 100, and 200 μm; (I–L) SEM images of the CS/PLA-LMS composite scaffold, highlighting the integration of LMS within the matrix. Scale bars: 20, 100, and 200 μm; (M) Elemental mapping images showing the distribution of carbon (C), oxygen (O), sulfur (S), and calcium (Ca) elements, confirming LMS incorporation. Scale bar: 1 mm; (N and O) Cell adhesion experiments performed in the blank scaffold and composite scaffold groups proved that composite scaffolds have good cell adhesion ability. Scale bar: 100 μm. (P) *In vitro* antibacterial test showing greater inhibition zones around the CS/PLA-LMS scaffold compared to CS/PLA. Abbreviations: CS, calcium sulfate; LMS, linezolid-loaded microsphere; PLA, polylactic acid; SEM, scanning electron microscopy.

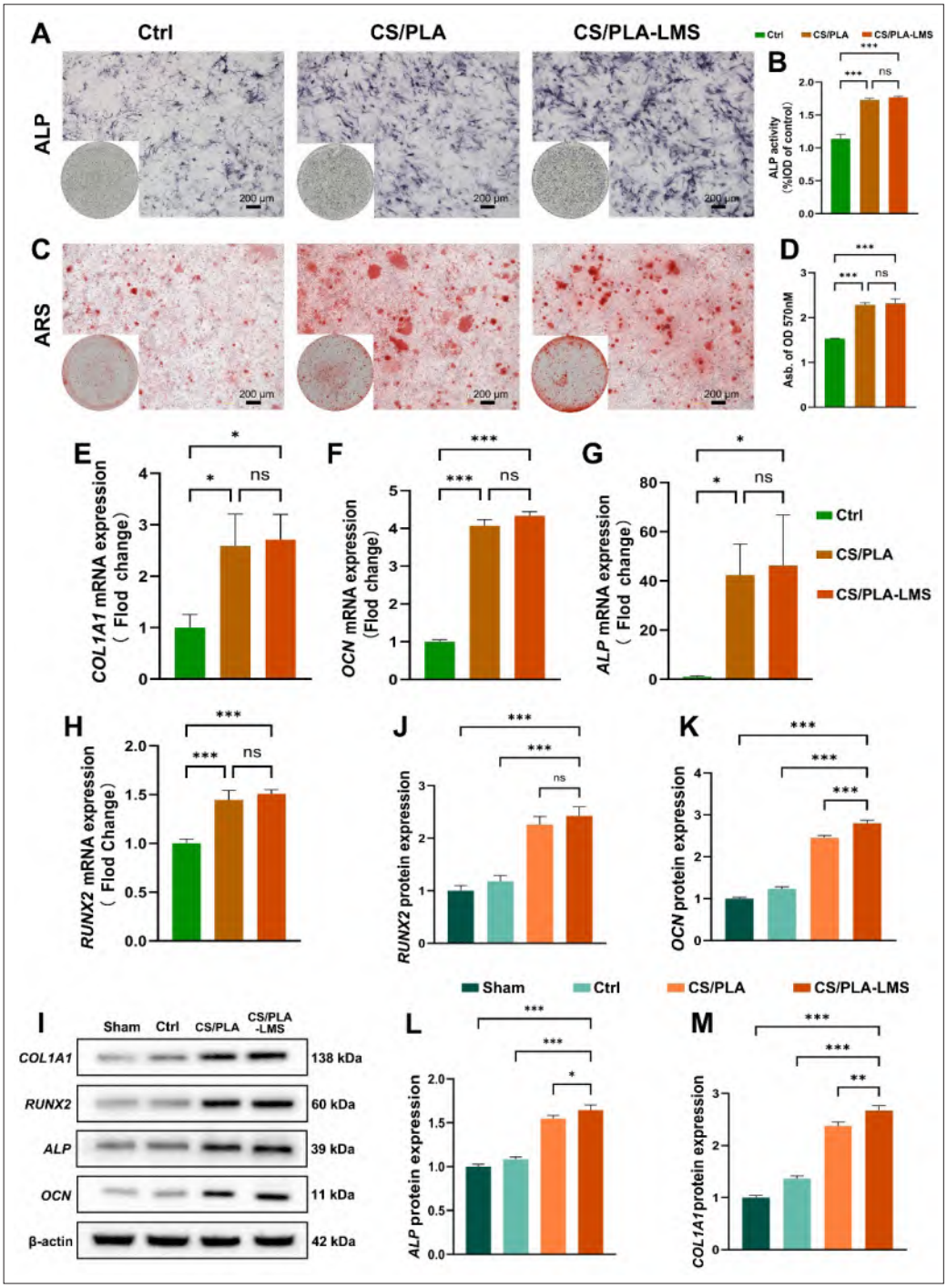


Figure 3. The osteogenic capability of BMSCs co-cultured with various scaffolds *in vitro*. (A) Microscopic images and macroscopic observations of ALP staining in BMSCs after 7 days of culture with different scaffold extracts. Scale bar: 200 μm. (B) Quantification of ALP activity, showing the osteogenic activity in the composite scaffold group. (C) Microscopic images and macroscopic observations of Alizarin Red (ARS) staining in BMSCs after 21 days of osteogenic induction, visualizing mineralization. Scale bar: 200 μm. (D) Quantification of ARS staining, indicating the degree of mineralization. (E–H) Gene expression analysis of osteogenic markers in BMSCs co-cultured with scaffold extracts, including *Col1a1* (E), *Ocn* (F), *Alp* (G), and *Runx2* (H). The composite scaffold group upregulates the expression of osteogenic genes. (I–M) Protein expression levels of BMSCs cultured in different scaffold extracts: RUNX2 (J), OCN (K), ALP (L), and *Col1a1* (M). Significant differences in protein expression were observed, with enhanced expression in the CS/PLA and CS/PLA-LMS group. All statistical data are represented as mean ± standard deviation ($n = 3$; *$p < 0.05$; **$p < 0.01$; ***$p < 0.001$). Abbreviations: ALP, alkaline phosphatase; BMSC, bone marrow stromal cell; COL1A1: Collagen type 1; CS, calcium sulfate; Ctrl, Control; LMS, linezolid-loaded microsphere; ns, non-significant; OCN, osteocalcin; OD, optical density; PLA, polylactic acid; RUNX2, runt-related transcription factor 2.

Alizarin Red S staining was subsequently performed on BMSCs co-cultured with scaffold extracts (Figure 3C and D). After 21 days of culture, both scaffold groups showed a significant increase in calcium nodule formation relative to the control group. qPCR analysis demonstrated that, compared to the control group, the expression levels of osteogenesis-related genes (*Runx2*, *Ocn*, *Alp*, and *Col1a1*) were upregulated in BMSCs co-cultured with the two scaffold extract groups (Figure 3E–H). Western blot analysis revealed that the expression levels of osteogenic proteins (RUNX2, OCN, ALP, and *Col1a1*) were significantly elevated in both scaffold groups compared to the control and uninduced (Sham) groups (Figure 3I–M). These results suggest that the CS/PLA-LMS scaffold has strong osteogenic-promoting properties.

3.6. Osteogenesis mechanism of calcium sulfate/polylactic acid-linezolid-loaded microsphere scaffold

Building on the results of previous experiments, we conducted mRNA sequencing on BMSCs from different treatment groups to further investigate the potential mechanisms by which CS/PLA-LMS promotes bone formation. Principal component analysis and differential gene clustering demonstrated a clear distinction between the two sample groups (Figure 4A and C). In total, 4118 differential genes were identified, with 181 genes upregulated and 250 genes downregulated (Figure 4B). GO functional enrichment analysis was performed based on the expression of these differential genes. The differential genes were significantly enriched in the cytoplasm, reaction to stimulus, developmental processes, and catalytic activity, as seen in Figure 4D. Additionally, KEGG pathway analysis revealed a notable enrichment of differential genes in the PI3K-Akt signaling pathway and protein processing in the endoplasmic reticulum (Figure 4E).

To validate this mechanism, we examined the expression and phosphorylation levels of key PI3K/Akt pathway proteins (PI3K and Akt) in the blank group (non-osteogenic induction), control group, CS/PLA group, and CS/PLA-LMS group using western blot. The CS/PLA and CS/PLA-LMS groups showed higher phosphorylation levels of PI3K and Akt than the control and blank groups, according to both western blot and quantitative data (Figure 4F–H). This activation effect was significantly reduced after the treatment of CS/PLA and CS/PLA-LMS groups with the specific PI3K inhibitor LY294002 (Figure 4I and J). Subsequent experiments revealed that LY294002 treatment significantly downregulated the expression levels of key osteogenic markers (*Col1a1*, RUNX2, ALP, and OCN) compared to other groups (Figure 4K–O), with levels markedly lower than the control group. These findings confirm that CS/PLA-LMS enhances osteogenic activity through the PI3K-Akt signaling pathway.

3.7. *In vivo* evaluation of calcium sulfate/polylactic acid-linezolid-loaded microsphere scaffolds

This study evaluated the therapeutic effect of composite stents by establishing a femoral condyle defect model (Figure S5, Supporting Information). Micro-CT reconstruction and quantitative analysis revealed that the CS/PLA-LMS scaffold group exhibited remarkable temporal advantages in bone defect repair (Figure 5A and B). At 4 weeks post-implantation, the BV/TV in the CS/PLA-LMS group reached 63.12%, representing a 3.2-fold increase compared to the control group (19.79%) and significantly exceeding the CS/PLA group (48.29%). The trabecular thickness (165.98 μm) in the CS/PLA-LMS group achieved 97.6% of normal bone levels (~170 μm), while the trabecular spacing (141.16 μm) demonstrated a 50.1% reduction relative to the control group (282.49 μm), indicating early formation of dense osseous structures.

By 8 weeks post-operation, the CS/PLA-LMS group displayed advanced regenerative characteristics: BV/TV further increased to 63.30%. Trabecular thickness (133.14 μm) and trabecular number (0.0048 mm^{-1}) exhibited 21.3% and 25.1% increases compared to the 4-week timepoint, respectively. Dynamic comparison demonstrated that the CS/PLA-LMS group maintained a stable weekly bone formation rate (ΔBV/TV: 0.04%), surpassing the control group (0.004%).

Neo-bone development and maturation were confirmed by histological evaluation using Masson's trichrome staining and H&E. At 4 weeks post-implantation, minimal osseous regeneration was observed in the control group, with defect regions predominantly occupied by marrow cells (Figure 5C). In contrast, scaffold pores in both CS/PLA and CS/PLA-LMS groups were infiltrated with fibrous tissue, accompanied by newly formed osseous tissue surrounding the fibrous matrices. By 8 weeks, fibrous components in experimental groups were replaced by organized bone tissue, while the control group exhibited persistent soft tissue infiltration. Masson's trichrome staining revealed more mature collagen organization in the CS/PLA-LMS group, demonstrating intense blue staining characteristic of mature bone (Figure 5D), consistent with the micro-CT findings.

Immunofluorescence staining of osteogenic-related proteins (*Col1a1*, OCN, and RUNX2) was performed on tissues harvested at 4 and 8 weeks postoperatively (Figure 6A and B). Compared to the control group, both the CS/PLA and CS/PLA-LMS groups showed a marked increase in the expression levels of these proteins.

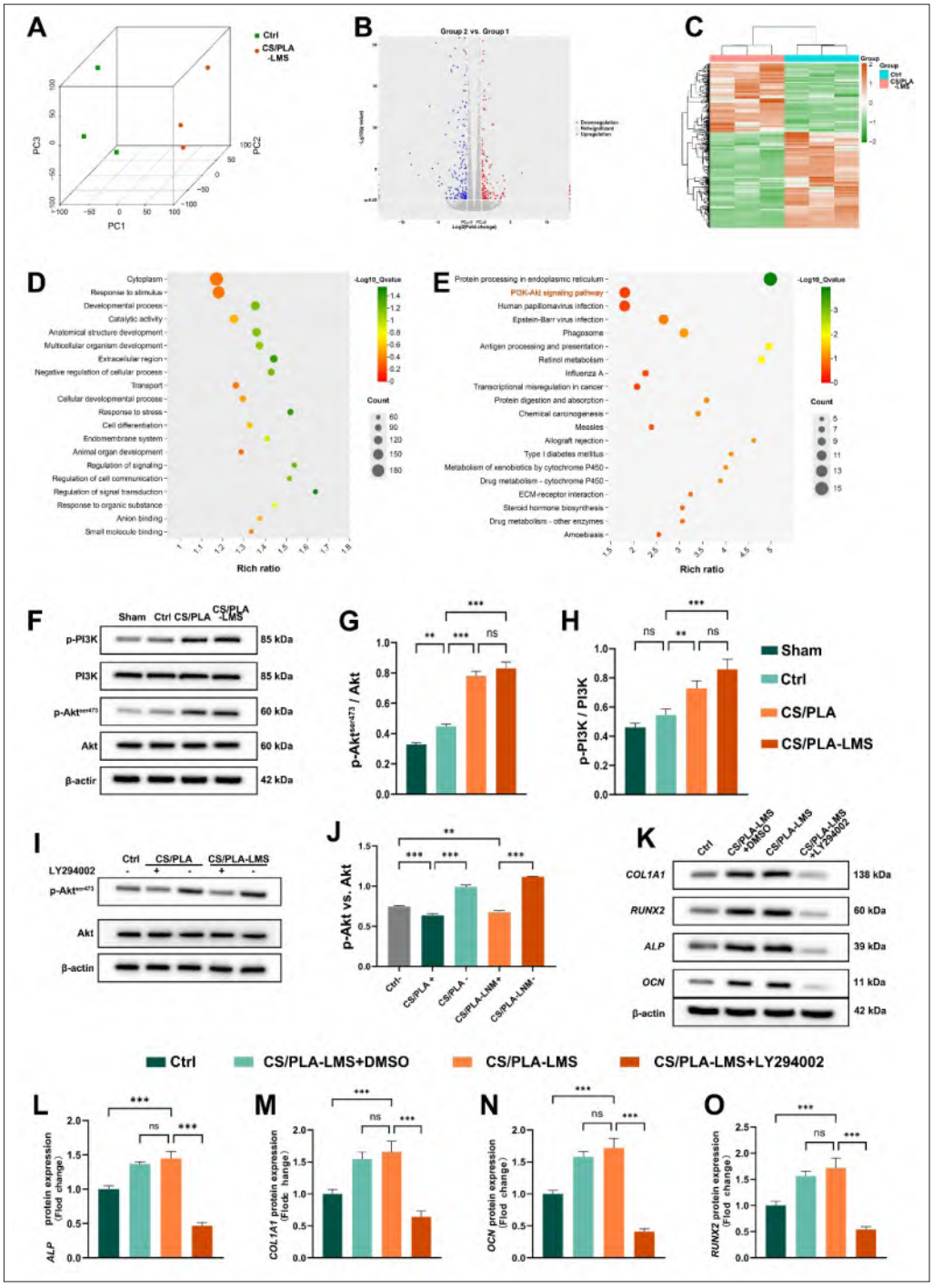


Figure 4. The CS/PLA-LMS scaffold promotes osteogenesis through the PI3K/Akt signaling pathway. (A) Principal component (PC) analysis showing the distribution of different groups. (B) Volcano plot illustrating differentially expressed genes between the groups. (C) Heatmap representing the differential gene expression patterns among the groups. (D) Gene ontology (GO) enrichment analysis of differentially expressed genes, highlighting the key biological processes involved. (E) KEGG pathway enrichment analysis, showing the most significantly enriched pathways in the different groups. (F–H) Western blot analysis of the phosphorylation levels of PI3K-Akt in BMSCs cultured with CS/PLA-LMS extracts. (I and J) Inhibition of the PI3K-Akt pathway using LY294002 and its effect on phosphorylation levels. (K–O) Expression levels of osteogenic-related proteins: ALP (L), *Col1a1* (M), OCN (N), and RUNX2 (O) after PI3K-Akt pathway inhibition. All statistical data are represented as mean ± standard deviation ($n = 3$; $^{*}p < 0.05$; $^{**}p < 0.01$; $^{***}p < 0.001$). Abbreviations: Akt, protein kinase B; ALP, alkaline phosphatase; BMSC, bone marrow stromal cell; COL1A1, Collagen type 1; CS, calcium sulfate; Ctrl, Control; DMSO, dimethyl sulfoxide; KEGG: Kyoto Encyclopedia of Genes and Genomes; LMS, linezolid-loaded microsphere; ns, non-significant; OCN, osteocalcin; PI3K, phosphoinositide 3-kinase; PLA, polylactic acid; RUNX2, runt-related transcription factor 2.

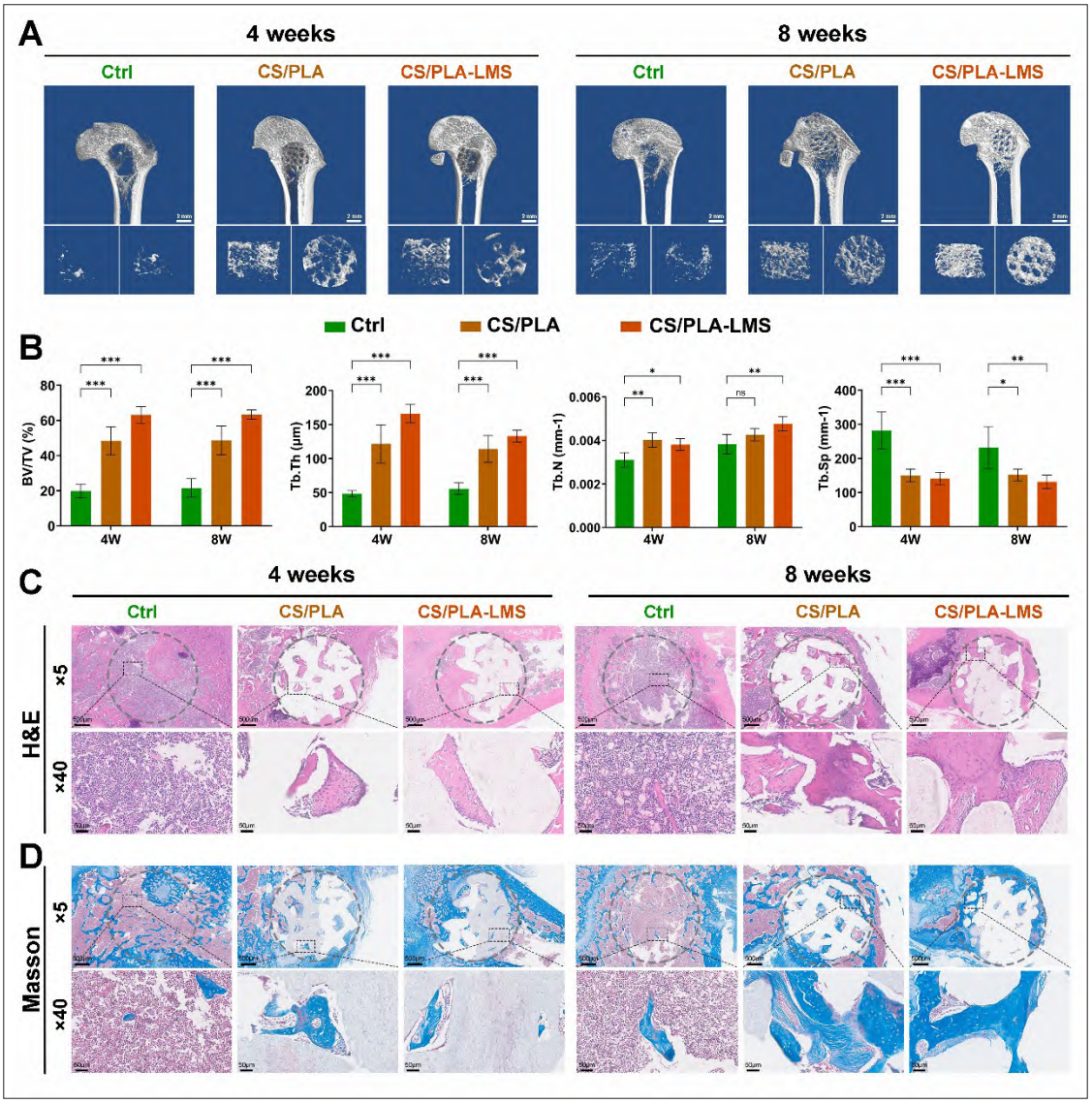


Figure 5. Evaluation of osteogenic capability at 4- and 8-weeks post-scaffold implantation. (A) Three-dimensional reconstructed micro-CT images of bone defects treated with different scaffolds at 4 and 8 weeks, showing the progression of bone healing. Scale bar: 2 mm (B) Quantitative analysis of micro-CT results, including bone volume/total volume (BV/TV), trabecular thickness (Tb.Th), trabecular number (Tb.N), and trabecular separation (Tb.Sp) at both 4 and 8 weeks. (C) Hematoxylin and eosin (H&E) staining of bone tissue sections at 4 and 8 weeks, showing tissue morphology and bone regeneration. Scale bars: 500 μm and 50 μm; magnifications: 5× and 40×. (D) Masson's trichrome staining of bone tissue sections at 4 and 8 weeks, visualizing collagen deposition and bone matrix formation. Scale bars: 500 and 50 μm; magnifications: 5× and 40×. All statistical data are represented as mean ± standard deviation ($n = 4$; $^{*}p < 0.05$; $^{**}p < 0.01$; $^{***}p < 0.001$). Abbreviations: CS, calcium sulfate; CT, computed tomography; Ctrl: control; LMS, linezolid-loaded microsphere; ns, non-significant; PLA, polylactic acid.

These findings validate the critical role of the composite scaffold in promoting bone regeneration through two synergistic mechanisms. First, the scaffold provides mechanical support and a porous microenvironment, which synergistically establishes an optimal osteogenic niche for bone repair. Secondly, as a drug delivery system, microspheres can release LN continuously, thus achieving the effect of long-term prevention of infection.

Additionally, H&E staining was performed on the animals' internal organs (heart, liver, spleen, lung, and kidney) (Figure S6, Supporting Information). No obvious pathological changes, such as inflammatory infiltration,

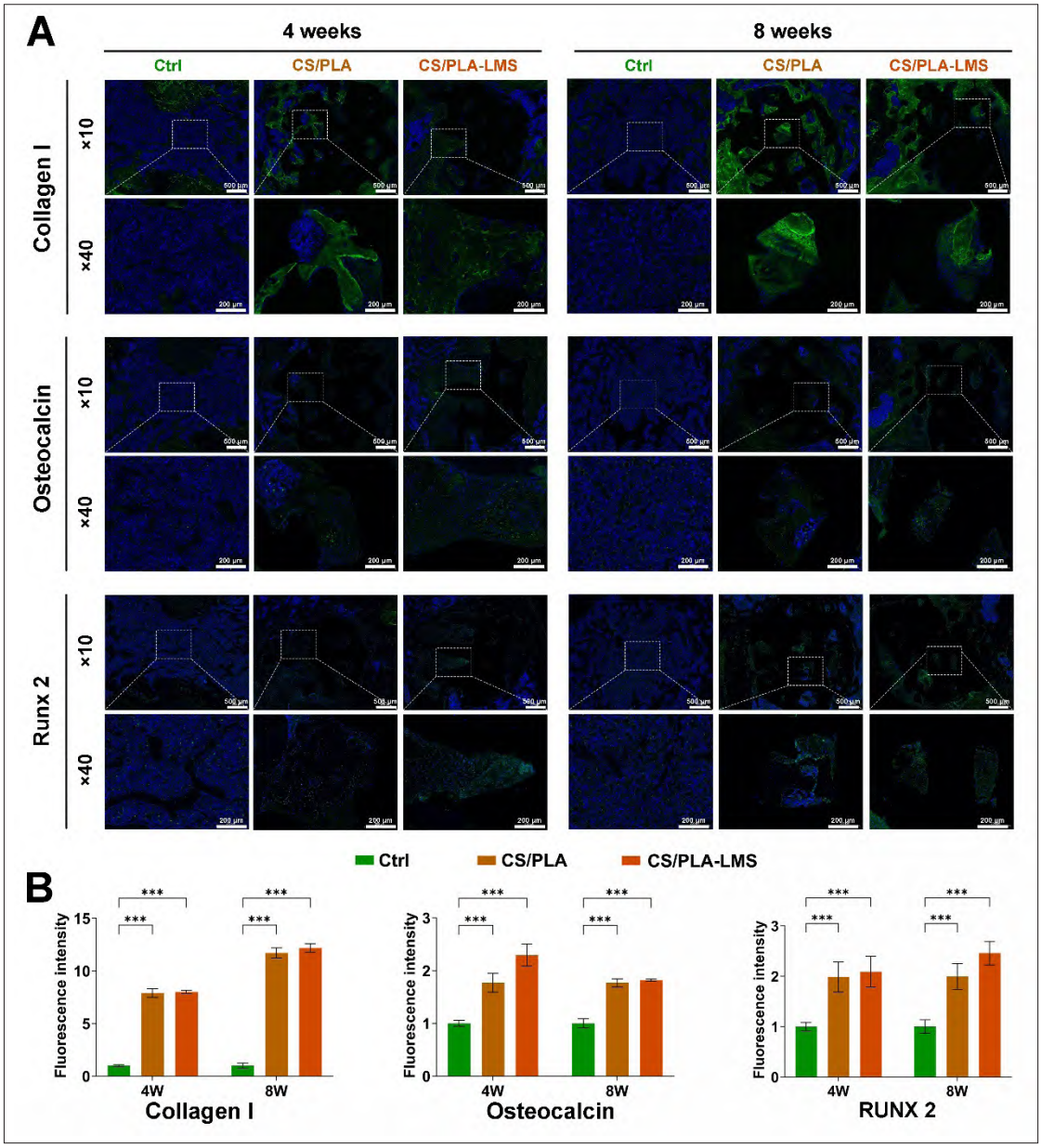


Figure 6. Immunofluorescence staining analysis of osteogenic activity. (A) Immunofluorescence staining for collagen I, osteocalcin, and RUNX2 at 4- and 8-weeks post-implantation, showing expression in bone tissue. Scale bars: 200 and 500 μm; magnifications: 10× and 40×. (B) Quantitative analysis of the fluorescence intensity for collagen I, osteocalcin, and RUNX2 at 4 and 8 weeks, indicating the osteogenic activity in the different scaffold groups. All statistical data are represented as mean ± standard deviation ($n = 4$; $^{*}p < 0.05$; $^{**}p < 0.01$; $^{***}p < 0.001$). Abbreviations: CS, calcium sulfate; Ctrl, control; LMS, linezolid-loaded microsphere; ns, non-significant; PLA, polylactic acid; RUNX2, runt-related transcription factor 2.

apoptosis, or necrosis, were observed in any groups, demonstrating the safety of the scaffold.

4. Discussion

In this study, we successfully developed a multifunctional composite scaffold (CS/PLA-LMS) using dual-nozzle 3D printing technology, which combined infection prevention and enhanced osteogenesis. The scaffold, incorporating LMS, demonstrated significant improvements in both antibacterial properties and bone regeneration. The results indicated that the scaffold effectively supported bone repair in a rat femoral condyle defect model while simultaneously preventing infection.

Research on carrier materials and preparation techniques for drug-loaded sustained-release microsphere systems provides innovative strategies for treating chronic

diseases, including infections and cancer.[36] In this study, the PLGA microsphere material, a commonly used polymeric carrier, was employed due to its biodegradability and non-toxicity in humans.[37] Additionally, the European Medicines Agency and the United States Food and Drug Administration have approved PLGA, citing its superior safety, degradability, and biocompatibility. These attributes make PLGA highly suitable for applications in biomedical engineering and drug delivery systems.[38,39] Yuan *et al.*[40] achieved controlled release of magnesium ions to promote bone regeneration by co-embedding magnesium oxide and magnesium carbonate in PLGA microspheres.[40] Moreover, Hickey *et al.*[41] developed a novel dexamethasone/PLGA microsphere system that provides immediate release of dexamethasone and sustained release for over a month, suitable for continuous delivery of anti-inflammatory drugs in implantable medical devices.[41]

Three-dimensional-printed scaffolds are viewed as ideal clinical bone substitute materials due to their controllable internal structures featuring pores that support cell survival and metabolism, facilitating nutrient exchange and accelerating osteogenesis.[42] In this experiment, the chosen scaffold materials are PLA and CS. PLA is highly biocompatible, produces biodegradable byproducts (such as lactic acid) that the body can metabolize and eliminate, and degrades at controlled rates, making it widely employed in the production of bone biomaterials.[43] To heal major bone lesions, Wang *et al.*[44] used fused deposition modeling-3D printing technology to create PLA/nano β-tricalcium phosphate composite scaffolds for bone tissue engineering.[44] Similarly, Senatov *et al.*[45] integrated bone morphogenetic protein-2 and erythropoietin into PLA scaffolds to develop recombinant protein scaffolds for bone defect repair. Additionally, CS, an inorganic component of bone, enhances scaffold biocompatibility, mechanical strength, and hydrophilicity. The incorporation of CS facilitates bone cell differentiation and proliferation, promoting calcium and phosphate mineral deposition within the scaffold and thereby accelerating new bone formation.[46] Liu *et al.*[47] further highlighted the effectiveness of α-CS hemihydrate/nano-hydroxyapatite composites loaded with metformin in promoting bone regeneration in a rat cranial defect model. A key advantage of this experiment is the utilization of computer-aided design to create the scaffold's internal structure. Compared to traditional immersion methods, the dual-nozzle 3D printing technology enables precise and uniform distribution of drug carrier microspheres within the scaffold's pores, thus addressing the issue of uneven distribution.[48] Uneven distribution could result in insufficient residual drug microspheres as the scaffold degrades, potentially failing to achieve effective antibacterial concentrations.

In large complex bone defects, perioperative infection constitutes a pivotal determinant of surgical outcome. Drug release kinetics revealed sustained release from the microsphere system over 20 days, with cumulative drug release reaching 87.53 ± 1.79%, demonstrating the capacity for extended antimicrobial protection. The sustained release profile corresponds with established clinical guidelines advocating LN trough levels exceeding 2.0 μg/mL to mitigate resistance emergence. Critically, the microsphere-mediated drug release consistently surpassed minimum therapeutic thresholds, ensuring robust infection prophylaxis.[49]

Despite the elastic modulus of this scaffold (87 MPa) being slightly higher than the 2–12 MPa range of human cancellous bone,[50] it remains significantly lower than that of clinically prevalent titanium metal implants.[51] Stress shielding occurs when the implant absorbs most mechanical loads, thereby reducing the load borne by surrounding bone tissue, which may inhibit bone remodeling and regeneration.[52] While the scaffold can provide short-term support for bone defect areas, future research should further optimize its mechanical properties to better match the elastic modulus of natural bone, thereby achieving biomechanical compatibility with native bone tissue.

Our findings also show that the CS/PLA-LMS scaffold activates the PI3K-Akt signaling pathway, which plays a key role in osteoblast differentiation and bone formation.[53] *In vitro* experiments showed that the CS/PLA-LMS scaffold significantly upregulated osteogenic markers such as RUNX2, OCN, ALP, and *Col1a1*. *In vivo* results further confirmed this mechanism.

Histological and micro-CT evaluations showed significant improvements in bone regeneration. In the *in vivo* rat model, the CS/PLA-LMS scaffold group exhibited a 3.2-fold increase in BV/TV and a 50% reduction in trabecular spacing compared to the control group. Histological analysis revealed well-organized bone tissue in the scaffold-treated groups, indicating accelerated bone healing. These observations are consistent with the osteogenic capabilities of the scaffold. Although the CS/PLA-LMS scaffold group demonstrated superior osteogenesis-related parameters in both radiographic and histopathological analyses compared to the CS/PLA group, no statistically significant difference was observed between the two groups. We hypothesized that this phenomenon may be associated with subclinical infection: while some animals showed no overt infection symptoms, low-virulence bacterial colonization might still exist. Such "occult infections" could compromise bone healing quality. The CS/PLA-LMS scaffold creates a more favorable

microenvironment for bone regeneration by preventing and controlling these subclinical infections.

5. Conclusion

In conclusion, we engineered a new CS/PLA-LMS scaffold with a unique porous architecture that enhances cell growth, metabolism, and proliferation within its pores, and assists in the treatment of pathological bone defects. The LMS has characteristics of sustained release. Using dual-nozzle 3D printing technology, these microspheres were uniformly distributed within the pores of the CS/PLA scaffold and released the drug gradually as the scaffold degraded. The osteogenic properties of CS/PLA-LMS were realized through the activation of the PI3K/Akt signaling pathway, and the inhibition of this pathway markedly reduced the osteogenic capacity of CS/PLA-LMS. Furthermore, tests on animals and *in vitro* cells demonstrated that the composite scaffold has outstanding biomechanical performance, compatibility, and degradability without cytotoxic effects, successfully facilitating osteogenesis and the restoration of bone defect areas. The creation of more effective multifunctional biomimetic scaffolds to address the therapeutic needs of complicated complex bone defects is anticipated with the help of additional optimization of the CS/PLA-LMS scaffold to improve its mechanical strength and prevent infection.

Acknowledgments

None.

Funding

This study was supported by the Taishan Scholar Project of Shandong Province, China (No.tstp 20250511).

Conflict of interest

The authors declare that they have no conflict of interest.

Author contributions

Conceptualization: Hai Huang, Tongshuai Xu
Data curation: Jiale Shao
Formal analysis: Jiale Shao
Funding acquisition: Yongming Xi
Investigation: Shannan Cao, Changlin Lv
Methodology: Shuqing Chen, Wenkang Yang
Resources: Shannan Cao, Changlin Lv
Supervision: Yongming Xi
Visualization: Xiaofan Du
Writing–original draft: Xiaojie Tang, Chenxu Li, Yanan Wang
Writing–review & editing: Yukun Du, Yongming Xi

Ethics approval

All animal-related experiments in this study adhered to the guidelines for the care and use of laboratory animals set forth by the National Institutes of Health (NIH). The experimental animals were provided by the Yantai Campus of Binzhou Medical University. All animal experiments were approved by the Animal Experimentation Committee of Yantai Campus, Binzhou Medical University (Animal Research Approval No.: 2024-L066).

Consent for publication

Not applicable.

Availability of data

Data will be made available upon request to the corresponding author.

References

1. Jihan M, Qi B, Bayaniahangar R, *et al*. Nanomaterials for bone tissue regeneration: updates and future perspectives. *Nanomedicine (Lond)*. 2019;14(22):2987-3006.
doi: 10.2217/nnm-2018-0445

2. Spicer PP, Kretlow JD, Young S, Jansen JA, Kasper FK, Mikos AG. Evaluation of bone regeneration using the rat critical size calvarial defect. *Nat Protoc*. 2012;7(10): 1918-1929.
doi: 10.1038/nprot.2012.113

3. Gugala Z, Gogolewski S. Regeneration of segmental diaphyseal defects in sheep tibiae using resorbable polymeric membranes: a preliminary study. *J Orthop Trauma*. 1999;13(3):187-195.
doi: 10.1097/00005131-199903000-00006

4. Dimitriou R, Jones E, McGonagle D, Giannoudis PV. Bone regeneration: current concepts and future directions. *BMC Med*. 2011;9:66.
doi: 10.1186/1741-7015-9-66

5. Campana V, Milano G, Pagano E, *et al*. Bone substitutes in orthopaedic surgery: from basic science to clinical practice. *J Mater Sci Mater Med*. 2014;25(10):2445-2461.
doi: 10.1007/s10856-014-5240-2

6. Roberts TT, Rosenbaum AJ. Bone grafts, bone substitutes and orthobiologics: the bridge between basic science and clinical advancements in fracture healing. *Organogenesis*. 2012;8(4):114-124.
doi: 10.4161/org.23306

7. Nazeer MA, Onder OC, Sevgili I, Yilgor E, Kavakli IH, Yilgor I. 3D printed poly (lactic acid) scaffolds modified with chitosan and hydroxyapatite for bone repair applications. *Mater Today Commun*. 2020;25:101515.
doi: 10.1016/j.mtcomm.2020.101515

8. Khan SN, Cammisa FP Jr, Sandhu HS, Diwan AD, Girardi FP, Lane JM. The biology of bone grafting. *J Am Acad Orthop Surg*. 2005;13(1):77-86.
doi: 10.5435/00124635-200501000-00009

9. Chiarello E, Cadossi M, Tedesco G, *et al*. Autograft, allograft and bone substitutes in reconstructive orthopedic surgery. *Aging Clin Exp Res*. 2013;25(Suppl 1):S101-S103.
doi: 10.1007/s40520-013-0088-8

10. Stevenson S, Horowitz M. The response to bone allografts. *J Bone Joint Surg Am*. 1992;74(6):939-950.
doi: 10.2106/00004623-199274060-00009

11. Stevenson S. The immune response to osteochondral allografts in dogs. *J Bone Joint Surg Am*. 1987;69(4):573-582.

12. Stevenson S, Li XQ, Martin B. The fate of cancellous and cortical bone after transplantation of fresh and frozen tissue-antigen-matched and mismatched osteochondral allografts in dogs. *J Bone Joint Surg Am*. 1991;73(8):1143-1156.

13. Kavanagh N, Ryan EJ, Widaa A, *et al*. Staphylococcal osteomyelitis: disease progression, treatment challenges, and future directions. *Clin Microbiol Rev*. 2018;31(2): e00084-17.
doi: 10.1128/CMR.00084-17

14. Yıldırım A, Kapukaya A, Mertsoy Y, Yiğit Ş, Çaçan MA, Atiç R. Management of open fractures using a noncontact locking plate as an internal fixator. *Indian J Orthop*. 2017;51(3):312-317.
doi: 10.4103/0019-5413.205686

15. Masters EA, Ricciardi BF, Bentley KLdM, Moriarty TF, Schwarz EM, Muthukrishnan G. Skeletal infections: microbial pathogenesis, immunity and clinical management. *Nat Rev Microbiol*. 2022;20(7):385-400.
doi: 10.1038/s41579-022-00686-0

16. Vallet-Regí M, Lozano D, González B, Izquierdo-Barba I. Biomaterials against bone infection. *Adv Healthc Mater*. 2020;9(6):e1901647.
doi: 10.1002/adhm.201901647

17. Prince GE, Yang X, Fu J, *et al*. Yolk-porous shell biphasic bioceramic granules enhancing bone regeneration and repair beyond homogenous hybrid. *Mater Sci Eng C Mater Biol Appl*. 2019;100:433-444.
doi: 10.1016/j.msec.2019.03.026

18. Yang Y, Chu L, Yang S, *et al*. Dual-functional 3D-printed composite scaffold for inhibiting bacterial infection and promoting bone regeneration in infected bone defect models. *Acta Biomater*. 2018;79:265-275.
doi: 10.1016/j.actbio.2018.08.015

19. Zhang L, Yang G, Johnson BN, Jia X. Three-dimensional (3D) printed scaffold and material selection for bone repair. *Acta Biomater*. 2019;84:16-33.
doi: 10.1016/j.actbio.2018.11.039

20. Liu W, Li J, Cheng M, *et al*. A surface-engineered polyetheretherketone biomaterial implant with direct and immunoregulatory antibacterial activity against methicillin-resistant Staphylococcus aureus. *Biomaterials*. 2019;208:8-20.
doi: 10.1016/j.biomaterials.2019.04.008

21. El-Rashidy AA, Roether JA, Harhaus L, Kneser U, Boccaccini AR. Regenerating bone with bioactive glass scaffolds: a review of in vivo studies in bone defect models. *Acta Biomater*. 2017;62:1-28.
doi: 10.1016/j.actbio.2017.08.030

22. Lopes MS, Jardini A, Maciel Filho R. Poly (lactic acid) production for tissue engineering applications. *Procedia Eng*. 2012;42:1402-1413.

23. Maadani AM, Salahinejad E. Performance comparison of PLA- and PLGA-coated porous bioceramic scaffolds: mechanical, biodegradability, bioactivity, delivery and biocompatibility assessments. *J Control Release*. 2022;351:1-7.
doi: 10.1016/j.jconrel.2022.09.022

24. Ma B, Han J, Zhang S, *et al*. Hydroxyapatite nanobelt/polylactic acid Janus membrane with osteoinduction/barrier dual functions for precise bone defect repair. *Acta Biomater*. 2018;71:108-117.
doi: 10.1016/j.actbio.2018.02.033

25. Tyler B, Gullotti D, Mangraviti A, Utsuki T, Brem H. Polylactic acid (PLA) controlled delivery carriers for biomedical applications. *Adv Drug Deliv Rev*. 2016;107:163-175.
doi: 10.1016/j.addr.2016.06.018

26. Zwingenberger S, Nich C, Valladares RD, Yao Z, Stiehler M, Goodman SB. Recommendations and considerations for the use of biologics in orthopedic surgery. *BioDrugs*. 2012;26(4):245-256.
doi: 10.2165/11631680-000000000-00000

27. Kumar RA, Sivashanmugam A, Deepthi S, Bumgardner JD, Nair SV, Jayakumar R. Nano-fibrin stabilized CaSO4 crystals incorporated injectable chitin composite hydrogel for enhanced angiogenesis & osteogenesis. *Carbohydrate Polym*. 2016;140:144-153.
doi: 10.1016/j.carbpol.2015.12.077

28. Zhou Z, Buchanan F, Mitchell C, Dunne N. Printability of calcium phosphate: calcium sulfate powders for the application of tissue engineered bone scaffolds using the 3D printing technique. *Mater Sci Eng C Mater Biol Appl*. 2014;38:1-10.
doi: 10.1016/j.msec.2014.01.033

29. Aquino-Martínez R, Angelo AP, Pujol FV. Calcium-containing scaffolds induce bone regeneration by regulating mesenchymal stem cell differentiation and migration. *Stem Cell Res Ther*. 2017;8(1):265.
doi: 10.1186/s13287-017-0713-0

30. Mitragotri S, Burke PA, Langer R. Overcoming the challenges in administering biopharmaceuticals: formulation and delivery strategies. *Nat Rev Drug Discov*. 2014;13(9):655-672.

doi: 10.1038/nrd4363

31. Wright JC, Burgess DJ. *Long Acting Injections and Implants*. Springer Science & Business Media; 2011.

32. Jain R, Shah NH, Malick AW, Rhodes CT. Controlled drug delivery by biodegradable poly (ester) devices: different preparative approaches. *Drug Dev Ind Pharm*. 1998;24(8):703-727.
doi: 10.3109/03639049809047401

33. Li J, Li K, Du Y, *et al*. Dual-nozzle 3D printed nano-hydroxyapatite scaffold loaded with vancomycin sustained-release microspheres for enhancing bone regeneration. *Int J Nanomed*. 2023;18:307-322.
doi: 10.2147/ijn.S394366

34. Wang L, Wang J, Zhou X, *et al*. A new self-healing hydrogel containing hucMSC-derived exosomes promotes bone regeneration. *Front Bioeng Biotechnol*. 2020;8:564731.
doi: 10.3389/fbioe.2020.564731

35. Wang L, Wei X, He X, *et al*. Osteoinductive dental pulp stem cell-derived extracellular vesicle-loaded multifunctional hydrogel for bone regeneration. *ACS Nano*. 2024;18(12):8777-8797.
doi: 10.1021/acsnano.3c11542

36. Davidson BL, Hilfinger JM, Beer SJ. Extended release of adenovirus from polymer microspheres: potential use in gene therapy for brain tumors. *Adv Drug Deliv Rev*. 1997;27(1):59-66.

37. Rocha CV, Gonçalves V, da Silva MC, Bañobre-López M, Gallo J. PLGA-based composites for various biomedical applications. *Int J Mol Sci*. 2022;23(4):2034.
doi: 10.3390/ijms23042034

38. Wang Y, Qin B, Xia G, Choi SH. FDA's poly (lactic-co-glycolic acid) research program and regulatory outcomes. *AAPS J*. 2021;23(4):92.
doi: 10.1208/s12248-021-00611-y

39. Wan B, Bao Q, Burgess D. Long-acting PLGA microspheres: advances in excipient and product analysis toward improved product understanding. *Adv Drug Deliv Rev*. 2023;198:114857.
doi: 10.1016/j.addr.2023.114857

40. Yuan Z, Wei P, Huang Y, *et al*. Injectable PLGA microspheres with tunable magnesium ion release for promoting bone regeneration. *Acta Biomater*. 2019;85:294-309.
doi: 10.1016/j.actbio.2018.12.017

41. Hickey T, Kreutzer D, Burgess DJ, Moussy F. Dexamethasone/PLGA microspheres for continuous delivery of an anti-inflammatory drug for implantable medical devices. *Biomaterials*. 2002;23(7):1649-1656.
doi: 10.1016/s0142-9612(01)00291-5

42. Huiwen W, Shuai L, Jia X, *et al*. 3D-printed nanohydroxyapatite/methylacrylylated silk fibroin scaffold for repairing rat skull defects. *J Biol Eng*. 2024;18(1):22.
doi: 10.1186/s13036-024-00416-5

43. Sitthisang S, Hou X, Treetong A, *et al*. Nanomechanical mapping of PLA hydroxyapatite composite scaffolds links surface homogeneity to stem cell differentiation. *Sci Rep*. 2024;14(1):21097.
doi: 10.1038/s41598-024-72073-z

44. Wang W, Liu P, Zhang B, *et al*. Fused deposition modeling printed PLA/Nano β-TCP composite bone tissue engineering scaffolds for promoting osteogenic induction function. *Int J Nanomedicine*. 2023;18:5815-5830.
doi: 10.2147/ijn.S416098

45. Senatov F, Zimina A, Chubrik A, *et al*. Effect of recombinant BMP-2 and erythropoietin on osteogenic properties of biomimetic PLA/PCL/HA and PHB/HA scaffolds in critical-size cranial defects model. *Mater Sci Eng C Mater Biol Appl*. 2022;135:112680.
doi: 10.1016/j.msec.2022.112680

46. Gao S, Li J, Lei Q, *et al*. Calcium sulfate-Cu(2+) delivery system improves 3D-printed calcium silicate artificial bone to repair large bone defects. *Front Bioeng Biotechnol*. 2023;11:1224557.
doi: 10.3389/fbioe.2023.1224557

47. Liu S, Fu H, Lv Y, *et al*. α-Hemihydrate calcium sulfate/n-hydroxyapatite combined with metformin promotes osteogenesis in vitro and in vivo. *Front Bioeng Biotechnol*. 2022;10:899157.
doi: 10.3389/fbioe.2022.899157

48. Macedo J, Marques R, Vervaet C, Pinto JF. Production of bi-compartmental tablets by FDM 3D printing for the withdrawal of diazepam. *Pharmaceutics*. 2023;15(2):538.
doi: 10.3390/pharmaceutics15020538

49. Morata L, Cuesta M, Rojas JF, *et al*. Risk factors for a low linezolid trough plasma concentration in acute infections. *Antimicrob Agents Chemother*. 2013;57(4):1913-1917.
doi: 10.1128/aac.01694-12

50. Mandal S, Viraj, Nandi SK, Roy M. Effects of multiscale porosity and pore interconnectivity on in vitro and in vivo degradation and biocompatibility of Fe-Mn-Cu scaffolds. *J Mater Chem B*. 2021;9(21):4340-4354.
doi: 10.1039/d1tb00641j

51. Qin Y, Jing Z, Zou D, *et al*. A metamaterial scaffold beyond modulus limits: enhanced osteogenesis and angiogenesis of critical bone defects. *Nat Commun*. 2025;16(1):2180.
doi: 10.1038/s41467-025-57609-9

52. Wang Q, Chen Y, Ding H, *et al*. Optogenetic activation of mechanical nociceptions to enhance implant osseointegration. *Nat Commun*. 2025;16(1):3093.
doi: 10.1038/s41467-025-58336-x

53. Zhao SJ, Kong FQ, Jie J, *et al*. Macrophage MSR1 promotes BMSC osteogenic differentiation and M2-like polarization by activating PI3K/AKT/GSK3β/β-catenin pathway. *Theranostics*. 2020;10(1):17-35.
doi: 10.7150/thno.36930

ACCSCIENCE PUBLISHING

International Journal of Bioprinting

RESEARCH ARTICLE

Thermally tunable and biodegradable copolymer ink for 3D-printed implantable drug delivery depots

Yun Geun Jeong[1†], Joon Yeong Park[1†], Moon Hee Lim[1], James J. Yoo[2], Sang Jin Lee[2], and Moon Suk Kim[1,3*]

[1]Department of Molecular Science and Technology, Ajou University, Suwon, Gyeonggi, South Korea

[2]Wake Forest Institute for Regenerative Medicine, Wake Forest School of Medicine, Winston-Salem, North Carolina, United States of America

[3]Research Institute, Medipolymer, Suwon, Gyeonggi, South Korea

Abstract

Three-dimensional (3D) printing enables precise, patient-tailored drug delivery, but its broader potential is limited by the lack of polymers that combine low processing temperatures with tunable biodegradability. This study presents the rational design, synthesis, and characterization of poly(ε-caprolactone-ran-lactide) (CL) polymer inks with tunable printability and controllable biodegradability for 3D-printed implantable drug delivery applications. By varying the poly(lactide) (PLA) content (1–20 mol%) within the poly(ε-caprolactone) backbone, the thermal and mechanical properties of the CL copolymers were precisely adjusted to meet both printing and biological performance criteria. Differential scanning calorimetry revealed that increasing PLA content systematically reduced the melting temperature (from 57 to 40°C), enabling thermal modulation of printability and depot shape retention. Rheological and printability assessments, conducted under optimized chamber temperature, feed rate, and extrusion pressure, demonstrated excellent filament continuity, layer stacking fidelity, and shape preservation. Among the synthesized variants, CL1–CL3 maintained structural stability above 40°C and were selected for detailed evaluation. The polymer inks were further validated through the fabrication of dexamethasone (Dex)-loaded CL (Dex-CL) depots, which achieved high encapsulation efficiency (>90%) and exhibited sustained drug release over 30 days in both *in vitro* and *in vivo* models. Notably, the lower melting point of Dex-CL3 contributed to accelerated release kinetics, confirming the utility of PLA content as a tunable parameter for degradation control. *In vivo* studies demonstrated prolonged Dex retention with minimal local inflammation, as confirmed by histological analysis. The CL polymer inks showed excellent biocompatibility and tissue integration, underscoring their potential for biomedical implantation. Collectively, these findings demonstrate that CL polymer inks provide a robust platform for 3D printing implantable drug depots with customizable degradation profiles, reliable structural performance, and immunological safety, supporting their use in sustained and responsive therapeutic delivery systems.

Keywords: 3D printing; Biocompatibility; Biodegradability; Drug delivery; Polymer inks; Printability

†These authors contributed equally to this work.

***Corresponding author:**
Moon Suk Kim
(moonskim@ajou.ac.kr)

Citation: Jeong YG, Park JY, Lim MH, Yoo JJ, Lee SJ, Kim MS. Thermally tunable and biodegradable copolymer ink for 3D-printed implantable drug delivery depots. *Int J Bioprint*. 2025;11(5):350-370. doi: 10.36922/IJB025290294

Received: July 18, 2025
1st revised: August 22, 2025
2nd revised: August 25, 2025
Accepted: August 26, 2025
Published online: August 26, 2025

Copyright: © 2025 Author(s). This is an Open Access article distributed under the terms of the Creative Commons Attribution License, permitting distribution, and reproduction in any medium, provided the original work is properly cited.

Publisher's Note: AccScience Publishing remains neutral with regard to jurisdictional claims in published maps and institutional affiliations.

1. Introduction

Drug delivery systems (DDS) are essential in modern medicine, enabling targeted, sustained, and controlled release of therapeutic agents while minimizing systemic side effects. Traditional DDS platforms, including tablets, microparticles, and hydrogels, have enabled varying degrees of temporal control over drug release.[1,2] However, these systems often fall short in terms of spatial targeting, consistent release kinetics, and adaptability to patient-specific needs. To address these limitations, three-dimensional (3D) printing has recently garnered increasing attention as a powerful tool for next-generation DDS, enabling precise spatial and temporal control over drug release and the fabrication of patient-tailored geometries.[3,4]

Among various 3D printing methods, semi-solid extrusion prints viscoelastic pastes or gels at ambient or moderately elevated temperatures, thereby minimizing thermal degradation and better preserving heat-sensitive components. However, it often necessitates solvent removal or post-printing crosslinking, which may reduce microarchitectural precision and introduce residual solvents. By contrast, fused deposition modeling (FDM) is particularly well suited for DDS applications because it provides simplicity, cost-effectiveness, and high reproducibility in producing multilayered drug delivery architectures.[5–7] Nevertheless, FDM requires polymer melting above the softening point, which can compromise the stability of thermolabile drugs or materials with narrow processing windows.

Thus, while FDM enables precise, solvent-free fabrication, its reliance on high processing temperatures remains a critical limitation. Addressing this challenge requires the development of polymer formulations with sufficiently low melting points (T_m), yet adequate mechanical strength, degradability, and biocompatibility.[8]

Biodegradable aliphatic polyesters, such as poly(ε-caprolactone) (PCL) and poly(lactide) (PLA), are among the most widely studied materials for 3D-printed DDS.[9] PCL is known for its excellent biocompatibility, flexibility, and relatively low T_m (~60°C), making it well-suited for low-temperature printing.[10,11] However, its slow degradation rate significantly limits its utility in applications requiring controlled or timely drug release.[12,13] In contrast, PLA degrades more rapidly but has a high T_m (~175°C), restricting its use in thermally sensitive FDM processes.[14]

Random copolymerization of PCL and PLA to form poly(ε-caprolactone-ran-lactide) (CL) offers a promising strategy to overcome these individual drawbacks, allowing the development of materials with tunable thermal, mechanical, and degradation properties. By adjusting the PLA content within the PCL matrix, both the T_m and biodegradation rate can be modulated simultaneously, enabling CL polymer inks optimized for printability and therapeutic performance.[15,16] Such customized formulations not only offer the potential for precise drug release profiles but also enhanced structural fidelity during FDM printing.[17–20]

In this study, dexamethasone (Dex)—a corticosteroid widely applied for anti-inflammatory treatment—was selected as the model drug owing to its well-established anti-inflammatory efficacy, extensive use in preclinical DDS evaluations, and compatibility with both *in vitro* and *in vivo* assays.[21] Although Dex possesses high thermal stability (reportedly up to ~200°C) and can be processed using high-melting polymers such as PLA, our primary objective was to demonstrate the feasibility, long-term stability, and sustained-release performance of the CL-based implantable DDS platform under clinically relevant conditions. Given that our DDS is intended for long-term, localized delivery, Dex was chosen for its proven stability over extended implantation periods and its therapeutic relevance in chronic inflammatory disorders. To validate their utility as drug delivery vehicles, Dex was incorporated into the CL polymer inks and formulated into Dex-loaded CL (Dex-CL) depots. These depots were comprehensively evaluated through *in vitro* and *in vivo* studies to examine drug release kinetics and inflammatory response. Collectively, these analyses establish the CL polymer inks as a versatile platform for 3D-printed implantable drug depots. This work demonstrates the rational design of CL polymer inks with tunable printability and degradability, offering promising potential for advanced, sustained-release therapeutic systems.

2. Materials and methods

2.1. Materials

Methoxy poly(ethylene glycol) (MPEG) (M_n = 750), tin(II) 2-ethylhexanoate ($Sn(Oct)_2$), and dexamethasone 21-phosphate disodium salt (Dex) were purchased from Sigma-Aldrich (United States of America [USA]). ε-caprolactone was obtained from TCI Chemicals (Japan) and distilled over calcium hydride under reduced pressure. L-lactide (Boehringer Ingelheim, France) was purified via two recrystallizations using ethyl acetate. Chloroform-D was purchased from Cambridge Isotope Laboratories, Inc. (USA). Toluene, dichloromethane, n-hexane, ethyl ether, and acetone were purchased from Samchun (Korea). Formalin (10%) and ethanol (100%) were obtained from Sigma-Aldrich. Mayer's hematoxylin solution was purchased from Corning (USA), and the anti-cluster of differentiation (CD) 68 antibody (ED1

antibody; AB303565) was obtained from Abcam (United Kingdom [UK]).

2.2. Synthesis and characterization of CL polymer inks

All glassware was heat-treated and vacuum-dried prior to use to eliminate residual moisture and contaminants. For the synthesis of the CL1 polymer ink, MPEG (0.075 g, 0.1 mmol) was placed in a pre-dried flask under a nitrogen atmosphere and dissolved in 90 mL of toluene. Azeotropic distillation was carried out at 150°C for 3 h to remove residual moisture. After distilling off 40 mL of toluene, ε-caprolactone (4.937 g, 43.254 mmol) and L-lactide (0.063 g, 0.437 mmol) were added to the flask. Subsequently, 0.2 mL of 0.1 M $Sn(Oct)_2$ solution was introduced as the catalyst, and ring-opening polymerization was conducted at 130°C for 24 h.

Following polymerization, the resulting copolymer was precipitated in a n-hexane/diethyl ether mixture (v/v = 4:1) to remove unreacted monomers and byproducts. The precipitate was then dissolved in dichloromethane, filtered, and concentrated using a rotary evaporator. The final CL1 polymer ink was obtained through vacuum drying to eliminate residual solvents.

Other CL polymer inks were synthesized using the same protocol with varying monomer feed ratios. The chemical composition and molecular weight of the synthesized polymer inks were characterized by proton nuclear magnetic resonance spectroscopy (^{1}H NMR). The molar ratio of L-lactide to ε-caprolactone was determined by integrating the characteristic peaks: methoxy protons of MPEG (δ = 3.38 ppm), methine protons of PLA (δ = 5.2 ppm), and methylene protons of PCL (δ = 2.3 ppm). The resulting compositions, designated as CL0 ($C_{100}L_0$), CL1 ($C_{99}L_1$), CL2 ($C_{91}L_9$), CL3 ($C_{85}L_{15}$), and CL4 ($C_{78}L_{22}$), were verified by ^{1}H NMR analysis, which showed that the polymers were obtained with ratios closely matching the intended feed compositions.

Molecular weight and polydispersity index were measured using gel permeation chromatography (GPC) on a Futecs GPC 500 system (Korea) equipped with a Shodex 201H refractive index detector (Shoko Scientific, Japan). Separation was performed using Shodex K-802, K-803, and K-804 polystyrene gel columns with $CHCl_3$ as the eluent, at a flow rate of 1 mL/min and a column temperature of 40°C.

Thermal properties, including the T_m and enthalpy of fusion (ΔH_m), were analyzed via differential scanning calorimetry (DSC) using a DSC 25 system (TA Instruments, USA). Approximately, 4 mg of each sample was sealed in an aluminum pan. For thermal analysis, the samples were heated from −80 to 200°C at a rate of 10°C/min, cooled back to −80°C at the same rate, and then reheated to 200°C. This cycle was used to eliminate thermal history and ensure reproducibility of thermal transitions.

2.3. Thermal stability assessment of CL polymer inks

To assess the thermal stability and processing feasibility of the CL polymer inks for 3D printing applications, 0.3 g of each sample was placed in a 4 mL glass vial and subjected to controlled heating at 25, 40, 60, 80, 100, and 120°C for either 1 or 2 h. Following thermal exposure, the samples were cooled to room temperature before analysis. The molecular weight distribution of the heat-treated polymer inks was analyzed by GPC, as described previously, to identify any signs of thermal degradation or structural alteration in the polymers.

2.4. Rheological characterization of CL polymer inks

The rheological properties of the CL0 to CL4 polymer inks were evaluated using a rheometer (MCR 102, Anton Paar, Germany) equipped with a temperature-controlled Peltier lower plate and a stainless-steel parallel plate geometry (25.0 mm diameter). The gap between the plates was fixed at 0.2 mm for all measurements, which were conducted at 80 and 100°C.

For the time sweep test, measurements were performed over a time range of 0–600 s with an oscillation frequency of 1 Hz, a gamma amplitude of 0.1%, and an oscillatory strain of 1%. For the strain sweep test, the strain range was set to 0–1000% with a gamma amplitude of 0.1% and a frequency of 1 Hz. For the linear ramp test, viscosity was measured over a shear rate range of 0–100 s^{-1}. The storage modulus (G'), strain (γ, %), shear rate (s^{-1}), and viscosity (Pa s) were calculated using the instrument's built-in software.

2.5. *In vitro* biodegradation of CL polymer inks

The *in vitro* biodegradation behavior of the CL polymer inks was evaluated by placing 0.1 g of each sample into a glass vial containing 5 mL of distilled water (DW). The vials were sealed and incubated at 50°C with continuous shaking at 100 rpm for 4 weeks. After incubation, the samples were sequentially frozen at −10°C for 24 h and −80°C for an additional 48 h to prepare for freeze-drying. Lyophilization was subsequently carried out to ensure complete drying.

The freeze-dried polymer inks were dissolved in chloroform, filtered to remove any undissolved residues, concentrated using a rotary evaporator, and vacuum-dried for 4 days. The recovered polymers were then analyzed using GPC to assess changes in molecular weight and the extent of degradation. Additionally, ^{1}H NMR spectroscopy was performed to investigate structural modifications in the CL copolymer backbone resulting from degradation.

2.6. Preparation of Dex-CL polymer inks

Dex-CL polymer inks were prepared by dissolving 1 g of each CL formulation (CL0, CL1, CL2, CL3, or CL4) in 30 mL of dichloromethane, while Dex was separately dissolved in 30 mL of acetone. These formulations correspond to the following monomer feed ratios: CL0 ($C_{100}L_0$), CL1 ($C_{99}L_1$), CL2 ($C_{91}L_9$), CL3 ($C_{85}L_{15}$), and CL4 ($C_{78}L_{22}$), as described in **Section 2.2**. The Dex solution was then combined with the corresponding CL solution, followed by thorough mixing to ensure uniform distribution of Dex within the CL matrix. The resulting mixture was subjected to rotary evaporation under reduced pressure at room temperature to remove the majority of the organic solvents, followed by additional vacuum drying at 40°C for 48 h to ensure complete elimination of any residual dichloromethane, acetone, or other volatile components. The absence of residual solvent was confirmed by ^{1}H NMR spectroscopy, which showed no detectable solvent peaks in the final polymer ink samples. The dried, homogeneous Dex-loaded CL polymer inks were then utilized for subsequent FDM 3D printing. CL4 ($C_{78}L_{22}$) was excluded from further drug-loading and printing experiments due to its relatively low mechanical stability and rapid softening at the optimized printing temperatures, which could compromise structural fidelity.

2.7. 3D printing process and printability assessment

Polymer ink depots were fabricated using a solid freeform fabrication 3D plotter (Protek Korea, Korea) equipped with a heating chamber, a stainless-steel syringe, and a micronozzle (200 μm internal orifice, 0.4 mm outer diameter). Material deposition along the *x*-, *y*-, and *z*-axes was precisely controlled via an air pressure-driven dispensing mechanism. Depot geometries were designed using Depot Path Generation software (Korea Institute of Machinery and Materials, Korea) to ensure uniform and reproducible structural specifications.

Each polymer ink formulation was loaded into the upper chamber of the FDM system, and the chamber temperature was adjusted between 80 and 120°C according to the thermal characteristics of the respective formulation. Printing was performed in a layer-by-layer manner onto a substrate maintained at 23–25°C, yielding circular depots (5 mm diameter, 1 mm height) with an internal pore size of 300 μm. Printing speed (50–400 mm/min) and extrusion pressure (100–500 kPa) were optimized to ensure continuous filament deposition, accurate layer stacking, and high geometric fidelity. A micronozzle (200 μm internal orifice, 0.4 mm outer diameter) was used for all prints.

After the printing process, the printed depots were cooled and solidified at ambient temperature. Printability was assessed by measuring filament widths and internal pore dimensions at multiple random locations using ImageJ software (Wayne Rasband, USA). Deviations from the designed line width and pore area were calculated to quantify structural accuracy and reproducibility. These metrics were used to determine the suitability of each CL polymer ink formulation for FDM-based 3D printing of drug delivery depots.

2.8. 3D printing of Dex-CL depots and post-printing evaluation

For the fabrication of Dex-CL depots, 1 g of each prepared polymer ink was loaded into the heating chamber of the 3D printer. The printing temperature was set 10–30°C above the T_m of the respective polymer ink to ensure smooth extrusion while maintaining structural integrity. Printing was conducted using a micronozzle (200 μm internal orifice, 0.4 mm outer diameter) at a feed rate of 400 mm/min and an extrusion pressure of 500 kPa. To ensure reproducibility, each formulation was printed in triplicate batches, with a minimum of 10 replicates per condition. Structural consistency was assessed by measuring dimensional accuracy and evaluating the uniformity of layer deposition. The printing time for a single Dex-CL depot was approximately 3 min. Additionally, the Dex and CL mixture was stored at 100°C for 2 h, and subsequent ^{1}H NMR analysis revealed no significant structural changes.

Following fabrication, the printed depots were incubated at 25°C (ambient) and 37°C (physiological) for 6 h to assess thermal stability under relevant environmental conditions. Structural changes were monitored using optical microscopy and scanning electron microscopy (SEM; JSM-7900F, JEOL, Japan). SEM was used to evaluate surface morphology, pore architecture, and microstructural integrity, providing insights into physical features that could influence subsequent drug release behavior.

2.9. Encapsulation efficiency and *in vitro* Dex release from Dex-CL depots

The encapsulation efficiency and *in vitro* release profiles of Dex from Dex-CL depots were quantified using high-performance liquid chromatography (HPLC; 1200 Series, Agilent Technologies, USA). Chromatographic separation was performed on a Hypersil C18 column (4.6 mm; Agilent Technologies, Germany) with a mobile phase consisting of acetonitrile (ACN) and DW (60:40, v/v) at a flow rate of 1.0 mL/min. Dex was detected and quantified based on its retention time and a standard calibration curve prepared in phosphate-buffered saline (PBS, pH 7.4).

To determine the encapsulation efficiency of Dex in the Dex-CL depots, freeze-dried Dex-CL samples were dissolved in 0.5 mL of ACN and stirred continuously at room temperature for 10 min. Subsequently, 0.5 mL of

DW was added, and the mixture was vortexed thoroughly for an additional 10 min to ensure complete extraction of Dex from the polymer matrix. The resulting solution was filtered through a 0.22 μm syringe filter to remove undissolved polymer residues. The encapsulation efficiency was calculated using the following equation:

$$(\text{weight of Dex in Dex-CL/weight of Dex initially fed}) \times 100 \quad \text{(I)}$$

For the release study, circular Dex-CL depots (5 mm diameter, 1 mm height) were individually immersed in 3 mL of PBS (pH 7.4) in 4 mL vials and incubated at 37°C with continuous agitation (100 rpm) to mimic physiological conditions. At predetermined intervals over the 4-week study period, 1 mL of the release medium was withdrawn and immediately replaced with fresh PBS within 10 s to maintain sink conditions. All experiments were conducted in triplicate ($n = 3$). Dex concentrations in the collected samples were quantified using HPLC (1200 Series, Agilent Technologies, USA) under the same chromatographic conditions described above. Cumulative release profiles were calculated based on the measured Dex concentrations and are presented as mean ± standard deviation.

2.10. *In vivo* implantation and evaluation of CL and Dex-CL depots

All animal experiments were approved by the Institutional Animal Care and Use Committee of Ajou University School of Medicine (Approval No. 2024-0030) and conducted in accordance with institutional ethical guidelines. Six-week-old male Sprague–Dawley (SD) rats (280–300 g; total $n = 36$) were used to evaluate the *in vivo* biocompatibility and drug release behavior of CL and Dex-CL depots. No experiments involving human subjects were conducted in this study.

Anesthesia was induced via intraperitoneal injection of tiletamine–zolazepam (Zoletil™ 50; Virbac, France) combined with xylazine (Rompun; Bayer Korea, Korea). After shaving and disinfecting the surgical site with povidone–iodine, the depots (5 mm diameter, 1 mm in height) were implanted into the subcutaneous tissue via a small incision. All depots were sterilized using ethylene oxide gas prior to implantation. Incisions were closed with absorbable sutures, and animals were housed under standard laboratory conditions with free access to food and water. At designated time points, rats were euthanized via carbon dioxide inhalation following institutional protocols. Implanted depots were retrieved for evaluation of drug release kinetics, structural integrity, degradation, and histological response, enabling a comprehensive assessment of *in vivo* performance.

2.11. Morphological and drug release analyses of *in vivo* Dex-CL depots

At designated post-implantation time points (Weeks 1, 2, 3, and 4), rats were euthanized, and the subcutaneously implanted Dex-CL depots were carefully excised from the dorsal region for subsequent morphological, structural, and drug release evaluations. All experiments were conducted in triplicate ($n = 3$) at each predetermined interval during the 4-week study period.

For morphological assessment, the retrieved depots were initially examined using a Camscope system (Sometech, Korea) and an optical microscope (Labophot-2, Nikon, Japan) at magnifications of 100× and 300×. Fine structural features were further analyzed using field-emission SEM, as previously described in **Section 2.8**. To preserve native morphology, the samples were flash-frozen in liquid nitrogen and lyophilized at −75°C for 5 days. The depots were then cryosectioned under liquid nitrogen to minimize structural disruption. Prior to SEM imaging, samples were gold-coated using a PS-1200 plasma sputter coater (Para One, Korea) under an argon atmosphere.

To quantify the residual Dex content in the depots, surface-adhered tissue was gently removed. Each depot was placed in a test tube containing 8 mL of ACN, homogenized at 16,000 rpm for 10 min at 25°C, and subsequently sonicated at the same temperature for 30 min. The homogenate was then centrifuged at 2000 rpm for 10 min at 4°C, and the supernatant was filtered through a 0.45 μm polytetrafluoroethylene membrane. ACN was removed by rotary evaporation under reduced pressure, and the resulting residue was reconstituted and analyzed by HPLC, as previously described in **Section 2.9**. Dex concentrations were determined using calibration curves prepared from known standards. All *in vivo* drug release experiments were independently conducted in three rats per condition, and results are expressed as mean ± standard deviation. These analyses provided comprehensive insights into depot morphology, *in vivo* structural stability, and Dex release kinetics over the 4-week period.

2.12. Histological and immunohistochemical analysis of host tissue response

At 2 and 4 weeks post-implantation, Dex-CL depots were explanted along with the surrounding tissues, which were immediately fixed in 10% neutral-buffered formalin to preserve morphology. The fixed tissues were processed into paraffin blocks, and 5 μm-thick sections were prepared using a microtome. The slides were incubated at 60°C for 2 h to ensure complete paraffin removal.

For hematoxylin and eosin (H&E) staining, deparaffinization was performed by immersing the slides in xylene for 10 min. It is important to note that during xylene treatment, the CL polymer inks were completely dissolved and removed, leaving only the host tissue for histological evaluation. This was followed by rehydration through a graded ethanol series (100%, 95%, 90%, 80%, and 70%; 10 min each). Sections were then stained with Harris hematoxylin (Sigma, USA) for 5 min, rinsed with DW for 2 min, and counterstained with 20% eosin solution (Sigma) for 5 min. After a final rinse in DW (1 min), the sections were dehydrated sequentially in ethanol (70–100%; 30 s each) and mounted using a permanent mounting medium (Muto Pure Chemicals, Japan).

For immunohistochemical staining of ED1 (CD68), paraffin sections were similarly deparaffinized and rehydrated. Antigen retrieval was conducted using citrate buffer (Sigma) at 120–130°C for 10 min, followed by cooling and two washes in PBS (5 min each). The slides were then incubated in PBST (0.05% Tween 20 in PBS) for 10 min. To block non-specific binding, the sections were treated with 5% horse serum (HS; Gibco, New Zealand) and 5% bovine serum albumin (BSA; Bovogen, Australia) in PBS for 90 min at 37 °C.

The primary antibody, mouse anti-rat CD68 (ED1; Abcam, UK), was diluted 1:1000 in antibody diluent (DAKO, Denmark) and applied overnight at 4°C. After washing twice with PBS and once with PBST, the sections were incubated with goat anti-mouse immunoglobulin G conjugated with Alexa Fluor 594 (Invitrogen, USA), diluted 1:200 in 1% BSA, for 3 h at room temperature. Nuclear counterstaining was performed using ProLong™ Gold Antifade Reagent with 4',6-diamidino-2-phenylindole (DAPI; Life Technologies, USA). The slides were mounted and visualized using an Axio Imager A1 fluorescence microscope (Carl Zeiss Microimaging GmbH, Germany), and images were acquired using Axiovision software (Rel. 4.8). Quantitative analysis of ED1-positive cells was performed using ImageJ, with data averaged from three specimens per group ($n = 3$). These evaluations provided detailed insights into tissue morphology and immune cell infiltration surrounding the implanted depots (Figure 1).

2.13. Statistical analyses

All data are presented as mean ± standard deviation from three independent experiments. Statistical comparisons were performed using one-way analysis of variance followed by Bonferroni's post hoc test for multiple comparisons. Analyses were conducted using SPSS version 12.0 (SPSS Inc., USA). A p-value of less than 0.05 was considered statistically significant.

3. Results

3.1. Synthesis of CL polymer inks

ε-caprolactone polymer inks were successfully synthesized by incorporating 1–20 mol% of PLA into the PCL backbone of the copolymers, yielding copolymers with an average molecular weight of approximately 50,000 g/mol. As summarized in Table 1, the resulting polymer inks were colorless and exhibited precipitation yields exceeding 90%. The ^{1}H NMR spectra displayed characteristic peaks corresponding to PCL, PLA, and MPEG, confirming the successful random incorporation of all monomeric units (Figure 2A). Moreover, the molecular weights and compositional ratios of PCL and PLA, calculated from signal integration in the ^{1}H NMR spectra, closely matched the theoretical feed ratios. These findings demonstrate the successful synthesis of CL-based copolymers with precisely controlled PCL and PLA contents, supporting their potential as tunable polymer inks for biomedical applications.

3.2. Thermal characterization of CL polymer inks for fused deposition modeling 3D printing

To assess their thermal suitability for FDM 3D printing, DSC was performed on CL copolymers containing 1–20 mol% PLA. The DSC analysis revealed no melting peaks near 175°C, the typical T_m of crystalline PLA, suggesting a high degree of phase compatibility between the PCL and PLA segments despite their random incorporation.

As shown in Table 1 and Figure 2B, both the T_m and the enthalpy of fusion (ΔH_m) decreased progressively with increasing PLA content. Specifically, T_m decreased from approximately 56 to 40°C, while ΔH_m declined from 60 to 17 J/g. These results indicate that increasing PLA content disrupts the crystalline order of the PCL matrix, thereby lowering its thermal transition parameters.

Among the tested CL copolymers, CL4 exhibited the lowest T_m (~40°C), approaching physiological temperature (~38°C), suggesting potential softening or partial dissolution under biological conditions.

Overall, these results demonstrate that the thermal behavior of CL-based copolymers can be precisely tuned by adjusting the PLA content. This thermal tunability offers a strategic advantage for optimizing printability and functional performance in FDM-based drug delivery systems.

3.3. Thermal stability of CL polymer inks under fused deposition modeling 3D printing conditions

The thermal stability of CL polymer inks was evaluated to determine their suitability for FDM 3D printing. For effective printing, polymer inks must melt efficiently within the heating chamber, flow smoothly through the nozzle

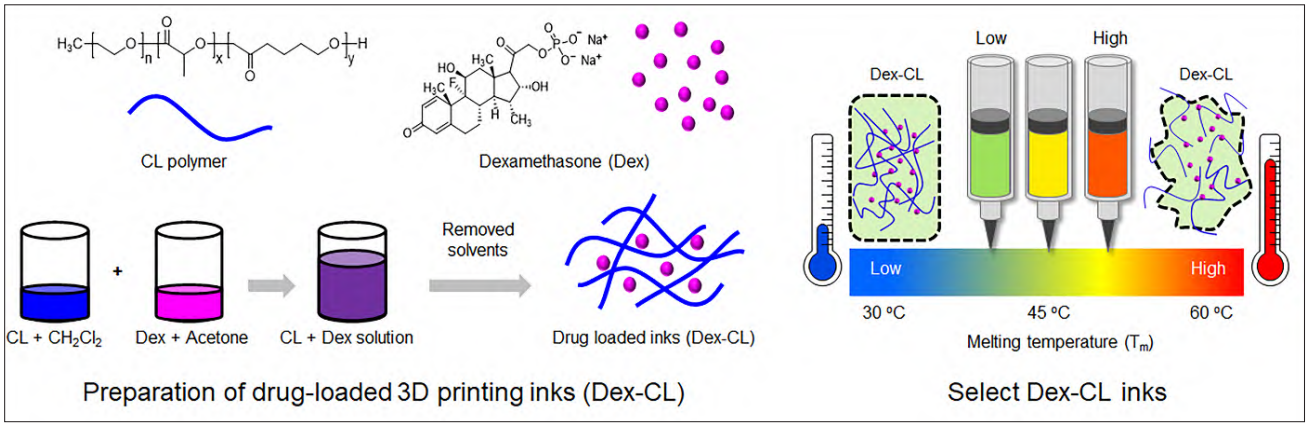


Figure 1. Schematic representation of the fabrication process for 3D-printed CL depots loaded with Dex. Abbreviations: CL, poly(ε-caprolactone-ran-lactide); Dex-CL, dexamethasone-loaded CL.

Table 1. Preparation and characterization of poly(ε-caprolactone-ran-lactide) (CL) polymer inks

No.	Theory molar ratio (%) [C:L][a]	Obtained molar ratio (%) [C:L][b]	MW[b]	T_m (°C)[c]	ΔH (J/g)[c]	Yield (%)	M_w/M_n[d]	Printability
CL0	$C_{100}L_0$	$C_{100}L0$	50,000	56.0	60.2	95	1.1	O
CL1	$C_{99}L_1$	$C_{99}L_1$	56,000	55.1	58.7	90	1.3	O
CL2	$C_{90}L_{10}$	$C_{91}L_9$	51,000	47.3	48.2	91	1.2	O
CL3	$C_{84}L_{16}$	$C_{85}L_{15}$	50,000	41.9	32.5	90	1.2	O~Δ
CL4	$C_{80}L_{20}$	$C_{78}L_{22}$	52,000	39.7	17.3	93	1.3	Δ~X

Abbreviations: M_n, number average molecular weight; MW, molecular weight; M_w, weight average molecular weight; O, (**High fidelity**: accurate line width and well-defined pores); O~Δ, (**Moderate fidelity**: acceptable line width and pore structure, with minor deviations from design); T_m, melting point; Δ*H*, enthalpy of fusion; Δ~X, (**Low fidelity**: a irregular or collapsed line width and pores, resulting in poor structural definition).

[a]C: ε-caprolactone, L: L-Lactide.

[b]Determined by proton nuclear magnetic resonance spectroscopy.

[c]Determined by differential scanning calorimetry.

[d]Measured by gel permeation chromatography, using polystyrene standards.

under pressure, and solidify into a stable 3D structure at room temperature (23–25°C). To assess thermal resistance, CL polymer inks were incubated in the printer chamber at various temperatures for 2 h. GPC analysis (Figure 2C) showed negligible changes in molecular weight, even after exposure to temperatures up to 120°C. These results confirm the excellent thermal stability of CL polymer inks, indicating resistance to heat-induced degradation and preservation of molecular characteristics throughout the printing process.

This thermal stability is essential for maintaining the structural integrity and reproducibility of printed constructs in biomedical applications. Collectively, these findings demonstrate that CL polymer inks are well-suited for use in temperature-sensitive FDM printing processes, particularly in the fabrication of drug delivery systems.

3.4. Rheological evaluation of CL polymer inks at printing temperatures

To predict the flowability and printability of CL0–CL4 polymer inks under FDM 3D printing conditions, rheological behaviors at 80, 100, and 120°C were analyzed using time sweep, strain sweep, and linear ramp measurements (Figure 3).

In the time sweep measurements, *G*' values were consistently lower at elevated temperatures (100 and 120°C) compared to 80°C, indicating that higher thermal input weakens the intermolecular interactions between polymer chains within the CL polymer inks. Nevertheless, all polymer inks maintained relatively stable *G*' values throughout the measurement period, suggesting that their viscoelastic integrity was preserved over time.

The strain sweep results revealed that across all tested temperatures, CL0 and CL1 exhibited a rapid decrease

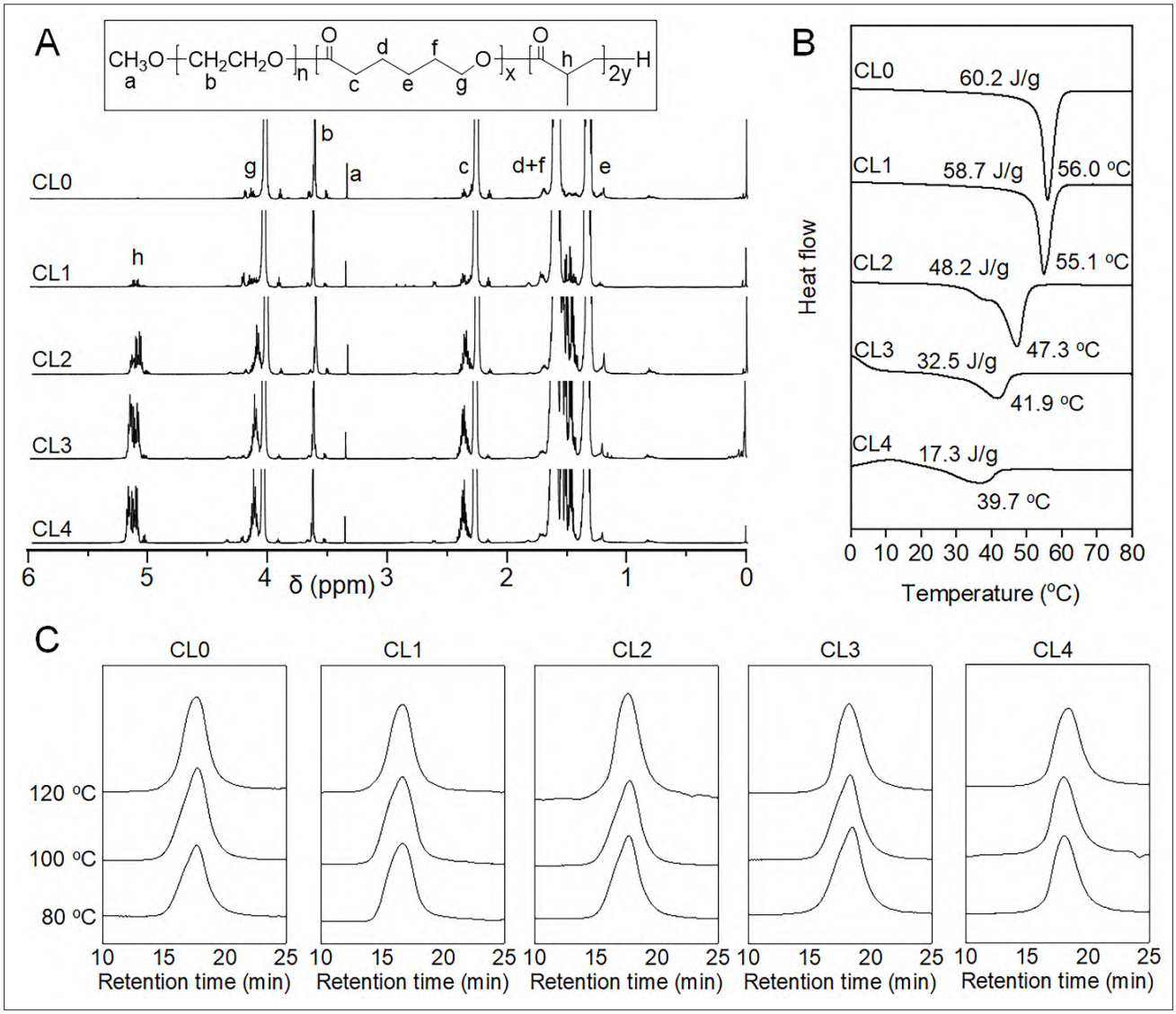


Figure 2. Physicochemical characterization of CL0, CL1, CL2, CL3, and CL4 polymer inks. (A) Representative proton nuclear magnetic resonance spectroscopy spectra confirming the chemical composition and monomer ratio of each copolymer formulation. (B) Differential scanning calorimetry thermograms illustrating the thermal transitions and crystallinity profiles of the CL polymer inks. (C) Gel permeation chromatography profiles obtained after 2 h of heating at 80–120°C, demonstrating the thermal stability of each formulation based on changes in molecular weight distribution. Note: Molar ratio of L-lactide to ε-caprolactone for CL0 = $C_{100}L_0$, CL1 = $C_{99}L_1$, CL2 = $C_{91}L_9$, CL3 = $C_{85}L_{15}$, and CL4 = $C_{78}L_{22}$. Abbreviation: CL, poly(ε-caprolactone-ran-lactide).

in *G*' at low strain levels, whereas CL2 showed a smaller initial drop. In contrast, CL3 and CL4 maintained nearly constant *G*' values across the entire strain range. This behavior can be attributed to the higher lactide content in CL3 and CL4, which reduces crystallinity and increases chain flexibility, thereby limiting the reduction in *G*' under increasing strain.

In the linear ramp tests, CL0 and CL1 showed a pronounced decrease in viscosity (Pa s) with increasing shear rate, consistent with their higher crystallinity and stronger chain entanglement at low shear rates. By contrast, CL2, CL3, and CL4—having higher lactide content, lower crystallinity, and weaker intermolecular interactions—exhibited only a modest additional decrease in viscosity. In all cases, viscosities were lower at elevated temperatures (100 and 120°C) than at 80°C, likely due to increased molecular mobility of polymer chains.

Overall, these findings indicate that both copolymer composition (CL:lactide ratio) and printing temperature strongly influence the flow behavior of the polymer inks

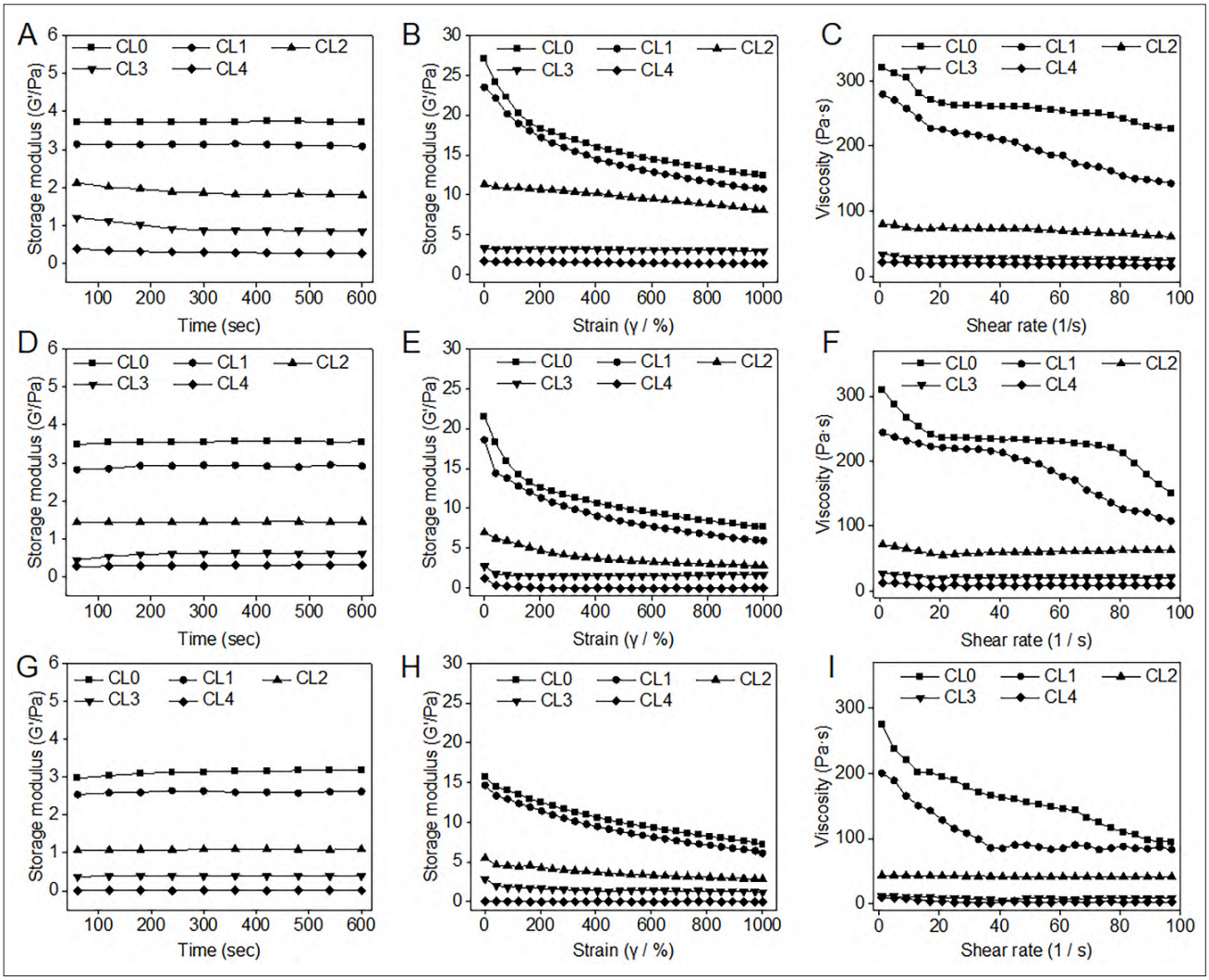


Figure 3. Rheological characterization of CL bioinks at (A–C) 80°C, (D–F) 100°C, and (G–I) 120°C. (A, D, G) Time sweep test; (B, E, H) strain sweep test; (C, F, I) linear ramp measurements. Note: Molar ratio of L-lactide to ε-caprolactone for CL0 = $C_{100}L_0$, CL1 = $C_{99}L_1$, CL2 = $C_{91}L_9$, CL3 = $C_{85}L_{15}$, and CL4 = $C_{78}L_{22}$. Abbreviation: CL, poly(ε-caprolactone-ran-lactide).

through the printer nozzle and the structural fidelity of the resulting printed constructs.

3.5. Printability and structural fidelity of CL polymer inks for fused deposition modeling 3D printing

The printability and structural fidelity of CL polymer inks were systematically evaluated to determine their suitability for FDM 3D printing (Figures 4 and S1, Supporting Information). Successful FDM printing requires that the polymer ink melts efficiently within the heating chamber, flows consistently under applied pressure, and rapidly solidifies at ambient temperature (23–25°C) to preserve the intended geometry. Variations in extrusion pressure or printing speed can affect line width and resolution. Therefore, optimizing these parameters is essential for high-fidelity fabrication.

First, the influence of chamber temperature was assessed across the 80–120°C range, previously verified to preserve the thermal stability of CL polymer inks. At temperatures below 80°C, extrusion was inconsistent and prone to nozzle clogging. At temperatures above 120°C, excessive fluidity led to over-extrusion, pore collapse, and yellow discoloration, likely due to thermal oxidation or degradation. It should be noted that the observed yellow discoloration at 120°C does not contradict the GPC results, indicating unchanged molecular weight distribution. GPC primarily detects polymer chain scission or crosslinking events, whereas discoloration can arise from minor thermo-

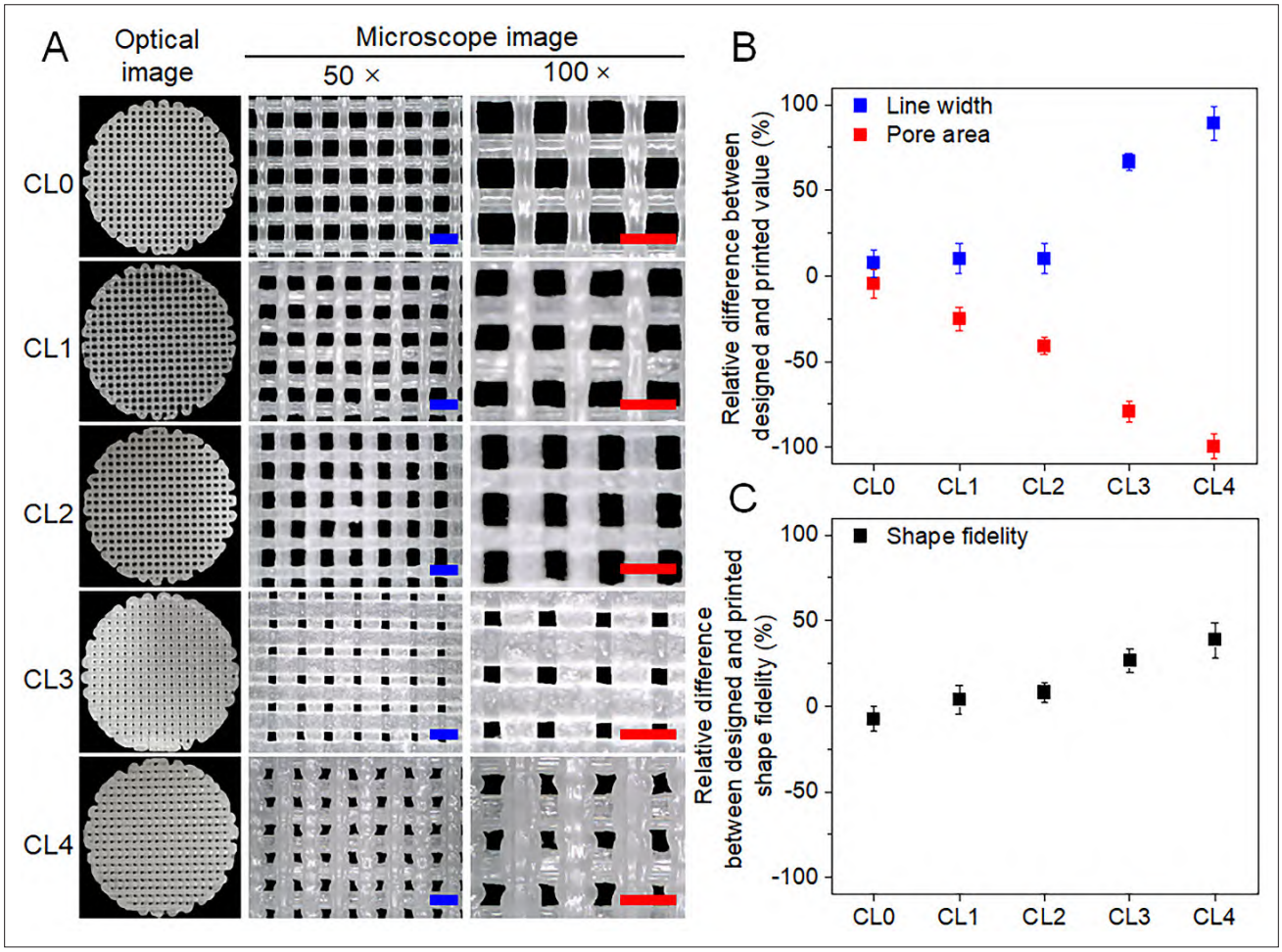


Figure 4. Printability and structural fidelity of CL polymer inks under fused deposition modeling 3D printing conditions. (A) Optical and microscopic images of 3D-printed CL polymer ink depots (CL0–CL3) showing strand morphology and pore architecture (scale bar = 1 mm; magnifications = 50× and 100×). (B) Quantitative comparison between designed and actual printed features, including relative deviations in line width and pore area, across different CL polymer inks. (C) Relative shape fidelity of printed depots, calculated by integrating the deviations in both line width and pore area. Note: Molar ratio of L-lactide to ε-caprolactone for CL0 = $C_{100}L_0$, CL1 = $C_{99}L_1$, CL2 = $C_{91}L_9$, CL3 = $C_{85}L_{15}$, and CL4 = $C_{78}L_{22}$. Abbreviation: CL, poly(ε-caprolactone-ran-lactide).

oxidative surface reactions, catalyst residue interactions, or trace impurity degradation—none of which necessarily alter the bulk chain length. These subtle chemical changes, while not impacting molecular weight, can still affect visual appearance and potentially surface-related performance.

During fabrication at the optimized chamber temperature of 100°C, individual DDS units required approximately 3–5 min of continuous heating from polymer ink loading to completion of printing. For multi-unit production runs, the copolymer–drug mixture remained in the heated chamber for up to 25 min, which was the longest duration tested under practical conditions. Notably, GPC analysis after simulated heating for 2 h at 100°C confirmed no detectable molecular weight degradation, indicating that all actual processing times in this study fell well within the thermally safe window for CL polymer inks.

Next, the effects of printing speed (50–400 mm/min) and extrusion pressure (100–500 kPa) were evaluated at a fixed chamber temperature of 100°C. Over-extrusion occurred at high pressure (500 kPa) and low speed (50 mm/min), while under-extrusion was observed at low pressure (100 kPa) and high speed (400 mm/min), highlighting the interdependent roles of pressure, polymer ink viscosity, and solidification rate during extrusion.

Optimal printing conditions were determined to be a chamber temperature of 100°C, an ambient platform temperature, a printing speed of 200 mm/min, and an extrusion pressure of 400 kPa. Under these conditions, drug delivery depots with a designed pore size of 300 μm

and a line width of 350 μm were fabricated using different CL formulations (CL0–CL4). Structural fidelity was evaluated based on the measured line width and pore area of the printed depots (Figure 4). Representative optical microscopic images (Figure 4A) showed that CL0, CL1, and CL2 produced stable geometries closely matching the designed specifications (Figure 4B). In contrast, CL3 and CL4 displayed excessive material extrusion due to lower viscosities, leading to an 80–90% increase in line width and a >60 % reduction in pore area, resulting in near-complete pore collapse.

These deviations in printed geometry are not merely superficial but critically impact the microarchitecture of the drug delivery depots—including pore size uniformity, interconnectivity, and surface-to-volume ratio. Such structural parameters govern drug diffusion and degradation-mediated release rates. Excessive widening of printed lines or pore collapse (as observed in CL3 and CL4) reduces effective surface area and alters internal diffusion pathways, leading to slower or less predictable release kinetics. Conversely, high-resolution, dimensionally accurate prints (CL0–CL2) preserve the designed porosity and geometry, ensuring consistent drug loading distribution and predictable release profiles throughout the intended therapeutic period. Under these optimized printing conditions, the dimensional accuracy of CL0–CL2 remained within ±10% of the design, indicating minimal geometry-induced variation in internal surface area. This suggests that, for high-fidelity prints, drug release kinetics are primarily dictated by the CL polymer ink composition and degradation behavior, with geometry-related effects being negligible.

It is well recognized that the geometry of 3D-printed depots can modulate drug release by altering the surface-to-volume ratio and diffusion pathways. In our study, the printing fidelity of CL0–CL2 formulations ensured near-identical pore architecture and line width, minimizing geometry-driven variability. Consequently, the *in vitro* release profiles primarily reflect the intrinsic degradation and diffusion characteristics of each CL polymer ink, rather than differences in printed geometry. This supports the interpretation that, under the optimized FDM parameters, the controlled nature of the DDS arises from material properties, with geometry effects held constant.

Shape fidelity analysis further confirmed that CL0–CL2 maintained 90–100% fidelity, with dimensional accuracy within ±10% of design values (Figure 4C), whereas CL3 and CL4 deviated substantially due to excessive flow and low mechanical integrity of the extruded lines. Collectively, these results demonstrate that the PCL-to-PLA ratio critically influences print performance, and that precise control of copolymer composition, alongside optimized printing parameters, is essential for achieving reproducible, high-resolution 3D-printed drug delivery depots. Among all formulations, CL4 exhibited the poorest printability, characterized by filament collapse, fused layers, and structural distortion—effects attributed to its low T_m and excessively low viscosity. These deficiencies, along with its thermal instability during FDM-based printing and observable clumping and deformation at physiological temperatures, led to its exclusion from further experiments, as it was deemed unsuitable for use as a stable implantable drug carrier.

3.6. *In vitro* biodegradation behavior of CL polymer inks

In our previous study, CL polymers showed almost no degradation at 37°C even after 14 weeks.[20] Building on this observation, the present study investigated the *in vitro* biodegradation profiles of CL polymer inks with varying PCL-to-PLA molar ratios at 37°C (physiological conditions), as well as at 50°C, where accelerated degradation enabled clearer assessment of compositional effects.

First, GPC analysis demonstrated that the molecular weights of the CL polymer inks remained largely unchanged across all formulations, suggesting that bulk degradation was minimal during the incubation period.

In contrast, ^{1}H NMR provided greater sensitivity to subtle chemical alterations. CL0 showed no detectable structural changes at either temperature, confirming its high chemical stability (Figures 5 and S2, Supporting Information). CL1 and CL2 exhibited minor but noticeable spectral changes at 4.45 and 1.55 ppm, with CL2 showing a more pronounced additional peak at 50°C. These low-intensity signals, although minor compared to the major intact polymer peaks, suggest partial hydrolytic cleavage of lactide-derived segments. Importantly, CL3 demonstrated an even stronger degradation pattern than CL2, particularly at 50°C, which can be attributed to its higher lactide content, reduced crystallinity, and increased hydrophilicity—factors that collectively enhance water uptake and accelerate hydrolysis.

Collectively, these findings demonstrate that the *in vitro* degradation behavior and structural integrity of CL polymer inks are governed by copolymer composition. This underscores the compositional tuning as a key design strategy, enabling the development of CL-based polymer inks with tailored biodegradation profiles.

3.7. Preparation and characterization of 3D-printed Dex-CL depots

To fabricate printable drug delivery depots and evaluate their drug-loading performance, Dex was incorporated

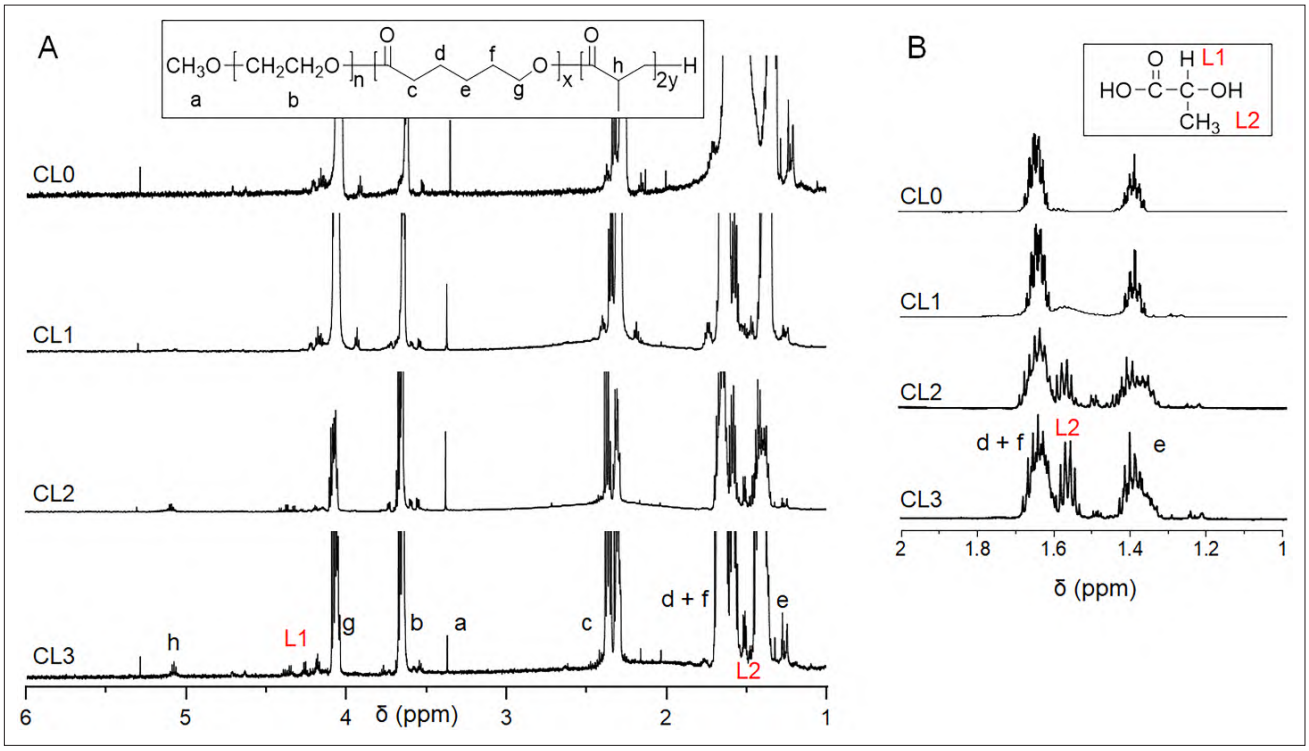


Figure 5. Hydrolytic degradation analysis of CL0, CL1, CL2, and CL3 polymer inks via proton nuclear magnetic resonance spectroscopy (^{1}H NMR) after incubation in distilled water at 50°C. (a) Full ^{1}H NMR spectra of the incubated samples, showing the overall chemical structure of each formulation. (b) Magnified view of the L2 region (1.0–2.0 ppm), highlighting the methyl proton signals of lactide units to assess hydrolytic cleavage and degradation behavior over time. Note: Molar ratio of L-lactide to ε-caprolactone for CL0 = $C_{100}L_0$, CL1 = $C_{99}L_1$, CL2 = $C_{91}L_9$, and CL3 = $C_{85}L_{15}$. Abbreviation: CL, poly(ε-caprolactone-ran-lactide).

into CL0, CL1, CL2, and CL3 polymer ink powders at concentrations ranging from 1 to 5 wt% to produce homogeneous mixtures.

Differential scanning calorimetry analysis revealed that, similar to CL polymer inks, no melting peak appeared near 175°C, the typical T_m of crystalline PLA. This indicates that the incorporation of Dex did not significantly alter the crystallization behavior within the CL copolymer matrix.

As shown in Table 2 and Figure S3, Supporting Information, all Dex-CL formulations exhibited slight decreases in both T_m and ΔH_m upon incorporation of Dex. While Dex disrupted the crystallization of the CL polymer inks to some extent, thereby lowering thermal transition parameters, the magnitude of this effect was minimal. Collectively, these results suggest that the addition of Dex exerts only a negligible influence on the thermal behavior of CL polymer inks. Consequently, Dex can be effectively loaded without compromising the printability or functional performance of the depot formulations.

Each Dex-loaded CL formulation was subsequently processed in the heating chamber of the FDM printer and fabricated under the previously optimized thermal conditions to generate 3D-printed drug depots. As shown in Figure 6, all printed depots retained well-defined circular geometries and regular pore structures across all Dex concentrations. The depots were fabricated in a layer-by-layer orthogonal pattern according to a computer-generated design (5 mm diameter, 1 mm height), featuring strand widths of 200 μm and inter-strand pore sizes of 300 μm (top view). At ambient temperature (25°C), Dex-CL0, CL1, and CL2 depots successfully preserved their intended architectures. In contrast, Dex-CL3 depots showed minor filament deformation, such as partial fusion and strand flattening, likely due to their lower mechanical stability.

Among the tested formulations, Dex-CL2 demonstrated the highest consistency in maintaining pore structure and geometric fidelity across all Dex concentrations. Encapsulation efficiency was uniformly high for all groups, averaging approximately 90% (Figure 6E), confirming efficient drug incorporation and retention during the printing process.

To assess the stability of the printed depots under physiological conditions, samples were incubated at 37°C

Table 2. Preparation and characterization of Dex-CL depots for printability

No.	Dex (wt%)	T_m (°C)[a]	ΔH (J/g)[a]	Printability	Encapsulation[b]
CL0	3	53.4	57.3	O	95
CL1	3	53.1	52.8	O	89
CL2	1	46.1	46.4	O	91
	3	45.9	43.9		93
	5	44.7	40.9		88
CL3	3	40.9	31.2	O~Δ	84
CL4	3	37.9	15.8	Δ~X	-

Abbreviations: CL, poly(ε-caprolactone-ran-lactide); Dex, dexamethasone; Dex-CL, dexamethasone-loaded CL; O, (**high fidelity**: accurate line width and well-defined pores); O~Δ, (**moderate fidelity**: acceptable line width and pore structure, with minor deviations from design); Δ~X, (**low fidelity**: a irregular or collapsed line width and pores, resulting in poor structural definition).

[a]Determined by differential scanning calorimetry measurement.

[b]Determined by high-performance liquid chromatography.

for 6 h, followed by optical and SEM imaging (Figure 6B and D). Dex-CL0, CL1, and CL2 depots generally retained their original shapes and pore architectures, indicating excellent thermal and structural stability. In particular, Dex(3)-CL0, Dex(3)-CL1, Dex(1)-CL2, Dex(3)-CL2, and Dex(5)-CL2 displayed outstanding shape fidelity and uniform surface morphology, supporting their potential use as implantable sustained-release drug depots.

In contrast, Dex-CL3 depots exhibited complete filament fusion and significant pore collapse after incubation at 37°C. This behavior confirms that the low T_m of CL3 (~40°C) compromises structural integrity under physiological conditions. However, this thermal sensitivity may be advantageous for rapid-release applications, where matrix dissolution is triggered at body temperature.

Collectively, these findings suggest that Dex-CL0, CL1, and CL2 depots offer sufficient mechanical robustness and thermal stability for sustained drug delivery. In contrast, CL3 may be better suited for scenarios requiring thermally responsive, rapid-release drug delivery systems.

3.8. *In vitro* Dex release from 3D-printed Dex-CL depots

The release behavior of Dex, incorporated as dexamethasone 21-phosphate disodium salt, was evaluated under

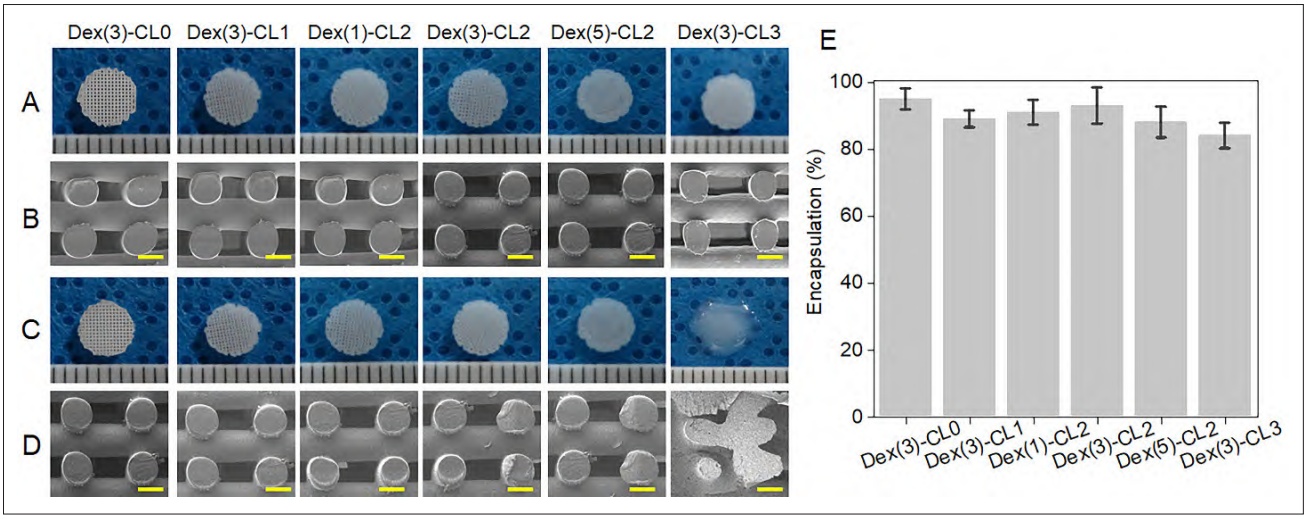


Figure 6. Characterization of 3D-printed Dex-CL depots. Optical photographs of Dex-CL depots incubated at (A) 25°C and (C) 37°C after 6 h of incubation. Scanning electron microscopy images of cross-sections of Dex-CL depots after 6 h of (B) 25°C and (D) 37°C incubation (scale bar = 100 μm; magnification = 100×), with numbers indicating the Dex concentration. (E) Encapsulation efficiency of Dex within the Dex-CL depots. Abbreviations: CL, poly(ε-caprolactone-ran-lactide); Dex-CL, dexamethasone-loaded CL.

physiological conditions. Given its hydrophilic nature, Dex release from the 3D-printed Dex-CL depots into PBS at 37°C was expected to occur through a combination of dissolution and diffusion mechanisms.

As shown in Figure 7, all Dex-CL depots exhibited sustained release profiles over a 30-day period, with minimal initial burst release. The early-phase release rate was influenced by the thermal properties of the CL polymer inks, particularly their T_m relative to the incubation temperature. Depots fabricated with lower-T_m polymer inks, such as CL3, showed a modestly accelerated initial release. However, following the early phase, all formulations converged toward similar sustained release profiles, demonstrating comparable long-term release behavior across all depot types.

Furthermore, the cumulative amount of Dex released increased proportionally with the initial loading concentration (1%, 3%, and 5%), indicating a clear dose-dependent release trend. These results underscore the importance of both the thermal characteristics of the polymer ink and the Dex loading level in modulating drug release kinetics. In summary, the 3D-printed Dex-CL depots enabled controlled and tunable drug release over extended durations, highlighting their potential for use in long-term therapeutic applications.

3.9. *In vivo* application of 3D-printed Dex-CL depot and Dex release profile

To evaluate the *in vivo* release kinetics and biocompatibility of 3D-printed Dex-CL depots, the constructs were subcutaneously implanted in SD rats and monitored over a 4-week period. The implantation procedure was well tolerated, with no observable adverse effects or signs of inflammation, indicating excellent biocompatibility of the CL polymer inks (Figure 8A).

Depot integrity was examined at 2 and 4 weeks post-implantation using optical and SEM imaging (Figure 8B and C). Most depots, especially those fabricated from Dex-CL0, CL1, and CL2, maintained their structural integrity throughout the study. Within the Dex-CL2 group, varying Dex concentrations did not result in noticeable morphological differences. In contrast, Dex-CL3 depots exhibited significant softening, filament fusion, and structural collapse by Week 2, attributed to their low T_m (~40°C), which closely approaches physiological temperature and compromises *in vivo* stability.

Cumulative Dex release was measured at Weeks 1, 2, 3, and 4 (Figure 9). All depots with equivalent Dex loading showed an initial burst release during the first week, followed by sustained release over the remaining period. After 1 week, cumulative release reached approximately 18%, 22%, and 38% for Dex-CL1, CL2, and CL3 depots,

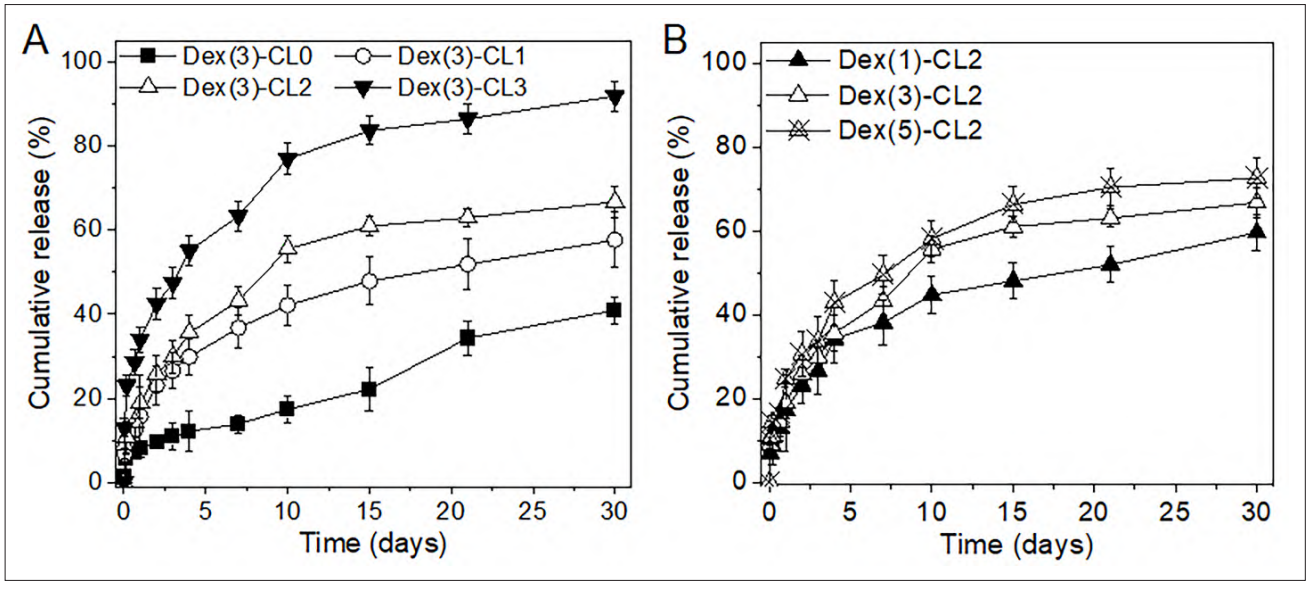


Figure 7. *In vitro* cumulative release profiles of Dex from Dex-CL depots over a 30-day period. (A) Dex release profiles from Dex-CL depots formulated with different polymer inks: CL0, CL1, CL2, and CL3. (B) Dex release profiles from Dex-CL2 depots with varying Dex concentrations (1, 3, and 5 wt%). Note: Molar ratio of L-lactide to ε-caprolactone for CL0 = $C_{100}L_0$, CL1 = $C_{99}L_1$, CL2 = $C_{91}L_9$, and CL3 = $C_{85}L_{15}$. Abbreviations: CL, poly(ε-caprolactone-ran-lactide); Dex, dexamethasone; Dex-CL, dexamethasone-loaded CL.

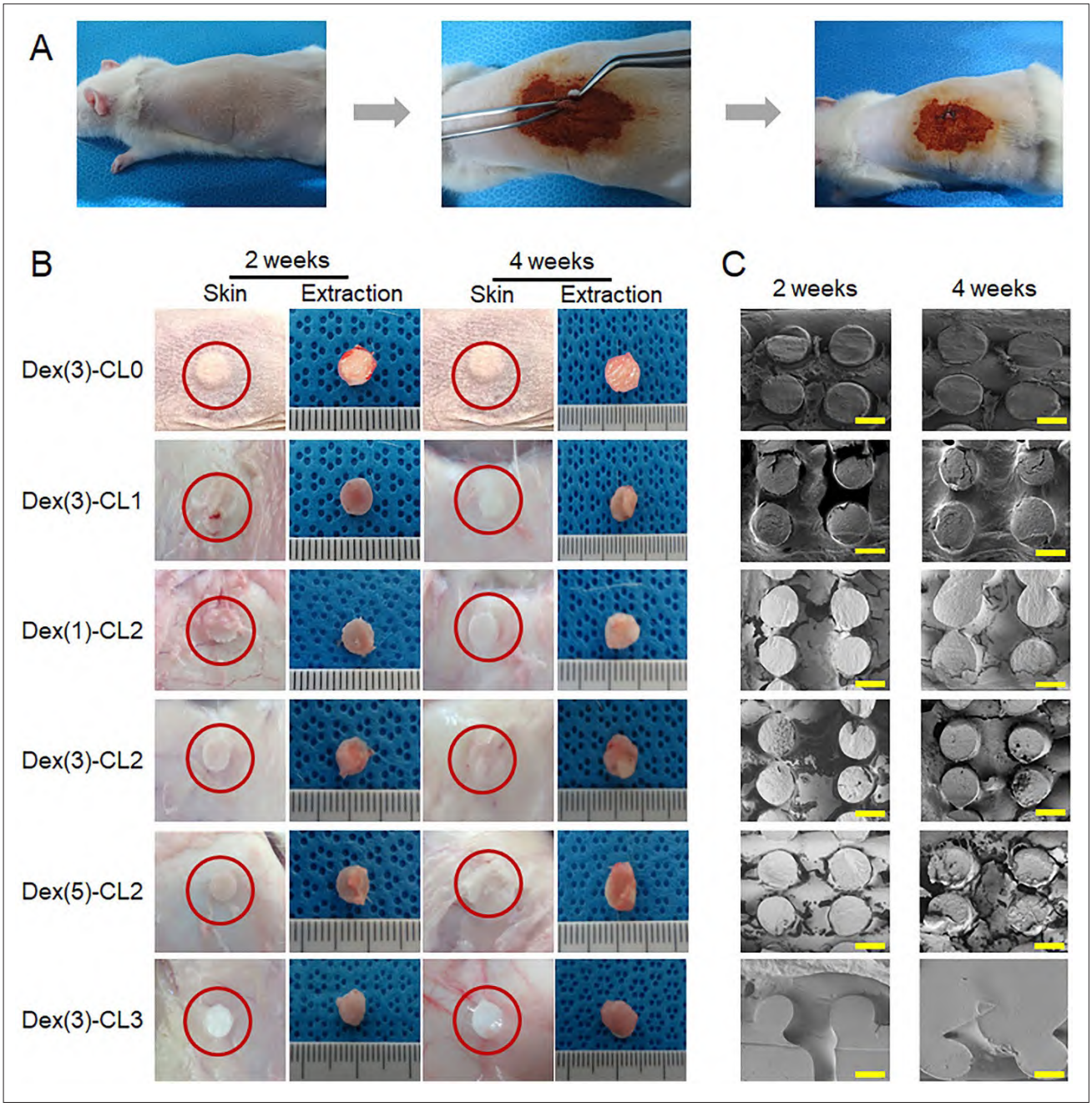


Figure 8. *In vivo* implantation of printed Dex-CL depots. (a) Subcutaneous implantation of Dex-CL depots in Sprague–Dawley rats. (b) Photographs and (c) scanning electron microscopy images (scale bar = 100 μm; magnification = 100×) of the Dex-CL depots on the skin and of the explanted Dex-CL depots at 2 and 4 weeks post-implantation. Abbreviations: CL, poly(ε-caprolactone-ran-lactide); Dex, dexamethasone; Dex-CL, dexamethasone-loaded CL.

respectively. The higher initial release from Dex-CL3 likely reflects enhanced surface diffusion and matrix softening at body temperature, improving drug accessibility at the depot–tissue interface. Although polymer melting alone does not fully account for the burst release, thermally induced matrix swelling appears to accelerate drug diffusion from the outer layers.

Following the initial phase, Dex was steadily released over the subsequent 3 weeks, consistent with a diffusion-dominated mechanism. For Dex-CL2 depots, higher Dex loading concentrations produced proportionally greater initial release, while long-term release rates remained relatively consistent, suggesting that drug loading affects

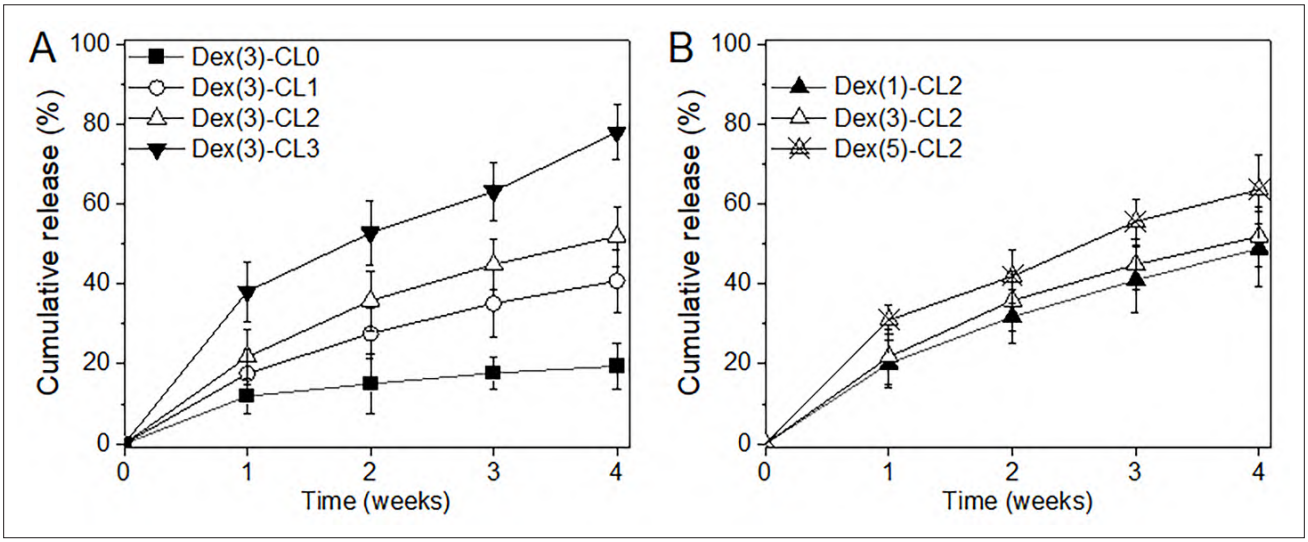


Figure 9. *In vivo* cumulative release of Dex from Dex-CL depots over 4 weeks. (A) Dex release profiles from Dex-CL depots formulated with different polymer inks: CL0, CL1, CL2, and CL3. (b) Dex release profiles from Dex-CL2 depots with varying Dex concentrations. Note: Molar ratio of L-lactide to ε-caprolactone for CL0 = $C_{100}L_0$, CL1 = $C_{99}L_1$, CL2 = $C_{91}L_9$, and CL3 = $C_{85}L_{15}$. Abbreviations: CL, poly(ε-caprolactone-ran-lactide); Dex: dexamethasone; Dex-CL, dexamethasone-loaded CL.

the magnitude of burst release without substantially altering sustained release behavior.

The *in vivo* drug release evaluation of the Dex-CL depots demonstrated that controlled release can be achieved by tuning the T_m of the polymer over the 4-week implantation period. Rheological analysis confirmed that polymers with T_m values closer to body temperature exhibited enhanced chain mobility, supporting the design rationale of this study. However, direct *in vivo* validation of thermal responsiveness was not performed in this work, and future studies will investigate the effects of carrier T_m and other thermal property changes on drug release behavior.

3.10. *In vivo* host response to 3D-printed Dex-CL depots

Biocompatibility and immunomodulatory effects were assessed by subcutaneously implanting the 3D-printed Dex(1)-CL2, Dex(3)-CL2, Dex(5)-CL2, and Dex-CL3 depots in rats. Histological evaluations were performed at 2 and 4 weeks post-implantation using H&E staining and ED1 immunostaining to examine local tissue response and macrophage infiltration.

Histological analysis confirmed that all depot types generally maintained their structural integrity, with host tissue and neovasculature encapsulating the implants. H&E staining showed evidence of new tissue formation in all groups, with only minor histological differences among the depot types (Figure 10A). Notably, Dex-CL depots exhibited enhanced tissue remodeling compared to their Dex-free counterparts, suggesting that sustained Dex release modulated the local tissue microenvironment to support integration.

Among the tested formulations, Dex-CL3 exhibited partial dissolution *in vivo* due to its low T_m (~40°C), leading to accelerated Dex release and deeper tissue infiltration. This was accompanied by a noticeable reduction in inflammatory cell infiltration. However, the thermal softening of Dex-CL3 also contributed to structural collapse, which may limit long-term mechanical stability.

To further evaluate the immune response, ED1 immunostaining was used to detect macrophage infiltration (Figure 10B). ED1-positive cells (red) and DAPI-stained nuclei (blue) were observed along the depot surface and in surrounding tissues across all groups. Quantitative analysis (Figure 10C) revealed that Dex-CL depots induced significantly lower macrophage infiltration. In all groups, macrophage counts peaked at 2 weeks and decreased by Week 4, consistent with the resolution phase of acute inflammation.

Importantly, Dex-CL depots demonstrated a more pronounced decline in ED1-positive cell counts over time, indicating that sustained Dex release effectively attenuated the host immune response. These results highlight the dual functionality of Dex-CL depots in providing both structural support and localized immunomodulation. By fine-tuning Dex release kinetics alongside thermal and mechanical properties, 3D-printed Dex-CL depots present

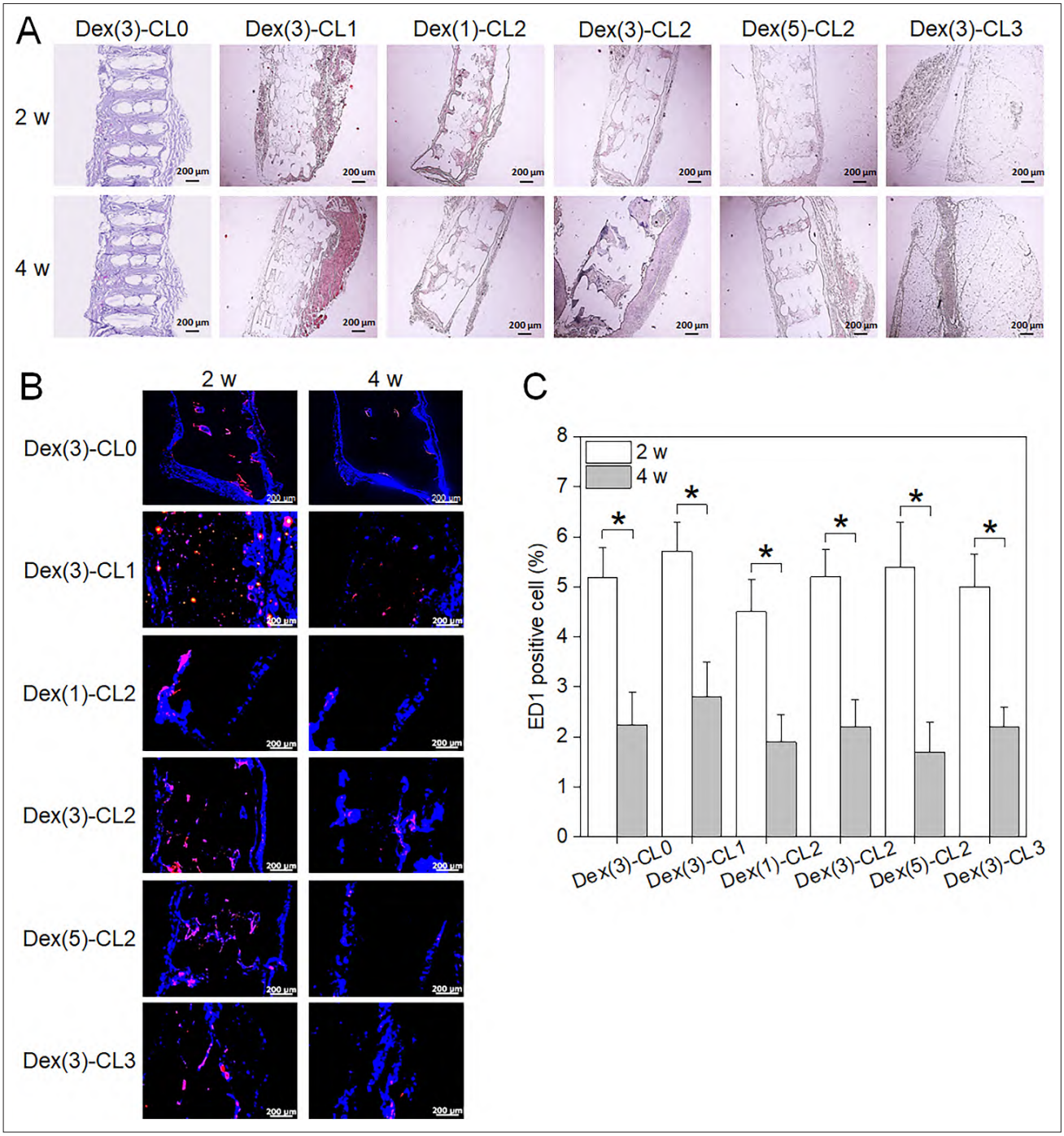


Figure 10. Hematoxylin and eosin (H&E) staining and immunofluorescence ED1 staining of Dex-CL depots explanted at 2 and 4 weeks post-implantation. Representative histological images showing tissue morphological changes over the implantation period: (A) H&E staining, (B) ED1 staining, and (C) quantification of ED1-positive area to assess inflammatory cell infiltration (magnification: 100×; scale bar: 200 μm). Data represent inflammatory ED1 expression. Note: $^*p < 0.05$. Abbreviation: Dex-CL, dexamethasone-loaded CL.

strong potential as subcutaneously implantable drug delivery platforms for long-term therapeutic applications.

4. Discussion

This study investigated the feasibility of using CL copolymer inks as thermally tunable matrices for fabricating implantable drug delivery depots via FDM. Unlike PLA, a commonly used FDM filament that requires high processing temperatures,[22] CL copolymers exhibit controllable melting transitions within a clinically relevant range of 40–60°C. This tunability enables the rational design of depots with controlled degradation and tailored release kinetics, addressing critical needs in localized and personalized drug delivery.[23–27]

Among available printing methods, FDM offers reproducibility, geometric fidelity, and structural stability without the need for solvents or crosslinking. In contrast, semi-solid extrusion allows lower-temperature processing but often requires solvent evaporation or chemical curing, which can limit precision and introduce cytotoxic residues. In this work, CL copolymer inks for FDM were designed to provide a balanced approach, yielding reliable microarchitecture, interconnected porosity, and mechanical robustness suitable for long-term implantation. Furthermore, rheological analysis confirmed that printability was strongly governed by the T_m and viscoelastic properties of the copolymer formulations.

A key consideration in this study was the effect of copolymer composition on microstructural fidelity. High-fidelity depots produced with CL0–CL2 maintained the designed geometry within ±10% accuracy, demonstrating the suitability of these copolymers as reliable printing inks. By contrast, CL3 and, in particular, CL4 exhibited pore collapse and excessive line widening, resulting in reduced structural fidelity. These findings suggest that while dimensional accuracy can be partially optimized through printing conditions, variations in copolymer composition—and the resulting physicochemical differences—play a decisive role in determining the structural fidelity of printed depots.

Beyond microstructural considerations, *in vivo* evaluations of Dex-CL depots confirmed stable and sustained release of Dex over a 4-week period. However, depots fabricated from CL copolymer inks with T_m relatively close to body temperature exhibited greater softening under physiological conditions, leading to accelerated release and reduced predictability. These results imply that melting transitions near physiological temperatures can influence release kinetics by enhancing copolymer chain mobility and swelling.

The substrate platform was maintained at ambient laboratory temperature (23–25°C) without active cooling, while only the enclosed printing chamber surrounding the extrusion nozzle was heated to the designated range of 80–120°C. This configuration ensured that the deposited filaments rapidly solidified upon contact with the cooler substrate, thereby preserving structural fidelity. Notably, chamber temperatures up to 100°C (the optimal printing condition) were substantially lower than the T_m of pure PLA (>160°C), underscoring the rationale for employing CL copolymer inks designed to achieve melt processability at reduced temperatures. The upper limit of 120°C was investigated solely to assess comparative processability and was not used for final DDS fabrication. Importantly, the short residence time of the CL copolymer inks in the heated chamber (3–5 min per unit, maximum 25 min for multi-unit runs) further minimized the risk of drug degradation.

Within this context, Dex was selected as the model drug due to its well-documented thermal stability up to ~200°C,[21] making it highly compatible with the FDM process at ~100°C. However, such conditions may not be appropriate for thermolabile drugs. To address this limitation, CL copolymer ink design strategies—such as adjusting the CL content—can be employed to lower the melting transition and enable printing below 100°C. Through careful compositional tuning, it is anticipated that depots containing moderately heat-sensitive drugs can be fabricated under optimized conditions while preserving drug stability. Although this approach may not extend to highly unstable proteins or peptides, which generally cannot withstand even slight elevations above body temperature, it remains well-suited for a wide range of small-molecule therapeutics, including corticosteroids, anti-inflammatory agents, and thermally stable antibiotics. Future studies will systematically explore these drug classes to broaden the clinical applicability of this platform.

Regarding biocompatibility, the present short-term implantation studies (4 weeks) revealed no significant inflammation or tissue damage, suggesting the safety of Dex-CL depots. Nevertheless, it should be noted that lactide degradation can generate acidic byproducts, which may influence local tissue responses over longer implantation periods.[28] Comprehensive long-term studies will therefore be required to fully establish clinical safety and confirm compatibility for chronic use.

5. Conclusion

This work establishes CL copolymers as versatile polymer inks for FDM-based implantable DDS. By integrating tunable composition, structural fidelity, and degradation behavior, the system enables controlled release of stable

small molecules over clinically relevant timescales. Limitations include the need for direct validation of thermal responsiveness and extension to more thermolabile drugs. Even so, the rational design framework presented here provides a promising foundation for developing 3D-printed depots with customizable release profiles, potentially advancing treatments for chronic inflammation, localized cancer therapy, and other conditions requiring sustained drug delivery. Furthermore, our ongoing studies are exploring advanced implant depot designs incorporating psychotropic drugs and distinct CL copolymer inks. These constructs are intended to enable spatially controlled, sequential drug release, thereby expanding the versatility of CL-based FDM systems.

Acknowledgments

None.

Funding

This study was supported by grants from the National Research Foundation of Korea (NRF), the Science, Technology, Engineering, Arts, and Mathematics (STEAM) Program (RS-2024-00458419), and the Ministry of Small & Medium-sized Enterprises and Startups (20224371).

Conflict of interest

Moon Suk Kim serves as an Editorial Board Member of the journal but was not involved in the editorial or peer-review process for this manuscript, either directly or indirectly. The other authors declare no competing interests.

Author contributions

Conceptualization: Moon Suk Kim, Yun Geun Jeong, Joon Yeong Park, Sang Jin Lee, James J. Yoo
Formal analysis: Moon Suk Kim, Yun Geun Jeong
Investigation: Yun Geun Jeong, Joon Yeong Park, Moon Hee Lim
Methodology: Moon Suk Kim, Yun Geun Jeong, Joon Yeong Park, Sang Jin Lee, James J. Yoo
Writing–original draft: Yun Geun Jeong, Moon Suk Kim
Writing–review & editing: Moon Suk Kim

Ethics approval and consent to participate

All animal experiments were approved by the Institutional Animal Care and Use Committee of Ajou University School of Medicine (Approval No. 2024-0030) and conducted in accordance with institutional ethical guidelines. Six-week-old male Sprague–Dawley (SD) rats (280–300 g) were used to evaluate the *in vivo* biocompatibility and drug release behavior of CL and Dex-CL depots. No experiments involving human subjects were conducted in this study.

Consent for publication

Not applicable.

Availability of data

Data are available from the corresponding author upon reasonable request.

Further disclosure

Part or all of the findings have been presented at the following academic conferences:

1. Poster presentation: Yungeun Jeong (presenter), Joon Yeong Park (co-author), and Moon Suk Kim (corresponding author) at The 12th World Biomaterials Congress (WBC 2024), held from May 26 to 31, 2024, at EXCO, Daegu, Republic of Korea.
2. Poster presentation: Yungeun Jeong (presenter), Joon Yeong Park (co-author), and Moon Suk Kim (corresponding author) at The 2024 KSBM Fall Meeting & Tutorial Symposium, held from November 21 to 23, 2024, at SONO Belle JEJU, Jeju, Republic of Korea.
3. Poster presentation: Yungeun Jeong (presenter), Joon Yeong Park (co-author), and Moon Suk Kim (corresponding author) at The 25th Annual Conference of the Korean Tissue Engineering and Regenerative Medicine Society (KTERMS 2025), held from May 2 to 3, 2025, at CHA Bio Complex, Seongnam, Republic of Korea.
4. Poster presentation: Yungeun Jeong (presenter), Joon Yeong Park (co-author), and Moon Suk Kim (corresponding author) at The 36th International Symposium on Polymer Analysis and Characterization (ISPAC 2025), held from June 23 to 27, 2025, at Nanyang Technological University, Singapore.
5. Poster presentation: Joon Yeong Park (presenter) and Moon Suk Kim (corresponding author) at the 6th World Congress of the Tissue Engineering and Regenerative Medicine International Society (TERMIS2021) (Note: some of the printing-related data were submitted to the World Congress, but the presentation did not take place due to the COVID-19 pandemic in 2021.)

References

1. Sadia M, Arafat B, Ahmed W, Forbes RT, Alhnan MA, 2018, Channelled tablets: An innovative approach to accelerating drug release from 3D printed tablets. *J Control Release*, 269:355–363.
doi: 10.1016/j.jconrel.2017.11.022

2. Melocchi A, Uboldi M, Maroni A, Foppoli A, Palugan L, Zema L, Gazzaniga A, 2020, 3D printing by fused deposition modeling of single- and multi-compartment hollow systems for oral delivery: A review. *Int J Pharm*, 579:119155.
doi: 10.1016/j.ijpharm.2020.119155

3. Yuan X, Wang Z, Che L, Lv X, Xu J, Shan S, Guo B, 2024, Recent developments and challenges of 3D bioprinting technologies. *Int J Bioprinting*, 10(2):1752.
doi: 10.36922/ijb.1752

4. Jeong YG, Yoo JJ, Lee SJ, Kim MS, 2024, 3D digital light process bioprinting: Cutting-edge platforms for resolution of organ fabrication. *Mater Today Bio*, 26:101284.
doi: 10.1016/j.mtbio.2024.101284

5. Ivorra-Martinez J, Ferrer I, Aguado R, Delgado-Aguilar M, Garcia-Romeu ML, Boronat T, 2024, Development of P(3HB-co-3HHx) nanohydroxyapatite (nHA) composites for scaffolds manufacturing by means of fused deposition modeling. *Int J Bioprinting*, 10(1):0156.
doi: 10.36922/ijb.0156

6. Ji YB, Park JY, Kang Y, Lee S, Ju HJ, Choi S, Lee BY, Kim MS, 2021, Scaffold printing using biodegradable poly(1,4-butylene carbonate) ink: Printability, *in vivo* physicochemical properties, and biocompatibility. *Mater Today Bio*, 12:100129.
doi: 10.1016/j.mtbio.2021.100129

7. Kwon DY, Park JY, Lee BY, Kim MS, 2020, Comparison of scaffolds fabricated via 3D printing and salt leaching: *In vivo* imaging, biodegradation, and inflammation. *Polymers*, 12(10):2210.
doi: 10.3390/polym12102210

8. Hou Y, Liu X, Wang X, Ji S, Gu Q, 2024, The application of 3D bioprinting technology in liver manufacturing: Progress, challenges, and prospects. *Int J Bioprinting*, 10(5):3819.
doi: 10.36922/ijb.3819

9. Balla E, Daniilidis V, Karlioti G, Kalamas T, Stefanidou M, Bikiaris ND, Vlachopoulos A, Koumentakou I, Bikiaris DN, 2021, Poly(lactic acid): A versatile biobased polymer for the future with multifunctional properties—From monomer synthesis, polymerization techniques and molecular weight increase to PLA applications. *Polymers*, 13(11):1822.
doi: 10.3390/polym13111822

10. Park JH, Park SH, Park JY, Ju HJ, Ji YB, Kim JH, Min BH, Kim MS, 2020, Preparation and characterization of biodegradable and hemocompatible copolymers. *React Funct Polym*, 146:104373.
doi: 10.1016/j.reactfunctpolym.2019.104373

11. Park JH, Lee BK, Park SH, Kim MG, Lee JW, Lee HY, Lee HB, Kim JH, Kim MS, 2017, Preparation of biodegradable and elastic poly(ε-caprolactone-co-lactide) copolymers and evaluation as a localized and sustained drug delivery carrier. *Int J Mol Sci*, 18(3):671.
doi: 10.3390/ijms18030671

12. Park JY, Park SH, Ju HJ, Ji YB, Yun HW, Min BH, Kim MS, 2020, Preparation of a cross-linked cartilage acellular matrix-poly(caprolactone-ran-lactide-ran-glycolide) film and testing its feasibility as an anti-adhesive film. *Mater Sci Eng C*, 117:111283.
doi: 10.1016/j.msec.2020.111283

13. Shi Y, Wang L, Sun L, Qiu Z, Qu X, Dang J, Zhang Z, He J, Fan H, 2023, Melt electrospinning writing PCL scaffolds after alkaline modification with outstanding cytocompatibility and osteoinduction. *Int J Bioprinting*, 9(6):1071.
doi: 10.36922/ijb.1071

14. Slavković V, Hanželič B, Plesec V, Milenković S, Harih G, 2024, Thermo mechanical behavior and strain rate sensitivity of 3D printed polylactic acid (PLA) below glass transition temperature. *Polymers*, 16(11):1526.
doi: 10.3390/polym16111526

15. Chen XB, Anvari-Yazdi AF, Duan X, Zimmerling A, Gharraei R, Sharma NK, Sweilem S, Ning L, 2023, Biomaterials / polymer inks and extrusion bioprinting. *Bioact Mater*, 28:511–536.
doi: 10.1016/j.bioactmat.2023.06.006

16. Hyun H, Kim MS, Jeong SC, Kim YH, Lee SY, Lee HB, Khang G, 2006, Preparation of diblock copolymers consisting of methoxy poly(ethylene glycol) and poly(ε-caprolactone)/poly(L-lactide) and their degradation property. *Polym Eng Sci*, 46(7): 1004–1011.
doi: 10.1002/pen.20581

17. Xu F, Rui S, Yang C, Jiang X, Wu W, Tang X, Armstrong DG, Ma Y, Deng W, 2023, Bioprinting technology for the management of diabetic foot disease: Emerging applications, challenges, and prospects. *Int J Bioprinting*, 9(6):0142.
doi: 10.36922/ijb.0142

18. Popescu D, Stochioiu C, Baciu F, Iacob MC, 2023, 3D-printed polycaprolactone mechanical characterization and suitability assessment for producing wrist–hand orthoses. *Polymers*, 15(3):576.
doi: 10.3390/polym15030576

19. Park HS, Park JH, Oh M, Yu K, 2024, Advancements in 3D bioprinting for precision medicine: Enhancing patient-derived organoids and extracellular vesicle applications in inflammatory diseases. *Int J Bioprinting*, 10(5):4054.
doi: 10.36922/ijb.4054

20. Rahul VG, Wilson J, Thomas LV, Nair PD, 2022, Assessing the 3D printability of an elastomeric poly(caprolactone-co-lactide) copolymer as a potential material for 3D printing tracheal scaffolds. *ACS Omega*, 7(8):7006–7016.
doi: 10.1021/acsomega.1c06679

21. Domsta V, Boralewski T, Ulbricht M, Schick P, Krause J, Seidlitz A, 2024, Stability of dexamethasone during hot-melt extrusion of filaments based on Eudragit® RS, ethyl cellulose and polyethylene oxide. *Int J Pharm*, 8:100263.
doi: 10.1016/j.ijpx.2024.100263

22. Mazur J, Sobczak P, Panasiewicz M, et al., 2025, Mechanical properties and biodegradability of samples obtained by 3D printing using FDM technology from PLA filament with by-products. *Sci Rep*, 15:5847.
doi: 10.1038/s41598-025-89984-0

23. Botlhoko OJ, Ramontja J, Ray SS, 2018, A new insight into morphological, thermal, and mechanical properties of melt-processed polylactide/poly(ε-caprolactone) blends. *Polym Degrad Stab*, 154:84–95.
doi: 10.1016/j.polymdegradstab.2018.05.025

24. Navarro-Baena I, Sessini V, Dominici F, Torre L, Kenny JM, Peponi L, 2016, Design of biodegradable blends based on PLA and PCL: From morphological, thermal and mechanical studies to shape memory behavior. *Polym Degrad Stab*, 132:97–108.
doi: 10.1016/j.polymdegradstab.2016.03.037

25. Urquijo J, Guerrica-Echevarría G, Eguiazábal JI, 2015, Melt processed PLA/PCL blends: Effect of processing method on phase structure, morphology, and mechanical properties. *J Appl Polym Sci*, 132(29):42641.
doi: 10.1002/app.42641

26. Gao H, Li J, Li Z, Li Y, Wang X, Jiang J, Li Q, 2023, Enhancing interfacial interaction of immiscible PCL/PLA blends by in-situ crosslinking to improve the foamability. *Polym Test*, 124:108063.
doi: 10.1016/j.polymertesting.2023.108063

27. Cerveto T, Denis L, Stoops M, Lechanteur A, Choisnard L, 2024, The promising role of semi-solid extrusion technology in custom drug formulation for pediatric medicine. *Int J Bioprinting*, 10(6):4063.
doi: 10.18063/ijb.v10i6.4063

28. Wang X, Liu D, 2024, Macrophage polarization: A novel target and strategy for pathological scarring. *Tissue Eng Regen Med*, 21:1109–1124.
doi: 10.1007/s13770-024-00509-7

ACCSCIENCE PUBLISHING

International Journal of Bioprinting

RESEARCH ARTICLE

Personalized 3D-printed tantalum-coated titanium alloy pelvic reconstruction prosthesis for complex pelvic defects: A prospective randomized controlled trial

Zhaoyang Ran[1,2,3†], Boran Pang[1,2,3†], Yulin Tian[4], Dinghao Luo[1,2,3], Junxiang Wu[1,2,3], Lei Wang[1,2,3], Kai Xie[1,2,3], Jingke Fu[1,2,3], Liang Deng[1,2,3*], Wei Li[4*], and Yongqiang Hao[1,2,3*]

[1]Shanghai Key Laboratory of Orthopaedic Implants, Department of Orthopaedic Surgery, Shanghai Ninth People's Hospital, Shanghai Jiao Tong University School of Medicine, Shanghai, China

[2]Clinical and Translational Research Center for 3D Printing Technology, Shanghai Ninth People's Hospital, Shanghai Jiao Tong University School of Medicine, Shanghai, China

[3]Shanghai Engineering Research Center of Innovative Orthopaedic Instruments and Personalized Medicine, Shanghai Ninth People's Hospital, Shanghai Jiao Tong University School of Medicine, Shanghai, China

[4]School of Materials Science and Engineering, Shanghai Jiao Tong University, Shanghai, China

[†]These authors contributed equally to this work.

***Corresponding authors:**
Yongqiang Hao (hyq_9hospital@hotmail.com)

Wei Li (weilee@sjtu.edu.cn)

Liang Deng (676471883@qq.com)

Citation: Ran Z, Pang B, Tian Y, *et al.* Personalized 3D-printed tantalum-coated titanium alloy pelvic reconstruction prosthesis for complex pelvic defects: A prospective randomized controlled trial. *Int J Bioprint.* 2025;11(5):371-384. doi: 10.36922/IJB025310312

Received: July 7, 2025
Revised: August 2, 2025
Accepted: August 21, 2025
Published online: August 25, 2025

Copyright: © 2025 Author(s). This is an Open Access article distributed under the terms of the Creative Commons Attribution License, permitting distribution and reproduction in any medium, provided the original work is properly cited.

Publisher's Note: AccScience Publishing remains neutral with regard to jurisdictional claims in published maps and institutional affiliations.

Abstract

The functional reconstruction of complex pelvic defects remains a global challenge. To address this, a personalized 3D-printed tantalum-coated titanium alloy pelvic reconstruction prosthesis was independently developed to enhance the osteogenic activity of existing titanium alloy prostheses. This prospective randomized controlled trial evaluated its efficacy, safety, and early clinical outcomes in 21 patients with complex pelvic defects. The patients were randomly assigned to an experimental group (11 cases of tantalum-coated prostheses) or a control group (10 cases of uncoated prostheses). The coated prostheses were designed using preoperative imaging data and coated with an approximately 15-μm tantalum coating through plasma immersion ion implantation. After post-treatment and sterilization, the prostheses were implanted during surgery. Operation time, intraoperative blood loss, and laboratory indices were recorded and compared between groups. Postoperative follow-up assessments included imaging assessments, complication monitoring, bone ingrowth analysis at the prosthesis–bone interface, and functional evaluation with the Harris Hip Score. All 21 surgeries achieved primary wound healing without early complications. Mean follow-up time was 15.1 ± 7.1 months. There was no significant difference in operation time, intraoperative blood loss, and abnormal laboratory indices. The prosthesis shape matched well with the bone defects, ensuring good stability. In the experimental group, one periprosthetic infection and one artificial femoral head dislocation occurred, compared to two periprosthetic infections and one dislocation in the control group. At final follow-up, the experimental group demonstrated significantly higher Harris Hip Scores ($p < 0.01$) and bone ingrowth rates (90.9% vs. 30.0% in control; $p < 0.001$). In conclusion, the personalized 3D-printed tantalum-coated titanium alloy pelvic

reconstruction prosthesis effectively promotes bone ingrowth, enhances prosthesis stability, and improves lower limb function, representing an effective approach for reconstructing complex pelvic defects.

Keywords: 3D printing; Complex pelvic defect; Pelvic reconstruction prosthesis; Tantalum coating; Titanium alloy

1. Introduction

Complex pelvic defects caused by trauma, tumor resection, inflammation, or infection remain a global orthopedic challenge due to irregular morphology, extensive bone loss, and the high mechanical demands of pelvic reconstruction. While autologous and allogeneic bone grafts serve as conventional clinical solutions for bone defect repair, they exhibit inherent limitations, including inadequate initial mechanical strength, limited donor availability, risks of disease transmission, and immunological rejection.[1–3]

Metal implants have gained attention as alternative reconstruction materials due to their abundance, favorable mechanical properties, and corrosion resistance. However, early-generation metal prostheses, such as saddle-shaped prostheses and ice-cream cone prostheses, demonstrated suboptimal clinical outcomes, primarily limited by conventional design concepts and manufacturing techniques.[4] Recent advancements in computer-aided design and metal additive manufacturing (3D printing) have enabled the development of patient-specific prostheses that simultaneously satisfy both biomechanical requirements and anatomical compatibility for pelvic reconstruction. These technological innovations have substantially improved the precision of defect restoration while maintaining essential load-bearing capacities, thereby advancing clinical management of complex pelvic defects.

Since 2014, pioneering clinical implementation of metal 3D printing technology for fabricating patient-specific pelvic prostheses has been reported.[5,6] A titanium alloy pelvic prosthesis featuring an anatomically adaptive design and surface structure optimization was developed through additive manufacturing. Animal experiments confirmed that the diamond-like porous structure facilitates trabecular bone ingrowth within 3–6 months post-implantation, achieving long-term osseointegration and mechanical stability.[5] Furthermore, a retrospective clinical study conducted by our group revealed that personalized 3D-printed titanium alloy pelvic prostheses for limb-salvage reconstruction in pelvic tumor patients yielded favorable early postoperative outcomes. The intervention was associated with reduced complication rates, satisfactory short-term functional recovery, and promising prosthesis survival rates.[6]

Osseointegration at the prosthesis–host bone interface is a fundamental determinant of long-term implant survival. Accelerating this interfacial osseointegration through material innovation and structural optimization has become a shared objective for both materials scientists and clinicians. Rapid prosthesis–bone interface integration offers two critical clinical advantages: (i) expedited achievement of biological fixation, thereby reducing dependence on mechanical fixation (primarily screw-based stabilization) during the early postoperative phase and minimizing stress-related failure risks; (ii) decreased susceptibility to periprosthetic infection. However, Ti-6Al-4V alloy is inherently bioinert and lacks osteoinductive capacity at the bone–implant interface. Current limitations persist regarding the insufficient osseointegration depth within porous titanium structures fabricated via 3D printing, with bone ingrowth typically restricted to superficial regions of the porous matrix.[7,8] These biological constraints highlight the urgent need for advanced modifications to existing 3D-printed pelvic prostheses. Enhancing both the velocity and depth of bone–implant interface integration represents a crucial research direction with significant clinical implications, particularly for improving prosthesis longevity and reducing revision surgery requirements in complex pelvic reconstructions. Therefore, there is an urgent need to develop a surface-modified titanium alloy prosthesis that simultaneously satisfies mechanical-performance requirements and actively promotes osseointegration.

Tantalum exhibits moderate hardness, exceptional wear resistance, and chemical inertness, conferring excellent biocompatibility and corrosion resistance.[9] Notably, tantalum demonstrates lower bacterial adhesion propensity and enhanced osteoinduction and bone regeneration compared to titanium alloys, making it a promising functional material for orthopedic implants.[10,11] *In vitro* studies by Guo *et al.*[12] demonstrated tantalum's capacity to enhance the proliferation, adhesion, and osteogenic differentiation of bone marrow mesenchymal stem cells. Corresponding *in vivo* evaluations revealed that tantalum scaffolds significantly promote new bone formation and osseointegration.

However, clinical application of bulk tantalum implants faces substantial limitations. The high density (16.6 g/cm^3) of tantalum increases prosthesis weight, particularly problematic for large-scale bone defects, while elevating manufacturing costs. Furthermore, pure tantalum's elastic modulus (180 GPa) dramatically exceeds that of human bone (10–30 GPa), predisposing implants to stress-shielding effects.

Surface tantalum coating technology emerges as an effective strategy to circumvent these limitations while preserving tantalum's bioactivity. This approach significantly reduces implant weight, production costs, and elastic modulus mismatch. Plasma immersion ion implantation (PIII) is a versatile surface modification technique with applications in precision manufacturing, aerospace, and biomedical engineering.[13] The PIII process utilizes active screen and hollow cathode coupling to generate high-density plasma, enabling bombardment of tantalum plasma onto heated substrate surfaces. Subsequent adsorption and diffusion processes form uniform surface alloy layers.[14] A key advantage of PIII is the complete immersion of substrates in plasma, enabling uniform coating deposition within complex geometries, including porous structures, making PIII particularly suitable for surface alloying of geometrically complex 3D-printed components.[15] The PIII technique induces metallurgical bonding between implanted ions and substrate particles, creating novel phase structures that preserve mechanical properties while enhancing surface characteristics. This technology achieves exceptional coating efficiency, cost-effectiveness, and environmental sustainability compared to conventional coating methods. These attributes position PIII as a transformative approach for developing next-generation tantalum-coated orthopedic implants with optimized biomechanical compatibility and enhanced osseointegration potential.

Therefore, this study developed a novel 3D-printed pelvic reconstruction prosthesis integrating porous titanium alloy substrates with PIII-derived tantalum coatings. This dual-phase design synergistically combines the structural–mechanical compatibility of porous titanium frameworks with the bioactive advantages of tantalum surface modifications. Through systematic clinical investigations, this study evaluated the safety profile and therapeutic efficacy of these customized prostheses in managing complex pelvic defects, demonstrating their potential to address both biomechanical requirements and biological integration challenges. The findings provide valuable insights into the development of functionally enhanced orthopedic solutions for critical bone defects.

2. Methods

2.1. Patient enrollment

This study was approved by the Ethics Committee of Shanghai Ninth People's Hospital affiliated to Shanghai Jiao Tong University School of Medicine (approval no.: SH9H-2020-T206-1). The clinical prospective randomized controlled trial was registered at the Chinese Clinical Trial Registry (www.chictr.org.cn) on September 25, 2020 (registration no.: ChiCTR2000037020). Patients were enrolled according to predefined inclusion and exclusion criteria. This study was conducted in accordance with the Consolidated Standards of Reporting Trials (CONSORT) guidelines.[16]

The inclusion criteria included:

(i) Chinese citizens aged 16–85 years;

(ii) Good systemic condition with surgical tolerance;

(iii) Absence of active infectious diseases (e.g., hepatitis A/B/C and tuberculosis);

(iv) Complex pelvic defects requiring prosthetic replacement surgery due to tumors, revision needs, or other indications;

(v) Normal hematological parameters and hepatic/renal function;

(vi) No participation in other clinical trials within three months;

(vii) Willingness to provide written informed consent; and

(viii) No contraindications for implantation.

The exclusion criteria included:

(i) Systemic or localized active infections;

(ii) Failure to undergo hemipelvic replacement surgery at our institution;

(iii) Incurable comorbidities with life expectancy ≤2 years;

(iv) Allergies to implant materials;

(v) Inability to accept innovative techniques in this trial; and

(vi) Poor compliance with follow-up or protocol requirements.

This randomized controlled trial enrolled 21 patients (10 males, 11 females) with complex pelvic defects who met the rigorous inclusion criteria. An independent third-party statistician, blinded to study implementation and data analysis, generated the 1:1 allocation sequence

using SAS® software (SAS, United States [US]) with block randomization methodology. Allocation concealment was ensured through sequentially numbered, opaque, sealed envelopes (SNOSE) containing group assignment information. Following completion of enrollment procedures and informed consent documentation, a designated independent staff member sequentially opened these sealed envelopes to disclose group assignments according to the predetermined randomization sequence, with participant blinding being rigorously maintained throughout this allocation process. Patients in the control group underwent pelvic defect reconstruction using personalized 3D-printed titanium alloy prostheses, while those in the experimental group received reconstruction with 3D-printed titanium prostheses with tantalum-coated surfaces. All surgical procedures were performed at our institution between September 2020 and August 2023. Participants had a mean age of 51.9 ± 13.3 years (range: 21–70 years), and all provided written informed consent. Detailed demographic and clinical characteristics are presented in Table 1.

2.2. Prothesis design

Following admission, all patients underwent preoperative evaluations, including complete blood count, coagulation profile, biochemical panels, and ancillary tests to assess surgical fitness. Standard radiographic assessment comprised pelvic X-ray and thin-slice pelvic computed tomography (CT) scans. Tumor patients received additional diagnostic workups: contrast-enhanced pelvic magnetic resonance imaging, chest CT, whole-body bone scintigraphy, and pathological examinations to evaluate tumor progression and metastasis, facilitating clinical decision-making regarding therapeutic strategies. Pelvic defect parameters were determined through 3D reconstruction of CT data using Mimics Medical 20.0 software (Materialise, Belgium; Figure 1), including defect area quantification and characterization of the acetabular center, dimensions, and orientation. Prosthetic design was executed in Unigraphics NX software (Siemens Digital Industries Software, USA), incorporating guidance positioning screws and locking screw channels within the implant structure. Bone–implant interface optimization was performed with porous trabecular structures (pore size: 600–800 μm, porosity: 60–80%). The finalized prosthetic model was exported in STL format and manufactured via electron beam melting additive manufacturing using Ti-6Al-4V titanium alloy powder.

The surface coating of prostheses was prepared using PIII technology, where tantalum was deposited via a high-energy plasma surface alloying system. Prior to coating, the prostheses were ultrasonically cleaned in anhydrous ethanol and deionized water, followed by drying. During this process, the cathode assembly consisted of the 3D-printed prosthesis combined with a tantalum mesh and rods, functioning as an active screen plasma device. The argon pressure was maintained at 22.5 Pa with other parameters adjusted accordingly. Throughout the coating process, the temperature remained more than 1000˚C for approximately 4 h. Subsequently, the vacuum pump was deactivated, and high-purity argon was introduced into the chamber to achieve rapid cooling to ambient temperature. Finally, the prostheses underwent 5-min ultrasonic cleaning in anhydrous ethanol, followed by standard sterilization protocols prior to surgical implantation. The surface morphology of the coated prostheses was examined using a high-resolution analytical scanning electron microscope (MIRA3, TESCAN, Czech Republic) at various magnifications, with elemental composition analysis performed by energy dispersive X-ray spectroscopy (EDS). Coating adhesion strength was evaluated using a micro-scratch tester (MFT-4000, Huahui, China) with a constant loading rate of 5 N/min.

2.3. Surgical process

Following general anesthesia induction, patients were positioned in the lateral floating orientation with the affected side elevated. The torso and unaffected limbs were immobilized on the operating table, followed by standard antiseptic preparation and draping. A classical ilioinguinal incision extending from the pubis to the sacroiliac joint was created, originating at the posterior superior iliac spine, coursing anteriorly along the iliac crest to the anterior superior iliac spine, then turning medially parallel to the inguinal ligament toward the lateral border of the pubic symphysis, with supplementary extensions

Table 1. Demographic data of the patients

Parameter	Experimental group (n = 11)	Control group (n = 10)	p-value
Gender			>0.05
Male	5 (45.5%)	5 (50%)	
Female	6 (54.5%)	5 (50%)	
Age (years)	47.9±13.6	56.2±11.4	>0.05

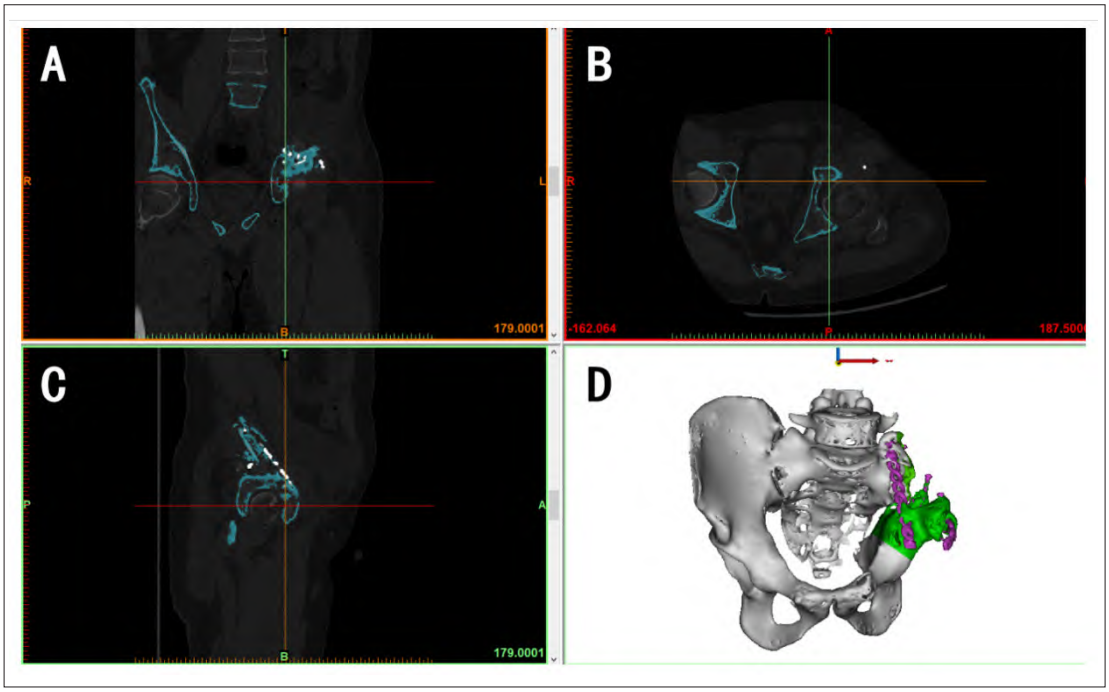


Figure 1. Three-dimensional pelvic model reconstruction utilizing patient computed tomography (CT) data. (A) CT coronal view. (B) CT axial view. (C) CT sagittal view. (D) 3D-reconstructed pelvic model.

as required. Layered dissection of skin and soft tissues exposed the osteotomy site, enabling precise implantation of the customized 3D-printed pelvic prosthesis secured through conventional and locking screws via pre-designed screw channels, supplemented by bone cement augmentation at the acetabular interface. Intraoperative fluoroscopy confirmed proper prosthesis alignment. The surgical site was irrigated, a closed suction drainage system was placed, and closure was achieved through layered fascial approximation (Figure 2). Operative duration and intraoperative blood loss were systematically recorded.

2.4. Postoperative management

Patients were maintained on strict bed rest with continuous vital sign monitoring. Affected limbs were immobilized using anti-rotation boots for 14 days. Surgical drains were removed when daily output fell below 50 mL. Thromboembolism prophylaxis included daily compression stockings. Prophylactic third-generation cephalosporins were administered according to institutional protocols. Hematological monitoring (complete blood count, coagulation profiles, and hepatic/renal function) was performed on postoperative days 1, 7, and 14, with laboratory deviations >50% from preoperative baselines flagged as abnormal. Clinical significance was assessed in the context of surgical blood loss or wound infection for parameters such as erythrocyte/leukocyte counts. Dietary intake was gradually resumed following bowel function recovery. Pelvic radiography and CT scans were conducted on postoperative day 14. Patients meeting discharge criteria (afebrile status, wound stability, and normalized inflammatory markers) were discharged with customized rehabilitation protocols. Progressive hip joint functional training was initiated at 2 months postoperatively.

2.5. Follow-up

All patients underwent regular postoperative follow-up consisting of clinical consultations, physical examinations, pelvic radiography, CT scans, and lower extremity functional assessments. Safety evaluations included monitoring of laboratory parameters (complete blood count, hepatic/renal function, and coagulation profiles); detection of mechanical complications (prosthesis loosening, dislocation, and periprosthetic fractures); and identification of non-mechanical complications (periprosthetic infections, surgical site infections, and systemic infections). Mechanical complications were radiologically assessed through pelvic X-ray and CT imaging, while non-mechanical complications were evaluated using combined laboratory and imaging data. Physicians conducted comprehensive assessments through medical history review and physical examination.

Lower extremity functionality was quantified using the Harris Hip Score system. Osseointegration

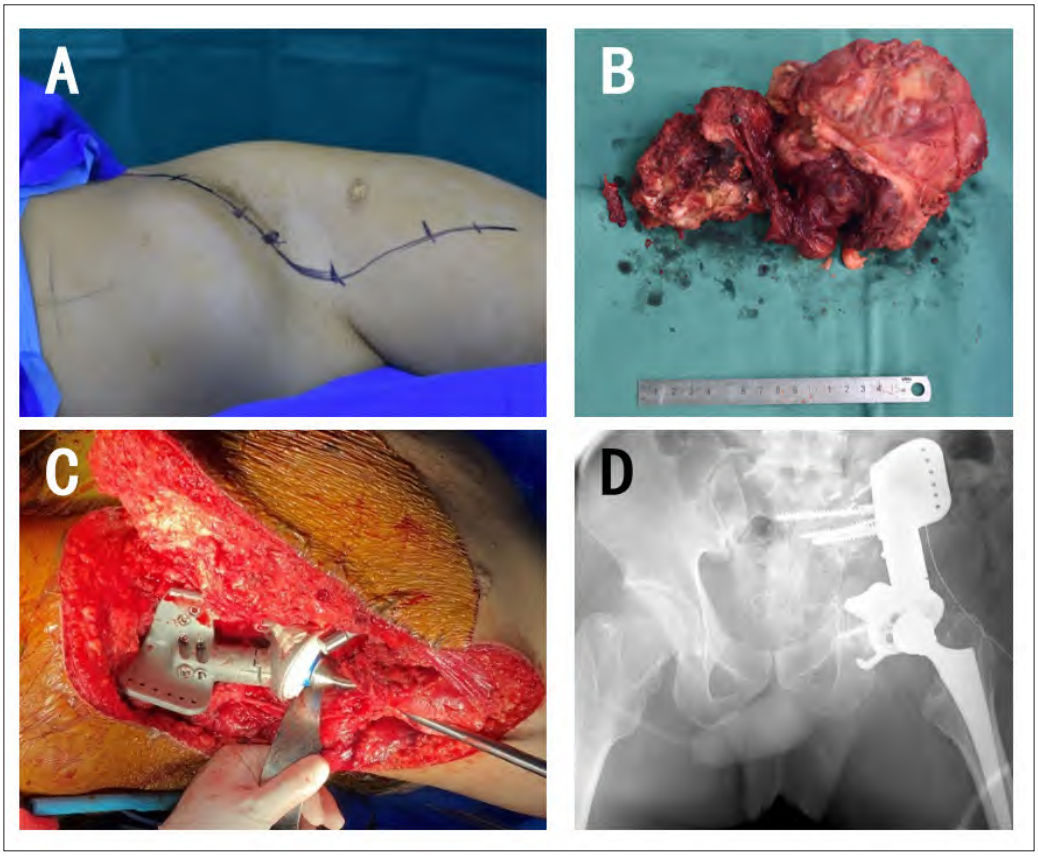


Figure 2. Limb salvage surgery for pelvic tumors. (A) Incision. (B) Pelvic tumor resection. (C) Personalized 3D-printed prosthesis implantation. (D) Intraoperative fluoroscopy of the prosthesis.

at the prosthesis–bone interface was analyzed through 0.625-mm-thin-slice CT reconstructions during final follow-up, with bone ingrowth criteria defined as:

- Excellent: Trabecular bone ingrowth >80% at perpendicular prosthesis–bone interface.
- Good: Partial trabecular integration (20–80%).
- Fair: Minimal ingrowth (0–20%).
- Poor: No detectable osseous incorporation.

All postoperative CT datasets were anonymized by an independent technician who removed patient identifiers and group labels, replacing them with unique randomized codes. All imaging assessments underwent dual independent evaluation by two senior orthopedic surgeons. They were both blinded to group allocation. Final grading determinations were achieved through consensus evaluation, thereby ensuring assessment reliability within the study's methodological constraints. Clinical classifications were determined through consensus review, integrating radiographic findings, physical examination data, and patient-reported functional outcomes.

2.6. Statistical analysis

Statistical analyses were conducted using SPSS version 29.0 software (IBM, US). Continuous variables are presented as means ± standard deviations and were compared via independent *t*-tests. Repeated-measures ANOVA was applied to compare outcomes at different time points. Categorical data are expressed as percentages (%) and were analyzed via the Chi-square test. Differences between groups were considered statistically significant at $p<0.05$.

3. Results

The surface morphology of personalized 3D-printed pelvic prostheses with tantalum coating is shown in Figure 3. Low-magnification scanning electron microscopy (SEM) images confirmed well-bonded tantalum coatings prepared through PIII technology, demonstrating no visible defects such as cracks or peeling. High-magnification SEM observations revealed numerous honeycomb-like microporous structures on the coating surface, with these fine pores increasing surface roughness to facilitate cellular adhesion and promote early osseointegration at the prosthesis–bone interface. EDS analysis further indicated

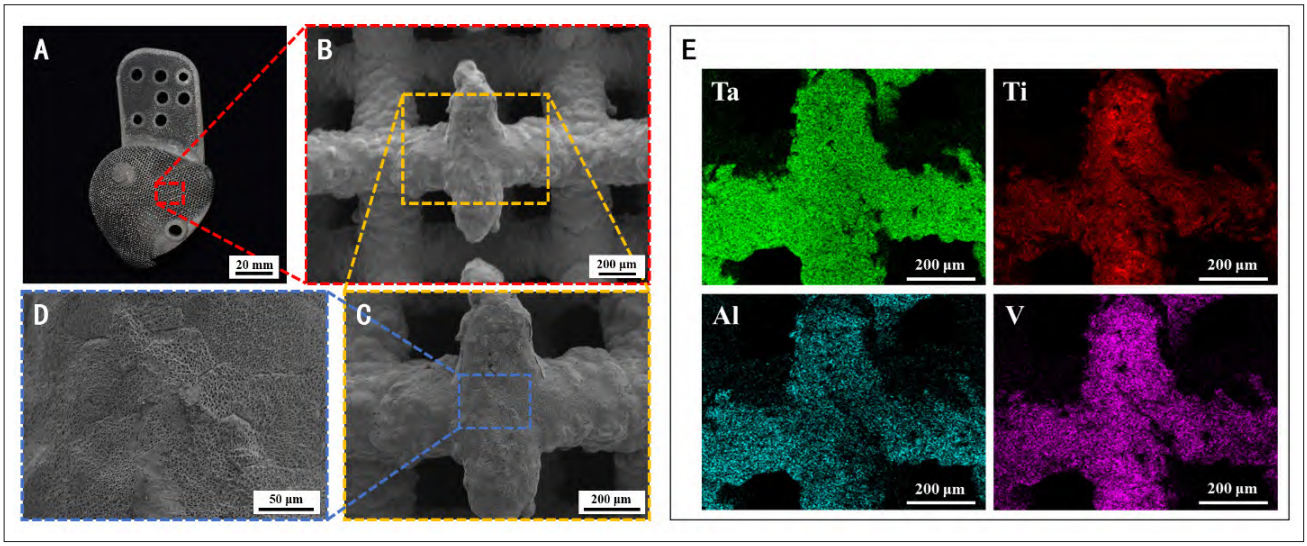


Figure 3. Macro/micromorphology and energy dispersive X-ray spectroscopy (EDS) analysis of a tantalum-coated prosthesis. (A) Macroscopic view of a tantalum-coated prosthesis (scale bar: 20 mm; magnification: 1×). (B–D) Scanning electron microscopy images at different magnifications: (B) magnification: 100× (scale bar: 200 μm), (C) magnification: 250× (scale bar: 200 μm), and (D) magnification: 1000× (scale bar: 50 μm). (E) EDS analysis (scale bar: 200 μm; magnification: 250×).

uniformly distributed high tantalum content across the coating surface, confirming the homogeneous nature of the prepared coating and its potential to enhance tantalum's osteogenic biological functions. Scratch testing revealed an adhesion strength of 123 MPa for the PIII-deposited tantalum coating, indicating robust bonding between the coating and the substrate.

Figure 4 illustrates the complete workflow encompassing personalized prosthesis design, manufacturing, implantation, and postoperative follow-up. In accordance with established inclusion/exclusion criteria, 21 patients with complex pelvic defects were enrolled, assiging to an experimental group (n = 11; 5 males [45.5%] and 6 females [54.5%]; mean age: 47.9 ± 13.6 years) or a control group (n = 10; 5 males [50.0%] and 5 females [50.0%]; mean age: 56.2 ± 11.4 years), with no significant differences in gender distribution or age between groups ($p > 0.05$), as detailed in Table 1.

All 21 participants successfully underwent pelvic defect reconstruction, with the experimental group demonstrating a mean operative duration of 306.6 ± 118.7 min and an intraoperative blood loss of 1886 ± 854 mL, compared to 297.1 ± 30.4 min and 2810 ± 1524 mL in controls. No significant differences were observed in operative duration or hemorrhage volume ($p > 0.05$), confirming the comparable intraoperative safety profile of tantalum-coated prostheses.

Safety assessments of tantalum-coated prostheses were conducted through hematological tests, hepatic/renal function, and coagulation profiles on postoperative day 14, revealing no significant differences in abnormal laboratory parameters between the experimental and control groups ($p > 0.05$). Prosthesis-related complications included one incision infection and one prosthetic femoral head dislocation in the experimental group, compared to two incision infections and one dislocation in controls. All three cases of incision infections (one experimental and two controls) resolved completely with antibiotic therapy, while both dislocated cases underwent successful open reduction without recurrence. The absence of significant differences in complication rates ($p > 0.05$) confirmed the postoperative safety equivalence of tantalum-coated prostheses. The detailed safety evaluation metrics are presented in Table 2.

At final follow-up, all patients survived, with one case of tumor recurrence in each group, maintaining survival with recurrent tumors. As shown in Figure 5, the experimental group demonstrated stable prosthesis positioning on postoperative X-rays at 1, 3, 6, and 22 months, with significant improvement in hip inclination from preoperative pathological elevation to near-symmetrical alignment by 6 months. This group showed a median follow-up of 15 months (range: 3–29 months) and significantly higher Harris Hip Scores (81.8 ± 5.7 vs. 69.8 ± 7.0 in controls, $p < 0.001$). Thin-slice CT evaluations by two surgeons revealed 4 excellent, 6 good, 1 fair, and 0 poor osseointegration cases (90.9% excellent/good rate) in the tantalum group versus 0 excellent, 3

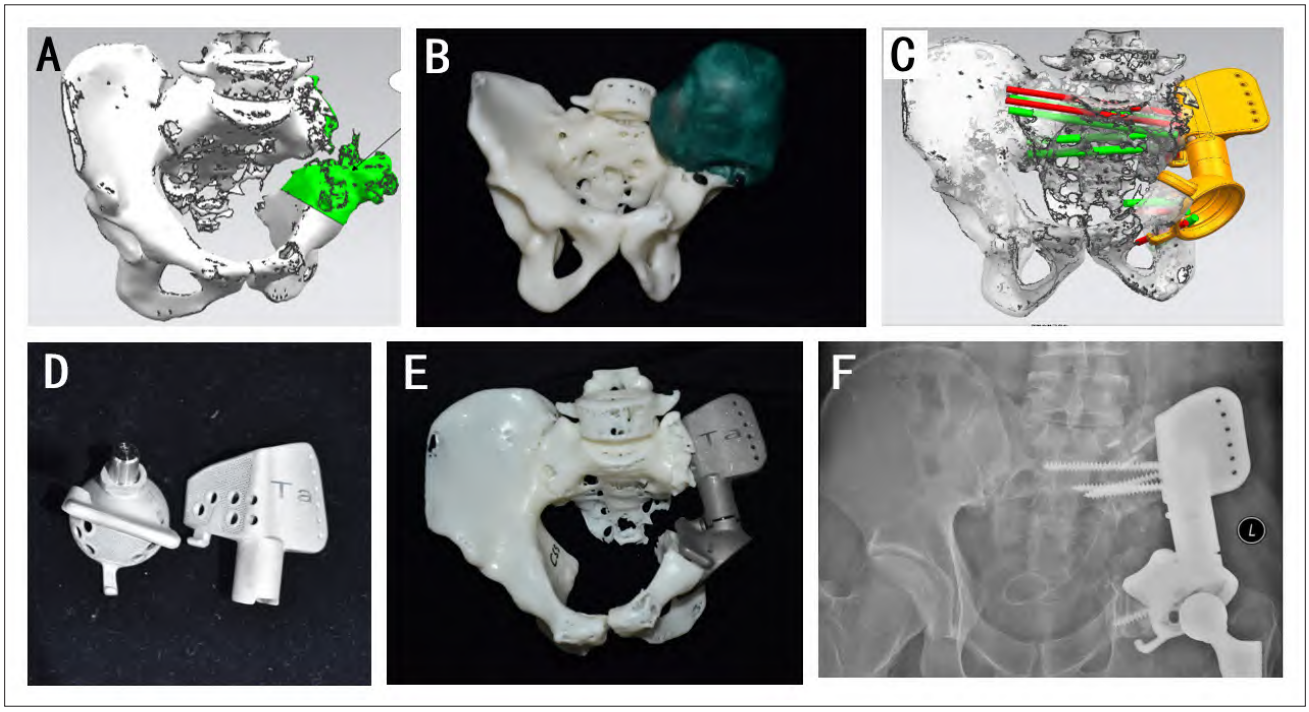


Figure 4. The entire process of personalized prosthesis design, preparation, and implantation. (A) 3D reconstruction of the lesion model. (B) 3D-printed pelvic lesion model. (C) Personalized prosthesis design. (D) 3D-printed personalized tantalum-coated titanium alloy pelvic reconstruction prosthesis. (E) *In vitro* simulation installation. (F) X-ray images at 3 months after the implantation of the 3D-printed personalized tantalum-coated titanium alloy pelvic reconstruction prosthesis.

good, 6 fair, and 1 poor (30.0% excellent/good rate) in controls. As shown in Figure 6, CT imaging confirmed enhanced trabecular bone formation at the prosthesis–bone interface, consistent with prior animal studies.[17] The detailed effectiveness data are provided in Table 3.

4. Discussion

Reconstructing complex pelvic defects necessitates both anatomical restoration and functional rehabilitation, requiring implants that not only restore bone continuity but also replicate native bone tissue to regain biomechanical stability and biological function. Therefore, implants must possess sufficient mechanical strength, excellent biocompatibility, and most critically, the ability to accelerate bone defect repair and osseointegration. Traditional bone defect treatments, such as autologous or allogeneic bone grafting, fail to meet the high weight-bearing demands of pelvic defect reconstruction or to provide early mechanical stability. Although 3D-printed porous titanium alloy pelvic prostheses manifest adequate mechanical strength

Table 2. Safety evaluation indices

Parameters	Experimental group (n = 11)	Control group (n = 10)	p-value
Operative duration (min)	306.6 ± 118.7	297.1 ± 30.4	>0.05
Intraoperative blood loss (mL)	1886 ± 854	2810 ± 1524	>0.05
Abnormal laboratory findings			
Blood tests	1 (9.1%)	2 (20%)	0.587
Liver function	1 (9.1%)	2 (20%)	0.587
Renal function	0 (0.0%)	1 (10%)	0.474
Postoperative complications			
Peri-incisional infection	1 (9.1%)	2 (20%)	0.587
Prosthetic femoral head dislocation	1 (9.1%)	1 (10%)	1.000

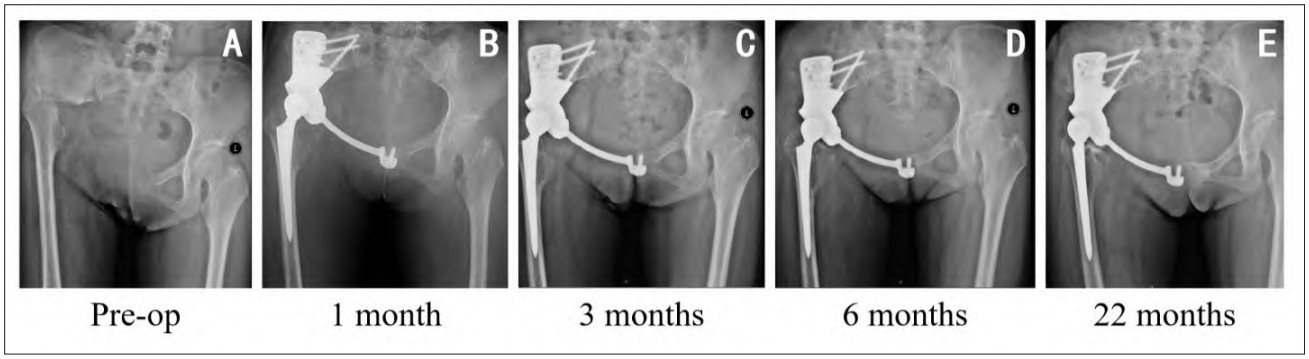


Figure 5. X-ray images of a middle-aged female with a pelvic defect at different time points (A) before and (B–E) after surgery: (B) 1 month, (C) 3 months, (D) 6 months, and (E) 22 months. The tantalum-coated prosthesis remained stable within a year after surgery. Abbreviation: Pre-op, preoperation.

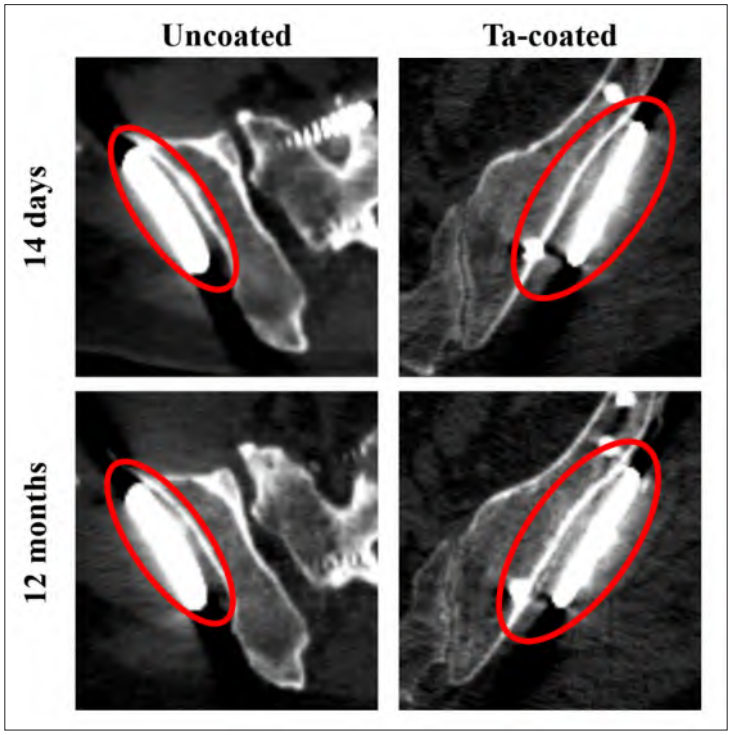


Figure 6. Computed tomography images of patients in the experimental (Ta-coated) and control (uncoated) groups on the 14th day after surgery and 12 months of follow-up. The red circles represent the bone trabeculae formed at the prosthesis–bone interface.

Table 3. Effectiveness evaluation index

Parameters	Experimental group (n = 11)	Control group (n = 10)	p-value
Harris Hip Score	81.8 ± 5.7	69.8 ± 7.0	0.001
Bone ingrowth grade			
Excellent	4	0	
Good	6	3	
Fair	1	6	
Poor	0	1	
Excellent/good rate (%)	90.9	30.0	

and favorable biocompatibility, their capacity to promote osteogenesis remains unsatisfactory. To address this limitation, this study applied PIII technology to deposit a tantalum coating on the surface of 3D-printed porous titanium alloy prostheses, thereby endowing them with osteogenic biological functionality. Clinical studies have substantiated that the personalized 3D-printed tantalum-coated titanium alloy pelvic reconstruction prostheses, independently developed by our research team, significantly enhance new bone ingrowth at the prosthesis–bone interface, thereby improving prosthesis stability, restoring lower limb function in patients, and ultimately representing a more effective approach for managing complex pelvic defects.

Aseptic loosening of orthopedic implants can lead to significant complications, including pain, functional impairment, and ultimately implant failure requiring revision surgery. A primary contributor to aseptic prosthetic loosening is inadequate osseointegration between the implant and host bone.[18,19] While robust osseointegration is paramount for implant success, conventional titanium alloys widely used in clinical orthopedic implants inherently lack the biological capacity to promote neo-osteogenesis. Substantial research efforts have been devoted to enhancing the osseointegration efficiency of existing titanium alloy prostheses to combat implant loosening.

Hydroxyapatite (HA) coating on implant surfaces has a well-established history, with studies as early as 1991 demonstrating that plasma-sprayed HA coatings on titanium alloys induced greater intramedullary neo-osteogenesis, thereby enhancing implant osseointegration.[20] Multiple clinical investigations have confirmed that plasma-sprayed HA coatings on titanium surfaces can stimulate cancellous bone formation.[21,22] However, HA coatings deposited via plasma spraying undergo progressive degradation *in vivo*, potentially leading to inflammatory reactions, coating disintegration, and subsequent implant loosening.[23]

Chemical surface modifications through sandblasting, acid-etching, or their combination have been clinically proven to enhance osseointegration, improve implant stability, and reduce healing duration.[24–26] Nevertheless, these techniques are predominantly applied to smaller oral/dental implants in maxillofacial regions rather than orthopedic clinical implants. In summary, although rational surface modifications and coating technologies can effectively improve titanium alloy osseointegration performance, current methodologies exhibit respective limitations, urgently necessitating the development of novel approaches to address the persistent clinical challenge of suboptimal osseointegration efficiency in titanium alloy prostheses.

Tantalum manifests significant potential for enhancing osseointegration due to its exceptional biocompatibility and corrosion resistance. The remarkable osteogenic capacity of tantalum has gained international recognition, positioning it as a promising novel material for orthopedic implants. While pure tantalum exhibits several limitations as an implant material, current strategies focus on fabricating porous tantalum prostheses or depositing tantalum coatings onto implant surfaces.[27–29] For example, Ying *et al.*[30] employed 3D-printed tantalum acetabular augments to address acetabular defects during total hip arthroplasty revision, achieving effective acetabular reconstruction with restored hip rotation center and improved hip function. Similarly, Li *et al.*[31] reported successful reconstruction of massive pelvic defects following iliac chondrosarcoma resection using 3D-printed tantalum prostheses, with the patient achieving ambulation at 1 month postoperatively and maintaining tumor-free status without implant loosening or mechanical failure during 12-month follow-up. Nevertheless, widespread clinical implementation of 3D-printed porous tantalum prostheses remains constrained by the prohibitively high cost of raw spherical tantalum powder required for fabrication.[32]

Tantalum coatings enhance surface roughness and microtopography, creating a favorable microenvironment for cell adhesion and promoting early osseointegration. Our research team previously fabricated 3D-printed porous tantalum scaffolds, with cellular and animal experiments confirming their exceptional osteogenic activity and biosafety in bone regeneration.[12] Zimmer Biomet (USA) developed a porous tantalum material through chemical vapor deposition technology, featuring 40–60-μm-thick tantalum coatings deposited on low-density vitreous carbon scaffolds.[33] This porous tantalum has achieved widespread clinical application for bone defect filling with documented economic and therapeutic benefits.[34,35] However, three critical limitations persist: First, its low elastic modulus prevents customization of patient-specific porous tantalum reconstruction prostheses.[17] Second, the inherent mechanical weakness of the carbon scaffold substrate becomes particularly problematic when applied to weight-bearing regions such as the pelvis.[36] Third, the mechanical properties of porous tantalum primarily hinge on the thickness of the tantalum coating on its surface. To guarantee the prosthesis's mechanical strength, the tantalum coating on the surface typically needs to exceed 40 μm in thickness, which necessitates a prolonged coating duration and incurs higher manufacturing costs.

Our research team pioneered the application of PIII technology to uniformly deposit tantalum coatings on personalized 3D-printed titanium alloy prostheses, with coating thickness maintained below 20 μm. This methodology simultaneously fulfills prosthetic morphological requirements, maintains structural integrity under mechanical loading, and preserves tantalum's biological functionality, thereby enabling functional reconstruction of complex pelvic defects. The coatings fabricated through PIII technology demonstrate exceptional density and uniformity while maintaining robust adhesion to the substrate.[37,38] Compared with solid pure tantalum implants, our surface-modified prostheses exhibit a significantly reduced elastic modulus closer to bone tissue, substantial weight reduction, and improved cost-effectiveness. The PIII-derived coatings completely cover all internal and external surfaces of porous prostheses without compromising osseous ingrowth into the porous architecture.[39,40] Our preliminary investigations demonstrated that 3D-printed titanium alloy implants maintained comparable mechanical properties before and after PIII deposited tantalum coating, with no significant changes in elastic modulus or compressive strength.[41] These findings suggest that the observed clinical improvements are principally attributable to tantalum's inherent osteoinductive capacity and bioactive properties that potentiate bone regeneration.

Through synergistic interaction with porous structures, tantalum further enhances osseointegration at the prosthesis–bone interface, thereby reducing the incidence of postoperative aseptic loosening of the prosthesis and ensuring a more secure union between the implant and the bone. Owing to its non-line-of-sight deposition characteristics and excellent adaptability, PIII tantalum-coating technology should be broadly compatible with various types of 3D-printed titanium implants—including acetabular cups, spinal fusion cages, and dental fixtures—while its process characteristics guarantee conformity with complex topologies and lattice architectures. Compared with conventional hydroxyapatite or micro-arc oxidation coatings, this technique demonstrates superior osseointegration-promoting capacity, while simultaneously enabling synergetic enhancement of mechanical adaptability and biological activity through topology-optimization strategies. Although the high-temperature process may increase manufacturing costs, batch processing and parameter optimization can effectively contain cost increments, thereby ensuring seamless integration into both clinical and commercial workflows.

Regarding safety considerations, tantalum-coated prostheses maintain identical design principles, manufacturing processes, surgical techniques, and perioperative management compared to conventional titanium alloy implants. The only distinction lies in the surface coating modification, which does not increase surgical complexity or procedural requirements, thereby ensuring equivalent intraoperative safety. Postoperative safety was evaluated through monitoring biochemical parameters and complication rates. In this study, no significant differences were observed between preoperative and postoperative indicators in the experimental group, with no severe complications reported. Both the experimental and control groups showed comparable prosthesis stability and equivalent patient survival rates. These results confirm that tantalum-coated prostheses exhibit favorable postoperative safety and are clinically applicable for complex pelvic reconstruction.

Given the inability to obtain prosthesis–bone interface specimens for histological or cellular analysis, the osteogenic capacity of tantalum coatings was evaluated exclusively through radiographic assessment. Currently, no established imaging criteria exist for quantifying bone ingrowth at prosthesis–bone interfaces. In this study, pelvic CT scans were utilized to evaluate trabecular bone formation perpendicular to the interface as the primary indicator of osseointegration. Comparative analysis revealed that the tantalum-coated group exhibited significantly higher bone ingrowth grades and superior clinical success rates compared to uncoated controls, thereby confirming the coating's enhanced osseointegration potential, findings consistent with previous cellular and animal experimental outcomes. The enhanced osseointegration observed with the tantalum coating may be attributed to its superior bioactivity, surface energy, and potential to modulate osteoblast behavior, as suggested in prior studies.[41] Furthermore, patients with tantalum-coated prostheses exhibited superior postoperative lower limb function scores and sustained implant positional stability, thereby confirming the enhanced postoperative stability and biomechanical performance characteristics of the tantalum-coated implants.

In summary, personalized 3D-printed tantalum-coated titanium alloy prostheses, fabricated through PIII, demonstrate clinical safety in the treatment of complex bone defects while exhibiting promising efficacy in promoting bone regeneration and restoring lower limb function. Its remarkable bone integration potential suggests the likelihood of long-term prosthesis stability, potentially leading to a significant reduction in long-term loosening rates and ultimately contributing to sustained improvements in patients' limb function and mobility. Nevertheless, potential long-term complications, such as late-onset infections, coating fatigue, and wear debris

reactions, necessitate further evaluation through extended observation periods.

This study has several limitations. First, the relatively small sample size, inherent to the rarity of complex pelvic defects requiring such reconstruction, may limit the statistical power and generalizability of the findings. Second, heterogeneity in follow-up durations among patients introduces potential bias in the assessment of complications and functional outcomes, particularly for long-term effects. Third, the lack of long-term follow-up data precludes definitive conclusions regarding the durability and long-term clinical efficacy of the prosthesis. Consequently, there is a need for long-term, multicenter studies with a larger cohort to comprehensively assess the long-term safety and effectiveness of a tantalum-coated prosthesis in treating complex bone defects, and to validate its potential in enhancing patients' long-term quality of life.

5. Conclusion

The personalized 3D-printed tantalum-coated titanium alloy pelvic prostheses fabricated via PIII demonstrate clinical safety and efficacy in reconstructing complex pelvic defects. These prostheses enhance osseointegration at the bone–implant interface, improve mechanical stability, and effectively restore lower limb function. Collectively, these advantages establish this technology as a superior therapeutic strategy for complex pelvic reconstruction. The findings confirm the significant clinical potential of functional tantalum-coated prostheses for orthopedic applications.

Acknowledgments

None.

Funding

This work was financially supported by the National Key Research & Development Program of China (2024YFB3814700), National Key Research & Development Program of China (2022YFC2406000), National Natural Science Foundation of China (52401056), Shanghai Municipal Commission of Economy and Informatization (2024-GZL-RGZN-01023), Domestic Science and Technology Cooperation Projects of Shanghai Municipal Science and Technology Commission (24010701700), Key Research & Development Programs of Ningxia, China (2020BCH01001), Shanghai Engineering Research Center of Innovative Orthopedic Instruments and Personalized Medicine (19DZ2250200), Biomaterials and Regenerative Medicine Institute Cooperative Research Project, Shanghai Jiao Tong University School of Medicine (2022LHA01), 3-year Action Plan of Shenkang Development Center (SHDC2020CR2019B) and Shanghai Pujiang Program (23PJ1421600).

Conflict of interest

The authors declare they have no competing interests.

Author contributions

Conceptualization: Yongqiang Hao, Wei Li, Liang Deng
Formal analysis: Zhaoyang Ran
Investigation: Zhaoyang Ran, Boran Pang, Junxiang Wu, Lei Wang, Jingke Fu
Methodology: Zhaoyang Ran, Boran Pang, Yulin Tian, Dinghao Luo
Writing–original draft: Zhaoyang Ran, Boran Pang
Writing–review & editing: Yongqiang Hao, Liang Deng, Wei Li, Kai Xie

Ethics approval and consent to participate

The study was approved by the Ethics Committee of Shanghai Ninth People's Hospital affiliated to Shanghai Jiao Tong University School of Medicine (approval no.: SH9H-2020-T206-1). Written informed consent to participate was obtained from all participants and/or their legal guardian(s)

Consent for publication

We confirmed that written informed consent for publication was obtained from all the subjects and/or their legal guardian(s).

Availability of data

The datasets used or analyzed during the current study are available from the corresponding author upon reasonable request.

References

1. Dimitriou R, Mataliotakis GI, Angoules AG, Kanakaris NK, Giannoudis PV. Complications following autologous bone graft harvesting from the iliac crest and using the RIA: a systematic review. *Injury*. 2011;42(Suppl 2):S3-S15. doi: 10.1016/j.injury.2011.06.015

2. Campana V, Milano G, Pagano E, *et al*. Bone substitutes in orthopaedic surgery: from basic science to clinical practice. *J Mater Sci Mater Med*. 2014;25(10):2445-2461. doi: 10.1007/s10856-014-5240-2

3. Ran ZY, Wang Y, Li JX, *et al*. 3D-printed biodegradable magnesium alloy scaffolds with zoledronic acid-loaded

ceramic composite coating promote osteoporotic bone defect repair. *Int J Bioprinting*. 2023;9(5):401-417. doi: 10.18063/ijb.769

4. Wang J, Min L, Lu M, *et al*. Three-dimensional-printed custom-made hemipelvic endoprosthesis for primary malignancies involving acetabulum: the design solution and surgical techniques. *J Orthop Surg Res*. 2019;14(1):389. doi: 10.1186/s13018-019-1455-8
5. Li GY, Wang L, Pan W, *et al*. In vitro and in vivo study of additive manufactured porous Ti6Al4V scaffolds for repairing bone defects. *Sci Rep*. 2016;6:34072. doi: 10.1038/srep34072
6. Wu JX, Xie K, Luo DH, *et al*. Three-dimensional printing-based personalized limb salvage and reconstruction treatment of pelvic tumors. *J Surg Oncol*. 2021;124(3):420-430. doi: 10.1002/jso.26516
7. Xue T, Attarilar S, Liu SF, *et al*. Surface modification techniques of titanium and its alloys to functionally optimize their biomedical properties: a thematic review. *Front Bioeng Biotechnol*. 2020;8:603072. doi: 10.3389/fbioe.2020.603072
8. Souza JCM, Sordi MB, Kanazawa M, *et al*. Nano-scale modification of titanium implant surfaces to enhance osseointegration. *Acta Biomater*. 2019;94:112-131. doi: 10.1016/j.actbio.2019.05.045
9. Wang X, Liu WT, Yu XD, *et al*. Advances in surface modification of tantalum and porous tantalum for rapid osseointegration: a thematic review. *Front Bioeng Biotechnol*. 2022;10:983695. doi: 10.3389/fbioe.2022.983695
10. Schildhauer TA, Robie B, Muhr G, Köller M. Bacterial adherence to tantalum versus commonly used orthopedic metallic implant materials. *J Orthop Trauma*. 2006;20(7):476-484. doi: 10.1097/00005131-200608000-00005
11. Wang Q, Qiao YQ, Cheng MQ, *et al*. Tantalum implanted entangled porous titanium promotes surface osseointegration and bone ingrowth. *Sci Rep*. 2016;6:26248. doi: 10.1038/srep26248
12. Guo Y, Xie K, Jiang WB, *et al*. In vitro and in vivo study of 3D-printed porous tantalum scaffolds for repairing bone defects. *ACS Biomater Sci Eng*. 2019;5(2):1123-1133. doi: 10.1021/acsbiomaterials.8b01094
13. Li WY, Li XY, Dong HS. Effect of tensile stress on the formation of S-phase during low-temperature plasma carburizing of 316L foil. *Acta Mater*. 2011;59(14):5765-5774. doi: 10.1016/j.actamat.2011.05.053
14. Ueda M, Silva C, Marcondes AR, Reuther H, de Souza GB. Recent experiments on plasma immersion ion implantation (and deposition) using discharges inside metal tubes. *Surf Coat Technol*. 2018;355:98-110. doi: 10.1016/j.surfcoat.2018.05.009
15. Zhang LC, Chen LY, Wang LQ. Surface modification of titanium and titanium alloys: technologies, developments, and future interests. *Adv Eng Mater*. 2020;22(5): 1901258. doi: 10.1002/adem.201901258
16. Schulz KF, Altman DG, Moher D; CONSORT Group. CONSORT 2010 statement: updated guidelines for reporting parallel group randomised trials. *J Clin Epidemiol*. 2010;63(8):834-840. doi: 10.1016/j.jclinepi.2010.02.005
17. Li X, Wang L, Yu XM, *et al*. Tantalum coating on porous Ti6Al4V scaffold using chemical vapor deposition and preliminary biological evaluation. *Mater Sci Eng C Mater Biol Appl*. 2013;33(5):2987-2994. doi: 10.1016/j.msec.2013.03.027
18. Agarwal R, Garcia AJ. Biomaterial strategies for engineering implants for enhanced osseointegration and bone repair. *Adv Drug Deliv Rev*. 2015;94:53-62. doi: 10.1016/j.addr.2015.03.013
19. Bohara S, Suthakorn J. Surface coating of orthopedic implant to enhance the osseointegration and reduction of bacterial colonization: a review. *Biomater Res*. 2022;26(1):26. doi: 10.1186/s40824-022-00269-3
20. Jansen JA, van de Waerden JP, Wolke JG, de Groot K. Histologic evaluation of the osseous adaptation to titanium and hydroxyapatite-coated titanium implants. *J Biomed Mater Res*. 1991;25(8):973-989. doi: 10.1002/jbm.820250805
21. D'Antonio JA, Capello WN, Jaffe WL. Hydroxylapatite-coated hip implants: multicenter three-year clinical and roentgenographic results. *Clin Orthop Relat Res*. 1992;285:102-115 doi: 10.1097/00003086-199212000-00015
22. D'Lima DD, Walker RH, Colwell CW Jr. Omnifit-HA stem in total hip arthroplasty: a 2- to 5-year follow-up. *Clin Orthop Relat Res*. 1999;363:163-169.

    doi: 10.1097/00003086-199906000-00021
23. Landor I, Vavrik P, Sosna A, Jahoda D, Hahn H, Daniel M. Hydroxyapatite porous coating and the osteointegration of the total hip replacement. *Arch Orthop Trauma Surg*. 2007;127(2):81-89. doi: 10.1007/s00402-006-0235-1
24. Bornstein MM, Hart CN, Halbritter SA, Morton D, Buser D. Early loading of nonsubmerged titanium implants with a chemically modified sand-blasted and acid-etched surface: 6-month results of a prospective case series study in the posterior mandible focusing on peri-implant crestal bone changes and ISQ values. *Clin Implant Dent Relat Res*. 2009;11(4):338-347. doi: 10.1111/j.1708-8208.2009.00148.x

25. Schatzle M, Mannchen R, Balbach U, Hammerle CH, Toutenburg H, Jung RE. Stability change of chemically modified sandblasted/acid-etched titanium palatal implants: a randomized-controlled clinical trial. *Clin Oral Implants Res*. 2009;20(5):489-495.
doi: 10.1111/j.1600-0501.2008.01694.x

26. Markovic A, Colic S, Scepanovic M, Misic T, Ethinic A, Bhusal DS. A 1-year prospective clinical and radiographic study of early-loaded bone level implants in the posterior maxilla. *Clin Implant Dent Relat Res*. 2015;17(5):1004-1013.
doi: 10.1111/cid.12201

27. Zhang C, Chen H, Fan H, *et al*. Carpal bone replacement using personalized 3D printed tantalum prosthesis. *Front Bioeng Biotechnol*. 2023;11:1234052.
doi: 10.3389/fbioe.2023.1234052

28. Girerd D, Parratte S, Lunebourg A, *et al*. Total knee arthroplasty revision with trabecular tantalum cones: preliminary retrospective study of 51 patients from two centres with a minimal 2-year follow-up. *Orthop Traumatol Surg Res*. 2016;102(4):429-433.
doi: 10.1016/j.otsr.2016.02.010

29. Shi LY, Wang A, Zang FZ, Wang JX, Pan XW, Chen HJ. Tantalum-coated pedicle screws enhance implant integration. *Colloids Surf B Biointerfaces*. 2017;160:22-32.
doi: 10.1016/j.colsurfb.2017.08.059

30. Ying J, Cheng L, Li J, *et al*. Treatment of acetabular bone defect in revision of total hip arthroplasty using 3D printed tantalum acetabular augment. *Orthop Surg*. 2023;15(5):1264-1271.
doi: 10.1111/os.13691

31. Li Z, Chen G, Xiang Y, *et al*. Treatment of massive iliac chondrosarcoma with personalized three-dimensional printed tantalum implant: a case report and literature review. *J Int Med Res*. 2020;48(10):300060520959508.
doi: 10.1177/0300060520959508

32. Wei XW, Zhao DW, Wang BJ, *et al*. Tantalum coating of porous carbon scaffold supplemented with autologous bone marrow stromal stem cells for bone regeneration in vitro and in vivo. *Exp Biol Med (Maywood)*. 2016;241(6):592-602.
doi: 10.1177/1535370216629578

33. Levine BR, Sporer S, Poggie RA, Della Valle CJ, Jacobs JJ. Experimental and clinical performance of porous tantalum in orthopedic surgery. *Biomaterials*. 2006;27(27):4671-4681.
doi: 10.1016/j.biomaterials.2006.04.041

34. Rajgopal A, Panda I, Yadav S, Wakde O. Stacked tantalum cones as a method for treating severe distal femoral bone deficiency in total knee arthroplasty. *J Knee Surg*. 2019;32(9):833-840.
doi: 10.1055/s-0038-1669789

35. Liu GH, Wang J, Yang SH, Xu WH, Ye SN, Xia TA. Effect of a porous tantalum rod on early and intermediate stages of necrosis of the femoral head. *Biomed Mater*. 2010;5(6):065003.
doi: 10.1088/1748-6041/5/6/065003

36. Chalkin B, Minter J. Limb salvage and abductor reattachment using a custom prosthesis with porous tantalum components: case report. *J Arthroplasty*. 2005;20(1):127-130.
doi: 10.1016/j.arth.2004.09.029

37. Zhou Y, Li M, Cheng Y, Zheng YF, Xi TF, Wei SC. Tantalum coated NiTi alloy by PIIID for biomedical application. *Surf Coat Technol*. 2013;228:S2-S6.
doi: 10.1016/j.surfcoat.2012.11.002

38. Lu T, Wen J, Qian S, *et al*. Enhanced osteointegration on tantalum-implanted polyetheretherketone surface with bone-like elastic modulus. *Biomaterials*. 2015;51:173-183.
doi: 10.1016/j.biomaterials.2015.02.018

39. Bobyn JD, Stackpool GJ, Hacking SA, Tanzer M, Krygier JJ. Characteristics of bone ingrowth and interface mechanics of a new porous tantalum biomaterial. *J Bone Joint Surg Br*. 1999;81-B(5):907-914.
doi: 10.1302/0301-620X.81B5.9283

40. Bobyn JD, Poggie RA, Krygier JJ, *et al*. Clinical validation of a structural porous tantalum biomaterial for adult reconstruction. *J Bone Joint Surg Am*. 2004;86-A (Suppl 2):123-129.
doi: 10.2106/00004623-200412002-00017

41. Tian YL, Jiang WB, Deng L, *et al*. A fractal-like hierarchical bionic scaffold for osseointegration. *Adv Funct Mater*. 2025;35(8):2415880.
doi: 10.1002/adfm.202415880

ACCSCIENCE PUBLISHING

International Journal of Bioprinting

RESEARCH ARTICLE

Bioprinting and *in vitro* characterization of alginate–gelatin constructs incorporating human umbilical vein endothelial cells for potential cardiac tissue engineering

Farinaz Ketabat[1], Reza Gharraei[1], Alex Guinle[1,2], Nicole J. Sylvain[3], Michael E. Kelly[1,3], Ildiko Badea[4]*, and Xiongbiao Chen[1,5]*

[1]Division of Biomedical Engineering, Department of Mechanical Engineering, College of Engineering, University of Saskatchewan, Saskatoon, Saskatchewan, Canada

[2]Catholic Institute of Arts and Crafts Bretagne Campus, Vannes, Bretagne, France

[3]Department of Surgery, College of Medicine, University of Saskatchewan, Saskatoon, Saskatchewan, Canada.

[4]College of Pharmacy and Nutrition, University of Saskatchewan, Saskatoon, Saskatchewan, Canada

[5]Department of Mechanical Engineering, College of Engineering, University of Saskatchewan, Saskatoon, Saskatchewan, Canada

(This article belongs to the *Special Issue*: *Three-Dimensional (3D) Bioprinting for Tissue Engineering and Food Printing*)

***Corresponding authors:**
Ildiko Badea
(ildiko.badea@usask.ca)

Xiongbiao Chen
(xbc719@mail.usask.ca)

Citation: Ketabat F, Gharraei R, Guinle A, *et al.* Bioprinting and *in vitro* characterization of alginate–gelatin constructs incorporating human umbilical vein endothelial cells for potential cardiac tissue engineering. *Int J Bioprint.* 2025;11(5):385-407. doi: 10.36922/IJB025280280

Received: July 10, 2025
1st revised: August 11, 2025
2nd revised: August 26, 2025
Accepted: August 28, 2025
Published online: August 28, 2025

Copyright: © 2025 Author(s). This is an Open Access article distributed under the terms of the Creative Commons Attribution License, permitting distribution, and reproduction in any medium, provided the original work is properly cited.

Publisher's Note: AccScience Publishing remains neutral with regard to jurisdictional claims in published maps and institutional affiliations.

Abstract

Three-dimensional (3D) bioprinting offers transformative potential for cardiac tissue engineering by enabling the fabrication of cell-laden constructs. However, key challenges remain, including maintaining cell viability within bioprinted constructs and understanding how embedded cells affect their physical and mechanical properties. This study addresses these challenges by incorporating human umbilical vein endothelial cells (HUVECs) into alginate–gelatin hydrogels and evaluating their impact on mechanical, physical, and rheological properties. Bioinks or hydrogels were prepared with or without HUVECs, and their rheological properties were assessed. Computational fluid dynamics (CFD) simulation was employed to determine the appropriate bioprinting pressure while minimizing cell damage. Constructs were designed and 3D-printed with an angular pattern to replicate the orientation of cardiac myofibrils and were characterized over a 21-day period for viscoelasticity, elastic modulus, swelling, mass loss, morphology, and cell viability. The incorporation of cells increased the storage and loss moduli of the bioink, demonstrating shear-thinning behavior as described by the Cross model. CFD simulation combined with preliminary cell viability assays identified 25 kPa as a suitable 3D-printing pressure, effectively preserving cell viability. Both cell-free and cell-laden constructs exhibited viscoelastic properties; however, cell-laden constructs displayed a lower elastic modulus under linear compression, reduced swelling, and greater mass retention. High cell viability was observed immediately post-bioprinting and was maintained for more than 1 week. These findings provide a framework for developing structurally robust, cell-laden constructs with enhanced functional fidelity, supporting their application in cardiac tissue engineering.

Keywords: Cell viability; Computational fluid dynamics modeling; Physical properties; Rheology; Viscoelastic behavior

1. Introduction

Heart disease remains one of the leading causes of death worldwide, largely due to the limited regenerative capacity of the adult heart.[1–3] In many cases, heart disease leads to compromised ventricular function, including impaired filling and/or ejection of blood, resulting in heart failure (HF), a common end-stage manifestation of structural and functional cardiac disorders.[4] While heart transplantation remains the gold standard therapy for selected HF patients, offering excellent post-transplant survival, its full potential is constrained by several complications. These include immunological rejection, heightened susceptibility to infections, medication-related issues, the complex ischemic milieu, and the persistent traditional risk factors of coronary disease.[5] Consequently, regenerative therapeutic strategies have been developed to repair or replace damaged cardiac tissue.[6] However, both cell-free and cell-based approaches face limitations, including poor delivery and retention as well as limited therapeutic efficacy,[6] highlighting the need for more advanced regenerative strategies.

Cardiac tissue engineering (CTE) is a promising approach for developing functional cardiac tissue, either for *in vivo* transplantation aimed at regenerative repair or for creating *in vitro* models to study disease mechanisms and facilitate drug discovery.[7,8] Despite its promise, the success of conventional CTE depends on meeting several critical requirements that remain only partially addressed.[9] These include limited control over scaffold microarchitecture, inadequate and/or non-functional vascularization to ensure perfusion, immunogenic responses, scalability challenges, and the absence of essential cell types required for myocardial repair.[9,10]

The advancement of three-dimensional (3D) printing, one of the most widely used techniques in additive manufacturing, offers a promising avenue to overcome the aforementioned limitations.[9] More specifically, the utilization of 3D-printing to fabricate functional living constructs from biological materials—such as cells, biomaterials, and growth factors—in a spatially controlled, layer-by-layer manner is referred to as 3D-bioprinting.[9,11,12] 3D-bioprinting can be used to develop engineered tissues through two main approaches: the top-down approach, in which living cells are introduced or seeded after scaffold fabrication, and the bottom-up approach, in which living cells are incorporated during scaffold fabrication.[13,14] Although both approaches have advantages and limitations, and many recent cardiac tissue constructs employ a combination of the two, the bottom-up approach is gaining greater recognition for its effectiveness in developing vascularized tissues.[13,14]

Extrusion bioprinting is recognized as a cost-effective 3D-bioprinting technique, utilizing pneumatic- or mechanically driven fluid dispensing systems to deposit bioink with cell densities closely resembling physiological levels onto a platform.[7,15] However, excessive dispensing pressure during printing can increase shear forces acting on cells within the bioink, particularly when extruding high-viscosity bioinks or using a thin nozzle, which may reduce cell viability.[7,16] The magnitude of these shear forces is influenced by the rheological properties of the bioink and can adversely affect cell viability and proliferation, thereby impairing the biological function of the engineered tissue.[17]

Additionally, the presence of living cells can influence the physical and mechanical properties of engineered constructs.[18,19] Therefore, when bioprinting cell-laden constructs, it is important to consider: (i) applying appropriate mechanical forces during printing to minimize cell damage while ensuring proper extrudability, and (ii) characterizing their *in vitro* properties post-printing, as these may differ significantly from cell-free scaffolds. Such differences could further influence their suitability for *in vivo* applications. To the best of our knowledge, the underlying rationales for these considerations have not been thoroughly studied or reported in the literature.

Motivated by these considerations, this study aims to fabricate 3D-bioprinted constructs from alginate–gelatin hydrogel containing endothelial cells, with the goal of promoting vascularization and advancing the development of engineered cardiac tissue. The specific objectives of this study are: (i) to determine the appropriate bioprinting pressure required to maintain cell viability and apply this pressure to fabricate both cell-free scaffolds and cell-laden constructs, and (ii) to investigate the influence of incorporated cells on the physical, mechanical, and morphological properties of bioprinted constructs over time compared with cell-free scaffolds.

We first characterized the rheological behavior of the bioink composed of human umbilical vein endothelial cells (HUVECs) encapsulated in alginate–gelatin hydrogels. Rheological data were then used in computational fluid

dynamics (CFD) simulations to estimate the average velocity of the bioink during extrusion.

Based on the CFD outcomes, preliminary cell viability assays conducted over 21 days, and findings from our previous work,[20] we identified a bioprinting pressure that effectively maintained cell viability. Using this pressure, both cell-laden constructs and cell-free scaffolds (controls) were fabricated. Their mechanical and physical properties—including elastic modulus, swelling behavior, mass loss, and morphology—were evaluated over a 21-day period. Additionally, cell viability within the cell-laden constructs was assessed to confirm sustained cellular function post-bioprinting.

2. Materials and experimental methods

2.1. Hydrogel preparation

Hydrogel solutions were prepared from brown algae (A2033, Sigma-Aldrich, USA) and gelatin (Type A, gel strength approximately 300 g Bloom; G1890, Sigma-Aldrich, USA), following the method established in a previous study,[20] which demonstrated that a solution of alginate 3 wt% (Alg3) and gelatin 1 wt% (Gel1)—referred to as Alg3Gel1—was favorable for HUVECs and exhibited enhanced mechanical strength. Specifically, Gel1 was prepared by dissolving gelatin in saline solution at approximately 55°C, after which alginate powder was added to Gel1 and stirred at the same temperature until fully dissolved, forming Alg3Gel1.

In this study, Alg3Gel1 was prepared at a concentration 70% higher than that used in the previous study[20] (i.e., 4.2% instead of 3%). This allowed for subsequent dilution with the cell solution to achieve the desired final concentration of 3%. HUVECs were suspended at a density of 6×10^6 cells/mL in culture medium, following the method established in a previous study that demonstrated successful vascular network formation at this cell density.[21] The cell suspension, which comprised 30% of the bioink volume, was then combined with the hydrogel mixture to create cell-laden Alg3Gel1.

2.2. Cell culture

HUVECs (ATCC CRL-1730, American Type Culture Collection, USA) were cultured in Dulbecco's Modified Eagle Medium (SH30243.01, HyClone, Cytiva, USA) supplemented with 2% sodium hypoxanthine–aminopterin–thymidine supplement (50× stock, Gibco™, Thermo Fisher Scientific, USA), 10% fetal bovine serum (Gibco®, Invitrogen, USA), and 1% antibiotic–antimycotic (100×) containing 10,000 units/mL penicillin, 10,000 μg/mL streptomycin, and 25 μg/mL Fungizone (Thermo Fisher Scientific, USA). The cells were incubated at 37°C with 5% CO_2 and were detached using 0.25% trypsin-EDTA (Gibco®, Invitrogen, USA) once they reached approximately 80–90% confluency.

2.3. Rheological properties of the bioink

The rheological behavior of the bioinks was investigated using a rheometer. Notably, bioinks can exhibit thixotropic, viscoelastic, or shear-thinning behavior,[22] and the rheological properties of alginate-based hydrogels encapsulating HUVECs have not yet been reported in the literature.

The hydrogels were prepared according to the method described in **Section 2.1** on the day prior to testing and stored at 4°C. On the day of testing, HUVECs were counted and suspended in complete culture medium for the preparation of cell-laden bioink, while only complete culture medium was used for cell-free hydrogels. The mixtures were then gently combined to create the bioink and allowed to stand for approximately 2 h to minimize stirring effects. The hydrogels were subsequently placed onto the rheometer's lower geometry at a set temperature of 37°C using a spatula.

The flow behavior of the hydrogels and bioink was assessed using a Discovery Hybrid Rheometer HR20 (TA Instruments, USA) with a 20-mm parallel plate geometry at a shear rate range of 0.01–1000 s^{-1}. A dynamic frequency sweep test was performed at 10% strain and an angular frequency of 0.1–100 rad/s to determine the solid- and liquid-like behavior of the hydrogels and the bioink.

2.4. Determining the three-dimensional bioprinting pressure

To preserve cell viability, the appropriate 3D-printing pressure was carefully determined based on CFD simulations (to reveal process-induced forces) and preliminary cell viability assay results, as outlined below.

2.4.1. Computational fluid dynamics simulation

The bioink flow during the extrusion process was simulated using CFD. Ansys Fluent 2021-R1 finite-volume CFD software (Ansys, USA) was used to establish and solve the governing equations for bioink flow. The geometry of a 10 mL syringe connected to a luer lock GA27 tapered dispensing tip (Figure 1) was developed using SOLIDWORKS (Dassault Systèmes, France). The computational domain for fluid flow simulation was then extracted using Ansys SpaceClaim (Ansys, USA).

The bioink flow, considered incompressible, was calculated using the following equations (**Equations I–III**)[23]:

(i) Continuity:

$$\nabla \vec{U} = 0 \quad \text{(I)}$$

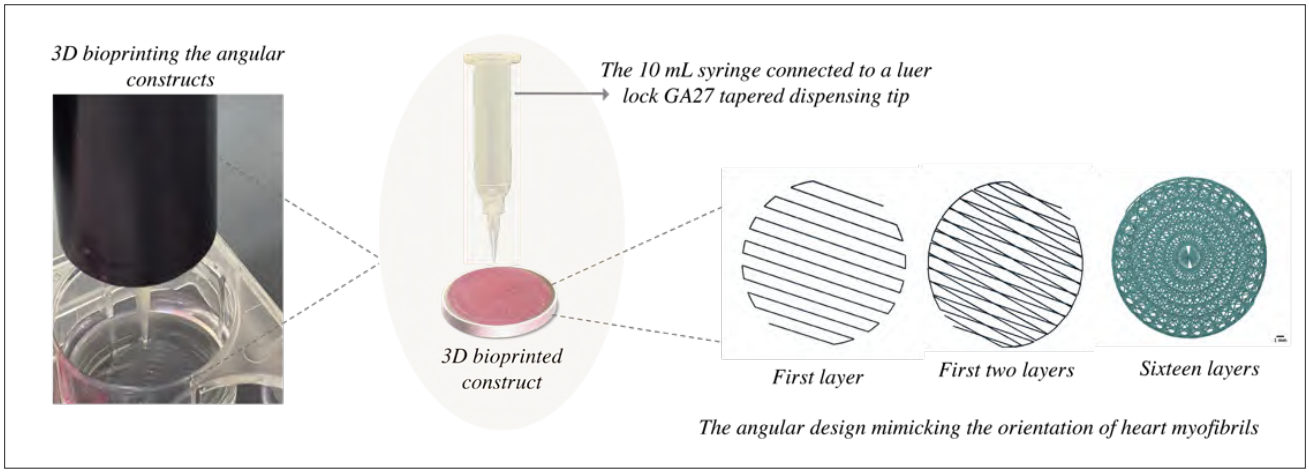


Figure 1. bioprinting of angular constructs using a 10 mL syringe equipped with a GA27 tapered dispensing tip. The construct design replicates the angular orientation of heart myofibrils. Abbreviation: 3D, three-dimensional.

(ii) Momentum:

$$\rho \frac{DU}{Dt} = \nabla.\sigma + \rho\vec{g} \quad \text{(II)}$$

$$\sigma = -pI + \tau \quad \text{(III)}$$

where $\overrightarrow{U}$ represents the fluid velocity vector, $\vec{g}$ indicates the gravitational acceleration vector, p denotes fluid pressure, ρ represents fluid density, and I is the unit tensor.[23] τ represents the shear stress tensor, which, for a Newtonian fluid, equals the shear rate tensor ($\dot{\gamma}$) multiplied by the dynamic viscosity η, according to Newton's viscosity law.[23]

$$\tau = \eta\dot{\gamma} \quad \text{(IV)}$$

For non-Newtonian fluids, the generalized form of **Equation IV** is used, where η is replaced with an apparent viscosity that varies with shear rate.[23]

The mathematical model that best fit the flow behavior data was extracted using TRIOS software (TA Instruments, USA). The computational solution of **Equations I–III**, with appropriate boundary conditions and a suitable flow behavior model (**Equation IV**), provides a detailed description of the flow inside the syringe and dispensing tip during extrusion. The boundary conditions were defined as follows: "pressure inlet" at the free surface of the bioink inside the syringe; "pressure outlet" at the environmental gauge pressure; and a "no-slip" condition on all solid walls. The computational simulations, performed using Ansys Fluent 2021-R1 software, yielded the distribution of velocity components, pressure, shear rate, and shear stress.

2.4.2. Cell viability

To evaluate the effect of printing pressure on cell viability, bioinks were extruded at 20 kPa and 30 kPa to fabricate single-layer constructs. Cell viability was assessed immediately after printing and again on the following day. In addition, 16-layer constructs were bioprinted, and cell viability was evaluated on days 1, 7, and 21 using a live/dead assay. The assay employed calcein-AM (1 μg/mL) and propidium iodide (10 μg/mL) in complete culture medium to stain live and dead cells, respectively. After 40 min of incubation at room temperature, the single-layer constructs were imaged using a BioTek Lionheart LX automated microscope (Biotek Instruments, Winooski, VT, USA), and the 16-layer constructs were imaged using a Leica TCS SPEII confocal microscope (Leica Microsystems, Wetzlar, Germany)). All live/dead assays were performed using the same protocol to ensure consistency and reproducibility across experiments.

2.5. Three-dimensional printing or bioprinting

Cylindrical constructs (20 mm × 20 mm) were designed and printed with a strand diameter of 0.15 mm and an infill distance of 1.5 mm. These parameters were selected based on a previous study, in which angular scaffolds fabricated from the Alg3Gel1 formulation (infill distance: 1.5 mm; strand diameter: 0.15 mm) exhibited the highest support

for cell viability and superior elastic modulus among the tested groups.[20] Cell-free scaffolds and cell-laden constructs were printed in 16 layers using a 27G SmoothFlow tapered tip with an inner diameter of 0.2 mm (Nordson EFD, USA) on a BioScaffolder 3.2 (Gesim, Germany). The scaffolds were printed with a gradual angular change in each layer (Figure 1), using a printing speed of 4 mm/s and a pressure of 25 kPa. The first layer was deposited at a −70° angle, with each successive layer rotated by 10°, until the final layer, which was deposited at +80° angle.

The day before printing, 6-well plates were coated with 0.1% polyethyleneimine (PEI; molecular weight 60,000; 50% w/w aqueous solution) (Thermo Fisher Scientific, USA) and incubated at 37°C. On the day of printing, the PEI solution was replaced with 50 mM calcium chloride prepared in 0.1% PEI solution. The scaffolds were printed directly into wells containing the prepared solution and left for 15 min post-printing to ensure effective crosslinking. They were then washed three times with culture medium and transferred to complete culture medium.

2.6. Rheological, mechanical, swelling, and mass retention properties of constructs

The physical properties of the printed constructs were assessed by evaluating their rheological properties, elastic modulus, swelling behavior, and mass retention percentages.

2.6.1. Mechanical and rheological properties

The elastic modulus (Young's modulus) of both cell-free and cell-laden constructs was assessed using the ElectroForce Biodynamic 5100 series (TA Instruments, USA). A compression force was applied to the printed constructs at a rate of 0.01 mm/s until they were compressed to 50% of their initial height. The stress–strain curve for each scaffold was then plotted, and the elastic modulus was calculated as the slope of the linear region.

Given that the viscoelasticity of the myocardium is crucial for cardiac function, it was essential to evaluate both the storage modulus (G') and the loss modulus (G"). Before conducting the frequency sweep test, a strain sweep was performed on the scaffolds using the HR-20 equipped with linear dynamic mechanical analysis capability. The strain sweep, conducted at an angular frequency of 1 Hz, involved an amplitude range of 1–100 μm to determine the linear region. A strain value within this range (3%) was selected for the frequency sweep test. The frequency sweep test was performed on the printed constructs at 37°C to obtain G' and G" as functions of frequency over the range of 1–16 s^{-1}. The initial strain was set to 5% of the initial height of the scaffolds.

2.6.2. Swelling and mass retention

The swelling and mass retention percentages of the constructs play an important role in regulating cell growth and function. Constructs with a high degree of swelling may promote cell attachment, while degradation that occurs neither too early nor too late provides adequate support for cell growth and proliferation.[14] Swelling and mass retention of the constructs were assessed over 21 days while being maintained in complete culture medium in an incubator at 37°C and 5% CO_2. After the constructs were printed, crosslinked, and washed three times with Dulbecco's Modified Eagle Medium, they were blotted and weighed under sterile conditions to record their initial weight (W_0). Subsequently, the constructs were maintained in complete culture medium at 37°C with 5% CO_2. At different time points (days 1, 3, 7, and 21), the constructs were removed, blotted, and weighed (W_t). The swelling percentage was then calculated using **Equation V**:

$$Swelling\ (\%) = \frac{W_t - W_0}{W_0} \times 100 \quad \text{(V)}$$

where W_0 is the initial weight of the constructs immediately after printing, and W_t is the wet weight of the constructs at different time points (days 1, 3, 7, and 21).

The same constructs were also used for the mass retention test. In this case, the constructs were lyophilized after weighing at different time points, and their dry weight was recorded (W_t). To determine the initial dry mass of the constructs, separate constructs were printed, and their average weight was designated as the initial lyophilized mass (W_0). The mass retention percentage was then calculated using **Equation VI**[24]:

$$Mass\ retention\ (\%) = 100 - \frac{W_0 - W_t}{W_0} \times 100 \quad \text{(VI)}$$

For each time point, the swelling and mass retention percentages were calculated using at least six replicates.

2.7. Field emission scanning electron microscopy

The microstructure and morphology of the printed constructs were examined using a Hitachi SU8010 field emission scanning electron microscope (FESEM) (Hitachi, Japan). After lyophilization, the constructs were sputter-coated with gold and observed under FESEM at a voltage of 3 kV and a current of 10 μA, at two different magnifications.

2.8. Statistics

All quantitative data are presented as mean ± standard deviation. Statistical analyses were performed using one-

way analysis of variance (ANOVA), followed by Tukey's post hoc test for multiple comparisons. All analyses were conducted using GraphPad Prism version 10.4.0 (GraphPad Software, USA).

3. Results

3.1. Rheological properties of the bioink

To examine the impact of incorporating cells into the Alg3Gel1 bioink and to determine appropriate 3D-printing parameters for bioprinting, the rheological behavior of cell-laden Alg3Gel1 was compared with that of Alg3Gel1 and Alg3. Figure 2 illustrates the shear stress and viscosity of the hydrogels and bioink as functions of shear rate. Figure 2A presents the relationship between shear stress and shear rate for Alg3, Alg3Gel1, and cell-laden Alg3Gel1. The non-linear relationship observed in all three samples indicates their non-Newtonian fluid behavior. The cell-laden Alg3Gel1 showed the highest shear stress across the tested shear rates, likely due to the presence of cells acting as suspended particles, thereby increasing the viscosity of the suspension compared to the base fluid.

At lower shear rates, Alg3Gel1 exhibited higher shear stress than Alg3, suggesting that the addition of Gel1 influences fluid behavior, particularly under lower-shear conditions. Figure 2B plots the viscosity against shear rate for the same three samples. All samples exhibited lower viscosities at higher shear rates—a characteristic of shear-thinning fluids. The cell-laden Alg3Gel1 displayed the highest viscosity at lower shear rates, which decreased rapidly with increasing shear rate, indicating pronounced shear-thinning behavior. While both Alg3 and Alg3Gel1 demonstrated shear-thinning properties, the addition of Gel1 consistently resulted in higher viscosities across most of the shear-rate range.

Based on the mathematical model fitting using TRIOS software, the Cross time-independent model provided the best fit for the data in Figure 2B among the array of models available. This model describes the flow behavior of shear-thinning fluids across a wide range of shear rates (**Equation VII**).

$$\frac{\eta-\eta_\infty}{\eta_0-\eta_\infty}=\frac{1}{1+k\dot{\gamma}^n} \quad \text{(VII)}$$

where k and n are fitting parameters, η_0 is the limiting viscosity at low shear rates, and η_∞ is the limiting viscosity at high shear rates.[25] Table 1 presents the parameters of the Cross model characterizing the flow behavior of cell-laden Alg3Gel at 37°C.

Figure 3 shows the rheological properties of the hydrogels and bioink as a function of frequency. Figure 3A depicts the storage modulus (G'), which reflects the solid-like behavior of the samples. Among all samples, the cell-laden Alg3Gel1 exhibited the highest G', indicating the most solid-like behavior. In contrast, Alg3 showed the lowest G', demonstrating the least solid-like behavior. Interestingly, while Alg3Gel1 showed the second-highest G' in its unloaded form, the presence of cells in the cell-laden Alg3Gel1 further increased its stiffness.

Figure 3B illustrates the loss modulus (G"), which reflects the liquid-like behavior of the samples. Similar to the storage modulus, the cell-laden Alg3Gel1 exhibited the highest G" among all samples, while Alg3 displayed a lower G" than the cell-laden Alg3Gel1. Alg3 also exhibited the lowest G" overall. Taken together, the cell-laden Alg3Gel1 exhibited the highest G' and G" among all samples.

Figure 3C shows the ratio of G" to G' (tan δ) for both cell-free and cell-laden hydrogels. The data indicate that the cell-laden Alg3Gel1 had a higher G" than G', suggesting more solid-like behavior in the cell-laden Alg3Gel1. In contrast, both Alg3Gel1 and Alg3 exhibited the opposite trend, with a greater loss modulus than storage modulus.

3.2. Preliminary cell viability and computational fluid dynamics modeling

In this study, the bioprinting process parameters were determined based on CFD simulations and preliminary cell viability tests. As demonstrated in our previous study,[20] printing Alg3Gel1 scaffolds at 20 kPa of pressure and 4 mm/s speed resulted in scaffolds with a high elastic modulus, high swelling percentage, minimal mass loss, excellent printability, and high cell viability, making them ideal for engineered cardiac tissue. However, incorporating cells into the bioprinting process introduces a critical challenge—potential cell damage caused by bioprinting process-induced forces.

3.2.1. Preliminary cell viability analysis

A preliminary cell viability assay was employed to assess the effect of 3D-bioprinting pressure on cell viability.

Table 1. Parameters of the Cross model used to describe the flow behavior of the bioink at 37°C

Fluid	η_0 (Pa·s)	η_∞ (Pa·s)	k (s)	n
Cell-laden Alg3Gel1	110.34	9.16×10^{-16}	1.01	0.62

Notes: k and n are fitting parameters, η_0 is the limiting viscosity at low shear rates, and η_∞ is the limiting viscosity at high shear rates.

Abbreviation: Alg3Gel1, alginate 3 wt%–gelatin 1 wt%.

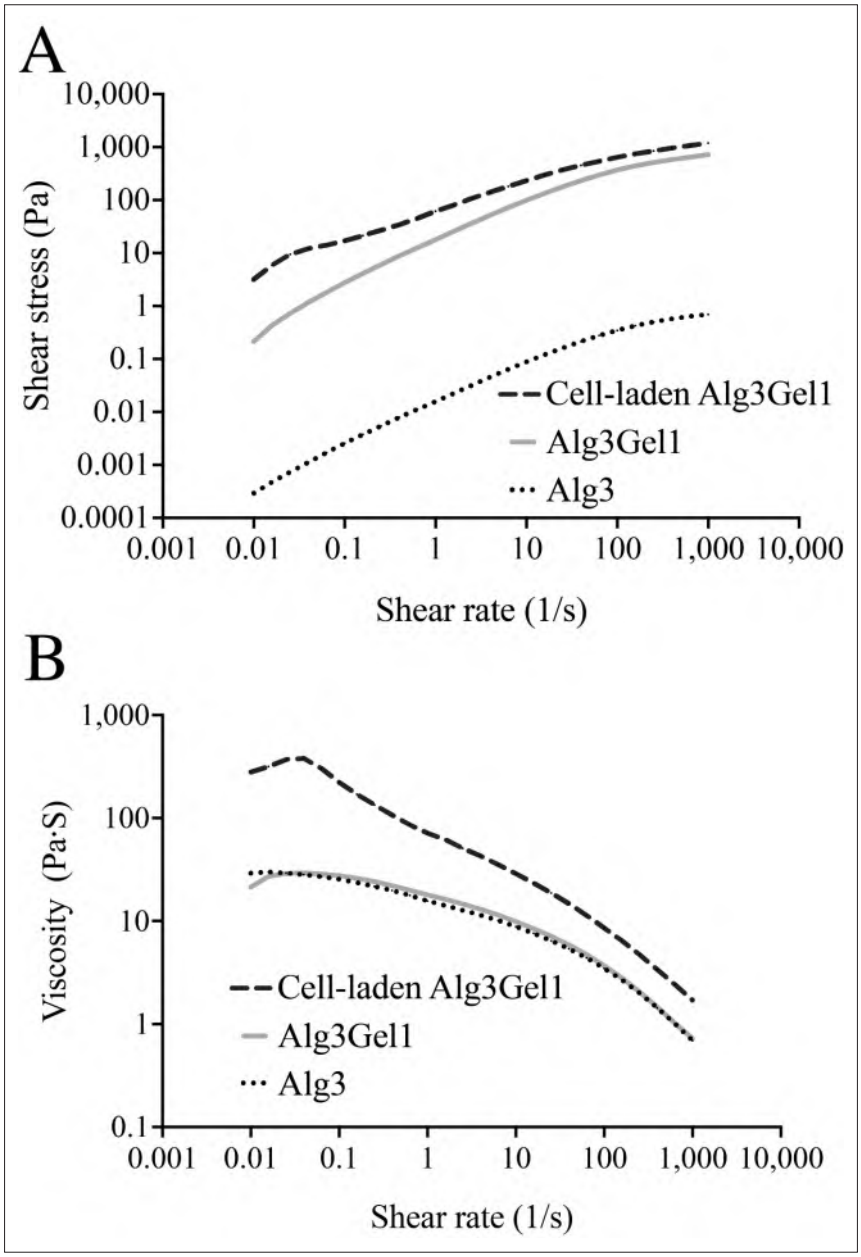


Figure 2. Rheological behavior of the hydrogels as a function of shear rate: (A) Shear stress vs. shear rate and (B) viscosity vs. shear rate. Abbreviations: Alg3, alginate 3 wt%; Alg3Gel1, alginate 3 wt%–gelatin 1 wt%.

In this study, the bioink was 3D-bioprinted into a single layer at pressures of 20 and 30 kPa. The theoretical fiber thickness was 0.15 mm, and the infill distance was 1.5 mm. For the 20 kPa pressure, the fiber thickness and infill distances were adjusted in terms of printability, mechanical properties, and the ability to support high cell viability, as determined in our previous study on cell-free scaffolds.[20]

Following the live/dead assay, all constructs exhibited high cell viability both immediately after bioprinting and on the following day. No noticeable differences in immediate post-printing viability were observed between constructs printed at 20 and 30 kPa. This is likely due to the delayed onset of mechanical stress-induced cellular responses, which typically require at least overnight incubation before detection via viability measurements.

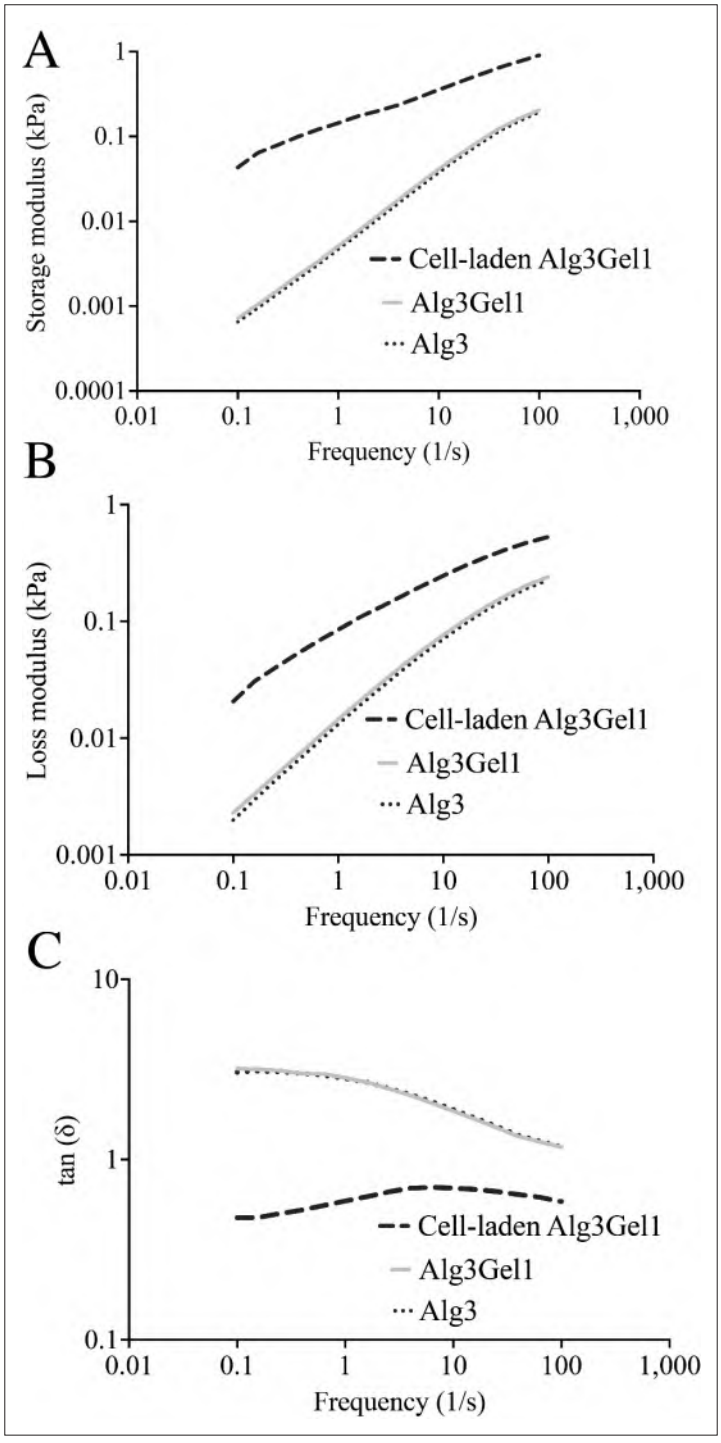


Figure 3. Frequency-dependent rheological properties of hydrogels and bioink: (A) Storage modulus (kPa) of cell-laden Alg3Gel1, Alg3Gel1 without cells, and Alg3 across a range of frequencies, (B) loss modulus (kPa) of the same groups, illustrating the viscous response under varying frequencies, and (C) tan δ (ratio of loss modulus to storage modulus) as a function of frequency. Abbreviations: Alg3, alginate 3 wt%; Alg3Gel1, alginate 3 wt%–gelatin 1 wt%.

The only noticeable difference was that a pressure of 30 kPa resulted in fibers with a greater thickness of approximately 0.6 mm, compared to the layer printed at 20 kPa, which had an approximate thickness of 0.3 mm (Figure S1). However, when 16-layer constructs were 3D-bioprinted using pressures of 20 and 30 kPa, significant differences were observed (Figure S2). On the first day after 3D-bioprinting, constructs printed at 20 kPa exhibited high cell viability. By day 21, the total cell count—including both viable and non-viable cells—significantly decreased for constructs printed at 30 kPa. Preliminary visual observations revealed that 3D-bioprinted constructs printed at 20 kPa exhibited fibers that appeared narrower compared to both cell-free fibers printed under the same pressure and cell–laden hydrogels printed at 30 kPa. These narrower fibers subsequently disintegrated after 21 days.

3.2.2. Computational fluid dynamics modeling

The numerical solution of the governing equations, along with specified boundary conditions, provides the distribution of velocity and pressure within the bioink as it flows through the syringe and nozzle. Additionally, the distribution of shear stress is calculated based on velocity gradients and the apparent viscosity distribution. Figure 4 illustrates the distribution of shear stress inside the syringe and printing nozzle. Simulations with different printing pressures revealed varying shear stress values near the nozzle outlet. Comparing the shear stress values for each printing pressure indicates an increase in shear stress with higher printing pressures. Table 2 lists the maximum shear stress values inside the nozzle for different printing pressures. Given the direct relationship between cell damage and shear stress, the CFD results suggest that the lowest applicable pressure capable of producing a stable fiber is the appropriate choice for printing.

The average velocity of bioink at the nozzle outlet can be calculated by area-weighted averaging of the normal component of velocity at the outlet. Applying different values of pressure boundary conditions on the bioink surface inside the syringe results in corresponding differences in the average velocity at the nozzle outlet. The average outlet velocity of extruded cell-laden Alg3Gel1 at a printing speed of 4 mm/s for different printing pressures, ranging from 20 to 40 kPa, is shown in Figure 5.

Given that the printing speed was set to 4 mm/s, only a pressure of 25 kPa resulted in an average outlet velocity of 4.26 mm/s (deposition speed), which is close to the printing speed. Minimizing the difference between deposition and printing speeds in extrusion bioprinting facilitates smooth and uniform bioink flow during extrusion from the nozzle, thereby improving printability. If the printing speed exceeds the deposition speed, the strand will be stretched,

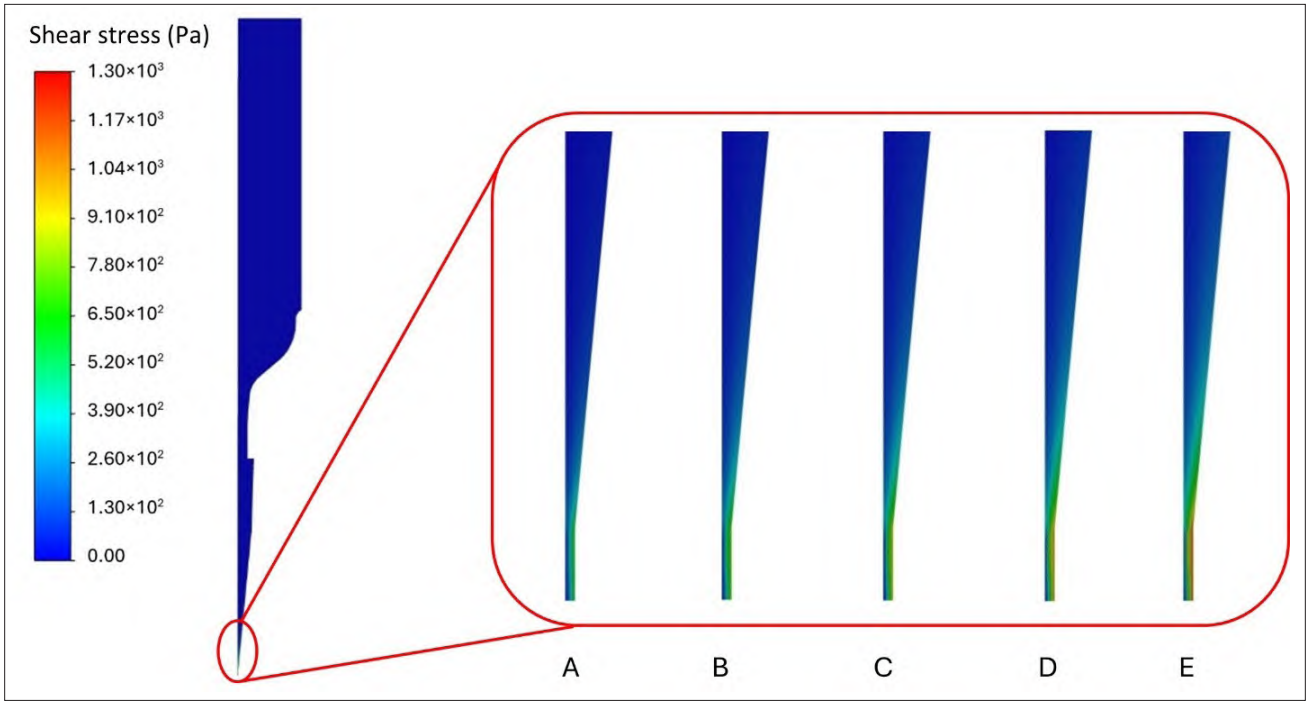


Figure 4. Distribution of shear stress inside the syringe and printing nozzle; magnified view of shear stress distribution near the nozzle outlet at printing pressures of (A) 20 kPa, (B) 25 kPa, (C) 30 kPa, (D) 35kPa, and (E) 40 kPa.

Table 2. Maximum shear stress values within the nozzle at different printing pressures

Printing pressure (kPa)	Maximum shear stress
20	685.37
25	839.76
30	992.34
35	1143.58
40	1293.79

causing cells to experience extensional stress that may damage their membranes.

Although compressive forces from hydrostatic pressure are minor, cell membranes may twist and stretch, potentially leading to cell damage if shear forces exceed physiological thresholds. Cells are particularly vulnerable when passing through the needle's constrictive region, where they are directly stretched and exposed to extensional stress.[26] A printing pressure of 20 kPa produces the minimum shear stress among the aforementioned cases. However, strands printed at 20 kPa are prone to lower printability and reduced cell viability due to the difference between dispensing and printing speeds. Therefore, a pressure of 25 kPa appears more suitable for bioprinting cell-laden Alg3Gel1 hydrogel constructs, ensuring adequate structural integrity and longevity. Consequently, we proceeded with the rest of the experiments using this pressure.

3.3. Mechanical, rheological, swelling, and mass retention properties of constructs

3.3.1. Mechanical and rheological properties

The elastic modulus of both cell-free and cell-laden Alg3Gel1 constructs is shown in Figure 6. The elastic modulus of cell-free scaffolds was measured as 9.24 ± 1.65 kPa, 10.08 ± 2.62 kPa, 11.27 ± 1.72 kPa, 7.20 ± 1.74 kPa, and 6.17 ± 1.27 kPa on days 0, 1, 3, 7, and 21, respectively. Similarly, the elastic modulus of cell-laden constructs was measured as 3.50 ± 0.71 kPa, 11.16 ± 2.43 kPa, 4.88 ± 1.37 kPa, 5.18 ± 2.42 kPa, and 4.65 ± 1.50 kPa on days 0, 1, 3, 7, and 21, respectively.

The elastic modulus of cell-free scaffolds showed an increasing trend from day 0 to day 3, followed by a decrease from day 7 to day 21. Day 3 exhibited the highest elastic modulus among all observed time points for cell-free scaffolds. Similarly, the elastic modulus of cell-laden constructs showed an initial increase from day 0 to day 1, followed by a decrease from day 1 to day 3. There was a slight increase on day 7, followed by a slight decrease on day 21. Although the elastic modulus values for cell-

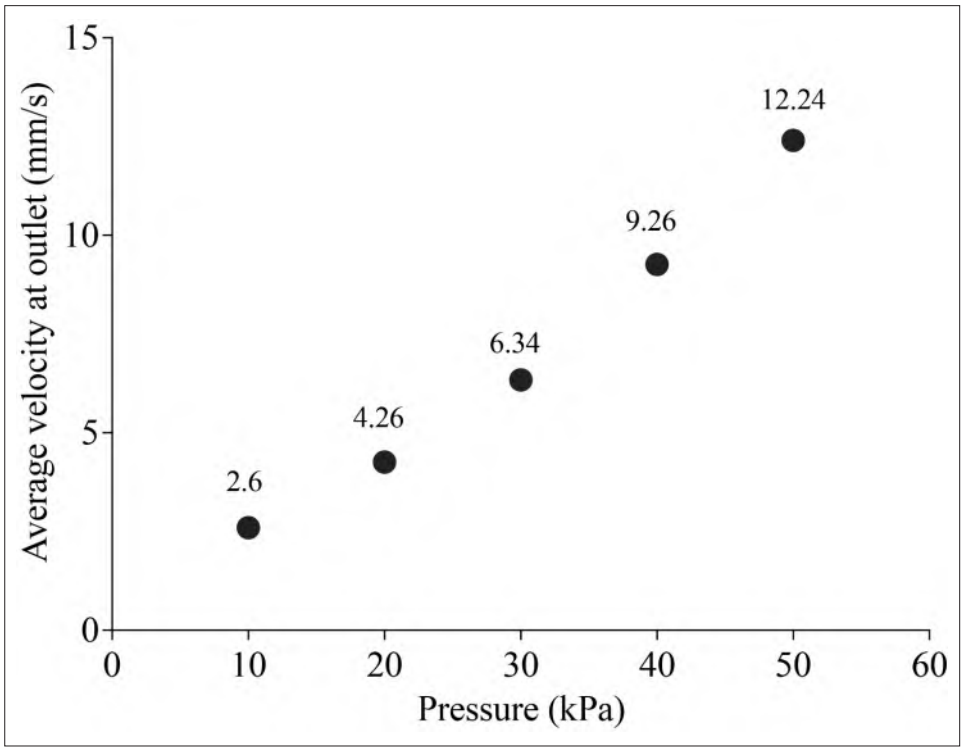


Figure 5. Calculated average outlet velocity at different printing pressures using the Cross model.

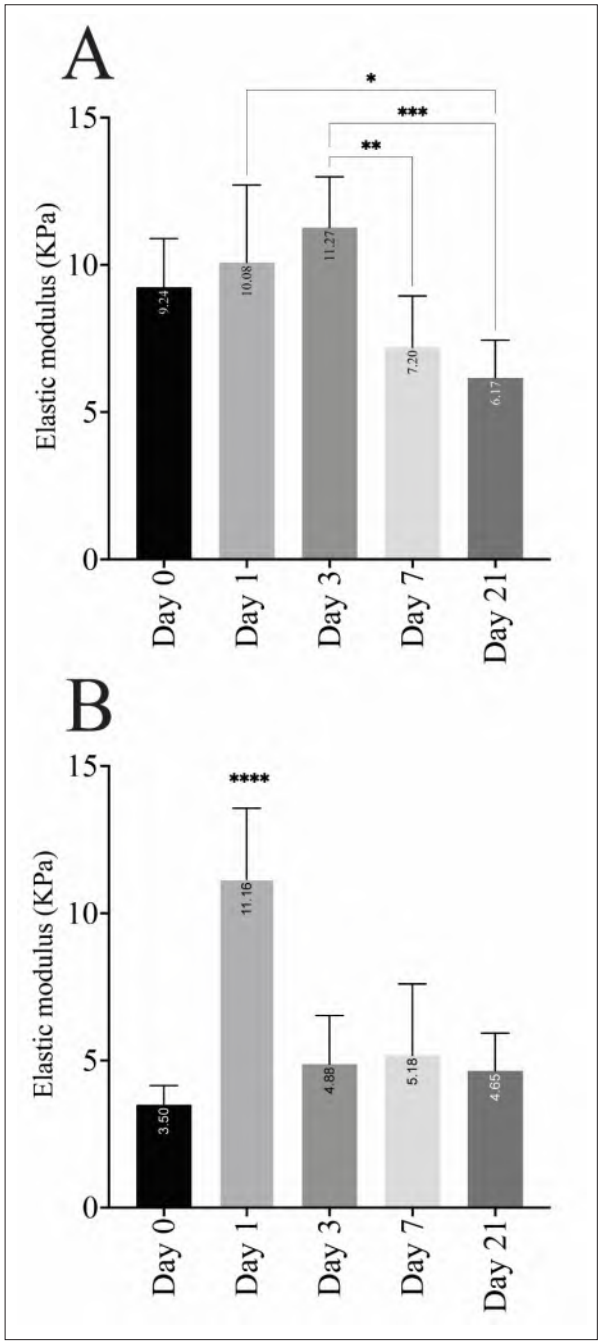


Figure 6. Elastic modulus of (A) three-dimensional-printed scaffolds and (B) cell-laden constructs. Statistical comparisons were performed using *one-way ANOVA* followed by Tukey's *post hoc test*. Significance thresholds: *$p < 0.05$, **$p < 0.01$, *** $p < 0.001$, ****$p < 0.0001$.

laden constructs are generally lower than those of cell-free scaffolds across most time points, they are significantly lower only on day 0 ($p = 0.000110$) and day 3 ($p < 0.000001$) compared to the cell-free scaffolds.

The storage (G') and loss (G") moduli versus frequency for both cell-free and cell-laden constructs are presented in Figure 7A and B, respectively. The G' of cell-free scaffolds was 3.94 kPa at 1 Hz and decreased to 2.37 kPa at 16 Hz. Concurrently, the G" was 0.83 kPa at 1 Hz and increased to 7.70 kPa at 16 Hz. For cell-laden constructs, the G' was 0.1 kPa at 1 Hz and decreased to 0.06 kPa at 16 Hz, while the G" was 0.04 kPa at 1 Hz and increased to 0.33

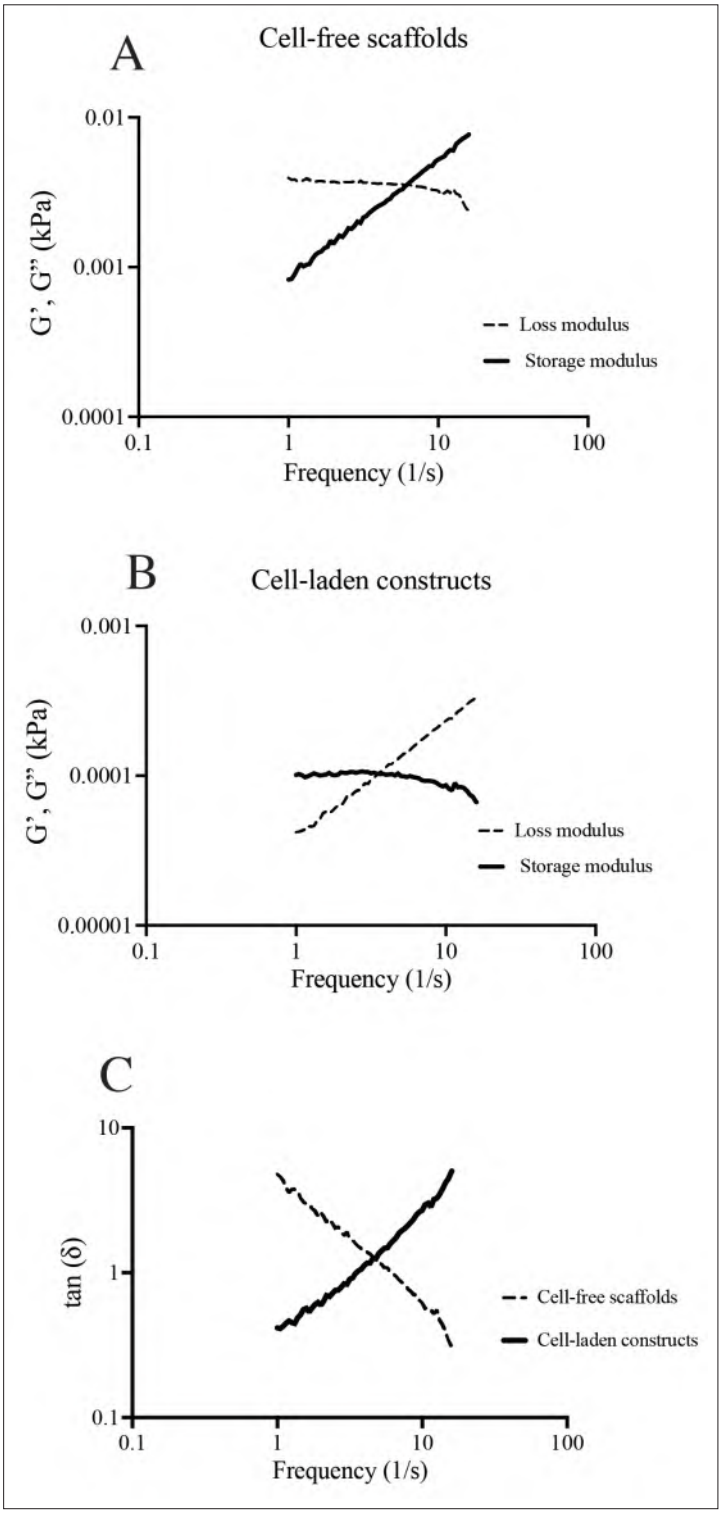


Figure 7. Viscoelastic behavior of three-dimensional-printed scaffolds and constructs: (A) Storage and loss moduli of cell-free scaffolds, (B) storage and loss moduli of Cell-laden constructs, and (C) tan δ of both cell-free scaffolds and cell-laden constructs.

kPa at 16 Hz. These findings indicate that both cell-free and cell-laden constructs exhibited viscoelastic behavior. However, the cell-laden constructs demonstrated less solid-like and more liquid-like behavior compared to the cell-free scaffolds. Figure 7C shows the damping factor (tan δ) for both cell-free and cell-laden constructs. For cell-laden constructs, tan δ was less than 1 at low frequencies, indicating more solid-like behavior, and exceeded 1 at higher frequencies, suggesting more liquid-like behavior. In contrast, cell-free scaffolds displayed the opposite trend, with tan δ greater than 1 at low frequencies and less than 1 at higher frequencies.

3.3.2. Swelling and mass retention percentages

The swelling and mass retention percentages of the cell-free and cell-laden constructs following incubation in complete culture medium over 21 days are shown in Figure 8**.** The swelling percentage of cell-free scaffolds was measured as 76.78, 80.25, 60.49, and 80.42% on days 1, 3, 7, and 21, respectively (Figure 8A). These scaffolds maintained a consistent swelling percentage throughout the experimental period, except on day 7, where they exhibited a statistically lower swelling percentage compared to days 3 and 21 ($p < 0.05$). Similarly, the cell-laden constructs maintained a consistent swelling percentage throughout the experiment, with a slight increase observed on day 21 post-printing, reaching statistical significance compared to day 7 ($p < 0.05$). The swelling percentage of cell-laden constructs was 62.33, 60.97, 53.45, and 72.98% on days 1, 3, 7, and 21, respectively (Figure 8C). While the swelling percentage of cell-free scaffolds was higher compared to that of the cell-laden constructs at each time point, no statistical difference was observed between them on any respective day, as determined by a one-way ANOVA with Tukey's post hoc multiple comparisons test.

The mass retention percentages of cell-free scaffolds (Figure 8B) demonstrated that these scaffolds retained more than 70% of their initial mass throughout the experimental period. Specifically, on day 1, the mass retention was 72.04%, followed by a significant increase ($p < 0.01$) to 83.95% on day 3. Conversely, a significant decrease in mass retention percentage was observed on day 7 ($p < 0.01$), decreasing to 73.62%. Interestingly, on day 21, a significant gain in mass ($p < 0.05$) was observed, reaching 83.82%. These findings highlight the dynamic nature of mass changes in the cell-free scaffolds over the experimental period. In contrast, the cell-laden constructs consistently exhibited nearly 100% mass retention over the 21-day period (Figure 8D). Overall, the mass retention percentage of cell-laden constructs was higher than that of the cell-free scaffolds at each time point ($p < 0.0001$), as determined by a one-way ANOVA with Tukey's post hoc multiple comparisons test.

3.4. Field emission scanning electron microscopy analysis

To examine the morphological changes of the printed structures over time, FESEM was employed to capture images of the lyophilized cell-free scaffolds (Figure 9) and cell-laden constructs (Figure 10).

The FESEM images of the cell-free scaffolds displayed signs of mass loss, which were noticeable from day 1. These changes became more pronounced by day 7 and peaked on day 21, providing visual insights into the progressive mass loss of the scaffolds over the 21-day period. The images of the cell-laden constructs revealed a more pronounced mass loss from day 1 to day 7 compared to the cell-free scaffolds. Surprisingly, by day 21, the cell-laden constructs exhibited a more uniform structure while maintaining their angular and hierarchical characteristics.

3.5. Cell viability analysis

To evaluate the distribution and viability of the 3D-bioprinted cells within the constructs, a live/dead assay was conducted over a 21-day period (Figure 11). The findings revealed that the majority of the cells were viable post-printing (Figure 9A–C). During the first 3 days post-printing, a notable increase in the density of viable cells was observed, along with the detection of a small population of dead cells. From day 7 to day 21, both the viable and dead cell populations decreased. These findings suggest that HUVECs tolerated 3D-printing well, with only minor adverse effects.

4. Discussion

Understanding the rheology and flow behavior of inks, particularly bioinks, before proceeding with extrusion 3D-printing is essential to ensure the fabrication of precise 3D-bioprinted constructs with high cell viability. Higher ink viscosity improves the mechanical properties of the ink, potentially resulting in improved printing resolution and greater printing fidelity.[27,28] While a controlled applied load on living cells may promote growth, locomotion, and differentiation, increasing the applied pressure can elevate nozzle–wall shear stress, leading to clogging of the printing nozzle, which could negatively affect cell viability and cell phenotype.[29,30] Bioprinting may reduce cell viability to below 60%, depending on the cell type.[31] Here, a primary challenge was to determine the appropriate printing pressure for fabricating a cell-laden construct using a bottom-up approach, ensuring high cell viability while maintaining printing parameters comparable to those used in previously fabricated structures with the top-

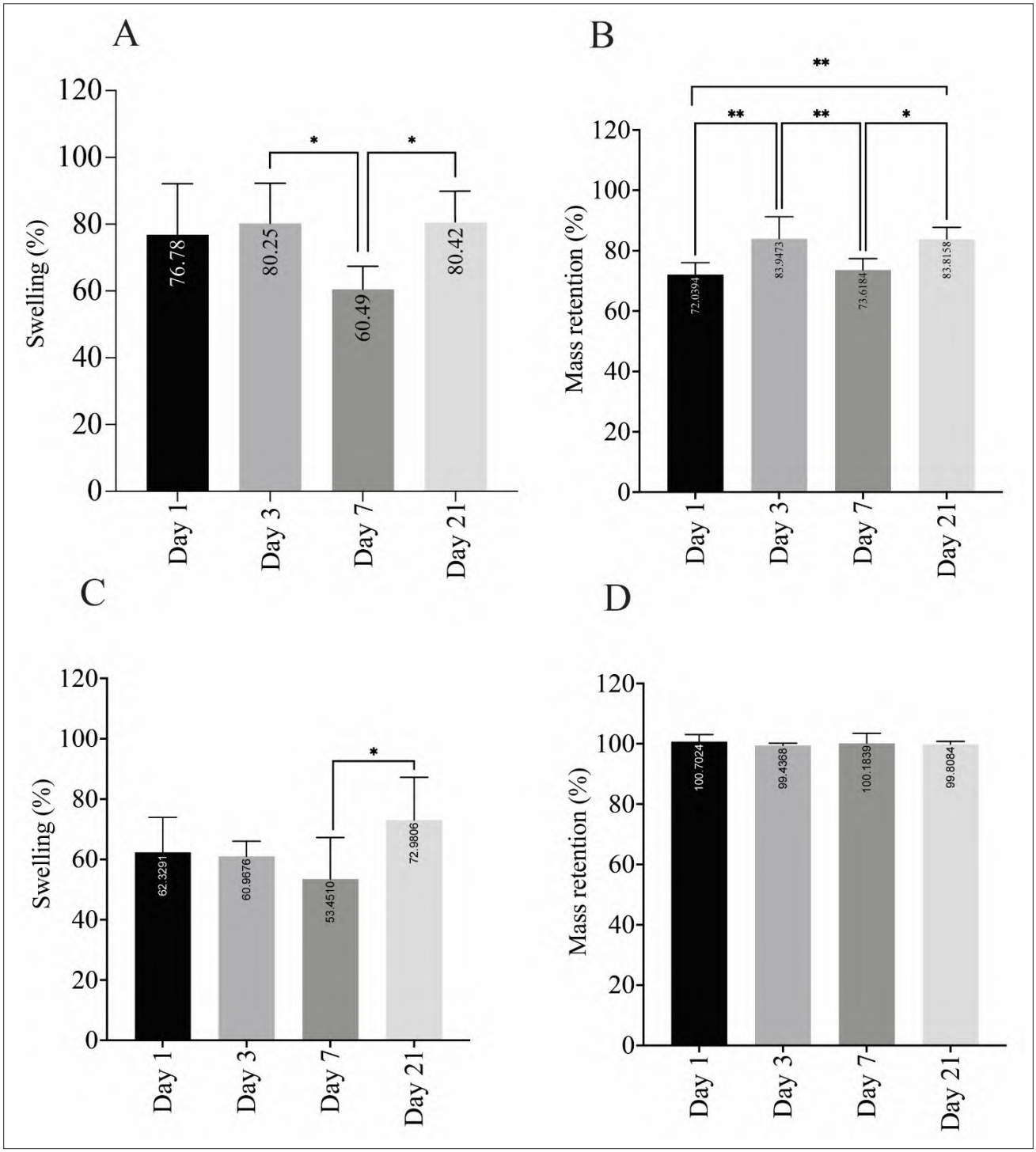


Figure 8. Swelling and mass retention percentage for cell-free scaffolds and cell-laden constructs: (A) the swelling percentage of cell-free scaffolds, (B) the mass retention percentage of cell-free scaffolds, (C) the swelling percentage of cell-laden constructs, and (D) the mass retention percentage of cell-laden constructs. The data in each graph were compared within the same graph using one-way ANOVA followed by Tukey's post hoc test. Significance thresholds: *$p < 0.05$, **$p < 0.01$.

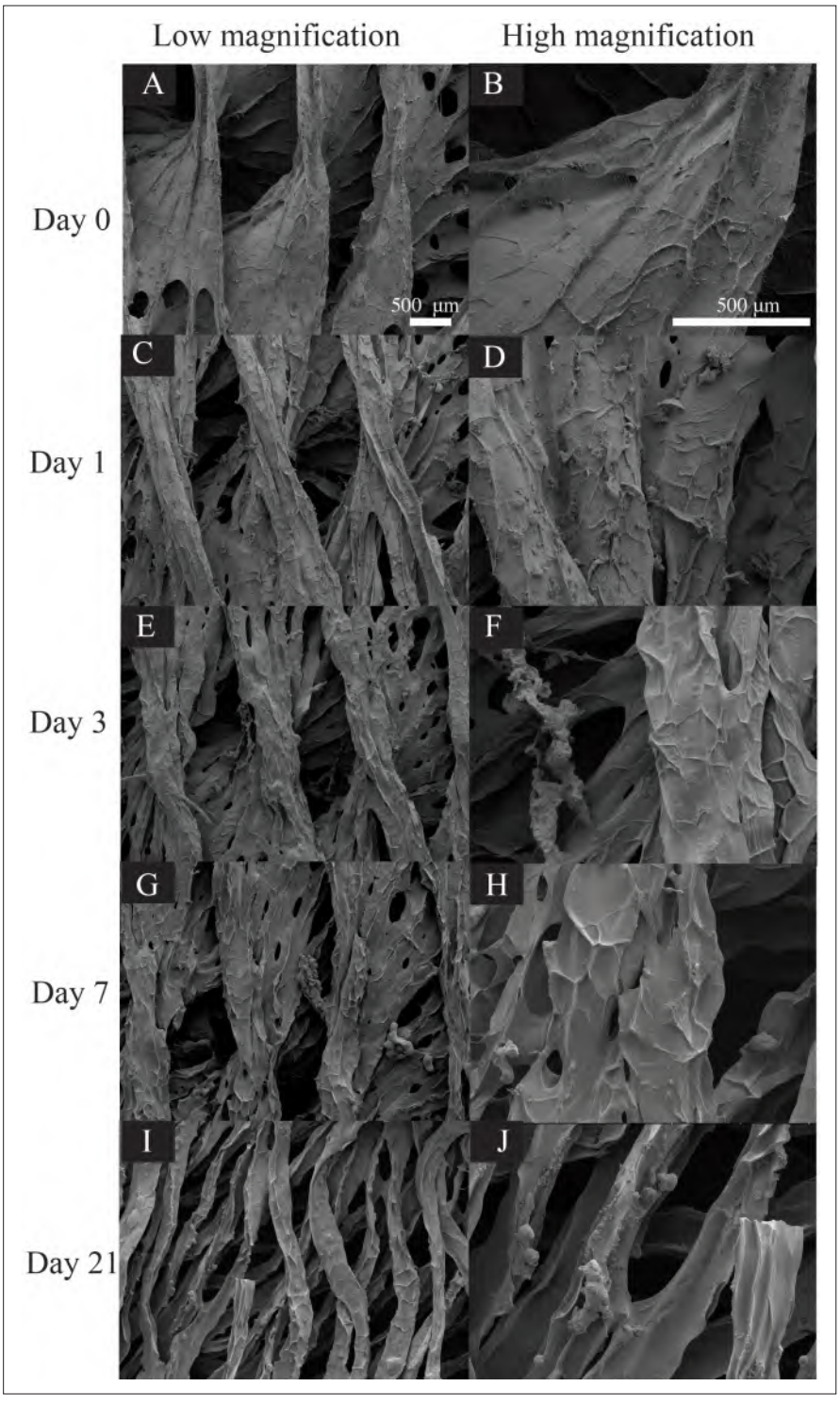


Figure 9. Field emission scanning electron microscopy images of lyophilized cell-free scaffolds at different time points. Low magnification images on (A) day 0, (C) day 1, (E) day 3, (G) day 7, and (I) day 21 (scale bar: 500 μm; magnification: 30×), and corresponding higher-magnification images on (B) day 0, (D) day 1, (F) day 3, (H) day 7, and (J) day 21 (scale bar: 500 μm; magnification: 100×).

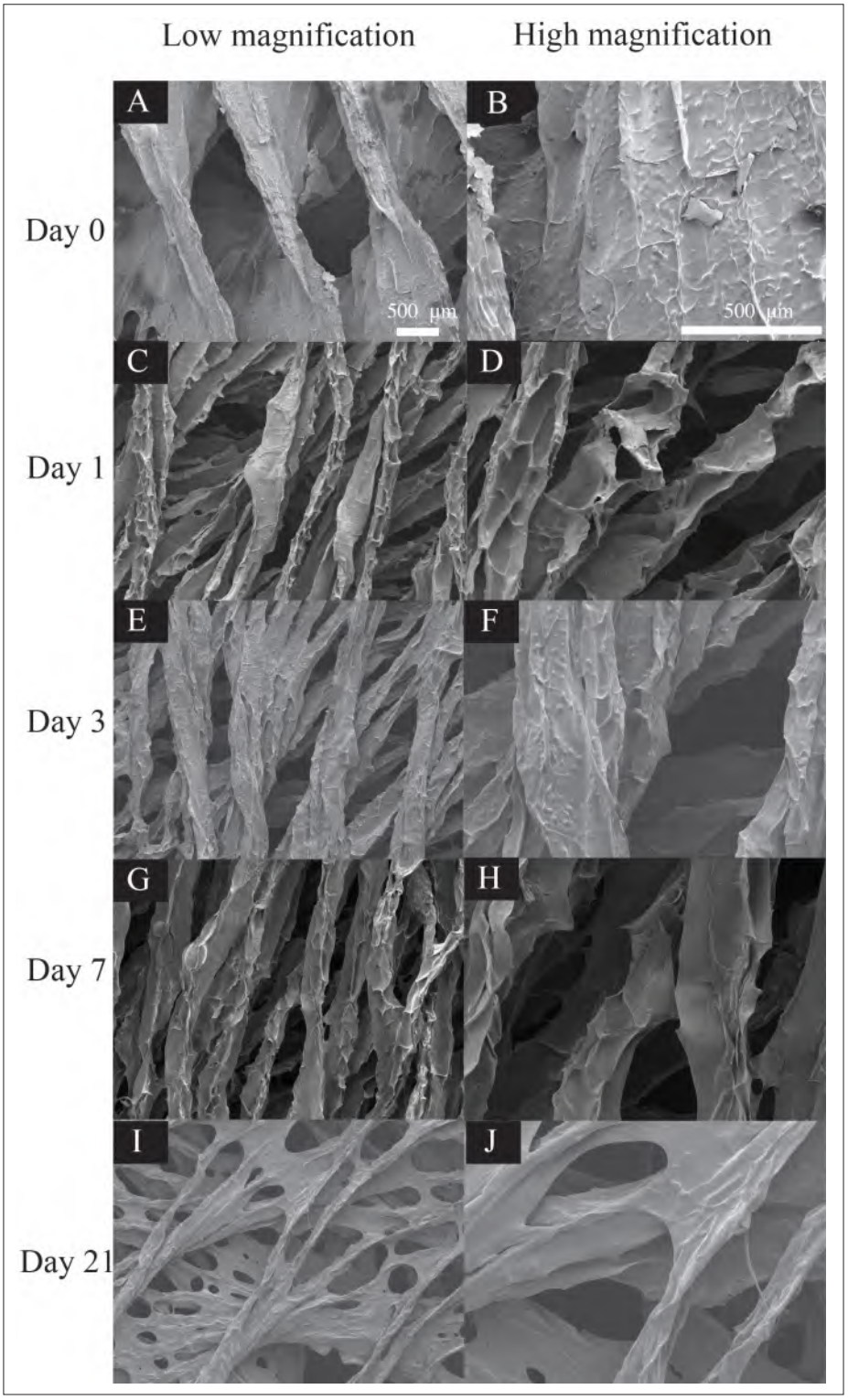


Figure 10. Field emission scanning electron microscopy images of lyophilized cell-laden constructs at different time points. Low magnification images on (A) day 0, (C) day 1, (E) day 3, (G) day 7, and (I) day 21 (scale bar: 500 μm; magnification: 30×), and corresponding higher-magnification images on (B) day 0, (D) day 1, (F) day 3, (H) day 7, and (J) day 21 (scale bar: 500 μm; magnification: 100×).

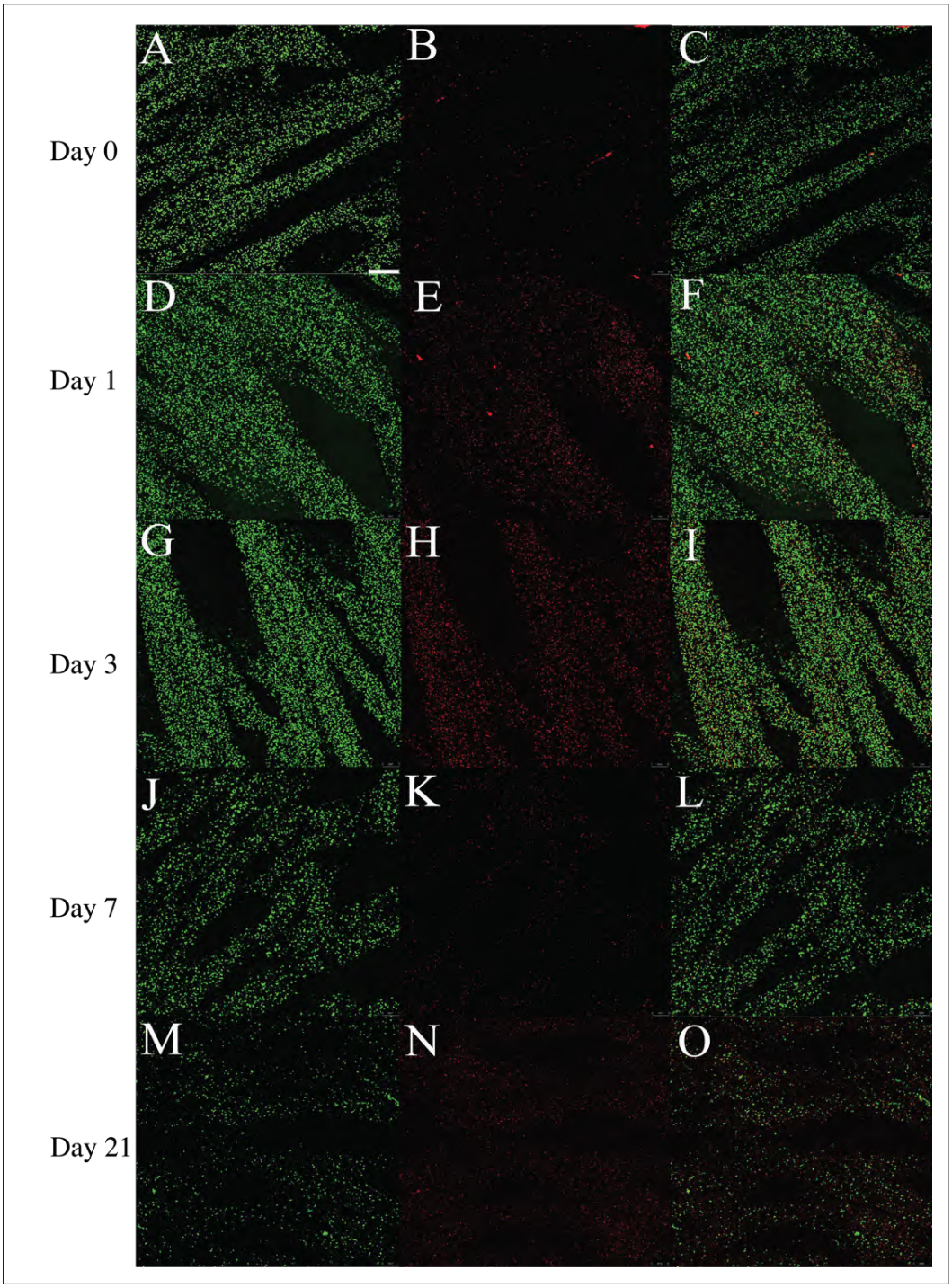


Figure 11. Cell viability assessment using the live/dead assay for three-dimensional-bioprinted constructs at different time points: (A–C) day 0, (D–F) day 1, (G–I) day 3, (J–L) day 7, and (M–O) day 21. The left column (A, D, G, J, M) displays live cells stained with calcein-AM, the middle column (B, E, H, K, N) shows dead cells stained with propidium iodide, and the right column (C, F, I, L, O) presents merged images of live and dead cells (scale bar: 500 μm; magnification: 5×).

down approach.[20] Subsequently, cell-free and cell-laden constructs were fabricated to evaluate the effect of cell presence on the physical and morphological properties of the constructs over time.

During the process of extrusion 3D-bioprinting, cells encounter various mechanical forces that can impact their viability and functionality. Among these forces, shear stress is considered particularly detrimental to cell viability and survival.[32] It is an inherent mechanical stress experienced by cells in all bioprinting approaches, posing a significant risk of cell damage and death depending on its intensity.[32] Controlling the shear forces generated within the bioprinting nozzle can enhance cell survival and proliferation post-3D-bioprinting.[33]

To minimize shear forces during 3D-bioprinting, it is essential to adjust the printing pressure to the minimum level that ensures a steady flow of bioink through the bioprinting nozzle, while also extruding the bioink at a deposition speed that closely matches the intended printing speed. Rheological studies on the bioink, including both steady shear and oscillatory shear tests, are essential for evaluating the bioink's suitability for 3D-bioprinting. These studies also provide crucial data for computational modeling of bioink flow behavior, supporting CFD simulations. CFD helps determine the appropriate pressure and printing speed, resulting in good printability and enhanced cell viability for printed constructs.

The findings of this study highlight the significant impact of cells on the viscosity of the bioink. While many studies on 3D-bioprinting have focused solely on the rheological behavior of the bioink without considering the presence of cells, our findings indicate that HUVECs can indeed have a significant effect on bioink rheology. The rheological behavior of both cell-free Alg3Gel1 and cell-laden Alg3Gel1 constructs exhibited shear-thinning behavior, which is advantageous for 3D-printing or bioprinting. This shear-thinning property is a key factor in ensuring proper printability and maintaining shape fidelity in extrusion printing.[28] The incorporation of cells increased the viscosity of the hydrogel from 21.27 to 167.95 Pa·s at a shear rate of 0.009992 s^{-1} and from 0.72 to 6.41 Pa·s at a shear rate of 999.95 s^{-1}. These findings are consistent with previous studies that indicate an increase in viscosity with higher cell densities.[34] However, these findings also contradict other studies that demonstrate a decrease in viscosity upon introducing cells or with increasing cell concentration,[35,36] suggesting a possible dependency on cell type, cell density, and hydrogel composition.

In this study, the increased viscosity of the cell-laden Alg3Gel1 construct is mostly related to the introduction of additional particulate matter in the bioink and potential interactions among the cell–hydrogel and/or cell–cell components. Because cells act as non-soluble microparticles suspended within the hydrogel, the system shifts from a single-phase to a two-phase structure.[37] This also explains the higher G' and G" of cell-laden bioink compared to cell-free Alg3Gel1. It is worth noting that the cell-laden Alg3Gel1 constructs exhibited a higher G' than G" compared to the Alg3Gel1 and Alg3 samples. This characteristic is advantageous for 3D-printing , as it ensures that the material can be extruded while maintaining its shape after extrusion.[38]

The higher viscosity of cell-laden bioink may require greater extrusion forces, leading to increased shear stresses experienced by the cells.[39] This can result in potential cell damage or even death. Therefore, based on the initial study of printability and the determination of a suitable printing pressure and speed for achieving a printable structure, a computational technique can be employed to determine the appropriate printing speed and pressure. This ensures that the difference between the defined printing velocity and the outlet velocity is minimized. Furthermore, the appropriate printing speed and pressure for producing scaffold fibers can be refined by conducting viability assays to determine the final appropriate parameters. This approach ensures high cell viability along with high printability and structural fidelity.

The rheological and mechanical properties, swelling behavior, and degradation of the structures were investigated by assessing the viscoelasticity, elastic modulus, swelling, and mass retention percentages of both cell-free and cell-laden constructs to determine the influence of living cells on these parameters. Evaluating both the elastic modulus and the viscoelastic properties (storage and loss modulus) provides a more comprehensive understanding of the mechanical behavior of the constructs. Although the static elastic modulus provides insights into the yielding strain (or stress) and the linear stress–strain response of a material, it cannot reveal the complex modulus, which encompasses both the storage (elastic) and loss (viscous) components.[40] This distinction is crucial, as no material is purely elastic or viscous. Instead, a material's behavior can range from solid-like to liquid-like depending on the frequency of the applied force. Therefore, evaluating a construct's response to dynamic stimuli is crucial in fields where frequency-dependent variations in modulus are significant.[40]

The myocardium exhibits dynamic viscoelastic behavior— its stiffness can vary depending on the speed and extent of the stretch it experiences. However, myocardial viscoelasticity often increases in myocardial

diseases, which can lead to reduced cardiac output by impeding diastolic filling.[41] Although many studies have measured the elasticity of the human heart, measuring its viscosity remains a challenge.[42] Simulations within the physiological range of the human heartbeat suggest that the viscous component of the human heart has a minor influence on its overall behavior, indicating that the human heart is hyperelastic.[42] Although both cell-free and cell-laden constructs exhibited viscoelastic behavior, the cell-laden constructs displayed more solid-like behavior at lower frequencies and more liquid-like behavior at higher frequencies, whereas the cell-free constructs exhibited the opposite trend.

The high water content in cell-laden constructs—since water accounts for 70% or more of total cell mass[43]—is most likely responsible for the more liquid-like response of the cell-laden constructs compared to the cell-free scaffolds.[44] This was confirmed by compressive mechanical tests measuring the elastic modulus of the constructs, which generally showed a lower elastic modulus for cell-laden constructs compared to cell-free scaffolds. However, only two out of the five time points showed a statistically significant difference.

Although there is limited knowledge comparing the mechanical properties of cell-free and cell-laden constructs, our findings are supported by a previous study[45] on hyaluronic acid-based constructs for cartilage tissue engineering, where the cell-laden constructs exhibited a lower elastic modulus compared to cell-free scaffolds on day 1. The mechanical properties of these constructs can vary depending on several factors, such as the specific type of cells used, the scaffold material, or the method by which the cells are incorporated into the scaffolds. For example, in a study involving smooth muscle cells, both smooth muscle cell-seeded and unseeded elastin-modified collagen sheets showed a lower Young's modulus compared to unseeded collagen sheets over 3 weeks, highlighting how different experimental conditions can influence the mechanical outcomes.[46]

A healthy myocardium has a stiffness of 10–15 kPa, while an infarcted myocardium has a stiffness of 35–70 kPa. To maintain their striations and a beating frequency of 1 Hz, cardiac myocytes should be grown on a substrate with stiffness comparable to that of a healthy myocardium. In contrast, growing cardiac cells on stiffer matrices may lead to a shorter beating period.[47,48] In this study, both cell-free and cell-laden constructs exhibited an elastic modulus of less than 15 kPa over time, indicating their potential suitability as substrates for culturing cardiac myocytes. The cell-laden constructs contain cells with high water content, which affects their viscoelastic behavior and elastic modulus. This could explain the lower swelling percentage of cell-laden constructs compared to cell-free scaffolds, although the difference is not statistically significant.

While the mass retention percentages showed a trend similar to that of the swelling percentages for cell-free scaffolds, the mass retention for cell-laden constructs demonstrated almost no mass loss. The higher mass retention in cell-laden constructs compared to cell-free scaffolds could be attributed to their lower swelling percentages, resulting in reduced hydrolytic mass loss. Additionally, the high swelling percentage of cell-free alginate-based scaffolds is likely associated with a lower content of calcium ions.[49] This relationship may be slightly altered in cell-laden constructs due to potential interactions between the cells and the calcium ions present within the construct.

However, the FESEM images of cell-laden constructs revealed significant signs of mass loss over time, similar to cell-free scaffolds. While this was anticipated for cell-free scaffolds based on the mass retention percentage, it was not expected for cell-laden constructs, which exhibited an almost 100% mass retention percentage. Interestingly, the FESEM images revealed that the cell-laden constructs exhibited more signs of mass loss until day 7, but by day 21, they exhibited a more integrated structure compared to cell-free scaffolds. This suggests that weight-based mass retention characterization may not be an appropriate method for assessing mass loss in cell-laden constructs.

Although there is limited knowledge regarding the impact of cells on the physical and mechanical properties of engineered tissues, our findings highlight the complex influence of HUVECs in these constructs. This underscores the need for further research on the mechanical properties of cell-laden engineered tissues, especially in contexts involving cell encapsulation for both *in vitro* and *in vivo* studies. Additionally, the cell viability assay exhibited high cell viability after 3D-bioprinting until day 7. The cells may have entered a resting phase after 7 days due to prolonged stationary incubation or inadequate nutrient supply, leading to cell death.[50] This suggests that the cell-laden constructs reached their maximum cellular capacity after 7 days.[50]

The primary objective of this study was to monitor cell viability following bioprinting, rather than to assess long-term proliferation or functionality. We have successfully achieved this goal, demonstrating high post-printing cell viability. Future studies aiming to develop functional vascular networks will require the incorporation of targeted treatments, such as supplementation with specific growth factors to promote vascularization, and the

assessment of long-term cellular functionality. In contrast, the present work was deliberately focused on preserving viable cells during and after printing and on examining how their presence affects the mechanical, rheological, and microstructural properties of the scaffolds.

5. Conclusion

Developing 3D-bioprinted tissue constructs offers promising opportunities for replicating complex, tissue-like structures. However, key challenges persist, particularly in maintaining high cell viability during printing and in understanding how living cells influence the mechanical and physical properties of the constructs. To address these challenges, we incorporated HUVECs into alginate–gelatin hydrogels and bioprinted them under optimized conditions, focusing on minimizing printing pressure-induced cell damage and elucidating the effects of incorporated cells.

The mechanical and rheological properties of both cell-free and cell-laden constructs were evaluated to assess the long-term influence of cells on these properties. Key findings revealed that cell-laden constructs exhibited higher viscosity and a greater storage modulus than the loss modulus compared to cell-free constructs. Based on preliminary cell viability data, CFD modeling, and experimental observations, 25 kPa was identified as the appropriate pressure for bioprinting these constructs. This pressure minimizes process-induced forces on the cells while maintaining a steady bioink flow through the nozzle, thereby reducing strand deformation and cell stretching during deposition.

Although both cell-laden and cell-free constructs exhibited viscoelastic behavior, the cell-laden constructs displayed more fluid-like characteristics, as evidenced by a lower elastic modulus relative to cell-free scaffolds. The cell-free scaffolds also exhibited a higher swelling percentage than the cell-laden constructs. While mass retention assays suggested minimal degradation over time, FESEM imaging revealed distinct signs of degradation in cell-free constructs. Furthermore, high cell viability was maintained in the 3D-bioprinted constructs for at least 7 days post-printing.

Our findings demonstrate the potential of cell-laden constructs with an angular design mimicking the orientation of heart myofibrils as suitable substrates for cardiomyocyte growth, particularly following vascularization within the constructs. As the present study primarily focused on maintaining cell viability post-printing rather than assessing cellular functionality, future research should investigate the functional behavior of incorporated endothelial cells, with the aim of promoting vascularization to support cardiomyocyte integration and maturation in these bioprinted constructs.

Acknowledgments

The authors express their gratitude to Dr. Graham George and Dr. Ingrid J. Pickering for generously providing access to the confocal microscope. Special thanks are also extended to Peyman Asadi for designing the graphical abstract.

Funding

This study was supported by the Natural Sciences and Engineering Research Council of Canada (grant number: PGPIN 06396-2019). Additional support was provided through the Saskatchewan Research Chair in Clinical Stroke Research, awarded to MK by the Heart and Stroke Foundation, the Saskatchewan Health Research Foundation, and the University of Saskatchewan College of Medicine. The study was further supported by a Dean's Scholarship and a Biomedical Engineering Devolved Scholarship, both awarded to FK by the University of Saskatchewan.

Conflict of interest

Xiongbiao Chen serves as the Editorial Board Member of the journal, but did not in any way involve in the editorial and peer-review process conducted for this paper, directly or indirectly. Other authors declare they have no competing interests.

Author contributions

Conceptualization: Farinaz Ketabat, Michael E. Kelly, Ildiko Badea, Xiongbiao Chen
Data curation: Farinaz Ketabat
Formal analysis: Farinaz Ketabat, Reza Gharraei, Alex Guinle
Funding acquisition: Michael E. Kelly, Ildiko Badea, Xiongbiao Chen
Investigation: Farinaz Ketabat, Reza Gharraei, Alex Guinle, Nicole J. Sylvain
Methodology: Farinaz Ketabat, Reza Gharraei, Alex Guinle
Resources: Michael E. Kelly, Ildiko Badea, Xiongbiao Chen
Supervision: Michael E. Kelly, Ildiko Badea, Xiongbiao Chen
Writing – original draft: Farinaz Ketabat
Writing – review & editing: All authors

Ethics approval and consent to participate

Not applicable.

Consent for publication

Not applicable.

Availability of data

Data is available from the corresponding author upon reasonable request.

Further disclosure

This work was previously presented at the 2024 CSPS/CCCRS Annual Symposium (June 10–13, 2024, Edmonton, Alberta, Canada) as a poster. During the preparation of this work, FK used ChatGPT 4.0 and Copilot in order to improve language and readability. After using this tool/service, FK reviewed and edited the content as needed and takes full responsibility for the content of the publication.

References

1. Cho S, Discher DE, Leong KW, Vunjak-Novakovic G, Wu JC. Challenges and opportunities for the next generation of cardiovascular tissue engineering. *Nat Methods*. 2022;19(9):1064-1071. doi: 10.1038/s41592-022-01591-3
2. Garbern JC, Lee RT. Heart regeneration: 20 years of progress and renewed optimism. *Dev Cell*. 2022;57(4):424-439. doi: 10.1016/j.devcel.2022.01.012
3. Izadifar M, Chapman D, Babyn P, Chen X, Kelly ME. UV-assisted 3D-bioprinting of nanoreinforced hybrid cardiac patch for myocardial tissue engineering. *Tissue Eng Part C Methods*. 2018;24(2):74-88. doi: 10.1089/ten.tec.2017.0346
4. Sobanski PZ, Alt-Epping B, Currow DC, *et al*. Palliative care for people living with heart failure: European Association for Palliative Care Task Force expert position statement. *Cardiovasc Res*. 2020;116(1):12-27. doi: 10.1093/cvr/cvz200
5. Truby LK, Rogers JG. Advanced heart failure: epidemiology, diagnosis, and therapeutic approaches. *Heart Fail*. 2020;8(7):523-536. doi: 10.1016/j.jchf.2020.01.014
6. Tenreiro MF, Louro AF, Alves PM, Serra M. Next generation of heart regenerative therapies: progress and promise of cardiac tissue engineering. *NPJ Regen Med*. 2021;6(1):30. doi: 10.1038/s41536-021-00140-4
7. Wang Z, Wang L, Li T, *et al*. 3D-bioprinting in cardiac tissue engineering. *Theranostics*. 2021;11(16):7948. doi: 10.7150/thno.61621
8. Liu N, Ye X, Yao B, *et al*. Advances in 3D-bioprinting technology for cardiac tissue engineering and regeneration. *Bioact Mater*. 2021;6(5):1388-1401. doi: 10.1016/j.bioactmat.2020.10.021
9. Agarwal T, Fortunato GM, Hann SY, *et al*. Recent advances in bioprinting technologies for engineering cardiac tissue. *Mater Sci Eng C*. 2021;124:112057. doi: 10.1016/j.msec.2021.112057
10. Chang YC, Mirhaidari G, Kelly J, Breuer C. Current challenges and solutions to tissue engineering of large-scale cardiac constructs. *Curr Cardiol Rep*. 2021;5(47):1-6. doi: 10.1007/s11886-021-01474-7
11. Ning L, Betancourt N, Schreyer DJ, Chen X. Characterization of cell damage and proliferative ability during and after bioprinting. *ACS Biomater Sci Eng*. 2018;4(11):3906-3918. doi: 10.1021/acsbiomaterials.8b00714
12. Noroozi R, Arif ZU, Taghvaei H, *et al*. 3D and 4D bioprinting technologies: a game changer for the biomedical sector? *Ann Biomed Eng*. 2023;51(8):1683-1712. doi: 10.1007/s10439-023-03243-9
13. Tiruvannamalai-Annamalai R, Armant DR, Matthew HWT. A glycosaminoglycan based, modular tissue scaffold system for rapid assembly of perfusable, high cell density, engineered tissues. *PLoS One*. 2014;9(1):e84287. doi: 10.1371/journal.pone.0084287
14. Ketabat F, Alcorn J, Kelly ME, Badea I, Chen X. Cardiac tissue engineering: a journey from scaffold fabrication to in vitro characterization. *Small Sci*. 2024;4(9):2400079. doi: 10.1002/smsc.202400079
15. Chen XB, Anvari-Yazdi AF, Duan X, *et al*. Biomaterials/bioinks and extrusion bioprinting. *Bioact Mater*. 2023;28:511-536. doi: 10.1016/j.bioactmat.2023.06.006
16. Ning L, Chen X. A brief review of extrusion-based tissue scaffold bio-printing. *Biotechnol J*. 2017;12(8):1600671. doi: 10.1002/biot.201600671
17. Lemarié L, Anandan A, Petiot E, Marquette C, Courtial EJ. Rheology, simulation and data analysis toward bioprinting cell viability awareness. *Bioprinting*. 2021;21:e00119. doi: 10.1016/j.bprint.2020.e00119
18. Krishnamoorthy S, Noorani B, Xu C. Effects of encapsulated cells on the physical–mechanical properties and microstructure of gelatin methacrylate hydrogels. *Int J Mol Sci*. 2019;20(20):5061. doi: 10.3390/ijms20205061
19. Otto IA, Levato R, Webb WR, *et al*. Progenitor cells in auricular cartilage demonstrate cartilage-forming capacity in 3D hydrogel culture. *Eur Cell Mater*. 2018;35:132. doi: 10.22203/eCM.v035a10
20. Ketabat F, Maris T, Duan X, *et al*. Optimization of 3D-printing and in vitro characterization of alginate/gelatin lattice and angular scaffolds for potential cardiac tissue engineering. *Front Bioeng Biotechnol*. 2023;11:1161804. doi: 10.3389/fbioe.2023.1161804
21. Maiullari F, Costantini M, Milan M, *et al*. A multi-cellular 3D-bioprinting approach for vascularized heart tissue engineering based on HUVECs and iPSC-derived cardiomyocytes. *Sci Rep*. 2018;8(1):13532. doi: 10.1038/s41598-018-31848-x

22. Sánchez-Sánchez R, Rodríguez-Rego JM, Macías-García A, Mendoza-Cerezo L, Díaz-Parralejo A. Relationship between shear-thinning rheological properties of bioinks and bioprinting parameters. *Int J Bioprint*. 2023;9(2):687. doi: 10.18063/ijb.687

23. Frank MW. *Viscous Fluid Flow. International Edition, 2nd ed. New York, NY: McGraw-Hill;* 1991.

24. Vey E, Rodger C, Booth J, Claybourn M, Miller AF, Saiani A. Degradation kinetics of poly (lactic-co-glycolic) acid block copolymer cast films in phosphate buffer solution as revealed by infrared and Raman spectroscopies. *Polym Degrad Stab*. 2011;96(10):1882-1889. doi: 10.1016/j.polymdegradstab.2011.07.011

25. Cross MM. Rheology of non-Newtonian fluids: a new flow equation for pseudoplastic systems. *J Colloid Sci*. 1965;20(5):417-437. doi: 10.1016/0095-8522(65)90022-X

26. Chen DXB. *Extrusion Bioprinting of Scaffolds for Tissue Engineering*. 2nd ed. Cham, Switzerland: Springer International Publishing AG; 2025. doi: 10.1007/978-3-031-72471-8

27. Bercea M. Rheology as a tool for fine-tuning the properties of printable bioinspired gels. *Molecules*. 2023;28(6):2766. doi: 10.3390/molecules28062766

28. Bom S, Ribeiro R, Ribeiro HM, Santos C, Marto J. On the progress of hydrogel-based 3D-printing: Correlating rheological properties with printing behaviour. *Int J Pharm*. 2022;615:121506. doi: 10.1016/j.ijpharm.2022.121506

29. Habib, M. A., Khoda, B. Rheological analysis of bio-ink for 3D-bio-printing processes. *J Manuf Process*. 2022;76:708–718. doi: 10.1016/j.jmapro.2022.02.048

30. Chopin-Doroteo M, Mandujano-Tinoco EA, Krötzsch E. Tailoring of the rheological properties of bioinks to improve bioprinting and bioassembly for tissue replacement. *Biochim Biophys Acta Gen Subj*. 2021;1865(2):129782. doi: 10.1016/j.bbagen.2020.129782

31. Ning L, Gil CJ, Hwang B, *et al*. Biomechanical factors in three-dimensional tissue bioprinting. *Appl Phys Rev*. 2020;7(4):041319. doi: 10.1063/5.0023206

32. Boularaoui S, Al Hussein G, Khan KA, Christoforou N, Stefanini C. An overview of extrusion-based bioprinting with a focus on induced shear stress and its effect on cell viability. *Bioprinting*. 2020;20:e00093. doi: 10.1016/j.bprint.2020.e00093

33. Persaud A, Maus A, Strait L, Zhu D. 3D-bioprinting with live cells. *Eng Regen*. 2022;3(3):292-309. doi: 10.1016/j.engreg.2022.07.002

34. Diamantides N, Dugopolski C, Blahut E, Kennedy S, Bonassar LJ. High density cell seeding affects the rheology and printability of collagen bioinks. *Biofabrication*. 2019;11(4):045016. doi: 10.1088/1758-5090/ab3524

35. Majumder N, Mishra A, Ghosh S. Effect of varying cell densities on the rheological properties of the bioink. *Bioprinting*. 2022;28:e00241. doi: 10.1016/j.bprint.2022.e00241

36. Ouyang L, Yao R, Zhao Y, Sun W. Effect of bioink properties on printability and cell viability for 3D bioplotting of embryonic stem cells. *Biofabrication*. 2016; 8(3):035020. doi: 10.1088/1758-5090/8/3/035020

37. Chen DXB. Preparation of Scaffold solutions and characterization of their flow behavior. In: *Extrusion Bioprinting of Scaffolds for Tissue Engineering Applications*. Cham, Switzerland: Springer; 2019:91-115. doi: 10.1007/978-3-030-03460-3_5

38. Kimbell G, Azad MA. Chapter fifteen — 3D-printing: bioinspired materials for drug delivery. In: Nurunnabi M, ed. *Bioinspired and Biomimetic Materials for Drug Delivery*. Woodhead Publishing Series in Biomaterials. Cambridge, UK: Woodhead Publishing; 2021: 295-318. doi: 10.1016/B978-0-12-821352-0.00011-3

39. Gao T, Gillispie GJ, Copus JS, *et al*. Optimization of gelatin–alginate composite bioink printability using rheological parameters: a systematic approach. *Biofabrication*. 2018;10(3):034106. doi: 10.1088/1758-5090/aacdc7

40. Patra S, Ajayan PM, Narayanan TN. Dynamic mechanical analysis in materials science: the Novice's Tale. *Oxf Open Mater Sci*. 2021;1(1):itaa001. doi: 10.1093/oxfmat/itaa001

41. Caporizzo MA, Prosser BL. Need for speed: the importance of physiological strain rates in determining myocardial stiffness. *Front Physiol*. 2021;12:696694. doi: 10.3389/fphys.2021.696694

42. Tikenoğulları OZ, Costabal FS, Yao J, Marsden A, Kuhl E. How viscous is the beating heart? Insights from a computational study. *Comput Mech*. 2022;70(3):565-579. doi: 10.1007/s00466-022-02180-z

43. Wang Z, St-Onge MP, Lecumberri B, *et al*. Body cell mass: model development and validation at the cellular level of body composition. *Am J Physiol Endocrinol Metab*. 2004;286(1):E123-E128. doi: 10.1152/ajpendo.00227.2003

44. Hasan A, Ragaert K, Swieszkowski W, *et al*. Biomechanical properties of native and tissue engineered heart valve constructs. *J Biomech*. 2014;47(9):1949-1963. doi: 10.1016/j.jbiomech.2013.09.023

45. Levett PA, Hutmacher DW, Malda J, Klein TJ. Hyaluronic acid enhances the mechanical properties of tissue-

engineered cartilage constructs. *PLoS One*. 2014; 9(12):e113216.
doi: 10.1371/journal.pone.0113216

46. Ghazanfari S, Alberti KA, Xu Q, Khademhosseini A. Evaluation of an elastic decellularized tendon-derived scaffold for the vascular tissue engineering application. *J Biomed Mater Res A*. 2019;107(6):1225-1234.
doi: 10.1002/jbm.a.36622

47. Janmey, P. A., Miller, R. T. Mechanisms of mechanical signaling in development and disease. *J Cell Sci*. 2011;124(1):9-18.
doi: 10.1242/jcs.071001

48. Engler AJ, Carag-Krieger C, Johnson CP, *et al*. Embryonic cardiomyocytes beat best on a matrix with heart-like elasticity: scar-like rigidity inhibits beating. *J Cell Sci*. 2008;121(22):3794-3802.
doi: 10.1242/jcs.029678

49. Moreno-Castellanos N, Velásquez-Rincón MC, Rodríguez-Sanabria AV, Cuartas-Gómez E, Vargas-Ceballos O. Encapsulation of beta-pancreatic cells in a hydrogel based on alginate and graphene oxide with high potential application in the diabetes treatment. *J Mater Res*. 2023;38(10):2823-2837.
doi: 10.1557/s43578-023-01009-6

50. Mohammadrezaei D, Moghimi N, Vandvajdi S, Powathil G, Hamis S, Kohandel M. Predicting and elucidating the post-printing behavior of 3D-printed cancer cells in hydrogel structures by integrating in-vitro and in-silico experiments. *Sci Rep*. 2023;13(1):1211.
doi: 10.1038/s41598-023-28286-9

ACCSCIENCE PUBLISHING

International Journal of Bioprinting

RESEARCH ARTICLE

3D-printed aerogel scaffolds with sodium para-aminosalicylate-encapsulated liposomes for intelligent drug delivery

Kefeng Wang[1†], Yutong Chen[1,2†], Yan Xu[1*], Subramanian Sundarrajan[2], Zhitao Yin[1], Jingtao Hu[1], Jian Chao[1], Shun Zhang[1], Miaomiao Zheng[1], and Seeram Ramakrishna[2*]

[1]School of Mechanical Engineering, Xinjiang University, Urumqi, Xinjiang, China

[2]Department of Mechanical Engineering, College of Design and Engineering, National University of Singapore, Singapore

Abstract

Uncontrollable local drug release from drug-loaded scaffolds is a critical challenge in treating bone tuberculosis (BTB), often leading to bacterial resistance and treatment failure. This study proposes an intelligent composite aerogel scaffold that integrates external stimulus response, sustained-release, and structural design. Using direct ink writing and freeze-drying, we integrated sodium para-aminosalicylate-encapsulated liposomes and silk fibroin-modified superparamagnetic iron oxide nanoparticles into a hydroxyapatite scaffold, thereby constructing an aerogel scaffold with an extracellular matrix-like structure and controlled-release capacity. The incorporation of liposomes significantly suppressed drug burst release and extended the effective drug release period to 336 h. Furthermore, under remote, non-invasive triggering by an external alternating magnetic field, the scaffold maintained a stable local temperature at 42°C. This enabled an accelerated, on-demand release of the drug, overcoming the limitations of uncontrolled delivery. By combining precise three-dimensional printing, liposome-based sustained release, and dynamic magnetic regulation, the intelligent scaffold offers a promising new strategy for personalized treatment of BTB.

Keywords: Aerogel; Bone tuberculosis; Drug release; Liposome; Magnetic thermal response; Three-dimensional printing;

†These authors contributed equally to this work.

***Corresponding authors:**
Yan Xu (xuyan2018@xju.edu.cn)

Seeram Ramakrishna (seeram@nus.edu.sg)

Citation: Wang K, Chen Y, Xu Y, *et. al.* 3D-printed aerogel scaffolds with sodium para-aminosalicylate-encapsulated liposomes for intelligent drug delivery. *Int J Bioprint.* 2025;11(5):408-430. doi: 10.36922/IJB025290296

Received: July 18, 2025
Revised: September 2, 2025
Accepted: September 3, 2025
Published online: September 9, 2025

Copyright: © 2025 Author(s). This is an Open Access article distributed under the terms of the Creative Commons Attribution License, permitting distribution, and reproduction in any medium, provided the original work is properly cited.

Publisher's Note: AccScience Publishing remains neutral with regard to jurisdictional claims in published maps and institutional affiliations.

1. Introduction

Tuberculosis, a highly contagious disease caused by *Mycobacterium tuberculosis*, remains a significant global health threat. Bone tuberculosis (BTB) is one of the most common forms of extrapulmonary tuberculosis[1] and is particularly challenging due to its characteristically long treatment duration.[2] In the clinical treatment of BTB, there is a possibility of disease recurrence or exacerbation.[3] Oral anti-tuberculosis drugs are typically used to address worsening conditions. However, traditional oral administration has significant limitations, such as prolonged treatment duration, low drug concentrations at the lesion site, and severe systemic side effects.[4,5] For conventional

drug-loaded scaffold treatment regimens,[6] it is impossible to dynamically regulate the effective drug concentration in the local lesion area without an external stimulus source. Therefore, there is an urgent need to design an intelligent drug delivery system that can achieve long-term drug release within the body while enabling non-invasive regulation of drug release from implanted scaffolds.

Owing to its compatibility with diverse material systems and its high manufacturing efficiency, direct ink writing (DIW) is a widely adopted technique for fabricating scaffolds with complex three-dimensional (3D) architectures. Moreover, mild post-processing techniques, such as freeze-drying[7,8] and supercritical carbon dioxide drying technology,[9,10] effectively preserve the activity of embedded bioactive molecules, including drugs and growth factors.[11] Therefore, the combination of these two strategies provides a robust foundation for the personalized customization of functional drug-loaded biomimetic scaffolds. In terms of drug loading processes, while drug encapsulation within scaffolds can achieve sustained drug release in localized lesion areas,[12] this simple drug delivery system carries the risk of a burst release. Researchers have developed various novel scaffolds (e.g., microsphere scaffolds,[13–15] liposome scaffolds,[16,17] and electrostatic spinning scaffolds[18]) to address the issues of initial drug burst release and insufficient drug release cycles. Among these, liposomes, as biocompatible lipids, are currently a research hotspot for addressing drug burst release.

Liposomes are amphiphilic drug carriers capable of encapsulating therapeutic agents both within their bilayer lipid membrane and in their internal aqueous core. When phospholipid molecules are dispersed in an aqueous environment, their hydrophobic tails rearrange to minimize exposure to water, while the hydrophilic heads orient toward the aqueous phase, spontaneously forming closed bilayer vesicles.[19] This amphiphilic nature allows liposomes to simultaneously carry both lipophilic and hydrophilic drugs, making them an ideal platform for drug delivery. Compared to traditional drug carriers such as microspheres, liposomes not only enable a sustained drug release but also exhibit thermosensitive properties due to their bilayer phospholipid structure.[20] When heated to the liquid crystal phase transition temperature of the phospholipids, the bilayer becomes more permeable due to an increase in its volume, thereby enabling rapid drug release into the surrounding medium.[21,22] Moreover, liposomes can be uniformly dispersed within an aerogel precursor (hydrogel), forming a stable system for subsequent drug delivery applications. The non-covalent interactions between liposomes and the hydrogel network further enhance the mechanical properties and uniformity of the composite material,[19] making it well-suited for constructing composite aerogel scaffolds with improved drug delivery performance.

Since implantable drug-eluting bone scaffolds are placed inside the human body, direct regulation of drug concentration at the local lesion site from the outside is not feasible. To overcome this limitation, external stimuli are employed to control drug release. Currently, the most widely used external triggers include near-infrared (NIR) light, alternating magnetic fields (AMF), and ultrasound. Studies have shown that NIR light-responsive scaffolds can regulate local temperature at the lesion site, enabling controlled drug release via an "NIR light–heat–drug release rate" mechanism[23–25] while simultaneously offering photothermal therapy and promoting bone regeneration. Alternating magnetic fields provide a simple, non-invasive approach based on the generation of localized heat through interactions between magnetic fields and magnetic nanoparticles, enabling both anticancer and antibacterial effects. Compared to NIR-based photothermal therapy, AMF offers deeper tissue penetration and more precise temperature control. However, within the field of bone tissue engineering, AMF has primarily been explored in the contexts of magnetic hyperthermia (to enhance bone regeneration)[4,26,27] and chemotherapy (to suppress tumor growth),[28] with relatively few studies focused on drug release regulation from implanted scaffolds.[29] In magnetic hyperthermia applications, superparamagnetic iron oxide nanoparticles (SPIONs) have exhibited excellent magnetic heating capabilities[30] and are biodegradable via the endogenous iron metabolism pathway,[31] making them well-suited for *in vivo* use. However, unmodified SPIONs can exhibit cytotoxicity[22] and often require surface modification to improve their biocompatibility.[32] Among various coating materials, silk fibroin (SF) has demonstrated excellent biocompatibility and has been shown to enhance the compatibility of nanoparticles.[33] Currently, limited research has explored the combined application of modified SPIONs, liposomes, and alternating magnetic fields for early-stage treatment of bone tuberculosis, particularly in achieving controlled drug release from 3D-printed implants. The integration of liposomes, SPIONs, and aerogel-based composite scaffolds holds significant promise for enabling non-invasive, externally triggered drug release from implanted scaffolds via alternating magnetic fields. Furthermore, this locally heat-generating scaffold has been shown to have therapeutic effects on osteosarcoma and promote bone tissue regeneration.[34–36]

Sodium para-aminosalicylate (PAS-Na), as an anti-tuberculosis drug, has not yet been proven to have a direct effect on promoting bone tissue regeneration and repair. PAS-Na plays an indirect role in promoting bone tissue

regeneration in the treatment of bone tuberculosis-induced bone defects.[37,38] It can kill *Mycobacterium tuberculosis* in the local lesion area, inhibiting inflammatory responses and creating a favorable microenvironment for bone tissue repair.

Given the challenges faced by traditional drug-eluting stents in the treatment of BTB, such as structural uncontrollability, drug burst release, and subsequent release control issues, this study proposes a multi-technology synergistic solution. By combining the macro-structural customization capabilities of DIW with the micro-porous construction technology of freeze-drying, we have successfully designed and fabricated a multifunctional composite aerogel scaffold for the first time. The scaffold integrates liposomes as the sustained-release unit, SPIONs as the magnetic-thermal response core, and the anti-tuberculosis drug PAS-Na, all uniformly embedded within a bioactive n-HA/PVA matrix. In this study, we prepared iron (II, III) oxide (Fe_3O_4)@SF nanoparticles using one-pot and stepwise methods, and investigated the effects of preparation methods and impregnation time on the microstructure, magnetic-thermal properties, and biocompatibility of magnetic nanoparticles. Additionally, we optimized the lipid preparation process, investigating the effects of the phospholipid-to-drug ratio, phospholipid-to-cholesterol ratio, and ultrasonication time on the encapsulation of PAS-Na by liposomes. We systematically prepared and characterized composite aerogel scaffolds (PAS-Na@Lipo/SPIONs/cellulose nanofibers [CNFs]/nano-hydroxyapatite [n-HA]/polyvinyl alcohol [PVA]) and investigated the dose–response relationships between liposome loading and mechanical properties, and drug release performance, with a focus on mechanical properties, sustained drug release capability, and intelligent response behavior enabling an "on-demand" drug release under external AMF. This work aims to provide a safe, efficient, and precisely controllable new drug delivery strategy to address the clinical challenge of uncontrollable drug concentrations in localized chemotherapy for BTB.

2. Materials and methods

2.1. Materials

Carboxylated cellulose nanofibers, soybean phospholipids (biotechnology grade, 99%), cholesterol (biotechnology grade, 99%), ferrous chloride tetrahydrate ($FeCl_2{\cdot}4H_2O$), ferric chloride hexahydrate ($FeCl_3{\cdot}6H_2O$), ammonium dihydrogen phosphate ($[NH_4]_2HPO_4$, reagent grade, 99%), sucrose (biotechnology grade, 98%), lactose (reagent grade, 98%), mannitol (biotechnology grade, 99%), dexamethasone (98%), ascorbic acid (99%), sodium β-glycerophosphate (98%), and dimethyl sulfoxide were purchased from Shanghai McLean Biochemical Technology (China). PAS-Na and SF were purchased from Shanghai Yuanye Biotechnology (China). Phosphate-buffered saline (PBS) at pH 7.2 was purchased from Thermo Fisher Scientific (United States). PVA 124 was purchased from China National Pharmaceutical Group Chemical Reagents, China. Mouse embryonic cranial fibrocartilage cells (MC3T3-E1), Dulbecco's Modified Eagle Medium (DMEM; high glucose) culture medium (KGL1208-500), trypsin-ethylenediaminetetraacetic acid digestion solution (KGM25200), and the 3-(4, 5-dimethylthiazolyl-2)-2, 5-diphenyltetrazolium bromide (MTT) cell proliferation and cytotoxicity assay kit (KGA311) were purchased from Jiangsu Kaiji Biotechnology, China. Live/dead cell staining kit (Calcein-acetoxymethyl ester [AM]·propidium iodide [PI], BTN140632) was purchased from Beijing Bio-Lab Technology (China). The 5-bromo-4-chloro-3-indolyl-phosphate (BCIP)/nitro blue tetrazolium (NBT) alkaline phosphatase (ALP) color development kit was purchased from Beyotime, China. The BCA protein assay kit was purchased from Biosharp (China), while the ALP assay kit was purchased from Solarbio (China). The alpha Minimum Essential Medium and fetal bovine serum were purchased from Stemmer Biologicals (China). Calcium nitrate tetrahydrate ($Ca[NO_3]_2{\cdot}4H_2O$, ACS reagent, 99%) was purchased from Merck KGaA, Germany.

2.2. Preparation of iron (II, III) oxide@silk fibroin magnetocaloric nanoparticles using the one-pot method

A total amount of 2.703 g of $FeCl_3{\cdot}6H_2O$ was dissolved in 25 mL of deionized water. A magnetic stir bar was placed into the solution, and the beaker was positioned on a magnetic stirrer with heating (Model D1J1C-120S, Lichen Instruments, China). Then, 1.448 g of $FeCl_2{\cdot}4H_2O$ and 1 g of SF were weighed and quickly added to the solution. The solution was stirred at 400 rpm for 30 s, then 8 mL of 28% ammonia solution was rapidly added. The beaker was immediately sealed with sealing film, and the solution was allowed to react for an hour. After the reaction, the formed Fe_3O_4 nanoparticles were collected using a block magnet. The formed product was washed three times with ultrapure water and ethanol. Finally, the resulting black material was air-dried naturally in a drying oven to obtain the desired black powder.

2.3. Preparation of iron (II, III) oxide@silk fibroin magnetocaloric nanoparticles using the stepwise method

A total amount of 2.703 g of $FeCl_3{\cdot}6H_2O$ was dissolved in 25 mL of deionized water. A magnetic stir bar was added, and the beaker was placed on a magnetic stirrer with heating, set to 70°C. Subsequently, 1.448 g of $FeCl_2{\cdot}4H_2O$ was weighed and quickly added to the solution. The solution

was stirred at 400 rpm for 30 s, then 8 mL of 28% ammonia solution was rapidly added. The beaker was immediately sealed with sealing film, and the solution was allowed to react for an hour. After the reaction, the formed Fe_3O_4 nanoparticles were collected using a block magnet. The formed precipitate was washed three times with ultrapure water and ethanol to obtain moist Fe_3O_4. Next, 1 g of SF was dissolved in 25 mL of deionized water, and the solution was added to the container containing moist Fe_3O_4. The mixture was stirred, then allowed to stand for 12, 24, and 48 h, respectively. After each time point, the precipitate was collected using a magnetic field, rinsed three times with ultrapure water and ethanol, and the resulting black material was placed in a drying oven to air-dry naturally, yielding the desired black powder. The preparation of unmodified Fe_3O_4 followed the same procedure, except that the moist Fe_3O_4 was directly air-dried without silk protein peptide treatment.

2.4. Preparation of nano-hydroxyapatite

A concentration of 0.116 mol of $Ca(NO_3)_2{\cdot}4H_2O$ and 0.1 mol of $(NH_4)_2HPO_4$ were dissolved in 200 mL of distilled water, mixed thoroughly, and stirred for 30 min. Then, the $(NH_4)_2HPO_4$ solution was slowly added to the stirred solution, allowing the components to react at 25°C for an hour. The solution pH was maintained at 11 by continuously adding ammonia solution. Under controlled temperature and pH conditions, the reaction was allowed to continue for 5 h. Upon completion of the reaction, the mixture was filtered under vacuum. The filtrate was washed multiple times with distilled water to remove impurities formed during the reaction. The filter cake was dried in a 90°C oven for 12 h, and the powder was sintered in a muffle furnace (CW1200, Carbolite Gero, United Kingdom) at 800°C for 2 h to obtain the HA powder.[39] The powder was ball-milled in a ball mill (PM200, Retsch, Germany) for 4 h, followed by grinding in a grinding mill (RM200; Retsch, Germany) for 30 min, yielding uniformly sized n-HA powder.

2.5. Preparation of sodium para-aminosalicylate-encapsulated liposomes and freeze-dried powder

2.5.1. Preparation of sodium para-aminosalicylate-encapsulated liposomes

Drug-loaded liposomes were prepared using the thin-film hydration method.[40] A specified ratio of soybean phospholipids and cholesterol was weighed into a 25 mL beaker and fully dissolved in 10 mL of anhydrous ethanol. The resulting solution was transferred to a 250 mL round-bottom flask. Under a pressure of 0.09 MPa and at a water bath temperature of 30°C, the flask was rotated on a rotary evaporator for 30 min to remove the ethanol. The flask was then placed under vacuum for further drying to ensure complete removal of the residual solvent, resulting in the formation of a thin lipid film on the inner wall of the flask. Next, 10 mL of 0.1 mol/L PBS containing a predetermined amount of PAS-Na was added to the flask. The film was hydrated at 60°C with stirring at 400 rpm for 15 min, producing a turbid liposomal suspension. Finally, the suspension was sonicated (power: 320 W, duration: 8 min, with 3 s on and 3 s off, using an ice water bath) to obtain a uniform liposome dispersion.

2.5.2. Preparation of freeze-dried powder

A specified amount of sucrose, lactose, and mannitol was dissolved in deionized water and mixed with the lipid particle suspension at a predetermined ratio. The mixture was then frozen at −40°C for 24 h, followed by placement in a freeze dryer (Model LC-12N-50A, Lichen Technology Co., Ltd., China) for 6 h of pre-freezing and subsequently freeze-dried for an additional 24 h.

2.6. Preparation of magnetic-thermal scaffolds

A specified amount of PAS-Na@Lipo and PAS-Na was mixed, followed by the addition of CNFs, n-HA, and PVA gel in predetermined proportions. The mixture was thoroughly homogenized and loaded into an extrusion-based printing nozzle. Scaffolds were fabricated using a multi-material, high-precision bio-3D printer (BIO X6, CELLINK, Sweden) following pre-set parameters for printing path, extrusion pressure, and printing speed. After printing, the scaffolds were placed in a −40°C freezer for 24 h of pre-freezing, followed by freeze-drying in a freeze dryer for an additional 24 h.

2.7. Determination of the sodium para-aminosalicylate standard curve

Accurately weighed 50 mg of PAS-Na was dissolved in 100 mL of PBS to prepare a 500 μg/mL stock solution. This stock solution was diluted to obtain standard solutions with concentrations of 10, 20, 30, 40, and 50 μg/mL PAS-Na. The absorbance of each solution was measured using an ultraviolet-visible spectrophotometer (UV-3600, Shimadzu Corporation, Japan).

2.8. Magnetothermal properties of superparamagnetic iron oxide nanoparticles

Five milligram each of Fe_3O_4@SF-12h, Fe_3O_4@SF-24h, and Fe_3O_4@SF-48h were weighed separately and dispersed in 5 mL of deionized water. The suspensions were sonicated at room temperature for 900 s to achieve uniform black suspensions. The samples were then placed in a high-frequency induction heating device (AMF, SPG-06A-1, Shenzhen Shuangping Power Technology Co., Ltd., China), which operated at a constant current of 15.5 A. Temperature changes were monitored in real time using a fluorescence-based fiber optic temperature sensor

(IF-C2A6F20, Fuzhou Yinnuo Electronic Technology Co., Ltd., China).

2.9. Characterization of sodium para-aminosalicylate-encapsulated liposomes

2.9.1. Determination of the encapsulation efficiency of sodium para-aminosalicylate-encapsulated liposomes

The encapsulation efficiency of PAS-Na@Lipo was determined using an ultraviolet-visible spectrophotometer. Before analysis, the suspension was centrifuged at 7000 rpm for 40 min using a bench-top high-speed refrigerated centrifuge (TGL16M, Changzhou Jintan High-Tech Instrument Factory, China) equipped with a 30 kDa ultrafiltration centrifuge tube. An aliquot of the supernatant was collected via pipette and diluted to the appropriate concentration. The absorbance of the resulting solution was then measured using an ultraviolet-visible spectrophotometer.

2.9.2. Zeta potential and particle size distribution of sodium para-aminosalicylate-encapsulated liposomes

The particle size of PAS-Na@Lipo was measured using a Zetasizer Nano ZS90 (Malvern Instruments, United Kingdom). A 20-fold diluted aqueous solution of PAS-Na@Lipo was loaded into appropriate cuvettes, and measurements were conducted with the Zetasizer. Three parallel samples were analyzed for each group.

2.10. Characterization of composite aerogel scaffolds

2.10.1. Mechanical properties of the scaffolds

Specified ratios of CNFs, n-HA, and PVA hydrogel were thoroughly mixed by physical stirring and poured into custom molds. The molds were frozen at −20°C for 24 h, then pre-frozen at −40°C for 6 h in a low-temperature freeze dryer. Finally, samples were vacuum freeze-dried for 24 h. The top and bottom surfaces of each sample were ground flat, yielding specimens with a diameter of 10 mm and a height of 12 mm. The mechanical properties of the scaffolds were evaluated in compression using an electronic universal testing machine (E44.304, MTS, China). Three samples per group were tested, with a compression load applied at a rate of 1 mm/min until a predetermined strain was reached, at which point the test was terminated.

2.10.2. In vitro drug release experiment of the scaffold

Three parallel samples with similar masses were prepared in each group. Scaffold masses were measured using a high-precision electronic balance. Each scaffold was placed in a test tube, and a precise volume of PBS was added before incubating the tubes in a water bath shaker (SHA-B, Bonatech, China) at 37°C and 110 rpm. Samples were collected at predetermined time points, with an equal volume of fresh PBS added after each collection. Absorbance at each time point was measured using a ultraviolet-visible spectrophotometer, and the released drug concentration was calculated based on a standard calibration curve.

2.11. *In vitro* cell experiments

The cell culture and seeding process were as follows. MC3T3-E1 cells were cultured in flasks with 5 mL of DMEM culture medium, with an additional addition of 3 mL of DMEM culture medium. The cells were maintained in a humidified incubator at 37°C and 5% carbon dioxide and were subcultured every 3 days. For seeding, cells were detached from the flask using trypsin, which was then neutralized with a complete medium. The cells were pelleted by centrifugation and resuspended to form a uniform suspension. After determining the cell concentration, the cell concentration was adjusted to a density of 2×10^4 cells/cm^2. Finally, the cells were then seeded into a 96-well plate by adding 100 μL of the suspension to each well and incubated in a 5% carbon dioxide incubator (Forma 371, Thermo Fisher Scientific, United States) at 37°C until cell adherence.

2.11.1. Cellular toxicity of superparamagnetic iron oxide nanoparticles

Suspensions of unmodified Fe_3O_4 and Fe_3O_4@SF-12h at a concentration of 1 mg/mL were prepared. Then, the serum-containing culture medium was removed, followed by the addition of two SPION suspensions to each well, and incubation for 24 h. After 24 h, the old solution was removed, and 0.5 mg/mL of MTT solution was added, followed by incubation for 4 h. After 4 h, the supernatant was aspirated, and 100 μL of dimethyl sulfoxide was added to the wells. The 96-well plate was then placed in an enzyme-linked immunosorbent assay reader (Synergy HTX, Biotek, United States) to measure the absorbance at 490 nm. The steps for cell incubation for 72 h were the same as above.

2.11.2. Cytotoxicity of scaffolds with different superparamagnetic iron oxide nanoparticle concentrations

Scaffolds containing different concentrations of SPIONs were first sterilized using high-temperature steam for 8 h. To prepare the extract, the sterilized scaffolds were incubated at 4°C in a carbon dioxide incubator for 4 h. Following the extraction, the conditioned medium was collected and then diluted with complete culture medium. Then, the resulting scaffold extract was incubated in a carbon dioxide incubator at 37°C with 5% carbon dioxide for 24 h. Subsequent experimental procedures were then performed as described previously.

2.11.3. Cell viability staining of composite scaffolds

The extraction solution and culture process for the composite scaffolds were the same as described above. After removing the culture medium from the well plates, cells were washed three times with PBS buffer. Then, 200 μL of green staining solution (diluted 1:1000) was added to each well and incubated in the dark for 15 min. The stain solution was removed, and cells were washed three times with PBS. Next, 200 μL of red staining solution (diluted 1:5000) was added to each well and incubated in the dark for 5 min. After aspirating the staining solution, the cells were washed three times with PBS. Finally, the cells were observed in fluorescence channels and bright fields using a laser confocal laser scanning microscope (LSM 880, Zeiss, Germany).

2.12. Microstructure observation

The microstructure of the SPIONs was examined using a high-resolution transmission electron microscope (TEM; Tecnai 12, Philips, the Netherlands). The TEM was operated at an acceleration voltage of 80 kV to observe their surface morphology. Particle size distribution was determined by analyzing the TEM images with ImageJ software (version 1.54g).

The microstructure of PAS-Na@Lipo was examined using a TEM (Tecnai 12, Philips, the Netherlands). The TEM was operated at an acceleration voltage of 80 kV to observe the surface morphology of the liposomes. Prior to imaging, the liposome suspension was stained with phosphotungstic acid solution.

The microstructure of the aerogel scaffold was examined using a scanning electron microscope (SEM; Regulus8220, Hitachi, Japan) operated at 5 kV. Before imaging, the aerogel scaffold was sputter-coated with gold to enhance conductivity.

2.13. Morphology observation

The infrared analysis of SPIONs, CNFs, PVA, n-HA, and composite aerogel scaffolds was conducted using a Fourier transform infrared spectrometer (FTIR; INVENIO R, Bruker, Germany). The samples were tested at room temperature, with a spectral wavenumber range of 400–4000 cm^{-1} and a scanning resolution of 4 cm^{-1}.

The X-ray diffraction analysis of SPIONs was performed using a high-resolution X-ray diffractometer (Smartlab 9 kW, Rigaku, Japan) with CuKα radiation (λ = 0.154 nm) in the 2θ range of 25–80°.

2.14. Osteogenic differentiation of MC3T3-E1 cells

2.14.1. Osteogenic induction

After acclimatization, the cells were inoculated into 24-well plates, and at 70%–80% confluence, the cells were induced and incubated. The control group was replaced with control medium, and the sample group was replaced with diluted conditioned medium. After 7 and 14 days of osteogenic induction, the cells were stained and imaged using the BCIP/NBTALP chromogenic kit at and the precipitated cell samples were assayed for ALP activity using the ALP assay kit.

2.14.2. Alkaline phosphatase measurement

The precipitated samples from each group of cells at −80°C were measured, followed by the addition of 200 μL of extraction solution to each sample. The cells were lysed through ultrasonication (ice bath, power 200 W, ultrasonication for 3 s, 7-s intervals, repeated 30 times), followed by centrifugation at 10,000 *g* at 4°C for 10 min. The supernatant was placed on ice to be measured. The total protein concentration in the samples was quantified by converting the enzyme activity of each sample to protein concentration and calculating the ALP activity according to the protein concentration.

2.14.3. Alkaline phosphatase staining

The cells of each group were fixed in 4% paraformaldehyde and washed with PBS three to five times for 3–5 min each. Each solution was added according to a certain proportion and mixed well to form the working solution for staining. After the last wash, the washing solution was removed, and an appropriate amount of staining solution was added to ensure sufficient coverage of the sample. The samples were incubated at room temperature and away from light for 1–2 h until the color developed to the desired shade. The working solution was removed, and the samples were washed with distilled water one to two times to terminate the color development reaction. The morphology of each group was observed using confocal microscopy (DSZ2000X, Aopu, China).

2.14.4. Alizarin red S staining

After 21 days of osteogenic induction culture, the samples were washed once with PBS and fixed in fixative for 20 min. The samples were then washed three times with PBS. The cells were stained using the Alizarin red staining kit (Osteoblast Mineralisation Nodule Staining Kit) (Alizarin Red S Method, Biyuntian China) for 30 min, then washed thoroughly with distilled water before acquiring imaging results.

2.15. Statistical analysis

In the study, all data were expressed as mean ± standard deviation. Significant difference was considered when $p<0.05$ ($^{*}p < 0.05$, $^{**}p < 0.01$, and $^{***}p < 0.001$; non-significant at $p \geq 0.05$). All results were verified through at least three independent experimental repeats.

3. Results and discussion

3.1. Performance analysis of superparamagnetic iron oxide nanoparticles

3.1.1. Microstructural morphology of superparamagnetic iron oxide nanoparticles

Since SPIONs release iron ions in the body, and excessive iron ion accumulation may affect protein synthesis in neurons or damage brain neurons,[33] improving the biocompatibility of SPIONs is crucial. In this study, we used a one-pot method and a stepwise method to prepare SF-modified SPIONs to enhance their biocompatibility. TEM analysis (Figure 1A) revealed that Fe_3O_4@SF nanoparticles prepared using the one-pot method exhibited severe agglomeration, irregular particle shapes, and square-shaped particles.[41] In contrast, Fe_3O_4@SF composite particles prepared using the stepwise method exhibited spherical shapes[42] and good dispersion. During the stepwise preparation process, we focused on investigating the effects of impregnation time on the cytotoxicity and microstructure of Fe_3O_4@SF nanoparticles. TEM (Figure 1A) revealed that Fe_3O_4@SF nanoparticles impregnated for 12, 24, and 48 h exhibited similar dispersion and microstructure. The Fe_3O_4 surface was covered with an amorphous coating after different impregnation times, confirming that SF successfully coated the Fe_3O_4 nanoparticles. The average particle size of nanoparticles impregnated with SF for 12 h was 12.13 ± 1.2 nm (Figure 1Bi), and the average particle sizes of nanoparticles impregnated for 24 and 48 h were also less than 15 nm (Figure 1Bii and Biii), all of which belong to SPIONs[43] and are suitable for biomedical applications. The effect of different immersion times on the thickness of the amorphous SF coating on the Fe_3O_4 surface was relatively small. After immersion for 12, 24, and 48 h, the thicknesses of the amorphous coatings on the Fe_3O_4 surface were 0.98, 1.10, and 1.54 nm, respectively. The coating thickness exhibited a non-linear increase with a slight growth trend as the immersion time increased. This non-linear growth pattern is primarily attributed to the high number of active sites on the SPIONs surface during the initial immersion stage and the structural changes of the SF configuration on the Fe_3O_4 surface during the immersion process.

3.1.2. Chemical properties of superparamagnetic iron oxide nanoparticles

The FTIR of Fe_3O_4@SF nanoparticles (Figure 1C) indicated that the FTIR of SPIONs prepared using the one-pot method and the stepwise method are essentially identical, suggesting that SF failed to effectively coat the Fe_3O_4 surface. This phenomenon may be attributed to the SF coating being too thin or severe agglomeration of Fe_3O_4, resulting in the peptide chains being encapsulated within the agglomerates. Based on the TEM, the stepwise method was adopted for the subsequent preparation of SPIONs.

The FTIR of SF-modified SPIONs (Figure 1C) showed characteristic peaks at 1624 and 1524 cm^{-1}, which correspond to the amide I and amide II bands of SF, respectively,[44] confirming the presence of a β-folded conformation on the surface of Fe_3O_4 after modification.[45] This result, together with TEM analysis, confirmed that SF was successfully coated on the surface of Fe_3O_4 nanoparticles. Additionally, the characteristic stretching vibration peak of the Fe–O bond at 567 cm^{-1} did not shift after SF modification, indicating that SF did not affect the local bonding environment of Fe_3O_4, thereby ensuring the stability of magnetic functionality in subsequent studies.

X-ray diffraction characterization of the SPIONs showed that the diffraction patterns of both untreated and SF-modified samples matched the standard pattern of Fe_3O_4 (Figure 1D). Both displayed characteristic peaks at 220, 311, 222, 400, 422, 511, 440, and 533 cm^{-1}, confirming the presence of pure spinel-structured Fe_3O_4.[41] The minor shifts in key peak positions and the consistent half-peak widths indicated that the SF modification did not significantly alter the crystal structure of Fe_3O_4.

3.1.3. Magnetic-thermal performance analysis of superparamagnetic iron oxide nanoparticles

The magnetic-thermal curves of SPIONs treated with different immersion times (Figure 1E) showed that when a 1 mg/mL dispersion was exposed to an alternating magnetic field for 300 s, the temperatures of Fe_3O_4@SF-12h, Fe_3O_4@SF-24h, and Fe_3O_4@SF-48h dispersions reached 45.1, 33.7, and 33.1°C, respectively. The specific loss power (SLP) was calculated using **Equation (I)**[46]:

$$SLP\left(\mathrm{W/g}\right) = \mathrm{C} - \frac{m_s}{m_p} \times \frac{dT}{dt} \quad \text{(I)}$$

where C is the specific heat capacity of the magnetic nanoparticle suspension (4.18 J/cm^3/K), m_s and m_p are the masses of the magnetic nanoparticle suspension and the magnetic nanoparticles, respectively, and $\frac{dT}{dt}$ denotes the initial slope of the magnetothermal heating curve.

The SLP values of the dispersions of Fe_3O_4@SF-12h, Fe_3O_4@SF-24h, and Fe_3O_4@SF-48h were 261.56189, 113.67705, and 105.55427 W/g, respectively. The magnetic-to-thermal conversion efficiency of Fe_3O_4@SF-12h was significantly higher than that of the other two (Figure 1E), which corresponds to the SLP values. This magnetic-thermal performance difference was

attributed to the SF coating amount. The peptide chains of SF constrain Fe_3O_4, suppressing its Brownian relaxation, while the coating also hinders magnetic hysteresis loss, collectively reducing the magnetic-thermal conversion efficiency of the magnetic nanoparticles. The temperature rise curve of Fe_3O_4@SF-12h remained stable after multiple heating cycles, demonstrating excellent magnetic-thermal cycling stability (Figure 1F). Observing the macroscopic morphology of the three samples at a concentration of 1 mg/mL (Figure 1G), the Fe_3O_4@SF-12h dispersion exhibited a uniform dark color after ultrasonication for 900 s, confirming its good dispersion. After 300 s under an alternating magnetic field with a constant current of 15.5 A, Fe_3O_4@SF-12h showed no significant agglomeration, while Fe_3O_4@SF-24h and Fe_3O_4@SF-48h exhibited agglomeration and precipitation after exposure to the alternating magnetic field. This phenomenon is related to the increased proportion of β-folded conformations in the SF coating due to impregnation. Excessive rigid β-folded structures restrict steric hindrance, leading to easier agglomeration of magnetic nanoparticles under an alternating magnetic field. Excessive SF coating reduces the saturation magnetization of SPIONs. To ensure optimal magnetic-thermal heating performance at minimal dosage, Fe_3O_4@SF-12h was selected as the SPIONs for subsequent experiments to serve as magnetic-thermal heating agents.

3.2. Performance analysis of *sodium para-aminosalicylate-encapsulated liposomes*

3.2.1. Preparation of the standard curve for sodium para-aminosalicylate-encapsulated liposomes

Before optimizing the lipid preparation process, a quantitative analysis of PAS-Na was first conducted. A solution of 5 μg/mL PAS-Na was prepared, and an ultraviolet-visible spectrophotometer was used to scan the solution in the 200–800 nm range. Characteristic peaks were observed at 208, 264.5, and 298.5 nm (Figure 2A). The 298.5 nm peak was selected as the characteristic peak for plotting the PAS-Na standard curve. The corresponding absorbance of PAS-Na solutions at concentrations of 10, 20, 30, 40, and 50 μg/mL (Figure 2B) was measured to create the standard curve (Figure 2C), with absorbance = 0.04472c − 0.00511 and R^2 = 0.9996.

3.2.2. Effect of different processes on the encapsulation efficiency of sodium para-aminosalicylate-encapsulated liposomes

Thin film hydration is the most common and simplest method for preparing liposomes in the laboratory.[47] Experimental results indicated that process parameters significantly influence the encapsulation efficiency of PAS-Na by liposomes (Figure 2D–F). The optimal drug encapsulation efficiency of the liposomes prepared in this study was approximately 25%, which is relatively low. This is because the thin film hydration method for encapsulating water-soluble drugs is a passive encapsulation process, and PAS-Na has extremely high hydrophilicity, making it more prone to migrating to the external aqueous phase and less likely to be encapsulated by the lipid bilayer's internal aqueous phase. To improve the encapsulation efficiency, further investigations were conducted by varying the mass ratio of phospholipids to PAS-Na, the mass ratio of phospholipids to cholesterol, and the ultrasonication time. As the mass ratio of phospholipids to PAS-Na increased, the encapsulation efficiency and drug loading first increased and then decreased (Figure 2D), reaching a maximum value when the ratio was 6:1. Further analysis revealed that within a certain range, when the amount of phospholipids added is too low, liposomes struggle to capture PAS-Na molecules, resulting in a lower encapsulation efficiency. However, when the amount of PAS-Na exceeds the load capacity of phospholipids, liposome stability decreases, leading to an increase in the free-phase drug content. As ultrasonication time increases, the duration of the strong pressure pulses generated by ultrasonication exceeds the "ultrasonic cavitation equilibrium point," causing damage to the bilipid membrane structure and a decrease in PAS-Na content in the aqueous phase of the liposomes (Figure 2E). Cholesterol plays a stabilizing role in the bilayer phospholipid membrane of liposomes. Generally, the higher the cholesterol-to-phospholipid ratio, the higher the encapsulation efficiency. However, beyond the equilibrium point, excessive cholesterol negatively affects the fluidity and permeability of the phospholipid membrane, leading to crystallization and membrane rupture, thereby reducing encapsulation efficiency (Figure 2F). In this study, the encapsulation efficiency reached its maximum value when the phospholipid-to-drug mass ratio was 6:1, the ultrasound time was 8 min, and the phospholipid-to-cholesterol mass ratio was 4:1.

3.2.3. Microscopic morphology and stability analysis of sodium para-aminosalicylate-encapsulated liposomes

Transmission electron microscopy images after phosphotungstic acid staining (Figure 2G) revealed that the liposomes exhibited a spherical morphology with well-defined lipid bilayers, and their particle size distribution was consistent with the results from the Zeta potential measurements.

Zeta potential measurements indicated that drug-loaded liposomes with a phospholipid-to-cholesterol ratio of 4:1 had an average particle size of 158.57 ± 3.70 nm and a zeta potential of –0.796 ± 0.132 mV, consistent with previous reports. The liposomes displayed a single peak

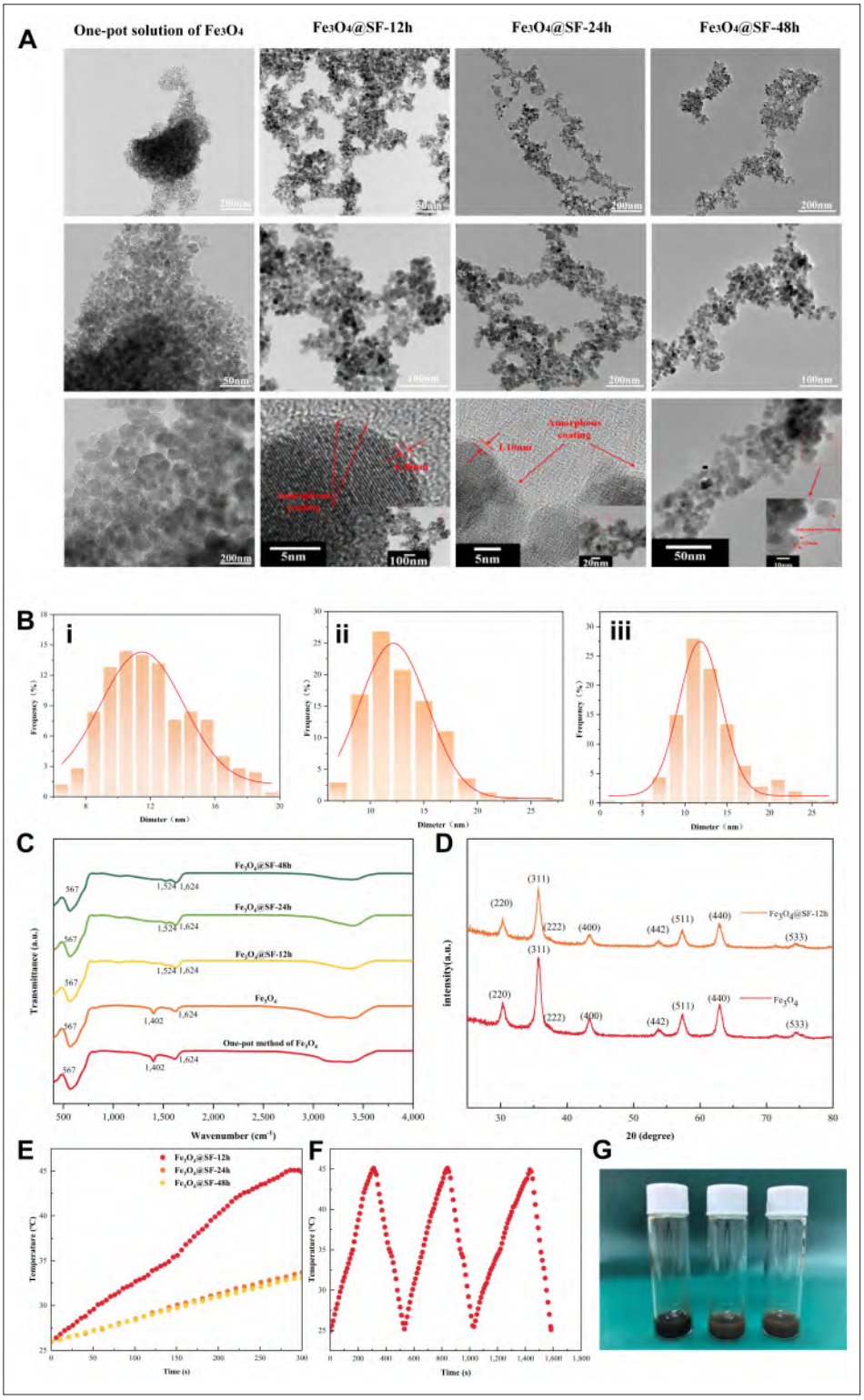


Figure 1. Characterization of superparamagnetic iron oxide nanoparticles (SPIONs). (A) Scanning electron microscopy of SPIONs. Scale bars: 5, 20, 50, 100, and 200 nm. (B) The average particle size of SPIONs immersed for (i) 12 h, (ii) 24 h, and (iii) 48 h. (C) Fourier transform infrared spectrometry of SPIONs. (D) X-ray diffraction analysis of SPIONs. (E) Magnetic-thermal heating performance of SPIONs with different immersion times. (F) Magnetic-thermal cycling heating performance of Fe_3O_4@SF-12h nanoparticles. (G) Cytotoxicity assessment of Fe_3O_4@SF-12h and Fe_3O_4 nanoparticles. Abbreviations: Fe_3O_4, Iron (II, III) oxide; SF, silk fibroin.

(Figure 2Gv) with a polydispersity index of 0.383 ± 0.093, indicating a relatively uniform particle size distribution.

3.2.4. Effect of different freeze-drying protective agents on the quality of sodium para-aminosalicylate-encapsulated liposomes freeze-dried powder

Observations of the macroscopic morphology of lyophilized liposome powders at different ratios revealed that both the type and amount of protective agent significantly affected the powder's quality. Specifically, when the phospholipid-to-lactose ratio was 1:3, the lyophilized powder displayed a smooth and relatively porous surface with no signs of crystallization. This powder is well-suited for preparing 3D printing extrusion slurries (Table 1).

3.2.5. Effect of different lyophilization protectants on the printability of the printing slurry

This study focused on the printing requirements of blended slurries using pneumatic 3D printing technology. We systematically screened and optimized the ratios of freeze-dried protectants—such as sucrose, lactose, and mannitol—and refined the physicochemical properties of the resulting powders. This optimization allows the freeze-dried powders to be readily dissolvable and blended with biomaterial slurries to form bioinks with suitable rheological properties, thereby ensuring optimal shear-thinning behavior, precise shaping, and structural stability during extrusion-based 3D printing.

Rheological tests (Figure 2H) demonstrated that different formulations of liposome freeze-dried powders influenced the rheological properties of PVA-liposome blended hydrogels but did not alter the intrinsic shear-thinning characteristics of the PVA gel. In PVA-liposome freeze-dried powder-PVA co-emulsion gels containing sucrose and lactose, a rapid enhancement in shear-thinning ability was observed (Figure 2Hi and Hii). This effect may be attributed to weaker hydrogen bonding interactions between sucrose/lactose and PVA hydroxyl groups compared to those between PVA chains. As mannitol content increased, the hydrogel exhibited a gradual increase in shear-thinning behavior (Figure 2Hiii).

Under equivalent drug loading conditions, a higher protectant-to-phospholipid ratio in the freeze-dried powder requires a greater amount of powder during printing. Moreover, excessive protectants may disrupt the gel network, potentially compromising the scaffold's mechanical properties. Considering powder quality, mechanical strength, rheological behavior, and drug loading efficiency, this study selected a formulation with a soy phospholipid-to-lactose ratio of 1:3.

3.3. Performance analysis of composite aerogel scaffolds

3.3.1. Microstructure and elemental composition of composite aerogel scaffolds with different formulations

Scanning electron microscopy images showed that the microstructures of the scaffolds without CNFs and those with 1% CNFs were similar (Figure 3Ai and ii), while the 2% CNF group exhibited more distinct and denser plate-like structures (Figure 3Gi–iv), which may explain its superior mechanical properties compared to the other two groups. As the PVA concentration increased, the plate-like structures became more pronounced, which was attributed to two factors. First, as the PVA content increases, both the hydrogen bond network between PVA molecules and the hydrogen bond network formed between the hydroxyl groups of PVA and the carboxyl and hydroxyl groups of CNFs become more robust, enabling the gel to retain more plate-like structures after freeze-drying[48] (Figure 3Ci–Dii). As n-HA content increases, the deposition of hydroxyapatite on the surface of PVA lamellar structures significantly increases, and agglomeration becomes more pronounced. These

Table 1. Evaluation of the effect of protective agents on the quality of freeze-dried powders

Types of lyophilized protectants	Soy phospholipids: lyophilized protective agent (mg: mg)	Macro-image
Sucrose	1:3	Denser, flat
Sucrose	1:6	Loose
Sucrose	1:9	Dry cracking, loose
Lactose	1:3	Rather loose, flat
Lactose	1:6	Dense, structural leveling
Lactose	1:9	Loose, flatter
Mannitol	1:3	Denser
Mannitol	1:6	Loose
Mannitol	1:9	Loose

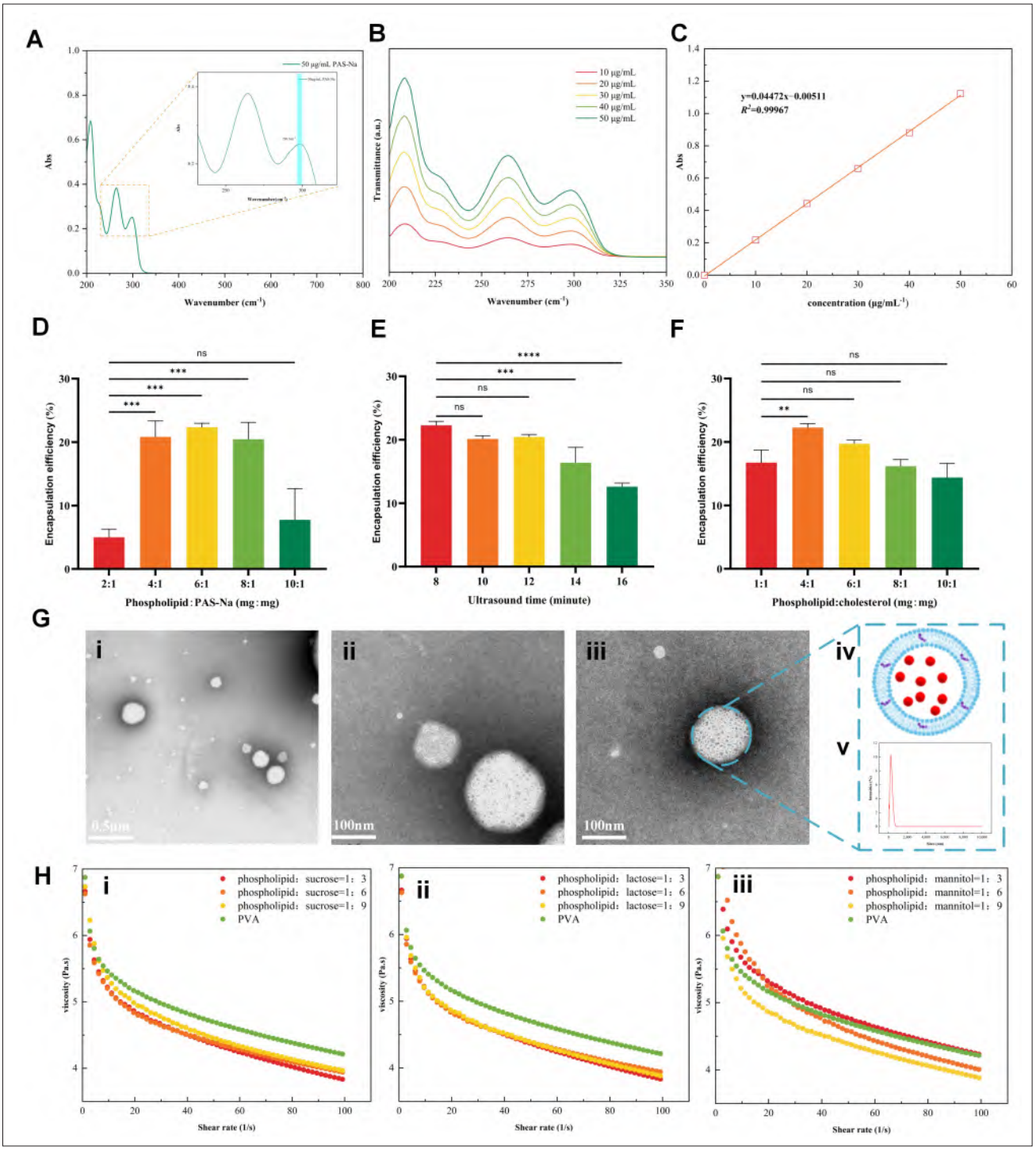


Figure 2. Characterization of liposomes. (A) Absorbance curve of PAS-Na in the 200–800 nm wavelength range. (B) Absorbance curves of PAS-Na at different concentrations. (C) Standard curve of PAS-Na in PBS buffer. (D) Effect of ultrasonication time on the encapsulation efficiency of liposomes. (E) Effect of the phospholipid-to-cholesterol ratio on liposome encapsulation efficiency. (F) Effect of phospholipid on the PAS-Na ratio on liposome encapsulation efficiency. (G) (i, ii, iii) Transmission electron microscopy of liposomes; scale bars: 0.5 μm and 100 nm; magnifications: Figure 2Gi 10,000X, Figure 2Gii 20,000X, (iv) a schematic diagram of liposomes, and (v) the particle size distribution of liposomes. (H) Speed–viscosity plot of polyvinyl alcohol (PVA) gel under different protective agents. *$p < 0.05$, **$p < 0.01$, and ***$p < 0.001$; non-significant (ns) at $p \geq 0.05$. Abbreviation: PAS-Na, sodium para-aminosalicylate; PBS, phosphate-buffered saline.

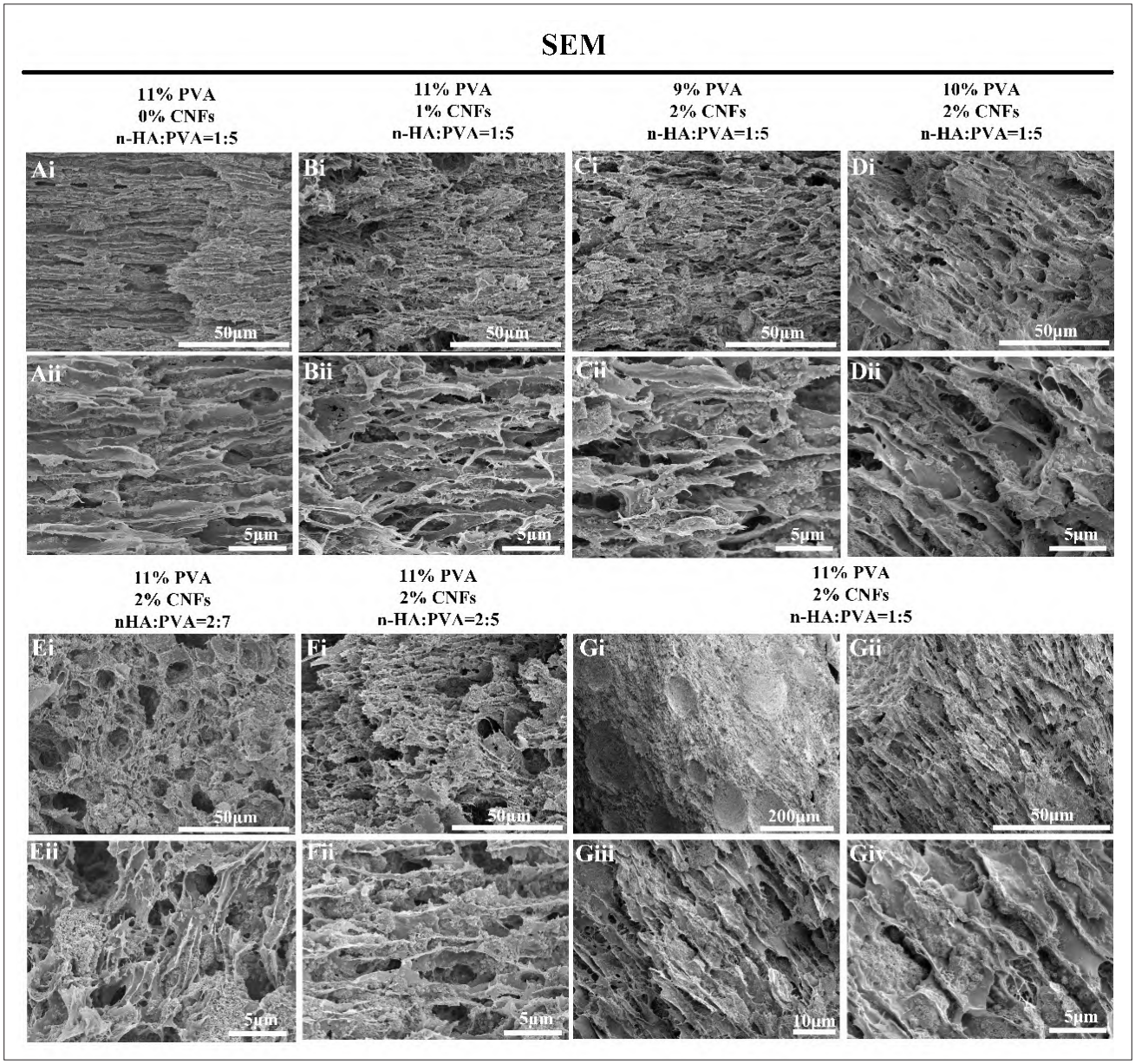


Figure 3. SEM of composite aerogel scaffolds under different ratios. CNFs added at (Ai and ii) 0%, (Bi and ii) 1%, and (Gi–iv) 2%. PVA concentration at (Ci and ii) 9% and (Di and ii) 10%. n-HA to PVA ratio of (Ei and ii) 2:7 and (Fi and ii) 2:5. Scale bars: 1, 5, 10, and 100 μm; Magnification of 5, 50, 200, and 10 μm corresponds to 5000X, 1000X, 100X, and 2000X, respectively. Abbreviations: CNF, cellulose nanofiber; n-HA, nano-hydroxyapatite; PVA, polyvinyl alcohol; SEM, scanning electron microscopy.

agglomerates act as stress concentration points, making the scaffold more prone to localized stress concentration during compression. This is likely the primary reason for the increased brittleness and susceptibility to compression collapse observed in scaffolds with n-HA/PVA ratios of 2:7 and 2:5 (Figure 3Ei–Fii). In scaffolds prepared with the optimal formulation of 2% CNFs, an n-HA:PVA ratio of 1:5, and a PVA concentration of 11%, the PVA exhibited a sheet-like structure, with spherical n-HA uniformly distributed on the PVA sheet-like structure. The scaffold features irregular, large pore sizes and an interconnected porous structure (Figure 3Gi–iv).

3.3.2. Energy dispersive spectroscopy of scaffolds

The molecular formulas of n-HA, PVA, and CNFs are $Ca_{10}(PO_4)_6(OH)_2$, $[C_2H_4O]_n$, and $[C_6H_{10}O_5]_n$, respectively. Since n-HA contains characteristic elements calcium (Ca) and phosphorus (P), elemental mapping was used for its

characterization. Energy dispersive spectroscopy (EDS) showed that Ca and P were uniformly distributed across the PVA surface (Figure 4A), confirming that n-HA was evenly dispersed within the aerogel scaffold.

3.3.3. Chemical properties of composite aerogel scaffolds

The FTIR of the individual components and composite scaffolds (Figure 4B) revealed that pure n-HA exhibited bending vibration peaks of PO_4^{3-} at 567 and 599 cm^{-1}, an asymmetric stretching vibration peak of PO_4^{3-} at 1040 cm^{-1}, and a sharp peak at 3571 cm^{-1} corresponding to O–H stretching vibrations.[49] All characteristic peaks of n-HA were also present in the FTIR of the composite aerogel scaffold. Pure PVA showed absorption peaks at 3346, 2919, 1415, 1322, and 1063 cm^{-1}, attributed respectively to O–H stretching, C–H stretching, the C–O group, C–H bending, and the C–O group.[50] For CNFs, a broad absorption peak at 3307 cm^{-1} corresponds to O–H bond stretching, while another peak at 2943 cm^{-1} is due to C–H bond stretching vibrations. The FTIR of the composite aerogel scaffold displayed characteristic peaks of n-HA, PVA, and CNFs. Additionally, a broad absorption band between 1011 and 1100 cm^{-1} arose from the overlapping bending vibration of PO_4^{3-} in n-HA and the stretching vibration of C–O in PVA, resulting in mutual reinforcement. Moreover, the O–H stretching vibration peak of PVA broadened and shifted to a lower frequency at 3399 cm^{-1} in the composite scaffold, indicating the formation of strong hydrogen bonds between CNFs and PVA.

3.3.4. Mechanical properties of scaffolds under different formulations

We investigated the effects of PVA concentration, CNF addition amount, and PVA: n-HA mass ratio on the mechanical properties of the scaffold. With a constant PVA: n-HA ratio and PVA concentration, samples were divided into three groups based on CNF content: 0%, 1%, and 2%. The stress–strain curves for these groups showed similar trends, with the 2% CNF group exhibiting higher stress values than the others (Figure 4C and F). Scaffolds containing 1% CNF showed a slight improvement in mechanical properties compared to those without CNFs, likely due to hydrogen bonding between the hydroxyl and carboxyl groups of CNFs and the hydroxyl groups of PVA, which enhanced scaffold cross-linking. However, this effect was limited by the low CNF content.

When CNF content reached 2%, the mechanical properties improved significantly. This enhancement can be attributed to three main factors. First, the carboxyl and hydroxyl groups in CNFs form multiple hydrogen bonds with PVA's hydroxyl groups, increasing the gel network's toughness. Additionally, hydrogen bonds form not only between PVA and CNFs but also among CNFs themselves, creating a composite hydrogen-bond network.[51] Finally, entanglement between CNF molecules and the long chains of PVA results in a mechanically interlocked network.[52] Considering the mechanical performance requirements of implantable bone scaffolds, after determining the CNF addition amount to be 2%, the effects of other factors on mechanical performance were investigated.

At constant CNF content and PVA: n-HA ratio, the stress–strain curves showed an overall upward trend with increasing PVA concentration (Figure 4D and G). This is due to two factors: first, higher PVA concentrations increase the solid content of the aerogel, making its structure denser; second, at 11% PVA, more hydroxyl groups are available to form hydrogen bonds with carboxyl groups on the carboxylated CNFs, strengthening both hydrogen bonding and entanglement between PVA and CNFs chains, thereby significantly enhancing mechanical properties.[48]

With CNF's content and PVA concentration fixed, the PVA: n-HA ratio had a pronounced effect on scaffold behavior. When the PVA: n-HA ratio was 2:7 (Sample 6), the stress at collapse was lower than that of the 2:5 group (Sample 7), but the strain at collapse was higher. SEM observations revealed that the 2:5 group had more n-HA attached to the PVA chains, providing greater mechanical reinforcement. However, the more severe agglomeration in this group created additional stress concentration points, increasing scaffold brittleness. Experimentally, scaffolds with n-HA: PVA ratios of 2:7 and 2:5 failed at strains of 44.5% and 26.3% (Figure 4E and H), respectively, indicating that these highly brittle scaffolds are unsuitable for implantation.

3.3.5. Effect of cellulose nanofiber content on the rheological properties of hydrogels

The storage modulus (*G*') and loss modulus (*G*") of hydrogels are key viscoelastic properties of hydrogels that define their mechanical behavior. The relative magnitudes of these moduli indicate whether the material is predominantly solid-like or liquid-like. When *G*' exceeds *G*", elastic deformation dominates, and the hydrogel behaves like a solid; when *G*" exceeds *G*', viscous deformation prevails, indicating more liquid-like behavior. The point where *G*' equals *G*" corresponds to the gel–sol transition or shear yield point. Before this yield point, the storage modulus remains higher than the loss modulus, signifying the formation of an elastic network within the composite hydrogel, which helps maintain the printed structure's shape stability and integrity.

As the CNF content increases, both the storage modulus and shear modulus of the composite hydrogel increase (Figure 4I). This enhancement is mainly due to the increased CNFs, as CNFs promote hydrogen bonding between the hydroxyl groups of PVA and the carboxyl and hydroxyl groups of CNFs, and strengthen the physical entanglement between CNFs and PVA molecular chains. Simultaneously, the gel–sol transition temperature shifted progressively higher with increasing CNF content.

All composite hydrogels exhibited shear-thinning behavior, with viscosity decreasing as shear rate increased (Figure 4J), indicating their suitability for extrusion-based 3D printing. Hydrogels containing 6% and 8% CNFs showed higher viscosities than those with 2% and 4%. Notably, although the hydrogel with 8% CNFs had significantly higher viscosity than that with 6%, their shear rate–viscosity curves were nearly identical. This is because at 8% CNFs, the high surface activity of CNFs promotes fiber aggregation, disrupting network order and reducing the polymer chains' ability to rearrange under flow. Based on these rheological results, the composite hydrogel containing 8% CNFs was selected for subsequent experiments.

3.3.6. Investigation of printing processes

In extrusion-based 3D printing, extrusion pressure and printing speed significantly affect both the viscosity of the extruded filaments and their diameter as they exit the nozzle. Therefore, optimizing these printing parameters is essential to ensure slurry uniformity during extrusion and achieve accurate printed parts. We designed a double-layer printed structure (Figure 5A) to study the printing process. All printing was performed under constant platform temperature, layer height, and gap settings, while extrusion pressure and printing speed were varied between 105–135 kPa and 1–3 mm/s, respectively.

We investigated how extrusion pressure and printing speed influenced the extrusion behavior, shape stability, and consistency of the printed structures (Figure 5G). The images framed in green and red represent "good quality" and "poor quality" printed supports, respectively. The results showed that at an extrusion pressure of 150 kPa, printing speeds exceeding 1.5 mm/s can lead to issues such as reduced filament diameter and poor adhesion between filaments and the underlying layer. When the printing material fails to adhere properly to the surface, filament adhesion deteriorates, resulting in overall poor print quality. Increasing the extrusion pressure can help by enlarging the filament diameter and improving adhesion. However, at extrusion pressures of 120, 135, 150, and 165 kPa, lower printing speeds cause excessive filament diameter and over-adhesion, which also compromise print quality. Notably, at 135 kPa and a printing speed of 3 mm/s, uneven filament extrusion and thinner filaments were observed.

According to our observations, the scaffold exhibited outstanding forming performance when extrusion pressure and printing speed are properly matched, as shown by the green-bordered pictures in the figure (Figure 5G). Using the composite scaffold design (Figure 5B), printing at 150 kPa and 3 mm/s proceeds smoothly, thereby yielding well-formed hydrogels (Figure 5C) and resulting in high-quality composite scaffolds (Figure 5D and E). Additionally, statistical analysis of filament diameters under various process conditions revealed that filament diameter is inversely proportional to printing speed and roughly proportional to extrusion pressure (Figure 5F).

3.4. Performance analysis of composite aerogel scaffolds

3.4.1. Morphological observation and elemental composition of composite aerogel scaffolds

Scanning electron microscopy observation of the surface and cross-sectional microstructure of the composite aerogel bone scaffold (Figure 6A) revealed micrometer-scale and nanometer-scale irregular pore structures on the aerogel scaffold surface. This is attributed to the hydrogen bond network formed between PVA and CNFs during freeze-drying, combined with the rigid support provided by n-HA, which prevents pore collapse caused by ice crystal sublimation. EDS analysis (Figure 6B) revealed the presence of Ca, Cl, C, Fe, Na, P, and O elements on the surface and within the cross-section of the scaffold. Among these, Ca and P elements were distributed uniformly, confirming the homogeneous dispersion of n-HA within the scaffold; Fe and Cl elements were uniformly distributed on the surface and within the cross-section of the scaffold, indicating that SPIONs have successfully penetrated the scaffold and are uniformly distributed. The presence of Cl elements was attributed to residual Cl^{-1} from the SPIONs preparation process. Additionally, fibrous structures with micrometer-length fibers were observed in the cross-section, which, based on the previous analysis, are likely CNFs. Compared to the EDS results of the unloaded scaffold (Figure 4I), the composite scaffold exhibited characteristic peaks of Na, indicating that PAS-Na has been loaded into the composite system (PAS-Na@Lipo/SPIONs/CNFs/n-HA/PVA).

3.4.2. Mechanical properties of scaffolds with different liposome loading quantities

The overall trend of the strain–strain curves for the four groups of scaffolds was consistent (Figure 7C), which aligns with the stress–strain curves previously reported for aerogel scaffolds. The composite scaffold can achieve

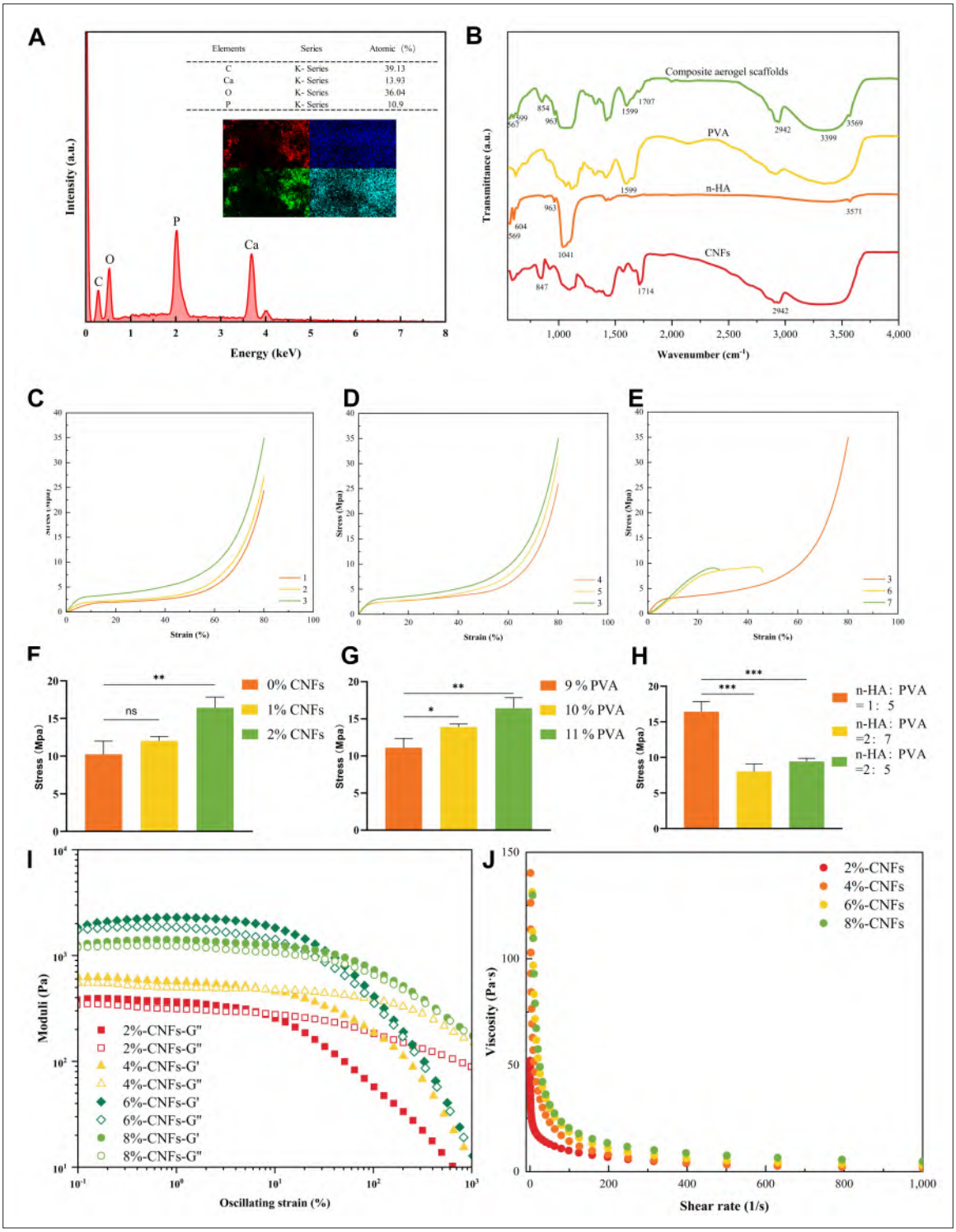


Figure 4. Performance characterization of slurries. (A) EDS of the composite scaffold. (B) FTIR of the composite scaffold and its components. (C) Stress–strain curves at different CNF contents. (D) Stress–strain curves at different PVA concentrations. (E) Stress–strain curves at different n-HA: PVA ratios. (F) Stress at 70% strain for scaffolds with different CNF content. (G) Stress at 70% strain for scaffolds with different PVA concentrations. (H) For the n-HA: PVA ratio of 1:5, the stress was measured at 70% strain. For ratios of 2:7 and 2:5, the stress at collapse was recorded. (I) Oscillation–strain curves for different CNF contents. (J) Speed-viscosity curves for different CNF contents. *$p < 0.05$, **$p < 0.01$, and ***$p < 0.001$; non-significant (ns) at $p \geq 0.05$. Abbreviations: CNF, cellulose nanofiber; EDS, energy dispersive spectroscopy; FTIR, Fourier transform infrared spectroscopy; n-HA, nano-hydroxyapatite; PVA, polyvinyl alcohol.

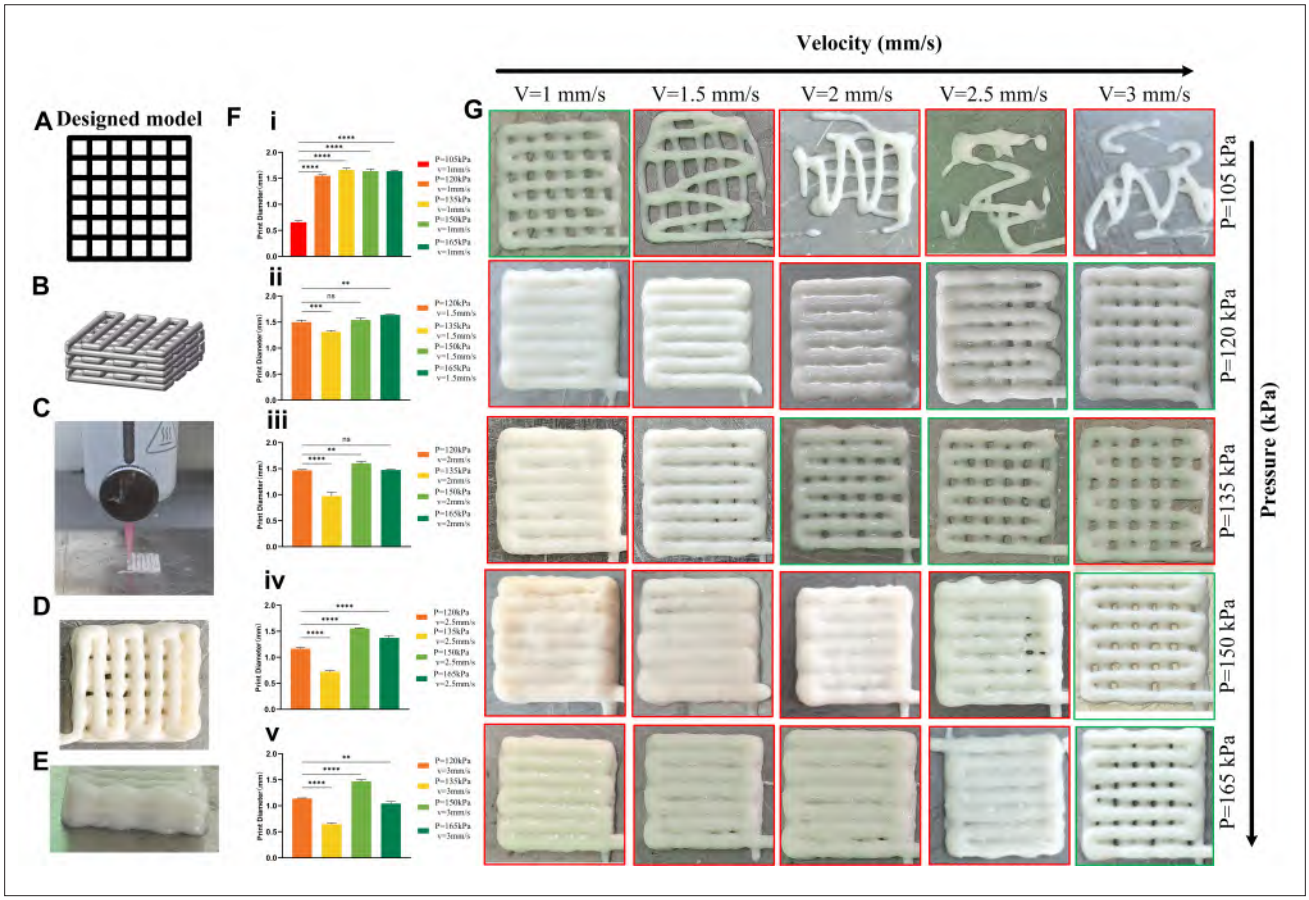


Figure 5. Research on the printing process of composite slurry. (A) Process exploration model. (B) Composite scaffold model. (C) Printing process. (D) Top view of composite scaffold. (E) Side view of composite scaffold. (F) Fine wire diameter under different printing parameters. (G) Forming condition under different printing parameters. *$p < 0.05$, **$p < 0.01$, and ***$p < 0.001$; non-significant (ns) at $p \geq 0.05$.

80% deformation without collapsing, indicating that the aerogel scaffold possesses excellent flexibility and mechanical properties. This is attributed to the high-strength hydrogen bond network formed between CNF chains and PVA chains, as well as between PVA chains themselves, which provides a buffering effect during compression. Mechanical testing showed that as the amount of lipid powder added increases, the mechanical properties of the scaffold exhibited a trend where it first increased and then decreased (Figure 6D). According to previous studies,[19] the initial increase in scaffold mechanical properties after adding liposomes is attributed to the formation of a composite hydrogen bond network between the phosphate groups of phospholipid molecules in liposomes, the hydroxyl groups of PVA molecules, and the carboxyl and hydroxyl groups of CNFs after liposomes disperse into the hydrogel network, thereby enhancing the mechanical properties of the scaffold. Additionally, the filling effect of liposomes on the gel network further enhances mechanical performance. The decrease in scaffold mechanical properties can be explained as follows. First, the added lactose competes with PVA and CNFs to form hydrogen bonds, disrupting the hydrogen bond network between CNFs and PVA and between PVA chains. Additionally, when lactose is added in excess, it undergoes self-association[53] which weakens the hydrogen bonding between lactose and CNFs/PVA. Furthermore, the fusion and hydrophobic interactions between excess liposomes reduce the hydrogen bonding cross-linking between liposomes and CNFs/PVA. These factors collectively lead to a decrease in the mechanical properties of the scaffold when the addition amount reaches 5%.

3.4.3. In vitro drug release of composite aerogel scaffolds without alternating magnetic fields

In vitro drug release experiments of aerogel scaffolds (Figure 6G) showed that the drug release rate of aerogel scaffolds with liposomes was slower than that of aerogel scaffolds with pure drugs. This was expected because the drugs encapsulated in liposomes need to pass through

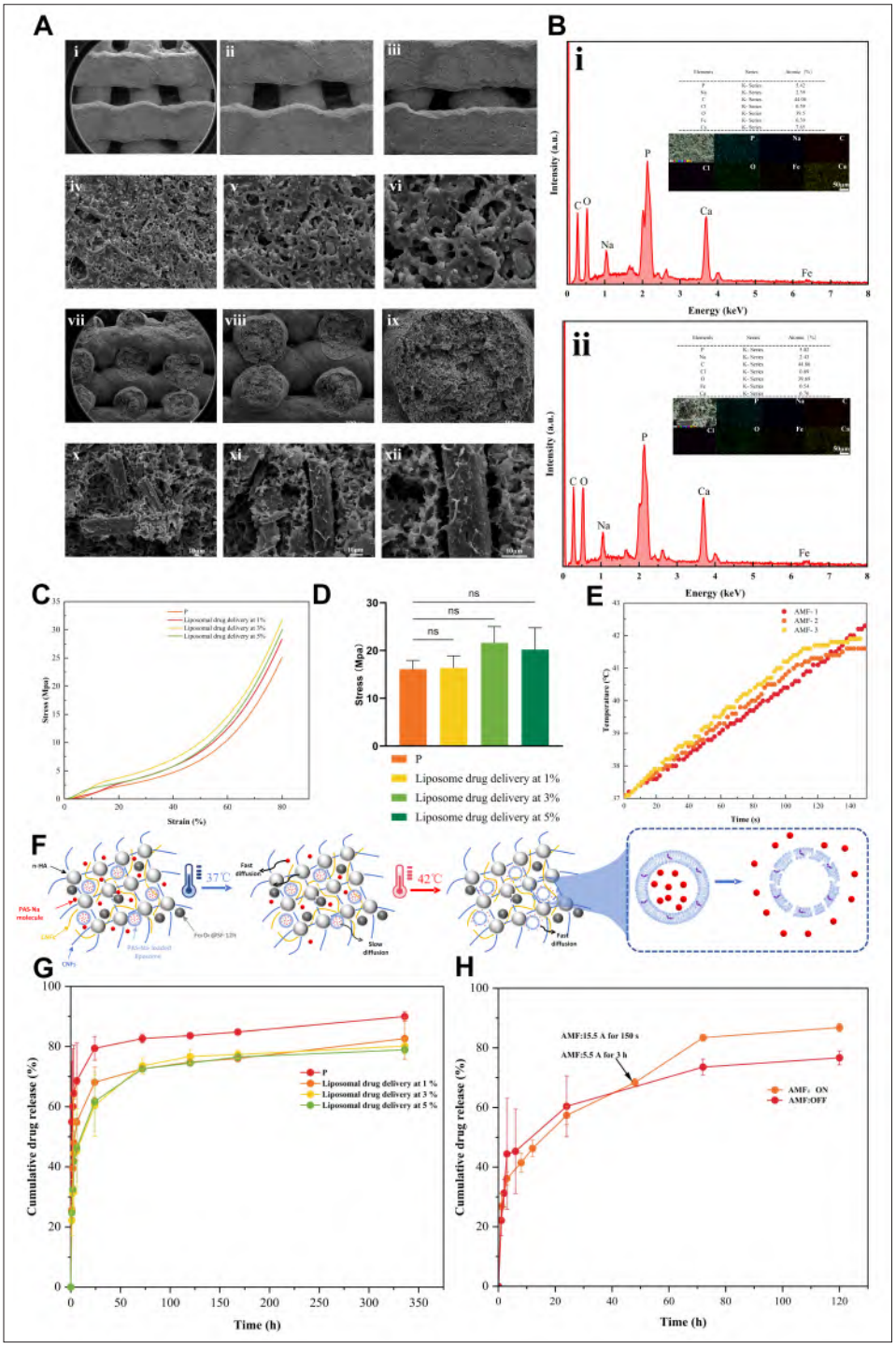


Figure 6. Performance characterization of composite aerogel scaffolds. (A) SEM of the surface of composite aerogel scaffolds at different magnifications (i–vi) and (vii–xii) cross-sections at different magnifications. Scale bar: 10 μm; magnification: Figures 6A a1–a6 are 25×, 35×, 35×, 300×, 1000×, and 2000×, respectively. Magnification for Figures 6A a7–a12 is identical to that for Figures 6A a1–a6. (B) EDS of the surface of (i) composite aerogel scaffolds and (ii) composite aerogel scaffold cross-section. Scale bar: 50 μm; Magnification: Figure 6B is 500X. (C) Stress–strain curves of aerogel scaffolds with different liposome content. (D) Stress values at 70% strain for scaffolds with different liposome content. Ns refers to not significant. (E) Magnetic-thermal heating curves of the composite scaffold under a constant current AMF of 15.5 A. (F) Drug release mechanism diagram of the composite aerogel scaffold. (G) Cumulative drug release curves of pure drug scaffolds and scaffolds with 1%, 3%, and 5% liposome content. (H) Cumulative drug release curves under AMF and without AMF. Abbreviations: AMF, alternating magnetic field; CNF, cellulose nanofiber; EDS, energy dispersive spectroscopy; n-HA, nano-hydroxyapatite; PAS-Na, sodium para-aminosalicylate; PVA, polyvinyl alcohol; SEM, scanning electron microscopy.

two diffusion media before reaching the release medium. On the other hand, when comparing aerogel scaffolds loaded with different drug-loaded liposomes, the pure drug aerogel scaffold exhibited a cumulative drug release of 79.40% at 24 h, while the cumulative drug releases for 1%, 3%, and 5% drug-loaded liposomes were 68.11%, 60.40%, and 61.74%, respectively. The drug release from lipid-loaded scaffolds was slower than that from pure drug scaffolds, indicating that the addition of lipid particles effectively reduced the initial drug release in the early stages. The sustained-release performance of the scaffolds increased non-linearly with the addition of lipid particles, and there were no significant differences in the drug release curves and parameters between 3% and 5% lipid-loaded scaffolds. This may be due to the excessive addition of lactose, which reduced the cross-linking degree of the gel network, increased the diffusion coefficient of the drug in the aerogel network, and accelerated drug release. This promoting effect on drug release counteracts the inhibitory effect of liposomes on drug release, resulting in no significant improvement in sustained drug release efficacy of the 5% liposome-loaded scaffold compared to the 3% scaffold. Additionally, the addition of liposomes delayed the drug release cycle. The cumulative drug release rate of the 3% liposome-loaded scaffold reached 80.18% at 336 h, which was 9.80% lower than that of the pure drug scaffold. The 3% liposome aerogel scaffold exhibited excellent sustained-release properties and mechanical performance.

3.4.4. In vitro drug release of composite aerogel scaffolds under alternating magnetic fields

To address the challenge of uncontrolled drug release during the early treatment of BMT, we introduced an AMF to locally raise the temperature of bone implants via the magnetothermal effect, thereby regulating the cumulative drug release from the scaffold. Due to the early burst release characteristic of water-soluble drugs, the AMF was applied after collecting the release solution on the second day. First, the AMF was applied for 150 s at a constant current of 15.5 A, raising the scaffold temperature to the phase transition temperature of the lipid bilayer membrane (42°C) (Figure 6E), followed by a reduction of the current to 5.5 A and maintenance for 3 h.

Following the AMF application, drug release was significantly accelerated (Figure 6H). The cumulative drug release rate from the composite scaffold without AMF was 73.57 ± 2.66% on Day 3, which increased to 83.27 ± 1.14% after AMF treatment—an improvement of nearly 10%. This effect can be attributed to two main factors. First, when the local temperature reached 42°C, the liposomal bilayer membrane ruptured, releasing the encapsulated PAS-Na into the scaffold (Figure 6F). Second, the temperature increase enhanced the diffusion coefficient of PAS-Na in PBS buffer, further promoting drug release. This *in vitro* drug release regulation method not only controls the release of water-soluble drugs during early-stage bone tuberculosis treatment but also allows for modulation of lipophilic drug release during later stages.

3.5. In vitro cell compatibility of superparamagnetic iron oxide nanoparticles and composite scaffolds

3.5.1. Biocompatibility of superparamagnetic iron oxide nanoparticles

To verify the role of SF in enhancing the biocompatibility of Fe_3O_4, we used the MTT method to detect the effects of Fe_3O_4 and Fe_3O_4@SF-12h on the proliferation of MC3T3-E1 cells. The cell survival rate was calculated using the following formula (**Equation II**):

$$\text{Cell viability}(\%) = \frac{OD_{treated} - OD_{blank}}{OD_{control} - OD_{blank}} \times 100 \quad \text{(II)}$$

where $OD_{control}$ is the optical density of untreated cells, $OD_{treated}$ indicates the optical density of cells treated with the extraction solution, and OD_{blank} is the blank group without cells.

Cell culture results (Figure 7A) showed that the cytotoxicity of pure Fe_3O_4 toward MC3T3-E1 cells was 88.89 ± 2.84% and 65.67 ± 2.80% after 1 and 3 days of culture, respectively, indicating that pure Fe_3O_4 exhibited certain cytotoxicity toward MC3T3-E1 cells. However, the cell viability of Fe_3O_4@SF-12h after 1 and 3 days of culture was 90.50 ± 4.26% and 80.29 ± 2.7%, respectively, suggesting that SF mitigated the cytotoxicity of Fe_3O_4 toward MC3T3-E1 cells. Fe_3O_4@SF-12h showed cell viability of 90.50 ± 4.26% and 80.29 ± 2.7% after 1 and 3 days, respectively. This suggests that the carboxyl and hydroxyl groups in the peptide chains of SF chelated iron ions in Fe_3O_4, effectively reducing the diffusion of Fe^{2+} and Fe^{3+}, thereby lowering the cytotoxicity of SPIONs.

3.5.2. Cell toxicity of scaffolds with different superparamagnetic iron oxide nanoparticle content

Cell culture results (Figure 7B) showed that the number of surviving cells in the three experimental groups was similar on Day 3 of culture. By Day 5 of cell culture, significant proliferation of MC3T3-E1 cells was observed in all groups, with similar cell viability. Based on the above results, this phenomenon can be attributed to two factors: first, the carboxyl and hydroxyl groups of SF chelated Fe^{2+} and Fe^{3+}; second, the hydrogen bond cross-linking network increased the mass transfer resistance of Fe^{2+} and Fe^{3+} within the scaffold. Under the combined influence

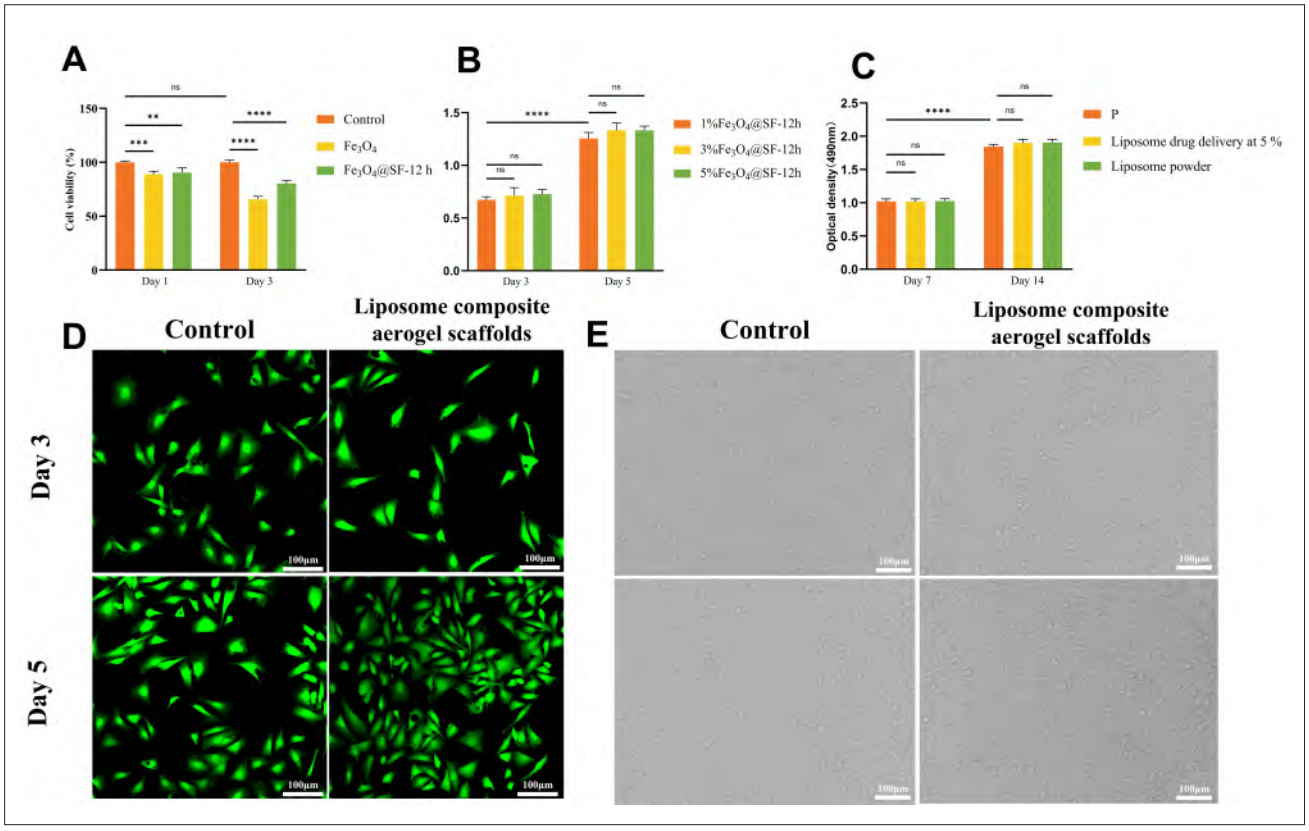


Figure 7. Cell experiments with superparamagnetic iron oxide nanoparticles (SPIONs) and composite aerogel scaffolds. (A) Cell viability of Fe_3O_4 and Fe_3O_4@SF after 1 and 3 days of cell culture. (B) OD values of scaffolds with different SPIONs content after 3 and 5 days of cell culture. (C) OD values of PAS-Na@Lipo and pure drug-loaded aerogel scaffolds and lipid-loaded aerogel scaffolds after 7 and 14 days of cell culture. (D) Confocal microscopy images of composite aerogel scaffolds after 3 and 5 days of cell culture. Scale bar: 100 μm; magnification: Figure 7D 20×. (E) Optical microscopy images of composite aerogel scaffolds after 3 and 5 days of cell culture. Scale bar: 100 μm; magnification; Figure 7E 20×. *$p < 0.05$, **$p < 0.01$, and ***$p < 0.001$; non-significant (ns) at $p \geq 0.05$. Abbreviations: OD, optical density; PAS-Na@Lipo, sodium para-aminosalicylate-encapsulated liposomes; SF, silk fibroin.

of these two factors, the iron ion content in the extract of composite aerogel scaffolds was lower, ensuring that the composite aerogel scaffolds with different SPIONs loading levels maintained low cytotoxicity toward MC3T3-E1 cells.

3.5.3 Cell viability staining of composite aerogel scaffolds

We evaluated the biocompatibility of the scaffold material with MC3T3-E1 cells using the immersion extraction method. Laser confocal microscopy observations (Figure 7C and D) showed that on Day 3 of cell culture, the number of viable cells in the control group and the composite aerogel scaffold group were similar. By Day 5 of cell culture, both the control group and the composite aerogel scaffold group exhibited cell proliferation, with the composite aerogel group showing a higher cell viability than the control group, indicating that the composite scaffold effectively promoted the proliferation of MC3T3-E1 cells. This phenomenon can be attributed to the low cytotoxicity of the composite aerogel scaffold material toward MC3T3-E1 cells.

In addition, we evaluated the cell growth of PAS-Na-unloaded liposome aerogel scaffolds, PAS-Na-loaded liposome aerogel scaffolds, and PAS-Na@Lipo at Days 7 and 14 of cell culture. The cell viability of the three groups was similar on Day 7 of cell culture. On Day 14, the cell viability of the lipid-loaded aerogel scaffold and PAS-Na@Lipo was higher than that of the aerogel scaffold loaded with PAS-Na but not with lipids. This indicates that PAS-Na@Lipo inherently possessed good biocompatibility and exhibited low cytotoxicity toward MC3T3-E1 cells. This composite aerogel scaffold loaded with liposomes, which exhibited good biocompatibility, provides a new strategy for bone tissue repair.

3.5.4. Cell osteogenic differentiation

Alkaline phosphatase is involved in the early stage of bone mineralization, and the increase of ALP activity is

an important sign of MC3T3-E1 differentiation toward osteoblasts. From the results of Days 7 and 14 of culture, the ALP activity of both liposome-loaded aerogel scaffolds and pure drug-loaded aerogel scaffolds groups was higher than that of the control group, and the difference was more significant with the extension of the culture time, which indicated that the composite aerogel scaffolds could promote the proliferation and differentiation of MC3T3-E1. In addition, MC3T3-E1 in the liposome-loaded aerogel scaffold group showed deeper and more intense staining, with stronger pro-cell proliferation and differentiation ability, and this phenomenon indicated that PAS-Na@Lipo could play a role in promoting the proliferation and differentiation of MC3T3-E1 cells, and the quantitative analysis of ALP also showed the same trend. In Alizarin red staining of cellular calcium nodules, greater calcium deposition was observed in both pure drug-loaded aerogel scaffolds and liposome-loaded aerogel scaffolds, indicating the superior mineralization capacity of the latter (Figure 8).

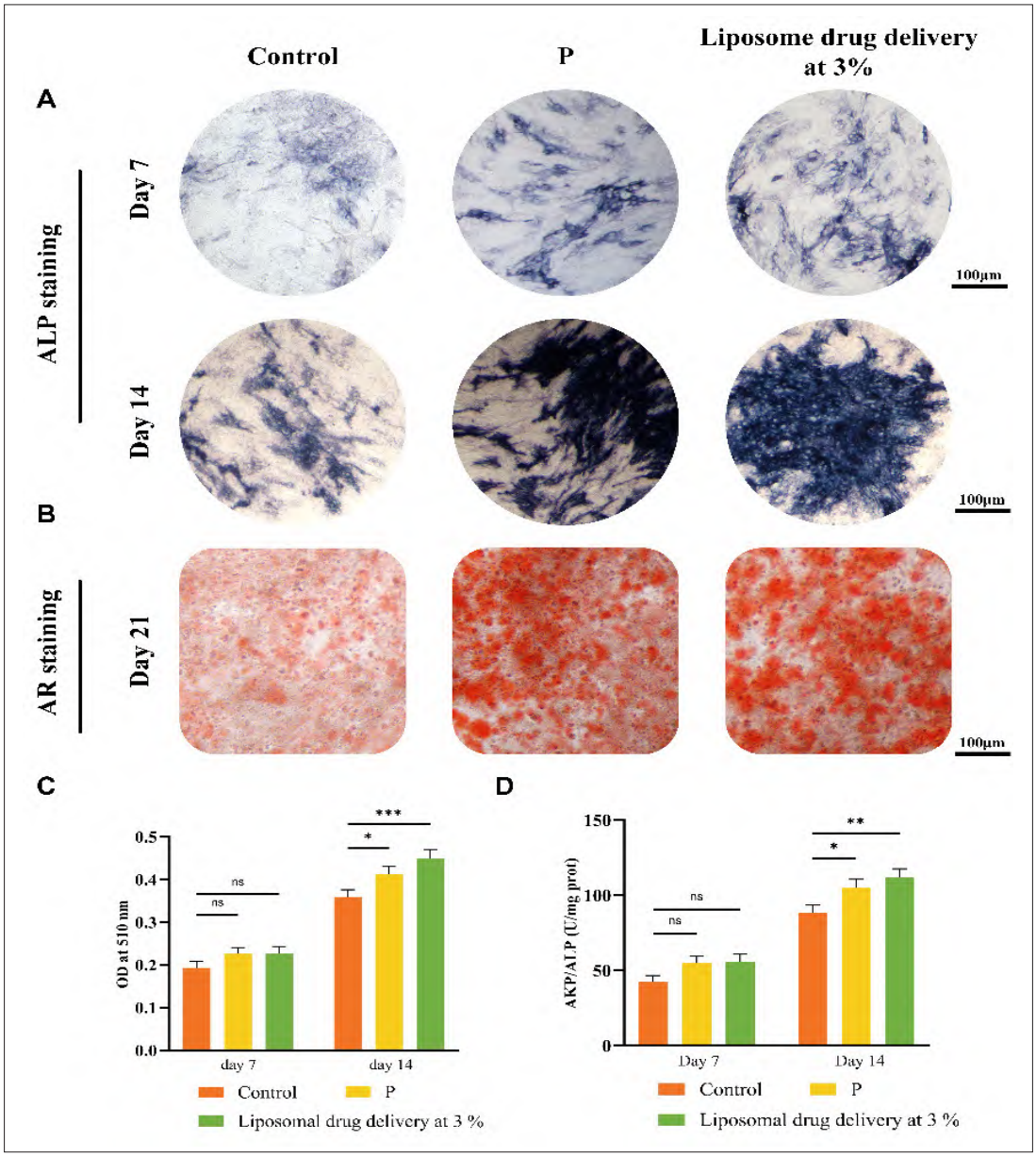


Figure 8. Osteogenic differentiation and mineralization of MC3T3-E1 *in vitro* at different culture stages. (A) Alkaline phosphatase (ALP) staining. (B) Alizarin red (AR) staining. Scale bar: 100 μm; magnification Figure A (100×), Figure B (200×). (C) The optical density (OD) value of ALP. (D) Quantitative analysis of ALP activity. $^{*}p < 0.05$, $^{**}p < 0.01$, and $^{***}p < 0.001$; non-significant (ns) at $p \geq 0.05$.

4. Conclusion

To achieve more precise and effective treatment of bone tuberculosis, this study proposed a 3D printing strategy to fabricate a composite scaffold (PAS-Na@Lipo/SPIONs/CNFs/n-HA/PVA). Liposomes effectively mitigated the initial burst release and extended the drug release cycle, while the phosphate groups of liposomes formed hydrogen bonds with CNFs and PVA, enhancing the mechanical properties of the aerogel scaffold. The incorporation of CNFs established multiple hydrogen bonds with PVA and entangled with PVA molecular chains, creating an interlocking network that significantly improved the scaffold's mechanical properties. Additionally, SPIONs modified with SF were introduced alongside alternating magnetic fields. Through the magnetothermal heating effect of SPIONs under these fields, dynamic *in vitro* regulation of drug release from the implant was achieved. *In vitro* cell studies demonstrated that the composite aerogel scaffold promoted MC3T3-E1 cell proliferation. This composite scaffold not only effectively overcomes the severe initial drug release shortcomings of traditional aerogel scaffolds but also offers real-time drug release control, excellent mechanical performance, and biocompatibility, providing a novel approach for the early treatment of BTB.

Acknowledgments

None.

Funding

This work was supported by the National Natural Science Foundation of China (52365053), the Excellent Doctoral Graduate Innovation Project of Xinjiang University, China (XJU2024BS101), and the China Scholarship Council (202407010013).

Conflict of interest

The authors declare they have no competing interests.

Author contributions

Conceptualization: Kefeng Wang, Yan Xu, Seeram Ramakrishna, Zhitao Yin

Formal analysis: Kefeng Wang, Shun Zhang, Miaomiao Zheng

Investigation: Kefeng Wang

Methodology: Kefeng Wang, Yutong Chen

Writing–original draft: Kefeng Wang, Yutong Chen

Writing–review & editing: Subramanian Sundarrajan, Jingtao Hu, Jian Chao

Ethics approval and consent to participate

Not applicable.

Consent for publication

Not applicable.

Availability of data

Data will be made available upon request to the corresponding author.

References

1. Qin X, Qin B, Zhou C, *et al.* A multicenter, epidemiological study of bone tuberculosis in Southwest China from 2011 to 2023. *J Epidemiol Glob Health.* 2024;14(4):1678-1692. doi: 10.1007/s44197-024-00325-2
2. Ding Y, Li B, Yi Y, *et al.* Progress in the role of nanoparticles in the diagnosis and treatment of bone and joint tuberculosis. *Front Med (Lausanne).* 2025;12:1536547. doi: 10.3389/fmed.2025.1536547
3. Yang L, Liu Z. Analysis and therapeutic schedule of the postoperative recurrence of bone tuberculosis. *J Orthop Surg Res.* 2013;8:47. doi: 10.1186/1749-799X-8-47
4. Huang J, Li H, Mei Y, *et al.* An injectable hydrogel bioimplant loaded with engineered exosomes and triple anti-tuberculosis drugs with potential for treating bone and joint tuberculosis. *Int J Nanomedicine.* 2025;20:1285-1302. doi: 10.2147/IJN.S480288
5. Fernández-Paz C, Fernández-Paz E, Salcedo-Abraira P, *et al.* Microencapsulated isoniazid-loaded metal-organic frameworks for pulmonary administration of antituberculosis drugs. *Molecules.* 2021;26(21):6408. doi: 10.3390/molecules26216408
6. Hua L, Qian H, Lei T, *et al.* Anti-tuberculosis drug delivery for tuberculous bone defects. *Expert Opin Drug Deliv.* 2021;18(12):1815-1827. doi: 10.1080/17425247.2021.1878328
7. Olmos-Juste R, Guaresti O, Calvo-Correas T, Gabilondo N, Eceiza A. Design of drug-loaded 3D printing biomaterial inks and tailor-made pharmaceutical forms for controlled release. *Int J Pharm.* 2021;609:121124. doi: 10.1016/j.ijpharm.2021.121124
8. Sun H, Hu C, Zhou C, *et al.* 3D printing of calcium phosphate scaffolds with controlled release of antibacterial functions for jaw bone repair. *Mater Design.* 2020;189:108536. doi: 10.1016/j.matdes.2020.108536
9. Iglesias-Mejuto A, García-González CA. 3D-printed, dual crosslinked and sterile aerogel scaffolds for bone tissue engineering. *Polymers (Basel).* 2022;14(6):1145.

doi: 10.3390/polym14061145

10. Menshutina N, Abramov A, Tsygankov P, Lovskaya D. Extrusion-based 3D printing for highly porous alginate materials production. *Gels.* 2021;7(3):128. doi: 10.3390/gels7030128

11. Son W-S, Park HJ, Lee C-J, *et al*. Supercritical drying of vascular endothelial growth factor in mesenchymal stem cells culture fluids. *J Supercrit Fluids.* 2020;157:104723. doi: 10.1016/j.supflu.2020.104723

12. Yuan J, Zhen P, Zhao H, *et al*. The preliminary performance study of the 3D printing of a tricalcium phosphate scaffold for the loading of sustained release anti-tuberculosis drugs. *J Mater Sci.* 2015;50(5):2138-2147. doi: 10.1007/s10853-014-8776-0

13. Cao X, Dai L, Sun S, Ma R, Liu X. Preparation and performance of porous hydroxyapatite/poly(lactic-co-glycolic acid) drug-loaded microsphere scaffolds for gentamicin sulfate delivery. *J Mater Sci.* 2021;56(27):15278-15298. doi: 10.1007/s10853-021-06183-8

14. Dang Z, Huang W, Cai X, Ye J, Xu W. Dual cytokine release from microsphere-containing decellularized extracellular matrix immune regulation promotes bone repair and regeneration. *Appl Mater Today.* 2024;40:102433. doi: 10.1016/j.apmt.2024.102433

15. Luo X, Zhang L, Luo Y, *et al*. Charge-driven self-assembled microspheres hydrogel scaffolds for combined drug delivery and photothermal therapy of diabetic wounds. *Adv Funct Mater.* 2023;33(26):2214036. doi: 10.1002/adfm.202214036

16. Mufamadi MS, Kumar P, du Toit LC, *et al*. Liposome-embedded, polymeric scaffold for extended delivery of galantamine. *J Drug Deliv Sci Technol.* 2019;50:255-265. doi: 10.1016/j.jddst.2019.101208

17. Sarkar N, Bose S. Liposome-encapsulated curcumin-loaded 3D printed scaffold for bone tissue engineering. *ACS Appl Mater Interfaces.* 2019;11(19):17184-17192. doi: 10.1021/acsami.9b20223

18. Mohammadian F, Eatemadi A. Drug loading and delivery using nanofibers scaffolds. *Artif Cells Nanomed Biotechnol.* 2017;45(5):881-888. doi: 10.1080/21691401.2016.1177901

19. Cheng R, Yan Y, Liu H, *et al*. Mechanically enhanced lipo-hydrogel with controlled release of multi-type drugs for bone regeneration. *Appl Mater Today.* 2018;12:294-308. doi: 10.1016/j.apmt.2018.04.003

20. Amin M, Lammers TLM ten Hagen. Temperature-sensitive polymers to promote heat-triggered drug release from liposomes: towards bypassing EPR. *Adv Drug Deliv Rev.* 2022;189:114503. doi: 10.1016/j.addr.2022.114503

21. Bejarano J, Rojas A, Ramirez-Sagredo A, *et al*. Light-induced release of the cardioprotective peptide angiotensin-(1-9) from thermosensitive liposomes with gold nanoclusters. *J Control Release.* 2020;328:859-872. doi: 10.1016/j.jconrel.2020.08.029

22. Liu G, Gao J, Ai H, Chen X. Applications and potential toxicity of magnetic iron oxide nanoparticles. *Small.* 2013;9(9-10):1533-1545. doi: 10.1002/smll.201201531

23. Al-Jawuschi N, Chen S, Abie N, Fischer T, Fare S, Maleki HH. Self-assembly-driven Bi_2S_3 nanobelts integrated a silk-fibroin-based 3D-printed aerogel-based scaffold with a dual-network structure for photothermal bone cancer therapy. *Langmuir.* 2023;39(12):4326-4337. doi: 10.1021/acs.langmuir.2c03334

24. Zhao Y, Chen H, Fu J, Wang A, Liu X, Jiang X. Drug-loaded microspheres on NIR-responsive PLA/MXene scaffolds: controlled release and bone tissue regeneration. *ACS Appl Bio Mater.* 2025;8(1):285-298. doi: 10.1021/acsabm.4c01175

25. Gu C, Chen H, Zhao Y, *et al*. $Ti_3C_2T_x$@PLGA/Icaritin microspheres-modified PLGA/β-TCP scaffolds modulate Icaritin release to enhance bone regeneration through near-infrared response. *Biomed Mater.* 2024; 19(5):055014. doi: 10.1088/1748-605X/ad6dc9

26. Deng C, Li Z, Lu L, *et al*. Sophisticated magneto-mechanical actuation promotes in situ stem cell assembly and chondrogenesis for treating osteoarthritis. *ACS Nano.* 2023;17(21):21690-21707. doi: 10.1021/acsnano.3c08367

27. Saranya M, da Silva AM, Karjalainen H, *et al*. Magnetic-responsive carbon nanotubes composite scaffolds for chondrogenic tissue engineering. *Adv Healthc Mater.* 2023;12(30):e2301040. doi: 10.1002/adhm.202300104

28. Beola L, Iturrioz-Rodriguez N, Pucci C, Bertorelli R, Ciofani G. Drug-loaded lipid magnetic nanoparticles for combined local hyperthermia and chemotherapy against glioblastoma multiforme. *ACS Nano.* 2023;17(18):18441-18455. doi: 10.1021/acsnano.3c10627

29. Kang T, Cha GD, Park OK, *et al*. Penetrative and sustained drug delivery using injectable hydrogel nanocomposites for postsurgical brain tumor treatment. *ACS Nano.* 2023;17(6):5435-5447. doi: 10.1021/acsnano.2c11409

30. Usov NA. Iron oxide nanoparticles for magnetic hyperthermia. *Spin.* 2019;9(2):1950006. doi: 10.3390/spin9020006

31. Zhang Z-Q, Song S-C. Thermosensitive/superparamagnetic iron oxide nanoparticle-loaded nanocapsule hydrogels for multiple cancer hyperthermia. *Biomaterials.* 2016; 106:13-23. doi: 10.1016/j.biomaterials.2016.07.029

32. Bardestani A, Ebrahimpour S, Esmaeili A, Esmaeili A. Quercetin attenuates neurotoxicity induced by iron oxide nanoparticles. *J Nanobiotechnol.* 2021;19(1):68. doi: 10.1186/s12951-021-00817-y

33. Zhang H, Ma X, Cao C, Wang M, Zhu Y. Multifunctional iron oxide/silk-fibroin (Fe_3O_4-SF) composite microspheres for the delivery of cancer therapeutics. *RSC Adv.* 2014;4(78):41572-41577. doi: 10.1039/C4RA07974E

34. Lee H, Han G, Na Y, *et al*. 3D-printed tissue-specific nanospike-based adhesive materials for time-regulated synergistic tumor therapy and tissue regeneration *in vivo*. *Adv Funct Mater.* 2024;34(48):2408622. doi: 10.1002/adfm.2024008622

35. Huang H, Qiang L, Fan MJ, *et al*. 3D-printed tri-element-doped hydroxyapatite/polycaprolactone composite scaffolds with antibacterial potential for osteosarcoma therapy and bone regeneration. *Bioact Mater.* 2024;31:18-37. doi: 10.1016/j.bioactmat.2024.02.013

36. Chen S, Hassan N, Kopp A, *et al*. Theragenerative injectable bone-adhesive hydrogels for combined photothermal osteosarcoma therapy and bone repair. *Biomater Sci.* 2025;13(13):751-766. doi: 10.1039/d4bm01489f

37. Cheung Y-MM, Van K, Lan L, *et al*. Hypothyroidism associated with therapy for multi-drug-resistant tuberculosis in Australia. *Intern Med J.* 2019;49(3):364-372. doi: 10.1111/imj.14238

38. Qiao J, Yang L, Feng J, Dai X, Xu F, Xia P. Analysis of efficacy and safety of linezolid-based chemotherapeutic regimens for patients with postoperative multidrug-resistant spinal tuberculosis. *Int J Infect Dis.* 2022;118:264-269. doi: 10.1016/j.ijid.2022.05.073

39. Mahmutoglu G, Topsakal A, Altan E, *et al*. Effects of temperature and pH on the synthesis of nanohydroxyapatite powders by chemical precipitation. *J Aust Ceram Soc.* 2023;59(5):1433-1441. doi: 10.1007/s41779-023-00893-0

40. Saroglu O, Karakas CY, Yildirim RM, *et al*. Liposomal propolis loaded xanthan gum-salep hydrogels: Preparation, characterization, and in vitro bioaccessibility of phenolics. *Int J Biol Macromol.* 2025;300:125859. doi: 10.1016/j.ijbiomac.2024.12.245

41. Deng M, Huang Z, Zou Y, Yin G, Liu J, Gu J. Fabrication and neuron cytocompatibility of iron oxide nanoparticles coated with silk-fibroin peptides. *Colloids Surf B Biointerfaces.* 2014;116:465-471. doi: 10.1016/j.colsurfb.2014.01.021

42. Akbar M, Cagli E, Erel-Goktepe I. Layer-by-layer modified superparamagnetic iron oxide nanoparticles with stimuli-responsive drug release properties. *Macromol Chem Phys.* 2019;220(4):1800316. doi: 10.1002/macp.201800316

43. Mallick N, Anwar M, Asfer M, *et al*. Chondroitin sulfate-capped super-paramagnetic iron oxide nanoparticles as potential carriers of doxorubicin hydrochloride. *Carbohydr Polym.* 2016;151:546-556. doi: 10.1016/j.carbpol.2016.06.040

44. Carissimi G, Baronio CM, Montalban MG, Villora G, Barth A. On the secondary structure of silk fibroin nanoparticles obtained using ionic liquids: an infrared spectroscopy study. *Polymers.* 2020;12(6):1494. doi: 10.3390/polymers12061494

45. Del Bianco L, Spizzo F, Yang YJ, *et al*. Silk fibroin films with embedded magnetic nanoparticles: evaluation of the magneto-mechanical stimulation effect on osteogenic differentiation of stem cells. *Nanoscale.* 2022;14(39):14558-14574. doi: 10.1039/d2nr04350a

46. Zheng Y, Yang R, Yu X, Zhang W, Shao Y. Effect of manganese ion doping on magnetic properties and magnetic induction heating of Zn-Al ferrite nanoparticles. *J Alloys Compd.* 2023;966:171827. doi: 10.1016/j.jallcom.2023.171827

47. Zhang H. Thin-film hydration followed by extrusion method for liposome preparation. In: Dsouza GGM, Zhang H, eds. *Liposomes, 3rd ed.* Vol 2622. New York, NY: Springer; 2023:57-63. doi: 10.1007/978-1-0716-3939-3_5

48. Zhang H, Fu C, Yong LC, Sun N, Liu FG. Flexible and transparent PVA/CNF hydrogel with ultrahigh dielectric constant. *ACS Appl Polymer Mater.* 2024;6(10):5706-5713. doi: 10.1021/acsapm.4c00649

49. Babaei M, Ghaee A, Nourmohammadi J. Poly (sodium 4-styrene sulfonate)-modified hydroxyapatite nanoparticles in zein-based scaffold as a drug carrier for vancomycin. *Mater Sci Eng C Mater Biol Appl.* 2019;100:874-885. doi: 10.1016/j.msec.2019.03.023

50. Aki D, Ulag S, Unal S, *et al*. 3D printing of PVA/hexagonal boron nitride/bacterial cellulose composite scaffolds for bone tissue engineering. *Mater Design.* 2020;196:109123. doi: 10.1016/j.matdes.2020.109123

51. Zou S, Xi L. CNF/PVA aerogel-based eutectic composite phase change materials with high strength and form stability for energy efficient building applications. *J Energy Storage.* 2025;127:106234. doi: 10.1016/j.est.2024.107870

52. Abe K, Tomobe Y, Yano H. The reinforcement effect of cellulose nanofiber on Young's modulus of polyvinyl alcohol gel produced through the freeze/thaw method. *J Polymer Res.* 2020;27(8):238. doi: 10.1007/s10965-020-02200-8

53. Fan XD, Hsieh YL, Krochta JM. Thermal and mechanical behaviors of poly(vinyl alcohol)-lactose blends. *J Appl Polymer Sci.* 2002;83(4):929-935. doi: 10.1002/app.10520

ACCSCIENCE PUBLISHING

International Journal of Bioprinting

RESEARCH ARTICLE

3D-printed patient-specific titanium implant for mandibular reconstruction with local drug release: Optimization, *in vivo* evaluation, and functional assessment

Chiao-Min Chang[1,2], Shao-Fu Huang[1,2], Hsuan-Wen Wang[1,2], Lu-Yi Yu[1,2], Tzu-Huan Huang[1,3], Chun-Liang Lo[1,2], and Chun-Li Lin[1,2]*

[1]Department of Biomedical Engineering, National Yang Ming Chiao Tung University, Taipei, Taiwan

[2]Department of Biomedical Engineering, Medical Device Innovation and Translation Center, National Yang Ming Chaio Tung University, Taipei, Taiwan

[3]Department of Oral and Maxillofacial Surgery, MacKay Memorial Hospital, Taipei, Taiwan

Abstract

Reconstruction of severe mandibular defects remains a significant clinical challenge due to high recurrence rates, inadequate anatomical restoration, and the limited efficacy of systemic chemotherapy. To address these limitations, a patient-specific, 3D-printed titanium mandibular implant was developed with an integrated refillable drug storage tank for localized cisplatin release. The tank surface geometry and the hydrogel formulation were optimized using the Taguchi method and incorporated into anatomically matched implants. *In vivo* evaluation in six porcine mandibular defect models demonstrated systemic safety over 12 weeks, with plasma platinum levels reduced by more than 60% compared to systemic administration. Hematological and biochemical indicators—including white blood cell count, liver enzymes, and renal function markers—remained within normal ranges throughout the observation period, confirming physiological stability and biocompatibility. No significant complications or implant loosening were observed. Functional validation was further performed on three representative human mandibular large-defect models. Finite element analysis revealed implant stresses well below the yield strength of Ti6Al4V (<40%), and four-point bending fatigue tests confirmed structural endurance beyond one million loading cycles. This study presents the first functional and biocompatible patient-specific mandibular implant with integrated, refillable drug delivery, offering a clinically translatable strategy for simultaneous reconstruction and localized chemotherapy in head and neck oncology.

Keywords: 3D printing; Drug release; Functional test; Patient-specific implant; Taguchi

***Corresponding author:**
Chun-Li Lin
(cllin2@nycu.edu.tw)

Citation: Chang CM, Huang SF, Wang HW, *et al.* 3D-printed patient-specific titanium implant for mandibular reconstruction with local drug release: Optimization, *in vivo* evaluation, and functional assessment. *Int J Bioprint*. 2025;11(5):431-450. doi: 10.36922/IJB025260250

Received: June 27, 2025
Revised: July 17, 2025
Accepted: July 21, 2025
Published Online: July 21, 2025

Copyright: © 2025 Author(s). This is an Open Access article distributed under the terms of the Creative Commons Attribution License, permitting distribution, and reproduction in any medium, provided the original work is properly cited.

Publisher's Note: AccScience Publishing remains neutral with regard to jurisdictional claims in published maps and institutional affiliations.

1. Introduction

Fibula-free flap surgery (FFS) combined with a traditional reconstruction plate remains the gold standard for the reconstruction of severe mandibular defects. The subsequent

administration of chemotherapy and radiotherapy in clinical practice has further improved the overall success rate of mandibular reconstruction.[1–6] Nevertheless, the recurrence rate of mandibular reconstruction is still as high as 32.7% according to the literature.[7] Contributing factors may include altered biomechanical behavior after reconstruction surgery and the limited efficacy of chemotherapy and radiotherapy.

Maintaining the structural integrity of the mandible after FFS continues to be a significant challenge, as the grafted bone often fails to restore optimal anatomical configuration. Complications such as plate deformation or fracture, screw loosening, and loss of masticatory function are frequently reported.[1,2,6,8–11] To address these issues, patient-specific mandibular implants have been developed through the integration of medical image processing, computer-aided design (CAD), and metal 3D printing (additive manufacturing), aiming to improve both esthetic outcomes and biomechanical performance.[1,5,12,13] Our previous study proposed a design criterion for patient-specific reconstructed implants with lightweight structural optimization for various mandibular continuity defects.[5] The sizes and positions of the internal support beams in the reconstructed implant were defined parametrically based on the corresponding segmental bone length, width, and height. In accordance with the Food and Drug Administration (FDA) regulations, functional and biomechanical fatigue tests confirmed that all mandibular continuity defects reconstructed using 3D-printed implants can withstand cyclic dynamic loading.

Another key factor contributing to recurrence is the suboptimal efficacy of chemotherapy and radiation therapy, often necessitating increased drug dosages. However, higher systemic drug concentrations can lead to widespread toxicity and adverse side effects.[14–17] In contrast, local drug delivery enables sustained therapeutic levels at target sites that are otherwise difficult to reach, thereby minimizing systemic exposure and reducing side effects. Given the anatomical variability of mandibular defects, local precision therapy may be more appropriate than traditional systemic approaches. As a result, there is a growing interest in implant systems integrated with drug delivery functionalities.[4,15,18–24]

Combining anticancer drugs with 3D-printed titanium alloy (Ti6Al4V) implants has been proposed as a promising strategy following surgical resection and perioperative radiotherapy.[24–26] These implants can provide antibacterial, antitumor, and osseointegration benefits while maintaining biocompatibility and minimizing damage to healthy tissues. Therefore, incorporating drug storage tanks within patient-specific 3D-printed reconstruction implants—allowing drug release through the surface lattice—may help maintain localized therapeutic concentrations (Figure 1). This concept also allows for post-surgical drug refilling, offering a potentially viable solution for treating severe mandibular defects in compliance with FDA regulations.

However, integrating drug storage tanks into a patient-specific 3D-printed mandibular reconstruction implant presents two critical challenges. First, anticancer drugs are typically pre-mixed with hydrogel before being loaded into the drug storage tank, from which they are gradually released. The release rate must be carefully controlled to ensure a sustained therapeutic effect, as timing plays a significant role in maintaining drug efficacy.[27] The efficiency of drug diffusion from the tank surface to the surrounding soft tissue is influenced by several key design factors, including the lattice geometry of the tank surface (e.g., lattice type, thickness, and density), as well as the formulation of the drug–hydrogel mixture. Therefore, it is essential to investigate these design parameters within the constraints of the metal 3D printing process. Second, when drug storage tanks are incorporated into mandibular continuity defect reconstruction implants, the number and spatial placement of these tanks may impact the biomechanical stability of the overall structure. Accordingly, a systematic evaluation is required to determine the mechanical implications of integrating drug storage tanks across different anatomical regions of the mandible.

This study aims to identify the optimal parameter combination using the Taguchi method for four variables, including lattice type, lattice thickness, lattice density of the 3D-printed titanium alloy drug storage tank surface, and hydrogel concentration. Drug release experiments were conducted to determine the best combination. The optimized drug storage tank design was then incorporated into patient-specific porcine mandibular reconstruction implants for *in vivo* porcine evaluation, assessing systemic blood safety following local drug release after surgery. Subsequently, finite element (FE) analysis was performed on human reconstruction implants with integrated drug storage tanks, based on three representative large mandibular defect models. In addition, fatigue mechanical tests compliant with FDA guidelines were conducted on the 3D-printed large-scale reconstruction implants to evaluate their structural stability and clinical feasibility.

2. Materials and methods

2.1. Release profile of cisplatin from hydrogel loaded into 3D-printed drug tank

In this study, the selected drug carriers were Pluronic® F-127 (PF127; Sigma-Aldrich, USA) and polyethylene glycol (PEG; average Mn 6000; Sigma-Aldrich, USA), both

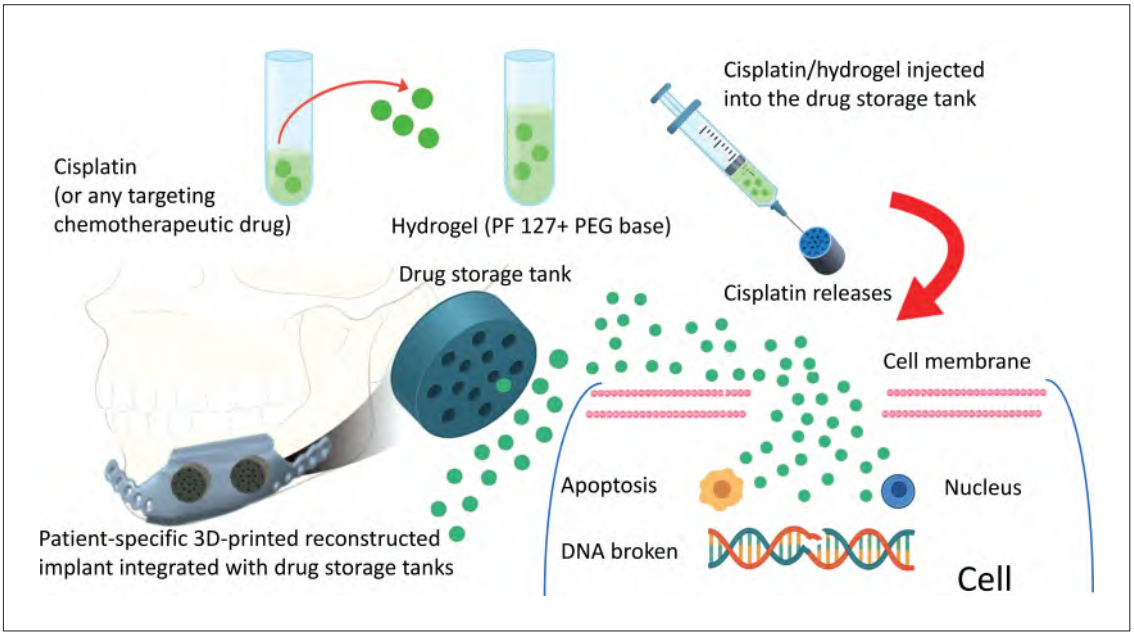


Figure 1. Illustration of the integration of drug storage tanks within patient-specific 3D-printed reconstruction implants for the treatment of severe mandibular defects. Abbreviations: PEG, polyethylene glycol; PF127, Pluronic® F-127

of which are non-toxic, biodegradable hydrogels. PF127 exhibits a temperature-dependent solution–gel transition, making it suitable for drug loading at low temperatures and sustained release under physiological conditions.

Since the molecular weight and concentration of PEG can influence drug release efficiency and gel stability, we first investigated how these parameters affect cisplatin release and the gelation behavior of the hydrogel. Drug release experiments were performed using various combinations of PF127 and PEG containing cisplatin. Cisplatin was dissolved in deionized water, followed by the addition of PF127 and PEG to obtain a final cisplatin concentration of 3 mg/mL.

To fabricate the hydrogels, 30% (w/v) PF127 was mixed with PEG at different concentrations (5%, 7.5%, and 10%) and molecular weights (1000, 3000, and 6000 Da), then stirred continuously at 4 °C until a clear solution was obtained. This resulted in nine different hydrogel formulations. At room temperature, the PF127/PEG solution underwent gelation.

These PF127–PEG composite hydrogels were subsequently loaded into 3D-printed drug reservoirs (diameter: 7 mm; height: 4.5 mm) fabricated using a photopolymerization-based printer (Objet30 Prime, Stratasys Ltd., Israel). The reservoirs featured circular openings and perforated surfaces. The reservoirs were fabricated using MED610™ (Stratasys Ltd., Israel), a biocompatible material suitable for medical applications. Drug release profiles from the various hydrogel formulations were evaluated over 28 days in phosphate-buffered saline (PBS) at 37 °C. On days 3, 7, 14, 21, and 28, the release medium was collected and replaced with 1 mL of fresh PBS to maintain sink conditions. The amount of released cisplatin was then quantified using inductively coupled plasma tandem mass spectrometry (ICP-MS/MS; NexION 2000, PerkinElmer Inc., USA).

2.2. Taguchi experimental design for optimizing drug storage tank parameters and 3D printing fabrication

The drug release behavior and duration are influenced by several design parameters of the storage tank, including the surface lattice pattern (type, thickness, and density) and the hydrogel formulation. To efficiently optimize these parameters, the Taguchi method was employed to minimize the number of experimental groups while identifying the optimal levels of control factors for achieving sustained drug release. This method utilizes an orthogonal array to significantly reduce the total number of required experiments by selecting a representative subset of all possible combinations, thus enabling a balanced comparison of factor levels.[28–31]

Four design factors, each at three levels, were considered to evaluate the drug release profile from a metal 3D-printed drug storage tank with a diameter of 7 mm and a length of 4.5 mm. The factors were the following:

(i) lattice type (hexagon, square, triangle); (ii) lattice thickness (0.5, 1.0, 1.5 mm); (iii) lattice density (40%, 30%, 20%, defined as the percentage of remaining material in the tank's cross-sectional area) (Figure 2A); and (iv) hydrogel formulation (30% PF127 combined with 5%, 3%, or 2.5% PEG of 6000 Da molecular weight) (Table 1). A complete factorial design would require 81 experiments to evaluate all combinations of these factors.[31] However, the Taguchi method requires only nine experiments, as defined by the L9 orthogonal array shown in Table 1.[31] This array consists of nine rows, each representing an experimental run, and four columns corresponding to the four factors, with each entry indicating the selected level of the respective factor.

Nine 3D drug storage tank models were designed using a CAD system (Creo Parametric v6.0, PTC, USA) based on the parameter combinations defined by the Taguchi method (Table 1) and subsequently converted into STL files for additive manufacturing (Figure 2B). Fabrication was performed using a metal 3D printer (A100, BLT Ltd. Co., China) with titanium alloy powder (Ti6Al4V ELI) of particle sizes ranging from 15 to 45 μm. The printing parameters included a laser power of 200 W, a scanning speed of 0.6 m/s, and an exposure time of 125 s. The laser selectively melted the powder to enable layer-by-layer solidification and formation of the components. Both printing resolution and layer thickness were maintained at 30 μm.

Following fabrication, the tanks underwent a post-processing procedure, including deburring and polishing using a magnetic polisher equipped with stainless steel pins (Ø = 1 mm, L = 3 mm) rotating at 2700 rpm. This step was followed by acid etching to eliminate residual sandblasting particles and final cleaning via ultrasonic agitation (Table 1).[4]

2.3. Drug delivery and Taguchi analysis

Cisplatin is one of the most commonly used chemotherapeutic agents for treating mandibular tumors, and its physicochemical properties make it suitable for *in vitro* release studies involving hydrogel and implant systems.[32–34] An *in vitro* release experiment was conducted to evaluate the sustained drug release behavior of the 3D-printed drug storage tank. Each drug storage tank, containing cisplatin-loaded hydrogel, was placed into a separate 2 mL Eppendorf tube containing 1 mL of PBS (pH 7.4). The tubes were incubated at 37°C with continuous shaking at 100 rpm to simulate physiological conditions. At predetermined time points (days 1, 7, and 14), the entire release medium was collected and replaced with fresh PBS to maintain sink conditions.

The concentration of cisplatin in the collected PBS samples was quantified using ICP-MS. Drug release percentages were calculated based on the measured concentration, dilution factor, and the total amount of drug initially loaded.

Nine experimental groups were prepared according to the L9 orthogonal array from the Taguchi design (Table 1), with each group tested in triplicate. The cumulative

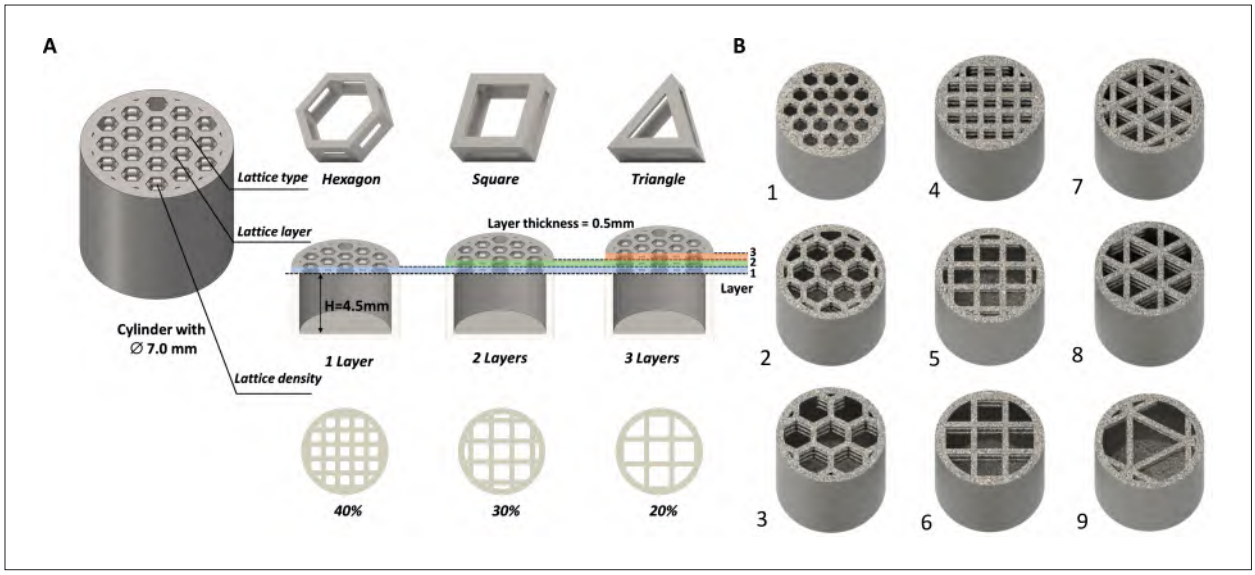


Figure 2. Design parameters and structural models of 3D-printed drug storage tanks. (A) Three design factors of the drug storage tank (7 mm diameter, 4.5 mm length), each at three levels: lattice type (hexagon, square, triangle), lattice thickness (0.5, 1.0, 1.5 mm), and lattice density (40%, 30%, 20%). (B) Nine solid models of the drug storage tank corresponding to **Table 1**.

Table 1. Taguchi L9 orthogonal array showing the four investigated parameters, corresponding drug storage tank features, and cumulative cisplatin release percentages on days 1, 4, and 7

No.	Lattice type	Lattice thickness (layers)	Lattice density	Hydrogel formulation	Tank surface	3D-printed drug storage tank	Cumulative release percentage		
							Day 1	Day 4	Day 7
1	Hex	L1-0.5 mm	D1-40%	C1-30%PF127+5%PEG			85%	95%	97%
2	Hex	L2-1.0 mm	D2-30%	C2-30%PF127+3%PEG			60%	70%	71%
3	Hex	L3-1.5 mm	D3-20%	C3-30%PF127+2.5% PEG			52%	62%	63%
4	Squ	L1-0.5 mm	D2-30%	C3-30%PF127+2.5% PEG			55%	62%	62%
5	Squ	L2-1.0 mm	D3-20%	C1-30%PF127+5%PEG			100%	100%	100%
6	Squ	L3-1.5 mm	D1-40%	C2-30%PF127+3%PEG			53%	65%	67%
7	Tri	L1-0.5 mm	D3-20%	C2-30%PF127+3%PEG			61%	69%	71%
8	Tri	L2-1.0 mm	D1-40%	C3-30%PF127+2.5% PEG			39%	51%	53%
9	Tri	L3-1.5 mm	D2-30%	C1-30%PF127+5%PEG			45%	56%	57%

Abbreviations: Hex, hexagon; PEG, polyethylene glycol; PF127, Pluronic® F-127; Squ, square; Tri, triangle.

drug release profiles served as the response variables for subsequent statistical analysis. Based on the release data, Taguchi analysis was used to determine the influence of each design factor—including lattice type, lattice thickness, lattice density, and hydrogel composition—on the *in vitro* release behavior. The optimal combination of parameters was identified for future functional and safety assessments.

The cumulative drug release percentage at time point t was calculated as follows:

$$\text{Cumulative release (\%)} = (\text{Concentration} \times \text{Dilution factor})/\text{Total drug loaded} \times 100 \quad \text{(I)}$$

To obtain the cumulative percentage at each time point:

$$\text{Cumulative percentage} = P(t-1) + Pt \quad \text{(II)}$$

where Pt = percentage released at time t, and $P(t-1)$ = percentage released prior to time t.

Cumulative cisplatin release percentages were recorded for each of the nine drug storage tank designs at days 1, 7, and 14. The main effects of each factor level on drug release percentage were computed.[28,29] The sum of squares for each design factor was estimated by performing ANOVA (Minitab version 12.23, Minitab, Inc., USA).

2.4. Design and fabrication of mandibular reconstruction implant integrated with drug tanks for porcine models

To evaluate the safety of large-sized mandibular implants integrated with drug storage tanks, six Lanyu miniature porcine (average age: 8 weeks; average weight: 58.37 kg) underwent segmental mandibular reconstruction surgery. Each porcine received a custom-designed implant conforming to its mandibular anatomy, incorporating three centrally positioned drug storage tanks. The porcine were randomly assigned to two groups as follows: in the experimental group (n = 3), the drug storage tanks were filled with cisplatin; in the control group (n = 3), the tanks remained empty, and systemic cisplatin was administered at defined intervals based on body weight. Postoperative physiological monitoring was conducted over a 12-week period, with cisplatin residue levels evaluated at the endpoint.

Before surgery, computed tomography (CT) scans of each pig's mandible were acquired at a slice thickness of 1 mm. These Digital Imaging and Communications in Medicine images were imported into the image processing software (Mimics Innovation Suite, Materialise NV, Belgium) to reconstruct 3D digital models of the mandible. A standardized segmental defect was virtually simulated, extending from the second premolar to the first molar. The osteotomy line and implant fixation sites were defined and transferred into Creo for precise implant and surgical guide design (Figure 3).

The implant design was inspired by soft-tissue preservation principles used in FFS procedures in human mandibular reconstruction.[5] Accordingly, the implant height was set to 50% of the native mandible height (occluso-gingival), and two-thirds of the bucco-lingual dimension at the mesiodistal midpoint, reserving space for future flap coverage. The buccal contour preserved the original anatomical curvature. Structurally, the implant featured a 0.5-mm-thick hollow shell configuration with two lateral "wings" at the mesial and distal ends, each containing three holes for 2.8 mm cortical screws to facilitate rigid fixation (Figure 3).

Three cylindrical drug storage tanks (7 mm diameter, 4.5 mm depth) were integrated at the center of the implant. Each tank was internally structured using a triangular lattice pattern with a layer thickness of 1.5 mm and a density of 30%, as determined through prior Taguchi optimization analysis. Titanium alloy implants were fabricated using the same 3D printer and underwent identical post-processing steps and ultrasonic cleaning (Figure 3).

A custom surgical guide was designed for each implant to ensure accurate intraoperative placement. The guide was offset by 2 mm from the buccal mandibular surface and extended to cover the occlusal surfaces of the teeth to engage the dental arch for enhanced stability. A 2-mm-wide cutting slot was incorporated at the planned resection zone (between the second premolar and first molar) for saw alignment. Additionally, two guide holes were created at the mesial and distal ends to pre-drill screw trajectories for wing fixation. All surgical guides were manufactured using a high-resolution 3D printer with ABS-430 material (U-printer, Stratasys, Israel) (Figure 3).

2.5. Safety evaluation of porcine mandibular reconstruction implants integrated with drug tanks

On the day of surgery, the pigs were fasted for 8 h and sedated via intramuscular injection of a mixed anesthetic (Zoletil, 2.5 mg/kg, Virbac, France; Rompun, 3.33 mg/kg, Bayer, Germany; atropine, 0.033 mg/kg, Taiwan Biotech, Taiwan). General anesthesia was subsequently induced and maintained with 3.0–5.0% isoflurane (Baoling Biotech, Taiwan) delivered through an oxygen-supplemented rebreathing circuit. Throughout the procedure, vital signs—including heart rate, respiratory rate, and oxygen saturation—were continuously monitored to ensure adequate anesthetic depth and physiological stability.

A horizontal skin incision approximately 4–5 cm in length was made below the mandible. The skin and underlying soft tissues were dissected layer-by-layer to

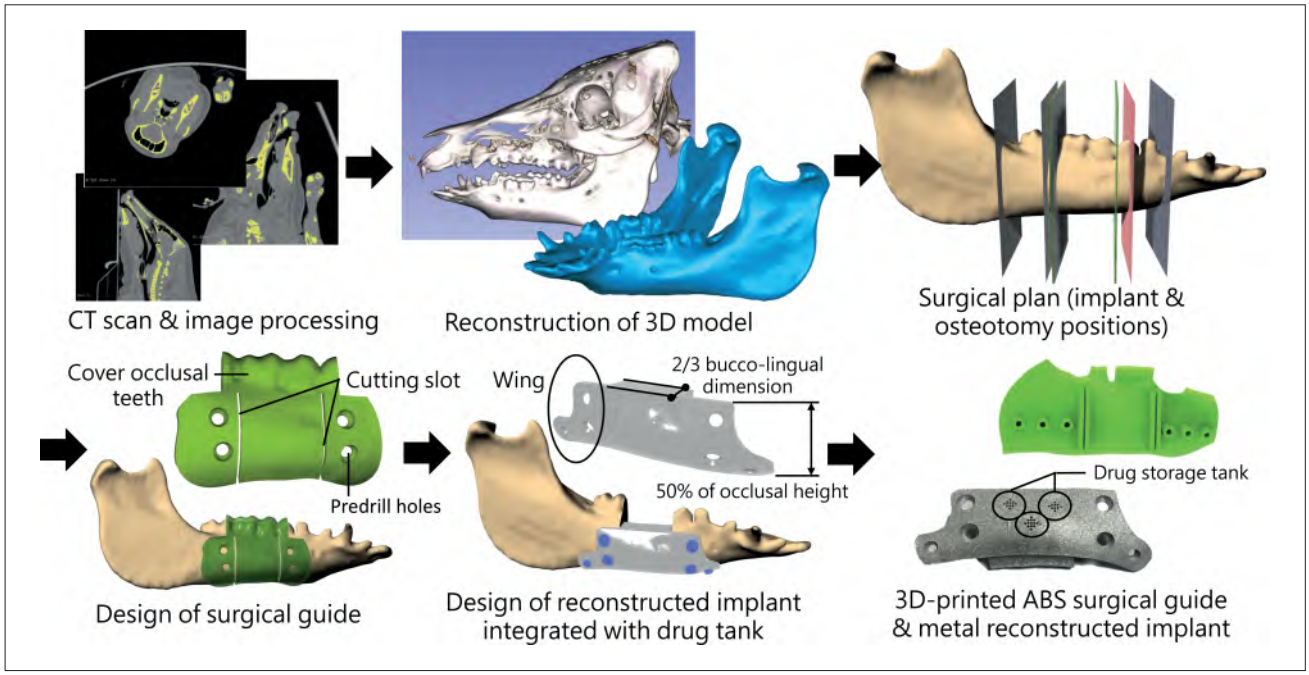


Figure 3. Illustration of the mandibular reconstructed implant and corresponding surgical guide design and manufacturing using 3D printing. Abbreviation: ABS, American Board of Surgery.

expose the mandibular surface. A pre-designed surgical guide was fitted onto the occlusal teeth in the planned resection area to ensure precise positioning. Pre-drilling was performed through the guide's pilot holes, followed by a linear segmental mandibular osteotomy from the second premolar to the first molar using a surgical saw, thereby creating a standardized bone defect model (Figure 4).

The reconstruction implant, integrated with three drug storage tanks and a 3D-printed titanium alloy structure, was custom-designed based on the anatomical morphology of each pig. Prior to implantation, the device underwent ultrasonic cleaning and moist heat sterilization at 121°C for 26 min. The implant was then positioned along the inferior border of the mandible and secured to the residual bone at both ends using 2.8 mm cortical screws through the fixation wings. A cisplatin-loaded hydrogel (2.5 μg/mL of cisplatin; composed of PF127 and PEG) was injected into the surface pores of the drug storage tanks (three units) to achieve localized drug release (Figure 4).

Following implantation, layered wound closure was performed using absorbable sutures (Vicryl 3-0, Ethicon, USA) across the periosteum, muscular layer, and skin. Postoperative analgesia (meloxicam, 0.2 mg/kg, Swiss Pharmaceutical Co., Taiwan) and antibiotic prophylaxis (Enrofloxacin, 5–10 mg/kg, YF Chemical Corporation, Taiwan) were administered subcutaneously for 3 consecutive days to ensure animal welfare. Postoperatively, animals were monitored daily for 90 days (12 weeks) to assess clinical signs, including behavior, appetite, activity level, wound healing, and signs of implant loosening. Body weight was recorded weekly. Blood samples were collected every week to quantify plasma platinum concentrations, reflecting systemic cisplatin exposure. Additionally, biweekly blood biochemistry and hematological analyses (glutamic pyruvic transaminase [GPT], glutamic oxaloacetic transaminase [GOT], white blood cells [WBC], red blood cells, platelets, hemoglobin, blood urea nitrogen [BUN], and creatinine [CRE]) were performed to evaluate systemic toxicity. Lateral mandibular radiographs were taken at week 5 to assess implant position and stability. At week 12, the animals were euthanized, followed by CT imaging to evaluate bone integration and new bone formation.

2.6. Finite element analysis of patient-specific 3D-printed implants integrated with drug tanks

To ensure the mechanical integrity of large mandibular reconstruction implants incorporating drug tanks for human applications, we designed three large-scale mandibular defects based on the worst-case representative mandible, as defined by image reconstruction in a previous study[5], and conducted FE mechanical analyses.

The mandible was divided into three segments—A, B, and C—according to the literature (Figure 5)[5]: Segment A spans from the third molar to the ramus; Segment B spans

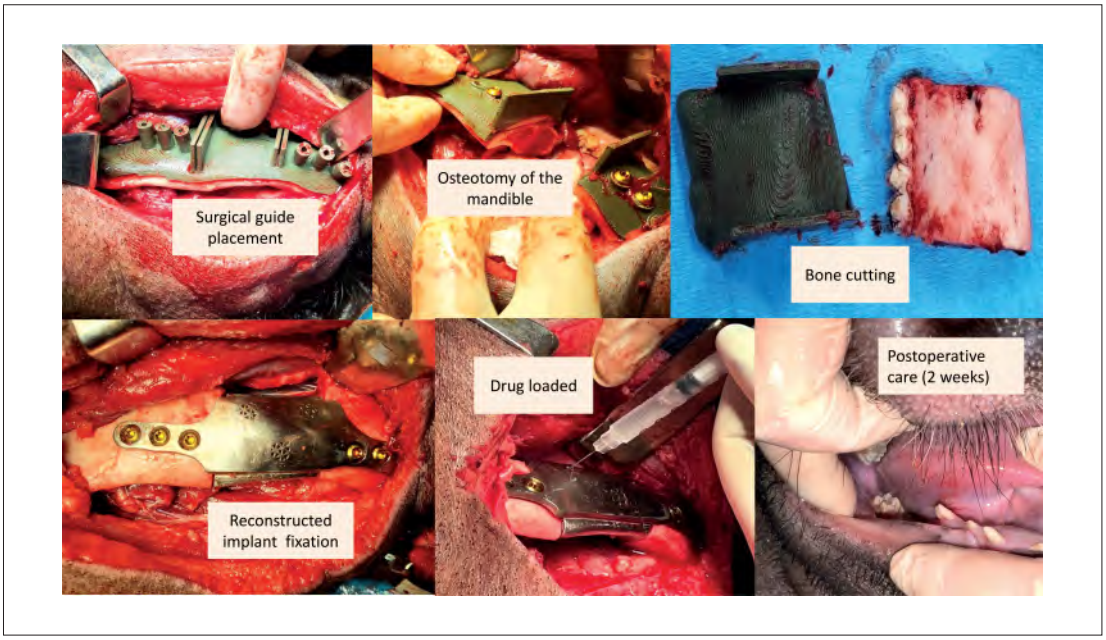


Figure 4. Surgical procedures in pigs, including bone osteotomy using a surgical guide, implant fixation, drug injection, and postoperative care.

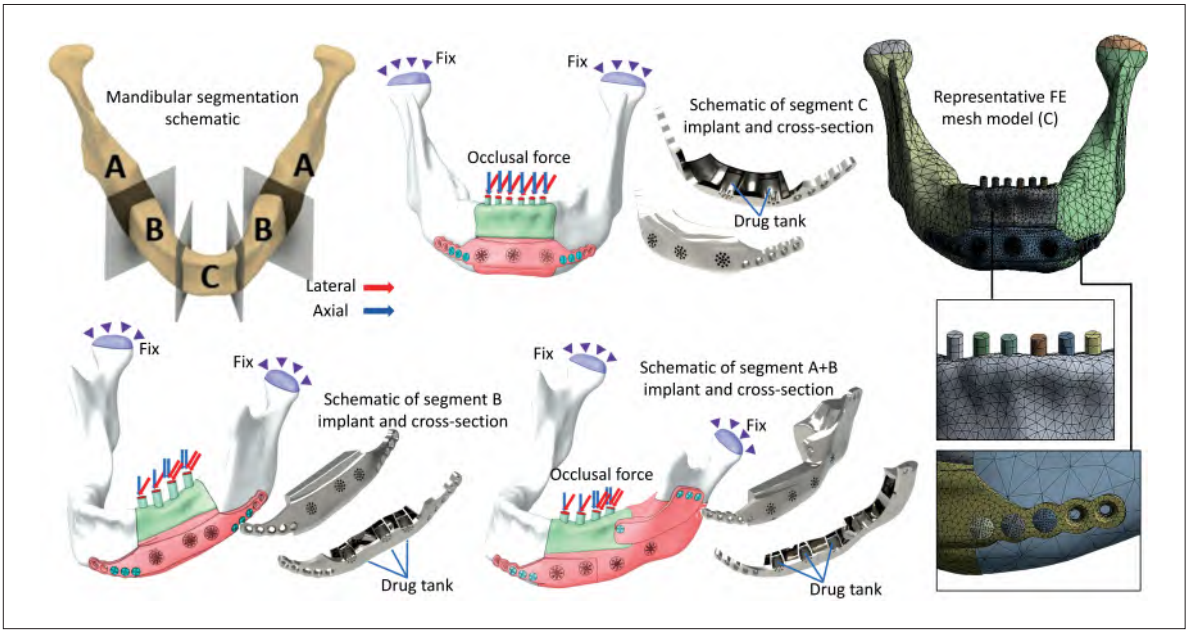


Figure 5. Finite element (FE) models of Segments C, B, and A+B of the mandible, showing loading and boundary conditions, as well as representative mesh patterns.

from the first premolar to the third molar; and Segment C represents a segmental defect from the left to the right canine. Accordingly, the three major mandibular defect zones were defined as Zone C, Zone B, and Zone A+B. The design criteria for the three reconstructed implant models incorporating drug tanks were as follows: (i) the implant shell thickness was set at 0.5 mm; (ii) internal supporting beam structures were designed based on the corresponding occlusal conditions determined through weighted topology optimization for each zone, as previously described[5]; (iii) implant height was set to one-half of the bone segment height, with space reserved at the top for postoperative prosthesis placement, and implant thickness was set to two-thirds of the bone segment thickness to allow

clearance for the flap, vascular pedicle, and soft tissue; (iv) a lateral wing extension with a thickness of 2.8 mm was included in the design, incorporating 3–5 reserved holes for fixation using 2.8 mm bone screws; and (v) a total of three and four drug storage tanks were placed in the B/C and A+B implants, respectively, within the space between the internal supporting beams (Figure 5). All three implant models were constructed using Creo software and imported into the FE package (ANSYS Workbench v19, ANSYS Inc., USA).

Three corresponding FE models of restored mandibular defects were established, each including the remaining mandible, graft bone, and dental implants based on the reconstructed implants (C, B, A+B) with integrated drug storage tanks. The number of elements and nodes for each model is listed in Table 2. To evaluate the mechanical responses, combined axial and lateral loads of 100 N were applied to the teeth, with specific loading conditions defined for each segment.[5] Boundary conditions were applied by fully constraining the nodes at both condyles to prevent movement (Figure 5). The von Mises stress of the reconstructed implants and the maximum principal stress in the remaining bone were calculated and compared to implant models without drug storage tanks.

2.7. Functional testing of patient-specific 3D-printed implants integrated with drug tanks

Three reconstructed implants integrated with drug storage tanks, corresponding to segments C, B, and A+B, were fabricated using the same 3D printer with titanium alloy powder, followed by post-processing and ultrasonic cleaning (Figure 6).

To comprehensively evaluate the mechanical strength of these implants for large mandibular bone defects, four-point bending tests were conducted in accordance with the American Society for Testing and Materials (ASTM) standard F382-17, using an Instron E3000 testing machine (INSTRON, USA). Two additional groups for the same segments were included for comparison as follows: (i) patient-specific reconstructed implants without integrated drug storage tanks, and (ii) traditional straight titanium reconstruction plates, both derived from our previous study.[5]

Static tests were first performed to determine the proof load. Since the reconstructed implants lack a symmetric and sufficiently long straight section, rigid extension segments were used to increase their effective length for mechanical testing. The proximal and distal geometries of these extensions were designed to match the corresponding contact surfaces of each implant and were fabricated using the same 3D printing process. The implants were mounted onto their respective extension segments. The loading rollers were positioned to contact the rigid extensions during testing (Figure 6). The center span (a)—the distance between the two loading rollers—was 100 mm for all samples, while the loading span distance (h)—the distance between a loading roller and the nearest support roller was 35 mm for the C, B, and A+B implants. Each group consisted of three samples subjected to loading at a crosshead rate of 0.05 mm/s until failure.

Fatigue tests for the three reconstructed implant groups were then conducted based on the proof load values obtained from the static tests. These tests employed a sinusoidal cyclic loading waveform at a constant frequency of 5 Hz using the same four-point bending configuration. Testing was terminated when either (i) failure occurred (via crack formation or plastic deformation), or (ii) one million cycles were completed without failure. Three samples were tested under each loading condition, and the corresponding bending moment resistance was recorded for implants that successfully withstood one million cycles.

2.8. Statistical analysis

All analyses were performed using IBM SPSS Statistics 29.0 (IBM, USA). The Kruskal–Wallis H test was used to compare hematological and biochemical parameters,

Table 2. Number of nodes and elements for the three finite element models, along with the material properties of all simulated materials

Model	Node number	Element number	Material	Elastic modulus	Poisson's ratio
C	434,135	281,560	Cortical bone	13,700 MPa	0.3
			Cancellous bone	1,370 MPa	0.3
B	273,641	173,786	Reconstructed implant and fixation screw (Ti6Al4V)	110 GPa	0.35
A+B	981,555	600,418	Bone graft	13,700 MPa	0.3
			Dental implant	110 GPa	0.35

Abbreviations: Ti6Al4V, 3D-printed titanium alloy

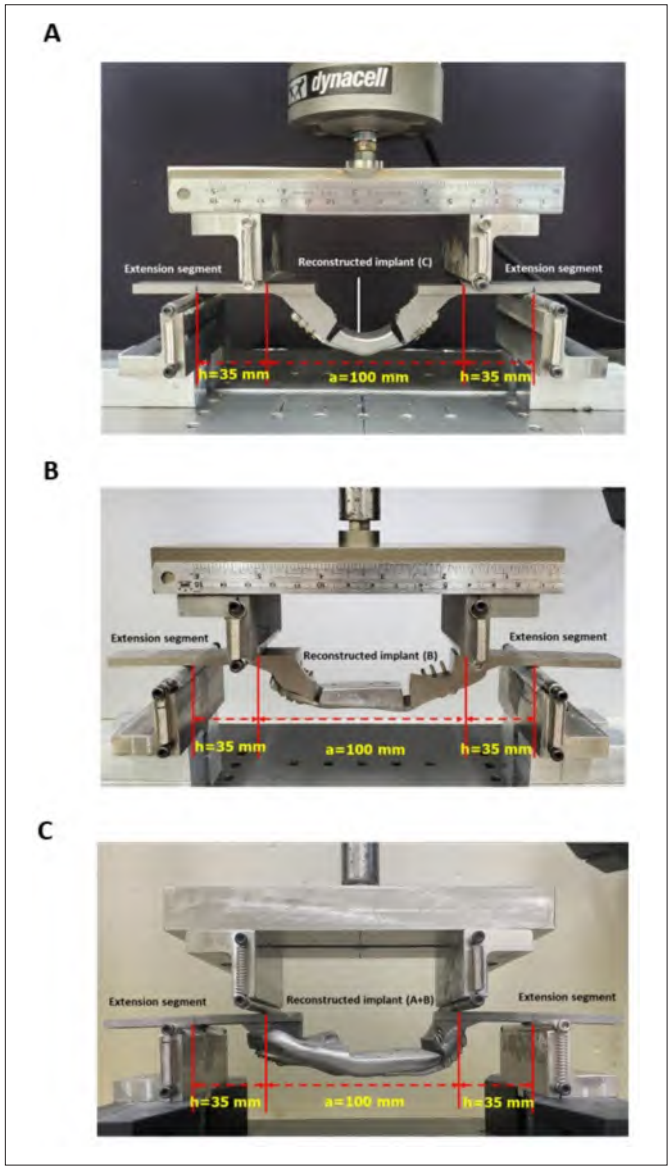


Figure 6. Illustration of the four-point bending tests for (A) Segment C; (B) Segment B, and (C) Segment A+B. Notes: a, center span distance; h, loading span distance.

platinum concentration, and body weight between the local (tank) and systemic (IV therapy) treatment groups at multiple time points (weeks 0, 1, 2, 3, 4, 5, and 9–12). This non-parametric test was selected due to the relatively small sample size in our study. A p-value < 0.05 was considered statistically significant.

3. Results

3.1. Drug release

According to the results of cisplatin drug release experiments, different PEG concentrations and molecular weights significantly affect drug release behavior. The overall trend showed that each sample group entered a rapid release phase within the first 5 days, after which the release rate stabilized. Among them, the group with 5% PEG concentration and a molecular weight of 6000 Da showed the best release efficiency, reaching a cumulative release of approximately 60% by day 7.5 and maintaining this level stably until day 30. This result is likely related to the formation of a moderately porous network structure in this formulation, which facilitates the sustained release of cisplatin molecules (Figure 7).

In contrast, the group with 10% PEG concentration and a molecular weight of 3000 Da demonstrated the lowest

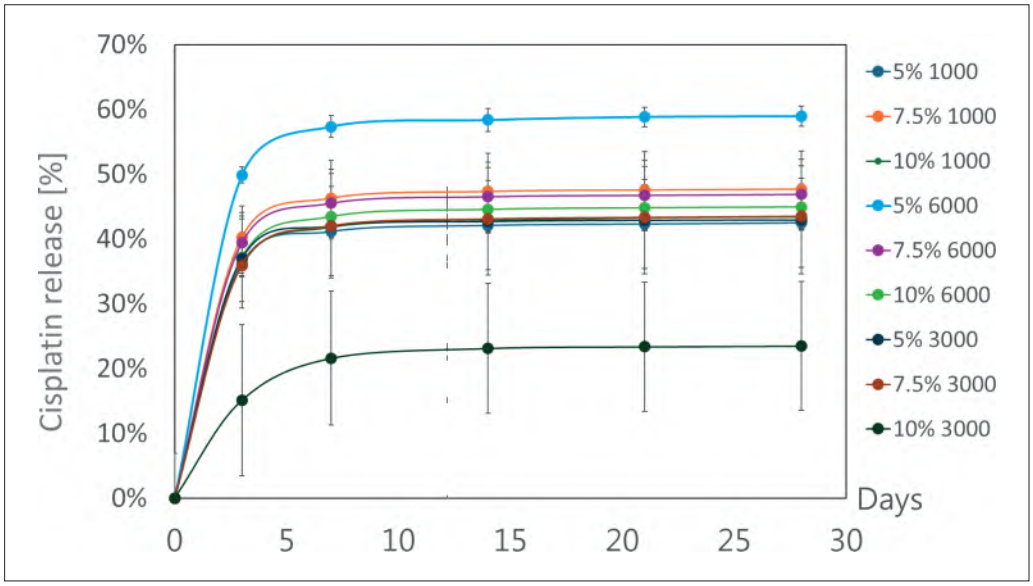


Figure 7. Cisplatin release percentages at days 3, 7, 14, 21, and 28 for different polyethylene glycol concentrations and molecular weight combinations.

release performance, with an overall release rate of only about 20% and a slow release trend. This phenomenon may be attributed to an overly dense hydrogel network formed by the combination of high PEG concentration and medium molecular weight, which inhibits drug diffusion and release.

Overall, when PEG concentration was held constant, the effect of molecular weight on release behavior showed a nonlinear trend. For example, at a 5% concentration, increasing the molecular weight from 1000 to 6000 Da significantly improved release efficiency. However, at higher concentrations (7.5% or 10%), the colloidal structure became overly compact, significantly reducing drug release efficiency (Figure 7).

3.2. Taguchi analysis and factorial percentage contribution

The cumulative cisplatin release percentages at days 1, 7, and 14 are listed in Table 3. A lower drug release percentage at 14 days postoperatively is considered favorable, as it contributes to prolonged and sustained drug delivery. The main effects of lattice type, lattice layer (thickness), lattice density, and hydrogel formulation at each level for days 1, 7, and 14 are shown in Figure 8. The relative importance of each factor is summarized in Table 3. With respect to cumulative cisplatin release at day 14, the hydrogel formulation was the most influential factor (43%), followed by lattice type (22%), lattice density (19%), and lattice thickness (16%) (Table 3). Based on the main-effect plot at day 14 (Figure 8), a triangle lattice, three lattice layers (1.5 mm), and 30% lattice density resulted in the greatest reduction in cisplatin release, making these the optimal parameters for tank surface design. Among the hydrogel formulation tested, the most effective was composed of 30% PF127 and 2.5% PEG (molecular weight 6000 Da).

3.3. Safety evaluation of porcine mandibular reconstruction implant integrated with drug tanks

In the *in vivo* porcine experiment, a total of six pigs underwent reconstructive implant surgery using

Table 3. ANOVA results for the four-factor, three-level fractional factorial design

Day of release	Day 1	Day 4	Day 7
Factor	Sum of squares % contribution (rank)		
Lattice type	24.91% (2)	23.70% (2)	22% (2)
Lattice layer	18.30% (3)	15.89% (4)	16% (4)
Lattice density	16.41% (4)	17.55% (3)	19% (3)
Hydrogel combination	40.38% (1)	42.86% (1)	43% (1)

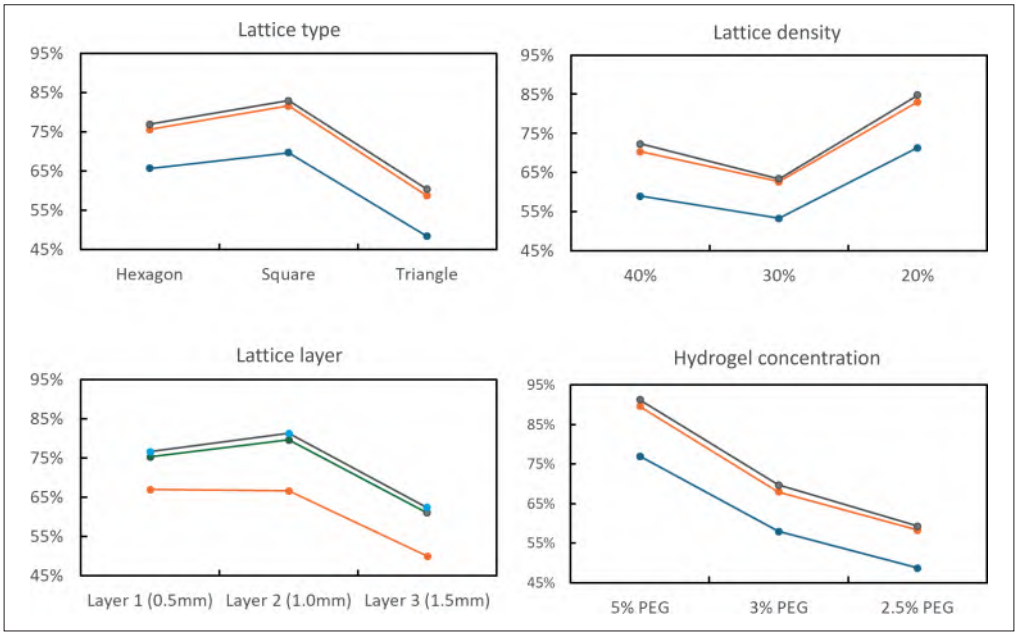


Figure 8. Main effects of lattice type, thickness, and density of the drug tank surface, and hydrogel formulation, at each level for days 1, 7, and 14.

implants integrated with drug storage tanks. Based on X-ray evaluations performed 5 weeks postoperatively, all implants demonstrated satisfactory initial fixation stability, with no signs of overall loosening. However, one implant showed loosening of a single fixation screw (Figure 9).

Regarding systemic physiological responses, the local drug release group exhibited more stable trends in key indicators, including WBC count, liver function markers (GPT, GOT), kidney function markers (BUN, CRE), and body weight, compared to the control group that received intravenous cisplatin. These findings suggest that local administration may offer superior systemic safety (Figure 10).

In vivo analysis of plasma platinum concentration revealed that the local release group consistently maintained significantly lower platinum levels than the intravenous chemotherapy group throughout the 12-week observation period. This indicates that the drug remained largely localized, effectively minimizing systemic exposure. In addition, body weight in the local delivery group remained relatively stable over the 12 weeks, with no significant weight loss observed, further supporting the biocompatibility and systemic safety of this treatment approach (Figure 11).

Postmortem CT imaging and gross examination revealed substantial spontaneous regeneration and osseointegration around the mandibular defect site. According to previous studies, this phenomenon is likely associated with the acute nature of the intrabony defects, which are known to exhibit enhanced spontaneous regenerative and osseointegrative capacities. This finding warrants further investigation in future studies (Figure 12).

3.4. Finite element simulation of human mandibular reconstructed implants

The results of FE analysis showed that the maximum stresses observed in both the implants and the surrounding bone were significantly lower than the failure strengths of their respective materials for the C, B, and A+B segments (Ti6Al4V ≈ 950 MPa; bone ≈ 150 MPa), indicating that the structural designs provided adequate mechanical safety (Figure 13).

In Segment B, the maximum implant stresses were 54.45 and 52.40 MPa for the models without and with drug tanks, respectively, while the corresponding bone stresses were 40.82 and 39.74 MPa—demonstrating minimal differences. A similar trend was observed in Segment A+B, where the integration of drug tanks had a negligible impact on stress distribution (implant stress ≈ 369 MPa; bone stress ≈ 100 MPa). However, in Segment C, the implant stress increased significantly following the integration of drug tanks, rising from 125.05 to 205.42 MPa. This finding suggests that the anterior region is more susceptible to stress concentration, and careful consideration should be given to structural support and load distribution in this area (Figure 13).

In summary, the integration of drug tanks did not introduce additional mechanical stress to the implant

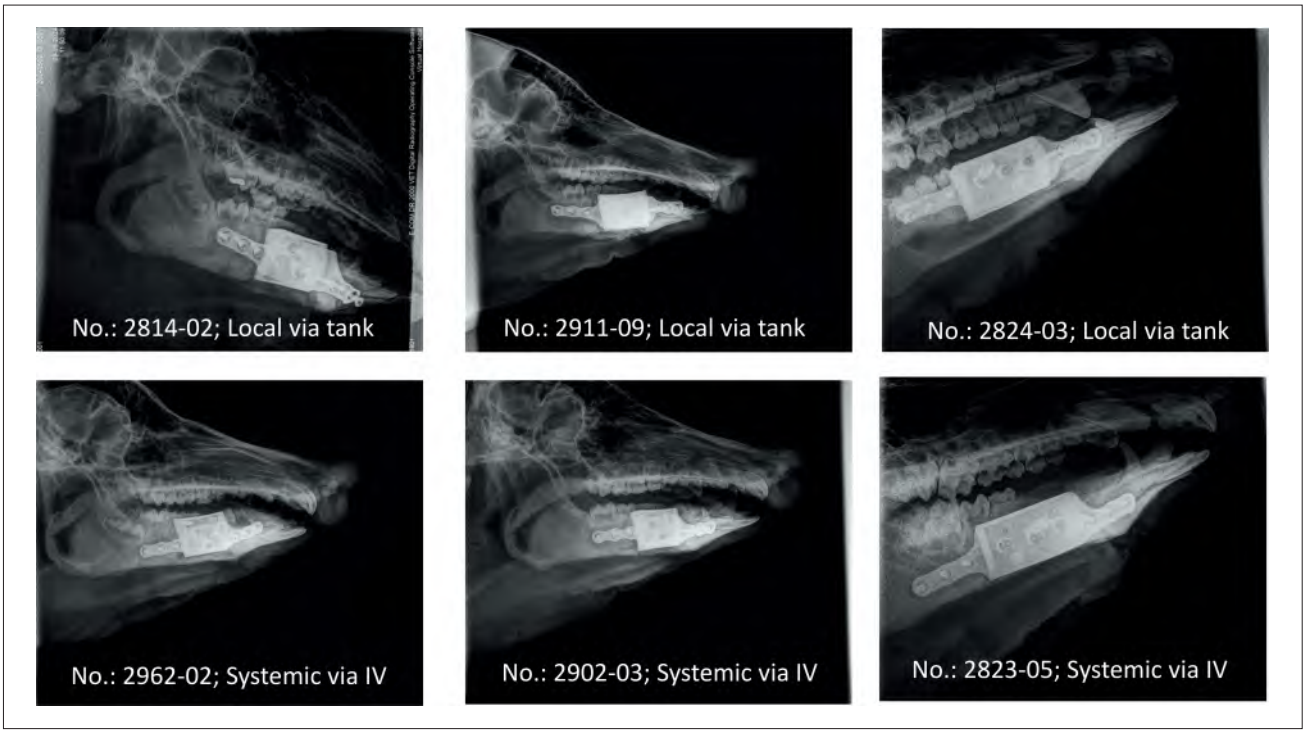


Figure 9. X-ray images of six *in vivo* mandibular reconstruction implants, 5 weeks after surgery. Abbreviation: IV, intravenous.

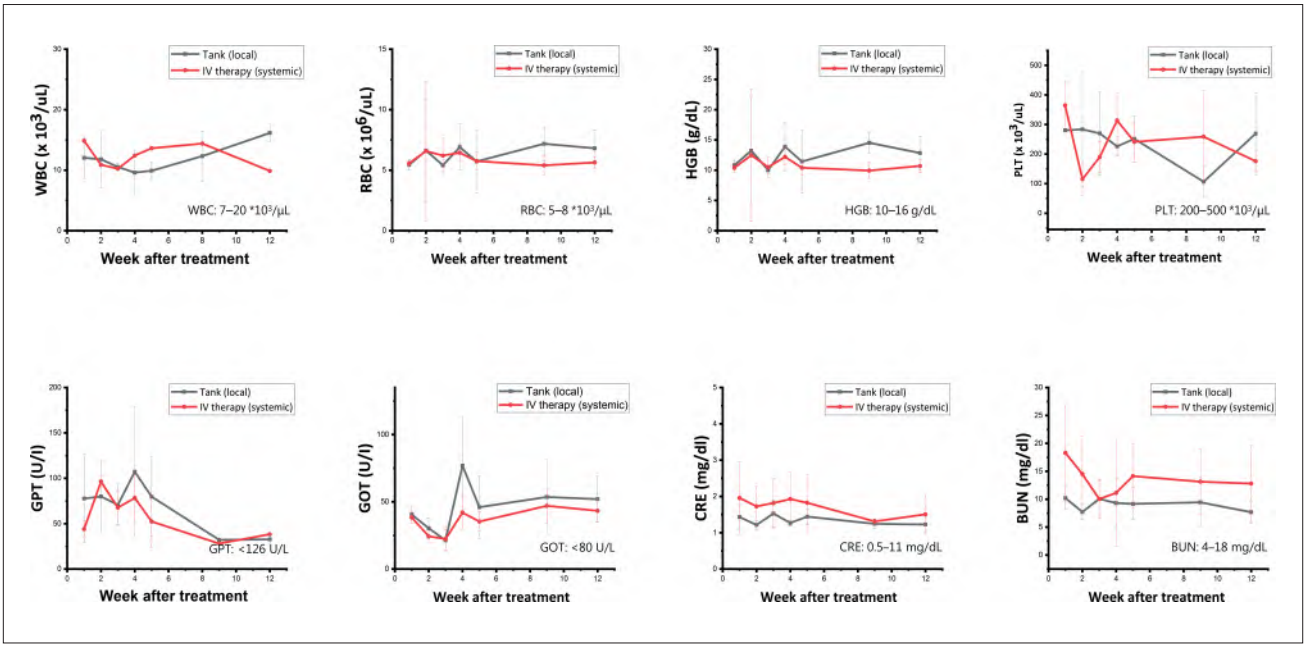


Figure 10. Various blood physiological indicators, including white blood cell (WBC), red blood cell (RBC), hemoglobin (HGB), platelet (PLT), glutamic pyruvic transaminase (GPT), glutamic oxaloacetic transaminase (GOT), creatinine (CRE), and blood urea nitrogen (BUN), used to evaluate systemic toxicity from local drug release versus systemic chemotherapy.

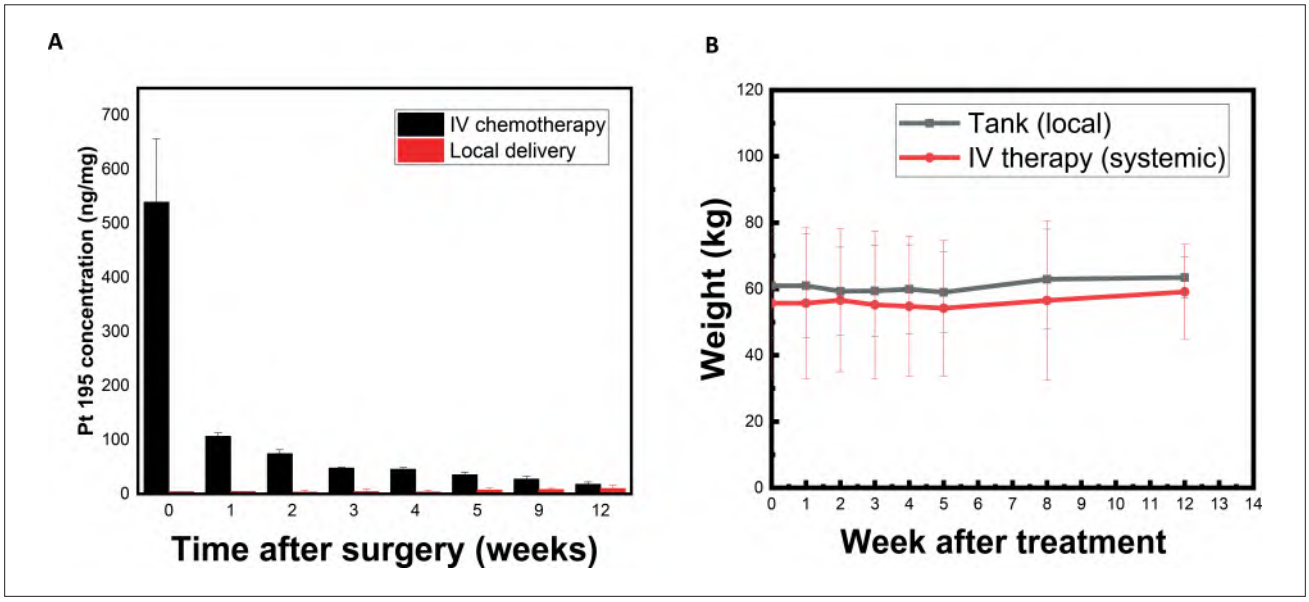


Figure 11. Cisplatin distribution and body weight changes following systemic and local treatment. (A) Platinum (Pt) concentrations and (B) body weight in groups receiving local drug release versus systemic chemotherapy.

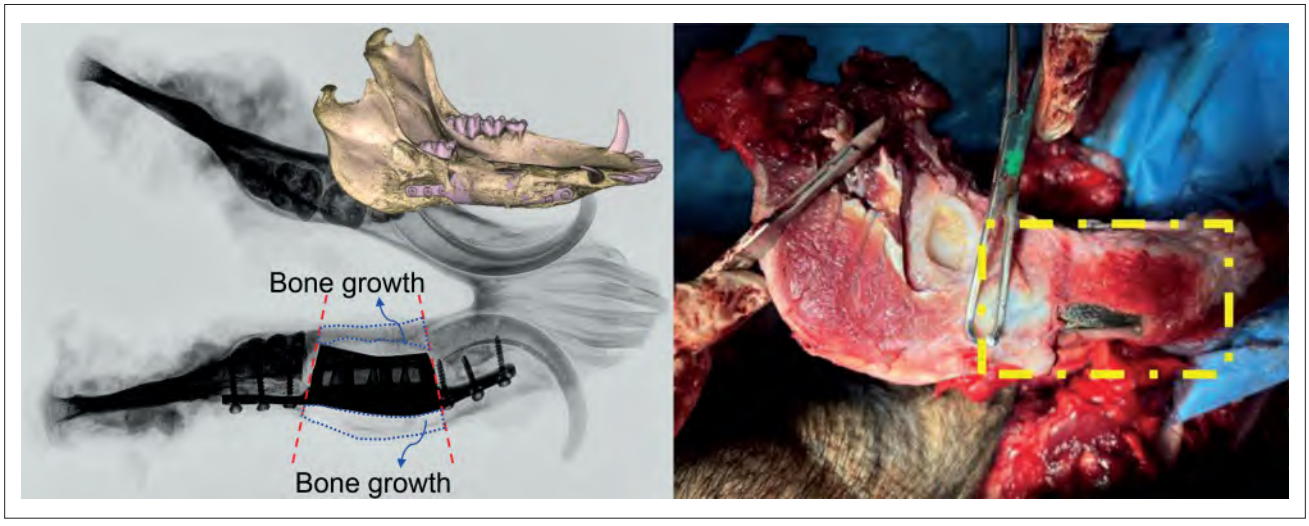
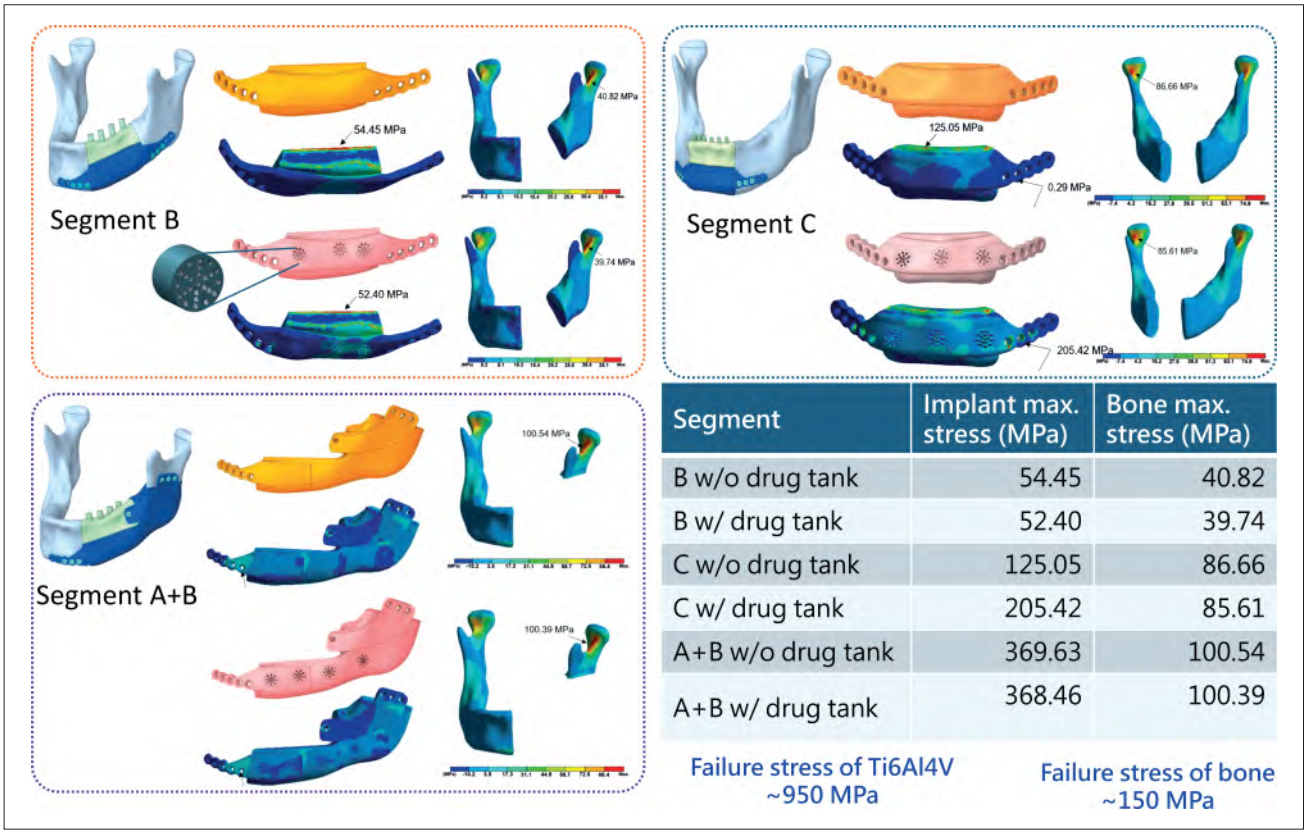


Figure 12. Representative computed tomography image of a pig after euthanasia, showing the outcome of mandibular reconstruction with the implant. A high degree of spontaneous bone regeneration and osseointegration is evident around the defect site.

or bone in most reconstruction scenarios, indicating that this functional implant design offers promising mechanical stability and clinical applicability. Nonetheless, specific anatomical regions such as the anterior segment may require further structural optimization to mitigate potential localized stress concentrations.

3.5. Functional testing of human mandibular reconstructed implants

Figure 14 presents a comparison of the mechanical strengths of the three mandibular reconstruction segment implants under static and dynamic four-point bending tests. As shown in the static failure bending moment results (Figure 14A), the integration of the drug tank had minimal impact on the maximum bending moment in Segments B and C, with only slight differences observed between the two conditions. However, in Segment A+B, the implant with an integrated drug tank exhibited a significantly lower failure bending moment compared to the design without a drug tank, suggesting that the inclusion of the drug tank may slightly reduce the overall structural rigidity in large-scale reconstructions. Nevertheless, all



Segment	Implant max. stress (MPa)	Bone max. stress (MPa)
B w/o drug tank	54.45	40.82
B w/ drug tank	52.40	39.74
C w/o drug tank	125.05	86.66
C w/ drug tank	205.42	85.61
A+B w/o drug tank	369.63	100.54
A+B w/ drug tank	368.46	100.39

Failure stress of Ti6Al4V ~950 MPa

Failure stress of bone ~150 MPa

Figure 13. Finite element analysis results showing stress distribution and locations with maximum (max.) stress values in both the implant and surrounding bone, comparing implants with (w/) and without (w/o) integrated drug storage tanks.

implant groups—regardless of whether they contained a drug tank—demonstrated failure bending moments substantially higher than that of the commercially available reconstruction plate (2192 N·mm), indicating that the new implant designs maintain a sufficient safety margin under static loading conditions.

In the dynamic fatigue test (Figure 14B), the implants with integrated drug tanks in Segments B and A+B showed higher fatigue resistance, with bending moments reaching 3028 and 2625 N·mm, respectively, both exceeding the values of their corresponding non-tank designs. In Segment C, the implant with a drug tank reached 1925 N·mm, slightly lower than the 2148 N·mm recorded for the implant without a drug tank; however, the difference was minimal, and both values surpassed the fatigue strength threshold of the standard reconstruction plate (1863.45 N·mm), meeting clinically acceptable criteria.

These results indicate that integrating drug tanks into the implant design does not compromise mechanical performance under fatigue loading in most reconstruction segments. On the contrary, in some cases, the integrated design may enhance fatigue resistance, highlighting its mechanical reliability and clinical application potential.

4. Discussion

Conventional straight plates or general patient-specific 3D-printed implants for mandibular reconstruction are primarily designed for mechanical stabilization, with limited capacity to support postoperative tumor control or adjunctive therapy. In contrast, the patient-specific 3D-printed implant developed in this study integrates both mechanical support and local drug release within a single construct. The reconstructed implant features a refillable drug tank embedded within the mandible that can be engineered to carry anticancer drug agents and offers a novel, system-integrated approach to the postoperative management of head and neck cancer patients.

Therefore, incorporating drug storage into patient-specific 3D-printed reconstruction implants—with drug release facilitated through the surface lattice—may help sustain localized therapeutic concentrations (Figure 1). Furthermore, this design enables post-surgical drug refilling and presents a viable approach for treating severe

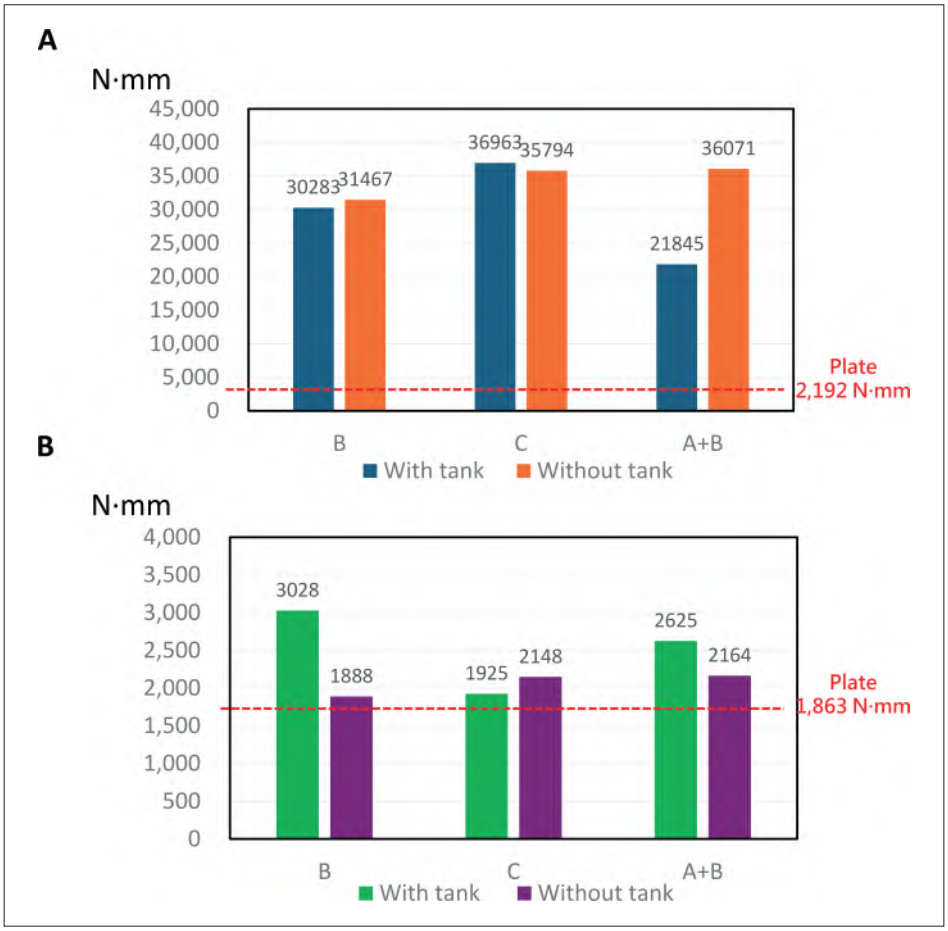


Figure 14. Comparison of the mechanical strengths (bending moment) of the three mandibular reconstruction segment implants under (A) static and (B) dynamic four-point bending tests.

mandibular defects in accordance with FDA regulatory standards, making it an attractive alternative treatment strategy with the potential for clinical translation. The refillable drug tank is designed with an integrated lattice geometry on the tank surface. Using fluoroscopy-guided or CT-guided injections to locate the refill pore allows for percutaneous refilling using a standard syringe and needle under sterile conditions. Similar approaches are already used in implantable drug delivery devices, such as Ommaya reservoirs and intrathecal pumps, demonstrating a precedent in clinical settings.

More importantly, this design is made possible by the geometric freedom and process integration capabilities uniquely offered by 3D printing. This enables the integration of complex geometries such as lattice type, density, and refill channels for the drug storage tank, all of which are extremely challenging or even infeasible with traditional subtractive machining. The implant demonstrates not only structural–functional integration but also the capability for post-surgical intervention and sustained release of anticancer drugs, thereby enhancing its therapeutic utility beyond the initial implantation.

For the drug storage tank design, results from the Taguchi-based parameter optimization identified hydrogel formulation as a key determinant of the cisplatin release rate (influential rate: 40.38–43.20%). In parallel, lattice design parameters—including pattern type, thickness, and density—collectively contributed to 56.80–59.62% of the observed drug release behavior. The optimal configuration—tri-lattice surface, 1.5 mm lattice layer, 30% lattice density, and a 30% PF127 + 2.5% PEG hydrogel—demonstrates a synergistic interplay between structural diffusion constraints and hydrogel composition. Denser and thicker lattice structures introduced physical barriers to drug permeation, effectively reducing the apparent diffusion coefficient and enabling sustained local release, as predicted by classical diffusion theory.

According to the FE analysis results, the integration of the drug tank had a minimal impact on implant stress

and strength, except in Segment C (anterior region). Based on ASTM F382, the four-point bending test is an FDA-recommended specification and test method for evaluating the functional performance of bone plates, including mandibular reconstruction plates. This standard provides a comprehensive reference for defining the geometric and performance characteristics of bone plates. However, it does not prescribe performance thresholds or predict case-specific clinical outcomes due to the lack of sufficient data regarding patient-specific activities of daily living.[35,36] The results of the static four-point bending test confirmed that all implant designs met the baseline safety requirements. Under dynamic fatigue loading, certain implant variants (Segments B and A+B) exhibited superior performance, likely due to optimized internal structural configurations. These findings offer strong engineering validation for the structural integrity and mechanical reliability of the drug-tank-integrated implants. However, the dynamic test results for Segment C showed trends consistent with the FE analysis, suggesting that further design refinement, such as modifying the support beam configuration or incorporating stress-dissipating geometries, may be necessary to enhance load distribution and reduce mechanical risk in this region.

Among various chemotherapeutic agents, cisplatin is primarily used as a first-line treatment for locally advanced or recurrent/metastatic oral squamous cell carcinoma. Based on previous studies, cisplatin has demonstrated superior efficacy compared to other chemotherapeutic agents.[34,37] Therefore, cisplatin was selected as the anticancer drug in this study. In future investigations, additional agents such as carboplatin, 5-fluorouracil, paclitaxel, and docetaxel will also be evaluated.

The interaction between PEG concentration and molecular weight plays a critical role in modulating the microstructure and drug release behavior of PF127-based hydrogels. In this study, varying concentrations of PEG were incorporated into PF127 hydrogels to tailor gel network density and diffusivity. Among the tested formulations, the combination of 30% PF127 with PEG (molecular weight 6000 Da) exhibited the most favorable drug release profile, achieving sustained and controlled cisplatin release over an extended duration. Meanwhile, a notable phenomenon was observed—lower PEG concentrations resulted in more sustained cisplatin release. Therefore, PEG concentrations ≤5% (specifically 5%, 3%, and 2.5%) were selected for subsequent hydrogel formulations. The reduced PEG content likely decreased the hydrophilicity and swelling capacity of the hydrogel matrix due to a lower degree of polymer–water interaction. This contributed to slower gel erosion and delayed cisplatin diffusion, thereby enhancing local drug retention. Additionally, high-molecular-weight PEG (molecular weight 6,000 Da) may act as a structural co-polymer in PF127-based hydrogel.

Importantly, the *in vivo* safety test in porcine demonstrated favorable outcomes—as evidenced by stable blood platinum levels, preserved liver and kidney function, and minimal weight loss. These findings support the biocompatibility and systemic safety of the implant system, indicating strong potential for clinical translation and enabling personalized, precision treatment approaches. However, the clinical application of localized drug delivery systems aimed at reducing systemic toxicity and maintaining therapeutic concentrations in head and neck cancer remains limited by several challenges. The complex anatomy of the head and neck region, variability in surgical margins, and limited accessibility to the residual tumor bed present significant obstacles to the stable placement and long-term retention of drug-eluting implants.[1] In addition, the dynamic local environment—including salivary flow, muscle movement, and inflammatory responses—can affect drug diffusion and decrease retention. As a result, this study did not assess the therapeutic efficacy or local drug concentration at the tumor site in the porcine model. This aspect is currently under investigation, as its evaluation requires addressing multiple layers of biological and technical complexity.

Nevertheless, recent advances in additive manufacturing, biocompatible materials, and personalized implant design have enabled the development of patient-specific drug delivery platforms tailored to individual surgical deficiencies. The combination of refillable drug reservoirs and programmable release profiles further enhances the flexibility of these systems in postoperative management. As local recurrence remains the leading cause of treatment failure in head and neck cancer, site-specific drug delivery is an effective strategy to complement surgical resection and radiation therapy while minimizing systemic toxicity.[38] Future work should focus on validating these platforms in long-term tumor models, optimizing combinatorial payloads, and advancing clinical translation through robust manufacturing and regulatory frameworks.

This study provides a closed-loop development framework involving image-based modeling, CAD, topology optimization, FE analysis, physical prototyping, and experimental testing. The drug tank's lattice geometry and the hydrogel release profile were iteratively optimized through the Taguchi method and data-informed refinement, highlighting the importance of experiment-driven design feedback in advanced biomedical prototyping. Together, this study not only presents a novel implant design but also establishes a quantifiable, optimizable, and scalable

prototype development process, contributing to future applications and clinical translation.

However, this study still has several limitations. For instance, in the porcine safety study, cisplatin release was evaluated *in vitro* by measuring platinum concentration; however, this may not accurately reflect *in vivo* drug behavior, the tumor microenvironment, or the actual inhibitory effects on adjacent tumor cells. Furthermore, critical factors such as the frequency of drug refilling, interactions with physiological conditions, penetration efficiency under tumor-specific environments, and the long-term stability of the drug tank were not assessed and should be systematically addressed in future *in vivo* studies.

Another limitation of this study is that the refilling frequency and clinical feasibility were not validated. After the initial implantation and soft tissue healing, the lattice port would remain palpable and could potentially be image-guided (e.g., ultrasound-assisted or fluoroscopy-guided injection) if necessary, enabling accurate needle placement without the need for surgical re-exposure. However, in real clinical settings, similar subcutaneous ports for chronic administration in cancer patients have been associated with low complication rates when managed with proper aseptic techniques. For example, CT-guided intratumoral cisplatin injection has been reported as a clinically feasible approach with minimal risks. The refilling frequency would depend on the physician's assessment, based on whether local recurrence occurs.[39,40]

5. Conclusion

This study introduces a novel, patient-specific mandibular reconstruction implant with integrated drug-release capability, developed through a closed-loop virtual and physical prototyping workflow. By leveraging image-based modeling, topology optimization, metal 3D printing, and experimental validation, we successfully embedded a refillable drug tank into a structurally optimized titanium implant. The drug release profile was fine-tuned via hydrogel formulation (PF127 + PEG) and lattice design using Taguchi parameter optimization. FE analysis and mechanical testing confirmed structural integrity, while *in vivo* porcine studies demonstrated systemic safety and biocompatibility. Although challenges remain regarding intratumoral drug diffusion and long-term refillability, our findings underscore the potential of combining mechanical support and localized chemotherapy in a single implant system. This integrated approach opens new avenues for functional, patient-specific implants in head and neck cancer treatment and lays the groundwork for future clinical translation.

Acknowledgments

The authors would like to thank Anji Company for providing 3D printing services.

Funding

This study was supported in part by the National Science and Technology Council project (project no.: 113-2327-B-A49-001), Taiwan.

Conflict of interest

No potential conflict of interest was reported by the authors.

Author contributions

Conceptualization: Chiao-Min Chang, Chun-Li Lin
Methodology: Chiao-Min Chang, Tzu-Huan Huang, Hsuan-Wen Wang, Lu-Yi Yu, Shao-Fu Huang
Writing—original draft preparation: Chun-Liang Lo
Writing—reviewing and editing: Chun-Li Lin

Ethics approval and consent to participate

All animal procedures were approved by the Institutional Animal Care and Use Committee (IACUC) of Master Laboratory Co., Ltd., New Taipei City, Taiwan (Approval No.: 24T10-0203). The approval was granted on February 16, 2024.

Consent for publication

Not applicable.

Availability of data

The data supporting the findings of this study are available from the corresponding author upon reasonable request.

Reference

1. Li CH, Wu CH, Lin CL. Design of a patient-specific mandible reconstruction implant with dental prosthesis for metal 3D printing using integrated weighted topology optimization and finite element analysis. *J Mech Behav Biomed Mater*. 2020;105:103700.
doi: 10.1016/j.jmbbm.2020.103700

2. Lee SW, Kim HG, Ham MJ, *et al*. Custom implant for reconstruction of mandibular continuity defect. *J Oral Maxillofac Surg*. 2018;76(6):1370-1376.
doi: 10.1016/j.joms.2017.12.003

3. Patel A, Harrison P, Cheng A, *et al*. Fibular reconstruction of the maxilla and mandible with immediate implant-supported prosthetic rehabilitation: jaw in a day. *Oral Maxillofac Surg Clin North Am*. 2019;31(3):369-386.
doi: 10.1016/j.coms.2019.03.002

4. Toure G, Gouet E. Use of a 3-dimensional custom-made porous titanium prosthesis for mandibular body reconstruction with prosthetic dental rehabilitation and lipofilling. *J Oral Maxillofac Surg.* 2019;77(6):1305-1313. doi: 10.1016/j.coms.2018.12.026

5. Lin CL, Wang YT, Chang CM, *et al*. Design criteria for patient-specific mandibular continuity defect reconstructed implant with lightweight structure using weighted topology optimization and validated with biomechanical fatigue testing. *Int J Bioprint*. 2022;8(1):437. doi: 10.18063/ijb.v8i1.437

6. Kumar BP, Venkatesh V, Kumar KA, *et al*. Mandibular reconstruction: overview. *J Maxillofac Oral Surg.* 2016;15(4):425-441. doi: 10.1007/s12663-015-0766-5

7. Wang B, Zhang S, Yue K, *et al*. The recurrence and survival of oral squamous cell carcinoma: a report of 275 cases. *Chin J Cancer.* 2013;32(11):614-618. doi: 10.5732/cjc.012.10219

8. Pinheiro M, Alves JL. The feasibility of a custom-made endoprosthesis in mandibular reconstruction: implant design and finite element analysis. *J Craniomaxillofac Surg.* 2015;43(10):2116-2128. doi: 10.1016/j.jcms.2015.10.004

9. Stoor P, Suomalainen A, Mesimaki K, *et al*. Rapid prototyped patient specific guiding implants in critical mandibular reconstruction. *J Craniomaxillofac Surg.* 2017;45(1):63-70. doi: 10.1016/j.jcms.2016.10.021

10. Yusa K, Yamanouchi H, Yoshida Y, *et al*. Evaluation of quality of life and masticatory function in patients treated with mandibular reconstruction followed by occlusal rehabilitation with dental implants: a preliminary report. *J Oral Maxillofac Surg Med Pathol***.** 2017;29(6):499-503. doi: 10.1016/j.ajoms.2017.06.004

11. Cheng K, Liu Y, Yao C, *et al*. A personalized mandibular implant with supporting and porous structures designed with topology optimization – a case study of canine. *Rapid Prototyping J.* 2019;25(2):417-426. doi: 10.1108/rpj-11-2017-0231

12. Chen CF, Chen CM, Chen HS, *et al*. The use of customized three-dimensionally printed mandible prostheses with a pressure-reducing device: a finite element analysis in different chewing positions, biomechanical testing, and *in vivo* animal study using lanyu pigs. *Biomed Res Int.* 2022;2022:9880454. doi: 10.1155/2022/9880454

13. Chen CF, Chen CM, Huang WC, *et al*. The use of customized 3D-printed mandibular prostheses with pressure-reducing device: a clinical trial. *Head Neck*. 2024;46(7):1614-1624. doi: 10.1002/hed.27660

14. Domsta V, Seidlitz A. 3D-printing of drug-eluting implants: an overview of the current developments described in the literature. *Molecules.* 2021;26(13):4066. doi: 10.3390/molecules26134066

15. Chen C, Chen J, Luo T, *et al*. Late toxicities, failure patterns, local tumor control, and survival of esophageal squamous cell carcinoma patients after chemoradiotherapy with a simultaneous integrated boost: a 5-year phase II study. *Front Oncol.* 2021;11:738936. doi: 10.3389/fonc.2021.738936

16. Lang K, Held T, Meixner E, *et al*. Frequency of osteoradionecrosis of the lower jaw after radiotherapy of oral cancer patients correlated with dosimetric parameters and other risk factors. *Head Face Med.* 2022;18(1):7. doi: 10.1186/s13005-022-00311-8

17. Muzumder S, Srikantia N, Udayashankar AH, *et al*. Late toxicities in locally advanced head and neck squamous cell carcinoma treated with intensity modulated radiation therapy. *Radiat Oncol J*. 2021;39(3):184-192. doi: 10.3857/roj.2020.00913

18. Ma X, Gao Y, Zhao D, *et al*. Titanium implants and local drug delivery systems become mutual promoters in orthopedic clinics. *Nanomaterials (Basel).* 2021;12(1):47. doi: 10.3390/nano12010047

19. Kong X, Feng M, Wu L, *et al*. Biodegradable gemcitabine-loaded microdevice with sustained local drug delivery and improved tumor recurrence inhibition abilities for postoperative pancreatic tumor treatment. *Drug Deliv.* 2022;29(1):1595-1607. doi: 10.1080/10717544.2022.2075984

20. Yang N, Chen H, Han H, *et al*. 3D printing and coating to fabricate a hollow bullet-shaped implant with porous surface for controlled cytoxan release. *Int J Pharm.* 2018;552(1-2):91-98. doi: 10.1016/ijpharm.2018.09.042

21. Yang G, Liu H, Li A, *et al*. Antibacterial structure design of porous Ti6Al4V by 3D printing and anodic oxidation. *Materials (Basel).* 2023;16(15):5206. doi: 10.3390/ma16155206

22. Park YS, Cho JY, Lee SJ, *et al*. Modified titanium implant as a gateway to the human body: the implant mediated drug delivery system. *Biomed Res Int*. 2014;2014:801358. doi: 10.1155/2014/801358

23. Fayazfar H, Salarian M, Rogalsky A, *et al*. A critical review of powder-based additive manufacturing of ferrous alloys: process parameters, microstructure and mechanical properties. *Mater Design.* 2018;144:98-128. doi: 10.1016/j.matdes.2018.02.018

24. Fan D, Zhang C, Wang H, *et al*. Fabrication of a composite 3D-printed titanium alloy combined with controlled in situ drug release to prevent osteosarcoma recurrence. *Mater Today Bio*. 2023;20:100683. doi: 10.1016/j.mtbio.2023.100683

25. Li R, Ting YH, Youssef SH, *et al*. Three-dimensional printing for cancer applications: research landscape and technologies. *Pharmaceuticals (Basel)*. 2021;14(8):787. doi: 10.3390/ph14080787

26. Belz JE, Kumar R, Baldwin P, *et al*. Sustained release talazoparib implants for localized treatment of BRCA1-deficient breast cancer. *Theranostics*. 2017;7(17):4340-4349. doi: 10.7150/thno.18563

27. Adepu S, Ramakrishna S. Controlled drug delivery systems: current status and future directions. *Molecules*. 2021;26(19):302. doi: 10.3390/pharmaceutics11070302

28. Lee WC, Zhang M. Design of monolimb using finite element modelling and statistics-based Taguchi method. *Clin Biomech (Bristol)*. 2005;20(7):759-766. doi: 10.1016/j.clinbiomech.2005.03.015

29. Huang S-F, Lo L-J, Lin C-L. Factorial analysis of variables influencing mechanical characteristics in Le Fort I osteotomy using FEA and statistics-based Taguchi method. *J Med Biol Eng*. 2016;36(4):495-505. doi: 10.1007/s40846-016-0157-5

30. Maazinejad B, Mohammadnia O, Ali GAM, *et al*. Taguchi L9 (34) orthogonal array study based on methylene blue removal by single-walled carbon nanotubes-amine: adsorption optimization using the experimental design method, kinetics, equilibrium and thermodynamics. *J Mol Liq*. 2020;298:112001. doi: 10.1016/j.molliq.2019.112001

31. Lin CL, Chang SH, Chang WJ, *et al*. Factorial analysis of variables influencing mechanical characteristics of a single tooth implant placed in the maxilla using finite element analysis and the statistics-based Taguchi method. *Eur J Oral Sci*. 2007;115(5):408-416. doi: 10.1111/j.1600-0722.2007.00473.x

32. Zhuang B, Chen T, Xiao Z, *et al*. Drug-loaded implantable surgical cavity-adaptive hydrogels for prevention of local tumor recurrence. *Int J Pharm*. 2020;577:119048. doi: 10.1016/j.ijpharm.2020.119048

33. Jing Z, Ni R, Wang J, *et al*. Practical strategy to construct anti-osteosarcoma bone substitutes by loading cisplatin into 3D-printed titanium alloy implants using a thermosensitive hydrogel. *Bioact Mater*. 2021;6(12): 4542-4557. doi: 10.1016/j.bioactmat.2021.05.007

34. Madhulaxmi M, Iyer K, Periasamy R, *et al*. Role of cisplatin in oral squamous cell carcinoma—a review. *J Adv Pharm Educ Res*. 2017;7:39–42.

35. U.S. Food and Drug Administration. Orthopedic Non-Spinal Bone Plates, Screws, and Washers – Premarket Notification (510(k)) Submissions: Guidance for Industry and FDA Staff. Silver Spring (MD): FDA; 2024. Available from: https://www.fda.gov/media/177663/download

36. Qin M, Liu Y, Wang L, *et al*. Design and optimization of the fixing plate for customized mandible implants. *J Craniomaxillofac Surg*. 2015;43(7):1296-1302. doi: 10.1016/j.jcms.2015.06.003

37. Ono K, Sato K, Nakamura T, *et al*. Reproduction of the antitumor effect of cisplatin and cetuximab using a three-dimensional spheroid model in oral cancer. *Int J Med Sci*. 2022;19(8):1320-1333. doi: 10.7150/ijms.74109

38. Meng F, Yin Z, Ren X. *et al*. Construction of local drug delivery system on titanium-based implants to improve osseointegration. *Pharmaceutics*. 2022;14(5):1069. doi: 10.3390/pharmaceutics14051069

39. Mittal L, Kalra M, Mahajan A. Study of feasibility and acceptability of subcutaneous implantable ports (SIPs) in cancer patients. *Indian J Pediatr*. 2012;79(12):1601-1604. doi: 10.1007/s12098-012-0711-2

40. Vogl TJ, Engelmann K, Mack MG, *et al*. CT-guided intratumoural administration of cisplatin/epinephrine gel for treatment of malignant liver tumours. *Br J Cancer*. 2002;86(4):524-529. doi: 10.1038/sj.bjc.6600116

ACCSCIENCE PUBLISHING

International Journal of Bioprinting

CASE STUDY

Customized 3D-printed prosthesis for reconstruction of complex bilateral traumatic knee bone defects: A case report

Gang Zhao[1], Yongqiang Zhang[1], Longfei Liu[1], Longxin An[2], Futian Zhang[1], Da Huo[1], Xuecheng Sun[1], Xiaoming Yang[1]*, and Naibo Feng[1]*

[1]Department of Trauma Orthopedics, Weifang People's Hospital, Shandong Second Medical University, Weifang, Shandong, China

[2]Clinical Medical College, Shandong Second Medical University, Weifang, Shandong, China

(This article belongs to the *Special Issue*: *Multifunctional Bioprinting for Tissue/Organ Engineering*)

Abstract

Composite knee tissue defects involving bone, meniscus, and ligaments caused by high-energy trauma are rare and present significant reconstructive challenges. Herein, we report a case of a 50-year-old woman with bilateral asymmetric knee injuries arising from a traffic accident, including right medial femoral condyle loss with medial collateral ligament (MCL) deficiency, and complex defect involving left-sided bone, meniscus, and MCL, accompanied by degloving injury involving 20% total body surface area. Treatment was performed in the following three stages: debridement, soft tissue coverage, and final reconstruction using data-driven mirror modeling to design patient-specific 3D-printed titanium implants. The right MCL was reconstructed using a LARS artificial ligament. At 12-month follow-up, stable bone–implant integration, flap viability, and functional recovery were observed, with knee flexion of 120° (left) and 80° (right), and Knee Society Scores of 65 and 70. This case highlights the feasibility of personalized 3D-printed implants in complex bilateral knee reconstruction.

Keywords: 3D printing; Knee bone defect; LARS ligament; Medial collateral ligament; Perforator flap

***Corresponding authors:**
Xiaoming Yang
(fristxinmeng@126.com)

Naibo Feng
(Fengnaibo@sdsmu.edu.cn)

Citation: Zhao G, Zhang Y, Liu L, *et al*. Customized 3D-printed prosthesis for reconstruction of complex bilateral traumatic knee defects: A case report. *Int J Bioprint*. 2025;11(5):451-459. doi: 10.36922/IJB025290292

Received: July 17, 2025
Revised: August 7, 2025
Accepted: August 8, 2025
Published Online: August 8, 2025

Copyright: © 2025 Author(s). This is an Open Access article distributed under the terms of the Creative Commons Attribution License, permitting distribution, and reproduction in any medium, provided the original work is properly cited.

Publisher's Note: AccScience Publishing remains neutral with regard to jurisdictional claims in published maps and institutional affiliations.

1. Background

Composite tissue defects of the knee involving the skin, bone, and ligaments represent a severe form of injury that can result in permanent lower limb dysfunction. The management of such injuries remains a significant challenge for orthopedic surgeons. Arthrodesis can address irreparable instability, inadequate soft tissue coverage, and recurrent failure following multiple revisions of joint arthroplasty.[1,2] However, in cases with extensive bone loss at the distal femur and/or proximal tibia, acute limb shortening and compromised vascular integrity caused by altered anatomical alignment may severely impact the patient's quality of life. Therefore, more advanced reconstructive strategies are required to manage these complex injuries.[3]

In the present case, the patient sustained large bilateral knee defects involving both osseous and soft tissue structures. We developed an innovative treatment strategy leveraging recent advancements in 3D printing technology. Using computer modeling and data-driven design, we fabricated customized titanium implants even in the absence of complete CT imaging, and simultaneously reconstructed the medial collateral ligament (MCL) using a LARS synthetic ligament. This approach aimed to restore anatomical integrity, improve functional outcomes, and enhance long-term durability. This case provides new insights into personalized orthopedic solutions for managing complex open knee injuries with extensive bone defect.

2. Case presentation

A 50-year-old female sustained bilateral open knee bone defects accompanied by hemorrhagic shock after being dragged by a motor vehicle during a traffic accident. Radiographic examination revealed a partial defect of the right medial femoral condyle measuring 3.2 × 2.8 cm^2, and a full-thickness defect of the left tibial plateau and femoral condyle measuring 4.5 × 3.6 cm^2. The total area of skin avulsion reached approximately 20% of the body surface area. The patient had no significant past medical history.

On physical examination, the left lower limb showed extensive injury. The anterior knee presented with lacerations, while large areas of skin were lost from the anterior and medial thigh, medial knee, and medial lower leg, involving approximately 4% of the total body surface area. Partial muscle loss was observed in the distal portions of the vastus medialis, hamstrings, and sartorius. There was extensive osseoligamentous loss, affecting the medial femoral condyle, medial tibial plateau, and medial collateral ligament. Distal perfusion was preserved. Additional skin defects were noted at the medial heel and the medial aspect of the first metatarsophalangeal joint (Figure 1A–D). On the right side, there was approximately 3% skin loss involving the medial knee and anterior thigh. The distal vastus medialis was partially missing, and the bone defect involved the medial femoral condyle with associated loss of the medial collateral ligament (Figure 1E). Vascular supply to the distal limb remained intact. Bilateral radiographs confirmed bone defects of both knees (Figure 1F).

2.1. Stage 1: Emergency radical debridement

Under general anesthesia with endotracheal intubation, the patient underwent thorough wound exploration and radical debridement. A "carpet rolling" technique was utilized to remove all contaminated and necrotic soft tissue, as well as devitalized bone fragments, preparing the wounds for subsequent flap coverage and prosthetic reconstruction. Intraoperative findings on the left side revealed complete loss of the medial femoral condyle and medial tibial plateau, while both the anterior and posterior cruciate ligaments remained intact (Figure 2A). On the right side, there was a partial defect of the medial femoral condyle involving the articular surface, along with the absence of the medial collateral ligament (Figure 2B). Following debridement, the wounds were covered with VAC® polyurethane foam dressings (Figure 2C and D).

Once the patient's condition stabilized, a second debridement was performed to remove necrotic subcutaneous tissue and contaminated bone. The bone defects were temporarily filled with polymethyl methacrylate (PMMA) cement, and local skin was mobilized to reduce wound dimensions and minimize exudate (Figure 2E and F). The left lower limb was additionally stabilized with an external fixation brace (Figure 2E). VAC® dressings were reapplied to maintain wound management.

2.2. Stage 2: Flap coverage of the wounds

After emergency debridement and stabilization, early flap coverage was initiated. A 22 × 14 cm^2 left deep inferior epigastric perforator (DIEP) flap was used to cover the right medial knee defect (Figure 3A–C). Microvascular anastomosis was performed between the deep inferior epigastric vessels and the descending branch of the lateral circumflex femoral artery and veins. Sensory nerve coaptation involved intercostal nerve branches and branches of the lateral femoral cutaneous or femoral nerve (Figure 3D).

One week later, after flap stabilization, a 30 × 10 cm^2 latissimus dorsi musculocutaneous flap was used to cover the left knee defect (Figure 3E–G). Anastomosis was performed between the thoracodorsal vessels and the same recipient vessels, with sensory coaptation between thoracodorsal nerve branches and femoral cutaneous nerves. Both flaps survived without complications. Throughout the treatment course, physical therapists guided early mobilization and rehabilitation (Figure 3H and I).

2.3. Stage 3: 3D-printed prosthesis design, implantation, and knee function reconstruction

The third stage involved reconstructing the knee bone defects using data-driven modeling to restore the right medial femoral condyle (Figure 4A–E; Video S1). The left femoral condyle and tibial plateau were reconstructed by



Figure 1. External wounds and radiographic evidence of bone defects. (A–D) Traumatic injuries of the patient's left lower limb, showing extensive soft tissue and skin loss around the knee, thigh, and lower leg. (E) Soft tissue defect over the medial aspect of the right knee and anterior thigh. (F) X-ray images showing bone defects of both knees.

mirroring the anatomy of the reconstructed right knee (Figure 4F–N). A dual-tunnel channel was designed on the tibial side for MCL reconstruction using a LARS synthetic ligament (Figure 4J; Video S2). The 3D-printed prostheses were implanted 6 weeks after flap repair. During this interval, we closely monitored complete blood count, C-reactive protein, and erythrocyte sedimentation rate, proceeding with surgery once all infection-related markers normalized. Postoperative radiographs confirmed accurate prosthesis placement (Figure 5A–D) and proper restoration of lower limb alignment (Figure 5E).

2.4. Follow-up

At the 3-month follow-up, there were no signs of infection or flap necrosis. The patient walked independently with a near-normal range of motion in the right knee. The left knee showed limited flexion but preserved extension (Figure 6A–F). He could walk over 500 m unaided with minimal pain (VAS score: 1/10; Video S3). By 12 months postoperatively, the patient could already walk almost normally, with only a slight limp (Video S4).

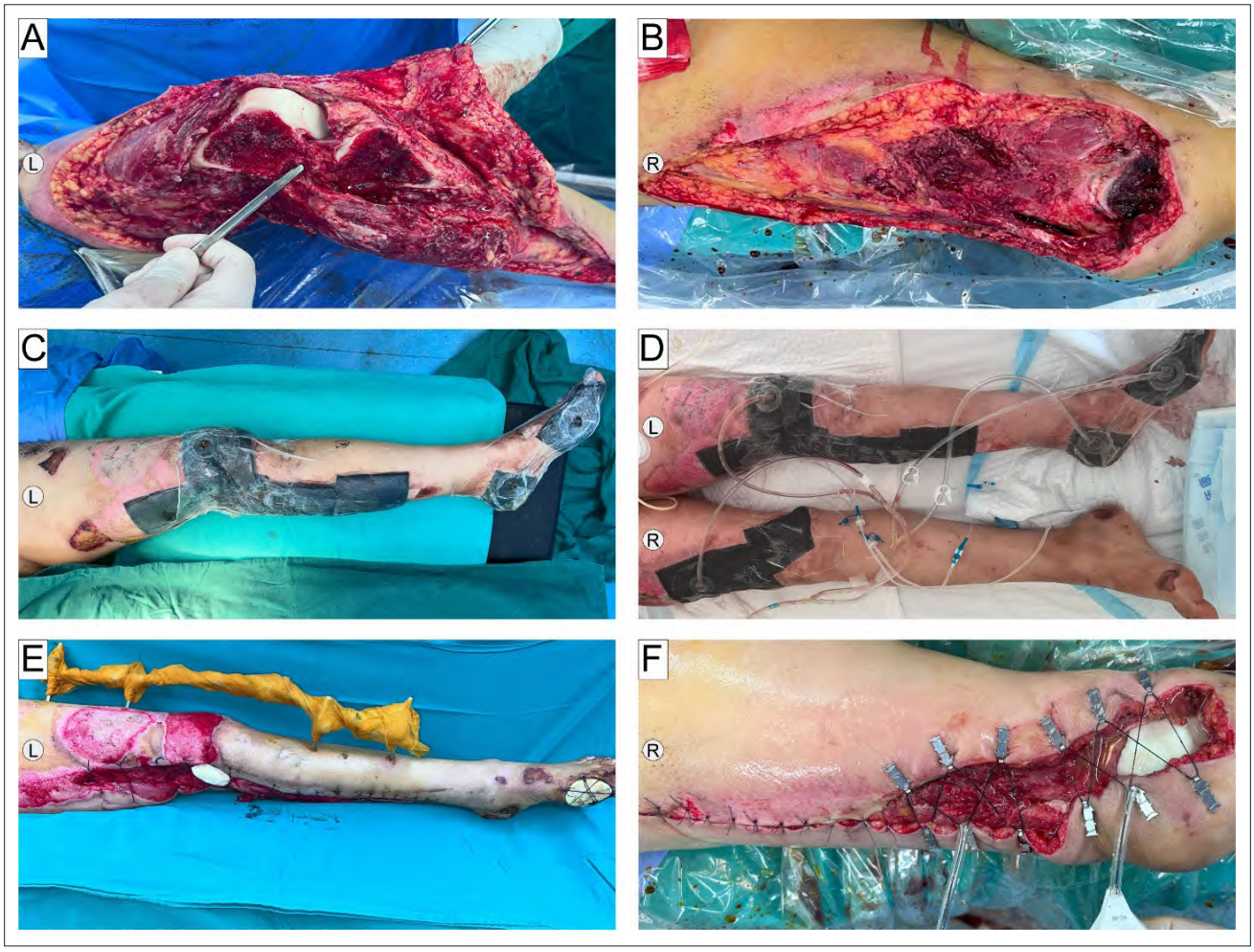


Figure 2. Multiple debridements removing necrotic subcutaneous tissue and contaminated bone, with limb stabilization. (A) Post-debridement exploration of the left knee showing complete loss of the medial femoral condyle and medial tibial plateau, with intact anterior and posterior cruciate ligaments. (B) Partial defect of the medial femoral condyle and absence of the medial collateral ligament on the right knee. (C–D) Wounds covered with VAC® polyurethane foam dressings. (E) Left lower limb stabilized with an external fixation frame following the second debridement. (F) Right lower limb after debridement.

3. Discussion

Periarticular bone and soft tissue defects of the knee caused by high-energy trauma such as traffic accidents, machine crush injuries, and falls from height remain a significant challenge for orthopedic surgeons.[4] The knee joint comprises critical bony structures, including the distal femur, tibial plateau, patella, and proximal tibia, which serve as attachment sites for muscles such as the quadriceps, rectus femoris, and hamstrings. High-energy trauma often results in open fractures and extensive bone and soft tissue loss following emergent debridement, necessitating staged treatment approaches. Conventional management typically involves free flap transfer combined with bone reconstruction techniques such as autologous or allogeneic bone grafting,[5] Masquelet's induced membrane technique,[6] Ilizarov bone transport,[7] and vascularized fibular grafting.[8] However, these approaches often require multiple debridements, prolonged external fixation crossing the knee joint, and are associated with high complication rates, including flap insufficiency, bone exposure, and nonunion. Currently, there is no universally accepted standard treatment for complex bilateral knee defects.

In severe bilateral knee bone defects, patient-specific 3D-printed prostheses offer a promising solution. These implants enable precise anatomical reconstruction with excellent biomechanical properties and biocompatibility.[9] They facilitate accurate anatomic reconstruction, enhanced biomechanical support, and customized integration with surrounding tissues.[10] Recent studies show that 3D-printed

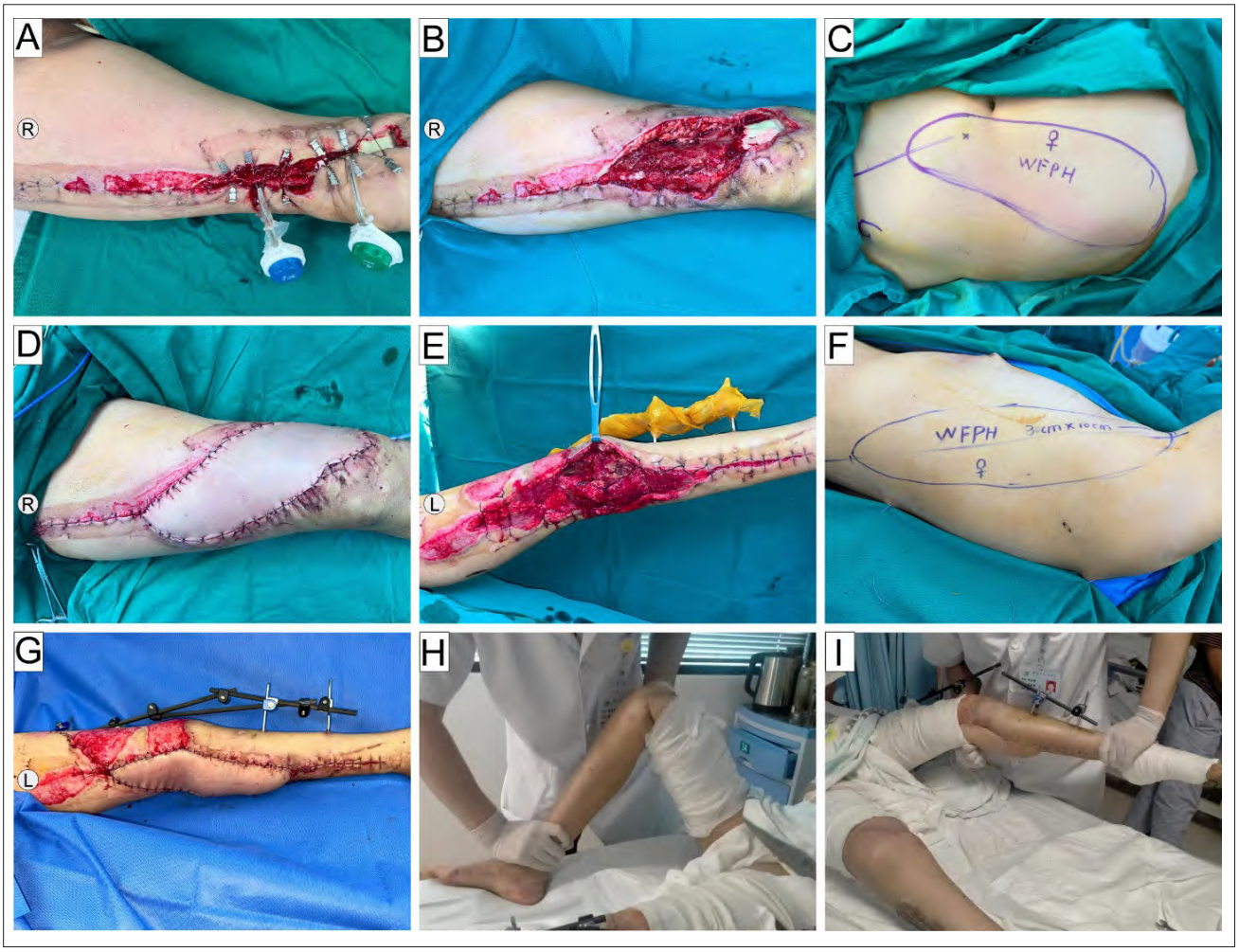


Figure 3. Flap coverage of the wounds. (A, B) Preoperative wound status of the right lower limb. (C) DIEP flap (22 × 14 cm^2) selected for right knee coverage. (D) Revascularization of the right knee DIEP flap. (E) Preoperative wound status of the left lower limb. (F) Latissimus dorsi musculocutaneous flap (30 × 10 cm^2) selected for left knee coverage. (G) Revascularization of the left knee latissimus dorsi flap. (H) Active knee flexion and extension rehabilitation of the right affected limb. (I) Removal of external fixation and initiation of knee flexion and extension rehabilitation of the left affected limb.

titanium prostheses, produced via selective laser sintering, achieve optimal pore size (300–800 μm) and porosity (60–80%), promoting osteoblast migration and vascular ingrowth—effectively overcoming the limitations of traditional grafts in managing large metaphyseal defects.[11] This case highlights a successful staged approach involving radical debridement and early wound coverage, combined with timely functional rehabilitation to prepare for prosthetic implantation. Based on previous research, we designed custom 3D-printed titanium implants using additively manufactured porous scaffolds with a target pore size of 300–400 μm, which are suitable for repairing large segmental bone defects.[12] The design also incorporated tunnels for MCL reconstruction using LARS ligaments, which exhibit excellent biocompatibility, rapid fibroblast ingrowth, and sufficient mechanical tensile strength while minimizing deformation.[13] This integrated approach reflects the growing role of 3D printing in osteochondral-ligamentous reconstruction, enabling simultaneous bone and soft tissue repair. Bilateral MCL reconstruction with LARS provided joint stability and promoted recovery. Postoperative imaging confirmed restored alignment, supporting the feasibility of bilateral 3D-printed knee prostheses for traumatic defects. At 12 months, the patient achieved 120° (left) and 80° (right) knee flexion, Knee Society Scores of 65 and 70, and could walk with small steps, maintaining good quality of life.[14] Mid-term studies report 85–92% 5-year survival rates for 3D-printed implants, affirming their reliability.[15] Patient-specific solutions, like the 3D-printed prosthesis in this

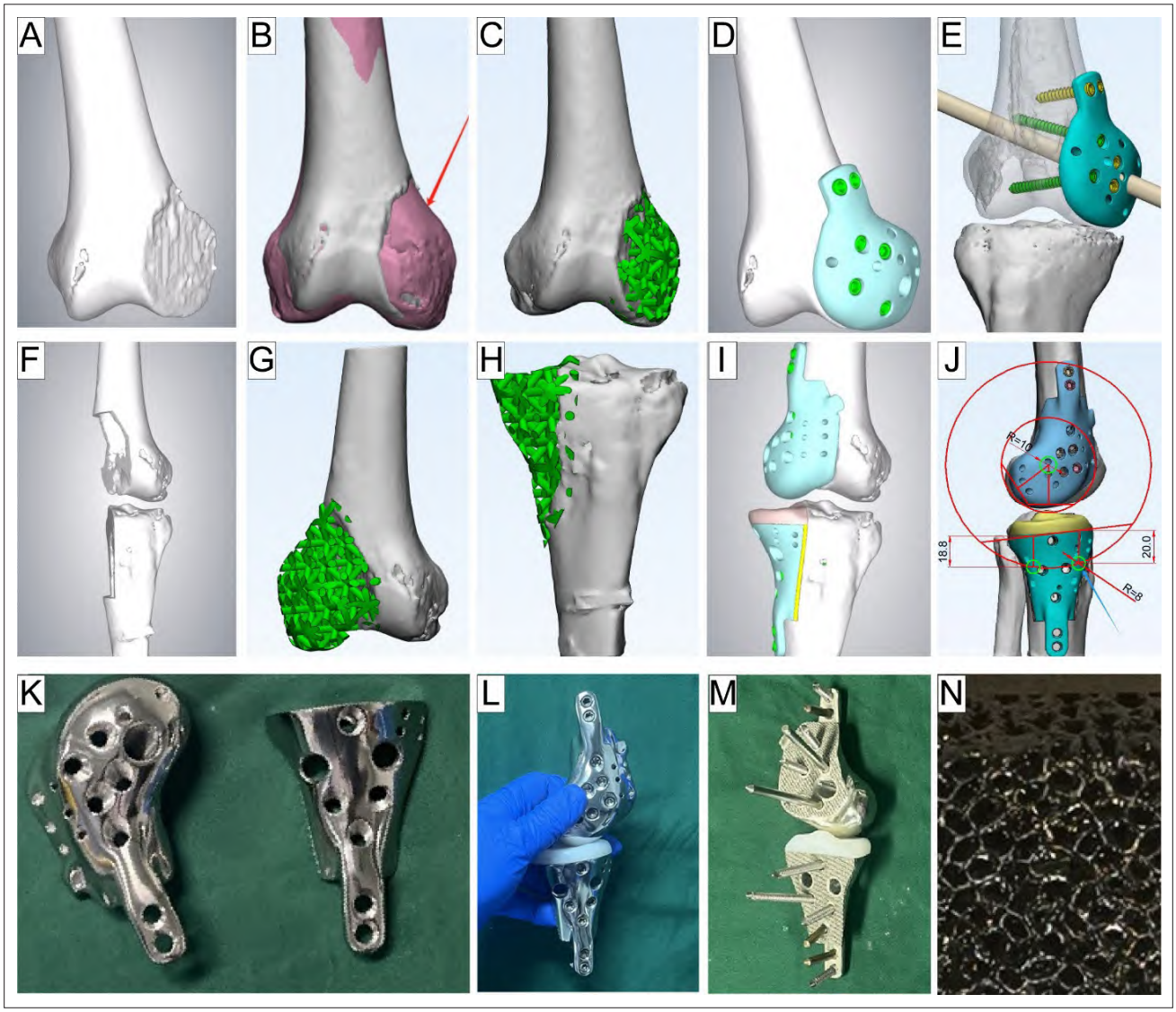


Figure 4. 3D-printed prosthesis design. (A–D) Design of the right medial femoral condyle prosthesis based on data-driven modeling. (E) Confirmation of the prosthesis design including the MCL reconstruction tunnel. (F–I) 3D-printed left knee prosthesis designed by mirroring the reconstructed right knee anatomy. (J) Design of the position and orientation of the MCL (all measurements in the schematic are shown in millimeters). (K, L) External view and assembly method of the left 3D-printed prosthesis. (M) Bone-contacting surface of the left prosthesis. (N) Surface coating of the bone-contacting interface. Abbreviation: MCL, medial collateral ligament.

study, represent a paradigm shift in managing complex joint injuries, but cost-effectiveness needs to be considered in future by adopting standardized designs.

4. Conclusion

The current case demonstrates that when direct mirroring is not feasible for bilateral knee defects, a prosthesis can first be designed for the less affected side using a data-driven approach. After successful implantation, the contralateral prosthesis can then be created by mirroring the reconstructed side. Combined with LARS ligament reconstruction, this staged strategy effectively restored joint stability and function despite extensive bone and ligament loss. It offers a promising solution for complex bilateral knee injuries and may be applicable to other challenging joint reconstructions.

Supplemental information

Video S1. Intraoperative range of motion of the right knee after prosthesis implantation.

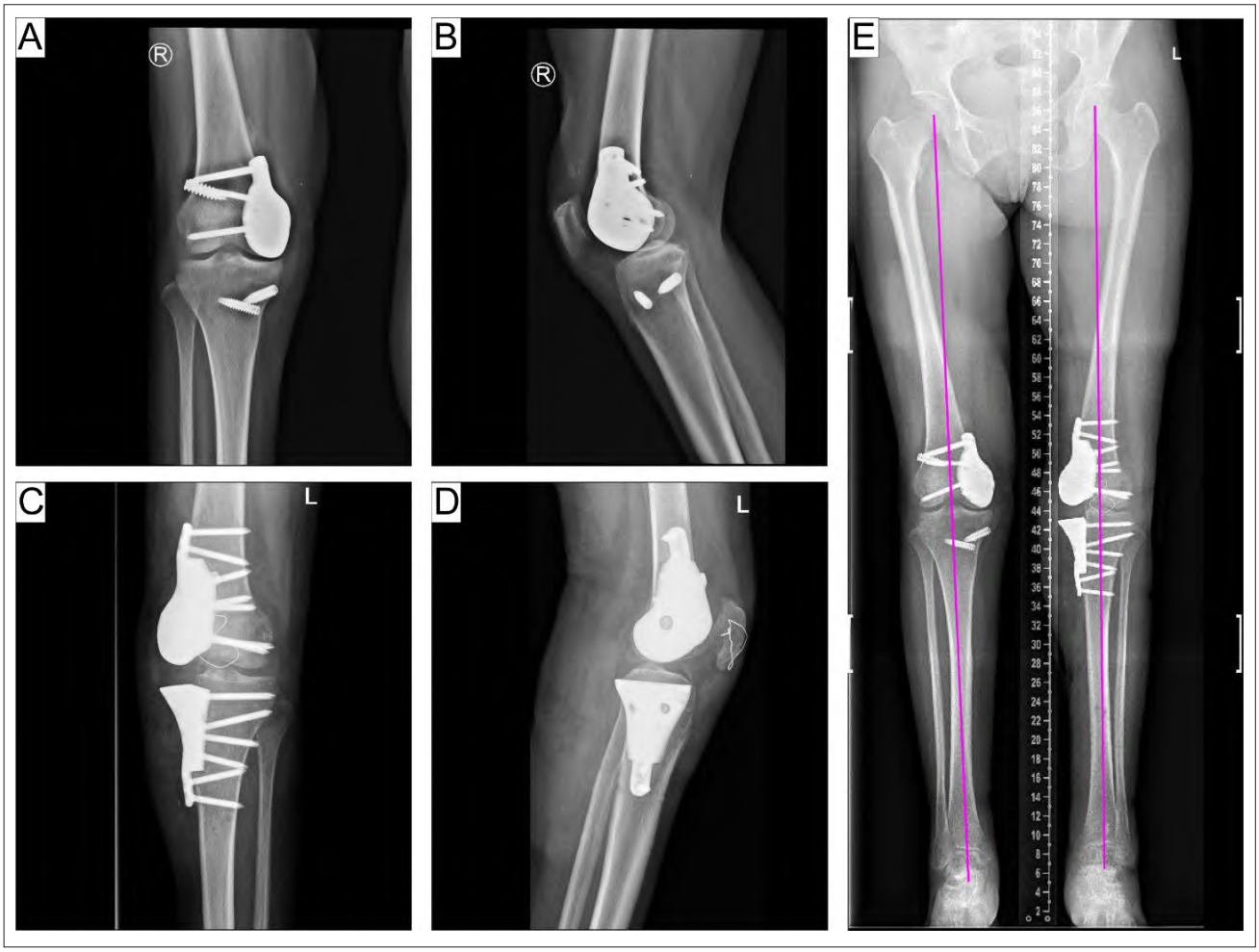


Figure 5. Postoperative radiographs. (A) Anteroposterior radiograph of the right knee post-reconstruction. (B) Lateral radiograph of the right knee post-reconstruction. (C) Anteroposterior radiograph of the left knee post-reconstruction. (D) Lateral radiograph of the left knee post-reconstruction. (E) Full-length lower limb radiograph demonstrating mechanical alignment after bilateral knee reconstructions (lines represent the mechanical axis of both lower limbs).

Video S2. Intraoperative range of motion of the left knee after prosthesis implantation

Video S3. Patient walking condition at 3 months postoperatively.

Video S4. Patient walking condition at 12 months postoperatively.

Acknowledgments

None.

Funding

This work was supported by the National Natural Science Foundation of China (No. 82302031) and the Natural Science Foundation of Shandong Province (No. ZR2024QH033).

Conflict of interest

The authors declare that they have no conflicts of interest.

Author contributions

Conceptualization: Gang Zhao, Xiaoming Yang, Xuecheng Sun, Naibo Feng
Investigation: All authors
Methodology: Gang Zhao, Yongqiang Zhang, Longfei Liu, Futian Zhang, Da Huo, Xiaoming Yang
Writing–original draft: Gang Zhao, Longxin An
Writing–review & editing: Xiaoming Yang, Naibo Feng

Ethics approval and consent to participate

This study was approved by the Ethics Committee of the First Affiliated Hospital of Shandong Second Medical

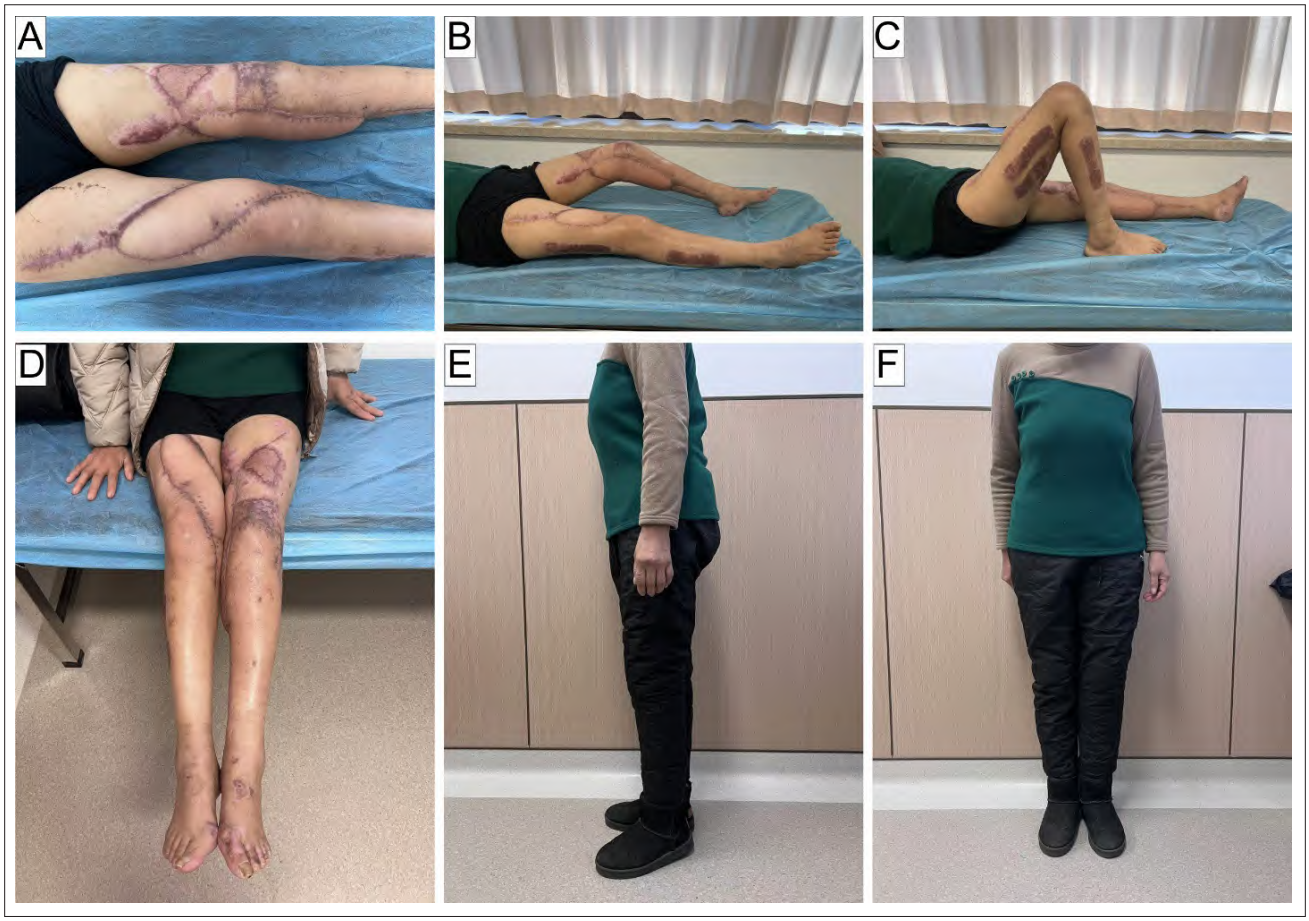


Figure 6. Follow-up. (A) External appearance of both lower limbs at 3 months postoperatively. (B) Active knee flexion of the left leg. (C) Active knee flexion of the right leg. (D) Bilateral lower limb extension. (E) Patient bearing weight normally on both lower limbs at 3 months post-operatively.

University (Approval No. KYLL20250521-7), and informed consent was obtained from the patient.

Consent for publication

Signed consent was obtained from the patient and guardians for the publication of patient-related test results in this paper.

Availability of data

Data will be made available from the corresponding author upon reasonable request.

References

1. Manzotti A, Pullen C, Deromedis B, *et al*. Knee arthrodesis after infected total knee arthroplasty using the Ilizarov method. *Clin Orthop Relat Res*. 2001;(389):143-149. doi: 10.1097/00003086-200108000-00020
2. Oostenbroek HJ, van Roermund PM. Arthrodesis of the knee after an infected arthroplasty using the Ilizarov method. *J Bone Joint Surg Br*. 2001;83(1):50-54. doi: 10.1302/0301-620x.83b1.10572
3. Barwick TW, Montgomery RJ. Knee arthrodesis with lengthening: experience of using Ilizarov techniques to salvage large asymmetric defects following infected peri-articular fractures. *Injury*. 2013;44(8):1043-1048. doi: 10.1016/j.injury.2013.02.017
4. Gupta R, Weisberger J, Herzog I, *et al*. Utilization of the gastrocnemius flap for post-traumatic knee reconstruction: a systematic review. *Eur J Orthop Surg Traumatol*. 2024;34(5):2255-2261. doi: 10.1007/s00590-024-03938-2
5. Azi ML, Aprato A, Santi I, *et al*. Autologous bone graft in the treatment of post-traumatic bone defects: a systematic review and meta-analysis. *BMC Musculoskelet Disord*. 2016;17(1): 465. doi: 10.1186/s12891-016-1312-4

6. Masquelet A, Kanakaris NK, Obert L, *et al*. Bone repair using the masquelet technique. *J Bone Joint Surg Am*. 2019;101(11):1024-1036.
doi: 10.2106/jbjs.18.00842

7. Blázquez-Carmona P, Mora-Macías J, Morgaz J, *et al*. Mechanobiology of bone consolidation during distraction osteogenesis: bone lengthening vs. bone transport. *Ann Biomed Eng*. 2021;49(4): 1209-1221.
doi: 10.1007/s10439-020-02665-z

8. Dheenadhayalan J, Imran A, Devendra A, *et al*. Can locking plate fixation and free vascularised fibular transfer with skin island achieve good functional outcome in the treatment of large bone defects of Tibia ? A study of 26 cases. *Injury*. 2024;55(Suppl 2):111465.
doi: 10.1016/j.injury.2024.111465

9. Meng M, Wang J, Huang H, *et al*. 3D printing metal implants in orthopedic surgery: methods, applications and future prospects. *J Orthop Translat*. 2023;42:94-112.
doi: 10.1016/j.jot.2023.08.004

10. Jing S, Yu A, Dong S, *et al*. 3D-printed prosthesis for traumatic trapezium bone defect: a case report. *Arch Orthop Trauma Surg*. 2025;145(1):182.
doi: 10.1007/s00402-025-05789-w

11. Qu Z, Yue J, Song N, *et al*. Innovations in three-dimensional-printed individualized bone prosthesis materials: revolutionizing orthopedic surgery: a review. *Int J Surg*. 2024;110(10):6748-6762.
doi: 10.1097/js9.0000000000001842

12. Li G, Wang L, Pan W, *et al*. In vitro and in vivo study of additive manufactured porous Ti6Al4V scaffolds for repairing bone defects. *Sci Rep*. 2016;6:34072.
doi: 10.1038/srep34072

13. Core M, Anract P, Raffin J, *et al*. Traumatic patellar tendon rupture repair using synthetic ligament augmentation. *J Knee Surg*. 2020;33(8):804-809.
doi: 10.1055/s-0039-1688564

14. Miralles-Muñoz FA, Gonzalez-Parreño S, Martinez-Mendez D, *et al*. A validated outcome categorization of the knee society score for total knee arthroplasty. *Knee Surg Sports Traumatol Arthrosc*. 2022;30(4):1266-1272.
doi: 10.1007/s00167-021-06563-2

15. Fang S, Wang Y, Xu P, *et al*. Three-dimensional-printed titanium implants for severe acetabular bone defects in revision hip arthroplasty: short- and mid-term results. *Int Orthop*. 2022;46(6):1289-1297.
doi: 10.1007/s00264-022-05390-5

ACCSCIENCE PUBLISHING

International Journal of Bioprinting

COMMENTARY

From platelet-rich plasma to personalized implants: A commentary on "3D-printed vascularized biofunctional scaffolds for bone regeneration"

Hyun-Do Jung*

Department of Bioengineering, College of Engineering, Hanyang University, Seoul, Republic of Korea

Abstract

Bone defects require simultaneous vascularization and sustained osteoinductive signaling to achieve functional repair—two goals that conventional grafts frequently fail to meet. The study under discussion explores the use of platelet-rich plasma (PRP) as a natural, multi-factor source, embedded in a methacrylated gelatin/methacrylated alginate (GA) hydrogel and modified with laponite (Lap) to regulate growth factor release. The resulting PRP–GA@Lap bioink is co-printed with polycaprolactone to create structurally reinforced scaffolds. *In vitro*, PRP–GA@Lap stimulated bone marrow mesenchymal stem cell proliferation, migration, and osteogenic differentiation, enhanced endothelial tube formation, and polarized macrophages toward a pro-regenerative M2 phenotype. *In vivo*, hybrid scaffolds accelerated vascular ingrowth and improved bone volume, mineral density, and defect integration in rat femoral condyles. By coupling biologically broad PRP signaling with engineered release kinetics and mechanical stability, this approach offers a clinically adaptable, patient-specific strategy for complex bone repair, with strong potential for personalized regenerative therapy.

Keywords: Bone regeneration; Immunomodulation; Laponite; Platelet-rich plasma; Three-dimensional printing; Vascularization

***Corresponding author:**
Hyun-Do Jung
(hdjung@hanyang.ac.kr)

Citation: Jung H. From platelet-rich plasma to personalized implants: A commentary on "3D-printed vascularized biofunctional scaffolds for bone regeneration". *Int J Bioprint*. 2025;11(5):460-463. doi: 10.36922/IJB025340338

Received: August 19, 2025
Published online: August 20, 2025

Copyright: © 2025 Author(s). This is an Open Access article distributed under the terms of the Creative Commons Attribution License, permitting distribution, and reproduction in any medium, provided the original work is properly cited.

Publisher's Note: AccScience Publishing remains neutral with regard to jurisdictional claims in published maps and institutional affiliations.

1. Introduction

Critical-sized bone defects pose a considerable challenge in orthopedic, craniofacial, and reconstructive surgery.[1,2] These flaws, frequently arising from significant trauma, tumor excision, infection, or congenital abnormalities, surpass the bone's natural regeneration ability and necessitate surgical intervention.[3,4] The optimal treatment must address both the anatomical and biomechanical issues in the affected region while minimizing complications at the donor site, reducing immunological responses, and limiting the necessity for revision procedures.[5] Autologous bone grafting has traditionally been considered the gold standard; however, it has significant drawbacks, including restricted tissue availability, extended surgical time, ongoing donor site pain,

and variable resorption rates.[6] Allogeneic bone grafts and synthetic substitutes address particular challenges; even so, they often fail to attain long-term integration, primarily due to insufficient graft vascularization.

Vascularization is crucial for effective bone regeneration due to the metabolic demands of newly produced bone.[7] It necessitates the continuous provision of oxygen, nutrients, and osteoinductive signals, effectively eliminating waste products. In the absence of rapid neovascularization, implanted materials may undergo fibrosis or necrosis, resulting in inadequate healing and mechanical instability.[8] In instances with considerable inadequacies, the distance to the next capillary bed is frequently inadequate for effective diffusion to maintain cellular viability, highlighting the need to develop structures that facilitate vascular ingrowth. Platelet-rich plasma (PRP) contains a broad spectrum of growth factors—such as vascular endothelial growth factor (VEGF), platelet-derived growth factor (PDGF), and transforming growth factor-beta (TGF-β)—that collectively promote angiogenesis, osteogenesis, and tissue remodeling.[9–11] However, when applied directly, PRP releases its factors rapidly, limiting its long-term regenerative effect. Recent advancements in tissue engineering have concentrated on amalgamating osteogenic and angiogenic signals into a unified therapeutic framework. Additive manufacturing, also known as three-dimensional (3D) printing, has emerged as an effective method for producing patient-specific scaffolds with very precise construction.[12–14] This approach enables exact regulation of pore size, porosity, interconnectivity, and mechanical properties, all critical for bone growth and vascular infiltration. Moreover, 3D printing enhances the spatial arrangement of bioactive molecules, enabling the fabrication of scaffolds that replicate the varied biological conditions essential for natural bone regeneration.

Cao *et al.*'s study on 3D-printed vascularized biofunctional scaffolds for bone regeneration efficiently demonstrates this technology.[15] They address this limitation by incorporating PRP into a methacrylated gelatin/methacrylated alginate (GA) hydrogel, further modified with the nanoclay laponite (Lap). Lap serves as a release modulator, binding growth factors electrostatically and extending their availability for up to two weeks. This PRP–GA@Lap bioink is co-printed with polycaprolactone (PCL) to create hybrid scaffolds that combine biological activity with structural stability. The authors hypothesize that this design will promote rapid vascular ingrowth, enhance bone marrow mesenchymal stem cell osteogenesis, and establish a pro-regenerative immune environment *in vivo*. This commentary will encapsulate the principal findings, examine the methodologies and implications, and discuss potential applications of this research in clinical practice.

2. Discussion

Incorporating Lap into PRP–GA hydrogel significantly altered the material's physical and biological performance. Adding Lap improved mechanical stiffness, reduced swelling, and slowed degradation, enabling the scaffold to maintain its form during early healing. Importantly, enzyme-linked immunosorbent assays confirmed that Lap extended the release of key PRP-derived growth factors—including VEGF, platelet-derived growth factor-BB, and TGF-β—from a rapid burst to a steady release profile lasting up to 14 days. This timing aligns well with the physiological sequence of fracture healing, in which angiogenic and osteogenic signals must persist during the early and mid-stage repair.

Bone marrow mesenchymal stem cells cultured on PRP–GA@Lap hydrogel showed increased proliferation and migration compared to PRP–GA and GA controls. Osteogenic differentiation was also enhanced, as evidenced by elevated alkaline phosphatase activity at day 5, upregulation of osteogenic markers (Runt-related transcription factor 2, osteocalcin), and greater mineralized matrix deposition at day 14. On the vascular side, human umbilical vein endothelial cells exposed to PRP–GA@Lap-conditioned media displayed robust proliferation, chemotaxis, and tube formation—indicating that the sustained release of PRP factors effectively supports angiogenesis. Macrophage polarization assays revealed a clear shift toward the M2 (pro-regenerative) phenotype when cultured with PRP–GA@Lap hydrogel. Expression of M1 markers (inducible nitric oxide synthase, C–C chemokine receptor type 7) decreased, while M2 markers (arginase 1, CD206) increased, suggesting that the scaffold actively modulates the immune environment to favor tissue repair and integration.

Hybrid scaffolds composed of PRP–GA@Lap bioink and PCL were tested in rat subcutaneous implantation and femoral condyle defect models. In subcutaneous sites, the PRP–GA@Lap/PCL group showed more mature and perfused blood vessels (alpha-smooth muscle actin$^+$, CD31$^+$) than controls. In femoral condyle defects, micro-computed tomography analysis demonstrated greater bone volume fraction and bone mineral density in the PRP–GA@Lap/PCL group, along with more complete defect bridging. Histological staining confirmed the presence of well-integrated new bone with active vascularization throughout the regenerated area.

Cao *et al.*'s[15] work represents a deliberate shift in bone tissue engineering strategy—from reliance on single recombinant growth factors to a multi-factor, endogenously derived bioactive system. By using PRP as the biological payload, the authors circumvent some cost

and safety issues associated with supraphysiologic doses of bone morphogenetic protein 2 or VEGF, while retaining a physiologic breadth of angiogenic and osteogenic cues. The integration of Lap as a release modulator is particularly noteworthy. Instead of relying on covalent tethering or synthetic carriers, Lap achieves sustained factor delivery through electrostatic interactions, preserving bioactivity and avoiding additional chemical modifications that might complicate regulatory approval. However, this approach also raises critical questions. The inherent variability of PRP composition between donors—affected by age, comorbidities, and preparation method—could introduce inconsistent scaffold performance, potentially impacting reproducibility and standardization. Furthermore, the current study focused on short-term endpoints in small animal models; it remains unclear whether the same immunomodulatory and regenerative benefits will persist in long-term, load-bearing, or large-defect scenarios. Looking forward, this strategy could evolve into a personalized, autologous scaffold platform if integrated with point-of-care PRP preparation and on-demand 3D printing. Future studies should aim to map the correlation between specific PRP factor release profiles and *in vivo* regenerative outcomes, potentially enabling predictive tailoring of scaffold formulations for individual patients. Additionally, combining PRP's multi-factor environment with gene-edited cells or responsive biomaterials could further refine temporal control over healing processes. By framing growth factor delivery as a kinetic engineering problem rather than a single-factor supplementation challenge, this work opens a compelling avenue for more physiologically aligned and clinically adaptable bone regeneration therapies.

3. Conclusion

The use of PRP–GA hydrogel modified with Lap, combined with PCL structural reinforcement, presents a well-integrated solution to the dual challenges of vascularization and osteoinduction in bone regeneration.[15] Sustained release of multiple endogenous growth factors from PRP supports a coordinated sequence of endothelial, osteogenic, and immunomodulatory events, leading to superior tissue integration and functional repair in preclinical models. Although further studies are needed to optimize PRP concentration, Lap content, and long-term mechanical performance—especially in load-bearing environments—this platform demonstrates strong translational potential. Its reliance on autologous PRP, combined with a modular and customizable 3D-printing process, makes it an attractive candidate for clinical application in complex bone defect repair. By engineering the release kinetics rather than relying solely on single-factor delivery, Cao *et al.*'s[15] work offers a biologically nuanced and technically practical pathway toward next-generation bone tissue scaffolds.

Acknowledgments

None.

Funding

This work was supported by the National Research Foundation of Korea (NRF) grant funded by the Korean government (MSIT) (RS-2024-00405381, and RS-2025-00513935), the Korea Institute of Marine Science & Technology Promotion (KIMST) funded by the Ministry of Oceans and Fisheries (RS-2024-00405273), and the Korean Fund for Regenerative Medicine (KFRM) grant funded by the Korean government (the Ministry of Science and ICT, the Ministry of Health & Welfare, KFRM 24A0105L1).

Conflict of interest

Hyun-Do Jung is an Editorial Board Member of this journal, but was not in any way involved in the editorial and peer-review process conducted for this paper, directly or indirectly. Separately, the author declares no known competing financial interests or personal relationships that could have influenced the work reported in this paper.

Author contributions

This is a single-author article.

Ethics approval and consent to participate

Not applicable.

Consent for publication

Not applicable.

Availability of data

Not applicable.

References

1. Lee H, Han G, Na Y, *et al*. 3D-printed tissue-specific nanospike-based adhesive materials for time-regulated synergistic tumor therapy and tissue regeneration in vivo. *Adv Funct Mater*. 2024;34(48):2406237. doi: 10.1002/adfm.202406237

2. Choi JW, Kim JJ. Strategies for the patient-specific implant angle of bone scaffolds using optimization. *Tissue Eng Regen Med*. 2025;22(6):805-816. doi: 10.1007/s13770-025-00730-z

3. Migliorini F, La Padula G, Torsiello E, Spiezia F, Oliva F, Maffulli N. Strategies for large bone defect reconstruction after trauma, infections or tumour excision: a comprehensive review of the literature. *Eur J Med Res*. 2021;26(1):118. doi: 10.1186/s40001-021-00593-9

4. Yao J, Zu D, Dong Q, *et al*. Functionalized periosteum-derived microsphere-hydrogel with sequential release of E7 short peptide/miR217 for large bone defect repairing. *Biomater Res*. 2025;29:0127. doi: 10.34133/bmr.0127

5. Kontogianni G-I, Loukelis K, Bonatti AF, *et al*. A mechanically stimulated Co-culture in 3-dimensional composite scaffolds promotes osteogenic and anti-osteoclastogenic activity and M2 macrophage polarization. *Biomater Res*. 2025;29:0135. doi: 10.34133/bmr.0135

6. Dong H, Hu B, Zhang W, *et al*. Robotic-assisted automated in situ bioprinting. *Int J Bioprint*. 2022;9(1):629. doi: 10.18063/ijb.v9i1.629

7. Kim JI, Kieu TTT, Lee J-C. A novel strategy to enhance the bone healing efficacy of composite scaffolds via induction of cell recruitment and vascularization. *Biomater Res*. 2025;29:0185. doi: 10.34133/bmr.0185

8. Yi L, Tang R, Shao C, *et al*. A biodegradable zinc alloy membrane with regulation of macrophage polarization for early vascularized bone regeneration. *Biomater Res*. 2025;29:0223. doi: 10.34133/bmr.0223

9. Lee S, Nam J, Kim HS, Yoo JJ. Phenotype-preserving co-culture of osteoblasts and chondrocytes enhances bone-cartilage interface integration in a PRP-augmented scaffold. *Tissue Eng Regen Med*. 2025;22(6):791-803. doi: 10.1007/s13770-025-00727-8

10. Kim MJ, Song YJ, Kwon TG, Lee JH, Chun SY, Oh SH. Platelet-rich plasma-embedded porous polycaprolactone film with a large surface area for effective hemostasis. *Tissue Eng Regen Med*. 2024;21(7):995-1005. doi: 10.1007/s13770-024-00656-y

11. Kim M, Park S, Kim S, Seo J, Roh S. A novel cell-penetrating peptide–vascular endothelial growth factor small interfering ribonucleic acid complex that mediates the inhibition of angiogenesis by human umbilical vein endothelial cells and in an ex vivo mouse aorta ring model. *Biomater Res*. 2025;29:0120. doi: 10.34133/bmr.0120

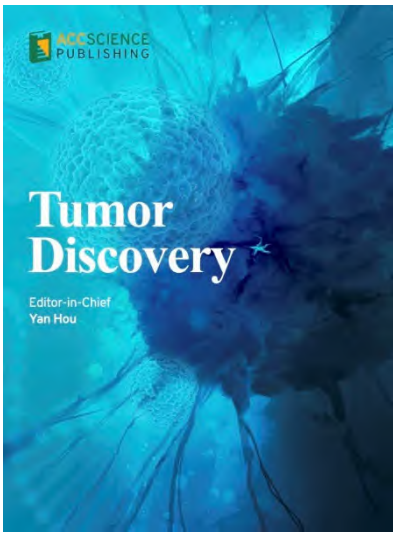
12. Kim N, Lee H, Han G, *et al*. 3D-printed functional hydrogel by DNA-induced biomineralization for accelerated diabetic wound healing. *Adv Sci*. 2023;10(17):2300816. doi: 10.1002/advs.202300816

13. Lee H, Won D-S, Park S, *et al*. 3D-printed versatile biliary stents with nanoengineered surface for anti-hyperplasia and antibiofilm formation. *Bioact Mater*. 2024;37:172-190. doi: 10.1016/j.bioactmat.2024.03.018

14. Shi W, Zheng J, Zhang J, *et al*. Desktop-stereolithography 3D printing of a decellularized extracellular matrix/mesenchymal stem cell exosome bioink for vaginal reconstruction. *Tissue Eng Regen Med*. 2024;21(6):943-957. doi: 10.1007/s13770-024-00649-x

15. Cao B, Lin J, Tan J, *et al*. 3D-printed vascularized biofunctional scaffold for bone regeneration. *Int J Bioprint*. 2023;9(3):702. doi: 10.18063/ijb.702

Our Journals



Tumor Discovery is a peer-reviewed and open-access journal that aims to present new cancer research with strong emphasis on fundamental and translational studies. *Tumor Discovery* covers topics, including but not limited to the following:

- Etiology and pathogenesis of cancer
- Mechanisms and molecular pathways underlying cancer initiation and progression
- Tumor metastasis
- Tumor evolution and heterogeneity
- Tumor microenvironment and tumor-host interactions
- Cancer genetics and genomics
- Cancer characterization using omics approaches
- Discovery and validation of cancer biomarker
- Discovery of new therapeutic targets
- New approaches of diagnostic and treatment modalities
- Statistical methods in cancer research

Global Translational Medicine is a quarterly journal that focuses on medicine, biological sciences, and biomaterials engineering. The goal of *Global Translational Medicine* is to provide a platform to researchers for showcasing their latest research works in translational medicine so as to advance the field towards the betterment of human health. Despite the advancement of omics and new technologies, the process of transforming these technologies and scientific research results into effective therapies and putting them into clinical use still has a long way to go. *Global Translational Medicine* provides a platform to fill the gaps in preclinical and inter-disciplinary research, to promote clinical translation of scientific research results, and to contribute to the conception of new and improved preventive measures as well as diagnostic and therapeutic techniques of diseases.

Global Translational Medicine covers the following themes: cardiovascular disease, metabolism/diabetes/obesity, neuroscience/neurology, cancer, biomaterials and their applications in medicine, proteomics/metabolomics, pharmacogenomics, biomarkers, bioinformatics and data mining, animal and clinical research, and medical methods arising from interdisciplinary crossover.



Start a new journal

Write to us via email if you are interested to start a new journal with AccScience Publishing. Please attach your CV, professional profile page and a brief pitch proposal in your email. We shall inform you of our decision whether we are interested to collaborate in starting a new journal.

Contact: info@accscience.com

https://accscience.com/journal/IJB



Contact
www.accscience.com
9 Raffles Place, Republic Plaza 1 #06-00 Singapore 048619
Email: editorial@accscience.com
Phone: +65 8182 1586